

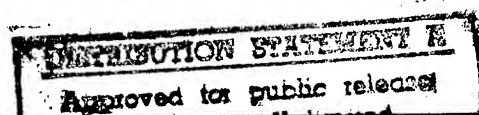
FIFTEENTH
**INTERNATIONAL
CONFERENCE ON THERMOELECTRICS**

**PROCEEDINGS
ICT '96**

**MARCH 26-29, 1996
PASADENA, CA USA**

20 SESSIONS — 105 PAPERS

- Bulk TE materials
- Theory
- TE Devices, Systems and Applications
- Cooling
- Power Generation
- Detectors and Sensors
- TE Measurements
- Thin Film Thermoelectrics



SPONSORED BY:



The International Thermoelectric Society



**The Institute of Electrical and
Electronics Engineers, Inc.**



**The Components, Packaging, and
Manufacturing Technology Society, IEEE**

**The Thermoelectric Group,
Jet Propulsion Laboratory/Cal Tech**

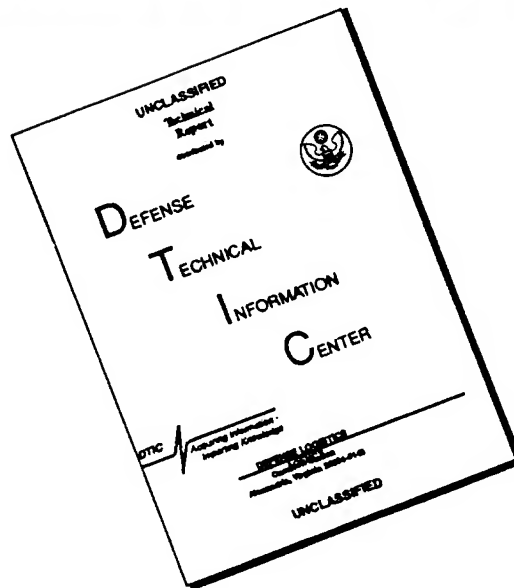
The U.S. Office of Naval Research

The U.S. Department of Energy

19961008 077

**IEEE CATALOG NUMBER 96TH8169
LIBRARY OF CONGRESS NUMBER 96-75531**

DISCLAIMER NOTICE



THIS DOCUMENT IS BEST QUALITY AVAILABLE. THE COPY FURNISHED TO DTIC CONTAINED A SIGNIFICANT NUMBER OF PAGES WHICH DO NOT REPRODUCE LEGIBLY.

[31,735.10]

REPORT DOCUMENTATION PAGE			Form Approved. OMB No. 0704-0188	
<small>Public reporting burden for this collection of information is estimated to average 1 hour per response, including the time for reviewing instructions, searching existing data sources, gathering and maintaining the data needed, and completing and reviewing the collection of information. Send comments regarding this burden estimate or any other aspect of this collection of information, including suggestions for reducing this burden, to Washington Headquarters Services, Directorate for Information Operations and Reports, 1215 Jefferson Davis Highway, Suite 1204, Arlington, VA 22202-4302, and to the Office of Management and Budget, Paperwork Reduction Project (0704-0188), Washington, DC 20503.</small>				
1. AGENCY USE ONLY (Leave blank)	2. REPORT DATE 1 October 96	3. REPORT TYPE AND DATES COVERED Final Report 1 Mar - 30 Sept 96		
4. TITLE AND SUBTITLE Proceedings of 15th International Conference on Thermoelectrics		5. FUNDING NUMBERS ONR Grant No. N00014-96-1-0620		
6. AUTHOR(S) Jean-Pierre Fleurial, Chief Editor				
7. PERFORMING ORGANIZATION NAME(S) AND ADDRESS(ES) Jet Propulsion Laboratory 4800 Oak Grove Drive Pasadena, CA 91109, USA		8. PERFORMING ORGANIZATION REPORT NUMBER		
9. SPONSORING/MONITORING AGENCY NAME(S) AND ADDRESS(ES) Midwest Research Institute 425 Volker Boulevard Kansas City, MO 64110		10. SPONSORING/MONITORING AGENCY REPORT NUMBER MRI Project No. RA-1409-01		
11. SUPPLEMENTARY NOTES IEEE Catalog No. 96TH8169 Library of Congress No. 96-75531				
12a. DISTRIBUTION/AVAILABILITY STATEMENT Approved for Public Release		12b. DISTRIBUTION CODE		
13. ABSTRACT (Maximum 200 words) The proceedings include all the technical papers presented at the 15th International Conference on Thermoelectrics, held on 26-29 March 1996 at Pasadena, California, USA. There were 10 invited presentations and over 110 regular presentations in this conference. The presentations were made in 20 technical sessions and are organized accordingly in this proceedings.				
14. SUBJECT TERMS Thermoelectric (TE) Materials, TE devices, TE Cooling, TE Detectors, TE Measurements, Thin Film TE			15. NUMBER OF PAGES 507	
			16. PRICE CODE	
17. SECURITY CLASSIFICATION OF REPORT Unclassified	18. SECURITY CLASSIFICATION OF THIS PAGE Unclassified	19. SECURITY CLASSIFICATION OF ABSTRACT Unclassified	20. LIMITATION OF ABSTRACT Unlimited	

NSN 7540-01-280-5500

Standard Form 298 (Rev. 2-89)
Prescribed by ANSI Std. Z39-18
298-102

FIFTEENTH

INTERNATIONAL CONFERENCE ON THERMOELECTRICS

The **International Conference on Thermoelectrics** is the principal annual meeting for the presentation of thermoelectrics research and development. The meeting provides scientists, engineers, manufacturers and users with a forum for the exchange of information and for discussions at the forefront of thermoelectrics. The 110 technical presentations, coupled with two short courses and over a dozen exhibits, give the attendee a rich opportunity for interchange. ICT has rotated between Western Europe, Russia/Asia, and the United States.

We invite you to consider presenting a paper at ICT in Dresden, Germany in 1997, or in Nagoya, Japan in 1998, and we look forward to again hosting the ICT in the United States in 1999.

The 1996 ICT is organized by the Thermoelectric Group of the Jet Propulsion Laboratory, California Institute of Technology, with support from the U.S. Office of Naval Research and the U.S. Department of Energy.

This year's conference is sponsored by the Components, Packaging, & Manufacturing Technology (CPMT) Society, one of the 35+ technical groups within the Institute of Electrical and Electronics Engineers, and by the International Thermoelectric Society (ITS).

CPMT is chartered within the IEEE as the focus for the application of technology, with a strong emphasis on thermal phenomena, electronics packaging, process development and optimization, and component, subassembly, and semiconductor manufacturing. CPMT's Technical Committee on Thermal Management is the liaison to the 1996 ICT Committee. It publishes three international journals and a quarterly Newsletter.

ITS is a nonprofit organization dedicated to the advancement of thermoelectric science, industry, and technology, and serving the advancing field of thermoelectrics research and development, with centers of activity in many countries. It publishes a Newsletter.

We invite you to consider membership in either Society, and to participate with us in furthering advancements in these fields. Refer to the back cover for additional information.

**March 26-29, 1996
DoubleTree Hotel
Pasadena, CA USA**

DTIC QUALITY INSPECTED &

1996 PROCEEDINGS, Fifteenth IEEE International Conference on Thermoelectrics (ICT)

PERMISSION TO REPRINT OR COPY:

Abstracting is permitted with credit to the source. Libraries are permitted to photocopy beyond the limits of U.S. copyright law for private use of patrons those articles in this volume that carry a code at the bottom of the first page, provided the per-copy fee indicated in the code is paid through the Copyright Clearance Center, 222 Rosewood Drive, Danvers, MA 01923 U.S.A. Instructors are permitted to photocopy isolated articles for non-commercial classroom use without fee. For other copying, reprint, or re-publication permission, write to IEEE Copyrights Manager; 445 Hoes Lane, PO Box 1331; Piscataway, NJ 08855 U.S.A. All rights reserved.

Copyright ©1996 by the Institute of Electrical and Electronics Engineers, Inc.

PRINTED IN THE UNITED STATES OF AMERICA

Additional copies of this PROCEEDINGS may be purchased from:

IEEE Service Center
445 Hoes Lane
Piscataway, NJ 08855-1331 USA
Phone: (908) 981-0060
or 1-800-678-IEEE

Refer to the IEEE Catalog Number, printed below.

IEEE Catalog Number	96TH8169
ISBN	0-7803-3221-0 Softbound Edition 0-7803-3222-9 Microfiche Edition
Library of Congress Number	96-75531

*Layout, composition, and compilation by
Chappell Enterprises*

Letter from the Conference Chairman

The XVth International Conference on Thermoelectrics, ICT96, was held at the DoubleTree Hotel, Pasadena, California, USA, March 26- 29, 1996. On the day preceding the conference, two half-day short courses were arranged. The conference was organized by the Thermoelectrics Team of the Jet Propulsion Laboratory/California Institute of Technology (JPL). The conference was supported by the International Thermoelectric Society (ITS), a non-profit organization, and sponsored by the US Office of Naval Research and the Department of Energy.

ICT96 featured technical sessions covering a broad range of topics in thermoelectrics R&D. The meeting provided a total of 190 scientists, engineers, manufacturers and users with a forum for the exchange of discussions and information at the forefront of thermoelectrics. This was the largest attendance for an ICT conference in the United States and it indicates that the interest in thermoelectrics is growing worldwide. The largest delegations were from the United States (97) and Japan (38). All major regions of the world were represented: Russia and Ukraine (17), Western Europe (20), Israel (1), Japan, Korea and Australia (47), North America (104) and even South Africa (1).

A total of 110 papers were actually presented during parallel sessions at the conference. The parallel sessions were held in adjacent rooms at the DoubleTree hotel which allowed the attendees to easily switch from one room to the other. By organizing 10 invited presentations, the goal of the ICT96 Organizing Committee was to emphasize promising

new approaches in thermoelectrics, such as novel materials and heterostructures (materials research) or thermal management and waste heat recovery applications (thermoelectric cooling and power generation). In addition, important topics which needed to get more exposure were selected, such as thin films, Bi-Sb alloys, theoretical calculations (materials research) and detectors, microdevices and commercial potential (applications).

A large number of regular papers were devoted to novel materials and structures, and several major discoveries were reported at this meeting. Other highlights of the conference included a plenary session showcasing the interest of U.S. federal agencies in thermoelectrics, a lively and stimulating 2-hour panel session, a technical exhibition featuring 14 different private companies and a visit to JPL and its thermoelectric facilities.

In addition to the very full technical schedule of the conference, the ICT96 Organizing committee managed to keep the attendees busy and entertained in the evenings. It appears that ICT96 was a success if the Organizing Committee can judge from the excellent feedback it has received from some of the attendees. As chairman of this conference, I am especially proud of the always improving quality of the International Thermoelectric Society meetings and I would like to thank the members of the Organizing Committee for their dedication and perseverance through many months of effort, the Jet Propulsion Laboratory for its support and the Office of Naval Research and the Department of Energy for their sponsoring.

Jean-Pierre Fleurial

ICT96 Conference Chairman

XV International Conference on Thermoelectrics

Organizing Committee

J.-P. Fleurial, Jet Propulsion Laboratory	Conference Chairman
T. Caillat, Jet Propulsion Laboratory	Technical Program Chairman
J. W. Vandersande, Jet Propulsion Laboratory	Treasurer
A. Borshchevsky, Jet Propulsion Laboratory	Secretary
A. Zoltan, Jet Propulsion Laboratory	Technical Assistant
D. Zoltan, Jet Propulsion Laboratory	Technical Assistant
F. Caillat	Social Program Coordinator
F. Grardin	Social Program Coordinator

Supporting Organizations

Jet Propulsion Laboratory/California Institute of Technology
International Thermoelectric Society
City of Pasadena

Sponsors

Department of Energy
Office of Naval Research

Exhibitors

ASARCO Inc.	Denver, Colorado, USA
Crioterm Ltd.	St. Petersburg, RUSSIA
Crystal, Ltd.	Moscow, RUSSIA
Hi-Z Technology, Inc.	San Diego, California, USA
Institute of Thermoelectricity	Chernivtsi, UKRAINE
International Thermoelectric Inc.	Chelmsford, Massachusetts, USA
Marlow Industries, Inc.	Dallas, Texas, USA
Melcor Corporation	Trenton, New Jersey, USA
Midwest Research Institute	Kansas City, Missouri, USA
MMR Technologies Inc.	Mountain View, California, USA
Noranda Advanced Materials	Saint-Laurent, Quebec, CANADA
Quantum Design	San Diego, California, USA
TE Technology, Inc.	Traverse City, Michigan, USA
Thermion	Odessa, UKRAINE

Preface

The present volume constitutes the proceedings of the XV International Conference on Thermoelectrics (ICT) held at the DoubleTree Hotel, Pasadena, California, USA, on March 26-29, 1996. The ICT provided a total of 190 scientists, engineers, manufacturers, and users with an opportunity to present and discuss the most recent findings and developments in thermoelectric research and applications. The growing attendance indicates the increasing interest in thermoelectrics worldwide.

For the first time in this series of conference, a plenary session was organized to give an opportunity to several US government agencies to outline their interest in thermoelectrics. This session generated a lot of interest from the attendees as well as the panel session. This year, the topic for the panel session was: "Increase demand for thermoelectrics: high ZT or cost the driver?".

Over 110 papers were presented at the conference, including 10 invited presentations. They are organized in these proceedings in technical sessions covering all aspects of thermoelectric research and technology. In most cases, the papers have been included in the proceedings as received. We are grateful to the authors for their cooperation and efforts to submit clear and technically sound manuscripts for publication.

Many individuals have worked hard to plan and organize this conference. They are listed in the committee section of these proceedings and deserve credit for this success. The organization of this conference was truly a team effort. Finally, I would like to take this opportunity to thank all the authors, speakers, and session chairpersons for their time and efforts spent to make the ICT96 such a success.

Thierry Caillat, Jet Propulsion Laboratory

Chief Editor and Technical Program Chairman

A. Borshchevsky, Jet Propulsion Laboratory

Associate Editor

J.-P. Fleurial, Jet Propulsion Laboratory

Associate Editor

SESSION A1: State-of-the-art thermoelectric materials - BiSb alloys

Bi-Sb alloys: an update (*invited paper*) 1

B. Lenoir¹, A. Dauscher¹, X. Devaux¹, R. Martin-Lopez¹, Yu. I. Ravich², H. Scherrer¹, and S. Scherrer¹

¹Laboratoire de Métallurgie Physique et Science des Matériaux, URA CNRS 155, Ecole des Mines,
Parc de Saurupt, 54042 Nancy, France

²Ioffe Physico-Technical Institute, St. Petersburg, Russia

Effect of anisotropy of the Seebeck coefficient on the thermal conductivity of polycrystalline Bi-Sb alloys 14

H. J. Goldsmid and J. W. Sharp

Marlow Industries, Inc., 10451 Vista Park Road, Dallas, TX 75238-1645, USA

Thermoelectric properties of Bi-Sb composite prepared by mechanical alloying method 18

M. Miyajima¹, K. Takagi², H. Okamura², G. Guen Lee³, Y. Noda³, and R. Watanabe³

¹DAIKIN Industries, 3 Banchi, Miyukigaoka, Tsukuba, Ibaraki 305, Japan

²Graduate students, Faculty of Engineering, Tohoku University, Sendai 980-77, Japan

³Faculty of Engineering, Tohoku University, Sendai 980-77, Japan

Observation of the effect of grain size on the lattice thermal conductivity of polycrystalline Bi-Sb 22

E. H. Volckmann, H. J. Goldsmid, and J. Sharp

Marlow Industries, Inc., 10451 Vista Park Road, Dallas, TX 75238-1645, USA

Thermoelectric properties of doped Bismuth-Antimony single crystals 27

V. M. Grabov¹, O. N. Uryupin², and M. G. Bondarenko¹

¹Herzen Russian State Pedagogical University, St. Petersburg, Russia

²A. F. Ioffe Physical-Technical Institute, St. Petersburg, Russia

SESSION A2: State-of-the-art thermoelectric materials - Bi₂Te₃-based alloys

Doping with organic halogen-containing compounds the Bi₂(Te,Se)₃ solid solutions 32

O. B. Sokolov, S. Ya. Skipidarov, N. I. Duvankov, and E. V. Zaitsev

NORD, Joint-Stock Company Moscow, Russia

Orientational distribution and procedure parameters in hot pressed (Bi₂Te₃)_{0.90}(Bi₂Se₃)_{0.10} 37

K. Fukuda¹, H. Imaizumi¹, T. Ishii¹, F. Toyoda², M. Yamanashi², and Y. Kibayashi²

¹Research Center, Komatsu Ltd., Hiratsuka 254, Japan

²Komatsu Electronics Inc., Hiratsuka 254, Japan

Charge carrier mobility in n-Bi₂Te_{3-x}Se_x (x < 0.4) solid solution with excess of Te 42

V. A. Kutasov, L. N. Luk'yanova, P. P. Konstantinov, and G. T. Alekseeva

A. F. Ioffe Physical-Technical Institute, Russian Academy of Sciences, Russia

High performance properties of sintered Bi₂Te₃-based thermoelectric material 46

S. Sugihara, S. Tomita, K. Asakawa, and H. Suda

Department of Materials Science and Ceramic Technology, Shonan Institute of Technology,

1-1-25, Tsujido Nishikaigan, Fujisawa, Japan 251

**A New n-type and improved p-type pseudo-ternary
(Bi₂Te₃)(Sb₂Te₃)(Sb₂Se₃) alloy for Peltier cooling 52**

M. H. Ettenberg, W. A. Jesser, and F. D. Rosi

University of Virginia, Department of Materials Science and Engineering, Charlottesville, VA 22903-2442, USA

SESSION B1: State-of-the-art thermoelectric materials - β -FeSi₂

**Thermopower and electrical resistivity of undoped and
Co-doped β -FeSi₂ single crystals and β -FeSi_{2+x} thin films 57**

A. Heinrich¹, A. Burkov^{1,3}, C. Gladun¹, G. Behr¹, K. Herz², J. Schumann¹, and H. Powalla²

¹*Institut für Festkörper- und Werkstofforschung Dresden e. V., D-01171 Dresden, Germany*

²*Zentrum für Sonnenenergie- und Wasserstofforschung, D-70565 Stuttgart, Germany*

³*A. F. Ioffe Physico-Technical Institute, St. Petersburg, 194021 Russia*

Electrical properties of β -FeSi₂ bulk crystal grown by horizontal gradient freeze method 62

H. Shibata¹, Y. Makita¹, H. Kakemoto^{1,2}, Y. Tsai³, S. Sakuragi³, H. Katsumata^{1,4},

A. Obara¹, N. Kobayashi¹, S. Uekusa⁴, T. Tsukamoto², T. Tsunoda⁵, and Y. Imai⁵

¹*Electrotechnical Laboratory, 1-1-4 Umezono, Tsukuba, Ibaraki 305, Japan*

²*Science University of Tokyo, 1-3 Kagurazaka, Shinjuku, Tokyo 162, Japan.*

³*Union Material, 1640 Osido-kyodai, Tonemachi, Ibaraki 270-12, Japan*

⁴*Meiji University, 1-1-1 Higashi-mita, Tama, Kawasaki, Kanagawa 214, Japan*

⁵*National Institute of Material and Chemical Research, 1-1 Tsukuba-Higashi, Ibaraki 305, Japan*

Preparation and characterization of thermoelectric β -FeSi₂ phase dispersed with Si 67

B. -G. Min¹, K. -W. Jang², and D. -H. Lee¹

¹*Department of Metallurgical Engineering, Yonsei University 134 Shinchon-dong, Seodaemun-gu, Seoul, 120-749, Korea*

²*Department of Material Science and Engineering, Hanseo University, 360 Daegok-ri, Haemi, Seosan, Chung-Nam, 352-820, Korea*

Plasma spray forming as a novel production method for thermoelectric materials 71

J. Schilz¹, M. Riffel¹, R. Mathesius², G. Schiller³, R. Henne³, and R. W. Smith⁴

¹*Institut für Werkstoff-Forschung, Deutsche Forschungsanstalt für Luft- und Raumfahrt (DLR), D-51140 Köln, Germany*

²*RWTH-Aachen, Werkstoffwissenschaften, Jülicher Str. 342, D-52056 Aachen, Germany*

³*Institut für Technische Thermodynamik, Deutsche Forschungsanstalt für Luft- und Raumfahrt (DLR), D-70503 Stuttgart, Germany*

⁴*Drexel University, Materials Engineering Department, 31 & Market Streets, Philadelphia, PA 1910, USA*

Properties of iron disilicide doped with Ru, Rh and Pd 75

M. I. Fedorov, M. A. Khazan, A. E. Kaliazin, V. K. Zaitsev, N. F. Kartenko, and A. E. Engalychev

A. F. Ioffe Physical-Technical Institute, St. Petersburg, 194021, Russia

Analysis of quadrupole splitting of transition metal doped β -FeSi₂ 79

S. Kondo, M. Hasaka, and T. Morimura

Department of Materials Science and Engineering, Faculty of Engineering, Nagasaki University,

1-14 Bunkyo-machi, Nagasaki 852, Japan

SESSION C1: Novel thermoelectric materials - Skutterudites I

Electronic and vibrational properties of skutterudites (*invited paper*) 84

D. J. Singh, L. Nordstrom, W. E. Pickett, and J. L. Feldman
Naval Research Laboratory, Code 6691, Washington, DC 20375, USA

High figure of merit in Ce-Filled skutterudites 91

J. -P. Fleurial¹, A. Borshchevsky¹, T. Caillat¹, D. T. Morelli², and G. Meisner²
¹*Jet Propulsion Laboratory/ California Institute of Technology, Pasadena, California, USA*
²*General Motors Corporation, Warren, Michigan, USA*

Electronic transport properties of the skutterudite CoSb₃ and mixed alloys 96

K. Matsubara¹, T. Sakakibara², Y. Notohara³, H. Anno¹, H. Shimizu¹, and T. Koyanagi⁴
¹*Science University of Tokyo in Yamaguchi, Yamaguchi, Japan*
²*Aisin Cosmos R&D Co., Ltd., Japan*
³*Kyushu Matsushita Electric Co., Ltd., Japan*
⁴*Yamaguchi University, Japan*

SESSION C2: Novel thermoelectric materials - Skutterudites II

Skutterudites for thermoelectric applications (*invited paper*) 100

T. Caillat, J. -P. Fleurial, and A. Borshchevsky
*Jet Propulsion Laboratory/California Institute of Technology,
4800 Oak Grove Drive, Pasadena, CA 91109 USA*

Thermoelectric properties of Co(M_xSb_{1-x})₃ (M=Ge, Sn, Pb) compounds 107

T. Koyanagi¹, T. Tsubouchi¹, M. Ohtani¹, K. Kishimoto¹, H. Anno², and K. Matsubara²
¹*Department of Electrical and Electronic Engineering, Yamaguchi University, 2557, Tokiwadai, Ube 755, Japan*
²*Science University of Tokyo in Yamaguchi, Yamaguchi, Japan*

Solid solution formation: improving the thermoelectric properties of skutterudites 112

A. Borshchevsky, T. Caillat, and J. -P. Fleurial
Jet Propulsion Laboratory/California Institute of Technology, 4800 Oak Grove Drive, Pasadena, CA 91109 USA

Thermoelectric properties of CoSb₃ prepared by copper mold quenching technique 117

H. Nakagawa¹, H. Tanaka¹, A. Kasama¹, K. Miyamura¹, H. Masumoto¹, and K. Matsubara²
¹*Japan Ultra-High Temperature Materials Research Institute, Okiube 573-3, Ube City,
Yamaguchi Prefecture 755, Japan*
²*Science University of Tokyo in Yamaguchi, 1-1-1 Daigaku-Dori, Onoda City,
Yamaguchi Prefecture 756, Japan*

SESSION C3: Materials - Tellurides, silicides, and intermetallics

TiNiSn: a gateway to the (1,1,1) intermetallic compounds 122

B. A. Cook¹, J. L. Harringa¹, Z. S. Tan², and W. A. Jesser²
¹*Ames Laboratory, Iowa State University, Ames, Iowa 50011-3020, USA*
²*Department of Materials Science and Engineering, University of Virginia, Charlottesville, VA 22903, USA*

Thermoelectric properties of sintered magnesium compounds 128

T. Kajikawa, I. Katsube, S. Sugihara, and K. Soejima
*Faculty of Engineering, Shonan Institute of Technology,
1-1-25 Tsujido-nishikaigan, Fujisawa, Kanagawa, Japan 251*

Mechanically alloyed $\text{Mg}_2\text{Si}_{1-x}\text{Sn}_x$ solid solutions as thermoelectric materials 133

M. Riffel and J. Schilz
*Institut für Werkstoff-Forschung, Deutsche Forschungsanstalt für Luft- und Raumfahrt (DLR),
D-51140 Köln, Germany*

**Comparison of different pressing techniques for the preparation
of n-type silicon-germanium thermoelectric alloys 137**

J. L. Harringa, and B. A. Cook
Ames Laboratory, Iowa State University, Ames, Iowa 50010-3020, USA

**Precipitation study of lead and chalcogens
in single crystals of PbSe-PbTe solid solution 142**

V. L. Kuznetsov
A. F. Ioffe Physical-Technical Institute, 194021, St. Petersburg, Russia

**High efficient program and carrier concentration
FGM thermoelectric materials in the intermediate temperature region 146**

Y. Noda¹, M. Orihashi¹, H. Kaibe², Y. Imai³, I. Shiota⁴, and I. A. Nishida³
¹*Tohoku University, Sendai 980-77, Japan*
²*Tokyo Metropolitan University, Tokyo 192-03, Japan*
³*Kogakuin University, Tokyo 192, Japan*
⁴*National Research Institute for Metals, Ibaraki 305, Japan*

SESSION D1: Novel thermoelectric materials - Other materials

A low thermal conductivity compound for thermoelectric applications: $\beta\text{-Zn}_4\text{Sb}_3$ 151

T. Caillat, J. -P. Fleurial, and A. Borshchevsky
Jet Propulsion Laboratory/California Institute of Technology, 4800 Oak Grove Drive, Pasadena, CA 91109 USA

Crystal growth of narrow gap semiconductors for thermoelectric applications 155

C. Kloc, K. Fess, W. Kaefer, K. Friemelt, H. Riazhi-Nejad, M. Wendl, and E. Bucher
Faculty of Physics, University of Konstanz, P.O.Box 5560, D-78434 Konstanz, Germany

**Thermoelectric properties and structures of the sintered compact
of $\text{Cu:Sn:S}=8:1:4$ composition 159**

M. Hasaka, T. Morimura, T. Aki, and S. Kondo
*Department of Materials Science and Engineering, Faculty of Engineering, Nagasaki University,
1-14 Bunkyo-machi, Nagasaki 852, Japan*

Electronic transport properties of highly conducting vapor-grown carbon fiber composites 164

K. L. Stokes¹, T. M. Tritt¹, W. W. Fuller-Mora¹, A. C. Ehrlich¹, and R. L. Jacobsen²
¹*Materials Science Division, Naval Research Laboratory, Washington DC 20375, USA*
²*Applied Sciences Inc., 141 W. Xenia Ave., Cedarville, OH 45314, USA*

SESSION D2: Novel thermoelectric materials - Oxides

Electrical properties of porous oxides of alkaline-earth metals with high thermoelectric efficiency 168

E. M. Sher
A. F. Ioffe Physical-Technical Institute, RAS, St. Petersburg, Russia

Thermoelectric characteristics of homologous compounds with layer structures in the $\text{ZnO-In}_2\text{O}_3$ system 172

K. Koumoto, H. Ohta, and W. -S. Seo
*Department of Applied Chemistry, School of Engineering, Nagoya University,
Furo-cho, Chikusa-ku, Nagoya 464-01, Japan*

Electronic transport properties of $\text{PrBa}_2\text{Cu}_{3-x}\text{Ga}_x\text{O}_{7-\delta}$ 176

W. W. Fuller-Mora¹, K. L. Stokes¹, T. M. Tritt¹, A. C. Ehrlich¹, J. Z. Liu², and R. N. Shelton²
¹*Materials Physics Branch, Naval Research Laboratory, Washington DC 20375, USA*
²*University of California, Davis, Department of Physics, Davis, CA 95616, USA*

Thermoelectric properties of $\text{La}_{(2-x)}\text{Sr}_x\text{CuO}_4$ 180

M. Shiloh*, B. Dabrowski, D. G. Hinks, J. Mitchell, K. Zhang, and R. Mogilevski
** Permanent address: Dept. of Solid State Physics, Soreq N.R.C., Yavne 81800, Israel*

SESSION E1: Theory - Analysis of ZT

Possible ways for efficiency improvement of thermoelectric materials 183

B. Moyzhes
SPI, 621 River Oaks Parkway, San Jose, CA 95134, USA

Remarks on a possible physical sense of the value $\text{ZT}=1$ for semiconductor thermoelectrics 188

M. V. Vedernikov and Y. I. Ravich
A. F. Ioffe Physical-Technical Institute, 194021, St. Petersburg, Russia

Texture influence on the forming of thermoelectric properties of pressed semiconductors 191

L. I. Anatychuk, S. V. Kosyachenko, and S. V. Melnichuk
Institute of Thermoelectricity, Chernivtsi, Ukraine

Effective figure of merit increase at the large temperature drops 194

V. B. Yurchenko
*Institute of Radiophysics and Electronics, National Academy of Sciences of Ukraine,
12 Proskura St., Kharkov, 310085, Ukraine*

The theoretical analysis of thermoelectric semiconducting crystalline materials figure of merit 197

L. P. Bulat and V. S. Zakordonets
Institute of Thermoelectricity, Chernivtsi, Ukraine

Thermoelectric figure of merit of bounded semiconductors 201

G. N. Logvinov and V. S. Zakordonets
Institute of Thermoelectricity, Chernivtsi, Ukraine

SESSION E2: Theory - Transport properties

The phonon drag effect on thermopower in p-CdTe 204

Y. G. Gurevich¹, S. Vackova², and K. Zdansky³

¹Centro de Investigacion y de Estudios Avanzados del I.P.N., México, Distrito Federal, México

²Department of Semiconductors, Charles University, Prague, Czech Republic

³Academy of Sciences of the Czech Republic, Prague, Czech Republic

Theory of phonon drag thermopower 206

P. G. Klemens

Dept. of Physics and Inst. of Materials Science, University of Connecticut, Storrs, CT 06269, USA

Thermoelectric power in disordered mixed crystals 209

P. J. Lin-Chung and A. K. Rajagopal

Naval Research Laboratory, Washington, D. C. 20375, USA.

On the role of the bulk and surface recombination in the thermopower in bipolar semiconductors 213

Yu. G. Gurevich¹, G. N. Logvinov², O. I. Lyubimov³, and O. Y. Titov¹

¹Departamento de Física, CINVESTAV—I.P.N., Apartado Postal 14-740, México D.F. 07000, México

²Teacher Training University, Avenue Krivonosa 2, Ternopil 282009, Ukraine

³Kharkov State University, Square Svobodi 4, Kharkov 310077, Ukraine

Interacted electron and phonon thermal waves in semiconductors: application to photothermal effects 217

G. González de la Cruz and Y. G. Gurevich

Departamento de Física, Centro de Investigacion y de Estudios Avanzados del I.P.N.,

Apartado Postal 14-740, 07000, México, Distrito Federal, México

SESSION F1: Thermoelectric cooling - Design and analysis I

Optimum design in thermoelectric cooling systems 220

M. Yamanashi, Y. Kibayashi, F. Toyoda, and M. Azechi

Komatsu Electronics, Inc., 2597 Shinomiya, Hiratuka-shi, Kanagawa-ken, 254, Japan

Optimal functions as an effective method of thermoelectric devices design 223

L. I. Anatychuk, O. J. Luste, and L. N. Vikhor

Institute of Thermoelectricity, Chernivtsi, Ukraine

Temperature and time dependent finite-element model of a thermoelectric couple 227

P. G. Lau and R. J. Buist

TE Technology, Inc., 1590 Keane Drive, Traverse City, MI 49686, USA

Theoretical analysis of thermoelectric cooling performance enhancement via thermal and electrical pulsing 234

R. J. Buist and P. G. Lau

TE Technology, Inc., 1590 Keane Drive, Traverse City, MI 49686, USA

Temperature analysis of thermoelectric device of Cu₄SnS₄ with two-dimension by boundary element method	238
---	------------

S. Kondo, M. Hasaka, and T. Morimura
*Department of Materials Science and Engineering, Faculty of Engineering, Nagasaki University,
 1-14 Bunkyo-machi, Nagasaki 852, Japan*

Reliability theory in thermoelectricity	243
--	------------

L. I. Anatychuk and O. J. Luste
Institute of Thermoelectricity, Chernivtsi, Ukraine

The Design problems of thermoelectric heat pumps for transportation facilities	247
---	------------

A. A. Aivazov, Y. I. Stern, K. B. Makharchev, and A. V. Morgal
Moscow Institute of Electronic Engineering, Terif Ltd., Russia

SESSION F2: Thermoelectric cooling - Devices and applications

Thermal management of power electronics using thermoelectric coolers (invited paper)	252
---	------------

J. W. Vandersande and J. -P. Fleurial
Jet Propulsion Laboratory/California Institute of Technology, Pasadena CA 91109, USA

Application of bismuth-telluride thermoelectrics in driving DNA amplification and sequencing reactions	256
---	------------

J. Hansen and M. Nussbaum
M. J. Research, Inc., 149 Grove Street, Watertown, MA 02172, USA

Thermoelectricity applied to the cryoconcentration of orange juice	259
---	------------

M. A. Sanz-Bobi, R. Palacios¹, and A. Arenas²
*¹Instituto de Investigación Tecnológica, ²Laboratory of Heat and Mechanical Fluids,
 Universidad Pontificia Comillas, Alberto Aguilera 23, 28015 Madrid, Spain*

A new concept of porous thermoelectric module using a reciprocating flow for cooling/heating system	264
--	------------

S. Tada, R. Echigo, and H. Yoshida
*Energy Phenomena Lab., Dept. of Mechanical Engineering and Science, Faculty of Engineering,
 Tokyo Institute of Technology, 2-12-1 Ohokayama, Meguro-ku, Tokyo 152, Japan*

Fabrication and testing of thermoelectric thin film devices	269
--	------------

A. V. Wagner, R. J. Foreman, L. J. Summers, T. W. Barbee Jr., and J. C. Farmer
*Chemistry and Materials Science Department, Lawrence Livermore National Laboratory,
 Livermore, California 94550, USA*

Robust thin film thermoelectric devices	274
--	------------

C. L. Chu
Tecstar, 15251 Don Julian Rd., City of Industry, CA, 91745-1002, USA

SESSION F3: Thermoelectric cooling - Design and analysis II

Physical principles of microminiaturization in thermoelectricity (*invited paper*) 279

L. I. Anatychuk and O. J. Luste
Institute of Thermoelectricity, Chernivtsi, Ukraine

Transient analysis of thermal junctions within a thermoelectric cooling assembly 288

M. J. Nagy and R. J. Buist
TE Technology, Inc., 1590 Keane Drive, Traverse City, MI 49686, USA

Evaluation of thermal junction quality in thermoelectric assemblies using transient analysis technology (TAT) 293

T. M. Ritzer, M. J. Nagy, and R. J. Buist
TE Technology, Inc., 1590 Keane Drive, Traverse City, MI 49686, USA

Rational conditions and prospects for two-stage cooling modules use 298

L. I. Anatychuk¹, L. N. Vikhor¹, K. Misawa², and N. Suzuki²
¹*Institute of Thermoelectricity, Chernivtsi, Ukraine*
²*Inst. of Photonic and Electronic Tech. Fujitaka Co., Ltd. Japan*

Thermoelectric coolers with small response time 301

V. A. Semenouk¹ and T. V. Pilipenko²
¹*THERMION Company, Odessa, Ukraine*
²*Odessa State Academy of Refrigeration, Odessa, Ukraine*

Optimization of multistage thermoelectric cooling system concerning maximum C.O.P. 307

T. Wartanowicz and A. Czarnecki
Heat Engineering Institute, Warsaw University of Technology, ul. Nowowiejska 25, 00-665, Warsaw, Poland

Influence of air heat sink geometry on the performance of thermoelectric cooling modules 311

W. Zheng¹ and G. Xu²
¹*Cannon Instrument Company, State College, PA, 16804, USA*
²*Pennsylvania State University*

SESSION G1: Thermoelectric devices - Detectors and sensors

A view to recent developments in thermoelectric sensors (*invited paper*) 315

R. Fetting
Universität Karlsruhe, Institut für Angewandte Physik, Kaiserstr. 12, 76128 Karlsruhe, Germany

Ultrafast response and high sensitivity semiconductor thermocouple 321

Z. Dashevsky¹, D. Rabinovich¹, G. Fish², S. Kokolova², and A. Lewis²
¹*Ben-Gurion University of the Negev, Materials Engineering Department, P.O.B. 653, Beer-Sheva 84105, Israel*
²*The Hebrew University, Department of Applied Physics, Jerusalem 91904, Israel*

Multi-element thermoelectric converters 326

L. I. Anatychuk and B. -P. N. Demchuk
Institute of Thermoelectricity, General Post Office, Box 86, 274000, Chernivtsi, Ukraine

Investigations of the properties of a thermoelectric I-R detector for low working temperature 332

R. Fettig¹, T. Henkel¹, and E. Müller²

¹Universität Karlsruhe, Institut für Angewandte Physik, Germany

²Martin-Luther-Universität Halle-Wittenberg, Fachgruppe Angewandte Physik, Germany

The thermoelectric power on p-n junction 336

Z. Dashevsky¹, S. Ashmontas², L. Vingelis², I. Gradauskas², and A. I. Kasian³

¹Ben Gurion University of the Negev, Materials Engineering Department, P.O.B. 653, Beer-Sheva 84105, Israel

²Institute of Semiconductor Physics, Academy of Sciences of Lithuania, 232600, Vilnius, Lithuania

³Kishinev Polytechnical Institute, 277028, Kishinev, Moldova

SESSION H1: Thermoelectric power generation - Space and high temperature applications

Thermoelectric power generation systems recovering heat from combustible solid waste in Japan (*invited paper*) 343

T. Kajikawa

Department of Electrical Engineering, Shonan Institute of Technology, 1-1-25 Tsujido-nishikaigan, Fujisawa, Kanagawa, 251 Japan

Thermoelectric generators in photovoltaic hybrid systems 352

R. Kügele, W. Roth, W. Schulz, and A. Steinhüser

Fraunhofer Institute for Solar Energy Systems, Oltmannsstr. 5, D-79100 Freiburg, Germany

Power performance of U.S. space radioisotope thermoelectric generators 357

G. L. Bennett¹ and E. A. Skrabek²

¹Metaspaces Enterprises, 5000 Butte Road, Emmett, Idaho 83617-9500, USA

²Orbital Sciences Corporation, 20301 Century Boulevard, Germantown, MD 20874, USA

Thermoelectric generation and related properties of conventional type module based on Si-Ge alloy 373

M. Kobayashi¹, K. Ikoma¹, K. Furuya¹, K. Shinohara¹, H. Takao¹, M. Miyoshi², Y. Imanishi², and T. Watanabe²

¹NISSAN Motor Co., Ltd., 1 Natsushima-cho, Yokosuka, 237 Japan

²NGK Insulators, Ltd., 2-56 Suda-cho, Mizuho-ku, Nagoya, 467 Japan

Use, application and testing of the HZ-14 thermoelectric module 378

F. A. Leavitt, N. B. Elsner, and J. C. Bass

Hi-Z Technology, Inc., 6373 Nancy Ridge Dr, San Diego 92121, CA, USA

SESSION I1: Thermoelectric power generation - Terrestrial applications

Potential applications of advanced thermoelectrics in the automobile industry (*invited paper*) 383

D. T. Morelli

Physics and Physical Chemistry Department, General Motors Research and Development Center, Warren, MI 48090, USA

Miniature thermoelectric generators (TEG) with catalytic heating 387

L. I. Anatychuk, V. Y. Mikhailovskii, and V. V. Konopelnyuk
Institute of Thermoelectricity, General Post Office, Box 86, 274000, Chernivtsi, Ukraine

A stove-top generator for cold areas 390

A. Killander¹ and J. C. Bass²
¹*Royal Institute of Technology, Stockholm, Sweden*
²*Hi-Z Technology, Inc., San Diego, CA, USA*

Free convection and electrical generation with thermoelectrics 394

J. Buffet
2 Av. Dode de la Brunerie, 75016, Paris, France

SESSION J1: Materials characterization and measurements

Electronic structure of semimetals from transport and fermiology experiments (*invited paper*) 397

A. C. Ehrlich, and D. J. Gillespie
U. S. Naval Research Laboratory, Washington, DC 20375, USA

Dense semiconductor-insulator nanocomposites for Navy thermoelectric applications 402

D. Demske
Naval Surface Warfare Center, Carderock Division-White Oak, Code 682, 10901 New Hampshire Ave., Silver Spring, MD 20903-5640, USA

Evaluation of metal-Bi₂Te₃ contacts by electron tunneling spectroscopy 404

J. Nagao¹, E. Hatta², and K. Mukasa²
¹*Materials Division, Hokkaido National Industrial Research Institute, MITI 2-17-2-1 Tsukisamu-Higashi, Toyohira-Ku, Sapporo 062, Japan*
²*Faculty of Engineering, Hokkaido University, N-13 W-8 Kita-Ku, Sapporo 060, Japan*

Tunneling spectroscopy of band edge structures of Bi₂Te₃ and Sb₂Te₃ 408

K. Funagai¹, Y. Miyahara¹, H. Ozaki¹, and V. A. Kulbachinskii²
¹*Department of Electrical Engineering, Waseda University, Ohkubo 3-4-1, Shinjuku-ku, Tokyo 169 Japan*
²*Low Temperature Physics Department, Physics Faculty, Moscow State University, 119899, Moscow, Russia*

Determination of the thermal band gap from the change of the Seebeck coefficient at the pn-transition in (Bi_{0.5}Sb_{0.5/2})Te₃ 412

E. Müller, W. Heiliger, P. Reinshaus, and H. Süßmann
Martin-Luther-Universität Halle-Wittenberg, Fachgruppe Angew. Physik, Germany

Validation of thermoelectrics measurements II 417

J. W. Sharp¹, E. H. Volckmann¹, H. B. Lyon Jr.¹, D. J. Gillespie², G. N. Kamm², and A. C. Ehrlich²
¹*Marlow Industries Inc., 10451 Vista Park Road, Dallas, TX 75238-1645*
²*Naval Research Laboratory, Washington, D. C. 20375, Code 6341, U. S. A.*

SESSION K1: Thin films and heterostructures - Thin films I

Deposition of $(\text{Bi,Sb})_2\text{Te}_3$ films by magnetron co-sputtering from two targets - first results 422

M. Stölzer, V. Bechstein, and J. Meusel
Martin Luther University Halle-Wittenberg, Department of Physics, Institute of Applied Physics,
06099 Halle (Saale), Germany

Thin film thermoelectric generator cell of Bi-Sb-Te-Se system 425

I. -H. Kim and D. -H. Lee
Department of Metallurgical Engineering, Yonsei University, 134 Shinchon-dong, Seodaemun-gu,
Seoul, 120-749, Korea

Low temperature MOCVD growth of V/VI materials via a $\text{Me}_3\text{SiNMe}_2$ elimination reaction 430

T. J. Groshens, R. W. Gedridge Jr., R. Scheri, and T. Cole
Naval Air Warfare Center Weapons Division, Research and Technology Division, China Lake, CA 93555, USA

Thermoelectric properties of RF-sputtered CoSb_3 films 435

H. Anno¹, K. Matsubara¹, Y. Notohara², T. Sakakibara³, K. Kishimoto⁴, and T. Koyanagi⁴
¹Science University of Tokyo in Yamaguchi, Yamaguchi, Japan
²Kyushu Matsushita Electric Co., Ltd., Japan
³Aisin Cosmos R&D Co., Ltd.
⁴Yamaguchi University, Japan

Radiation defects induced by ion implantation as a promising method of doping semiconductor type A^{IV}B^{VI} films 440

Z. M. Dashevsky
Ben-Gurion University of the Negev, Materials Engineering Department, P.O.B. 653, Beer-Sheva 84105, Israel

Preparation of highly effective $\text{p-Bi}_{0.5}\text{Sb}_{1.5}\text{Te}_3$ and $\text{n-Bi}_2\text{Te}_{2.7}\text{Se}_{0.3}$ films 445

M. Stölzer, M. Stordeur, and I. Stark
Martin Luther University Halle-Wittenberg, Department of Physics, Institute of Applied Physics,
06099 Halle (Saale), Germany

SESSION K2: Thin films and heterostructures - Quantum-wells and superlattices

Experimental study of the effect of quantum-well structures on the thermoelectric figure of merit (*invited paper*) 450

L. D. Hicks¹, T. C. Harman², X. Sun¹, and M. S. Dresselhaus¹
¹Massachusetts Institute of Technology, Cambridge, MA 02139, USA
²Lincoln Laboratory, Massachusetts Institute of Technology, Lexington, MA 02173-9108, USA

Experimental evidence of high power factors and low thermal conductivity in $\text{Bi}_2\text{Te}_3/\text{Sb}_2\text{Te}_3$ superlattice thin-films 454

R. Venkatasubramanian, T. Colpitts, E. Watko, and J. Hutchby
Research Triangle Institute, Research Triangle Park, NC 27709, USA

Synthesis and evaluation of thermoelectric multilayer films 459

A. V. Wagner, R. J. Foreman, L. J. Summers, T. W. Barbee, Jr., and J. C. Farmer
*Chemistry and Materials Science Department, Lawrence Livermore National Laboratory,
7000 East Avenue, Livermore, California 94550, USA*

Thermoelectric figure of merit of Si-Ge multilayered thin films 464

A. Yamamoto and T. Ohta
Electrotechnical Laboratory, Umezono 1-1-4, Tsukuba, Ibaraki 305, Japan

Thermoelectric performance of B_4C/B_5C heterostructures 469

S. Ghamaty¹, N. Elsner¹, K. Wang², and Q. Xiang²
¹*Hi-Z Technology, San Diego, California, USA*
²*University of California, Los Angeles, USA*

SESSION K3: Thin films and heterostructures - Thin films II

Structure and transport properties of Ga-doped semi- and polycrystalline $Si_{1-x}Ge_x$ films 474

F. Edelmann¹, M. Stölzer², P. Werner³, and R. Butz⁴
¹*Materials Engineering Faculty, Technion-Israel, Institute of Technology, Haifa, Israel*
²*Martin Luther University Halle-Wittenberg, Department of Physics, Institute of Applied Physics,
Hoher Weg 7, D-06120 Halle (Saale), Germany*
³*Max-Planck Institut für Mikrostrukturphysik, Weinberg 2, D-06120 Halle (Saale), Germany*
⁴*Institut für Schicht und Ionentechnik (ISI), Forschungszentrum Jülich, D-5170 Jülich, Germany*

**Optical, electrical and structural properties of polycrystalline β -FeSi₂ thin films
fabricated by electron beam evaporation of ferrosilicon 479**

H. Katsumata¹, Y. Makita², H. Takahashi³, H. Shibata², N. Kobayashi²,
M. Hasegawa², S. Kimura², A. Obara², J. Tanabe³, and S. Uekusa¹
¹*Meiji University, 1-1-1 Higashi-mita, Tama, Kawasaki, Kanagawa 214, Japan*
²*Electrotechnical Laboratory, 1-1-4 Umezono, Tsukuba, Ibaraki 305, Japan*
³*Nippon Inst. of Tech., 4-1 Gakuendai, Miyashiro, Minami-Saitama, Saitama 345, Japan*

Structure and thermoelectric properties of nano-crystalline Re_xSi_{1-x} thin film composites 484

A. Burkov, A. Heinrich, C. Gladun, W. Pitschke and J. Schumann
¹*Institute of Solid State and Materials Research, D-01171 Dresden, Germany*

A microstructural analysis of thin film TiNiSn 491

D. N. Compton, A. W. R. Leitch, J. H. Neethling, and V. V. Kozyrkov
*Department of Physics, University of Port Elizabeth, PO Box 1600,
Port Elizabeth 6000, Republic of South Africa*

**Large transverse Seebeck voltage in oxygen-reduced
 $YBa_2Cu_3O_{7-x}$ and $Y_{1-x}Pr_xBa_2Cu_3O_{7-x}$ thin films 494**

F. Lankes, E. V. Pechen, T. Honke, and K. F. Renk
Institut für Angewandte Physik, Universität Regensburg, D-93040 Regensburg, Germany

Structure and phase formation in amorphous Ir_xSi_{1-x} thin films at high temperatures 499

W. Pitschke¹, R. Kurt¹, A. Heinrich¹, J. Schumann¹, and M. Mäder²
¹*Institut für Festkörper- und Werkstoffforschung Dresden e.V., D-01171 Dresden, Germany*
²*Forschungszentrum Rossendorf e.V., D-01314 Dresden, Germany*

Bi-Sb Alloys : an Update

B. Lenoir, A. Dauscher, X. Devaux, R. Martin-Lopez, Yu.I. Ravich*, H. Scherrer and S. Scherrer

Laboratoire de Métallurgie Physique et Science des Matériaux

Ecole des Mines / Parc de Saurupt

F-54042 Nancy, France

*Ioffe Institut, St Petersburg, Russia

Abstract

This paper is devoted to a survey of the principal studies performed on Bi-Sb thermoelectric materials over the last forty years. Bi-Sb alloys are still the best *n*-type materials for refrigeration at low temperatures nowadays. After a brief introduction of their physical characteristics (cristallography and band structure), the elaboration, characterization and transport properties (thermoelectric and galvanomagnetic) of the Bi-Sb alloys will be presented. The results obtained on bulk materials, in single crystalline and polycrystalline forms, and thin films will be discussed.

Introduction

Among semimetals and narrow band gap semiconductors, bismuth-antimony alloys have received particular attention these last forty years not only because they present interesting physical properties from a fundamental point of view, but also for their interest as engineering materials. The structure of their conduction and valence bands strongly depends on various parameters such as alloy composition [1-3], temperature [4], external pressure [5, 6] and magnetic field [7, 8]. Such peculiarities have yielded to the observation of several exciting properties like for example the observation of a transition to a gapless state [9, 10].

The study of the transport properties of $\text{Bi}_{1-x}\text{Sb}_x$ alloys realized by Smith and Wolfe in 1962 [11] and extended by Yim and Amith ten years later [12] has shown that such alloys may be attractive *n*-type materials for electronic refrigeration. Actually, properly oriented Bi-rich bismuth-antimony crystals have been reported as having higher thermoelectric performances than Bi_2Te_3 compounds for temperatures lower than 220 K [11]. These interesting properties could however not give rise to any application for solid state cooling devices at this time because no *p*-type material having compatible thermoelectric properties at low temperatures was available.

The figure of merit Z_{np} , which is the thermoelectric index of efficiency of a thermocouple constituted of *n* and *p* legs [13], is defined as :

$$Z_{np} = \frac{(\alpha_p - \alpha_n)^2}{\left[(\rho_p \lambda_p)^{1/2} + (\rho_n \lambda_n)^{1/2} \right]^2} \quad (1)$$

where $\alpha_{n,p}$ is the thermoelectric power, $\rho_{n,p}$ the electrical resistivity and $\lambda_{n,p}$ the thermal conductivity of the *n* and *p* legs, respectively.

From relation (1), it is clear that if the *p* leg has far lower thermoelectric performances than the *n* leg, the figure of merit of the *n*-*p* couple will be decreased and thus the potential performances of solid state cooling devices will even be

considerably reduced. Fortunately, the discovery of high T_c superconductors has fundamentally modified the situation. Actually, a thermocouple constituted of a *n*-type Bi-Sb leg and of a *p*-type high T_c superconductor leg, thermoelectrically passive, will possess a figure of merit close to that of the *n* leg [14]. Several workers have investigated the figure of merit of thermocouples composed of high T_c superconducting *p* leg for their application in solid state devices [15-18].

The advantage of using Bi-Sb single crystals with regard to conventional *n*-type materials is still more important in the presence of a transverse magnetic field, as first pointed out by Wolfe and Smith [19] for a $\text{Bi}_{0.88}\text{Sb}_{0.12}$ single crystal. They reported a dimensionless figure of merit ZT greater than unity between 125 K and 275 K by applying an optimum magnetic field. These values are two times, and even more, greater than the zero field values. This large improvement is due to the presence of transverse thermomagnetic effects [19]. These effects are particularly great for dilute Bi-Sb alloys, making them very attractive materials for Ettingshausen cooling devices [20-22].

After a brief introduction of the principal physical properties of Bi-Sb alloys, the salient results pertaining to thermoelectric properties will be discussed. Both bulk materials and thin films will be reviewed. The transport properties will only be described qualitatively because the band structure is strongly correlated to antimony content and temperature.

Although the effect of a magnetic field presents considerable interest for Bi-Sb solid solutions, we will essentially deal with zero-field coefficients. Goldsmid [23] has recently reviewed the interest of using Bi-Sb alloys for thermomagnetic cooling.

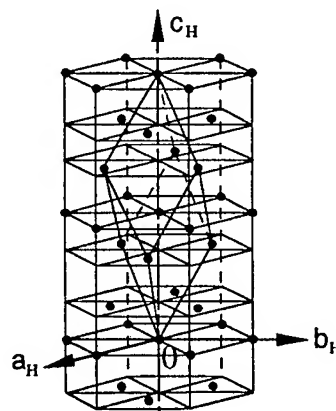


Fig. 1 Hexagonal representation of the A_7 structure. The basal planes are perpendicular to the trigonal axis c_H .

Survey of the band structure of $\text{Bi}_{1-x}\text{Sb}_x$ alloys

Bismuth and antimony (group V) are semimetals that both exhibit a similar rhomboedral crystal structure (often called the A_7 structure) of $R\bar{3}m$ point group. They present very close lattice parameters and two atoms per unit cell. The set of axes usually used is such that 1-axis is parallel to a binary axis, 3-axis is parallel to the trigonal axis and 2-axis, called the bisectrix axis, is normal to the two other axes so as to obtain a right handed orthonormal set (1,2,3). The hexagonal representation shows that the A_7 structure is lamellar (Fig. 1) in the same way as in bismuth telluride compounds. Crystals can be cleaved along the basal planes (perpendicularly to the trigonal axis) but not so easily as in bismuth telluride.

The most important crystallographic feature of these semimetals is that the A_7 structure can be considered as a slightly deformed cubic lattice [24]. The band structure resulting from the distortion from cubic symmetry distinguishes the group V semimetals from the more commonly known isotropic insulators or metallic conductors.

Since bismuth and antimony have similar lattice parameters, it is not surprising that Bi-Sb alloys form a solid solution over the whole composition range. Cucka and Barrett [25] have reported that the hexagonal lattice parameters of $\text{Bi}_{1-x}\text{Sb}_x$ satisfy the Vegard's rule when $0 \leq x \leq 0.3$.

From symmetry arguments, it can be shown that the tensors of the three zero field transport properties, i.e. α , ρ and λ , have only two independent components, one along the trigonal axis (index 33) and one in the basal plane (index 11 or 22).

Reviews concerning the electronic band structure of bismuth and antimony and the properties of electrons in bismuth have been reported by Dresselhaus [26] and Edelman [27], respectively. In the following section, we will only summarize the aspects of the band structure of the pure components and alloys that are relevant to the understanding of the transport properties.

The small distortion from the simple cubic lattice induces that bismuth and antimony are semimetals characterized by a small overlap of the fifth and sixth bands, leading to the presence of a small equal number of electrons and holes at every temperature. In bismuth, the pockets of electrons are located at the L points of the Brillouin zone whereas the pockets of holes are located at the T points (Fig. 2). The hole Fermi surface corresponds to an ellipsoid of revolution along the trigonal axis whereas the electron Fermi surfaces consist in

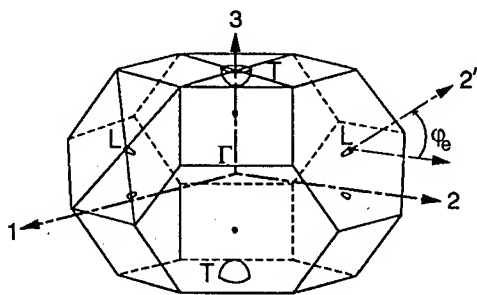


Fig. 2 Location of the Fermi surfaces of bismuth in the Brillouin zone. Axes 1, 2 and 3 are parallel to the binary, bisectrix and trigonal axes, respectively. ϕ_e is the tilt angle of the electron ellipsoids.

three quasi-ellipsoids strongly elongated along a direction which is near from the bisectrix axis. This highly anisotropic shape leads to unusual very small effective masses along two directions inducing very high electron mobilities.

The same structure occurs for the "light" L hole band, which is separated from the conduction band by a narrow energy gap E_g ($E_g = 13.6$ meV at 0 K [28]) and is coupled to it by the $\mathbf{k} \cdot \mathbf{p}$ interaction, causing a highly non-parabolic dispersion relationship of the two bands and a non quasimomentum dependence of the Bloch amplitude. The simplest dispersion relation for the L-bands is the two-band model of Lax and Mavroides [29]. Expressed in coordinates fixed to the ellipsoid axes, the energy dispersion follows the law :

$$E \left(1 + \frac{E}{E_g} \right) = \frac{\hbar^2}{2m_0} \bar{\mathbf{k}} \bar{\mathbf{m}}^{-1} \bar{\mathbf{k}} \quad (2)$$

where m_0 is the free electron mass, $\bar{\mathbf{m}}$ the effective mass tensor of electrons and L holes near the band edges and $\bar{\mathbf{k}}$ the wave vector. The non-parabolicity alters the effective masses. In the previous model, an effective mass tensor element m^* depends on energy E as :

$$m^*(E) = m \left(1 + 2 \frac{E}{E_g} \right) \quad (3)$$

In antimony, the pockets of electrons are also located at the L points of the Brillouin zone whereas holes are located at the six equivalent H points. The departure from cubic symmetry is more pronounced in antimony than in bismuth, resulting in a larger carrier density in antimony than in bismuth. It should be noted that L, T and H hole bands differ greatly with regard to the density of state effective mass m_d . Values reported at the helium temperature are respectively : $m_{d,L} = 0.02 m_0$, $m_{d,T} = 0.14 m_0$ and $m_{d,H} = 0.5 m_0$ [26].

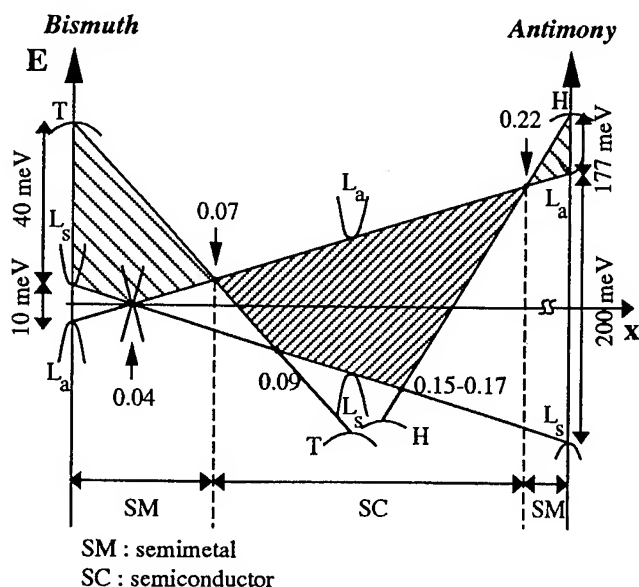


Fig. 3 Schematic diagram of the band edge configuration of $\text{Bi}_{1-x}\text{Sb}_x$ alloys as a function of x , at $T \cong 0$ K. In the semiconducting range, the band gap is maximum around $x = 0.15-0.17$.

The substitution of Bi atoms by Sb atoms in the Bi lattice modifies drastically the band structure of bismuth. Fig. 2 represents the band structure evolution of $\text{Bi}_{1-x}\text{Sb}_x$ alloys as a function of x , at low temperature. These results were obtained from powerful oscillatory techniques like magnetoreflexion or cyclotron resonance.

As it can be seen in Fig. 3, alloying affects mainly three band parameters :

- the overlap between L and T bands,
- the value of the direct energy gap E_g ,
- the energy of the top of the H bands.

Between $0 \leq x < 0.04$, the overlap as well as the band gap decrease. At $x \approx 0.04$, a gapless state appears [30,31]. Beyond this composition, the bonding L_s and antibonding L_a bands are inverted and the band gap increases with enhancing antimony concentration. At $x \approx 0.07$, there is no more overlap between the conduction band at the L point and the valence band at the T point. The material loses then its semimetallic character and becomes a semiconductor [32,33]. However, because the top of the H band increases with enhancing antimony concentration, a second transition takes place at $x \approx 0.22$ [34,35]. Beyond this composition, the band structure of the alloys evolves up to the band structure of pure antimony. So, between $0.07 < x < 0.22$, $\text{Bi}_{1-x}\text{Sb}_x$ alloys are narrow band gap semiconductors with a maximal band gap around 15-17 at. % Sb.

Since the energy gap associated with the electron pockets at the L point is very small, it is not surprising that all the band parameters associated with the electron carriers are strongly temperature dependent. These observations were first reported by Vecchi and Dresselhaus [28] for pure bismuth and were further extended to some Bi-rich alloys by Mendez [4]. Their results show drastic relative variations of the energy band gap with regard to the value at 0 K, compared to typical semiconductors. For $T > 80$ K, extrema of L_s and L_a bands increase and decrease in energy, respectively, when the temperature is enhanced. The effective masses at the L bands extrema were also reported as being very sensitive to temperature. Nothing is "à priori" known about the temperature dependence of band parameters for T and H bands in Bi-Sb alloys.

All these unusual features allow us to understand, at this stage, why it is difficult to analyse the transport properties of such alloys, the difficulties arising in part from the strong non-parabolicity and the large temperature dependence of the band parameters at the L points of the Brillouin zone.

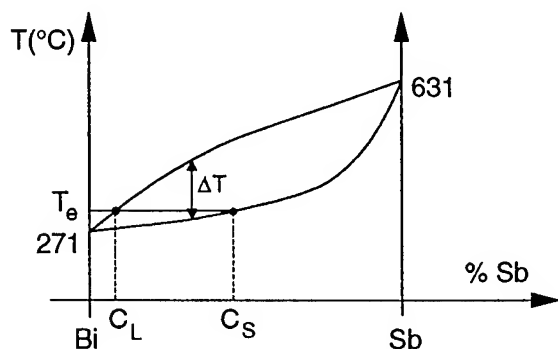


Fig. 4 Phase diagram of the Bi-Sb system.

The situation is still more complex when several valence bands contribute to the transport properties. This matter of fact prevails when alloys are semiconductors, and it is precisely when the thermoelectric performances are the most interesting.

Preparation

Although bismuth and antimony are completely miscible in both the liquid and solid states, there is a large temperature difference between the liquidus and the solidus (Fig. 4). A similar situation is encountered for silicon-germanium alloys which are the best thermoelectric materials for high temperature uses. According to the phase diagram of the Bi-Sb system, a liquid of C_L composition will start to crystallise a solid with the C_S composition, enriched in Sb with regard to the melt, as seen Fig. 4. Further lowering the temperature modifies both the compositions of the liquid along the liquidus line and of the grown ingot along the solidus line. Due to very low diffusion rates in the solid, the resulting ingot exhibits severe segregation. It results that the preparation of homogeneous solids requires either to maintain constant the composition of the melt during the growth or to use some process to homogenize the solid phase.

Bi-Sb alloys have been extensively prepared in the single crystalline form and to a less extent via powder metallurgy.

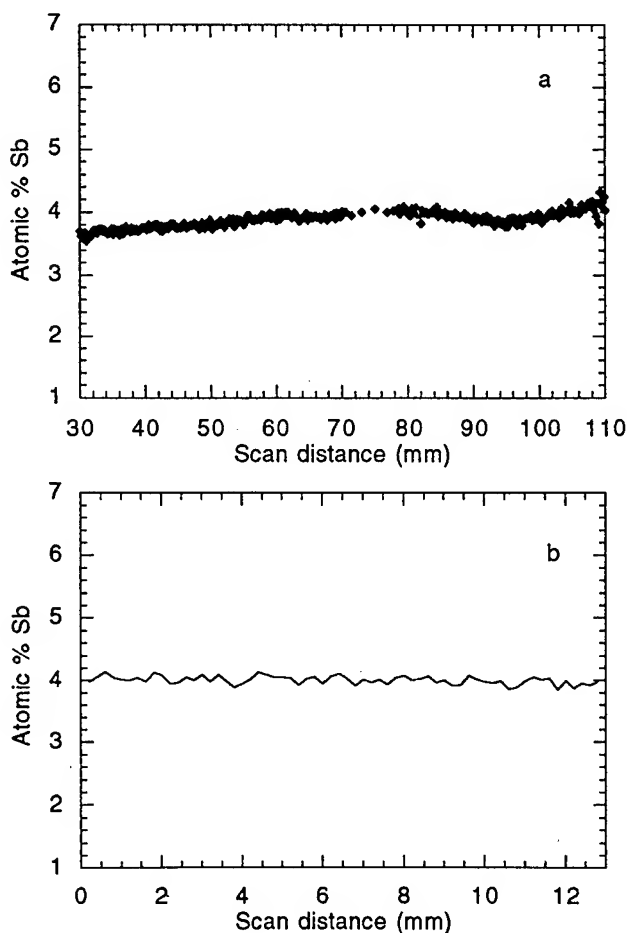


Fig. 5 Longitudinal (a) and radial (b) variation in Sb content as determined by electron microprobe analysis on a 150 mm in length and 15 mm in diameter $\text{Bi}_{0.96}\text{Sb}_{0.04}$ alloy elaborated by T.H.M.

Although Bi-Sb samples were mostly prepared without any intentional doping, effects on the thermoelectric properties of donor (Te [36,37], Se [36]) and acceptor (Sn [12,37,38], Pb [11,39], Ga [40]) centers have been considered.

Single crystals

Among the various preparation methods mentioned in the literature, the repeated pass zone melting was principally used to produce single crystals, the growth rate ranging from 0.1 to 51 mm h⁻¹ [1,11,36,41-46]. This elaboration method can overcome excessive macro-segregations in the alloys whereas the micro-homogeneity in composition can only be achieved from slow growth rates. Micro-inhomogeneities arise from the detrimental effect of constitutional supercooling. Constitutional supercooling can be eliminated [47] or at least reduced substantially if the applied growth rate R satisfy the relation :

$$R < DG/\Delta T \quad (4)$$

where D is the binary alloy liquid diffusion constant (about 10⁻⁵ cm²s⁻¹ at 300°C as reported by Brown and Heumann [41]), G the temperature gradient at the solidification interface and ΔT the temperature difference between the liquidus and the solidus. It is however difficult to produce large temperature gradients due to the low melting temperatures of the alloys. Consequently, small G gradients associated with large ΔT constrain to use small growth rates R .

Contrarily to multi-pass zone melting, a single-pass zone levelling technique [48] or a Traveling Heater Method (T.H.M.) [49] were successfully used to grow very homogeneous single crystals. These processes are methods of solvent zone transfer through a polycrystalline source ingot in a quartz ampoule sealed under vacuum. The compositions of the source ingot C_S and of the solvent zone C_L are chosen in such a way that the liquid and the solid are in equilibrium at the solidification interface T_e (Fig. 4). An example of longitudinal and radial homogeneities is reported Fig. 5 for a Bi_{0.96}Sb_{0.04} alloy elaborated by the T.H.M. method. It must be pointed out that temperatures used for the growth are much lower for zone levelling or T.H.M. methods than for zone melting processes.

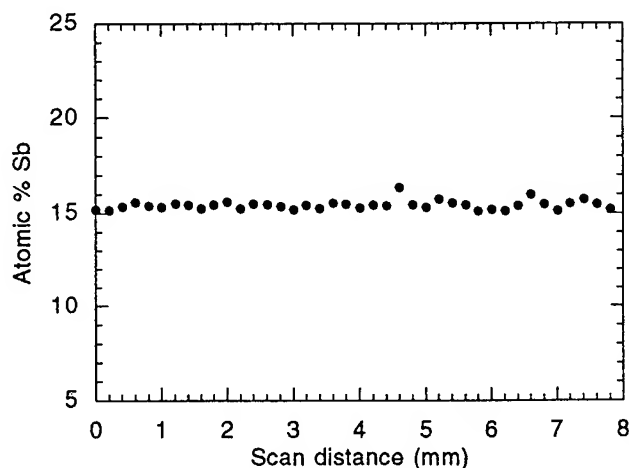


Fig. 6 Electron microprobe scanning along compacted Bi_{0.85}Sb_{0.15} powders elaborated by mechanical alloying (ball to powder weight ratio : 10/1, particle sizes > 100 μ m, 15 h of milling time), after [56].

The Czochralski pulling technique was also successfully used to grow homogeneous doped (Te, Sn) and undoped Bi-Sb alloys up to 18 % at. Sb [50]. Large single crystals (20-25 mm in diameter) of high degree of crystalline perfection have been obtained. Recently the melt-injection technique [51] was also developed to prepare these mixed crystals.

Powder metallurgy

The use of Bi-Sb single crystals in low temperature stages of solid state coolers is still restrained up to now. The main reason is that the Bi-Sb single crystalline leg possesses a low bending strength and a low tension strength along the trigonal axis leading to slippings in the cleavage planes. Unfortunately, it is precisely in that direction that the figure of merit is the best. Special attention was devoted to enhance the mechanical properties of Bi-Sb single crystals. Belava et al. [52] have investigated the influence of the growth parameters on the bending strength of Czochralsky grown ingots as well as the influences of the size and the surface quality of the samples. Quite remarkable works on extrusion of single crystals have been performed by Sidorenko and co-authors [53-55] as an attempt to improve the mechanical properties, without any large decrease of the thermoelectric performances.

Another way to improve the durability of the material is to produce Bi-Sb polycrystalline alloys via powder metallurgy. They are easier to synthesize, dimension, and handle than single crystals. The microstructure produced by powder metallurgy also eliminates the danger of catastrophic failure due to cleavage.

Nowadays, in the light of the scarce published works on Bi-Sb powder alloys, there are three obtention techniques : mechanical alloying [56], arc-plasma spraying [57,58], and the grinding of zone-melted rods [59,60]. Mechanical alloying allows the elaboration of homogeneous powders (Fig. 6) with grain sizes about 10 μ m, in relatively low milling times (4-15 hours, depending on the milling conditions) [56]. Arc-plasma technique also permits to elaborate fine powders (Fig. 7) of controlled stoichiometry and granulometry (0.025 to 0.8 μ m) [58].

Galvanomagnetic properties

Galvanomagnetic investigations are well adapted to study the evolution of carrier mobilities and densities with temperature. The 80-200 K temperature range is particularly interesting for the use of Bi-Sb alloys in thermoelectric devices.

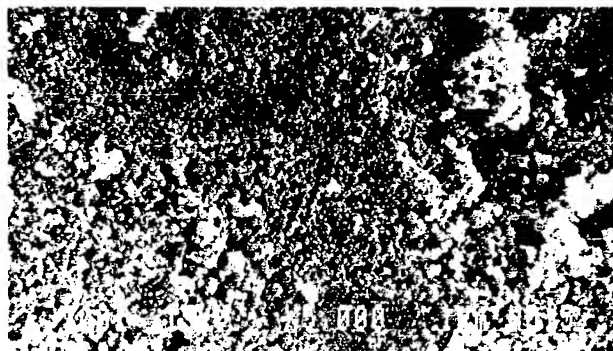


Fig. 7 Scanning electron micrograph of a Bi_{0.875}Sb_{0.125} powder elaborated by arc plasma spraying (mean particle size < 1 μ m), after [58].

To compute the band model parameters in a straightforward way from the galvanomagnetic data, one approach is to turn to low field measurements, that is fields for which $\mu B \ll 1$, where μ is some carrier mobility and B the magnetic induction, and in this case the effects are very small. Different attempts to obtain informations about band parameters have been performed on some alloys [45,61]. Nevertheless, the conclusions obtained by these authors need substantial reconsideration because of the use of an incorrect band model for the alloys. Moreover, by studying the galvanomagnetic effects in weak magnetic fields, the Hall factor and the magnetoresistance factor, both governed by the energy dependence of the relaxation time, are assumed to be close to unity in bismuth and in alloys. When the non-parabolicity is taken into account, these factors may be considerably increased for electrons when there is no strong statistical degeneracy. Ravich and Rapoport [62] have clearly shown that these factors differ greatly from unity in bismuth for temperatures exceeding 100 K.

Quite recently, Demouge et al. [63] have investigated the galvanomagnetic tensor of $\text{Bi}_{0.96}\text{Sb}_{0.04}$ in the temperature range 77-180 K under strict isothermal conditions, rigorously satisfying the low field conditions. Their experimental results have been analysed from a two band model taking into account the non-parabolicity and a mixed scattering model : the scattering by acoustical phonons and interband (recombinaison) scattering due to electron transitions between the conduction band and the valence band (T band). As expected, the authors have also found that the Hall and magnetoresistance factors differ from unity. The temperature dependence of the carrier mobilities is reported Fig. 8. It is seen that the T-holes mobilities are smaller in the alloy than in bismuth, suggesting that holes are more affected by alloying than electrons.

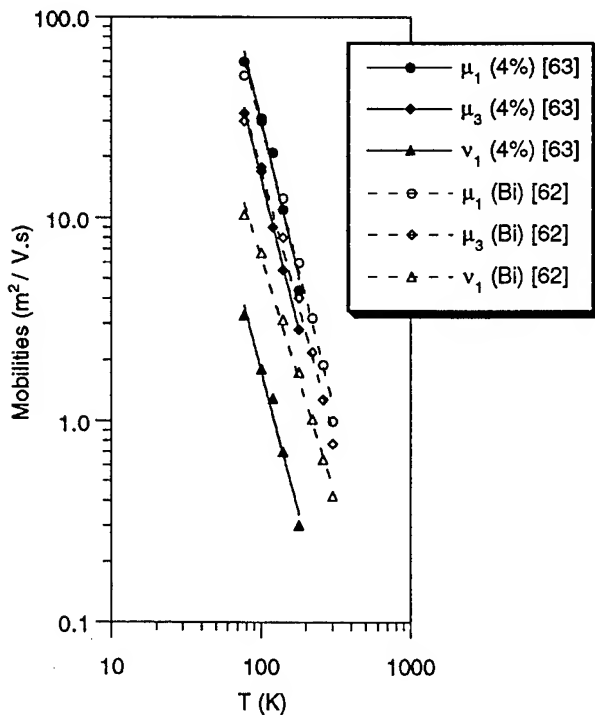


Fig. 8 Evolution of the electron mobilities μ_i and hole mobilities v_i with temperature of $\text{Bi}_{0.96}\text{Sb}_{0.04}$ and Bi (index i refers to the directions to the principal axes of the ellipsoids).

Transport properties

Single crystals

Electrical resistivity

The electrical transport coefficients ρ_{11} and/or ρ_{33} of Bi-rich Bi-Sb alloys have been measured by many authors within the 4.2 - 300 K temperature range [1,11,12,36,42,44,46,64-71]. The general trends are similar in most of the studies except at low temperatures where the crystalline quality and the concentration of residual impurities play an important role. The different temperature dependences of the electrical resistivity encountered in $\text{Bi}_x\text{Sb}_{1-x}$ alloys ($x < 0.20$) are schematized Fig. 9.

Above 150 K, the electrical resistivity increases almost linearly whatever the measurement direction and the alloy composition. At 300 K, the value of the resistivity is about $1.5 \mu\Omega \cdot \text{m}$. This value, near from that of pure bismuth ($\approx 1.2 \mu\Omega \cdot \text{m}$), is only two orders of magnitude higher than the value of typical metals. For bismuth, the low number of carriers (10^{17} - 10^{18} cm^{-3} [72]) is compensated by their very high mobilities in some directions, as compared to metals, due to very small effective masses. Since the density of carriers in Bi-Sb alloys is of the same order of magnitude than in pure bismuth, we can expect that the mobilities are still very high in the solid solution at room temperature.

Below 150 K, a clear difference in the electrical resistivity behaviours appears. For $x < 0.07$, the electrical resistivity of the semimetallic alloys decreases with diminishing the temperature, quite similarly to what happens for pure bismuth. For $0.07 < x < 0.20$, the resistivity first decreases down to a minimum and then three temperature dependences can be observed as the temperature decreases (Fig. 9) :

- a continuous increase of the resistivity,
- an increase with a subsequent transition to saturation,
- an increase up to a maximum and then a decrease down to a saturation limit.

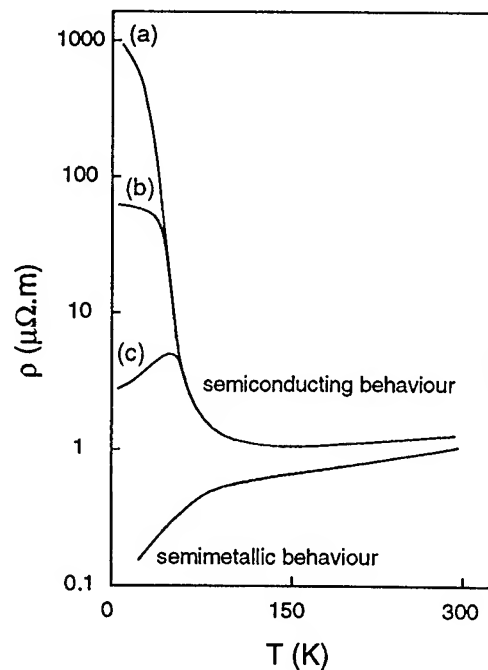


Fig. 9 Schematic temperature dependence of the electrical resistivity in Bi-Sb alloys.

This unusual behaviour at low temperature in the semiconducting range for undoped alloys can be qualitatively understood according to the hydrogenoid model. Actually, due to a large dielectric constant (≈ 100) and to small effective masses ($\approx 0.02 m_0$), the ionization energy of the bound states and the Bohr radius are abnormally low and high, respectively, leading to the formation of an impurity band for low impurity concentrations n_i (for Bi-Sb alloys, $n_i < 10^{12} \text{ cm}^{-3}$ to have bound states). These considerations explain why, even in very pure materials, a large residual conductivity can be expected at $T = 4.2 \text{ K}$.

When the intrinsic carrier concentration is greater than the impurity density n_i , the resistivity decreases. The variations observed as a function of temperature are then similar to those of a semiconductor having a narrow band gap. The thermal band gap ΔE was estimated by many authors on the assumption that the resistivity follows an exponential law :

$$\rho = \rho_0 \exp (-\Delta E/2kT) \quad (5)$$

The results are reported Fig. 10. Despite the approximation of such temperature dependence, the obtained results describe qualitatively the evolution of the band structure as a function of composition at low temperature when the investigated samples are homogeneous. It results from the small value of the thermal gap that the electrical resistivity increases when the thermal energy kT is of the same order of magnitude as ΔE .

The anisotropy of the electrical resistivity is not very important for $T > 50 \text{ K}$ and depends on the antimony content [12,70].

Thermoelectric power

The substitution of Bi atoms by Sb atoms results in larger absolute values of the thermoelectric power for both thermoelectric powers α_{11} and α_{33} , with regard to those of pure bismuth (Fig. 11). It is due to the decrease of the overlap between L and T bands, and to the appearance of a semiconducting state. It was shown experimentally by many authors that the thermoelectric power of semiconducting alloys is always negative in the region of intrinsic conductivity [11,12,64,65,68-70,73] whereas it can be either positive or negative in the region of extrinsic conductivity according to the type of doping (intentional or not).

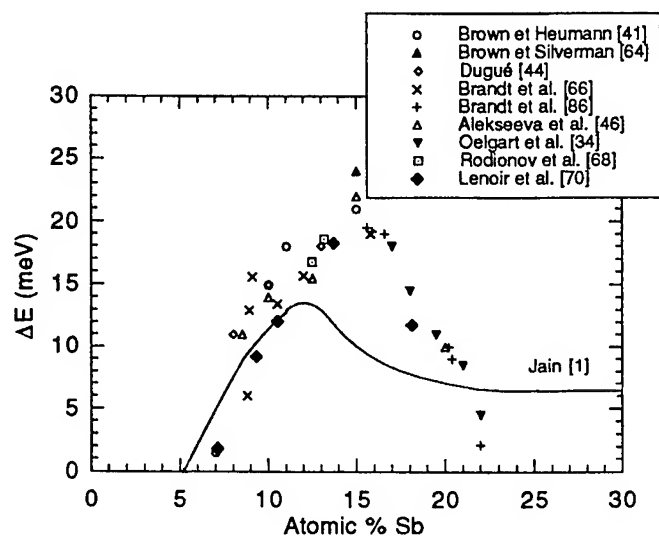


Fig. 10 Estimation of the thermal gap ΔE of Bi-Sb alloys from relation (5), according to several authors.

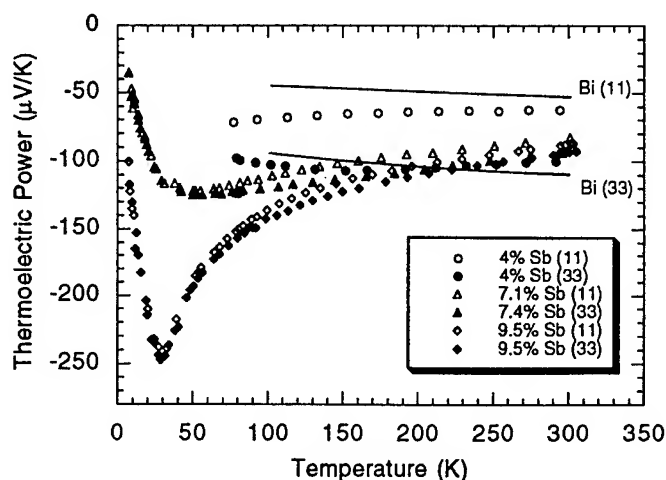


Fig. 11 Thermoelectric power of various Bi-Sb alloys as a function of temperature along directions parallel (α_{33}) or perpendicular (α_{11}) to the trigonal axis, after [70]. (— represents the measurements for Bi [87]).

A lot of studies have been performed by Red'ko and co-authors [68,74-76] on the measurement of the thermoelectric power on p or n $\text{Bi}_{1-x}\text{Sb}_x$ ($0.085 \leq x \leq 0.17$) alloys at low temperatures ($T < 100 \text{ K}$) with the attempt to correlate their results with the complex valence band structure. By varying the impurity carrier densities, they have investigated the carrier scattering mechanism in a single-band state (only light holes participate in the transport phenomena) or in a many-band state (both the light holes and the heavy holes are involved in the transport effects). Very large values of the thermoelectric power were reported at very low temperature in a series of samples (Fig. 12). Due to the narrow band gap of the semiconducting alloys, the transition from extrinsic to intrinsic conductivity takes place at low temperature.

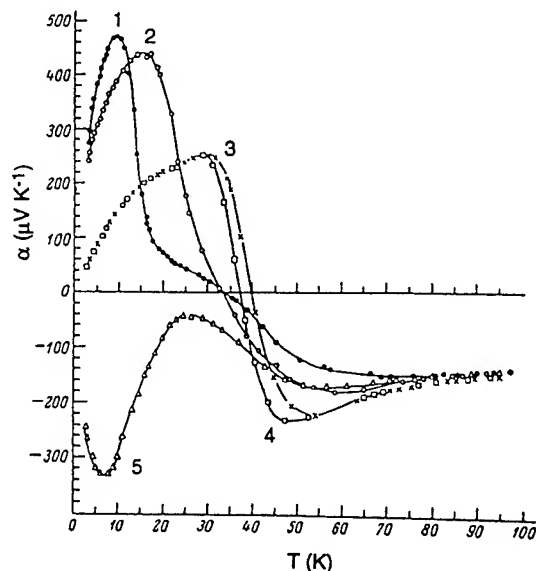


Fig. 12 Temperature dependence of the thermoelectric power as a function of hole and electron densities p and n , respectively : 1) α_{22} , $p = 3.4 \cdot 10^{13} \text{ cm}^{-3}$; 2) α_{22} , $p = 2.1 \cdot 10^{14} \text{ cm}^{-3}$; 3) α_{22} and 4) α_{33} , $p = 4.6 \cdot 10^{14} \text{ cm}^{-3}$; 5) α_{33} , $n = 4.1 \cdot 10^{13} \text{ cm}^{-3}$, after [68].

An increase of the carrier concentration at low temperature only leads to the shift of the transition temperature towards higher temperature, as can be seen Fig. 12.

The negative sign of the thermoelectric power in the intrinsic range reflects only the higher mobilities of electrons compared to those of holes. Actually, the total diffusion thermoelectric power α_{ii} is expressed in terms of the corresponding partial contributions as :

$$\alpha_{ii} = \frac{\alpha^e \sigma_{ii}^e + \alpha^h \sigma_{ii}^h}{\sigma_{ii}^e + \sigma_{ii}^h} \quad (6)$$

where σ_{ii}^j is the partial contribution of carriers to the total electrical conductivity in the considered direction (index j refers to electrons or holes) and α^j are the partial diffusion thermopowers. For holes, L, T and H bands may contribute to the partial contributions. In first approximation, we can suppose that the numerical partial thermopowers are of the same order of magnitude. Following this assumption, an expression can be found for α_{ii} :

$$\alpha_{ii} \cong \frac{\alpha^e \left(1 - \frac{\sigma_{ii}^h}{\sigma_{ii}^e} \right)}{1 + \frac{\sigma_{ii}^h}{\sigma_{ii}^e}} \quad (7)$$

Since the contribution of light and/or heavy holes to the intrinsic conductivity is small in comparison with that of electrons, because the mobility of electrons is much higher than that of holes, the ratio of the partial conductivities is less than unity and α_{ii} is negative.

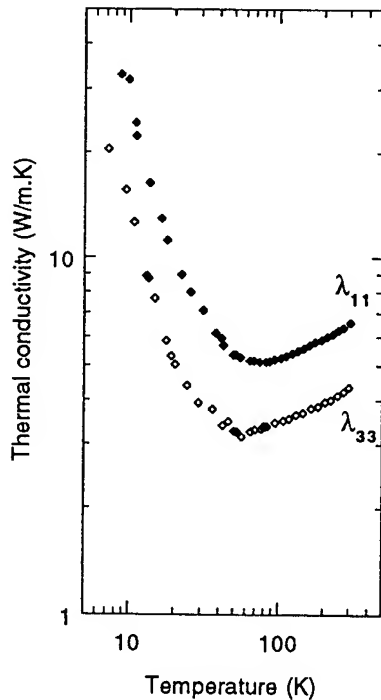


Fig. 13 Anisotropy of the thermal conductivity represented for a $\text{Bi}_{0.93}\text{Sb}_{0.07}$ alloy, after [70].

Thermal conductivity

The temperature dependence of the thermal conductivity is illustrated in Fig. 13 for a $\text{Bi}_{0.93}\text{Sb}_{0.07}$. A strong anisotropy is observed ($\lambda_{11}/\lambda_{33} \cong 1.7$).

In these materials, the thermal conductivity λ is principally the sum of two terms : an electronic contribution λ_E (including both unipolar and bipolar terms) and a contribution associated with the lattice phonons λ_L :

$$\lambda = \lambda_E + \lambda_L \quad (8)$$

In pure bismuth, in the range 2-20 K, the thermal conductivity λ_{11} is only due to the lattice contribution. The relative contribution of λ_E increases with increasing temperature. Uher and Goldsmid [77] have reported that λ_E contributes to 14 % of the total conductivity at 35 K and to 42 % at 140 K. The knowledge of the relative contributions of carriers and phonons has also been studied in the alloys [65,69,78-81]. The most remarkable results have been obtained by Kagan and Red'ko [80,81] who succeeded to separate the relative contributions by applying a strong magnetic field ($\mu B > 1$) (Fig. 14). As might be expected, below 20 K the heat is still primarily transported by phonons, and at higher temperatures the electronic component becomes more important as the temperature increases. However, alloying reduces strongly the lattice thermal conductivity with regard to pure bismuth because of strong point defect scattering. The relaxation time τ for this process is expressed by [82]:

$$\tau^{-1} = A \Gamma \omega^4 \quad (9)$$

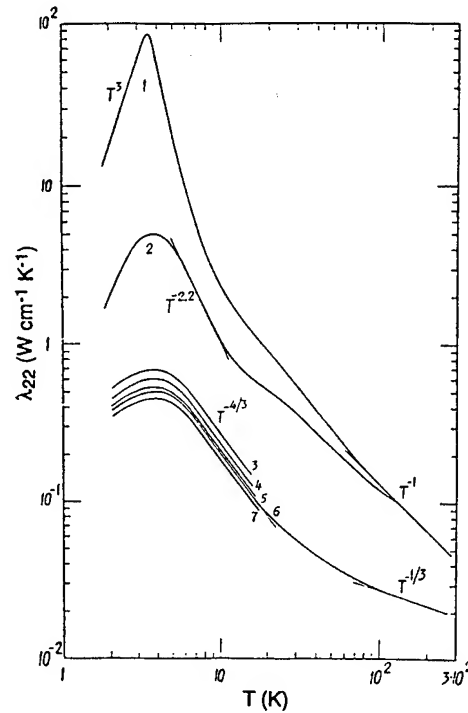


Fig. 14 Temperature dependence of the phonon thermal conductivity λ_{22} of single-crystal samples. 1) pure bismuth ; (2-7) $\text{Bi}_{1-x}\text{Sb}_x$ alloys of the compositions $x=0.001$ (2), 0.085 (3), 0.1 (4), 0.12 (5), 0.135 (6), 0.15 (7), after [81]. Dimensions of the sample were : $4 \times 4 \times 40 \text{ mm}^3$. As in Bi, a size effect was observed in $\text{Bi}_{1-x}\text{Sb}_x$ alloys.

where A is a constant, ω refers to the phonons frequency and Γ , which is a measurement of the strength of the scattering, is given by :

$$\Gamma = \sum_i f_i \left(1 - \frac{M_i}{\bar{M}}\right)^2 \quad (10)$$

where M_i is the mass of the i^{th} type of impurity, \bar{M} the mean atomic mass and f_i the fractional concentration of this impurity. Since the atomic masses of bismuth and antimony largely differs ($M_{\text{Bi}} \approx 209$ and $M_{\text{Sb}} \approx 122$), point-defect scattering phenomena are relatively important.

The decrease of the lattice thermal conductivity with respect to bismuth is spectacular near the dielectric maximum where the defects have a far greater effect on the thermal conductivity than at higher temperature (Fig. 14).

Thermoelectric figure of merit

The larger values of the Seebeck coefficient and the lower values of the lattice thermal conductivity in the alloys result in higher values of the figure of merit than for pure bismuth (Fig. 15). Values measured along the trigonal axis are higher than those measured in the basal plane (Fig. 15). This strong anisotropy reflects mainly the strong anisotropy of the thermal conductivity. The temperature dependence of the figure of merit is similar whatever the composition. It increases slowly from 300 K up to a maximum around 70 K and then drops sharply at low temperature.

Lenoir et al. [83] have observed the presence of two maxima in the curve of the figure of merit versus Sb content at 70 K in undoped Bi-Sb alloys (Fig. 16) corresponding to the situation where the tops of T and H bands are on the same level than L bands, for $x \approx 0.09$ and $x \approx 0.16$. Such behaviour was previously reported by Grabov et al. [84] for $T = 82$ and $T = 95$ K. Lenoir et al. [83] have qualitatively interpreted this dependence as arising from interband hole scattering. Within the composition range $0.09 \leq x \leq 0.16$, the interband scattering is maximal when the heavy hole extremum is on the same level than the light hole maximum. The figure of merit may be lowered outside this range because of the decrease of the thermal gap. Therefore, the interband hole scattering may explain the existence of the two maxima in the evolution of the figure of merit with Sb content at low temperatures. The same mechanism can certainly also explain why the bismuth-antimony alloys cannot be good p -type thermoelectric materials.

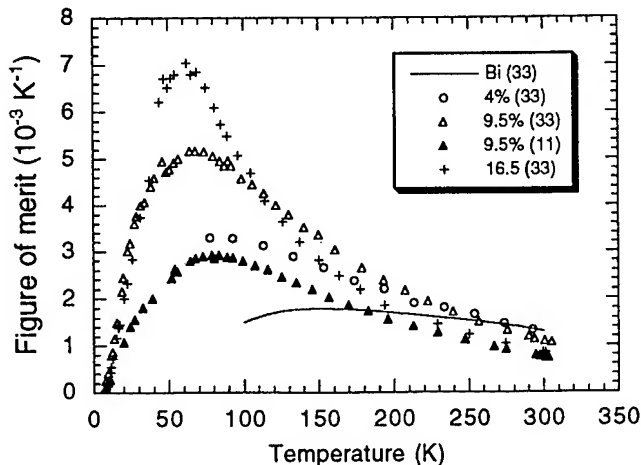


Fig. 15 Temperature dependence of the figure of merit of various $\text{Bi}_{1-x}\text{Sb}_x$ alloys [70,83,87].

Some recent results obtained on doped, by tin or tellurium, samples [37] do not present any substantial increase of the figure of merit for $T > 80$ K, as previously observed by other authors [11,12]. At lower temperature, it is possible to obtain a p -type thermoelement with acceptor impurities [11,12,85] over a small range of temperature of about 40 K. However, as was discussed by Red'ko [85], the conditions are not favourable to obtain a high p -type figure of merit (the reported values never exceed $1 \cdot 10^{-3} \text{ K}^{-1}$) due to the peculiarities of the complex valence band structure.

Polycrystalline samples

Powder metallurgy has the advantage to improve the mechanical properties of $\text{Bi}_{1-x}\text{Sb}_x$ alloys but is detrimental to the figure of merit as a result of the random orientations of the grains. However this adverse effect may be hindered by significant reduction of the thermal conductivity resulting from phonon scattering at grain boundaries at temperatures higher than the Debye temperature θ_D ($\theta_D = 120$ K in bismuth) like it is known to occur at high temperature for Si-Ge alloys.

An early work performed by Cochrane and Youdelis [59] on $\text{Bi}_{0.88}\text{Sb}_{0.12}$ alloys synthesized by grinding zone melted rods has however not shown preferential scattering by a particular powder size, the main effects affecting the figure of merit being the variations in electrical resistivity. Impurities, such as oxygen insertion during powder elaboration may be an hindering factor to improve the figure of merit as well as the fact that the powder particles were too large ($> 38 \mu\text{m}$) to see any effect. However, a recent study by Suse et al. [57] performed on the same alloy composition elaborated by arc-plasma showed an enhancement of the figure of merit by a factor two as compared to a single crystal (Fig. 17), for temperatures greater than 150 K, that was attributed to phonon scattering at grain boundaries (particle size $1\text{-}5 \mu\text{m}$).

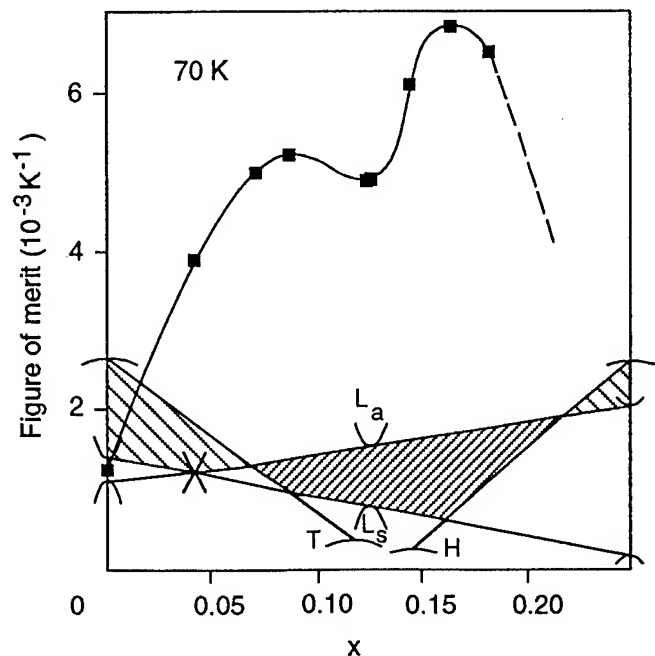


Fig. 16 Antimony content dependence of the thermoelectric figure of merit at 70 K of $\text{Bi}_{1-x}\text{Sb}_x$ alloys, as reported in [83].

The value of the thermal conductivity ($1.2 \text{ Wm}^{-1}\text{K}^{-1}$) measured at room temperature was found to be two thirds of that of a single crystal along the trigonal axis. Recently, Goldsmid et al. [88] determined the conditions for high temperature boundary scattering in solid solutions by a simplified theory. They concluded that it is possible to obtain even larger reductions in the thermal conductivity if the grain size is decreased to a fraction of a micrometer (reduction of 50 % for a size of $0.13 \mu\text{m}$). However they have not discussed the change in electrical resistivity that accompany boundary scattering.

Another way to improve the figure of merit of polycrystalline samples is to texture the powder by extrusion. Banaga et al. [60] have shown that the figure of merit of extruded $\text{Bi}_{0.88}\text{Sb}_{0.12}$ alloys prepared by grinding zone melted rods exceed the computed average value for single crystals (Fig. 17) in the entire temperature range studied (80-300 K), due to both the presence of a favourable texture and potential barriers.

Thin films

Data reported on the transport properties of Bi-Sb thin films are relatively scarce [89-94]. The comparison between the several results is rendered difficult because of the differences in thickness of the prepared films as well as of measurement problems concerning the thermal conductivity.

Films have been prepared by ion beam mixing [89], thermal evaporation [91,92], molecular beam epitaxy [93] or sputtering [94,95].

The thickness dependences of the thermal conductivity and figure of merit have been reported by Völklein and Kessler for several compositions of $\text{Bi}_x\text{Sb}_{1-x}$ alloys [91]. The figure of merit decreases with decreasing thickness, whatever the alloy composition and the temperature. Such effect has also been observed by Boyer and Cissé [92] for $\text{Bi}_{0.87}\text{Sb}_{0.13}$ thin films alloys. Both authors [91,92] have observed that the figure of merit of bulk materials is reached at room temperature for this specific composition since a film thickness of about 150 nm.

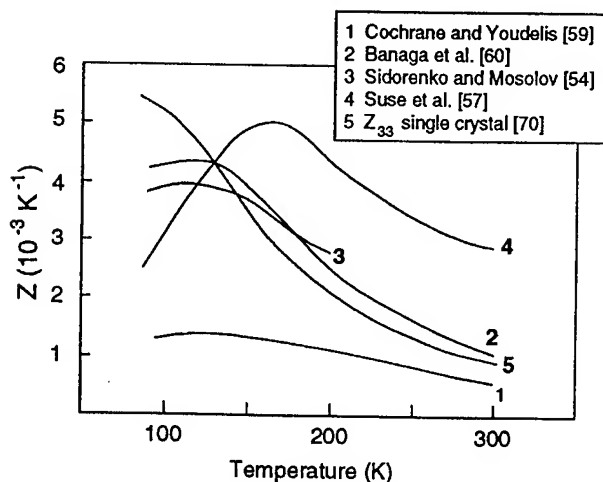


Fig. 17 Temperature dependence of the figure of merit of $\text{Bi}_{0.88}\text{Sb}_{0.12}$ polycrystalline samples. The shift of maximum towards higher temperature with regard to the single crystal seems to be a simple consequence of the drop of Z at low temperature where any defects strongly manifest.

Temperature dependence behaviours of the semiconducting thin films show that the maximum of the figure of merit is located in the temperature range between 200 and 300 K, shifted towards higher temperature by comparison with bulk materials, as it has already been observed for compacted powder materials [56,57]. The highest value of the figure of merit is however one order of magnitude lower for thin films than for bulk single crystalline materials.

In order to enhance the film quality for further uses in quantum wells as it has been predicted an improvement of the figure of merit in such structures [96], $\text{Bi}_{0.86}\text{Sb}_{0.14}$ films were recently grown epitaxially on BaF_2 substrates by sputtering [95]. Electrical measurements show an enhancement of the electrical resistivity as compared to bismuth films as it is also happening with bulk materials. The thickness of the films was nevertheless not mentioned.

Concluding remarks

The main aspects of Bi-Sb alloys have been presented in this survey including both the preparation and the transport properties. Most of the experimental results have been qualitatively described. For a quantitative analyse, the effects of band non-parabolicity and the large temperature dependence of the band parameters have to be taken into consideration. Moreover, the scattering mechanisms still remain a challenge to our understanding of these materials particularly in the intrinsic range.

The great thermoelectric performances of Bi-Sb single crystals around 80 K are due to the peculiarities of the electronic L-band. Little or none improvement in the figure of merit of single crystals has been achieved since the first works of Smith and Wolfe [11]. The observed discrepancies are generally linked to the problem of sample homogeneity. Even doping attempts were unsuccessful.

Some promising results obtained on bulk samples prepared via powder metallurgy make these materials, also mechanically strong, good prospects for use in solid state devices working around 150 K. However, sample preparation and history are important and need to be taken into consideration before conclusions can be drawn about the degree of effectiveness of grain boundary scattering in improving thermoelectric materials.

The possibility of improve figure of merit cannot be dismissed and work with this aim should be encouraged.

Acknowledgements

The authors would like to express their gratitude to the Unité de Physico-Chimie et de Physique des Matériaux of Louvain-La-Neuve (Belgium) for fruitful collaboration. The authors would also like to apologize for any inadvertent omissions or misstatements of fact or opinion attributed to others.

References

- [1] A.L. Jain, "Temperature dependence of the electrical properties of bismuth-antimony alloys", *Phys. Rev.*, 114(6), pp. 1518-1528 (1959).
- [2] S. Golin, "Band model for bismuth-antimony alloys", *Phys. Rev.* 176(3), pp. 830-832 (1968).
- [3] N.B. Brandt, R. Hermann, G.I. Golysheva, L.I. Devyatkova, D. Kusnik, W. Kraak and Ya.G. Ponomarev, "Electron Fermi surface of semimetallic alloys $\text{Bi}_{1-x}\text{Sb}_x$

- ($0.23 \leq x < 0.56$)", Sov. Phys. JETP, 56(6), pp. 1247-1256 (1982).
- [4] E.E. Mendez, Ph. D. Thesis, MIT, (1979).
 - [5] N.B. Brandt and S.M. Chudinov, "Oscillation effects in semimetallic $Bi_{1-x}Sb_x$ alloys under pressure", Sov. Phys. JETP, 32(5), pp. 815-822 (1971).
 - [6] E.E. Mendez, A. Misu and M.S. Dresselhaus, "Pressure-dependent magnetoreflection studies of Bi and $Bi_{1-x}Sb_x$ alloys", Phys. Rev. B, 24(2), pp. 639-648 (1981).
 - [7] N.B. Brandt and E.A. Svistova, "Electron transitions in strong magnetic fields", J. Low Temp. Phys., 2(1), pp. 1-35 (1970).
 - [8] K. Hiruma, G. Kido, K. Kawauchi and N. Miura, "Shubnikov-de Haas effect and semiconductor transition in bismuth-antimony alloys in high magnetic fields", Solid State Comm., 33, pp. 257-260 (1980).
 - [9] N.B. Brandt, S.M. Chudinov and V.G. Karavaev, "Investigation of gapless states in bismuth-antimony alloys under pressure", Sov. Phys. JETP, 34(2), pp. 368-375 (1972).
 - [10] N.B. Brandt, Ya.G. Ponomarev and S.M. Chudinov, "Investigation of the gapless state in bismuth-antimony alloys", J. Low Temp. Phys., 8(5-6), pp. 369-420 (1972).
 - [11] G.E. Smith and R. Wolfe, "Thermoelectric properties of bismuth-antimony alloys", J. Appl. Phys., 33(3), pp. 841-846 (1962).
 - [12] W.M. Yim and A. Amith, "Bi-Sb alloys for magnetothermoelectric and thermomagnetic cooling", Solid-State Electronics, 15, pp. 1141-1165 (1972).
 - [13] A.F. Ioffe, *Semiconductor Thermoelements and Thermoelectric Cooling*, Infosearch, London, p. 39 (1957).
 - [14] K.K. Gopinathan, H.J. Goldsmid, D.N. Matthews and K.N.R. Taylor, "Passive thermoelements", Proceeding of the VII International Conference on Thermoelectrics, Arlington, pp. 58-61 (1988).
 - [15] Z.M. Dashevskii, N.A. Sidorenko, S.Ya. Skipidarov, N.A. Tsvetkova and A.B. Mocolov, "Cryogenic thermoelectric coolers with passive high T_c superconductor legs", Proceeding of the X International Conference on Thermoelectrics, Cardiff, pp. 142-146 (1991).
 - [16] M.V. Vedernikov, V.L. Kuznetsov, A.V. Ditman, B.T. Melekh and A.T. Burkov, "Efficient thermoelectric cooler with a thermoelectrically passive, high- T_c superconducting leg", Proceeding of the X International Conference on Thermoelectrics, Cardiff, pp. 96-101 (1991).
 - [17] M.G. Fee, "Peltier refrigerator using a high T_c superconductor", Appl. Phys. Lett., 62(10), pp. 1161-1163 (1993).
 - [18] V.L. Kuznetsov, M.V. Vedernikov, P. Yandl and U. Birkholz, "Exploring the limits of thermoelectric refrigeration at liquid nitrogen temperatures", Tech. Phys. Lett., 20(9) pp. 757-758 (1994).
 - [19] R. Wolfe and G.E. Smith, "Effects of a magnetic field on the thermoelectric properties of a bismuth-antimony alloy", Appl. Phys. Lett., 1(1), pp. 5-7 (1962).
 - [20] K.F. Cuff, R.B. Horst, J.L. Weaver, S.R. Hawkins, C.F. Kooi and G.M. Enslow, "The thermomagnetic figure of merit and Ettingshausen cooling in Bi-Sb alloys", Appl. Phys. Lett., 2(8), pp. 145-146 (1963).
 - [21] R. B. Horst and L.R. Williams, "Application of solid state cooling to spaceborne infrared focal planes", Proceeding of the III International Conference on Thermoelectric Conversion, Arlington, pp. 183-199 (1980).
 - [22] P. Jandl, "Optimization of the thermogalvanomagnetic properties of $Bi_{95}Sb_5$ by Sn-doping for Ettingshausen cooling in weak magnetic fields", Proceeding of the XI International Conference on Thermoelectrics, Arlington, pp. 254-259 (1992).
 - [23] H. J. Goldsmid, *CRC Handbook of Thermoelectrics*, edited by D.M. Rowe, CRC Press, p. 75 (1995).
 - [24] A.A. Abricosov and L.A. Falkovskii, "Theory of the electron energy spectrum of metals with a bismuth type lattice", Sov. Phys. JETP, 16(3), pp. 769-777 (1963).
 - [25] P. Cucka and C.S. Barrett, "The crystal structure of Bi and solid solutions of Pb, Sn, Sb and Te in Bi", Acta Cryst., 15, pp. 865-872 (1962).
 - [26] M.S. Dresselhaus, "Electronic properties of group V semimetals", J. Phys. Chem. Sol., 32, Suppl. 1, pp. 3-33 (1971).
 - [27] V.S. Edelman, "Electrons in bismuth", Adv. Phys., 25(6), pp. 555-613 (1976).
 - [28] M.P. Vecchi and M.S. Dresselhaus, "Temperature dependence of the band parameters of bismuth", Phys. Rev. B, 10(2), pp. 771-774 (1974).
 - [29] B. Lax and J.G. Mavroides, *Advances in Solid State Physics*, edited by F. Seitz and D. Turnbull, Academic Press New York, Vol. 11, p. 261 (1960).
 - [30] E.J. Tichovolsky and J.G. Mavroides, "Magnetoreflection studies on the band structure of bismuth-antimony alloys", Solid State Comm., 7, pp. 927-931 (1969).
 - [31] G. Oelgart and R. Herrmann, "Cyclotron masses in semiconducting $Bi_{1-x}Sb_x$ alloys", Phys. Stat. Sol. (b), 75, pp. 189-196 (1976).
 - [32] M.R. Ellett, R.B. Horst, L.R. Williams and K.F. Cuff, "Shubnikov-de Haas investigations of the $Bi_{1-x}Sb_x$ ($0 < x < 0.3$) system", J. Phys. Soc. Jpn, 21(Suppl.), pp. 666-672 (1966).
 - [33] P.W. Chao, H.T. Chu and Y.H. Kao, "Nonlinear band-parameter variations in dilute bismuth-antimony alloys", Phys. Rev. B, 9(10), pp. 4030-4034 (1974).
 - [34] G. Oelgart, G. Schneider, W. Kraak and R. Herrmann, "The semiconductor-semimetal transition in $Bi_{1-x}Sb_x$ alloys", Phys. Stat. Sol. (b), 74, pp. K75-K78 (1976).
 - [35] W. Kraak, G. Oelgart, G. Schneider and R. Herrmann, "The semiconductor-semimetal transition in $Bi_{1-x}Sb_x$ alloys with $x \geq 0.22$ ", Phys. Stat. Sol. (b), 88, pp. 105-110 (1978).
 - [36] G.A. Ivanov, V.A. Kulikov, V.L. Naletov, A.F. Panarin and A.R. Regel, "Thermoelectric figure of merit of pure and doped bismuth-antimony alloys in magnetic

- fields", Sov. Phys. Semicond., 6(7), pp. 1134-1137 (1973).
- [37] A.D. Belaya, S.A. Zayakin and V.S. Zemskov, "Single crystals of Bi-Sb solid solutions for magnetothermoelectric and galvano-themomagnetic cooling", J. Adv. Mater., 1(2), pp.158-165 (1994).
- [38] R. B. Horst and L.R. Williams, "Potential figure of merit of the BiSb alloys", Proceeding of the III International Conference on Thermoelectric Conversion, Arlington, pp. 139-173 (1980).
- [39] M.M. Tagiev, Z.F. Agaev and D. Sh. Abidinov, "Thermoelectric properties of extruded specimens of $Bi_{0.85}Sb_{0.15}$ doped with lead", Neorg. Mater., 29(6), pp. 868-869 (1992).
- [40] T. Okumura, M. Yamashita and Y. Kibayashi, "Ga doped n-type Bi-Sb alloys prepared by sintering process", Proceeding of the X International Conference on Thermoelectrics, Cardiff, pp. 44-48 (1991).
- [41] D.M. Brown and F.K. Heumann, "Growth of bismuth-antimony single-crystal alloys", J. Appl. Phys., 35(6), pp. 1947-1951 (1964).
- [42] G.A. Ivanov and A.M. Popov, "Electrical properties of bismuth-antimony alloys", Soviet Physics - Solid State, 5(9), pp.1754-1761 (1964).
- [43] M.A. Short and J.J. Schott, "Preparation of homogeneous single-crystal bismuth-antimony alloys", J. Appl. Phys., 36, pp. 659-660 (1965).
- [44] M. Dugué, "Propriétés électriques des solutions solides bismuth-antimoine", Phys. Stat. Sol., 11, pp. 149-158 (1965).
- [45] T. Yazaki and Y. Abe, "Galvanomagnetic investigations of the $Bi_{1-x}Sb_x$ ($0 < x \leq 0.15$) system at 77°K", J. Phys. Soc. Jpn., 24(2), pp. 290-295 (1968).
- [46] V.G. Alekseeva, N.F. Zaets, A.A. Kudryashov and A.B. Ormont, "Dependence of the forbidden band width of Bi-Sb semiconducting solid solutions on antimony concentration", Sov. Phys. Semicond., 10(12), 1332-1334 (1976).
- [47] W.A. Tiller, K.A. Jackson, J.W. Rutter and B. Chalmers, "The redistribution of solute atoms during the solidification of metals", Acta Met., 1, pp. 428-437 (1953).
- [48] W.M. Yim and J.P. Dismukes, "Growth of homogeneous Bi-Sb alloy single crystals", Proceeding of an International Conference on Crystal Growth, p. 187-195 (1966).
- [49] B. Lenoir, A. Demouge, D. Perrin, H. Scherrer, S. Scherrer, M. Cassart and J-P. Michenaud, "Growth of $Bi_{1-x}Sb_x$ alloys by the traveling heater method", J. Phys. Chem. Solids, 56(1), pp. 99-105 (1995).
- [50] V.S. Zemskov, A.D. Belaya and G.N. Kozhemyakin, "Growth of single crystals of bismuth-antimony alloys by Czochralski method", J. Crystal Growth, 71, pp.243-245 (1985).
- [51] H.J. Koh, P. Rudolph and T. Fukuda, "Growth of $Bi_{1-x}Sb_x$ mixed crystals by a new melt injection technique", J. Crystal Growth, 154, 151-155 (1995).
- [52] A.D. Belava, S.A. Zayakin and V.S. Zemskov, "Mechanical properties of Bi-Sb single crystal solid solutions grown by Czochralski method", Proceeding of the XIV International Conference on Thermoelectrics, St Petersburg, pp. 37-41 (1995).
- [53] N.V. Kolomoetz, S. Ya. Skipidarov, N.A. Sidorenko and R.S. Erofeev, "Cryogenic temperature level thermoelectric coolers", Proceeding of the IX International Conference on Thermoelectrics, Pasadena, pp. 128-135 (1990).
- [54] N.A. Sidorenko and A.B. Mosolov, "Cryogenic thermoelectric coolers with passive high- T_c superconducting legs", Proceeding of the XI International Conference on Thermoelectrics, Arlington, pp. 289-298 (1992).
- [55] N.A. Sidorenko, "Brittle thermoelectric semiconductors extrusion under high hydrostatic pressure", Proceeding of the XIII International Conference on Thermoelectrics, Kansas City, pp. 260-266 (1994).
- [56] R. Martin-Lopez, B. Lenoir, A. Dauscher, X. Devaux, H. Scherrer, S. Scherrer and M. Zandona, "Bi-Sb semiconductor alloy synthesized by mechanical alloying", Proceedings of the Second European Workshop on Thermoelectrics, Nancy, pp.34-37 (1995).
- [57] Y. Suse, Y.H. Lee, H. Morimoto, T. Koyonagi, K. Matsubara and A. Kawamoto, "Structure and thermoelectric properties of $Bi_{88}Sb_{12}$ ceramics using fine particles produced by hydrogen arc-plasma", Proceeding of the XII International Conference on Thermoelectrics, Yokohama, pp. 248-251 (1993).
- [58] X. Devaux, F. Brochin, A. Dauscher, B. Lenoir, R. Martin-Lopez, H. Scherrer and S. Scherrer, "Elaboration and consolidation of ultrafine Bi-Sb alloys powders", Proceedings of the Second European Workshop on Thermoelectrics, Nancy, pp. 58-61 (1995).
- [59] G. Cochrane and W.V. Youdelis, "Transport and thermoelectric properties of bismuth and Bi-12 at. pct Sb alloy powder compacts", Metal. Trans., 3, pp. 2843-2850 (1972).
- [60] M.P. Banaga, O.B. Sokolov, T.E. Benderskaya, L.D. Dudkin, A.B. Ivanova and I.I. Fridman, "Peculiarities of the structure and thermoelectric properties of extruded samples of $Bi_{0.88}Sb_{0.12}$ ", Neorg. Mater., 22(4), pp. 619-622 (1986).
- [61] D.M. Jacobson, "Magnetoresistance anisotropy in bismuth and bismuth-antimony crystals", Phys. Stat. Sol. (b), 58, pp. 243-250 (1973).
- [62] Yu. I. Ravich and A.V. Rapoport, "Temperature dependences of the carrier mobilities and densities in bismuth", Sov. Phys. Solid State, 34(6), pp. 960-963 (1992).
- [63] A. Demouge, B. Lenoir, Yu. Ravich, H. Scherrer and S. Scherrer, "Estimation of carrier mobilities and densities in $Bi_{0.96}Sb_{0.04}$ alloys from galvanomagnetic coefficients", J. Phys. Chem. Solids, 56(9), pp. 1155-1164 (1995).
- [64] D.M. Brown and S.J. Silverman, "Electrons in Bi-Sb alloys", Phys. Rev., 136(1A), pp. 290-299 (1964).

- [65] T. Yazaki, "Thermal conductivity of bismuth-antimony alloy single crystals", J. Phys. Soc. Jpn., 25(4), pp. 1054-1060 (1968).
- [66] N. B. Brandt, E.A. Svistova and R.G. Valeev, "Investigation of the semiconductor-metal transition in the bismuth-antimony system in a magnetic field", Soviet Physics JETP, 28(2), pp. 245-254 (1969).
- [67] R. Kuhl, W. Kraak, H. Haefner and R. Herrmann, "The semimetal-semiconductor transition in bismuth-antimony alloys", Phys. Stat. Sol. (b), 77, pp. K109-K111 (1976).
- [68] N.A. Rodionov, N.A. Red'ko and G.A. Ivanov, "Transport effects in $\text{Bi}_{0.88}\text{Sb}_{0.12}$ alloys with low hole densities in the L_S band", Sov. Phys. Solid State, 21(9), pp. 1473-1476 (1979).
- [69] S.D. Probert and C.B. Thomas, "Transport properties of some bismuth-antimony alloys", Applied Energy, 5, pp. 127-140 (1979).
- [70] B. Lenoir, M. Cassart, J.-P. Michenaud, H. Scherrer and S. Scherrer, "Transport properties of Bi-rich Bi-Sb alloys", J. Phys. Chem. Solids, 57(1), pp. 89-99 (1996).
- [71] V.M. Grabov, G.A. Ivanov, V.L. Naliotov, M.G. Bondarenko and O.N. Uryupin, "Thermoelectric figure of merit of horizontal zone-leveling prepared bismuth-antimony single crystals", Proceeding of the XIV International Conference on Thermoelectrics, St Petersburg, pp. 115-118 (1995).
- [72] J.-P. Michenaud and J.-P. Issi, "Electron and hole transport in bismuth", J. Phys. C, 5, pp. 3061-3072 (1972).
- [73] N.A. Rodionov, G.A. Ivanov and N.A. Red'ko, "Thermoelectric efficiency of $\text{Bi}_{1-x}\text{Sb}_x$ ($0.12 \leq x < 0.14$) p-type alloys at low temperatures", Sov. Phys. Solid State, 24(6), pp. 1074-1075 (1982).
- [74] N.A. Rodionov, G.A. Ivanov and N.A. Red'ko, "Anomalous temperature dependence of the thermoelectric power of holes in semiconducting $\text{Bi}_{1-x}\text{Sb}_x$ alloys", Sov. Phys. Solid State, 23(7), pp. 1231-1234 (1981).
- [75] O.S. Gryaznov, G.A. Ivanov, B. Ya. Moizhes, V.N. Naumov, V.A. Nemchinskii, N.A. Rodionov and N.A. Red'ko, "The effect of interband scattering on kinetic phenomena in p-type $\text{Bi}_{1-x}\text{Sb}_x$ ", Sov. Phys. Solid State, 24(8), pp. 1326-1330 (1982).
- [76] N.A. Red'ko, V.I. Belitskii, V.V. Kosarev, N.A. Rodionov and V.I. Pol'shin, "Bands of heavy holes and sign of the thermoelectric power of Bi-Sb alloys", Sov. Phys. Solid State, 28(12), pp. 2111-2112 (1986).
- [77] C. Uher and H.J. Goldsmid, "Separation of the electronic and lattice thermal conductivities in bismuth crystals", Phys. Stat. Sol., 65, pp. 765-772 (1974).
- [78] K.D. Chaudhuri and T.K. Dey, "Heat conduction in bismuth-antimony alloy single crystals between 4.2 and 300 K", J. Low Temp. Phys., 20(3/4), pp. 397-405 (1975).
- [79] N.A. Red'ko, "Thermal conductivity of bismuth alloys under conditions of combined phonon-impurity scattering of phonons", Sov. Tech. Phys. Lett., 16(11), pp. 868-869 (1990).
- [80] V.D. Kagan and N.A. Red'ko, "Phonon thermal conductivity of bismuth alloys", Sov. Phys. JETP, 73(4), pp. 664-671 (1991).
- [81] V.D. Kagan and N.A. Red'ko, "Phonon thermal conductivity of the thermoelectric Bi-Sb alloys", Proceeding of the XIV International Conference on Thermoelectrics, St Petersburg, pp. 78-81 (1995).
- [82] P.G. Klemens, "The scattering of low frequency lattice waves by lattice imperfections", Proc. Phys. Soc. A, 68, p. 1113 (1955).
- [83] B. Lenoir, M. Cassart, A. Dauscher, Yu. I. Ravich and H. Scherrer, "Highest figure of merit in undoped $\text{Bi}_{1-x}\text{Sb}_x$ alloys", Proceeding of the XIV International Conference on Thermoelectrics, St Petersburg, pp. 96-99 (1995).
- [84] V.M. Grabov, G.A. Ivanov, V.L. Naliotov and A.F. Panarin, "Interband scattering of charge carriers and thermoelectric figure of merit of bismuth-antimony alloys", Soviet Seminar of Semiconductor Materials for Thermoelectric Conversion, Leningrad, pp.30-31 (1985), (in Russian).
- [85] N.A. Red'ko, "Thermoelectric efficiency of semiconducting Bi-Sb alloys", Proceeding of the XIV International Conference on Thermoelectrics, St Petersburg, pp. 82-84 (1995).
- [86] N.B. Brandt, E.A. Svistova and M.V. Semenov, "Electron transitions in antimony-rich bismuth-antimony alloys in strong magnetic fields", Soviet Phys. JETP, 32(2), pp. 238-243 (1971).
- [87] C.F. Gallo, B.S. Chandrasekhar and P.H. Sutter, "Transport properties of bismuth single crystals", J. Appl. Phys., 34(1), pp. 144-152 (1963).
- [88] H.J. Goldsmid, H.B. Lyon and E.H. Volckmann, "A simplified theory of phonon boundary scattering in solid solutions", Proceeding of the XIV International Conference on Thermoelectrics, St Petersburg, pp. 16-19 (1995).
- [89] A.M. Ibrahim and D.A. Thompson, "Ion beam mixing to produce Bi/Sb alloys for thin film thermoelectric devices", Nuclear Instruments & Methods in Phys. Res. B, 7/8, pp. 566-570 (1985).
- [90] F. Völklein and E. Kessler, "Temperature and thickness dependence of electrical and thermal transport coefficients of $\text{Bi}_{1-x}\text{Sb}_x$ films in an anisotropic, non-degenerate two-band model", Phys. Stat. Sol. (b), 134, pp. 351-362 (1986).
- [91] F. Völklein and E. Kessler, "Thermal conductivity and thermoelectric figure of merit of $\text{Bi}_{1-x}\text{Sb}_x$ films with $0 < x \leq 0.3$ ", Phys. Stat. Sol. (b), 143, pp. 121-130 (1987).
- [92] A. Boyer and E. Cissé, "Properties of thin film thermoelectric materials: application to sensors using the Seebeck effect", Mater. Sci. Engin. B, 13, pp. 103-11 (1992).
- [93] I. Yoshida, S. Tanuma, T. Irie and J. Takahashi, "Thermoelectric properties of multilayer films of semimetals", Proceeding of the XII International Conference on Thermoelectrics, Yokohama, pp. 334-339 (1993).

- [94] J.C. Farmer, T.W. Barbee, G.C. Chapline, R.J. Foreman, L.J. Summers, M.S. Dresselhaus and L.D. Hicks, "*Sputter deposition of multilayer thermoelectric films : an approach to the fabrication of two-dimensional quantum wells*", Proceeding of the XIII International Conference on Thermoelectrics, Kansas City, pp. 217-225 (1994).
- [95] A.V. Wagner, R.J. Foreman, L.J. Summers, T.W. Barbee and J.C. Farmer, "*Multilayer thin film thermoelectrics produced by sputtering*", Proceeding of the XIV International Conference on Thermoelectrics, St Petersburg, pp. 283-287 (1995).
- [96] L.D. Hicks and M.S. Dresselhaus, "*Effect of quantum-well structures on the thermoelectric figure of merit*", Phys. Rev. B, 47(19), pp. 12727-12731 (1993).

Effect of Anisotropy of the Seebeck Coefficient on the Thermal Conductivity of Polycrystalline BiSb Alloys

H.J. Goldsmid, J.W. Sharp
Marlow Industries Inc.
10451 Vista Park Road, Dallas, TX 75238-1645

Abstract

In 1961, Cosgrove, McHugh and Tiller reported the effect of micro-segregation in fast-grown bismuth telluride on the thermal conductivity. They attributed a significant increase in this property to the presence of circulating electric currents associated with the non-uniform Seebeck coefficient in the inhomogeneous material. If this effect is an important one, then it could seriously impair the performance of thermoelements made from polycrystalline BiSb alloys since, even if such materials are chemically homogeneous, they will have local variations of the Seebeck coefficient associated with the anisotropy of this parameter in single crystals.

We now think that circulating thermoelectric currents are not the main reason for the increase of thermal conductivity in inhomogeneous bismuth telluride. Such currents should have an even smaller effect in BiSb alloys and should not cause any substantial decrease in the figure of merit. This is borne out by measurements on the thermal conductivity of large-grained polycrystalline BiSb alloys. Using a technique for the determination of the electronic component that is described elsewhere, it has been found that the residual thermal conductivity is very close to the lattice component that is predicted from observations on single crystals. This would not be so if there were any significant heat transfer by internal circulating currents.

Introduction

An important step towards the production of consistently good thermoelectric material was made by Cosgrove et al.¹ in 1961 when they observed the effects of growth rate and temperature gradient in a Bridgman furnace on the properties of BiSbTe₃. They paid particular attention to the thermal conductivity, λ . After subtracting the Wiedemann-Franz electronic component, $\lambda_{W,F}$, they found that the remaining term showed considerable variation from sample to sample. It became larger when either the temperature gradient, dT/dZ , in the furnace was reduced or the rate of movement, V , of the liquid-solid interface was increased. Their observations are summarized in Fig. 1.

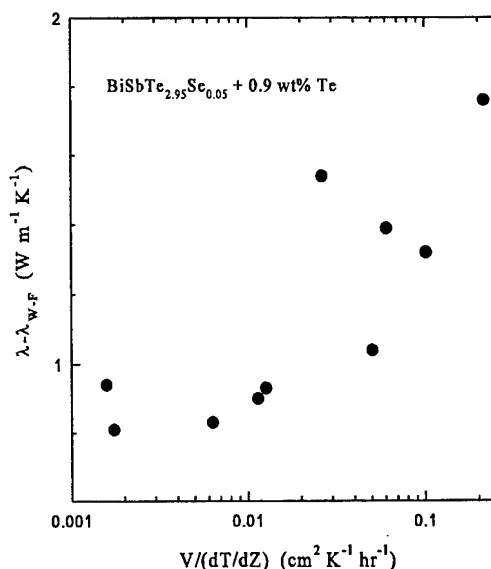


Figure 1. Plot of residual thermal conductivity against the ratio of growth rate to furnace gradient according to Cosgrove et al.

The explanation for the behavior shown in Fig. 1 was claimed by the authors¹ to lie in non-uniformity of the material, arising from the micro-segregation or constitutional supercooling that occurred when $V/(dT/dZ)$ became large. They stated that this non-uniformity would lead to local variations of the Seebeck coefficient so that, when a temperature gradient was applied, circulating thermoelectric currents would flow. These currents would transfer heat through the Peltier effect. Presumably such circulatory effects will be present in any material in which the Seebeck coefficient is non-uniform.

Since the time when Cosgrove and his colleagues carried out their work, there has been considerable interest in the use of polycrystalline bismuth telluride alloys prepared by sintering. Such alloys may be chemically uniform but their thermoelectric properties may vary within a sample due to the anisotropy of the single crystal parameters. However, the Seebeck coefficient is either isotropic or nearly so, and the possibility of internal circulating thermoelectric currents does not arise. On the other hand, in BiSb alloys the Seebeck coefficient is strongly anisotropic. Thus, if circulating

thermoelectric currents degrade the figure of merit in non-uniform bismuth telluride alloys, through an increase in the thermal conductivity, so might they be expected to do so in uniform but randomly oriented polycrystals of BiSb.

Bismuth Telluride

Let us first examine the origin of the high thermal conductivity in bismuth telluride that has been grown too fast. It is certainly true that internal currents will flow if the Seebeck coefficient is non-uniform. However, let us consider the magnitude of the effect in the rather extreme case where half the material consists of p-type bismuth telluride with a Seebeck coefficient, α_1 , of 200 $\mu\text{V/K}$, and the other half consists of n-type material with a Seebeck coefficient, α_2 , of -200 $\mu\text{V/K}$. This would surely lead to the largest possible circulatory effect.

We can get some idea of the magnitude of the effect from the studies of the thermal conductance of thermoelectric modules in the open-circuit and short-circuit conditions.^{2,3} The difference between the two thermal conductances has been used to determine the figure of merit in an alternative technique⁴ to that employed by Harman.⁵ Briefly, if K^* is the short-circuited thermal conductance and K is the usual open-circuit value,

$$K^* = K(1+zT), \quad (1)$$

where zT is the dimensionless figure of merit.

The situation in the non-uniform sample that we are discussing is somewhat similar to that for a bipolar conductor. It can be shown⁶ that the bipolar contribution to the thermal conductivity of a mixed conductor is

$$\lambda_{\text{bip}} = \{\sigma_1 \sigma_2 / (\sigma_1 + \sigma_2)\} (\alpha_1 - \alpha_2) T \quad (2)$$

Where σ_1 and σ_2 are the partial electrical conductivities of the holes and electrons respectively. The only difference between the non-uniform case and the bipolar case is that, in the former, each type of material contributes its own lattice conductivity while, in the latter, the lattice conductivity is shared by the two types of conductor. Consequently, equation (1), rather than equation (2), gives the thermal conductance of a non-uniform sample containing two constituents.

Now the very largest value for the dimensionless figure of merit of a thermocouple composed of bismuth telluride alloys is close to unity.⁷ We see, then, that it would be possible, in principle, for the thermal conductivity of a bismuth telluride alloy, such as that studied by Cosgrove et al., to be almost doubled by internally circulating thermoelectric currents. However, it would be virtually impossible to obtain a material with the specific non-uniformity described by our

model and, in practice, one would expect a very much smaller contribution to the thermal conductivity from internal currents. This is much more consistent with the observations of Yim and Rosi⁷, who also studied the effect of growth rate and furnace gradient on the thermoelectric properties. The dependence of the residual thermal conductivity, $\lambda - \lambda_{W-F}$, on the growth rate for p-type and n-type alloys is shown in Fig. 2. The temperature gradient was said to be 25 K cm^{-1} and, at the highest growth rate of about 10 cm hr^{-1} , the value of $V/(dT/dZ)$ was close to 0.4 $\text{cm}^2 \text{K}^{-1} \text{hr}^{-1}$. The rise of the residual thermal conductivity with growth rate was appreciably less than that reported by Cosgrove et al., especially for the p-type material.

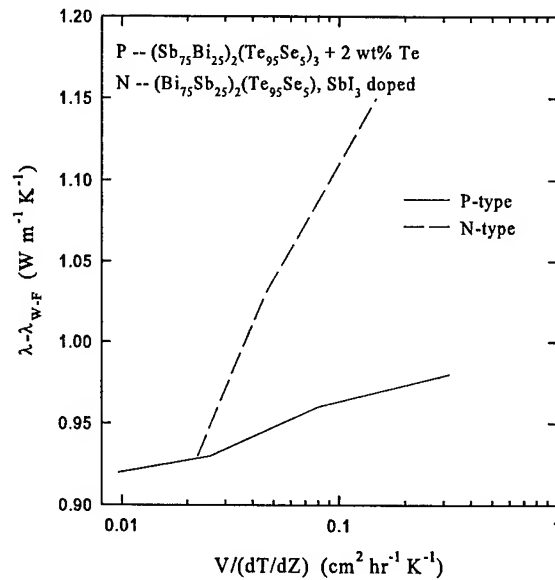


Figure 2. Residual thermal conductivity plotted against growth rate for the alloys used by Yim and Rosi.

Is it possible to account of the fact that Cosgrove et al. observed almost twice the residual thermal conductivity for rapidly grown BiSbTe₃ compared with that for slowly grown material? It is, perhaps, difficult to explain quite such a large increase as this, but we may go some way towards an explanation if we consider the effect of the variation of thermal conductivity with carrier concentration in uniform samples of this alloy.

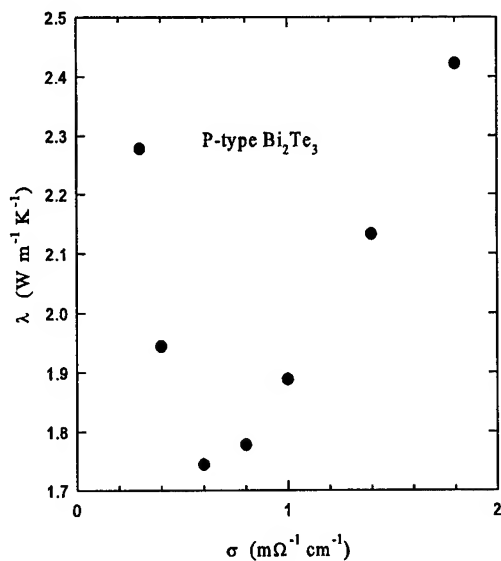


Figure 3. Variation of thermal conductivity with electrical conductivity for p-type bismuth telluride at 300K.

Undoped samples of BiSbTe₃ that are melt grown are not stoichiometric but are p-type with a typical electrical conductivity of between 0.5 and 1.0 mΩ⁻¹ cm⁻¹. There are interesting consequences for the Lorenz number and, thus, for the electronic thermal conductivity when the carrier concentration rises or falls. When the electronic conductivity becomes greater, the electronic thermal conductivity rises even more rapidly as the Lorenz number approaches its value for metals, which is larger than that for extrinsic semiconductors. When the electronic conductivity falls, the Lorenz number becomes very much greater due to bipolar heat conduction⁸ so that the electronic thermal conductivity again rises. The effects are illustrated for bismuth telluride in Fig. 3 and would be relatively greater for BiSbTe₃ since the lattice conductivity of the alloy is appreciably less than that of the compound. According to Rosi et al.⁹ the lattice conductivity of BiSbTe₃ is about 0.6 W m⁻¹ K⁻¹ and, as shown in Fig. 3, the electronic component in bismuth telluride rises by this much on either side of its minimum value. It appears, then, that Cosgrove and his co-workers were misled in calculating a residual thermal conductivity by subtracting an electronic component determined using a Lorenz number that is typical for non-degenerate extrinsic semiconductors. If they had taken account of the larger Lorenz numbers that would have been appropriate for much of the non-uniform material, they would probably have deduced only a minor contribution to the thermal conductivity from circulating currents.

Bismuth-Antimony

The BiSb alloys differ from bismuth telluride alloys in that, because of their smaller (or non-existent) energy gap, they

contain both holes and electrons even when produced with the thermoelectric application in mind. The Seebeck coefficient can be calculated from

$$\alpha = (\alpha_1 \sigma_1 + \alpha_2 \sigma_2) / (\sigma_1 + \sigma_2) \quad (3)$$

and is different in the "a" and "c" directions. Thus, even if the material is chemically homogeneous, the Seebeck coefficient will vary from point to point in a sample according to the direction of the current. Thus, the conditions exist for internal circulating currents to occur. The question is, whether or not these currents are large enough to have any appreciable effect on the thermal conductivity.

We consider first the case of pure bismuth. The necessary data for this element have been given by Gallo et al.¹⁰ who made measurements on single crystals along the principal axes. The data at 100 K are shown in Table 1.

	α (mV K ⁻¹)	σ (Ω ⁻¹ m ⁻¹)	λ (Wm ⁻¹ K ⁻¹)
"a" axis	-40	2.5 x 10 ⁶	18
"c" axis	-90	2.5 x 10 ⁶	13

Table 1 Properties of bismuth in the "a" and "c" directions at 100K.

Thus, the figure of merit, z , of a couple between two crystals of bismuth aligned respectively in the "a" and "c" directions is 1.0×10^{-4} K⁻¹, with ZT equal to 1.0×10^{-2} .

This means the contribution of circulating currents to the thermal conductivity of polycrystalline bismuth could not be more than 1%. In fact, we would expect it to be much smaller than this because the grains within a sintered sample would not be aligned at right angles to one another but would take up all possible orientations.

Turning to the BiSb alloys, we might expect the anisotropy of the Seebeck coefficient to be of the same order as for pure bismuth but the lattice thermal conductivity would be reduced and one may predict that the figure of merit of a couple formed from two single crystals of a typical alloy, aligned respectively in the "a" and "c" directions, would be a few times higher than for Bi. Nevertheless, in any randomly oriented sample the contribution to the thermal conductivity from circulating currents would have to be on the order of 1%.

Experimental Results for Bi₈₈Sb₁₂

We report elsewhere a technique that we have used to determine the lattice thermal conductivity of BiSb alloys. Briefly, we have measured the thermal and electrical

conductivities in transverse magnetic fields of up to 1 Tesla. By comparing the field dependencies of the two conductivities we have been able to estimate the electronic component of the thermal conductivity, and we have thus been able to obtain the residual contribution, λ_L .

Applying this technique to a large grained (50 μ m) sample of Bi₈₈Sb₁₂ for which boundary scattering of the phonons can safely be ignored, we find a residual thermal conductivity of 2.3 W m⁻¹ K⁻¹ at 80K. We selected this composition and temperature because Horst and Williams¹¹ have determined the lattice conductivity of a single crystal of Bi₈₈Sb₁₂ at 80 K. They found λ_L to be 3.1 W m⁻¹ K⁻¹ in the "a" direction and 1.5 W m⁻¹ K⁻¹ in the "c" direction. Now there are two "a" directions to one "c" direction in the bismuth crystal structure. Thus, if we wish to estimate the lattice conductivity of polycrystalline material from the single crystal values we should perhaps take a mean that is weighted 2:1 in favor of the "a" direction. The weighted mean has a value of 2.6 W m⁻¹ K⁻¹. The fact that the experimentally determined residual thermal conductivity for the polycrystalline material is not greater than this predicted value (it is marginally less) seems to be a good indication that circulating thermoelectric currents can be ignored.

Conclusions

We have shown that, while circulating thermoelectric currents undoubtedly flow in non-uniform bismuth telluride and its alloys, they are unlikely to make a large contribution to the thermal conductivity. The high thermal conductivities observed by Cosgrove and his colleagues for BiSbTe₃, grown under conditions in which constitutional supercooling occurred, can be more probably be explained in terms of the high electronic thermal conductivities on either side of the optimum thermoelectric composition.

It has been shown that the figure of merit of a couple formed from crystals of bismuth or BiSb oriented in the "a" and "c" directions is too small to allow circulating thermoelectric currents to make any significant contribution to the heat flow. This is supported by experimental data on polycrystalline and single crystal Bi₈₈Sb₁₂.

References

- [1] G.J. Cosgrove, P.P. McHugh, W.A. Tiller, *J. Appl. Phys.* **32**, 621 (1961).
- [2] I.S. Lisker, *Sov. Phys. Solid State* **8**, 1042 (1966).
- [3] W.B. Berry, *Energy Convers.* **9**, 133, (1969).
- [4] T.A.A. Al-Obaidi, H.J. Goldsmid, *Energy Convers.* **9**, 131 (1969).
- [5] T.C. Harman, *J. Appl. Phys.* **29**, 1373, (1958).
- [6] H.J. Goldsmid, "Electronic Refrigeration", Pion,

London, p. 45 (1986).

- [7] W.M. Yim, F.D. Rosi, *Solid-state Electron* **15**, 1121 (1972).
- [8] H.J. Goldsmid, *Proc. Phys. Soc. B*, **69**, London, 203 (1956).
- [9] F.D. Rosi, B. Abeles, R.V. Jensen, *J. Phys. Chem. Solids* **10**, 156 (1959).
- [10] C.F. Gallo, B.S. Chandrasekhar, Sutter, *J. Appl. Phys.* **34**, 144 (1963).
- [11] R.B. Horst, L.R. Williams, *Proceedings, Third International Conference on Thermoelectric Energy Conversion*, Arlington, Texas (New York: IEEE), p. 139 (1980).

Thermoelectric Properties of Bi-Sb Composite Prepared by Mechanical Alloying Method

Masafumi Miyajima¹, Kenta Takagi², Hiroshi Okamura²
Gil Geun Lee³, Yasutoshi Noda³ and Ryuzo Watanabe³

1. DAIKIN Industries, 3 Banchi, Miyukigaoka, Tsukuba, Ibaraki 305, Japan
2. Graduate Student, Faculty of Engineering, Tohoku University, Sendai 980-77, Japan
3. Faculty of Engineering, Tohoku University, Sendai 980-77, Japan

Abstract

To study the mechanical alloying process and the properties of thermoelectric semiconductor with fine dispersed ceramic particles, Bi-Sb alloys with addition of fine BN and ZrO₂ were prepared by mechanical alloying. The milled powders were sintered by hot pressing. The Bi_{92.5}Sb_{7.5} solid solution with fine dispersion of BN and ZrO₂ ceramic particles were successfully synthesized. The sintered composites show very fine microstructures in which average grain size are less than one micron. The thermal properties of composites were measured by laser flash method at room temperature. The electrical properties were measured by Van der Pauw method at room temperature and at 77 K. The BN addition has obtained larger reduction of thermal conductivity compared to ZrO₂. The thermal conductivity has been reduced to 20% of the reported value of Bi-Sb single crystal, which achieved with 10 vol% addition of BN.

1. Introduction

The mechanical alloying (MA) method has been applied in various fields⁽¹⁾⁻⁽³⁾ of material research. MA process has such practical merits that:

- (1) very wide scale of alloy composition is available
- (2) multi phase composite can be prepared
- (3) nano scale crystal structure can be realized.

With these characteristics, sintered composites made by MA powders, have very fine crystal grains and very large amount of grain boundary. The phonons which carry the heat energy in semiconductor crystals are scattered at grain boundary, so, we can expect enhancement of the thermoelectric figure of merit by sintering MA powder.

Furthermore, the method of introducing ultrafine scattering center for phonon, is considered to be effective for reducing thermal conductivity of thermoelectric materials. Fleurial⁽⁴⁾⁻⁽⁵⁾ calculated the reduction of thermal conductivity by dispersed nano scale fine ceramic particles. Such fine particle dispersion will be prepared also by MA process.

The present work concentrates on MA process and the effect of fine dispersed ceramic powders in thermoelectric materials. The n-type Bi-Sb⁽⁶⁾⁻⁽⁷⁾ solid solution, which is the known best material in low temperature region thermoelectric conversion, used as the model material. The effect of milling condition and the additive amount on the microstructure development and on the thermoelectrical properties were studied.

2. Experimental Procedure

(1) mechanical alloying

The average particle size and the transport properties of starting powders, Bi, Sb, BN and ZrO₂, are shown in Table 1. The composition of Bi-Sb solid solution is fixed to 7.5 at% Sb. The reported works⁽⁶⁾⁻⁽⁷⁾ on Bi-Sb solid solution show that this system becomes spontaneously n-type semiconductor, and the best thermoelectric performance appears in Sb content region from 7 to 12 at%. In considering these results, we used the lower end of this region as the trying composition.

The volume fraction of dispersed fine ceramic powders are changed to 2.0, 6.0 and 10.0 vol%. The blended powders are mechanical alloyed using stainless tumbler vessel and carbon steel milling balls. The milling time were changed to 48, 100, 200 h long. The Ar atmosphere was used in MA. The size of the milling pot was 70 mm in diameter, 135 mm in length. And the milling ball size was 12.7 mm in diameter. The filling ratio of milling ball was 50 vol % of the milling pot. The weight ratio of filled powder to the milling balls is 1 / 62.

(2) compaction and sintering

The milled powders were compacted in metal die at a pressure of 110 MPa, then cold isostatic pressed at 200 MPa. The compacts were sintered by hot pressing in Al₂O₃ die under a pressure of 70 MPa at 543K for 60 min. The sintering atmosphere was Ar + 5%H₂ gas flow.

(3) heat treatment

Some of the as-sintered BiSb composites were heat treated to clarify the influence of recovery and recrystallization of the microstructure on the thermoelectric properties. The treatment was done in 10⁻³Torr vacuum level at 543 K for 48 h.

(4) microstructure evaluation

To see the completeness of alloying process, starting powders and milled powders were examined by x-ray diffraction. The microstructure of sintered composites were observed with TEM. The TEM samples are prepared by polishing with Al₂O₃ paste and by Ar ion milling.

(5) measurement of thermal conductivity

The thermal conductivity of sintered Bi-Sb composites was measured by laser flash method at room temperature. The samples were prepared by cutting the samples into a cylindrical shape of 10mm in diameter and 1mm in thickness.

(6) measurement of electrical properties

The electrical resistivity and the Hall coefficient of the sintered composites were measured by Van der Pauw method at 77 K and at 300 K. With the measured Hall coefficient the carrier density and the carrier mobility were calculated. The measuring current was 10 mA and the magnetic field was 3078 G.

Table 1 Thermal and electrical properties and average particle size of the starting powders.

STARTING MATERIAL	Thermal Conductivity at 300 K [W/cmK ⁻¹]	Electrical Resistivity at 300 K [Ω cm]	Average Particle Size [μ m]
Bi	1.9×10^{-2}	1.16×10^{-2}	15.6
Sb	4.2×10^{-2}	4.2×10^{-2}	55
h-BN	$6.3 \times 10^{+2}$	1×10^{-2}	5
ZrO ₂ (3mol%Y ₂ O ₃)	3.3×10^{-2}	$> 10^{-2}$	0.3

3. Results and Discussion

Phase analysis

The x-ray diffraction patterns of blended powder (before M.A.) and mechanical alloyed Bi-7.5at%Sb powders with 6vol%BN and 6vol%ZrO₂ additives are shown in Fig.1. The diffraction peaks of Sb had vanished after mechanical alloying, and the profile shows formation of Bi-Sb solid solution. The peaks from BN and ZrO₂ single phases were not detected.

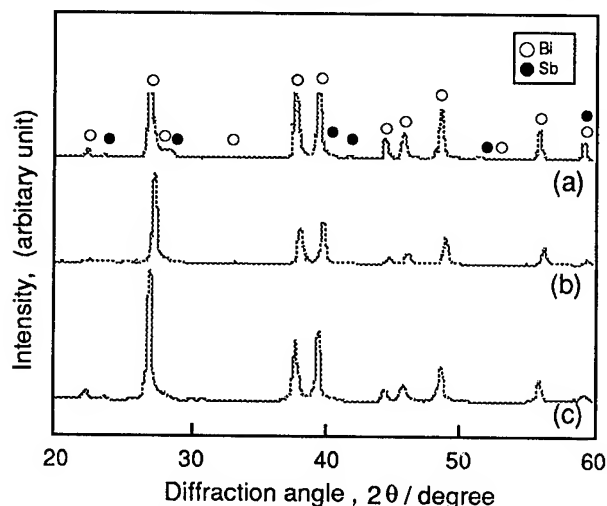


Fig.1 XRD patterns of sintered Bi-7.5at%Sb composites. (a) starting powder (b) MA with 6vol% BN and sintered (c) MA with 6vol% ZrO₂ and sintered.

TEM observation

The TEM micrographs of sintered Bi-Sb composites are shown in Fig.2. Micrograph (a) shows Bi-Sb with 6vol% BN addition, milled for 48 h. Micrograph (b) shows Bi-Sb with 6vol% BN addition milled for 100 h. Micrograph (c) shows Bi-Sb with 6vol% ZrO₂ addition, milled for 100 h. The average grain sizes were 130nm in (a), 90nm in (b) and 300nm in (c). As shown in the micrographs, the grain size of Bi-Sb composite was influenced by MA condition very much. The grain size varies from nano scale order to submicron scale order for the same chemical composition. Comparing the fineness of crystal grain structure, with BN addition the finer grain structure was obtained compared to the ZrO₂ addition of the same milling time. In case of MA without ceramic additives, the average grain size become about 50 nm, which is still finer than the

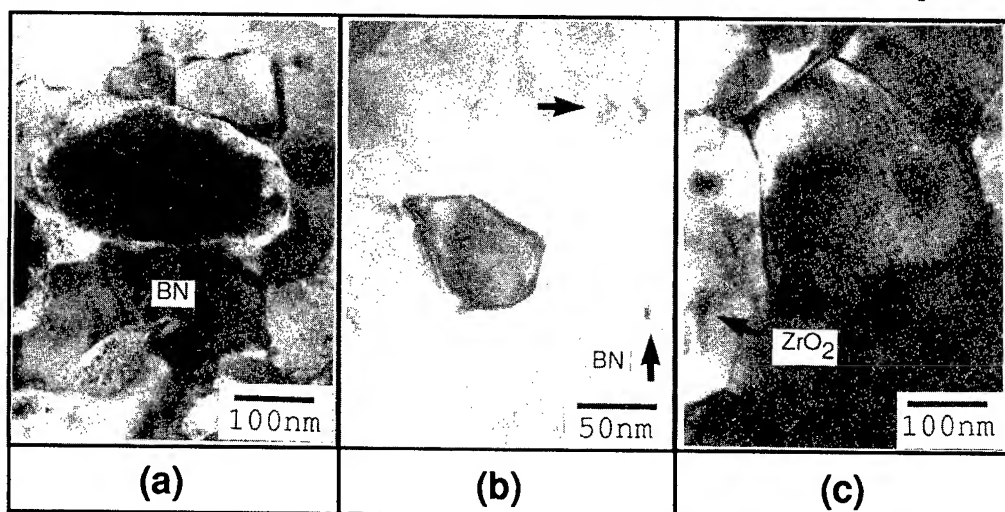


Fig.2 TEM images of mechanical alloyed and hot pressed Bi-7.5at%Sb powders. (a) addition of 6vol%BN, MA 24h (b) addition of 6vol%BN, MA 100h (c) addition of 6vol%ZrO₂, MA 100h.

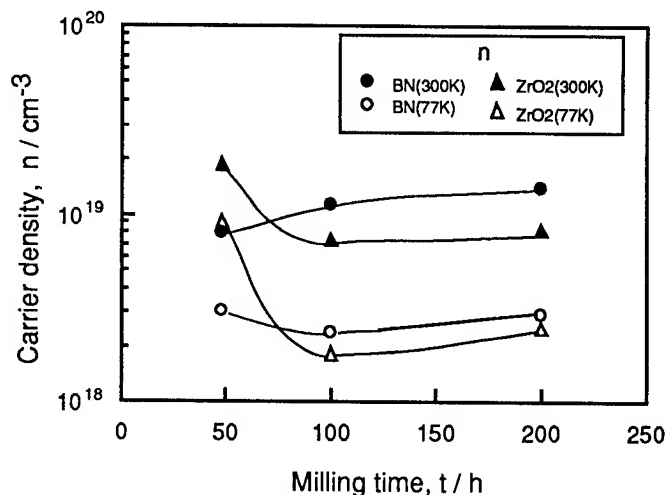


Fig.3 Carrier density of mechanical alloyed and hot pressed Bi-7.5at% Sb powders, with addition of 6vol%BN or 6vol% ZrO₂, as a function of milling time.

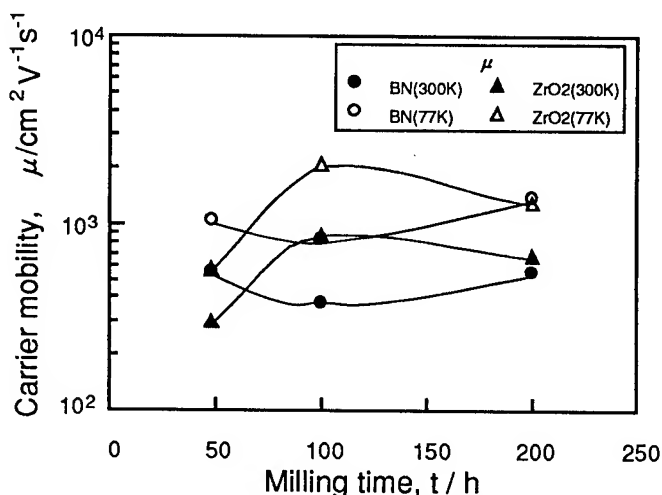


Fig.4 Carrier mobility of mechanical alloyed and hot pressed Bi-7.5at% Sb powders, with addition of 6vol%BN or 6vol% ZrO₂, as a function of milling time.

grain sizes with ceramic addition. The ceramic particles are considered to act as an inhibitor of fine crystal grain formation. The uniformity of ceramic particle dispersion is also influenced

by milling time. Comparing micrograph (a) and (b), the dispersion of BN particle become more uniform with increasing milling time.

Carrier density

The carrier density of the mechanical alloyed Bi-Sb composites are shown in Fig.3 as a function of milling time. The additive amount was 6 vol% for both of BN and ZrO₂. The all samples showed negative seebeck coefficient, so the majority carrier is considered to be electron. The carrier density at 300 K are higher than those at 77 K for all samples, which is considered to be caused by thermal activation of conduction electrons. The carrier density decreased with milling time at first, then increase slightly with milling time. It is considered that these changes are related to the amount of lattice defects which accumulated through MA process. If the lattice defects work as donor sites, the carrier density change can be related to the microstructure development in MA process. The variation of the influence of the ceramic particles on carrier density change, is also considered to be caused by different way of microstructure development.

Carrier mobility

In Fig.4, the carrier mobility of the mechanical alloyed Bi-Sb composites with 6 vol% for both of BN and ZrO₂ are shown as a function of milling time. The mobility at 77K were higher

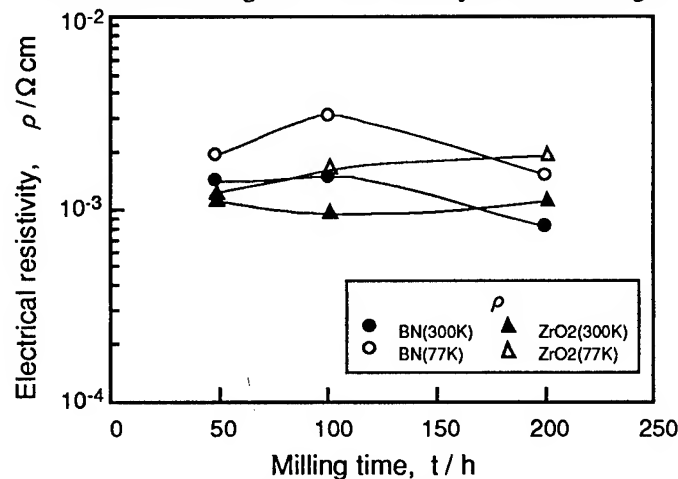


Fig.5 Electrical resistivity of mechanical alloyed and hot pressed Bi-7.5at.%Sb powders, with addition of 6vol% BN or 6vol% ZrO₂, as a function of milling time.

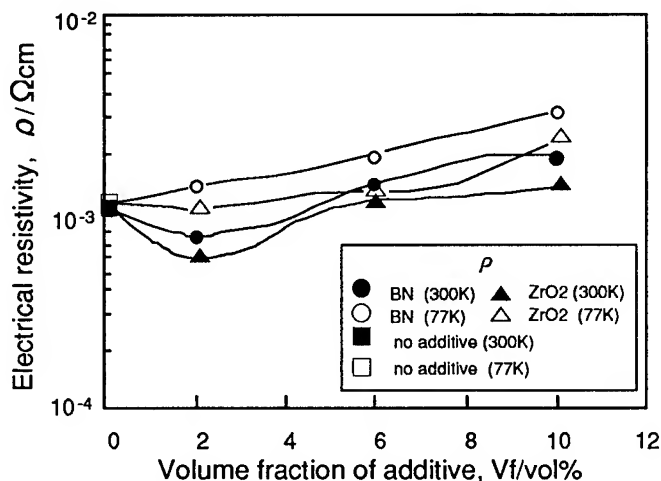


Fig.6 Electrical resistivity of mechanical alloyed and hot pressed Bi-7.5at.%Sb powders, as a function of volume fraction of additive. (MA milling time: 48h)

than those at 300 K which implies the small scattering probabilities of electrons in low temperature region. The relation between the milling time and the carrier mobility is not simply discriminated, because in the present work, dispersion of BN or ZrO₂ fine particles occur simultaneously with MA progress. This problem should be examined separately through another way of composite preparation, i.e., using prealloyed Bi-Sb powders as starting material.

Electrical resistivity

In Fig.5, the electrical resistivity of the mechanical alloyed Bi-Sb composites with the same BN and ZrO₂ content are shown as a function of milling time. In the case of BN addition, the electrical resistivity increased first slightly with milling time, then decreased for longer milling time. This may be related to the accumulation of lattice defects in MA process, as is already mentioned. On the other hand, with ZrO₂ addition, the electrical resistivity did not show appreciable variation with milling time. This is considered to be due to slow progress of ZrO₂ dispersion, as shown in micrograph (c) in Fig.2.

In Fig.6, the electrical resistivity versus volume fraction of additives, are shown. The milling time were fixed to 48 h. With increase in additive amounts, the electrical resistivity increased for all samples. This is considered to be caused by the enhancement of electron scattering at the boundaries of Bi-Sb matrix and ceramic powder particles, that is, non conductive materials, as shown in Table 1.

Thermal conductivity

The thermal conductivity of the mechanical alloyed Bi-Sb composites are shown in Fig.7 as a function of milling time. The thermal conductivity decreased with increase in milling time. This is considered to be caused by:

- (1) increase grain boundary area in MA progress
- (2) finer dispersion of additives in MA progress.

The thermal conductivity reduction was not same for BN and ZrO₂. The difference came from the different influence of each additives on microstructure formation in MA process. But the thermal conductivity values became almost constant for both additives, at the milling time of more than 100 h. It is related to full dispersion of added materials under the ball milling energy condition of the present work.

The thermal conductivities as a function of volume fraction of additives for the mechanical alloyed Bi-Sb composites are shown in Fig.8. The milling time were 48 h for all plots. Though the thermal conductivity of BN and ZrO₂ were higher than that of the Bi-Sb alloy, the thermal conductivity of the

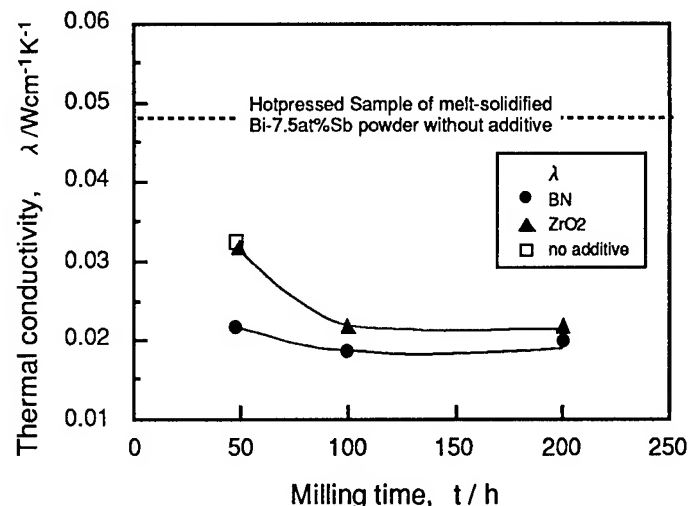


Fig.7 Thermal conductivity of mechanical alloyed and hot pressed Bi-7.5at.%Sb powders, with addition of 6vol% BN or 6vol% ZrO₂, as a function of milling time.

composites decreased with increase in ceramic additive amount. This implies the enhancement of phonon scattering at the boundary between the Bi-Sb matrix and the ceramic additives occurred effectively. The thermal conductivity was reduced to 20% of reported value of Bi-Sb single crystal⁽⁸⁾ with the condition of 10vol% BN addition and milling time for 48 h.

As described above, by sintering the Bi-Sb powders which were prepared via mechanical alloying with addition of fine ceramic particles, we can obtain Bi-Sb composite with nano scale fine grain structure. Such fine microstructure showed very large thermal conductivity reduction, but at the same time the electrical resistivity increased. To reduce the electrical resistivity retaining the low thermal conductivity, heat treatment experiment of the composites were examined. The thermal and the electrical properties of as-sintered and annealed Bi-Sb composites are shown in Table 2. The additive was ZrO_2 and the amount were 6 vol% and 10 vol%. The annealing was done at 533 K for 48 h in 10^{-3} Torr vacuum. After annealing, the electrical resistivity decreased. The electrical resistivity could be reduced to 60% in this condition. It should be studied in more detail how to gain optimum condition for reduction of electrical resistivity, keeping the low level thermal conductivity.

4. Summary

Bi-Sb thermoelectric semiconductor composite powders with dispersion of ceramic particles were prepared by mechanical alloying. The influence of BN and ZrO_2 dispersion on the microstructure formation in MA process and the thermoelectric properties of the sintered composites from the MA powders were studied. The following results were obtained.

- (1) Bi-7.5at%Sb thermoelectric powder with fine dispersed BN and ZrO_2 additives were prepared successfully by MA.
- (2) The prepared powders were fully densified by hot pressing and the composites had submicron size structure. The grain size changed with milling time of MA. The dispersion of the ceramic particles has become more uniform with increase in MA time.

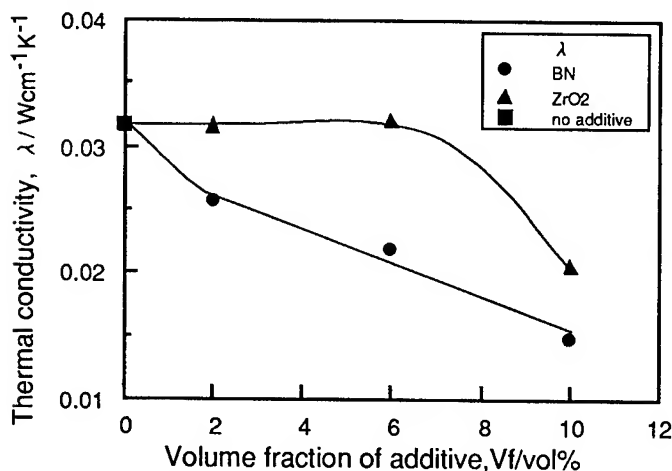


Fig.8 Thermal conductivity of mechanical alloyed and hot pressed Bi-7.5at%Sb powders, as a function of the volume fraction of additive. (MA milling time : 48h)

- (3) With increase in volume fraction of the ceramic particles up to 10 vol%, the thermal conductivity of sintered composite decreased for the all samples.
- (4) Within the total milling time of 200 h, BN addition resulted in smaller thermal conductivity and also smaller electrical resistivity, compared to the ZrO_2 addition.
- (5) The best thermal conductivity reduction was achieved with the condition of 10vol% BN addition and milling time for 48 h. The reduced value was 20% of the reported single crystal Bi-Sb thermal conductivity.

Table 2 Thermal and electrical properties of as-sintered and annealed (533K / 48h / vacuum) Bi-7.5at%Sb composites with ZrO_2 additive.

		6vol% ZrO_2 MA48h		6vol% ZrO_2 MA100h		10vol% ZrO_2 MA48h	
		not annealed	annealed	not annealed	annealed	not annealed	annealed
Electrical resistivity ($10^{-2} \Omega \text{ cm}$)	300K	1.12	0.688	0.987	0.548	1.34	0.820
	77K	1.21	1.11	1.66	1.05	2.35	1.69
Thermal conductivity ($10^{-2} \text{ W/cm}^2 \text{ K}$)		3.20	2.75	2.16	3.12	2.06	2.91

Reference

- [1] B.Cook, B.Beaudry and J.Harrnga, " Optimization of the P/Ga RATIO in n-type $Si_{80}Ge_{20}$ ", Proc. 9th ICT, pp 28-32 (1990).
- [2] K.Hasezaki, M.Nishimura, M.Umata, H.Tsukuda and M.Araoka, "Mechanical Alloying of Thermoelectric Materials ", Proc. 12th ICT, pp 307-310 (1994).
- [3] S.Shiga, K.Fujimoto and M.Umemoto, " Thermoelectric Properties of $FeSi_{1-x}Ge_x$ Compound Prepared by Mechanical Alloying ", Proc. 12th ICT, pp 311-315 (1994).
- [4] Jean-Pierre Fleurial, "Evaluation of the Improvement in the Figure of merit of Bi_2Te_3 based alloys with addition of ultrafine scattering centers", Proc. 12th ICT, pp1-6 (1993).
- [5] Jan W.Vandersande, Jean-Pierre Fleurial, Nancy Scoville and Jon L.Rolfe, " Thermal Conductivity Reduction in p-type $Si_{80}Ge_{20}$ alloys due to Ultrafine Insulating Particulates", Proc. 12th ICT, pp11-14 (1993).
- [6] W.Yim and A.Amith, " Bi-Sb Alloys for Magneto-Thermoelectric and Thermomagnetic Cooling ", Sol.-St.Electron., vol.15, pp1141-1165 (1972).
- [7] R.B.Horst and L.R.Williams, "Potential Figure of Merit of the BiSb alloys ", Proc. 3rd ICT, pp139-173 (1980).
- [8] Y.S.Touloukian, R.W.Powell, C.Y.Ho and P.G.Klemens (Ed.), *Thermophysical Properties of Matter, vol.1 Thermal Conductivity-Metallic Elements and Alloys*, IFI/PLENUM, p 502 (1970).

OBSERVATION OF THE EFFECT OF GRAIN SIZE ON THE LATTICE THERMAL CONDUCTIVITY OF POLYCRYSTALLINE BISMUTH ANTIMONY

E. H. Volckmann, H. J. Goldsmid, J. Sharp
Marlow Industries Inc.
10451 Vista Park Road, Dallas, TX 75238-1645

Abstract

The thermal conductivity of polycrystalline sintered BiSb has been measured from 80 to 300 K. The samples had mean grain sizes between 1 μm and 19 μm . The electronic contribution to the thermal conductivity was determined by a technique that involves the comparison of the magneto-resistance and the magneto-thermal resistance effects in transverse fields of up to 1.0 tesla. The electronic thermal conductivity seems to be somewhat smaller than expected, bearing in mind that there should be a significant bipolar contribution, yet the technique is believed to be sound since it yields a lattice thermal conductivity for large-grained samples that is intermediate between the values for single crystals in the principal crystal directions. The lattice thermal conductivity is found to decrease as the grain size is reduced. Such a decrease has been predicted on the basis of grain boundary scattering of phonons but it is occurring at grain sizes somewhat larger than expected. It is possible that the effect may be due to the scattering of phonons on point or line defects that have been introduced as a consequence of powder metallurgy. Nevertheless, grain boundary scattering cannot be ruled out as the cause, in view of the simplifications that were made in the theory.

Introduction

Of the known n-type thermoelectric materials, Bi-rich alloys between Bi and Sb exhibit the highest thermoelectric figure of merit (Z) for temperatures below about 210 K. The best thermoelectric properties are observed along the trigonal axis of single crystals, but the propensity of BiSb crystals to cleave along the trigonal planes has largely prevented utilization of BiSb alloys in thermoelectric coolers.

Synthesizing polycrystalline BiSb alloys with a fine grain size eliminates the cleavage problem and offers the possibility of decreasing the lattice thermal conductivity (λ_L). Recent theory predicts that as the grain size is reduced, phonon boundary scattering should become noticeable at a grain size of about 5 μm [1].

The purpose of the present work was to determine if the predicted λ_L reduction could be observed experimentally. Two groups of samples, with varying grain size, were prepared and characterized metallurgically and electrically.

Experiment

The grain size (L) of each sample was equal to the particle size of the powder from which it was made. The powder used in the first sample series was prepared by crushing a $\text{Bi}_{88}\text{Sb}_{12}$ ingot with a porcelain mortar and pestle followed by sieving to obtain four size fractions. The smallest mean particle size was 6.4 μm , and there was little size difference between the coarser fractions (6.4, 12.3, 14.8 and 15.8 μm). The crushed particles were irregular in shape with some platelet-like nature.

A second lot of powder was produced, at Ames Laboratory, by high pressure inert gas atomization (HPGA) and fractions with mean sizes of 19.0, 5.0, 2.5 and 1.1 μm were separated in an air classifier. The powder composition was $\text{Bi}_{91}\text{Sb}_9$ indicating that some Sb was lost during atomization. The HPGA particles were spherical in shape and each particle contained multiple grains as shown in Figure 1.

The powders were hot-consolidated to nearly full density. Grain growth, which becomes more energetically favorable as L decreases, occurred during consolidation as shown in Figure 2. However, growth was restricted to the prior particle boundaries so L became equal to the starting mean particle size.

The composition of powders was determined by atomic emission spectroscopy and wavelength dispersive spectroscopy. Oxygen concentrations were determined by the inert gas fusion method and Auger spectroscopy was used to estimate the oxide thickness on particle surfaces.

The grain size in consolidated samples was taken from photomicrographs of polished cross-sections etched with HNO_3 using the Heyn procedure [2]. The Archimedes method was used for determining density. Seebeck coefficient (α), electrical resistivity (ρ) and thermal conductivity (λ) were measured from 80 to 300 K (-213 to 27 °C) using a modified Harman method.

For separation of the electronic component, (λ_e), and the lattice component, (λ_L), of the thermal conductivity, transport measurements were also performed in a transverse field of weak to intermediate strength. If it is assumed that λ_e and ρ vary with magnetic field strength in the same manner as follows:

$$\rho = \rho(0)(1 + cB^2) \quad (1)$$

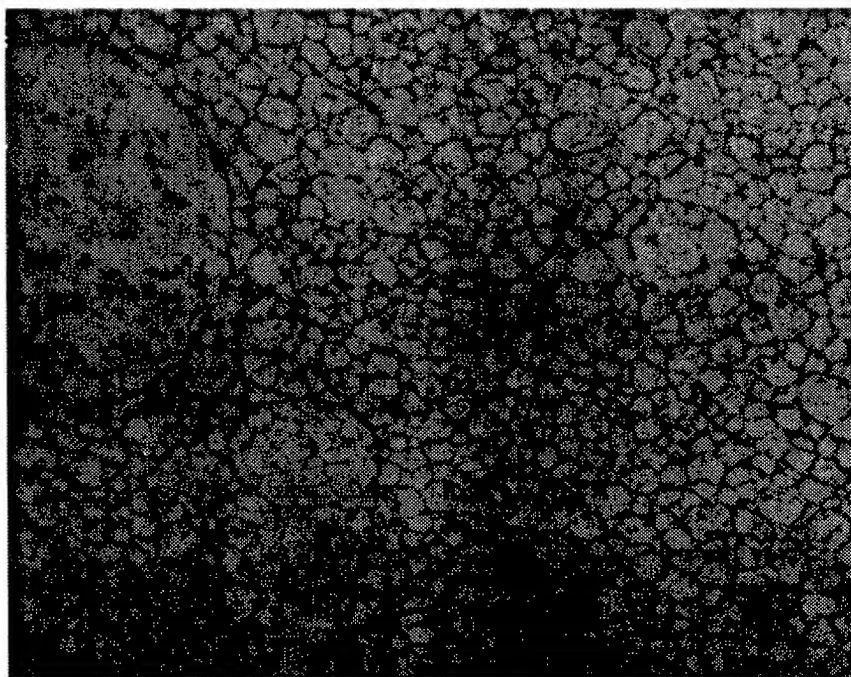


Figure 1 Microstructure of compact cold pressed from HPGA powder. 1000 X, dilute HNO_3 etch.



Figure 2. BiSb hot consolidated from 5 μm HPGA powder. 1000 X, dilute HNO_3 etch.

and

$$\lambda_e = \lambda_e(0)/(1 + cB^2) , \quad (2)$$

then combining the equations to eliminate B gives

$$\lambda_e = \lambda_e(0) \frac{\rho(0)}{\rho} . \quad (3)$$

Therefore

$$\lambda_{tot} = \lambda_L + \lambda_e = \lambda_L + \lambda_e(0) \frac{\rho(0)}{\rho} , \quad (4)$$

where λ_L is the intercept and $\lambda_e(0)$ is the slope from the plot of λ_{tot} versus $\rho(0)/\rho$. Such a plot is shown in Figure 3. In actuality, ρ and λ_e did not depend on B as expected from equations (1) and (2) but the deviance of the parameters was the same allowing the use of equation (3). The fact that all the points in Figure 3 lie so close to the line of best fit supports the validity of equation (4) and the assumptions on which it is based. Further support is also provided by the fact that the value of λ_L , obtained from equation (4) for polycrystals of large grain size, lies between the values of the principal directions for single crystals of the same composition [3].

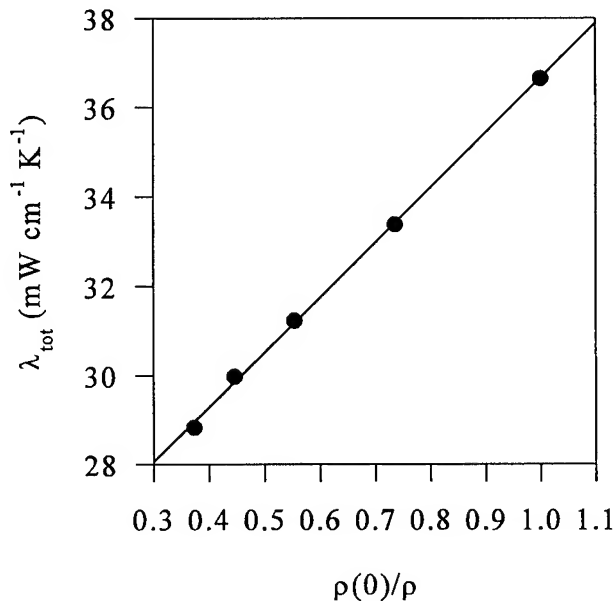


Figure 3. Plot of λ_{tot} vs $\rho(0)/\rho$ produced by testing $\text{Bi}_{88}\text{Sb}_{12}$ ($L \sim 45 \mu\text{m}$) at 160 K in magnetic fields up to 0.6 T. Linear regression gives $\lambda_L = 24.4 \text{ mW cm}^{-1} \text{ K}^{-1}$ and $\lambda_e(0) = 12.3 \text{ mW cm}^{-1} \text{ K}^{-1}$.

Discussion

The predicted relationship between λ_L and L is

$$\lambda_L = \lambda_s - \frac{2}{3} \lambda_0 \sqrt{\frac{l}{3L}} , \quad (5)$$

where λ_s is the lattice thermal conductivity of a large crystal of the solid solution, λ_0 is the lattice thermal conductivity in the absence of point defect scattering, l is the phonon mean free path, and L is the grain diameter [1].

Curves generated from equation 5 are plotted in Figures 4 and 5. Since λ_L of BiSb single crystals is significantly anisotropic, a value somewhere between $\lambda_{L,33}$ (along the trigonal axis) and $\lambda_{L,11}$ (along the binary axis) should be used for λ_s . For this reason, λ_L of large grained (50 to 75 μm) BiSb was taken as an effective λ_L for a "single crystal of an intermediate orientation" and this value was used for λ_s . Likewise, an intermediate value of λ_L for pure Bi was estimated from the data of Uher and Goldsmid [4] and used as λ_0 .

Actual 120 K data is also shown in Figures 4 and 5. Although much of the data from the first sample series is for a narrow range of L (Figure 4), it shows that λ_L decreases with L . The second sample series, which was made from HPGA powder, covers a broader size range and clearly reveals the dependence of λ_L on L (Figure 5). It should be noted that λ_e , which was smaller than expected for a material that should have a significant bipolar contribution, also decreased with L .

The experimental data is consistent with the theory that boundary scattering can produce significant reductions in λ_L using grains of reasonable dimensions, but further work is needed to confirm that boundary scattering is responsible for the reduced λ_L . The fact that λ_L begins to decrease at larger grain sizes than predicted may be a consequence of simplifications made in the theory or could be a manifestation of an additional scattering mechanism. The effect of inclusions in the form of porosity or second phase oxides, was considered.

Auger spectroscopy indicated that all particle surfaces were covered with an oxide layer about 100 Å thick. If this layer was not disrupted during consolidation, carrier tunneling would be required for conduction. However, tunneling cannot be taking place since the electrical resistivity is too low and is independent of the applied voltage. Consequently, the oxides in the sintered material must be in the form of inclusions.

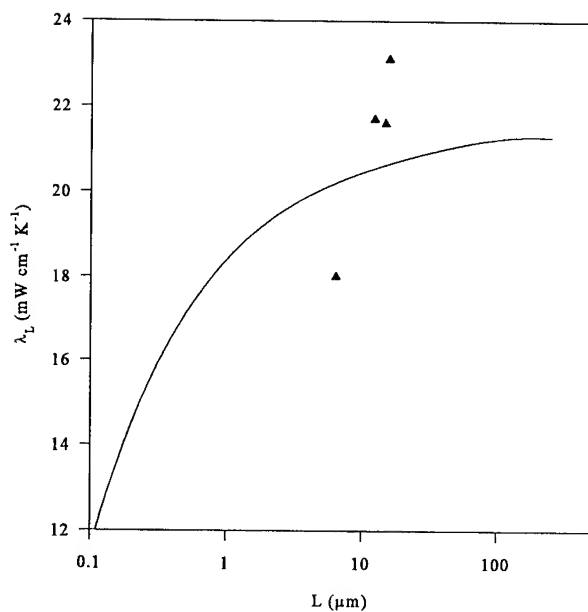


Figure 4. Predicted grain size dependence of λ_L (curve) and experimental data; $\text{Bi}_{88}\text{Sb}_{12}$ at 120 K.

Kingery [5] has shown that the effect of insulating inclusions on the electrical conductivity is given by

$$\sigma_2 = \sigma_1 \frac{(1-x)}{(1+\frac{x}{2})}, \quad (6)$$

where σ_1 and σ_2 are the electrical conductivity of single- and two phase- material respectively and x is the inclusion volume fraction.

In the sample made from 1.1 μm HPGA powder, the oxide fraction was 0.04 so one might have expected a 6% reduction in electrical conductivity, σ , due to the inclusions rather than the observed decrease of about 75% shown in Figure 6. The effect on the thermal conductivity would have been even smaller than 6%, since oxide inclusions would have a thermal conductivity comparable with BiSb. Clearly, the fall of about 20% in λ_L of $\text{Bi}_{91}\text{Sb}_9$ made from 1.1 μm powder is much too large to be explained in this way.

Hall measurements indicate that a reduction in mobility, of both electrons and holes, is largely responsible for the σ behavior shown in Figure 6. It is not yet clear whether the increasing level of carrier scattering with decreasing grain size is due to more defects or if the grain size is approaching the carrier mean free path.

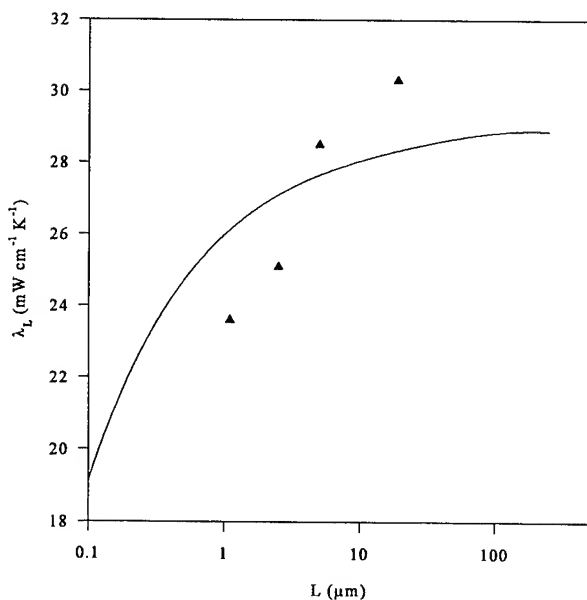


Figure 5. Predicted grain size dependence of λ_L (curve) and experimental data; $\text{Bi}_{91}\text{Sb}_9$ at 120 K.

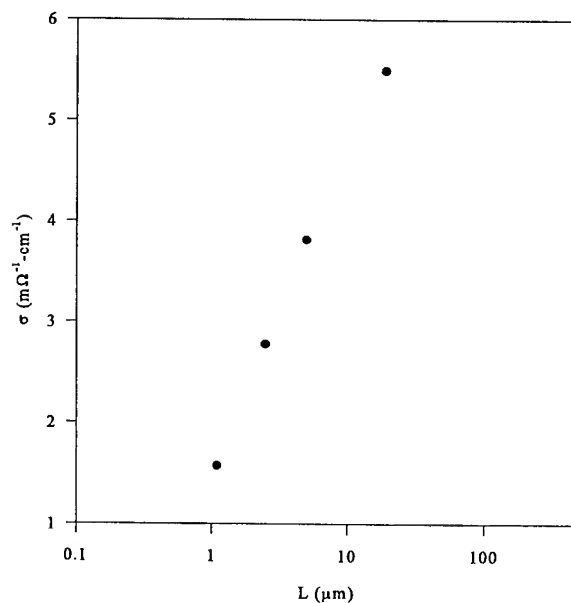


Figure 6. Observed grain size dependence of σ for $\text{Bi}_{91}\text{Sb}_9$ at 120 K.

Conclusions

The polycrystalline BiSb samples that were prepared exhibited thermal conductivities that decreased with grain size but an enhanced figure of merit was not realized due to a dominating, concurrent decrease in electrical conductivity. The lower values of thermal conductivity were a result of decreases in both the electronic and the lattice components. Porosity or dispersed second phase inclusions cannot account for the observed reductions of the lattice thermal conductivity and electrical conductivity. While the apparent dependence of the lattice thermal conductivity on grain size suggests that boundary scattering of phonons is occurring, further work is required to rule out other explanations such as phonon scattering by defects or impurities whose concentration depend on grain size.

Acknowledgments

Thanks goes: to Dr. John Prater and the Army Research Office for their support, to Drs. Iver Anderson, Bruce Cook and Matthew Kramer at Ames Laboratory for HPGA powder production and powder characterization, and to Drs. Hylan Lyon and Ctirad Uher for their advice throughout the project.

References

- [1] Goldsmid, H. J., Lyon, H. B., Volckmann, E. H., In Proceedings for XIV International Conference on Thermoelectrics St. Petersburg, 16 1995.
- [2] ASTM Designation E 112 - 88.
- [3] Horst, R. B., Williams, L. R., In Proceeding for III International Conference on Thermoelectrics, 139, 1980.
- [4] Uher, C., Goldsmid, H. J., *Physica Status Solidi B*, **65** 765 1974.
- [5] Kingery, W. D., *Introduction to Ceramics*, Wiley, 1960.

Thermoelectric Properties of Doped Bismuth-Antimony Single Crystals

V.M.Grabov¹, O.N.Uryupin², M.G.Bondarenko¹

¹ Herzen Russian State Pedagogical University, St. Petersburg, Russia

² A.F.Ioffe Physical-Technical Institute, St. Petersburg, Russia

Abstract

The thermoelectric phenomena in bismuth-antimony crystals doped by tellurium donor and tin acceptor impurities in temperature range $80 \div 300$ K have been investigated. Crystals have been grown by horizontal zone recrystallization method with the use of regimes which provide their homogeneity. The area ranges of doping bismuth-antimony crystals in which thermoelectric figure of merit appears higher than in undoped crystals have been determined. The transport phenomena and thermoelectric figure of merit of $\text{Bi}_{0.93}\text{Sb}_{0.07} < y >$ crystals at $y \leq 0.001$ at.% Sn and Te have been investigated in detail. It was shown that thermoelectric figure of merit of $\text{Bi}_{0.93}\text{Sb}_{0.07} < y >$ crystals doped $y = 0.001$ at.% Sn in temperature range $80 \div 300$ K exceeds thermoelectric figure of merit undoped and doped $y \leq 0.001$ at.% Te crystals.

Introduction

The $\text{Bi}_{1-x}\text{Sb}_x$ crystals have the highest thermoelectric figure of merit Z_{33}

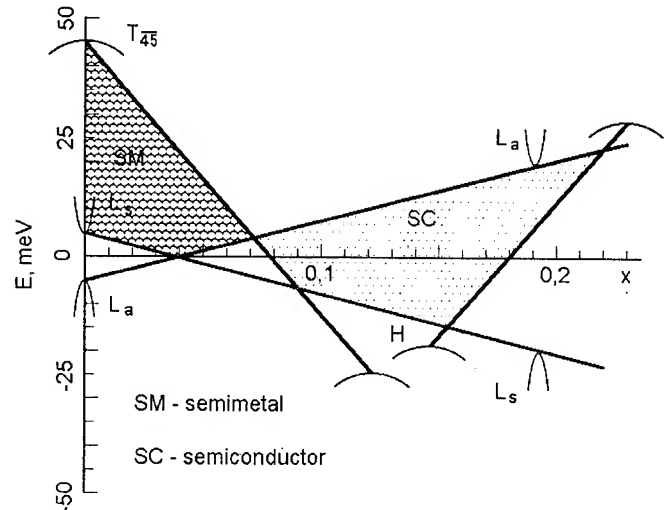
$$Z = \frac{\alpha^2}{\rho \cdot \kappa}$$

among the low temperature thermoelectric materials in the semimetal-semiconductor transition region in $\text{Bi}_{1-x}\text{Sb}_x$ system, (Fig. 1) [1]-[5]. The high Z_{33} of n-type materials is due to electron contribution predominance in transport properties of $\text{Bi}_{1-x}\text{Sb}_x$ crystals. However, the chemical potential level is shifted to conduction band with temperature increase in because of density of state mass difference for valence and conductivity bands. Thus its position can be not optimum for all temperatures in $80 - 300$ K range.

Panarin [7] performed preliminary calculations doping impurities influence on Z of $\text{Bi}_{1-x}\text{Sb}_x$ crystals. However, he only experimentally determined the optimum doping impurities content in $\text{Bi}_{0.88}\text{Sb}_{0.12}$ crystals. For temperature range: $80 - 100$ K optimum concentration $y = 0.001$ at.% Te, for $100 - 140$ K - undoped crystals, $T > 140$ K - $y = 0.002 - 0.005$ at.% Sn [7]. Zemskov *et al.* [8, 9] investigated low ($10^{-5} - 10^{-3}$ at.%) Sn and Te content influence on the Z_{33} of $\text{Bi}_{1-x}\text{Sb}_x$ crystals at $x=0.09, 0.15$ grown by Chokhralsky method. Slightly (by 2 - 6%) increase of Z_{33} in doped crystal is detected.

Our recent investigations have demonstrated that the increase of bismuth purity degree and $\text{Bi}_{1-x}\text{Sb}_x$ single

Figure 1: Evolutoin of the band structure of $\text{Bi}_{1-x}\text{Sb}_x$ homogeneous single crystals versus x at low temperature.



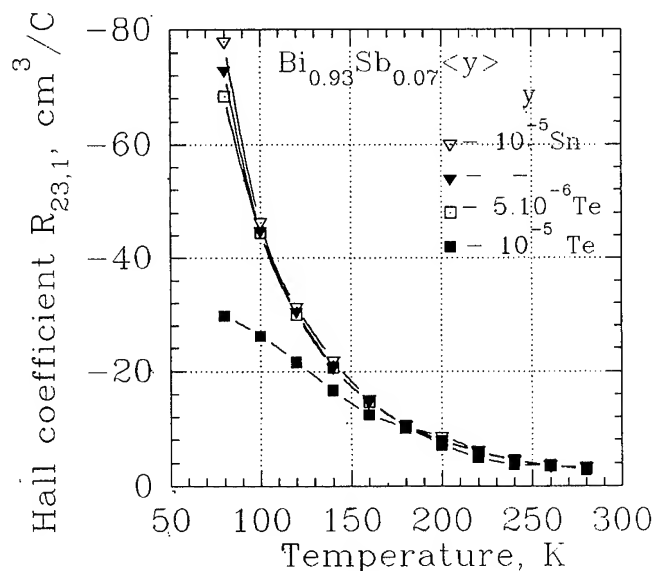
crystals homogeneity at growing by zone recrystallization method with the use of the low growth speed $V \leq 0.5$ mm/h and the small temperature gradient in crystallization front $G \leq 20$ K/cm leads to little reduction of thermoelectric figure of merit Z_{33} in the area of semiconducting state of $\text{Bi}_{1-x}\text{Sb}_x$ in comparison with the results [2, 3, 5], including the results of doped crystals investigation [7, 8, 9]. Hence, the problem of optimization of the chemical potential level position for obtaining maximum Z_{33} in homogeneous crystals $\text{Bi}_{1-x}\text{Sb}_x$ by doping donor and acceptor impurities is actual.

Experimental procedure

Preparing $\text{Bi}_{1-x}\text{Sb}_x$ single crystals with horizontal zone-leveling technique, the analysis of their composition and quality, preparing the samples and the measurement of transport coefficients in the temperature range $77-300$ K have been carried out according to the method reported during previous conference [4]. The ingots of doped alloys $\text{Bi}_{1-x}\text{Sb}_x$ were preliminary undergone by zone equalization of the content at the even number passages of the molten zone at $V=2$ cm/h with following single crystals preparation at the odd passage of the molten zone at

$v = 0.5 \text{ mm/h}$ and $G \leq 20 \text{ K/cm}$.

Figure 2: Hall coefficient as a function of temperature for $\text{Bi}_{0.93}\text{Sb}_{0.07} < y >$ homogeneous single crystals.



The distribution of the alloy composition (x) and doping impurities content (y) in the central part of ingot was homogenous with the concentration close to the concentration inserted during loading. The data [10] show that the doping impurities of Bi - type crystals in the used quantity change the concentration of carriers and chemical potential level without changing the parameters of initial energy spectrum of charge carriers. Acceptor impurities doping (tin) causes the increase of holes concentration and the shift of chemical potential level to valence band. Donor impurities doping (tellurium) causes the increase of electrons concentration and the shift of chemical potential level to conductivity band (Fig. 1). The analysis of doping impurities content has been carried out according to the results of measurement of Hall coefficient (Fig. 2).

Results and discussion

The influence of the doping impurities on Seebeck coefficient of bismuth and $\text{Bi}_{0.93}\text{Sb}_{0.07} < y >$ crystals in the temperature range 80-300 K

The measurements of Seebeck coefficient α_{33} dependence on the content of doping impurities Te, Sn at the temperature 80 and 273 K for bismuth crystals having the greatest overlapping of bands and for $\text{Bi}_{0.93}\text{Sb}_{0.07} < y >$ crystals having thermal energy gap approximating the maximum for composition $0 < x < 0.20$ (Fig. 1) have been carried out to determine the possible content range of doping impurities for the optimization of thermoelectric parameters of $\text{Bi}_{1-x}\text{Sb}_x$ crystals. The results of these investigations are shown in Fig. 3, 4.

It is obvious that the maximum values of thermoelec-

Figure 3: Seebeck coefficient as a function of the doping impurities content $< y >$ for $\text{Bi}_{1-y} < y >$ single crystals for two temperatures.

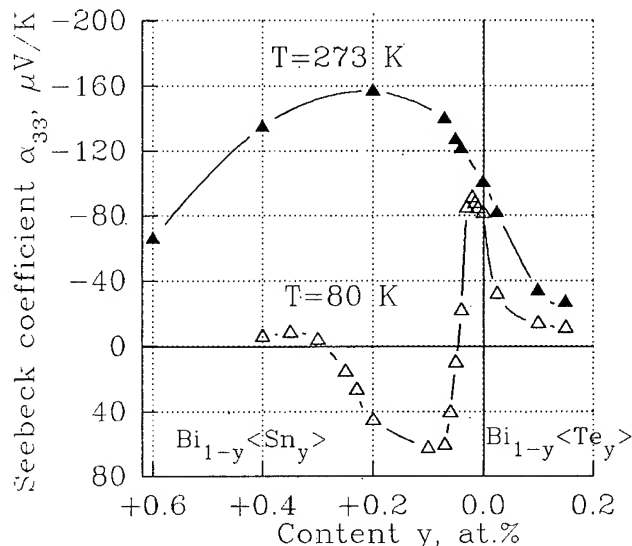
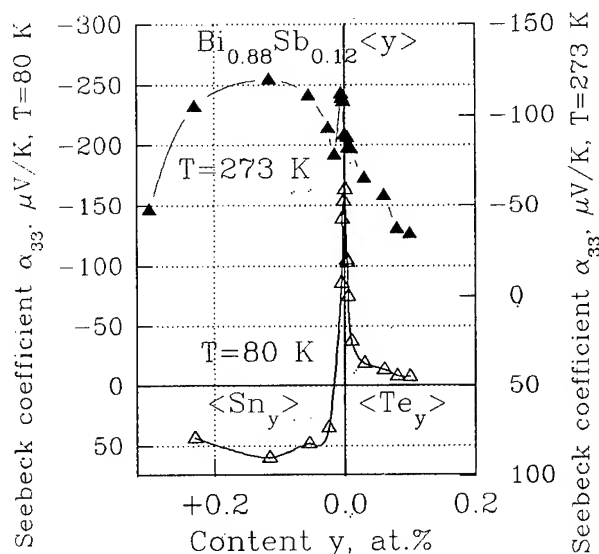


Figure 4: Seebeck coefficient as a function of the doping impurities content for $\text{Bi}_{1-x}\text{Sb}_x < y >$ homogeneous single crystals for two temperatures.



tric figure of merit for n-type materials should be looked for in the vicinity of the maximum of Seebeck coefficient absolute value, in the region of negative Seebeck coefficient. The maximum of α_{33} and Z_{33} in bismuth crystals for temperature range near the room temperature is reached at the doping the acceptor impurities 0.1 – 0.2 at.% Sn. In decreasing the temperature and passing from bands overlapping to the gap (from $x=0$ to $x=0.12$) the Seebeck coefficient α_{33} maximum becomes more sharp and is shifted to the low concentration area of acceptor impurity $Sn \sim 10^{-3}$, approximating the intrinsic conductivity state. The Z_{33} maximum is also shifted to the low concentration interval area of doping acceptor impurity and then - to the intrinsic conductivity area and even the low concentration of donor impurities, which is proved by the results [7] for $x=0.12$. Changing the Seebeck coefficient sign to negative one at increasing the content of Sn in bismuth crystals at low temperatures (Fig. 3), and also nonmonotonous Seebeck coefficient dependence on the tin doping impurities content in crystals ($x=0.12$), (Fig. 4), are determined by complicate band structure and contribution of interband scattering [6].

In this paper we demonstrate the results of the experimental investigation of the influence of tin and tellurium doping impurities ($y \leq 0.001$ at.%) on the transport coefficients and thermoelectric figure of merit of $Bi_{1-x}Sb_x$, $x=0.07$ crystals in the temperature range 80-300 K, which are corresponded with the maximum of Z in homogeneous undoped crystals [4].

Electrical resistance

The temperature dependence of electrical resistance ρ_{33} of $Bi_{0.93}Sb_{0.07} < y >$ crystals doped by tin and tellurium is shown in Fig. 5.

Electrical resistance depends essentially on the content and type of doping impurities at $T < 180$ K, but at higher temperature they have similar values.

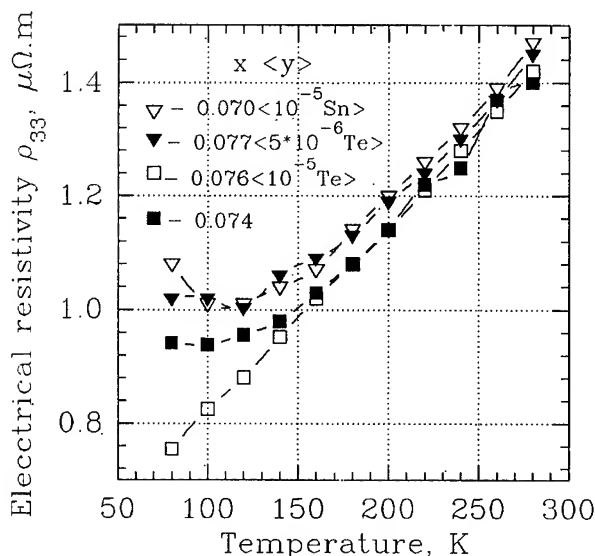
Tin doping results to the shift of the chemical potential level in energy gap E_g , Fig. 1. In this case the concentration of the light charge carriers of L-extrema decreases that causes increase of electrical resistance in low temperature area.

First, tellurium doping leads to the increase of the electric resistance and its further decrease at tellurium content increasing. Nonmonotonous dependence of electrical resistance on the doping impurities content is determined not only by changing the electron and hole concentrations but the essential changing of intravalley, intervalley, interband and recombination scattering of charge carriers by phonons.

Seebeck coefficient

Seebeck coefficient of all the investigated crystals in the temperature range 80-300 K has negative sign, Fig. 6, which proves the predominant contribution of conductivity band electrons. Seebeck coefficient of $Bi_{0.93}Sb_{0.07}$ crystals doped by tin exceeds the Seebeck coefficient of

Figure 5: Electrical resistivity as a function of temperature for $Bi_{1-x}Sb_x < y >$ homogeneous single crystals.



undoped crystals. Tin doping, $Bi_{0.93}Sb_{0.07} < 10^{-5}Sn >$, approaches Seebeck coefficient to the maximum shown in Fig. 2, 3, in the temperature range 80-300 K, Fig. 6. The maximum in the temperature dependence of Seebeck coefficient in the investigated interval for crystal $Bi_{0.93}Sb_{0.07} < 10^{-5}Te >$ is connected with the transition to the temperature dependence of Seebeck coefficient typical for metals. In the range 80-300 K Seebeck coefficient decreases monotonously in the crystals with less content of doping impurities and in the undoped crystals.

Thermal conductivity

Increasing of thermal conductivity (κ) at the temperature grown in investigated crystals (Fig. 7) is determined by the essential contribution of the ambipolar diffusion of charge carriers to the heat transport. Relative contribution of ambipolar diffusion increases with tin doping the $Bi_{0.93}Sb_{0.07} < y >$ crystals because of approaching to the equalization of electron and hole contributions, that causes the increase of $d\kappa/dT$. Doping does not causes the substantial changing of lattice thermal conductivity of $Bi_{0.93}Sb_{0.07} < y >$ crystals, as impurities concentration is in the several orders less than content of antimony in the alloy, so the observed difference in value of thermal conductivity (Fig. 7) is determined by charge carriers contribution changing.

Thermoelectric figure of merit

The results of thermoelectric figure of merit Z_{33} calculation are shown in Fig. 8. At $T > 200$ K thermoelectric figure of merit of all the investigated crystals has

Figure 6: Seebeck coefficient as a function of temperature for $\text{Bi}_{1-x}\text{Sb}_x < y >$ homogeneous single crystals.

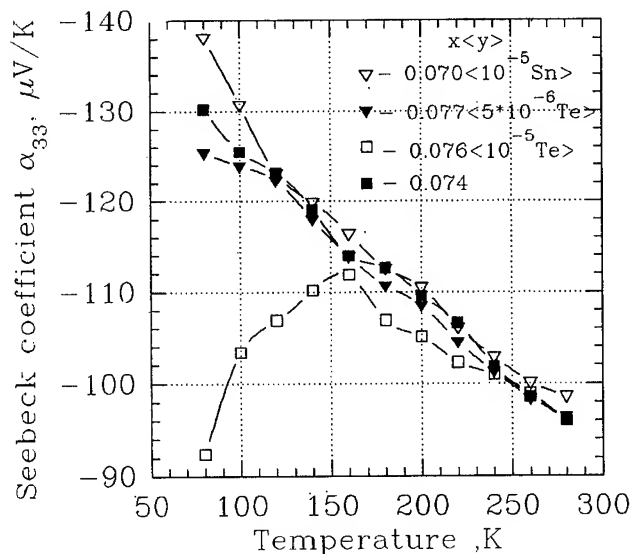
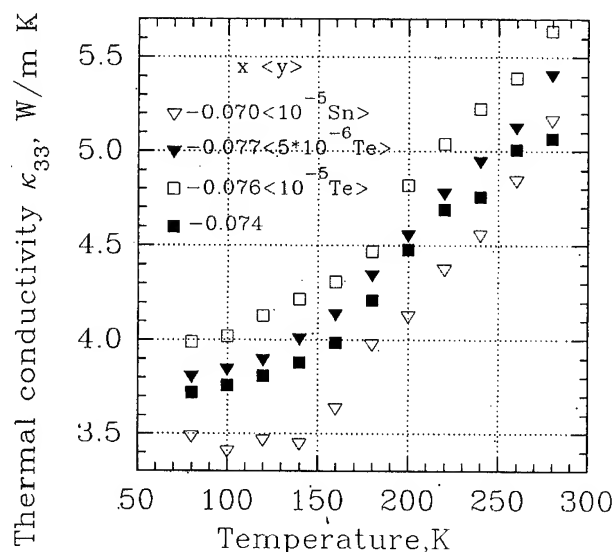


Figure 7: Thermal conductivity as a function of temperature for $\text{Bi}_{1-x}\text{Sb}_x < y >$ homogeneous single crystals.



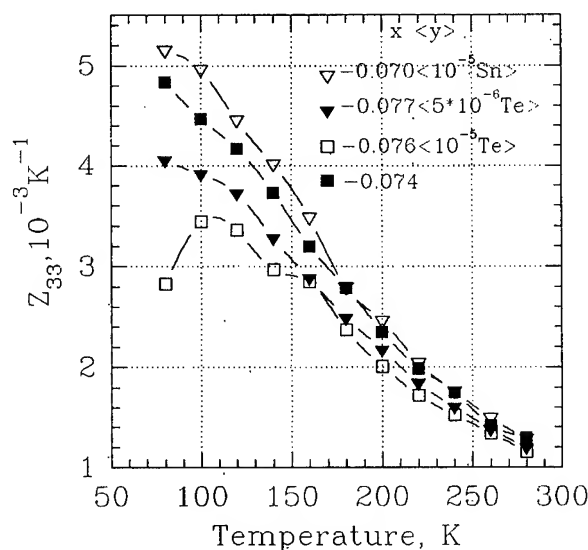
near values. In the temperature range 80-200 K Z_{33} of $\text{Bi}_{0.93}\text{Sb}_{0.07} < 10^{-5}\text{Sn} >$ crystal noticeably exceeds the value for all the investigated crystals. In this way, the maximum of Z for $x = 0.07$ in the temperature range 80-300 K is achieved at the tin acceptor impurity content about 0.001 at.%. Tellurium donor impurity doping removes the chemical potential level from the optimum position in the given temperature range and causes the decrease of Z_{33} . As, due to the complexity of charge carriers energy spectrum in Bi-Sb crystals, Fig. 1, the change of electrons and holes contributions to transport phenomena at doping is determined by the changing of relative contributions of various kinds of scattering [6], the dependence of Seebeck coefficient on temperature and doping impurities content (Fig. 3,4) show only the general picture of thermoelectric properties changing.

To identify compositions with maximum $Z(x,T)$ it is necessary to determine exactly the optimum doping level of Bi-Sb crystals with given (x). It demands the experimental investigation of the complex of transport coefficients.

Conclusions

1. The thermoelectric figure of merit Z_{33} of homogeneous $\text{Bi}_{0.93}\text{Sb}_{0.07} < y >$ crystals in the temperature range 80-200 K has the maximum in the area of tin acceptor impurity doping ($y = 0.01$ at.%) ($y = 0.01$ at.%) and exceeds Z_{33} of undoped crystals.
2. The thermoelectric figure of merit Z_{33} of homogeneous $\text{Bi}_{0.93}\text{Sb}_{0.07} < y >$ crystals, doped by tellurium, appears to be lower than Z_{33} of undoped crystals in the whole investigated temperature range.

Figure 8: Figure of merit as a function of temperature for $\text{Bi}_{1-x}\text{Sb}_x < y >$ homogeneous single crystals.



3. Due to the complexity of energy spectrum of charge carriers and scattering mechanisms the calculation of the optimum doping level of $\text{Bi}_{1-x}\text{Sb}_x$ $< y >$ crystals [7] has only the character of estimation. The most exact picture can be obtained using experimental values of Seebeck coefficient (Fig. 2, 3). The most reliable values of the optimum doping level can be obtained in experimental investigation of the complex of the transport coefficients. The estimating calculation and experimental data on Seebeck coefficient essentially narrow the area of searching the optimum compositions.

References

- [1] G. E. Smith and R. Wolfe. Thermoelectric Properties of Bismuth-Antimony Alloys. *J. Appl. Phys.*, v.33, No.3, pp.841-846, (1962).
- [2] Ivanov G.A., Kulikov B.A., Naletov V.L., Panarin A.F., Regel A.R. Thermoelectric figure of merit at magnetic field of pure and doped bismuth-antimony single crystals. *Fizika i tehnika poluprovodnikov*, v.6, No.7, pp.1296-1299, (1972), (in Russian).
- [3] Yim W.M., Amith A. Bi-Sb alloys for magnetothermoelectric and thermomagnetic cooling. *Solid State Electronics*, v.15, No.10, pp.1141-1165, (1972).
- [4] Grabov V.M., Ivanov G.A., Naletov V.L., Bondarenko M.G., Uriypin O.N. Thermoelectric figure of merit of horizontal zone-leveling prepared bismuth-antimony single crystals. *Proc. of the XIV International Conference on Thermoelectrics*. pp.115-118, (1995).
- [5] B.Lenoir, M.Cassart, A.Dauscher, Yu.I.Ravich, H.Scherrer Highest Figure of Merit in Undoped $\text{Bi}_{1-x}\text{Sb}_x$ Alloys. *Proc. of the XIV International Conference on Thermoelectrics*. pp.115-118, (1995).
- [6] Grabov V.M., Ivanov G.A., Naletov V.L., Panarin A.F. Intervalley and interband scattering and thermoelectric figure of merit of Bismuth-Antimony Alloys. in *Poluprovodnicovye materialy dlia termoelektricheskikh preobrazovatelei*. Leningrad. Fiz. Teh. Inst. im. Ioffe, pp. 30-31, (1985), (in Russian).
- [7] Panarin A.F. The physical concept thermoelectric parameters optimisation of bismuth-antimony alloys. *Dissertatsiya kandidata fiziko-matematicheskikh nauk*. Leningrad, 144 p., (1976), (in Russian).
- [8] Zemskov V.S., Belaya A.D., Borodin P.G. Thermoelectric figure of merit of tin doped Bismuth-Antimony Alloys. *Izvestiya AN SSSR. Neorganicheskie materialy*. v.18, No.6, pp.1154-1157, (1982), (in Russian).
- [9] Zemskov V.S., Belaya A.D., Zayakin S.A., Bultova N.A. The magnetic field influence on the thermoelectric properties of tin doped $\text{Bi}_{0.91}\text{Sb}_{0.09}$ alloys.

Izvestiya AN SSSR. Neorganicheskie materialy. v.23, No.4, pp.554-557, (1987), (in Russian).

- [10] Shoenberg D. *Magnetic oscillations in metals*. Cambridge University Press, 612 p., (1984).

DOPING WITH ORGANIC HALOGEN-CONTAINING COMPOUNDS THE $Bi_2(Te,Se)_3$ SOLID SOLUTIONS

O.B.Sokolov, S.Ya.Skipidarov, N.I.Duvankov, E.V.Zaitsev
Nord Co., Moscow, RUSSIA

The paper considers the opportunity for the doping with organic halogen-containing compounds the $Bi_2(Te,Se)_3$ solid solutions. The advantages of their application as compared to that of inorganic halogen-containing compounds are described.

INTRODUCTION

For the doping of $Bi_2(Te,Se)_3$ solid solutions the following elements and compounds are used as donor additions[1,2]:

- halogens (Cl_2 , Br_2 , I_2);
- metals of the secondary subgroup of group I (Cu , Ag , Au);
- metals of the secondary subgroup of group II (Zn , Cd , Hg);
- halides of metals of group I ($AgCl$, $AgBr$, CuI , etc.);
- halides of metals of group II ($ZnCl_2$, $ZnBr_2$, ZnI_2 , $CdCl_2$, $CdBr_2$, CdI_2 , Hg_2Cl_2 , etc.);
- chlorides and iodides of bismuth and antimony ($SbCl_3$, $BiCl_3$, SbI_3 , BiI_3);
- chloreoxides of metals ($BiClO$, $SbClO$).

In actual practice for the doping of low-temperature thermoelectric materials, which are employed in cooling modules, chlorides of metals are usually used. To our view, of all these compounds mercury chloride (Hg_2Cl_2) is the most suitable dope. However it is liable to a breakdown in the presence of light. It is also hygroscopic, and liable to static-charge accumulation. All these factors may lead to errors in the process of its dosing. Furthermore, the presence of mercury in its composition does not allow to use this dope for thermoelectric materials intended for the application under higher temperatures.

CHOOSING A DOPE

According to Gibbs phase rule [3] the number of degrees of freedom in the system (F), i.e., the system variability, is unambiguously determined by the number of the system components (k) and by the number of co-existing phases (r): $F = k + 2 - r$.

Liberation of metal due to decomposition occurring in the process of doping with halogen-containing inorganic compounds results in the growth of the number of components in the system per unit. At the same time the number of phases does not change. Consequently, the number of degrees of freedom per unit increases.

The latter may negatively affect the reproducibility of properties of a thermoelectric material in the process of its formation, as well as the stability of its operating characteristics. In the context of the above mentioned the search for new dopes has been undertaken.

Undoubtedly, of certain interest for the study are the substances with high content of easily splitted-out halogen and which are free from elements negatively affecting the properties of the material. This condition is readily met by organic halogen-containing compounds. The molecule of such compounds is expressed by the following empirical formula: C_mX_n , where $X = Cl, Br, I$. The presence of carbon (C) in molecules of such compounds cannot be considered an obstacle for their application. Carbon does not actually react with the material components and does not dissolve in it. Consequently, a certain amount of carbon is consumed for the reduction of tellurium, bismuth and selenium oxides which are present in small amounts in the initial components. One can expect the residual carbon setting on the walls of a synthesis container in a graphite phase.

For the practical investigation of the doping efficiency of organic halogen-containing compounds hexachloroethane (C_2Cl_6) and hexachlorobenzole (C_6Cl_6) have been chosen. Table 1 below presents basic characteristics of the chosen organic halogen-containing compounds compared to those of one of inorganic halogen-containing compounds (mercurous chloride) [4].

Table 1

Alloying Additions Characteristics

Matter	Hg_2Cl_2	C_2Cl_6	C_6Cl_6
Appearance	White free-flow powder	White free-flow powder	White free-flow powder
Molecular mass	472.2	237	285
Density, g/cm ³	7.151	2.091	2.044
Melting point, K	-	462	501
Boiling point, K	-	-	605
Sublimation point, K	657	458	-
Chlorine content, mass. %	15.04	89.87	74.74

One should note, that the chosen organic compounds are not hygroscopic, but they are resistant to light, not liable to the accumulation of static charge and characterized by a high degree of chemical stability.

THE ANALYSIS OF THE BEHAVIOUR OF AN DOPES IN THE PROCESS OF SYNTHESIS

The synthesis of $Bi_2(Te,Se)_3$ solid solution was effected via the melting of components with a stoichiometric ratio in evacuated sealed-off quartz ampoules with an inside pressure $P = 0.1$ Pa under temperature $T = 1073$ K. For the identification of the composition of products formed in the process of thermal decomposition of dopes under consideration the authors have carried out a thermodynamic analysis using the parameters which meet the conditions of the synthesis ($P = 0.1$ Pa, $T = 1073$ K). The technique described in [5] has been used. The results of the analysis are presented in Table 2.

Note: condensed products formed in the process of thermal decomposition are marked by**.

From the above presented data one can come to the conclusion that under prescribed conditions of the synthesis the rates of doping of the material with the use of C_2Cl_6 and C_6Cl_6 are higher than those observed in such cases when calomel is used, as their thermal decomposition results in the formation of larger amounts of an active doping agent, monatomic chlorine in this case. The amount of products formed in the process of the dope incomplete decomposition is negligible in all cases. Nearly all the amount of carbon emitted in the process of C_2Cl_6 and C_6Cl_6 decomposition is in the condensed phase (graphite). The latter can be considered a favourable indicator, as it allows to eliminate the stage of quartz ampoules graphitization in the technological process, as the amount of graphite emitted in the process of thermal decomposition of the dopes under consideration is sufficient enough for the formation of a continuous film on the surface of the ampoules.

Through thermodynamic analysis the authors have assessed the influence of temperature and

pressure of the completeness of emission of the doping agent (chlorine) in the process of thermal decomposition of dopes. The results of the above mentioned assessment are presented in Table 3.

The Results of the Analysis of the Equilibrium Composition of the Products formed in the Process of Thermal Decomposition of Dopes (due account is given to the possible ionization)

Components Content, mol/kg					
Mercurous chloride		Hexachlorathan		Hexachlorbensole	
Cl	2.6366	Cl	12.0090	Cl	9.9832
Cl ₂	0.7839	Cl ₂	6.6675	Cl ₂	5.5427
Hg**	0.0000	C **	8.4481	C **	21.0690
Hg	4.2204	C	$3.498 \cdot 10^{-20}$	C	$2.908 \cdot 10^{-20}$
Hg ₂	$1.2283 \cdot 10^{-9}$	C ₂	0.0000	C ₂	0.0000
HgCl	0.3968	C ₃	0.0000	C ₃	0.0000
HgCl ₂ **	0.0000	C ₄	0.0000	C ₄	0.0000
HgCl ₂	0.0161	C ₅	0.0000	C ₅	0.0000
Hg ₂ Cl ₂ *	0.0000	CCl	$2.131 \cdot 10^{-12}$	CCl	$1.772 \cdot 10^{-12}$
Cl-	$2.077 \cdot 10^{-16}$	CCl ₂	$5.8397 \cdot 10^{-9}$	CCl ₂	$4.8545 \cdot 10^{-9}$
Hg+	$2.077 \cdot 10^{-16}$	CCl ₃	$5.3477 \cdot 10^{-9}$	CCl ₃	$4.4455 \cdot 10^{-9}$
		CCl ₄	$7.0033 \cdot 10^{-9}$	CCl ₄	$5.8219 \cdot 10^{-9}$
		C ₂ Cl	$2.166 \cdot 10^{-14}$	C ₂ Cl	$1.801 \cdot 10^{-14}$
		C ₂ Cl ₂	$1.9842 \cdot 10^{-7}$	C ₂ Cl ₂	$1.6495 \cdot 10^{-7}$
		C ₂ Cl ₃	$3.967 \cdot 10^{-13}$	C ₂ Cl ₃	$3.298 \cdot 10^{-13}$
		C ₂ Cl ₄	$1.322 \cdot 10^{-11}$	C ₂ Cl ₄	$1.099 \cdot 10^{-11}$
		C ₂ Cl ₅	$5.863 \cdot 10^{-20}$	C ₂ Cl ₅	$4.874 \cdot 10^{-20}$
		C ₂ Cl ₆	$5.203 \cdot 10^{-20}$	C ₂ Cl ₆	$4.325 \cdot 10^{-20}$
		Cl-	$1.071 \cdot 10^{-20}$	Cl-	$1.058 \cdot 10^{-20}$
		C+	0.0000	C+	0.0000
		C-	0.0000	C-	0.0000
		C ₂ +	0.0000	C ₂ +	0.0000
		C ₂ -	0.0000	C ₂ -	0.0000

Table 3
Temperature Dependence of the Amount (mol/kg) of Monatomic and Molecular Chlorine Emitted in the Process of the Dope Pyrolysis ($P = 0.1$ Pa)

T, K	Hg_2Cl_2		C_2Cl_6		C_6Cl_6	
	Cl	Cl_2	Cl	Cl_2	Cl	Cl_2
700	0.00003	0.00045	0.00839	12.6680	0.00698	10.5310
800	0.00380	0.03895	0.11872	12.6130	0.09869	10.4850
900	0.14133	0.71564	0.93742	12.2030	0.77926	10.1450
1000	1.18120	1.36160	4.83630	10.2540	4.02040	8.52410
1100	3.14070	5.41810	15.3110	5.01650	12.7280	4.17020
1200	4.06030	8.79690	23.3410	1.00150	19.4040	0.83253

The results of the analysis show that within the investigated temperature range the degree of dissociation to monoatoms of molecular chlorine which is emitted in the process of decomposition of alloying additions largely depends upon the temperature. As to mercury chloride is concerned, with the temperature growth the proportional growth of molecular and monoatomic chlorine content in decomposition products is observed. It means, that it is the first stage of the process, i.e. the emission of molecular chlorine, which is the limiting factor. As to C_2Cl_6 and C_6Cl_6 are concerned, high content of molecular chlorine in decomposition products is observed as early as under 700 K temperature. And temperature growth results in the decrease of its content accompanied by the growth of monoatomic chlorine content. That is, it is the second stage of the process, or dissociation of chlorine molecules, that is predominantly in progress. It is evident, that higher content of monoatomic chlorine (which is characterized by the highest chemical reactivity) in decomposition products will provide for the higher doping efficiency of organic chlorine-containing dopes as compared to that of mercurous chloride.

The assessment of the influence of the pressure made in the process of thermodynamic analysis (Table 4) shows that the increase of pressure in a quartz

ampoule in the process of synthesis of a semiconductive material may cause the reduction of monatomic chlorine content, and, as a result, the inhibition of the process of doping.

It is even more true for the cases when mercurous chloride is used, as for both hexachloroethane and hexachlorobenzene the level of critical pressure, at which the content of monoatomic chlorine dramatically decreases, is higher by 50 - 100 times and even more.

In the process of thermodynamic analysis the assessment of the opportunity for the application of the following organic fluorine-, bromine- and iodine-containing compounds, for instance, polyfluorethylene ($(C_2F_4)_n$), bromoform ($CHBr_3$) and iodoform (CHI_3), as dopes has been made. The calculations have been made on the basis of the values of such parameters which meet the conditions of the synthesis of a semi-conductive material (Table 5).

Table 5
The Results of the Calculation of the Equilibrium Composition of the Main Products of Thermal Decomposition of Polyfluorethylene, Bromoform and Iodoform ($T=1073$ K, $P=0.1$ Pa)

Components Content, mol/kg					
$(C_2F_4)_n$		$CHBr_3$		CHI_3	
F	0.00002	Br	7.8509	I	7.4826
C **	24.1860	Br_2	0.0319	I_2	0.0006
CF_2	0.00004	C **	3.9568	C **	2.5398
CF_3	0.00001	H	0.00001	H	0.00005
CF_4	8.06200	H_2	0.0005	H_2	1.2021
		HBr	3.9557	HI	0.1356

The data on the composition of products of thermal decomposition shows that fluorene-containing substances are rather stable even under high temperatures, and the content of monatomic fluorene in the products of pyrolysis is very low to provide for the efficient doping of a semiconductive material.

The above bromine- and iodine-containing substances may be used as dopes because in the process of their pyrolysis a substantial amount of an active doping

Table 4
Pressure Influence on the Amount (mol/kg) of Monatomic and Molecular Chlorine Emitted in the Process of Dope Pyrolysis ($T = 1073$ K)

P, Pa	Hg_2Cl_2		C_2Cl_6		C_6Cl_6	
	Cl	Cl_2	Cl	Cl_2	Cl	Cl_2
0.01	3.91720	0.15937	21.8500	1.74690	18.1640	1.45230
0.05	3.14670	0.53955	15.3480	4.99820	12.7590	4.15500
0.10	2.63660	0.78388	12.0090	6.66740	9.98350	5.54260
0.50	1.42550	1.26630	5.92960	9.70730	4.92920	8.06970
1.00	1.00220	1.32190	4.25150	10.5460	3.53430	8.76720
5.00	0.34510	0.93244	1.92310	11.7110	1.59860	9.73500

agent, in this case it is monatomic bromine or monatomic iodine, as well as hydrobromic and hydroiodic acids are formed. Small amount of emitted hydrogen creates (together with carbon) a favourable environment for the deoxidation of the initial components. Carbon initially contained in bromoform and iodoform is nearly completely emitted in a solid phase (graphite).

TEST RESULTS

With the use of the vertical zone-melting technique [6], three process runs (Fig.1) and temperature gradient at the solid-liquid interface of 18-19 K/mm zone-melted ingots of $N\text{-Bi}_2(\text{Te},\text{Se})_3$ material have been produced.

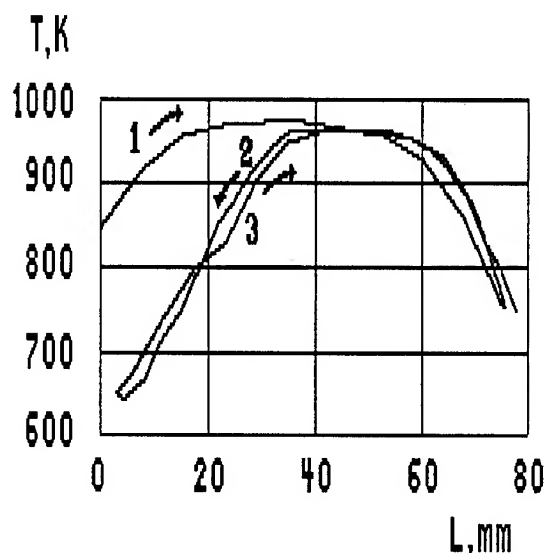


Fig.1. Changing of the Material Temperature in the Process of the Ingot Growth: 1 - first run, (heater temperature $T_h = 1133$ K); 2 - second run, ($T_h = 1123$ K); 3 - third run, ($T_h = 1123$ K).

The ingot diameter is 20 and 45 mm, and length is 200 - 220 mm. All measurements of properties have been taken in parallel to the growth direction. Figures 2 and 3 present dope content dependence of thermoelectric characteristics of $N\text{-Bi}_2(\text{Te},\text{Se})_3$. They prove that for the doping with organic halogen-containing compounds high thermoelectric figure of merit is retained, and it allows to identify an optimum content of an dope.

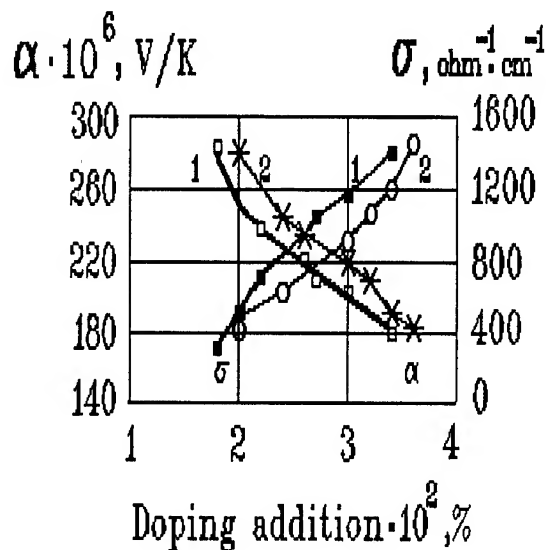


Fig.2. Dope Content Dependence of Seebeck Coefficient () and Conductivity () of $\text{Bi}_2(\text{Te}_{0.90}\text{Se}_{0.10})_3$ under 300 K: 1 - C_2Cl_6 , 2- C_6Cl_6 .

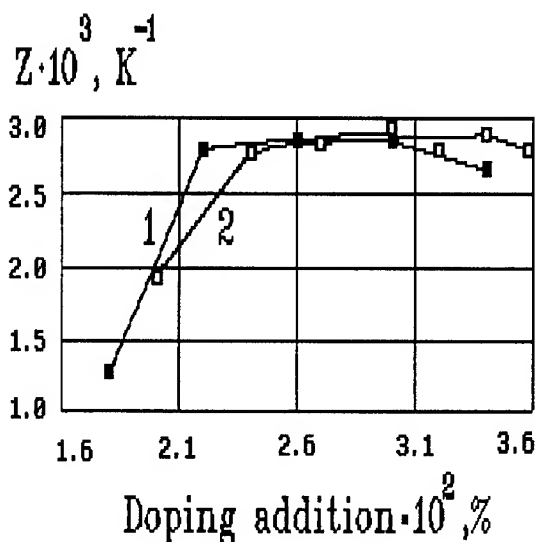


Fig.3. Dope Content Dependence of the Thermoelectric Figure of Merit (Z) of $\text{Bi}_2(\text{Te}_{0.90}\text{Se}_{0.10})_3$ under 300 K: 1 - C_2Cl_6 , 2- C_6Cl_6 .

Data presented in Table 6 proves that all the investigated additions have an equal doping efficiency with an equal optimum content of the doping agent (chlorine). It shows that mercury (if calomel is used) does not produce a doping effect.

Table 6

Doping Efficiency of Dopes and a Doping Agent

Dope	Hg ₂ Cl ₂	C ₂ Cl ₆	C ₆ Cl ₆
Optimum content, mass. %	0.15	0.026	0.031
Doping Agent (Chlorine) Content, mass. %	0.023	0.023	0.023
Conductivity, Ohm ⁻¹ ·cm ⁻¹	1000	1000	1000
Seebeck coefficient, V/K	210-215	210-215	210-215
Figure of Merit × 10 ³ , K ⁻¹	2.80-3.00	2.80-3.00	2.80-3.00

CONCLUSIONS

1. The opportunity for the application of organic halogen-containing compounds as dopes for the synthesis of thermoelectrical semi-conductive material on the basis of bismuth telluride and bismuth selenide solid solutions is described.

2. Through the methods of thermodynamic analysis the advantages of organic halogen-containing compounds as compared to inorganic ones (for instance, mercurous chloride) are proved from the viewpoint of the pyrolysis of these dopes under conditions of the synthesis of the material and formation of the active doping agent, i.e. monatomic halogen.

3. As a practical example, the experimental research into the doping ability of hexachloroethane and hexachlorobenzole has been effected and high thermoelectric figure of merit of the synthesized semi-conductive material has been proved.

REFERENCES

1. J.Przytowski, K.Borkowski, "Doping of Bi₂Te₃ and its alloys", Proceedings 4th International Conference on Thermoelectric Energy Conversion, University of Texas at Arlington, Arlington, Texas, 1982, pp.157- 159.
2. B.M.Goltzman, B.A.Kudinov, I.A.Smirnov, "Semiconducting thermoelectric materials based on Bi₂Te₃", "Nauka Publishers", Moskow, 1972, 320 p. (in Russian)
3. A.Findley, "The phase rule and its applications", Longmans, Green and Co., London-NewYork-Toronto, 1931, 318 p.
4. V.A.Rabinovich, Z.Ya.Havin, "Abridged Reference Book on Chemistry", "Khimiya Publishers", L., 1977, 376 p. (in Russian)
5. G.B.Sinyarev, N.A.Vatolin, B.G.Trusov, G.K.Moiseev, "Computer-Aided Thermodynamic Analysis of Metallurgical Processes", M., "Nauka Publishers", 1982, 263 p. (in Russian)

6. A.I.Anukhin, S.Ya.Skipidarov, O.B.Sokolov, "Statistical micro-inhomogeneities in (Bi,Sb)₂Te₃ solid solutions grown from melt with excess content of tellurium", Proceedings 14th International Conference on Thermoelectric Energy Conversion, St-Petersburg, Russia, 1995, pp.65-71.

Orientational Distribution and Procedure Parameters in Hot Pressed $(\text{Bi}_2\text{Te}_3)_{0.90}(\text{Bi}_2\text{Se}_3)_{0.10}$

K. Fukuda¹, H. Imaizumi¹, T. Ishii¹, F. Toyoda², M. Yamanashi² and Y. Kibayashi²

¹Research Center, KOMATSU Ltd., Hiratsuka 254, Japan

²Komatsu Electronics Inc., Hiratsuka 254, Japan

Abstract

Single crystals of Bi_2Te_3 and its solid solutions with Bi_2Se_3 for n type material show anisotropy of thermoelectric property. Hot-pressed materials also show the anisotropy, but it is weaker than the single crystal's and the one directional polycrystal's. In a hot pressed material, crystal grains orient with an orientational distribution.

In this work, we compared the orientational distributions of hot-pressed materials which were made by different process conditions and attempted to lead the best procedure parameters of a hot-pressed material that give a high Z-value.

Introduction

The crystals of the Bi_2Te_3 and its alloys show uniaxial anisotropy in both electrical and thermal properties which are originated from the crystal structure [1][2]. The structure of these materials are hexagonal (or rhombohedral) [3]. These crystals have atomic layers which are stacked alternately along the c-axis in the sequence: -Te(1)-Bi-Te(2)-Bi-Te(1)-Te(1)-. The bonding of Te(1)-Te(1) is weak -van der Waal's force [4]. Therefore, these compounds are cleaved perpendicular to the c-axis.

Both thermal and electrical conductivities in the direction perpendicular to the c-axis (in the c-plane) are larger than that in the direction parallel to the c-axis. The Seebeck coefficient shows only a slight difference in anisotropy. The electrical conductivity in the c-plane is larger by about four times than the conductivity parallel to the c-axis in pure Bi_2Te_3 . On the other hand, the thermal conductivity in the c-plane is larger by about two times than parallel to the c-axis. The difference of the anisotropy ratios of each thermoelectric property causes the anisotropy of the figure of merit. The figure of merit in the direction perpendicular to the c-axis, which is called the a-direction and uses the notation small a in this paper, is approximately two times as large as the figure of merit along the c-axis, which is called the c-direction and uses the notation small c in this paper, in n-type alloys [5]. This difference is relatively small for p-type materials.

Sintered Bi_2Te_3 and its alloys also show anisotropy [6][7][8][9][10]. The conductivity in the pressed direction is smaller than that in perpendicular to that direction. The powder's shape of Bi_2Te_3 and its alloys are flaky because of their cleavage properties. When the powders are pressed, they slip along the cleavage planes. Each powder's c-axes tend to align to the pressed direction, but it is imperfect. The powders orient their c-axes with an orientational distribution. Of course, each of the

powders have anisotropic properties as the single crystal. Thus, the figure of merit of sintered materials depend on the distribution of the powder grain's orientation [11]. The orientational distribution can be determined by X-ray diffraction.

In the last work [12], we showed that the results which were calculated from two dimensional orientation distribution functions were in good agreement with the experimental results, and the figure of merit of hot pressed materials were decreased about 30% compared with the single crystal's.

Model

We consider electric and thermal conductivities in the direction with the angle θ to the a-axis in a anisotropy crystal such as Bi_2Te_3 [13]. The a-axis is selected from one of the directions in the c-plane freely. There are two cases to measure electrical and thermal conductivities. In one case, the electrical and thermal current density vectors are parallel to the axis of the sample and the electrical and thermal conductivities are measured parallel to these vectors. In the other case, the electrical and thermal gradient vectors are parallel to the axis of the sample. The electrical and thermal conductivities are measured parallel to these vectors. In the present study, we prepared near the rod shape sample in which the sample current was loaded along the rod. Then we adopted the first case. This case is shown in Fig.1

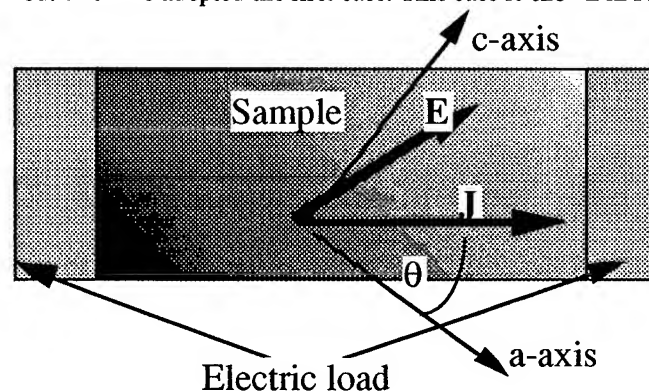


Fig. 1 Current density in a long rod. It makes the angle θ with the a-axis of crystal

Fig.1 illustrates the electric current density vectors with the angle θ to the a-axis. The electric current vector J is given by

$$J = (J \cos \theta, J \sin \theta), \quad (1)$$

where J is the magnitude of the electric current density vector. The electric resistivity tensor is given by

$$\rho = \begin{pmatrix} \rho_a & 0 \\ 0 & \rho_c \end{pmatrix} \quad (2)$$

where ρ_a is the electric resistivity parallel to the a-axis and ρ_c is the resistivity parallel to the c-axis. The electric field vector \mathbf{E} and electric resistivity $\rho(\theta)$ with the angle θ to the a-axis are given by

$$\mathbf{E} = \rho \mathbf{J} \quad (3)$$

and

$$\rho(\theta) = \mathbf{J} \cdot \mathbf{E} / J^2. \quad (4)$$

Then we obtain $\rho(\theta)$ as follows;

$$\rho(\theta) = \rho_a \cos^2 \theta + \rho_c \sin^2 \theta \quad (5)$$

and the electrical conductivity is defined by

$$\sigma(\theta) = 1/\rho(\theta). \quad (6)$$

The thermal conductivity is obtained similarly.

The conductivity of one grain which is in the hot pressed sample is calculated by this model. The c-axis of one grain oriented with angle θ to the rod shape sample is in the same condition as shown Fig.1. In the rod shape sample model, the normalized electric resistivity $\rho(\theta)$ and thermal resistivity $r(\theta)$ are given respectively by

$$\rho(\theta)/\rho_a = \cos^2 \theta + \rho_c/\rho_a \sin^2 \theta \quad (7)$$

and

$$r(\theta)/r_a = \cos^2 \theta + r_c/r_a \sin^2 \theta \quad (8)$$

where r_c is thermal resistivity parallel to the c-axis and r_a is resistivity in the c-plane.

The two dimensional orientational distribution function $\omega(\theta)$ is defined by how many crystal grains are oriented to the direction with angle θ which is made by their cleavage plane in the hot pressed ingot and the plane perpendicular to the pressed direction. The function is obtained by x-ray measurement [14].

The electric resistance in a hot pressed material is a series of each grain's resistance, which are defined in each orientation angle θ . Then, using the orientation distribution function $\omega(\theta)$, the electric resistivity in the direction perpendicular to the pressed direction ρ_A is normalized by ρ_a and given as

$$\begin{aligned} \rho_A / \rho_a &= \frac{1}{\rho_a} \int_0^{\pi/2} \rho(\theta) \omega(\theta) d\theta \\ &= \int_0^{\pi/2} (\cos^2 \theta + \rho_c / \rho_a \sin^2 \theta) \omega(\theta) d\theta \end{aligned} \quad (9)$$

and the normalized electric resistance in the direction parallel to the pressed direction ρ_C is given as

$$\begin{aligned} \rho_C / \rho_a &= \frac{1}{\rho_a} \int_0^{\pi/2} \rho(\theta) (\pi/2 - \theta) d\theta \\ &= \int_0^{\pi/2} (\rho_c / \rho_a \cos^2 \theta + \sin^2 \theta) \omega(\theta) d\theta \end{aligned} \quad (10)$$

where $\omega(\theta)$ is normalized for integration from 0 to $\pi/2$;

$$1 = \int_0^{\pi/2} \omega(\theta) d\theta \quad (11)$$

Notation A indicates the direction perpendicular to the pressed direction and notation C indicates the direction parallel to the pressed direction. With thermal resistivity, we can obtain this by changing a notation from " ρ " to " r ".

Experiments

Sample preparation

All raw materials were element materials with the grade of 99.999%. They were weighed with the ratio of stoichiometry of $(\text{Bi}_2\text{Te}_3)_{0.90}(\text{Bi}_2\text{Se}_3)_{0.10}$ and encapsulated in an evacuated Pyrex tube with 0.3 atom argon gas. Before encapsulating, HgCl_2 was added as a dopant. The raw materials and dopants which were encapsulated in the Pyrex tube were heated to above the melting point, and the melt in the tube was shaken sufficiently by the rocking furnace. The melt was solidified by the Bridgman method. The solidified ingot was ground into a powder in a ceramic mortar, and the powder was shifted between 200 and 400 mesh (74 micron and 37 micron). We used this powder and the fine powder which was passed through the 400 mesh sieve in the experiment. These powders were annealed at 620K for 10 hours in a reducing atmosphere of hydrogen gas, and hot pressing was accomplished in an argon atmosphere. The size of ingot was 40 x 40 x 20mm. Several ingots were prepared by using different procedure parameters; hot press temperatures, pressures and powder grain sizes.

X-ray Measurement

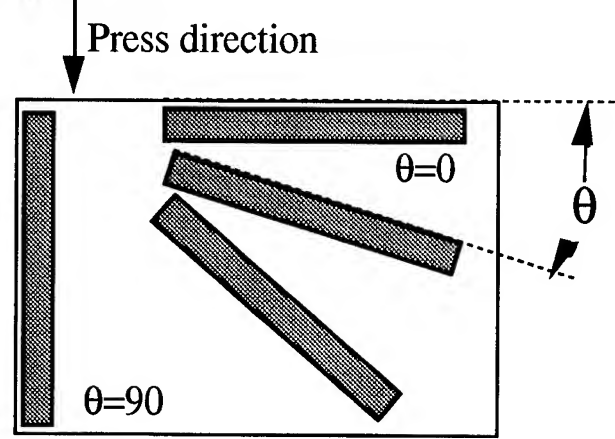


Fig.2 Test pieces cut from hot pressed ingot

Test pieces were cut from each hot pressed ingots with a tilting angle θ , as shown in Fig.2. The tilting angle was from 0 to 90 degrees. The size of the test piece was 25 x 7.5 x 1 mm. Each test piece was set in a X-ray diffractometer holder (CuK α radiation, 50KV and 150mA) and the area 25x7.5mm² was irradiated by the X-ray. Fig.3 and Fig.4 show XRD patterns of the hot pressed sample cut with tilted 0 degree and 90 degrees, (perpendicular press direction and parallel press direction), respectively at room temperature. Reflections such as (0,0,3), (0,0,6) and (0,0,15) were observed in the 0-degree sample very well, but their intensities became very weak in the 90-degree sample. We measured the integral intensities of the Bragg reflection (0,0,6) in dozen pieces which were tilted in angles from 0 to 90 degrees without any intensity correction. The intensities of each piece were plotted as variables of the tilted angles.

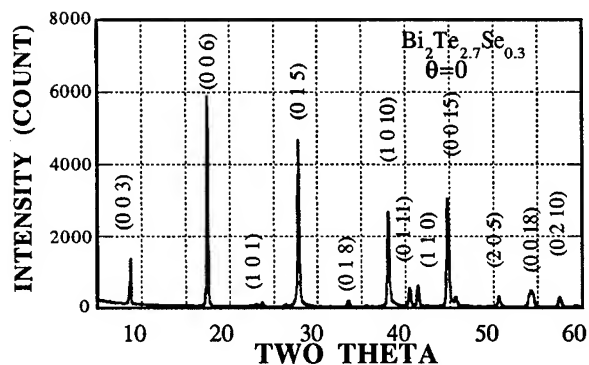


Fig. 3 XRD pattern of the hot pressed sample tilted 0 degree

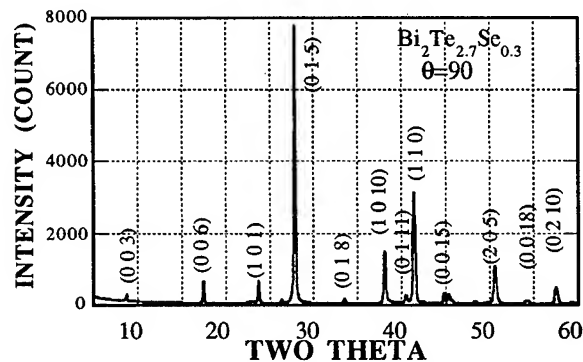


Fig. 4 XRD pattern of the hot pressed sample tilted 90 degrees

Measurement of the thermoelectric properties

The electrical resistivity, the Seebeck coefficient and the thermal conductivity were measured at room temperature (300K). The electrical resistance was obtained from the measurement of a.c. resistance. The Seebeck coefficient was obtained by measuring the thermopower which was caused by the temperature difference. The thermal conductivity was measured using TF101 Test System which was made by TE Technonlogy Inc.[15].

Results and discussion

We chose three parameters of the hot press procedure; hot press temperature, pressure and grain size, and made several hot pressed ingots by changing these parameters. Table 1 shows the procedure parameters of the each ingot. The thermoelectric properties of both the A and C direction of each hot pressed ingots, the anisotropies of the electrical resistivity and the anisotropies of the thermal conductivity and density ratios are

shown as Table 2.

Table 1 Procedure parameters

Ingot	Hot press temperature (K)	Hot press pressure (kg/cm ²)	Grain size (micron)
A	720	750	37-74
B	770	750	37-74
C	820	750	37-74
D	770	1000	37-74
E	770	500	37-74
F	770	750	under 37

Hot press temperature

Ingots A, B and C were pressed at 720K, 770K and 820K. They were made in the same conditions except for the hot press temperature.

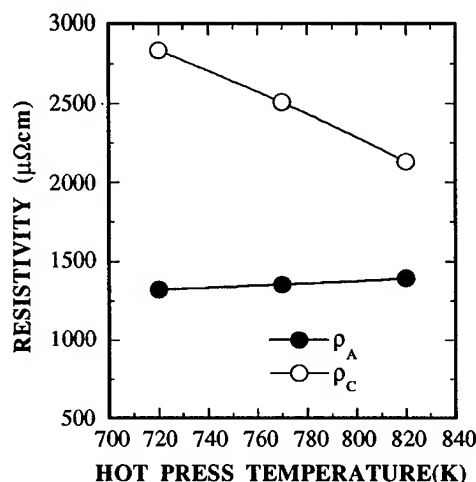


Fig.5 Electrical resistivities of both the directions of Ingots A, B and C

Fig.5 shows the hot press temperature and both electrical conductivities; ρ_A and ρ_C . Resistivity ρ_A is not changed by the hot press temperature in this range. On one hand, the resistivity ρ_C depends on the hot press temperature. It decreases linearly as the hot press temperature increases.

The anisotropy ratio ρ_C/ρ_A also decreases as the hot press

Table 2 Thermoelectric property of three hot pressed samples at 300K

Ingot	α_A ($\mu\text{V/deg}$)	α_C ($\mu\text{V/deg}$)	ρ_A ($\mu\Omega/\text{cm}$)	ρ_C ($\mu\Omega/\text{cm}$)	κ_A (mW/cmdeg)	κ_C (mW/cmdeg)	ρ_C/ρ_A	κ_A/κ_C	Density ratio%
A	207	202	1323	2835	15.19	9.82	2.14	1.55	99.3
B	208	203	1355	2506	14.29	10.74	1.85	1.33	99.8
C	208	205	1393	2132	13.92	11.02	1.53	1.26	99.8
D	210	204	1458	2698	14.66	10.17	1.85	1.44	99.8
E	207	204	1352	2445	14.67	10.82	1.81	1.36	99.8
F	238	239	2470	3386	12.38	11	1.37	1.13	98.3

temperature increases. In the last work, we showed that the anisotropy ratio depended on the orientational distribution of the ingot. Fig.6 shows the orientational distribution functions of three ingots, and Table 3 shows both the measured and the calculated anisotropy ratios of the electrical resistivity and thermal conductivities. The calculated ratios were obtained by using Eq. 9, 10 and each of the orientational distribution functions $\omega(\theta)$. We assumed that the anisotropy ratio of the electrical resistivity ρ_c/ρ_a in a single crystal is 4 and the anisotropy ratio of the thermal resistivity κ_c/κ_a in a single crystal is 2 respectively [5][13].

Ingots A and B have similar orientational distributions, and the ingot C has a weaker random distribution compared with the others.

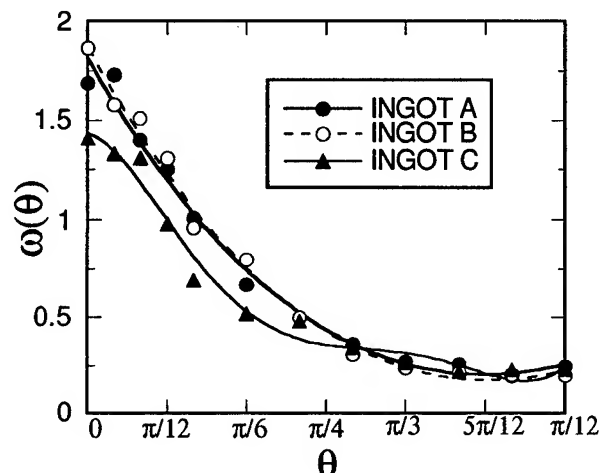


Fig.6 The orientational distribution function of three ingots made at different hot press temperatures.

Table 3 Comparison of the anisotropies in ingots A, B and C

Ingot	H.P.Temp.	Measurement		Calculation	
		ρ_c/ρ_a	κ_c/κ_a	ρ_c/ρ_a	κ_c/κ_a
A	720	2.14	1.55	1.80	1.38
B	770	1.85	1.33	1.88	1.45
C	820	1.53	1.26	1.71	1.34

Because these ingots have similar orientational distributions, the calculated results of the three ingots' anisotropy ratios are almost the same value. From these results, it is realized that the hot press temperature's dependence of ρ_c is not caused by the difference of the orientational distribution.

It is natural to think that the dependence of ρ_c is caused by the grain's binding. When an ingot is hot pressed, the grains in a hot pressed ingot seem to be bound anisotropically by the crystal's axis. If an ingot is hot pressed at a low temperature, the grains are not bound enough in the direction parallel to the c-axis, so the ρ_c is at high value. The imperfect binding along

the c-axis also influences the density ratio of ingot A, which is slightly smaller than the others.

The weaker random distribution of ingot C seems to be caused by the growing of the grains in the ingots under high temperature hot pressing.

Hot press pressure

Ingots D, B and E were pressed at the pressures 500, 750 and 1000 kg/cm². They were made in the same condition except for the pressure. Regarding the anisotropy ratio, there are not great differences in these ingots. The hot press pressure is not an important procedure parameter for the orientational distribution in this pressure range. At the present, we can not understand why the carriers decrease in ingot D.

Grain size.

Ingot F was made of the powder which size was under 37 microns. High values of α and ρ indicate low carrier density in ingot F. The reason of the decrease of carrier is not understood in detail, but it seems to be related with the surface of the powder. Fig.7 shows the orientational distribution functions of ingots B and F. The orientational distribution of ingot F shows more randomness than in ingot B. Random distribution makes both the electrical and the thermal conductivities decrease. Table 4 shows both the measured and calculated anisotropy ratios of the electrical resistivity and thermal conductivity. The calculated anisotropy ratios are in good agreement with the measurement ones. From these results, the decrease of both the electrical and thermal conductivities are only caused by random orientation. In this grain size, the grain boundary does not affect the electrical and thermal conductivities.

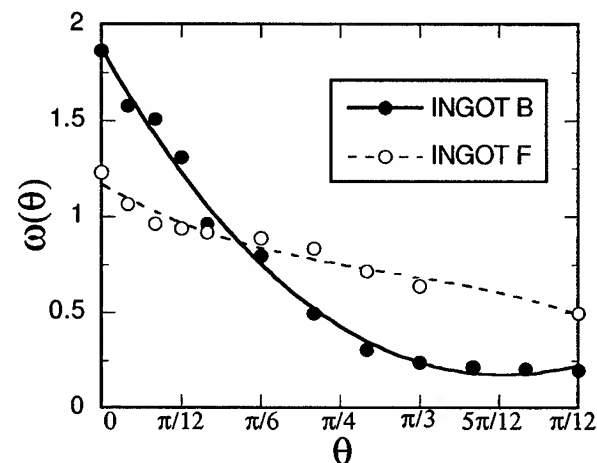


Fig.7 The orientational distribution function of two ingots made of different powder's grain size

Table 4 Comparison of the anisotropies in ingots B and F

Ingot	Grain size	Measurement		Calculation	
		ρ_c/ρ_a	κ_c/κ_a	ρ_c/ρ_a	κ_c/κ_a
B	37-74	1.85	1.33	1.88	1.45
F	under 37	1.37	1.12	1.20	1.18

Conclusion

We evaluated six ingots which were made in different procedure conditions. We especially noticed the orientation of grains in the hot press ingots. The hot press pressure did not affect the orientational distribution. The hot press temperature also did not affect the orientation, but it affected the binding of the grain. In the hot pressed ingot achieved at a low temperature, the binding between the cleavage planes was not enough. This imperfection of the binding made the anisotropies of the conductivities. The procedure parameter which was the most influenced in this experiment was the grain size. The hot pressed material which was produced by the fine powders tended to have random orientational distribution.

After completing this experiment, we could not improve the orientational distribution in hot pressed materials which give a high Z-value. We realize that further experimentation is required on this subject, and want to continue to research further.

Acknowledgments

We would like to thank to T.Hironiwa, K.Hara, T.Nakajima, A.Karita, T.Miyagi and M.Hamada for the measurement and the preparation samples. We also would like to thank to D.Wiseman for the helpful support.

References

- [1] J.R.Drabble, "Galvanomagnetic Effects in p-Type Bismuth Telluride", Proc. Phys. Soc. London, London, pp. 380 (1958).
- [2] J.R.Drabble, R.D.Groves, and R.Wolf, "Galvanomagnetic Effects in n-Type Bismuth Telluride", Proc. Phys. Soc. London, London, pp. 430 (1958).
- [3] R.Wiese and L.Muldawer, "Lattice Constants of Bi_2Te_3 - Bi_2Se_3 Solid Solution", J. Phys. Chem. Solids, vol.15, pp.13-16 (1960).
- [4] J.R.Drabble, "Chemical Bonding in Bismuth Telluride", J. Phys. Chem. Solids, vol.5, pp.142-144 (1958).
- [5] H.J.Goldschmid, "Recent Studies of Bismuth Telluride and its Alloys", J. Appl. Phys., vol.32, No.10, pp.2198-2202 (1961).
- [6] H.Imaizumi, et al., "Thermoelectric Properties N-Type $\text{Bi}_2(\text{Te},\text{Se})_3$ by Hot-Pressing". Proc. 7th International Conference on Thermoelectric Energy Conversion, Arlington USA, pp. 141-145 (1988).
- [7] I.J.Ohsugi, et al., "Analysis of The Anisotropic Resistivities and Hall Coefficients of Sintered, N-type Bi_2Te_3 ", Proc. 8th International Conference on Thermoelectric Energy Conversion, Nancy France, pp. 32-34 (1989).
- [8] I.J.Ohsugi, et al., "Evaluation of Anisotropic Thermoelectricity of Sintered Bi_2Te_3 on the Basis of the Orientation Distribution of Crystallites", J. Appl. Phys., vol.76, No.4, pp.2235-2239 (1994).
- [9] H.J.Goldschmid and M.Situmorang, "Sintered Bismuth Telluride Alloys-Problems of Orientation", Proc. 8th International Conference on Thermoelectric Energy Conversion, Nancy France, pp. 1-6 (1989).
- [10] R.Griot, G.Brun, and J.C.Tednac, "Orientation Effects in Sintered Thermoelectric Material", Proc. 8th International Conference on Thermoelectric Energy Conversion, Nancy, France, pp. 27-31 (1989).
- [11] A.W.Penn, "The Thermoelectric Properties of N-Type Single Crystals of Bismuth Seleno-Telluride and their Relationship those of Pressed Powder Compacts", Advanced Energy Conversion, vol.7, pp.257-264 (1968).
- [12] K.Fukuda et al., "Orientational Distribution in Hot pressed N-type Bi_2Te_3 ", International Conference on Thermoelectrics, St.Petersburg Russia, pp. 135-149 (1989).
- [13] J.H.Madigan, "Dependence of the Thermoelectric Figure of Merit on the Orientation in Uniaxial Crystals", J. Appl. Phys., vol.33, No.12, pp.3564-3567 (1962).
- [14] I.J.Ohsugi, T.Kojima, and I.A.Nishida, "Orientation Analysis of the Anisotropic Galvanomagnetism of Sintered Bi_2Te_3 ", J. Appl. Phys., vol.68, No.11, pp.5692-5695 (1990).
- [15] R.J.Buist, "The New Methodology for Testing Thermoelectric Materials and Devices", Arlington USA, pp. 196-209 (1992).

CHARGE CARRIER MOBILITY IN $\text{Bi}_2\text{Te}_{3-x}\text{Se}_x$ ($x < 0.4$) SOLID SOLUTION WITH EXCESS OF Te

Kutasov V.A., Luk'yanova L.N., Konstantinov P.P., Alekseeva G.T.
A.F. Ioffe Physical-Technical Institute, Russian Academy of Sciences, Russia

Abstract.

Thermoelectric and galvanomagnetic properties of $n\text{-Bi}_2\text{Te}_{3-x}\text{Se}_x$ ($x < 0.4$) solid solutions with the carrier density $\leq 1 \cdot 10^{18} \text{ cm}^{-3}$ are studied. Some peculiarities of the mobility temperature dependence with account of the effective scattering parameter r_{eff} are discussed.

Investigation of the possibility of a deep cooling by means of thermoelectric methods is initiated not only studies on high- T_c superconductivity but also achievements in the range of sensor techniques. Investigations of the materials based on solid solutions of Bi and Sb chalcogenides [1] are shown that a six cascades module may be produced maximum temperature difference $\Delta T_{\text{max}} = 150^\circ$ for hot junction temperature about 300 K. The results of these studies were shown that a decrease of the carrier density is allowed to use of the n-type materials at more low temperatures.

The parameter $(m^*/m)^{3/2} \mu_0$ (where m^* and μ_0 are the density of states effective mass and the mobility of charge carriers with account of degeneracy of an electron gas, m is the free electron mass) is the important value, that defines a figure of merit Z at considered temperature in the range of impurity conductivity. A comparison of the mobility value from data on different authors [2-5] are not always corrected because in refs. [2-3] the mobility in bismuth telluride and solid solutions is calculated from measurements of all indispensable galvanomagnetic effects and in refs. [4-5] from electroconductivity and Hall effect data only. Nevertheless temperature dependence of the mobility in Bi_2Te_3 is detail investigated since the carrier density is constant at studied temperatures and the dependence of $\mu_0(T)$ may be calculated from the experimental temperature dependence of $\sigma(T)$.

The electroconductivity temperature dependence for classical statistic and the acoustic mechanism of carrier scattering can be represented in the following form:

$$\sigma \sim T^{-3/2} m^{*-5/2} \quad (1)$$

The electroconductivity σ_0 is considered in the case of arbitrary degeneracy analogously of μ_0 .

The experimental dependences of $\sigma(T)$ in Bi_2Te_3 with carrier densities $(1 \div 10) \cdot 10^{19} \text{ cm}^{-3}$ are differed from $T^{-3/2}$ (from T^{-2} to $T^{-1.2}$) and are explained by weak temperature dependence of the density of states effective mass [6,7]. For low carrier density ($n < 10^{18} \text{ cm}^{-3}$) the more strong change of the mobility with temperature is observed: the dependence of the form $\mu_0 \sim T^{-2.3}$ [8] is explained by temperature dependence of m^* , a variation of the mobility

$\mu_0 \sim T^{-2.8}$ [9] is connected to influence of scattering on optical phonons for temperature below Debye one. The analogous of $\sigma(T)$ dependences are observed in Bi_2Te_3 -based on solid solutions with increase of the carrier density n . The index of a power in the dependence of $\sigma(T)$ for equal n is decreased in comparing with Bi_2Te_3 owing to additional scattering on the atoms of the second component of solid solution. Investigation of $\text{Bi}_2\text{Te}_{3-x}\text{Se}_x$ ($0 < x < 0.3$) solid solutions is limited usually by the range of the optimal carrier density $n = (1 \div 3) \cdot 10^{19} \text{ cm}^{-3}$ near the room temperature. These materials with low density ($n < 10^{18} \text{ cm}^{-3}$) is not studied systematically, but this range of concentrations is interested not only for practical application, but it is permitted to study specific peculiarities of scattering mechanism.

At the present work thermoelectric and galvanomagnetic properties of $n\text{-Bi}_2\text{Te}_{3-x}\text{Se}_x$ ($x = 0.3; 0.36$) solid solutions were measured in the range of temperature interval from 80 to 300 K. Samples for measurements were grown by directed crystallization method in the conditions excluding a concentration overcooling [10]. The temperature gradient on the front of crystallization was about 200 K cm^{-1} , a rate of crystallization was no more than 0.5 mm/min . Cleavage planes (0001) in the samples were oriented along crystallization axis, block-crystalline structure of the samples provided to cut single crystals for measurement of Hall effect.

Instead of widely used doping of ordinary impurities (halogenides of some metals) we now used excess Te for deviation from stoichiometric composition. This way permitted to exclude the influence of the additional scattering on donor impurities especially for low temperatures and to obtain the materials with controlled values of the carrier density.

Usually analysis of temperature dependences of the thermoelectric properties is carried out for the acoustic mechanism of carrier scattering (a scattering parameter $r = -0.5$, where r is the index of a power in the dependence of relaxation time τ on energy: $\tau = \tau_0 E^r$). Such analysis without account of complicated band structure and a mixed scattering mechanism in the solid solutions based on Bi_2Te_3 may be used for qualitative estimations. In ref. [11] the thermoelectric and the galvanomagnetic properties of $p\text{-Bi}_{2-x}\text{Sb}_x\text{Te}_3$ solid solutions are analyzed assuming a non-parabolic one-band model and mixed carrier scattering. The results of investigations of the thermoelectric and the galvanomagnetic properties in bismuth telluride and its solid solutions [12] are shown the necessity to use the effective scattering parameter r_{eff} . The parameter r_{eff} takes into account as peculiarities of the band structure as the mechanism of

carrier scattering. The value r_{eff} is changed from -0.38 to -0.82 on composition of solid solution, temperature and carrier density [12,13].

Temperature dependences of the thermoelectric power α and the electroconductivity σ in $\text{Bi}_2\text{Te}_{3-x}\text{Se}_x$ ($x = 0.3; 0.36$) solid solutions are shown in Fig.1,2. High values of the thermoelectric power in studied temperature interval (Fig.2, curves 1,2,4) point out to low carrier concentration of the samples. Sharp temperature dependence of the electroconductivity is connected with increasing of the mobility at low temperatures.

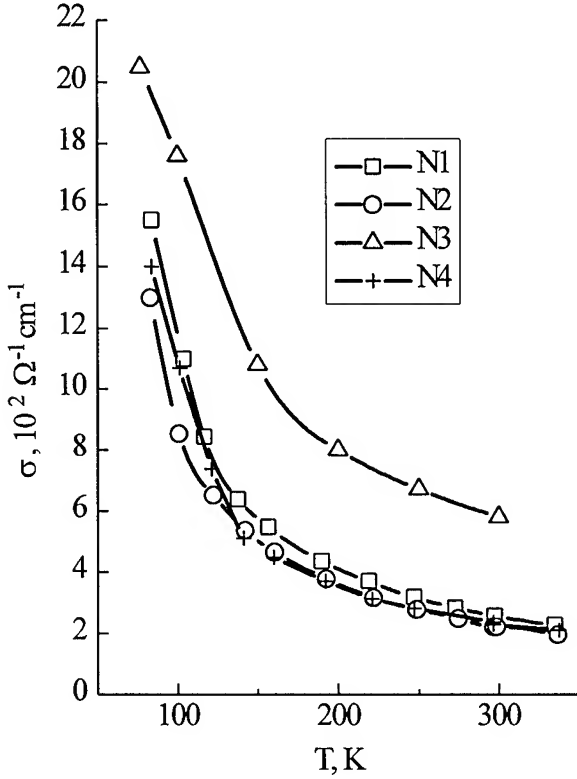


Fig.1 Temperature dependences of the electroconductivity σ in $\text{Bi}_2\text{Te}_{3-x}\text{Se}_x$ solid solutions.
x: 1, 2, 3 - 0.3; 4 - 0.36.

Analysis of the experimental data of $\alpha(T)$ and $\sigma(T)$ are carried out in accordance with the expressions applied for semiconductor in the range of impurity conductivity and a arbitrary degeneracy:

$$n = \frac{4(2\pi m^* k_0 T)^{3/2} F_{1/2}(\eta)}{\sqrt{\pi} h^3} \quad (2)$$

$$\sigma = en\mu \quad (3)$$

$$\mu = \frac{\sqrt{\pi}}{2} \frac{F_{r+1/2}(\eta)}{\Gamma(r+3/2) F_{1/2}(\eta)} \mu_0 \quad (4)$$

where η is a reduced Fermi level, $F(r, \eta)$ - Fermi integral:

$$F_r(\eta) = \int_0^\infty x^r [\exp(x - \eta) + 1]^{-1} dx \quad (5)$$

$\Gamma(t)$ - gamma function:

$$\Gamma(t) = \frac{1}{t} \int_0^\infty x^t \exp(-x) dx = \frac{\Gamma(t+1)}{t} \quad (6)$$

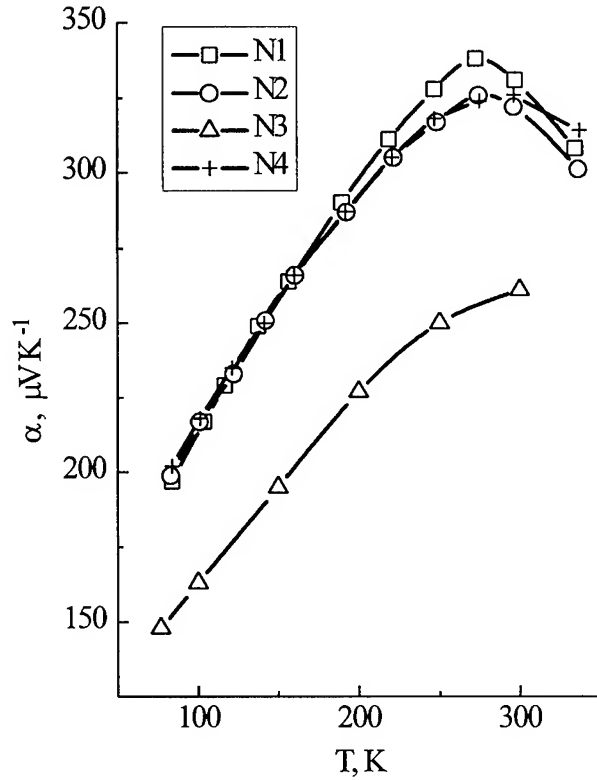


Fig.2 Temperature dependences of the thermoelectric power α in $\text{Bi}_2\text{Te}_{3-x}\text{Se}_x$.
x: 1, 2, 3, - 0.3; 4 - 0.36.

The parameter $(m^*/m)^{3/2} \mu_0$ may be obtained from the experimental data on α and σ in accordance with the expressions (2,3) for some assumption about scattering mechanism. For calculation of the mobility μ_0 and the effective mass m^*/m it is required to define a value of the carrier density. A calculation of the carrier density in anisotropic materials with complicated band structure besides Hall effect data is needed the data on galvanomagnetic effects and information about a scattering mechanism. In anisotropic materials the expression for the carrier density is given by:

$$n = \frac{A(r, \eta) B}{\rho_{23} e} \quad (7)$$

where $A(r, \eta)$ is a Hall-factor, B is an anisotropy parameter:

$$B = \left[\left(\frac{\rho_{11}\rho_{1133}}{\rho_{123}^2} + 1 \right) \beta(r_{\text{eff}}, \eta) \right]^{-1} \quad (8)$$

$\beta(r, \eta)$ is a degeneracy parameter, $\rho_{11}, \rho_{123}, \rho_{1133}$ - components of the resistance, Hall effect and magnetoresistivity tensors.

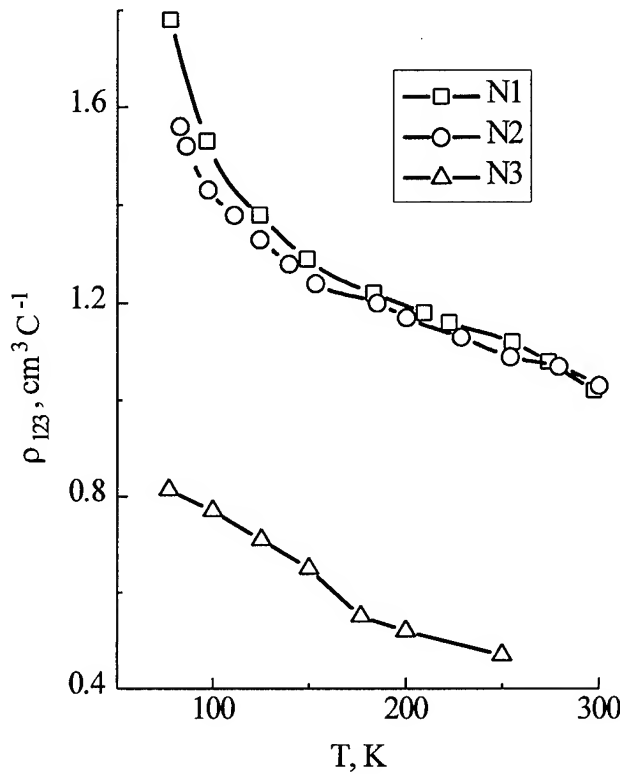


Fig. 3 Temperature dependences of the Hall coefficient ρ_{123} in $\text{Bi}_2\text{Te}_{3-x}\text{Se}_x$ ($x=0.3$) solid solutions. $n, 10^{18} \text{ cm}^{-3}$: 1 - 0.8; 2 - 1; 3 - 4.

The temperature dependences of Hall coefficient ρ_{123} are shown in Fig. 3. Estimations of the carrier density were carried out according to the expressions (7,8) with account of the dependences of $B = f(n)$ [13] and $\alpha = f(r_{\text{eff}}, n)$, $r_{\text{eff}} = f(n, T)$ [12,14]. The values of n for these two methods were closed and were equal to $(0.8 \div 1) \cdot 10^{18} \text{ cm}^{-3}$.

The form of $\rho_{123}(T)$ dependence (Fig.3) and also the carrier density n values show that a second band in the conduction band of the solid solution is not occupied (curves 1,2). Change of $\rho_{123}(T)$ may be explained with influence of anisotropy of the scattering. In the samples at $n = 4 \cdot 10^{18} \text{ cm}^{-3}$ the second band is occupied.

The temperature dependences of $\mu_0(T)$ are shown in Fig.4. Values of μ_0 more higher in one-band samples (curves 1,2,4) due to deficiency of interband scattering.

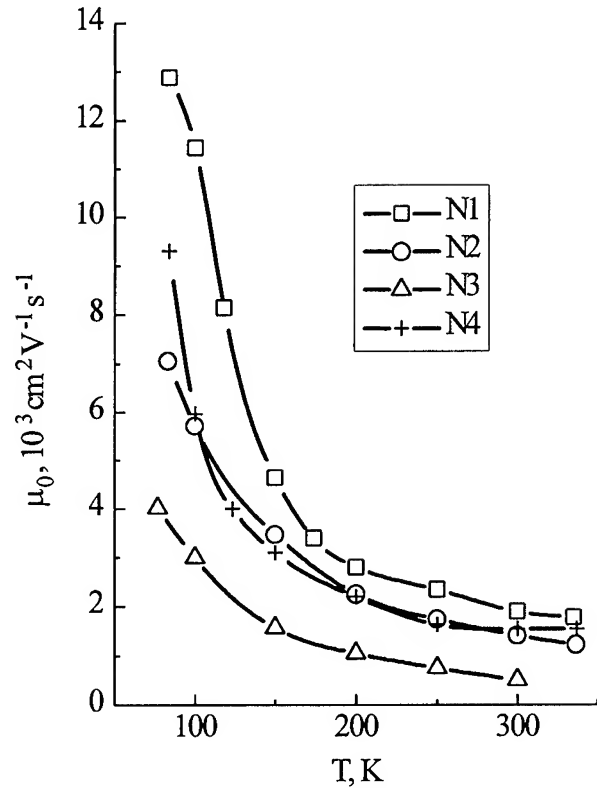


Fig. 4 Temperature dependences of the mobility μ_0 in $\text{Bi}_2\text{Te}_{3-x}\text{Se}_x$ solid solutions. x : 1, 2, 3, - 0.3; 4 - 0.36.

Analysis of $\mu_0(T)$ dependence with account of r_{eff} shows to some peculiarities in comparing with the analysis for the acoustic scattering mechanism. The expression for angle coefficients $s = d \ln \mu_0 / d \ln T$ are not linear function in considered temperature interval. However for low and high-temperature intervals $d \ln \mu_0 / d \ln T$ dependences may be studied as linear one. A change of s value is observed near Debye temperature ($T_D = 155 \text{ K}$ for Bi_2Te_3). In the solid solution with low carrier density $n = (1 \div 0.8) \cdot 10^{18} \text{ cm}^{-3}$ the angle coefficients are equal to $|s| = 1.75 \div 1.9$ at $T < T_D$, and $|s| = 1.2 \div 1.3$ at $T > T_D$. The values $|s|$ decreases to $(1.4 \div 1.6)$ with growth of the carrier density ($n = 4 \cdot 10^{18} \text{ cm}^{-3}$) at $T < T_D$ due to increasing of a number of the scattering centers.

The angle coefficients s may be also calculated from the temperature dependence of electroconductivity since the carrier density does not changed in the investigated temperature range. The values of $s = d \ln \sigma_0 / d \ln T$ for the acoustic mechanism of carrier scattering have some average values $(1.6 \div 1.7)$ in the interval to $80 \div 240 \text{ K}$ in accordance with [7,9]. Changing of $s = d \ln \mu_0 / d \ln T$ at temperature near T_D indicates to varying of the scattering mechanism: for $T < T_D$ a scattering on optical phonons become noticeable.

From the expressions (2-4) the density of states effective mass m^*/m (Fig.5) was obtained. A strong increase of m^*/m in the samples with high carrier density (Fig.5, curves 3) may be explained with influence of the additional band with more effective mass in the conduction band of solid solution.

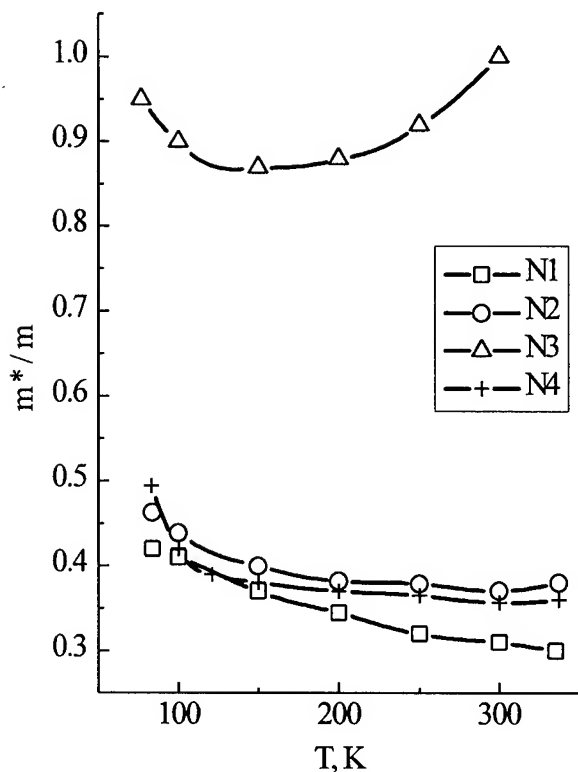


Fig.5 Temperature dependences of the effective mass m^*/m in $\text{Bi}_2\text{Te}_{3-x}\text{Se}_x$ solid solutions.
x: 1, 2, 3 - 0.3; 4 - 0.36.

The effective mass m^*/m may be presented in the exponential form ($m^*/m \sim T^t$) in the low-temperature range only for $T < T_D$ since $t = f(T)$. Therefore evaluation of t value from the thermoelectric power temperature dependence using the angle coefficients $d \ln F_{1/2} / d \ln T$ is possible only at low temperature. The angle coefficient t is equal to 0.2 for at low- and 0.4 at high-carrier density $T < T_D$.

Increasing of the mobility in the low-temperature range leads to increase of the figure of merit Z which was obtained from experimental data on thermoelectric power α , electroconductivity σ and thermoconductivity κ . The values of figure of merit Z are equal to: $Z = (2.0 \div 2.3) \cdot 10^{-3} \text{ K}^{-1}$ at $80 \div 100 \text{ K}$ in $\text{Bi}_2\text{Te}_{3-x}\text{Se}_x$ ($x = 0.3; 0.36$) solid solution samples with low carrier density $(0.8 \div 1) \cdot 10^{18} \text{ cm}^{-3}$ which is optimal at these temperatures.

References

[1] M.V. Vedernikov, V.A. Kutasov, V.L. Kuznetsov, L.N. Luk'yanova, P.P. Konstantinov, Yu. I. Ageev, G.T. Alekseeva, Yu. I. Ravich, M.I. Fedorov, E.A. Izupak, L.M. Gladkikh, I.M. Bash, Thermoelectric cooling to 130 K and Lower Temperature. XIII International Conference on Thermoelectrics, Kansas City, Missouri, USA, p.p.B4-3 (1994).
[2] O. Beckman, P. Bergval, K. Tripathi, Doping Studies of $\text{Bi}_2(\text{TeSe})_3$ Alloys, Arkiv fur Fysik, B. 28, Hf. 3, p.p.215-221 (1965).

[3] V.A. Kutasov, L.N. Luk'yanova, Influence of Scattering Effective Parameter on State Density Mass and Mobility in Solid Solutions Based on Bismuth and Antimony Chalcogenides, Fizika i Technika Poluprovodnikov, vol. 1, No. 23, p.p.652-656 (1989).
[4] J. Black, E.M. Conwell, L. Seigle, C.W. Spencer, Electrical and Optical Properties of Some $\text{M}_2^{\text{v}}\text{B}_3^{\text{vi}}\text{B}$ Semiconductors, The Physics and Chemistry Solids, vol. 2, p.p.240-251 (1957).
[5] C.H. Champness, A.L. Kipling, The Hall and Seebeck Effects in Nonstoichiometric Bismuth Telluride, Canadian Journal of Physics, vol. 44, No. 4, p.p.769-778 (1966).
[6] B.M. Gol'tsman, V.A. Kudinov, I.A. Smirnov, Semiconductor Thermoelectric Materials Based on Bi_2Te_3 , Nauka, Moskva, (in Russian), p.320, (1972).
[7] J.P.Fleurial, L. Gaillard, R. Tribolet, H. Scherer, S. Scherer, Thermal Properties of High Quality Single Crystals of Bismuth Telluride, part I, Experimental Characterisation, Journal of Physics and Chemistry of Solids, vol. 49, No. 10, p.p.1237-1247 (1988).
[8] Yu. A. Boikov, O.S. Gribanova, V.A. Danilov, V.A. Kutasov, Electrophysical Parameters of Epitaxial n-type Bi_2Te_3 films, Soviet Physics Solid State, vol. 33, No. 11, p. 1926-1929 (1991).
[9] R.W. Ure. Proceedings of the International Conference on the Physics of Semiconductors, Exeter, p.p.659-665 (1962).
[10] W.A. Tiller. Growth and Perfection of Crystals, John Wiley and Sons. Inc., New-York, p.329 (1958).
[11] H.SuBmann, E.Muller, Verification of a Transport Model for p-Type $(\text{Bi}_{0.5}\text{Sb}_{0.5})_2\text{Te}_3$ and $(\text{Bi}_{0.25}\text{Sb}_{0.75})\text{Te}_3$ Solid Solutions by Means of Temperature Dependent Thermoelectric Properties Below Room Temperature, Proceedings of the XIV International Conference on Thermoelectrics, St.Petersburg, Russia, p.p.1-6 (1995).
[12] V.A. Kutasov, L.N. Luk'yanova, Carrier Density Dependence of the Effective Scattering Parameter of Solid Solutions Based on Bismuth Telluride, Fizika Tverdogo Tela, Leningrad, vol. 26, No. 8, p.p.2501-2504 (1984) (Soviet Physics Solid State, vol. 26, No. 8, p.p.1515-1516 (1984)).
[13] V.A. Kutasov, L.N. Luk'yanova, Carrier Density Dependence of the Anisotropy Parameter of n-type Bi_2Te_3 and Solid Solutions Derived from it, Fizika Tverdogo Tela, Leningrad, vol. 28 No. 3, p.p.899-900 (1986), (Soviet Physics Solid State, vol. 28, No. 3, p.p.502-503 (1986)).
[14] G.T. Alekseeva, P.P. Konstantinov, V.A. Kutasov, L.N. Luk'yanova, T.E. Svechnikova, S.N. Chizhevskaya, Transport Phenomena in $\text{Bi}_{2-x}\text{In}_x\text{Te}_{2.85}\text{Se}_{0.15}$ Solid Solutions, Fizika Tverdogo Tela, Leningrad, vol.33, No.12, pp.3539-3542 (1991), (Soviet Physics Solid State, vol. 33, No. 12, p.p.1988-1991 (1991)).

High performance properties of sintered Bi_2Te_3 -based thermoelectric material

S.Sugihara, S.Tomita, K.Asakawa and H.Suda
Department of Materials Science and Ceramic Technology,
Shonan Institute of Technology,
1-1-25, Tsujido Nishikaigan, Fujisawa, Japan, 251.

Abstract

Bi_2Te_3 -based thermoelectric materials have been studied for fabrication parameters and orientation effects. The powder particle sizes were less than 150 μm and the mixtured grain sizes after sintering were observed in scanning electron microscope. As the results, electrical resistivity was 40% lower by reducing powders before pressing, and cold isostatic press took away the layer structures formed with pressing. The direction to the pressing and the measurements indicated lower resistivities (30-60%) for both p- and n- Bi_2Te_3 , then Z values were 2.05 and 2.23 K^{-1} for those types, respectively. It should be notified that the composites of large and small garains will mitigate an enhancement of electrical resistivity and reduce thermal conductivity in a sintered specimen.

Introduction

Bi_2Te_3 -based thermoelectric materials have been actively studied for a cooling devices for an electronic substrate and some other local cooling in these years. Fabrication method should be investigated for enhancement of figure of merit as well as that in the total system of the modules. The powder particle size dependencies of thermoelectrical properties were reported by Sugihara et al.[1]. Smaller powder particles will be better to obtain lower electrical resistivity, and the control of the microstructures after sintering are important in terms of the constituents of a larger grains and smaller ones.

As the other parameters, the reduction of the powder has been discussed to result in enhancement of electron mobility, then the increase of the Z value[2]. The orientation of the thermoelectric properties due to anisotropy were also reported to

indicate the better properties in the perpendicular direction to the pressing [2], [3], [4].

The purposes of present study are to clarify the effect on the thermoelectric properties of the powder reduction, cold isostatic press(CIP), anisotropy and to discuss the microstructures relating to the properties.

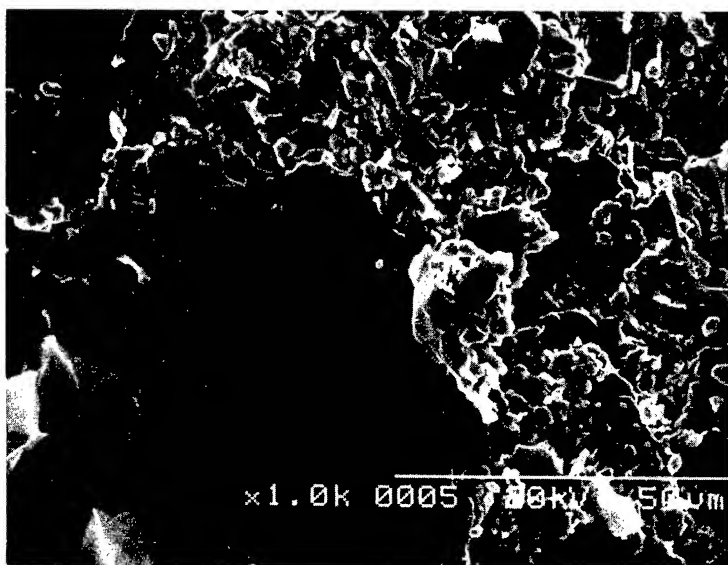
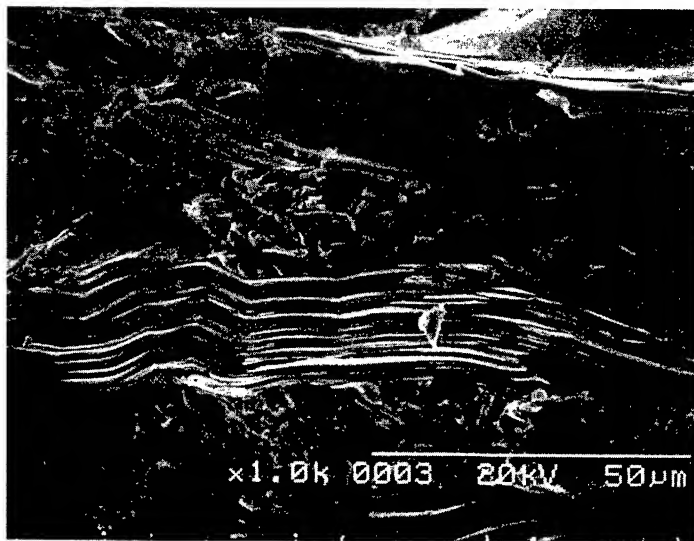
Experiment

The n- and p- bismuth telluride ingots(Ferro Tech. Co.Ltd.) are purverized in Ar atmosphere and sieved with the size less than 150 μm . The part of the powders are provided for reducing for 3 hrs in 93%Ar + 7% H_2 atmosphere (Ar+ H_2) at 300 $^{\circ}\text{C}$. The reduced powder and no-reduced powder(normal powder) were pressed at 200 MPa. The one group of green pellets was employed for CIP at 300 MPa followed by sintering for 2 hrs at 450 $^{\circ}\text{C}$ in the Ar and the another group was proceeded in Ar+ H_2 atmosphere. Moreover, no sintering process after the CIP was also studied. The size of sintered specimen was 12-13 mm in diameter and 13-14 mm in thickness, then slightly polished for obtaining the perpendicularity at the both ends. Seebeck coefficient and electrical resistivity were measured with a four- probe method and thermal conductivity was evaluated with a laser flash method. The microstructures were analyzed with scanning electron microscope (SEM).

Results and discussion

Effects of CIP

The layered structures were usually seen in perpendicular to the pressing direction when Bi_2Te_3 powder were pressed as shown in Fig. 1 (a) and the cross section at the pressed surface exhibited just flat, showing the large dark part of ingot or the plate-



PR3(r)). It was reasonable that the electrical resistivities were higher in both cases because of no sintering. The Seebeck coefficients for the CIPed specimens without sintering were apparently higher valued showing 200 to 230 $\mu\text{V/K}$ at 50 $^{\circ}\text{C}$ as illustrated in Fig. 2(a). Since Seebeck coefficient means the ratio of thermal flow to electric current, both phonons and carriers are scattered by the grain

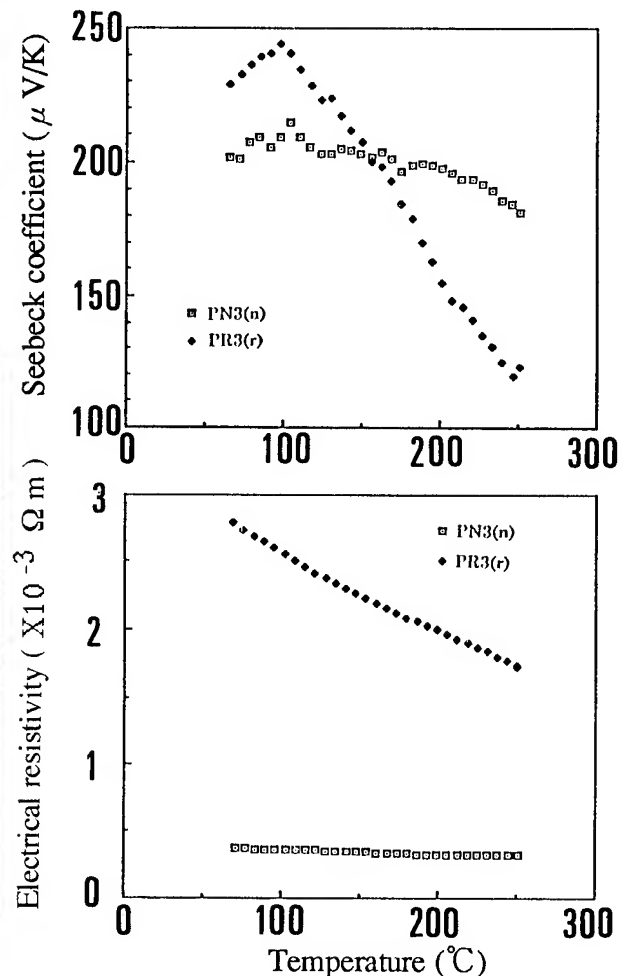


Fig.2 Seebeck coefficient(a) and resistivity(b) of CIPed green pellets; powder processing: PN3(n) in Ar and PR3(r) in Ar+H₂.

like grains with more than 100 μm after press in Fig.1(b). It is said that the anisotropy exhibits different thermoelectric properties [3]. Electrical conductivity, for instances, was shown to be much higher in perpendicular to the c-axis of the crystal [4], and it was evaluated by Hall coefficient that the crystal c-axis almost equals to the pressing direction [2]. Figure 2(a) and 2(b) show Seebeck coefficients and electrical resistivities for the CIPed green pellets by the p-type powders proceeded in Ar atmosphere (specimen No. PN3(n)) and in Ar+H₂ (specimen No.

boundaries much containing in the CIPed specimens without sintering and no phonon drag exists at high temperatures like 50 $^{\circ}\text{C}$ than the Debye temperature, then the ratio does not largely change as a result. After sintering, Seebeck coefficient and resistivity were 250 $\mu\text{V/K}$ and $1.14 \times 10^{-4} \Omega\text{m}$ for the p-type pellets by the reduced powder, respectively. By the CIP processing, layer structures were distorted as shown in Fig. 3(a) particularly, but the faces to the

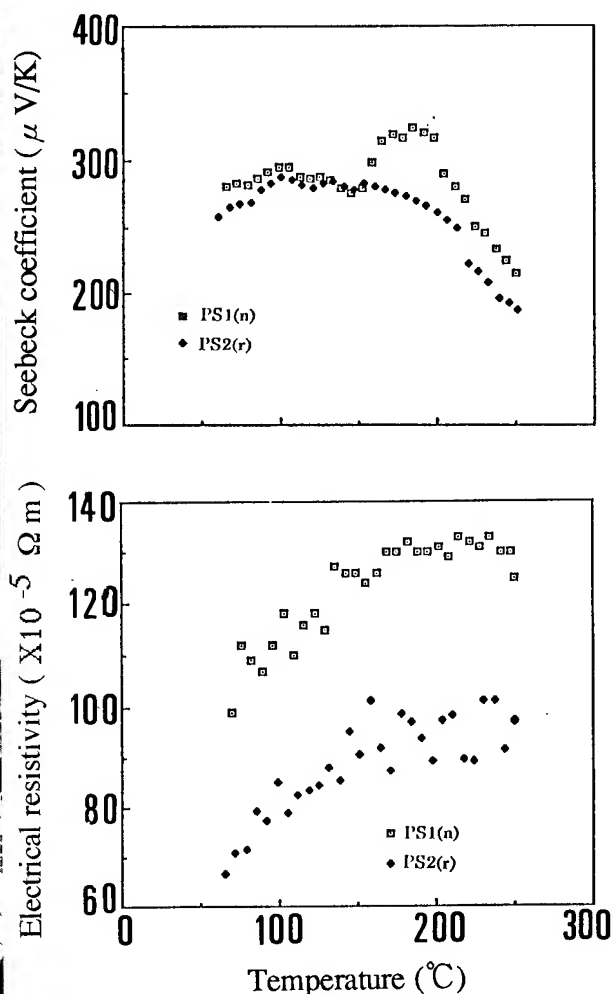
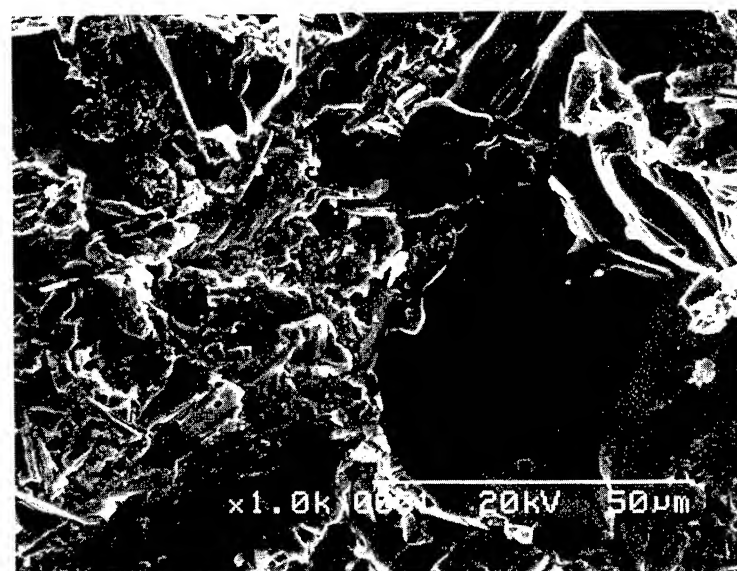
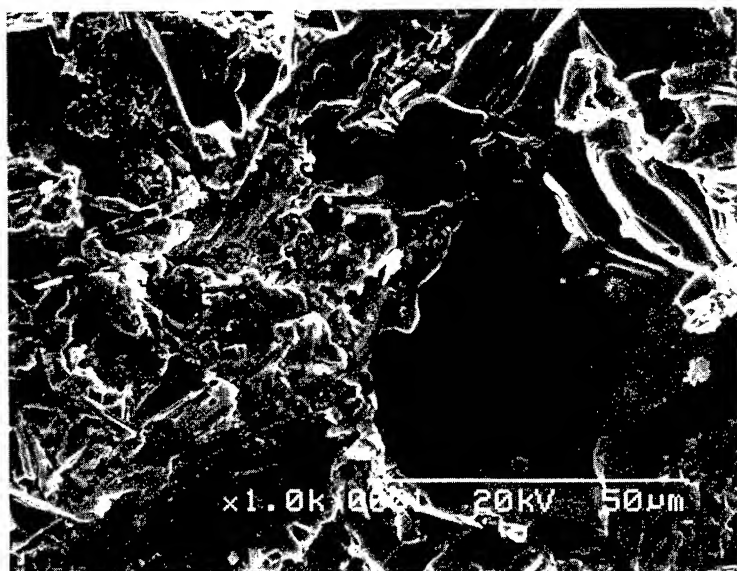


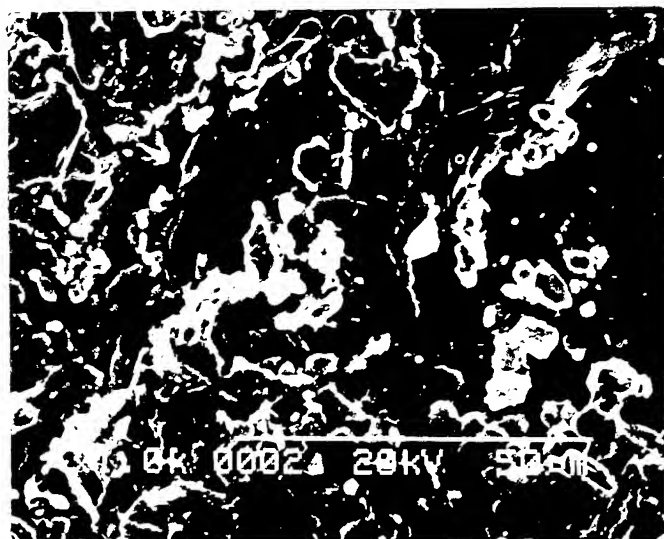
Fig. 4 Powder processing dependencies of Seebeck coefficient (a) and resistivity (b) for p-Bi₂Te₃; powder processing: PS1(n) in Ar and PS2(r) in Ar+H₂.

pressing direction in Fig. 3(b) did not differ from the specimen processed without CIP. The distortion of the layers by CIP was not much although anisotropy was alleviated.

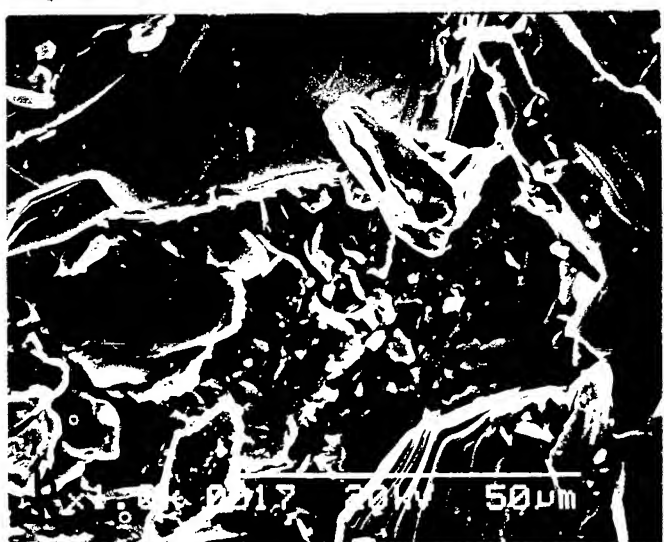
Powder reducing

As shown in Fig. 2(b), the resistivity of the CIPed pellet by the reduced powder in Ar + H₂ atmosphere was larger than that of the pellet by the processing in only Ar. The p-type sintered pellet by the powder heat-treated in Ar + H₂ had lower resistivity than

that of the pellet by the powder processed in Ar atmosphere as shown in Fig. 4(b), which tendency coincided with the result by Kaibe [2]. It is said to be the number of carrier reduced because of decreasing oxygen content but mobility increased leading to lower resistivity [2]. They did not report Seebeck coefficient which did not exhibit much differences in our results as seen Fig. 4(a). This fact is associated with that the grains already grew in the reducing powder at 450 $^{\circ}\text{C}$, and formed necking between grains after sintering as shown in Fig. 5(a) and 5(b). The resistivities were 10.5×10^{-5} and $8.0 \times 10^{-5} \Omega\text{m}$ for the sintered pellets by the powder processing in Ar and in Ar+H₂, respectively, which sintering were performed in the same atmosphere of



(a)



(b)

Fig.5 SEM photographs of p-Bi₂Te₃ by normal powder: sintering in Ar (a) and Ar+H₂ (b).

Ar. The pellets by the powder proceeded in Ar+H₂ presented 24 % lower resistivity than the pellets in Ar.

The sintered pellet is considered to be a composite of the part of a large alloy with the sintered area containing small grains. The relationship between thermal and electrical conductivity is qualitatively explained in the macroscopic mean; In the part of the alloy, electrical and thermal conductivity are larger due to less grain boundaries, while mean free path in the sintered area is shorter resulting in the lower thermal conductivity as shown in the following equation,

$$K = (\pi^2/3) k^2 T N \tau / m \quad (1)$$

as well known in Wiedemann-Franz law in pure metal, where, k , T and m are usual physical meanings and N ; the number of electrons and τ ; mean free path. Electrical conductivity (σ) is also described in the equation below,

$$\sigma = N e^2 \tau / m \quad (2)$$

As far as those equations are applied to the metal, both thermal and electrical conductivity are lower in the small grains than those in large grains. As shown in Fig.6, however, the contact area of large flat grains to small grains is larger when the smaller grains are sandwiched between flat large grains as compared to that the larger grains are sandwiched, in

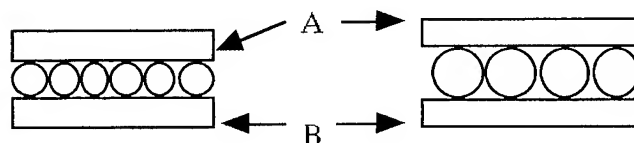


Fig. 6 Model for a composite of large grains and small grains- sandwiches.

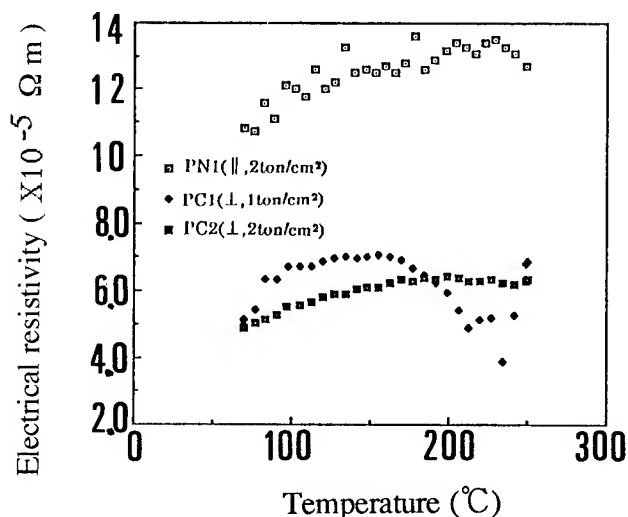
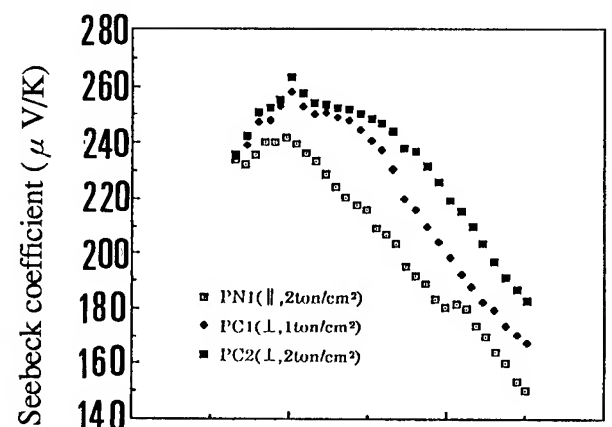


Fig.7 Seebeck coefficient(a) and resistivity(b) of p-Bi₂Te₃ for different measuring direction ;

which are analogous to the electrodes, hereby electrical conductivity can be improved. Meanwhile phonon can not transmit from the layer A to the B layer or vis-a-vis due to lower energy than electron, then thermal conductivity becomes lower.

Anisotropy of thermoelectric properties

Figure 7 shows the different directions of the measurement and to pressing pressure for electrical resistivities of p-type specimens. The measurement direction of perpendicular to the pressing exhibited about 60 % lower resistivities for both pressures than that in the parallel one. Those results can be understood by the microstructure of the layer as shown in Fig. 1. The anisotropic resistivities of the n-type specimens are indicated in Fig. 8, showing about 30% lower resistivity in perpendicular direction. These results coincided with the report that resistivity in perpendicular was lower in general[2]. There were not significantly depending on the direction in the Seebeck coefficient for both p- and n- type as shown in Table 1. Since the heat flow and electrical current take part in Seebeck coefficient, concerning problems are complicated, not only the direction (anisotropy) but also other factors should be considered. Moreover, the thermal conductivities for p- and n- types were 20 to 30 % lower in the perpendicular than those in parallel. The Z values of 2.05 and 2.23 K⁻¹ for p- and n- types, respectively, were obtained even in an about one order higher resistivity.

Conclusion

The sintered p- and n- type Bi₂Te₃ were studied with the process parameters such as powder reduction, cold isostatic press and the direction of the cut specimens and measurement to the pressing. The conclusions are as follows;

- 1) Electrical resistivity had a tendency to be one fourth lower by reducing the powders.
- 2) The layer structure after pressing was broken by cold isostatic press, which did not exhibit significant results of thermoelectricities although the anisotropy was taken away somewhat.
- 3) The direction to the pressing and the measurements indicated lower resistivities (30-60%) for both types, then Z values were 2.05 and 2.23 K⁻¹ for p- and n- type, respectively.

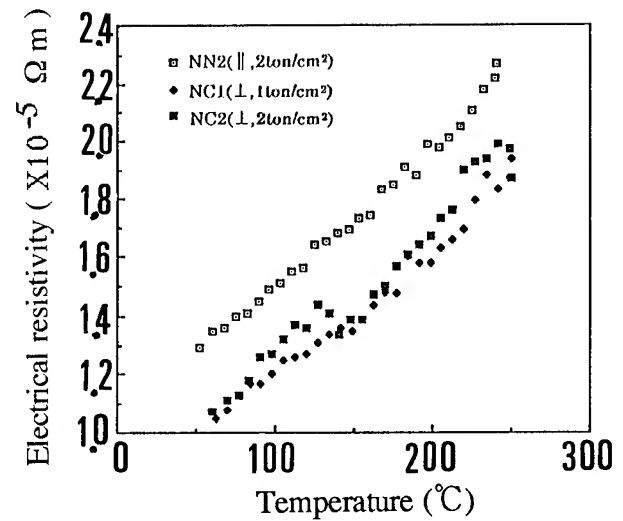


Fig. 8 Seebeck coefficient(a) and resistivity(b) of n-Bi₂Te₃ for different measuring direction;

Table 1 Thermoelectric properties of sintered p- and n-type Bi₂Te₃ at 50 °C (○; Cold Isostatic Press additionally, X; no CIP, *; perpendicular to press)

Specimen	CIP	α (μ V/K)	ρ (Ω m)	κ (W/mK)	Z (K ⁻¹)
p PR2	X	218	6.50×10^{-5}	0.61	1.22
PR4	○	250	1.14×10^{-4}	0.60	0.91
PN1	X	230	1.08×10^{-4}	0.74	0.66
PC2	X	230*	4.30×10^{-5} *	0.60	2.05
n NN1	○	-130	1.70×10^{-5}	0.80	1.24
NN2	○	-115	1.28×10^{-5}	0.50	2.07
NN5	X	-125	1.45×10^{-5}	0.70	1.54
NC2	X	-105*	1.01×10^{-5} *	0.49	2.23

- 4) The composite of large grains and small ones will mitigate an enhancement of electrical resistivity and reduce thermal conductivity in a sintered specimen. Thermoelectrical properties can be improved by the controlled constituents of the larger grains and the smaller ones.

Acknowledgement

The authors are grateful to Ferrotech. Co.Ltd. for supplying the ingots of Bi₂Te₃, and also wish to thankfulness to Professor Kajikawa and Mr.Katsube at Shonan Institute of Technology for measuring Seebeck coefficients.

References

- (1) S.Sugihara, M.Iizuka and Y.Katou;
"Thermoelectric properties of sintered n and p type Bi₂Te₃", Proceedings of XIII ICT, Kansas City, Mo., pp.282-284 (1994).

- (2) A. Kaibe, M. Sakata, Y. Isoda and I. Nishida; "Thermoelectric Properties of n-Type Sintered $\text{Bi}_2\text{Te}_{2.85}\text{Se}_{0.15}$ ", J. Japan Inst. Metals, Vol. 53, No. 9, pp. 958-963 (1989).
- (3) I. J. Ohsugi, T. Kojima and I. Nishida; "Orientation analysis of the anisotropic galvanomagnetism of sintered Bi_2Te_3 ", J. Appl. Phys., Vol. 68, No. 11, pp. 5692-5695 (1990).
- (4) R. Griot, G. Brun and J. C. Tedenac; "Orientation effects in sintered thermoelectric material", Proceedings of VII ICT, Nancy pp. 27-31 (1989).

A New n-type and Improved p-type Pseudo-ternary $(\text{Bi}_2\text{Te}_3)(\text{Sb}_2\text{Te}_3)(\text{Sb}_2\text{Se}_3)$ Alloy for Peltier Cooling

by

M. H. Ettenberg, W. A. Jesser, F.D. Rosi

University of Virginia, Department of Materials Science and Engineering

Abstract

The pseudo-ternary alloy of $(\text{Bi}_2\text{Te}_3)(\text{Sb}_2\text{Te}_3)(\text{Sb}_2\text{Se}_3)$ has been explored for over twenty-five years with little progress in the figure of merit, p-type $3.4 \times 10^{-3}/\text{K}$ and n-type $3.2 \times 10^{-3}/\text{K}$. [1-5] Using multiple dopants, Te and SbI_3 , higher figure of merit material can be achieved without creating more of the deleterious pure Te commonly found as a second phase in the p-type alloy, $(\text{Bi}_2\text{Te}_3)_{25}(\text{Sb}_2\text{Te}_3)_{72}(\text{Sb}_2\text{Se}_3)_3$. Using a combination of the two dopants figures of merit as high as $3.7 \times 10^{-3}/\text{K}$ have been achieved.

Using two dopants has also permitted the creation of an n-type alloy with a composition of $(\text{Bi}_2\text{Te}_3)_{70}(\text{Sb}_2\text{Te}_3)_{25}(\text{Sb}_2\text{Se}_3)_5$. Previously n-type doping could not be achieved with a single dopant because the alloy as grown always exhibits p-type conductivity. Using Te and SbI_3 together as dopants, or SbI_3 by itself in this alloy produces n-type material with a figure of merit of $3.4 \times 10^{-3}/\text{K}$.

Introduction

There has been only modest improvement in the thermoelectric properties of the $(\text{Bi}_2\text{Te}_3)(\text{Sb}_2\text{Te}_3)(\text{Sb}_2\text{Se}_3)$ since their inception in the late 1960's. [1-5] The p-type material had composition of $(\text{Bi}_2\text{Te}_3)_{25}(\text{Sb}_2\text{Te}_3)_{72}(\text{Sb}_2\text{Se}_3)_3$ and it was doped by adding excess Te. The Te content was beyond the solubility limit and caused a deleterious second phase to be found in the alloy. Figures of merit, Z (Equation 1)

$$Z = \alpha^2 / \kappa \rho \quad (1)$$

α -Seebeck Coefficient κ -thermal conductivity
 ρ -electrical resistivity
 have been reported as high as $3.4 \times 10^{-3}/\text{K}$. [3] The n-type alloy has been $(\text{Bi}_2\text{Te}_3)_{90}(\text{Sb}_2\text{Te}_3)_5(\text{Sb}_2\text{Se}_3)_5$ and the dopant is SbI_3 . The maximum figure of merit of the n-type alloy was reported as high as $3.2 \times 10^{-3}/\text{K}$. [3] The n-type alloy has a lower figure of merit than the p-type alloy primarily due to a higher lattice thermal conductivity (κ_{ph}) which leads to a higher total thermal conductivity (κ) at optimum carrier concentration. See Equation 2 [1]

$$\kappa = \kappa_{\text{ph}} + \kappa_{\text{el}} + \kappa_{\text{amb}} \quad (2)$$

κ_{ph} -phonon thermal conductivity
 κ_{el} -electronic thermal conductivity
 κ_{amb} -ambipolar thermal conductivity

In this alloy system the phonon thermal conductivity was measured by Yim and Rosi and has indicated at higher compositions of Bi_2Te_3 the phonon contribution to the thermal conductivity is lowered. This allows for higher figure of merit material at higher Sb_2Te_3 compositions. The material becomes more p-type in nature as the Sb_2Te_3 composition is increased. For this reason the n-type material is made from a low Sb_2Te_3 alloy with a suitable dopant to make it n-type. Yim and Rosi found three alloys in this system which could produce high figures of merit material, see Figure 1 [2-4]

Improvement in the n-type material was sought by changing composition to a higher level of Sb_2Te_3 . The research by Yim and Rosi indicated a peak in Z at $(\text{Bi}_2\text{Te}_3)_{70}(\text{Sb}_2\text{Te}_3)_{25}(\text{Sb}_2\text{Se}_3)_5$. [2] This peak is achieved through lower thermal conductivity and higher effective mass. They reported difficulty in doping that composition as n-type with the proper resistivity using a single dopant. [3] In the present work we focus on

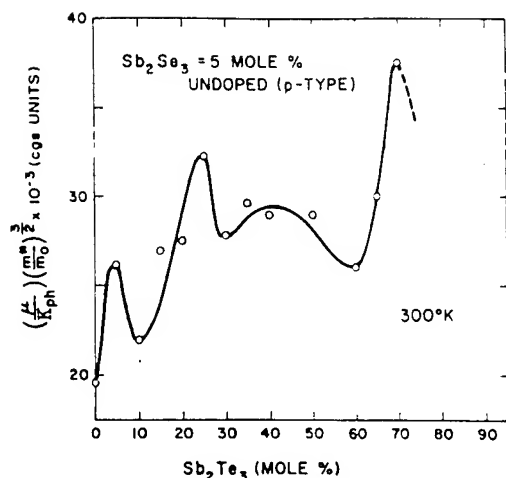


Figure 1-Theoretical prediction of maximum Z with various compositions in the $(\text{Bi}_2\text{Te}_3)(\text{Sb}_2\text{Te}_3)(\text{Sb}_2\text{Se}_3)$. [2]

making this material n-type using multiple dopants (Te and SbI_3) to reach the desired carrier concentration for optimum figure of merit.

The p-type alloy is presently doped with Te, an n-type conductor, that acts to compensate non-stoichiometric holes to achieve the desired conductivity. The problem with Te is the solubility limit is 0.2 wt% Te, as found by metallurgical analysis.[3] Using Te in conjunction with other n-type dopants (SbI_3 , TeCl_4 , and SbCl_3) one can create a greater range of dopant concentrations without exceeding the Te solubility limit further.[6] This approach is taken in the present research to improve the p-type material.

Experimental Procedure

Ingots were produced from 99.999% pure elements purchased from Alpha/Aesar. Alloys were produced in fused silica tubes by first evacuating with an absorption pump and then backfilling with Argon before being sealed. The alloys were melted and mixed for several hours in a radio frequency furnace. All ingots were grown using a vertical Bridgman furnace with a hot zone at 700°C and a temperature gradient at the melting temperature of $25^\circ\text{C}/\text{cm}$. The growth rate was about 5mm/hour.

Ingots were removed from the fused silica tubes and first tested for resistivity along the ingot's length. The resistivity was measured

using a 4 point probe method. Two probes were used to supply the current which was A/C. The current was measured using a Fluke 75 multimeter. The two voltage probes were gold coated blades 10mm apart connected to a Keithley 195A multimeter. Knowing the applied current (I), measured voltage (ΔV), point separation (L) and area of the piece (A) one could calculate the resistivity from equation 3.

$$\rho = \frac{\Delta V \cdot A}{I \cdot L} \quad (3)$$

Pieces were removed from the ingots for Seebeck coefficient and thermal conductivity measurements using a Mettler slow speed saw with a diamond tipped blade. Pieces were approximately 5-7mm long and 8-10mm in diameter. The sample was placed in an absolute testing device as schematically shown in figure 2. The sample was warmed from above and then from below. Using the thermocouples the temperature difference and the voltage produced across the sample could be measured and this in turn can be converted to an absolute Seebeck coefficient. The temperature difference across the sample as compared to the standard (fused silica) indicates the thermal conductivity. For further information please see thereferences.[1,6]

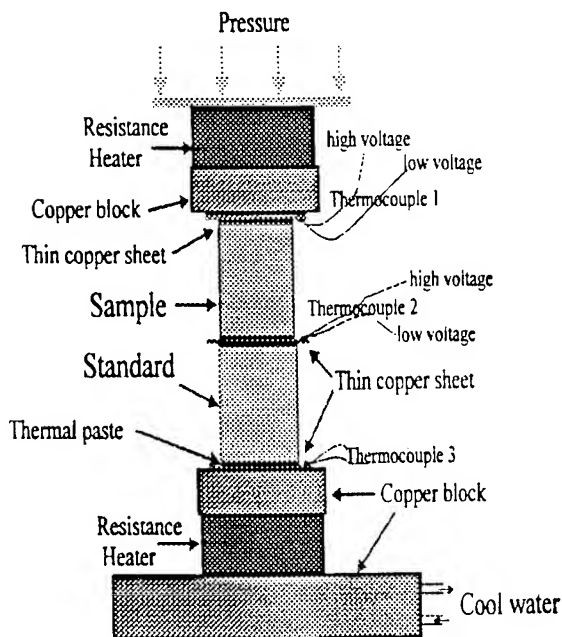


Figure 2-Absolute method used for measuring Seebeck coefficient and thermal conductivity

Experimental Results

New n-type alloy

The new n-type alloy, $(\text{Bi}_2\text{Te}_3)_{70}(\text{Sb}_2\text{Te}_3)_{25}(\text{Sb}_2\text{Se}_3)_5$, can be produced with either one or multiple dopants. Currently both doping methods produce ingots with resistivities that vary along the length when grown in a vertical Bridgman furnace. (Figure 3) The solubility limit for SbI_3 and excess Te in these alloys is predicted to be about 0.2wt%.[2] The material can be successfully made n-type while still being below the solid solubility of SbI_3 . Using Te and SbI_3 poses the problem of exceeding the Te solubility limit thus creating a detrimental second phase. In this study no second phase could be detected with the optical microscope. However, the combined dopants also appears to create ingots with greater variation of resistivity along the length than that found for a single dopant.

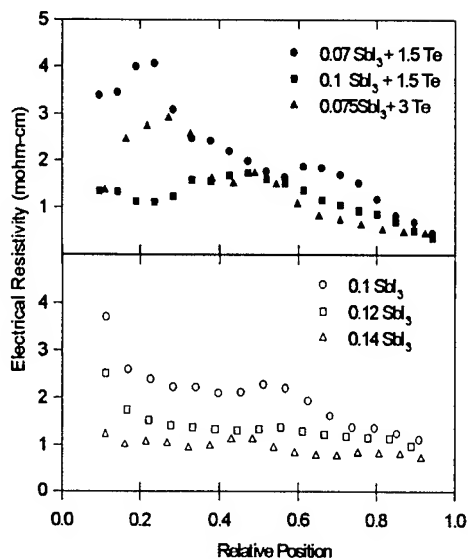


Figure 3- Electrical resistivity versus relative position for the new n-type alloy $(\text{Bi}_2\text{Te}_3)_{70}(\text{Sb}_2\text{Te}_3)_{25}(\text{Sb}_2\text{Se}_3)_5$. The upper graph shows the effect of multiple dopants while the lower shows the effect of a single dopant.

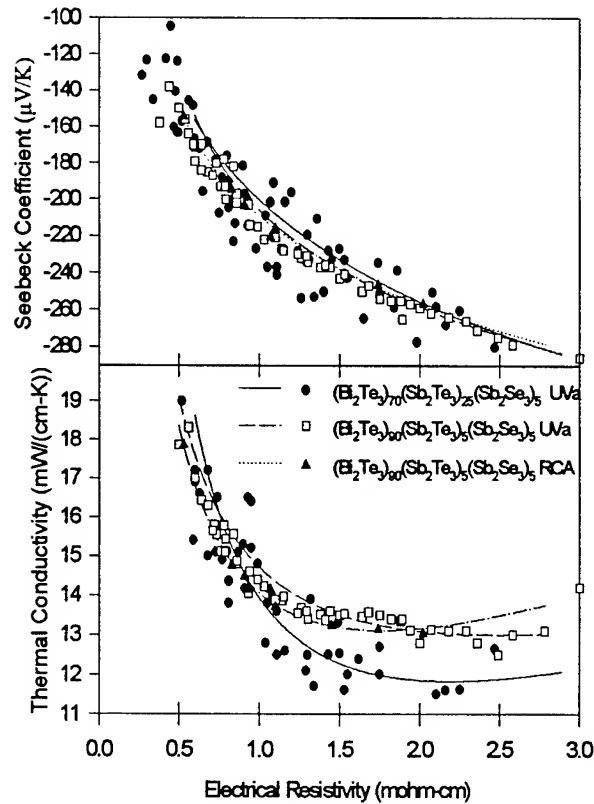


Figure 4-The new n-type alloy (●) versus the standard n-type alloy grown at UVa (□) and at RCA (▲) in terms of the Seebeck coefficient and thermal conductivity

Seebeck coefficient measurements of the new n-type alloy indicate similar properties to the standard n-type alloy produced at UVa, $(\text{Bi}_2\text{Te}_3)_{90}(\text{Sb}_2\text{Te}_3)_5(\text{Sb}_2\text{Se}_3)_5$. The standard n-type alloy produced at UVa is also similar to measurements taken by Yim and Rosi at RCA, see Figure 4.[2] The thermal conductivity measurements show an improvement in the new n-type alloy over the standard alloy. This is due to the lower κ_{ph} in the new alloy thus leading to a lower total thermal conductivity. This lower total thermal conductivity leads to a larger figure of merit, as predicted by Yim and Rosi.[2] A figure of merit as high as $3.4 \times 10^{-3}/\text{K}$ has been achieved in this alloy at a resistivity of 1.1 mohm-cm.

Improved p-type alloy

Using Te in conjunction with SbI_3 , TeCl_4 , PbCl_2 or SbCl_3 allowed greater variety in resistivity than can be achieved by using Te only. This greater resistivity variation has led to a

higher measured figure of merit of $3.8 \times 10^{-3}/K$. The $PbCl_2$ acted as a p-type dopant while the others acted as n-type dopants by compensating the holes. Figure 5 indicates that through the use of multiple dopants the resistivity versus position shows more variation along the length than using Te only as a dopant. Further studies are desired to see if excess Te can be reduced sufficiently to eliminate the deleterious second phase.

Measurement of Seebeck coefficient and thermal conductivity has indicated similar trends to that of the p-type material doped by only Te, see Figure 6. A distinct curve can not be drawn that distinguishes multiple dopant from singly doped material, due to the scatter in the data. The scatter in the data is believed to be due partly to the amount of second phase material present in the ingot. The multiple dopant material has produced figure of merit material consistently higher than was possible through single doping with Te. This increase we believe is due to an increase in the hole mobility and hence an increase in the Fermi energy. This increase in the Fermi energy leads to a higher Seebeck coefficient for the desired conductivity in the absence of a second phase. The thermal conductivity may be lowered also but not as dramatically.

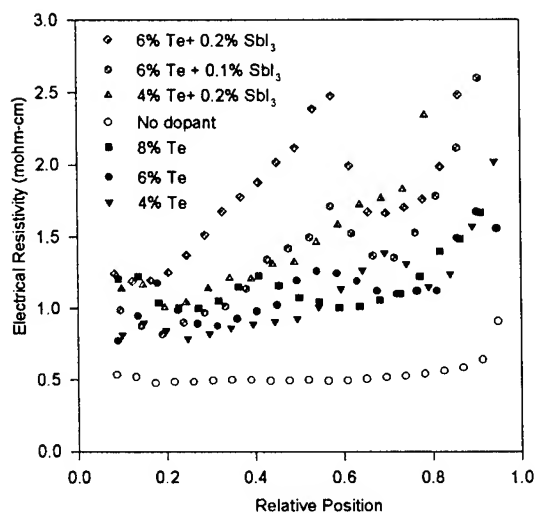


Figure 5- Resistivity versus relative position for several doping concentrations in the p-type alloy, $(Bi_2Te_3)_{25}(Sb_2Te_3)_{72}(Sb_2Se_3)_3$

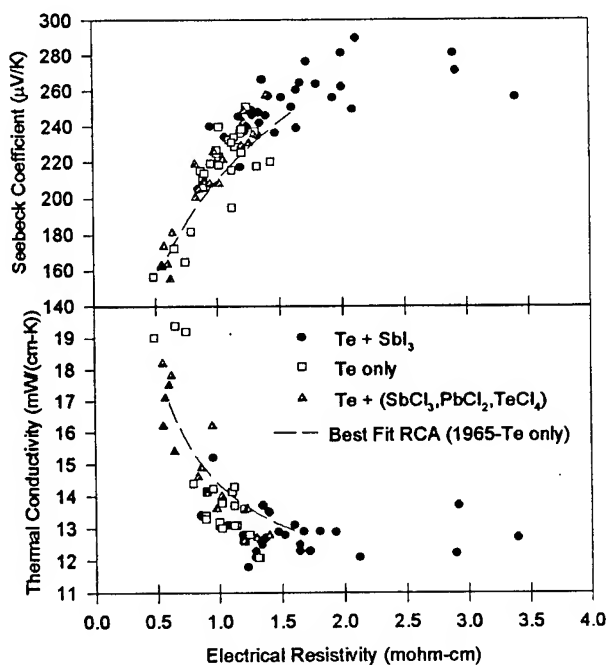


Figure 6- Seebeck coefficient and thermal conductivity versus electrical resistivity for the p-type material $(Bi_2Te_3)_{25}(Sb_2Te_3)_{72}(Sb_2Se_3)_3$ with varying dopant concentrations

Conclusions

Using SbI_3 or Te and SbI_3 as a compensator instead of only Te allows for production of a new n-type alloy that is improved over the present n-type alloys for cooling purposes. The new n-type alloy has a lower phonon thermal conductivity which leads to higher figure of merit material. The SbI_3 dopant can also be used in the p-type material to compensate it to the optimal doping concentration. In this study it appears to improve the present p-type alloy.

References

- [1] F. D. Rosi, B. Abeles, and R. V. Jensen, "Materials for Thermoelectric Refrigeration", *J. Phys. Chem. Solids*, 1959, pp. 191-200.
- [2] W. M. Yim, E. V. Fitzke, and F. D. Rosi, "Thermoelectric Properties of $(Bi_2Te_3)(Sb_2Te_3)(Sb_2Se_3)$ Pseudo Ternary....", *Journal of Mat. Sci.*, 1966.

- [3] W. M. Yim and F. D. Rosi, "Compound Tellurides and Their Alloys for Peltier Cooling", Solid State Electronics, 1972, pp. 1121-1140.
- [4] F. D. Rosi, "Thermoelectrics and Thermoelectric Power Generation", Solid State Electronics, 1968, pp. 833-868.
- [5] H. Jeon, H. Ha, D. Hyun and J. Shim, "Electrical and Thermoelectrical Properties of Undoped...", J. Phys. Chem. Solids 1991, pp 579-585.
- [6] R. Heikes and R Ure, Thermoelectricity: Science and Engineering, pp. 424, 1961.

Thermopower and Electrical Resistivity of Undoped and Co-Doped

β -FeSi₂ Single Crystals and β -FeSi_{2+x} Thin Films

A.Heinrich¹, A.Burkov^{1,3}, C.Gladun¹, G.Behr¹, K.Herz², J.Schumann¹ and H.Powalla²

¹ Institut für Festkörper- und Werkstofforschung Dresden, D-01171 Dresden, Germany

² Zentrum für Sonnenenergie- und Wasserstoffforschung, D-70565 Stuttgart, Germany

³ A.F.Ioffe Physico-Technical Institute, St. Petersburg, 194021 Russia

Abstract

Thermopower and electrical resistivity have been investigated of β -FeSi₂ single crystals and β -FeSi_{2+x} thin films in the temperature range from 40K to 1200K. The single crystals were grown by chemical transport reaction with source material of different purity and with a Si/Fe ratio between 1.5 and 2.5 to obtain crystals from the Fe-rich and Si-rich boundaries of the homogeneity range, respectively. The undoped and Co-doped thin films have been prepared in the range $-0.06 < x < 0.25$ by coevaporation. It is shown that the conductivity type of the single crystals changes from p-type to n-type with increasing purity of the starting material. Both thermopower and resistivity depend on the deviation from strict stoichiometry. The low temperature thermopower is mainly determined by phonon drag effect. The undoped films are of p-type. It is shown that the films are especially sensitive to doping at $x \approx 0.13$.

Introduction

Within the group of semiconducting silicides the compound β -FeSi₂ is known to be one of the most promising thermoelectric high temperature materials [1]. Many investigations have been carried out over more than twenty years to find suitable doping elements and optimum doping levels in both n-type and p-type material for a high thermoelectric figure of merit Z , see e.g. [2-14]. Most of the work was done with ceramic material [2-8], but also thin films have been investigated [9-14]. It is well established that doping with transition metals from the right side of Fe in the Periodic Table like Co and Ni yield n-type β -FeSi₂ and doping with transition metals from the left like Cr and Mn p-type material. But usually the effect of doping on the thermoelectric properties depends strongly on the preparation technology and with that on the kind of the dopant incorporation and on non-intentional doping. Deviations from stoichiometry can also occur and can give additional effects. As a consequence at the same level of intentional doping the transport behaviour can be quantitatively quite different.

To get a more detailed understanding of the transport behaviour of β -FeSi₂ also single crystals have been investigated [15-18]. Single crystals can be considered as systems with high structural order and defined stoichiometry. Their understanding should be a basis for further improvement of β -FeSi₂ ceramics and thin films. In [15,16] the Hall conductivity was measured and analyzed. It was shown that

the mobility can achieve at low temperature values up to $48\text{cm}^2\text{V}^{-1}\text{s}^{-1}$ in n-type and $1200\text{cm}^2\text{V}^{-1}\text{s}^{-1}$ in p-type crystals. These values are much higher than previously observed. From the analysis of the Hall data of p-type crystals a shallow impurity at 50meV has been obtained and an impurity band at about 100meV. The polar optical phonon scattering was found to be the dominant scattering mechanism above room temperature [19]. In [17] also photoconductivity was found in n-type crystals which might be important for optoelectronic and photovoltaic applications [18].

In [20] first results on the thermopower of β -FeSi₂ single crystals have been reported. Doping was performed with Cr, Co, Mn and Ni but also undoped crystals have been considered. It was found that between 40K and 1200K at least four temperature regions exist with specific transport behaviour. In the doped crystals these four regions are with increasing temperature [20]: (i) conduction within an impurity band up to about 100K, (ii) band conduction with an enhanced thermopower probably due to phonon drag up to about 250...300K, (iii) band conduction with strong electron-phonon scattering above room temperature and (iv) above 600K the onset of intrinsic conduction. In contrast to the doped samples the behaviour of the undoped samples was irregular caused by non-intentional doping which changes from sample to sample.

This paper is a continuation of [20]. In the first part the thermopower and resistivity will be discussed of undoped β -FeSi₂ single crystals in dependence on the purity of the source material. It will be shown that the type of conductivity is changed from p-type to n-type if the impurity concentration is reduced. These results will be compared with those of Co-doped single crystals. The second part is devoted to undoped and Co-doped β -FeSi_{2+x} thin films. It was found that in the whole temperature range the thermopower remains smaller than in single crystals and depends strongly on the deviation from stoichiometry. Possible explanations will be discussed for the different properties between thin films and single crystals.

Experimental

Sample preparation:

The β -FeSi₂ single crystals were grown in closed ampoules by chemical transport reaction using iodine as the transporting agent. In comparison with [20] we have changed kind and purity of the starting material. In [20] as starting

material FeSi_2 powder of 99.98% purity was used. The doping elements were added in a concentration of 2wt% resulting in a doping level $<0.1\text{at}\%$. Now instead of FeSi_2 powder a mixture of Fe and Si was used with high purity of both components up to 99.999%. Up to now only undoped crystals have been grown with this pure material. The composition of the starting powder was in most cases equal to the atomic ratio $\text{Si/Fe}=2$ of the disilicide. But also the ratios 2.5 and 1.5 were chosen to be sure to obtain crystals at the upper and lower boundary of the homogeneity range of $\beta\text{-FeSi}_2$.

The chemical vapour transport was performed in a horizontal configuration and proceeded from a source at the temperature $T_2=1050^\circ\text{C}$ to the crystallization zone kept at a lower temperature T_1 . In different runs T_1 was varied between 750°C and 950°C . The iodine content was $5\text{mg I}_2/\text{cm}^{-3}$, the total pressure at the processing temperatures about 3bar. The growth times were in between 1 and 2 weeks. For temperatures $T_1 \leq 850^\circ\text{C}$ needle-like crystals were obtained which are about 8-15mm long and have a diameter of 0.5-2mm. By X-ray diffraction the structure was checked. The measured peaks were correlated only to the orthorhombic $\beta\text{-FeSi}_2$ phase, no traces of $\alpha\text{-FeSi}_2$ were found. For $T_1=950^\circ\text{C}$ plate-like crystals were obtained of the phase $\alpha\text{-FeSi}_2$.

The $\beta\text{-FeSi}_{2+x}$ thin films were prepared by electron beam coevaporation of pure Fe and Si onto unheated glass substrates. The film thickness of the undoped samples was about 200nm, that of the doped ones about 650nm. Annealing after deposition was carried out at 1100K to obtain a crystalline structure. The doping with Co was achieved by a third source which was placed in the middle of the Fe and Si sources. According to the arrangement of the sources a concentration profile of the Si/Fe ratio is achieved across the substrate at almost constant Co concentration. This concentration profile allows to obtain FeSi_{2+x} films with a variation of the Si/Fe ratio by 0.4 in one run.

Transport measurements:

Thermopower and resistivity of the single crystals and thin films have been measured in the temperature range from 40K to 1200K. The thermopower was measured with a static temperature gradient, the resistivity by conventional four probe technique. The high temperature measurements were carried out in pure He atmosphere. By repeated heating and cooling cycles also the stability of the samples was tested. Due to limitations in sample size and stability of contacts high temperature results could not be obtained for all variants of crystal growth. The low temperature measurements were in some cases limited by high sample resistance.

Results on undoped $\beta\text{-FeSi}_2$ single crystals

Undoped single crystals have been investigated to obtain results about the influence of non-intentional doping and of the deviation from strict stoichiometry on the transport properties. The undoped samples in [20] grown with FeSi_2 powder of 99.98at% purity were in most cases high ohmic samples with a thermopower changing sign with increasing

temperature from positive to negative. Obviously such samples have a high concentration of deep impurities and are highly compensated [20]. With the new source material in form of a mixed powder of Si and Fe and with higher purity completely different results have been obtained.

The purity of the starting material was improved by two steps. In the first step carbonyl-iron was used and in the second step specially prepared Fe with 99.999% purity. The results of the thermopower of samples grown with carbonyl-iron are shown in Fig.1. These samples are of p-type and have a small resistivity which allows measurements at low temperatures. As shown in Fig.1 magnitude and temperature dependence of the thermopower $S(T)$ are very similar to the results found in Cr-doped single crystals [20]. $S(T)$ shows a maximum or a plateau at about 150K and a sharp decrease below 100K. The strong temperature dependence below 150K can be described by a T^3 -law. The same temperature dependence is also observed in the doped crystals. The T^3 -dependence is characteristic of a phonon drag contribution to the thermopower [21]. The large number of optical phonon branches in $\beta\text{-FeSi}_2$ makes it very likely that especially optical phonons contribute to the phonon drag thermopower.

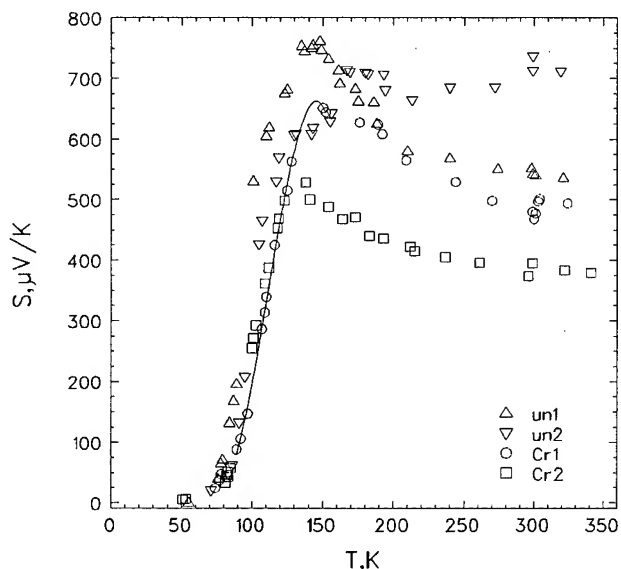


Fig. 1 Thermopower of undoped and Cr-doped ($\approx 0.1\text{at}\%$) p-type $\beta\text{-FeSi}_2$ single crystals (full line: T^3 -dependence)

Single crystals with the high purity source material were grown with different composition of the source material. In table 1 preparation conditions as described above are summarized and electrical data at room temperature are given. The values of the resistivity are not very accurately because of the irregular shape of the needle-like crystals, but they are correct at least in the order of magnitude and in their mutual relation. The main difference to the samples of Fig.1 is the negative sign of the thermopower. Obviously there is also a dependence of the properties on the deviation from strict stoichiometry, i.e. on the composition within the homogeneity range of $\beta\text{-FeSi}_2$. Samples grown with Si-rich source material are assumed to be at the upper boundary of the homogeneity range, those grown with Fe-rich powder at

Table 1 Preparation conditions and electrical parameters at room temperature of β -FeSi₂ single crystals

no	initial comp.	T ₂ /°C	T ₁ /°C	$\rho/\Omega\text{cm}$	S/ μVK^{-1}	E _A /meV
1	FeSi ₂	1050	750	20	-600	45
2	FeSi ₂	1050	800	230	-750	50
3	FeSi _{1.5}	1050	750	18	-650	23
4	FeSi _{2.5}	1050	750	8	-300	≈40

the lower. Different deposition temperatures T₂ will also yield different compositions within the homogeneity range. The main differences in table 1 are the smaller values of the resistivity and thermopower of sample 4 in comparison with all other samples, the small activation energy of sample 3 and the large resistivity of sample 2. Further differences can be seen in the temperature dependence of the transport parameters.

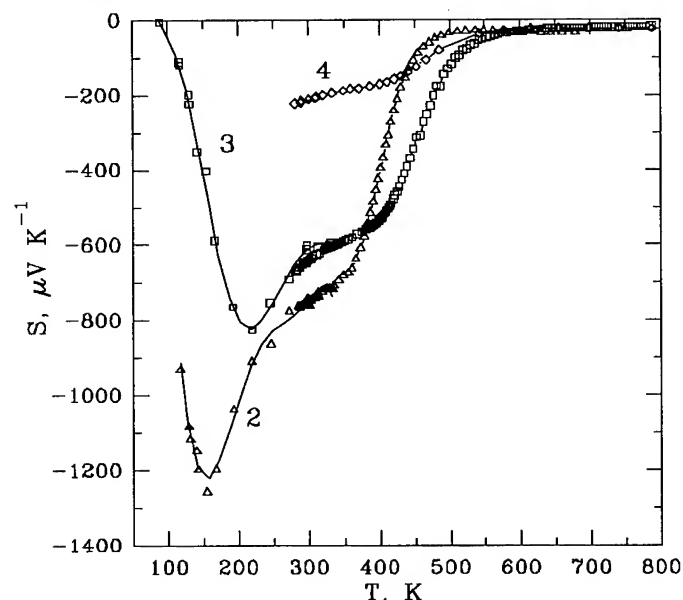


Fig. 2 Thermopower of β -FeSi₂ single crystals prepared with purified Fe (sample numbers refer to table 1)

In Fig. 2 the temperature dependence of the thermopower S is shown of samples 2 to 4. As for doped crystals [20] and also for sample 1 four temperature ranges can be defined with specific temperature dependence as discussed in the introduction. But there are several important differences to the behaviour of the doped crystals prepared with iron of 99.98at% purity. The low temperature minimum caused by the phonon drag thermopower can achieve much larger values (in one sample -2mV/K was measured) and depends probably on the deviation from strict stoichiometry. The decrease of the thermopower above room temperature caused by the onset of intrinsic conduction starts already at much lower temperatures. In sample 2 e.g. the thermopower S is decreased until 500K to 50 $\mu\text{V/K}$, but in the Co-doped only to 500 $\mu\text{V/K}$ [20]. The strong decrease of the thermopower S in the undoped crystals above 450K is probably the result of a

small density of impurity states in the energy gap region. The much smaller thermopower of sample 4 below 400K in comparison with all other samples is believed to be an effect of the Si excess at the upper phase boundary (deficit of Fe)

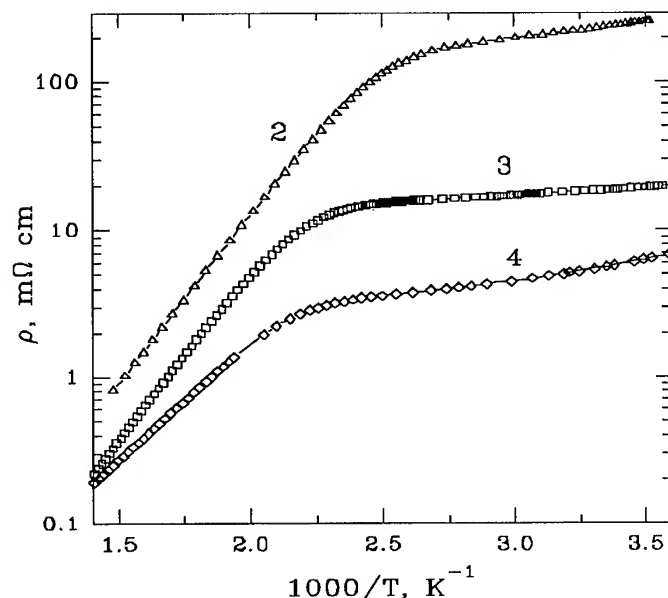


Fig. 3 Resistivity of β -FeSi₂ single crystals prepared with purified Fe (sample numbers refer to table 1)

In Fig. 3 the resistivity is shown of samples 2 to 4 in the plot $\lg \rho$ vs. T^{-1} . In all samples the activation energy of the resistivity above 450K is $(0.42 \pm 0.05)\text{eV}$, i.e. half of the energy gap as expected for intrinsic conduction. But there is a difference in the activation energy of the shallow impurity state determined from $\rho(T)$ below 400K. As shown in Fig. 3 and summarized in table 1 this activation energy is $>40\text{meV}$ in the samples prepared with stoichiometric composition and with Si excess of the source material but only 20meV in the sample grown with excess of Fe. This difference is a hint for the existence of another shallow impurity state at the lower phase boundary in comparison with the other parts of the homogeneity range of β -FeSi₂.

Results on β -FeSi_{2+x} thin films

Undoped thin films:

From the results on undoped single crystals one has to expect that non-intentional doping is also crucial for the transport properties of the thin films. Because the Fe ingot for the evaporation was not specially purified the undoped stoichiometric films were expected to be of p-type. In [10] it was found that the thermopower of β -FeSi_{2+x} thin films changes sign in dependence on composition. This change was observed with increasing x from positive to negative at $x=0.06$. To get more information about possible doping effects by such large deviations from stoichiometry we have again measured thermopower and resistivity in β -FeSi_{2+x} films.

In Figs. 4 and 5 the results are shown in the high temperature range for $0 \leq x \leq 0.25$. In the whole considered temperature range and for all compositions the thermopower is positive. There is no change in sign. The x-dependence of the

thermopower is non-monotonous with a maximum at $x=0.13$. The maximum in dependence on temperature lies in all samples between 500K and 550K. Below this maximum the thermopower strongly decreases to values between $30\mu\text{V/K}$ and $150\mu\text{V/K}$ at room temperature and decreases further below 300K (not shown in Fig.4). This behaviour is quite different from that in undoped and doped single crystals which can be explained by the suppression of the phonon drag effect.

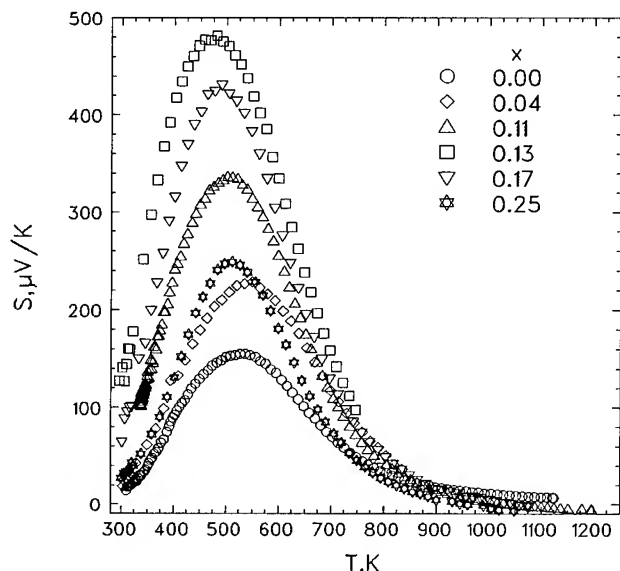


Fig. 4 Thermopower of undoped $\beta\text{-FeSi}_{2+x}$ thin films

From the temperature dependence of the resistivity $\rho(T)$ two activation energies can be estimated. As shown in Fig.5 in the high temperature range all samples have the same slope with $E_A=0.40\text{eV}$ corresponding to the half of the energy gap. Therefore this decrease of $\rho(T)$ as well as the decrease of $S(T)$ above 500K...550K are related to the onset of intrinsic conduction. The activation energy at room temperature is about 45meV. Such values have been often found [16,19] also in undoped single crystals (table 1).

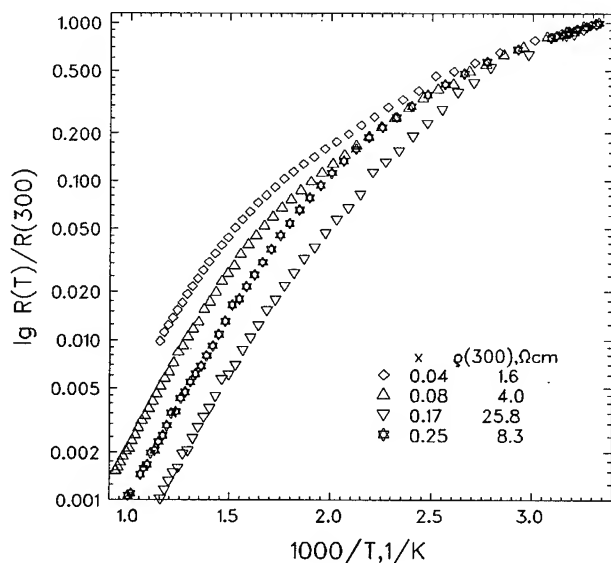


Fig. 5 Resistivity of undoped $\beta\text{-FeSi}_{2+x}$ thin films

Co-doped films:

For the preparation of the Co-doped films the same evaporation material was used as for the undoped films. Therefore, the non-intentional doping should be the same. But the Co-doping determines the type of conductivity already at concentrations much smaller than 0.1at%. In Fig.6 the high temperature thermopower is shown in the composition range $-0.06 < x < 0.16$ for a Co concentration of 0.8at%. With increasing Si/Fe ratio the thermopower increases and shows a broad maximum between 400 and 750K. Especially there is no strong decrease of the thermopower at $T > 600\text{K}$ as observed in Co-doped [20] and undoped single crystals due to the onset of intrinsic conduction.

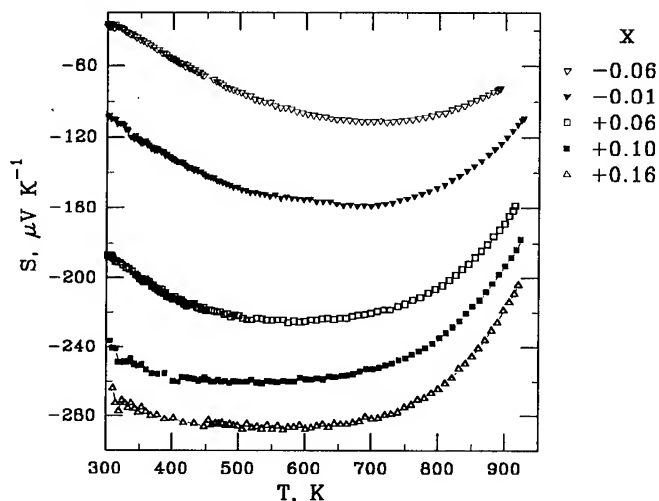


Fig. 6 Thermopower of Co-doped $\beta\text{-FeSi}_{2+x}$ thin films

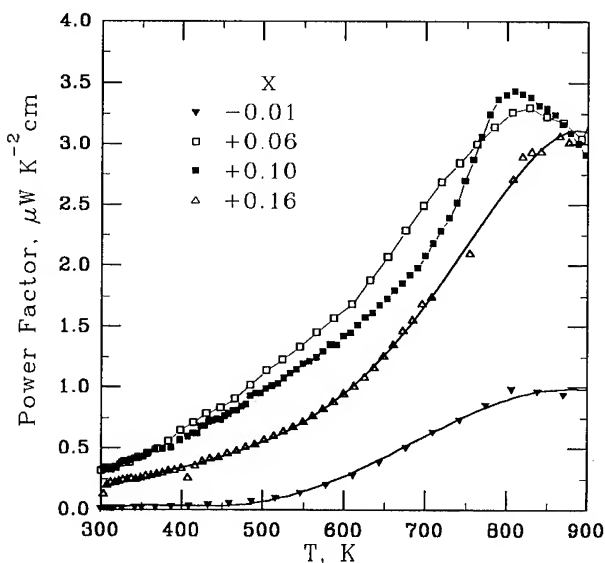


Fig. 7 Power factor of Co-doped $\beta\text{-FeSi}_{2+x}$ thin films

The x -dependence of the thermopower shows that the largest doping effect appears at $x=0.16$. This is approximately the same x -value where in undoped films the largest positive thermopower was found. This composition seems to be very sensitive with respect to doping. The resistivity of the Co-doped films lies in the same order of magnitude as found by

other authors, see e.g. [16]. The resulting power factors are shown in Fig.7. Note, that the largest values are found far from the stoichiometry at $x \approx 0.1$.

Conclusions

The effect of doping and of deviations from strict stoichiometry has been investigated on the thermopower and resistivity of β -FeSi₂ single crystals and β -FeSi_{2+x} thin films.

It has been shown that for β -FeSi₂ single crystals the purity of the source material and with that kind and degree of non-intentional doping has a determinant effect on the type of conductivity. The use of Fe with 99.999% purity results in n-type crystals, whereas p-type crystals have been obtained with Fe of lower purity.

By appropriate preparation conditions the n-type crystals have been grown with different compositions inside the homogeneity range of β -FeSi₂. It could be shown that crystals from the upper and lower boundaries as well as crystals grown at different crystallization temperatures have specific transport properties. Especially it was found that

- * the shallow impurity state has lowest energy at the lower phase boundary
- * resistivity and thermopower have lowest value in crystals at the upper phase boundary
- * the resistivity depends strongly on the crystallization temperature.

In the undoped of β -FeSi_{2+x} thin films in the whole considered composition range $-0.5 < x < 0.25$ only p-type conduction was found. This is obviously the result of non-intentional doping. Co-doped films are of n-type as expected.

There is a clear dependence of thermopower and power factor on the deviation from stoichiometry. The largest thermopower was found in undoped and doped films at $x=0.13$. This composition seems to be especially sensitive to doping. Also the power factor has the largest value near this composition.

Acknowledgements:

The authors would like to thank H. Lange (HMI Berlin) for many stimulating discussions. One of us (A.B.) is very grateful to the Wilhelm Heinrich und Else Heraeus Foundation (Hanau, Germany) for financial support.

References:

- [1] C.B.Vining, in *RCR Handbook of Thermoelectrics*, ed. D.M.Rowe, CRC Press, New York, p.277.
- [2] U.Birkholz and J.Schelm, *phys.stat.sol.* **27** (1968) 413.
- [3] I.Nishida, *J.Mat.Sci.Soc.(Japan)* **15** (1978) 15.
- [4] Y.Isoda, T.Ohkoshi, I.Nishida and H.Kaibe, *J. Mater. Science Soc. Jap.* **25** (1989) 311.
- [5] U.Stöhrer, R.Voggesberger, G.Wagner, U.Birkholz, *En. Conv. Mgmt.* **20** (1990) 143 and E.Groß and U.Stöhrer, in *Polycrystalline Semiconductors II*, Springer Proc. vol.54, Berlin, 1991, p.403.
- [6] C.B.Vining, *Proc. IX. ICT 1990, Pasadena, Calif. Inst. Techn. (1990)*, p.249.
- [7] T.Miki, Y.Matsui, Y.Teraoka, Y.Ebina, K.Matsubara and K.Kishimoto, *J. Appl. Phys.* **76** (1994) 2097.
- [8] Y.Isoda, M.A.Okamoto, T.Ohkoshi and I.A.Nishida, *Proc. XII. ICT 1993, Yokohama, Inst. Electr. Eng. Jap.*, 1994, p.192.
- [9] M.Kombayashi and S.Ido, *Jap.J.Appl.Phys.* **30** (1991) 2883 and *J.Cer.Soc.Jap. Int.Ed.* **100** (1992) 21.
- [10] M.Kombayashi, K.Hijikata and S.Ido, *Jap.J.Appl.Phys.* **29** (1990) 1118 and **30** (1991) 331.
- [11] K.Matsubara, K.Kishimoto, K.Nagao, O.Ueda, T.Miki, T.Koyanagi and I.Fujii, *Proc. XII. ICT 1993, Yokohama, Inst. Electr. Eng. Jap.*, 1994, p.223.
- [12] M.Powalla and K.Herz, *Appl. Surf. Science* **70/71** (1993) 593.
- [13] Y.Kizaki, H.Osada, H.Aoki, *Jpn. J. Appl. Phys.* **32** (1993) 5778.
- [14] A.Heinrich, C.Gladun, A.Burkov, J.Schumann and D.Elefant, *AIP Conf. Proc.* **316** (1995) 45.
- [15] E.Arushanov, Ch.Kloc and E.Bucher, *Phys.Rev. B* **50** (1994) 2653.
- [16] E.Arushanov, Ch.Kloc, H.Hohl and E.Bucher, *J. Appl. Phys.* **75** (1994) 5106.
- [17] E.Arushanov, E.Bucher, Ch.Kloc, O.Kulikowa, L.Kulyuk and A.Siminell, *Phys.Rev. B* **52** (1995) 20.
- [18] F.Fenske, H.Lange, G.Oertel, G.-U.Reinsperger, J.Schumann and B.Selle, *Symp. Proc. Int. Conf. Electr. Mater. (ICEM 94), Taiwan 1994, MRS Taiwan*, p.155.
- [19] E.Arushanov, S.Brehme and H.Lange, to be published.
- [20] A.Heinrich, C.Gladun, A.Burkov, Y.Tomm, S.Brehme and H.Lange, *Proc. XIV. ICT 1995, St.Petersburg, A.I. Ioffe Institute*, 1995, p.259.
- [21] R.D.Barnard, *Thermoelectricity in Metals and Alloys*, Taylor&Francis, London, 1972.

ELECTRICAL PROPERTIES OF β -FeSi₂ BULK CRYSTAL GROWN BY HORIZONTAL GRADIENT FREEZE METHOD

H. Shibata^a, Y. Makita^a, H. Kakemoto^{a,b}, Y. Tsai^c, S. Sakuragi^c, H. Katsumata^{a,d}, A. Obara^a, N. Kobayashi^a, S. Uekusa^d, T. Tsukamoto^b, T. Tsunoda^e and Y. Imai^e

a) Electrotechnical Laboratory, 1-1-4 Umezono, Tsukuba, Ibaraki 305, Japan.

b) Science University of Tokyo, 1-3 Kagurazaka, Shinjuku, Tokyo 162, Japan.

c) Union Material, 1640 Oshido-kyodai, Tonemachi, Ibaraki 270-12, Japan.

d) Meiji University, 1-1-1 Higashi-mita, Tama, Kawasaki, Kanagawa 214, Japan.

e) National Institute of Material and Chemical Research, 1-1 Tsukuba-Higashi, Ibaraki 305, Japan.

ABSTRACT

The growth of bulk iron silicide by Horizontal Gradient Freeze (HGF) method was achieved using different growth and annealing conditions. Two types of annealing process, in-situ annealing and ex-situ annealing, were examined. Three types of samples were prepared and examined; (i) samples which were not applied any annealing processes, (ii) samples which were applied in-situ annealing, and (iii) samples which were applied both in-situ and ex-situ annealing. The influence of annealing and growth conditions upon the material qualities was examined and discussed, putting special emphasis on the structural properties and electrical properties. Results of the X-ray diffraction revealed that only the in-situ annealing was not sufficient for the peritectic reaction from $\alpha + \epsilon$ eutectic to peritectic β -phase. However, it was revealed that, if the ex-situ annealing is applied after the in-situ annealing, the condition of 900°C for 200 hours is enough for the ex-situ annealing to obtain almost single β -phase. It was also confirmed in the aspect of electrical properties that ex-situ annealing at 900°C for 300 hours is enough to realize electrically semiconducting β -FeSi₂. The sample prepared under such a condition exhibited p-type conductivity with hole concentration and hole mobility about $5.68 \times 10^{17} \text{ cm}^{-3}$ and $1.36 \text{ cm}^2/\text{Vs}$, respectively.

INTRODUCTION

Semiconducting silicides have received considerable attention as very attractive materials for a variety of electronic applications [1,2]. Among them, beta-iron disilicides (β -FeSi₂) has received particular attention either for optoelectronic devices (such as light emitting devices and solar cells) integrated on highly advanced Si-technology, or for thermoelectric devices [3]. Advantages in using β -FeSi₂ arise mainly from (i) direct bandgap nature (around 0.87 eV), (ii) high optical absorption coefficient, and (iii) relatively high thermoelectric-power figure-of-merit in this material [3-7].

Thermodynamic phase diagram in iron-silicon system has been the subject of controversial consideration for a long time, particularly in the region where iron-silicon composition ratio Fe/Si is less than unity. According to a generally accepted study [8], iron-silicon system in the composition region has three types of thermodynamic phases named ζ_α , ζ_β and ϵ , which are called α , β and ϵ respectively in this paper. The composition ratio Fe/Si for α , β , and ϵ phases are reported to be 2/5, 1/2, and 1/1, respectively [8]. Among them, only β -

FeSi₂ phase and ϵ -FeSi phase are thermodynamically stable at room temperature. The α -Fe₂Si₅ phase is stable only between 937°C and 1220°C, while the ϵ -FeSi phase is stable below 1410°C. The composition ratio Fe/Si for the α -Fe₂Si₅ and ϵ -FeSi phases is exactly equal to that for the congruent melt. On the other hand, the β -FeSi₂ phase is a peritectic phase, and stable only below 982°C which is the peritectic temperature.

The phase diagram in iron-silicon system suggests that the transition from liquid phase to solid phase takes place at about 1212°C, when the iron-silicon mixture with Fe/Si composition ratio equal to 1/2 is cooled down from liquid phase. The solid obtained at the temperature is an eutectic material, which is the mixture of α -Fe₂Si₅ phase and ϵ -FeSi phase. Then the peritectic reaction takes place at 982°C. Therefore, the peritectic reaction is necessary to obtain β -FeSi₂ phase, if the material is prepared through such cooling and solidification process of liquid. However, the requirement for the peritectic reaction makes it very difficult to obtain homogenous and high quality β -FeSi₂ material. In addition, the speed of such a

peritectic reaction from $\alpha + \epsilon$ phase to β -phase is considered to be extremely low [9]. Therefore, the intensive annealing below 982°C is necessary to realize homogenous and high quality β -FeSi₂ when it is prepared through such types of crystal growth technique.

The important nature of the energy-band structure of the β -FeSi₂ phase has been shown recently [6] to be very sensitive to very small structural changes, such as distortion or hydrostatic deformation, which may induce a slight change in the first neighbor inter-atomic distance. Therefore, it is of great importance to synthesize high quality β -FeSi₂ bulk crystals for the full understanding of its intrinsic properties [9]. The bulk material will also be useful as a reference for studying the properties of strained or relaxed thin films, which may be subjected to structural change as pointed out above.

In this work, β -FeSi₂ bulk crystals were prepared through the combination of annealing technique with crystal growth method from liquid phase. Particularly, we examined two types of annealing process in this work; in-situ annealing and ex-situ annealing. The influence of annealing conditions and growth conditions upon the material qualities was examined and discussed, putting special emphasis on the structural properties (such as thermodynamic phases) and electrical properties.

EXPERIMENTAL

Commercially available chunk and powdered FeSi₂ materials were used as starting materials to grow β -FeSi₂ samples. High purity Fe (4N) and Si (9N) materials were also examined as starting materials to grow high purity β -FeSi₂

samples. Three kinds of the composition ratio Fe/Si were selected for this study in the starting materials, which were Fe/Si = 1/2, 2/5 and 1/3. The crucibles were made of high purity graphite covered with boron nitride (BN) powder. In this work, we used a technique named Horizontal Gradient Freeze (HGF) method, which requires the melting and solidification processes of the materials in crucible.

Non-wetting condition between crucible and liquid of the charged material is a very important point for any types of crystal growth technique using crucible, since the wetting condition gives rise to the inter-diffusion between crucible and charged material, which gives rise to undesirable contamination from crucible elements into charged material. Therefore, it is essential to realize the non-wetting condition to obtain high quality crystal. This condition strongly depends on the atmosphere in the furnace. Particularly, the reduction of the residual H₂O vapor in the furnace is essential to realize the non-wetting condition.

In order to reduce the residual H₂O vapor in the furnace, we adopted the following baking process, prior to charge the starting materials into the crucible, for both crucible and the HGF furnace: (i) insert empty crucible covered with BN powder into the HGF furnace, (ii) evacuate the furnace down to approximately 10⁻⁶ Torr, (iii) bake out the furnace at 400 - 500°C for two hours under the vacuum, (iv) cool and fill the furnace with high purity argon gas up to 760 Torr, (v) cool the furnace down to room temperature, (vi) repeat the processes (ii) - (v) for three times.

Then, the HGF furnace was opened and the crucible was taken out to be filled with starting materials. Then, we used the

TABLE 1 Growth and annealing conditions.

sample name	starting material	Fe/Si	cooling rate (°C/hour)	in-situ annealing conditions		ex-situ annealing conditions		remarks
				temperature (°C)	holding time (hour)	temperature (°C)	holding time (hour)	
FST-1a	FeSi ₂ powder (3N)	1/2	60	800°C	100h	-----	-----	sample 1
FST-1b	FeSi ₂ chunk (3N)	1/2	60	800°C	100h	-----	-----	
FST-2	Fe(4N)+Si(9N)	1/2	120	-----	-----	-----	-----	
FST-4	Fe(4N)+Si(9N)	1/2	60	900°C	100h	-----	-----	
FST-5	Fe(4N)+Si(9N)	1/2	60	900°C	100h	-----	-----	sample 2
FST-7	Fe(4N)+Si(9N)	1/2	120	900°C	100h	-----	-----	
FST-8	Fe(4N)+Si(9N)	1/2	120	-----	-----	-----	-----	
FST-9	Fe(4N)+Si(9N)	1/2	120	-----	-----	-----	-----	
FST-10	Fe(4N)+Si(9N)	1/2	100	-----	-----	-----	-----	sample 3
FST-11	Fe(4N)+Si(9N)	1/2	200	-----	-----	-----	-----	
FST-12	Fe(4N)+Si(9N)	2/5	120	-----	-----	-----	-----	
FST-13	Fe(4N)+Si(9N)	2/5	120	-----	-----	-----	-----	
FST-14	Fe(4N)+Si(9N)	1/3	120	900°C	100h	-----	-----	sample 4
FST-15	Fe(4N)+Si(9N)	1/3	120	-----	-----	-----	-----	
FST-16	Fe(4N)+Si(9N)	1/2	120	900°C	100h	900°C	200h	
FST-17	Fe(4N)+Si(9N)	1/2	120	900°C	100h	900°C	300h	
FST-18	Fe(4N)+Si(9N)	1/2	120	900°C	100h	900°C	1000h	sample 6

following procedure for the crystal growth and in-situ annealing: (i) fill the crucible with starting material and insert into the HGF furnace, (ii) evacuate the furnace down to approximately 10^{-6} Torr, (iii) bake out the furnace at 800°C for one hour under the vacuum, (iv) fill the furnace with high purity argon gas up to 760 Torr, (v) raise the furnace temperature up to 1450°C in the argon atmosphere, (vi) keep the furnace temperature at 1450°C during one hour for the reaction and homogenization of the molten material, (vii) cool the furnace at a cooling rate of R_c down to the in-situ annealing temperature T_1 , (viii) hold the furnace temperature at T_1 for the time duration of H_1 for in-situ annealing, (ix) cool the furnace down to room temperature.

For ex-situ annealing process, we adopted the following process: (i) insert the grown sample in quartz tube, (ii) evacuate the tube down to approximately 10^{-6} Torr and seal in vacuum, (iii) insert the tube in ex-situ annealing furnace and anneal at 900°C for the time duration of H_2 .

In summary, the following experimental parameters were taken as key parameters to efficiently promote the conversion from $\alpha + \epsilon$ to β -phase in this work: (i) Fe/Si; iron-silicon composition ratio in the starting materials, (ii) T_1 ; annealing temperature for the in-situ annealing, (iii) H_1 ; holding time for the in-situ annealing, (iv) R_c ; cooling rate for the cooling from 1450°C to in-situ annealing temperature, (v) H_2 ; holding time for the ex-situ annealing.

TABLE 1 shows the summary of their growth and annealing conditions (Fe/Si, R_c , T_1 , H_1 , H_2). Three types of samples were prepared and examined in this work; (i) samples which were not applied any annealing processes, (ii) samples which were applied in-situ annealing, and (iii) samples which were applied both in-situ and ex-situ annealing. The ex-situ annealing was applied to three samples named FST16 - 18. In this paper, however, experimental results obtained from only six samples were selected and discussed as the typical results. Name of the selected six typical specimens are refereed in the TABLE 1 as sample 1 - 6. Structural characterizations were carried out by X-ray Diffraction (XRD). The electrical properties were characterized by the van der Pauw method at room temperature.

RESULTS AND DISCUSSION

XRD study was performed in powdered condition for all the specimens (sample 1 - 6) to analyze their thermodynamic phases. Samples before powdering were also studied by XRD from specimens named sample 1 - 3 to characterize their crystal quality. The samples before powdering are refereed to "as-grown" samples in this paper. The as-grown samples were sliced in arbitrary direction and polished for the XRD study.

The XRD results obtained from specimens named sample 1

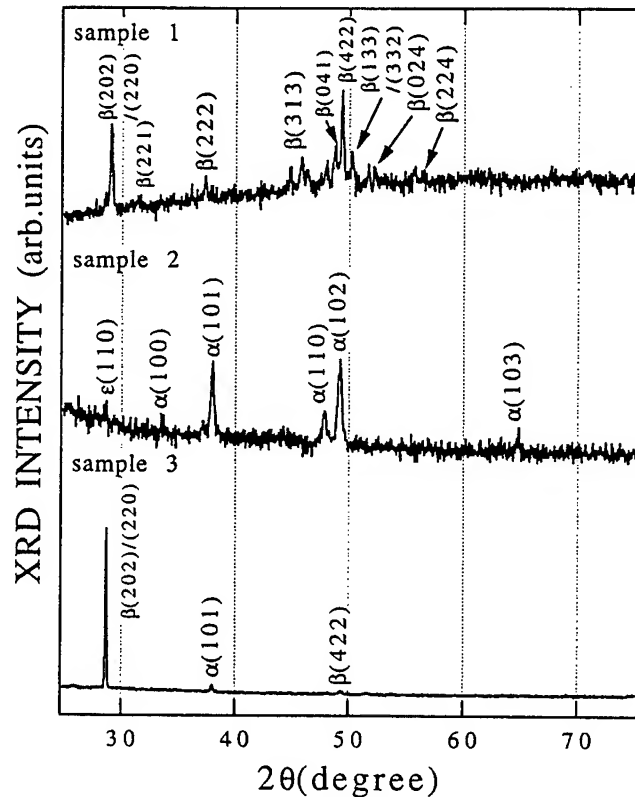


Fig. 1 X-ray diffraction patterns of sample 1 - 3 in as-grown condition.

- 3 in as-grown condition are shown in Fig. 1. The results exhibit that all the samples are polycrystalline materials. Therefore, it is strongly suggested that all the samples grown in this work by the HGF method must have polycrystalline properties. The XRD pattern of the sample 1 in Fig. 1 consists mainly of signals related to β -phase. On the other hand, the results obtained in sample 2 in the same figure exhibit almost α -phase related peaks and very weak ϵ -phase related one. The (202)/(220) reflection signal related to β -phase is dominant in the XRD spectrum of sample 3 in Fig. 1, while small $\alpha(101)$ peak is present.

The XRD results obtained from specimens named sample 1 - 3 in powdered condition are shown in Fig. 2. The results were inconsistent with those in Fig. 1. The XRD spectrum of sample 1 in Fig. 2 shows comparable α - and β -phase related peaks with very weak ϵ -phase related one, in contrast to the result in Fig. 1. Results obtained in sample 2 in Fig. 2 exhibit almost α -phase related peaks and very weak β -phase related one. Results obtained in sample 3 in Fig. 2 show comparable α - and β -phase related peaks, in contrast to the results in Fig. 1. Therefore, the results of XRD in Fig. 2 clearly suggest that only the in-situ annealing under the condition shown in TABLE 1 is not sufficient for the α -phase to be transformed into β -phase through the peritectic reaction.

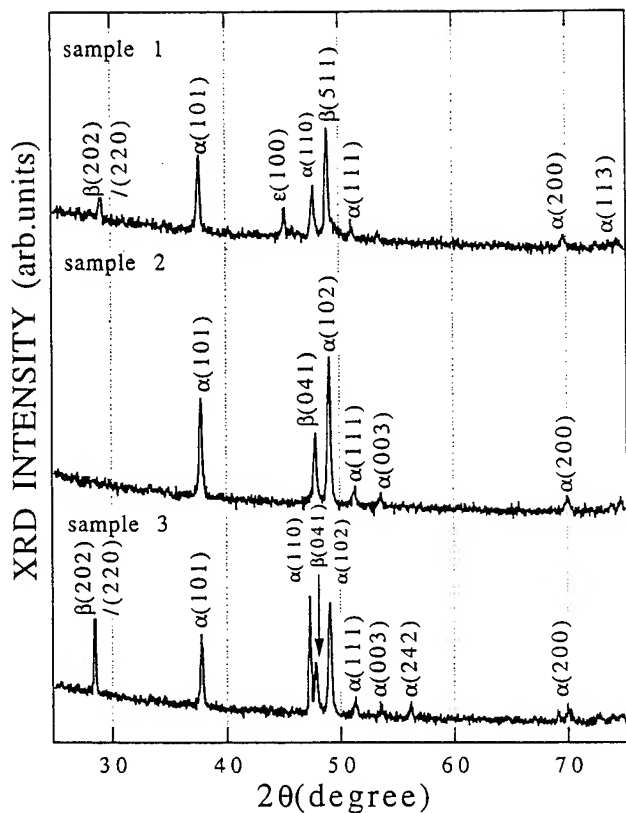


Fig.2 X-ray diffraction patterns of sample 1 - 3 in powdered condition.

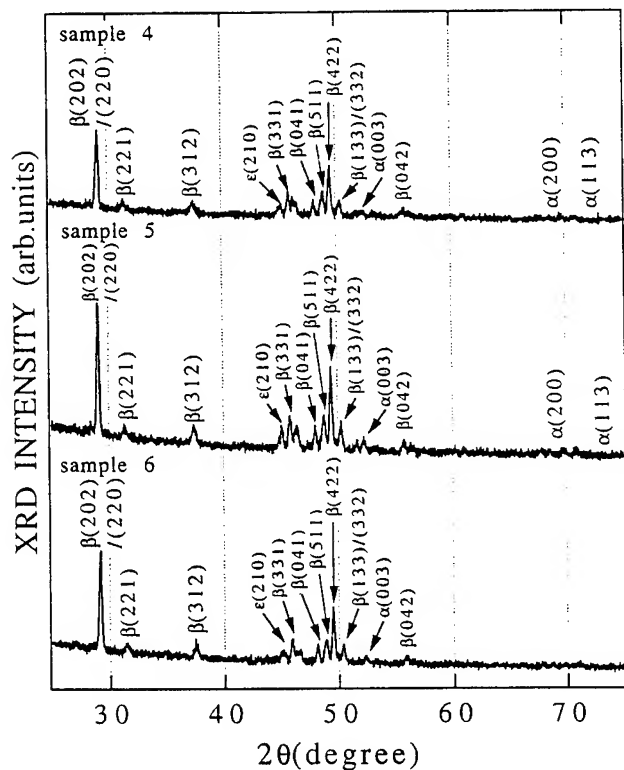


Fig. 3 X-ray diffraction patterns of sample 4 - 6 in powdered condition.

The XRD results obtained from specimens named sample 4 - 6 in powdered condition are shown in Fig. 3. The result should be considered in comparison with the results obtained from sample 1 shown in Fig. 2, since all the specimens named sample 1 and 4 - 6 were prepared under the same growth and in-situ annealing conditions. Three results shown in Fig. 3 are all nearly comparable each other. In addition, almost all the signals appeared in the spectra shown in Fig. 3 are related to only β -phase, although small peaks related to α - and ϵ -phases are observed as well. Therefore, it is strongly suggested from Fig. 3 that the thermodynamic phases in sample 4 - 6 are almost β -phase with very small amount of α - and ϵ -phases, in contrast to the sample 1. The result suggests that, condition of $T_2 = 200$ hours at 900°C is enough for the ex-situ annealing to obtain almost single β -phase, through the peritectic reaction.

The electrical properties were characterized for sample 5. The sample exhibited p-type conductivity. Hole concentration and hole mobility were estimated to be $5.68 \times 10^{17} \text{ cm}^{-3}$ and $1.36 \text{ cm}^2/\text{Vs}$, respectively. Therefore it was confirmed also in aspect of electrical properties that annealing condition of $T_2 = 300$ hours at 900°C is enough for the ex-situ annealing to realize electrically semiconducting β -FeSi₂.

CONCLUSIONS

The growth of bulk iron silicide by Horizontal Gradient Freeze (HGF) method was achieved using different growth and annealing conditions. Particularly, we examined two types of annealing process in this work; in-situ annealing and ex-situ annealing. Results of the XRD analysis revealed that only the in-situ annealing under the condition adopted for sample 1 - 3 is not sufficient for the α -phase to be transformed into β -phase, through the peritectic reaction from $\alpha + \epsilon$ eutectic to peritectic β -phase. However, it is also suggested that, if the ex-situ annealing was applied in addition, the annealing for 200 hours at 900°C was enough for the ex-situ annealing to obtain almost single β -phase. It was confirmed also in aspect of electrical properties that ex-situ annealing for 300 hours at 900°C is enough to realize electrically semiconducting β -FeSi₂. The sample prepared under such a condition exhibited p-type conductivity with hole concentration and hole mobility about $5.68 \times 10^{17} \text{ cm}^{-3}$ and $1.36 \text{ cm}^2/\text{Vs}$, respectively.

ACKNOWLEDGEMENTS

The authors would like to acknowledge S. Kimura, I. Sakamoto, N. Tsukada, T. Watanabe, Y. Ishii and Y. Takano for helpful discussions.

REFERENCE

- [1] J. Derrien, J. Chevrier, V. Le Tran, and J. E. Mahan, Appl.

Surface Sci. **56-58**, 382 (1992).

[2] S. Mantl, Nucl. Instrum. Methods Phys. Res. Sect. **B80/81**, 895 (1993).

[3] T. Miki, Y. Matsui, K. Matsubara, K. Kishimoto, K. Nagao, and Y. Fujii, in the Proceedings of the 12th International Conference on Thermoelectrics, edited by K. Matsuura (1993 November 9-11 Yokohama/Japan), p.29-33.

[4] H. Katsumata, H. L. Shen, N. Kobayashi, Y. Makita, M. Hasegawa, H. Shibata, S. Kimura, and A. Obara, in the Proceedings of the 9th International Conference on Ion Beam Modification of Materials (IBMM'95 Canberra, Australia, 5-10 February 1995).

[5] C. H. Holk, S. M. Yalisove and G. L. Doll, Phys. Rev. **B52**, 1692 (1995).

[6] L. Miglio and G. Malegori, Phys. Rev. **B52**, 1448 (1995).

[7] E. Arushanov, E. Bucher, Ch. Kloc, O Kulikova, L. Kulyuk, and A. Siminel, Phys. Rev. **B52**, 20 (1995).

[8] O. Kubaschewski, Iron-Binary Phase Diagram, Springer-Verlag, New York, p.136 (1982).

[9] Ch. Kloc, E. Arushanov, M. Wendl, H. Hohl, U. Malang, and E Bucher, J. of Alloys and Compounds **219**, 93 (1995).

Preparation and Characterization of Thermoelectric β -FeSi₂ Phase Dispersed with Si

Byoung-Gue Min, Kyung-Wook Jang* and Dong-Hi Lee

Department of Metallurgical Engineering, Yonsei University, Seoul, 120-749, Korea

*Department of Material Science and Engineering, Hansoo University, Chung-Nam, 352-820, Korea

Abstract

Heat treatment of α single phase of Fe-Si system produced eutectoid microstructures consisted of β and Si phases. The volume fraction of Si dispersoids, 0.1~0.25 μ m in size, was controlled by varying Si content within the compositional range of α single phase. The dispersed Si particles in the β matrix acted as effective scattering centers for carriers as well as phonons.

Introduction

As an effort for improving the figure of merit of the thermoelectrics, reduction of thermal conductivity has been attempted by inducing phonon scattering without any harmful effect on electrical conductivity and thermoelectric power (Seebeck coefficient). In this context, solid solution (for Bi₂Te₃-based materials) and grain refinement or dispersion of fine particles (for SiGe-based system) have been studied.[1~4] These, in other words, were related to the attempt to reduce lattice thermal conductivity by keeping other variables, including carrier concentration, to be constant.

During the preparation of stoichiometric β -FeSi₂, there undergo several complicated phase transitions. β , α (Fe₂Si₅), ϵ (FeSi) and Si phases take part in phase transformations of peritectoid, eutectoid and eutectic reactions (where α and ϵ phases show metallic properties[5,6]). Among the various transition phases, eutectoid phase of Si+ β mixture, from which it is possible to produce fine Si dispersoids in β matrix, are formed by decomposition of α phase when heat treated below the eutectoid temperature (937°C)[7,8].

Therefore, it is expected that if size of Si dispersoids is controlled to be fine enough to affect phonon scattering by heat treatment, the decrease in lattice thermal conductivity may be achieved.

Experimental

Button-shape ingots of α single phase were prepared from elemental Fe, Mn and Si of >99.9% purity by electron beam melting in vacuum (~10⁻⁶ torr), and they were remelted five times thereafter for compositional homogeneity.

Intrinsic FeSi₂ shows a very low electrical conductivity due to its high band gap of 0.9eV[9]. It is, therefore, necessary to add the dopant usable in the wide range of temperature. In these studies, Mn was chosen as a p-type dopant, and the amount of Mn was varied to control the doping effect (or carrier concentration). For the investigation into the effect of Si dispersion on thermoelectric properties, volume fraction of Si was subjected to change within the compositional range of

α single phase (69~71.2at%Si), where atomic ratio of Fe to Mn was fixed to be 98 to 2 (see Table 1).

Table 1. Chemical compositions of the specimens used in this experiment (wt%)

Specimen	Nominal composition	Fe	Si	Mn
1	(Fe _{0.98} Mn _{0.02})Si ₂ + 26vol% Si	42.38	56.67	0.87
2	(Fe _{0.98} Mn _{0.02})Si ₂ + 32vol% Si	39.63	59.29	0.96
3	(Fe _{0.90} Mn _{0.10})Si ₂ + 26vol% Si	41.93	53.58	4.49

The heat treatments for eutectoid reaction were carried out at temperatures of 730, 770, 810 and 850°C for up to 20 hours in Ar atmosphere. Among those, heat treating condition at 810°C showed the highest rate of eutectoid reaction.

Analyses on compositions and phase transformations were carried out by ICP and XRD respectively. Microstructures of heat treated specimens were observed by SEM, and the mean size and average interparticle spacing of Si dispersoids were measured by quantitative metallography.[10]

Thermoelectric properties (Seebeck coefficient, electrical conductivity and figure of merit) were measured at 500°C where the FeSi₂ based thermoelectrics were reported to show the best performance. There was no indication of transformation or microstructural changes at 500°C. Thermal conductivity was estimated from the values of figure of merit measured by Harman's method.

Results and Discussion

As shown in Table 1, the compositions of specimens were (Fe_{0.98}Mn_{0.02})Si₂ + 26vol%Si, (Fe_{0.98}Mn_{0.02})Si₂ + 32vol%Si and (Fe_{0.90}Mn_{0.10})Si₂ + 26vol%Si. They were designated as specimen 1, 2 and 3 respectively.

XRD patterns indicated that there existed only α phase for all specimens before heat treatment. But as it was shown in Fig. 1, α phase in the specimens transformed to β and Si phases when heat treated at 810°C for 20 hours.

Detailed comparison of integral intensities of Si (100) peak (2 θ =28.5°) and β peaks ([202]=29.09° and [220]=29.18°) showed a intensity ratio of 12 : 24 : 13 for specimens 1, 2 and 3, which means the fraction of Si dispersoid in specimen 2 was higher by about 2 times than in the other two specimens.

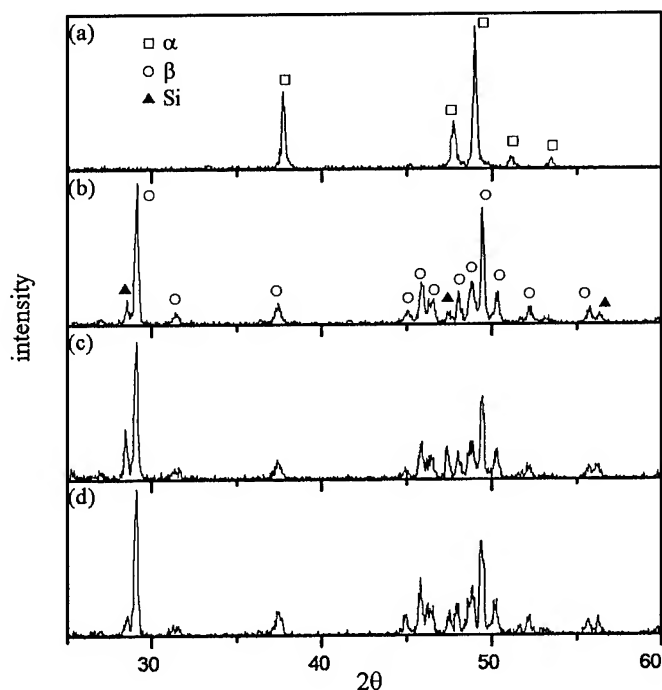


Fig. 1. XRD patterns of (a) ingot specimen, (b) specimen 1, (c) specimen 2 and (d) specimen 3 heat treated at 810°C for 20hr. (Cu K α)

The relative XRD intensity of Si to β phase was almost unchanged for the specimens of same composition irrespective of heat treatment temperature. This means that the phase fractions of Si and β were determined solely by the composition of α phase. It was also recognized that the size of Si dispersoids was increased with heating temperature for a given heating time period. But phase fraction was not varied much with heat treating time at a given temperature.

Photo. 1 shows the SEM photographs for specimen 1, 2 and 3 heat treated for 20 hours at different temperatures. Bright phases are Si dispersoids and dark background is β phase. The shape of the Si dispersoids was ellipsoidal rod having aspect ratio of ~ 30 . Mean size changed from $\sim 0.1\mu\text{m}$ to $\sim 0.25\mu\text{m}$ by heat treatment, but there were little variations in aspect ratio with heat treatment. The fractions of Si phase were found to be 27.0, 31.9 and 25.0 vol% for specimens 1, 2 and 3 respectively when heat treated at 850°C for 20 hours. In Figs. 2 and 3, the variations of mean size and interspacing of Si dispersoids with conditions of heat treatment were shown. Figs. 2-(a) and -(b) are for the variations with temperatures at fixed heating time of 20 hours, while Fig 3-(a) and -(b) for the heating time effect at a given temperature of 810°C. During the eutectoid reaction, higher temperatures enhanced interdiffusion rate of Fe and Si in the α phase. That, in turn, caused the increment of the size and interspacing of Si dispersoids as temperatures increased. It seemed that the mean size of Si dispersoids was changed more effectively by heat treating temperature than by time.

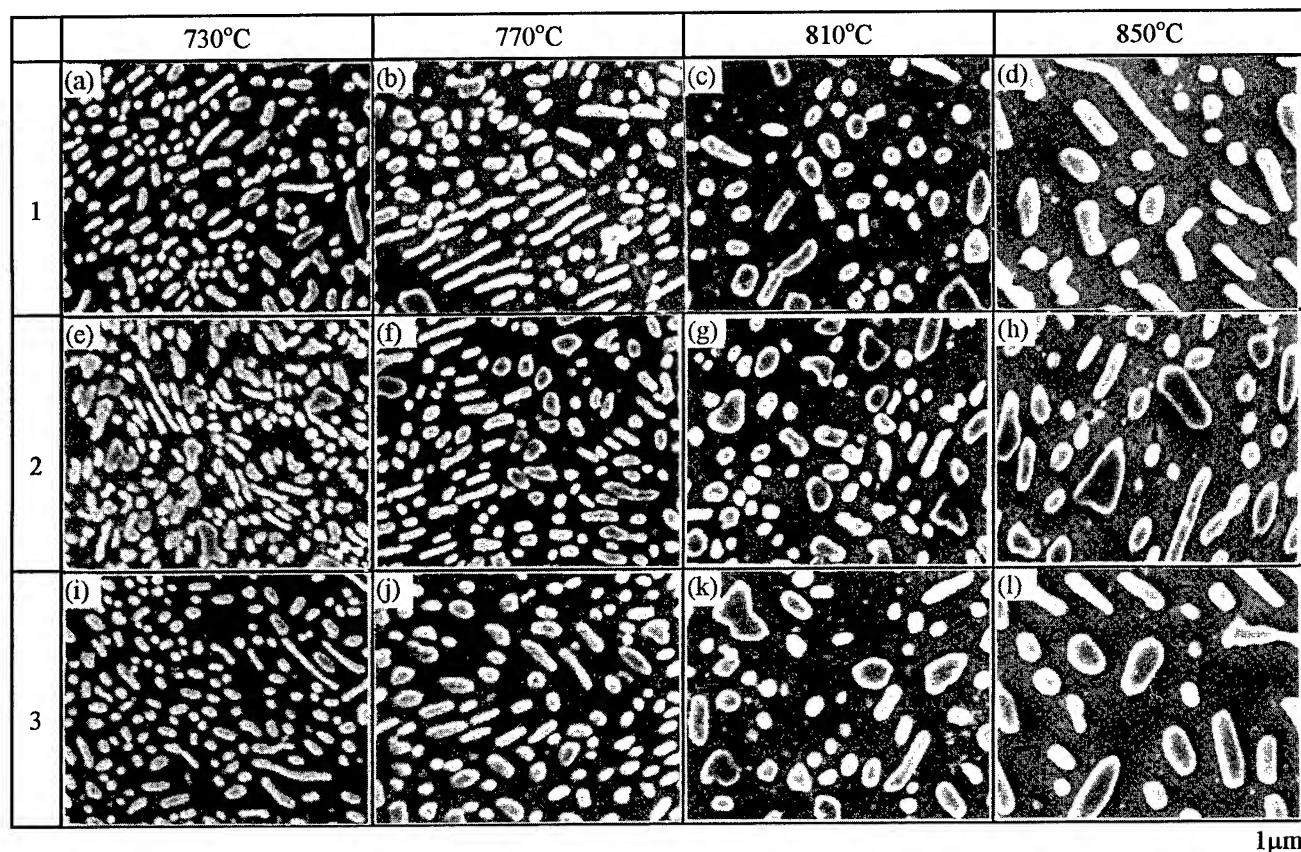


Photo. 1. SEM photographs of (a)~(d) specimen 1, (e)~(h) specimen 2 and (i)~(l) specimen 3 heat treated at various temperatures for 20 hours

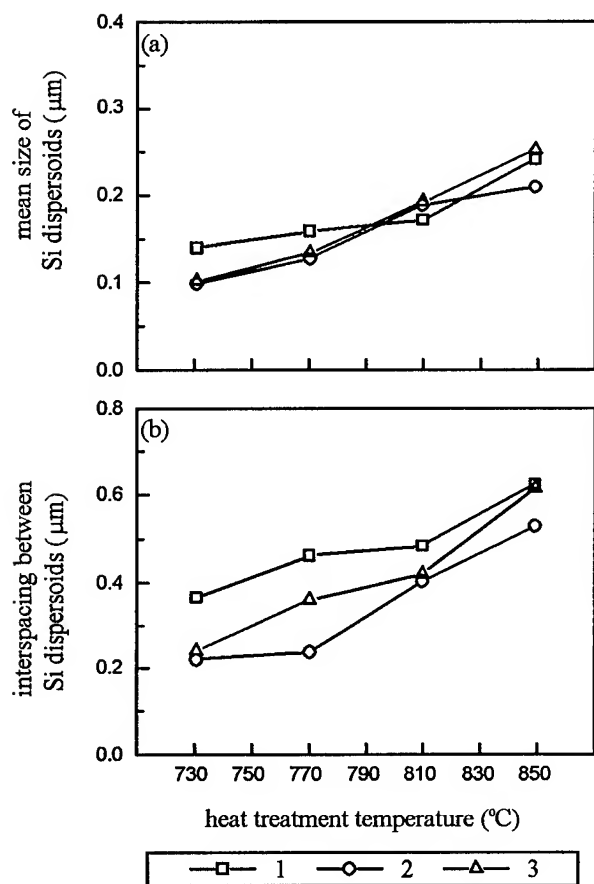


Fig. 2. Variations of mean size(a) and interspacing(b) of Si dispersoids with heat treating temperature. (20hr)

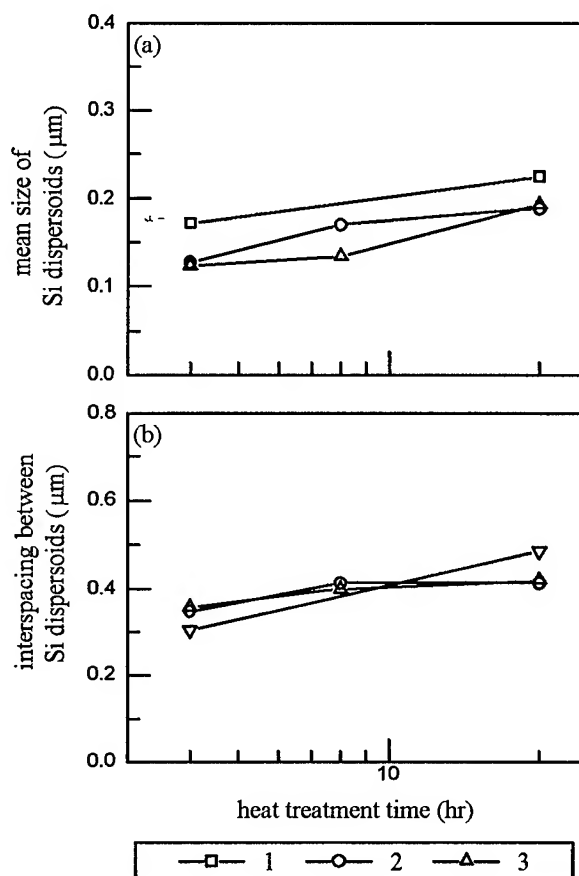


Fig. 3. Variations of mean size(a) and interspacing(b) of Si dispersoids with treatment time (heated at 810°C)

Fig. 4 shows the variations of thermoelectric properties measured at 500°C as a function of heat treating temperature, where the time for heat treatment was fixed at 20 hrs. Thermoelectric power of specimen 3 showed a clear tendency of increase with decreasing heat treating temperature, whereas in the cases of specimen 1 and 2, there was not such a dependency on the temperature. Electrical conductivity varied, as expected, reversely to the behavior of thermoelectric power, and higher values were observed for specimen 3 due to the comparatively high doping level. These differences of changes for specimen 3, therefore, are believed to be caused by its relatively high carrier concentration. In other words, the more the number of carriers, the higher was the effectiveness of carrier scattering with Si dispersoids. The values for thermoelectric power of specimen 2 were higher than those of specimen 1 at all heat treating temperatures, but values of electrical conductivity showed nearly same values for two specimens. Reason for this is thought to stem from the smaller interspacings of Si dispersoids for the case of specimen 2 at the same heat treatment condition(see Fig 2-(b)).

Thermoelectric figures of merit for all specimens showed considerably low values (~ one order less) compared with that of β single phase. Proper reason for this discrepancy was not possible to understand at present.

Fig. 5 shows the estimated thermal conductivities which were calculated from the measured thermoelectric power, electrical conductivity and figure of merit. These values are much lower than that of β single phase. Considering the fact that the thermal conductivities of β and Si phase are respectively $3\sim 6 \times 10^{-2}$ W/cmK[11] and 1.24 W/cmK[12], it is understood that the fine dispersoids of Si phase caused very effectively to reduce thermal conductivity of mixed phase. It is believed that the interface between β and Si phase is responsible for the scattering of phonons as well as carriers. The lack of data in the present study did not permit to analyze the quantitative contribution of dispersoids to carrier and phonon scattering, but the comparatively high overall effect of dispersoids on scattering process was clearly demonstrated by this work.

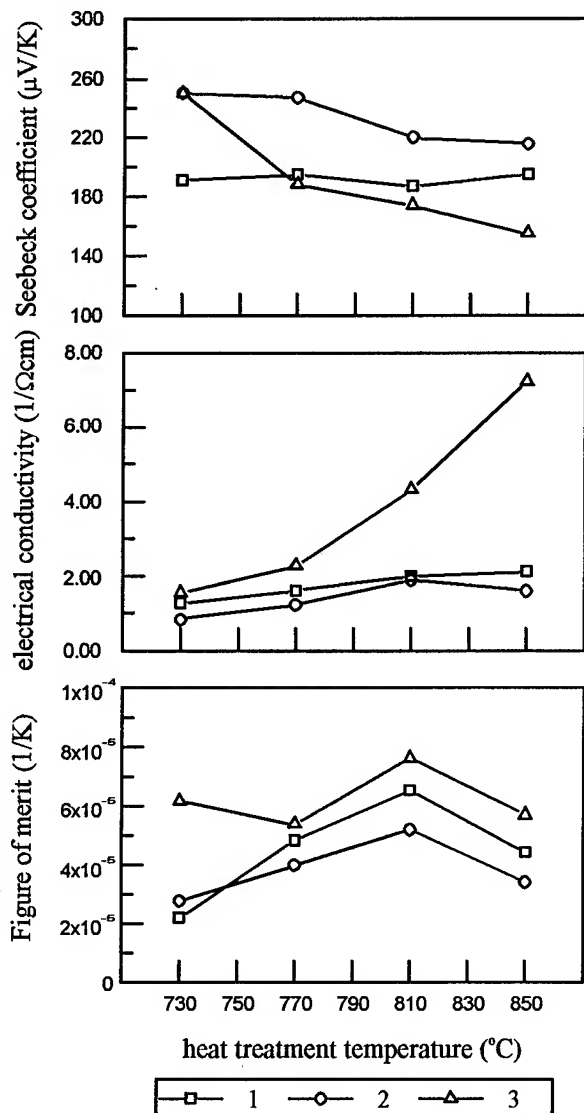


Fig. 4. Variations of thermoelectric properties of specimen 1, 2 and 3 as a function of heat treating temperatures

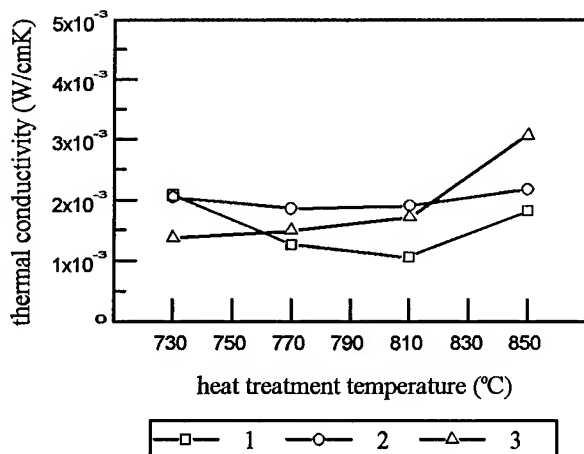


Fig. 5. Estimated thermal conductivities of specimens vs. heat treating temperatures (heated for 20hrs, measured at 500°C)

Conclusion

From the investigation into microstructure, constituent phases and thermoelectric properties of Fe-Si eutectoid system, following results were obtained :

- (1) Size of dispersed Si phases of ellipsoidal rod in β matrix was controllable within 0.1–0.25 μm range. The mean size and interspacing of Si dispersoids were increased with heat treating temperature and time.
- (2) Fine Si dispersoids acted as effective scattering sites for phonons and carriers, consequently electrical conductivity as well as thermal conductivity was lowered considerably, however, increase of thermoelectric power was not so profound.

References

- [1] A.F. Ioffe, *Semiconductor thermoelements and thermoelectric cooling*, Insforsearch Ltd., London, (1957).
- [2] K-W. Jang and D-H. Lee, "Properties of Bi_2Te_3 -based thermoelectrics fabricated with porous matrix", Proc. 12th ICT, pp115-120 (1993).
- [3] D.W. Rowe and V.S. Shukla, "The effect of grain boundary scattering on the lattice thermal conductivity and thermoelectric conversion efficiency of heavily doped fine grained Si-Ge alloys", J. of Appl. Phys., vol. 52, No. 12, pp7421-7426 (1981).
- [4] J.W. Vandersande, J-P. Fleurial, N. Scoville and J.L. Rolfe, "Thermal conductivity reduction in p-type $\text{Si}_{80}\text{Ge}_{20}$ alloys due to ultrafine insulating particulates", Proc. 12th ICT, pp11-14 (1993).
- [5] U. Birkholz and A. Fruhauf, "Magnetic susceptibility of semiconducting and metallic FeSi_2 ", Phys. Stat. Sol., vol. 34, ppK181-184 (1969).
- [6] I. Nishida, "Study of semiconductor-to-metal transition in Mn-doped FeSi_2 ", Phys. Rev. B, vol. 7, No. 6, pp2710-2713 (1973).
- [7] Y-H. Eun, B-G. Min and D-H. Lee, "Transformation behavior of high temperature thermoelectric FeSi_2 ", Korean J. Electron Microscopy, vol. 25, No. 3, pp90-98 (1995).
- [8] B-G. Min, Y-H. Eun and D-H. Lee, "Effect of additives on the phase transformation and thermoelectric properties of FeSi_2 ", Proc. of 3rd IUMRS-ICA, pp185-191 (1995).
- [9] U. Birkholz and J. Schelm, "Electrical investigation of the semiconductor-to-metal transition in FeSi_2 ", Phys. Stat. Sol., vol. 34, ppK177-180 (1969).
- [10] E.E. Underwood, *Quantitative stereology*, Addison-Wesley, p22 (1970).
- [11] E. Grob, M. Riffel and U. Stohrer, "Thermoelectric generators made of FeSi_2 and HMS: fabrication and measurement", J. Mater. Res., vol. 10, No. 1, pp34-40 (1995).
- [12] C.W Robert, *CRC Handbook of Chemistry and Physics*, 68th, pE-102 (1987).

Plasma spray forming as a novel production method for thermoelectric materials

Jürgen Schilz, Michael Riffel

Institut für Werkstoff-Forschung, Deutsche Forschungsanstalt für Luft- und Raumfahrt (DLR), D-51140 Köln, Germany,
Tel.: +49/2203/601-3556, Fax: +49/2203/696480, E-mail: juergen.schilz@dlr.de

Robert Mathesius

RWTH-Aachen, Werkstoffwissenschaften, Jülicher Str. 342, D-52056 Aachen, Germany

Günter Schiller, Rudolf Henne

Inst. für Technische Thermodynamik, Deutsche Forschungsanstalt für Luft- und Raumfahrt (DLR), D-70503 Stuttgart, Germany

Ronald W. Smith

Drexel University, Materials Engineering Department, 31 & Market Streets, Philadelphia PA 1910, USA

Abstract

To date the development of thermoelectric materials and technology has reached a level, that allows the fabrication of reliable generators. It now turns out that the main impediment on the way to large scale, commercial (terrestrial) applications is primarily not the comparable low efficiency of the devices, but the high investment costs, which are still on the order of several ten Dollars per Watt.

Necessary conditions for cost reduction are the availability of (i) cheap, non-toxic materials in large quantities and (ii) processing methods which allow efficient production; preferably the formation of complete device structures within a single, automatized manufacturing step.

This paper introduces plasma spraying as a forming process with the potential to fulfil the above stated condition. The paper reports on first studies on the consolidation and characterization of iron disilicide (FeSi_2). It was found that plasma spray forming is applicable to produce dense materials with properties comparable to hot-pressed ones.

Introduction

Thermoelectric (TE) generators have shown their reliability in space applications and there are already a number of efforts to bring TE generation of electricity into large scale terrestrial, commercial applications (i.e. [1,2]). Requirement, however, are lower investment costs for the modules, and — according to ecologic standards — the employment of non-toxic materials.

In terms of cost efficiency it is indispensable to develop manufacturing processes for TE devices, which not only consolidate the powders in automatized procedures, but also have the potential of lateral shape forming and composition control of the material. This would give the possibility to form complete elements, modules, or functionally adapted TE devices, i.e. integrated TE circuits, in a single manufacturing step.

Here, we introduce plasma spray forming of powders as a process with the required capabilities. As first TE material to be processed by plasma spray forming, we have chosen iron disilicide (FeSi_2), which has an indeed low conversion efficiency, but it meets the condition of being cheap, non-toxic, and easy to handle [3]. Additionally it can be synthesized by inert gas atomization [4], i.e. by an industrial mass production process and thus at comparable low costs.

Due to its well known properties, the processing of FeSi_2 allows a valuation of the novel method's applicability.

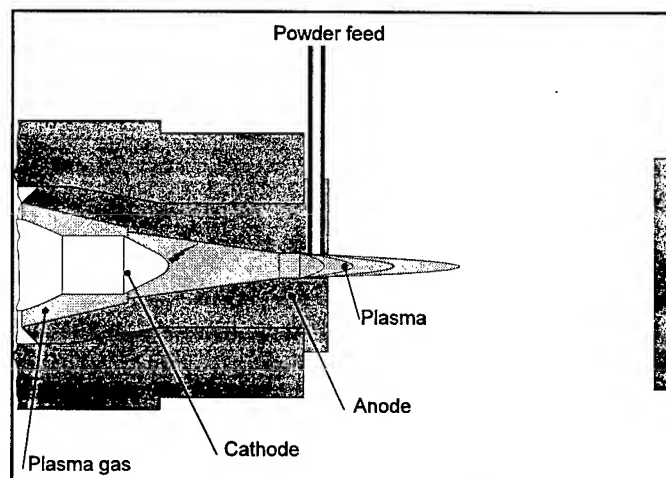


Fig. 1: Sketch of a plasma spray gun.

Plasma spray forming

Plasma spraying is a technology that has been widely used in the aircraft industry for coating both metals and ceramics since 40 years. Coatings are formed by blowing powder into a plasma jet, which is produced by an electric discharge in a gas. Due to the thermal expansion (temperature about 10000 K), the plasma

gains a velocity on the order of 1000 m/s. The powder particles are heated and partially molten by the hot plasma and the then pasty droplets catapulted with a velocity around 400 m/s onto the substrate forming flake-like structures (cf. Fig. 1) [5]. In the present case, however, the spraying process is not applied with the aim to form a coating of a substrate, but to form bulk material, which itself has functional aspects, i.e. which TE properties will be exploited.

It is standard, that the feeding of several different powders and the moving of the plasma gun (or the target) is computerized. Additionally, the facility allows a partly shading of the beam, which gives the possibility to "write" structures consisting of e.g. alternate layers of differently doped TE-material as the one sketched in Fig. 2. The beam has a diameter around 10 mm and, by masking the powder flow, structures with sizes of several mm are possible [6]. Plasma spray forming can be used to built up multi-layer thermoelectric modules of much smaller dimensions than by conventional hot-pressing procedures.

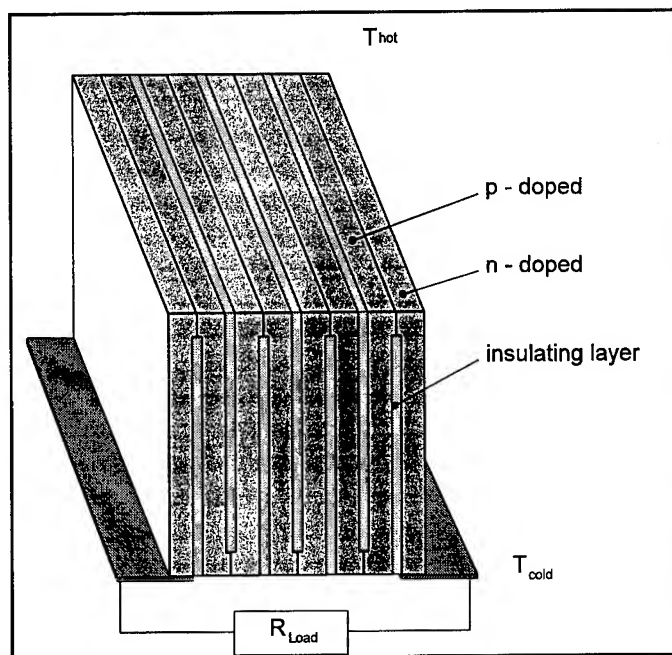


Fig. 2: It is possible to produce TE-devices with a quasi-layer structure by plasma spray forming.

Experiment

Gas atomized, Co- and Al-doped, FeSi_2 powders with mean particle diameter of 70 μm were plasma sprayed (PS) onto targets made of conventional steel St37 or of Ti-6Al-4V. The latter substrate's thermal expansion coefficient is well matched to that of FeSi_2 .

Spraying distance was 70 mm and PS powers between 20 and 30 kW with pure argon as plasma gas, and 30 kW with hydrogen-addition were used to prepare samples.

Material was sprayed in air (APS), with an argon shroud to aggravate oxidation (SPS), and finally in so-called vacuum, i.e. in a closed chamber operated below atmospheric pressure at

200 mbar inert argon gas (VPS).

For APS and SPS, the chosen spray parameters were appropriate to produce FeSi_2 layers up to a thickness of 3 mm, which showed a mechanical strength almost identical to that of hot-pressed material. Thus, there were no problems in cutting and machining samples to be tested. In the case of VPS, however, it turned out that the chosen spray parameters together with the quite large powder size did not lead to a sufficiently melting of the particles.

Whereas with APS and SPS at a powder feed rate of 30 g/Min every scan produced a layer of 0.1 mm thickness, VPS deposited layers did not exceed 0.02 mm per scan. Preliminary experiments with FeSi_2 powder synthesized by self propagating heating synthesis (SHS) and subsequent ball milling produced much better results in terms of deposition ability and layer density [7]. The material itself, however, was not optimized for TE purposes and is therefore not comparable. Here, we will mainly focus on the APS and SPS results.

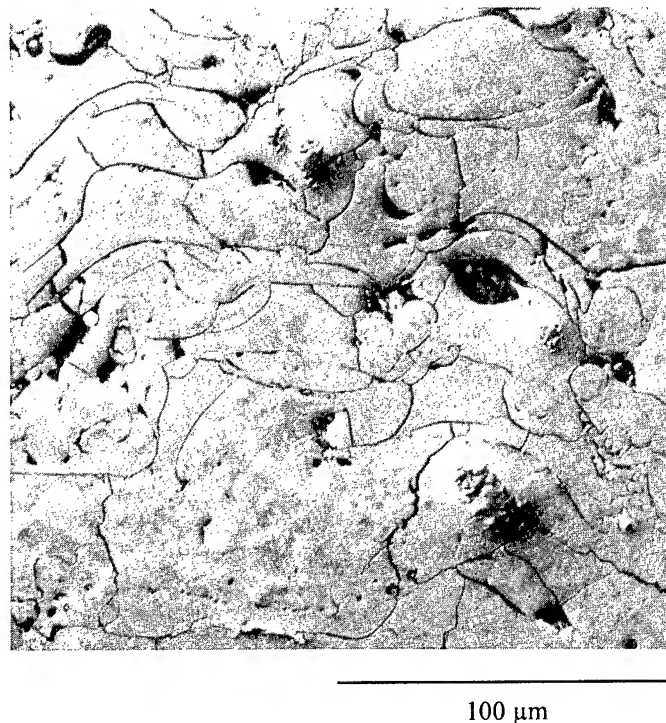


Fig. 3: Optical micrograph of argon shrouded plasma sprayed (SPS) FeSi_2 sample.

Results and discussion

Metallography

Fig. 3 shows an optical micrograph perpendicular to the growth direction of an as-sprayed SPS FeSi_2 sample deposited at 30 kW. We covered the sample with a thin film of ZnSe, which enhances optical contrast and thus makes the inner grain structure visible. The former droplets, referred to as splats, can clearly be distinguished, because they are surrounded by thin oxide layers, which developed during the flight in spite of the argon shroud. Compared to APS samples, the oxide contents is reduced, but only the employment of VPS prevented oxidation efficiently. The larger structures are pores, which area sums up

to a fraction of 4.5% as determined by optical image processing [8]. The porosity was found to be a function of the spraying power. At the highest energy setting bulk material could be produced, where the pores covered only a fraction of 1.6%. However, Al-doped p-type FeSi₂ showed systematically a 20% higher porosity than Co-doped material. A similar behaviour was observed with hot-pressed material — Al- and Co-doped FeSi₂ show a significant difference in compactibility.

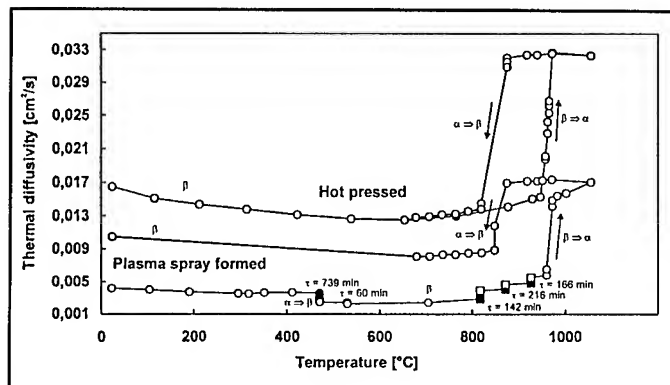


Fig. 4: Thermal diffusivity as a function of temperature of plasma spray formed Co-doped n-type FeSi₂.

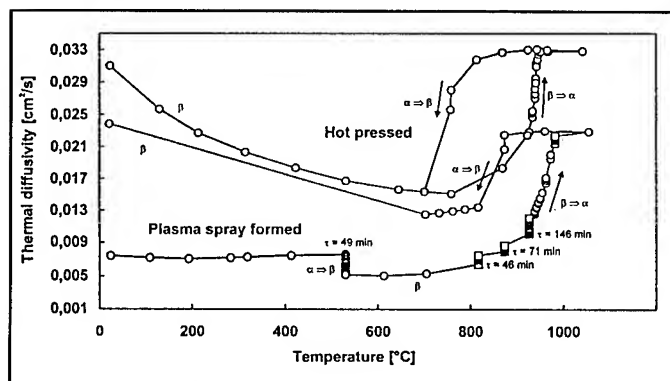


Fig. 5: Thermal diffusivity as a function of temperature of plasma spray formed Al-doped p-type FeSi₂.

Thermal conductivity

Due to the rapid solidification during the spraying procedure, the quenched FeSi₂ is still in its metallic α -phase as revealed by x-ray diffraction (XRD). In spite of this, the thermal diffusivity, D_{th} , at room temperature is by a factor of 3.5 lower compared to hot-pressed material from the same powder batch (cf. Figs. 4 and 5). Heating the sample to an intermediate temperature, T , between 400 and 700°C and maintaining the temperature fixed, a decrease in D_{th} is observable. Concomitant XRD investigations proved this to be the transition from the (metastable) α into the semiconducting β -phase. Plotting D_{th} as a function of time reveals an exponential decrease with a time constant, τ . The value of τ again is a function of the transition temperature obeying $\tau = \tau_0 \exp(E_a/RT)$ with E_a an activation energy, R the universal gas constant, and τ_0 a scaling parameter. Evaluation of $\tau(T)$ on different samples at different T revealed an activation

energy for the α to β -transition of 200 kJ/mol for the Co-doped n-type and 260 kJ/mol for the Al-doped p-type plasma spray formed FeSi₂ [9].

When further rising the temperature to a value at or above 800°C, one finds an increase in D_{th} with time. The time constants in this case, however, do not show any particular correlation with temperature, which disregards any simple activated process.

The measurement cycle is continued by heating up to 1050°C, which brings the material again into the α -phase and then slowly cooling down to room temperature allowing the transition into the β -phase to occur. It is seen in Figs. 4 and 5 that the D_{th} -values after the heat treatment are approaching those of the hot-pressed FeSi₂. Indeed, a plot of room temperature thermal conductivity, κ , vs. heat treatment time at 1000°C shows, that the PS FeSi₂ obviously undergoes a microstructural change eventually reaching the value of hot-pressed material (cf. Fig. 6). Material inspection by means of optical metallography did not detect any obvious reason for the aging process. Possible mechanisms can be crystallization of initially (pseudo-) amorphous regions or the relaxation of flat micropores in the bond regions between the splats [10]. A small amount of such laminar type of pores can be very effective, as they exhibit a large scattering cross section.

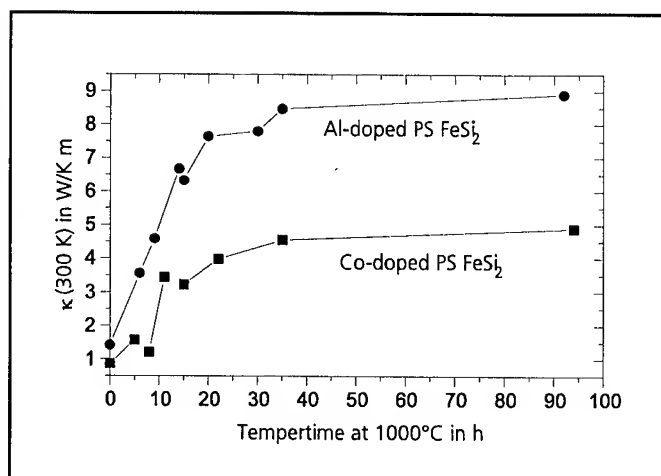


Fig. 6: Room temperature thermal diffusivity values of plasma spray formed FeSi₂ as a function of heat treatment time at 1000°C.

Electrical conductivity and thermopower

SPS FeSi₂ shows an extremely low electrical conductivity, σ (cf. Fig. 7). Compared to hot-pressed material it is by a factor of 5 lower. We contribute this behaviour to the oxide contents in the samples. This assumption is supported by the observation that APS FeSi₂ shown even a 20% lower σ . As seen from Fig. 7, in contrast to the thermal conductivity, σ does not show any significant dependence on the aging properties of the material. Table 1 lists room temperature values of κ , σ , S , and carrier concentration, n , for "as sprayed" (i.e. only the α -to- β -transition has been induced) and 50 h tempered n-type FeSi₂ together with

data of hot-pressed samples from the same powder batch. It can be seen that the thermopower, S , for PS FeSi_2 is the same than for hot-pressed material. Also here, no dependence on the heat treatment process was observed.

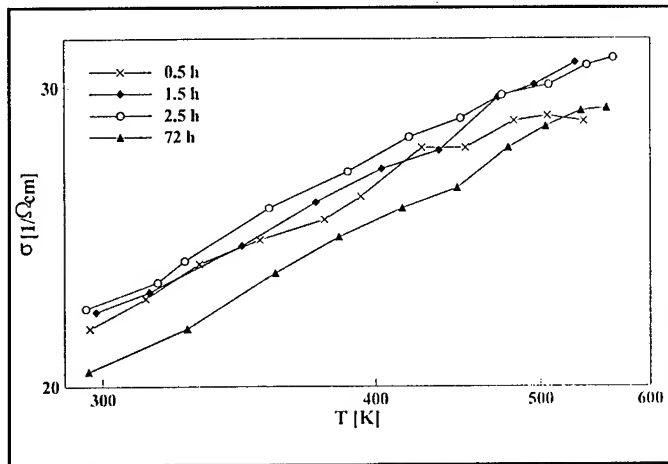


Fig. 7: Electrical conductivity of plasma spray formed Co-doped n-type FeSi_2 after different heat treatment durations at 800°C .

	Plasma "as sprayed"	sprayed 50 h	Hot pressed
Porosity	4.5 %	4.5 %	2 %
κ in W/mK	1.5	4.5	4.9
S in $\mu\text{V/K}$	180	180	165
σ in $1/\Omega\text{cm}$	22	20	100
n in cm^{-3}	$2 \cdot 10^{21}$	—	$2 \cdot 10^{21}$

Table 1: Room temperature characteristics of plasma sprayed and hot-pressed Co-doped n-type FeSi_2 .

Conclusions

Our experiments found that the employed Co- and Al-doped gas atomized iron disilicide powders exhibit a good sprayability in case of APS and SPS deposition. For VPS, the particle sizes of $70 \mu\text{m}$ average were found to be too large. Melting in the much faster VPS jet was not sufficient to achieve a substantial deposition rate. Plasma spray formed layers have to undergo a post-deposition annealing process in order to obtain the semi-conducting β -phase. It seems to be desirable to develop a process, which directly obtains the required semiconducting material.

Regarding thermoelectric properties, APS formed TE-material can be disregarded, because of the too high oxide content. Employing SPS reduces the amount of oxides somewhat, but there

is a demand for further improvement, as the electrical conductivity is still extremely low.

The PS FeSi_2 is not thermally stable. An aging process occurs, which may be due to recrystallisation and/or micropore relaxation. Interesting is the fact, that the aging process only affects the thermal diffusivity (conductivity), whereas the electrical conductivity and the thermopower remain unchanged. As seen from Table 1, in spite of the low σ , the ZT -value of "as sprayed" FeSi_2 is almost that of hot pressed material due to the extremely low thermal conductivity.

This work was supported by the Deutsche Forschungsgemeinschaft, Schwerpunktprogramm Gradientenwerkstoffe. We gratefully acknowledge the continuous support by W.A. Kaysser and E. Lugscheider.

References

- [1] T. Kajikawa, M. Ito, I. Katsube, E. Shibuya, "Development of thermoelectric power generation system utilizing heat of combustible solid waste", Proc. of the XIII Int. Conf. on Thermoelectrics, Kansas City (1994), AIP Conf. Proc. **316** (1995) 314.
- [2] J.C. Bass, N.B. Elsner, F.A. Leavitt, "Performance of the 1 kW thermoelectric generator for Diesel engines", Proc. of the XIII Int. Conf. on Thermoelectrics, Kansas City (1994), AIP Conf. Proc. **316** (1995) 295.
- [3] R.M. Ware, D.J. McNeill, "Iron disilicide as a thermoelectric generator material", Proc. IEE **111** (1964) 178.
- [4] U. Stöhrer, U. Taibon, E. Gross, U. Birkholz, "Figure of merit of cold and hot pressed FeSi_2 measured with the Kohlrausch method", Proc. IX Int. Conf. on Thermoelectrics, Pasadena CA, (1990) 242.
- [5] R.W. Smith, R. Novak, *Advances and Applications in U.S. Thermal Spray Technology*, pmi **23** (1991).
- [6] R. Henne, E. Fendler, M. Lang, Proc. 8th National Thermal Spray Conf., Houston, TX, ASM International, USA (1995) 533.
- [7] R.W. Smith, M. Barsoum, E. Lugscheider, P. Remer, R. Henne, J. Schilz, "Thermal spray formed FeSi_2 for thermoelectric applications", Thermal spraying conference (TS'96), Essen, Germany, March (1996).
- [8] M. Riffel, J. Schilz, E. Paulussen, S. Sous, F. Dourado, W. Kaysser, R. Mathesius, D. Koch, E. Lugscheider, R. Henne, "Preliminary results on plasma sprayed FeSi_2 ", Proc. of the 2nd European Workshop on Thermoelectrics (ETS2), Nancy (1995) 11.
- [9] J. Schilz, S.A. Sous, W.A. Kaysser, R. Mathesius, E. Lugscheider, "Thermal diffusivity of hot-pressed and thermal spray formed iron disilicide", Proc. of the First Southeast Asian Symp. on Thermophysical Properties (SEAS'95), Kuala Lumpur, Malaysia (1995).
- [10] H.E. Eaton, J.R. Linsey, R.B. Dinwiddie, "The effect of thermal aging on the thermal conductivity of plasma sprayed fully stabilized zirconia", In: *Thermal conductivity* **22**, Ed. T.W. Wong, Technomic (1994) p. 289.

Properties of iron disilicide doped with Ru, Rh and Pd

M.I.Fedorov, M.A.Khazan, A.E.Kaliazin, V.K.Zaitsev, N.F.Kartenko, A.E.Engalychev*

A.F.Ioffe Physical-Technical Institute, St. Petersburg, 194021, Russia

Abstract

This paper shows the results of a study of electrical resistivity and thermopower of semiconductor iron disilicide β -FeSi₂ doped with Ru, Rh and Pd in the temperature range 300-1000 K. Polycrystalline samples for measurement were prepared by the vacuum-casting method. The limits of each dopant solubility in iron disilicide were estimated by X-ray diffraction measurements. It is shown that if non-band conductivity mechanism takes place in pure iron disilicide, the addition of the heavy metals results in change of conductivity mechanism. The results obtained are discussed from the point of optical phonon drag effect.

Introduction

Semiconductor iron disilicide is a very interesting thermoelectric. It has low electrical conductivity, high thermal conductivity of crystal lattice and notwithstanding these points doped iron disilicide has a sufficient figure of merit $Z \approx 0.4 \cdot 10^{-3} \text{ K}^{-1}$. Thermopower (α) of pure iron disilicide has a maximum value up to $500 \mu\text{V/K}$ [1] and its temperature dependence is a bell-shape curve [1,2]. This bell-shape temperature dependence of thermopower is observed not only on pure iron disilicide but on iron disilicide doped by manganese and cobalt either [1-4]. If the first results were obtained on polycrystalline samples [1,2,4] and could be connected with boundary effects [5], the last results were obtained on single crystals [3] and so the hypothesis of boundary effects can be neglected. One can say there is no good explanation of such a temperature dependence of thermopower.

A few years ago it was suggested [6] that a drag of current carriers by longitudinal optical phonons could take place in this material. This work is devoted to an experimental check of this hypothesis. Until now mainly cobalt, manganese and aluminum were used as dopants in any systematic study of iron disilicide thermopower. The mass and size of manganese and cobalt atoms are very close to those of iron atoms. The mass and size of aluminum atom are close to those of silicon atoms. Therefore such impurities cannot essentially change conditions of creation and scattering of phonons in solid solutions of iron disilicide with aluminum, manganese or cobalt. If the hypothesis of drag by optical phonons is correct, doping by atoms with mass much greater or much less than that of iron or silicon can drastically change the shape of the temperature dependence of thermopower.

In this work we studied temperature dependencies of thermopower and electrical conductivity of solid solutions of iron disilicide with Pd, Rh and Ru. The masses of these atoms are nearly twice those of iron. Therefore doping with these atoms can result in increase of phonon scattering and decrease of optical phonon drag contribution in thermopower.

Samples and measurement

Polycrystalline samples for measurements were made by vacuum-casting method [7] as ingots 50 mm in length and 8 mm in diameter and then cut with a diamond disk. The final length of a specimen was 18 mm. The total amount of uncontrolled impurities was less than 0.03 mas.%. All samples were annealed for 100 h at 1000 K to obtain the semiconductor phase of iron disilicide. X-ray diffraction measurements were used to check the phase composition of the samples and solubility of dopants. It was shown that more than 5 at.% of Rh, less than 3 at.% of Ru and less than 2 at.% of Pd can be dissolved in iron disilicide. Measurements of temperature dependencies of thermopower and electrical conductivity were carried out simultaneously with automatic installation. Accuracy of thermopower and electrical conductivity measurement was better than 5%.

Experimental results

Figure 1 shows the temperature dependencies of electrical conductivity of pure iron disilicide and iron disilicide doped with palladium. There are two temperature regions for all dependencies. Activation dependence of electrical conductivity on temperature takes place in both regions. Intrinsic electrical conductivity at higher temperature is characterized by the same energy of activation ($E_1=0.43 \text{ eV}$) for all samples. At lower temperature the activation energy decreases when concentration of palladium increases (see Table 1). Similar dependence of activation energy on impurity content was observed earlier [1,2]. Figure 2 shows the temperature dependencies of thermopower measured on the same samples. There is a systematic modification of the dependencies which can be caused by compensation holes by electrons and then by increase of electron concentration. The variation of shape of the dependencies will be discussed later.

Figure 3 shows the temperature dependencies of electrical conductivity of pure iron disilicide and iron disilicide doped with ruthenium and rhodium. Figure 4 shows the relationships of temperature and thermopower for the same samples. The behavior of electrical conductivity for both dopants is the same as that for palladium doped samples. Moreover, the samples containing 3 and 5 at% of Rh show

*Present address: Joint-stock venture "EKROS", pr. Lunacharskogo, 47, St. Petersburg, 194291, Russia

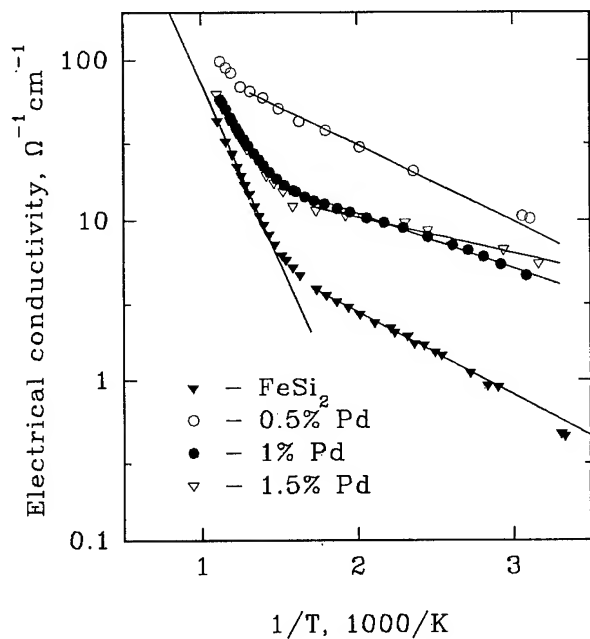


Figure 1: Electrical conductivity of β -FeSi₂, pure and doped with Pd. Symbols correspond to experimental data and solid lines to calculated dependencies

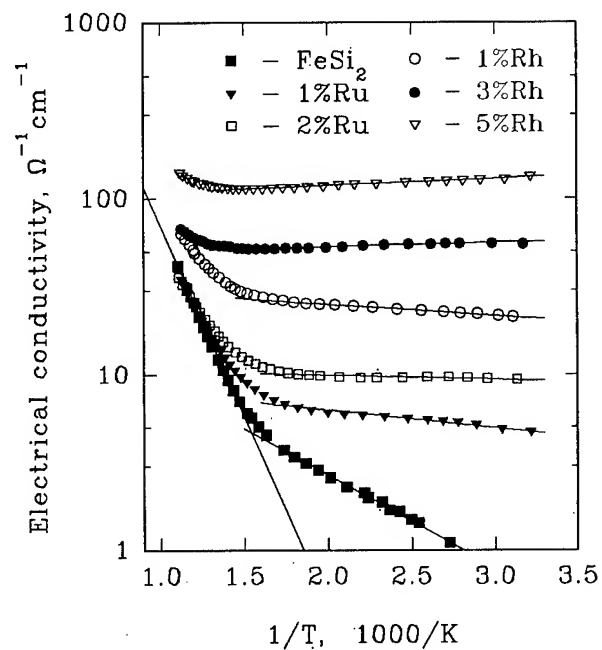


Figure 3: Electrical conductivity of β -FeSi₂, pure and doped with Rh and Ru. Symbols correspond to experimental data and solid lines to calculated dependencies

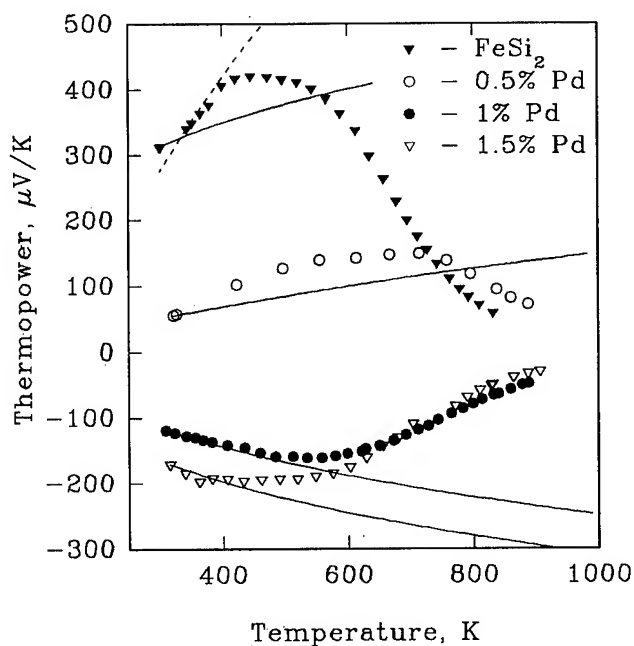


Figure 2: Thermopower of β -FeSi₂, pure and doped with Pd. Symbols correspond to experimental data. Solid lines correspond to dependencies calculated for usual one-band conductivity and dashed line to that for optical phonon drag

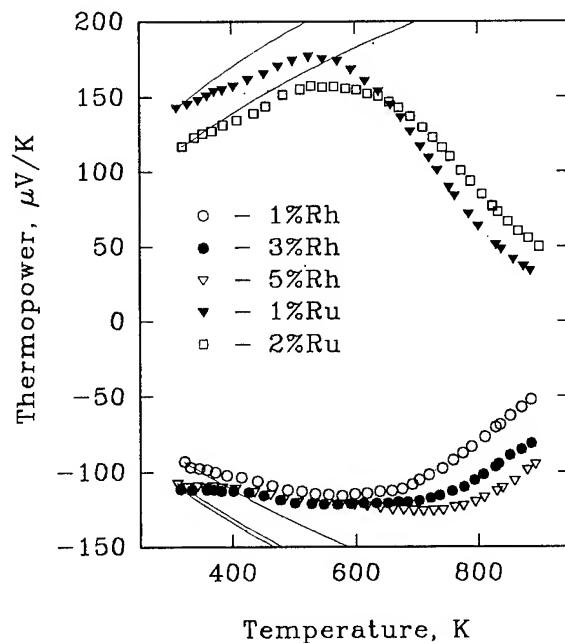


Figure 4: Thermopower of β -FeSi₂, pure and doped with Ru and Rh. Symbols correspond to experimental data. Solid lines correspond to dependencies calculated for usual one-band conductivity.

metallic characteristics of conductivity in lower temperature region. The behavior of thermopower for rhodium doped samples can be described as being caused by electron concentration increase when rhodium concentration increases. The behavior of thermopower for ruthenium doped samples can be caused by compensation of holes by electrons.

Table 1.

Activation energy of electrical conductivity in lower temperature region.

Impurity type	Impurity content %	Activation energy eV
none	0	0.10
Pd	0.5	0.09
Pd	1.0	0.07
Pd	1.5	0.04
Ru	1.0	0.02
Ru	2.0	0.005
Rh	1.0	0.01

Discussion

There is no theory which can describe complete behavior of electrical conductivity and thermopower in iron disilicide. Another difficulty exists - temperature dependencies of thermopower obtained by various authors for pure iron disilicide and doped materials of similar composition differ significantly [1,2,4]. Figure 5 shows temperature dependencies of thermopower measured by various authors on undoped iron disilicide of various degree of purity. Samples of β -FeSi₂ doped with Co and Mn usually have shape of thermopower temperature dependence close to that measured by Birkholz and Schelm [2] (Figure 5 - curve 3).

It can be suggested that various conductivity mechanisms prevail in various temperature range. Changing the conditions of obtaining iron disilicide can change the contribution of various mechanisms in conductivity and thermopower. A common feature of thermopower measurement on a majority of samples of pure β -FeSi₂ and doped by Co, Mn, Cr, Al is a very abrupt slope of thermopower temperature dependence at low temperature best described as $\alpha \sim \exp(-T_0/T)$. The results of fitting the experimental curves using this formula is shown on the Figure 5 in solid lines. Such a slope can hardly be caused by transition from band to polaron conductivity because there is no similar growth of electrical conductivity in this temperature region. Polaron theory also does not predict such a behavior of thermopower [8]. When the existence of optical phonon drag effect is supposed [4], thermopower is given by the formula:

$$\alpha = \frac{1}{3} \frac{k_B}{e} \frac{v_{lo}^2 \tau_{ph}}{D_{pol}} \cdot e^{-\frac{\Theta}{T}} \quad (1)$$

where k_B - Boltzman constant, e - electron charge, v_{lo} - group velocity, τ_{ph} - phonon transport time, D_{pol} - polaron diffusion coefficient, Θ - Debye temperature. We calculated thermopower using the formula (1) for pure β -FeSi₂ (Figure 2, dotted line).

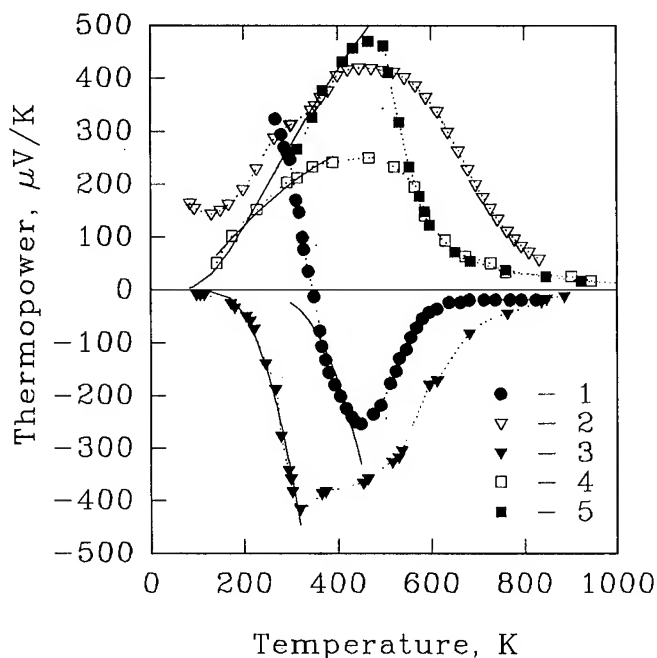


Figure 5. Thermopower of pure β -FeSi₂ measured by various author. 1 - [3], 2 - [4], 3 - [2], 4 - [1, low purity], 5 - [1, high purity]. Solid lines correspond to dependencies calculated using formula 1.

We calculated either thermopower for one-band model using the value of thermopower at 300 K. These curves are drawn in solid lines on Figures 2 and 4. As Figure 2 shows, the thermopower of pure β -FeSi₂ at lower temperature is well described by formula 1. The curve for the one-band model passes significantly lower than experimental data. When iron disilicide is doped with 0.5 at.% of palladium, the one-band curve is much closer to experimental data. When the amount of the impurity is not less than 1 at.% experimental data at lower temperatures either are well described by the one-band model or the theoretical curve passes higher than the data. Hence it is possible to suggest that doping by high metals results in destroying optical phonon drag. Similar results are obtained when β -FeSi₂ is doped with germanium [9].

Conclusion

So, one can say, that doping with heavy metals results in a drastic change of temperature dependence of thermopower in comparison with traditional doping. Hence, the hypothesis of

optical phonon drag effect in β -iron disilicide probably is correct and should be studied in more detail.

Acknowledgments

This work was supported by the Russian Foundation for Basic Research, grant No 95-02-04103-a.

References

- [1]. Kojima T. "Semiconducting and thermoelectrical properties of sintered iron disilicide", Phys. stat. sol. (a), vol.111, No.1, pp.233-242, (1989)
- [2]. Birkholz U., Schelm J. "Mechanism of electrical conduction in β -FeSi₂", Phys.Stat.sol., vol.27, No.1, pp.413-425, (1968)
- [3]. Heinrich A., Gladun C., Burkov A., Tomm Y., Brehme S., Lange H. "Thermopower and electrical resistivity of β -FeSi₂ single crystals doped with Co, Cr and Mn". Proceedings of the XIV International Conference on Thermoelectrics, St.Petersburg, pp.259-263, (1995)
- [4]. Zaitsev V.K., Ktitorov S.A., Kaliazin A.E., Fedorov M.I. "Thermoelectric properties of small mobility materials in the hopping regime", Proceedings of the XIV International Conference on Thermoelectrics, St.Petersburg, pp.210-211, (1995).
- [5]. Bogomolov V.N., Kurdyukov D.A., Prokofiev A.V., Ravich Yu.I., Samoilovich L.A., Samoilovich S.M. "Cluster superlattice as 3D-array of thermoionic energy converters", Proceedings of the XIV International Conference on Thermoelectrics, St.Petersburg, pp.280-282, (1995)
- [6]. Zaitsev V.K., Ktitorov S.A., Petrov Yu.V. "Small polaron drag", Materials for thermoelectric converters, Leningrad, p.36, (1987)
- [7]. Fedorov M.I., Engalychev A.E., Zaitsev V.K., Kaliazin A.E., Solomkin F.Yu. "Universal thermoelectric unit." AIP Conference Proceedings, vol.316, Thirteenth International Conference on Thermoelectrics, N.Y., pp.324-327, (1995)
- [8]. *Polarons*, ed.by Yu.A.Firsov, Moscow, 424 p., (1975)
- [9]. Fedorov M.I. et al., "Properties of β -FeSi₂ doped with heavy impurities." (to be published)

Analysis of Quadrupole Splitting of Transition Metal Doped β -FeSi₂

S. KONDO M.HASAKA and T.MORIMURA

Department of Materials Science and Engineering, Faculty of Engineering, Nagasaki University, Nagasaki 852, Japan

Abstract

Large quadrupole splittings ($Q.S.$) are observed in Co doped specimen, compared with other transition metal doped specimens while isomer shifts ($I.S.$) do not show large value. Since $Q.S.$ is associated with the electric field gradient at nucleus of iron atom; we calculate the potential at nucleus site, assuming the interaction between LA-phonon-conduction electron. Through the calculations, it is found that electric field gradient increase with the number of phonons attached to a conduction electron ($= \langle N_{ph} \rangle$). Accordingly large $Q.S.$ for Co doped specimen are considered to be due to large $\langle N_{ph} \rangle$ in comparison with those for other transition metal doped specimen.

Introduction

Intermetallic compound β -FeSi₂^[1-3] is expected to be applied to thermoelectric device because of high efficiency of changing heat into electric power. Especially Co or Mn doped β -FeSi₂ are very important material in the industrial fields; hence we measured Mössbauer effects of transition metal (Ti, Cr, Mn, Co or Ni) doped specimen at room temperature and analyzed $Q.S.$ for the purpose of investigating the changes in electronic structure owing to doping element.

Experimental Procedures

Fe₃₀Si₇₀ alloys, Fe_{30-x}Co_xSi₇₀ ($x=1, 3$) and Fe₂₈M₂Si₇₀ (M=Ti, Cr, Mn, Co or Ni) were prepared from electrolytic iron (99.9%), pure silicon (99.999%), electrolytic cobalt (99.93%), manganese (99.99%), titanium (99.9%), nickel (99.95%) and chromium (99.99%). The alloys were melted with a high-frequency furnace in vacuum to prohibit oxidation. For the purpose of forming a β -FeSi₂ phase, bars cut from the alloy ingots were annealed in sealed quartz ampoules for 240 hours at 1063K and then cooled slowly in a furnace. After the heat treatment, the bars were powdered for the measurement of Mössbauer effects. Mössbauer spectra of ⁵⁷Fe were taken at room temperature (about 296K) in a velocity range of -4mm/sec to +4mm/sec. Thermoelectromotive force for each alloy was measured in the temperature difference of up to 100K between hot and cold junction with temperature of cold junction remaining room temperature (about 296K to 302K).

Experimental Results

β -FeSi₂ has very complex structure with 48 atoms per unit cell: there exist two iron sites with different atomic configurations in a unit cell.

Figure 1 shows two different iron sites (I site and II site) as stated above. An iron atom in each site is surrounded by eight silicon atoms. As shown in Fig.1,

symmetry of each iron site is very low; accordingly $Q.S.$ for each iron site is supposed to be large.

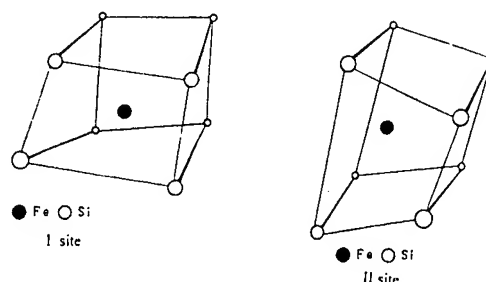


Fig.1 Schematic illustration of both iron sites (I site and II site)

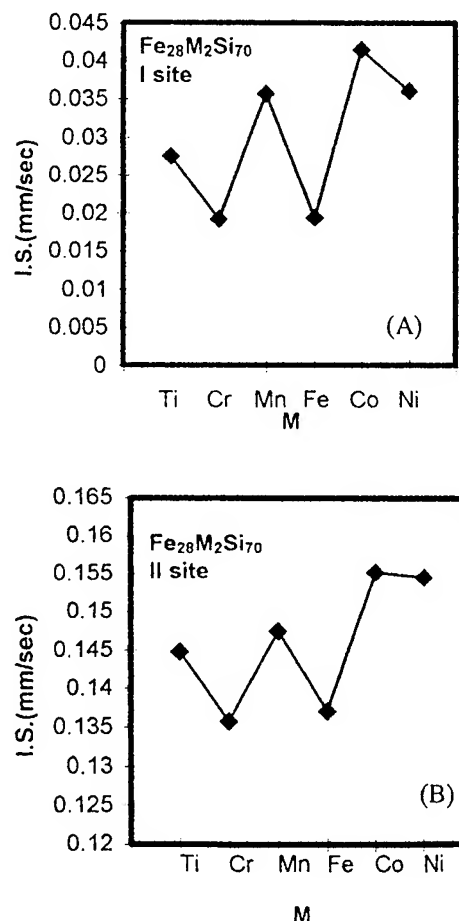


Fig.2 $I.S.$ of both iron sites for Fe₂₈M₂Si₇₀ alloys

Figure 2(A) and (B) show the isomer shifts (*I.S.*) of I site and II site for $\text{Fe}_{28}\text{M}_2\text{Si}_{70}$ alloy ($\text{M}=\text{Ti}, \text{Cr}, \text{Mn}, \text{Fe}, \text{Co}$ or Ni). Both *I.S.* of doped specimens tend to be large in comparison with those of non doped specimens

Figure 3 shows the *Q.S.* of the I site and II site for $\text{Fe}_{28}\text{M}_2\text{Si}_{70}$ alloy ($\text{M}=\text{Ti}, \text{Cr}, \text{Mn}, \text{Fe}, \text{Co}$ or Ni). As shown in Fig.3, *Q.S.* of both iron sites for Co doped specimen seem large.

Figure 4 shows *Q.S.* of both iron sites for $\text{Fe}_{30-x}\text{Co}_x\text{Si}_{70}$ alloy ($x=1,2,3$). *Q.S.* of both iron sites increase with Co concentration.

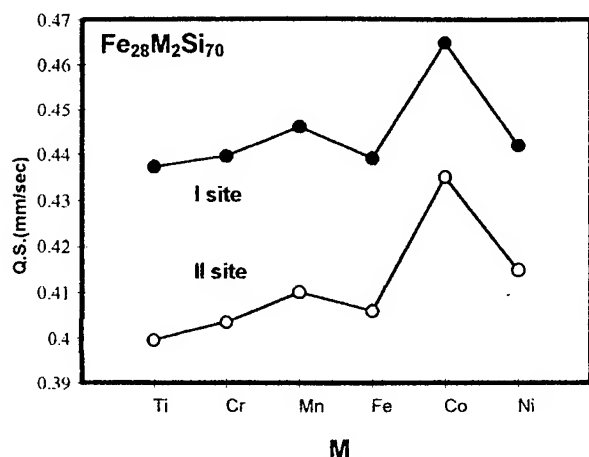


Fig.3 *Q.S.* of both iron sites for $\text{Fe}_{28}\text{M}_2\text{Si}_{70}$ alloys

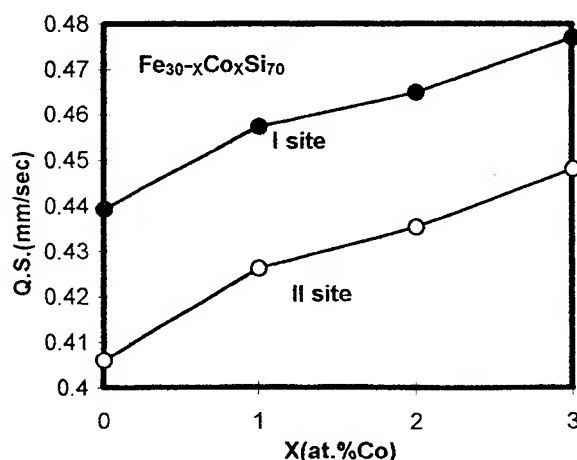


Fig.4 *Q.S.* of both iron sites for $\text{Fe}_{30-x}\text{Co}_x\text{Si}_{70}$ alloys

Figure 5 shows thermoelectromotive force for $\text{Fe}_{28}\text{M}_2\text{Si}_{70}$ ($\text{M}=\text{Ti}, \text{Cr}, \text{Mn}, \text{Co}$, or Ni) alloys. Thermoelectromotive force increases almost linearly with temperature of hot junction. Positive thermoelectromotive force is observed in the case of $\text{M}=\text{Ti}, \text{Cr}$ or Mn whereas negative one is observed in the case of $\text{M}=\text{Co}$ or Ni . It should be noted that thermoelectromotive force is negative when atomic number of doping element is larger than Fe ($\text{M}=\text{Co}$ or Ni) and is

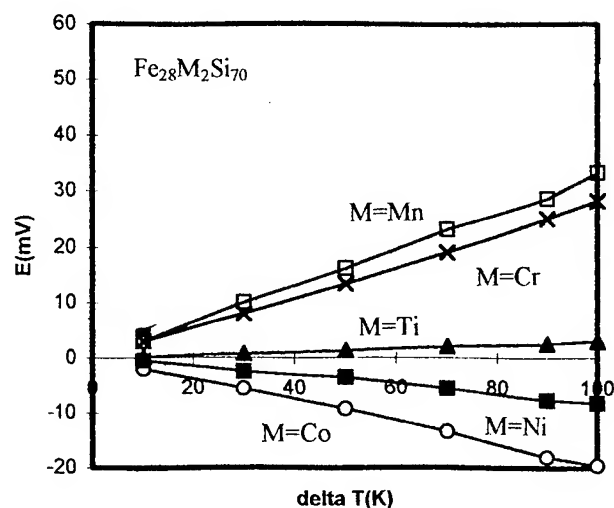


Fig.5 Thermoelectromotive force for $\text{Fe}_{28}\text{M}_2\text{Si}_{70}$ alloys where $\Delta T(\text{K}) = T_h - T_c$: T_h and T_c are temperature of hot and cold junction.

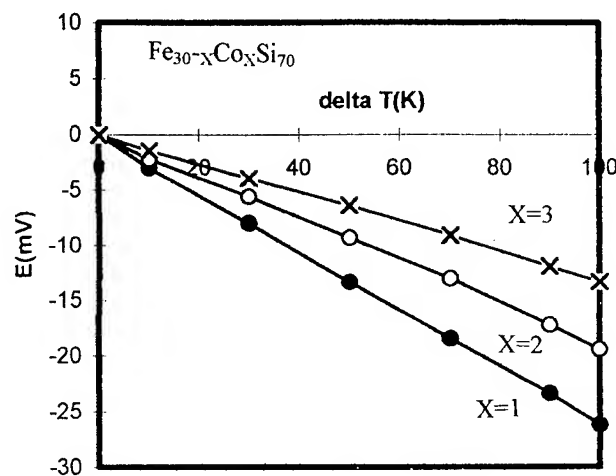


Fig.6 Thermoelectromotive force for $\text{Fe}_{30-x}\text{Co}_x\text{Si}_{70}$ alloys

positive when smaller than Fe ($\text{M}=\text{Ti}, \text{Cr}$ or Mn). From the sign of thermoelectromotive force, carrier of Ti, Cr or Mn doped specimen is supposed to be hole while that of Co or Ni doped specimen to be conduction electron.

Figure 6 shows thermoelectromotive force for $\text{Fe}_{30-x}\text{Co}_x\text{Si}_{70}$ alloy ($x=1,2,3$). Thermoelectromotive force increases linearly with the temperature of hot junction. As shown in Fig.6, thermoelectromotive force decreases with increase in Co concentration; accordingly absolute value of Seebeck coefficient decreases with increase in Co concentration.

Discussion

As shown in Fig.2 (A) and (B), *I.S.* of both iron sites for Co doped specimen seems not so remarkably large, compared with those for other transition metal such as Ni or

Mn doped specimen; however $Q.S.$ of Co doped specimen are large. Since Co doped β -FeSi₂ is industrially important material with good figure of merit; accordingly it seems essential to examine the mechanism of large $Q.S.$

At first let consider the direct effect of Co atoms, providing that electric charge of each atom is approximately expressed as point charge (namely, point charge approximation as used often in the $Q.S.$ analysis for ionic materials). $Q.S.$ is given in the well-known form as follows:

$$Q.S. = \frac{1}{2} e^2 q Q (1 + \frac{\eta^2}{3})^{1/2} \quad (1)$$

and

$$eq = |V_{zz}| \quad (2)$$

$$\eta = \frac{V_{xx} - V_{yy}}{V_{zz}}$$

Q is quadrupole moment and V_{xx} , V_{yy} , and V_{zz} are field gradient of x, y and z direction at ⁵⁷Fe nucleus. η is an asymmetric constant. Furthermore V_{xx} , V_{yy} and V_{zz} satisfy $|V_{xx}| \leq |V_{yy}| \leq |V_{zz}|$.

Then, based on the point charge approximation, each field gradient tensor V_{ij} at nucleus site is easily written down

$$V_{ij} = \left(\frac{\partial^2 V}{\partial i \partial j} \right)_{r=0} = \left(\frac{\partial^2}{\partial i \partial j} \sum_m \frac{q_m}{|\mathbf{r} - \mathbf{R}_m|} \right)_{r=0} \quad (3)$$

where q_m and \mathbf{R}_m are effective charge of m-th atom and vector from ⁵⁷Fe nucleus to m-th atom and i, j mean x, y and z. From eq. (3), V_{ij} is found to be expressed as a summation of $C_m q_m |\mathbf{R}_m|^{-3}$ (C_m is some arbitrary constant). Consequently atomic distance from ⁵⁷Fe nucleus to Co atom plays very important role in determining the electric field gradient, namely, $Q.S.$

Table 1 shows atomic distance in each Fe site. As illustrated in the table, the nearest atomic distance from the Fe I site to the Fe II site is 0.297nm and from the Fe II site to another Fe II site is 0.402nm. From the report of Kondo et al.^[4], it is disclosed that Co atoms mainly occupy site II through the analysis of intensity of Mössbauer spectra. Thereby the influence of Co atom to electric field gradient in Fe II site should be concluded to be much smaller than that in Fe I site because of the term of $|\mathbf{R}_m|^{-3}$. This means that the change in $Q.S.$ for Fe I site is larger than that for Fe II site. However experimental results, as shown in Fig 3 and 4, say that increase in $Q.S.$ for both iron sites is observed; influence of Co atom itself can not explain the both increase in $Q.S.$

From the above discussion, it is disclosed that local effect such as the direct influence of Co atom can not explain experimental results as shown in Fig.3 and 4; we

Table I Atomic distance for Fe I and Fe II sites, where Si I and Si II represent Si I and Si II sites, respectively.

x (SITE)	DISTANCE (Fe I SITE - x) nm	x (SITE)	DISTANCE (Fe II SITE - x) nm
Si I	0.2338	Si I	0.2347
Si I	0.2338	Si I	0.2347
Si I	0.2376	Si I	0.2333
Si I	0.2376	Si I	0.2333
Si II	0.2385	Si II	0.2429
Si II	0.2385	Si II	0.2429
Si II	0.2339	Si II	0.2335
Si II	0.2339	Si II	0.2335
Fe I	0.3957	Fe I	0.2967
Fe I	0.3957	Fe I	0.2967
Fe I	0.3978	Fe I	0.3975
Fe I	0.3978	Fe I	0.3975
Fe II	0.2967	Fe II	0.4022
Fe II	0.2967	Fe II	0.4022
Fe II	0.3975	Fe II	0.4027
Fe II	0.3975	Fe II	0.4027

need to introduce another factor. It seems, therefore, reasonable to consider the role of conduction electron, since conduction electrons spread all over the crystal, not localized and in addition, Co doped specimen shows n-type behavior of semiconductor.

To clarify the role of conduction electron, we divide the electron charge density $\rho(\mathbf{r})$ into two parts,

$$\rho(\mathbf{r}) = \rho_{in}(\mathbf{r}) + \rho_c(\mathbf{r}) \quad (4)$$

where $\rho_{in}(\mathbf{r})$ and $\rho_c(\mathbf{r})$ are charge density of inner and conduction electrons, respectively. Hence potential $V(\mathbf{r})$ can be divided into two parts:

$$V(\mathbf{r}) = V_{in}(\mathbf{r}) + V_c(\mathbf{r}) \quad (5)$$

In eq.(5), potential $V_{in}(\mathbf{r})$ and $V_c(\mathbf{r})$ are potentials due to inner and conduction electrons, respectively. Since $V_{in}(\mathbf{r})$ is considered to be constant, regardless of doping elements, the change in $Q.S.$ due to doping can be concluded to be ascribed to that in $V_c(\mathbf{r})$. Then $V_c(\mathbf{r})$ is given in the below form,

$$V_c(\mathbf{r}) = \iiint \frac{\rho_c(\mathbf{R})}{|\mathbf{R} - \mathbf{r}|} d\mathbf{R} \quad (6)$$

And we can write down $\rho_c(\mathbf{r})$, using Bloch state $\phi_{\mathbf{k}}(\mathbf{r})$

$$\rho_c(\mathbf{R}) = \sum_{\mathbf{k}} |\phi_{\mathbf{k}}(\mathbf{R})|^2 \quad (7)$$

Substituting eq.(7) into eq.(6), we can get

$$V_c(\mathbf{r}) = \sum_{\mathbf{k}} \langle \mathbf{k} | \frac{1}{|\mathbf{R} - \mathbf{r}|} | \mathbf{k} \rangle \quad (8)$$

where

$$| \mathbf{k} \rangle = \varphi_{\mathbf{k}}(\mathbf{R})$$

For simplifying the discussion, let conduction electron be free electron, then $| \mathbf{k} \rangle = \exp(i\mathbf{k}\mathbf{R}) / \sqrt{\Omega}$ (Ω is volume of the system), consequently eq.(8) is

$$V_c(r) = \frac{1}{\Omega} \sum_{\mathbf{k}} \iiint \frac{d\mathbf{R}}{|\mathbf{R} - \mathbf{r}|} = \frac{N}{\Omega} \pi \left(2R_0^2 - \frac{2}{3}r^2 \right) \quad (9)$$

where $4\pi R_0^3/3 = \Omega$ and $r = |\mathbf{r}|$. N is the number of conduction electrons.

Hence we can get electric field gradient tensor V_{ij} as following form:

$$V_{ij} = -\frac{4}{3} \pi \frac{N}{\Omega} \begin{bmatrix} 1 & 0 & 0 \\ 0 & 1 & 0 \\ 0 & 0 & 1 \end{bmatrix} \quad (10)$$

Combining eq.(10) with eq.(1) and (2), we can conclude $Q.S.$ to be proportional to N/Ω namely, conduction electron density. Hence increase in $Q.S.$ for both iron sites, as illustrated in Fig.4, can be interpreted as increase in conduction electron density due to the increase in Co concentration.

Next we consider the Seebeck coefficient. Seebeck coefficient S is considered to be proportional to $1/n$ (n : carrier density); as illustrated in Fig.6, decrease in thermoelectromotive force with increase in Co concentration can be explained by increase in electron charge density. However Seebeck coefficient for Ni doped specimen, as illustrated in Fig.5, is smaller than that for Co doped one, which implies that carrier density of Ni doped specimen is larger than that of Co doped one. If carrier density (conduction electron density = N/Ω) of Ni doped specimen is larger than that of Co doped specimen, then we cannot explain large $Q.S.$ for both iron sites in Co doped specimen because of $Q.S. \propto N/\Omega$. Hence we can not explain large $Q.S.$ by above discussion.

As stated above, effect of conduction electron itself can not explain experimental results, with implying other interaction. Hence it appears reasonable to consider the interaction between conduction electrons and phonons. Then let introduce LA-phonon-conduction electron interaction for explaining the experimental results, especially large $Q.S.$ for both iron sites in Co doped specimen. Hamiltonian for the system is well-known form^[5],

$$H = H_0 + H'$$

$$H_0 | \mathbf{k}, 0 \rangle = E_{\mathbf{k}}^0 | \mathbf{k}, 0 \rangle$$

and

$$H' = iC_1 \sum_{\mathbf{k}} \sum_{\mathbf{q}} \frac{|\mathbf{q}|}{\sqrt{2\rho_0 w_{\mathbf{q}}}} (a_{\mathbf{q}} - a_{-\mathbf{q}}^+) c_{\mathbf{k}+\mathbf{q}}^+ c_{\mathbf{k}} \quad (11)$$

where $| \mathbf{k}, 0 \rangle$ is Bloch state with no perturbation, $a_{\mathbf{q}}^+$ and $a_{\mathbf{q}}$ are formation and annihilation operators of phonon with \mathbf{q} . $c_{\mathbf{k}}^+$ and $c_{\mathbf{k}}$ are formation and annihilation operators of conduction electron with \mathbf{k} . C_1 and ρ_0 are deformation potential constant and density of specimen. In the first order of perturbation, Bloch state is expressed as

$$| \mathbf{k} \rangle = | \mathbf{k}, 0 \rangle + \sum_{\mathbf{q}} \frac{\langle \mathbf{k} - \mathbf{q}, 1\mathbf{q} | H' | \mathbf{k}, 0 \rangle}{E_{\mathbf{k}}^0 - E_{\mathbf{k}-\mathbf{q}}^0 - w_{\mathbf{q}}} | \mathbf{k} - \mathbf{q}, 1\mathbf{q} \rangle \quad (12)$$

Substituting eq.(12) into eq.(8), we get

$$V_c(\mathbf{r}) = \sum_{\mathbf{k}} \langle \mathbf{k}, 0 | \frac{1}{|\mathbf{R} - \mathbf{r}|} | \mathbf{k}, 0 \rangle + \sum_{\mathbf{k}} \sum_{\mathbf{q}} |\lambda(\mathbf{k}, \mathbf{q})|^2 \langle \mathbf{k} - \mathbf{q}, 1\mathbf{q} | \frac{1}{|\mathbf{R} - \mathbf{r}|} | \mathbf{k} - \mathbf{q}, 1\mathbf{q} \rangle \quad (13)$$

where

$$\lambda(\mathbf{k}, \mathbf{q}) = \frac{\langle \mathbf{k} - \mathbf{q}, 1\mathbf{q} | H' | \mathbf{k}, 0 \rangle}{E_{\mathbf{k}}^0 - E_{\mathbf{k}-\mathbf{q}}^0 - w_{\mathbf{q}}}$$

The number of phonons attached to a conduction electron with \mathbf{k} ($= \langle N_{ph} \rangle$) is

$$\langle N_{ph} \rangle = \langle \mathbf{k} | \sum_{\mathbf{q}} a_{\mathbf{q}}^+ a_{\mathbf{q}} | \mathbf{k} \rangle = \sum_{\mathbf{q}} |\lambda(\mathbf{k}, \mathbf{q})|^2 \quad (14)$$

if we assume conduction electron to be free electron as discussed previously, then potential $V_c(\mathbf{r})$ is

$$V_c(\mathbf{r}) = \frac{1}{\Omega} \sum_{\mathbf{k}} \iiint \frac{d\mathbf{R}}{|\mathbf{R} - \mathbf{r}|} + \frac{1}{\Omega} \sum_{\mathbf{k}} \sum_{\mathbf{q}} |\lambda(\mathbf{k}, \mathbf{q})|^2 \iiint \frac{d\mathbf{R}}{|\mathbf{R} - \mathbf{r}|}$$

$$= \frac{1}{\Omega} \left(N + \sum_{\mathbf{k}} \sum_{\mathbf{q}} |\lambda(\mathbf{k}, \mathbf{q})|^2 \right) \iiint \frac{d\mathbf{R}}{|\mathbf{R} - \mathbf{r}|}$$

$$= \frac{N}{\Omega} \left(1 + \langle N_{ph} \rangle \right) \left(2\pi R_0^2 - 2\pi r^2 / 3 \right) \quad (15)$$

Hence, finally we get

$$\left| \frac{\partial^2}{\partial z^2} V_c(\mathbf{r}) \right|_{r=0} = \frac{4\pi}{3} \frac{N}{\Omega} \left(1 + \langle N_{ph} \rangle \right) \quad (16)$$

Based on the eq.(16), large $Q.S.$ observed in Co doped specimen is supposed to be due to the term of

$\langle N_{ph} \rangle$: the number of phonon attached to one electron is large in Co doped specimen., compared with other transition metal doped one. Hence, though (N/Ω) for Ni doped specimen is larger, as illustrated in Fig.5, than that for Co doped one, large $Q.S.$ appears in Co doped specimen due to the term of $(1 + \langle N_{ph} \rangle)$ in eq.(16).

Conclusion

Large $Q.S.$ is observed in Co doped specimen. Since $Q.S.$ is associated with electric field gradient at nucleus of iron atom, we evaluate electric charge density of conduction electron, assuming LA-phonon-conduction electron interaction. Electric field gradient at nucleus of iron atom is found to increase with $\langle N_{ph} \rangle$; hence large $Q.S.$ observed in Co doped specimen is concluded to be due to large $\langle N_{ph} \rangle$.

References

- [1] T.Kojima, M.Okamoto and I.Nishida, Proc.5th Int. Conf. Thermoelectric Energy Conv., Arlington, March 1984, p.56.
- [2] R.W.Ware and D.J.McNeill, Proc.Inst.Electr.Eng. 111 (1964)178.
- [3] U.Birkholz and J.Schelm, Phys.Status.Solidi 27(1968)413.
- [4] S.Kondo, M.Hasaka, T.Morimura and Y.Miyajima, Physica B 198(1994)332
- [5] J.Bardeen and W.Shockley, Phys.Rev. 80(1950)72.

Electronic and Vibrational Properties of Skutterudites

D.J. Singh, L. Nordstrom, W.E. Pickett and J.L. Feldman
Naval Research Laboratory

Abstract

Advances in theoretical understanding, numerical algorithms and computing technology have made practical the determination of electronic, vibrational and other properties from first principles, even for complex materials like advanced thermoelectrics. These approaches require a minimum of experimental input, typically only composition and crystal structure. As such they may be viewed as a new window on the materials, which in combination with experiment may lead to new insights and better understanding of the variation of properties with variables like composition. This may then lead to more efficient optimization of thermoelectric materials and help in searches for new materials. This paper illustrates how theory is being applied in the search for high ZT thermoelectrics, mostly through examples.

Density Functional Methods

Thermoelectric (TE) research aimed at finding new high ZT materials faces certain difficulties, not the least of which is narrowing the search to a number of possibilities that can be feasibly studied. While this is a generic problem in exploratory materials research, it is particularly significant in TE efforts. This is because of the strong dependence of electrical transport properties of semiconductors on the doping level (n), which makes it necessary to optimize n in order to evaluate a given material, combined with the fact that TE research focuses on materials with at least potentially low thermal conductivity (κ) often leading to the consideration of materials with large complex unit cells. Among the more recent advances in this area of research are a number of improved automated characterization methods and the development of predictive material-specific computational tools, particularly first principles methods based on density functional theory. This paper discusses the use of these first principles tools, particularly the linearized augmented planewave (LAPW) method [1] for TE research using the binary and Ce-filled skutterudites as examples [2,3].

The basic approach in first principles studies is to start with the understanding that solids are essentially collections of electrons and nuclei governed by the rules of quantum mechanics and then to calculate as well as possible the properties with minimal experimental input. Modern calculations are based on density functional theory, usually within the local density approximation (LDA). Crystal structure data is the only experimental input, although some structural data, like internal coordinates, can be calculated. Because such calculations are not fits to or extrapolations from experimental measurements they can provide information

on materials for which experimental data is lacking or is unreliable. In this sense first principles calculations may be viewed as a new window on the materials, supplementing experimental studies.

Density functional theory reduces the intractable problem of solving the many body Schrodinger equation for the strongly interacting electron system to that of finding solutions to a set of single particle like equations coupled through a density dependent potential, $v_{xc}(\rho)$.

$$[T + V_{eff}(\mathbf{r}) - \epsilon_i] \phi_i(\mathbf{r}) = 0 \quad (1)$$

where T is the single particle kinetic energy and $v_{eff}(\mathbf{r})$ is an effective potential that includes the electron ion interaction as well as electron electron Hartree and v_{xc} contributions, which depend on the charge density,

$$\rho(\mathbf{r}) = \sum_{occ} \phi_i^*(\mathbf{r}) \phi_i(\mathbf{r}) \quad (2)$$

where the sum is over the occupied states. An excellent review of density functional theory is in the book of Lundqvist and March [4].

The local density approximation consists in the use of the local exchange correlation energy and potential of a uniform electron gas with the local density $\rho(\mathbf{r})$.

Density functional theory rigorously gives ground state properties, such as the charge density and the total energy. These may be computed as a function of the ionic positions within the Born-Oppenheimer approximation, to calculate minimum energy structures, phonon frequencies and elastic properties. Although there is no rigorous connection between the eigenvalues, ϵ_i and the physical excitation spectra, numerous calculations have shown that for transition metal compounds, the density functional band structure is ordinarily a very close approximation to the physical band structure.

Most methods for solving these equations in solids are based on basis set expansions of the wavefunctions, or at least can be shown to be equivalent to this. The differences between methods are in the particular basis set used (planewaves, local orbitals, muffin tin orbitals, etc.) and the representations of the density and potential. Additionally, some methods remove core states from the problem by employing pseudopotentials constructed to reproduce the chemical environment sensitive valence bands and energy.

The calculations discussed in this paper were performed within the LDA using an extended general potential LAPW

method [1]. This is an all electron method employing general expansions of the charge density and potential in all regions and a flexible basis. It is generally regarded as state-of-the-art for LDA calculations on complex transition metal compounds. Since Ref. 1 gives a general review of the method, only details specific to the present calculations are provided here.

Electronic Properties of IrSb₃, CoSb₃ and CoAs₃

The skutterudite pnictides, MA₃, where M is Co, Rh or Ir have been under investigation as a possible basis for new TE materials [5-7]. The binary skutterudites, which tend to form p-type, show very high mobilities, μ , coupled with reasonable Seebeck coefficients, S , in as synthesized form. Although the thermal conductivities, κ , are not as low as would be desired for a good TE material, estimates of the minimum thermal conductivity [5] imply that considerable reduction in the lattice thermal conductivity, κ_l is possible if suitable modifications can be found, and in fact measurements for Ce filled skutterudites do show strongly reduced κ [8].

The skutterudites occur in a bcc $Im\bar{3}$ structure with four formula units per cell. The structure is derived from an expanded simple cubic transition metal sublattice, with body center positions alternately filled with x-, y- and z- oriented A₄ rings or (one in four) empty. Besides the lattice parameter, there are two structural parameters, conventionally denoted u and v , which give the positions of the A atoms.

The binary skutterudites are conventionally regarded as doped semiconductors with moderate gaps, such as the 1.4 eV measured spectroscopically in IrSb₃ [5], although Ackermann and Wold reported that they did not find a convincingly clean optical gap in CoSb₃ [9]. As will be discussed below, our calculations also do not show clean gaps in these materials, although with an interesting twist for the case A=Sb, and this view is also supported by some more recent measurements [6,7].

As mentioned our calculations were performed using the general potential LAPW method. Experimental crystal structures were used [10,11]. Spin-orbit interactions were included for IrSb₃, where they were found to have only minor effects on the energy bands. The calculations employed the Hedin-Lundqvist parameterization of the exchange correlation functional along with well converged basis sets.

The calculated band structures of IrSb₃ and CoAs₃ are shown in Figs. 1 and 2 respectively. The electronic density of states (DOS) for IrSb₃ is shown in Fig. 3. The DOS of the Co based materials are qualitatively the same.

In all three materials there is a well-defined gap separating manifolds of valence and conduction bands, and this is evident in the DOS, which approximates what will be seen in spectroscopic experiments. Both manifolds are derived from hybridized combinations of transition metal d and pnictogen p states. Neglecting the (important) gap crossing state, discussed below, all the materials show an indirect gap from Γ to P. The LDA values of these pseudogaps are 0.71, 0.57 and 0.73 eV for IrSb₃, CoSb₃ and CoAs₃, respectively. The direct gaps at Γ are larger, e.g. 1.21 eV for IrSb₃, which

corresponds reasonably with an optical value of 1.4 eV [5]. However, electrical transport properties are determined by the band structure near the Fermi energy (E_F); here differences from the assumed picture of these materials are seen.

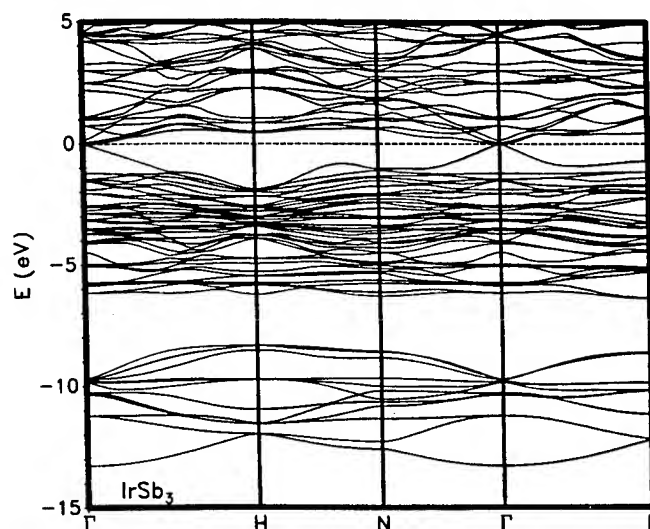


Fig. 1 Band structure of IrSb₃. The dashed line denotes E_F .

What is unexpected is the existence of a gap crossing band, in addition to the valence and conduction manifolds. This is present in all three materials, and disperses upwards from the valence manifold, touching or nearly touching (dependent on the material) the conduction band manifold at the Γ point. Like the other bands, this state has hybridized transition metal d, pnictogen p character.

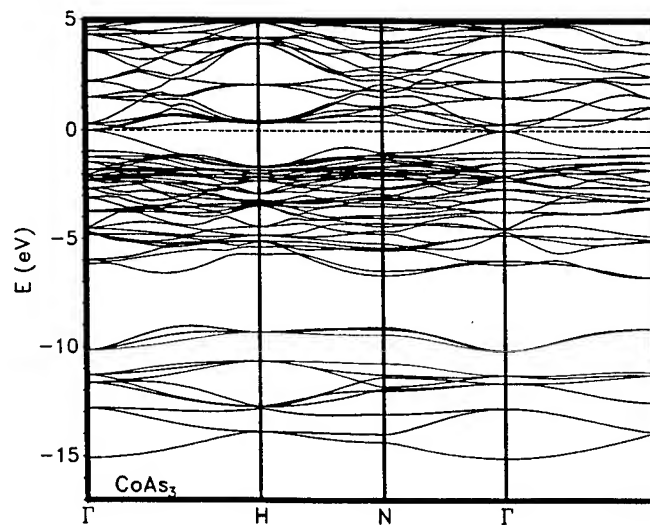


Fig. 2 Band structure of CoAs₃.

CoSb₃ is predicted to have a very small gap of only 50 meV, while CoAs₃ is predicted to be a true zero gap semiconductor. IrSb₃ is borderline in the sense that when the older handbook crystal structure [10] is used zero gap behavior is predicted, while with the probably more accurate internal parameters of Kjekshus and Rakke [11] a small 100 meV gap occurs. These differences are due to different orderings of the bands at the bottom of the conduction manifold resulting from the 0.05 Å

differences in Sb position.

The discovery of CoAs₃ as a new gapless semiconductor is notable because of the apparent stability of the skutterudites allowing the growth of high quality samples. In particular, there are strong theoretical indications that novel electronic states will develop at low temperatures in clean zero gap semiconductors [12-14], but these have not been realized experimentally because of difficulties in making sufficiently clean crystals of known materials like Hg chalcogenides and grey tin.

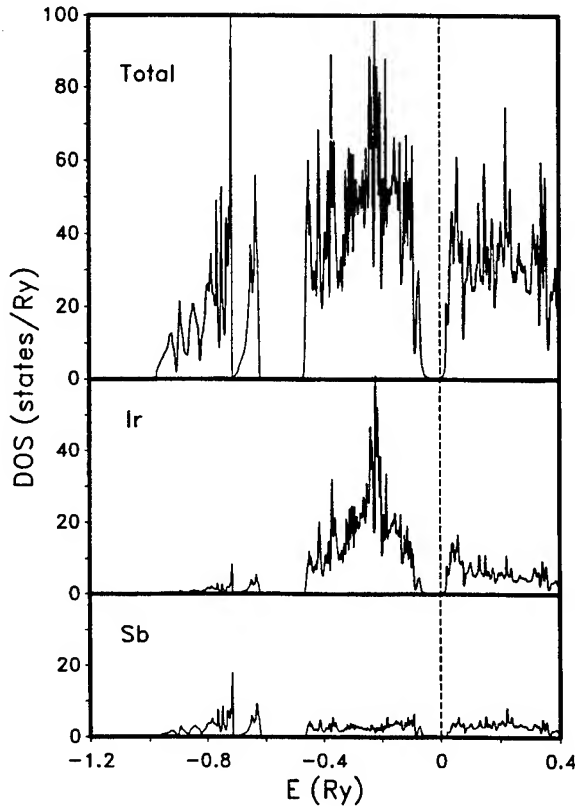


Fig. 3 Electronic DOS and projections for IrSb₃. The projections are on a per atom basis, while the DOS is per formula unit.

The fact that the gap crossing states in skutterudites had not been clearly seen experimentally is related to the complexity of these materials, and illustrates the importance of first principles studies. In particular, the band is difficult to see because of its strong dispersion and the large number of bands in the valence and conduction manifolds, both of which make it a relatively weak contributor to the DOS.

The dispersion of the gap crossing band is remarkable. Although a normal parabolic shape is evident in CoAs₃ the dispersion is linear practically to the maximum in IrSb₃ and CoSb₃. The parabolic region near Γ amounts to roughly 10^{-5} of the zone, corresponding to hole doping levels of $\sim 3 \times 10^{16} \text{ cm}^{-3}$. This is nearly three orders of magnitude below the doping levels normally found in TE materials and is below the

doping levels of reported p-type samples, and accordingly transport measurements on p-type material are determined by this linear behavior. The slopes of the linear dispersing bands are $\alpha = -3.45 \text{ eV \AA}$ and -3.10 eV \AA in IrSb₃ and CoSb₃, respectively.

As mentioned, reported p-type doping levels are within this linear dispersing regime, where transport properties are expected to deviate from standard semiconductor behavior. Here the DOS has a quadratic rather than square root dependence on E_F relative to the band edge, while the number of carriers, n , varies as E_F^3 rather than $E_F^{3/2}$ in the degenerate case. The inverse effective mass tensor $\nabla_i \nabla_j \epsilon(\mathbf{k})$, which is normally diagonal and constant near a band edge is entirely off diagonal. The transport mass normal to the Fermi surface is then formally infinite and the cyclotron mass is n dependent and given by k/α . Here k is the magnitude of the Fermi wavevector. The carrier density has the same dependence on k as in the standard parabolic case and the standard Hall determination of this quantity holds. In the constant scattering time approximation, the mobility is predicted to vary as $n^{-1/3}$ and the Seebeck coefficient is given by

$$S = -\frac{2\pi k_B^2 T}{3e\alpha} \left(\frac{\pi}{3n} \right)^{1/3} \quad (3)$$

As in the ordinary parabolic case, there is a linear T dependence and the scattering time does not enter the expression. However, the doping dependence is different.

With the doping level determined by Slack and Tsoukala [5] for their sample, $n = 1.1 \times 10^{19} \text{ cm}^{-3}$ and the calculated value of α for IrSb₃, we obtain $S = 62 \mu\text{V/K}$ at 300K and $123 \mu\text{V/K}$ at 600K, in good agreement with the measured values of $72 \mu\text{V/K}$ and $126 \mu\text{V/K}$. More recently, the doping level dependence of S has been measured for a series of p-type CoSb₃ samples [6] in apparent agreement with the predictions of Eqn. 3.

These band structures have certain implications for TE applications. First of all, in p-type antimonides, the doping dependence of the power factor, σS^2 will be weak, and this combined with the relatively high measured κ means that modifications beyond optimizing n will be needed to make these competitive. Secondly, reasonably high values of the effective mass ($\sim 0.5 m_e$) are predicted for n-type material. If the electron mobilities are comparable to the effective mobilities for p-type material, the TE performance comparable to the best present materials (i.e. $ZT \sim 1$) is possible with n-type doping.

Lattice Dynamics of CoSb₃

One of the key issues in TE research is understanding the thermal conductivity and devising strategies for its reduction. Measurements on binary skutterudites have shown thermal conductivities as much as 50 times higher than the estimated minimum for this structure [5]. In this section, use of first

principles calculations to understand the lattice dynamics of skutterudites is illustrated by application to CoSb_3 [15]. This is a prerequisite to understanding the thermal conductivity. Despite the fact the CoSb_3 is probably the best studied material as regards lattice dynamics, published information remains scant.

Infrared (IR) measurements have provided information on seven of the 19 distinct Γ point frequencies. Very recently, Nolas and co-workers [17] have measured some Raman frequencies in several skutterudites. Here we report LDA frozen phonon calculations of frequencies and eigenvectors for A_g and A_u Γ point modes. Certain cubic anharmonic parameters were also determined along with the bulk modulus and its pressure derivative. These were obtained by the usual approach of calculating total energies as a function of the atomic displacements compatible with the above symmetries. The experimentally determined IR frequencies and the new LDA "data" were then combined to fit force-constant models. These were used in turn to calculate complete phonon dispersions for CoSb_3 .

The electronic structure of CoSb_3 is strongly covalent. This view is supported by the short interatomic distances and the existence of high hole mobilities. This leads to certain expectations regarding the lattice dynamics. Strong two body interactions between nearest neighbor Co and Sb atoms and between neighboring Sb atoms in the rings are anticipated. Additionally, three body interactions may be expected associated with the covalent bonds. LO-TO splittings and Born effective charges may also be enhanced due to the covalency, and as such the Born effective charges should not be viewed as similar to ionic charges.

The lattice parameter, and bulk modulus and its pressure derivative were determined by computing the total energy as a function of volume and fitting to the Birch equation of state. The internal parameters, u and v , were fixed at their zero pressure values of 0.33537 and 0.15788, respectively. Accordingly, the value obtained is a constrained, rather than physical bulk modulus. This value is an upper bound on the physical modulus, which is then calculated from the force constant model, discussed below.

Our LDA calculations yield a lattice parameter of 8.937 Å or 1.1% below the measured value at room temperature. Lattice parameters smaller than experiment by 1-2% are typical in LDA calculations. The constrained bulk modulus is 105 GPa with a pressure derivative of 4.3.

The A_g symmetry modes are associated with changes in u and v retaining full crystal symmetry. Calculations of the total energy were performed for 13 values of (u,v) within 0.005 of the experimental values. A fit retaining all terms up to third order yielded a standard deviation of 0.02 mRy. The calculated minimum energy values of u and v were 0.333 and 0.160. The A_g Raman frequencies were obtained as 150 cm^{-1} and 178 cm^{-1} , with polarization vectors nearly parallel to the edges of the Sb_4 rings; the lower (higher) frequency mode modulates the longer (shorter) sides of the ring.

There are two independent A_u modes. This symmetry destroys

inversion, and as such the energy must be an even function of such coordinates. In particular there cannot be cubic terms in the energy as a function of these coordinates alone. We performed calculations for 4 sets of displacements consistent with A_u symmetry and used a quadratic least squares fit. A_u frequencies of 110 cm^{-1} and 241 cm^{-1} resulted.

TABLE I. Zone center phonon frequencies (cm^{-1}) for CoSb_3 . The experimental data is from Ref. 16. Elastic constants are in GPa. The bulk modulus is the LDA value less relaxation from the force constant model.

Mode	LK	Present	Expt.	LDA
A_g	162	149		150
	183	177		178
A_u	69	109		110
	250	242		241
F_u	79	78	78	
	119	120	120	
	143	145	144	
	174	176	174	
	242	242	247	
	258	260	257	
E_g	277	275	275	
	140	141		
	194	181		
F_g	71	84		
	103	96		
	162	158		
	188	176		
E_u	95	139		
	275	262		
C_{44}	22	44		
c'	81	74		
B	105	102		

As mentioned, Lutz and Kliche (LK) measured IR frequencies for CoSb_3 . They also present an analysis of these frequencies in terms of a central force model. Their model yields quite good agreement with three of the four LDA frequencies and the bulk modulus that we calculate, even though data on these phonons was not available when the model was constructed. The model fails for the lowest A_u mode, for which it yields 69 cm^{-1} . This mode involves a twisting motion of the Sb_4 rings along with concerted motion of Co and Sb atoms to minimize bond length changes. The bond stretching forces are relatively unimportant for this mode, and instead bond-angle forces related to covalency and/or long range forces will dominate. The LK model does not include bond angle forces.

We attempted to refit the LK model using the IR frequencies and our LDA results, but reasonable fits could not be obtained. Accordingly, we constructed a new model (actually we tested four similar models, which yielded insignificantly different results) and fit this to the data. The main difference

from the LK model was the inclusion of bond angle forces associated with the two distinct Sb-Sb-Co angles and an additional Co-Sb stretching parameter operating between the neighbors near 4.4 Å apart. This stretching constant was not included in the LK model even though it did include Co-Co forces, which act over a longer distance. We did not include Sb-Sb interactions across the Sb₄ ring diagonal, since these are probably not large in view of the nature of the A_g eigenvectors. Phonon frequencies and elastic properties as obtained from our model are given in Table 1 along with those of LK and the LDA and experimental data. Besides the lower A_u phonon, discussed above, the largest discrepancy is for the low frequency E_u mode and the c₄₄ elastic constant.

The phonon DOS, G is presented in Fig. 4. Notable features are a gap around 100 cm⁻¹, which is not present in the LK spectrum, and a rather sudden departure from parabolic behavior at ~70 cm⁻¹. This departure arises from optic branches in this frequency range. These are modes involving, for the most part, rigid motions of the Sb₄ rings. Sb-Sb bond bending and bond stretching behaviors are prominent around 110 cm⁻¹ and 150-175 cm⁻¹, respectively, while modes with large Co motions occur around 250 cm⁻¹.

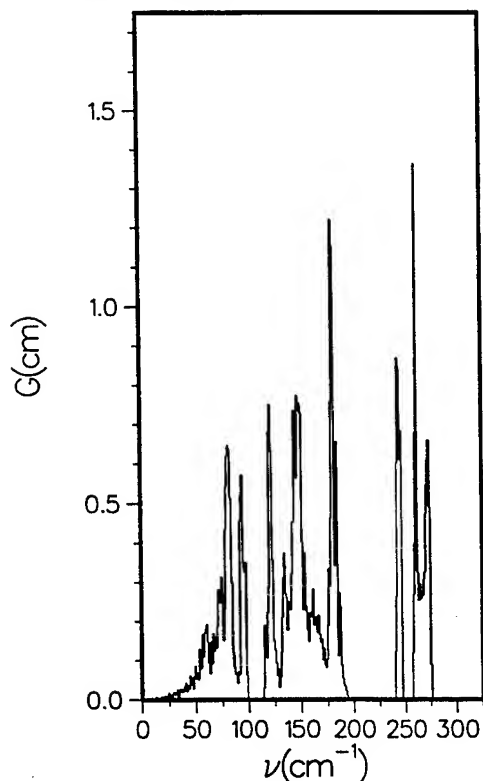


Fig. 4 Phonon DOS for CoSb₃. The normalization is 48 corresponding to the number of modes per 16 atom cell.

In order to start addressing the question of thermal conductivity, we have plotted a histogram of $\langle v^2 \rangle G$, where v is the group velocity, in Fig. 5. This function can give a qualitative understanding of which modes might contribute to the lattice thermal conductivity, as related quantities enter a relaxation time approximation to the Boltzmann-Peierls theory of thermal conductivity. In CoSb₃, $\langle v^2 \rangle G$ is seen to be

appreciable for certain optic modes as well as acoustic modes, although it should be noted that this is less so in our model than in the phonon dispersion of the LK model. Based on these results, the modes that are important in thermal conduction are the acoustic modes and those optic modes involving more or less rigid motions of the Sb₄ rings.

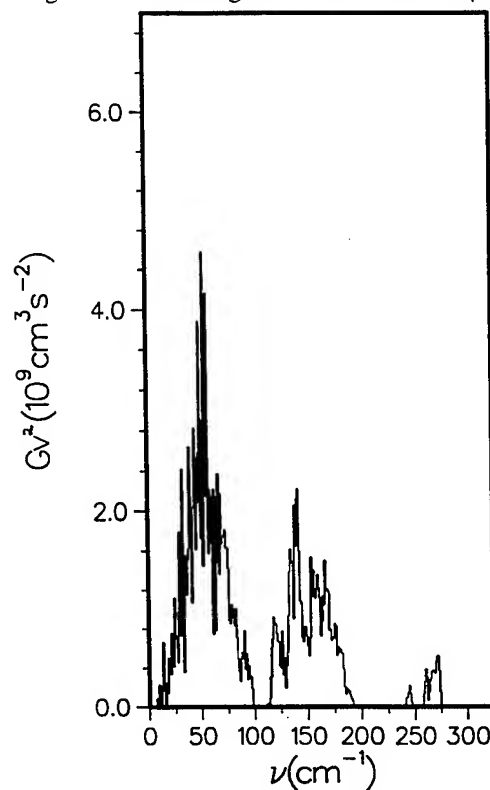


Fig. 5 $\langle v^2 \rangle G$ for CoSb₃ as determined from the force constant model.

Ce-filled Skutterudites

Morelli and Meisner [8] have recently reported transport measurements of CeFe₄Sb₁₂ showing a strongly reduced thermal conductivity relative to unfilled skutterudites. They measured a Seebeck coefficient of $S \sim 70 \mu\text{V/K}$ at 300K on their unoptimized p-type sample, with S still rising linearly with T .

Here we report studies of the electronic structure of this material and CeFe₄P₁₂ using LDA calculations. Two distinct views of the electronic structure have been suggested. First, it has been suggested that Ce is tetravalent in these compounds leading to a close correspondence in electronic structure with the unfilled skutterudites CoSb₃ and CoP₃. On the other hand, Meisner *et al.* [18] noting the relationship with U and Th filled skutterudites, argued that Ce is probably trivalent and semiconductivity in CeFe₄As₁₂ and CeFe₄P₁₂ is due to hybridization between valence states and Ce 4f states. This view is also supported by recent electron spin resonance [19] and transport measurements [8].

The electronic structures were calculated at the experimental lattice parameters of 7.792 Å and 9.135 Å for CeFe₄P₁₂ and CeFe₄Sb₁₂, respectively. Experimental values of u and v were used for CeFe₄P₁₂ ($u=0.3522$, $v=0.1501$), while in the

absence of experimental data, we calculated u and v for $\text{CeFe}_4\text{Sb}_{12}$ from the LDA total energy variation. In this way we obtain $u=0.333$ and $v=0.163$ with A_g Raman frequencies of 137 cm^{-1} and 157 cm^{-1} .

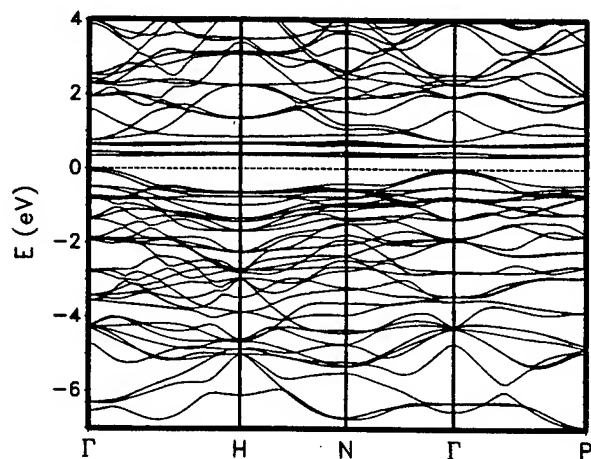


Fig. 6 Band structure of $\text{CeFe}_4\text{P}_{12}$

The band structures are shown in Figs. 6 and 7. From these it is immediately apparent that both materials are predicted to be narrow gap semiconductors. The band gaps are 340 meV and 100 meV for $\text{CeFe}_4\text{P}_{12}$ and $\text{CeFe}_4\text{Sb}_{12}$, respectively. The highest valence bands have hybridized Fe 3d pnictogen p character, while the lower lying ones are mostly pnictogen derived. This is qualitatively the same as in CoSb_3 and CoAs_3 , discussed above. The lowest lying conduction bands are dominated by the narrow spin-orbit split Ce 4f bands, which at first sight appear to be in a gap dug out of the other conduction bands. However, an analysis of the DOS (not shown) shows substantial Ce 4f contributions to the valence bands.

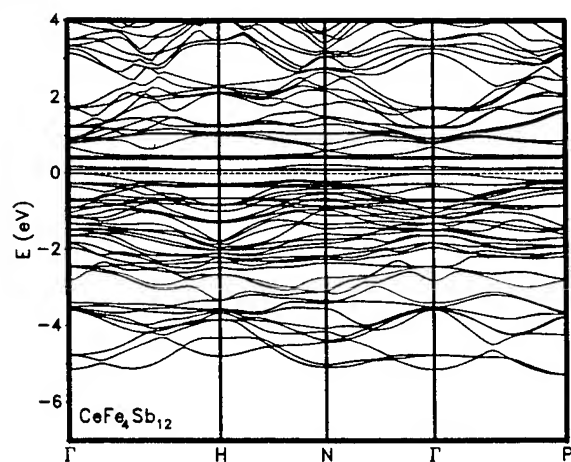


Fig. 7 Band structure of $\text{CeFe}_4\text{Sb}_{12}$.

Although the band structures are qualitatively similar there are differences near the nominal E_F . In the phosphide, there are two parabolic bands at the Γ point valence band maximum (VBM), while in the antimonide the highest valence band is singly degenerate at Γ . The corresponding band in the phosphide, based on its symmetry and orbital character, is the

second highest valence band. These singly degenerate bands are of primarily Fe 3d character ($\sim 80\%$) and have zero Ce 4f character. The top band in the phosphide, corresponds closely to the fourth highest band in the antimonide, which is situated 400 meV below the VBM. These bands have strong Ce 4f character ($\sim 50\%$) at Γ , and are derived from strongly hybridized Ce 4f, Fe 3d and pnictogen p states. Although the Ce character of this band decreases moving away from the zone center, it is apparent that Ce 4f states are important below E_F .

An important consequence of this is the occurrence of high band masses even in the valence bands. The calculated valence band masses are 0.8 and $2.2 m_e$ for the phosphide and the antimonide, respectively. This is significant for TE applications. The conduction bands have even higher masses. Although there is some uncertainty in the present calculation, we estimate these masses at 10-20 m_e for $\text{CeFe}_4\text{Sb}_{12}$ and 6-8 m_e for $\text{CeFe}_4\text{P}_{12}$.

Valency and ionicity in f-band materials are useful but somewhat ambiguous quantities, and this has led to a degree of confusion in the literature. Here we discuss valency in two ways: (1) in terms of the occupancy of the 4f orbital, so that $4f^0$ is tetravalent and $4f^1$ is trivalent; and (2) in terms of the ionicity of the Ce atom, i.e. the amount of charge that is associated with the Ce atom in an ionic construction of the crystal charge density.

Integrating the components of the electronic DOS, decomposed into angular momentum components within each LAPW sphere, we obtain 1.0 f electrons in $\text{CeFe}_4\text{P}_{12}$ and 1.2 f electrons in $\text{CeFe}_4\text{Sb}_{12}$, reflecting the f character contained in the valence bands. For the states like the spatially localized 4f orbitals, this procedure is quantitative. Many body correlation effects beyond the LDA would tend to favor integer occupations, although the strength of this effect cannot be easily estimated from the present calculations. In any case, in terms of f-occupancy both materials are clearly trivalent.

In order to determine the ionic charge on the Ce atom, we compare the density of overlapping ions with various charges to the self-consistently determined charge density from the LAPW calculations. The ionic densities are obtained from atomic calculations, where negative ions are stabilized with a circumscribing Watson sphere. In our tests we transfer charge between the Ce and Fe atoms, to find the best fit. This was quantified by calculating the positions of the 4d core levels and 4f bands relative to those obtained with the true LAPW charge densities. Some additional tests were performed where charge was transferred between the Fe and pnictogen atoms, but this did not affect the results as regards the Ce ionicity. The fit showed that a Ce $4f^1$ configuration was needed to obtain a reasonable f band position, and best results were obtained with an additional 0.5-1.0 valence (Ce 5d) electrons indicating a substantial covalency of the Ce bonding.

Thus we conclude that Ce is trivalent in these compounds and that the Ce 4f states are active in the bonding through hybridization with the Fe 3d and pnictogen p derived bands. In fact, this hybridization is crucial for the formation of the

band gaps around the Fermi level, which we find in both compounds. It is known that the LDA has certain deficiencies in describing 4f orbitals, and in particular underestimates intra-atomic correlation effects and as a result overestimates the degree of hybridization. Based on this one may expect that our calculated band gaps are higher than the actual gaps. This may account for the conclusion of experimental studies that $\text{CeFe}_4\text{Sb}_{12}$ is metallic, although the observation of high Seebeck coefficients, and the fact that apparently only fairly heavily doped p-type material has been studied, suggest that clean samples should be looked at in order to establish where there is in fact a small band gap.

The combination of very small gaps and large effective masses is unusual. This combination and the observed low values of κ are favorable for TE. These compounds deserve detailed experimental investigation in this context, particularly $\text{CeFe}_4\text{Sb}_{12}$ and $\text{CeFe}_4\text{As}_{12}$ (intermediate between the phosphide and antimonide) and as a function of p- and n-type doping level.

Acknowledgements

We are grateful for helpful discussions with F.J. DiSalvo, J.P. Fleurial, H.B. Lyon, M.J. Mehl, G.P. Meisner, D.T. Morelli, G.S. Nolas and G.A. Slack. Computations were performed using the DoD High Performance Computing Modernization Facilities at NAVO and CEWES. Work at the Naval Research Laboratory is supported by the Office of Naval Research.

References

- [1] D.J. Singh, *Planewaves, Pseudopotentials and the LAPW Method*, Kluwer, Boston (1994).
- [2] D.J. Singh and W.E. Pickett, *Skutterudite antimonides: Quasilinear bands and unusual transport*, Phys. Rev. B **50**, 11235-11238 (1994).
- [3] L. Nordstrom and D.J. Singh, *Electronic structure of Ce-filled skutterudites*, Phys. Rev. B **53**, 1103-1108 (1996).
- [4] S. Lundqvist and N.H. March, *Theory of the Inhomogeneous Electron Gas*, Plenum, New York (1983).
- [5] G.A. Slack and V.G. Tsoukala, *Some properties of semiconducting IrSb_3* , J. Appl. Phys. **76**, 1665-1671 (1994).
- [6] D.T. Morelli, T. Caillat, J.P. Fleurial, A. Borshchevsky, J. Vandersande, B. Chen and C. Uher, *Low-temperature properties of p-type CoSb_3* , Phys. Rev. B **51**, 9622-9628 (1995).
- [7] D. Mandrus, A. Migliori, T.W. Darling, M.F. Hundley, E.J. Peterson and J.D. Thompson, *Electronic transport in lightly doped CoSb_3* , Phys. Rev. B **52**, 4926-4931 (1995).
- [8] D.T. Morelli and G.P. Meisner, *Low temperature properties of the filled skutterudite $\text{CeFe}_4\text{Sb}_{12}$* , J. Appl. Phys. **77**, 3777-3781 (1995).
- [9] J. Ackermann and A. Wold, *The preparation and characterization of the cobalt skutterudites CoP_3 , CoAs_3 and CoSb_3* , J. Phys. Chem. Solids **38**, 1013-1016 (1977).
- [10] P. Villars and L.D. Calvert, *Pearsons Handbook of Crystallographic Data for Intermetallic Phases*, 2nd ed., American Society for Metals, Metals Park, OH (1991).
- [11] A. Kjekshus and T. Rakke, *Compounds with the Skutterudite Type Crystal Structure III Structural Data for Arsenides and Antimonides*, Acta Chem. Scand. A **28**, 99-103 (1974).
- [12] B.I. Halperin and T.M. Rice, *Possible Anomalies at a Semimetal-Semiconductor Transition*, Rev. Mod. Phys. **40**, 755-766 (1968).
- [13] D. Sherrington and W. Kohn, *Speculations about Grey Tin*, Rev. Mod. Phys. **40**, 767-769 (1968).
- [14] A.A. Abrikosov and S.D. Beneslavskii, *Some Properties of Gapless Semiconductors of the Second Kind*, J. Low Temp. Phys. **5**, 141-154 (1971).
- [15] J.L. Feldman and D.J. Singh, *Lattice dynamics of skutterudites: first principles and model calculations for CoSb_3* , Phys. Rev. B **53**, 6273-6282 (1996).
- [16] H.D. Lutz and G. Kliche, *Far-Infrared reflections spectra, optical dielectric constants, effective charges and lattice dynamics of the skutterudites CoP_3 , CoAs_3 and CoSb_3* , Phys. Stat. Sol. (b) **112**, 549-557 (1982).
- [17] G.S. Nolas, G.A. Slack, T. Caillat and G.P. Meisner, *Raman scattering study of antimony-based skutterudites*, J. Appl. Phys. **79**, 2622-2626 (1996).
- [18] G.P. Meisner, M.S. Torikachvilli, K.N. Yang, M.B. Maple and R.P. Guertin, *UF_6P_{12} and $\text{CeFe}_4\text{P}_{12}$: Nonmetallic isotypes of superconducting $\text{LaFe}_4\text{P}_{12}$* , J. Appl. Phys. **57**, 3073-3075 (1985).
- [19] G.B. Martins, M.A. Pires, G.E. Barberis, C. Rettori and M.S. Torikachvilli, *Electron spin resonance of Nd^{3+} and Yb^{3+} in $\text{CeFe}_4\text{P}_{12}$* , Phys. Rev. B **50**, 14822-14826 (1994).

High Figure of Merit in Ce-Filled Skutterudites

Jean-Pierre Fleurial, Alex Borshchevsky, Thierry Caillat

Jet Propulsion Laboratory/ California Institute of Technology, Pasadena, California, USA

Donald T. Morelli and Gregory P. Meisner

General Motors Research and Development Center, Warren, Michigan, USA

Abstract

New thermoelectric materials with superior transport properties at high temperatures have been discovered. These materials are part of the large family of skutterudites, a class of compounds which have shown a good potential for thermoelectric applications [1-4]. The composition of these novel materials, called filled skutterudites, is derived from the skutterudite crystal structure and can be represented by the formula $\text{LnT}_4\text{Pn}_{12}$ (Ln = rare earth, Th; T = Fe, Ru, Os, Co, Rh, Ir; Pn = P, As, Sb). In these compounds, the empty octants of the skutterudite structure which are formed in the TPn_3 ($\sim \text{T}_4\text{Pn}_{12}$) framework are filled with a rare earth element [5,6]. Some of these compositions, based on $\text{CeFe}_4\text{Sb}_{12}$, have been prepared by a combination of melting and powder metallurgy techniques and have shown exceptional thermoelectric properties in the 350-700°C temperature range. At room temperature, $\text{CeFe}_4\text{Sb}_{12}$ behaves as a p-type semimetal, but with a low thermal conductivity and surprisingly large Seebeck coefficient. These results are consistent with some recent band structure calculations on these compounds [7]. Replacing Fe with Co in $\text{CeFe}_4\text{Sb}_{12}$ and increasing the Co:Fe atomic ratio resulted in an increase in the Seebeck coefficient values. The possibility of obtaining n-type conductivity filled skutterudites for Co:Fe values higher than 1:3 is currently being investigated. Measurements on bulk samples with a $\text{CeFe}_{3.5}\text{Co}_{0.5}\text{Sb}_{12}$ atomic composition and p-type conductivity resulted in dimensionless figure of merit ZT values of 1.4 at 600°C.

Introduction

A systematic search for advanced thermoelectric materials was initiated at JPL several years ago and resulted in the discovery of a new family of promising semiconducting materials with the skutterudite crystal structure [1]. The skutterudite structure was originally attributed to a mineral from Skutterud (Norway) with a general formula $(\text{Fe}, \text{Co}, \text{Ni})\text{As}_3$ [8]. The unit cell of the skutterudite structure (cubic, space group $\text{Im}\bar{3}$, prototype CoAs_3) contains square radicals $[\text{As}_4]^{4-}$. This anion located in the center of the smaller cube is surrounded by 8 Co^{3+} cations. The unit cell was found to consist of 8 smaller cubes (octants) described above but two of them do not have the anions $[\text{As}_4]^{4-}$ in the center. This is necessary to keep the ratio $\text{Co}^{3+}: [\text{As}_4]^{4-} = 4:3$. Thus, a typical coordination structure results with $\text{Co}_8[\text{As}_4]_6 = 2\text{Co}_4[\text{As}_4]_3$ composition and 32 atoms per cell.

A low lattice thermal conductivity and a high carrier mobility are desirable for improved figures of merit in new thermoelectric materials. High carrier mobility values are usually found in crystal structures with a high degree of covalency. It has been shown that the bonding is predominantly covalent in the skutterudite structure [9] and high hole mobility values have been measured recently on several skutterudite compounds: IrSb_3 [10], RhSb_3 [11], CoSb_3 [12] and RhP_3 [13]. The unit cell is relatively large and contains 32 atoms which indicate that low lattice thermal conductivity might be possible. For state-of-the-art thermoelectric materials such as PbTe and Bi_2Te_3 alloys, the number of isostructural compounds is limited and the possibilities to optimize their properties for maximum performance at different temperatures of operation are also very limited. This is not the case for the skutterudite family of materials, where eleven binary compounds and several solid solutions and related phases are known to exist [1]. These materials cover a large range of decomposition temperatures and bandgaps which offers the possibility to adjust composition and doping level for a specific temperature range of application.

However, the room temperature thermal conductivity of binary skutterudites ($100\text{-}150 \text{ mWcm}^{-1}\text{K}^{-1}$) was found to be too high to result in high ZT values. Substantial reductions in the lattice thermal conductivity must be obtained to achieve values comparable to those of state of the art thermoelectric materials ($10\text{-}40 \text{ mWcm}^{-1}\text{K}^{-1}$). One approach to the reduction of the lattice thermal conductivity of skutterudites is to prepare and characterize filled skutterudite compositions derived from the binary compounds. This requires filling the two empty octants present in the 32 atom unit cell and conserving the valence electron count to retain good semiconducting properties.

Low Thermal Conductivity in Filled Skutterudites

A large number of materials with a filled skutterudite crystal structure has already been synthesized (see for example [14-18]). The composition of these types of compounds can be represented by the formula $\text{LnT}_4\text{Pn}_{12}$ (Ln = La, Ce, Pr, Nd, Sm, Eu, Gd, Th and U; T = Fe, Ru, Os; Pn = P, As, Sb). In these compounds, the empty octants of the skutterudite structure (see Figure 1) which are formed in the TPn_3 ($\sim \text{T}_4\text{Pn}_{12}$) framework are filled with a rare earth element.

Because the T_4Pn_{12} groups using Fe, Ru or Os are electron-deficient (by 4 e^-) relative to the skutterudite electronic structure (using Co, Rh or Ir), the introduction of the rare earth atom compensates this deficiency by adding free electrons. However, the number of valence electrons given up by the rare earth atoms is generally insufficient: for example, La has a 3+ oxidation state, Ce can be 3+ or 4+. This means that most of these compounds behave as metals, or very heavily doped p-type semimetals.

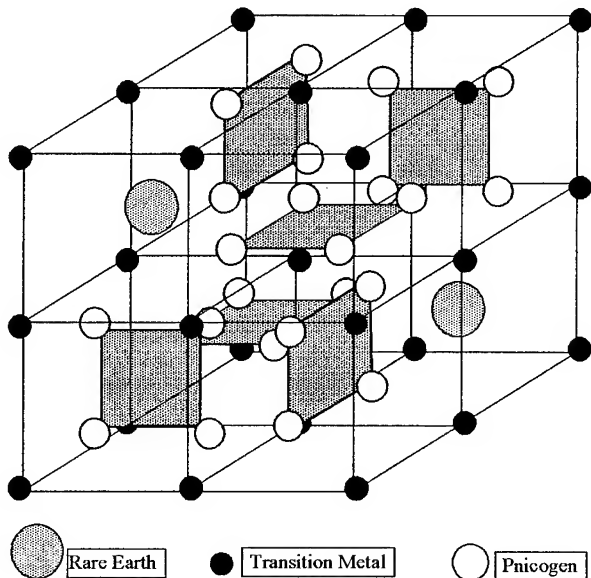


Figure 1: Schematic of the filled skutterudite 34 atom unit cell of the novel thermoelectric materials. Each cell contains 8 transition metal atoms: Fe, Ru, Os, Co, Rh, Ir, Ni, Pd or Pt; 24 pnictogen atoms: P, As, Sb (substitution by S, Se or Te possible); 2 rare-earth atoms filling the vacant octants in the skutterudite structure: La, Ce, Pr, Nd, Sm, Eu, Gd, Th and U.

However, the introduction of a filling atom into the skutterudite structure is expected to substantially reduce the lattice thermal conductivity of the original binary compound with minimal decrease in carrier mobility. The heavy filling atom would “rattle” within its octant “cage” and thus scatter phonons quite effectively. Also because it is filling an empty octant, its contribution to the electrical transport would be minimal, though the increased phonon scattering rate should somewhat impact the carrier scattering rate (carrier-phonon interaction). Recent experimental results on filled skutterudite samples have confirmed that the thermal conductivity values are much lower in these materials than in $CoSb_3$ or $IrSb_3$, even taking into account the high porosity of the samples [5,6].

To conserve the excellent semiconducting behavior of the unfilled binary skutterudites, it is necessary to introduce a “compensating” atom for the addition of the “filling” atom into the structure. The ratio of compensating atoms to filling atoms is determined exclusively from the number of valence

electrons of the filling atom. Thus, if Ce (the most stable valence number is 3) is introduced into the two empty octants of the 32 atoms $CoSb_3$ unit cell, 6 atoms of Fe (each providing one acceptor per atom) will have to be substituted for Co: $CoSb_3$ (or Co_8Sb_{24}) will become $Ce_2Fe_6Co_2Sb_{24}$ (or $CeFe_3CoSb_{12}$). This composition is very close to the compound $CeFe_4Sb_{12}$ whose existence was previously reported. The same approach can be applied to replacing Sb by Ge, resulting in $CeCo_4Ge_3Sb_9$ or both Co and Sb by Fe and Te, resulting in $CeFe_4Sb_{11}Te$. Moreover, the doping level and conductivity type might be controlled by changing the compensating to filling atomic ratio. It is important to note that because compensating atoms need to be introduced in quantity, they could also bring a substantial increase in phonon scattering (mass and volume differences) and carrier scattering (ionized impurity, disorder) rates.

Experimental Results and Discussion

The filled skutterudite compositions based on $CeFe_4Sb_{12}$ were prepared by a combination of melting and powder metallurgy techniques. X-ray diffraction analysis indicated that the samples were mostly filled skutterudites with the presence of some $FeSb_2$ and $CeSb_2$. After synthesis, mass density measurements showed that the geometrical density of the cylindrical pellets (about 10 mm long and 6.4 mm in diameter) were close to 98% of the theoretical values calculated from the experimentally determined lattice parameters (see Table 1). The electron microprobe analysis of the samples confirmed the previous X-ray diffraction results, indicating the presence of only about 5% in volume of $FeSb_2$ and $CeSb_2$ in the $CeFe_4Sb_{12}$, $CeFe_{3.5}Co_{0.5}Sb_{12}$ and $CeFe_3CoSb_{12}$ samples. The compositions of the filled skutterudite phase in these samples were found to be very close to the nominal atomic concentrations.

The high temperature electrical and thermal transport properties of the filled skutterudite samples were measured from 25 up to 650°C. The room temperature results are reported in Table 1.

Table 1: Room temperature properties of Ce-based filled skutterudite samples where a_0 is the lattice parameter (Å), cc is the carrier concentration (cm^{-3}), μ_H is the Hall mobility ($cm^2 V^{-1} s^{-1}$), ρ is the electrical resistivity ($m\Omega cm$), S is the Seebeck coefficient (μVK^{-1}) and λ is the thermal conductivity ($mW cm^{-1} K^{-1}$).

Composition	a_0	cc	μ_H	ρ	S	λ
$CeFe_4Sb_{12}$	9.1460	5.5×10^{21}	1.5	0.75	59	14
$CeFe_{3.5}Co_{0.5}Sb_{12}$	9.1349	5.7×10^{21}	1.5	0.71	76	22
$CeFe_3CoSb_{12}$	9.1145	4.4×10^{21}	1.7	0.84	106	19
$CeFe_2Co_2Sb_{12}$	9.0909	6.5×10^{20}	2.9	3.89	125	28
Co_4Sb_{12}	9.0385	4.4×10^{18}	1944	0.74	138	118

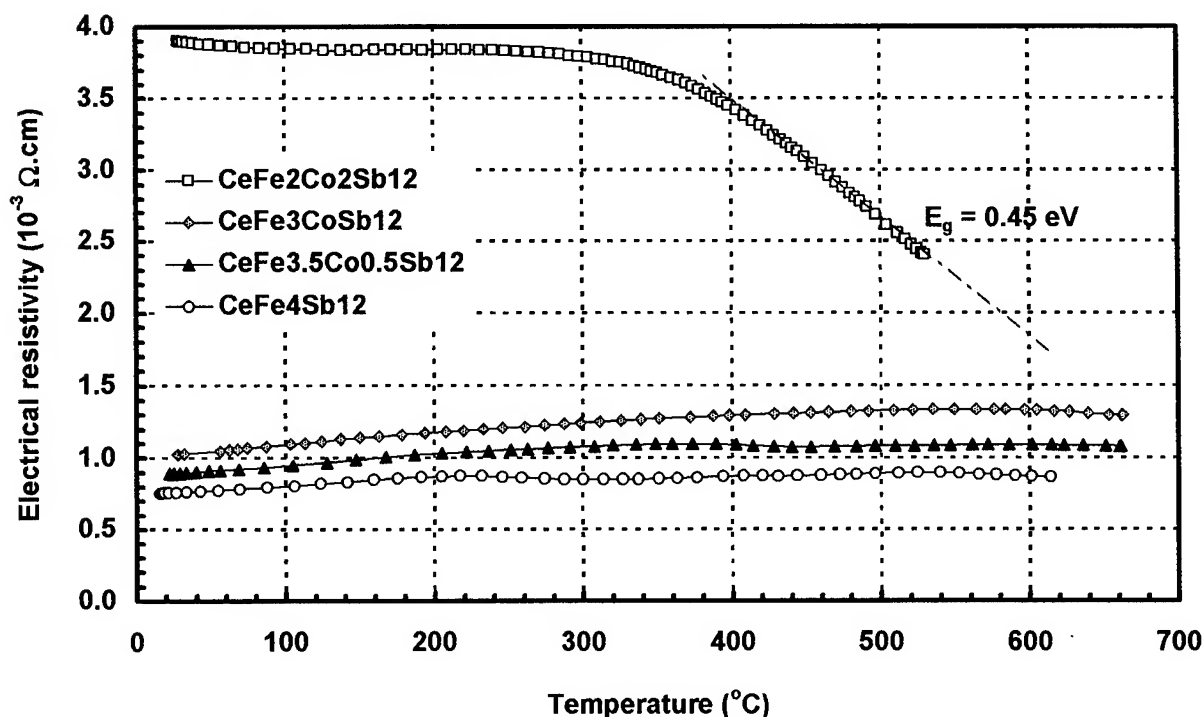


Figure 2: High temperature variations of the electrical resistivity of Ce-filled skutterudite samples

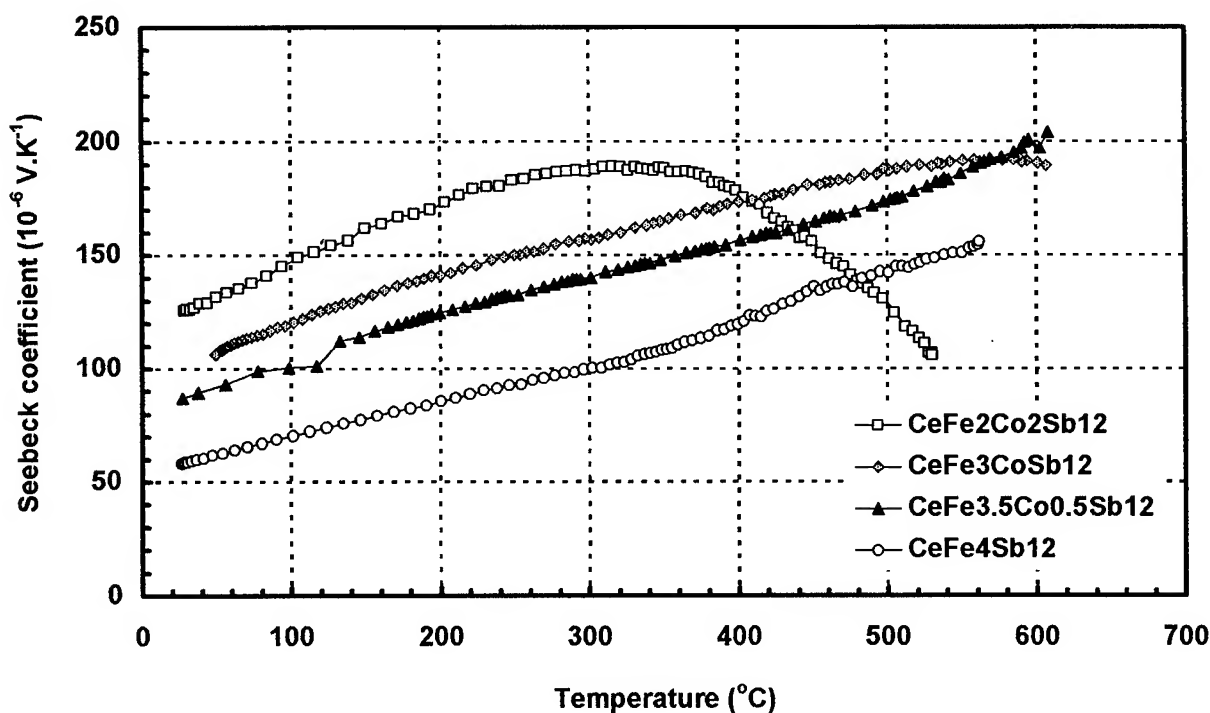


Figure 3: High temperature variations of the Seebeck coefficient of Ce-filled skutterudite samples

The temperature dependence of the electrical resistivity, Seebeck coefficient and thermal conductivity are reported in Figures 2, 3 and 4, respectively. The results show that the Fe-rich compositions have a semi-metallic behavior (very high carrier concentration of about $5 \times 10^{21} \text{ cm}^{-3}$ and low carrier mobilities,) with a low electrical resistivity, which

increases slightly with temperature. However, the $\text{CeFe}_2\text{Co}_2\text{Sb}_{12}$ sample demonstrated a semiconducting behavior, with a bandgap value of 0.45 eV determined from high temperature electrical resistivity measurements. What is most surprising is the magnitude of the Seebeck coefficients, ranging from 55 to $125 \mu\text{V.K}^{-1}$ at 25°C and increasing steadily with temperature. Again, the intrinsic

regime is obtained in $\text{CeFe}_2\text{Co}_2\text{Sb}_{12}$ for temperatures over 350°C . These values are comparable to those obtained for other p-type binary skutterudites except that here the carrier concentration is two to three orders of magnitude higher. This is attributed to the fact that these materials behave

similarly to heavy fermions systems: the hybridization between Ce and the transition metal (Fe or Co here) creates a small bandgap and carriers possess large effective masses resulting in a low mobility but unusually high Seebeck coefficient [5,7].

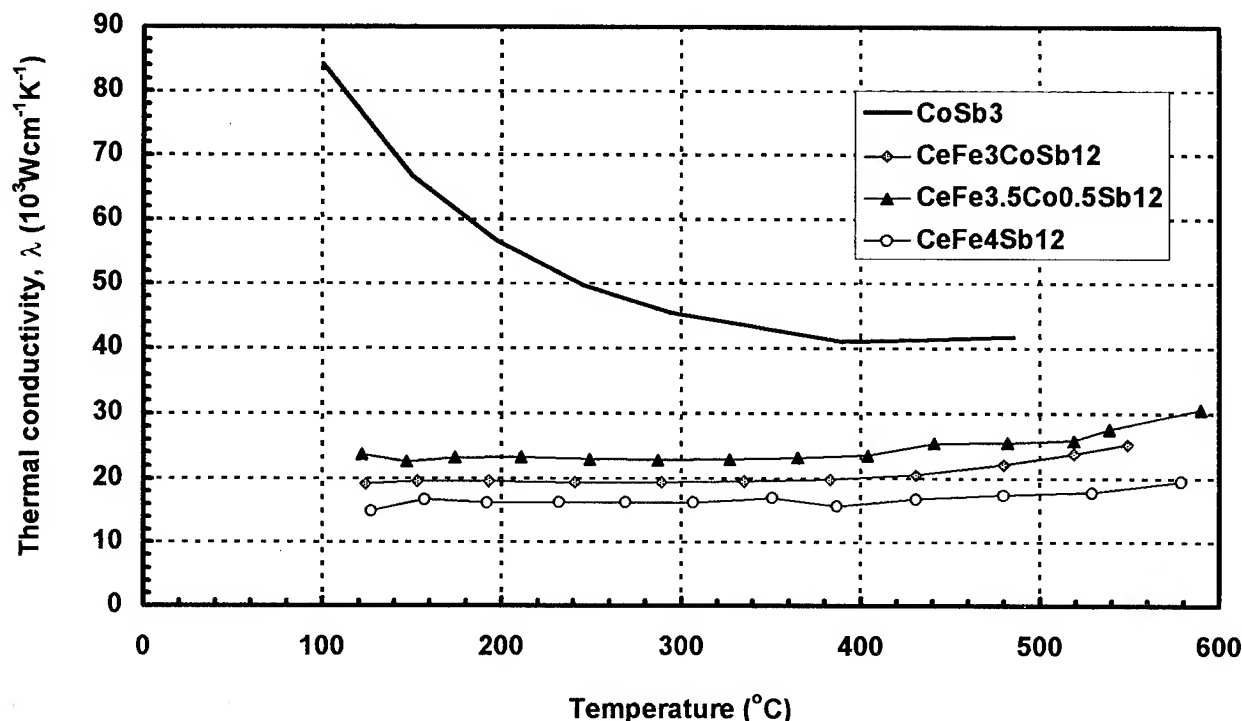


Figure 4: High temperature variations of the thermal conductivity of Ce-filled skutterudite samples

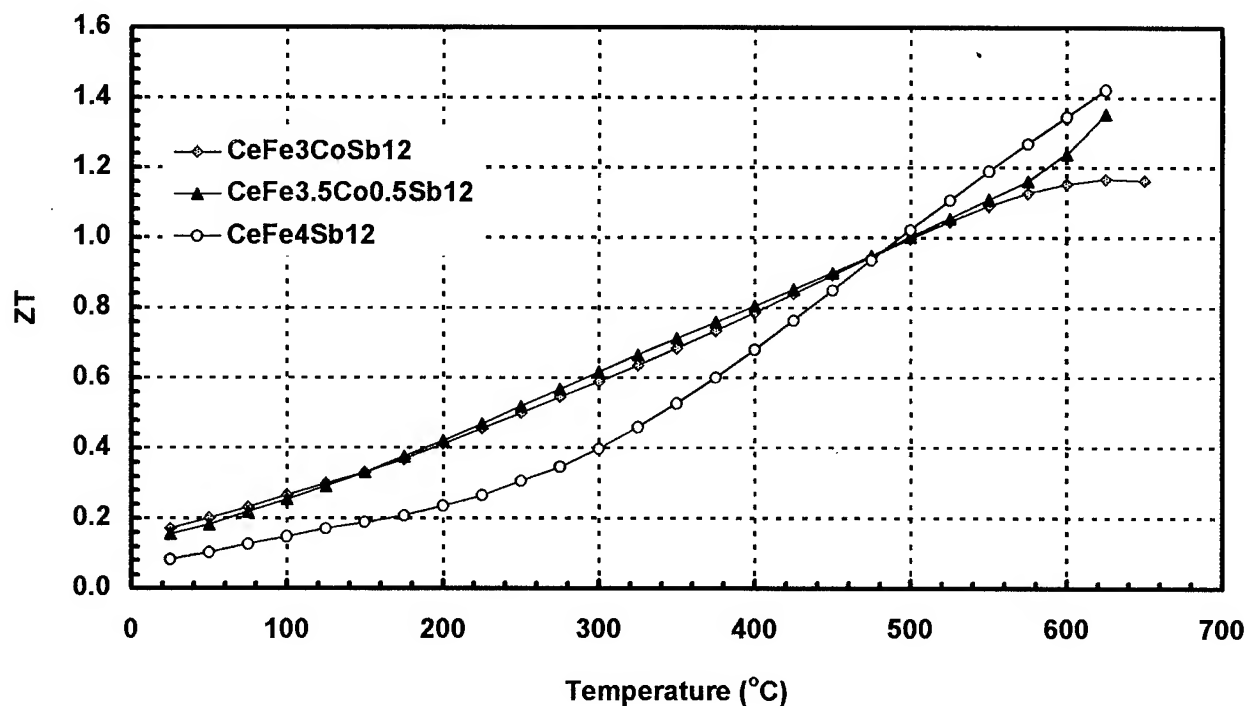


Figure 5: Dimensionless figure of merit ZT as a function of temperature for Ce-filled skutterudite samples with different compositions.

The thermal conductivity of those materials is much lower than for CoSb_3 . The $\text{CeFe}_4\text{Sb}_{12}$ sample has a low thermal conductivity of about $14 \text{ mWcm}^{-1}\text{K}^{-1}$ at room temperature and increasing up to $20 \text{ mWcm}^{-1}\text{K}^{-1}$ at 575°C . Such low values indicate that nearly all of the thermal conductivity is from an electronic contribution. This demonstrates that the combination of the "rattling" atom and very high carrier concentration very effectively scatter the phonons, and results in an extremely low lattice thermal conductivity.

The $\text{CeFe}_{3.5}\text{Co}_{0.5}\text{Sb}_{12}$ and $\text{CeFe}_3\text{CoSb}_{12}$ samples also show low thermal conductivity values with a temperature dependence identical to that of $\text{CeFe}_4\text{Sb}_{12}$. It is quite interesting to note that both the room temperature Seebeck coefficient and thermal conductivity tend to increase as the amount of Co is increased from 0 at.% to 12 at.%. This suggests that the introduction of Co alters the strength of the Ce-Fe interactions. However, even for the $\text{CeFe}_2\text{Co}_2\text{Sb}_{12}$ composition (with 12 at.% of Co), the carrier concentration is still very high, indicating that the compensation effects between Fe and Co might be neutralized by valence fluctuations. As discussed above, the introduction of Ir, or Te instead of Co might lead to very different results.

The combination of the low electrical resistivity, moderate Seebeck coefficient and low thermal conductivity resulted in high ZT values at temperatures above 400°C . A maximum ZT value of 1.4 has been achieved to date at a temperature of 600°C . However, it appears that ZT keeps on increasing with temperature for those filled skutterudite samples, as expected from the metallic behavior of the electrical properties. This means that if those materials were determined to remain stable at higher temperatures, even higher ZT would be obtained. The results, displayed on Figure 5, are higher than for any other state of the art materials (p-type or n-type).

High ZT values in lower or higher temperature ranges, as well as n-type conductivity samples might be obtained by controlling the composition and doping levels. For these materials to be useful at lower temperatures for cooling applications, the Seebeck coefficient must be increased, which requires a lower doping level. For example, this might be achieved by increasing the Co to Fe atomic ratio ($\text{CeFe}_{4-x}\text{Co}_x\text{Sb}_{12}$ with $1 < x \leq 4$) or combining Co with Te or Se. Replacing Co by Ir in the filled skutterudites would certainly result in higher decomposition temperatures allowing their use in power generation applications at temperatures close to 1000°C . In addition, the heavier and larger Ir atom will introduce additional scattering of the phonons, resulting in a decrease in lattice thermal conductivity.

Acknowledgments

Part of the work described in this paper was carried out at the Jet Propulsion Laboratory/California Institute of Technology, under contract with the National Aeronautics and Space Administration.

References:

- [1] J.-P. Fleurial, T. Caillat, and A. Borshchevsky, *Proc. XIV Intl. Conf. Thermoelectrics*, St. Petersburg, Russia, June 27-30, 231 (1995).
- [2] T. Caillat, A. Borshchevsky, and J.-P. Fleurial, J.-P., *Proc. XIII Intl. Conf. on Thermoelectrics*, AIP Press No. 316, 58-61, Kansas City, MO (1994).
- [3] T. Caillat, A. Borshchevsky, and J.-P. Fleurial, J.-P., *Proc. XIII Intl. Conf. on Thermoelectrics*, AIP Press No. 316, 31-34, Kansas City, MO (1994).
- [4] T. Caillat, A. Borshchevsky, and J.-P. Fleurial, *Proc. XIII Intl. Conf. on Thermoelectrics*, AIP Press No. 316, 209-211, Kansas City, MO (1994).
- [5] D.T. Morelli and G.P. Meisner, *J. Applied Physics* 77, 3777 (1995)
- [6] G.S. Nolas, G.A. Slack, T.M. Tritt and D.T. Morelli, *Proc. XIV Intl. Conf. on Thermoelectrics*, St. Petersburg, Russia, June 27-30, 236 (1995).
- [7] L. Nordstrom and D. Singh, *Phys. Rev. B*, 53 (3) 1103 (1996).
- [8] Oftedal, I., *Z. Kristallogr.*, 66, 517 (1928).
- [9] A. Kjekshus, D. G. Nicholson, T. Rakke, *Acta Chem. Scand.*, 27, 4 (1973).
- [10] T. Caillat, A. Borshchevsky, J. P. Fleurial, in K. R. Rao (ed.), *Proc. XIth Int. Conf. Thermoelectrics*, Arlington, TX, The University of Texas, Arlington, 98 (1993).
- [11] T. Caillat, J.-P. Fleurial, and A. Borshchevsky, *J. Cryst. Growth*, 4204 (1995).
- [12] D.T. Morelli, T. Caillat, J.-P. Fleurial, A. Borshchevsky, J.W. Vandersande, B. Chen and C. Uher, *Phys. Rev. B* 51, 9622 (1995).
- [13] J. P. Odile, S. Soled, C. A. Castro, A. Wold, *Inorganic Chemistry*, 17, 2, 283 (1978).
- [14] G. P. Meisner, M. S. Torikachvili, K. N. Yang, M. B. Maple, R. P. Guertin, *J. Appl. Phys.*, 57, 1, 3073 (1985).
- [15] D. Jung, M. H. Whangbo, S. Alvarez, *Inorganic Chemistry*, 29, 2252 (1990).
- [16] F. Grandjean, A. Gérard, D. J. Braun, W. Jeitschko, *J. Phys. Chem. Solids*, 45, 8/9, 877 (1984).
- [17] N. T. Stetson, S. M. Kauzlarich, H. Hope, *Journal of Solid State Chemistry*, 91, 140 (1991).
- [18] W. Jeitschko and D. Braun, *Acta Cryst. B* 33, 3401 (1977).

Electronic Transport Properties of the Skutterudite CoSb₃ and Mixed Alloys

K.Matsubara¹, T.Sakakibara², Y.Notohara³, H.Anno¹, H.Shimizu¹ and T.Koyanagi⁴

¹Science University of Tokyo in Yamaguchi, Faculty of Science and Engineering

1-1-1 Daigaku-Dori, Onoda, Yamaguchi 756, Japan

²Aisin Cosmos R&D Co.,Ltd., ³Kyushu Matsushita Electric Co.,Ltd., ⁴Yamaguchi University

Abstract

We present some results on physical and electrical properties of the Skutterudites CoSb₃ and mixed alloys. Most of samples measured were polycrystalline, which have been prepared by hot-pressing of powders under 10⁷ Pa at ~650°C and ~750°C, and a few measurements on CoSb₃ single crystals were performed. We report some results of the Hall mobility, Seebeck coefficient and electrical conductivity measurements on CoSb₃ and mixed alloys. Based on the experimental results, we make clear important factors which have influence on the electronic transport properties, in particular, on the Hall mobility of the materials.

1. Introduction

The Skutterudites MSb₃ (M: Co, Rh and Ir) with antimony have been a topic of a new promising thermoelectric material, because of its peculiar band structure and unusual electronic transport properties. The crystal structure of the Skutterudite CoSb₃ is shown in Fig.1, which is formed by a cubic-lattice of 8-cobalt atoms and by 4-planary rings of Sb atoms, and cobalt atoms are octahedrally surrounded by six-antimony atoms. Figure 2 shows a band scheme, and this is based on a model for transition metal chalcogenides proposed by Ackermann [1]. The energy band gap is formed by the occupied bonding σ_{a-m} band and the antibonding σ_{a-m}^* band. The Sb₄-rings are achieved through the overlap of anion- sp^3 orbitals to form the two σ bands. Recently, it has been reported by David *et al* [2] that the Skutterudite antimonides have a band structure of a pseudogap around the Fermi level and the band gap dispersion remarkably cross over to linear behavior extremely close to the band edge, and that the unusual transport properties of the antimonides are determined by the linear dispersion.

The research of the Skutterudite was first made on CoSb₃ by Dudkin in 1957 [3], and a phase diagram of the binary system Co-Sb and the thermoelectric properties of the semiconducting CoSb₃ with Sn, Te and Ni impurities were investigated extensively [4]. The most attractive point is an extremely large hole mobility for the *p*-type Skutterudites. Morelli *et al* [5] have shown that single crystals of CoSb₃ exhibit large hole mobilities up to 3000 cm²/Vs at room temperature. In recent studies, Caillat *et al* [6] demonstrated at room temperature *p*-type hole mobility of about 3445 cm²/Vs for single crystals CoSb₃ at a carrier concentration of 4×10¹⁷ cm⁻³, which were grown by a gradient-freeze technique. In addition, Mandrus *et al* [7] measured a value of 1940 cm²/Vs for a very lightly doped ($1/qR_H = 7.0 \times 10^{16}$

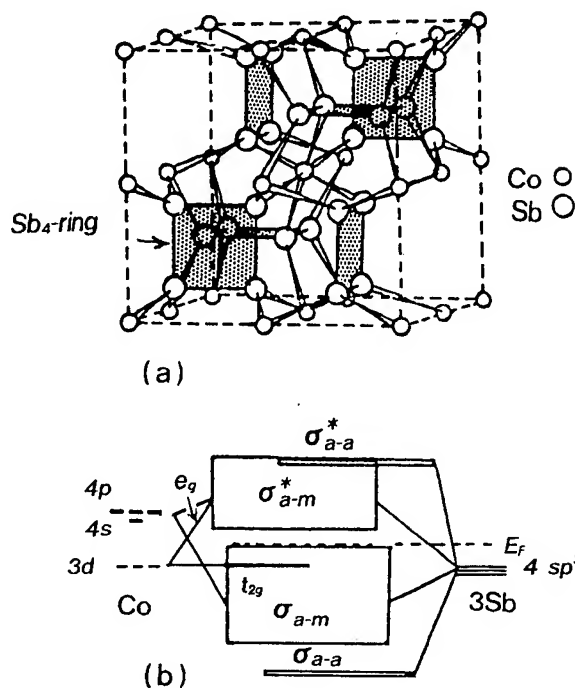


Fig.1 Crystal structure for CoSb₃ (a) and a proposed energy band model (b).

holes/cm³) single crystal of CoSb₃, which was grown from a Sb-rich melt. For our hot-pressed CoSb₃ samples, however, the hole mobility value at room temperature was as low as 60 to 80 cm²/Vs up to now [8,9]. In short, there is a great variation in the measured values of the hole mobility in CoSb₃ (*p*-type) samples.

The purpose of this study, therefore, is to find important factors which have a great influence on the hole mobility of CoSb₃ (*p*-type). Major factors which have a considerable influence on the hole mobility of CoSb₃ (*p*-type) can be considered to be (1) crystal quality, (2) nonstoichiometry, (3) impurities.

2. Experimental procedure

2.1 Sample preparation

The starting materials used are cobalts (Co), which have the three varieties of purity of (1) 99.87%, (2) 99.92% and (3) 99.998%, and antimony (Sb) is "extra pure" of 6N. Prime impurities in cobalt are nickel, and the contents are 450ppm

for (1), 230ppm for (2), and undetectable for (3), respectively.

The sample preparation was made by annealing stoichiometric mixtures of cobalt and antimony in evacuated quartz tubes (600°C, 2 days), that is, a solid phase reaction, followed by hot-pressing under 600kgf/cm² at 650°C for 1hr (sample C01) and at 750°C for 3hr(sample C03), respectively. The all samples were polycrystalline structures, and X-ray powder diffraction methods were used to verify the stoichiometry after hot-pressing. The quantitative analyses of the starting materials and the hot-pressed samples were made by ICP emission spectroscopy and electron-probe microanalysis (EPMA).

2.2 Characterization

Powder X-ray diffraction pattern of samples obtained in this way showed an insensitive peak along a (310) plane, which is characteristic of the stoichiometric CoSb₃ with the lattice constant $a = 9.016\text{\AA}$. The density of samples was determined by hydrostatic weighing, and the densities were about 95% of the theoretical value of CoSb₃ (7.69g/cm³). The microstructure and homogeneity of samples were studied by the observation of scanning electron microscope (SEM) on the crystal habit of the sample surface after polishing using 0.5 μm diamond paste up to mirror-like surface and etching with 20% HNO₃.

3. Experimental results

Figure 3 shows the Hall mobility of our hot-pressed CoSb₃ samples as a function of temperature, compared with the results for two p -type single crystals: one was grown by a normal gradient freezing method [6] and the other was grown from a Sb-rich melt [7].

As shown in this figure, a room temperature hole mobility of 2000 cm²/Vs is obtained for the CoSb₃ hot-pressed sample (C03), when cobalt of nickel-free was used as a raw material. This result suggests that the hole mobility values for the p -type CoSb₃ samples are very sensitive to impurity nickel in cobalt. For the samples, below 300K the hole mobility increases with increasing temperature, and the mobility varies as $T^{3/2}$. The temperature dependence is similar to the result of Mandrus *et al* [7], which is explained in terms of an ionized impurity scattering model.

On the dominant scattering mechanism for the p -type CoSb₃, there is no denying a thermally activated hopping due to a small polaron or bipolaron. In general, for materials which are characterized by narrow band gap in the vicinity of the Fermi energy, as the case of the materials, the electron-phonon coupling should be considered explicitly. Electronic interactions between electrons (or holes) and an adjacent atom give rise to a localized atomic distortion. Such distortions of this type can move with electrons in the crystal lattice, and this is called "small polaron". When the distortions are sufficiently large, electrons (or holes) will be trapped in a lattice site associated with the atomic distortions, that is, a localized potential well.

Schematic view of the small polaron is illustrated in Fig.3. Free carriers will conduct only by means of thermally activated hopping at ordinary temperatures [10]. A small

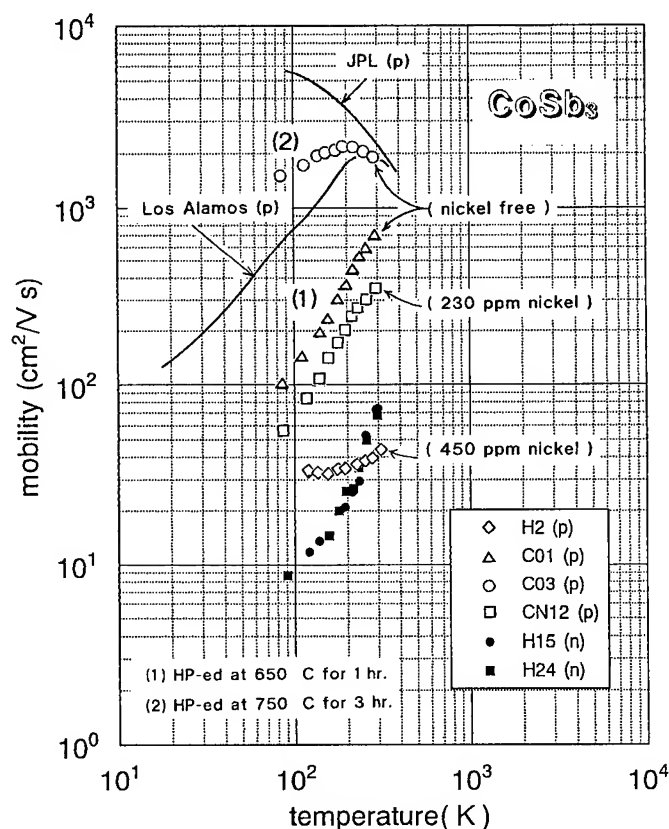


Fig.2 Hall mobilities of our hot-pressed CoSb₃ samples as a function of temperature, compared with two single crystal CoSb₃ samples.

polaron consists of a self-bound charge carrier in the localized potential well, and two carriers bound in a potential well form a small bipolaron. In both cases, increasing temperature causes atomic distortions on sites neighboring the polarons. Such distortions aid the motion of the charge carrier, and results in an increase of the mobility with increasing temperature. The mobility is expressed as follows: [11]

$$\mu = (qa^2\nu/k_B T) \exp(-E_a/k_B T),$$

where q is the electron charge, a is the mean distance for the hopping of carriers, ν is a characteristic vibrational frequency, k_B is the Boltzman constant, and E_a is the activation energy to produce an atomic distortion on sites neighboring the small polaron.

The exponential factors of the Hall mobility for samples vary inversely with temperature, and plots of the logarithm of (μT) versus $1/T$ were linear at low temperatures up to 300K. The activation energy E_a obtained from the slope of the plots was fairly small (0.016 to 0.042 eV). The value of the activation energy is about 1/10 as compared with those for β -FeSi₂ (0.3 to 0.4 eV) [12]. CoSb₃ is probably of a charge-transfer type [13], for which the transport properties of carriers are directly related to the electronegativity of anion atoms. Therefore, it is likely that the atomic distortion can be

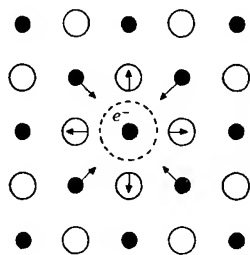


Fig.3 Schematic view of a small polaron model. Increasing temperature causes atomic distortions on sites neighboring the polaron, and such distortions aid the motion of carriers. Free carriers will conduct only by means of thermally activated hopping.

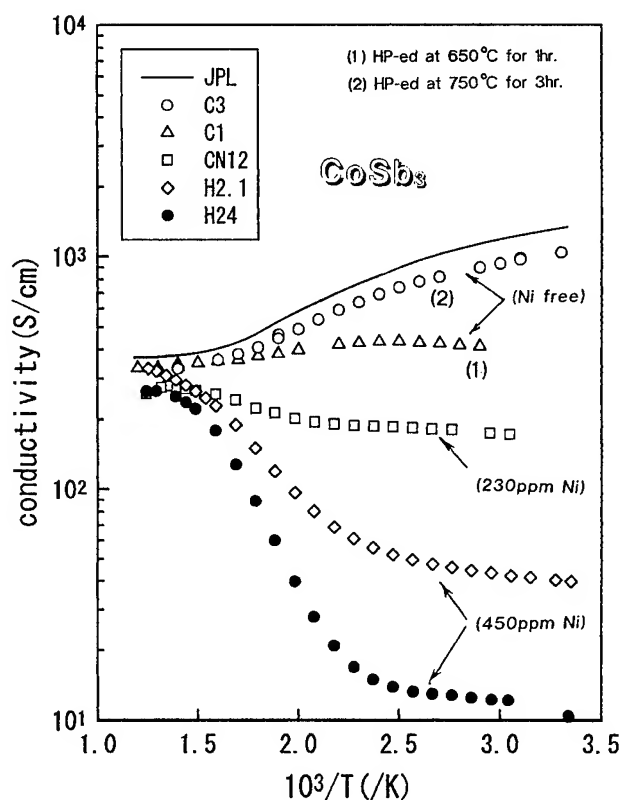


Fig.4 Electrical conductivities for the hot-pressed CoSb_3 samples as a function of temperature.

produced by mainly thermal motion of the constituent atoms. This is substantially different from the transport properties for high-spin Fe^{+3} or Mn^{+2} compounds as the case of $\beta\text{-FeSi}_2$. In the latter case, the transport properties of carriers are strongly suppressed because of the high energies of the $d-d$ Coulomb and exchange interactions, resulting in low carrier mobilities. In fact, the carrier mobilities (electron and hole) of $\beta\text{-FeSi}_2$ are as low as 0.3 to 4.0 cm^2/Vs [14].

Figure 5 shows the electrical conductivity for the CoSb_3 samples versus inverse temperature. The carrier concentra-

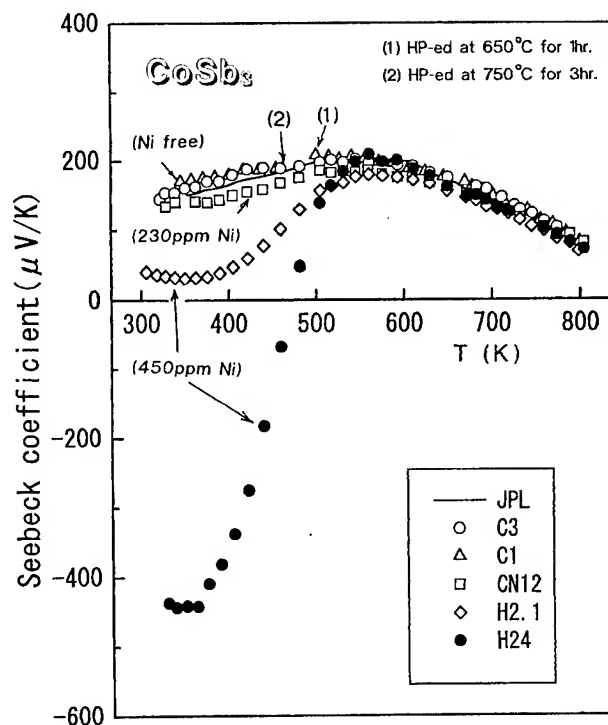


Fig.5 Seebeck coefficient for the hot-pressed CoSb_3 samples as a function of temperature.

tions of the samples (C01 and, C03) were about $1/(qR_H) = 10^{18}/\text{cm}^3$, which is lower than the degenerate concentration estimated to be $10^{20}/\text{cm}^3$. Therefore, the positive temperature dependence of conductivity σ for the samples should be considered in relation to a quasi-band gap peculiar to the Skutterudite structure. It is also possible to consider that the band gap is formed by additional doping of nickel in the crystal lattice.

Figure 6 shows the Seebeck coefficient S for the samples as a function of temperature. The two samples (C01 and C03) which were prepared using nickel-free cobalt and antimony of 6N are of p -type. The values of S are about $200\mu\text{V/K}$ at temperatures ranging from 430 to 600K are less dependent on temperature.

On the other hand, for the other samples which contain nickel as an impurity, the Seebeck coefficient is found to be highly dependent on the concentration of nickel substituted in the crystal. For example, the samples containing 450 ppm nickel (samples: H2.1 and H24) indicate a large temperature dependence of the Seebeck coefficient. For the sample of the stoichiometric composition (H2.1), the value of the p -type Seebeck coefficient decreases as compared with those for the nickel-free samples (C01 and C03) below 500K. This suggests that the nickel as an impurity acts as a donor and the hole concentration in the p -type CoSb_3 is partially compensated in the crystal lattice. For the sample of missing antimony atoms (H24), which has a composition of $\text{CoSb}_{2.7}$, the Seebeck coefficient varies from n -type to p -type at about 470K, suggesting that the excess of cobalt atoms causes an anion vacancy as a donor. On the contrary, it was found that

samples with excess antimony led to the positive thermoelectric powers ("hole conducting"), which were fairly lower than those of the stoichiometric CoSb_3 .

Conclusion

Major results obtained in this study are as follows:

(1) A great variation in the measured values in hole mobility in CoSb_3 (p -type) can be attributed in impurities, in particular, nickel in cobalt as a raw material is highly sensitive to the hole mobility of the material. By using nickel-free cobalt as a raw material, a room temperature hole mobility of $2000 \text{ cm}^2/\text{Vs}$ can be obtained for hot-pressed polycrystals.

(2) Nickel as an impurity acts as a donor in the crystal lattice of CoSb_3 ; that is, a partially compensated material.

(3) From the low temperature dependence of the Hall mobility below 300K for CoSb_3 , a form of scattering by thermally activated hopping of holes (small polarons or bipolarons) can be expected to predominate.

(4) Non-stoichiometry also have a pronounced effect on the electric transport properties of the Skutterudite CoSb_3 .

Acknowledgement

This study has been performed by a financial support of the Yamaguchi Prefectural Government and the Yamaguchi Industrial Technology Development Organization. The authors would like to thank Dr. Jan W. Vandersande, Dr. T. Caillat, Dr. J.-P. Fleurial, and Dr. A. Borshchevsky of Jet Propulsion Laboratory for their available discussions.

Reference

- [1] J.Ackermann and A.Wold, "The preparation and characterization of the cobalt skutterudites CoP_3 , CoAs_3 and CoSb_3 ", J. Phys. Chem. Solid, Vol.38, pp. 1013-1016 (1977).
- [2] David J.Singh and Warren E.Pickett, "Skutterudite anti-monides: Quasilinear bands and unusual transport", Phys. Rev. B, Vol.50, No.5, pp 11235-11238 (1994).
- [3] L.D.Dudkin and N.Kh.Abriskosov, "Effect of nickel on the properties of the semiconducting compound CoSb_3 ", J. Inorganic Chem., Vol.2, No.1, pp 212-221 (1957).
- [4] B.N.Zobrina and L.D.Dudkin, "Investigation of the thermoelectric properties of CoSb_3 with Sn, Te and Ni impurities", Sov. Phys. Solid State, Vol.1, pp 1668-1674 (1960).
- [5] D.T.Morelli, T.Caillat, J.-P.Fleurial, A.Borshchevsky, J.Vandesande, B.Chen, and C.Uher, "Low-temperature transport properties of p -type CoSb_3 ", Phys. Rev. B, Vol.51, No.15, pp. 9622-9628 (1995).
- [6] T.Caillat, J.-P.Fleurial and A.Borshchevsky, "Bridgman-solution crystal growth and characterization of the skutterudite compounds CoSb_3 and RhSb_3 ", J. Crys. Growth, (1995) to be published.
- [7] D.Mandrus, A.Migliori, T.W.Darling, M.F.Hundley, E.J.Peterson and J.D.Thompson, "Electronic transport in lightly doped CoSb_3 ", Phys. Rev. B, Vol.52, No.7, pp. 4926-4931 (1995).
- [8] K.Matsubara, T.Iyanaga, T.Tsubouchi, K.Kishimoto, and T.Koyanagi, "Thermoelectric properties of $(\text{Pd},\text{Co})\text{Sb}_3$ compounds with the skutterudite structure", AIP Conf. Proc. 316, pp.226-229 (1994).
- [9] K.Matsubara, T.Iyanaga, T.Tsubouchi, K.Kishimoto, T.Koyanagi, and H.Anno, "Thermoelectric properties of the skutterudite $(\text{Pd},\text{Co})\text{Sb}_3$ ", T.IEE Japan, Vol.116-A, No.3, pp.268-272 (1996).
- [10] A.David and F.Julius, "Electrical and optical properties of narrow-band materials", Phys. Rev. B, Vol.2, No.8, pp.3112-3134 (1970).
- [11] T.L.Aselage and D.Emin, "Electronic transport properties in boroncarbides", CRC Handbook of Thermoelectrics (Edited by D.M.Rowe), pp. 373-386 (1995).
- [12] N.E.Christensen, "Electronic structure of $\beta\text{-FeSi}_2$ ", Phys. Rev. B, Vol.42, No.11, pp. 7148-7153 (1990).
- [13] J.Zaanen, G.A.Sawatzky, and J.W.Allen, "Band gaps and electronic structure of transition-metal compounds", Phys. Rev. Lett., Vol.55, No.4, pp. 418-421 (1985).

Skutterudites for Thermoelectric Applications

Thierry Caillat*, Jean-Pierre Fleurial, and Alex Borshchevsky

Jet Propulsion Laboratory/California Institute of Technology

4800 Oak Grove Drive

Pasadena, CA 91109 USA

*e-mail: thierry.caillat@jpl.nasa.gov

Abstract

Thermoelectric generators and cooling devices present several advantages compared to other energy conversion technologies: they are reliable, can operate unattended in hostile environments, and are also environmentally friendly. However, their application has been limited up to now because of the relatively low conversion efficiency of traditional thermoelectric materials used in the devices. New more efficient materials are needed. A new class of semiconducting materials was identified at JPL a few years ago and the study of the properties of these materials for thermoelectric and other applications has been subject to a growing interest. Recent findings on the physical-chemical and transport properties of skutterudite materials are reviewed. Results obtained on binary compounds showed that their lattice thermal conductivity is too high to achieve high thermoelectric figures of merit. Several approaches have been recently proposed to decrease the lattice thermal conductivity of skutterudite materials. They are described and illustrated by recent experimental results. It is shown that low thermal conductivity can be achieved and high ZT values are possible for skutterudites.

Introduction

Skutterudite materials have generated considerable interest as new thermoelectric materials over the past few years [1,2]. The value of a material for thermoelectric power generation or cooling applications is defined by the thermoelectric figure of merit Z which is a function of the Seebeck coefficient (α), electrical resistivity (ρ), and thermal conductivity (λ), and is defined as $Z = \alpha^2/\rho\lambda$. Skutterudite materials have interesting transport properties, in particular high hole mobilities [3,4]. The work on skutterudites initially focused on the study of the properties of the binary compounds IrSb₃ and CoSb₃ [1-3]. The most completely characterized binary compound is CoSb₃. Both n- and p-type single crystals were grown over a wide carrier concentration range and their thermoelectric properties measured [4,5]. In the first section of this paper, the thermoelectric properties of CoSb₃ are reviewed. The thermoelectric properties of other binary compounds, when known, seem to follow the trends established for CoSb₃. Band structures calculations of skutterudite compounds were also recently performed [6,7]. These studies showed that the binary skutterudite compounds appear to be small band gap semiconductors with highly nonparabolic valence bands in the case of the antimonides which result in unusual transport properties. Although the binary compounds have good

electrical properties, their thermoelectric figure of merit is limited by their relatively high thermal conductivity (about 110 mW/cmK at room temperature for IrSb₃ and CoSb₃). If the lattice thermal conductivity of the binary compounds could be significantly reduced, high thermoelectric figure of merit values might be possible [2].

Several approaches were recently considered to reduce the lattice thermal conductivity of these materials. Such reduction have been observed in solid solutions, ternary compounds, filled skutterudites, and also heavily doped n-type samples. The corresponding phonon scattering mechanisms are reviewed in the second part of this paper and illustrated by experimental data obtained for several skutterudite materials. It is shown that low thermal conductivity skutterudite materials can be obtained and high ZT values are possible.

Thermoelectric properties of CoSb₃

We present in this section some properties of the binary skutterudite compound CoSb₃ at room temperature. As we mentioned before, this compound is the most characterized of the binary skutterudite compounds MA₃, where M is Co, Rh, or Ir and A is Sb, As, or P. The data obtained on the other binary compounds showed that the trends established for CoSb₃ are also valid for these compounds. CoSb₃ single crystals grown from Sb-rich melts have p-type conductivity and were obtained with carrier concentrations from 1×10^{17} to $1 \times 10^{19} \text{ cm}^{-3}$ [4]. N-type single crystals were obtained by doping with Pd or Te with carrier concentrations from 1×10^{18} to $1 \times 10^{21} \text{ cm}^{-3}$ [4]. According to band structure calculations, CoSb₃ was predicted to have an indirect pseudo-gap of 0.57 eV but there is a band crossing the pseudo-gap and, in fact, CoSb₃ would have a small gap of only 50 meV [6,7].

The room temperature variations of hole and electron mobilities in CoSb₃ are shown in Fig. 1. The hole mobilities are very large but the electron mobilities are much smaller. According to the predictions of Singh and Pickett [6,7], for hole concentration above $3 \times 10^{16} \text{ cm}^{-3}$, the hole mobility should vary as $p^{-1/3}$ as determined by the linear dispersions of the bands. For a parabolic band, the mobility should vary as $p^{-2/3}$. In Fig. 1, the $p^{-1/3}$ predicted behavior is compared with the experimental data. For carrier concentrations from 1×10^{18} to $1 \times 10^{19} \text{ cm}^{-3}$, the experimental data seem to agree reasonably well with the model predictions. However, for lower carrier concentrations, the hole mobilities seem to flatten out and vary only weakly with carrier concentration. This is presumably due to a change in the carrier scattering

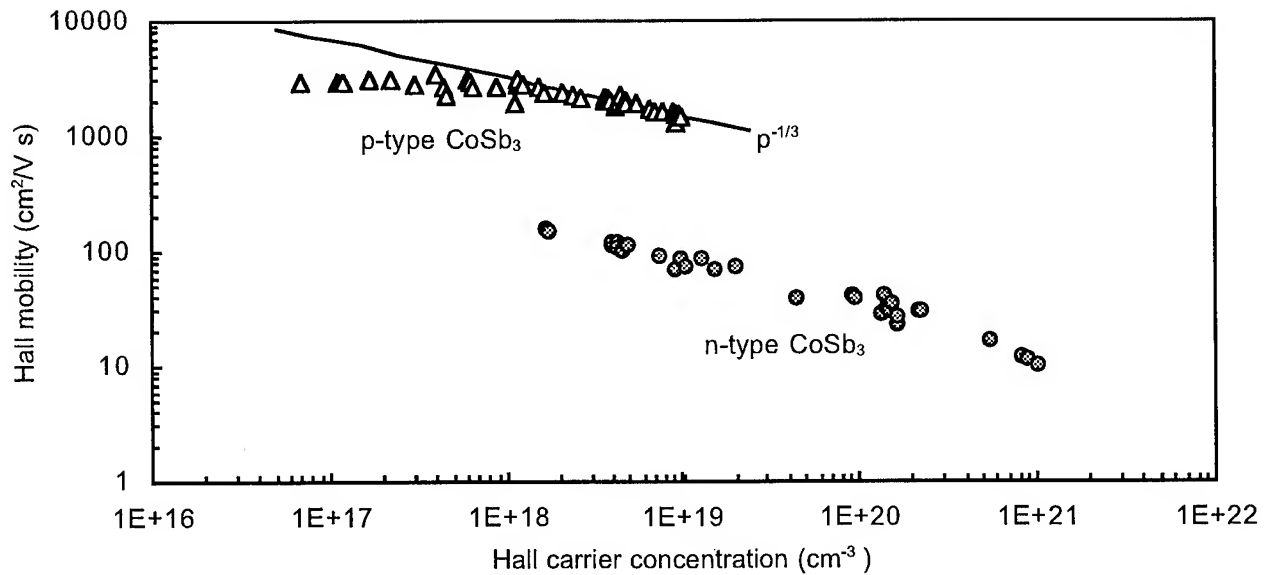


Figure 1. The room temperature Hall mobility values for n- and p-type CoSb₃ crystals as a function of the Hall carrier concentration. The solid line represents the predicted behavior derived from band structure calculations.⁶

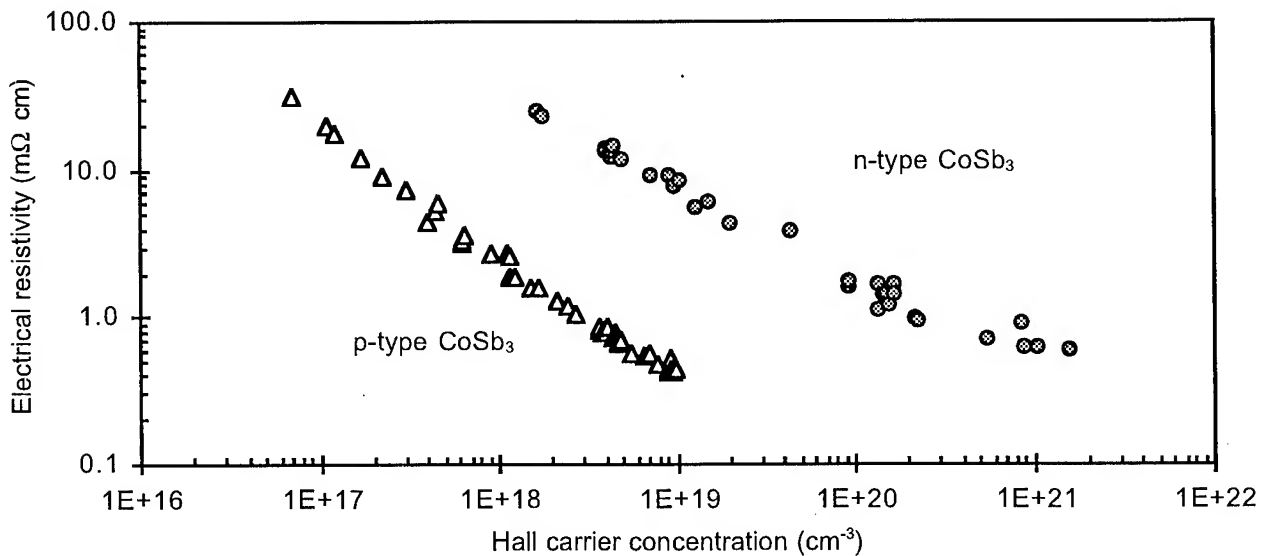


Figure 2. The room temperature electrical resistivity values for n- and p-type CoSb₃ crystals as a function of the Hall carrier concentration

mechanisms as it was observed in InSb and other small gap semiconductors [8]. As a result of the large difference between the electron and hole mobilities, the electrical resistivity values are larger for n-type samples than for p-type at a given carrier concentration (see Fig.2). However, electrical resistivity values about 1 mΩ cm were obtained for both p- and n-type but at a carrier concentration of $3 \times 10^{18} \text{ cm}^{-3}$ for p-type and $1.5 \times 10^{20} \text{ cm}^{-3}$ for n-type. An estimation of the carrier effective masses was carried out using a parabolic band model and acoustic phonons scattering for the carriers [5]. The results showed that the effective mass of the electrons is about 10 times larger than the hole effective mass. At a carrier concentration of $1 \times 10^{18} \text{ cm}^{-3}$, the hole effective mass is $0.13 m_0$ and the electron effective mass is $1.4 m_0$. The hole

effective mass shows some dependence on the doping level which suggests some degree of non-parabolicity for the valence band.

The room temperature Seebeck coefficients values are shown in Fig 3. for CoSb₃. As a result of the large difference between electron and hole effective mass, the n-type Seebeck coefficient values are much larger than p-type at a given carrier concentration. In the constant scattering time approximation, the Seebeck coefficient is given by [6]

$$\alpha = - \left(\frac{2\pi k_B^2 T}{3es} \right) \left(\frac{\pi}{3p} \right)^{1/3}, \quad (1)$$

where s is the slope of the linear dispersing band, p the hole carrier concentration, and $s = -3.10 \text{ eV Å}$. The calculated

Seebeck coefficient values using equation (1) are also plotted on Fig 3. and seem to agree fairly well with the experimental data, supporting the model proposed [4].

The calculated power factor values (α^2/ρ) are shown in Fig 4. for p- and n-type CoSb₃ single crystals. The power factor values are relatively large and comparable to those for state-of-the-art thermoelectric materials. Although a maximum power factor value of about 30 $\mu\text{W}/\text{cm K}^2$ was obtained for both p- and n-type, the maximum occurs at a carrier concentration of about an order of magnitude lower for p-type than for n-type which can also be attributed to the difference in effective masses. Based on band structure calculations, it was predicted

that for p-type antimonides, the doping dependence of the power factor would be weak [9] but the experimental data suggests that the power factor is somewhat dependent on the carrier concentration.

The minimum thermal conductivity at high temperatures was estimated at 3.11 mW/cmK for CoSb₃ [10]. Using a parabolic band model, acoustic phonon scattering for the carriers, and assuming that the thermal conductivity has its minimum value of 3.11 mW/cmK, a maximum room temperature ZT value of 1.59 would be obtained for n-type CoSb₃ at $2 \times 10^{19} \text{ cm}^{-3}$ and 0.98 for p-type at $5 \times 10^{17} \text{ cm}^{-3}$. Unfortunately, the intrinsic thermal conductivity of CoSb₃ at room temperature

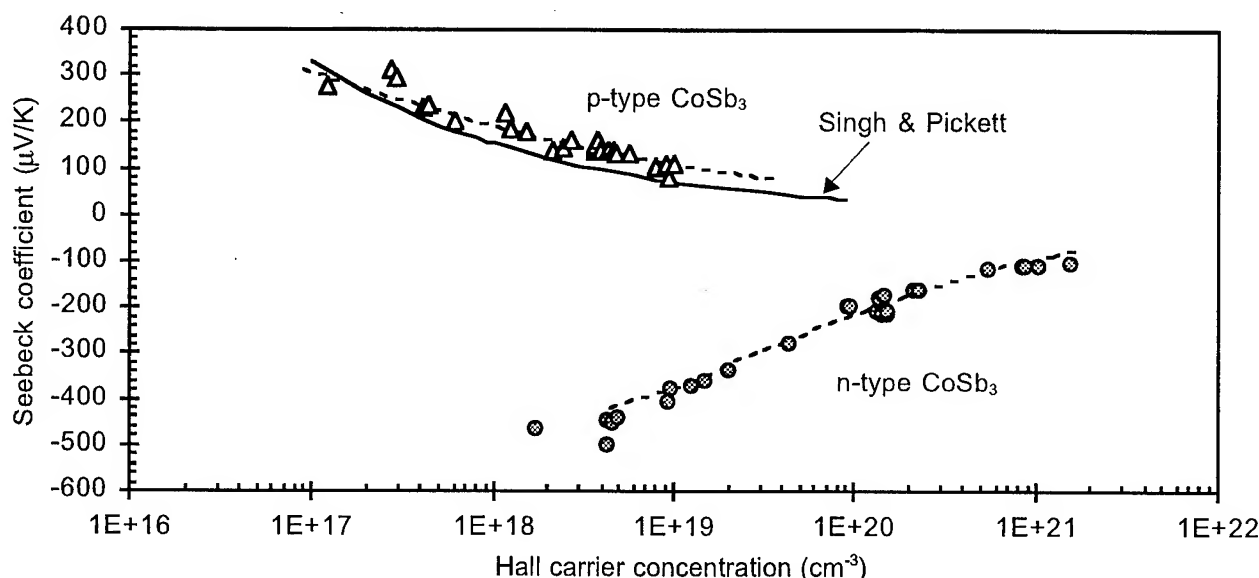


Figure 3. The room temperature Seebeck coefficient values for n- and p-type CoSb₃ crystals as a function of the Hall carrier concentration. The dashed lines represent the best-fit of the experimental data.

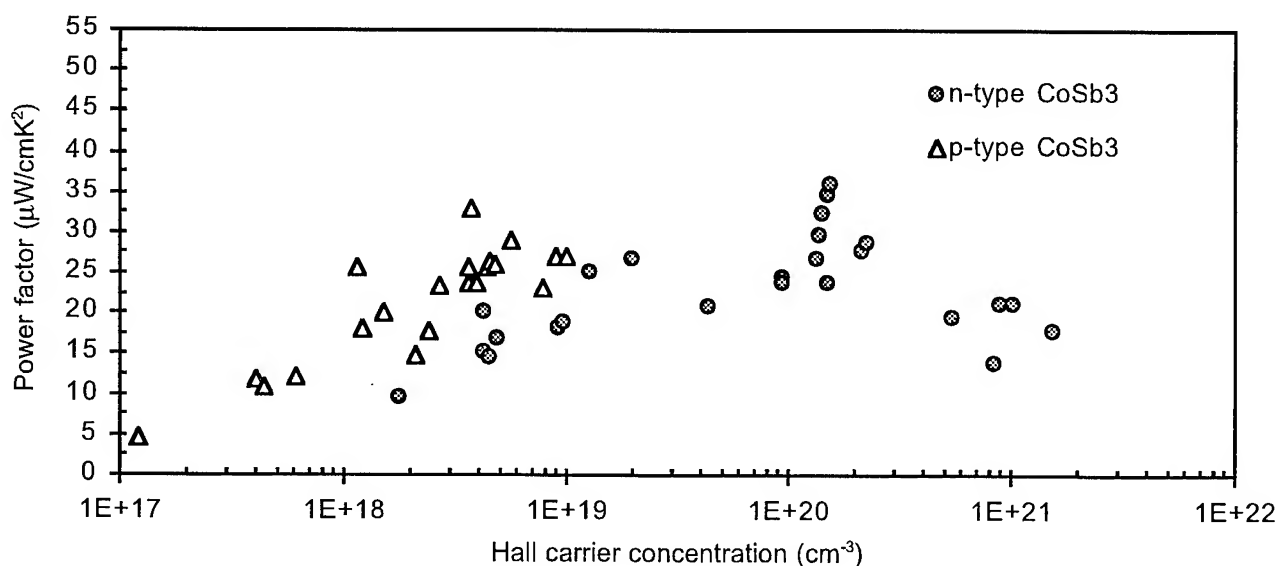


Figure 4. The power factor (α^2/ρ) values as a function of the Hall carrier concentration for p- and n-type CoSb₃ at room temperature

is about 100 mW/cmK and the ZT values are low. Existing thermal conductivity data on other binary compounds show that their thermal conductivity is also too high to outperform state-of-the-art thermoelectric materials. It is clear that the efforts should now focus on lattice thermal conductivity reduction. Recent studies on skutterudite materials have shown that several phonon scattering mechanisms can successfully lower the lattice thermal conductivity of skutterudites and initial results have shown that high ZT values can be obtained. The different approaches are reviewed in the next section.

Lattice thermal conductivity reduction in skutterudites

We recently reviewed the mechanisms which were successfully used to reduce the lattice thermal conductivity of skutterudites [10]. The four major mechanisms are mass and strain fluctuation, electron-phonon scattering in heavily doped samples, electron charge transfer in mixed-valence ternary compounds, and void filling in the skutterudite structure. These mechanisms are briefly described in the next paragraphs and illustrated by experimental data.

Skutterudite solid solutions

All state-of-the-art thermoelectric materials are solid solutions and using mass and strain fluctuations in solid solutions is a well known approach to reduce the lattice thermal conductivity. This type of phonon scattering would tend to scatter high frequency phonons but would also result in some carrier mobility reduction. Thus, improvements in the thermoelectric properties can be obtained if the ratio between carrier mobility and lattice thermal conductivity (μ/λ_L) is larger for the solid solutions. A number of solid solutions between skutterudite compounds were reported in the literature [2,11-13]. More recent studies showed that many more solid solutions can be formed and initial results showed that some reduction in lattice thermal conductivity can be obtained [14]. For example, a room temperature lattice thermal conductivity of 29 mW/cmK was obtained for a solid solution $(\text{IrSb}_3)_{0.12}(\text{CoSb}_3)_{0.88}$. This represents a threefold reduction compared to either one of the end members in this system. Results obtained for a solid solution $(\text{RhSb}_3)_{0.5}(\text{IrSb}_3)_{0.5}$ showed that its room temperature lattice thermal conductivity was 90 mW/cmK [2]. The reduction is not as large as for the solid solution $(\text{IrSb}_3)_{0.12}(\text{CoSb}_3)_{0.88}$ and can be attributed to the fact that the decrease is only due to mass fluctuation in this system and that there is no strain fluctuation. In order to help selecting the most promising solid solutions systems, the effect of mass and strain fluctuation scattering of phonons was calculated for skutterudites using the theory developed by Callaway and Von Baeyer [15]. The details of the calculations and the results will be published later. The major findings are:

1. Skutterudite alloys with small mass and volume fluctuations (such as $\text{CoSb}_3\text{-Fe}_{0.5}\text{Ni}_{0.5}\text{Sb}_3$, $\text{IrSb}_3\text{-RhSb}_3$ and $\text{IrSb}_3\text{-RuSb}_2\text{Te}$) exhibit relatively small decrease in thermal conductivity.
2. Alloys between ternary and binary skutterudites do not result in lower thermal conductivity values compared to those obtained for optimum binary skutterudite alloys.

3. The lowest thermal conductivity values are achieved for alloys maximizing mass and volume fluctuations, such as $\text{CoSb}_3\text{-IrP}_3$ with 8 mW/cmK for a 50 mole% concentration.

These calculations show that point defect scattering can be a very efficient phonon scattering mechanism in some skutterudite solid solutions. More work is needed to determine the solubility limit of some of these solid solutions and efforts are currently underway to prepare samples of the most promising systems and compare the experimental data with the theoretical predictions.

Heavily doped CoSb_3

The thermal conductivity of heavily doped n-type CoSb_3 sample was recently measured [5]. The thermal conductivity data are shown in Fig. 5. For lightly doped samples, the room temperature lattice thermal conductivity is about 100 but for more heavily doped samples, the value decreases to about 57 mW/cmK. The temperature dependence of the lattice thermal conductivity varies with the doping level of the samples, becoming smaller for heavily doped samples. These results suggest that electron-phonon scattering is responsible for the large decrease in lattice thermal conductivity in heavily doped samples. This is an interesting finding because charge carrier phonon scattering would scatter the phonons with low frequency and if coupled with point defect scattering could result in very low lattice thermal conductivity values. The combination of point defects and charge carrier scattering was utilized in Si-Ge alloys [16]. Up to now, this scattering mechanism appears to be much weaker in p-type samples.

Ternary compounds

The properties of the ternary skutterudite phase $\text{Ru}_{0.5}\text{Pd}_{0.5}\text{Sb}_3$ were recently studied in details [17]. The thermal conductivity data are shown in Fig. 6. The total room temperature thermal conductivity is 30 mW/cmK and the lattice component is about 16 mW/cmK, about five times lower than for p-type CoSb_3 . The substitution of Ru and Pd for Rh in RhSb_3 is expected to create some mass and volume disorder in the structure, resulting in lower thermal conductivity. However, Ru and Pd have only slightly different atomic masses and atomic radii. Therefore, the large decrease in lattice thermal conductivity does not appear to be only due to mass and volume fluctuations. A possible explanation for the unusually high scattering rates of charge carriers and phonons in $\text{Ru}_{0.5}\text{Pd}_{0.5}\text{Sb}_3$ could be that ruthenium has a mixed valence states and electrons are transferred between the two ions, scattering the phonons. The binary compound CoSb_3 can be described by its ionic formula: $\text{Co}^{3+}\text{Sb}_3^{-1}$. For the stoichiometric $\text{Ru}_{0.5}\text{Pd}_{0.5}\text{Sb}_3$, we assume that the valence state of Ru, Pd, and Sb would be Ru^{2+} , Pd^{4+} , and Sb^{-1} . A systematic shift from the stoichiometry $\text{Ru}_{0.5}\text{Pd}_{0.5}\text{Sb}_3$ was revealed by microprobe analysis. To compensate for the Pd deficit and excess Sb in the samples, the Ru might take a mixed valence state, i.e., Ru^{2+} and Ru^{4+} . Based on the microprobe results, we calculated that 48% of the Ru would be in the Ru^{4+} state in our samples. In a study of the thermal conductivity of Fe_3O_4 , Slack [18] has shown that the phonon scattering caused by interaction of the phonons by local disorder in the magnetic lattice was significant.

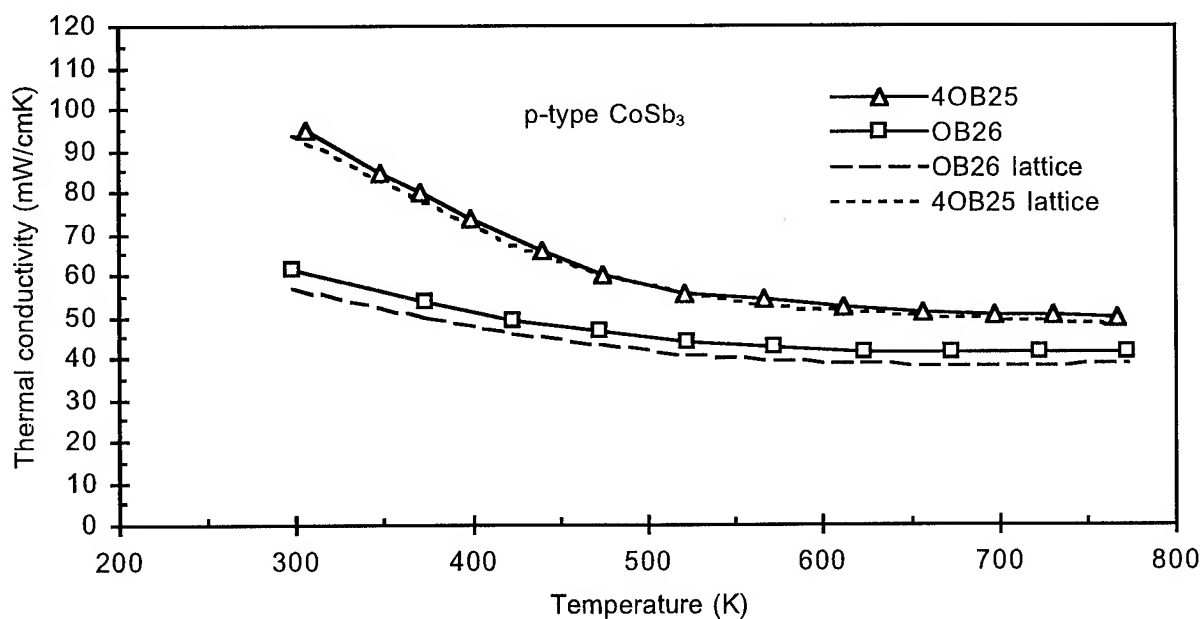


Figure 5. The thermal conductivity values as a function of temperature for n-type CoSb_3 samples with different doping levels: 4OB25 ($2 \times 10^{19} \text{ cm}^{-3}$) and OB26 ($2 \times 10^{20} \text{ cm}^{-3}$). The dashed lines correspond to the lattice thermal conductivity.

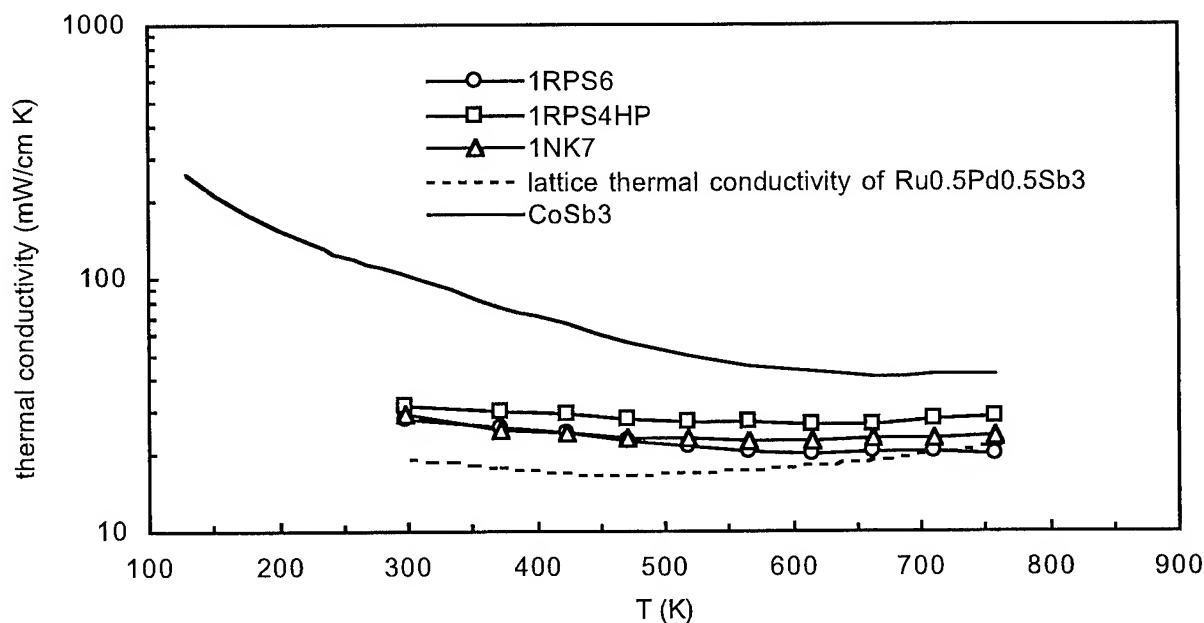


Figure 6. Thermal conductivity versus temperature for three hot-pressed $\text{Ru}_{0.5}\text{Pd}_{0.5}\text{Sb}_3$ samples. The solid line corresponds to the typical thermal conductivity values for p-type CoSb_3 and the dashed line is the calculated lattice thermal conductivity for sample 1RPS4HP.

Similarly, for $\text{Ru}_{0.5}\text{Pd}_{0.5}\text{Sb}_3$, electron exchange between the Ru^{2+} and Ru^{4+} ions and/or Pd^{4+} might occur which could explain why a large decrease in carrier mobility was observed. Similarly to Fe_3O_4 , the nearly temperature independent thermal conductivity might be caused (at least partially) by the same electron exchange between the ions in this

compound. This scattering mechanism might also be at the origin of the low thermal conductivity observed on other ternary skutterudite compounds [19]. Although ternary compounds have rather low thermal conductivity values, it was not found yet how to control their electrical properties. The ZT values for these compounds are relatively low but

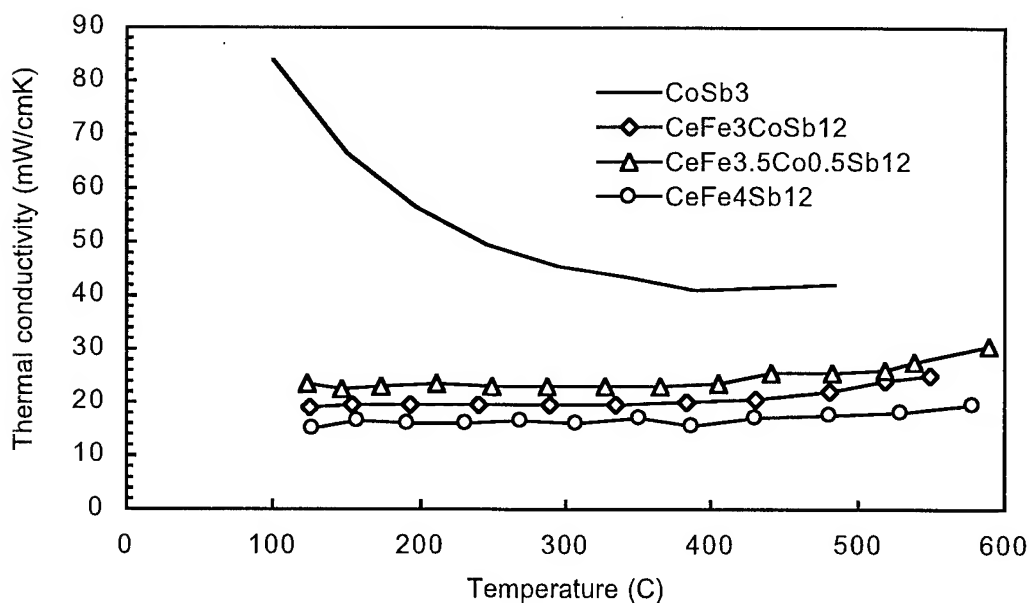


Figure 7. Thermal conductivity versus temperature for three $\text{CeFe}_{4-x}\text{Co}_x\text{Sb}_{12}$ filled skutterudite compositions.

efforts should focus on controlling the doping level, preparing n-type samples, and investigate their properties.

Filled skutterudites

Finally, the last approach which was considered to lower the lattice thermal conductivity of skutterudite materials is to fill the voids present in the skutterudite structure with rare earth elements. Slack [20] first suggested that the "rattling" of the rare earth element would produce a significant phonon scattering and reduce the thermal conductivity. Experimental evidence of this enhanced phonon scattering was since published in the literature [21-24]. This approach seems to be particularly promising in light of recent results obtained on $\text{CeFe}_{4-x}\text{Co}_x\text{Sb}_{12}$ materials [24]. The thermal conductivity data of some of these compositions are shown in Fig. 7. The room temperature lattice thermal conductivity of $\text{CeFe}_4\text{Sb}_{12}$ is about 12 mW/cmK. As a result of these low thermal conductivity values and good transport properties of these semi-metallic compositions, ZT values up to 1.4 at 600°C were measured. Numerous filled skutterudites with the formula RM_4B_{12} , where $\text{M}=\text{Fe}$, Ru or Os and $\text{B}=\text{P}$, As or Sb , are known. The calculated band gaps for $\text{CeFe}_4\text{Sb}_{12}$ and $\text{CeFe}_4\text{P}_{12}$ are 0.1 and 0.34 eV, respectively [7]. In addition, band structure calculations determined that these compounds should possess large effective masses which should result in large Seebeck coefficients. The properties of these compounds will be investigated further.

Summary

The thermoelectric properties of the binary skutterudite compound CoSb_3 have been reviewed and we have shown that this compound possesses good electric properties but the thermoelectric figure of merit value are limited by the relatively high thermal conductivity values. We have also reviewed several phonon scattering mechanisms which can

reduce the lattice thermal conductivity of skutterudites. Among these mechanisms, mass and strain fluctuation and void filling appear to be the most promising. Ultimately, a combination of these mechanisms should be employed to reach lattice thermal conductivity close to the theoretical minimum. Initial results show that high ZT values are obtainable for skutterudites. Efforts are currently underway at JPL to investigate the various approaches described in this paper to reduce the lattice thermal conductivity.

Acknowledgments

The work described in this paper was carried out at the Jet Propulsion Laboratory/California Institute of Technology, under contract with the National Aeronautics and Space Administration. The authors would like to thank Prof. G. A. Slack for valuable discussions.

References

1. T. Caillat, A. Borshchevsky, and J. -P. Fleurial, in Proceedings of the XIth International Conference on Thermoelectrics, University of Texas at Arlington, 1992, edited by K. R. Rao (University of Texas at Arlington Press, Arlington), 98 (1993).
2. G. Slack and V. G. Tsoukala, J. Appl. Phys. 76, 1665 (1994).
3. D. T. Morelli, T. Caillat, J. -P. Fleurial, A. Borshchevsky, J. Vandersande, B. Chen, and C. Uher, Phys. Rev. B 51, 9622 (1995).
4. T. Caillat, J. -P. Fleurial, and A. Borshchevsky, J. Cryst. Growth, accepted for publication (1996).
5. T. Caillat, J. -P. Fleurial, and A. Borshchevsky submitted to J. Appl. Phys. for publication (1996).
6. D. J. Singh and W. E. Pickett, Phys. Rev. B, 50, 15, 11235 (1994).

7. L. Nordtröm and D. J. Singh, Phys. Rev. B, 53, 3, 1103 (1996).
8. W. Zawadski, Adv. Phys. 23, 435 (1974).
9. D. J. Singh, L. Nordtröm, W. E. Pickett, and J. L. Feldman, this conference.
10. G. A. Slack, J. -P. Fleurial, and T. Caillat, to be published in Naval Research Reviews (1996).
11. A. Borshchevsky, J. -P. Fleurial, E. Allevato., and T. Caillat, in Proceedings of the XIIIth International Conference on Thermoelectrics, Kansas City, MO, USA, edited by B. Mathiprakasam and P. Heenan (AIP Conference 316, New York), 31 (1995).
12. N. Mandel, J. Donohue, Acta Cryst., B27, 2288 (1971).
13. H. D. Lutz, G. Kliche, Journal of Solid State Chemistry, 40, 64 (1981).
14. A. Borshchevsky, J. -P. Fleurial, and T. Caillat, this conference.
15. T. Callaway and H. C. Von Baeyer, Phys. Rev., 120, 1149 (1960).
16. J. P. Dismukes, L. Esktröm, E. F. Steigmeier, I. Kudman, and D. S. Beers, J. Appl. Phys. 35, 2899 (1964).
17. T. Caillat, J. Kulleck, A. Borshchevsky, and J. -P. Fleurial, J. Appl. Phys. 79, 11, 1141 (1996)
18. G. A. Slack, Phys. Rev 126, 427 (1962).
19. J. -P. Fleurial, A. Borshchevsky, and T. Caillat (to be published).
20. G. A. Slack, Thermoelectric Handbook, edited by M. Rowe (Chemical Rubber, Boca Raton, FL) 1995, p. 407.
21. D. T. Morelli and G. P. Meisner, J. Appl. Phys. 77, 3777 (1995).
22. G. S. Nolas, G. A. Slack, T. M. Tritt, and D. T. Morelli Proceedings of XIVth International Conference on Thermoelectrics, St. Petersburg, Russia, edited by M. V. Vedernikov, A. F. Ioffe Physical-Technical Institute, 194201, St- Petersburg, Russia, 236 (1995).
23. G. S. Nolas, G. A. Slack, T. Caillat, and G. P. Meisner, J. Appl. Phys, Vol. 79, 5, 2622 (1996).
24. J. -P. Fleurial, A. Borshchevsky, T. Caillat, D. T. Morelli, and G. P. Meisner, this conference

Thermoelectric Properties of $\text{Co}(\text{M}_x\text{Sb}_{1-x})_3$ ($\text{M}=\text{Ge}, \text{Sn}, \text{Pb}$) Compounds

T. Koyanagi, T. Tsubouchi, M. Ohtani, K. Kishimoto, H. Anno*, and K. Matsubara*

Department of Electrical and Electronic Engineering, Yamaguchi University

**Department of Electronics and Computer Science, Science University of Tokyo in Yamaguchi*

Abstract

The thermoelectric properties of CoSb_3 , which was doped with IV elements of Sn, Ge and Pb, were investigated in order to improve the p -type thermoelectric performance of non-doped CoSb_3 . $\text{Co}(\text{M}_x\text{Sb}_{1-x})_3$ ($\text{M}=\text{Ge}, \text{Sn}, \text{Pb}$) compounds were prepared by hot-pressing. The solubility limit of these dopants was determined from measurements of the x-ray photoelectron spectroscopy (XPS). The solubility limit of Ge and Sn are estimated to be about 1.4 and 2.4%, respectively, while Pb hardly substitutes for Sb. The Hall measurements reveal that the maximum carrier concentrations at room temperature were $1.5 \times 10^{19} \text{cm}^{-3}$ for Ge and $2.9 \times 10^{19} \text{cm}^{-3}$ for Sn. The change in the mobility with x can be explained qualitatively by taking account of conduction of both holes and electrons in doped CoSb_3 . The electrical conductivity σ and Seebeck coefficient S of these samples were measured in the temperature range from 300 to 800K. The p -type conduction is achieved in the whole temperature range by introducing Ge and Sn in CoSb_3 . The values of the power factor $S^2\sigma$ for $\text{Co}(\text{Sn}_x\text{Sb}_{1-x})_3$ with $x=1\%$ are of the order of 10^{-5}W/cmK^2 and 2~10 times as high as those of the non-doped CoSb_3 in the wide temperature range.

Introduction

Many skutterudite compounds have been investigated as new thermoelectric materials [1-13]. These compounds have an extraordinarily high hole mobility, compared with those of state-of-the-art semiconductors. Further, the thermal conductivity of skutterudite compounds is relatively low because of their large unit cell. These natures are favorable for a thermoelectric material. In these skutterudite families, CoSb_3 have been investigated actively as is the case with IrSb_3 [1-3,7-11,13]. Non-doped CoSb_3 shows p -type conduction due to its high hole mobility. For CoSb_3 with n -type conduction, Ni, Pd and Te have been used as a dopant [2,3,7,8,11]. We found that the substitution of Pd for Co in sintered CoSb_3 allowed one to enhance the n -type thermoelectric performance [8]. On the other hand, although Fe and Sn are known as a dopant for p -type CoSb_3 , few studies on the doping for p -type CoSb_3 have been made [2,3,11]. Since the bonding of CoSb_3 is predominantly covalent, the substitution of IV elements, such as Ge, Sn and Pb, for Sb (V element) is expected to be effective for generation of holes, that is, enhancement of p -type thermoelectric performance.

In this paper, we report some results of CoSb_3 which was doped with IV elements of Sn, Ge and Pb by substituting for

Sb. The solubility limit of these dopant in CoSb_3 is discussed based on the results of the x-ray photoelectron spectroscopy (XPS). The dependence of the carrier concentration and the mobility for $\text{Co}(\text{M}_x\text{Sb}_{1-x})_3$ ($\text{M}=\text{Ge}, \text{Sn}$) on the introduced dopant concentration x are also discussed. For the thermoelectric properties of $\text{Co}(\text{M}_x\text{Sb}_{1-x})_3$ ($\text{M}=\text{Ge}, \text{Sn}$), results of the electrical conductivity and the Seebeck coefficient are described, and the thermoelectric figure of merit is estimated.

Experiment

CoSb_3 doped with Ge, Sn and Pb was sintered by hot-pressing. Co (99.9%) and Sb (99.9999%) ingots were mixed in the molar ratio $\text{Co:Sb}=1:3.1$, which took account of deficiency of Sb due to evaporation during the following process. The ingots of Ge (99.9999%), Sn (99.999%) and Pb (99.9999%) were also mixed as a dopant with the mixture of Co and Sb. The introduced dopant concentration x were changed from 0.5% to 5% of an Sb amount. The mixture of these ingots was arc-melted together in an Ar atmosphere, and the resultant alloy was crushed and ground by ball-milling to powder diameters of several μm . The obtained powder was hot-pressed at 600°C and 60MPa for 3 hours in an Ar atmosphere.

The dopant concentration in the sintered CoSb_3 was measured and the bonding state of the dopant was investigated simultaneously by the x-ray photoelectron spectroscopy (XPS). The crystal structure was checked by the x-ray diffractometry (XRD) analysis. The Hall measurements were made at room temperature to examine the carrier concentration and the mobility. The carrier concentration p was calculated from the Hall coefficient R_H using the simple equation $p=1/(eR_H)$. The Hall mobility μ_H was determined from the zero-field conductivity σ and R_H using the equation $\mu_H=R_H\sigma$. The electrical conductivity σ and Seebeck coefficient S were measured in the temperature range from 300 to 800K.

Results and Discussion

Sintered $\text{Co}(\text{M}_x\text{Sb}_{1-x})_3$ ($\text{M}=\text{Ge}, \text{Sn}, \text{Pb}$) had a skutterudite structure and was highly dense within $x=0\sim 5\%$. The powder of $\text{Co}(\text{M}_x\text{Sb}_{1-x})_3$ showed a typical x-ray diffraction pattern of CoSb_3 powder and no diffraction peak from other phases could be observed in the patterns. The measured densities of all samples were found to be over 96% of the theoretical CoSb_3 density.

Figure 1 shows the dopant concentrations, which were measured by XPS, as a function of the introduced dopant

concentration x . For Ge and Sn, their concentrations in CoSb_3 are almost equal to x , and Ge and Sn remain in CoSb_3 through the arc-melting and the hot-pressing processes. On the other hand, Pb concentration becomes lower than the introduced Pb concentration x .

Figures 2 (a), (b) and (c) show the XPS spectra of Ge $2p_{3/2}$ core electron for $\text{Co}(\text{Ge}_x\text{Sb}_{1-x})_3$, Sn $3d_{3/2}$ for $\text{Co}(\text{Sn}_x\text{Sb}_{1-x})_3$ and Pb $4f_{7/2}$ for $\text{Co}(\text{Pb}_x\text{Sb}_{1-x})_3$ with different introduced dopant concentrations x , respectively. In these figures, "m" and "c" indicate the XPS peak of the non-substituted metallic dopant and the substituted dopant for Sb in a CoSb_3 crystal, respectively. The "c" peaks shift toward higher energies, as

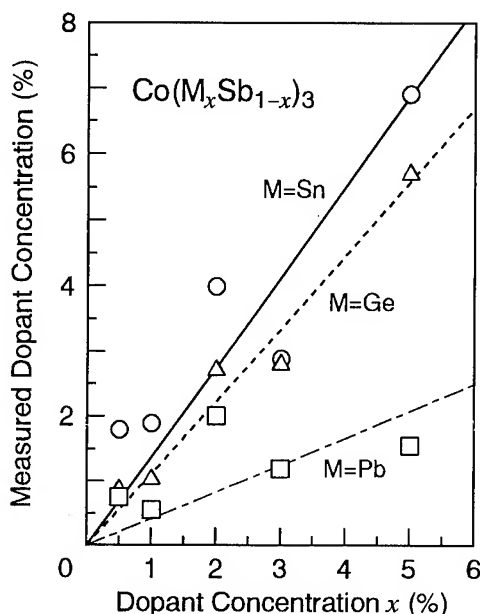


Fig.1 Measured dopant concentration vs. introduced dopant concentration.

compared with the "m" peaks, resulting from the formation of covalent bonds of dopant atoms in the skutterudite crystal. For Ge and Sn, although the "c" peaks are dominant for $x \leq 2\%$, the "m" peaks become higher than "c" peaks as x increases above $x=3\%$. Figure 3 shows the XPS peak area ratio $S_c/(S_c+S_m)$ of the "c" peak to these two peaks as a function of x . The peak ratios $S_c/(S_c+S_m)$ for Ge and Sn hardly change up to $x=2\%$, and rapidly decrease above $x=2\%$. From the results of Fig.1 and Fig.3, the solubility limits of Ge and Sn could be estimated to be about 1.4% and 2.4%, respectively.

On the other hand, for Pb the "m" peak appears even at $x=0.5\%$ in Fig.2 (c), and the peak ratio $S_c/(S_c+S_m)$ is not dependent on x . These results suggest that Pb is not substituted for Sb in an appreciable amount. Bi, of which tetrahedral covalent radius is almost equal to that of Pb, was reported to be hardly substituted for Sb [2]. The electrical conductivity σ hardly changed even if Pb was introduced up to $x=5\%$. Accordingly, it is concluded that the tetrahedral covalent radius of Pb is too large for Pb to substitute for Sb.

Figure 4 shows the carrier concentrations (n or p) at room temperature for $\text{Co}(\text{Ge}_x\text{Sb}_{1-x})_3$ and $\text{Co}(\text{Sn}_x\text{Sb}_{1-x})_3$ as a function of the introduced dopant concentration x . Non-doped CoSb_3 shows n -type conduction. This is related to the deficiency of Sb during the arc-melting and the hot-pressing processes [11] and/or n -type impurities such as Ni in Co powder. As x increases, the carrier concentration decreases and the conduction changes from n -type to p -type. The dopant concentration x_c at which the conduction changes from n -type to p -type is approximately $x_c=1.3\%$ for $\text{Co}(\text{Ge}_x\text{Sb}_{1-x})_3$ and $x_c=0.7\%$ for $\text{Co}(\text{Sn}_x\text{Sb}_{1-x})_3$. At about $x=3\%$, each carrier concentration reaches the maximum and decreases slightly above $x=3\%$. The maximum values of hole concentration p are $1.5 \times 10^{19} \text{ cm}^{-3}$ and $2.9 \times 10^{19} \text{ cm}^{-3}$ for $\text{Co}(\text{Ge}_x\text{Sb}_{1-x})_3$ and $\text{Co}(\text{Sn}_x\text{Sb}_{1-x})_3$, respectively. For $\text{Co}(\text{Ge}_x\text{Sb}_{1-x})_3$, p is lower and

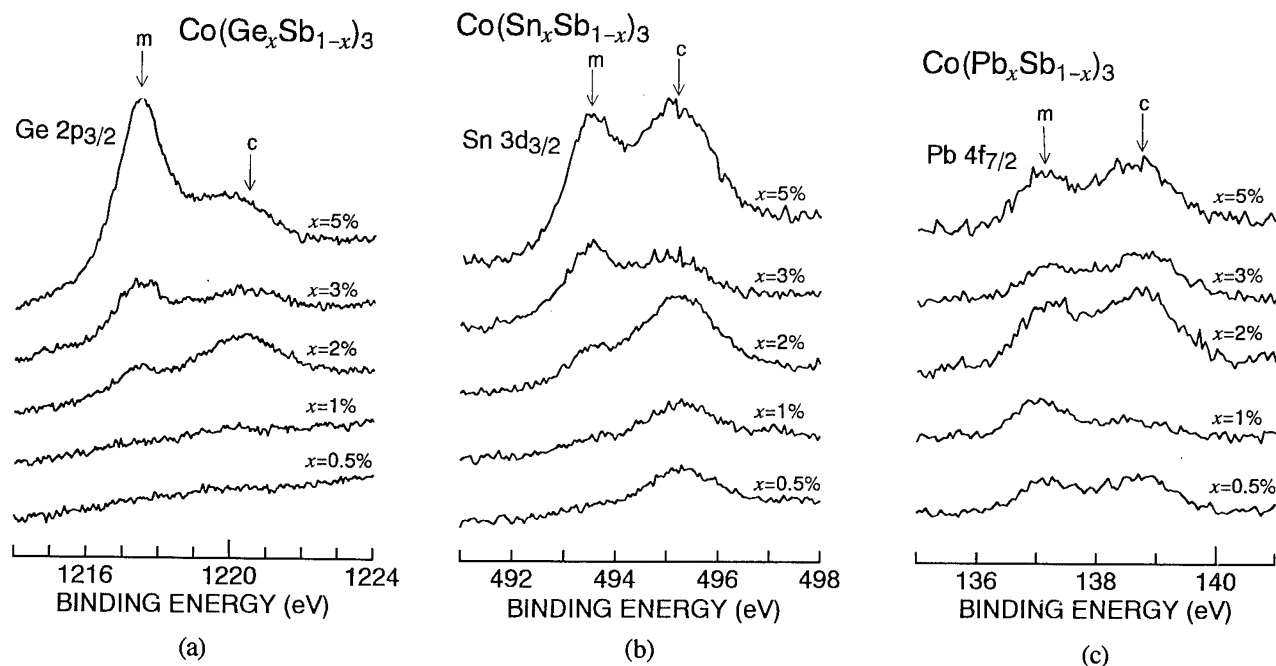


Fig.2 XPS spectra of (a) Ge $2p_{3/2}$ core electron for Ge-, (b) Sn $3d_{3/2}$ for Sn- and (c) Pb $4f_{7/2}$ for Pb-doped CoSb_3 with different x .

x_c is higher than those for $\text{Co}(\text{Sn}_x\text{Sb}_{1-x})_3$. This is attributed to the lower solubility limit for $\text{Co}(\text{Ge}_x\text{Sb}_{1-x})_3$ than that for $\text{Co}(\text{Sn}_x\text{Sb}_{1-x})_3$. The Ge and Sn atomic concentrations in the CoSb_3 crystal, which were estimated from the values of solubility limit, are $4.6 \times 10^{20}\text{cm}^{-3}$ and $7.8 \times 10^{20}\text{cm}^{-3}$, respectively. A few percent of dopant atoms substituted for Sb is found to be active as an acceptor.

Figure 5 shows the Hall mobility μ_H at room temperature for $\text{Co}(\text{Ge}_x\text{Sb}_{1-x})_3$ and $\text{Co}(\text{Sn}_x\text{Sb}_{1-x})_3$ as a function of the introduced dopant concentration x . The values of μ_H are lower than those of single crystals due to the scattering at grain boundaries in the sintered CoSb_3 . The μ_H increases with increasing x and

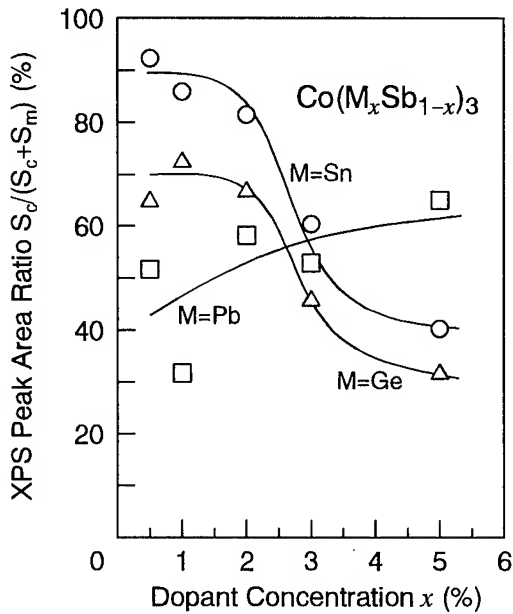


Fig.3 XPS peak area ratio $S_c/(S_c+S_m)$ as a function of x for Ge-, Sn- and Pb-doped CoSb_3 .

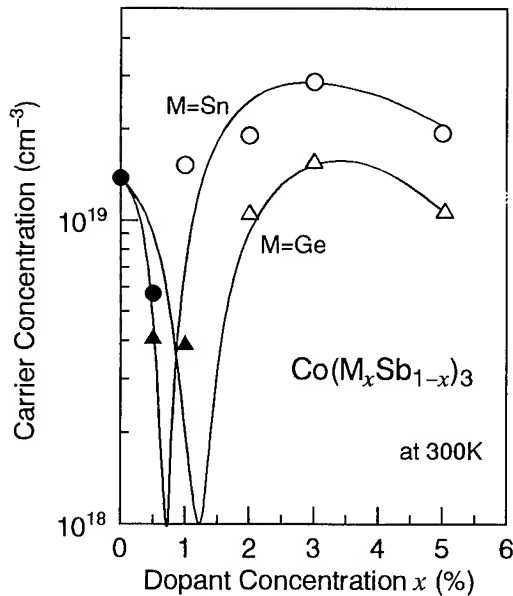


Fig.4 Carrier concentration n/p at room temperature as a function of x for Ge- and Sn-doped CoSb_3 .

tends to be saturated above about $x=3\%$. When both electrons and holes coexist in a semiconductor, the mobility μ is given as the following equation.

$$\mu = \frac{|\mu_p^2 p - \mu_n^2 n|}{\mu_p p + \mu_n n} \quad (1)$$

where μ_p and μ_n are mobilities for holes and electrons, respectively. CoSb_3 has an extraordinarily high hole mobility μ_p ($\sim 3000\text{cm}^2/\text{Vs}$ [7]) and a relatively low electron mobility μ_n ($\sim 100\text{cm}^2/\text{Vs}$ [7]). Accordingly, as the hole concentration p increases, the mobility μ increases according to Eq.(1). $\text{Co}(\text{Ge}_x\text{Sb}_{1-x})_3$ shows lower values of μ_H in the whole dopant concentration range than those of $\text{Co}(\text{Sn}_x\text{Sb}_{1-x})_3$, since the phonon scattering is enhanced due to a large mass difference between Sb and Ge.

Figures 6 (a) and (b) show the temperature dependence of electrical conductivity σ for $\text{Co}(\text{Ge}_x\text{Sb}_{1-x})_3$ and $\text{Co}(\text{Sn}_x\text{Sb}_{1-x})_3$, respectively. The electrical conductivities σ for both doped CoSb_3 increase rapidly at the dopant concentration x at which the conduction changes from n -type to p -type. Since the carrier conduction state is degenerate, σ of the doped CoSb_3 with higher x decreases with an increase in temperature according to a decrease in the mobility. The mobility μ of the samples with higher x was calculated assuming that the carrier concentrations is constant. For $\text{Co}(\text{Ge}_x\text{Sb}_{1-x})_3$ with $x=2\%$ and $\text{Co}(\text{Sn}_x\text{Sb}_{1-x})_3$ with $x=1\%$, μ almost obeys the relation $\mu \propto T^{-1.5}$, suggesting that carriers are mainly scattered by acoustic phonons. As x increases above $x=2\%$ for $\text{Co}(\text{Ge}_x\text{Sb}_{1-x})_3$ and $x=1\%$ for $\text{Co}(\text{Sn}_x\text{Sb}_{1-x})_3$, μ deviates from the relation $\mu \propto T^{-1.5}$ by the other scattering such as the ionized impurity scattering.

Figures 7 (a) and (b) show the temperature dependence of Seebeck coefficient S for $\text{Co}(\text{Ge}_x\text{Sb}_{1-x})_3$ and $\text{Co}(\text{Sn}_x\text{Sb}_{1-x})_3$, respectively. For non-doped CoSb_3 , $\text{Co}(\text{Ge}_x\text{Sb}_{1-x})_3$ ($x \leq 1\%$) and $\text{Co}(\text{Sn}_x\text{Sb}_{1-x})_3$ ($x=0.5\%$), the sign of S is negative at lower

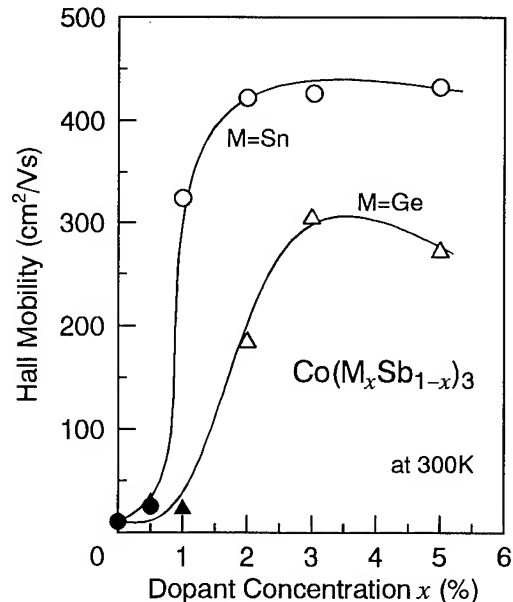


Fig.5 Hall mobility μ_H at room temperature as a function of x for Ge- and Sn-doped CoSb_3 .

temperatures and changes to positive at higher temperatures. The temperature dependence of S for these samples is very similar to that of the hot-pressed CoSb_3 [11]. For the samples with higher x , the sign of S is positive in the whole temperature range, and the p -type conduction can successfully be obtained. As the dopant concentration x increases, the values of S decreases slightly, and the temperature at which S shows the maximum shifts toward higher temperatures. This behavior can be explained by an increase in the carrier concentration.

Figure 8 shows the temperature dependence of the power factor $S^2\sigma$ for $\text{Co}(\text{Ge}_x\text{Sb}_{1-x})_3$ with $x=2\%$ and $\text{Co}(\text{Sn}_x\text{Sb}_{1-x})_3$ with $x=1\%$, which showed the highest $S^2\sigma$ at 600K of

$\text{Co}(\text{Ge}_x\text{Sb}_{1-x})_3$ and $\text{Co}(\text{Sn}_x\text{Sb}_{1-x})_3$, respectively. In this figure, the power factor $S^2\sigma$ for non-doped CoSb_3 is compared. Note that for non-doped CoSb_3 the conduction changes from n -type to p -type at about 450K. The values of $S^2\sigma$ for doped CoSb_3 are 2~10 times as high as those for non-doped CoSb_3 . Although the value of $S^2\sigma$ is almost same between $\text{Co}(\text{Ge}_x\text{Sb}_{1-x})_3$ and $\text{Co}(\text{Sn}_x\text{Sb}_{1-x})_3$ above about 580K, $S^2\sigma$ of $\text{Co}(\text{Sn}_x\text{Sb}_{1-x})_3$ is improved better than that of $\text{Co}(\text{Ge}_x\text{Sb}_{1-x})_3$ below about 580K. For $\text{Co}(\text{Sn}_x\text{Sb}_{1-x})_3$, the value of $S^2\sigma$ is almost constant and of the order of 10^{-5}W/cmK^2 in the temperature range from 300 to 600K. From these values, the maximum value of the non-dimensional thermoelectric figure of merit ZT was estimated using the values of thermal

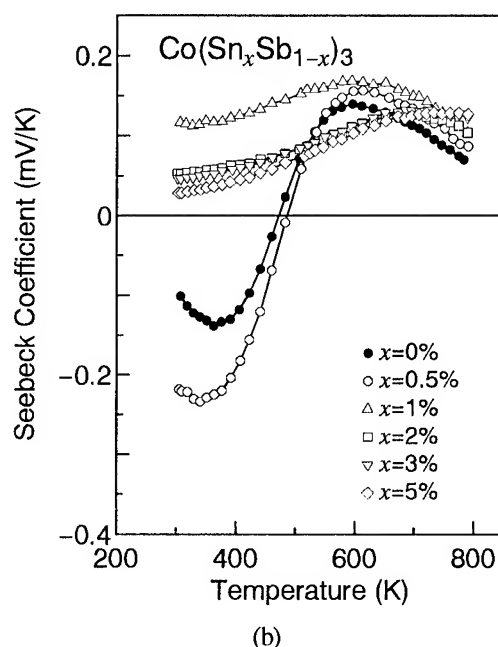
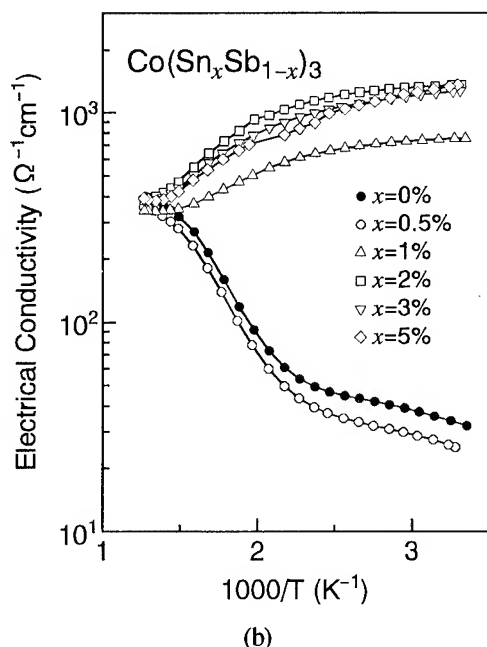
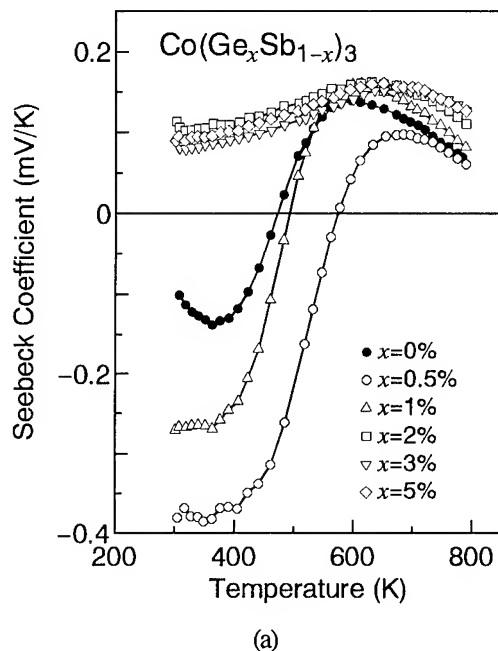
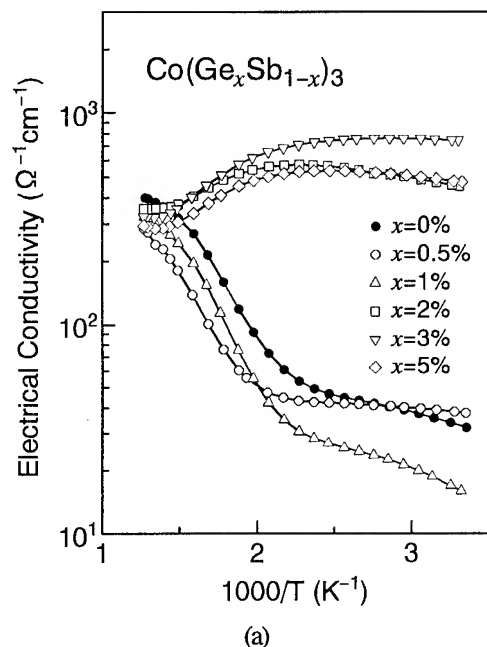


Fig.6 Temperature dependence of conductivity σ for (a) Ge- and (b) Sn-doped CoSb_3 with different x .

Fig.7 Temperature dependence of Seebeck coefficient S for (a) Ge- and (b) Sn-doped CoSb_3 with different x .

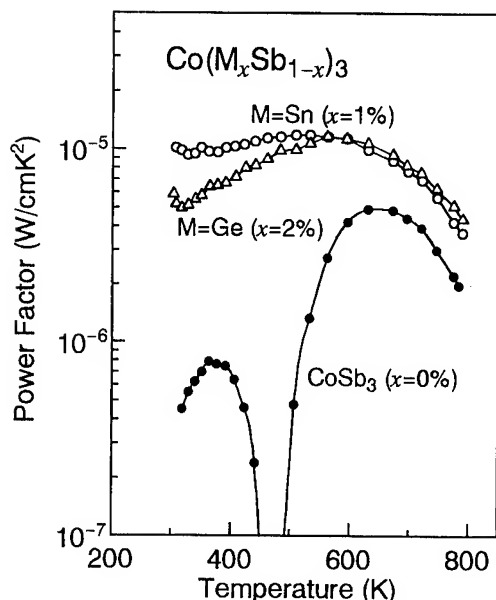


Fig.8 Temperature dependence of power factor $S^2\sigma$ for Ge- ($x=2\%$) and Sn-doped CoSb_3 ($x=1\%$), as compared with that of non-doped CoSb_3 .

conductivity κ of the hot-pressed non-doped CoSb_3 [11]. The maximum ZT of 0.15 was obtained at 600K. This value is comparable to that of non-doped single crystals [7]. An improvement of the figure of merit Z for these doped CoSb_3 would be achieved by suppressing minority carriers (electron) which give rise to a decrease in the mobility μ . The hot-pressed CoSb_3 , which was prepared using Co of high purity (99.998%) by solid reaction of Co and Sb, showed p -type conduction in the temperature range from 300 to 800K and a high mobility of the order of $1000\text{cm}^2/\text{Vs}$ at room temperature [13]. This result suggests that the value of ZT of these doped CoSb_3 is improved 2~3 times.

Conclusion

The thermoelectric properties of $\text{Co}(\text{M}_x\text{Sb}_{1-x})_3$ ($\text{M}=\text{Ge}, \text{Sn}, \text{Pb}$) compounds were investigated. The solubility limits of Ge and Sn are estimated to be 1.4 and 2.4%, respectively, while Pb hardly substitutes for Sb. The p -type conduction is achieved in the temperature range from 300 to 800K and the hole concentration at room temperature is in excess of 10^{19}cm^{-3} by doping CoSb_3 with Ge and Sn. The values of power factor $S^2\sigma$ for $\text{Co}(\text{Sn}_x\text{Sb}_{1-x})_3$ with $x=1\%$ are of the order of 10^{-5}W/cmK^2 in the wide temperature range, leading to the estimation of $ZT=0.15$ at 600K. The figure of merit Z for these doped CoSb_3 is expected to be increased by suppressing minority carriers (electron) which give rise to a decrease in the mobility μ . By improving the process of sintered CoSb_3 , Ge and Sn could become candidates for an effective p -type dopant.

Acknowledgement

This work is supported in part by the Yamaguchi prefectural government.

References

- [1] L.D. Dudkin and N.Kh. Abrikosov, "A Physicochemical Investigation of Cobalt Antimonides", *Russ. J. Inorg. Chem.* **1**, pp.169-180 (1956).
- [2] L.D. Dudkin and N.Kh. Abrikosov, "On the Doping of the Semiconductor Compound CoSb_3 ", *Sov. Phys. Solid State* **1**, pp.126-133 (1959).
- [3] B.N. Zobrina and L.D. Dudkin, "Investigation of the Thermoelectric Properties of CoSb_3 with Sn, Te, and Ni Impurities", *Sov. Phys. Solid State* **1**, pp.1688-1674 (1960).
- [4] T. Caillat and A. Borshchevsky and J.-P. Fleurial, "Novel Transition Metal Compounds with Promising Thermoelectric Properties", *Proc. XII Int. Conf. on Thermoelectrics*, IEEJ, Tokyo, Yokohama (Japan), pp.132-136 (1994).
- [5] G.A. Slack and V.G. Tsoukala, "Some Properties of Semiconducting IrSb_3 ", *J. Appl. Phys.* **76**(3), pp.1665-1671 (1994).
- [6] J.-P. Fleurial, T. Caillat and A. Borshchevsky, "Skutterudite: a New Class of Promising Thermoelectric Materials", *Proc. XIII Int. Conf. on Thermoelectrics*, AIP Press, New York, Kansas City (USA), pp.40-44 (1995).
- [7] T. Caillat, A. Borshchevsky and J.-F. Fleurial, "Preparation and Thermoelectric Properties of p - and n -type CoSb_3 ", *Proc. XIII Int. Conf. on Thermoelectrics*, AIP Press, New York, Kansas City (USA), pp.58-61 (1995).
- [8] K. Matsubara, T. Iyanaga, T. Tsubouchi, K. Kishimoto and T. Koyanagi, "Thermoelectric Properties of $(\text{Pd},\text{Co})\text{Sb}_3$ Compounds with Skutterudite Structure", *Proc. XIII Int. Conf. on Thermoelectrics*, AIP Press, New York, Kansas City (USA), pp.226-229 (1995).
- [9] D.T. Morelli, T. Caillat, J.-P. Fleurial, A. Borshchevsky, J. Vandersande, B. Chen and C. Uher, "Low-Temperature Transport Properties of p -type CoSb_3 ", *Phys. Rev. B* **51** (15), pp.9622-9628 (1995).
- [10] D. Mandrus, A. Migliori, T.W. Darling, M.F. Hundley, E.J. Peterson and J.D. Thompson, "Electronic Transport in Lightly Doped CoSb_3 ", *Phys. Rev. B* **52** (7), pp.4926-4931 (1995).
- [11] J.W. Sharp, E.C. Jones, R.K. Williams, P.M. Martin and B.C. Sales, "Thermoelectric Properties of CoSb_3 and Related Alloys", *J. Appl. Phys.* **78** (2), pp.1013-1018 (1995).
- [12] J.-P. Fleurial, T. Caillat and A. Borshchevsky, "Thermoelectric Materials with the Skutterudite Structure: New Results", *Proc. XIV Int. Conf. on Thermoelectrics*, A.F.Ioffe Physical-Technical Institute, St.Petersburg, St.Petersburg (Russia), pp.231-235 (1995).
- [13] K. Matsubara, H. Anno, T. Sakakibara, Y. Notohara, H. Shimizu and T. Koyanagi, "Electronic Transport Properties of CoSb_3 and Mixed Alloys", *Proc. XV Int. Conf. on Thermoelectrics* (in this conference), Pasadena (USA) (1996).

Solid Solution Formation: Improving the Thermoelectric Properties of Skutterudites

A. Borshchevsky, T. Caillat, and J.-P. Fleurial

Jet Propulsion Laboratory/California Institute of Technology

4800 Oak Grove Drive, MS 277-207, Pasadena, CA 91109

alexander.borshchevsky@jpl.nasa.gov

Abstract

Skutterudite semiconductors possess attractive transport properties and have a good potential for achieving high thermoelectric figures of merit, ZT . Low electrical resistivities and moderate to large Seebeck coefficients are obtained in binary skutterudite compounds such as CoSb_3 . However, their thermal conductivities are too high (100 to $150 \times 10^{-3} \text{ Wcm}^{-1}\text{K}^{-1}$ at 300K) to achieve high ZT values. It is well known that the formation of solid solutions, or alloying, can substantially reduce the lattice thermal conductivity of semiconductors. Because a large number of skutterudite compounds, solid solutions and related phases exist, these materials offer many possibilities for optimizing the thermal and electrical properties to a specific range of temperature. An overview of the formation of skutterudite solid solutions is given. It is shown that a substantial decrease of thermal conductivity can be achieved in cases where the fluctuations of atomic masses and volumes can be maximized and the possibility of achieving high ZT values is discussed.

Introduction

The chemical compounds with the skutterudite structure have been found to be attractive thermoelectric materials [1,2]. Most of the binary skutterudite compounds possess reasonably large Seebeck coefficient and good electrical conductivity, resulting in large power factor values comparable to state-of-the-art thermoelectric materials. However, their thermal conductivity remains too high to make these materials efficient thermoelectrics. The room temperature thermal conductivity values are about $100 \times 10^{-3} \text{ Wcm}^{-1}\text{K}^{-1}$ with 80% of lattice contribution. The formation of solid solution is a well known approach to lower the lattice thermal conductivity. It has already been shown that in solid solutions between IrSb_3 and CoSb_3 , the thermal conductivity can be substantially reduced, from 90 - 100 to 30 - $35 \times 10^{-3} \text{ Wcm}^{-1}\text{K}^{-1}$, at room temperature [3]. The formation of solid solutions in numerous systems (binary-binary, binary-ternary and ternary-ternary combinations) was investigated and thirteen new solid solutions were found.

Experimental

Polycrystalline samples were prepared by low temperature synthesis of elemental powders followed by hot pressing, resulting in dense cylinders of 5 - 15mm long and 6.35mm in diameter (95-97% of the theoretical density calculated from the lattice parameters). X-ray diffractometry, optical and electron microscopy, microprobe analysis, electrical and thermal measurements (Seebeck coefficient, electrical resistivity, thermal conductivity) and speed of sound measurements were performed to reveal the solid solution formation and evaluate their thermoelectric properties. The methods of preparation and measurements were described in details elsewhere [3,4].

Experimental results

Besides three solid solutions already known in the literature, CoP_3 - CoAs_3 , RhSb_3 - IrSb_3 , and CoAs_3 - CoSb_3 [2,5], a full range of solid solutions in the following two systems was found:

IrSb_3 - RuSb_2Te

$\text{Fe}_{0.5}\text{Ni}_{0.5}\text{Sb}_3$ - $\text{Ru}_{0.5}\text{Pd}_{0.5}\text{Sb}_3$.

Partial solid solutions were also found in the following eleven systems:

IrAs_3 - IrSb_3	CoSb_3 - $\text{Ru}_{0.5}\text{Pd}_{0.5}\text{Sb}_3$
CoAs_3 - IrAs_3	CoSb_3 - $\text{Fe}_{0.5}\text{Ni}_{0.5}\text{Sb}_3$
IrSb_3 - $\text{Fe}_{0.5}\text{Ni}_{0.5}\text{Sb}_3$	IrSb_3 - $\text{Ru}_{0.5}\text{Pd}_{0.5}\text{Sb}_3$
CoSb_3 - IrSb_3	CoSb_3 - FeSb_2Te
IrSb_3 - $\text{Ru}_{0.5}\text{Pd}_{0.5}\text{Sb}_3$	FeSb_2Te - RuSb_2Te
CoSb_3 - RuSb_2Te	

The existence of solid solutions is proved by lattice parameter-composition dependencies followed by the microstructure and microprobe analyses. Figs. 1 and 2 show such dependencies for three systems.

Based on experimental results achieved on binary skutterudite compounds, lattice thermal conductivity values in the order of about 10 to $15 \times 10^{-3} \text{ Wcm}^{-1}\text{K}^{-1}$ should be obtained in order to reach high figures of merit for skutterudite materials. Our

results show that alloying is an effective means to reduce the lattice thermal conductivity of binary compounds. Maximum reductions of lattice thermal conductivity values obtained experimentally are presented in Table 1 for some compositions of several systems. The lattice thermal conductivity values, reported in Table 1, were calculated using the Wiedemann-Franz law (based on electrical resistivity and Seebeck coefficient measurements). Some of the values were increased to account for sample porosity (in particular in the CoSb_3 - IrSb_3 system).

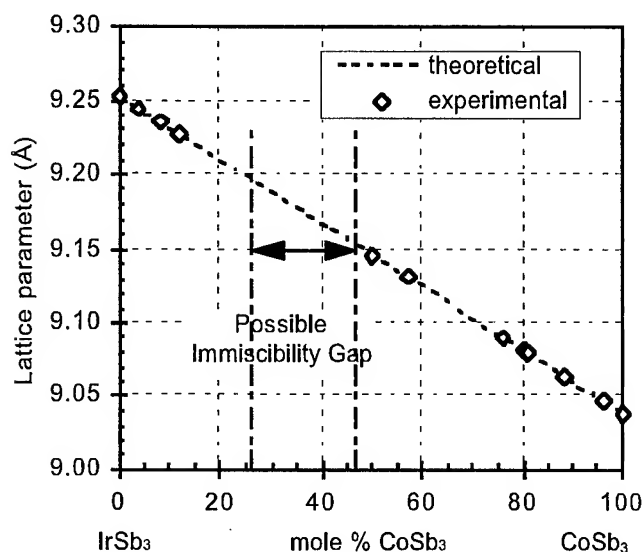


Fig. 1: $\text{Co}_{1-x}\text{Ir}_x\text{Sb}_3$ lattice parameter vs composition

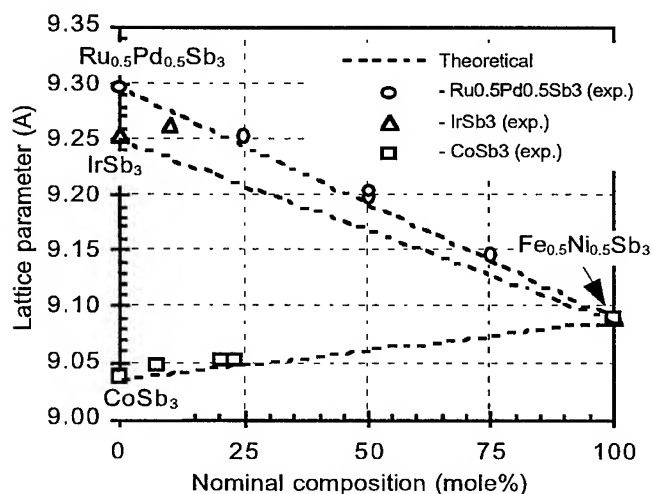


Fig. 2: Lattice parameter variations as a function of composition for $\text{Fe}_{0.5}\text{Ni}_{0.5}\text{Sb}_3$ -based alloys

Because of the large number of alloying possibilities, we used the experimental thermal conductivity data to perform some theoretical calculations on the effect of alloy scattering in skutterudites. The goal was to predict the maximum possible reduction in thermal conductivity and help select the most promising systems for further investigations. The results are presented in the following section.

Table 1: Lattice thermal conductivity values for some solid solutions ($10^{-3}\text{W cm}^{-1}\text{K}^{-1}$)

Solid solution	Alloy	1st member	2nd member
$(\text{CoSb}_3)_{0.96}-(\text{IrSb}_3)_{0.04}$	45	100	100
$(\text{CoSb}_3)_{0.90}-(\text{IrSb}_3)_{0.10}$	32	100	100
$(\text{CoSb}_3)_{0.88}-(\text{IrSb}_3)_{0.12}$	29	100	100
$(\text{CoAs}_3)_{0.98}-(\text{CoSb}_3)_{0.02}$	57	140	100
$(\text{CoSb}_3)_{0.90}-(\text{IrAs}_3)_{0.10}$	25	100	145
$(\text{CoSb}_3)_{0.90}-(\text{FeSb}_2\text{Se})_{0.10}$	31	100	-
$(\text{CoSb}_3)_{0.79}-(\text{Fe}_{0.5}\text{Ni}_{0.5}\text{Sb}_3)_{0.21}$	35	100	30
$(\text{IrSb}_3)_{0.90}-(\text{RuSb}_2\text{Te})_{0.10}$	42	100	32
$(\text{Ru}_{0.5}\text{Pd}_{0.5}\text{Sb}_3)_{0.5}-(\text{Fe}_{0.5}\text{Ni}_{0.5}\text{Sb}_3)_{0.5}$	24	14	30

Lattice thermal conductivity calculations

The effect of alloy scattering on the thermal conductivity of skutterudite compounds can be evaluated by using the theoretical work of Callaway and Von Baeyer [6,7]. The thermal conductivity of an alloy, λ_{alloy} , can be calculated from the experimental value obtained for the pure compound, λ_{pure} , as:

$$\lambda_{\text{alloy}} = \frac{\tan^{-1}(u)}{u} \cdot \lambda_{\text{pure}} \quad (1)$$

$$\text{with } u = \sqrt{3G\Gamma\lambda_{\text{pure}}} \quad (2)$$

$$\text{and } G = \frac{\pi^2 \theta_D \delta^3}{3h v_s^2} \quad (3)$$

where θ_D is the Debye temperature, δ^3 is the average volume per atom in the crystal, v_s is the average sound velocity, h is the Planck's constant, u is an alloy scattering scaling parameter and Γ is the alloy scattering parameter. Based on the speed of sound measurements, the calculated values for G for several skutterudites are reported in Table 2.

To determine the lattice thermal conductivity of the skutterudite alloys, the alloy scattering parameter Γ must now be calculated. Quaternary skutterudite alloys are considered in the following paragraphs, with the formula $\text{A}_x\text{B}_y\text{C}_z\text{D}_4$. There are only two sublattices present in skutterudites: the sublattice of the transition metal element (such as Co) and the sublattice of the pnictogen element (such as Sb). Mass and volume fluctuations can occur on only one sublattice, such as in $\text{Co}_{1-x}\text{Ir}_x\text{Sb}_3$, or in $\text{Fe}_x\text{Ir}_{1-x-y}\text{Ni}_y\text{Sb}_3$ alloys, or both sublattices, such as in $\text{Co}_{1-x}\text{Ir}_x\text{Sb}_{3-y}\text{As}_y$.

Table 2: Calculation of the G parameter for several skutterudite compounds

	d (Å)	Θ_D (K)	v_s ($\times 10^5$ cm.s ⁻¹)	G (cm K W ⁻¹)	λ (10^{-3} W cm ⁻¹ K ⁻¹)
CoSb ₃	2.8470	306.8	2.935	408.4	103
CoAs ₃	2.5846	425.4	3.695	267.4	140
IrSb ₃	2.9146	302.7	2.964	423.8	100
Ru _{0.5} Pd _{0.5} Sb ₃	2.9281	267.8	2.635	481.2	14
RuSb ₃ Te	2.9211	268.6	2.637	478.6	32

The scattering parameter for each atom located on one of these sublattices can be written as:

For the mass fluctuation term:

$$\Gamma_A^M = \sum_i f_i^A \left(1 - \frac{M_i}{\bar{M}_A} \right)^2 \quad (4)$$

where the average mass of the atoms on the A site is $\bar{M}_A = \sum_i f_i^A M_i$, f_i^A representing the relative proportion of each atom on a particular site ($\sum_i f_i^A = 1$).

For the volume fluctuation term:

$$\Gamma_A^V = \sum_i f_i^A \varepsilon_A \left(1 - \frac{r_i}{\bar{r}_A} \right)^2 \quad (5)$$

where the average radius of the atoms on the A site is $\bar{r}_A = \sum_i f_i^A r_i$

The parameters ε_A , ε_B , ε_C , and ε_D , are adjustable strain parameters, with values typically of the order of 10 to 100. For skutterudite alloys, only two different values of the strain parameters ε_i are considered, one for the transition metal site, ε_{tm} , and one for the pnictogen site, ε_{pn} .

The total average mass for the alloy is:

$$M = \sum_i p_i \bar{M}_i \quad (6)$$

with the atomic proportion of the A atoms in the compound

$$p_A = \frac{a}{a + b + c + d}$$

The total alloy scattering parameter is determined by:

$$\Gamma = \sum_i p_i \left(\left[\frac{\bar{M}_i}{M} \right] \Gamma_i^M + \Gamma_i^V \right) \quad (7)$$

Table 3 lists the atomic mass, radius and charge of the cations and anions used in the skutterudite structure. The use of the

cation and anion radii values instead of the usual covalent radii values is important when calculating the alloying effects in systems such as CoSb₃-Fe_{0.5}Ni_{0.5}Sb₃ or IrSb₃-RuSb₂Te.

Table 3: Atomic mass and ionic radius for the transition metal and pnictogen/chalcogen

Transition metal	Pnictogen/chalcogen	Ion charge	Mass (g)	Radius (Å)
Fe		2+	55.847	1.14
Ru		2+	101.07	1.26
Os		2+	190.2	1.25
Co		3+	58.9332	1.07
Rh		3+	102.905	1.19
Ir		3+	192.22	1.19
Ni		4+	58.7	1.15
Pd		4+	106.4	1.26
Pt		4+	195.09	1.28
	P	1-	30.9737	1.14
	As	1-	74.9216	1.26
	Sb	1-	121.75	1.45
	S	0	32.06	1.1
	Se	0	78.96	1.23
	Te	0	127.6	1.43

The strain parameter value for the transition metal site is calculated by considering experimental data obtained on several CoSb₃-rich CoSb₃-IrSb₃ alloys. The best match between experimental and calculated values was achieved for a value of $\varepsilon_{tm} = 398$. The strain parameter value for the pnictogen site is obtained by considering experimental data on CoSb₃-CoAs₃, CoSb₃-IrAs₃ and CoSb₃-FeSb₂Se samples. Because the CoSb₃-CoAs₃ and CoSb₃-IrAs₃ samples show mixed conduction effects at room temperature, only an upper limit to the lattice thermal conductivity of these alloys could be determined. The extrinsic (CoSb₃)_{0.9}-(FeSb₂Se)_{0.1} sample was used to calculate a value of $\varepsilon_{pn} = 225$.

The variations of the thermal conductivity of CoSb₃- and IrSb₃-based alloys could now be estimated. Some results of our calculations are reported in Fig. 3 for CoSb₃ alloys (similar calculations were performed for IrSb₃ alloys and some ternary-based compositions). It should be noticed, that Figure 3 is drawn in assumption that solid solutions form up to 50% mol. of the second component introduced into the base compound located at the right hand of the graph. Several conclusions can be drawn from these calculations:

- Skutterudite alloys with small mass and volume fluctuations result in relatively small decrease in thermal conductivity, such as CoSb₃-Fe_{0.5}Ni_{0.5}Sb₃, IrSb₃-RhSb₃ and IrSb₃-RuSb₂Te.

- Alloys between ternary and binary skutterudites do not result in lower thermal conductivity values than those obtained with optimum binary skutterudite alloys.
- The lowest thermal conductivity values are achieved for alloys maximizing mass and volume fluctuations, such as $\text{CoSb}_3\text{-IrP}_3$, with $8 \times 10^{-3} \text{ W cm}^{-1}\text{K}^{-1}$ for a 50 mol% alloy.

The low thermal conductivity achieved on ternary skutterudite compounds derived from binary compounds (such as RuSb_2Te and $\text{Ru}_{0.5}\text{Pd}_{0.5}\text{Sb}_3$ from RhSb_3) cannot be explained by mass and volume fluctuations alone. Moreover, a complete range of solid solutions exists between the $\text{Ru}_{0.5}\text{Pd}_{0.5}\text{Sb}_3$ and $\text{Fe}_{0.5}\text{Ni}_{0.5}\text{Sb}_3$ compounds, but the lattice thermal conductivity of 50-50 and 75-25 mol% samples is significantly higher, not lower as predicted from simple alloy scattering, than the value obtained for $\text{Ru}_{0.5}\text{Pd}_{0.5}\text{Sb}_3$. This means that other mechanisms, such as charge exchange between the ions, must be considered [4].

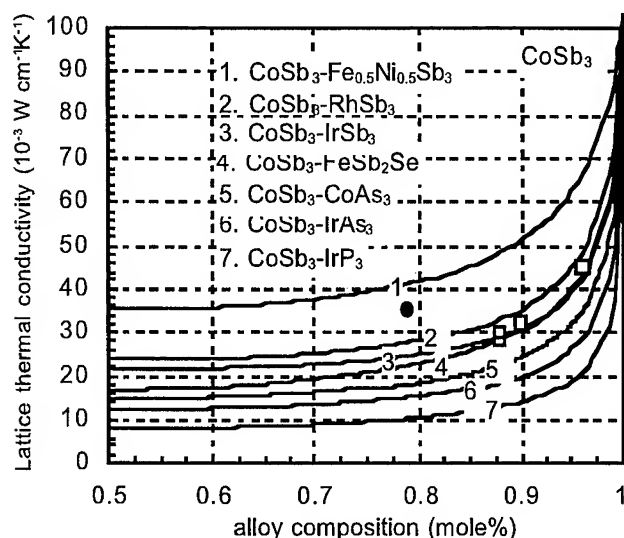


Fig. 3 Effect of alloy scattering on the room temperature lattice thermal conductivity of CoSb_3 . The symbols \square and \bullet are experimental data obtained for the systems 1 and 3, respectively.

These calculations do not take into account the effect of phonon scattering by charge carriers. This additional scattering is very much apparent in heavily doped n-type samples of CoSb_3 and $\text{CoSb}_3\text{-Fe}_{0.5}\text{Ni}_{0.5}\text{Sb}_3$ which have substantially lower thermal conductivity values than expected.

These calculations must now be further tested against additional experimental data. In particular, some good quality samples of the best alloy compositions should be prepared and measured to determine the validity of the theoretical findings. However, based on these preliminary results and considering the impact of electron-phonon scattering, it appears that a total thermal conductivity value of $15 \times 10^{-3} \text{ W cm}^{-1}\text{K}^{-1}$ or lower at room temperature might be achieved for an optimal skutterudite alloy, with an electrical resistivity of $1 \times 10^{-3} \Omega\text{cm}$ and a doping level between 10^{19} cm^{-3} and 10^{20} cm^{-3} . Considering the attractive electrical properties of

these materials, the possibility of obtaining such a low lattice thermal conductivity indicates that the study of alloying effects on skutterudites should be pursued.

To illustrate the potential of heavily doped CoSb_3 -based solid solutions, the improvement in ZT over current heavily doped CoSb_3 samples (Pd- or Te-doped) is plotted on Fig. 4. The graph shows that the optimum CoSb_3 -based solid solution could reach a ZT value of 1.75 at 600°C , a considerably higher value than obtained for state of the art thermoelectric materials. This value was calculated assuming a thermal conductivity of $15 \times 10^{-3} \text{ W cm}^{-1}\text{K}^{-1}$ and that there will not be any significant deterioration of the electrical properties compared to heavily doped n-type CoSb_3 samples. Indeed, considering the high doping levels required in n-type samples, it is likely that the carrier mobility of the alloy will only decrease a little compared to n-type CoSb_3 .

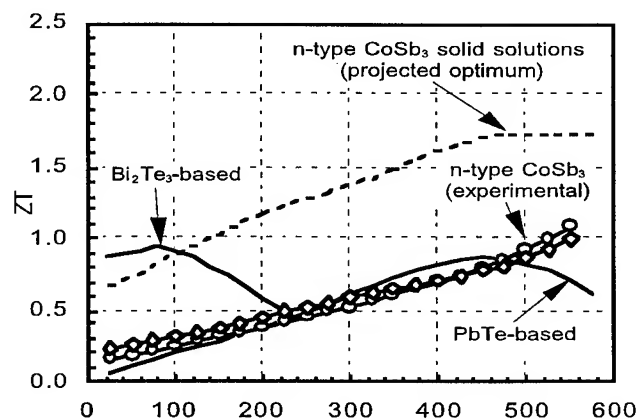


Fig. 4: Calculated improvement in ZT as a function of temperature for heavily doped n-type CoSb_3 -based solid solutions

Sources of new skutterudite solid solutions

Skutterudites were discovered last century by geologists looking for sources of elements on the earth. Large Seebeck coefficients have been measured on synthetic skutterudites several years ago. In the meantime, some of the natural skutterudites such as arsenides as well as phosphides have been synthesized. The diagram shown on Fig. 5 [8] depicts a skutterudite group of minerals available in the nature and based on a mixture of CoAs_3 , NiAs_3 and FeAs_3 compounds (the existence of the latter has not been proven).

All minerals (skutterudites, smaltites and chloanthites) are solid solutions with a similar crystal structure. As can be replaced by Sb and P, widening the number of possible solid solutions. Thus, the huge number of solid solutions with a skutterudite structure is available for researchers. No doubts, part of these materials are semiconductors with the possibility of attractive thermoelectric properties.

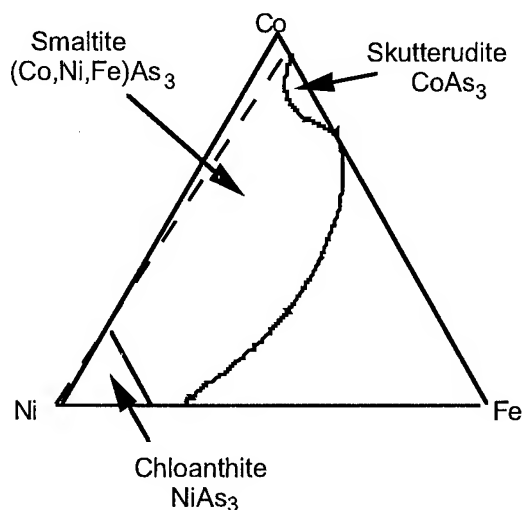


Fig. 5: Skutterudite group of minerals (compositions are idealized)

Conclusions

- Thirteen quasibinary systems have been studied: two were found to form solid solutions with full range of solubility and eleven with partial solid solubility.
- Significant reduction in thermal conductivity of binary compounds was achieved by solid solution formation.
- Theoretical calculation of lattice thermal conductivity for different systems of skutterudite solid solutions, at room temperature, was performed, and the lowest possible thermal conductivity value of about $8 \times 10^{-3} \text{ Wcm}^{-1}\text{K}^{-1}$ was predicted for the $\text{CoSb}_3\text{-IrP}_3$ system.
- Many more solid solutions within skutterudite group of materials are available for evaluation of their thermoelectric properties.

Acknowledgments

The work described in this paper was carried out at the Jet Propulsion Laboratory/California Institute of Technology, under contract with the National Aeronautics and space administration. The authors would like to thank Danny and Andy Zoltan for thermoelectric property measurements, Jim Kulleck for x-ray diffractometry, Paul Carpenter for microprobe analysis and Yoseph Bar-Cohen for sound velocity measurements.

References

1. T. Caillat, A. Borshchevsky, J.-P. Fleurial, Proc. 12th Int. Conf. on Thermoelectrics, Yokohama, Japan, 1994, p.p.132-136 (Inst. of Electrical Engineers of Japan)
2. G. A. Slack, V. G. Tsoukala, J. Appl. Phys. 76, 1665 (1994)
3. A. Borshchevsky, J.-P. Fleurial, E. Allevato, T. Caillat, American Institute of Physics, Conf. Proc. 316, p. 3 (XIII Int. Conf. on Thermoelectrics, Kansas City, MO, 1994), 1995
4. T. Caillat, J. Kulleck, A. Borshchevsky, J.-P. Fleurial, J. Appl. Physics 79, 11.....(1996)
5. H. D. Lutz and G. Kliche, J. Solid State Chemistry 40, 64 (1981)
6. J. Callaway and H. C. Baeyer, Phys. Rev. 120, 1149 (1960)
7. G. A. Slack, private communication
8. A. A. Godovikov "Mineralogy", Moscow, publ. house "Nedra", 1975, p.112 (in Russian)

Thermoelectric Properties of CoSb₃ Prepared by Copper Mold Quenching Technique

Hamazo Nakagawa¹, Hisao Tanaka¹, Akio Kasama¹, Kou Miyamura¹, Hiroki Masumoto¹ and Kakuei Matsubara²

¹ Japan Ultra-high Temperature Materials Research Institute,
Okube 573-3, Ube City, Yamaguchi Prefecture 755, JAPAN

² Science University of Tokyo / in Yamaguchi,
1-1-1 Daigaku-Dori, Onoda City, Yamaguchi Prefecture 756, JAPAN

Abstract

A novel technique to prepare CoSb₃ materials on a mass production level was studied. Co and Sb were melted together in an alumina crucible at 1373K, and cast in a copper mold to solidify the melts. The obtained alloyed ingots consist of mainly three phases of CoSb₃, CoSb₂ and Sb. To react Sb with CoSb₂ and get a CoSb₃ single phase, the ingots were annealed at 823-1073K. During the heat treatment, Sb and CoSb₂ phases changed to CoSb₃ phases and voids. The obtained CoSb₃ samples show n-type thermoelectric properties. Some factors affecting the properties, for example, Sb/Co atomic ratio, impurity content and density are discussed, based on the experimental data by X-ray diffractometry, optical microscopy, EPMA, chemical analysis and so on. On the other hand, an ingot was ground, mechanically alloyed and hot-pressed. The hot-pressed samples show p-type thermoelectric properties. Moreover, mechanical alloying is effective to reduce the thermal conductivity by refining the crystal grain size of CoSb₃. As a result, ZT value, 0.10 was obtained at a temperature of 669K.

1. Introduction

CoSb₃ and its doped alloys have recently been identified as promising candidates for advanced thermoelectric materials[1].

T. Caillat et al. [2] have grown CoSb₃ single crystals successfully using the gradient freeze technique from melts with 93at.%Sb in sealed quartz ampoules. The Co-Sb phase diagram [3] shows that CoSb₃ single crystals can only be grown from Sb rich melts between 90 to 97 at.%Sb. Although fully dense and high quality CoSb₃ can be obtained by the gradient freeze technique, it is not practical way because the yield of CoSb₃ single crystals is very low and the thermoelectric properties are not constant in the growing direction of the process.

An other method of preparing CoSb₃ is the powder processing of raw materials of Sb and Co powders. J. W. Sharp et al. [4] heated stoichiometric mixtures of Sb and Co powders in evacuated fused silica ampoules at 873-973K for two to three days. Following the powder reaction, 3/4-in.-diam pellets were formed by hot-pressing (10⁷Pa, 873-973K), or cold-pressing (10⁷ Pa) and sintering at 973K. The hot-pressed CoSb₃ showed n-type thermoelectric properties. On the other hand, cold-pressed and sintered CoSb₃ had p-type thermoelectric properties. They mentioned that the reason why the hot-pressed samples showed n-type thermoelectric properties was a slight Sb deficiency from the stoichiometry of CoSb₃. However, it is not clear.

In our studies, we aim to make clear the reason why some CoSb₃ materials show n-type conduction behaviors. The reason was supposed to be related to a processing method. During the powder processing, samples are easy to be contaminated especially by oxygen and milling materials. We chose an annealing method of solidified alloyed ingots. We believe the

method is more suitable for mass production than the gradient freeze technique, and the obtained materials by the method are less contaminated by oxygen and so on than by the powder processing.

2. Experimental procedure

2.1 Sample preparation

High purity Sb ingots (99.999%) and Co flakes (99.9%) were used as raw materials. They were placed in an alumina crucible in the various Sb/Co atomic ratios from 2.6 to 3.4, and heated up to 1373K in an induction furnace for the melting Sb and Co together in an Ar atmosphere. After the melts were kept for 5 minutes at the maximum temperature to make sure the homogeneity, the melts were poured into a copper mold for the solidification. After the 1mm thickness surface layers of the solidified alloyed ingots were removed, they were cut into pieces, which were annealed at 823-1073K for 20-100h in a covered alumina crucible in Ar. The annealed samples were cut into several pieces for the characterization. Especially, the samples for thermoelectric property measurements were cut from the middle of the materials.

After an Sb-rich Co-Sb alloy was crushed with an stamp mill under the size of 2mm, the granules were put in a stainless steel vessel and mechanically alloyed using steel arms and steel balls for 10h. The mechanically alloyed powders were recovered as a slurry in hexane to prevent a surface oxidation of powders. After the hexane was removed from the slurry in an Ar atmosphere, the powders were hot-pressed at 823K for 10h at a pressure of 29MPa in Ar. During the hot pressing, samples were enveloped by graphite foil. The surfaces of the hot-pressed samples were removed and cut into several pieces for the characterization and the thermoelectric property measurements.

2.2 Sample characterization

Cross sections of the samples were polished and examined by optical microscopy and EPMA. To determine those crystal grain size, they were etched with conc. nitric acid before the observation. And the samples were ground and the crystal phases were analyzed by powder X-ray diffractometry. Densities of the samples were calculated from the size and the mass. And also, impurity contents and Sb/Co atomic ratios were determined by chemical analysis.

2.3 Thermoelectric property measurement

Electrical resistivity and Seebeck coefficient were measured simultaneously using ULVAC ZEM-1 at room temperature to 700K in He. Thermal conductivity was calculated from the thermal diffusivity, the specific heat capacity and the density. The thermal diffusivity was obtained by the laser flash measurements on ULVAC TC-7000 at room temperature and 669K in vacuum. And the specific heat

capacity was measured using PERKIN ELMER DSC7 at room temperature to 723K in a nitrogen atmosphere. The specific heat capacity at 283K was determined by extrapolation method.

3. Results and discussion

3.1 Annealing of alloyed ingots

3.1.1 Characterization

The X-ray diffraction patterns of the alloyed ingots before the annealing with various Sb/Co atomic ratios between 2.6 and 3.4 are shown in Fig.1. From the Fig.1, we can see that every

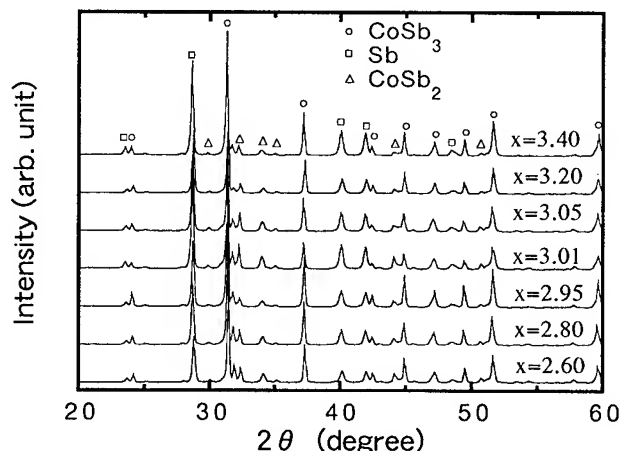


Fig.1. X-ray diffraction patterns of the alloyed CoSb_x before the annealing with various Sb/Co atomic ratios (x).

sample has CoSb_2 and Sb phases besides CoSb_3 phases. After the annealing of the samples at 823K for 100h, CoSb_2 and Sb phases disappear in Sb-rich and Co-rich alloys, respectively, as shown in the X-ray diffraction patterns in Fig.2. And the

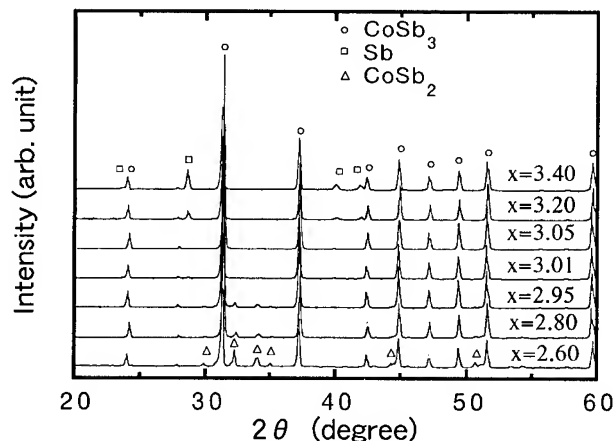


Fig.2. X-ray diffraction patterns of the annealed CoSb_x at 823K for 100h with various Sb/Co atomic ratios (x).

samples with near the stoichiometric ratio of CoSb_3 do not show the X-ray diffraction patterns of CoSb_2 and Sb phases. We calculated the volume percentages of the CoSb_3 , CoSb_2 and Sb phases for each Sb/Co atomic ratio of the annealed samples. In the case, it is supposed that only two phases among CoSb_3 , CoSb_2 and Sb exist in the samples. Theoretical densities of CoSb_3 , CoSb_2 and Sb used for the calculation are 7.69, 8.337 and 6.618 respectively. Table 1 shows the calculated results of

Table 1. Calculated results of the volume percentages of the CoSb_3 , CoSb_2 and Sb phases for the various Sb/Co atomic ratios.

Sb/Co atomic ratio	Volume percentage (%)		
	CoSb_3	CoSb_2	Sb
3.40	88.2	0	11.8
3.20	93.7	0	6.3
3.05	98.4	0	1.6
3.01	99.7	0	0.3
2.95	96.7	3.3	0
2.80	85.9	14.1	0
2.60	69.5	30.5	0

the volume percentages of the CoSb_3 , CoSb_2 and Sb phases for the various Sb/Co atomic ratios. Those calculated values are fairly close to the analytical results by EPMA.

Fig.3 shows the optical micrographs of before and after the annealing at 823K for 100h of alloyed ingots with the Sb/Co atomic ratio of 3.05. Before the annealing, the sample is dense

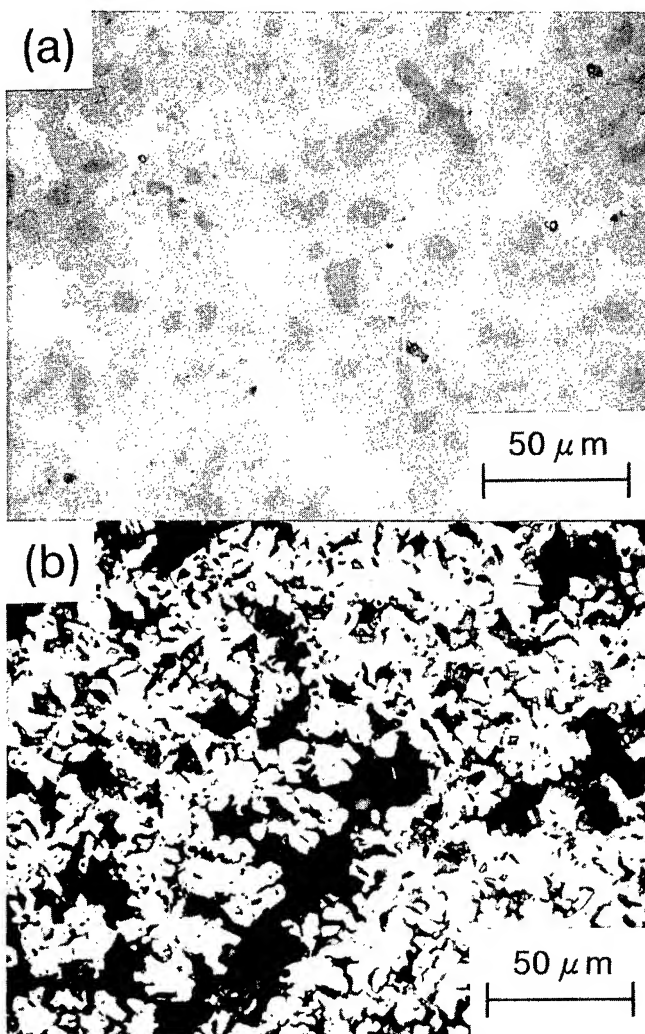


Fig.3. Optical micrographs of (a) as-cast $\text{CoSb}_{3.05}$ and (b) annealed $\text{CoSb}_{3.05}$ at 823K for 100h.

and consists of three regions of white, gray and dark colors, which are Sb, CoSb_3 and CoSb_2 phases respectively. After the annealing, lots of pores and CoSb_3 phases are observed, but Sb and CoSb_2 phases are not found. Only small amounts of Sb phases are detected by EPMA. In Fig.4, the densities of the annealed samples are compared with as-cast samples. We

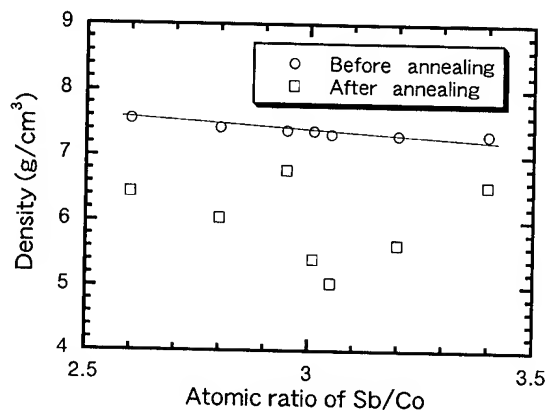


Fig.4. Density of as-cast CoSb_x and annealed CoSb_x at 823K for 100h, as a function of atomic ratio (x) of Sb/Co.

suppose that the reason why the density decrease during the annealing is the largest in the sample near the stoichiometric Sb/Co atomic ratio is because the amount of Sb and CoSb_2 to react are the largest in the sample. The reaction of Sb with CoSb_2 may cause to decrease the density.

The oxygen contents of all samples were less than 140 ppm. We think the oxygen content of 140 ppm is low enough, because the more than 1000ppm oxygen is contained in the samples by the powder processing usually. Other impurities detected are Fe of 40ppm, Ni of 10ppm, Cu of 40ppm and Si of 80ppm.

3.1.2 Thermoelectric properties

In Figs.5 and 6, Seebeck coefficient and electrical

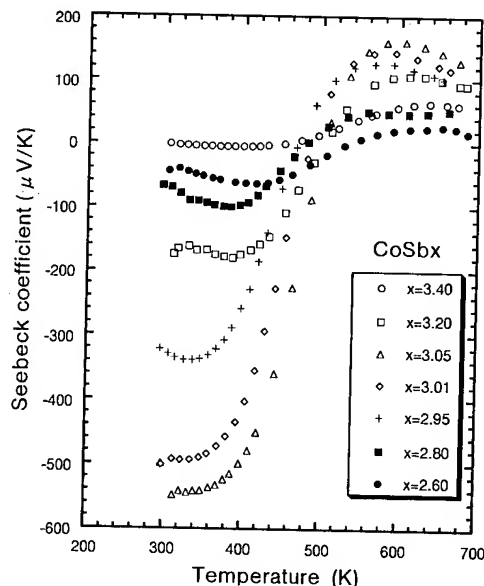


Fig.5. Seebeck coefficient as a function of temperature for the CoSb_x samples with various Sb/Co atomic ratios (x), which were annealed at 823K for 100h.

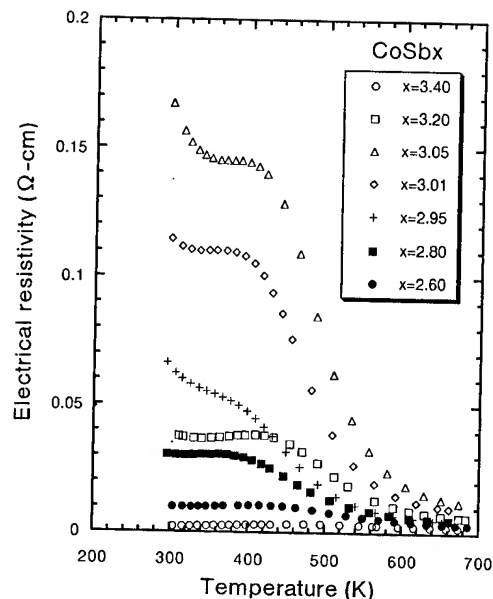


Fig.6. Electrical resistivity as a function of temperature for the CoSb_x samples with various Sb/Co atomic ratios (x), which were annealed at 823K for 100h.

resistivity as a function of temperature are shown for the samples with various Sb/Co atomic ratios, which were annealed at 823K for 100h in Ar. The sample with the Sb/Co atomic ratio of 3.05 has the largest negative Seebeck coefficient at a room temperature and the largest positive Seebeck coefficient at 600K. The deviations from the stoichiometric Sb/Co atomic ratio of CoSb_3 are larger, Seebeck coefficients are smaller. And there is a same tendency in the electrical resistivity, as shown in Fig.6. The sample with the Sb/Co atomic ratio of 3.05 show the highest resistivity at a whole temperature range measured.

Figs.7 and 8 show the Seebeck coefficient and the electrical

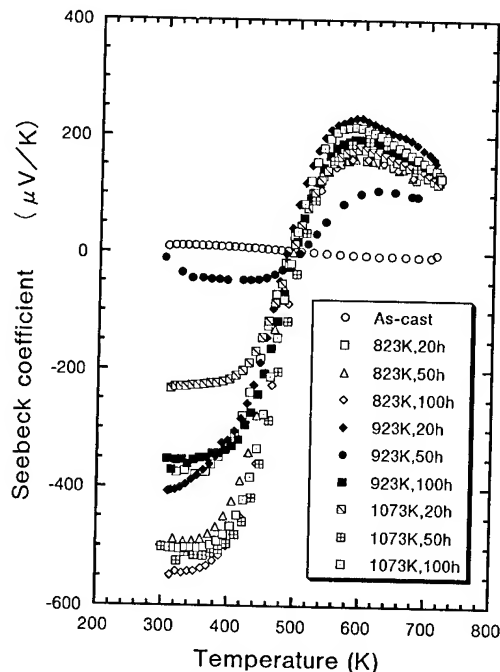


Fig.7. Seebeck coefficient as a function of temperature of the samples with the Sb/Co atomic ratio of 3.05, which were annealed at the various temperatures of 823-1073K for 20-100h.

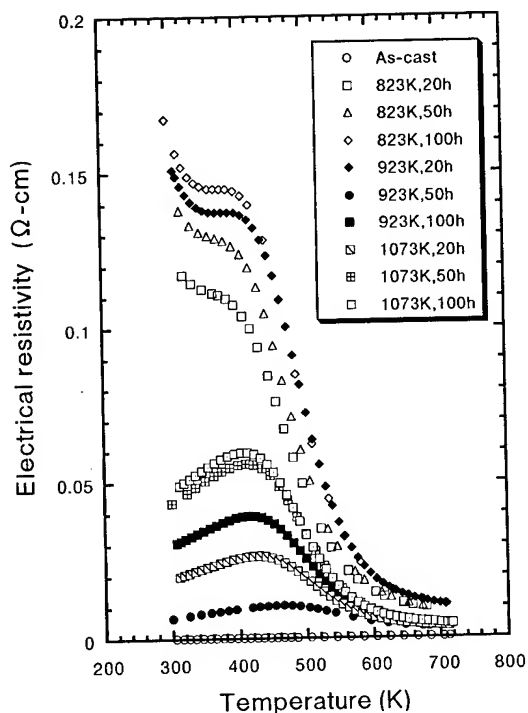


Fig.8. Electrical resistivity as a function of temperature of the samples with the Sb/Co atomic ratio of 3.05, which were annealed at the various temperatures of 823-1073K for 20-100h.

resistivity as a function of temperature when the samples with the Sb/Co atomic ratio of 3.05 were annealed at the various temperatures of 823-1073K for 20-100h. The Seebeck coefficients and the electrical resistivities change greatly depending on the heat treatment conditions, although the X-ray diffraction patterns are almost same. Higher oxygen contents in the materials make the electrical resistivities higher, but we can not explain the change of Seebeck coefficients only by the oxygen content. And the contents of other impurities are not dominant factors because those are supposed to be almost same in spite of the heat treatment conditions. There are slight correlations between the densities and the Seebeck coefficients or the electrical resistivities. In other words, the samples with low densities have large negative Seebeck coefficients and high electrical resistivities. Defects may be created in the sample, when the density changes during the annealing. Deviations from the stoichiometry of the CoSb_3 phase may happen and be different depending on the annealing conditions. We are now analyzing the Sb/Co atomic ratios of CoSb_3 phases by EPMA in the samples annealed at the various conditions, and trying to prove the factors to change the thermoelectric properties.

3.2 Mechanical alloying and hot-pressing

3.2.1 Properties of mechanically alloyed powder

The mechanically alloyed powder from the Sb-rich Co-Sb alloy has a particle size of several microns, which may contain agglomerates. And the powder contains oxygen of 2900ppm, Fe of 1500ppm, Al of 80ppm and Ni of 70ppm as the impurities. Most of the Ni atoms are from the raw material of Co. Oxygen, Fe and Al are contaminations during the crushing and the mechanical alloying. X-ray diffractometry shows broad CoSb_3 , CoSb_2 and Sb peaks, which mean alloying of those phases proceeds during the mechanical alloying.

3.2.2 Characterization of hot-pressed samples

Hot-pressed samples from the mechanically alloyed powder have Sb phases besides CoSb_3 phases, which were analyzed by X-ray diffractometry. And that the samples are constituted by CoSb_3 and Sb crystal grains with the size of submicrons to several microns is shown by optical microscopy and EPMA. And also, an Sb/Co atomic ratio is determined by chemical analysis to be 3.39. The samples have the density of 6.97g/cm^3 and contain 1800ppm oxygen.

3.2.3 Thermoelectric Properties

Seebeck coefficient and electrical resistivity of the hot-pressed sample as a function of temperature are shown in Fig.9.

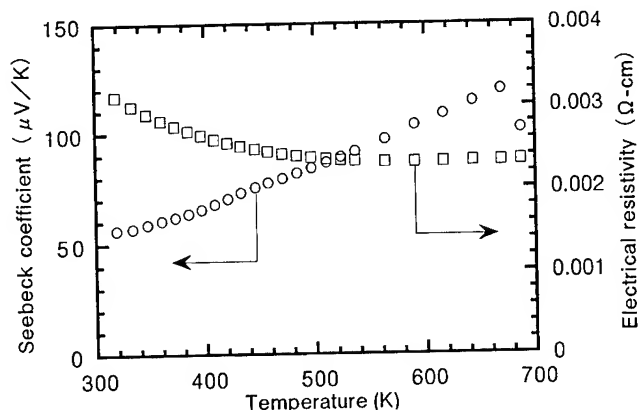


Fig.9. Seebeck coefficient and electrical resistivity of the mechanically alloyed and hot-pressed sample as a function of temperature.

This material shows p-type conduction. Although the Seebeck coefficients are not high enough compared to the value by T. Caillat et al. [2] and J. W. Sharp et al. [4], electrical resistivity is lower than J. W. Sharp et al. [4]. Especially, thermal conductivity at room temperature is reduced significantly compared to the annealed samples, as shown in Fig.10. The

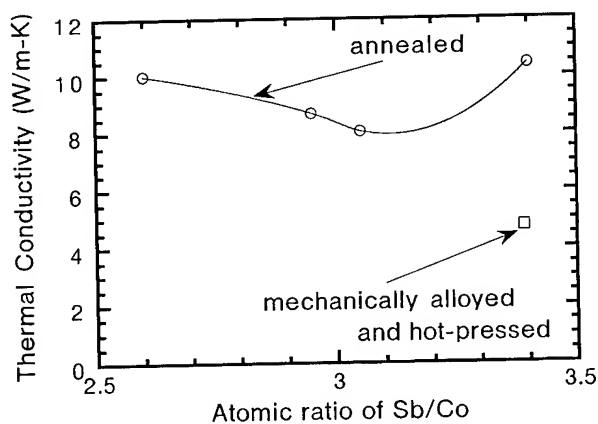


Fig.10. Thermal conductivity at 283K of the mechanically alloyed and hot-pressed sample compared with the annealed samples with various Sb/Co atomic ratios.

annealed samples have the densities of 6.6 to 7.1, which are comparable with the density of the hot-pressed sample. Oxygen contents of those annealed samples are between 10 and 20ppm. Thermal conductivity of the hot-pressed sample at a temperature of 669K is 3.94W/m-K . Using this value, ZT value 0.10 is obtained at 669K.

4. Conclusions

CoSb₃ materials can be obtained by the annealing of the alloyed ingots from the melts of Co and Sb. Although those materials consist of a single CoSb₃ phase from the X-ray diffractometry results, they show n-type conduction. During the annealing, densities of the materials decrease, which may cause some defects in the samples. We are now trying to analyze the CoSb₃ phases in the annealed samples more precisely by EPMA.

The ingot obtained from the melt was mechanically alloyed and the alloyed powder was hot-pressed. The hot-pressed materials show p-type conduction behavior. Moreover, mechanical alloying is very effective to reduce the thermal conductivity by refining the crystal grain size of CoSb₃. At a temperature of 669K, ZT value of 0.10 was obtained.

Acknowledgement

This work was financially supported by Yamaguchi Prefectural Government and Yamaguchi Industrial Technology Development Organization. The authors would also thank Professor Toshikatsu Miki in Yamaguchi University and Dr. Thierry Caillat in Jet Propulsion Laboratory for the helpful suggestions.

References

- [1] D. T. Morelli, T. Caillat, J. -P. Fleurial, A. Borshchevsky, J. Vandersande, B. Chen and C. Uher, "Low-temperature transport properties of p-type CoSb₃", *Physical Review B*, vol. 51, No. 15, pp.9622-9628 (1995).
- [2] T. Caillat, A. Borshchevsky and Jean-Pierre Fleurial, "Preparation and Thermoelectric Properties of p- and n-type CoSb₃", in *Proceedings of the XIIIth International Conference on Thermoelectrics*, edited by B. Mathiprakasam, New York, pp.58-61 (1994).
- [3] Thaddeus B. Massalski, *Binary Alloy Phase Diagrams*, Second Edition, edited by ASM International, USA, p.1234 (1990).
- [4] J. W. Sharp, E. C. Jones, R. K. Williams, P. M. Martin and B. C. Sales, "Thermoelectric properties of CoSb₃ and related alloys", *Journal of Applied Physics*, vol.78, No.2, pp.1013-1018 (1995).

TiNiSn: A Gateway to the (1,1,1) Intermetallic Compounds

B. A. Cook and J. L. Harringa
Ames Laboratory, Iowa State University
Ames, IA 50011-3020

Z. S. Tan and W.A. Jesser
Department of Materials Science and Engineering
University of Virginia, Charlottesville, VA 22903

Abstract

Recent awareness of the transport properties of Skutterudite pnictides has stimulated an interest in numerous other intermetallic compounds having a gap in the density of states at the Fermi level including the MNiSn compounds where $M=(\text{Ti, Zr, Hf})$. These intermetallic 'half-Heusler' compounds are characterized by high Seebeck coefficients (-150 to $-300 \mu\text{V/deg.}$) and reasonable carrier mobilities (30 to $50 \text{ cm}^2/\text{V-s}$) at room temperature which make them attractive candidates for intermediate temperature thermoelectric applications. Samples of TiNiSn were prepared by arc melting and homogenized by heat treatment. The temperature dependence of the electrical resistivity, Seebeck coefficient, and thermal diffusivity of these samples was characterized between 22°C and 900°C . The electrical resistivity and thermopower both decrease with temperature although the resistivity decreases at a faster rate. Electrical power factors in excess of $25 \mu\text{W/cm-}^\circ\text{C}^2$ were observed in nearly single phase alloys within a 300 to 600°C temperature range. A brief survey of other selected ternary intermetallic compounds is also presented.

Introduction

The search for new thermoelectric materials is shifting from binary to ternary and higher order compounds. While at least one transport parameter is known about most ($\sim 85\%$) of the 4,000 experimentally known binary alloys, this figure drops to only $\sim 5\%$ of the 161,700 ternary alloys. In other words, there are some 153,000 compounds that are essentially unknown in terms of structure and properties. Several recent studies of the transport properties of an interesting class of ternary intermetallic

compounds such as MNiSn ($M = \text{Ti, Zr, Hf}$) have shown that these compounds crystallize in the MgAgAs structure and are characterized by the existence of a gap or pseudo-gap in the density of states at the Fermi level [1,2,3,4]. This feature makes them attractive candidates for a survey of thermoelectric properties because the gap gives rise to semiconducting-like transport properties. The most intriguing property from a thermoelectric viewpoint is that of a large room temperature thermopower, on the order of $-300 \mu\text{V}/^\circ\text{C}$. Of the three primary macroscopic quantities that affect a material's figure of merit (electrical conductivity, thermopower, and thermal conductivity), the thermopower is probably the most difficult to predict a priori and also to engineer. Therefore, a good starting point for a systematic search for high figure of merit materials are high metal content compounds having large thermopowers, as is the case for TiNiSn. While the dimensionless figure of merit of TiNiSn itself is unlikely to exceed that of conventional materials, a good understanding of the transport properties of this interesting compound is expected to provide insight into the feasibility of similar ternary compounds through substitutional alloying. Previous studies have investigated substitutions for the Group IVA transition metal [5] and for the Group VIIIA transition metal [6]. Other systematics remain unexplored. Little published data exists on the orthorhombic TiNiSi and TiNiGe compounds. Although strictly not Heusler alloys, these systems may provide useful information on the differences between intermetallic compounds with and without a gap. While alloy theory predicts limited solubility for Si or Ge in TiNiSn, the extent of solid solubility as a substitutional replacement for tin and the effect on the band structure and the thermoelectric properties remains unknown. Other ternary compounds are known to crystallize in the MgAgAs structure [7], such as

the $R\text{PtSb}$ where R = heavy lanthanide element and may be of interest as thermoelectric materials. Furthermore, it is hoped that the results of this research, coupled with that of other laboratories, will motivate subsequent investigations into the myriad of ternary intermetallic compounds having semiconducting-like transport properties.

Experimental Details

Stoichiometric quantities of Ti, Ni, and Sn were weighed out and arranged on a water-cooled copper hearth. Arc melting was accomplished by first melting the Ni and Sn together and then adding the Ti to form a smooth button. The button was turned over six times and remelted before arc-casting into a rod. The as-cast rod was sectioned for metallography and Hall coefficient measurements. The remainder of the rod was wrapped in Ta, sealed in quartz, and heat treated at 840°C for 3 weeks. Another set of samples was cut for metallography and Hall coefficient from the heat treated rod and a portion of the remainder was subjected to a final heat treatment of 950°C for a period of 2 weeks. No discoloration on the inner surface of the quartz was observed nor was there any noticeable change in the ductility of the Ta wrapping. X-ray diffraction patterns of the samples were obtained with an automated powder diffractometer using $\text{Cu K}\alpha$ radiation. Disk-shaped samples were characterized for their electrical properties at room temperature by a Hall effect measurement. Following Hall effect measurement, the disks were sectioned into rectangular parallelepiped-shaped bars and instrumented for electrical resistivity and Seebeck coefficient measurements from 22°C to 900°C . The measurement procedures are described in a previous publication [8].

Two samples were prepared at the University of Virginia by a similar arc casting procedure. These samples were subsequently heat treated at 800°C for various amounts of time as described in a previous publication [9]. In their paper, values of the room temperature Seebeck coefficient, electrical resistivity, and thermal conductivity were shown after annealing for up to 6 weeks. The temperature dependence of the electrical resistivity and Seebeck

coefficient of their samples after 1 and 4 weeks at 800°C is presented and discussed later.

TiNiSi samples were also prepared for this survey by arc casting and heat treating. Dramatic differences between the cubic Sn and the orthorhombic Si compounds were observed.

Results and Discussion

I. Samples prepared at Ames Laboratory: Metallographic results showed the as-cast TiNiSn sample to be multiphase with clearly observed dendritic segregation, as shown in Fig. 1. The amount of segregation decreased upon application of a 3 week heat treatment at 840°C and a subsequent 2 week heat treatment at 950°C as shown in Figs. 2 and 3, respectively, albeit the material remained multiphased. The material was, however, clearly more homogeneous following the 950°C heat treatment, which gave rise to improved electrical properties as shown below.



Fig. 1. Microstructure of as-cast and electropolished TiNiSn (250X)

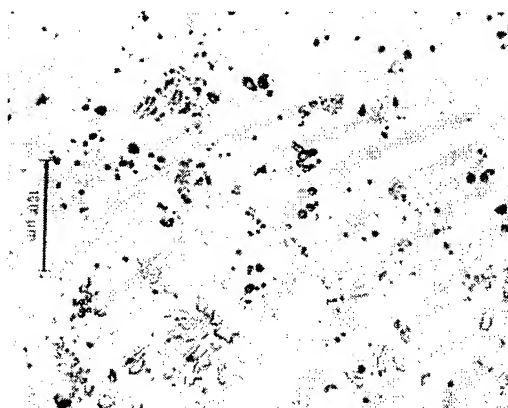


Fig. 2. Microstructure of TiNiSn after 3 week heat treatment at 840°C (250X)

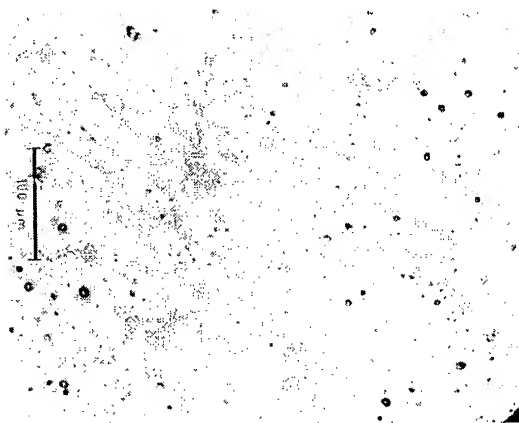


Fig. 3. Microstructure of TiNiSn after 3 week heat treatment at 840°C (Fig. 2) followed by an additional 2 week heat treatment at 950°C (250X)

A small amount of material was removed from the 2 week at 950°C heat treatment sample and ground for evaluation by X-ray diffraction. The pattern is reproduced in Fig. 4.

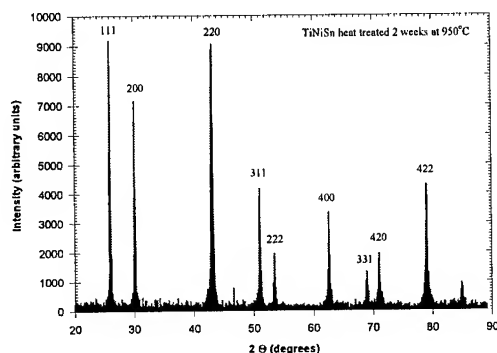


Fig. 4. X-ray Diffraction Pattern of TiNiSn Prepared by Arc Melting and Annealed for 2 Weeks at 950°C

All reflections can be indexed to a face centered cubic lattice and the amount of second phase is apparently less than five percent. The lattice parameter was determined to equal 0.5930 nm using a Nelson-Riley extrapolation routine, giving reasonable agreement with values reported by other researchers. In fact, the U. of Virginia group reported a lattice parameter of 0.5941 nm on their samples using different starting materials, a different heat treatment, and a different diffractometer. A summary of the room temperature electrical properties of some of these alloys is provided in Table I. The differences in the conduction mechanism between the semiconductor-like TiNiSn and semimetallic TiNiSi is obvious. From the slope of the intrinsic conductivity (see below) the

magnitude of the energy gap of TiNiSn is estimated from $\sigma = \sigma_0 \exp(-Q/kT)$ to be on the order of 0.1 to 0.2 eV. However, the TiNiSi, crystallizing in an orthorhombic structure, shows no evidence of a gap.

Table I. Room Temperature Electrical Properties of TiNiX Alloys (X=Si or Sn)

Sample	ρ (m Ω -cm)	n ($\times 10^{18}$ cm $^{-3}$)	μ (cm 2 /V-s)
TiNiSn IHT	14.8	8.0	53.0
TiNiSn IIHT	11.4	15.0	36.7
TiNiSi as cast	0.98	3140	2.0
TiNiSi HT	0.68	2670	3.4

note: IHT = 3 weeks at 840°C, IIHT = 2 weeks at 950°C
TiNiSi HT refers to 12 days at 1100°C

A usable thermoelectric material is generally expected to have a band gap of at least 5kT, which, at 300K has a value of 0.13eV. TiNiSn, which is intrinsic above room temperature, only marginally satisfies this requirement. Nonetheless, this material displays interesting electrical properties within the intrinsic conduction regime. The high temperature electrical resistivity, ρ , Seebeck coefficient, S , and power factor, S^2/ρ , of two TiNiSn alloys are melted at Ames and subsequently annealed are shown in Fig. 4.

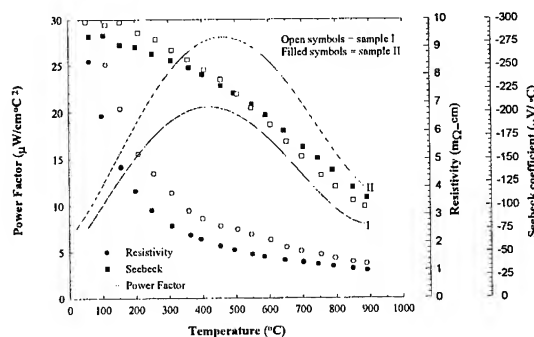


Figure 4. Electrical resistivity, Seebeck coefficient, and power factor of arc melted and annealed TiNiSn.

Sample I = 3 week heat treatment at 840°C,
Sample II = Sample I + additional 2 week heat treatment at 950°C.

Both samples display qualitatively similar electrical behavior although the resistivity of the material which had been heat treated at 950°C is lower than that of the corresponding sample heat treated at 840°C. This seems reasonable

considering that a more homogeneous microstructure will provide fewer second phase scattering sites. Clearly, control of microstructure will be a critical parameter in optimizing the thermoelectric properties of these alloys. The decrease in resistivity with temperature is consistent with that of an intrinsic semiconductor. The Seebeck coefficient of the two samples is similar and is sufficiently large to drive the power factor to a maximum of $27 \mu\text{W}/\text{cm-deg.}^2$ near 500°C in the material heat treated at 950°C for 2 weeks. Due to the higher resistivity, the power factor of the 840°C sample maximized at $21 \mu\text{W}/\text{cm-deg.}^2$. Interestingly, the power factor increases with increasing temperature in the lower temperature range, even though the material should be operating in or quite near the intrinsic conductivity range. The magnitude of the power factor is comparable with that of state-of-the-art silicon-germanium alloys, although Si-Ge can be used at a much higher operating temperature than TiNiSn. Continuous cooling data was obtained after reaching the maximum temperature and no evidence of hysteresis was observed.

II. Samples prepared at the Univ. of Virginia:

Two rectangular parallelepiped-shaped samples of TiNiSn were cut from an arc melted and heat treated sample prepared at the University of Virginia. These samples were instrumented and characterized for high temperature electrical resistivity and Seebeck coefficient in the same manner as applied to the alloys prepared at Ames. The results of these measurements are shown in Fig. 5.

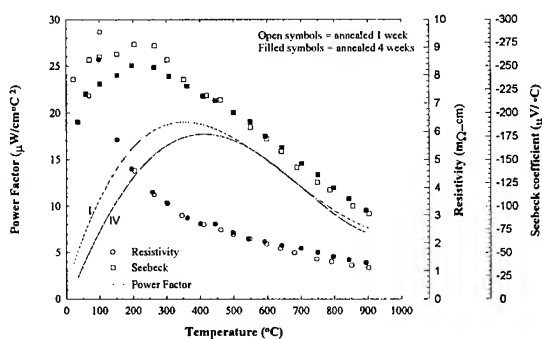


Figure 5. Electrical resistivity, Seebeck coefficient, and power factor of arc melted and 800°C annealed TiNiSn. Sample designation: I = 1 week heat treatment and IV = 4 week heat treatment. (Samples were prepared at the University of Virginia)

The Seebeck coefficient of both samples increases slightly with temperature to about 300°C and decreases thereafter. This behavior is qualitatively different from the samples prepared at Ames in that the latter alloys show a continuously decreasing Seebeck coefficient with temperature throughout the entire temperature range. The electrical resistivity of both sets of samples show similar behavior. The power factor of the U. of Virginia samples increases to a maximum of near $20 \mu\text{W}/\text{cm-deg.}^2$ in the 300 to 400°C range. It is noted that the maximum power factor of the Ames' 840°C heat treated sample is similar to that of the U of Virginia alloys but that the application of the additional heat treatment at 950°C has improved the power factor. The exact cause for the improvement is not known at this time, however, some differences in processing are worth mentioning. The U. of Virginia group placed the samples in alumina crucibles which were in turn sealed within quartz ampoules. They subsequently observed formation of a metallic coating on the inner wall of the ampoule following the heat treatment. In contrast, the Ames group wrapped the samples in Ta before sealing in quartz and no coating on the ampoules was observed. Moreover, no noticeable change in the ductility of the Ta was observed, which would have suggested that a reaction between the sample and the wrapping occurred. Clearly, additional studies are needed to identify and control the heat treatment conditions required for the optimum power factor.

The thermal conductivity of various heat treated specimens have been measured at room temperature by the Virginia group and found to lie in the 40 to $60 \text{ mW}/\text{cm-deg.}$ range. From the above data, the high temperature thermal transport in these alloys is expected to be dominated by an increasing electronic component which might offset any T^{-1} phonon scattering decrease. Taking the lower value for the thermal conductivity, a reasonable estimate for the optimized ZT of this material would be 0.45 to 0.50 within the 300°C to 600°C range.

III. Other (1,1,1) Compounds

A survey of the RPdBi system, where R = rare earth element has shown that large room temperature electrical power factors are possible within this family. These compounds were prepared by melting in sealed Ta ampoules and subsequently heat treated. They exhibit p-type

conductivity, as shown in Fig. 6. which displays the room temperature Seebeck coefficient vs. Lanthanide atomic number.

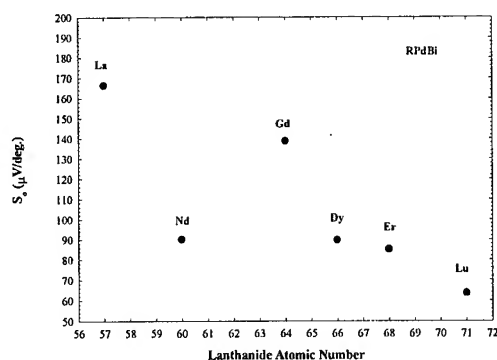


Fig. 6. Room Temperature Seebeck Coefficient of RPdBi Compounds as a Function of Atomic Number. (R = Rare Earth)

(The LaPdBi sample was not single phase)

The variation of Seebeck coefficient with atomic number is believed to be related to the number of unpaired 4f electrons in the lanthanide valence shell. The anomalous value for the La compound is not fully understood but is likely due to the presence of additional phases. A preliminary screening of the room temperature properties of these compounds indicate that some have room temperature power factors on the order of $30 \mu\text{W/cm-deg.}^2$ or higher. A summary of some of these properties is given in Table II.

Table II. Room Temperature Properties of RPdBi (R=Rare Earth)

Compound	ρ (m Ω -cm)	S_0 ($\mu\text{V/}^\circ\text{C}$)	PF ₀ ($\mu\text{W/cm}^2\text{-}^\circ\text{C}^2$)
LaPdBi	1.0	166.4	27.7
NdPdBi	1.8	90.2	4.5
GdPdBi	0.5	138.8	38.5
DyPdBi	2.0	89.8	4.0
ErPdBi	0.7	85.3	10.4
LuPdBi	1.1	63.6	3.7

Most of these compounds, however, have an energy gap on the order of 0.1 eV or less which would suggest that the Seebeck coefficient, and hence the power factor, would both decrease with increasing temperature. A few of these, particularly LaPdBi and GdPdBi, may, however, be attractive candidates for thermoelectric

cooling applications. Other compounds known to crystallize in the MgAgAs structure that may have semiconducting properties include the RPtSb system where R is a heavy rare earth element. Little transport data has been measured on these compounds to date.

Conclusions

Intermetallic compounds having a gap in the density of states at the Fermi level are attractive candidates for low and intermediate temperature thermoelectric applications. Preliminary transport measurements on annealed TiNiSn indicate that electrical power factors exceeding $25 \mu\text{W/cm}^2\text{-}^\circ\text{C}^2$ within the 300°C to 600°C temperature range are achievable. Control of microstructure is a critical processing variable in the optimization of these alloys.

Acknowledgment

The RPdBi compounds were prepared by T. Reidemann as part of a graduate thesis project. The Ames Laboratory is operated by Iowa State University for the United States Department of Energy under contract W-7405-ENG-82. This project was supported by the DOE Radioisotope Power Systems Division. The advice and assistance of Bernard Beaudry is gratefully acknowledged.

References

- [1] Z.M. Dashevsky, L.L. Dudkin, V.B. Eliseev, and R.V. Skolozdra, "New Materials for Thermoelectric Generation", X Int. Conf. on Thermoelectrics, D.M. Rowe, ed. (Babrow Press, Cardiff, UK, 1991) 186-190.
- [2] F.G. Aliev, *Physica B* **171** (1991) 199-205.
- [3] F.G. Aliev, N.B. Brandt, V.V. Moshchalkov, V.V. Kozyrkov, R.V. Skolozdra, and A.I. Belogorokhov, *Z. Phys. B - Condensed Matter* **75** (1989) 167-171.
- [4] S. Ogut and K.M. Rabe, *Phys. Rev. B* **51**, 16 (1995) 10443-10453.
- [5] F.G. Aliev, V.V. Kozyrkov, V.V. Moshchalkov, R.V. Skolozdra, and K. Durczewski, *Z. Phys. B - Condensed Matter* **80** (1990) 353-357.

- [6] A.H. El-Sayed, G.J. Nieuwenhuys, J.A. Mydosh, and K.H.J. Buschow, *J. Phys. F: Met. Phys.* **18** (1988) 2265-2281.
- [7] M. Kasaya, H. Suzuki, T. Yamaguchi, and K. Katoh, *J. Phys. Soc. Japan* **61** (1992) 4187-4192.
- [8] B.A. Cook, J.L. Haringa, S.H. Han, and C.B. Vining *J. Appl. Phys.* **78** (1995) 5474-5480.
- [9] Z.S. Tan and W.A. Jesser "Microstructure Analysis of Thermoelectric TiNiSn Alloy", Proc. XIV Int. Conf. on Thermoelectrics, A.F. Ioffe Physical-Technical Institute, St. Petersburg, Russia (1995).

THERMOELECTRIC PROPERTIES OF SINTERED MAGNESIUM COMPOUNDS

Takenobu Kajikawa, Izumi Katsube, Sunao Sugihara, and Kunihiro Soejima

Faculty of Engineering, Shonan Institute of Technology

1-1-25 Tsujido-nishikaigan, Fujisawa, Kanagawa, JAPAN 251

Tel:+81 466 34 4111, Fax:+81 466 35 8897, e-mail: kajikawa@elec.shonan-it.ac.jp

Abstract

The thermoelectric properties of the sintered magnesium compounds such as magnesium silicide and magnesium stannide have been researched in order to apply to a thermoelectric power generation system using combustion heat of municipal solid waste. Temperature dependencies of thermoelectric properties such as Seebeck coefficient, electrical resistivity and thermoelectric power factor are measured for the temperature range from 300K to 770K. The non-dimensional figure-of-merit for the sintered magnesium silicide is obtained about 0.4 at 600K in the initial stage. The durability of magnesium compound elements is also discussed.

Introduction

Intermetallic magnesium compounds such as magnesium silicide, magnesium stannide and magnesium germanium and their solid solutions have been known as the promising thermoelectric materials⁽¹⁾⁽²⁾⁽³⁾. The factor A ($m^{*1.5} \mu/k$; where m^* is the effective mass, μ is the mobility and k is the lattice thermal conductivity) representing the potential ability of thermoelectric performance by Ioffe is 14 for magnesium silicide as compared with 0.8 for iron silicide, 2.6 for silicon germanium and 1.4 for manganese silicide pointed out by C.Vining⁽⁴⁾. It has been also reported that the figure of merit of $Mg_2Si_{1-x}Ge_x$ solid solution at 300K was $0.69 \times 10^{-3} K^{-1}$ for n-type⁽⁵⁾. At present, the research on magnesium compounds is inactive because the degradation of the performance would be severe at high temperature atmosphere. However, if we

could modify the environment to use the module by some systematic arrangements, the performance degradation due to sublimation and oxidization of magnesium would be substantially reduced.

In this paper thermoelectric properties of the sintered thermoelectric materials such as magnesium silicide and magnesium stannide as compared with the casted materials are presented to establish the improved thermoelectric materials for the medium temperature range in consideration of the good effect due to the sintering process.

Experimental Procedure

Mg(4N, 3-5mm chunk) and Si(4N, 300 mesh powder) were used as the starting materials for magnesium silicide. The required amount of these materials were mixed and then melted in the graphite crucible by RF furnace in low pressure atmosphere to prepare Mg_2Si ingot. The ingot was powdered by

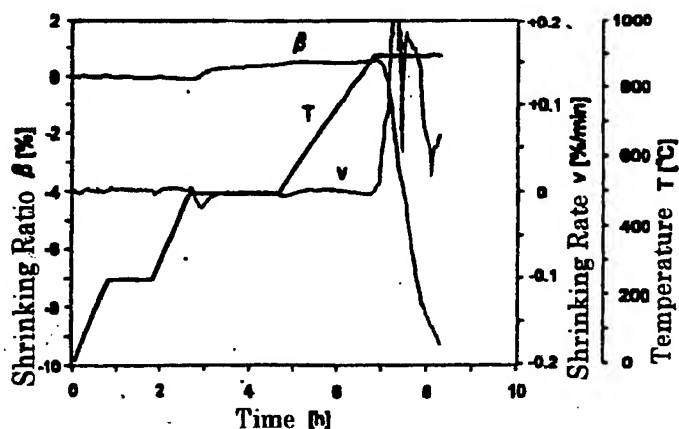


Fig.1 Sintering pattern of magnesium silicide element for shrinking rate control

a planetary ball mill. The powder was one-dimensionally pressed to be made the green samples of 7mm in diameter and 20 mm in length. The green samples covered with platinum cylinder were sintered by shrinking rate control sintering apparatus in argon atmosphere at the temperature range from 1073K to 1200K in consideration of 1375K in melting point of magnesium silicide. The sample temperature pattern of sintering is shown in Fig.1. The temperature at 773K was kept for 2 hours to remove the binder of PVA.

Concerning the magnesium stannide samples, the preparation procedure was similar to the above-mentioned. However, in this case the binder was not used because the powder was soft and adhesive. Small amount of antimony(4N) was added as a dopant at the alloying process. The samples of undoped Mg_2Sn , $Mg_2Sn+1wt\%Sb$, and $Mg_2Sn+2wt\% Sb$ were made. The sintering temperature was 945K, where the shrinking ratio was 3.4%. For the reference, both magnesium silicide and magnesium stannide were made by alloy casting method by RF furnace at the same time.

Results and Discussion

The characterization of the sample were determined by powder X-ray diffractometry(XRD) and scanning electron microscopy(SEM).

Seebeck coefficient and electrical resistivity were simultaneously measured by the thermoelectric power factor measurement apparatus⁽⁶⁾. Thermal diffusivity, heat capacity and thermal conductivity were measured by a laser flash method. The measurement of electrical resistivity and Hall coefficient were measured by Van-der-pauw method. The magnetic field of 0.3T was applied for it.

XRD for the sintered magnesium silicide and the sintered magnesium stannide are shown in Figs.2 and 3 respectively. The patterns exhibit most of lines of standard polycrystalline phases. For the sintered Mg_2Si elements, magnesium oxide, single element of silicon and magnesium were not observed. However, the small level of broad spectrum around $15-20^\circ$ of diffraction angle

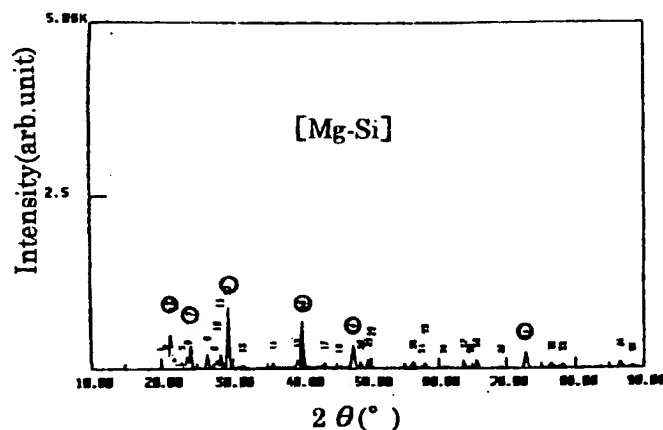


Fig.2 X-ray diffraction pattern of sintered Mg-Si

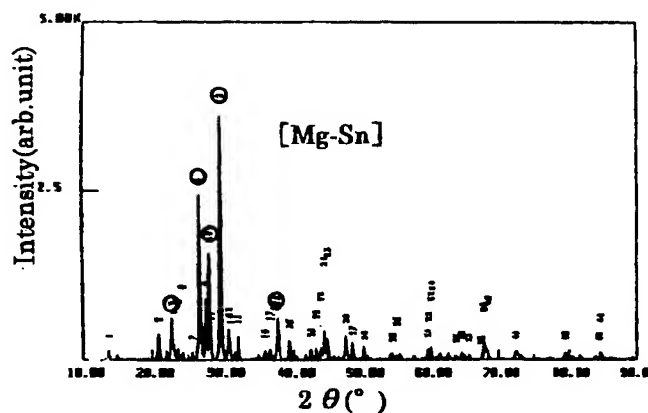


Fig.3 X-ray diffraction pattern of sintered Mg-Sn

suggested containing silicon oxide such as SiO_2 .

According to the SEM micrograph of the sintered Mg_2Si , many closed pores of about 10 micron in diameter are dispersed and other parts are dense sintering phase. The relative density in this case was about 92-95% based on 1.95g/cc in ideal density. The grain size was about 10 micron on the average. According to the SEM micrographs of the sintered and the casted Mg_2Sn , the relative density was about 95% based on 3.592g/cc in ideal state density. Figure 4 shows the dependencies of the Seebeck coefficient and the thermoelectric power factor on the temperature for the sintered Mg_2Si and the casted one. The undoped Mg_2Si was n-type semiconductor. The Seebeck coefficients for both the sintered and the casted increase with temperature and reach to the plateau as predicted

from the theoretical expression of thermoelectric motive force. The Seebeck coefficient of the first sintered sample, which has not been exposed in air at high temperature, is about twice larger than that of the casted due to various scattering effects. The power factor of the first sintered one can be obtained $3.5 \times 10^{-3} (\text{W/mK}^2)$ in the temperature range from 600K to 700K, while the value of the casted one is one tenth of the first sintered.

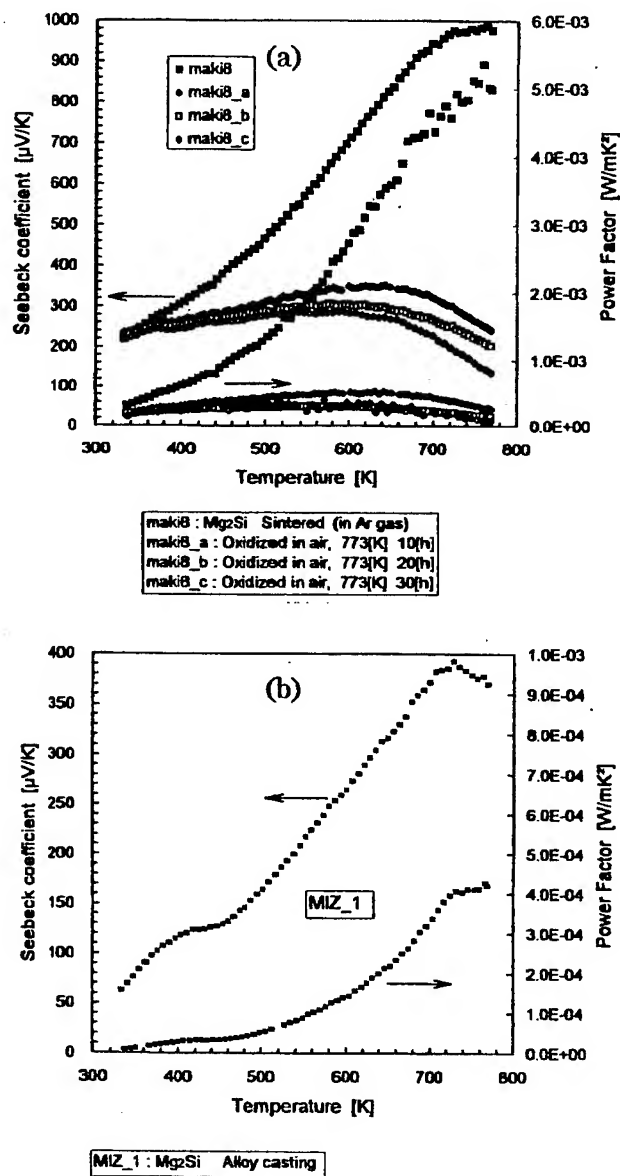


Fig.4 Dependencies of the Seebeck coefficient and thermoelectric power factor on the temperature for sintered at (a) and casted at (b)

In Fig.4(a) the results of the durability test, in

which the samples have been exposed at 773K for every 10 hours, are also shown. The performance is substantially degraded due to oxidation and sublimation and reach to the similar level of the casted one. It suggests that magnesium silicide element should be used in the inert atmosphere.

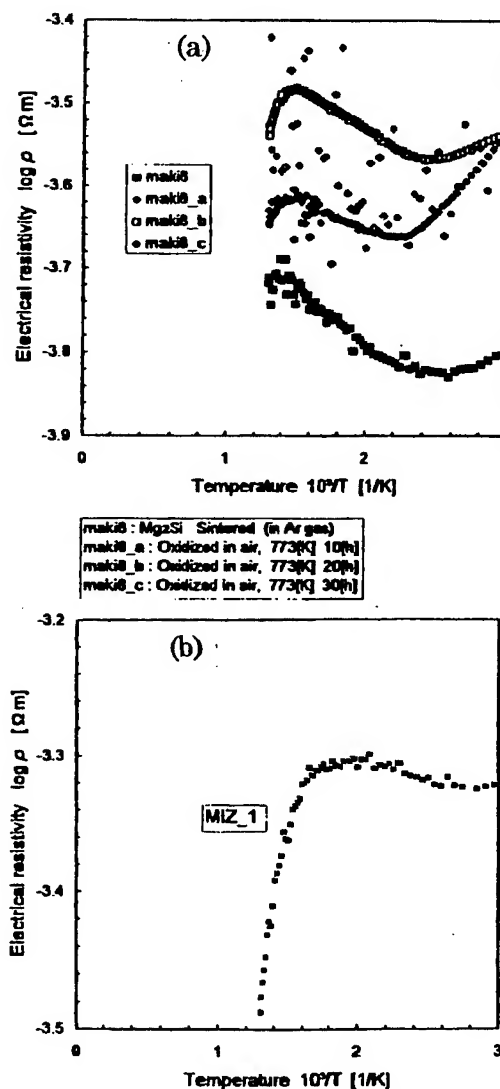


Fig.5 Temperature dependencies of electrical resistivity for sintered at (a) and for casted at (b)

The dependencies of the electrical resistivity on the temperature are shown in Fig.5. The width of the forbidden gap for magnesium silicide determined by the slope of the curve $\ln \rho = f(1/T)$ in the region of intrinsic conductivity, was found equal to 0.74eV, while the width was indicated about 0.77-0.8eV by Nikitin et al⁽¹⁾. The degradation effect also appears on the electrical resistivity due to oxidation. The

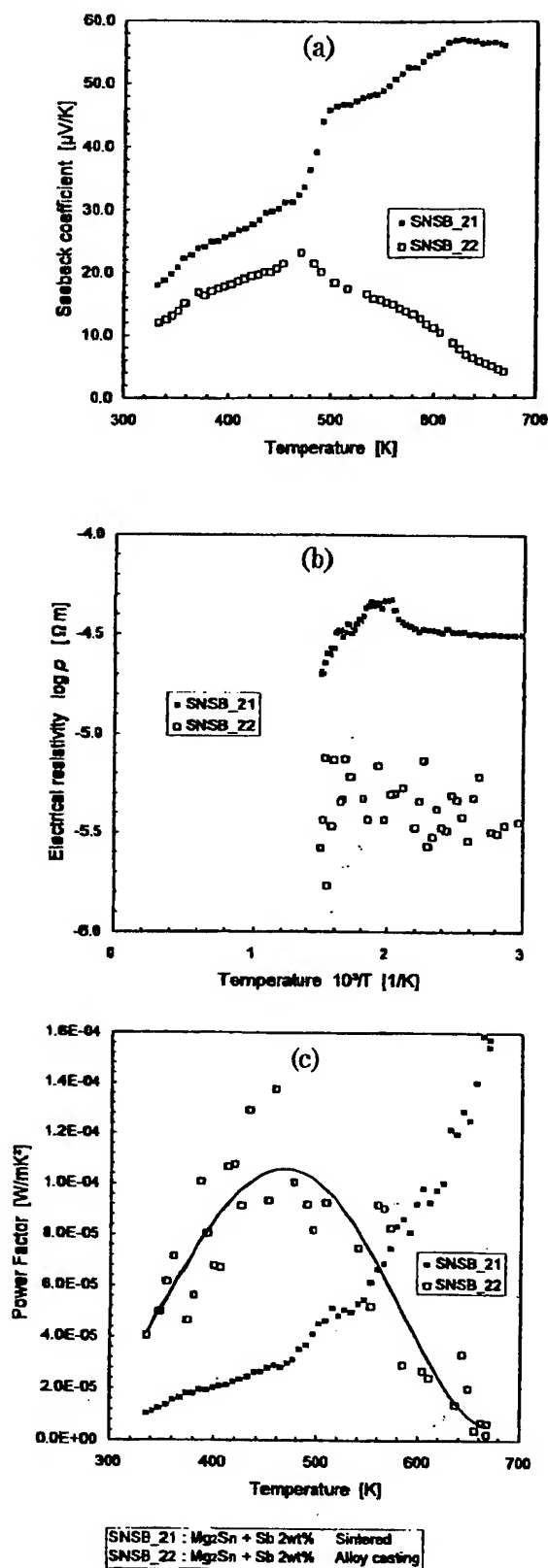


Fig.6 Temperature dependencies of the Seebeck coefficient at (a), electrical resistivity at (b) and thermoelectric power factor at (c) for magnesium stannide elements

value for the sintered one is rather superior to that for the casted one because it can be suggested for the XRD chart that the casted one has been oxidized a little during the alloy casting process.

Figure 6 shows the dependencies of the Seebeck coefficient, the electrical resistivity and the thermoelectric power factor on the temperature up to 700K for the sintered and the casted magnesium stannide doped 2wt% of antimony. The samples of undoped and Sb-doped one represented n-type semiconductor. According to the behavior of Seebeck coefficient the samples of magnesium stannide seem to have a kind of metallurgically transitional state at 460K to 480K.

The electrical resistivity is quite low as compared with magnesium silicide samples. The width of the forbidden gap for the samples doped 2wt% Sb was found to be equal to 0.54-0.6eV, while the undoped magnesium stannide alloy was reported to have 0.3-0.36eV⁽¹⁾. The thermoelectric power factor is obtained about 1.2×10^{-4} (W/mK²) at most, because the carrier concentration has not been optimized obviously.

Concerning the thermal properties, the thermal diffusivity, heat capacity, and thermal conductivity were measured 0.051 cm²/s, 0.82 J/gK, and 7.69 W/mK for the first sintered magnesiumsilicide by a laser flash method at room temperature. According to the reference⁽⁷⁾, thermal conductivity is proportional to $T^{-0.5}$ assuming the intensive phonon scattering due to point defects and is estimated 5.4 W/mK at 600K based on the observed value.

Conclusion

The Seebeck coefficient, electrical resistivity and thermoelectric power factor of the sintered elements of undoped Mg₂Si(n-type) and Sb-doped Mg₂Sn(n-type) have been investigated for the temperature range from 300K to 770K in order to aim the establishment of high efficiency, inexpensive thermoelectric element for medium temperature range.

On the basis of thermoelectric power factor at 600K and of the estimated thermal conductivity, the

non-dimensional figure of merit for the sintered magnesium silicide could be obtained about 0.4 at 600K in the initial stage. The durability tests at 770K in air suggested that the magnesium silicide element should be used in the inert atmosphere for a practical system.

Concerning the sintered magnesium stannide doped 2wt% of antimony, the thermoelectric power factor was obtained about $1.2 \times 10^{-4} (\text{W/mK}^2)$ at most. It suggested that the carrier concentration should be optimized. After that, the sintered element of the solid solution of magnesium silicide and magnesium stannide should be intensively investigated further.

Acknowledgment

We express our gratitude to Mr.S.Suzuki,SIT, Dr.I.Nishida, National Research Institute for Metals and Prof. Y.Noda, Tohoku University for continuous support and encouragement.

References

- 1.E.N.Nikitin,V.G.Bazanov,V.I.Tarasov, "Thermoelectric Properties of Solid Solution $\text{Mg}_2\text{Si-Mg}_2\text{Sn}$ ", Soviet Physics-Solid State,3,12,2648-2651(1962)
- 2.Y.Noda,H.Kon,Y.Furukawa, N.Otsuka, I.Nishida, and K.Masumoto,"Preparation and Thermoelectric Properties of $\text{Mg}_2\text{Si}_{1-x}\text{Ge}_x$ ($x=0.0-0.4$) Solid Semiconductor" Materials Transactions; JIM, 33, 9,845-850(1992)
- 3.M.Riffel, J.Schilz, "Mechanical Alloying of Mg_2Si ", Scripta Metallurgica et Materialia, 33, 12 ,pp1951-1955(1995)
- 4.C.Vining,"Silicides as Promising Thermoelectric Materials", Proc. of IX International Conference on Thermoelectrics, pp249-259(1991)
- 5.Y.Noda, H.Kon, Y.Furukawa, I.Nishida, K.Masumoto,"Temperature Dependence of Thermoelectric Properties of $\text{Mg}_2\text{Si}_{0.6}\text{Ge}_{0.4}$ ", Material Transaction, JIM,33,9,pp851-855(1992)
- 6.T.Kajikawa, I.Katsube, Y.Takada, K..Kuwabara, M.Inobe, T.Ohta," Rapid and Continuous Measurement of Power Factor of Thermoelectric

Material at Temperature up to 1300 K",Proc. of XII ICT,pp44-48(1994)

7.R.J.Zlalotz D.R.Mason, D.F.O'Kane, "The Thermoelectric Properties of Mixed Crystals of $\text{Mg}_2\text{Ge}_x\text{Si}_{1-x}$ ", J. of the Electrochemical Society, 110,2,pp127-134(1963)

Mechanically alloyed $\text{Mg}_2\text{Si}_{1-x}\text{Sn}_x$ solid solutions as thermoelectric materials

Michael Riffel, Jürgen Schilz

Institut für Werkstoff-Forschung, Deutsche Forschungsanstalt für Luft- und Raumfahrt (DLR), D-51140 Köln, Germany,
Tel.: +49/2203/601-4601, Fax: +49/2203/696480, E-mail: michael.riffel@dlr.de

Abstract

$\text{Mg}_2\text{Si}_{1-x}\text{Sn}_x$ solid solutions with ($0 \leq x \leq 0.4$) were prepared by mechanical alloying and subsequent hot-pressing. It was found that the alloying process during milling develops in one of two different directions. The first one leads to the nominal composition with only a small amount of iron impurities resulting from wear of the milling media. In the second route — which only occurs in the presence of Sn — an abrasive phase is formed and the Fe content may increase up to 50 at%. The Fe is bound in FeSi and consequently, the solid solution has a lack of Si.

The hot-pressing was performed at a temperature smaller than the peritectic temperature of the quasibinary Mg_2Si - Mg_2Sn system. A decomposition of the solid solutions occurs, which suggest changes on the miscibility gap in published phase diagrams. However, some transport measurements on the multiphase materials were performed, which revealed lower mobility values and lattice thermal conductivities compared to values published in the literature for single crystalline materials. The mobility of our materials was found to be independent from composition whereas the thermal conductivity decreases with increasing Sn content.

Introduction

Quasi-binary and quasi-ternary solid solutions of the Mg_2Si , Mg_2Sn , and Mg_2Ge intermetallic compounds have been proposed to be good candidates for high- ZT thermoelectric materials [1,2]. As wide ranges of solid solutions have been shown to exist, this material class possesses the additional potential to form temperature-field adapted, i.e. graded TE-devices without problems with chemical degradation.

Preparing the Mg-alloys by meltmetallurgical methods, however, is difficult due to the high vapour pressure of the Mg. Therefore we investigated material preparation via mechanical alloying in a planetary ball mill. The paper focuses on the synthesis and phase evolution of the alloy powders, and selected thermoelectric properties of hot-pressed Mg_2Si and $\text{Mg}_2\text{Si}_{1-x}\text{Sn}_x$ with x up to 0.4. The investigations complement the more phenomenological ones on the mechanical alloying of pure Mg_2Si [3].

Material synthesis

For the preparation of Mg_2Si and $\text{Mg}_2\text{Si}_{1-x}\text{Sn}_x$ by mechanical alloying, nominal compositions of Si, Mg, and Sn chunk pieces (≤ 5 mm) were filled into 500 ml steel vessels together with 100 steel grinding balls of 10 mm diameter and 150 ml n-hexane.

The vials were sealed under Ar-atmosphere. The milling occurred in a planetary ball mill Retsch PM4000DLR [ICT94] for 8 to 150 h. Powders were examined metallographically by scanning electron microscopy (SEM), standard x-ray diffraction (XRD), energy dispersive analysis of x-rays (EDX) in a transmission electron microscope (TEM), and by x-ray fluorescence analysis (XFA).

Consolidation of the powders occurred in a hot-uniaxial press (HUP) in vacuum ($p \leq 10^{-4}$ mbar) at a pressure of 50 MPa and at a temperature between 800 and 850°C. Mass and size of the ingots were determined to calculate their densities. The samples for the thermoelectric measurements were cut with a wire saw and the ones for the Hall measurements were etched prior to the evaporation of Indium contacts.

Material evolution during mechanical alloying

Mg_2Si

After some time of planetary ball milling, the vial load consists of loose powder and larger bulk rests. XRD investigations on the powder (separated from the bulk pieces by sieving at 25 mesh) revealed that it consists of pure Si and the desired Mg_2Si compound, but there is no Mg. Fig. 1 shows an XRD measurement on 8 h milled material. A quantitative analysis of the average powder composition by XFA as well as local composition measurements on single powder particles by means of EDX in a TEM (spot resolution 80 nm) showed, that the average and the local Mg concentrations never exceed the value of 69 at%, i.e. the stoichiometric composition.

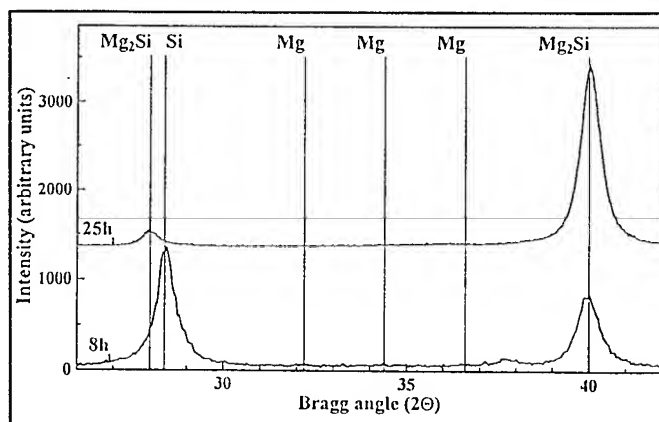


Fig 1: X-ray diffraction diagrams on 8 h and 25 h milled Mg_2Si .

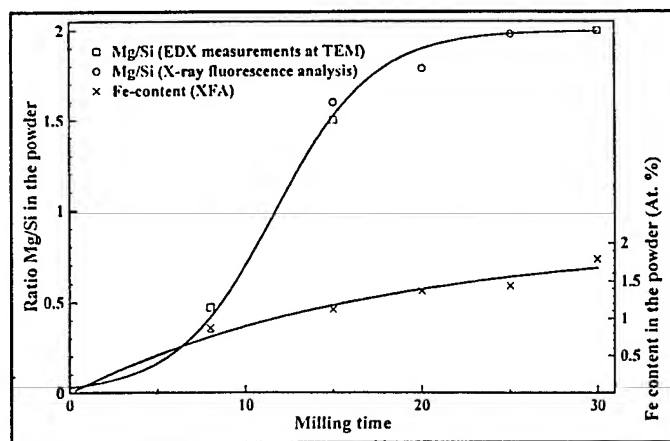


Fig. 2: Composition (Mg/Si ratio) and iron content of the powder.

The bulk rests on the other hand were found to consist of a core of pure Mg without any inclusions. The surface is covered with a thin layer (approx. 20 μm), which was found to be of the same composition as the loose powder. It consists of a ductile Mg_2Si matrix with inclusions of brittle Si. The layer is easily to be scatched off the bulk, which makes it possible that particles of pure silicon come into contact with the Mg-core and continuously form the intermetallic compound.

After a milling time of at least 25 hours no more bulk rests are left, and the XRD spectra only shows the Mg_2Si peaks as seen in Fig. 1.

These findings lead to the conclusion that mechanical alloying of Si and Mg to form Mg_2Si occurs on the surface of the chunky Mg. In the initial stages of milling, the Si is rapidly diminished to particles not exceeding 100 μm which start to abrade small amounts from the still large Mg pieces forming the intermetallic compound.

Concerning the picking up of impurities during the course of milling, a quantitative analysis showed that the Fe content resulting from the milling media does not exceed 2.5 at%.

The time evolution of the powder composition and the impurity contents is shown in Fig. 2.

$\text{Mg}_2\text{Si}_{1-x}\text{Sn}_x$

While the mechanical alloying of the pure Mg_2Si is straightforward, the milling of the solid solutions $\text{Mg}_2\text{Si}_{1-x}\text{Sn}_x$ show some unexpected effects. The most important one is that — apparently arbitrarily — the milling evolves into two different directions leading to completely different types of powder.

The "good" route leads to the nominal solid solution. If the batch develops into this direction, we always observed the occurrence of an intermediate product consisting of a metastable, i.e. high temperature Mg_2Sn -phase and pure Si in the powder, and Mg bulk rests. The metastable Mg_2Sn could never be observed together with the stable solid solution. Consequently, we conclude that there is a spontaneous transformation from the metastable Mg_2Sn into the stable phase with a concomitant

incorporation of silicon. The time required to receive the alloyed powder without bulk rests is much longer compared to the pure Mg_2Si . Milling had to proceed for 80 hours for the composition $\text{Mg}_2\text{Si}_{0.8}\text{Sn}_{0.2}$ and for 130 hours for $\text{Mg}_2\text{Si}_{0.6}\text{Sn}_{0.4}$. Nevertheless the iron content in these powders does not exceed 3 at%.

In the second evolution route even at early milling stages large amounts of iron powders are found which eventually form FeSi. Additionally, pure Sn can be observed. During further milling, there are the stable $\text{Mg}_2\text{Sn}(\text{Si})$ phase and FeSi in the powder together with Mg bulk rests. In this processing route the Fe content increases very fast and finally reaches a value of 50 at% after a milling time of 140 hours. Even in this stage of the milling, Mg bulk rests are still existing.

It is important to notice that neither FeSi nor Sn can be observed simultaneously with the metastable Mg_2Sn -phase and that FeSi and pure Sn are always observed together. This means that one of these phases must be an abrasive one causing the high iron concentration. Due to this high impurity concentration these powders cannot be used for the further processing steps.

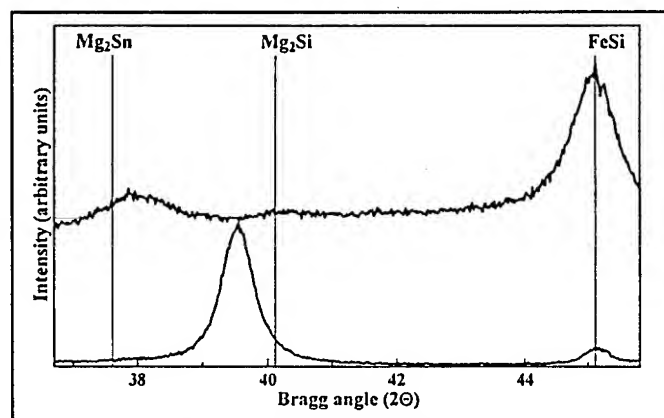


Fig. 3: X-ray diffraction measurement of $\text{Mg}_2\text{Si}_{0.8}\text{Sn}_{0.2}$ powders of the two different evolution routes.

The two different evolution routes are demonstrated by the XRD spectra of two powders which are processed in exactly the same way (cf. Fig. 3). The lower spectrum corresponds to the powder of the first, i.e. "good" evolution route and shows a large solid solution peak of the nominal composition and a small peak belonging to FeSi corresponding to an Fe concentration of 2.9 at%. The upper curve exhibits a large FeSi peak and only a small peak of the solid solution, which additionally is shifted to the tin-rich side, because the reduced content of available Si induced by the formation of FeSi. The iron content in the shown case is 44 at%.

Consolidation of mechanically alloyed powders

The parameters for the consolidation process were chosen according to available quasibinary phase diagrams on Mg_2Sn - Mg_2Si (Fig. 4) [5,6]. Both variants show a peritectic behaviour

with the peritectic temperature being about 860°C. Consequently, we have chosen 850°C as the pressing temperature.

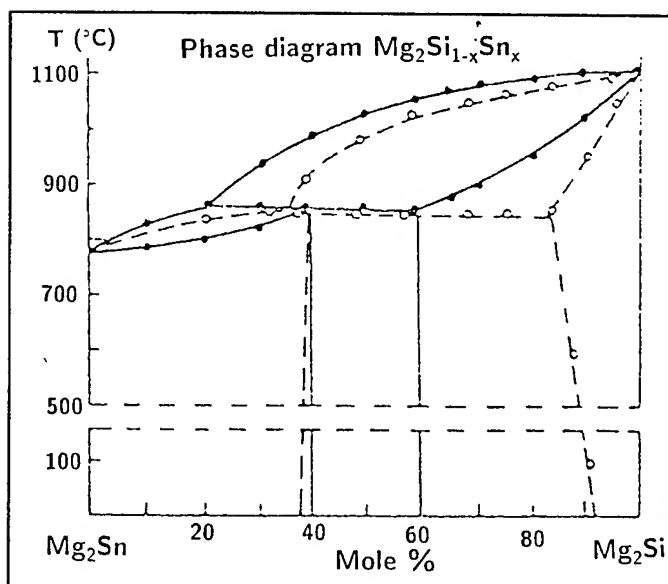


Fig. 4: Two different phase diagrams for the $\text{Mg}_2\text{Sn-Mg}_2\text{Si}$ quasi-binary system. Full curves [5], dotted curves [6].

After hot pressing, the ingots show a density close to the theoretical one, however, as MgO was detected in the samples, the density values are shifted to higher values.

XRD measurements show that the previous alloy peak, which was seen in the powder material, splits into three signals indicating a decomposition of the material (Fig. 5). One of the peaks still corresponds to the nominal composition and the other ones can be attributed to the decomposition values of the peritectic reaction.

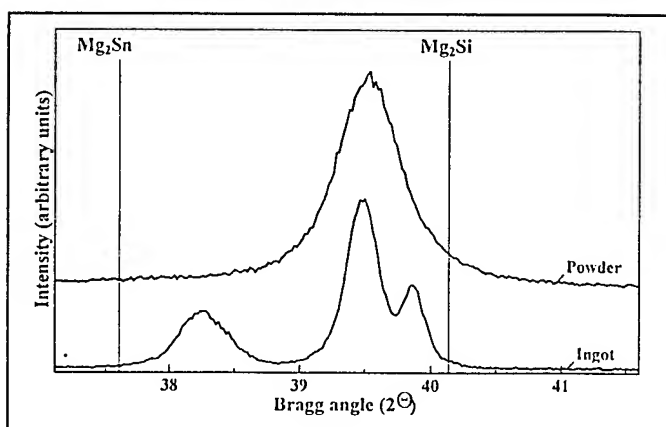


Fig. 5: X-ray diffraction measurement on mechanically alloyed $\text{Mg}_2\text{Si}_{0.8}\text{Sn}_{0.2}$ powder and the hot-pressed ingot.

The lattice parameters calculated from the XRD measurements of the powders agree well with Vegard's law. Following this,

we calculated the compositions of the split values from the lattice parameters determined by XRD measurements. The results indicated a solubility gap between 28 and 91 at%.

Comparing our result on the solubility gap with those shown in the published phase diagrams of Fig. 4 reveal large discrepancies. Nikitin *et al.* [5] report a gap between 40 and 60 mol% Mg_2Si , Mantyanu *et al.* [6] state 35 to 92 mol%. The upper limit agrees with that reported in [6], but the lower reported limit is obviously too high. Further investigations are needed on the way to a reliable phase diagram.

	Mg_2Si	$\text{Mg}_2\text{Si}_{0.8}\text{Sn}_{0.2}$	$\text{Mg}_2\text{Si}_{0.6}\text{Sn}_{0.4}$
ρ (g/cm ³)	1.94	2.35	2.85
σ (1/Ωcm)	0.11	600	450
n (1/cm ³)	$3 \cdot 10^{16}$	$2 \cdot 10^{20}$	$1 \cdot 10^{20}$
μ (cm ² /Vs)	21	18	20
κ (W/mK)	5.3	3.9	2.6
κ_{ph} (W/mK)	5.3	3.4	2.3
μ/κ (cm ² K/VJ)	400	530	870
S (μV/K)	-620	-65	-90
ZT	$4.4 \cdot 10^{-4}$	0.023	0.03

Table 1: Room temperature values of not intentionally doped, mechanically alloyed $\text{Mg}_2\text{Si}_{1-x}\text{Sn}_x$.

Thermoelectric properties

We performed transport measurements on the multiphase materials at room temperature. No dopants were intentionally added to the materials, and, according to the literature [e.g. 1, 7], all samples were of n-type. The ones containing Sn have a high carrier density, n , about $10^{20}/\text{cm}^3$. The carrier density of the pure Mg_2Si was much lower not exceeding $10^{17}/\text{cm}^3$. Both, the electrical conductivity, σ , and the Seebeck coefficient, S , correspond to the carrier density (see Tab.1).

The Hall mobility, μ , as calculated from n and σ , was found to be independent from composition about $20 \text{ cm}^2/\text{Vs}$. This value is significantly lower compared to the ones published by Winkler [7] who measured $370 \text{ cm}^2/\text{Vs}$ (Mg_2Si) and $210 \text{ cm}^2/\text{Vs}$ (Mg_2Sn) for single crystalline materials. This decrease may be caused by additional scattering mechanisms resulting from the grain and crystallite boundaries in the powdermetallurgical materials and from scattering at point defects, because the impurity concentration in our samples is much higher than in Winkler's material as can be seen from the difference in carrier concentration (for Mg_2Si , Winkler measured only $10^{14}/\text{cm}^3$).

The thermal conductivities, κ , for Mg_2Si , $\text{Mg}_2\text{Si}_{0.8}\text{Sn}_{0.2}$, and $\text{Mg}_2\text{Si}_{0.6}\text{Sn}_{0.4}$ were 5.3, 3.9, and 2.6 W/mK, respectively. Due to the low carrier density of the Mg_2Si the measured value is equal

to that of the lattice thermal conductivity, κ_{ph} . To receive the lattice thermal conductivities of the solid solutions, the measured values were corrected by the electronic part, κ_{El} , which can be calculated from the electrical conductivity by the Wiedeman-Franz-Lorentz law. Thus, the lattice thermal conductivities were estimated to 3.4 and 2.3 W/mK for $Mg_2Si_{0.8}Sn_{0.2}$ and $Mg_2Si_{0.6}Sn_{0.4}$, respectively. These values are about 30% lower than those published in the literature [1,8].

A quantity which may serve to value undoped materials for their thermoelectric suitability is the ratio of mobility to lattice thermal conductivity, μ/κ_{ph} . In the investigated composition range this quantity increases monotonously with increasing Sn content from 400 cm²K/VJ for Mg_2Si to 870 cm²K/VJ for $Mg_2Si_{0.6}Sn_{0.4}$. This result shows that the solid solution with a high Sn content is much more suitable for thermoelectric applications than the pure intermetallic compound.

Calculating a room temperature value for the dimensionless figure of merit, ZT , of the solid solution $Mg_2Si_{0.6}Sn_{0.4}$ leads to a value of 0.03, which is indeed a promising one, as the material is not optimized and not at the optimal temperature.

Conclusions

A preparation method for the $Mg_2Si_{1-x}Sn_x$ ($0 \leq x \leq 0.4$) solid solution based on mechanical alloying in a planetary ball mill and subsequent hot uniaxial pressing could be developed. During mechanical alloying two different evolution routes were observed from which only one leads to the desired end product. The consolidation causes a partial decomposition of the materials that is not in accordance to published quasibinary phase diagrams.

Room temperature transport parameters show that the solid solution (in spite of decomposition) is more suitable for thermoelectric applications than the pure intermetallic compound. However, for conclusive statements in terms of thermoelectric suitability the examination of doped materials is necessary.

This work was supported by the Deutsche Forschungsgemeinschaft, Schwerpunktprogramm Gradientenwerkstoffe. We gratefully acknowledge the continuous support by W.A. Kaysser.

References

- [1] R.J. LaBatz, D.R. Mason, D.F. O'Kane, "The thermoelectric properties of mixed crystals of $Mg_2Si_{1-x}Ge_x$ ", J. Electrochem. Soc. **110** (1963) 127.
- [2] Y. Noda, H. Kon, Y. Furukawa, I.A. Nishida, K. Masumoto, "Preparation and thermoelectric properties of $Mg_2Si_{1-x}Ge_x$ ", Proc. of the XIIth Int. Conf. on Thermoelectrics (ICT'93), Yokohama, Japan, 1993.
- [3] M. Riffel, J. Schilz, "Mechanical alloying of Mg_2Si ", Scr. Met. **32** (1995) 1951.
- [4] J. Schilz, K. Pixius, W. Amend, M. Plate, H.-J. Meyer, "Mechanical alloying of Si and Ge in a planetary ball mill", Proc. of the XIIIth Int. Conf. on Thermoelectrics (ICT'94), Kansas City MO, USA, 1994, AIP Conf. Proc. **316** (1995) 71.
- [5] E.N. Nikitin, E.N. Tkalenko, V.K. Zaitsev, A.I. Zaslavskii, A.K. Kuznetsov, "A study on the phase diagram for the Mg_2Si - Mg_2Sn system and properties of certain of its solid solutions", J. Inorganic Mater. **4** (1970) 1656.
- [6] S. Mantyanu, E.B. Sokolov, E.S. Makarov, Zh. Neorgan. Materialy, **2** (1966) 870.
- [7] U. Winkler, "Die elektrischen Eigenschaften der intermetallischen Verbindungen Mg_2Si , Mg_2Ge , Mg_2Sn und Mg_2Pb ", Helv. Phys. Acta **28** (1955) 633.
- [8] V.K. Zaitsev, E.N. Tkalenko, E.N. Nikitin, "Lattice thermal conductivity of Mg_2Si - Mg_2Sn , Mg_2Ge - Mg_2Sn , and Mg_2Si - Mg_2Ge solid solutions", Soviet Physics - Solid State **11** (1969) 221.

Comparison of Different Pressing Techniques for the Preparation of n-type Silicon-Germanium Thermoelectric Alloys

by J. L. Harringa and B. A. Cook

Ames Laboratory, Iowa State University, Ames, IA 50010-3020, USA.

Abstract

Improvements to state-of-the-art $\text{Si}_{80}\text{Ge}_{20}$ thermoelectric alloys have been observed in laboratory-scale samples by the application of the powder metallurgical techniques of mechanical alloying and hot pressing. Incorporating these improvements in large scale compacts for the production of thermoelectric generator elements is the next step in achieving higher efficiency RTG's. This paper discusses consolidation of large quantities of mechanically alloyed powders into production size compacts. Differences in thermoelectric properties are noted between the compacts prepared by the standard technique of hot uniaxial pressing and hot isostatic pressing. Most significant is the difference in carrier concentration between the alloys prepared by the two consolidation techniques.

Introduction

Silicon-germanium thermoelectric alloys have been used for many years in radioisotope thermoelectric generators for space applications. These alloys are typically manufactured via a melting, grinding, and hot pressing sequence [1]. Due to the large separation between the solidus and liquidus in the Si-Ge phase system, dendritic segregation is prevalent in these alloys. This requires that multiple hot pressing and grinding sequences be carried out in order to homogenize the alloys. Cook et al. [2] have shown the viability of mechanical alloying (MA) using a high energy ball mill applied to heavily doped Si-Ge alloys for thermoelectric applications. The advantage of MA over conventional techniques is that alloying is carried out at ambient temperatures and a homogeneous alloy is produced in a single MA + hot uniaxial pressing (HUP) step. A further advantage is that volatile phosphorous, the n-type dopant, is incorporated into the alloy at room temperature in a sealed vial rather than to a melt at high temperature as is conventionally done. Cook et al. [3] have shown that second phase oxygen has deleterious effects on the thermoelectric properties of n-type Si-Ge alloys. The MA process allows for the handling of precursor materials and the alloyed powders under a purified He atmosphere provided by a glove box, thus avoiding the reaction of the fine powders with air. Conventionally prepared material can contain a much higher level of second phase oxygen than MA materials due to powder handling.

Mechanical alloying has been applied to Si-Ge thermoelectric alloys on a laboratory scale. This is due to the fact that the milling equipment, a Spex 8000 mixer/mill, is

capable of alloying only 5-6 grams of powder at a time. Samples produced at the Ames Laboratory consist of vacuum hot pressed 1.27cm diameter cylinders approximately 2.5 cm in length. The scaleup from laboratory to industrial production requires larger volumes of powder to prepare large hot pressed billets called "pucks" from which thermoelements for RTG's are machined. Other milling equipment is available that is capable of producing MA powder in larger quantities. To avoid the problem of oxygen contamination, preparation of Si-Ge pucks needed to be carried out at the Ames Laboratory. Hot isostatic pressing (HIP) was thus attempted.

Experimental

As reported by Cook et al. [4] MA has been applied on the laboratory scale to prepare GaP and P doped n-type Si-Ge alloys with high figures of merit. Production of the MA powder for large scale HIPing was carried out in the same manner as for the laboratory scale alloys. Initial components consisted of Si (Hemlock Semiconductor), Ge (Cabot Berylco), GaP (Cerac) and P (Cerac). All of the starting materials were added to a round ended hardened steel vial as +20 mesh chunks in order to lower the oxygen content in the alloys introduced from surface oxide layers. The material was ball milled for 2 hours to form a mixed powder. Five grams of the premilled powder were removed and added to a flat ended hardened steel vial. This powder was then milled for 6 hours to form an alloy. Multiple MA millings were used to accumulate powder for HIPing whereas one 6 hour MA milling provided all the powder necessary for one HUP consolidation. Handling of the elemental components and MA powder was performed in a purified He filled glove box. Table 1 summarizes the sample compositions and consolidation technique. The greek letter designates an individual HUP sample consolidation.

HUP Samples

HUP samples were prepared by loading four grams of MA powder were loaded into a 1.27 cm graphoil lined graphite die. The powder was pressed in an RF vacuum furnace at 1130°C and an applied pressure of 140 MPa for 45 minutes after which the pressure was released and the sample was allowed to furnace cool. Samples were then sectioned from the compact and given a "reset" heat treatment at 1050°C for 20 minutes. One sample, A92β, was pressed for 60 minutes.

HIP Samples

HIP samples were prepared by packing the MA powder into a cylindrical graphoil lined Ta HIP vessel. A Ta lid was pressure fit into the vessel and e-beam welded under vacuum. Each HIP vessel was held in the vacuum port of the e-beam welder overnight to remove residual He in the vessel before the lid was e-beam welded in place.

Two types of HIP vessels were used. Initial HIP vessels were cylindrical Ta vessels with wall thickness of 0.05 cm, diameter of 1.91 cm, and height of 3.8 cm. This vessel type was used on samples designated HIP-2, HIP-5a,

compact. In the longitudinal direction HIP-5a has large grains in the 10-20 μ m range with most grains approximately 15 μ m. The transverse section showed a very fine grain structure with grain sizes of \sim 1 μ m and an occasional large grain of \sim 20 μ m.

The microstructure of HIP-10 exhibited longitudinal grains that appear to be in the 10-20 μ m range. The grains in the transverse section are larger and in the range of \sim 12 - \sim 40 μ m. The difference in grain size between the transverse and longitudinal directions does not appear to be as significant as for the HIP-5a compact. It would thus appear that the aspect ratio of the HIP vessel greatly influences the

Table 1 Composition and consolidation conditions for n-type Si₈₀Ge₂₀ alloys. All alloys were consolidated at 1130°C and 140 MPa.

Sample	Composition	Consolidation Method	Consolidation Time (minutes)
A92 α	Si _{0.785} Ge _{0.196} Ga _{0.006} P _{0.019}	HUP	45
A92 β	Si _{0.785} Ge _{0.196} Ga _{0.006} P _{0.019}	HUP	60
A93 α	Si _{0.780} Ge _{0.195} Ga _{0.013} P _{0.025}	HUP	45
A95 α	Si _{0.778} Ge _{0.195} Ga _{0.013} P _{0.028}	HUP	45
A96 β	Si _{0.776} Ge _{0.194} Ga _{0.013} P _{0.030}	HUP	45
A99 α	Si _{0.776} Ge _{0.194} Ga _{0.008} P _{0.030}	HUP	45
HIP-2	Si _{0.785} Ge _{0.196} Ga _{0.006} P _{0.019}	HIP	45
HIP-5a, 5b	Si _{0.788} Ge _{0.197} Ga _{0.005} P _{0.015}	HIP	45
HIP-7 through HIP-18	Si _{0.788} Ge _{0.197} Ga _{0.005} P _{0.015}	HIP	45
A101-1 through A101-4	Si _{0.791} Ge _{0.198} Ga _{0.004} P _{0.011}	HIP	45

and HIP-5b. The final vessels used for the production of large compacts were constructed from 0.05 cm thick Ta with 5.08 cm diameter x 3.81 cm length. These vessels were filled with approximately 80 gm of packed powder. The vessel was HIPed at 1130°C for 45 minutes under an applied pressure of 137 MPa. The furnace temperature was ramped from 25-900°C at 10°C/min, 900-1130°C at 5°C/min, and then furnace-cooled to room temperature following pressing. This heating schedule is the same as that for the HUP samples. Each HIP sample was given a 1050°C thermal treatment for 20 minutes. Samples designated HIP-7 through HIP-18 and A101-1 through A101-4 were produced in this manner. One important difference between the HUP and HIP is that the vacuum HUP used a die which was exposed to the vacuum system whereas the HIP samples were sealed in a Ta vessel thus trapping any P vapor that developed during the thermal excursion.

Characterization

Metallography

The HIP-5a and HIP-10 compacts were sectioned such that a longitudinal (top face) and transverse (side) portion could be examined by optical metallography. The grain size of HIP-5a was not uniform throughout the

size and shape of the grains. It is assumed that HIP-2 has the same type of microstructure as HIP-5a due to the identical type HIP vessel used.

Oxygen Determination

The oxygen content of selected HUP and HIP alloys was determined by neutron activation by Nicolet Imaging Systems-Radiation Processing Group. Values obtained for different alloys are presented in Table 2. These values are consistent with low oxygen n-type Si-Ge alloys prepared by Cook et al. [3].

Table 2. Total oxygen content determined by neutron activation. A92-H is a HUP alloy prepared identically to A92 α , the rest are HIP.

Sample	Oxygen (at.%)
HIP-2	0.4
HIP-10	0.05
A101-4	0.21
A92-H	0.2

Chemical Analysis

Several samples were examined by Inductively Couple Plasma-Atomic Emission Spectroscopy (ICP-AES) and Laser Ionization Mass Spectroscopy (LIMS). ICP-AES was used to determine P and Ga contents following hot consolidation. LIMS was used to characterize impurities from sources such as wear debris from the milling vessels.

Table 3 shows the nominal and measured P and Ga content in a number of the alloys. It can be seen that the actual amount of P in the HUP alloys varies substantially from the nominal amount. The measured amount of P is much closer to the nominal amount for the HIP alloys. HIP-7 through HIP-15 show that the final P content is consistent from one sample to the next. Note that HIP-5b has a lower P content than the remaining HIP samples with the same nominal composition. It is unknown why this sample would have a greater loss of P following hot consolidation.

Table 3. Nominal phosphorous and gallium concentrations. Actual P and Ga contents were determined by ICP-AES following hot consolidation.

Sample	Nominal P at. %	Actual P at. %
A90 α	1.25	1.1
A91 α	2.0	1.56
A92 α	1.8	1.28
A92 β	1.8	1.47
A93 α	2.5	1.87
HIP-2	1.8	1.56
HIP-5b	1.5	1.13
HIP-7	1.5	1.36
HIP-10	1.5	1.39
HIP-12	1.5	1.36
HIP-15	1.5	1.36

LIMS data for trace element impurities is presented in Table 4. A101-2 had a slightly lower Fe content than the other A101 compacts; but HIP15 was higher than A101-3 and A101-4. Portions of the Si-Ge in the A101-3 compact were in contact with the Ta HIP vessel, but this did not contribute to a higher Ta level in the alloy. The level of Ta contamination is low in all of the alloys. Graphoil facilitates the removal of the sample and does not appear to significantly affect the carbon content.

Table 4. Impurities in MA + HIP alloys as determined by Laser Ionization Mass Spectroscopy. The values are in ppm atomic. Determination of C is subject to relatively large errors. X-1 refers to a spot near the edge of the compact which was in direct contact with the Ta vessel graphoil. The x-2 refers to a spot near the center of the compact.

Sample ID	Fe	C	Ta
HIP-15	420	7.3	1.9
A101-2	170	58	2.9
A101-3 x-1	230	25	0.34
A101-3 x-2	320	40	0.62
A101-4	460	10	0.10

Properties

Electrical

Electrical characterization of the HIP and HUP alloys consisted of room temperature Hall effect measurements, shown in Table 5, and measurements of the temperature dependence of resistivity and Seebeck coefficients to 1000°C. The high temperature measurements are represented in Table 6 as integrated averages of resistivity, Seebeck coefficient, and power factor in the range of 300°C to 1000°C.

The carrier concentration values given in Table 5 illustrate the change in carrier concentration with sample composition. Nearly optimized figures of merit have been observed in Si-Ge alloys doped with GaP and P having a carrier concentration in the $2.5\text{--}3.0 \times 10^{20} \text{ cm}^{-3}$ range, as shown, for example, by Scoville et al. [5]. Alloys of the A92 composition fall within or close to that range and this composition was chosen for the first HIP sample, HIP-2. It can be seen in Table 5 that the HIP-2 alloy has a much higher carrier concentration than the corresponding HUP counterparts. The P content of HIP-2 is much higher than that of the HUP alloy A92 as discussed above, which indicates that the HIP approach does not allow the escape of P vapor during consolidation. The nominal phosphorus composition of alloys consolidated by HIPing must therefore be lower than corresponding HUP alloys to compensate for the fact that P is not lost to the vacuum system as it is in the HUP. The HIP-5 alloys had a nominal composition designed to lower the carrier concentration. It can be seen that this was achieved, but as mentioned above, these alloys possessed an anisotropic microstructure. The HIP-7 through HIP-18 compacts were prepared with larger diameter and shorter vessels. It can be seen that the carrier concentration increased for these alloys compared with the HIP-5 compacts. The HIP-5 compacts and the HIP-7-HIP-18 compacts have the same composition, but the carrier concentrations are much higher in the 2" diameter compacts. The behavior of the 2" compacts indicates that the nominal P level needs to be reduced in order to obtain Z similar to the laboratory scale samples of $0.94 \times 10^{-3} \text{ C}^{-1}$. The carrier concentration of all HIP billets with the A100 composition is too high, yet the mobility is the highest possible for the given carrier concentration based on extrapolating Dismukes zone leveled Si-Ge data to higher carrier concentration values.

The A101 alloys had a nominal composition intended to lower the carrier concentration to the $2.5 \times 10^{20} \text{ cm}^{-3}$ range. Hall measurements of A101-2 indicated that the target concentration n of $2.5 \times 10^{20} \text{ cm}^{-3}$ was not attained, but n was reduced by 14 percent. Although the desired carrier concentration was not achieved, it was lowered to the point where the figure of merit Z was improved, as discussed below. As seen in Table 5, the carrier concentration for the A101 series of alloys decreases with each subsequent sample. The carrier concentration for A101-4 is in the targeted range of $2.5\text{--}2.8 \times 10^{20} \text{ cm}^{-3}$, but the mobility is about 10% lower than the value of 45 expected with this carrier concentration.

One possible explanation for the low mobility in the A101-3 and A101-4 alloys is that increased wear debris from the grinding media would iron disilicide or germinide scattering centers. The LIMS data in Table 5 tends to supports this idea. Another possibility is that the actual HIP temperature was lower than 1130°C target. This would lead to smaller grain sizes and reduced mobility due to grain boundary scattering.

Table 5. Room temperature Hall effect properties for HUP and HIP alloys.

Sample	$n (\times 10^{20} \text{cm}^{-3})$	$\rho (\text{m}\Omega\text{-cm})$	$\mu (\text{cm}^2/\text{V-s})$
A92 α	2.78	0.599	37.7
A92 β	3.08	0.51	40.0
A93 α	3.10	0.50	40.4
A95 α	3.26	0.442	43.4
A96 β	3.80	0.445	37.0
A99 α	3.29	0.467	40.7
HIP-2, S-1	3.53	0.46	38.8
HIP-2, S-2	3.60	0.45	38.3
HIP-5a	2.45	0.51	50.0
HIP-5b	2.44	0.52	49.7
HIP-7	3.42	0.45	40.1
HIP-10	3.45	0.45	39.2
HIP-12	3.44	0.46	39.3
HIP-15	3.45	0.46	39.6
HIP-16	3.36	0.47	39.4
HIP-17	3.37	0.47	39.6
HIP-18	3.47	0.47	38.4
A101-2	2.95	0.51	41.4
A101-3	2.80	0.54	41.6
A101-4	2.76	0.55	41.2

The integrated average power factors for the HUP samples from Table 6 range from 31.4 for A92 α to 36.6 $\mu\text{W}/\text{cm}^2\text{C}^2$ for A93 α . The changes in composition affected the resistivity more than the Seebeck coefficient.

There is also a spread in the power factor data for the HIP alloys. HIP-2 did not duplicate the values in the A92 alloys. As was mentioned above, the carrier concentration of HIP-2 was much higher than that of the HUP counterpart. However, the integrated average power factor is higher for HIP-2 than for A92 α . The exact reason for this is not known, but it may be an artifact of the anisotropic microstructure. The loss of P in the hot consolidation of the MA powders plays an important role in properties of the HUP alloys.

Both HIP-5a and HIP-5b have higher integrated average power factors than HIP-2 and A92 α . This demonstrates that lowering the carrier concentration to the desired range results in higher performance. Comparing the integrated average resistivity, Seebeck, and power factor of the HIP-5 alloys with the HIP-7 - HIP-17 alloys, it can be seen that both the resistivity and Seebeck increased which lead to an overall decrease in the power factor. Changing the shape of the HIP vessel apparently led to higher P retention which resulted in a higher carrier concentration. These results again demonstrate the necessity for maintaining the carrier concentration in the correct range.

Table 6. Integrated average electrical high temperature property data from 300-1000°C for n-type $\text{Si}_{80}\text{Ge}_{20}$ alloys.

Sample	$\langle\rho\rangle (\text{m}\Omega\text{-cm})$	$\langle S\rangle (\mu\text{V}/^\circ\text{C})$	$\langle PF\rangle (\mu\text{W}/\text{cm}^2\text{C}^2)$
A92 α	1.38	-205.6	31.4
A92 β	1.17	-200.5	34.7
A93 α	1.17	-205.5	36.6
A95 α	1.21	-203.3	35.1
A96 β	1.15	-193.9	33.4
A99 α	1.13	-195.0	34.3
HIP-2	1.23	-204.0	34.8
HIP-5a	1.12	-215.5	41.4
HIP-5b	1.23	-217.7	38.6
HIP-7	1.26	-200.8	32.5
HIP-10	1.25	-201.0	32.3
HIP-15	1.25	-200.9	33.3
HIP-17	1.22	-201.1	33.7
A101-2	1.29	-210.7	35.3
A101-3	1.32	-210.3	34.4

The A101 series of alloys employed the same 5.08 cm diameter HIP vessels as HIP-7 through HIP-18, but the P and Ga levels were decreased in order to lower the carrier concentration. A101-2 demonstrated that the reduction in P from 1.5% to 1.1% gave an increase in the average Seebeck coefficient while the resistivity remained relatively unchanged. This led to A101-2 having an average power factor of 35.3 $\mu\text{W}/\text{cm}^2\text{C}^2$ compared to 32-33 $\mu\text{W}/\text{cm}^2\text{C}^2$ for the A100 composition samples. A101-3 had a 5-6% higher resistivity than A101-2. A portion of this sample was in contact with the Ta HIP vessel during consolidation, however LIMS analysis indicated that an increased Ta content did not affect the electrical properties. LIMS results indicated that this was probably not the case.

Thermal conductivity and Figure of Merit

Thermal diffusivity was measured using a laser flash diffusivity method as described in Kokos et al. [6]. Table 7 summarizes data for both HIP and HUP samples.

Table 7. Integrated average thermal conductivity λ and figure of merit Z from 300-1000°C for HUP and HIP n-type SiGe alloys.

Sample	$\langle\lambda\rangle (\text{mW}/\text{cm}^2\text{C})$	$\langle Z\rangle (\times 10^{-3} ^\circ\text{C}^{-1})$
HIP-2	44.0	0.80
HIP-5a	44.5	0.94
HIP-7	38.6	0.84
HIP-10	39.5	0.82
HIP-15	38.7	0.86
HIP-17	39.6	0.85
A101-2	38.7	0.92
A92 β	37.5	0.94

Both HIP-2 and HIP-5a have relatively high thermal conductivities typical of high mobility low oxygen n-type alloys. The thermal conductivities of both of these alloys is nearly identical to that measured in a previous study of HUPed n-type Si-Ge doped with 1.6 % GaP and a P/Ga ratio of 3.125:1 with a low oxygen content of 0.2 at. %³. As

previously mentioned, the grain structure of HIP-2 and HIP-5a was nonuniform. This may account for the high thermal conductivity values for these two samples. The thermal conductivity for the other HIP alloys using the A100 composition is fairly uniform, ranging from 38.6 to 39.6 mW/cm-°C.

A101-2 had an integrated average thermal conductivity similar to that of the 2" diameter compacts with the A100 composition. A101-3 has a higher thermal conductivity than A101-2, as well as a lower power factor as discussed above.

The highest Z attained was on HIP-5a, but that may be due to the anisotropic microstructure. HIP-7 through HIP-17 had lower integrated average Z's in the low 0.8 to 0.85 x 10⁻³ °C⁻¹ range. A101-2 had a higher Z, demonstrating the value of lowering the carrier concentration.

Summary

Two inch diameter compacts of P and GaP doped Si-Ge can be prepared via MA and HIPing. These alloys can attain the high power factors and figures of merit demonstrated by the laboratory scale samples. Due to the differences in hot consolidation between the HIP and HUP, it is impossible to identify one composition that will perform equally under both preparation techniques. Phosphorous loss and solubility is different in both consolidation techniques. Changing the HIP vessel shape can result in changes in carrier concentration.

Acknowledgment

The Ames Laboratory is operated by Iowa State University for the United States Department of Energy under contract W-7405-ENG-82. The advice and assistance of Bernard Beaudry is gratefully acknowledged. Hot isostatic pressing was performed by Lester Reed.

References

- [1]. Sandia National Laboratory Report number SLA-74-0046, (1974).
- [2]. B.A. Cook, B.J. Beaudry, J.L. Haringa, and W.J. Barnett, "The Preparation of SiGe Thermoelectric Alloys by Mechanical Alloying," Proc. of the 24th Intersoc. Energy Conv. Eng. Conf., ed. by W. D. Jackson, Washington, DC: Inst. IEEE, volume 2, 693-700 (1989).
- [3]. B.A. Cook, J.L. Haringa, S.H. Han, and B.J. Beaudry, J. Appl. Phys. 72 (1992) 1423-1428.
- [4]. B.A. Cook, J.L. Haringa, S.H. Han, and C.B. Vining, J. Appl. Phys. 78 (1995) 5474-5480.
- [5]. N. Scoville, C. Bajgar, J.P. Fleurial, and J.W. Vandersande, "Optimization of Heavily Doped SiGe Alloys,"

Proc. of the XI Int. Conf. on Thermoelectrics, University of Texas at Arlington, Oct 7-9, 1992, 70-73.

- [6]. G.B. Kokos, K.A. Gschneidner, B.A. Cook, and B.J. Beaudry, J. Appl. Phys., 66, (1989) 2356.

Precipitation study of lead and chalcogens in single crystals of PbSe-PbTe solid solution

V.L.Kuznetsov

A.F.Ioffe Physical-Technical Institute, 194021, St.-Petersburg, Russia

Abstract

Lead chalcogenides and their solid solutions exhibit a retrograde solubility of lead and chalcogens that can result in the precipitation of excess components and degradation of electrical properties when this materials are used at temperatures lower then their fabrication temperature. The kinetic of precipitation of lead and chalcogens from supersaturated single crystals PbSe, PbTe, and their solid solution has been studied in this work. Single crystals were grown from vapour phase by a sublimation procedure in a vertical quartz ampoules. Sample treatment times ranged from 2 min to several hundred hours at three temperatures for both lead- and chalcogen-saturated crystals. Based on the analysis of the kinetic data the activation energy of precipitation was estimated and compared with the activation energy of diffusion of lead and chalcogens.

Introduction

The electrical and thermoelectric properties of crystals depend on the composition and, consequently, on the fabrication method and preparation conditions. The composition of crystals grown from the melt corresponds to the homogeneity boundary at a growth temperature. Crystal of lead chalcogenides possessing the concentration of cations or anions close enough to the homogeneity boundary at a given temperature will become supersaturated in that ions at lower temperatures due to a retrograde solubility, i.e. a narrowing of the compound homogeneity range at lower temperature (Fig.1). The supersaturated component may be disposed of by an internal precipitation process, in which the excess atoms diffuse from normal sites to precipitation centers such as clusters, dislocations, grain boundaries where they deposit out as electrically neutral atoms forming microsegregations [1]-[3]. In this process the concentration of donor or acceptor levels in the crystals is reduced to the maximum value appropriate for the lower temperature that leads to the change of electrical properties (carrier concentration, thermopower, electrical conductivity). Changes in composition and electrical properties of crystals resulting from the precipitation of one of the components can cause the uncontrollable degradation of device characteristics during operation.

The concentration of nonstoichiometric lead or chalcogen atoms is related to the carrier concentration. This relationship is based on the assumption that each excess lead atom introduces a donor and each excess chalcogen atom introduces an acceptor. During the precipitation the

supersaturated atoms deposit out to the electrically inactive state. Therefore, the precipitation kinetic can be monitored by Hall effect measurements, a technique that provides direct means for determination the number of precipitated atoms.

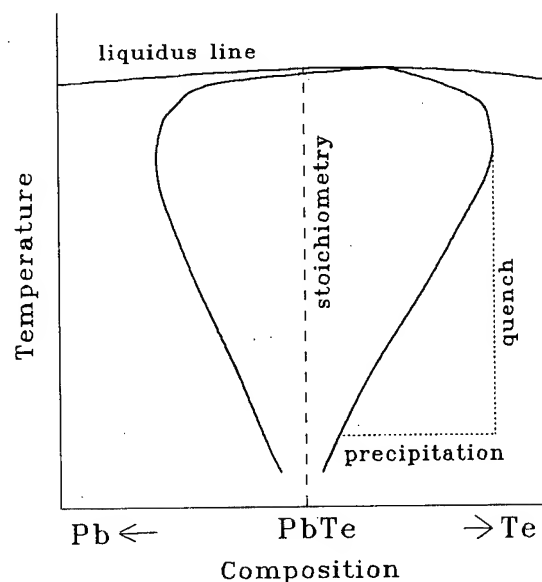


Fig.1 Schematic PbTe homogeneity range and precipitation process.

Material preparation

Single crystals of PbSe-PbTe solid solution were grown from vapour phase by a sublimation procedure in a vertical quartz ampoule [4]. A temperature profile of the growth furnace and an ampoule position is shown schematically in Fig.2. The evacuated quartz ampoule with a charge was placed into the furnace so that an upper vault was situated in the high-temperature furnace zone to clean the inner ampoule surface from the accidental crystallization centers. Then the ampoule was risen in the growth position as it is shown in Fig.2. When evaporated from the melt the vapour is condensed on the upper ampoule vault forming liquid drops. These drops were merged one with other forming a continuous liquid layer which covered totally the ampoule vault. The ampoule was risen and its upper vault turned out in lower temperature region where the crystallization of the melt could take place. The crystallization heat was taken away by means of a quartz rod soldered to the ampoule that promoted an appearance the only initial crystal in the central part of the vault opposite the rod.

The evaporation and condensation temperatures were selected experimentally so that during the growth process the crystal surface was separated from the vapour phase by thin liquid layer. The ampoule rise rate (0.2-0.4 mm/h) was close to the linear growth rate of the crystals to establish the stationary conditions in the growth ampoule. The growth process lasted 120-170 hours after that the crystals were cooled at a rate of 10-15 K/h. Single crystals were 16-20 mm in diameter and 30-40 cm long depending on the weight of the initial charge. Specimens with dimensions of $1.2 \times 2 \times 15 \text{ mm}^3$ were cut from the single crystals for further precipitation investigations.

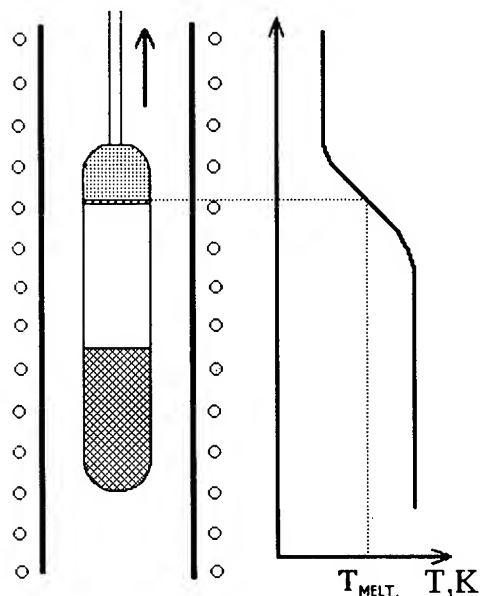


Fig.2 Scheme of the crystal growth procedure.

The dislocation density was measured by metallographic microscope on the samples chemically etched in a solution of 13 ml 50% KOH, 3 ml glycerol and 1 ml 30% H_2O_2 and was $1 \cdot 10^5 \text{ cm}^{-2}$ for PbTe and PbSe crystals and did not exceed $3 \cdot 10^5 \text{ cm}^{-2}$ for solid solution crystals.

The single crystals grown from the vapour phase have more crystallographic perfection and higher carrier mobility in comparison with those grown by Bridgman method. The material transfer through the vapour phase during the growth supplies the additional material cleaning and small temperature gradient (3-5 K/cm) in crystallization zone does not cause the thermal stresses into the growing crystal. These circumstances contribute to the growth of crystals with a high crystallographic perfection.

To investigate a precipitation kinetic in detail it is necessary to obtain samples of n- and p-type conductivity with a maximum initial saturation. The samples with a maximum solubility of lead and chalcogens were prepared by vapour diffusion of the excess component. The isothermal annealing of samples was performed in small evacuated quartz ampoules with a charge of $\text{Pb}_{0.51}(\text{Se}_{1-x}\text{Te}_x)_{0.49}$ or $\text{Pb}_{0.49}(\text{Se}_{1-x}\text{Te}_x)_{0.51}$ composition to prepare the crystals

of n- and p-type, respectively. The charge was separated from the crystals and acted as a vapour source. The mole fraction of lead telluride (x) in the charge and in the crystals was the same. Annealing conditions to prepare lead-saturated crystals were 1050-1120 K for 72 hours and to prepare chalcogen-saturated crystals - 923 K for 120 hours. After the annealing procedure ampoules were quenched in ice water and the specimens were polished to remove any remnants of vapour etching.

It is difficult to quench the lead chalcogenides crystals sufficiently rapidly from high temperature to freeze the composition established at the high temperature near the homogeneity boundary, thus the quenching rate from the temperatures above 923 K is considered to be ineffective [5]. Therefore, it is likely that some precipitation occurred during the quench after vapour treatment that resulted in the unreproducibility of solidus line determination for chalcogen rich lead chalcogenides [4, 5].

Precipitation study

The precipitation kinetic in single crystals PbSe, PbTe and their solid solutions was studied at temperatures 473K, 523 K for chalcogen-saturated crystals and at 673 K for lead-saturated crystals. It was accomplished by the periodic freezing the precipitation process by quenching and room temperature Hall effect measurement to determine the time dependence of carrier concentration.

The samples were placed in a 11-mm OD quartz ampoule about 7 mm long. The ampoule was evacuated, back-filled with argon at a pressure of about 300 Torr, and sealed. It was then placed in the center of a pre-heated resistance furnace containing a cylindrical stainless-steel liner. The sample temperature was monitored with a Pt-Pt,10% Rh thermocouple placed next to the ampoule. The annealing time ranged from 2 min to several hundred hours. Periodically the annealing was interrupted, the ampoules were quenched in cold water, opened and carrier concentration was measured. Then the specimens were sealed again and the annealing for another time was performed.

Several samples with a different thickness were used for each composition and at each annealing temperatures, thereby providing an indication of the independence of the heat treatment and quenching conditions upon the sample thickness. The carrier concentration difference of several samples with an equal composition and with different thickness was less than 7%.

Results and discussion

The isothermal annealing curves are presented in Figs. 3-5. After completion of precipitation process the carrier concentration was about an order of magnitude lower than initial one except for lead-saturated samples of PbTe and $\text{PbSe}_{0.08}\text{Te}_{0.92}$ where the concentration drop was negligible. The kinetic curves may be described by the following expression [6]:

$$f(t) = \frac{C_o - C_t}{C_o - C_e} = 1 - \exp(-(t/\tau)^n) \quad (1)$$

where $f(t)$ is the fraction precipitated after time t , parameters C_o , C_t , and C_e are, respectively, the carrier concentration at the initial moment $t = 0$, at moment of time t , and at equilibrium after completion of precipitation. τ is the time constant, n is the power constant. The time and power constants can provide information about the rate-limiting process and the shape of the precipitation

particles [6, 7]. If the equation (1) applies, then a plot of $\log(-\ln(1 - f(t)))$ vs. $\log(t)$ will be a straight line of slope n .

The typical form of $\log(-\ln(1 - f(t)))$ vs. $\log(t)$ dependence is plotted in Fig.6 by the results of the annealing at 473 K for p-type samples. The analogous plots for 523 K and 673 K are qualitatively similar. It is seen that the precipitation process can be divided into two stages, each of which forms a straight line. Initially the precipitation rate was fast and the slope n varied in the range of 0.9-1.1 depending on sample composition. After about 50-60% of

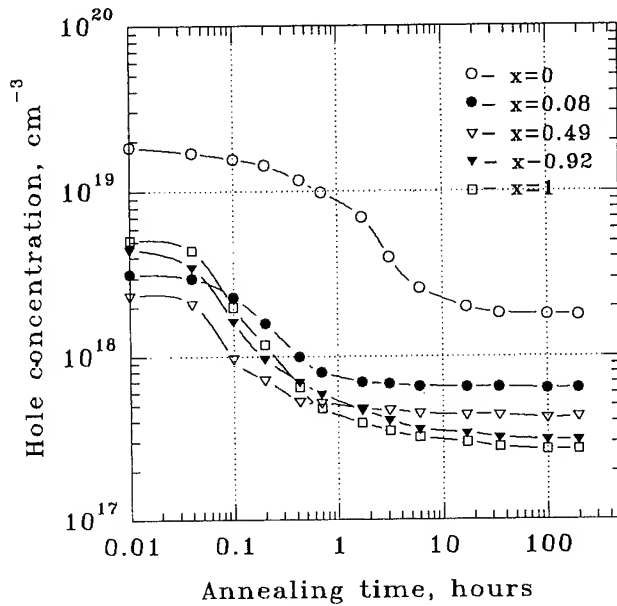


Fig.3 Kinetic curves of isothermal annealing of p-type $\text{PbSe}_{1-x}\text{Te}_x$ at 523 K.

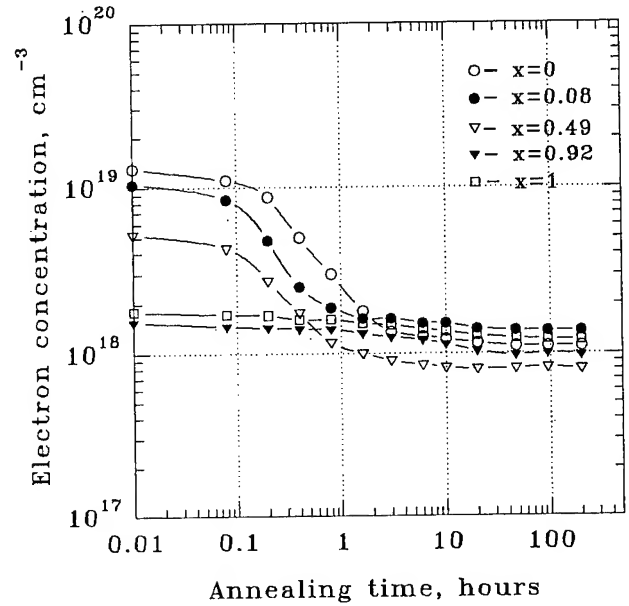


Fig.5 Kinetic curves of isothermal annealing of n-type $\text{PbSe}_{1-x}\text{Te}_x$ at 673 K.

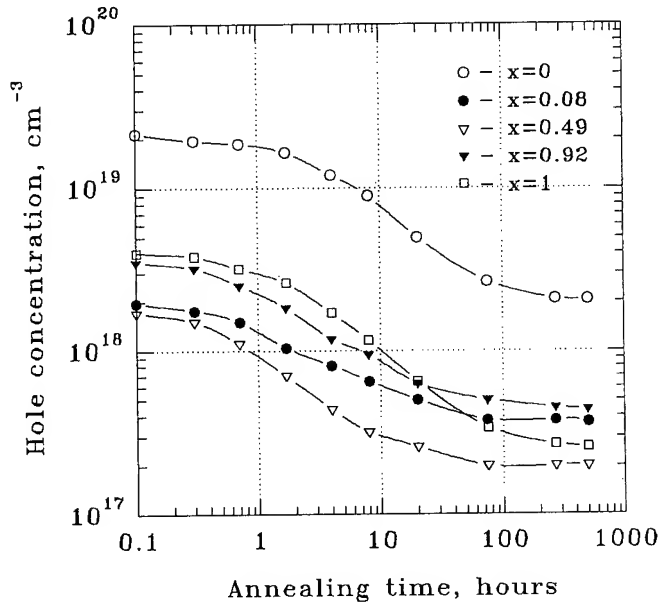


Fig.4 Kinetic curves of isothermal annealing of p-type $\text{PbSe}_{1-x}\text{Te}_x$ at 473 K.

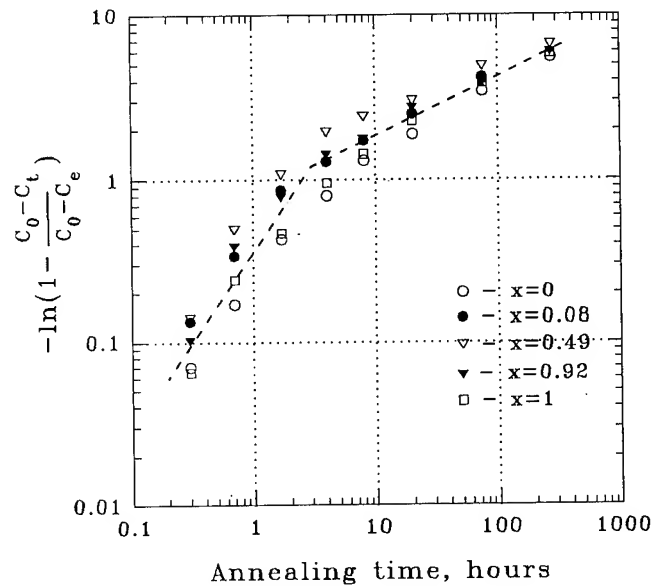


Fig.6 Fraction precipitated vs. annealing time for n-type $\text{PbSe}_{1-x}\text{Te}_x$ at 473 K.

the chalcogens have precipitated another kinetic process becomes rate-controlling as evidence by the change in slope to a value n in the range of 0.25-0.35.

From the straight-line parts of kinetic curves at 473K and 523 K the activation energies for precipitation of chalcogens were estimated. The first and second stages of precipitation are characterized by the activation energy of 0.85-0.9 eV and 1.2-1.4 eV, respectively, depending on sample composition. The activation energies of chalcogen diffusion was reported for p-type PbSe as 1.33 eV [8] or 1.2 eV [9] and for p-type PbTe as 1.04 eV [10] or 0.75 eV [9]. The close agreement the activation energy of diffusion and that of precipitation is evidence that diffusion plays an important role in the precipitation of chalcogens in $\text{PbSe}_{1-x}\text{Te}_x$ solid solution.

According to the theory of diffusion-limited precipitation [7] the value of $n=1$ is indicative of cylindrically shaped particles precipitated on dislocations. The value of slope (n) less than 1 indicates that the number of precipitation sites is diminishing with time or that the precipitation process is being supplanted by one or more slower competing processes leading to a lower carrier concentration. Such processes may be considered to be an interaction of point defects to form polyatomic molecules or polyvacancies, which may not carry a charge.

It may be noted that the estimated precipitation rate of the chalcogens at 673 K is two or three orders of magnitude faster than precipitation rate of lead in spite of the diffusion of lead is more than an order of magnitude faster than that of chalcogens [8]-[10]. This fact can be explained taking into account the predominant point defects which exist in n- and p-type lead chalcogenides. The possible model of predominant point defects in lead chalcogenides is based on the model of Frenkel disorder in metal sublattice [8, 10, 11], i.e. lead interstitials for n-type and lead vacancies for p-type. Therefore, if precipitation occurs by nucleation on vacancies then the number of vacancies, available as nucleation sites would be many orders of magnitude greater for chalcogen precipitation than for lead precipitation.

Conclusions

The present study shows that the crystals of lead chalcogenides become thermodynamically nonequilibrated when an initial concentration of excess component exceeds the maximum solubility of the component at operating temperature. This nonequilibrium results in precipitation of supersaturated component to electrically inactive state. The same phenomena can take place in case of doping of a compound with an excess of foreign electroactive dopant.

At temperatures 500-600 K the precipitation kinetic in lead chalcogenides is fast enough to diminish the concentration of supersaturated components to an order of magnitude and complete the precipitation process for one hundred hours. This changes cause the uncontrollable degradation of device characteristics during operation. Therefore, to improve the reliability of the materials operating at

relatively high temperatures an attention should be paid to the problem of possible supersaturation with a component or dopant due to a retrograde solubility.

References

- [1] W.W.Scannon, "Precipitation of Te and Pb in PbTe" *Phys. Rev.*, vol. 126, No. 2, pp. 509-513 (1962).
- [2] S.Scherrer, M.Rodot, M.Schneider, P.Manet, "Precipitation of selenium from lead selenide" *J.Phys.Lett.*, vol. 35, No. 2, pp. L15-L18 (1974).
- [3] V.Fano, "Precipitation in chalcogenides of groups II and IV" *J.Cryst.Growth*, vol. 106, pp.510-512 (1990).
- [4] V.L.Kuznetsov, A.M.Gas'kov, V.P.Zlomanov, A.V.Novoselova, "The growth of single crystals and determination of the solidus surface coordinates of the solid solution Pb-Se-Te" *Inorganic Materials*, vol.20, No. 9, pp. 1483-1485 (1984) (in Russian).
- [5] N.Chou, K.Komarek, E.Miller, "Retrograde solubility of PbS, PbSe, and PbTe" *Trans.Met.Soc. AIME*, vol. 245, No. 7, pp. 1553-1560 (1969).
- [6] D.Shaw, "The precipitation and out-diffusion of a solute in a solid during cooling" *Phys.stat.sol.(a)*, vol.60, No.1, pp. 251-263 (1980).
- [7] F.S.Ham, "Theory of diffusion-limited precipitation" *J.Phys.Chem.Solids*, vol.6, pp.335-351 (1958).
- [8] R.L.Guldi, J.N.Walpole, R.N.Rediker, "Diffusion of Pb and Se in PbSe" *J.Appl.Phys.*, vol.44, No. 11, pp. 4896-4907 (1973).
- [9] B.I.Boltaks, Yu.N.Mokhov, "Selfdiffusion and diffusion of impurities in lead telluride and lead selenide" *Soviet J.Tech.Phys.*, vol. 28, No. 5 pp. 1047-1050 (1958) (in Russian).
- [10] M.P.Gomez, D.A.Stevenson, R.A.Huggins, "Self-diffusion of Pb and Te in lead telluride" *J.Phys. Chem. Solids*, vol. 32, No. 2, pp. 335-344 (1971).
- [11] T.D.George, J.B.Wagner, "Trace diffusion of lead in lead telluride" *J.Appl.Phys.*, vol. 42, No. 1, pp.220-221 (1971).

High Efficient Program and Carrier Concentration FGM Thermoelectric Materials in the Intermediate Temperature Region

Y.Noda⁽¹⁾, M.Orihashi⁽¹⁾, H.Kaibe⁽²⁾, Y.Imai⁽³⁾, I.Shiota⁽⁴⁾ and I.A.Nishida⁽³⁾

(1)Tohoku University, Sendai 980-77, Japan

(2)Tokyo Metropolitan University, Tokyo 192-03, Japan

(3)Kogakuin University, Tokyo 192, Japan

(4)National Research Institute for Metals, Ibaraki 305, Japan

Abstract

As a part of the national project in Japan, the experimental examination and investigation have been carried out on PbTe compounds and their functionally graded material(FGM) with a view to an enhancement of thermoelectric energy conversion efficiency. The experiments consist of preparation and thermoelectric characterization of n-type PbTe melt-grown and sintered non-FGM and FGM. The electron concentration in the non-FGM single crystals was controlled in the range from 5×10^{23} to $5 \times 10^{25} / \text{m}^3$ by doping 700-6000 molppm PbI_2 . The FGM structure for PbTe was obtained through the unidirectional solidification in a special growth ampule by doping 1500 and 3400 molppm PbI_2 , in which carrier concentration varied continuously along the growth direction in one order of magnitude. An electron concentration at the bottom end of the FGM ingot doped with 1500 molppm PbI_2 was $0.82 \times 10^{25} / \text{m}^3$, and the figure of merit was estimated to be $2 \times 10^{-3} / \text{K}$ at 410 K. A 3-stage segmented FGM was prepared by hot-pressing subsequently the layers with electron concentrations of 3.6 , 2.6 and $2.2 \times 10^{25} / \text{m}^3$. It is found that the temperature dependence of electric figure of merit ($\alpha^2 \sigma$) for the sintered FGM showed a broad peak and never came lower than those for the component non-FGM. The results indicate that high efficiency in thermoelectric energy conversion will be expected for well-designed FGM structure.

Introduction

The figure of merit (Z) for a homogeneous thermoelectric material reaches its maximum (Z_{opt}) at a certain optimum temperature (T_{opt}), and rapidly decreases on deviation from T_{opt} [1]-[3]. Therefore, the thermoelectric materials are selected for low (less than 450 K), intermediate (450-840 K) and high temperature (more than 900 K), respectively.

Lead telluride is still among the best material used in construction of thermoelectric generators working at intermediate temperate. The PbTe generators were developed as the special application in space exploration in 1960's, and now constitute the power supply unit using heat of gas

combustion[2][3].

As for a thermoelement arm, Z_{opt} shifts from low to high temperature side with an increase of carrier concentration. Thus, a continuous control of carrier concentration along the temperature profile in the arm is expected to attain high conversion efficiency[4][5].

The present study pursued possibility to attain high efficiency by inspecting the existing data of Z values reported for n-type PbTe and performing the preparation of a functionally graded materials(FGM) with the carrier concentration and the investigation into the thermoelectric properties.

Inspection into high efficiency by FGM

Figure 1 shows the relationship between dimensionless figure of merit (ZT) and carrier concentration for n-type PbTe. The thin solid lines correspond to the relationships estimated on the basis of the experimental data for the homogeneous material measured by Stavitskaya[6], which show that the temperature (T_{max}) at the maximum ZT -value ($(ZT)_{\text{max}}$) in each curve shifts to high temperature side with an increase of electron concentration. The arrow indicates T_{opt} , which also shifts to high temperature side with an increase of electron

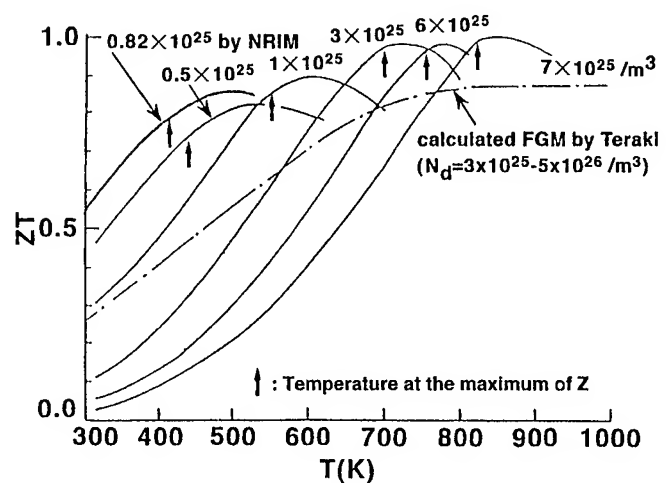


Fig.1 Temperature dependence of dimensionless figure of merit ZT for n-type PbTe.

concentration. For the practical application of the PbTe homogeneous thermoelectric material, the carrier concentration is adjusted at $n_{\text{opt}} = 3.5 \times 10^{25} \text{ m}^{-3}$, where the peak area in the Z-T curve is the largest.

The dashed line in the Fig.1 indicates the temperature dependence of $(ZT)_{\text{max}}$ calculated by Teraki[7] as a function of donor concentration in FGM. The curve shows that the high ZT or Z value can be expected in the wide temperature range for the FGM with the carrier concentration gradient. However, the calculation also shows that an increase of ZT value can not be expected below the T_{opt} at $n_{\text{opt}} = 3 \times 10^{25} \text{ m}^{-3}$. The observed high $(ZT)_{\text{max}}$ values at $T < 450 \text{ K}$ may have been caused from the temperature dependence of the physical properties in lead chalcogenides, which are the mobility(μ) proportional to $T^{-2.5} \sim T^{-3.5}$ and the decrease of the energy gap(E_g) with a decrease of temperature.

Experimental

The experiments consisted of the preparation and the thermoelectric characterization of the n-type PbTe of melt-grown and sintered non-FGM and FGM. The iodine doped single crystals(melt-grown non-FGM) were grown by the conventional Bridgman method after direct melting of constituent elements of Pb and Te(nominal purity of 99.9999 %). The growth ampule was made of quartz tube with dimension of 10 mm ID and 120 mm length. The weighed amount of the elements in the stoichiometric composition ($\text{Pb/Te}=1$) was vacuum sealed in the ampule with PbI_2 as the source of n-type dopant of iodine. The amount of the dopant was controlled by weighing 100 to 16000 molppm of PbI_2 . The growth was performed in the vertical electric furnace, the condition of which was the maximum temperature of 1223 K, the temperature gradient of about 1200 K/m at the melting point and the growth rate of 4 mm/h.

The melt-grown FGM was made by unidirectional solidification in the growth system shown in Fig. 2. The source elements and the dopant PbI_2 were vacuum sealed and melted in the ampule of the special shape. The melt was stirred sufficiently using the rocking and freezing furnace, and then solidified by cooling in the furnace under controlled temperature profile without mechanical motion. The temperature gradient and the cooling rate were 0.8 K/mm and 10 K/h, respectively. The FGM structure resulted due to the segregation of dopant.

On preparing the homogeneous sintered material, a part of melt-grown FGM was cut and ground, and then sieved at the powder size of 74-124 μm . The resultant powder was poured

into a mold and hot-pressed for 15 min at 1100 K under 3.3 MPa. The sintered FGM with 3-stage segmented structure was prepared by direct hot-press of three sections subsequently with high, medium and low electron concentrations. Each layer was adjusted to have a thickness of about 2 mm and a carrier concentration listed in Table 1.

The electrical conductivity(σ) and Hall coefficient(R_H) were measured by van der Pauw configuration using the Pt-wire electrode. All the carrier concentration was calculated using the equation $n = 1/eR_H$ (e: electric charge). The thermoelectric power(α) at room temperature was estimated from the linear relationship between thermoelectromotive force(EMF) and temperature difference within 5 K. The temperature dependence of thermoelectric properties was measured by using Pt-13 %Rh thermocouples under the temperature difference within 1 K, where Pt wire was adopted for the EMF probes. The thermal conductivity(κ) at room temperature was measured by the static comparison method using fused silica.

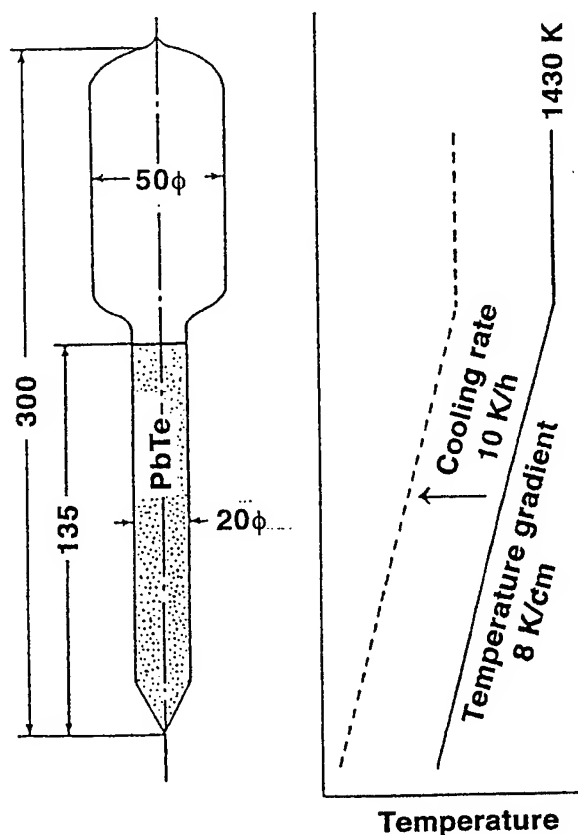


Fig.2 Schematic diagram of growth ampule and temperature profile for unidirectionally solidified FGM with a carrier concentration graded structure.

Results and discussion

A non-FGM ingot of undoped melt-grown PbTe was p-type with hole concentration of $3.1 \times 10^{24} \text{ m}^{-3}$. Figure 3 shows the relationship between carrier concentration and amount (M) of PbI_2 . At $M=750$ molppm, the conduction type changed from p- to n-type, and then carrier concentration monotonously increased with an increase of M. The solid line was drawn by assuming that an I atom occupies a Te site and acts as a singly ionizable donor. The electron concentration (n_e) was found to be controlled in the region of $n_e = 5 \times 10^{24} - 5 \times 10^{25} \text{ m}^{-3}$ at $M=700-6000$ molppm.

The relationship between n_e and position from the bottom end in the unidirectionally solidified ingots is shown in Fig. 4. The two ingots doped with 1500 and 3400 molppm PbI_2 resulted in the FGM structure of carrier concentration with $n_e = 0.82 \times 10^{24}$ and $2.21 \times 10^{25} \text{ m}^{-3}$ near at the bottom end A1 in the figure, respectively. In spite of the large difference in electron concentration between the two ingots, the Hall mobility was almost equal to $0.12 \text{ m}^2/\text{Vs}$.

Figure 5 shows the temperature dependence of the electric figure of merit (power factor, $\alpha^2 \sigma$) for the samples at A1 ($n_e = 0.820 \times 10^{25} \text{ m}^{-3}$) and B1 ($n_e = 0.153 \times 10^{25} \text{ m}^{-3}$) cut from the melt-grown FGM ingot doped with 1500 molppm PbI_2 . The maximum $\alpha^2 \sigma$ value for the sample A1 was $4.4 \times 10^{-3} \text{ W/K}^2 \text{ m}$ at 410 K, while the curve for B1 was low lying because of the low carrier concentration. The figure of merit estimated using the thermal conductivity of $\kappa = 2.15 \text{ W/mK}$ [8] was $2.0 \times 10^{-3} / \text{K}$. The ZT value for A1 was by 1.5 times larger than the existing data as shown in Fig. 1, which was comparable to that for the low-temperature thermoelectric material of the Bi-Te system.

The thermoelectric data measured for the sintered non-FGM were listed in Table 1 as the component materials (a), (b) and (c) for the FGM with high, medium and low carrier concentration, respectively. In the 3-step segmented FGM, the component layers were arranged from (a) for high temperature to (c) for low temperature through (b) for medium temperature.

The values of α and resistivity (ρ) for the FGM at room temperature were 128.2 mV/K and $7.91 \times 10^{-5} \Omega \text{ m}$, respectively, which exceeded those for each component layer. The high resistivity in case of the FGM may have been caused from the hot-pressing process, but the origin has not yet been clarified. The similar characteristic feature has been observed at

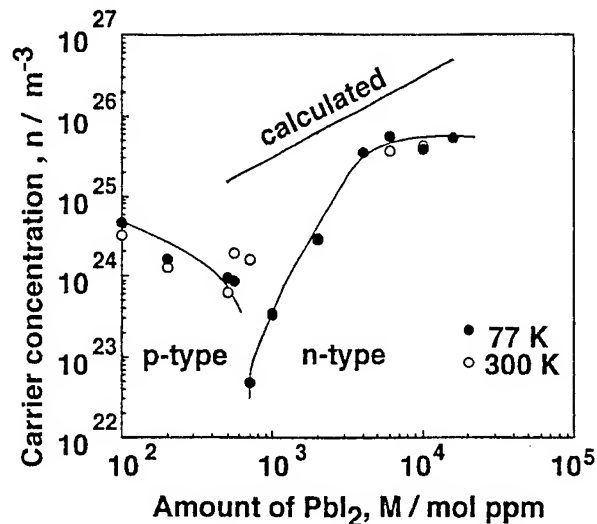


Fig.3 Plots of carrier concentration versus amount of PbI_2 in melt-grown PbTe single crystals.

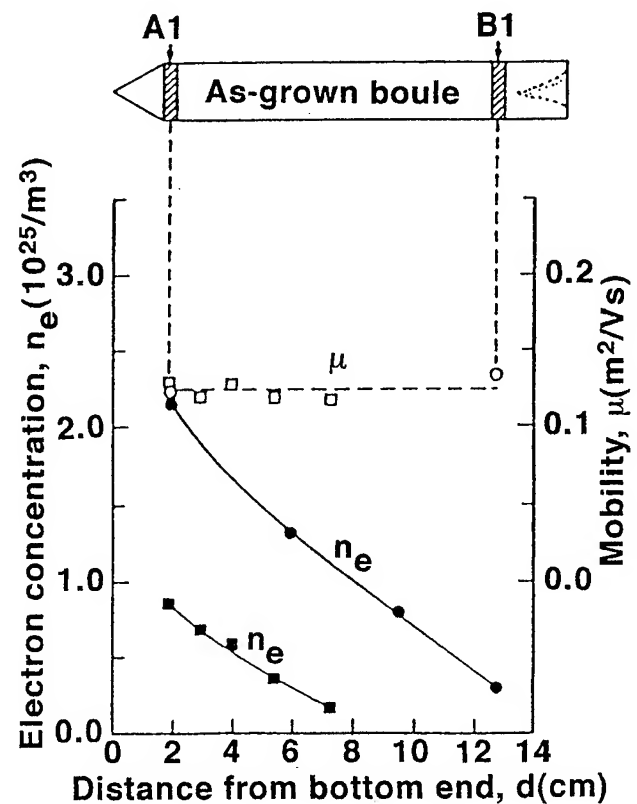


Fig.4 Plots of electron concentration n_e and mobility μ versus distance from the bottom end in the unidirectionally solidified FGM boules. The samples A1 and B1 were cut from the bottom and top ends, respectively. (■) and (●) for PbTe FGM doped with 1200 and 3400 molppm PbI_2 , respectively.

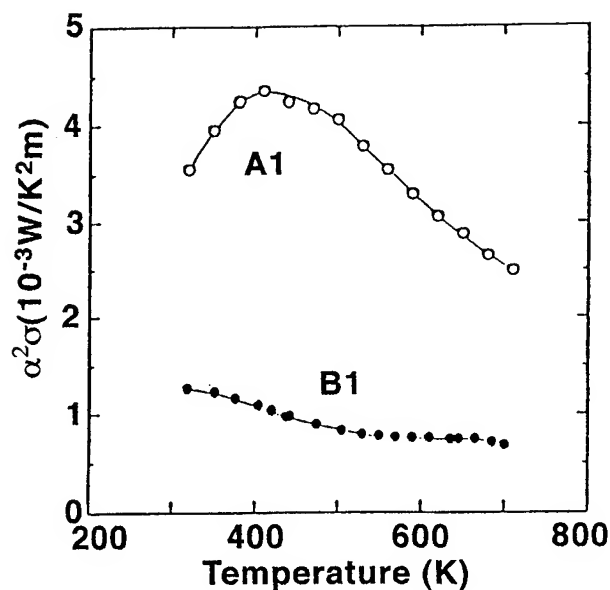


Fig.5 Temperature dependence of electrical figure of merit $\alpha^2\sigma$ for a unidirectionally solidified n-type PbTe FGM doped with 1500 molppm PbI_2 . A1 and B1 stand for the bottom and top end, respectively.

the interface of adjacent layers[9] in the 2-stage segmented Si-Ge FGM.

Figure 6 shows the temperature dependence of the resistivity for the sintered FGM and its component non-FGM samples of (a), (b) and (c). The resistivity of all the samples increased with an increase of temperature, indicating that the samples are the typical degenerated semiconductors. It is found that the FGM exerted its effect by a gradual increase in resistivity at high temperature compared with the cases of non-FGM samples.

Figure 7 and 8 show the temperature dependence of α and $\alpha^2\sigma$, respectively. The α curves for (a) and (b) monotonously increased with an increase of temperature, while that for the FGM showed a decrease of inclination at high temperature as was the case of resistivity. Each $\alpha^2\sigma$ curve showed the

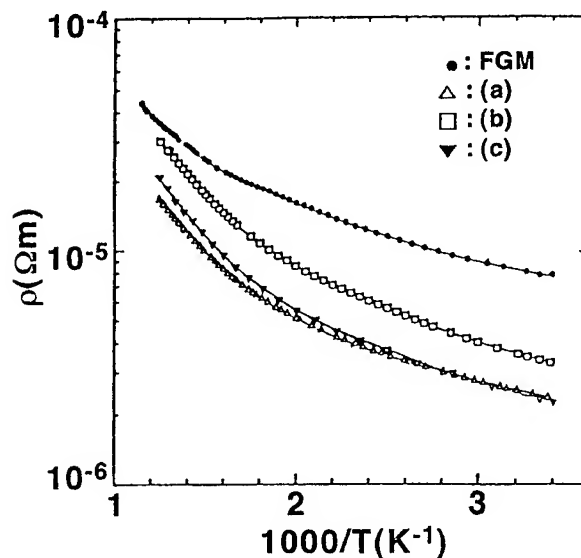


Fig.6 Temperature dependence of resistivity ρ for 3-stage segmented PbTe FGM shown with those for the component materials (a), (b) and (c) with different electron concentrations listed in Table 1.

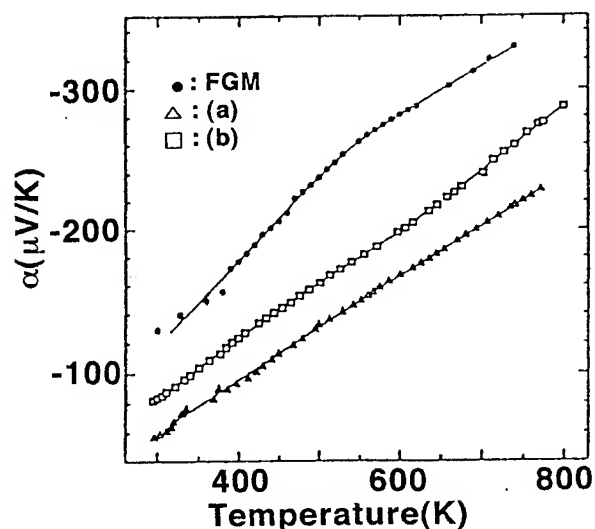


Fig.7 Temperature dependence of thermoelectric power α for 3-stage segmented PbTe FGM shown with those for the component materials (a) and (b) with different electron concentrations listed in Table 1.

Table 1 Thermoelectric properties of the 3-stage segmented PbTe FGM and its component materials(a), (b) and (c) at room temperature.

Sample	$\alpha(\text{mV/K})$	$\rho(10^{-6} \Omega \text{m})$	$R_H(10^{-6} \text{m}^3/\text{C})$	$n_e(10^{25} / \text{m}^3)$	$\mu_e(\text{m}^2/\text{Vs})$	$\alpha^2\sigma(\text{W/K}^2\text{m})$
(a)	-60.5	2.540	1.78×10^{-7}	3.51	7.00×10^{-2}	1.44×10^{-3}
(b)	-71.1	2.831	2.30×10^{-7}	2.60	8.12×10^{-2}	1.79×10^{-3}
(c)	-83.4	3.342	2.75×10^{-7}	2.26	8.22×10^{-2}	2.08×10^{-3}
FGM	-129.2	7.91	--	--	--	2.11×10^{-3}

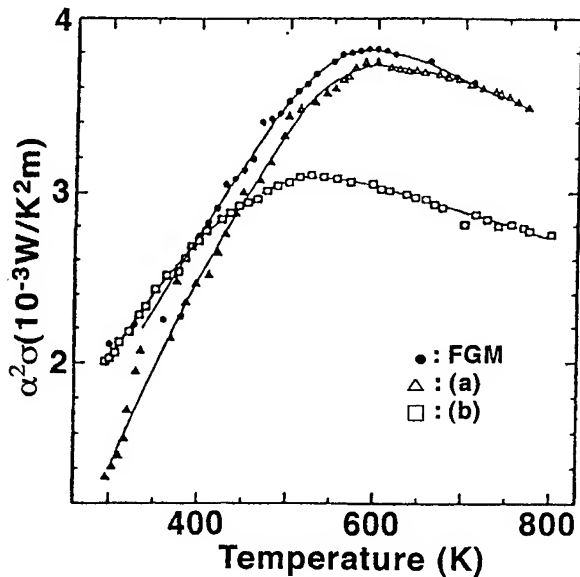


Fig.8 Temperature dependence of electrical figure of merit $\alpha^2\sigma$ for the 3-stage segmented PbTe FGM shown with those for the component materials (a) and (b) with different electron concentrations listed in Table 1.

maximum, the position of which was about 800 K for (a) and the FGM, while about 500 K for (b). At $T < 450$ K, the $\alpha^2\sigma$ value for (b) was larger than that for (a). The $\alpha^2\sigma$ value for the FGM never came lower than those for the non-FGM of (a) and (b) in the measured temperature range. By using the κ value of 2.95 W/mK measured for the-FGM at room temperature, the Z_{max} was estimated to be $1.29 \times 10^{-3} / \text{K}$, which was comparable to that of $1.43 \times 10^{-3} / \text{K}$ for the non-

FGM sample with optimum carrier concentration $n_e = 3 \times 10^{25} / \text{m}^3$. The effect of the FGM was also found in the broadening of the peak in the $\alpha^2\sigma$ -T curve, which is favorable to enhance the conversion efficiency. The results indicate the possibility to realize high efficiency of energy conversion with the well designed FGM structure.

References

- [1] I.B. Cardoff and E. Miler, Thermoelectric Materials and Devices, New York, Reinhold Publishing Co., (1960).
- [2] D.M. Rowe and C.M. Bhandari, Modern Thermoelectrics, London, Holt, Rinehart and Winston, (1983).
- [3] K. Uemura and I.A. Nishida, Thermoelectric Semiconductors and Their Applications, Nikkan Kogyo, (1988).
- [4] R.W Fritts, Direct Conversion of Heat to Electricity, eds. J.Kaye and J.A.Welsh, John Wiley, New York, p.1(1960).
- [5] M.Niino and L.Chen, Projected Research on High-Efficiency Hybrid Direct Energy Conversion System, Proc. 12ICT, Yokohama, p.527(1993).
- [6] T.S. Stavitskaya, Semiconducting Lead Chalcogenides, ed. Yu.I. Ravich, B.A.Efimova and I.A. Smirov, Plenum, New York, p.326(1970).
- [7] J. Teraki, Proc. 23rd FGM Workshop, FGM Society, p.13 (1994).
- [8] K. Sato, I. Shiota and I.A. Nishida, Proc. FGM Symposium(FGM94), p.189(1994).
- [9] K. Takahashi, T. Masuda, T. Mochimaru, T. Noguchi, Proc. FGM Symposium(FGM95), (1994), in print.

A Low Thermal Conductivity Compound for Thermoelectric Applications: β - Zn_4Sb_3

Thierry Caillat*, Jean-Pierre Fleurial, and Alex Borshchevsky
Jet Propulsion Laboratory/California Institute of Technology
4800 Oak Grove Drive
Pasadena, CA 91109 USA
*e-mail: thierry.caillat@jpl.nasa.gov

Abstract

The potential of the semiconducting compound β - Zn_4Sb_3 for thermoelectric energy conversion was investigated. The thermoelectric properties were measured on hot-pressed samples characterized by x-ray and microprobe analysis. All samples had p-type conductivity and the thermoelectric properties of the samples were measured between room temperature and 400°C. Exceptionally low thermal conductivity values were measured and the room temperature lattice thermal conductivity was estimated at $7 \text{ mW cm}^{-1} \text{ K}^{-1}$. High figures of merit were obtained between 200 and 400°C and a maximum dimensionless thermoelectric figure of merit ZT of about 1.3 was obtained at a temperature of 400°C. The stability of the compound was investigated by thermogravimetric studies and showed that the samples were stable under Ar atmosphere up to about 400°C and up to 250°C in dynamic vacuum. The high thermoelectric performance of β - Zn_4Sb_3 in the 200 to 400°C temperature range fills the gap established in the ZT spectrum of p-type state-of-the-art thermoelectric materials between Bi_2Te_3 -based alloys and PbTe-based alloys. This material, relatively inexpensive, could be used in more efficient thermoelectric generators for waste heat recovery and automobile industry applications, for example.

Introduction

Thermoelectric generators convert heat energy directly into electrical energy without moving parts. They are reliable, operate unattended in hostile environments and are also environmentally friendly. However, their applications have been limited until now because of the relatively low efficiency of the thermoelectric materials as well as their relatively high cost. New more efficient materials should be developed in order to expand the range of applications of thermoelectric generators. For applications such as heat recovery from processing plants of combustible solid waste, the materials have also to be inexpensive enough to make the thermoelectric power generation a viable option. Many new potential applications of thermoelectric generators have been recently described in the literature. For many of these applications, the heat source temperature ranges between 100 and about 400°C where there exists a gap in ZTs between the low temperature state-of-the-art thermoelectric materials (Bi_2Te_3 -based alloys) and the intermediate temperature materials (PbTe-based alloys) and TAGS (Te-Ag-Ge-Sb). Therefore, it is important to develop efficient thermoelectric materials in this temperature range.

Based on literature data and theoretical considerations, several new materials were investigated over the past few years as potential new thermoelectric materials at JPL. Several of these new materials have shown interesting potential for thermoelectric applications [1]. As part of this broad search for more efficient thermoelectric materials, we have prepared and investigated the properties of the semiconducting compound β - Zn_4Sb_3 . Three compounds have been well identified in the system Zn-Sb: ZnSb stable up to the melting point (546°C), Zn_3Sb_2 , metastable, and Zn_4Sb_3 , stable, which melts congruently at 566°C [2,3]. For Zn_4Sb_3 , three modifications are known: α -, β -, γ - Zn_4Sb_3 which are stable below -10°C, between -10 and 492°C, and above 492°C, respectively. The phase diagram has been re-investigated by Mayer et al. [2]. β - Zn_4Sb_3 is a hexagonal rhombohedral compound, space group $R\bar{3}C$ with $a = 12.231 \text{ \AA}$ and $c = 12.428 \text{ \AA}$ [2,4]. The unit cell contains 66 atoms.

A few investigations of the electrical and thermoelectric properties of β - Zn_4Sb_3 were performed [4-6] but the results were sometimes contradictory. Some attempts were also made to dope the compound with various impurities [7]. The optical properties were investigated and an optical band gap of about 1.2 eV was measured [4], in agreement with some estimations made from high temperature electrical measurements [5]. To our knowledge, the only thermal conductivity data available in the literature was published by Spitzer [8] who reported a room temperature lattice thermal conductivity value of $6.5 \text{ mW cm}^{-1} \text{ K}^{-1}$ on a polycrystalline sample of unknown density.

Experimental

Single phase, polycrystalline hot-pressed samples of β - Zn_4Sb_3 were prepared from pre-reacted mixtures of zinc (99.9999% pure) and antimony (99.999% pure). The samples (about 12 mm in diameter and about 2 cm long) were of good mechanical strength. The density of the samples was measured by the immersion technique using toluene as the liquid. The density of the hot-pressed sample was typically between 95 and 97% of the theoretical density. The microstructure of the samples, polished by standard metallographic techniques, was investigated using a Nikon optical microscope under both ordinary and polarized light. The microprobe analysis of selected samples was performed on a JEOL JXA-733 superprobe. XRD analyses were performed on a Siemens D-500 diffractometer using $\text{Cu-K}\alpha$ radiation with silicon as a standard. The thermal expansion coefficient was measured using a standard dilatometer.

Resistivity and Hall effect measurements were conducted on samples between room temperature and about 400°C. The high temperature resistivity (ρ) was measured using the van der Pauw technique with a current of 100 mA using a special high temperature apparatus [9]. The Hall coefficient (R_H) was measured in the same apparatus with a constant magnetic field value of 8000 Gauss. Assuming a scattering factor of 1 in a single carrier scheme, the carrier density was calculated from the Hall coefficient by $p = 1/R_H e$ where p is the density of holes and e is the electron charge. The Hall mobility (μ_H) was calculated from the Hall coefficient and the resistivity values by $\mu_H = R_H/\rho$. The error was estimated at $\pm 0.5\%$ and $\pm 2\%$ for the resistivity and Hall coefficient measurements, respectively. The Seebeck coefficient of the samples was measured on the same samples used for resistivity and Hall coefficient measurements using a high temperature light pulse technique [10]. The error of measurements of the Seebeck coefficient was estimated to be less than $\pm 1\%$. The thermal conductivity of the samples was calculated from the experimental density, heat capacity and thermal diffusivity. The heat capacity and thermal diffusivity were measured using a flash diffusivity technique [11] and the overall error in the thermal conductivity measurement was about $\pm 10\%$.

Results and Discussion

A total of about 30 samples were prepared and their properties measured. All samples had p-type conductivity and were heavily doped with similar thermoelectric properties and little variation in carrier concentration. The typical room temperature properties of hot-pressed β -Zn₄Sb₃ are listed in Table 1. The Hall mobility and Seebeck coefficient values are relatively large at this doping level. Hall mobility values in the order of $1000 \text{ cm}^2 \text{ V}^{-1} \text{ s}^{-1}$ were reported by Ugai et al. [5] at a doping level of $8.8 \times 10^{17} \text{ cm}^{-3}$ but were in contradiction to some results obtained later also by Ugai et al. [6]. The complexity of the Zn-Sb phase diagram makes the preparation of single phase samples difficult and might explain the discrepancies in the results. Unfortunately, no details were given by Ugai et al. [5] on the composition analysis of their samples.

Table 1. Some room temperature properties of β -Zn₄Sb₃

Property	β -Zn ₄ Sb ₃
Melting point (C)	566 [2,5]
Type of formation from the melt	congruent [2,5]
Structure type	hexa. rhom. [2,3]
Number of atoms/unit cell	66 [2]
Lattice parameter	$a=12.231, c=12.428\text{\AA}$ [2]
X-ray density (g cm^{-3})	6.077
Thermal expansion coefficient (C^{-1})	1.93×10^{-5}
Energy band gap (eV)	1.2 [3,4]
Conductivity type	p
Electrical resistivity ($\text{m}\Omega \text{ cm}$)	2
Hall mobility ($\text{cm}^2 \text{ V}^{-1} \text{ s}^{-1}$)	30
Hall carrier concentration (cm^{-3})	9×10^{19}
Seebeck coefficient ($\mu\text{V K}^{-1}$)	120
Thermal conductivity ($\text{mW cm}^{-1} \text{ K}^{-1}$)	9

Typical temperature dependence of the thermoelectric properties of hot-pressed β -Zn₄Sb₃ samples are shown in Fig. 1 (electrical resistivity), Fig. 2 (Seebeck coefficient), and Fig. 3 (power factor values). The Seebeck coefficient and electrical resistivity increase up to about 350°C where an onset of mixed conduction seems to appear, lowering the electrical resistivity and Seebeck coefficient. However, the intrinsic behavior is difficult to establish definitively because of the small temperature range where it seems to occur. Measurements were limited to 400°C because of transformation from the β to γ phase at higher temperatures. The results of the Seebeck coefficient measurements are in agreement with the results of Tapiero et al. [4]. A maximum power factor of $12.5 \mu\text{W cm}^{-1} \text{ K}^{-2}$ was calculated at 350°C.

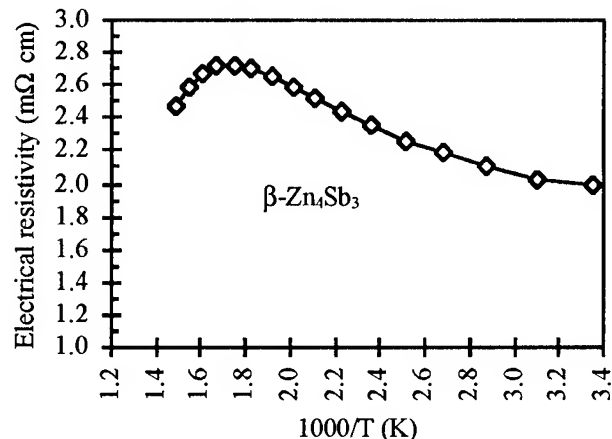


Figure 1: Typical electrical resistivity values as a function of inverse temperature for p-type β -Zn₄Sb₃

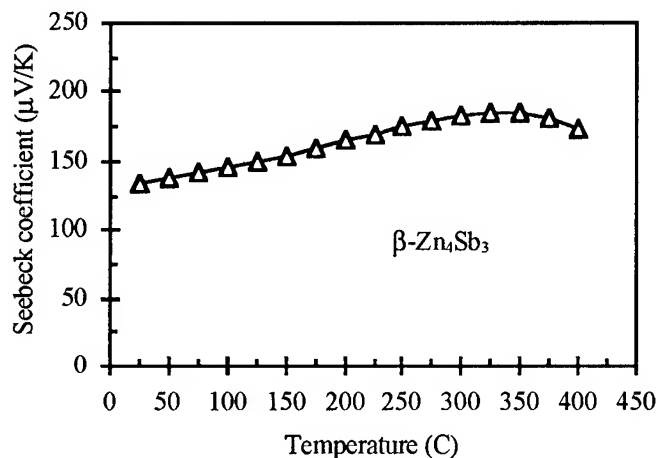


Figure 2: Typical Seebeck coefficient values as a function of temperature for p-type β -Zn₄Sb₃

Fig. 4 shows the thermal conductivity values of β -Zn₄Sb₃ between room temperature and about 250°C. The values for state-of-the-art p-type thermoelectric materials PbTe- and Bi₂Te₃-based alloys as well as TAGS (Te-Ag-Ge-Sb alloys) are also shown for comparison. The room temperature value is about $9 \text{ mW cm}^{-1} \text{ K}^{-1}$ for β -Zn₄Sb₃ samples. The thermal conductivity decreases to about $6 \text{ mW cm}^{-1} \text{ K}^{-1}$ at 250°C.

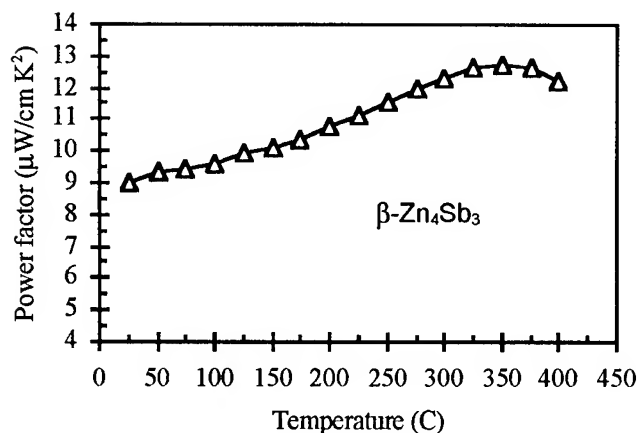


Figure 3: Typical power factor values (α^2/ρ) as a function of temperature for p-type $\beta\text{-Zn}_4\text{Sb}_3$

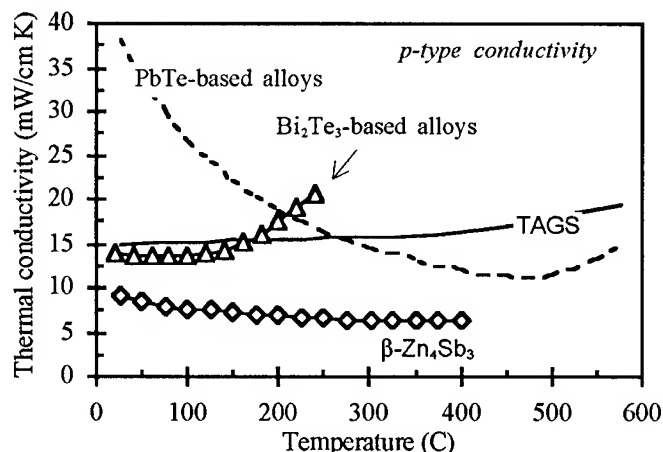


Figure 4: Typical thermal conductivity values as a function of temperature for p-type $\beta\text{-Zn}_4\text{Sb}_3$. Results are compared to state-of-the-art p-type thermoelectric materials PbTe- and Bi_2Te_3 -based alloys, and also TAGS (Te-Ag-Ge-Sb alloys).

Low thermal conductivity is one of the most interesting feature of $\beta\text{-Zn}_4\text{Sb}_3$. This is the lowest of all the thermoelectric materials known until now. As we mentioned before, the only value reported in the literature for $\beta\text{-Zn}_4\text{Sb}_3$ was a room temperature lattice thermal conductivity of $6.5 \text{ mW cm}^{-1} \text{ K}^{-1}$ [8] measured on a polycrystalline sample. We calculated a room temperature lattice thermal conductivity by subtracting the electronic component to the total thermal conductivity. We found a value of $7 \text{ mW cm}^{-1} \text{ K}^{-1}$, in good agreement with the literature results. The thermal conductivity values for $\beta\text{-Zn}_4\text{Sb}_3$ are typical of glass-like materials. This is due to its complex crystal structure and also most likely to the presence of some antistructure defects resulting in a highly disordered structure. However, glass-like materials have usually high electrical resistivity such as Ti_3AsSe_3 [12] which is not desirable to achieve high figure of merits. This is not the case for $\beta\text{-Zn}_4\text{Sb}_3$. In this compound, there is a unique combination of low thermal conductivity and good electrical resistivity which makes it a very interesting thermoelectric

material. The analysis of the low thermal conductivity values will be the object of a separate publication.

The dimensionless thermoelectric figure of merit ZT is a function of the electrical resistivity (ρ), the Seebeck coefficient (α) and the thermal conductivity (λ):

$$ZT = \alpha^2/\rho\lambda \quad (1)$$

The calculated figure of merit for several p-type $\beta\text{-Zn}_4\text{Sb}_3$ are shown in Fig. 5. This figure shows that there is a gap between the low temperature state-of-the-art thermoelectric materials (Bi_2Te_3 -based alloys) and the intermediate temperature materials (PbTe-based alloys) and TAGS (Te-Ag-Ge-Sb). P-type $\beta\text{-Zn}_4\text{Sb}_3$ fills in this gap in the 200 to 400°C temperature range.

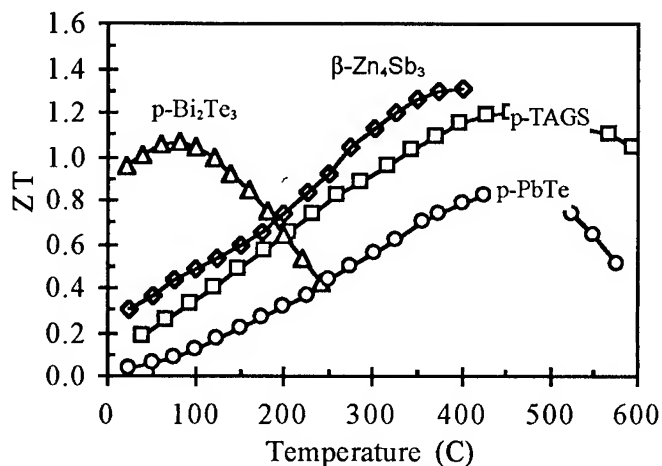


Figure 5: Dimensionless figure of merit ZT as a function of temperature for several p-type $\beta\text{-Zn}_4\text{Sb}_3$ samples. Results are compared to state-of-the-art p-type thermoelectric materials: PbTe- and Bi_2Te_3 -based alloys, and TAGS (Te-Ag-Ge-Sb alloys).

Although TAGS have also a good thermoelectric figure of merit in this temperature range, they have been little used due to their high sublimation rate and low temperature phase transition [13]. Thermogravimetric studies have shown that $\beta\text{-Zn}_4\text{Sb}_3$ samples did not loose any weight at all under argon atmosphere up to about 400°C and for up to 6 hours. Electrical resistivity measurements were conducted as a function of time in dynamic vacuum. It was found that no significant variations in electrical resistivity was observed for samples maintained at a temperature of 250°C for up to 5 days. Microprobe analysis of the same samples did not show any dissociation of the samples. However, for higher temperatures, some partial decomposition was observed in dynamic vacuum and some ZnSb inclusions were detected by microprobe analysis. The stability of the samples was also tested by annealing samples of $\beta\text{-Zn}_4\text{Sb}_3$ in sealed quartz ampoules under argon or vacuum at 400°C for about 5 days. In both cases, no significant changes in the electrical resistivity was found before and after the anneals and microprobe analysis of the annealed samples showed that no dissociation was observed. P-type $\beta\text{-Zn}_4\text{Sb}_3$ has the highest thermoelectric figure of merit in the 200 to 400°C temperature

range. Further improvements of the figure of merit could likely be obtained by optimizing the doping level of the samples. Also, for many applications using thermoelectric generators, the cost of the material is important. β -Zn₄Sb₃ is relatively inexpensive compared to state-of-the-art thermoelectric materials.

There are many potential applications for thermoelectric generators using β -Zn₄Sb₃. One of them is waste heat recovery. Large efforts in Japan have been recently initiated to develop thermoelectric power generation systems to recover waste heat from various sources: solid waste, geothermal, power plants and automobile [14]. Many potential applications have heat sources in the 100 to 400°C temperature range where the β -Zn₄Sb₃ thermoelectric properties are optimal. For example, a study of a thermoelectric generation system using the waste heat of phosphoric acid fuel cells was recently proposed [15]. In this system, the hot side of the heat source is at a temperature of about 200°C and the cold side is at room temperature. Another potential application was also recently described using geothermal heat from North Sea oil platforms [16]. Heat sources with temperatures between 100 to 200°C are available from these oil platforms and the potential use of a thermoelectric generator to recover this heat was described. The actual need for more efficient and cleaner cars has resulted in a strong interest from car manufacturers in recovering the waste heat generated by the vehicle exhaust to replace or supplement the alternator [17-19]. The temperature range for these applications would be in the 100 to 400°C temperature range where high ZT values have been measured on β -Zn₄Sb₃, and the relatively low cost of this material makes it an excellent candidate for these applications.

Conclusion

Thermoelectric properties of β -Zn₄Sb₃ were measured on hot-pressed samples. Exceptionally low thermal conductivity were measured and a maximum ZT value of 1.3 was measured at 400°C. The good thermoelectric performance of β -Zn₄Sb₃ fills a gap existing in ZT values between the low temperature state-of-the-art thermoelectric materials Bi₂Te₃-based alloys and the intermediate temperature materials PbTe-based alloys and TAGS (Te-Ag-Ge-Sb). The stability of the material was studied and it was found that the thermoelectric properties remain stable up to 400°C under static vacuum and argon. This material, relatively inexpensive, could be used in thermoelectric and generators and a brief description of the numerous potential applications was given.

References

1. T. Caillat, A. Borshchevsky and J. -P. Fleurial, this conference, 1996.
2. H. W. Mayer, I. Mikhail, and K. Schubert, *J. Less Common Metals* 59, p. 43(1978).
3. V. Tydlit, *Czech. J. Phys.* 9, p. 638 (1959).
4. M. Tapiero, S. Tarabichi, J. G. Gies, C. Noguet, J. P. Zielinger, M. Joucla, J. Loison, M. Robino, and J. Henrion, *Solar Energy Materials* 12, p. 257 (1985).
5. Ya. A. Ugai, E. M. Averbakh, and V. V. Lavrov, *Sov. Phys. Solid State* 4, p. 2393 (1963).
6. Ya. A. Ugai, T. A. Marshakova, V. Ya. Shevchenko, and N. P. Demina, *Inorg. Mat.* 5, p. 1180 (1969).
7. V. I. Psarev and N. L. Kostur, *Izv. Vyssh. Ucheb. Zaved. Fiz.* 10, (2), p. 34 (1967).
8. D. Spitzer, *J. Phys. Chem. Solids* 31, p. 19 (1970).
9. J. McCormack and J. -P. Fleurial, in *Modern Perspectives on Thermoelectric and Related Materials*, edited by D. D. Alred, C. B. Vining and G. A. Slack, Materials Research Society, Pittsburgh, p. 135 (1991).
10. C. Wood, D. Zoltan, and G. Stapfer, *Rev. Sci. Instrum.* 56, p. 179 (1985).
11. J. W. Vandersande, C. Wood, A. Zoltan, and D. Whittenberger, *Thermal Conductivity*, Plenum Press, New York, p. 445 (1988).
12. M. D. Ewbank, P. R. Newman, and H. Kuwamoto, *J. Appl. Phys.* 53, (9), p. 6450 (1982).
13. E. Skrabek and D. S. Trimmer, "Properties of the General TAGS System", ed. by D. M. Rowe, CRC Press, Boca Raton, p. 267 (1995).
14. T. Kajikawa, K. Nozaki and T. Ohta, *Proceedings of the XIth International Conference on Thermoelectrics*, The university of Texas at Arlington, p. 175, October 7-9 (1992).
15. H. Hori, T. Ito, and Y. Kuzuma, *Proceedings of the XIIIth International Conference on Thermoelectrics*, Kansas City, Missouri, American Institute of Physics, AIP Conference No. 316, p. 497 (1995).
16. M. Rowe, *MTS Journal* 27, 3, p. 43 (1994).
17. J. C. Bass, N. B. Elsner, and F. A. Levitt, *Proceedings of the XIIIth International Conference on Thermoelectrics*, Kansas City, Missouri, American Institute of Physics, AIP Conference No. 316, p. 295 (1995).
18. E. Takanose and H. Tamakoshi, *Proceedings of the XIIth International Conference on Thermoelectrics*, Yokohama, Japan, November 9-11, p. 467 (1993).
19. D. T. Morelli, General Motors, private communication.

Acknowledgments

The work described in this paper was carried out at the Jet Propulsion Laboratory/California Institute of Technology, under contract with the National Aeronautics and Space Administration. The authors would like to thank Danny Zoltan and Andy Zoltan for thermoelectric property measurements.

Crystal growth of narrow gap semiconductors for thermoelectric applications

Ch. Kloc, K. Fess, W. Kaefer, K. Friemelt, H. Riaz-Nejad, M. Wendl, and E. Bucher
Faculty of Physics, University of Konstanz, P.O.Box 5560, D-78434 Konstanz, Germany.
Tel:49-7531-882967; Fax: 49-7531-883895; e-mail:christian.kloc@uni-konstanz.de

Abstract

Recently, there has been a growing interest in small integrated cooling units. This prompted us to establish a screening program for the search of new efficient thermoelectric materials requiring the optimization of figure of merit. Preparation and crystal growth experiments on possible thermoelectric compounds: TiNiSn, ZrNiSn, CoSb₃, SrAs₃, β -FeSi₂, FeSi, NiS, La₃Cu₃Sb₄, Ce₃Cu₃Sb₄, Gd₃Cu₃Sb₄, are presented. Single crystals of congruently melting compounds were obtained by the Czochralski or Bridgman techniques. The peritectic decomposing compounds were prepared by flux-growth. Low defect crystals were obtained by vapor transport. Whenever it was possible, more than one technique was studied for the preparation of the same compound. Transport properties and thermoelectric properties were measured and discussed.

Introduction

Due to the high thermoelectric figure of merit, $Z = S^2\sigma/\kappa$, (where S is the Seebeck coefficient, σ electrical conductivity and κ thermal conductivity), Bi₂Te₃, Bi-Sb, and PbTe compound semiconductors are currently used as cooling materials in thermoelectric devices working at near room temperatures. Unfortunately, this highest achieved Z is still too small for the wider use of thermoelectric coolers or generators. Therefore a search for new thermoelectric materials has been the goal for numerous recent studies.

To achieve a large Seebeck coefficient, electrical conductivity and small thermal conductivity, narrow band gap semiconductors with optimized mobility and carrier concentration are needed.

Table 1.

Semiconductor or semimetal	Example
Elements	Bi, Sb, Bi-Sb, Si-Ge
Tetrahedral coordinated	CdTe, HgTe,
Complex structure, low symmetry	Bi - Te,
Multi anions	Skutterudite, SrAs ₃ , borides
Transition metal, rare earth	La ₃ Cu ₃ Sb ₄ , Ce ₃ Cu ₃ Sb ₄ , Gd ₃ Cu ₃ Sb ₄ .
Without translation symmetry	Al-Cu-Ru Icosahedral quasicrystal
Two- and one- dimensional compounds	CuP ₂

Today it is not possible to choose a priori a material or even a group of compounds whose properties could fit best the requirement for thermoelectric applications. Therefore, some electron transport measurements and their analyses are a rough guide for choosing the studied materials. The possible group of the considered compounds are presented in Table 1.

In the presented work we select some compounds due to:

- homonuclear bondings and reported [1] high mobility: CoSb₃ and SrAs₃,
- silicon compatible: β -FeSi₂,
- narrow band gap and simultaneously unusual magnetic properties, FeSi and NiS
- tetrahedral coordination: TiNiSn and ZrNiSn
- rare earth atoms: Ce₃Cu₃Sb₄ and Gd₃Cu₃Sb₄.

We were able to prepare all these compounds as pure phases and CoSb₃, β -FeSi₂, FeSi, NiS, TiNiSn and ZrNiSn as single crystals. We think that the single crystals will hardly be usefull in thermoelectric coolers, but that single crystals are very desirable for basic studies before a material will be choosen for applications.

The transport properties and thermopower were measured. The comparison of power factor $S^2\sigma$ with the currently known thermoelectric materials was conducted.

Skutterudite CoSb₃

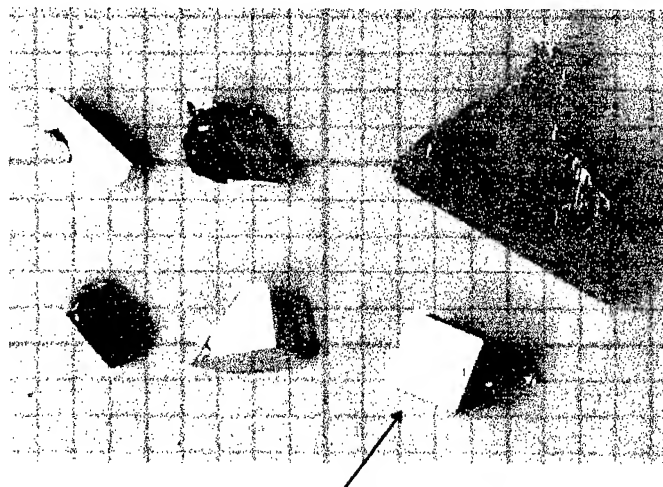


Fig. 1. Five CoSb₂ and one CoSb₃ crystals grown in the same quartz ampoule by chemical vapor transport with iodine as transport agent at 950-750°C.

CoSb₃ is stable only up to 873 °C. A steep liquidus near eutectic point at 97 atm % Sb in Co - Sb phase diagram forced us to growth this material from an antimony rich flux. Due to constitutional supercooling, a large temperature gradient on the solid/liquid interface was needed. The crystals were separated from the antimony by heating the flux in one end of the closed quartz ampoule at 650 °C and keeping the other end of the ampoule at room temperature. Such a separation procedure could shift the composition of CoSb₃ on the Co side of homogeneity range, in spite that the homogeneity range of CoSb₃ is supposed to be small. To

improve the crystal quality and to grow the crystals on the Sb side of homogeneity range, a chemical vapor transport with iodine or bromine as transport agent was used.

Unfortunately the low peritectical temperature of CoSb_3 forced us to use a low source temperature. Therefore, the growth rate was very low and the grown crystals were small (1 - 2 mm). To increase the crystals dimensions, the source was kept above decomposition temperature at 1050 or 950 °C. In these cases the metallic compounds, CoSb , and CoSb_2 , and a small amount of CoSb_3 were formed at the cold, 750 °C, ampoule part.

Two type of samples which show "metallic" or "semiconducting" (Fig. 2) conductivity characteristics, were prepared. The highest mobility was achieved in Sb saturated samples.

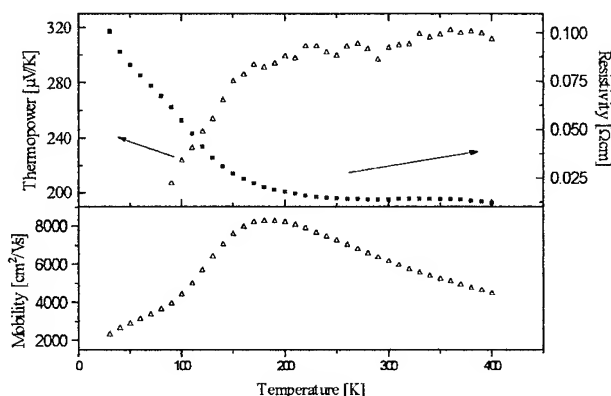


Fig. 2. Mobility, Seebeck coefficient and resistivity of CoSb_3 .

SrAs_3

SrAs_3 is known to have very high mobility [2]. It has a more complicated, monoclinic, C2/m structure than, cubic, $\text{Im}\bar{3}$ CoSb_3 . In CoSb_3 , each Sb atom overlaps three s^2p^3 orbitals in the Sb_4 ring and one s^2p^3 orbital hybridizes with 3d, 4s and 4p Co orbitals. As atoms in SrAs_3 form puckered layers containing, in contrast to CoSb_3 , no d valence electrons. Therefore, we supposed that SrAs_3 compounds could have better thermoelectric properties in respect to CoSb_3 .

SrAs_3 melts congruently, which simplifies the preparation procedure. In spite of the presence of alkaline earth metal, Sr, this compound is stable in ambient air. Up to now, we obtained only polycrystalline samples by directional freezing of SrAs_3 melt in a glassy carbon crucible sealed in a quartz ampoule. The specific resistivity of SrAs_3 samples are 1.4 - 2.4 $\text{m}\Omega\text{cm}$, but the Hall and Seebeck coefficients change signs, (Fig. 3) suggesting a complex band structure. Contrary to our expectation, the power factor is lower in SrAs_3 than in CoSb_3 , but the thermopower is high enough, 70 $\mu\text{V/K}$ at 150 K, to be worthy of more study.

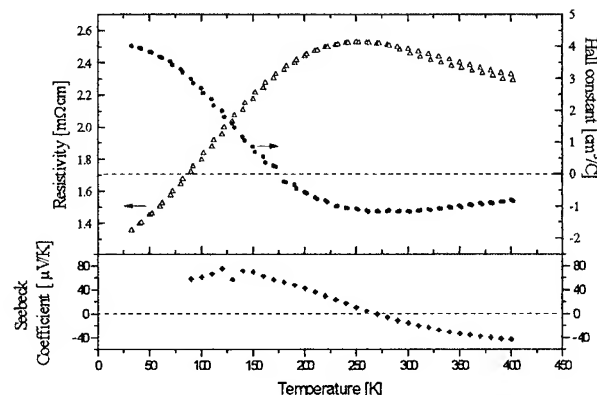


Fig. 3. Resistivity, Hall coefficient and thermopower of SrAs_3 polycrystalline sample.

Rare earth semiconductors: $\text{Ce}_3\text{Cu}_3\text{Sb}_4$ and $\text{Gd}_3\text{Cu}_3\text{Sb}_4$

The origin of the energy gap in these types of compounds is not well known. It was assumed that hybridization of f electrons with conduction electrons is responsible for band gap formation. Even the metallic or semiconducting transport character is the subject of discussion. The binary rare earth chalcogenides are very stable and have interesting thermoelectric properties.

The ternary pnictides were synthesized by melting components in vacuum sealed tantalum tubes and subsequently annealing them for 3 weeks at 600 °C. Pure phase samples were formed and examined by an x-ray method. The resistivity, decreasing with rising temperature, and the Seebeck coefficient, near one order of magnitude higher than in normal metals, indicate the semiconducting behavior of these compounds [3]. The power factor near room temperature is still lower than in the other narrow band gap semiconductors studied. The metallic conductivity found in numerous rare earth compounds are caused frequently by the low purity of used elements or the contamination of highly reactive elements by crucible material during preparation. However, the presence of f-electrons in these compounds, oft anomalous transport properties in low temperature and ten times larger than in normal metals thermopower in heavy-fermion compounds near the Kondo temperature [4], allow us to suggest rare earth semiconductors as very interesting materials for thermoelectric and galvanomagnetic study, in spite of their complicated technology.

TiNiSn , ZrNiSn

The analysis of bonds in a MgAgAs -type structure allowed to speculate that Sn in the tetrahedral positions could have sp^3 hybridization, and, therefore, high electron mobility. Thus, we began to study TiNiSn and ZrNiSn compounds. Phase diagram, or melting point and its stoichiometric or nonstoichiometric character are not known. We used crystallized TiNiSn or ZrNiSn from Sn flux by cooling from 1400 °C to 400 °C. The TiNiSn crystals are shown on Fig. 4.

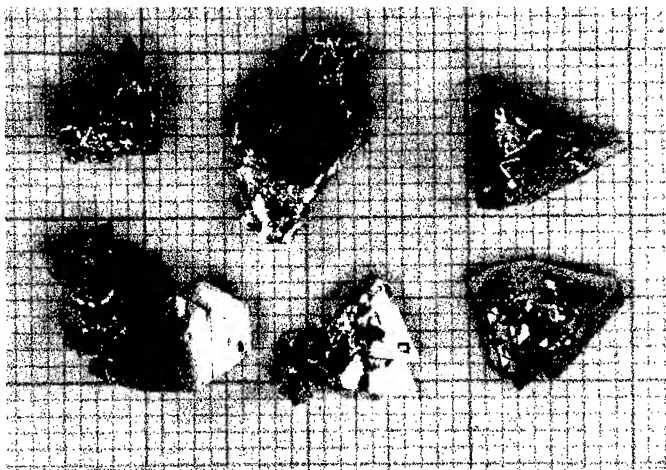


Fig. 4. TiNiSn grown from Sn flux.

The resistivity of both compounds lightly increased vs. increased temperature, but the transport measurements and the value of Seebeck coefficient confirmed that these intermetallic compounds are doped semiconductors (Fig. 5).

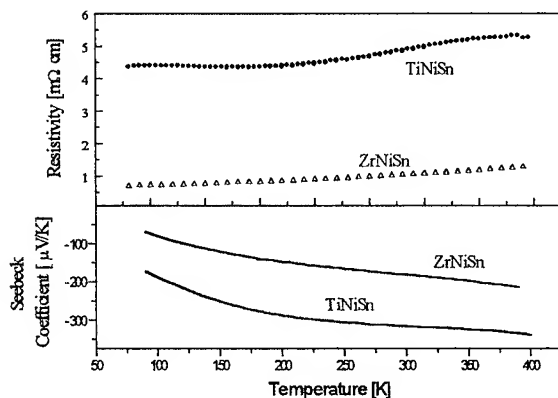


Fig. 5. Electric and thermoelectric properties of TiNiSn and ZrNiSn.

Because the thermal conductivity was measured only up to 120 K (ca. 10 W/Km) [5], the power factor, $S^2\sigma$, was calculated and compared with other materials (Fig. 9). Above 200 K power factor of ZrNiSn exceed IrSb₃. It is reasonable to hope that solid solution ZrNiSn - TiNiSn lowers thermal conductivity, and that this system would be one of the best thermoelectric materials in near room temperature thermoelectric applications.

NiS

The hexagonal, P6mmc, phase of NiS undergoes a metal - insulator transition between 150 and 260 K depending on sulfur content [6]. Below this temperature a small band gap, about 100 meV, caused by electron correlation opens. Above the transition temperature NiS shows Pauli paramagnetism; below NiS is antiferromagnetic. The band gap is formed between S 3p and Ni 3d orbitals.

Because it is very difficult to predict the thermoelectric properties of such a complex system, the preparation and measurements have been carried out. The single crystals were grown by the Bridgman method and

quenched in water to prevent forming the rhombohedral phase which is stable in room temperature (Fig. 6).

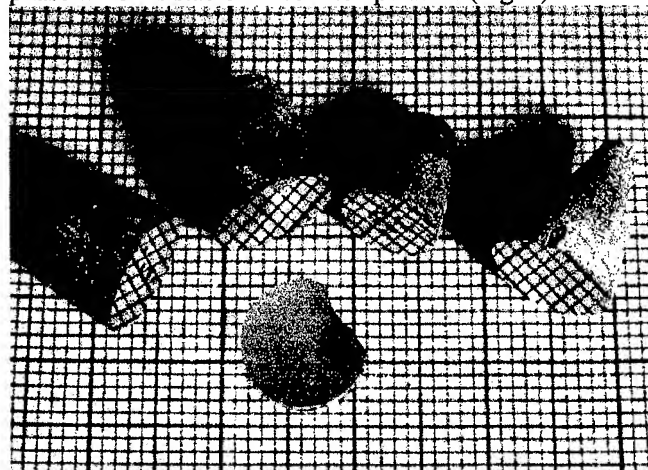


Fig. 6. NiS single crystals grown by Bridgman method

Resistivity measurements revealed existence of magnetic phase transition, but the Seebeck coefficient of the antiferromagnetic phase was only slightly larger than that of the paramagnetic phase.

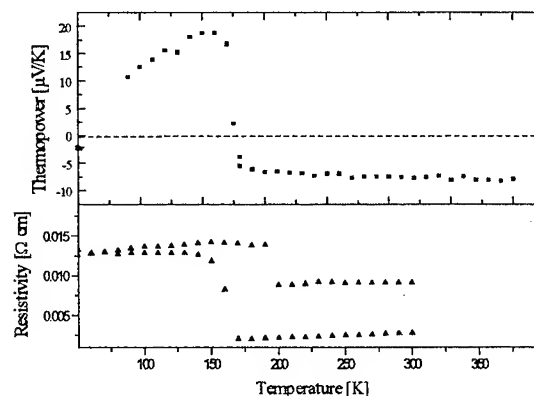


Fig. 7. Resistivity and thermopower of NiS near antiferromagnetic to paramagnetic phase transition.

FeSi and β -FeSi₂

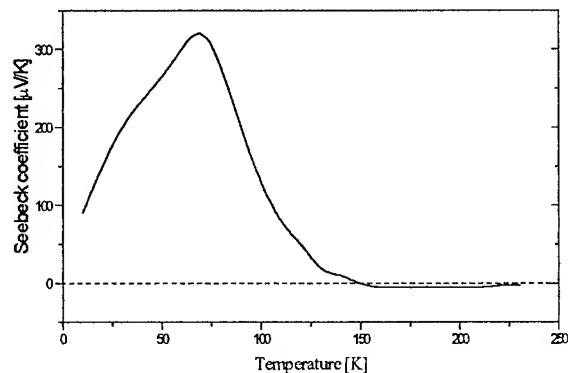


Fig. 8. Seebeck coefficient in FeSi single crystals

Single crystals of FeSi were grown using the Czochralski technique. Due to peritectic decomposition, the needle β -FeSi₂ crystals were grown by chemical vapor transport[7]. An example of FeSi crystals are presented in fig. 8. FeSi mobility shows a very small mobility, but the Seebeck coefficient forms a narrow maximum between 10 and 100 K. Such a characteristic could be well explained by electron - phonon interactions [8]. The band gap of β -FeSi₂, ca. 0.9 eV, prefers this material for high temperature applications.

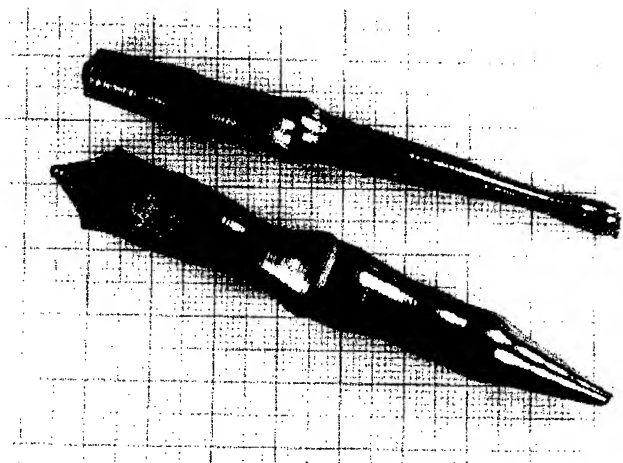


Fig. 8. Czochralski grown FeSi single crystals.

Conclusion

The narrow band gap semiconductors include very different families of compounds. The best thermoelectric properties are shown by compounds where metal - metal or nonmetal - nonmetal bondings are present. It means that pure covalent bondings or bondings with small ionic contribution are desirable. Strong ionic oxides or sulfides (NiS) are rarely used. Compounds containing weak pure covalent bonds frequently decompose before reaching the melting point. Also, it is easy to form defects or strongly dope such compounds ("metallic" conductivity). The elements used for thermoelectric materials are not typically used in microelectronic applications. As a result, they are hardly available in proper purity on the market. Compounds synthesized from such materials are not intentionally doped, and the solubility limit for dopant could be larger. The properties are very sensitive to the technology processes used. Therefore, detailed composition and defect characterization are very desirable. The elementary cells in these compounds are frequently large and not cubic, which makes interpretation of other physical properties very difficult in comparison to classical semiconductors.

The widely studied compounds of precious metals (Os, Ru, Rh, Ir or Pt) are excellent thermoelectric materials, but we think that TiNiSn, ZrNiSn and their solid solutions should be considered as promising thermoelectric materials due to the very high power factor (Fig. 9) and inexpensive price.

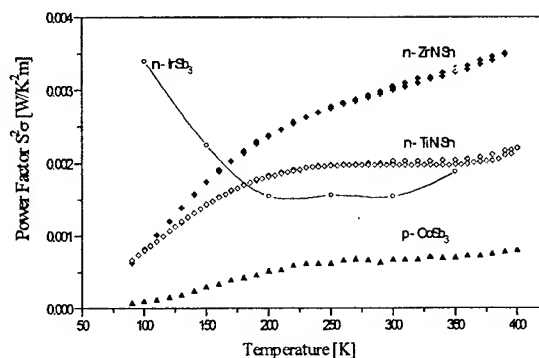


Fig. 9. Comparison of power factors for skutterudite IrSb₃ (calculated from [9]) and CoSb₃ with TiNiSn and ZrNiSn.

Additional improvement of figure of merit, in some materials, could be achieved by the application of magnetic field. The effects of a magnetic field on narrow band semiconductors containing transition metals or rare earth magnetic ions, seems especially worthy of study.

Acknowledgments

The authors wish to thank Dr. Ch.Gladun and Prof. A.Heinrich from IFW Dresden for making the measurements shown in Fig. 8.

References

- [1] T.Caillat, A.Borshchovsky, and J.-P.Fleurial, "Preparation and Thermoelectric Properties of p- and n-type CoSb₃" Proc. ICT 13, ed. B.Mathiprakasham and P.Heenan, 1994.
- [2] P.J.Klar and W.Bauhofer, "Galvanomagnetic Properties and Band Structure of Monoclinic SrAs₃" Phys. Rev. B50,5180(1994).
- [3] K.Fess, W.Kaefer, Ch.Kloc, K.Friemelt, and E.Bucher, "Growth and Characterization of the Semiconducting Ternary Rare-Earth Compounds R₃Cu₃Sb₄ (R=Ce, Gd)", Proc. of 10-ICTMC Stuttgart (1995).
- [4] K.H.Fisher "Thermoelectric power of heavy-fermion compounds", Z. Phys. B - Condensed Matter 76,315(1989).
- [5] F.G.Aliev, R.Villar, S.Vieira, and A.P.Levanyuk, "Thermal expansion of the disordered conductors MNiSn (M=Ti, Zr, Hf)" Phys. Rev. B 50, 17881(1994).
- [6] T.Ohtani, K.Kosuge, and S.Kachi, "Thermoelectric Power of Ni_{1-x}S", J.Phys.Soc.Japan 29,521(1970).
- [7] Ch.Kloc, E.Arushanov, M.Wendl, H.Hohl, U.Malang, and E.Bucher, "Preparation and properties of FeSi, α -FeSi₂ and β -FeSi₂ single crystals" J.Alloys Comp. 219,93(1995).
- [8] V.K.Zeitsev, S.A.Kitorov, and M.I.Fedorov, in: "CRC Handbook of Thermoelectrics" ed. D.M.Rowe, CRC Press, p. 311(1995).
- [9] T.Caillat, A.Borshchovsky, and J.-P.Fleurial, "Preparation and Thermoelectric Properties of p- and n-type IrSb₃" Proc. ICT 13, ed. B.Mathiprakasham and P.Heenan, 1994.

Thermoelectric Properties and Structures of the Sintered Compact of Cu:Sn:S=8:1:4 Composition

M. Hasaka, T. Morimura, T. Aki and S. Kondo

Department of Materials Science and Engineering
Faculty of Engineering, Nagasaki University

Abstract

The compact of Cu:Sn:S = 8:1:4 composition was prepared by sintering. The thermoelectric properties of the compact were measured as a function of temperature and annealing period. The microstructures were investigated by X-ray diffraction experiments and transmission electron microscopic observation. The compact is desirable in thermoelectric properties and thermal stability below 450K. The compact consists of mixtures of several compound structures.

Introduction

Good properties for thermoelectric energy conversion were reported in the Cu-Sn-S system. The compound structure of Cu_4SnS_4 has the electrical conductivity of 10S/cm, the Seebeck coefficient of 0.6mV/K, the figure of merit of 0.8×10^{-3} at 300K [1,2]. The electrical conductivity of the complex structure of Cu:Sn:S=8:1:6 composition is about 100S/cm at 300~400K [3].

The objective of this paper is to measure the thermoelectric properties as a function of temperature and annealing period in the sintered compact of Cu:Sn:S=8:1:4 composition, and also to identify the microstructures by X-ray diffraction experiments and transmission electron microscopic observation.

Experimental

The materials of 99.99% copper sheets, 99.99% tin particles, 99% sulfur powders were weighed in Cu:Sn:S=8:1:4 composition, and were evacuated to a vacuum in silica tubes. After the sulfur powders in the tubes were melted at 373K, they were absorbed by the other materials. The materials in the tubes were next melted for 3h at about 1200K, and were cooled to room temperature in a furnace. The product was ground into powders, which were pressed into the compact of 10 mm diameter, 2~3mm thickness for 15min under a uniaxial pressure of 200MPa in a vacuum. For the sake of comparison, the compacts of Cu:Sn:S=2:1:0 and 4:1:4 compositions were also made through the above procedure.

After each compact was sintered for 3h at 973K in a vacuum in a furnace, the electrical conductivity of each compact was measured with the four-probe method in a vacuum in a furnace. The

thermoelectromotive force was measured by heating one edge of the compact. The thermal conductivity was measured with an optical heating-pulse apparatus, Rigaku LF/TCM-FA8510B. The structures were identified with an X-ray diffractometer, Rigaku RINT 2200, using a copper target at room temperature. The microstructures were observed by using a transmission microscope, JEM-2000FX, at HVEM Lab, Kyushu University. The EDX spectra from twenty areas were measured with an electron beam size of 50 nm diameter.

Results and discussion

Thermoelectric properties

Fig. 1 shows that the thermoelectromotive force for the Cu:Sn:S=8:1:4 composition remains unchanged up to 8h during keeping a temperature difference of 150K, the cooling edge of 300K, and the heating edge of 450K in a vacuum, argon gas, or air. It is seen from the figure that the compact is useful for long period in

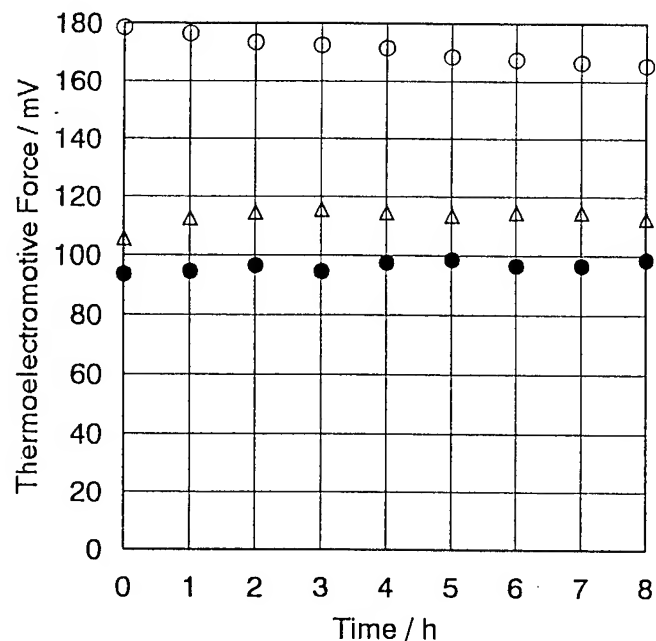


Fig.1 Thermoelectromotive force of the compact of the Cu:Sn:S=8:1:4 composition in a vacuum (O), in argon gas (●), and in air (Δ) with a temperature difference $\Delta T=150\text{K}$, the cooling edge of 300K, and the heating edge of 450K.

temperature range up to 450K. The large difference between the thermoelectromotive forces in a vacuum and in argon gas may be due to difficulties in controlling the microstructures of the compact.

Fig.2 shows that the thermoelectromotive force for the Cu:Sn:S=8:1:4 composition changes rapidly during keeping a temperature difference of 250K, the cooling edge of 300K, and the heating edge of 550K in a vacuum, or argon gas. The thermoelectromotive force reduces to the value of $\Delta T=100\text{K}$ within 1 h in a vacuum, or $\Delta T=150\text{K}$ after 3 h in argon gas, which suggests that the useful life of the compact depends on the atmospheric conditions.

Fig 3 shows the relation between temperature and the Seebeck coefficient for the Cu:Sn:S=8:1:4, 2:0:1, and 4:1:4 compositions. In the whole temperature range, the Seebeck coefficient remains constant, being higher for the 8:1:4 composition than for the 2:0:1 and 4:1:4 compositions.

Fig 4 shows the relation between temperature and the electrical conductivity for the Cu:Sn:S=8:1:4, 2:0:1, and 4:1:4 compositions. The electrical conductivity changes slightly with increasing temperature, while it remains higher for the 8:1:4 composition than for the 2:0:1 and 4:1:4 compositions.

Fig 5 shows the relation between temperature and the power factor for the Cu:Sn:S=8:1:4, 2:0:1, and 4:1:4 compositions. In the whole temperature range, the

power factor for the 8:1:4 composition is superior to the power factor for the 2:0:1 and 4:1:4 compositions. Since the thermal conductivity for the Cu:Sn:S=8:1:4 composition measures $0.004\sim 0.007\text{W/cmK}$ at room temperature, the figure of merit is estimated to be over $10^{-3}/\text{K}$.

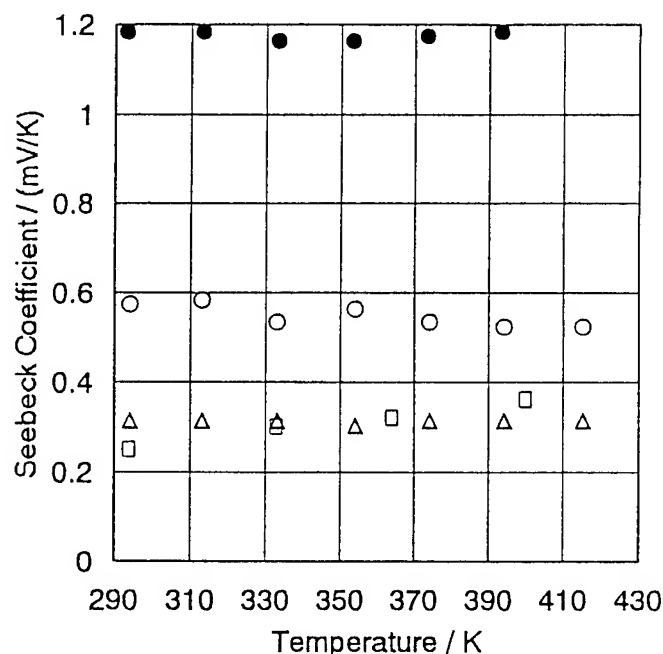


Fig.3 Relation between temperature and the Seebeck coefficient in the compacts of the Cu:Sn:S=8:1:4 (○, ●), 2:0:1 (□) and 4:1:4 (△) compositions.

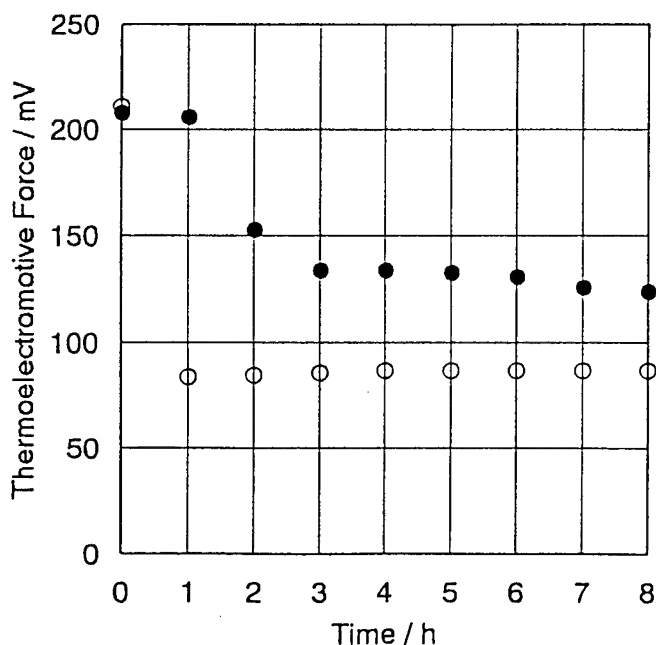


Fig.2 Thermoelectromotive force of the compact of the Cu:Sn:S=8:1:4 composition in a vacuum (○) and in argon gas (●) with a temperature difference $\Delta T=250\text{K}$, the cooling edge of 300K, and the heating edge of 550K.

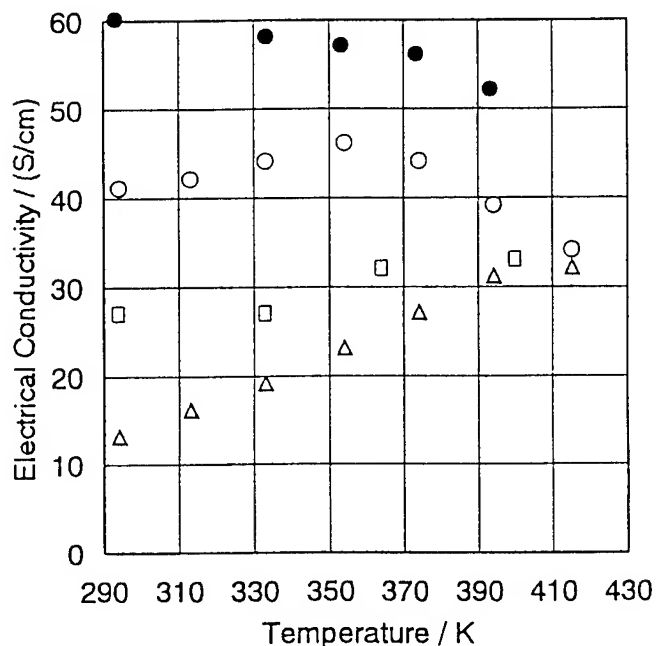


Fig.4 Relation between temperature and the electrical conductivity in the compacts of the Cu:Sn:S=8:1:4 (○, ●), 2:0:1 (□) and 4:1:4 (△) compositions.

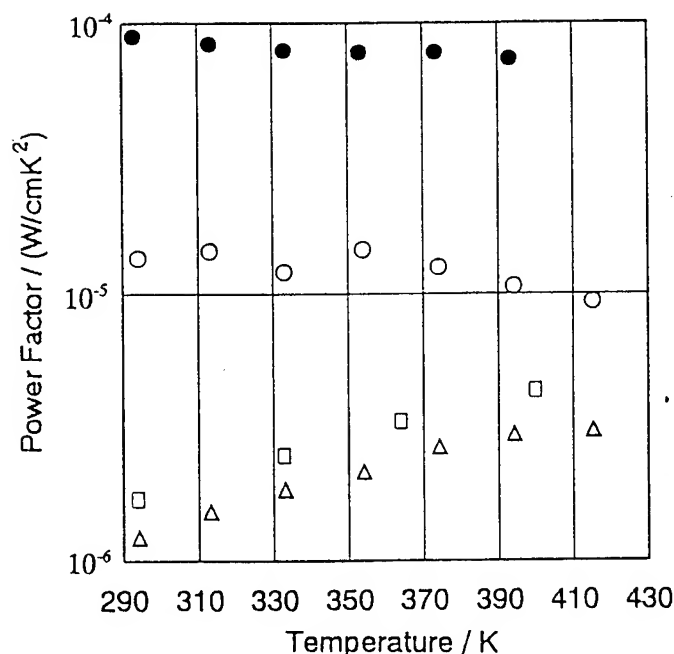


Fig 5 Relation between temperature and the power factor in the compacts of the Cu:Sn:S=8:1:4 (○, ●), 2:0:1 (□) and 4:1:4 (△) compositions.

Microstructures

X-ray diffraction peaks revealed that there exist the compound structures of $\text{Cu}_2\text{S}+\text{Cu}_{1.81}\text{S}+\text{Cu}_3\text{Sn}$ for the 8:1:4 composition. On the other hand, the EDX spectra from the twenty areas for the 8:1:4 composition presented more detailed information about microstructures, which is composed of four types of phase: Cu-S binary phase, Cu-Sn-S ternary phase, Cu phase, Cu-Sn binary phase. Since the Cu-S binary phase was most frequently observed, it is concluded to be major in the four phases which lead to good properties for thermoelectric energy conversion.

Electron diffraction patterns identified the Cu-S binary phase as the structures of $\text{Cu}_{1.81}\text{S}$, $\text{Cu}_{1.96}\text{S}$ and Cu_2S . Fig.6 shows the bright field image and 001 diffraction pattern of $\text{Cu}_{1.81}\text{S}$. Extra spots are observed in addition to main spots. The extra spots are due to long period order structure. Fig.7 shows the bright field image and 110 diffraction pattern of $\text{Cu}_{1.96}\text{S}$ super-imposed on 001 diffraction pattern of $\text{Cu}_{1.81}\text{S}$, where only the indices of $\text{Cu}_{1.96}\text{S}$ are indicated. The 111 spot of $\text{Cu}_{1.96}\text{S}$ overlaps with 120 spot of $\text{Cu}_{1.81}\text{S}$. Extra spots due to the long period order structure are also observed in addition to main spots. In the bright field image, the white lines are observed perpendicular to the [111] direction. Fig.8 shows the 111 diffraction pattern of $\text{Cu}_{1.96}\text{S}$ or 001 diffraction patterns of Cu_2S , where only the indices of $\text{Cu}_{1.96}\text{S}$ are indicated. The upper pattern was observed with a slight convergent electron beam, while the lower pattern was observed with a parallel beam. Although the same main spots are observed in the both patterns,

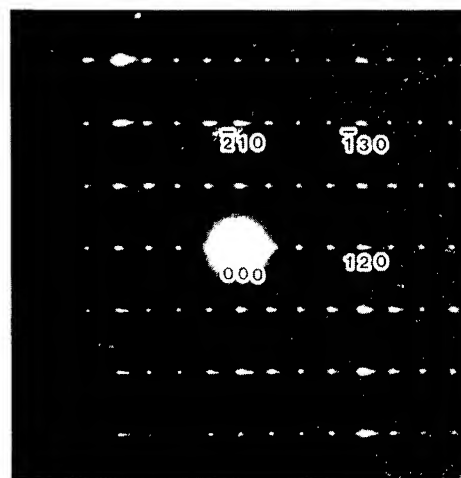


Fig.6 Bright field image and 001 diffraction pattern of $\text{Cu}_{1.81}\text{S}$.

the extra spots disappear in the upper pattern, which suggests that electron beam irradiation causes disordering transformation of vacancies and copper atoms in Cu_{2-x}S [4,5].

Fig.9 shows the bright field image and diffraction pattern of the Cu-Sn-S ternary phase. The pattern is indexed as $\text{Cu}_{1.96}\text{S}$ or Cu_2S with extra spots. Thus, the ternary phase is expected to have structure of $\text{Cu}_{1.96}\text{S}$ or Cu_2S containing tin atoms.

Conclusions

The thermoelectric properties of the compact were measured as a function of temperature and annealing period in the sintered compact of the Cu:Sn:S = 8:1:4 composition. The microstructures were investigated by X-ray diffraction experiments and transmission electron microscopic observation. The results are summarized as follows. The compact is promising because the thermoelectric properties and thermal stability are good below 450K. The figure of merit of the compact exceeds $10^{-3}/\text{K}$. The good properties are

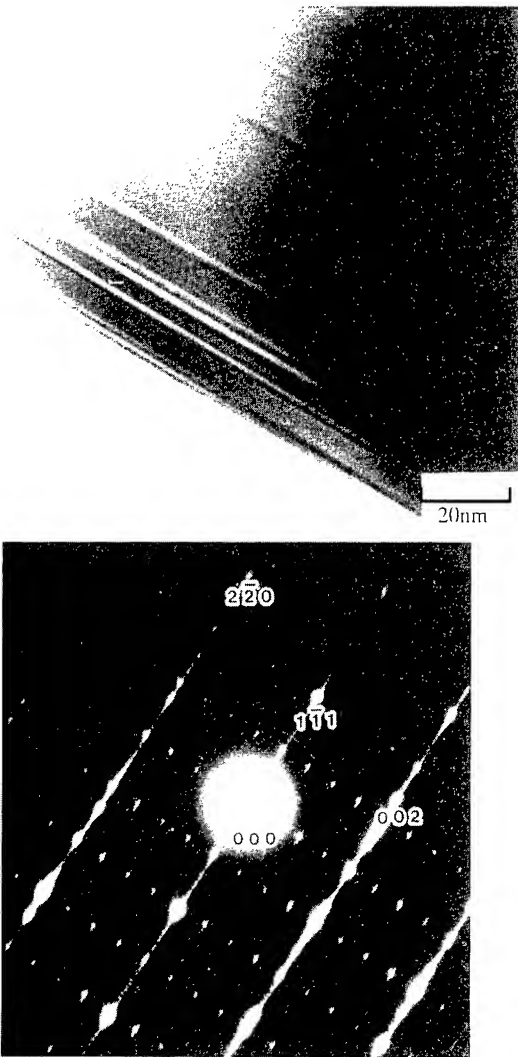


Fig.7 Bright field image and $\bar{1}\bar{1}0$ diffraction pattern of $\text{Cu}_{1.96}\text{S}$ superimposed on 001 diffraction pattern of $\text{Cu}_{1.81}\text{S}$. The indices are indicated for $\text{Cu}_{1.96}\text{S}$.

associated with the microstructures of the Cu-S, Cu-Sn-S, Cu, Cu-Sn phases, order-disorder transformation in the Cu-S or Cu-Sn-S phases, or mutual reaction among these phases.

References

1. M. Matoba, I. Inoue, T. Uemura, M. Watanabe, S. Anzai, J. Materials Science Society of Japan, vol.27, pp.299-301 (1990).
2. S. Anzai, K. Ozawa, "Effects of Pressure on the First-Order Phase Transition of Cu_4SnS_4 and Cu_8GeS_6 ", JAERI-M reports 84-059, pp.1-28(1984)
3. M. I. Aliev, D. G. Arasly and T. G. Dzhabrailov, "Thermal Properties of Cu_8SnS_6 ", Sov. Phys. Solid State, vol.24, pp.1978-1979(1982).

4. C. C-Conde-Amiano, D. Van Dyck, R. De Ridder, S. Amelinckx, "The Structure of Digenite (Cu_{2-x}S) Studied by Electron Microscopy and Electron Diffraction", Electron Microscopy, vol.1, pp.478-479(1980).
5. D. Van Dyck, C. Conde-Amiano, S. Amelinckx, "The Diffraction Pattern of Crystals Presenting a Digenite Type of Disorder", Phys. Stat. Sol. (a), vol.58, pp.451-466.(1980).

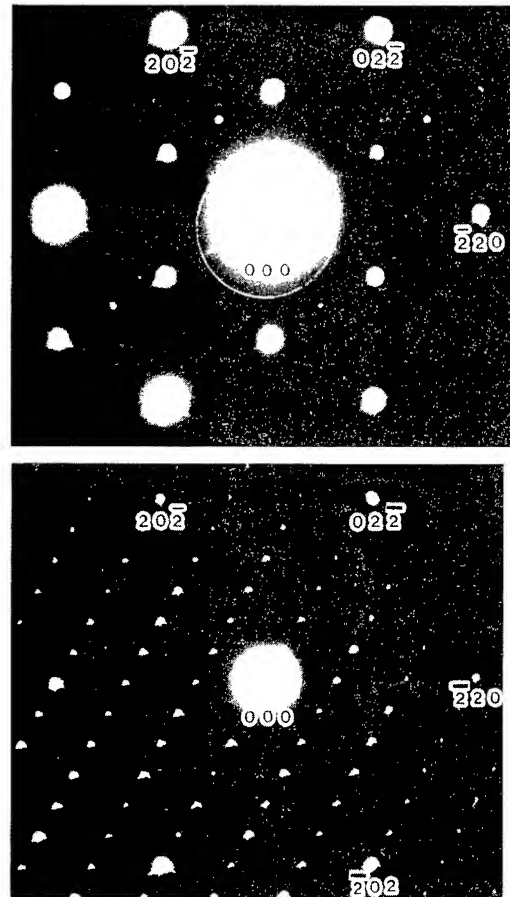


Fig.8 111 diffraction pattern of $\text{Cu}_{1.96}\text{S}$ or 001 diffraction patterns of Cu_2S . The indices of $\text{Cu}_{1.96}\text{S}$ are indicated. The upper pattern was observed with a slight convergent electron beam and the lower pattern was observed with a parallel beam.

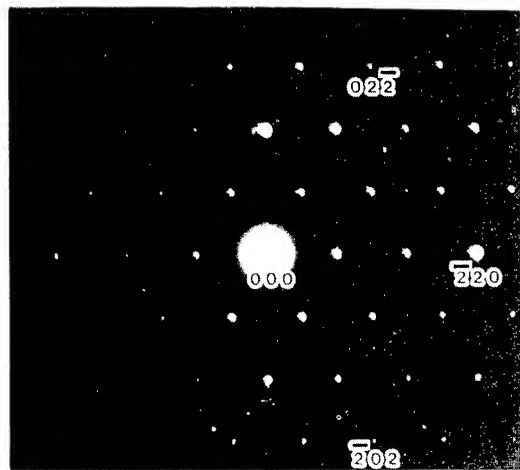


Fig.9 Bright field image and the diffraction pattern of the Cu-Sn-S ternary phase. The pattern can be indexed as 111 zone axis incidence of $\text{Cu}_{1.96}\text{S}$ or 001 of Cu_2S . The indices are indicated for $\text{Cu}_{1.96}\text{S}$.

ELECTRONIC TRANSPORT PROPERTIES OF HIGHLY CONDUCTING VAPOR-GROWN CARBON FIBER COMPOSITES

Kevin L. Stokes, Terry M. Tritt, Wendy W. Fuller-Mora and A.C. Ehrlich,
Materials Science Division, Naval Research Laboratory,
Washington, DC 20375, USA

and

R. L. Jacobsen,
Applied Sciences Inc., 141 Xenia Ave.,
Cedarville, OH 45314, USA

Abstract

We have measured the electrical resistivity and thermoelectric power of commercial vapor-grown carbon fibers and fiber composites from 4 K to 300 K. Post-growth heat treatment decreased the resistivity and moderately increased the magnitude of the thermopower. Thermoelectric measurements on fiber composites showed that the host material altered the resistivity but had little effect on the thermopower. Thermopower data suggest that the fibers in the composite material have a smaller degree of graphitization than isolated fibers.

Introduction

Carbon fiber composites have been used extensively for light-weight structural materials, but these materials also exhibit transport properties that make them valuable for other applications. By adjusting process variables and post-growth heat treatment, intrinsic carbon fibers can be fabricated to have a wide range of thermal conductivity (20 to 2000 W/m-K) [1] and electrical resistivity (3 to 0.07 m Ω ·cm) at room temperature [2]. Intercalation of the fibers, as is done for graphite, can alter the carrier concentration, phonon scattering and thermopower [3]. In fact, thermopowers of about 35 μ V/K for acceptor compounds and -25 μ V/K for donor compounds have been reported for intercalated graphite [4]. Intercalated fibers could be incorporated into different host materials to further alter the properties of the composite. This flexibility prompts us to investigate the properties of carbon fibers as a candidate for a thermoelectric material.

We present a preliminary study of the electrical and transport properties of vapor-grown carbon fibers. We have measured the resistivity and thermoelectric power as a function of temperature (4 K - 300 K) for a variety of differently-prepared fibers and composites.

Samples

Vapor-grown carbon fibers (VGCF) are produced in a catalytic reaction in which a hydrocarbon (in our case methane) pyrolytically decomposes on metal particles,

usually iron. These particles absorb carbon from the methane breakdown and then incorporate it into filaments that grow out of the particle [1,5]. The diameter of the carbon filament is nominally equal to the diameter of the catalyst particle which is approximately 10 nm. The length can be made anywhere from a few microns to several centimeters depending on the process parameters. Once the fibers' lengths are established, they are thickened to arbitrary diameter by chemical vapor deposition (CVD). Structurally, the carbon planes in the as-grown fibers form concentric circles (like tree rings). After heat treatment to sufficiently high temperature, the structure becomes graphitized and faceting is observed [1].

Two varieties of VGCF are manufactured by Applied Sciences, Inc., designated as Pyrograf-ITM and Pyrograf-IIITM. The Pyrograf-ITM fibers are grown in a one-dimensionally oriented mat and are about 2 cm long with 7 μ m diameter. Pyrograf-IIITM fibers are generally 100 μ m long and about 200 nm in diameter. They grow in random orientation and are entangled, like a cotton ball. Both of these types of VGCF have been incorporated into a variety of composites. For this study, we have investigated the thermoelectric properties of as-grown and heat-treated Pyrograf-ITM single fibers, Pyrograf-ITM fibers in cyanate ester resin (CER) and carbon matrices and Pyrograf-IIITM fibers in a nylon matrix.

Experiment

Standard four-probe resistance and thermopower measurements were performed using the same experimental set-up. The apparatus consisted of two small copper blocks, both containing heaters. One block was in thermal contact with an approximately 0.5 kg copper base plate and the other block was thermally isolated from the base plate. The sample was suspended between the Cu blocks; the ends of the sample were attached to the blocks with GE 7031 varnish. This entire assembly was placed inside a continuous-flow liquid He cryostat. The temperature of the heat-sunk end of the sample was determined using a Lake Shore calibrated Cernox sensor mounted inside the base plate. The temperature difference across the sample, ΔT , was measured with a 0.005" Au-0.07 at% Fe vs. Chromel differential thermocouple permanently embedded in the Cu blocks with Stycast epoxy. The leads for measuring the

voltage (for both thermopower and resistivity) were 0.003" Au wire attached to the sample with Ag paint. The sample was positioned so that the voltage leads were directly above the thermocouple junctions. The sample voltage (V_S) as well as the thermocouple voltage (V_{TC}) were measured with a Keithley 182 nanovoltmeter. The thermopower was measured with the standard differential technique [6] in which the thermopower is given by $V_S/\Delta T$ (with the current off) at each temperature, T . The ΔT was kept to approximately 1-5% of T . The linearity of this method was verified by comparing the slope of V_S vs. ΔT , with ΔT varied from -5% to +5% of T . This measurement was made at room temperature and at low temperature (nominally 20 K) for each sample. The absolute thermopower was estimated by subtracting the thermopower of the Au leads using published values [7]. The resistance of the sample was measured by reversing the current at each temperature and then taking an average V_S thereby canceling any thermal voltages. Typical sample currents were 0.01 - 1 mA. The measurements were taken while the sample was being cooled from 300 K to 4 K over a 12-16 hour period with data being collected approximately every 0.5 K. The measurements were repeated while warming the sample back to room temperature.

Results and Discussion

Resistivity and thermopower for two single Pyrograf-ITTM carbon fibers are shown in Figs. 1 and 2. One fiber was not subjected to any post-growth heat treatment and the other fiber was heat-treated at 2400° C. The resistivity shows little temperature dependence. This is not uncommon in turbostratic graphite systems and indicates that the carrier mobility is limited by scattering from boundaries and imperfections[1]. The resistivity for the heat-treated fiber is a factor of 10 less than that of the as-grown fiber over the entire temperature range.

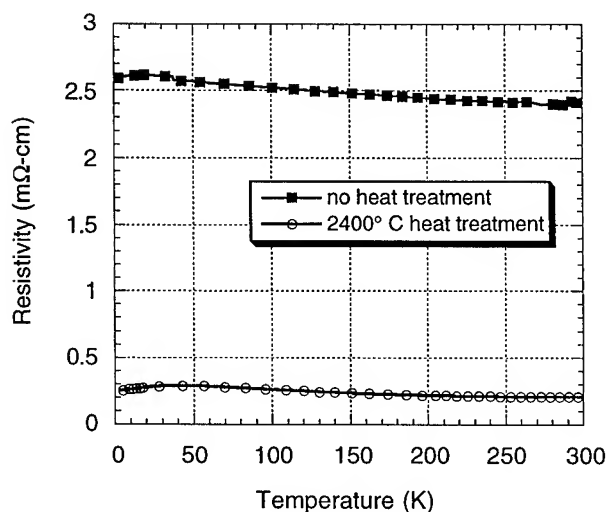


Fig. 1. Resistivity for two single Pyrograf-ITTM fibers. For clarity, the symbols mark only every 20th data point.

Striking differences are observed in the thermopower (Fig. 2). The thermopower is positive for the as-grown fiber with a positive peak at low temperature. The thermopower for the heat-treated sample is negative at room temperature with a negative phonon-drag peak at 35 K then shows a small positive peak at about 7 K.

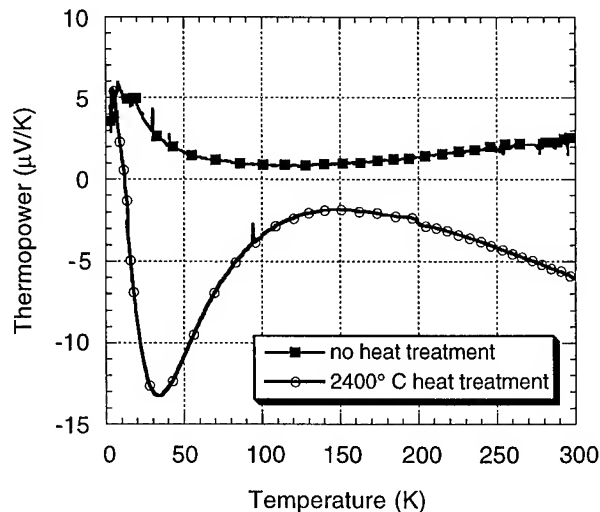


Fig. 2. Thermopower for two single Pyrograf-ITTM fibers.

This general behavior of the thermopower is characteristic of heat-treated VGCF and has been noted by other researchers for benzene-derived fibers [8], cyanoacetylene-derived fibers [9] and methane-derived fibers [10]. However, the details of the temperature dependence of the thermopower vary. For example, Endo, *et al.* and Heremans and Beetz both observe that the thermopower for as-grown VGCF is positive at room temperature but goes negative at about 150 K [8,10]. For our as-grown fibers, the thermopower is positive over the entire temperature range. After heat treatment, the benzene-derived VGCF's show a negative thermopower at room temperature, a broad positive peak between 190 K and 60 K, and then the large negative phonon-drag peak. The heat-treated methane-derived VGCF (Fig. 2 and Ref. [10]) and cyanoacetylene-derived VGCF [9] show no positive thermopower in this temperature region; in fact the thermopower is essentially translated by about -10 μV/K relative to that of the benzene-derived fibers.

These differences are not surprising since the thermopower is very sensitive to the carrier properties in these systems [1,10,11]. For a nearly compensated semimetal, a two-band electronic model must be considered in which there will be a contribution to the electric current density from both bands. The diffusion thermopower is then given as [11]

$$S_d = \frac{\sigma_h S_h + \sigma_e S_e}{\sigma_h + \sigma_e} \quad (1)$$

where $S_{e,h}$ is the partial Seebeck coefficient due to electron and hole conduction and $\sigma_{e,h}$ is the electrical conductivity

due to the electrons and holes. The partial thermopowers originating from the two bands oppose each other, $S_e = -S_h$, so that the resulting thermopower is small. If we express the partial conductivities in terms of the carrier density ratio $a = n_h/n_e$ and the carrier mobility ratio $b = \mu_e/\mu_h$, then Eq. (1) can be rewritten

$$S_d = \frac{aS_h + bS_e}{a+b} \quad (2)$$

For the nearly intrinsic case [11], $a=1$ since $n_h \approx n_e$, and

$$S_d \propto \frac{1-b}{1+b} \quad (3)$$

Consequently, the magnitude and sign of the thermopower is a sensitive function of the mobility ratio. For pyrolytic graphite, the mobility ratio is about 1.1 near room temperature [11].

There is agreement that the degree of graphitization can be qualitatively deduced from the thermopower data [1,8]. The thermopower is predominantly positive for turbostratic fibers and predominantly negative for three-dimensionally ordered fibers [1]. Also, the magnitude of the thermopower decreases with decreasing order; the smallest thermopowers are found for the as-grown VGCF [1]. The thermopower for benzene-derived VGCF heat treated to 3000° C is strikingly similar to the thermopower for single crystal graphite [8]. Our data in Fig. 2 agree with this characterization.

The evolution of the thermopower from the as-grown fiber (turbostratic) to the nearly graphite fiber is interesting. Endo, *et al.* [8] studied the thermopower as a function of heat-treatment temperature (T_{HT}) for benzene-derived VGCF. Their data show that the room temperature thermopower increases as a function of increasing T_{HT} from 1 $\mu\text{V/K}$ to a peak of about 20 $\mu\text{V/K}$ at a T_{HT} of 1900° C [8]. Increasing the T_{HT} further, they find that the thermopower decreases and becomes negative.

Resistivity and thermopower for two composites of heat-treated Pyrograf-ITM fibers are shown in Figs. 3 and 4. For both composites, the fiber fraction is about 50%. The thermopower was relatively insensitive to the host material, however, the phonon drag peak is shifted. For the fibers in the CER matrix, the phonon drag peak is at 27 K and for the carbon matrix the phonon drag peak is at 18 K. For the isolated heat-treated fiber (Fig. 2), the phonon-drag component is much broader and has maximum at 35 K. Notice, too, that the thermopower is positive at room temperature and crosses zero below 100 K and has no peak around 150 K like the isolated heat-treated fiber. The thermopower appears to be intermediate between the as-grown and heat-treated fiber. This would suggest that the process of fabricating the composite material has introduced some damage or disorder to the fibers.

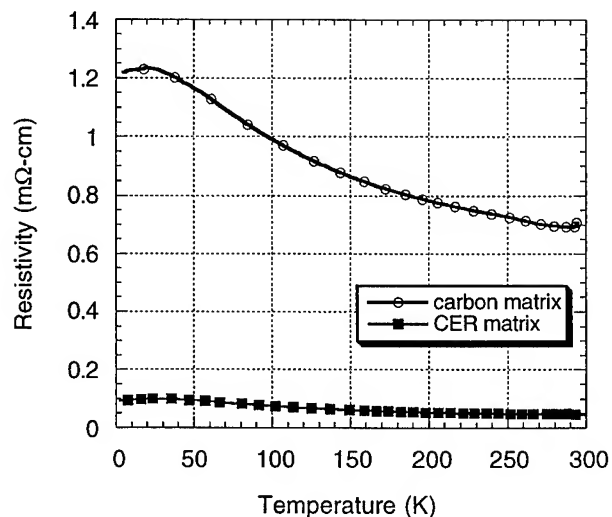


Fig. 3. Resistivity for Pyrograf-ITM fibers in different composite matrices. The fibers were heat-treated at 2800° C prior to incorporation into the composites.

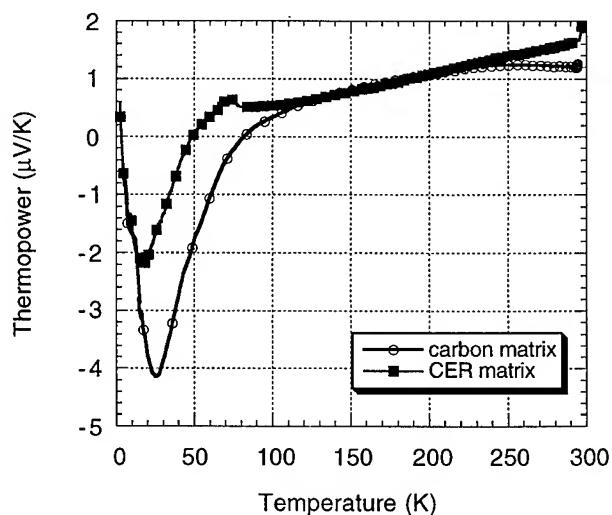


Fig. 4. Thermopower for Pyrograf-ITM fibers in different composite matrices as in Fig. 3.

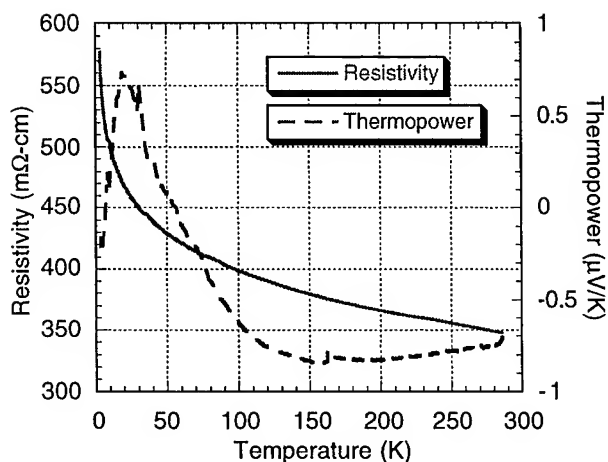


Fig. 5. Resistivity and thermopower for Pyrograf-III™ fibers in a nylon matrix.

Finally, Fig. 5 shows the resistivity and thermopower for Pyrograf-III™ fibers embedded in a nylon matrix. The fibers compose 75% of the composite. These fibers are only on the order of 100 μm long so they are not continuous along the length of the sample which was 15 mm. The fibers are also randomly oriented and entangled. As a result, the resistivity is two to three orders of magnitude larger than the other fiber composites (see Fig. 3). The thermopower data indicates the fibers have turbostratic graphite structure. The thermopower data is close in magnitude and form to the as-grown isolated fiber (Fig. 2). It was assumed that the as-grown Pyrograf-III™ fibers were more graphitic than the as-grown Pyrograf-I™ fibers since the Pyrograf-III™ fibers contain a higher fraction of catalytically-grown carbon. Our data suggests that both as-grown fibers have about the same degree of graphitization.

Summary

We have measured the resistivity and thermopower for differently-prepared VGCF and composites. Two types of commercial fibers were used, with and without post-growth heat treatment. We find that heat treatment significantly reduced the conductivity while moderately increasing the magnitude of the thermopower. The host material of the composite altered the resistivity but had little effect on the thermopower. Based on the thermopower data, the carbon fibers in the composites are less graphitized than the isolated fibers.

References

- [1] M.S. Dresselhaus, G. Dresselhaus, K. Sugihara, I.L. Spain and H.A. Goldberg, *Graphite Fibers and Filaments* (Springer-Verlag, New York, 1988)
- [2] J. Heremans, *Carbon* **23**:431, 1985.
- [3] M.S. Dresselhaus, *Phys. Today* **37** (3):60, 1984.
- [4] J.-P. Issi, B. Poulaert, J. Heremans and M.S. Dresselhaus, *Solid State Comm.* **44**:449, 1982.
- [5] N.M. Rodriguez, *J. Mater. Res.* **8**:3233 (1993).
- [6] F. J. Blatt, P.A. Schroeder, C.L. Foiles and D. Greig, *Thermoelectric Power of Metals* (Plenum, New York, 1976), Ch. 3.
- [7] C.L. Foiles, in *Landolt-Bornstein Vol. III/15b*, ed. by K.-H. Hellwege and O. Madelung (Springer-Verlag, Berlin, 1985) Ch. 3.3.
- [8] M. Endo, I. Tamagawa and T. Koyama, *Japan. J. Appl. Phys.* **16**:1771, 1977.
- [9] J. Tsukamoto, A. Takahashi, T. Tani and T. Ishiguro, *Carbon* **27**:919, 1989.
- [10] J. Heremans and C.P. Beetz, Jr., *Phys. Rev. B* **32**:1981, 1985.
- [11] C.A. Klein, *J. Appl. Phys.* **35**:2947, 1964.

Electrical Properties of Porous Oxides of Alkaline-Earth Metals with High Thermoelectric Efficiency

E.M.Sher

A.F.Ioffe Physico-Technical Institute, RAS, St. Petersburg, Russia

Abstract

Electrical properties of porous oxide layers investigated with the help of specially developed methods. The electrical conductivity measurements made in the wide range of electrical fields by developed pulse method. The method of thin metallic probes and measurements of their spreading resistance in o.l. used to receive the parameters of electron gas in pores. The value of electrical conductivity of contacts between small oxide grains separated from the value of electrical conductivity through electron gas in pores at high temperatures by measurements of spreading resistance and thermoemf, and their changes in magnetic field.

The results of these experiments are giving and discussed below.

Introduction

The most important characteristic of porous oxides (Ba,Sr)O and (Ba,Sr,Ca)O is the small value of their work function, about 1.7ev at 1000K. Such small work function and high porosity results in the pores filed with electron gas and thus reasonable high values of electrical conductivity and thermoemf is provided.

These peculiarities of oxide properties were the source for A.F.Ioffe and B.Ja.Moizhes idea about possibility of high thermoelectric efficiency in these materials [1,2].

This paper is the third part of the work about "Thermoelectric Properties of Porous Oxides of Alkaline-Earth Metals". The first part [3] presents the experimentally received data about thermoelectric efficiency of these materials. The second part [4] discusses the peculiarities of thermal conductivity of porous oxides at high temperatures

the connection of oxide structure and its thermoelectric efficiency.

Electrical conductivity of oxide layers in pulse regime. Because of small work function of oxide grains and high porosity of o.l.(~70-80%), at temperatures >900-1000K pores

are filling with electron gas. Due to this electron gas, the volt-ampere characteristic of o.l. must become nonlinear with rise of electrical field. The theoretical V-A-curve calculated [5] for o.l. in the wide range of electrical fields. The independence of electrons free path length l_0 assumed from their energy, emission direction and from electrical field E . The result of calculation is show on the fig.1. In so doing, the current density j threw o.l. with convex form grains is $j=4j_0L_a/l_0$. Here j_0 -is the current density from grain surface. L_a - is mean electron drift in electrical field E direction from the moment of electron emission until moment of its grain adsorption. On the fig.1 B -is dimensionless parameter: $B=eEl_0/2kT=f(E)$, $L_a/l_0=F(B)$. In the case of weak field ($B \ll 1$) $L_a/l_0=(2/3)B$ and:

$$j = \frac{4j_0}{3} \frac{e^2 n E}{\sqrt{2\pi} m k T} \quad (1)$$

In the case of strong field ($B \gg 1$), when the voltage drop on the free path length became about or more than kT/e , we have

$(L_a/l_0)=1$ and:

$$j=4j_0. \quad (2)$$

In general case:

$$j=4j_0 (L_a/l_0)=4j_0 F(B) \quad (3)$$

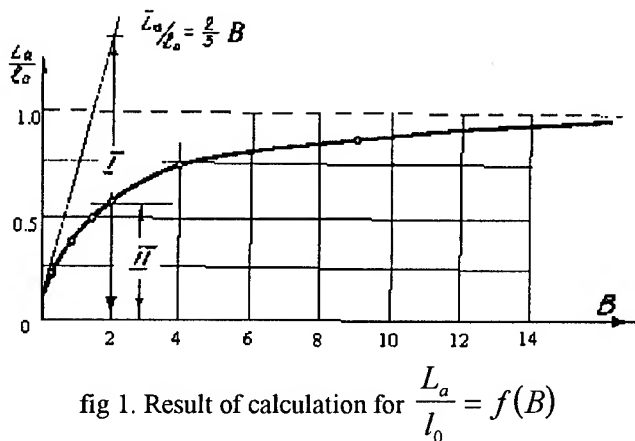


fig 1. Result of calculation for $\frac{L_a}{l_0} = f(B)$

($\geq 1000K$). Now, in the third part, we will describe the developed methods for investigation electrical properties of oxide layers and will analyze the experimental results with

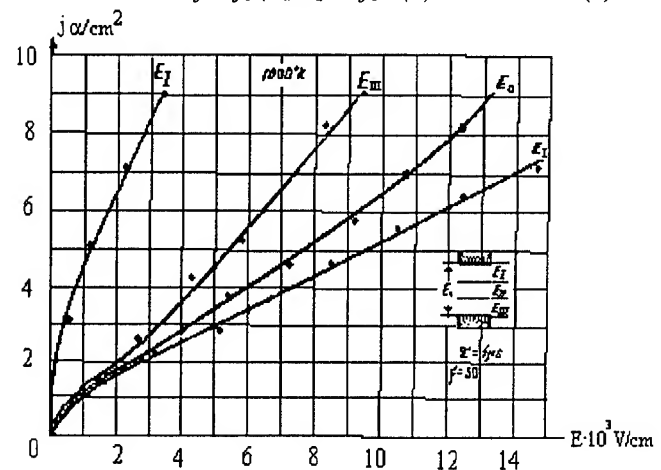


fig. 2. The dependence $j(E)$ for o.l. and its parts. Two probes(Ni) $\tau=1\text{msec}$; $f=50 \text{ imp/sec}$

Here: e and m - charge and mass of electron, k -Boltzman constant. Experimental V-A-characteristics measured in

pulse regime: pulse duration was 1 microsec, frequency repetition was 50 herz. Each sample of o.l. was located in vacuum ($\sim 10^{-7}$ Torr) between faced surfaces of two hollow cylindrical electrodes from Ni. Each electrode had its W-heater and thin Pt-PtRh thermocouple. The thickness of the samples was in the range of 100-300micron. The V-A-characteristics for a sample of o.l. with thickness 200micron and for its three parts (upper, middle and lower), divided by two probes, are given on the fig.2.

All these V-A-characteristics are roughly linear in the region of weak fields (below $E_w \sim 1.10^2$ v/cm). The electrical conductivity here is determined practically completely by electron gas in pores. The nonlinearity is arise when passing from this region to region of middle fields (till $E_m \sim 3.10^3$ v/cm). Here the experimental and theoretical V-A-characteristics are in sufficient agreement. In the strong fields (above $E_s \sim 4.10^3$ v/cm) they are in increasing non-conformity, probably, because of electrical or thermal breakdown of the contacts between oxide grains.

Therefore, as electrical conductivities through electron gas in pores and through contacts between grains are connected in parallel (see [3] and fig.4 here), the field above E_w will decrease the total σ_o and α_o of o.l. and can resulted in a drop of thermoelectric efficiency.

Method of thin metallic probes in the o.l.

The experimental investigations (in the weak fields region) of electrical conductivity σ of porous oxide layers and the parameters of electron gas in pores (concentration n , mobility u and free path length l_o of electrons) were made with the help of specially developed method of thin metallic probes. This method permits to establish the connection of σ and these parameters with the structure and work function ϕ on different depth of o.l. [3,6,7].

The method based on measurements of the probe spreading resistance and its changes in magnetic field. One (fig.3) thin metallic probe located in o.l. between two metallic electrodes (1). The spreading resistance $R_{sr} = V/I$ measured by passing the current I at potential difference V between the probe and two connected electrodes. The electrical conductivity σ of o.l. can be calculated from [3,6]:

$$\sigma = \frac{\ln \frac{r_o}{r}}{2\pi \cdot R_{sr} \cdot l_p}, \quad (4)$$

where r -probe radius ($r \ll d$), l_p --probe length and r_o :

$$r_o = 2 (d/p) \sin(\pi a/d), \quad (5)$$

where d -o.l. thickness, a - probe-electrode distance. The value r_o is a radius of equivalent concentric with probe metallic cylinder (o.l. located between this cylinder and the probe), which give the same spreading resistance as we receive it at real geometry of o.l. and the bases (electrodes). The structure of formulas (4) and (5) is such, that measurement mistakes in o.l. thickness d and in probe location a slightly (logarithmically) influence on measuring o.l. electrical conductivity σ . Therefore σ determination

from measuring R_{sr} is more precise method then usual used method from measuring probe potential when the definite current pass through o.l. It can be seen from (4), (5) that main value of spreading resistance is create by o.l. just located around the probe. Therefore, if o.l. electrical conductivity is changed across its

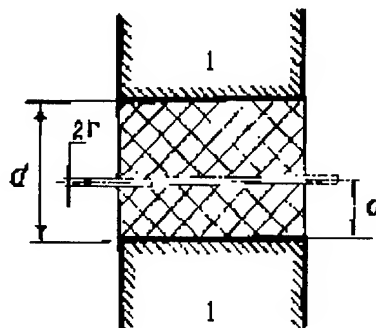


fig.3 Oxide layer with a probe between two cylindrical electrodes (1).

thickness, we can expect that σ calculated from formulas (4),(5) will give value close to local electrical conductivity near the probe. For determine parameters of electron gas in o.l. pores, was used method of spreading resistance changing in magnetic field H applied parallel to probe. In this case, the current j through o.l. will go under some angle to

electrical field E and in weak magnetic field H ($\frac{uH}{c} \ll 1$, where c -velocity of the light) the following usual formula for resistance change in magnetic field can be used

$$\frac{\Delta R_{sr}}{R_{sr}} = \frac{9\pi}{16} \left(\frac{uH}{c} \right)^2 \quad (6)$$

Thus from the measurements of spreading resistance changing in magnetic field we determine electron mobility u in pores of o.l. near the probe from (6). By using value of electrical

conductivity σ from (4) and value of mobility u , the electron concentration n in pores calculated from $\sigma = enu$. The electron free path length l_o in o.l. pores can be received from the following temperature dependence of electron mobility u (when l_o is not depend from electron energy):

$$u = \frac{4}{3} \frac{el}{\sqrt{2\pi \cdot mkT}} \quad (7)$$

The electron work function ϕ of oxide grains can be determined from measurements of thermoelectric temperature dependence or from measurements of electron concentration dependence from temperature. Experimental devices (tubes) with o.l. located between two cylindrical electrodes (see above and fig.3) used for investigation σ and parameters of electron gas in the pores. For the probe disposed in o.l. used wires from Ni ($\varnothing 17$ micron). The probe wire was heated by alternating current ($f=50$ Hz) to compensate cooling of o.l. around because of heat removal threw metallic wire-contacts.. For this sample (with thickness 100 micron) the

following values were measured: probe spreading resistance R_{sr} and its changing $\Delta R_{sr}/R_{sr}$ in magnetic field. These measurements allowed to receive the following parameters: electrical conductivity σ , mobility u , free path length l_o and concentration n of electron in pores and the work function ϕ for o.l. around the probe. From the measurements of R and $\Delta R/R$ for o.l. between two electrodes was received values of σ, l_o, u, n, ϕ - average throughout the all layer. All these parameters are listed in table 1 for three temperatures of o.l. From these data for electron free path length in pores near probe and for all o.l., it may be concluded that o.l. density was not uniform across its thickness. O.l. density near probe is higher than for all o.l. That non-uniformity of o.l. density is connected with technology of carbonate deposition on the probe. First layers of carbonate are more condensed (packed) during their pulverization on metallic surface of the probe. Because of smaller electron free path length of this thin oxide layer, electrical conductivity near probe was lower than the average o.l. electrical conductivity at high temperatures. A small change of σ near probe (in comparison with σ between two electrodes) produced only by structural cause and is not effect of activity changing of these layers. The last circumstance is confirmed by agreement (within the limits of 0.03-0.05eV) between work function of the layer around probe and average work function of the full layer thickness ϕ for three values of o.l. temperatures at which measurements made.

The correlation between values σ and oxide densities can be seen clearly in low temperature region (below curve bend of the relationship $\lg(1/T)$, fig.4). The smaller is the electron free path length in pores of oxide layer (near the probe), the greater σ is at low temperature. Hence, at low temperature the electrical conductivity σ is defined, in large part, by contacts between grains. The important role of the grain

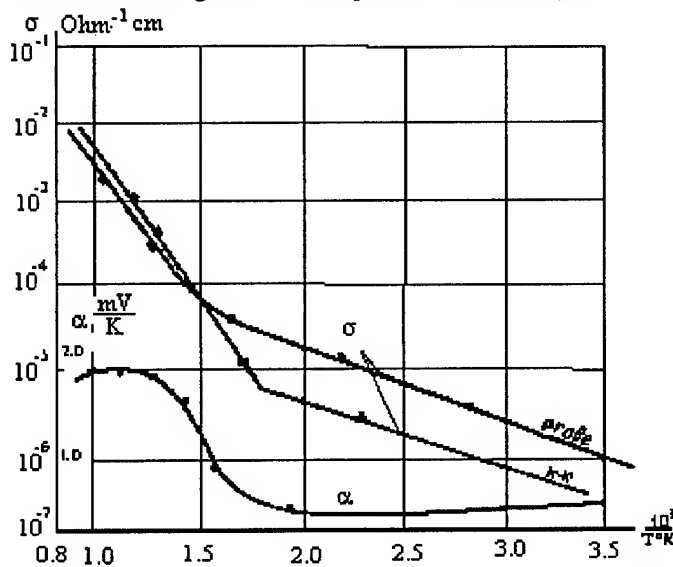


fig. 4 The dependences $\lg \sigma$ and α from $1/T$ for whole layer (k-k) and near the probe (Ni-wire).

contacts can be seen also from the data of thermal conductivity (see [4]) and from measurements of potential distribution when to the layer is applied a big pulse voltage

(see above). The developed method of metallic probe in o.l. is permit to separate the electrical conductivity of crystal frame (grains+contacts) σ_f from the o.l. total electrical conductivity σ_o . For this purpose, it must be measured the thermoelectric changing $\Delta\alpha/\alpha_o$ in magnetic field H simultaneously with the probe spreading resistance changing $\Delta R_{sr}/R_{sr}$ in this field. The ratio of frame electrical conductivity σ_f to the total electrical conductivity σ_o can be received with the help of equation, obtained by B.Ya.Moizhes [2]:

$$\frac{\sigma_f}{\sigma_o} = \frac{1-\gamma}{1-\gamma \frac{\alpha_f}{\alpha_o}} \quad (8)$$

where

$$\gamma = \left(1 + \frac{\Delta\alpha/\alpha_o}{\Delta R_{sr}/R_{sr}} \right)^{-1} \quad (9)$$

All values in (8) and (9) can be measured. The meaning of α_o is conventional to be equal 0,3 mV/°C. It is corresponded to average value of α_f , received by extrapolation the dependence $\alpha=f(1/T)$, (fig.4) from low to high temperature region. The error in α_f is scarcely affected on the calculated value of σ_f/σ_o , because $\alpha_f \ll \alpha_o$. The experimental results for two temperatures of o.l. are presented in tab.2. As it is seen from tab.2, the crystal frame electrical conductivity σ_f is not more then 5% from total value σ_o at temperatures above 1000K

Conclusions

The total electrical conductivity σ_o at high temperatures is determined (see fig.4 and [4]) by two mechanisms, acting in parallel: through electron gas in pores σ_p and through crystal frame σ_f (grains+contacts between them). From experimental determining the values of R_{sr} , $\frac{\Delta R_{sr}}{R_{sr}} = f(H^2)$ and $\frac{\Delta\alpha_o}{\alpha_o} = f(H^2)$ it was shown, that at high temperatures ($\geq 1000K$) electrical conductivity of crystal frame σ_f not exceeded $\sim 5\%$ from σ_o . Extrapolation from low temperature region of the dependence $\sigma_o = \lg(1/T)$ (where $\sigma_o = \sigma_f$), to region of high temperatures, confirm this estimate.

Such value of σ_f will not increase while the electrical field remains weak (till $E \sim 1 \cdot 10^{-2}$ v/cm). The proportion (quota) of electrical conductivity through crystal frame σ_f will rise, as the electrical field will increase. Finally that can lead to the drop in thermoelectric efficiency. Thus, within the range of high temperatures and weak fields, electrical conductivity σ_o is determined, almost completely, by the electron gas in pores, that is, by the work function ϕ of o.l. grains (as electron concentration in pores $n \sim \exp\{-e\phi/kT\}$). That is the most important property of o.l. electrical conductivity σ_o . As indicated in [4], the total thermal conductivity χ_o at $T \geq 1000K$ almost completely determined by transparency of porous o.l. By this means, the porous o.l. is an unique

material in which at $T \geq 1000\text{K}$ the values σ_o and χ_o are practically divorced from each other. It is because they determined by two independent mechanisms of charge and heat transfer. There is not such binding between them, as the Viedeman- Franz law. This is one of the main property of the material, which permitted to receive [3-4] high values of thermoelectric parameters $zT=1.2-1.7$ at $T \geq 1000\text{K}$.

Acknowledgments

Author would like to thank B.Ja.Moizhes for advises and discussion results during performance of this work.

References

- [1].A.F.Ioffe. Semiconductor Thermoelements (in Russian).M.-L., AS USSR, 188p (1960).
- [2].B.Ja.Moizhes. Physical Processes in Oxide Cathode (in Russian).M., "Science", 479p (1968).
- [3].E.M.Sher. "The Thermoelectric Efficiency of Dispersed Porous Oxides of Alkaline -Earth Metals", Proceedings of XII ICT, Yokohama, pp.54-59 (1993).

[4].E.M.Sher. "Effective Thermal Conductivity of Porous Oxides at Temperatures $T > 1000\text{K}$ ", Proceedings of XIV ICT, S.Petersburg, pp.277-279 (1995).

[5].B.Ja.Moizhes,I.N.Petrov,E.M.Sher. "Pulse Electrical Conductivity of Porous Oxide Covering", Radiotekhnika e Elektronica (in Russian, Radio Engineering and Electronics), vol.10, No. 10, pp.1845-1855 (1965).

[6].B.Ja.Moizhes, E.M.Sher, "Probes Method for Investigation of Work Function and Electrical Conductivity of Oxide Cathode", Electronnoe Priborostroenie (in Russian, Electronic Instrument Engineering), Issue 3, L., "Energy", pp.89-108 (1967).

[7].E.M.Sher, "Measurements of Electrical Conductivity and Work Function of Oxide Cathode Covering With Help of The Probe", Radiotekhnika e Elektronika (in Russian, Radio Engineering and Electronics), vol.11, No.9, pp.1721-1723 (1966).

Table 1. Electrical parameters of the o.l. near the probe and between electrodes.

$T_{o.l.}$		905K		996K		1111K	
param-s	units	elctr-elctr	probe	elctr-elctr	probe	elctr-elctr	probe
σ	$\text{Ohm}^{-1}.\text{cm}$	$2.5.10^{-3}$	$8.9.10^{-4}$	$5.8.10^{-3}$	$2.0.10^{-3}$	$1.1.10^{-2}$	$4.4.10^{-3}$
l_o	mkm	6.2	3.4	4.2	2.9	4.8	2.2
u	$\text{cm}^2/\text{v}.\text{sec}$	$4.9.10^4$	$2.7.10^4$	$3.2.10^4$	$2.2.10^4$	$3.5.10^4$	$1.62.10^4$
n	cm^{-3}	$3.2.10^{11}$	$2.1.10^{11}$	$1.1.10^{12}$	$5.6.10^{11}$	$1.9.10^{12}$	$1.7.10^{12}$
φ	ev	1.54	1.57	1.60	1.66	1.75	1.76

Table 2. Results of $\frac{\sigma_f}{\sigma_o}$ measurements from $\frac{\Delta R_{sr}}{R_{sr}}$ and $\frac{\Delta \alpha}{\alpha_o}$ data.

T	$\Delta R_{sr}/R_{sr}$	$\Delta \alpha/\alpha_o$	α_f	φ_p	α_o	σ_f/σ_o
K	(H=1400 Oe)	(H=1400 Oe)	mv / deg	ev	mv / deg	
915	0.322	0.0273	0.3	1.74	2.07	0.095
1090	0.212	0.0102	0.3	1.86	1.88	0.053

Thermoelectric Characteristics of Homologous Compounds with Layer Structures in the ZnO-In₂O₃ System

Kunihito Koumoto, Hiromichi Ohta and Won-Seon Seo

Department of Applied Chemistry, School of Engineering, Nagoya University

Furo-cho, Chikusa-ku, Nagoya 464-01, Japan

Abstract

Thermoelectric materials with high Z 's have been searched for recently among semiconducting oxide ceramics for the purpose of power generation at high temperatures in an air atmosphere. Metallic oxides consisting of non-transition metal elements which would possibly have large band widths and high carrier mobility have been the target materials. One possible oxide group is that having In₂O₃ as a main component. In the present study, homologous compounds of (ZnO)_mIn₂O₃ (m = integer) with layer structures were synthesized by reaction-sintering the powder mixtures of ZnO and In₂O₃ at 1823K for 2h in air. Their thermoelectric characteristics, i.e. electrical conductivity, Seebeck coefficient, and thermal conductivity were measured at 500 - 1000K. Their Z depended on the composition and the microstructure.

Introduction

Refractory ceramic semiconductors could be applied to high-temperature thermoelectric energy conversion because of their high thermal stability and corrosion resistance. Recently metallic oxides having rather high electrical conductivity, such as (Zn_{1-x}Al_x)O[1], In₂O₃-SnO₂[2], and CdIn₂O₄[3] have been investigated to seek for their possible thermoelectric applications. However, the most important problem we face is that refractory oxides of metals usually show only very low energy conversion efficiencies, and it is urgently desired to improve their thermoelectric properties.

Homologous compounds, (ZnO)_mIn₂O₃ (m =integer), have very unique crystal structures with space groups of $R\bar{3}m$ (for m =odd) or $P6_3/mmc$ (for m =even)[4-6] that are composed of layers of InO_{1.5}, (InZn)O_{2.5}, and ZnO periodically stacking in the c -axis direction. Combination of the semiconducting oxides having fairly high electrical conductivity with high carrier mobility would be expected to give rise to a complex oxide with good thermoelectric properties. Homologous compounds of (ZnO)_mIn₂O₃ were chosen from this point of view. This is the first report on the thermoelectric properties of (ZnO)_mIn₂O₃.

Experimental Procedure

Starting materials, ZnO powder and In₂O₃ powder(purity: 99.99%, average particle size :1 μ m for both powders) were weighed in specific proportions to give ZnO/In₂O₃ molar

ratios of 3 to 11 and mixed using an alumina mortar with ethanol. The mixed powders were dried and pressed into compacts under the isostatic pressure of 196MPa, and then reaction-sintered at 1823K for 2h in air. Crystalline phases of the sintered bodies were identified by powder X-ray diffraction(XRD) using CuK α radiation, and their microstructures were observed with a scanning electron microscope(SEM) and a transmission electron microscope(TEM). Compositions of the sintered bodies were measured using an inductively coupled plasma(ICP) spectroscopic analyser. Relative densities of the sintered bodies were measured by an Archimedes technique.

The specimens for electrical measurements were cut out of the sintered bodies into rectangular bars of 6 x 6 x 18mm with a diamond saw. Heads of the two Pt-Pt13%Rh thermocouples were embedded in the drilled holes at the ends of a specimen and they were fixed by platinum wires. Electrical conductivity and thermoelectromotive force were measured simultaneously for the same specimen at 500 to 1100K under Ar atmosphere.

Thermal diffusivity and specific heat capacity were measured by a usual laser flash method. The disk specimen was set in an electric furnace, and heated up to a target temperature in vacuum. After the temperature became stabilized, the front surface of the specimen was irradiated by a ruby laser pulse. The temperature variation at the rear surface was monitored with a Pt-Pt13%Rh thermocouple and an InSb infrared detector. The thermal conductivity(κ) was calculated from thermal diffusivity, specific heat capacity and density.

Results and Discussion

Crystalline phases and microstructure

Figure 1 shows the measured XRD patterns of the sintered bodies synthesized by reaction-sintering the ZnO and In₂O₃ mixed powders and those for (00l) reflections calculated from the lattice constants of a hexagonal cell which were calculated from the following equation proposed by Nakamura et al.[6],

$$c_{\text{calcd}} = \{ p + q + (m - 1) \cdot r \} \cdot z$$

where c_{calcd} is the thickness of the unit cell in the c -axis direction, p is the thickness of InO_{1.5} layer, q is the thickness of (InZn)O_{2.5} layer, r is the thickness of ZnO layer, and z is the number of formula unit in a unit cell.

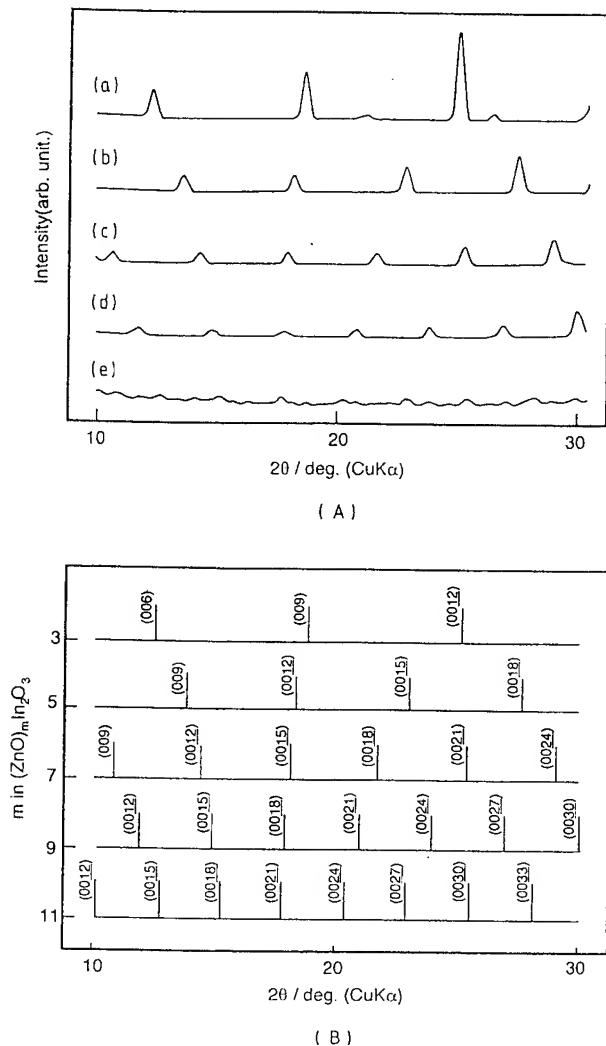


Fig. 1. (A) X-ray diffraction patterns of $(\text{ZnO})_m\text{In}_2\text{O}_3$ sintered bodies synthesized by reaction-sintering the ZnO and In_2O_3 mixed powders [$\text{ZnO}/\text{In}_2\text{O}_3$ molar ratios=(a) 3, (b) 5, (c) 7, (d) 9, and (e) 11] and (B) those calculated from the lattice constants of hexagonal axis.

The employed values are as follows; $(p + q) = 0.8951(\text{nm})$, $r = 0.2602(\text{nm})$, $z = 3$ for $m=\text{odd}$, and $z = 2$ for $m=\text{even}$. X-ray diffraction angles for the sintered bodies synthesized from $\text{ZnO}/\text{In}_2\text{O}_3$ molar ratios=5, 7, and 9 coincided with those calculated from the lattice constants. However, for other starting compositions, i. e. $m=3$ and 11, XRD patterns corresponding to either $m=4$ or unknown phases were additionally observed.

Figure 2(a) shows a typical SEM photograph of the microstructure of a single-phase sintered body polished and thermally etched at 1523K. It is interesting to note that parallel stripes can be seen in each grain. They may reflect the existence of planar defects, possibly stacking faults (twin and deformation faults), judging from the high-resolution TEM photograph shown in Fig. 2(b). However, no preferred crystal-axis orientation was observed in XRD patterns indicating that these planar defects are randomly

distributed in a whole sintered body. Sintered samples were almost fully dense and few pores were observed. Table 1 shows Zn/In atomic ratios obtained from ICP analyses, average grain sizes and bulk densities of the sintered bodies. The Zn/In ratios were in good

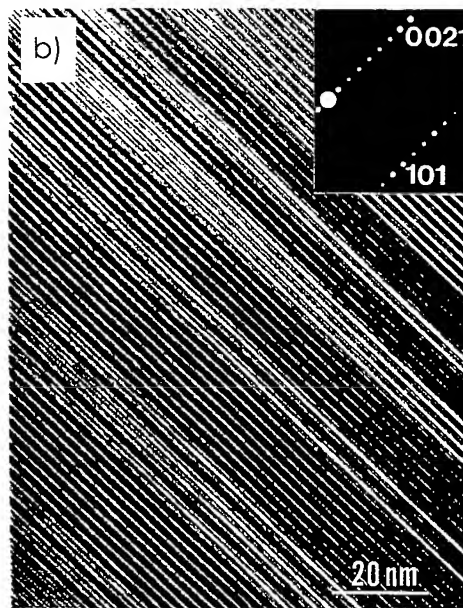


Fig. 2. (a) SEM photograph of the surface of $(\text{ZnO})_s\text{In}_2\text{O}_3$ sintered body polished and thermally etched at 1523K: (b) TEM photograph of a thin section.

accordance with those of starting compositions. Even though the average grain size decreased slightly with increasing m in $(\text{ZnO})_m\text{In}_2\text{O}_3$, their microstructures were basically similar.

Thermoelectric properties

Figure 3 shows the temperature dependences of Seebeck coefficient and electrical conductivity for $(\text{ZnO})_m\text{In}_2\text{O}_3$ ($m=5, 7$, and 9) specimens and a dense ZnO sintered body for comparison. Seebeck coefficients (Fig. 3(a)) were always negative, and the specimens were n-type semiconductors. It

should be noted that the absolute value of the Seebeck coefficient increased with increasing temperature. The observed temperature dependence is not usual, since the absolute value of Seebeck coefficient decreases with increasing carrier density in a common semiconductor.

Table 1 Analyzed Zn/ In atomic ratios (A.R.), average grain sizes (A.G.) and bulk densities (B.D.) of the (ZnO)_mIn₂O₃ sintered bodies.

m in (ZnO) _m In ₂ O ₃	A.R.	A.G.(μm)	B.D.(gcm ⁻³)
5	2.53	10.9	6.06
7	3.46	9.1	5.99
9	4.54	6.3	5.93

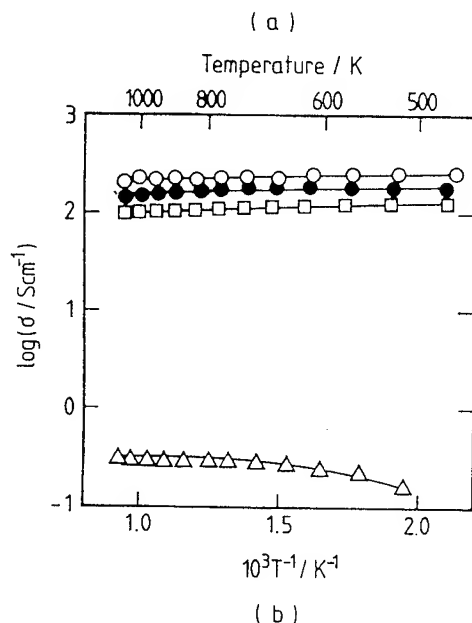
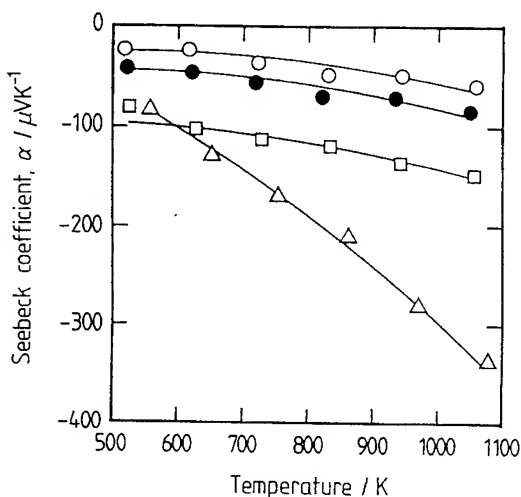
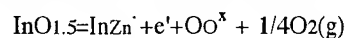


Fig. 3. Temperature dependence of Seebeck coefficient (a), and electrical conductivity (b) for (ZnO)_mIn₂O₃ sintered bodies; ○: m=5, ●: m=7, □: m=9, and △: pure ZnO.

However, similar tendency was also reported for β-SiC and

boron carbide, and was analyzed in terms of the phonon-drag effect[7] and the small polaron hopping conduction[8], respectively. The phonon drag effect was also observed for ZnO at 80 to 300K; Seebeck coefficient was 1200μVK⁻¹ at 300K and 30000μVK⁻¹ at 80K, respectively[9].

Figure 3(b) shows that the electrical conductivity decreased gradually with increasing temperature, which would indicate metallic conduction taking place at first sight. However, the electrical conductivity of (ZnO)_mIn₂O₃ is rather low and the Seebeck coefficient is rather large for metallic conduction. We would rather believe that the concentration of conduction electrons is quite high and fixed in the present temperature range possibly because the carrier density is determined by the valency control mechanism expressed as the following equation which was possibly induced by certain small deviations from stoichiometric compositions;



If this is the case for carrier generation and the carrier density is fixed in the present temperature range, the temperature dependence of electrical conductivity would have reflected that of carrier mobility decreasing with increasing temperature. However, the anomalous temperature dependence of Seebeck coefficient shown in Fig. 3(a) must then be attributed to a certain unusual mechanism, such as a phonon drag effect. On the contrary, if the carrier density decreases with increasing temperature possibly due to, for example, the reduction of In³⁺ to In²⁺, the observed temperature dependences of both electrical conductivity and Seebeck coefficient can be regarded as quite common and understandable. To clarify which mechanism dominantly works, Hall effect measurements for instance would be necessary, and a further detailed investigation on the electrical conduction mechanism will appear in our future publication.

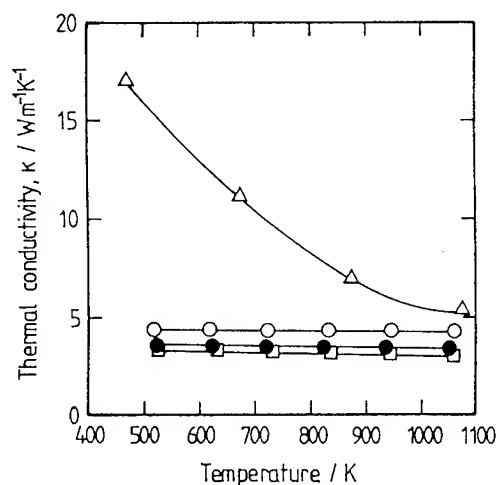


Fig. 4. Temperature dependence of thermal conductivity for (ZnO)_mIn₂O₃ sintered bodies; ○: m=5, ●: m=7, □: m=9, and △: pure ZnO.

Figure 4 shows the temperature dependence of the thermal conductivity calculated from specific heat capacity, thermal diffusivity, and bulk density. Specific heat capacity decreased and thermal diffusivity slightly increased leading to a decrease in thermal conductivity with increasing m in $(\text{ZnO})_m\text{In}_2\text{O}_3$. Thermal conductivity of ZnO estimated from the reported data[10] is much higher than those of $(\text{ZnO})_m\text{In}_2\text{O}_3$ at low temperatures, and similar at high temperatures. Thermal conductivity could be decreased by enhancing the phonon scattering generally, and the incorporation of In_2O_3 into ZnO constituting a layered structure must have enhanced the phonon scattering and hence lowered its thermal diffusivity.

Figure 5 shows the temperature dependence of the thermoelectric figure of merit, $Z(=\sigma\alpha^2/\kappa)$, calculated using the data shown in Figs. 3 and 4. The figure of merit increased with increasing temperature and increasing m in $(\text{ZnO})_m\text{In}_2\text{O}_3$. The figure of merit of ZnO is also shown in Fig. 5 for comparison. Although this result firmly suggests

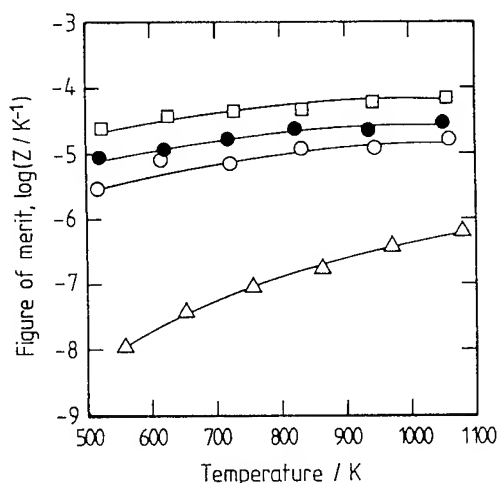


Fig. 5. Temperature dependence of figure of merit for $(\text{ZnO})_m\text{In}_2\text{O}_3$ sintered bodies; ○: $m=5$, ●: $m=7$, □: $m=9$, and △: pure ZnO.

that the optimum value of m in $(\text{ZnO})_m\text{In}_2\text{O}_3$ apparently exists between $m=9$ and $m=\infty$ (pure ZnO) giving the largest figure of merit, homologous compounds with the values of m larger than 9 were unable to synthesize in single phase forms and the optimum composition could not be determined. However, though the figures of merit of the homologous compounds are not so high compared to those of non-oxide thermoelectric materials, such as Bi_2Te_3 [11] and PbTe [12], they are comparable to or higher than those of other oxide materials so far reported. Moreover, as the figure of merit becomes large at relatively high temperatures, these compounds can be regarded as candidates for high-temperature applications. Appropriate doping and microstructure control would be effective to further improve the thermoelectric properties of this compound series.

References

- [1] T. Tsubota, M. Ohtaki, K. Eguchi and H. Arai, "Thermoelectric Properties of Mixed Oxides $(\text{Zn}_{1-x}\text{Al}_x)\text{O}$ ", pp.683, Proceedings of Annual Meeting of The Ceramic Society of Japan, 1995 (in Japanese).
- [2] M. Ohtaki, D. Ogura, K. Eguchi and H. Arai, "Thermoelectric Properties and Applicability of In_2O_3 -based Mixed Metal Oxides for Thermoelectric Conversion at High Temperature", pp.212-17, Proceedings of the 12th International Conference on Thermoelectrics (Yokohama, Japan, November, 1993). Edited by K. Matsuura.
- [3] R. D. Shannon, J. L. Gilson and R. J. Bouchard, "Single Crystal Synthesis and Electrical Properties of CdSnO_3 , Cd_2SnO_4 , In_2TeO_6 and CdIn_2O_4 ", J. Phys. Chem. Solids, **38** 877-881 (1977); W. S. Seo, H. Sinnachi and K. Koumoto, "Synthesis of Spinel-type Oxides and Their Thermoelectric Properties", pp.206, Proceedings of Annual Meeting of The Ceramic Society of Japan, 1994 (in Japanese).
- [4] H. Kasper, Z. Anorg. Allg. Chem., **349** 113-123 (1967).
- [5] P. J. Cannard and R. J. D. Tilley, "New Intergrowth Phases in the $\text{ZnO-In}_2\text{O}_3$ System," J. Solid State Chem., **73** 418-426 (1988).
- [6] M. Nakamura, N. Kimizuka and T. Mohri, "The Phase Relations in the $\text{In}_2\text{O}_3\text{-Fe}_2\text{ZnO}_4\text{-ZnO}$ System at 1350°C ," J. Solid State Chem., **86** 16-40 (1990).
- [7] K. Koumoto, M. Shimohigoshi, S. Takeda and H. Yanagida, "Microstructure and Thermoelectric Energy Conversion in Porous SiC Ceramics", pp. 501-510 in Ceramic Transactions, Silicon Carbide '87, Vol. 2, 1989 by The American Ceramic Society, Inc.
- [8] K. Koumoto, "Thermoelectric Properties of CVD Boron Carbide," Am. Ceram. Soc. Bull., **73** [10] 84-87 (1994).
- [9] A. R. Hutson, "Seebeck Effect in Zinc Oxide," Bull. Am. Phys. Soc., **2** 56 (1957).
- [10] W. D. Kingery, J. Franchl, R. L. Coble and T. Vasilos, "Thermal Conductivity : X, Data for Several Pure Oxide Materials Corrected to Zero Porosity," J. Am. Ceram. Soc., **37** [2] 107-110 (1954).
- [11] H. T. Kaibe, M. Sakata and I. A. Nishida, "Thermoelectric Cooling Properties of the p-Shaped Thermocouples Consisting of the Sintered Bi_2Te_3 and Sb_2Te_3 Based Compounds", pp. 212-217, Proceedings of the 12th International Conference on Thermoelectrics (Yokohama, Japan, November, 1993). Edited by K. Matsuura.
- [12] D. M. Rowe and C. M. Bhandari, "A Review of Lead Telluride Technology at UWIST", pp. 43-54, Proceedings of the 6th International Conference on Thermoelectric Energy Conversion (Arlington, 1986).

Thermoelectric Properties of $\text{La}_{2-x}\text{Sr}_x\text{CuO}_4$

M. Shiloh*, B. Dabrowski, D.G. Hinks, J. Mitchell, K. Zhang, R. Mogilevski, Materials Science Division, Argonne National Laboratory, Argonne, IL 60439, U.S.A.

Abstract

$\text{La}_{2-x}\text{Sr}_x\text{CuO}_4$ is unique among the high T_c superconductors with high values of Seebeck coefficient in the normal state for $x < 0.1$, in addition to a low thermal conductivity. Seebeck coefficient and electrical conductivity were measured for samples of sintered and single crystal $\text{La}_{1.95}\text{Sr}_{0.05}\text{CuO}_4$ in order to look for the optimum concentration of Sr as related to its thermoelectric properties at room temperature. At this doping level this material is in the region of metal-insulator transition. Room temperature values of $147 \mu\text{V/K}$ and $0.01 \Omega\text{cm}$ for the Seebeck coefficient and the electrical resistivity, respectively, were obtained for a sintered sample. For a single crystal of the same composition, the Seebeck coefficient parallel to the ab planes is $143 \mu\text{V/K}$ and along the c axis it is $156 \mu\text{V/K}$. The electrical resistivity was measured only along the ab planes, down to about 9K. The R.T. value was $0.03 \Omega\text{cm}$. No significant change was observed after annealing, either in oxygen or in vacuum. There is a significantly different behavior of the temperature dependence of the resistivity between the sintered and single crystal samples: the sintered sample has a metallic behavior from room temperature down to 80K, and there is no superconducting transition above 10K - whereas the single crystal shows semiconducting behavior from R.T. down to the superconducting transition with an onset temperature of 17K (along the lower resistivity ab planes). Our data are compared with published data of different values of x in the system $\text{La}_{2-x}\text{Sr}_x\text{CuO}_4$.

Introduction:

$\text{La}_{2-x}\text{Sr}_x\text{CuO}_4$ is unique among the high- T_c superconductors with high values of Seebeck coefficient in the normal state, in addition to a low thermal conductivity (1-5). The room temperature Seebeck coefficient data are discussed by some of us in a separate paper (6). Unlike in Bi_2Te_3 , there is a significant anisotropy of the Seebeck coefficient in this material, the ratio S_c/S_{ab} increases about ten-fold with increasing x (the dopant concentration), from 0.05 to 0.25 (4,6). On the other hand there is only a small decrease of the ratio ρ_c/ρ_{ab} with increasing x, with ρ_c two order of magnitude higher than ρ_{ab} (4). (where S is the Seebeck

coefficient, the electrical resistivity, ρ_c denotes the orientation parallel to the crystallographic c axis and ρ_{ab} denotes orientation parallel to the ab planes). In order to look for the optimum concentration of Sr, as related to thermoelectric properties, we measured the Seebeck coefficient and electrical resistivity of sintered and single crystal samples of $\text{La}_{1.95}\text{Sr}_{0.05}\text{CuO}_4$. At this doping level of strontium the material is within the region of metal-insulator transition, where the expected value of the Seebeck coefficient is in the range of $100\text{--}200 \mu\text{V/K}$. Above $x = 0.1$ the material has a metallic behavior (4).

Experimental:

Details of the preparation of the sintered samples as well as the growth of the single crystal by the float zone refining technique are reported in previous publications(6,7). Resistivity measurements, in the temperature range 9K - 300K, were done by the standard four-probe method, using samples with dimensions: $1 \times 1 \times 5 \text{ mm}^3$. The electrical contacts were made by a silver paint. Samples of single crystal were cut after orientation alignment by x-ray Laue photographs so that the a-b planes were parallel to the long dimension of the sample. Samples for Seebeck measurements were cut $2 \times 2 \times 2 \text{ mm}^3$ after being oriented by x-ray Laue photographs so that the c axis was perpendicular to one of the faces of the cube.

Results and Discussion:

Fig.1 shows powder x-ray diffraction of crushed sample of the single crystal, which shows that it is a single phase. Measured room temperature Seebeck data are given in table 1:

Table 1 - measured r.t. seebeck data for $\text{La}_{1.95}\text{Sr}_{0.05}\text{CuO}_4$

S_{sintered}	S_{a-b}	S_c	$S_{\text{calculated}}$	S_c/S_{a-b}
147	143	156	134	1.09
($\mu\text{V/K}$)	($\mu\text{V/K}$)	($\mu\text{V/K}$)	($\mu\text{V/K}$)	

The room temperature data were found to be temperature independent in the range used in our measurements: 298K - 313K.

* Permanent address: Dept. of Solid State Physics, Soreq N.R.C., Yavne 81800, Israel.

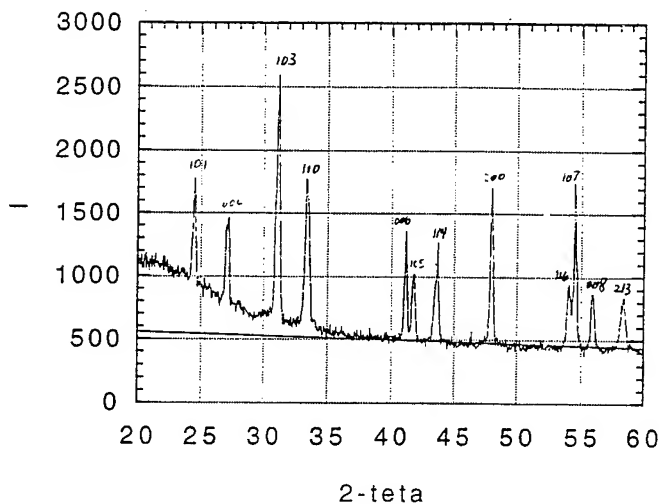
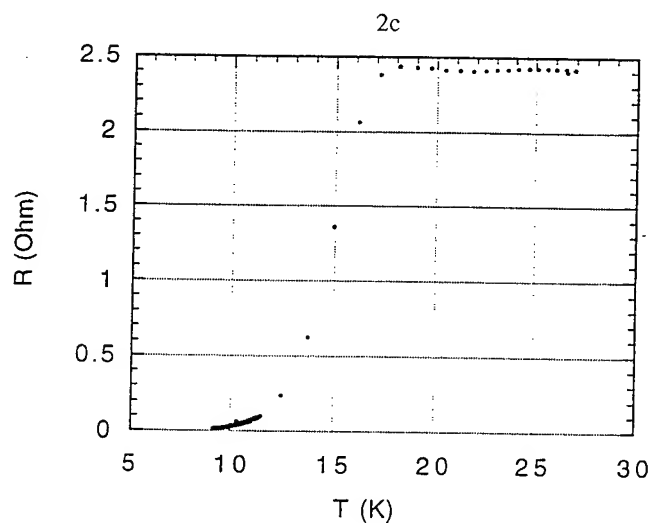
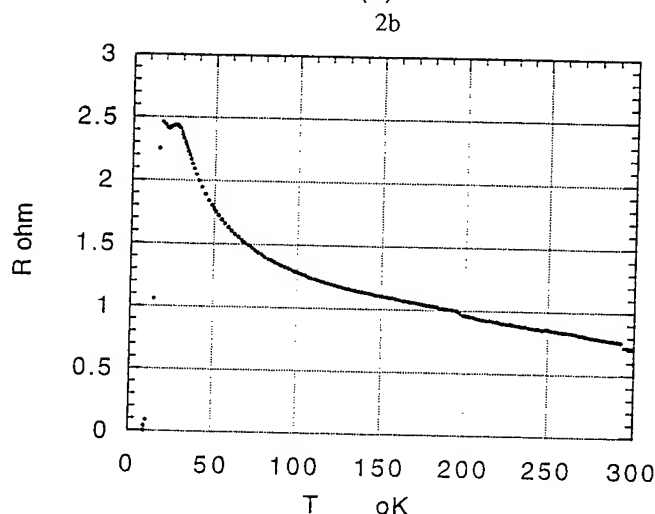
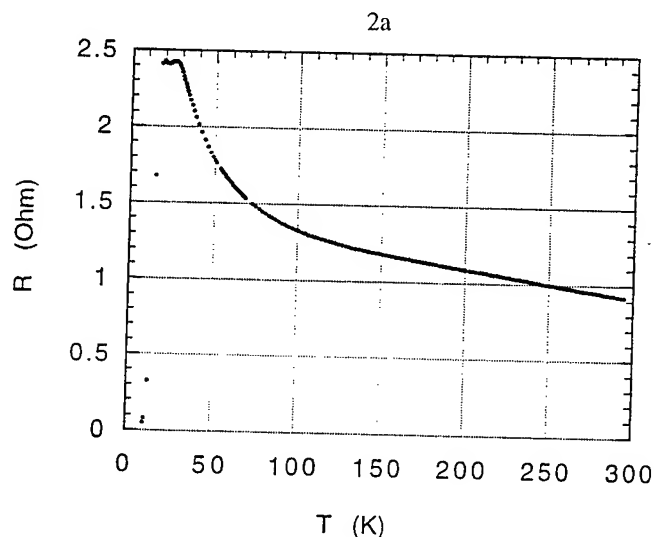


Fig. 1. XRD of crushed sample of single crystal $\text{La}_{1.95}\text{Sr}_{0.05}\text{CuO}_4$.

At this low doping level the anisotropy is small. (pure La_2CuO_4 is isotropic with respect to the Seebeck coefficient (6)). The value of S calculated from the Heikes formula (8) is in good agreement with the measured values. Assuming a random orientation for the sintered sample, a value of $S_{\text{random}} = 1/3S_c + 2/3S_{a-b}$ could be expected. From our data $S_{\text{random}} = 147 \mu\text{V/K}$ which coincides with the measured value for the sintered sample. At higher doping levels the values of S_{random} were always higher than the measured S_{sintered} , but always closer to the measured values of S_{a-b} (6).

Figs. 2a & 2b show the temperature dependence of the electrical resistance of a sample of single crystal $\text{La}_{1.95}\text{Sr}_{0.05}\text{CuO}_4$ in the (110) orientation (in the a-b planes). 2a is of a sample annealed in pure oxygen for 48 hrs. and 2b is of the same sample annealed in vacuum at 500C for 14 hrs. No significant difference between the two treatments is observed, which shows that the crystal did not released or absorbed oxygen under reducing or oxidizing conditions, respectively. Both measurements show a semiconducting behavior from room temperature down to the transition temperature, which indicates two transitions, one at about 26K (a very small fraction of the sample) and the second transition, of the main phase, with an onset at 17K. An expanded scale of figs. 2a and 2b near the transition temperature is shown in figs. 2c and 2d. The room temperature resistivity in the (110) direction, from this measurement, was $0.03 \Omega\text{cm}$.



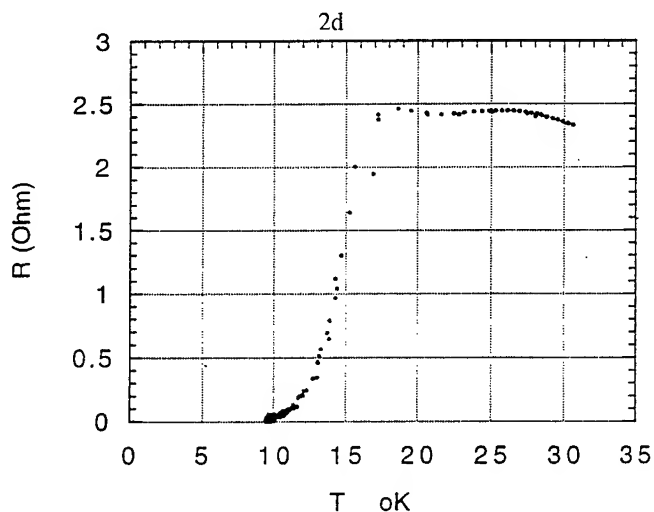


Fig. 2. Temperature dependence of the electrical resistance of single crystal $\text{La}_{1.95}\text{Sr}_{0.05}\text{CuO}_4$ in the (110) orientation. (a) sample annealed in pure oxygen for 48 hrs. (b) same sample annealed in vacuum at 500C for 14 hrs. (c) & (d) expanded scales of (a) & (b) near the superconducting transition temperature.

Fig. 3 shows the temperature dependence of the electrical resistance of a sintered sample of $\text{La}_{1.95}\text{Sr}_{0.05}\text{CuO}_4$. The behavior is entirely different: from room temperature down to about 80K it shows a metallic behavior and there is no superconducting transition above 10K (which was the minimum temperature that we could reach in our system). The room temperature resistivity from this measurement was $0.01 \Omega\text{cm}$.

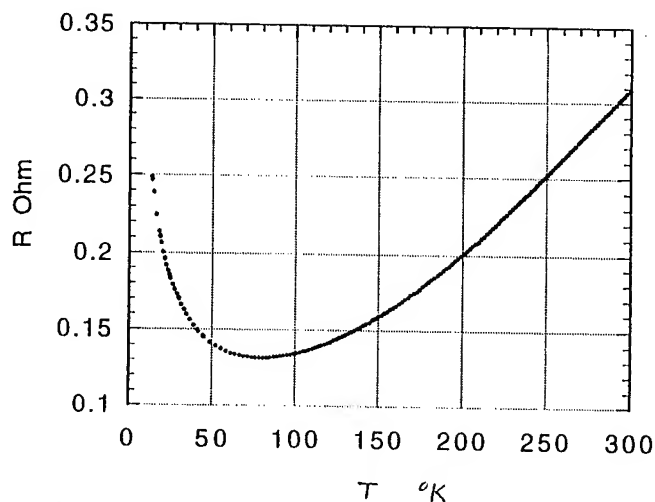


Fig. 3. Temperature dependence of the electrical resistance of a sintered sample of $\text{La}_{1.95}\text{Sr}_{0.05}\text{CuO}_4$.

Fig.4 shows the magnetic susceptibility of a sample of the single crystal $\text{La}_{1.95}\text{Sr}_{0.05}\text{CuO}_4$. The onset temperature of the superconducting transition is not sharp but similar to that measured by the electrical resistance, around 16K.

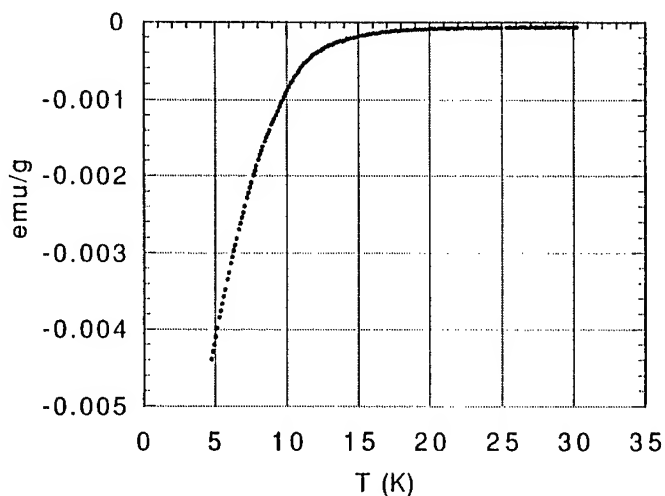


Fig. 4. Temperature dependence of the magnetic susceptibility of a single crystal $\text{La}_{1.95}\text{Sr}_{0.05}\text{CuO}_4$.

According to Kimura et.al. (9), for a sample with $x=0.06$, the resistivity shows a semiconducting behavior along the c axis and a metallic behavior from room temperature down to around 100K, in the a-b planes and a semiconducting behavior at lower temperatures down to the transition temperature. In this group of materials the general trend is a transition from a semiconducting phase to a metallic phase as the doping level (and holes concentration) is increased. The different behavior of the sintered sample and the single crystal along the a-b planes, arises from difference in holes concentration between the different samples and reflects the fact that this doping level is in the border between the semiconducting and metallic phases, so that relatively small changes in holes concentration can shift from one type of phase to the other. The resistivity along the c axis is more than two order of magnitudes higher compared with that in the a-b planes for the same value of x , and in addition, below $x = 0.1$ it shows a semiconducting behavior. Along the a-b planes the behavior is metallic down to $x = 0.1$ but as x is decreased a semiconducting behavior starts to show up at the low temperature range (4). Cieplak et. al.(10) measured the resistivities along the a-b planes of aligned films of polycrystals: as the values of x decreased the transition temperature from semiconducting to metallic phase increased, but even at $x = 0.03$ the transition to semiconducting behavior started much below room temperature, around 120K. Our measurements on single

crystal show for $x = 0.05$ a semiconducting behavior up to room temperature.

From our results for $x = 0.05$ it turns out that compared with $x = 0.1$ the thermoelectric figure of merit remains in the same order of magnitude because the increase in the Seebeck coefficient is compensated by the increase in resistivity: assuming a value of 0.03 W/cm.K (11) for the thermal conductivity, the room temperature figure of merit of the sintered $\text{La}_{1.95}\text{Sr}_{0.05}\text{CuO}_4$ is $0.7 \times 10^{-4} \text{ K}^{-1}$. For the single crystal in the a-b planes it is $0.2 \times 10^{-4} \text{ K}^{-1}$. From the data of Nakamura et al. (4) the values of the figures of merit for $x = 0.1$ and $x = 0.15$, in the a-b planes, are $0.7 \times 10^{-4} \text{ K}^{-1}$ and $0.3 \times 10^{-4} \text{ K}^{-1}$, respectively. The values in the a-b planes are overestimates because the value of the thermal conductivity along this direction is expected to be higher than that of a sintered sample. In any case it seems that reducing the doping level to shift from a metallic phase toward the semiconducting phase still leaves the thermoelectric figure of merit of this material in the same order of magnitude, which is more than one order of magnitude smaller than in bismuth telluride alloys. Cassart et al. (11) find the same order of magnitude for sintered samples of Ba doped lanthanum cuprate. They suggest a possible improvement of the figure of merit by taking advantage of the anisotropy of this material, based on the results of Sera et al. (2), who claim that $S_{a-b} > S_c$, contrary to all other published results which show that the transport properties along the a-b planes are always much more metallic than along the c axis.

References

- [1] J.R. Cooper, B. Alavi, L.W. Zhou, W.P. Beyermann and G. Gruner Phys.Rev. B, 35,p.8794 (1987).
- [2] M. Sera, S.Shamoto and M.Sato, Solid State Commun. 68, No.7, p.649 (1988).
- [3] M. Sera, T. Nishikawa and M. Sato, J. Phys. Soc. Japan, 62, No.1, p. 281 (1993).
- [4] Y. Nakamura and S. Uchida, Phys. Rev. B, 47, No.13, p. 8369 (1993).
- [5] C. Hohn, M. Galfy and A. Freimuth, Phys. Rev. B, 50, No.21, p. 15875 (1994).
- [6] M. Shiloh, K. Zhang, D.G. Hinks and R. Mogilevsky (to be published).
- [7] K. Zhang, R. Mogilevsky, D.G. Hinks, J. Mitchell, M. Shiloh, Y. Wang and M. St. Louis-Weber, 1995 Taiwan Int. Conf. on Superconductivity.
- [8] R.R. Heikes and R.W. Ure, "Thermoelectricity: Science & Engineering", chapter 4, Interscience (1961).
- [9] T. Kimura et.al. Physica C, 192, p. 247 (1992).
- [10] M.Z. Cieplak, M. Berkowski, S. Guha, E. Cheng, A.S. Vagelos, D.J. Rabinowitz, B. Wu, I.E. Trofimov and P. Lindenfeld, Appl. Phys. Lett., 65, (26) p. 3383 (1994).
- [11] M Cassart, L. Piraux and J.P. Issi, Proc. 8th Int. Conf. on Thermoelectric Energy Conversion, Nancy (1989), p. 121.

Electronic Transport Properties of $\text{PrBa}_2\text{Cu}_{3-x}\text{Ga}_x\text{O}_{7-\delta}$

W. W. Fuller-Mora, K. L. Stokes, T. M. Tritt, A. C. Ehrlich

Materials Physics Branch, Naval Research Laboratory,
Washington, DC 20375, USA

J. Z. Liu, R. N. Shelton

Department of Physics
University of California
Davis, CA 95616 USA

Abstract

We have measured the electrical resistivity, ρ , and the thermopower, S , of $\text{PrBa}_2\text{Cu}_{3-x}\text{Ga}_x\text{O}_{7-\delta}$ in a temperature range from 300 K down to approximately 100 K. Samples with varying amounts of Ga substitution ($x = 0.0, 0.2, 0.4, 0.6$, and 0.8) were studied, some of which were annealed in flowing O_2 for one week at 700°C . At room temperature the resistivity of the material increases by several orders of magnitude as Ga is substituted for the Cu. The thermopower increases from $100\ \mu\text{V/K}$ for $x = 0.0$ to approximately $300\ \mu\text{V/K}$ when $x = 0.2$. The value does not continue to increase as more Ga is substituted. The resistivity increases as the temperature is lowered, while the thermopower exhibits a complicated temperature dependence. Annealing the material in O_2 decreases the resistivity, but does not change the room temperature value of the thermopower. Although the resistivity may follow a 3D variable range hopping expression as a function of temperature, the thermopower does not. The thermopower may show indications of magnetic transitions. The power factor ($=S^2/\rho$) at room temperature is greatest for $x = 0.0$ with a value of $10^{-1}\ \mu\text{W}/(\text{K}^2\text{-cm})$, it decreases over several orders of magnitude as Ga is substituted. It also decreases as the temperature is lowered. We conclude that the system $\text{PrBa}_2\text{Cu}_{3-x}\text{Ga}_x\text{O}_{7-\delta}$ is probably not going to be useful as a thermoelectric material, even with other substitutions such as Y for Pr.

Introduction

In measuring the thermoelectric power of $\text{PrBa}_2\text{Cu}_3\text{O}_{7-\delta}$ we found that there is a large positive thermopower on the order of $100\ \mu\text{V}$ at room temperature. This material belongs to the family of copper oxides that include the high temperature superconductors. It is known that it is possible to modify the behavior of these materials by substitution of various elements [1]. The crystal structure of these materials is complicated; thus, a variety of substitutions and behaviors are possible. Measuring a sample with 40% Ga in place of the Cu increased the room temperature thermopower by a factor of three. This led us to initiate a systematic study of $\text{PrBa}_2\text{Cu}_{3-x}\text{Ga}_x\text{O}_{7-\delta}$. This system has been studied by several groups [2,3]. These groups measured the temperature dependence of the resistivity of ceramic samples. However, they did not perform a complete study of the thermoelectric power. The resistivity decreases with increased Ga concentration. We wish to study what happens to the thermopower with Ga substitution.

It is known that the quantity of interest for thermoelectric materials is the figure of merit [4]:

$$ZT = \frac{S^2 \sigma}{\lambda} T \quad (1)$$

where S is the thermopower, σ the electrical conductivity, and λ the thermal conductivity. A material which is a good candidate for thermoelectric applications will have a $ZT \geq 1$. Thus a good candidate material will have a large thermopower, large electrical conductivity, and small thermal conductivity. It is known [5] that as the carrier concentration increases, the thermal and electrical conductivities increase and the thermopower decreases. There is an optimum carrier concentration on the order of 10^{18} to $10^{19}/\text{cm}^3$ for thermoelectric materials. The power factor:

$$PF = S^2 \sigma \quad (2)$$

has a maximum at the optimum carrier concentration for good thermoelectric materials. Thus, by studying the electrical conductivity (or equivalently the resistivity) and the thermopower of a material, one obtains a very good indication of the usefulness that material might have as a thermoelectric.

Experimental Procedure

The materials we studied were made by the conventional solid state reaction method of heating oxides of the required elements in a furnace. This was followed by repeated grinding and sintering of the resulting powder. The powder was then pressed into disks about 2 mm in thickness by 12 mm in diameter. These disks were cut into rectangular prisms of 10 mm x 2 mm x 1 mm with a high speed diamond saw for our measurements. In order to study the effect of the O concentration we annealed some of the samples at 700°C for one week in flowing O_2 .

Standard four-probe resistance measurements were performed on all our samples. The voltage leads consisted of 3 mil Au wire attached to the sample with pressed In contacts, typically under 1 mm in width. The current leads were 5 mil Cu wire attached with Ag paint. Thermocouples, 0.005" Au-Fe (0.07 at%) vs. Cr, were attached to the samples with GE 7031 varnish to enable measurement of the temperature gradient across the sample. The sample voltage (V_S) as well as the thermocouple voltage (V_{TC}) were measured with a Keithley 182 nanovoltmeter. The Au-Fe vs. Cr

thermocouples provide adequate sensitivity even to the lowest temperatures ($T \approx 4\text{K}$). The temperature of the sample was determined using a Lake Shore calibrated Cernox sensor. Temperature control was provided by a Pt resistance thermometer. The resistance of the sample was taken by reversing the current at each temperature and measuring the sample voltage and then taking an average. Typical sample currents were $0.1 - 100 \mu\text{A}$. We attempted to keep the sample voltage under 10 mV to avoid self heating during the resistivity measurements, although this was not always possible.

The thermopower was measured in two ways. First a standard V_S vs. ΔT curve was taken at several temperatures with the gradient on the sample being swept from $-\Delta T$ to $+\Delta T$ with $\Delta T \approx 2-5\%$ of T . The slope was calculated and the Au lead contribution subtracted, thus giving the absolute thermopower of the material. We used this method to check our more typical method. In this method a ΔT of $2-5\%$ T was established across the sample. Then under computer control the sample current was cycled in the following sequence; (1.) $+I$, (2) $I = 0$, (3) $-I$, (4) $I = 0$, (5) $+I$, with sample current and voltage, absolute temperature and thermocouple voltage being read and recorded at each step. The sample resistance was calculated from averaging steps 1, 3, and 5 and the thermopower was calculated from an average of steps 2 and 4. Again the Au lead contribution was subtracted for the thermopower measurements. These quantities were monitored as the sample was slowly cooled from room temperature, typically at a rate of 0.4 K/min . Excellent agreement was found between the two methods. This standard procedure was modified for the most resistive samples. For these materials we found it necessary to obtain the thermopower data in a separate run. In this case the current source was disconnected, a ΔT of $2-5\%$ T was established, and the temperature of the sample slowly swept at 0.4 K/min . The ΔT was changed during the temperature sweep in order to maintain a value of $2-5\%$ T . We were not able to obtain thermopower data when the sample resistance reached $10 \text{ M}\Omega$ due to rf pickup in the system resulting in a dc offset.

Results and Discussion

We have measured the thermopower, S , and electrical resistivity, ρ , as a function of temperature for several concentrations of Ga. As can be seen in Figure 1, increasing the Ga concentration increases ρ by several orders of magnitude.

For each concentration, ρ increases as the temperature is lowered. Annealing the samples in O_2 decreases $\rho(300)$, by an order of magnitude. In the annealed samples, the resistivity also increases with decreasing temperature. The temperature dependence of ρ is best fit by a 3D variable range hopping model [6]. This model predicts that

$$\rho(T) = \rho_0 \exp(T_0/T)^{1/4} \quad (3)$$

In figure 2 we have plotted ρ as a function of $T^{-1/4}$ on a semilogarithmic graph. Plotted in this fashion a straight line would imply agreement with equation 3. As can be seen in figure 2, this model is consistent with the data. This expression fits both the unannealed and the annealed samples.

A semiconducting behavior, $\rho \sim \exp(\Delta/2k_B T)$, is not seen in these materials.

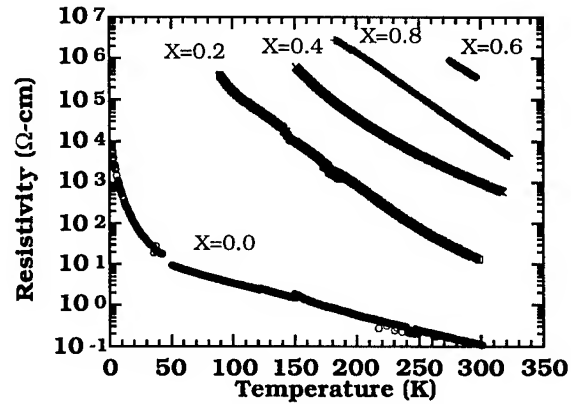


Fig. 1 The resistivity of $\text{PrBa}_2\text{Cu}_{3-x}\text{Ga}_x\text{O}_{7-\delta}$ as a function of temperature. These samples have not been annealed in O_2 .

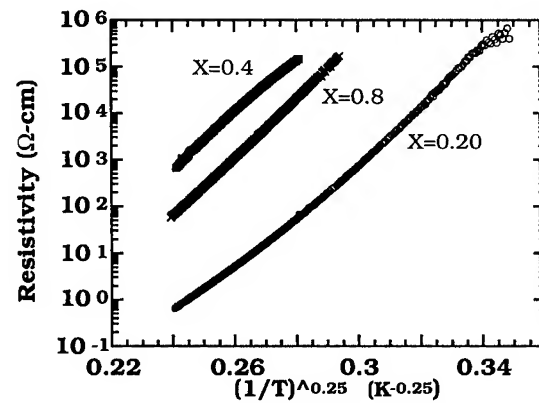


Fig. 2 The resistivity of $\text{PrBa}_2\text{Cu}_{3-x}\text{Ga}_x\text{O}_{7-\delta}$ plotted as a function of $T^{-1/4}$. These samples were annealed in O_2 .

The thermopower of these materials is more complicated as can be seen in figures 3 and 4. Over the temperature range that we studied, the thermopower is positive, implying hole carriers for all concentrations of Ga.

In the 3D variable range hopping model the thermopower (equation 4) is similar to that for the diffusion thermoelectric power as derived from standard Boltzmann theory [6]. From looking at the temperature dependence it is not possible to determine the difference between the two models. Both vary as $1/T$.

$$S(T) = \frac{1}{|e|} \frac{\langle \mu - E \rangle}{T} \quad (4)$$

In the variable range hopping model the quantity in the brackets represents the energy of the sites participating in the conduction. In the expression valid for diffusion thermopower the quantity is the difference between the chemical potential and the valence band.

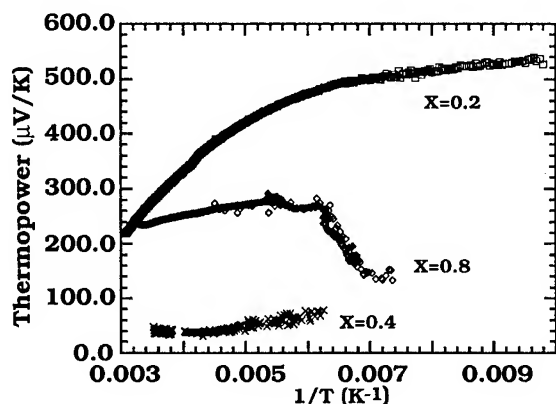


Fig. 3 The thermopower of $\text{PrBa}_2\text{Cu}_{3-x}\text{Ga}_x\text{O}_{7-\delta}$ plotted as a function of $1/T$. These samples were annealed in O_2 .

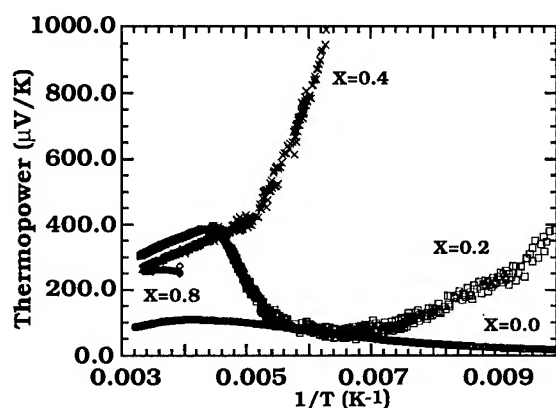


Fig. 4 The thermopower of $\text{PrBa}_2\text{Cu}_{3-x}\text{Ga}_x\text{O}_{7-\delta}$ plotted as a function of $1/T$. These samples were not annealed.

Looking at figures 3 and 4 it is readily seen that the data does not follow a $1/T$ dependence over any appreciable temperature range. It is possible that some of the features in the thermopower of these materials are due to magnetic transitions. Pr is known to order antiferromagnetically in this material [7].

In figure 5 we have plotted the power factor, equation 2, as a function of temperature for the unannealed samples. Figure 6 shows the power factor for the samples which were annealed in O_2 .

Comparing figures 5 and 6 one can see that substituting Ga for Cu decreases the power factor quite dramatically. Annealing the substituted samples increases the power factor. Thus the Ga substitution and the annealing of these materials did effect the carrier concentration. However the power factor is several orders of magnitude less than that for the "state of the art" thermoelectric, Bi_2Te_3 ($\text{PF} = 40 \mu\text{W}/\text{K}^2\text{-cm}$). We therefore conclude that $\text{PrBa}_2\text{Cu}_{3-x}\text{Ga}_x\text{O}_{7-\delta}$ will not be a useful system for thermoelectric applications.

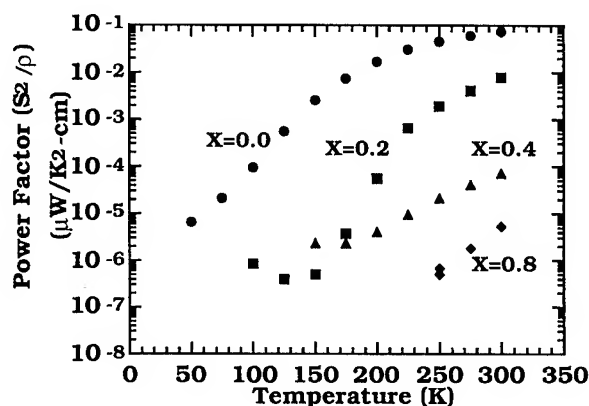


Fig. 5 The power factor for unannealed $\text{PrBa}_2\text{Cu}_{3-x}\text{Ga}_x\text{O}_{7-\delta}$

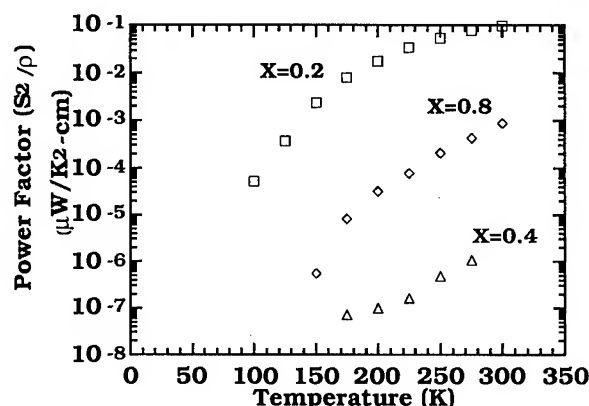


Fig. 6 The power factor for annealed $\text{PrBa}_2\text{Cu}_{3-x}\text{Ga}_x\text{O}_{7-\delta}$

References

- [1] For many examples see *Proceedings of the International Conference on Materials and Mechanisms of Superconductivity: High Temperature Superconductors IV*, ed. P. Wyder, North Holland, The Netherlands (1994), appeared in *Physica C* vol. **235-240** (1994).
- [2] B. Fisher, J. Genossar, L. Patlagan, "Two-band hopping conductivity in the nonmetallic barrier material $\text{PrBa}_2\text{Cu}_{2.8}\text{Ga}_{0.2}\text{O}_y$ ($y \sim 7$)", *Appl. Phys. Lett.* vol. **65**, No. 21, pp 2734-2736 (1994).
- [3] Yunhui Xu, Weiyan Guan, "Hopping Conductivity in the $\text{PrBa}_2\text{Cu}_{3-x}\text{Ga}_x\text{O}_{7-y}$ system", *Physica C*, vol. **206**, pp 59-69 (1993).
- [4] See H. J. Goldsmid, *Electronic Refrigeration*; Pion Limited, London, Chapter 1 (1985).
- [5] A. F. Ioffe, *Semiconductor Thermoelements and Thermoelectric Cooling*, Infosearch Limited, London, pg. 100 (1957).
- [6] N. F. Mott and E. A. Davis, *Electronic processes in Noncrystalline Materials*, Oxford, Chapter 2 (1979).
- [7] B. Fisher, J. Genossar, L. Patlagan, G. M. Reisner, C. K. Subramaniam, A. B. Kaiser, "Hopping conductivity in fully oxygenated $\text{PrBa}_2\text{Cu}_3\text{O}_y$, $\text{YBa}_2\text{Cu}_2\text{CoO}_y$, and $\text{PrBa}_2\text{Cu}_2\text{CoO}_y$ ", *Phys. Rev. B*, vol. **50**, No. 6, pp 4118-4124 (1994).

POSSIBLE WAYS FOR EFFICIENCY IMPROVEMENT OF THERMOELECTRIC MATERIALS

Boris Moyzhes
Space Power, Inc.
621 River Oaks Parkway
San Jose, CA 95134
(408) 434-9500

ABSTRACT

Various properties which influence zT can be improved by using modern technology for creation special submicron structures inside homogeneous thermoelectrics.

Barriers for electrons with $\epsilon < \mu$ can be used to increase thermopower. Modulation doping can be used to increase mobility. Due to diffusion these structures can be used only in materials for TE refrigeration especially $\text{Be}_{1-x}\text{Sb}_x$ alloys.

At high T the best thermoelectrics with $zT > 100$ is electron gas in vacuum due to full absence of lattice thermal conductivity. Even after taking into account the losses due to radiation and electrical lead to emitter the thermionic converter can have $zT \geq 20$.

In 1992 V. Nemchinsky and I presented to XI Int. Conf. on Thermoelectrics (Arlington, Texas) a paper [1] based on our calculations published in 70-ths in the Russian Confidential Journal on Energy Conversion. We discussed possibility to increase the figure of merit (zT) by introducing into a TE material special barriers for low energy electrons to increase Peltier coefficient ($\Pi = \alpha T$) that is entropy current accompanying the charge current. But, neither V Nemchinsky nor I could attend ICT92.

This year I am in position to come back to discussion of the problem: How to increase zT by using new microelectronics technology for goal-directed improvements of homogeneous TE materials?

1. Main Formula

Lets begin with undimensional figure of merit [2]

$$zT = \frac{\alpha^2 6 T}{\chi_L + \chi_e} \quad (1)$$

By using Wiedeman-Franz law

$$\chi_e = L_o \left(\frac{k}{q} \right)^2 6 T \quad (2)$$

we can rewrite (1) as

$$zT = \frac{\left(\frac{\alpha}{k/q} \right)^2}{L_o \left(1 + \frac{\chi_L}{\chi_e} \right)} \quad (3)$$

Usually L_o is constant equal to ~ 2 . Therefore, instead of four material parameters in (1), we have in (3) only two: $\alpha/(k/q)$ and χ_L/χ_e .

Then we have [3]

$$\alpha / \left(\frac{k}{q} \right) = \frac{\langle \epsilon \rangle_j - \mu}{kT} \quad (4)$$

where $\langle \epsilon \rangle_j$ is the mean electron energy in the current and μ is chemical potential of electrons. Thermalconductivity [3].

$$\chi = \frac{1}{3} C v L \quad (5)$$

Formula (5) can be applied to both phonons and electrons

$$C_e = \frac{3}{2} k n_e \quad (6)$$

$$C_L = 3 k N_a \quad (7)$$

From (4) ÷ (7) we obtain, that

$$zT = \frac{\left(\frac{\langle \epsilon \rangle_j - \mu}{kT} \right)^2}{L_o \left(1 + 2 \frac{V_{ph}}{V_e} \cdot \frac{L_{ph}}{L_e} \cdot \frac{N_a}{n_e} \right)} \quad (8)$$

where V_{ph} and V_e are mean velocities of phonons and electrons, L_{ph} and L_e are their mean free paths, and N_a and n_e are concentrations of atoms and electrons. We have

$$\mu = -kT \ln \frac{N_{st}}{n_e} \quad (9)$$

where $N_{st} = 4.82 \cdot 10^{15} T^{3/2} (m^*_d/m_0)^{3/2}$ is density of electron states at the edge of the band (Fig. 1).

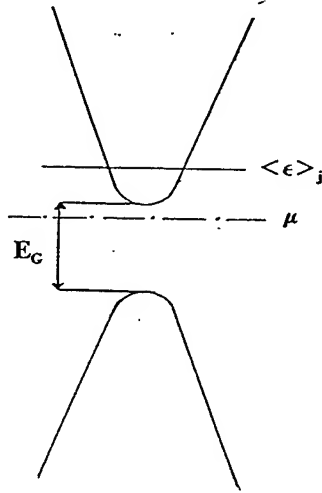


Figure 1 Bands in a semiconductor

By doping we can change n_e in (8) and (9) and find optimal n_e . Usually at $(n_e)_{opt}$ μ is a little below the band edge and $n_e \approx N_{st}$. We have also $L_o \approx 2$ and $\langle \epsilon \rangle_j / kT \sim 2$, therefore

$$(zT)_{max} \propto \frac{2}{1 + P_o} \quad (10)$$

where

$$P_o = \frac{\chi_L}{\chi_e (\mu=0)} = 2 \frac{V_{ph}}{V_e} \cdot \frac{L_{ph}}{L_e} \cdot \frac{N_a}{N_{st}} \quad (11)$$

Usually we have $V_{ph}/V_e \sim 2 \cdot 10^5 / 2 \cdot 10^7 \sim 10^{-2}$, $N_a/N_{st} \sim 3 \cdot 10^{22} / 10^{19} \sim 3 \cdot 10^3$. Approximately $L_e (\text{\AA}) \sim U (\text{cm}^2/\text{vsec})$ and $L_{ph} (\text{\AA}) \sim 2 \cdot 10^3 \chi_L (\text{W/cmK})$, therefore

$$P_o \sim 10^5 \frac{\chi_L \left(\frac{W}{\text{cmK}} \right)}{U \left(\frac{\text{cm}^2}{\text{vsec}} \right)} \quad (12)$$

For obtaining $P_o \leq 1$ we need materials with $\chi_L \leq 10^{-2} \text{ W/cmK}$ and in the same time $U \geq 1000 \text{ cm}^2/\text{vsec}$ and $\alpha \geq 200 \mu\text{V/K}$. Such materials are rather rare.

2. Classical Ways to Increase zT

Classical ways are as follow (A.F. Ioffe) [4]:

- To obtain by doping the optimal concentration.
- To use as dopant atoms with small electron scattering cross sections.
- To find appropriate solid solutions to decrease L_{ph} and in the same time not deteriorate L_e or to find special defects for strong phonon scattering for example vacancy and/or noncentral ions (off-ions) as Ge in GeTe where χ_L is very small.
- But what next?

To search for new TE materials or to search for new ways to improve existing ones? It seems that in (11) there are no parameters except L_{ph}/L_e for zT improvement. But, they do appear if we include into consideration inhomogeneous materials.

We can use inhomogeneities and potential barriers [1] to change electron spectrum (quantum mechanics problems) or to change $\langle \epsilon \rangle_j$ (classical mechanics). Below I am going to discuss some ideas based on classical transport theory.

3. Modulation Doping [5]

Charged dopants atoms scatter electrons and decrease L_e . Many TE have very large dielectric constant but nevertheless at low T impurity scattering becomes dominant. For example, at low T mobility in PbTe with low electron concentrations exceeds $10^6 \text{ cm}^2/\text{vsec}$ ($L_e \sim 10^2 \div 10^3 \text{ cm}$). But at higher concentrations mobility is much lower. Mobility is very important parameter in solid state electronics too. It determines for example the time of gates switching.

In the case of modulation doping the dopant atoms are located inside special layers in the heterostructure. For example -GaAs-Ga_{1-x}Al_xAs-GaAs-Ga_{1-x}Al_xAs- (Figure 2). Scattering is smaller due to decreasing electrons wave-functions inside layers with larger gap E_g . Mobility $U > 2 \cdot 10^6 \text{ cm}^2/\text{sec}$ were obtained in GaAs with modulation doping [5]. The distances between layers with dopant atoms has to be of the order of Debye length, i.e. $\sim 10^{-6} \text{ cm}$ at $n_e \sim 10^{18} \text{ cm}^{-3}$. It is necessary to have very good mirror reflection of electrons from contact surfaces.

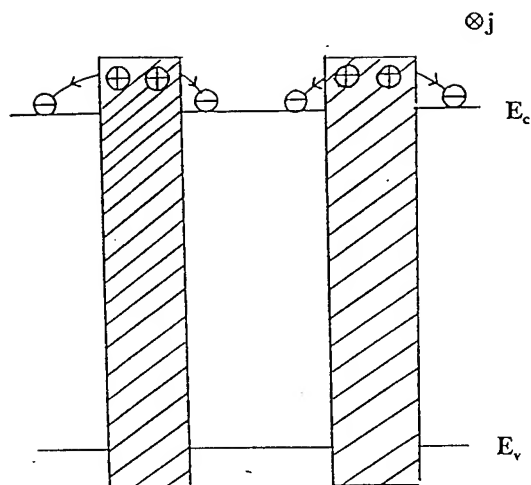


Figure 2 Modulation Doping

If a material has layered structure with different atoms in different layers, the modulation doping can be achieved without any heterostructures. For instance, modulation doping is widely used in high- T_c cuprate superconductors to preserve good translation symmetry inside superconducting CuO_2 layers.

4. TE Materials with Small Gaps (E_G)

From (4) it is obvious that all electrons with energy below μ decrease thermo power like holes. It is easy to show that such electrons decrease $\alpha^2\sigma$ too and besides increase χ_e .

To exclude holes in small gap TE materials, we can create periodic structure $-n^-n^+-n^-n^+$ (Figure 3). The distances L_B between barriers for the minority charge carriers have to be smaller than diffusion length: $L_B \ll L_D = \sqrt{D_e \tau_p}$ (D_e is diffusion coefficient, τ_p is generation-recombination time for holes). L_D at low T can be rather large, in $\text{Bi}_{0.9}\text{Sb}_{0.1}$ it is about several microns [1]. Effectiveness of small gap TE materials with high mobilities can be improved by transverse magnetic field. In such case several model of operation are possible: longitude (Peltier-Seebeck), transverse (Nernst-Ettingshausen) and combined one [6] when ∇T is directed parallel to entropy current and under some optimal angle to electrical current.

5. Barriers for Main Charge Carriers

Suppose we have degenerated electron gas in a semiconductor. All electrons with $\epsilon < \mu$ are harmful for $\alpha^2\sigma$ they are alike holes on Figure 3. To exclude such electrons from the charge and entropy currents we can use barriers as on Figure 4.

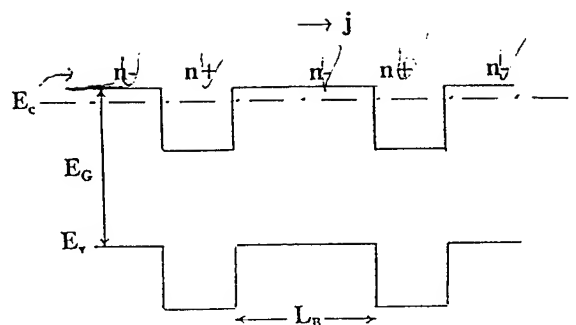


Figure 3 Barriers for Minority Charge Carriers

Inside the barriers only electrons with energy above the barrier can take part in the current. But, if scattering is elastic or almost elastic (defects and acoustical phonons) the flow of energy cannot change after one or even several scatterings which change electron impulse.

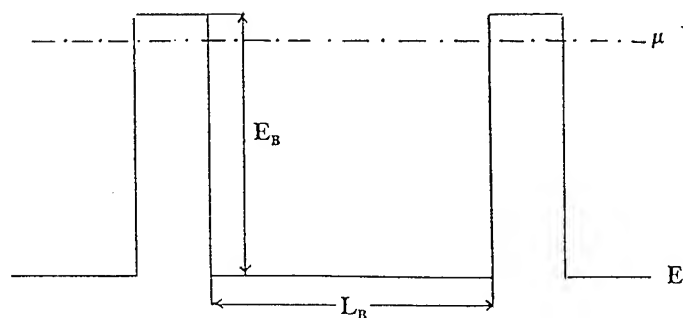


Figure 4 Barriers in the degenerated electron gas to increase $\alpha^2\sigma$

The distance from barrier, where distribution of charge carriers became normal is $L_e \sim \sqrt{D\tau_e}$, where τ_e is relaxation time of entropy current. If $\tau_e \gg \tau_p$ we have $L_e \gg L_p$. And if distances between barriers are smaller than the L_e Peltier coefficient between barriers is the same as inside the barriers. Therefore, we can have α as for non degenerated electron gas but the number of effective charge carriers is higher than in the case when μ is near the bottom of the band due larger effective density of states N_{μ} ($\epsilon \approx E_g$). Therefore such barrier structure can increase $\alpha^2\sigma$ in (1) or decrease χ_L/χ_e in (3) with simultaneous decrease of L_o .

Very important that electron-electron collisions cannot change significantly α or σ in the barrier structures, because in such collisions electrical current and entropy current do not change if Umklapp processes are absent.

It is easy to see [1] that all electrons with $(\epsilon - \mu) < 1/2 (\langle \epsilon \rangle_j - \mu)$ are harmful, i.e. they lower $\alpha^2\sigma$. Therefore, if we could increase scattering of these electrons and in the same time none or little disturb flow of electrons with higher energy we could obtain higher zT . It can be done by small barriers, resonance scattering [9] or interband scattering [10].

6. Vacuum as TE Material

Electron gas in vacuum between two hot emitting electrodes (Figure 5) has σ , α and χ_e as electrons in solids but $\chi_L = 0$. In such case $\mu = \phi$ (work function) and as it is easy to show that $L_o = 2$ and $\langle \epsilon \rangle_j/kT = 2$. Therefore:

$$(zT)_{vac} = \frac{1}{2} \left(\frac{\phi}{kT} + 2 \right)^2 \quad (13)$$

Figure of merit in (13) can be much higher than for solid TE materials. If for example $T = 1000K$ and $\phi = 1.4$ eV (emission current 10 A/cm²), $zT = 160$.

There are in thermionic converter (TIC) some inevitable losses of effectiveness due to the radiation heat transfer and the metallic lead to the emitter. Therefore, instead of (13) we have [7]:

$$(zT)_{TIC} = \frac{(\phi/kT + 2)^2}{\left(\sqrt{2 + \frac{4\epsilon_0 T^3}{2j(k/q)}} + \sqrt{\frac{\pi^2}{3}} \right)^2} \quad (14)$$

where $\epsilon_0 = 5.67 \cdot 10^{-12}$ W/cm²K⁴ is Stephan-Boltzmann constant; ϵ is the radiation emissivity of electrodes; $j = AT^2 \exp(-\phi/kT)$; $\pi^2/3$ is Lorentz number (L_o) for the metallic lead; and j is exchange current between the electrodes in thermodynamic equilibrium (Figure 5). From (14) it is possible to obtain $(zT)_{TIC} \geq 20$.

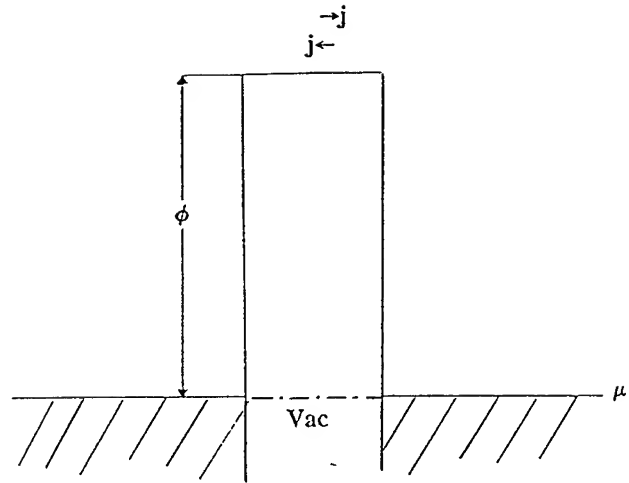


Figure 5 Electron gas in vacuum between two metallic electrodes

Conclusion

Because of diffusion proposed barrier structures can be used indeed only at low T , i.e. for improvement of TE materials for refrigeration.

In all cases there is very important not deteriorate mobilities of TE material between barriers. It seems that monocrystals $Bi_{1-x}Sb_x$ are the best candidate for application of these methods due to their high mobility and low lattice thermal conductivity [1,8].

It is worth to mention [1] that even at $\mu \approx 0$ and $n \approx n_{opt}$ all electrons with $(\epsilon - \mu) < 1/2 (\langle \epsilon \rangle_j - \mu)$ decrease $\alpha^2\sigma$ and increase χ_e , i.e. they are harmful.

This paper was inspired by many enlightening discussions with my late teachers A. Ioffe, A. Regel, L. Stil'baus and my colleagues V. Nemchinsky, I. Drabkin, Yu. Ravich and O. Gryazhov.

References

1. B. Y. Moyzhes, V. Nemchinsky "Nontraditional Methods of Improvement of the Thermoelectric Figure-of-Merit Based on Size Effects," Proc of XI Int. Conf on Thermoelectrics, Arlington, Tx (1992).
2. C. Wood "Material for Thermoelectric Energy Conversion," Reports on Progress in Physics, v. 51, N4, pp.459-539, (1988).

3. J. Ziman "Electrons and Phonons," Oxford Univ. Press, 1962.
4. A.F. Ioffe, B. Ya. Moizhes, L. S. Stil'bans "Thermoelectrics for the Energy Conversion," Fizika Tverdogo Tela v.2, pp.2834-2857, (1960), Russia.
5. K. Board "New Unorthodox Semiconductor Devices," Reports on Progr. in Phys., v. 48, N12, pp.1595-1635, (1985).
6. O. Gryaznov, B. Moizhes, V. Nemchinsky "Generalized Thermoelectirc Efficiency," Sov. Phys. Tech. Phys, v.23, N8, pp.975-978 (1978)
7. G. Fitzpatrick, B. Moyzhes, To be published in the Proceed ings of IECEC, Conf. 96, Washington DC.
8. A. Wagner, R. Foreman, L. Summers, T. Barbee Jr, J. Farmer "Multilayer Thermoelectric Films: A Strategy for the Enhancement of ZT," Proc. IECEC Conv., pp87-92, Orlando, Florida, 1995.
9. V.I. Kaydanov, Yu. I. Ravich "Deep and Resonance States in AIV and BVI Semiconductors," Sov. Phys. Uspekhi, v. 18, #1, pp.31-53, 1985.
10. N.V. Kolomoetz, Thesis, Semicond. Inst., Leningrad, 1962.

Remarks on a possible physical sense of the value $ZT=1$ for semiconductor thermoelectrics

M.V.Vedernikov, Yu.I.Ravich

A.F.Ioffe Physical-Technical Institute, 194021, St.Petersburg, Russia

Abstract

The problem of existence of an upper limit of thermoelectric figure of merit Z is of principal importance for thermoelectric energy conversion. It was discussed actively during the period of development of basic aspects of semiconductor thermoelectricity but was not solved. After long time of silence it attracts attention again. C.B.Vining at ICT'92 considered well known fact that dimensionless parameter $ZT \leq 1$ for all real thermoelectrics. He concluded that one doesn't know any physical reasons to consider this value as a specific one. Our paper indicates those rather general assumptions at which $ZT \approx 1$ for semiconductor at a qualitative evaluation. It is shown too that the dependence of ZT increase on decrease of lattice thermal conductivity is weaker for semiconductor with $ZT > 1$ than for one with $ZT < 1$.

Introduction

The problem of efficiency is principal one for any energy conversion process, if a possibility of its practical application is considered. Good perspectives of semiconductors for use as effective thermoelectrics were predicted by A.F.Ioffe. Later, in course of development of his theory of energy applications of semiconductors, he introduced in general use values of figure of merit of a thermoelectric Z and dimensionless figure of merit ZT (T - temperature). Ioffe found the expression for maximum Z in the simplest model of semiconductor [1]. During next several years Z_{max} were calculated by other authors for more sophisticated but more particular models. Then these efforts weakened together with general diminishing of interest to thermoelectric research. But after 1980, in parallel to an increase of activity in thermoelectric field, some new approaches to the problem of Z_{max} were made [2]-[5]. The problem was reviewed in monographs and handbooks too [6]-[8]. But the most significant expression of the interest to understand a possible bounds of Z (and often more convenient parameter ZT) were the publication of two analytical reviews by Vining: "The Thermoelectric Limit $ZT \sim 1$: Fact or Artifact" [9] and "Thermoelectric Materials of the Future" [10]. If one is interested to be acquainted with the problem in details, he could begin from these two papers which contain the full list of references too. As for us, we would like to make a few remarks to the problem formulated above in the title of the first Vining's paper. It is helpful to add one more question from the

abstract of this paper: "Is $ZT \sim 1$ a fundamental limit or merely characteristic of the materials examined to date?"

We would remind that any physical upper limit for parameter Z or ZT is not found till now; different models of thermoelectrics are described which result in $ZT \gg 1$; $ZT \approx 1$ is the maximum value for all real thermoelectrics till now.

We shall deal with the simplest model of semiconductor used by Ioffe: energy spectrum of one parabolic band, current carriers in nondegenerate state (classical statistics), carrier scattering by acoustic phonons only.

Discussion

An analysis of the maximum thermoelectric figure of merit for the model thermoelectric (described above) leads to the conclusion the optimal chemical potential μ is situated near the edge of the conductor band (for n-type material), while the maximum figure of merit is proportional [1]

$$Z_{max} \propto \frac{m^{*3/2} u T^{3/2}}{\kappa_l} \quad (1)$$

Here m^* is the density-of-states effective mass, u is the mobility of charge carriers, κ_l is the lattice (phonon) thermal conductivity. The main result of this theory is an increase of the maximum figure of merit in inverse ratio to the lattice thermal conductivity when this parameter is lowered. It is important that this result is obtained at assumption the lattice component is the main part of the total thermal conductivity and one can cancel the electronic component κ_e . It is not easy to evaluate quantitatively the $Z_{max}T$ parameter directly from formula (1). For such an evaluation one can remember the present practical limit $Z_{max}T \approx 1$ is realized when the electronic and phonon components of the thermal conductivity are of the same order-of-magnitude $\kappa_l \approx \kappa_e$. Using notation: σ - electrical conductivity, S - thermopower, $L = \kappa_e / \sigma T$ - Lorenz number - one can rewrite the general expression for ZT

$$ZT = \frac{S^2 \sigma T}{\kappa_l + \kappa_e} \quad (2)$$

to a simple form

$$ZT = \frac{S^2}{2L} \quad (3)$$

Provided $\mu = 0$:

$$S = 2 \frac{k_0}{e}, L = 2 \left(\frac{k_0}{e} \right)^2 \quad (4)$$

– and it just follows from (3) that $ZT \approx 1$ (k_0 – Boltzmann constant and e – electron charge).

Looking at the formula (2) again, one could imagine that the figure of merit can be enhanced maximally by factor 2 only, if κ_l would be small enough. Really however the optimal chemical potential should be changed essentially at very small lattice thermal conductivity. It have to move to a region of negative values $\mu < 0$ and results in increase S^2 at practically constant Lorenz number L . Therefore ZT will rise according to (3). Electrical conductivity σ , electron thermal conductivity κ_e and electron density n decrease when negative chemical potential moves down. All these quantities exponentially depend on the reduced chemical potential

$$\kappa_e \propto \sigma \propto n \propto e^{-|\mu^*|} \quad (5)$$

Optimal reduced chemical potential μ_{opt}^* and corresponding maximum figure of merit can be found as a function of a dimensionless parameter

$$K = \frac{\kappa_l}{\kappa_e|_{\mu=0}} \quad (6)$$

which is proportional to the lattice thermal conductivity and does not depend on a chemical potential. When we considered the special case $\mu^* = 0$, $\kappa_l = \kappa_e$, this parameter was $K = 1$. The ratio κ_l/κ_e at arbitrary μ can be expressed through K and μ^*

$$\frac{\kappa_l}{\kappa_e} = K e^{-\mu^*} \quad (7)$$

and the formula (2) comes to the form

$$ZT = \frac{S^2}{L(1 + K e^{-\mu^*})} \quad (8)$$

Substituting (4) in (8) we obtain:

$$ZT = \frac{(2 - \mu^*)^2}{2(1 + K e^{-\mu^*})} \quad (9)$$

The condition of maximum of ZT

$$\frac{d(ZT)}{d\mu^*} = 0 \quad (10)$$

gives an analytical expression for the optimal chemical potential in the form of an inverse function $K(\mu_{opt}^*)$

$$K = -\frac{2}{\mu_{opt}^*} e^{\mu_{opt}^*} \quad (11)$$

and the corresponding formula for maximum figure of merit is

$$Z_{max}T = -\mu_{opt}^* \left(1 - \frac{\mu_{opt}^*}{2} \right) \quad (12)$$

The problem looks perfectly like the problem of the optimal work function and the maximum parameter ZT in the superlattice of thermionic converters of submicron size [11]. The value $|\mu|$ in usual semiconducting thermoelectrics corresponds to work function φ in the mentioned composite.

The values μ_{opt}^* and ZT as functions of the parameter K together with corresponding thermopower S are presented in the table 1.

Table 1: The dependence of dimensionless figure of merit ZT , optimal reduced chemical potential μ_{opt}^* and thermopower S on parameter K .

K	μ_{opt}^*	ZT	$S, \mu V/K$
1	0	1.0	200
0.74	-1	1.5	260
0.135	-2	4.0	345
0.033	-3	7.5	430
0.009	-4	12	520

The table shows clearly that ZT increases not so fast as a value $1/K \propto 1/\kappa_l$ when ZT is more 1. For example, if one could diminish $\kappa_l \propto K$ by a factor $0.135^{-1} = 7.3$, ZT would increase by a factor 4 only (in comparison with situation $K = 1$, $ZT = 1$). The electron density should also be nearly one order of magnitude less than at $\mu = 0$.

Conclusion

First of all we would like to attract attention to the simple evaluation of $Z_{max}T$ for that values of thermal conductivity components which are typical for the best real thermoelectrics. This evaluation gives $Z_{max}T \approx 1$ in agreement with experiment. Of course this procedure is semiquantitative one only. Therefore $Z_{max}T$ may be equal to 2 perhaps, but hardly to 10.

If one could change a relation between thermal conductivity components in a favorable direction, he couldn't use the former criterion $Z_{max}T \propto 1/\kappa_l$: he should use method described above. But it means more hard demands to a lowering of κ_l .

Thus for semiconductors of classical type ("conventional thermoelectrics" according to Vining terminology [10]) $ZT = 1$ is that limit, above which it is possible to increase this parameter but it needs stronger decrease of κ_l than earlier. But the level of κ_l is low enough already. This is why the problem is so difficult.

It is not unlikely that mechanism described explains physical sense of $ZT = 1$ limit for conventional semiconductor thermoelectrics. This conclusion cannot be used automatically for other types of thermoelectrics of course, including more complicated semiconductors. But the best known thermoelectric materials seems rather similar to conventional semiconductors.

Acknowledgement

It is a great pleasure for one of the authors (M.V.V.) to thank *The John D. and Catherine T. MacArthur Foundation* for financial support of his participation in this Conference.

References

- [1] A.F.Ioffe, Semiconductor thermoelements and thermoelectric cooling, Inforsearch, London, pp.101-105 (1957).
- [2] G.D.Mahan, Figure of merit for thermoelectrics, *J.Appl.Phys.*, vol.65, No.4, pp.1578-1583 (1989).
- [3] G.A.Slack, M.A.Hussain, The maximum possible conversion efficiency of Si-Ge thermoelectric generators, *J.Appl.Phys.*, vol.70, No.5, pp.2694-2718 (1991).
- [4] J.-P.Fleurial, Thermal and electrical transport properties modelling of Bi_2Te_3 - based alloys, In "Proceedings of XI Intern. Conf. on Thermoelectrics", University of Texas at Arlington, ed. K.R.Rao, pp.276-281 (1992).
- [5] L.P.Bulat, V.S.Zakordonets, A limited thermoelectric figure of merit of crystalline semiconductor materials, *Phys.Tech.Semicond.*, vol.29, No.10, p.1743-1749 (1995) (In Russian).
- [6] D.M.Rowe, C.M.Bhandary, Modern Thermoelectrics. Holt, Rinehart and Winston Ltd, London (1983).
- [7] H.J.Goldsmid, Electronic refrigeration, Pion, London (1986).
- [8] CRC Handbook of Thermoelectrics, ed. D.M.Rowe, CRC Press, Boca Raton (1995).
- [9] C.B.Vining, The thermoelectric limit $ZT \sim 1$: fact or artifact. In "Proceedings of XI Intern. Conf. on Thermoelectrics", University of Texas at Arlington, ed. K.R.Rao, pp.223-231 (1992).
- [10] C.B.Vining, Thermoelectric materials of the future, In "Proceedings of XIIth Intern. Conf. on Thermoelectrics", ed. K.Matsuura, The Institute of Electrical Engineers of Japan, pp.126-131 (1994).
- [11] V.N.Bogomolov, D.A.Kurdyukov, A.V.Prokofiev, Yu.I.Ravich, Cluster superlattice as 3D-array of thermoionic energy convertors, In "Proceedings of XIV Intern. Conf. on Thermoelectrics", ed. M.V.Vedernikov, St.Petersburg, pp.280-282 (1995).

Texture influence on the forming of thermoelectric properties of pressed semiconductors.

Anatychuk L.I., Kosyachenko S.V., Melnichuk S.V.

Institute of Thermoelectricity, General Post-Office, Box 86, 274000, Chernivtsi, Ukraine

Abstract

The dependence of thermoelectric properties on the texture layer thickness was investigated. The electric and thermal conductivities decrease is caused by decrease of texture layer thickness. Seebeck coefficient and figure of merit remain constant.

Introduction

Pressed powder samples of Bi_2Te_3 retain some anisotropic properties of monocrystalline bismuth telluride [1-4]. The reason of this phenomenon is a creation of mainly oriented crystallite layers near the boundary surface or texture. The texture of pressed powder structures influence thermoelectric properties of such materials, in particular it causes anisotropy of these properties. Pressed powder Bi_2Te_3 kinetic properties were studied in [3-5]. The dependence upon item size, item orientation and annealing temperature has been found.

Analytical description of such materials properties is limited, as a rule, by effective medium approximation [6]. However, this approach does not allow us to find correlation between macroscopic properties and material microstructure. In this work dependence of thermoelectric properties on the texture layer thickness, item size and direction of mainly oriented crystallites was investigated. We used the calculation scheme which was proposed in [7-8].

The computer model and thermoelectric properties of pressed semiconductors.

Computer model for texture layer thickness calculation was developed. This model allows us to form powder structure from crystal grains which is characterized by cleavage planes. The algorithm may be described as follows:

- 2-dimensional powder structure is considered;
- uniform rectangles are structure items of powder;
- structure is forming by rectangles falling down on the horizontal plane;
- structural items are falling from random position with random orientation on the plane or items which have been fallen earlier.

Array of pseudorandom numbers γ_k was obtained by Lemer's method [9].

$$\gamma_k = 2^{-40} m_k, \quad (1)$$

where m_k array of intact numbers

$$m_{k+1} = 5^{17} m_k \pmod{2^{40}} \quad (2)$$

Formula (2) means, that number m_{k+1} is equal to the remainder of division $5^{17} m_k$ on 2^{40} . Pseudorandom numbers

determine rectangles center coordinates (x_0, y_0) . Vertice coordinates were obtained by formulae

$$\begin{aligned} x_1 &= x_0 - b \cos(\varphi) - a \sin(\varphi); \\ y_1 &= y_0 - b \sin(\varphi) + a \cos(\varphi); \\ x_2 &= x_0 - b \cos(\varphi) + a \sin(\varphi); \\ y_2 &= y_0 - b \sin(\varphi) - a \cos(\varphi); \\ x_3 &= x_0 + b \cos(\varphi) + a \sin(\varphi); \\ y_3 &= y_0 + b \sin(\varphi) - a \cos(\varphi); \\ x_4 &= x_0 + b \cos(\varphi) - a \sin(\varphi); \\ y_4 &= y_0 + b \sin(\varphi) + a \cos(\varphi); \end{aligned} \quad (3)$$

As a result model structure is forming. The boundary layer has strong rectangle orientation. This model allows us to determine the texture layer thickness. Results of modeling are illustrated in Fig.1.

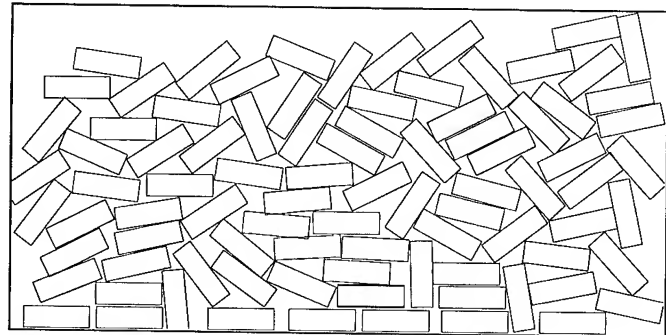


Fig.1 Crystallite powder computer model.

Texture layer thickness is determined by item size and relation between rectangle length ($2b$) and width ($2a$). This thickness dependence upon relation b/a is shown in Fig.2.

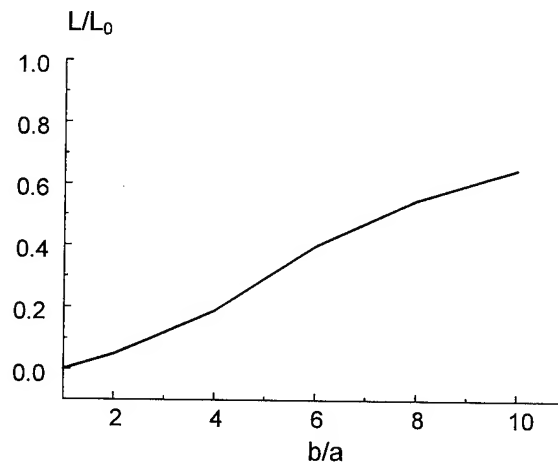


Fig.2 Relative texture layer thickness upon model rectangle relation b/a (L_0 - model region size).

Minimal crystallite width is limited by the distance between cleavage planes. Crystallite size decrease causes the decrease of texture layer thickness and percent of oriented grains (Fig.3)

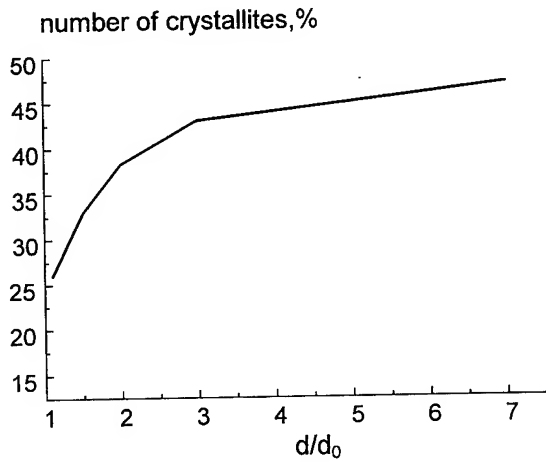


Fig.3 Relative number of crystallites which are oriented to the sample plane in the range $\pm 5^\circ$ upon crystallite size (d_0 is minimal width).

Real pressed samples of Bi_2Te_3 are 3-layered structures [5]. Layers are altering in the pressing direction. The middle part consists of randomly oriented grains. Boundary parts are texture layers with mainly oriented crystallites. To obtain such structure it is necessary to complicate modeling algorithm: rectangles may move to up and down boundary planes directions with equal probabilities. Then pressed powder model structure may be obtained (Fig.4).

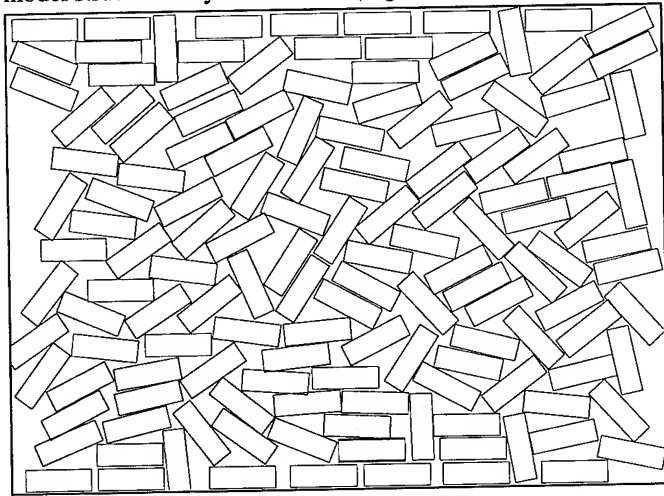


Fig.4 Pressed powder computer model.

In the case when electrical current is parallel to layers we can use method proposed in [7-8]. The calculation formulae are:

$$\begin{aligned} \rho_{xx}^{ef} &= \langle \rho_{xx} \rangle + d1 \cdot d2 \cdot \left[F1(\rho_{xy}^{(1)} - \rho_{xy}^{(2)}) + P1(\alpha_{xy}^{(1)} - \alpha_{xy}^{(2)}) \right], \\ \rho_{yx}^{ef} &= \langle \rho_{yx} \rangle + d1 \cdot d2 \cdot \left[F1(\rho_{yy}^{(1)} - \rho_{yy}^{(2)}) + P1(\alpha_{yx}^{(1)} - \alpha_{yx}^{(2)}) \right], \end{aligned} \quad (4)$$

where

$$F1 = (c1(-\kappa_{xx}) - f1\alpha_{yx}) / \Delta,$$

$$\Delta = \rho_{yy}(-\kappa_{xx}) - \alpha_{yx}\Pi_{xy},$$

$$\alpha = d2 \cdot \alpha^{(1)} + d2 \cdot \alpha^{(2)},$$

$$c = \rho_{yx}^{(1)} - \rho_{yx}^{(2)}, \quad f1 = \Pi_{xx}^{(2)} - \Pi_{xx}^{(1)}$$

$d1, d2$ - partial volumes of particular layers; Π - Peltier coefficient tensor

$$\alpha_{xy}^{ef} = \langle \alpha_{xy} \rangle + d1 \cdot d2 \cdot \left[F2(\rho_{xy}^{(1)} - \rho_{xy}^{(2)}) + P2(\alpha_{xx}^{(1)} - \alpha_{xx}^{(2)}) \right], \quad (5)$$

$$\alpha_{yy}^{ef} = \langle \alpha_{yy} \rangle + d1 \cdot d2 \cdot \left[F2(\rho_{yy}^{(1)} - \rho_{yy}^{(2)}) + P2(\alpha_{yx}^{(1)} - \alpha_{yx}^{(2)}) \right],$$

$$\kappa_{xy}^{ef} = \langle \kappa_{xx} \rangle + d1 \cdot d2 \cdot \left[-F2(\Pi_{xy}^{(1)} - \Pi_{xy}^{(2)}) + P2(\kappa_{xx}^{(1)} - \kappa_{xx}^{(2)}) \right],$$

$$\kappa_{yy}^{ef} = \langle \kappa_{yy} \rangle + d1 \cdot d2 \cdot \left[-F2(\Pi_{yy}^{(1)} - \Pi_{yy}^{(2)}) + P2(\kappa_{yx}^{(1)} - \kappa_{yx}^{(2)}) \right], \quad (6)$$

$$\alpha_{xx}^{ef} = \alpha_{xx}^{(2)} + d1 \cdot d2 \cdot \left[F4(\rho_{xy}^{(1)} - \rho_{xy}^{(2)}) + P4(\alpha_{xx}^{(1)} - \alpha_{xx}^{(2)}) \right], \quad (7)$$

$$\alpha_{yx}^{ef} = \alpha_{yx}^{(1)} + d1 \cdot d2 \cdot \left[F4(\rho_{yy}^{(1)} - \rho_{yy}^{(2)}) + P4(\alpha_{yx}^{(1)} - \alpha_{yx}^{(2)}) \right],$$

$$\kappa_{xx}^{ef} = \kappa_{xx}^{(2)} + d1 \cdot d2 \cdot \left[-F4(\Pi_{xy}^{(1)} - \Pi_{xy}^{(2)}) + P4(\kappa_{xx}^{(1)} - \kappa_{xx}^{(2)}) \right], \quad (8)$$

$$\kappa_{yx}^{ef} = \kappa_{xx}^{(2)} + d1 \cdot d2 \cdot \left[-F4(\Pi_{yy}^{(1)} - \Pi_{yy}^{(2)}) + P4(\kappa_{yx}^{(1)} - \kappa_{yx}^{(2)}) \right],$$

$$\rho_{xy}^{ef} = \rho_{xy}^{(2)} + d1 \cdot d2 \cdot \left[F3(\rho_{xy}^{(1)} - \rho_{xy}^{(2)}) + P3(\alpha_{xx}^{(1)} - \alpha_{xx}^{(2)}) \right], \quad (9)$$

$$\rho_{yy}^{ef} = \rho_{yy}^{(2)} + d1 \cdot d2 \cdot \left[F3(\rho_{yy}^{(1)} - \rho_{yy}^{(2)}) + P3(\alpha_{yx}^{(1)} - \alpha_{yx}^{(2)}) \right],$$

$$F2 = (c2(-\kappa_{xx}) - f2\alpha_{yx}) / \Delta,$$

$$c2 = \alpha_{yx}^{(1)} - \alpha_{yx}^{(2)}, \quad f2 = \kappa_{xx}^{(2)} - \kappa_{xx}^{(1)}$$

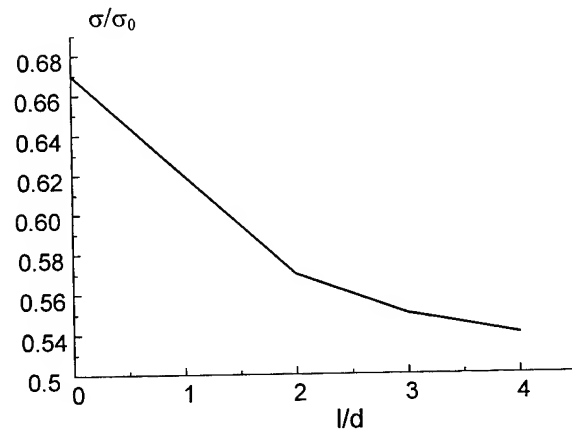


Fig.5 Relative conductivity dependence as a function of removed layer thickness. (σ_0 is conductivity of a single crystallite, l is removed layer thickness, d is crystallite effective size).

These relationships were used to set up a computer program for calculation of layer structures containing arbitrary number of arbitrary thickness layers of differently oriented materials.

Algorithm of 3-layer system calculation consists in replacement of 2-layer system with one layer one, with effective mean parameters and total thickness with added new homogeneous layer. For example, results of relative conductivity calculation for systems with different texture layers thickness are shown in Fig.5.

Conclusion

The conductivity decrease is caused by the decrease of texture layer thickness. This conclusion is in a qualitative agreement with experimental results [5]. The same dependence may be obtained for thermal conductivity. On the other hand, Seebeck coefficient is constant. That is why the figure of merit remains constant for powders where crystallite sizes are much more then electron and phonon mean free path.

References

- [1] Goltsman V.M.,Kudinov V.A., Smirnov I.A. *Bi₂Te₃ - based semiconductor thermoelectric materials.*, Nauka, Moscow.; pp.271-280(1972).
- [2] Lidorenko N.S.,Kagan A.S.,Chizhik S.P.,Kovalsky A.E.,Prokoshina S.M.,Sokolov O.V. "The "stack" texture of fragile materials.", Powder Metallurgy, No.10, pp.82-84 (1969).
- [3]Goldsmid H.T.,Underwood F.A. Study of orientation in polycrystalline bismuth telluride alloys.// - Advances Energy Conversion, No.7, pp.297-301 (1968).
- [4] Barash A.S.,Grinberg R.Z., Zhukova T.V.,Zaslavsky A.E. "Anisotropy nature in semi-elements cold-pressed from Bi-Te-Sb-Se alloys." Academy of Sciences News, USSR, Inorganic Materials., vol.8.,No.10.,pp.1765-1768. (1972).
- [5] Semizorov A.F. "Texture investigation in pressed samples made of Bi-Te-Se alloys."- Journal of Thermoelectricity., No.1, pp.90-95 (1994).
- [6]Privalko V.P.,NovikovV.V., Jankovsky J.P. *Heatphysics and reophysics bases of polymer materials.*, Naukova Dumka., Kiev, p.229 (1991).
- [7]Anatychuk L.I.,Melnichuk S.V.,Kosyachenko S.V.,Chernov V.M. "Powder materials characteristics calculation.", Journal of Thermoelectricity, No.4, pp.1-26(1994).
- [8] Anatychuk L.I.,Melnichuk S.V.,Kosyachenko S.V. Computer modelling of thermoelectric material anizotropic powder structures, in Proceedings of the XIV International Conference on Thermoelectrics, St.Petersburg, Russia, June 27-30, 1995, ,p.319-323.
- [9] Sobol I.M. *Monte-Carlo numerical methods.*, Nauka, Moscow, p.243(1973).

Effective Figure of Merit Increase at the Large Temperature Drops

Vladimir B. Yurchenko

Institute of Radiophysics and Electronics, National Academy of Sciences of Ukraine

12 Proskura St., Kharkov, 310085, Ukraine

Phone: 38 0572 44 8371, Fax: 38 0572 44 1105, E-mail: yurchenko@ire.kharkov.ua

Abstract

Optimum configuration, assembling and commutation of the cells in a thermoelectric device have been investigated taking into account the temperature dependence of resistivity, thermal conductivity and Seebeck coefficient of the material operating at the large temperature drop. A kind of the solution proposed which enables one to increase the effective figure of merit of the device as compared to the mean value of Z measured at the same temperature drop in a single wafer thermoelectric cell.

Introduction

Increasing the efficiency of thermoelectric devices is the main goal in thermoelectric activity. The efficiency could be estimated according to the relation $\eta \sim Z\Delta T_{12}$ where $Z = \alpha^2\sigma/\lambda$ is the figure of merit of the given material, α , σ and λ are the typical values of Seebeck coefficient, of the electrical conductivity, and of the heat conductivity, respectively, $\Delta T_{12} = T_2 - T_1$ is the temperature drop across the thermoelectric cell, T_1 and T_2 being the temperatures of the opposite surfaces. To increase the efficiency, one has to develop novel materials of greater Z , and to apply the large temperature drops ΔT_{12} .

When operating at the large temperature drop, thermoelectric materials reveal, however, the less figure of merit $< Z >$ than the maximum value of Z achieved at the optimum temperature T_{opt} . It is a result of the temperature dependence of α , σ and λ typical for any semiconductor material. The loss of the efficiency arises from the fact that the part of the cell operating at the optimum temperature T_{opt} , appears to be loaded by the other parts being at the less beneficial conditions. So, some additional thermoelectric power is dissipated in the cell as compared to the minimum loss achieved at the temperature T_{opt} .

The aim of this work was to consider the possibilities to avoid these additional losses by means of the optimum cell configuration, assembling and commutation in the complex thermoelectric device of a special structure.

Figure of Merit of a Single Wafer

Let us consider the plain thermoelectric cell made of a single semiconductor wafer of the thickness L , with the large temperature drop ΔT_{12} being applied to the wafer. Suppose the values of α , σ and λ are the functions of the temperature T . In this case, the densities of the heat flux and of the electrical current, q and j , respectively, are

determined by the equations

$$q = -\lambda(T)dT/dx, \quad (1)$$

$$j = -\sigma(T)\alpha(T)dT/dx - \sigma(T)d\tilde{\varphi}/dx \quad (2)$$

where $q = Q/S$, $j = I/S$, Q is the total heat flux, I is the total current, S is the area of the thermoelectric cell, $\tilde{\varphi}$ is the electrochemical potential. At the given temperature drop ΔT_{12} , the nonlinear differential equation (1) determines the temperature profile $T(x)$ across the wafer as well as the value of the total heat flux

$$Q = -(S/L) \int_{T_1}^{T_2} \lambda(T) dT. \quad (3)$$

The Eqs.(1), (2) lead to the relation

$$d\tilde{\varphi} = [Q\alpha(T)/\lambda(T) - I\sigma^{-1}(T)] dx/S \quad (4)$$

resulting in the current-voltage characteristics

$$U = U_{oc} - IR \quad (5)$$

where $U = \int_0^L d\tilde{\varphi}$ is the voltage applied, U_{oc} is the open-circuit voltage, R is the resistance of the cell. With the Eq.(1), the open-circuit voltage U_{oc} , the resistance R and the short-circuit current $I_{sc} = U_{oc}/R$ could be expressed in the form independent of the spatial variable x :

$$U_{oc} = - \int_{T_1}^{T_2} \alpha(T) dT, \quad (6)$$

$$R = Q_0^{-1} \int_{T_1}^{T_2} \lambda(T)\rho(T) dT, \quad (7)$$

$$I_{sc} = -Q_0 \int_{T_1}^{T_2} \alpha(T) dT / \int_{T_1}^{T_2} \lambda(T)\rho(T) dT \quad (8)$$

where $Q_0 = -Q$, $\rho(T) = \sigma^{-1}(T)$. As a result, the maximum thermoelectric power generated by the cell, P_{m0} , is calculated by the relation

$$P_{m0} = \frac{Q_0}{4} \left(\int_{T_1}^{T_2} \alpha(T) dT \right)^2 / \int_{T_1}^{T_2} \lambda(T) \rho(T) dT . \quad (9)$$

The efficiency of the cell could be evaluated by the formula $\eta = P_{m0}/Q_0 = 0.25 < Z > \Delta T_{12}$ where

$$\begin{aligned} < Z > = Z(T_1, T_2) = \\ &= \left(\int_{T_1}^{T_2} \alpha(T) dT \right)^2 / \left(\Delta T_{12} \int_{T_1}^{T_2} \lambda(T) \rho(T) dT \right) \end{aligned} \quad (10)$$

is the effective figure of merit of a single thermoelectric cell operating at the large temperature drop. Notice a special averaging procedure in the Eq.(10) arising from the fact that the different regions of the wafer operates with different efficiency since the local figure of merit Z depends on the local temperature: $Z = Z(T) = \alpha^2(T)\sigma(T)/\lambda(T)$. It is clear that the effective figure of merit $< Z >$ is less than the maximum value of $Z(T)$ in the temperature range considered.

Effective Figure of Merit of a Complex Structure

In order to reduce the loss of the efficiency mentioned above, let us divide the whole semiconductor wafer in a few layers which, in turn, to be divided in different cells connected in series within a layer. The goal is to equalize the power generated by the different layers operating at the different temperatures so that all the layers were in the equal conditions to avoid the electrical loading some of them by another ones.

We consider the case of the two-layer structure (Fig.1).

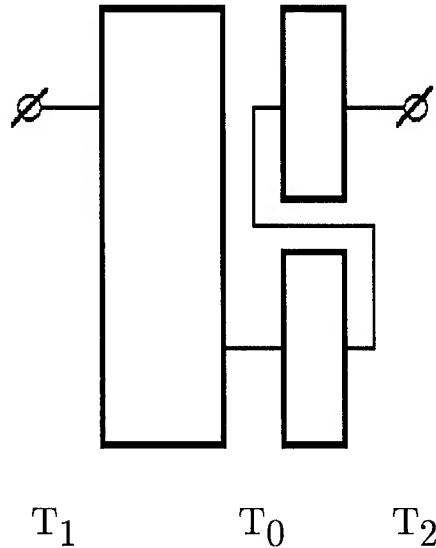


Fig.1 A scheme of the complex two-layer structure.

Suppose N_1 and N_2 are the numbers of the cells in the layers 1 and 2, respectively, S_1 and S_2 being the areas of the cells. Since the total device area is the same, one has

$$N_1 S_1 = N_2 S_2 . \quad (11)$$

The condition of the equal power generated by the different layers under the optional loading means that $U_{oc1} = U_{oc2}$ and $I_{sc1} = I_{sc2}$ where U_{oci} and I_{sci} are the open-circuit voltages and the short-circuit currents of the layers ($i = 1, 2$). For the cells connected in series, the open-circuit voltages are

$$\begin{aligned} U_{oc1} &= -N_1 \int_{T_1}^{T_0} \alpha(T) dT , \\ U_{oc2} &= -N_2 \int_{T_0}^{T_2} \alpha(T) dT \end{aligned} \quad (12)$$

where T_0 is the temperature at the plane x_0 dividing the wafer in the two layers. The resistances of the layers are, respectively,

$$\begin{aligned} R_1 &= (N_1/S_1) \int_0^{x_0} \rho(T) dx , \\ R_2 &= (N_2/S_2) \int_{x_0}^L \rho(T) dx . \end{aligned} \quad (13)$$

The requirement of the equal voltages means

$$N_1 \int_{T_1}^{T_0} \alpha(T) dT = N_2 \int_{T_1}^{T_0} \alpha(T) dT \quad (14)$$

while the condition of the equal currents implies

$$\frac{N_1}{S_1} \int_{T_1}^{T_0} \lambda(T) \rho(T) dT = \frac{N_2}{S_2} \int_{T_0}^{T_2} \lambda(T) \rho(T) dT . \quad (15)$$

The Eqs.(11), (14) and (15) yields the final equation in the temperature T_0 ,

$$\begin{aligned} &\left(\int_{T_1}^{T_0} \alpha(T) dT \right)^2 / \int_{T_1}^{T_0} \lambda(T) \rho(T) dT = \\ &= \left(\int_{T_0}^{T_2} \alpha(T) dT \right)^2 / \int_{T_0}^{T_2} \lambda(T) \rho(T) dT . \end{aligned} \quad (16)$$

The Eq.(16) enables one to determine the temperature T_0 and then, with the known temperature profile $T(x)$, to calculate the coordinate x_0 and the ratio of the cell numbers in the layers.

Notice the Eq.(16) is equivalent to the condition

$$Z(T_1, T_0) \Delta T_{10} = Z(T_0, T_2) \Delta T_{02} \quad (17)$$

where $\Delta T_{10} = T_0 - T_1$, $\Delta T_{02} = T_2 - T_0$. It is not a surprise since the requirement of the equal power produced by the layers was the starting point of the whole consideration. The consequence of this requirement is the increase of the total power and, therefore, of the effective figure of merit, Z_{eff} , of the complex thermoelectric device:

$$Z_{eff}(T_1, T_2) = 2 Z(T_1, T_0) \frac{\Delta T_{10}}{\Delta T_{12}} > Z(T_1, T_2). \quad (18)$$

The gain of the power $G = P_m/P_{m0}$ is evaluated by the formula

$$G = \frac{2 \left(\int_{T_1}^{T_0} \alpha(T) dT \right)^2 / \int_{T_1}^{T_0} \lambda(T) \rho(T) dT}{\left(\int_{T_1}^{T_2} \alpha(T) dT \right)^2 / \int_{T_1}^{T_2} \lambda(T) \rho(T) dT} \quad (19)$$

where $G > 1$ if the temperature T_0 satisfies the Eq.(16).

Numerical Results and Discussion

Theoretical analysis described in the previous sections has been applied to estimate the effect in the promising skutterudite materials. To solve the Eq.(16), numerical methods have been employed, and a special computer code in Fortran has been developed. The efficiency gain G , the thickness of the layers L_1 and L_2 , the ratio of the cell numbers $r_N = N_1/N_2$, and the ratio of the cell areas $r_S = S_1/S_2 = 1/r_N$ have been calculated on PC.

Material parameters of IrSb₃ and Ir₄LaGe₃Sb₉ published by Terry M. Tritt et. al. [1] have been used to approximate the functions $\alpha(T)$, $\rho(T)$ and $\lambda(T)$ in a wide temperature range. In the particular case of IrSb₃, the functions $\alpha(T)$, $\rho(T)$ and $\lambda(T)$ in the temperature range $T = 100 \dots 300K$ have been approximated as follows

$$\alpha(T) = \alpha_1 + \delta\alpha(T - T_1) \quad (20)$$

$$\rho(T) = \rho_1 + \delta\rho(T - T_1) \quad (21)$$

$$\lambda(T) = \lambda_1(T_1/T) \quad (22)$$

where $\alpha_1 = 35 \mu V/K$, $\delta\alpha = 0.2 \mu V/K^2$, $\rho_1 = 3.2 \cdot 10^{-4} \Omega cm$, $\delta\rho = 0.005 \cdot 10^{-4} \Omega cm/K$, $\lambda_1 = 45 W/(m K)$, $T_1 = 100 K$, $T_2 = 300 K$.

The calculations have shown that, at the given temperature drop $\Delta T_{12} = 200K$, the effective figure of merit of the complex structure based on the two layers of IrSb₃ makes $Z_{eff}(T_1, T_2) = 3.8 \cdot 10^{-5} K^{-1}$ while the initial figure of merit of a single wafer is $\langle Z \rangle = 3.4 \cdot 10^{-5} K^{-1}$.

To compare, the local figures of merit at the temperatures $T_1 = 100K$ and $T_2 = 300K$ are as follows: $Z(T_1) = 0.85 \cdot 10^{-5} K^{-1}$, $Z(T_2) = 8.9 \cdot 10^{-5} K^{-1}$.

Thus, the total efficiency gain of the two-layer structure is $G = 1.12$, i.e. the growth of the figure of merit is about 12% of the initial value measured in a single wafer. The optimum layer thickness ratio of the structure is estimated as $r_L = L_1/L_2 = 4.8$ ($T_0 = 248K$), the optimum number-of-the-cells ratio is $r_N = N_1/N_2 = 0.5$, and the area-of-the-cells ratio is $r_S = S_1/S_2 = 2.0$.

The similar calculations carried out for Ir₄LaGe₃Sb₉ have, however, revealed the very small efficiency gain being about $G = 1.06$. It is a result of the small initial difference in $Z(T_1)$ and $Z(T_2)$ arising from the very smooth temperature dependence of $\lambda(T)$ [1]. It means that for the material like Ir₄LaGe₃Sb₉, there is no need to complicate the structure since the mutual loading of the different parts of a single wafer cell is almost absent.

To accomplish the research, the case of the three-layer structure of IrSb₃ was also investigated. The gain of the efficiency $G = 1.15$ has been obtained. The results have shown a tendency for the efficiency saturation because of considerable elimination of the mutual loading of the different layers achieved even in the case of the two-layer structures.

Conclusion

At the large temperature drop, thermoelectric materials exhibit the less figure of merit $\langle Z \rangle$ than the maximum value Z_{max} because of the temperature dependence of the resistivity, thermal conductivity and Seebeck coefficient. The loss of the efficiency arises from the fact that the part of the device operating at the optimum temperature T_{opt} , appears to be loaded by the other parts being at the less beneficial conditions.

In this work, the problem of the optimum device configuration, assembling and commutation has been considered, with the aim to eliminate the negative effect mentioned above. A kind of the solution proposed which enables one to increase the effective figure of merit of the complex device as compared to the mean value $\langle Z \rangle$ measured at the same temperature drop in a single-wafer thermoelectric cell.

The effect has been evaluated for IrSb₃ and other skutterudite materials in the temperature range $T = 100 \dots 300K$. The results have shown that, in the case of IrSb₃, the effective value of Z of the complex device could be increased by 12% to 15% of the initial mean value $\langle Z \rangle$ of a single wafer depending on the kind of a solution accepted for the device arrangement.

References

- [1] Terry M. Tritt et al., "Low Temperature Transport Properties of IrSb₃", *Proc. the 14th Int. Conf. on Thermoelectrics*, M.V.Vedernikov, M.I.Fedorov and A.E.Kaliazin, Eds., St.Petersburg (1995).

THE THEORETICAL ANALYSIS OF THE THERMOELECTRIC SEMICONDUCTING CRYSTALLINE MATERIALS FIGURE OF MERIT

BULAT L.P., ZAKORDONETS V.S.

Institute of Thermoelectricity, Academy of Sciences of the Ukraine

Abstract

The thermoelectric figure of merit z is computed for bipolar semiconducting materials with a degenerate gas of current carriers and a nonparabolic band structure. The factors that affect the value of z are analyzed. It is established that the figure of merit of such materials increases monotonically with increasing band gap, in contrast with semiconductors with a parabolic band. It is shown that $zT < 3$ is always true in crystalline thermoelectric materials.

The efficiency of converting the thermal energy into the electric one is basically determined by the thermoelectric figure of merit (the dimensionless thermoelectric figure of merit) of the used thermoelectric materials

$$zT = \frac{\alpha^2 \sigma T}{\chi} \quad (1)$$

where α , σ , χ - respectively are the Seebeck coefficient, electric conductivity and heat conductivity, T is absolute temperature.

In the general case the thermoefficiency is in a complex manner dependent on the semiconductor material constants. Particularly, the zT value is influenced by the energy bands number, the dispersion law shape, the charge carriers scattering mechanism, the forbidden gap width, and so on.

A lot of works are dedicated to the influence of these factors on the figure of merit (see, for example, [1, 2]). The results given there were obtained in the parabolic dispersion law of the carriers approximation, and this law is true for the semiconductors with the forbidden band $E_g \gg k_0 T$ with the Fermi energy of the carriers $F \ll E_g$ [3].

In the middle-temperature and especially in the low-temperature thermoelectric materials, and also in the conduction of the high charge carriers concentration, when these requirements are not met anymore it is necessary to consider the dispersion law is not parabolic. For calculating the figure of merit let us consider the model of semiconductor with the elementary structure of the conductivity band and the valency band, and with non-parabolic dispersion law [3]

$$\frac{\eta^2 k^2}{2m_{e,p}} = \varepsilon \left(1 + \frac{\varepsilon}{E_g} \right), \quad (2)$$

where $m_{e,p}$ are the effective masses of the electrons and holes near the bottom of the conduction band and the top of the valence band, k is the wave vector of the carriers.

The effective mass near the energy extremum we consider the isotropic one

$$m(\varepsilon) = m_{e,p} \left(1 + \frac{2\varepsilon}{E_g} \right). \quad (3)$$

Because the most promising for thermoelectric use materials belong to the class of strongly doped ones, besides the

scattering on acoustic phonons we'll take into account also the scattering on ionized atoms of the impurity. The relaxation time for the separate scattering mechanism we'll write as follows

$$\tau(\varepsilon) = \tau_{or} \left[\frac{\varepsilon}{k_0 T} \left(1 + \frac{\varepsilon}{E_g} \right) \right]^{r-1/2} \left(1 + \frac{2\varepsilon}{E_g} \right)^{-1}, \quad (4)$$

where r is scattering factor, which has the values of $r = 0$ and $r = 2$ respectively for scattering on the acoustic phonons and the ionized dopes, k_0 is Boltzman constant.

Using the rule of the reverse relaxation times addition [3]

$$\frac{1}{\tau} = \sum_i \frac{1}{\tau_i}, \quad (5)$$

and considering (4) for the effective relaxation time when the both mechanisms act, we will get

$$\tau(\varepsilon) = \frac{\tau_{ol} \left[\frac{\varepsilon}{k_0 T} \left(1 + \frac{\varepsilon}{E_g} \right) \right]^{3/2}}{\left\{ b^2 + \left[\frac{\varepsilon}{k_0 T} \left(1 + \frac{\varepsilon}{E_g} \right) \right]^2 \right\} \left(1 + \frac{2\varepsilon}{E_g} \right)}, \quad (6)$$

where $b^2 = \tau_{ol}/\tau_{oi}$, τ_{ol} , τ_{oi} are the known functions of the temperature determined by the carriers scattering on the acoustic phonons and the ionized dopes, respectively. In the case of scattering on the acoustic phonons $\tau_{oi} \rightarrow \infty$, and $b = 0$, and in the case of ionized dopes $\tau_{ol} \rightarrow \infty$, and $b \rightarrow \infty$. We define the basic kinetic coefficients by the formulas

$$\alpha = \frac{\alpha_e \sigma_e}{\sigma} + \frac{\alpha_p \sigma_p}{\sigma}, \quad (7)$$

$$\sigma = \sigma_e + \sigma_p, \quad (8)$$

$$\chi = \chi_e + \chi_p + \chi_{ep} + \chi_{ph}, \quad (9)$$

where $\alpha_{e,p}$, $\sigma_{e,p}$, $\chi_{e,p}$ are the partial components of Seebeck coefficient, electric conductivity and the thermal conductivity.

$$\chi_{ep} = \frac{\sigma_e \cdot \sigma_p}{\sigma} (\alpha_e - \alpha_p)^2 T$$

is the bipolar thermal conductivity, χ_{ph} is the lattice component of the thermal conductivity.

Using (2), (3) and (6) we will find out the electron components of the kinetic coefficients

$$\alpha_e = -\frac{k_0}{e} \left(\frac{S_{3,2}^1(\eta, \beta, b)}{S_{3,2}^0(\eta, \beta, b)} - \eta \right), \quad (10)$$

$$\sigma_e = N_0 e \mu_{ce} \left(\frac{m_e}{m_0} \right)^{3/2} S_{3,2}^0(\eta, \beta, b), \quad (11)$$

$$\chi_e = \left(\frac{k_0}{e} \right)^2 L_e \sigma_e T, \quad (12)$$

where $N_0 = 2 \left(2\pi m_0 k_0 T / h^2 \right)^{3/2}$,

$$L_e = \frac{S_{3,2}^2(\eta, \beta, b)}{S_{3,2}^0(\eta, \beta, b)} - \left[\frac{S_{3,2}^1(\eta, \beta, b)}{S_{3,2}^2(\eta, \beta, b)} \right]^2$$
 is the dimensionless

Lorents number,

$$S_{n,k}^m(\eta, \beta, b) = \int_0^\infty \left(-\frac{\partial f_0}{\partial x} \right) \frac{x^m (x + \beta x^2)^n (1 + b^2/6)}{\left[b^2 + (x + \beta x^2)^2 \right] (1 + 2\beta x)^k} dx, \quad (1)$$

3)

are the triple-parameter integrals.

The calculating of the integrals was done by Simpson's method [4] with replacement of the infinitely big upper limit of integrating by the finishing ($x_0 = 30$). At this time the calculation accuracy provided was not worse than $\delta = 10^{-5}$.

Here, $f_0 = (1 + \exp(x - \eta))^{-1}$ is the Fermi-Dirac

distribution function, $\eta = \frac{\zeta}{k_0 T}$, ζ is the chemical potential of

electrons, $x = \frac{\varepsilon}{k_0 T}$ is the reduced energy, $\beta = \frac{k_0 T}{E_g}$ is the

coefficient of band non-parabolicity, m_0 is the free electron mass.

Replacing in (10), (11), (12) $-e \rightarrow e$, $m_e \rightarrow m_p$, $\eta \rightarrow \eta_p = -(\eta + E_g/k_0 T)$ we will get the hole components of the kinetic coefficients. Considering (7), (8), (9) for dimensionless thermoelectric figure of merit we will obtain

$$zT = \frac{(\alpha_{e0} - \Phi \alpha_{p0})^2 (1 + \Phi)^{-1}}{L_e + \Phi L_p + \frac{\Phi}{1 + \Phi} (\alpha_{e0} + \alpha_{p0})^2 + [BS_{3,2}^0(\eta, \beta, b)]^{-1}}, \quad (1)$$

4)

where $\alpha_{e0} = \frac{e}{k_0} \alpha_e$, $\Phi = \gamma \frac{S_{3,2}^0(\eta_p, \beta, b)}{S_{3,2}^0(\eta, \beta, b)}$, $\gamma = \frac{\mu_{cp} m_p^{3/2}}{\mu_{ce} m_e^{3/2}}$,

$$\mu_{ce, cp} = \frac{\mu_{ce, cp}^i \cdot \mu_{ce, cp}^j}{\mu_{ce, cp}^i + \mu_{ce, cp}^j}, \quad B = \left(\frac{k_0}{e} \right)^2 N_0 \left(\frac{eT}{\chi_{ph}} \right) \mu_{ce} \left(\frac{m_e}{m_0} \right)^{3/2}$$

is corrected in comparison with [5] dimensionless coefficient determining the quality of thermoelectric energy conversion, $\mu_{ce, cp}^i, \mu_{ce, cp}^j$ are the drift mobilities of the electrons, holes for the parabolic band case, the non-confluent statistics and when scattering on the acoustic phonons and the ionized dopes, respectively.

It follows from the given expressions that the thermoelectric figure of merit at a fixed temperature is a

function of the following dimensionless parameters: η, β, γ, B , and b .

Choosing as the main carriers the electrons, let us analyze the relation (14) by the numerical methods. For this let's estimate at first the maximum possible B parameter value. For hypothetical semiconductor which could combine the electric properties of III-V groups compounds with the thermal conductivity of the complex crystalline structures lattice, the value $B=0.55$ and for the real thermoelectric materials it is the limiting one. Let us note, that now the maximum $B=0.35$ is obtained for the semiconductive compounds based on bismuth telluride [7].

At fixed values of the dimensionless parameters β, γ, B , and b , the figure of merit is a function of only the chemical potential of the carriers, while $z(\eta)$ has an extremum. Maximizing the figure of merit with respect to the chemical potential, we investigate the effect on it of the parameters B, β, γ and b .

Figures 1-5 show typical dependences of the maximum quality factor on the enumerated parameters. It can be seen from Fig.1 that, when the electrons are scattered at acoustic phonons ($b=0$), $(zT)_{\max}$ decreases as the nonparabolicity coefficient increases. Beginning with values $\beta > 0.1$ ($E_g < 10k_0 T$), the effect of minority carriers will also be to decrease the figure of merit. If nonparabolicity is absent ($\beta=0$), the maximum figure of merit will lie in the interval $(zT)_{\max}=0.55-1.25$ for $B=0.20-0.55$ and acoustic scattering. When the carriers are scattered at ionized impurities ($b \rightarrow \infty$) (Fig.2) in the absence of nonparabolicity, the maximum figure of merit amount to $(zT)_{\max}=1.75-3$ for the same B values.

It can be seen from Figs.3 and 4 that, with a nonparabolic carrier dispersion law, the figure of merit monotonically increases with increasing band gap. The figure of merit would saturate only in the parabolic model and would actually occur when $E_g > 10k_0 T$, as was shown in Ref.2. However saturation does not occur in real, low-temperature thermoelectric materials.

Defining the limiting figure of merit in the case of the mixed scattering it is necessary to find precisely the b parameter value. In principle this parameter for the specific material can be obtained using calculating or empiric [7, 8] dependences of the carriers mobility on the temperature and impurity concentration.

As it is seen from the fig.5, increase of the limiting figure of merit is assisted by the parameter b increase, i.e. the increase of the carriers scattering on the ionized impurities.

To check the results obtained numerically, we analytically calculated the figure of merit for a nondegenerate semiconductor with a nonparabolic dispersion law. In the limiting case of the absence of degeneracy, the numerical results completely agree with the analytical results.

On the other hand, we assumed a spherical band model. Changing from a spherical isoenergetic surface to a more complex surface (elliptical, corrugated, etc.) naturally complicates the final result. However, a nonspherical band, like a multivalley band, has virtually no effect on the maximum figure of merit. Actually, we always can choose such values of the effective mass, mobility, and thermal conductivity for calculations in the spherical model that they

will correspond to the best values of these parameters in materials with a more complex band structure. It is precisely such best parameters that we used for the numerical calculations in the spherical band model.

We can thus consider it to be established in crystalline thermoelectric materials that the largest figure of merit, which

corresponds to the ideal combination of parameters of the material, is $(zT)_{\max} < 3$. We cannot exclude the possibility of substantially larger values of the maximum figure of merit in more complex structures.

The authors are deeply grateful to L.I. Anatychuk for fruitful discussions.

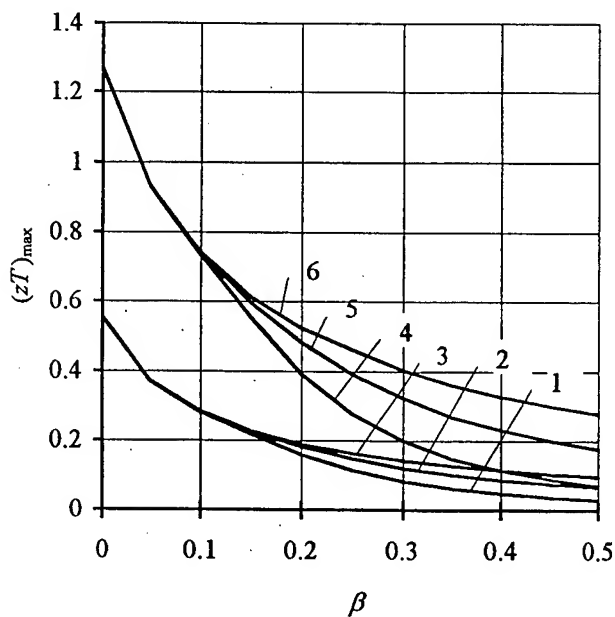


FIG.1. Maximum figure of merit $(zT)_{\max}$ vs the band-nonparabolicity coefficient β when the carriers are scattered at acoustic phonons. Curves 1-3 are constructed for $B=0.2$ for $\gamma=1$, $\gamma=0.2$ and $\gamma=0$, respectively; curves 4-6 are constructed for $B=0.55$ for $\gamma=1$, $\gamma=0.2$ and $\gamma=0$, respectively.

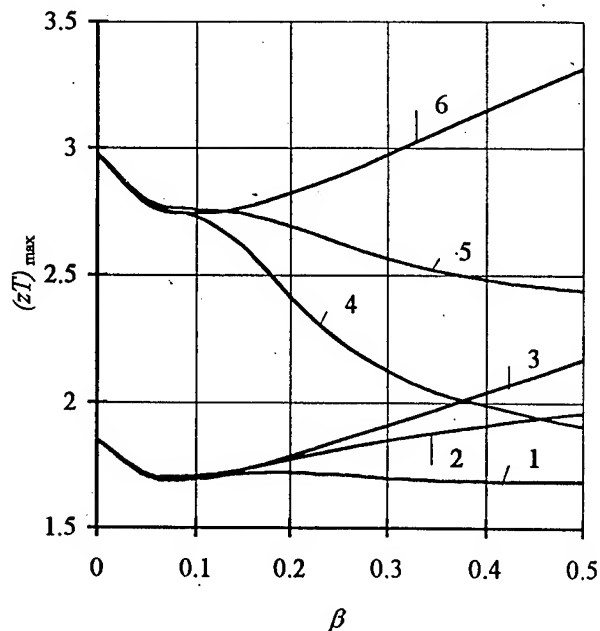


FIG.2. Maximum figure of merit $(zT)_{\max}$ vs the band-nonparabolicity coefficient β when the carriers are scattered at ionized impurities. Curves 1-3 are constructed for $B=0.2$ for $\gamma=1$, $\gamma=0.2$ and $\gamma=0$, respectively; curves 4-6 are constructed for $B=0.55$ for $\gamma=1$, $\gamma=0.2$ and $\gamma=0$, respectively.

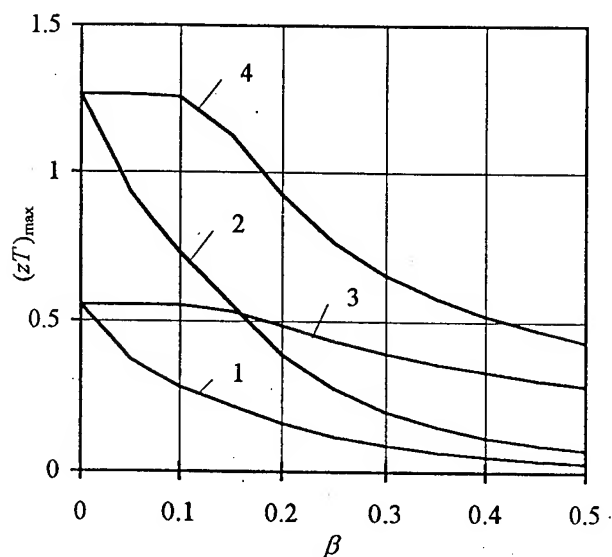


FIG.3. Maximum figure of merit $(zT)_{\max}$ vs the band-nonparabolicity coefficient β for $\gamma=1$ and for scattering of the carriers at acoustic phonons, taking into account nonparabolicity (curves 1 and 2) and neglecting it (curves 3 and 4). Curves 1 and 3 are constructed for $B=0.2$, and curves 2 and 4 are for $B=0.55$.

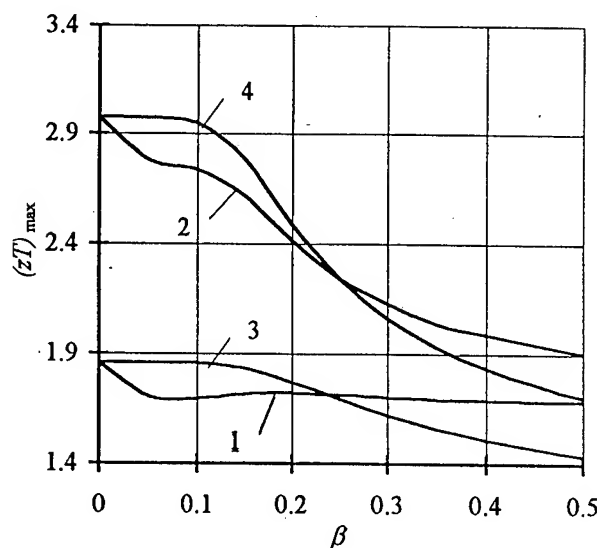


FIG.4. Maximum figure of merit $(zT)_{\max}$ vs the band-nonparabolicity coefficient β for $\gamma=1$ and for scattering of the carriers at ionized impurities, taking into account nonparabolicity (curves 1 and 2) and neglecting it (curves 3 and 4). Curves 1 and 3 are constructed for $B=0.2$, and curves 2 and 4 are for $B=0.55$.

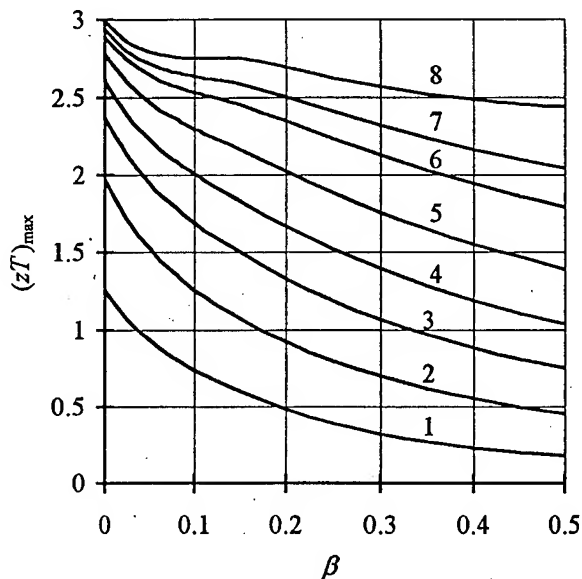


FIG.5. Dependence of $(zT)_{\max}$ on β when mixed carriers scattering, at $B = 0.55$ and $\gamma = 0.2$. Curves 1-8 are built respectively at $b \rightarrow 0$ (acoustic phonons scattering), $b = 3$, $b = 5$, $b = 7$, $b = 10$, $b = 15$, $b = 20$, $b \rightarrow \infty$ (ionized impurity scattering).

REFERENCES

1. Rowe D.M. and Bhandari C.M. Modern Thermoelectric. -1983. -P. 157.
2. Mahan G.D. Figure of merit for thermoelectrics//J.Appl. Phys.-1989.v.65-p.1578-1583.
3. Askerov B.M. Electron transmission phenomena in semiconductors M., Nauka, 1985, p 320
4. Diakonov V. P. Manual on algorithms and programs in BASIC for personal computers. M., Nauka, 1989, p.239.
5. Chsma R.P., Stratton R.J. Electron. Control. - 1959. v.7. p.52-75.
6. Bulat L.P., Zakordontes V.S. Maximum thermoelectric quality factor of semiconducting crystalline materials. FTP, 1995, v.29, N 10, p.1743-1749.
7. Anatychuk L.I., Semeniuk V.A. Optimum control of the thermoelectric materials and devices properties. Chernovtsy, Proot, 1992, p.263.
8. Goltsman B.M., Ikonnikova G.N., Kutasov V.A., Shapiro E.K. Influence of the intrinsic conduction on the thermoelectric properties of the solid solutions $\text{Bi}_2\text{Te}_{3-x}\text{Se}_x$. /FTT, 1970, v.12, N5. p.1402-1409.

THERMOELECTRIC FIGURE OF MERIT OF BOUNDED SEMICONDUCTORS

G.N Logvinov and V.S. Zakordonets

Institute of Thermoelectricity of Ukrainian Academy of Science, Chernivtsy, Ukraine

Abstract

The thermoelectric figure of merit is investigated under accounting as bulk so surface parameters. The electron and phonon temperatures are supposed different. It is shown that thermoelectric figure of merit increases under sample dimensions decreasing when electron subsystem has isotropic heat contact with thermostat and phonon subsystem has adiabatical one.

Thermoelectric materials are known to be characterized by thermoelectric figure of merit [1]

$$z = \frac{\alpha^2 \sigma}{\chi_e + \chi_p} \quad (1)$$

where α , σ , χ_e , χ_p are thermoelectric coefficient, electrical conductivity, electron and phonon components of thermal conductivity, respectively.

It is known so that formula (1) was obtained without considering of sample geometric dimensions. At the same time the real situation demands of there consideration under studying of thermoelectric properties [2]. It is naturally to formulate the current and heat boundary conditions in this case. The general heat flux which contains itself as electron's so phonon's heat transports is fix on the boundaries usually. At the same time experiments [3, 4] and there theoretical generalization [2] point out on the possibility of separating of these fluxes. This leads to that electron temperature T_e and phonon temperature T_p are different [5] at distances of order of the cooling length [6] from surfaces which contact with external thermostats.

Suppose a semiconductor sample has the form of a rectangular parallelepiped of the length $2a$ along the x axis, and its right and left faces are maintained at the

temperatures of T_1 and T_2 ($T_1 > T_2$). We consider the lateral faces of the sample to be adiabatically isolated, and the sample itself to be closed on the external metal load by the resistance R_m so that thermoelectric current $j \neq 0$.

We suppose that $(T_1 - T_2)/T \ll 1$ where $T = (T_1 + T_2)/2$ is the average temperature. Electronic gas in a semiconductor characterized by the isotropic parabolic law of dispersion, is considered to be nondegenerate. As a simplification, let us restrict ourselves to the scattering of charge carriers on the acoustic phonons. In the framework of the model chosen thermoelectric current and distribution of the electron and phonon temperatures were studied in detail in [7] and are represented by the following expressions:

$$T_{e,p}(x) = T - \frac{\Delta T}{2} \left\{ \frac{x}{a} - \frac{A_e + \beta A_p (1 + \Delta)}{A_e B_p + \beta A_p B_e} \cdot \frac{x}{a} - \frac{\gamma_{e,p} [\xi_e - \xi_p - B_p \Delta / ak]}{A_e B_p + \beta A_p B_e} \cdot \frac{sh(kx)}{ch(ka)} \right\} \quad (2)$$

where

$$A_{e,p} = 1 + \xi_{e,p} th(ak), \quad B_{e,p} = 1 + \xi_{e,p} ak,$$

$$k^2 = L^{-2} = k_e^2 + k_p^2, \quad \xi_{e,p} = (\chi_{es,ps} / \chi_{e,p}) (ak)^{-1},$$

$$k_{e,p}^2 = P / \chi_{e,p}, \quad \beta = k_p^2 / k_e^2 = \chi_e / \chi_p,$$

χ_{es} and χ_{ps} are the surface thermal conductivity of electrons and phonons, P is the parameter used to define the interaction intensity of electron and phonon subsystems [5], $\gamma_{e,p}$ is parameter taking the values of 1 and $-\beta$ for T_e and T_p

$$j = \frac{\alpha \Delta T}{R} G + \frac{\alpha_s \Delta}{R} T (1 - G), \quad (3)$$

where $R=R_0 + R_s + R_p + R_m$ is the sample resistance, R_s is the total resistance of its contacts, α_s is the thermal EMF of contacts:

$$\Delta = \frac{2aT(\alpha - \alpha_s)[G\alpha + (1-G)\alpha_s]}{\chi_e R}, \quad (4)$$

$$R_p = \frac{2aT(\alpha - \alpha_s)^2}{\chi_e} \cdot F,$$

$$G = 1 - \frac{(A_e + \beta A_p) - (\xi_e - \xi_p)th(ka)}{A_e B_p + \beta A_p B_e}, \quad (5)$$

$$F = \frac{\beta A_p + B_p [th(ka)/ka]}{A_e B_p + \beta A_p B_e}.$$

Let us use the common expression for the efficiency of thermoelectric converters

$$\eta = \frac{W}{q(x=-a)} \quad (6)$$

where $W = j^2 R_m$ is useful power,

$q = q_e(x=-a) + q_p(x=-a)$ is general heat flux which is leadered up to the hot surface.

Electron and phonon heat flux's components are determined by relation [5]

$$q_e = -\chi_e \frac{dT_e}{dx} + j(T_e)j \quad (7)$$

$$q_p = -\chi_p \frac{dT_p}{dx} \quad (8)$$

After uniting expressions (2), (7) and (8) we can obtaine

$$\eta = \frac{\Delta T}{T_1} \left[\frac{4}{z^* T_1} + \frac{T_e(x=-a)}{T_1} \cdot \frac{\alpha}{\alpha_s(1-G) + \alpha G} \cdot \frac{R}{R_m} \right]^{-1} \quad (9)$$

where

$$z^* = \frac{8a[\alpha_s(1-G) + \alpha G]^2 R_m}{\chi_p(1+\beta)R^2}.$$

$$\left[1 - \frac{A_e + \beta A_p(1+\Delta)}{A_e B_p + \beta A_p B_e} \right]^{-1} \quad (10)$$

is parameter which has the dimensions of the inverse temperature and can be defined as effective thermoelectric figure of merit.

The first term in the square brackets (9) is associated with nonreversible heat loos caused by thermal conductivity. The second term is associated which Peltier effect. Let us note that z^* depends not only bulk parameters but on surface characteristics too.

The expression (9) transfers to well known expression [8] in the limiting case of isothermic contact electron subsystems of bulk sample ($a/L \gg 1$) with thermostats ($\chi_{es} \gg \chi_e, \chi_{ps} \gg \chi_p$), $F = 0$, $G = 1$, $R_p = 0$, $T_e(x = -a) = T_1$ and under condition of reaching maximum power ($R_0 = R_m$) [8]

$$\eta_w = \frac{\Delta T}{T_1} \left[\frac{4}{z^* T_1} + 2 \right]^{-1} \quad (11)$$

where $z^* = z$.

The most interesting situation from the standpoint of thermoelectric energy conversion presents by the case when the phonon subsystem is adiabatically isolated, and the electron one makes the isothermal contact with the thermostats ($\chi_{es} \gg \chi_e, \chi_{ps} \ll \chi_p$).

This situation can take place, for example, under electron gas heating by electromagnetic wave [9]. The value of wave frequency must be the order or more than energy electron-phonon relaxation frequency. It this case the effective thermoelectric figure of merit is equal to

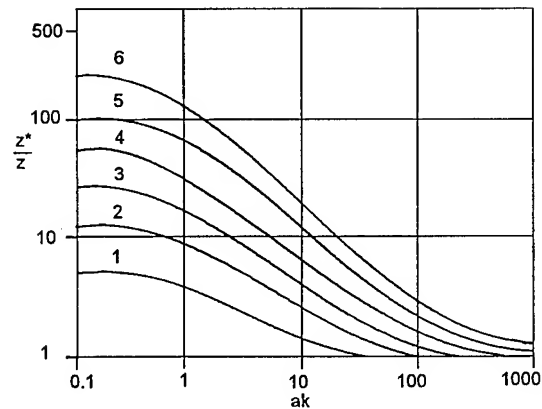
$$z^* = z \left(1 + \frac{1}{\beta a k} \right) \quad (12)$$

It the limitng case of semiconductor sample of submicron dimensions ($a/L \ll 1$)

$$z^* = z \left(1 + \frac{1}{\beta} \right) \quad [10] \quad (13)$$

Thus, from (11) it is seen that with adiabatical isolation of the phonon subsystem and with the reduction of linear sample dimensions the value of thermoelectric figure of merit increases. Its limiting value is in the sample of submicron dimensions. It is explained by the absence of bulk energy electron-phonon interaction, so the adiabatically isolated phonon subsystem "turns off" from heat transport process through sample and efficiency increases. The plot demonstrating this tendency is shown in the Figure.

9. S.Ashmontas. Electrogradient phenomena in



Dependence of z^*/z on linear dimensions of sample at different β values.

1 – 0.2, 2 – 0.1, 3 – 0.05, 4 – 0.025, 5 – 0.01, 6 – 0.005.

References

1. Anatychuk L.I. Thermocouples and thermoelectric devices. K.:Naukova Dumka, 1979, 766 p.
2. Granovsky M.Ja., Gurevich Ju.G. On the Theory of Thermoemagnetic Effects.// Phys. Techn. Poluprov. - 1975. - vol.9. -Issue 8. p.p.1552 -1544.
3. Klimovskaja A.I., Snitko O.V. Absorption of not electron energy by the semiconductor surface.//Letters to Journal of Exp. and Theoretical Physics.-1968. -Vol.7. -p. 194
4. Williams P.P., Sardaryan V.S., Dobrovolsky P.P., Kopylova S.V. Current nonlinearity in Ge films in magnetic field.//Letters to Journal of Exp. and Thor. Phis. -1969. -vol. 10. -p. 377-380.
5. Bass F.G., Bochkov V.S., Gurevich Yu.G. Electrons and phonons in bounded semiconductors. M.:Nauka, 1984. - 289 p. (in Russian).
6. Gribnikov Z.S., Melnikov V.I. Effect of Dimensions in Magnetoresistance of Semiconductors.// Journal of Exp. and Theor. Phys. -1966. -Vol. 51. Issue 6(12). -p. 1909-1913.
7. Gurevich Yu.G., Logvinov G.N. Thermal EMF and Thermal Current of Monopolar Semiconductors of Limited Dimensions.//Phys. Techn. Poluprov. - 1992. Vol. 26. Issue 11. -p.p. 1945-1951.
8. Thermoelectric generators.(Under Regel A.R.edition)-Moscow.:Atomizdat.-1976.-p.320.
9. S.Ashmontas. Electrogradient phenomena in semiconductors. Vlnius.:Mokslas.-1984.-p.182.
10. Logvinov G.N. Thermoelectric Figure of Merit of Semiconductor Submicron Layers. //Izvestija vuzov.Physics. -1993. -N 9. -p.p. 68-72.

The Phonon Drag Effect on Thermopower in p-CdTe

Yu. G. Gurevich, Svetla Vackova[†], Karel Zdansky[‡]

Centro de Investigacion y de Estudios Avanzados del I.P.N.,
México, Distrito Federal, México

[†]Department of Semiconductors, Charles University,
Prague, Czech Republik

[‡]Academy of Sciences of Czech Republik, Prague

Introduction

Cadmium teluride (CdTe) is a wide band-gap semiconductor which has many applications in various fields [1,2,3]—from detectors of nuclear radiation to infra-red diodes and solar cells. The aim of this paper is to describe the new observed experimental effect—the influence of temperature gradient ΔT on the electrical properties of the systems: Au/p-CdTe/Au (Au/CT/Au), Au/p-Cd_{0.96}Zn_{0.04}Te/Au (Au/CZT/Au). Its explanation based on the theory [4], the role of non-equilibrium carriers appearing due to ΔT , is given. Thirty years ago Plavitu [5] has published interesting theoretical work about the role of the optical phonons (optical phonon drag effect) in Seebeck effect and in related transport phenomena. While the acoustical phonon drag contribution can significantly enlarge the value of thermopower, on the contrary the optical phonon drag effect can reduce it. This was shown for the first time in 1972 [6] (measured on CdTe *n*- and *p*-types and even in CdSe). Later this observation was also verified by other authors [8]. Our paper represents a continuation of our previous papers [6,7,9,10]. The analysis of the rectifying properties of contacts Au/p-CdTe was published in [11,12]. The interpretation of the results is based on extended thermo emission-diffusion theories of charge carrier transport through a Schottky diode structure. The influence of Richardson constant was also considered for carriers passing from the metal into the semiconductor.

Experiment

Single-crystals of p-CT and p-CZT wafers were prepared in the laboratory of prof. O. Panchuk (State Chernivtsi University, Ukraine). Bulk resistivity of CT measured at room temperature by four point method was about 100 ohm/cm, Hall mobility 80 cm²/Vs, resp. bulk resistivity of CZT was about 4 ohm/cm, Hall mobility 76 cm²/Vs (from Hall measurements). The contacts were prepared by electroless deposition of gold on fresh surface (cut immediately before the deposition) in air. The gold stipes (1 x 3) mm² were deposited on fresh splitted orientated surface. The samples (15 x 3 x 2) mm³ were pressed between two copper blocks with electrical heaters inside. The contacts indicated rectifying properties.

The Seebeck effect

While the Seebeck effect in CT demonstrates significant phonon drag effect by optical phonons (see [6,7,10]), in

CZT the phonon drag effect disappears [7]. The reason is probably—as in other similar three compound semiconductors—in the fact that optical phonons are more scattered on impurity centers, and so the probability to interact with carriers in phonon drag is smaller. Moreover the thermopower increases with the decrease of temperature, when experimental values of thermopower are compared with calculated values from Hall measurements.

The description of observed effect

The experiment was in details described in our last papers [7,9,10]. In our paper [10] we described the experiment keeping the middle temperature T^* on the constant value as it is suggested in the theory [4], but the theory does not assume the rectifying properties of the contacts. For this reason we decided to keep the temperature of one contact Au/CT resp. Au/CZT constant and to increase or decrease the temperature of second one. The temperature gradient ΔT on the system Au/CT/Au resp. Au/CZT/Au significantly controls the electrical current through the sample, it can enlarge or diminish it in the dependence of the gradient direction. Typical set of $j - U$ characteristics for CT is shown in Fig. 1 (see our previous papers [7,9,10]). Nonohmic contacts moritor changes of the density of car-

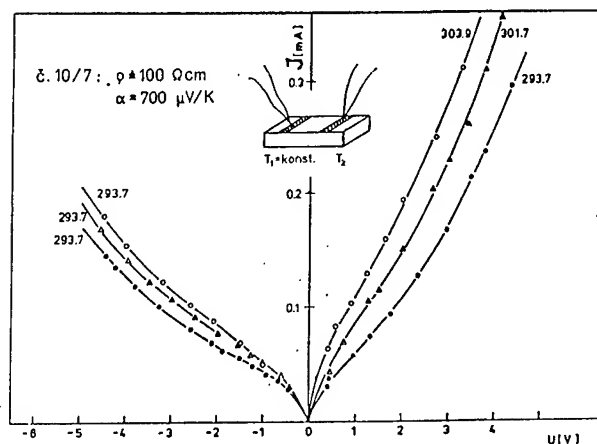


Figure 1: Typical set of $j - U$ characteristics of the system Au/CT/Au.

riers near the Au/CT or Au/CZT interface. Thus a significant shift on the measured $j - U$ characteristics with the temperature gradient is observed. The greater is the

termovoltage $\alpha\Delta T$, the greater is the current change

$$\log j_1 - \log j_0 = q\alpha\Delta T, \quad \text{for } U = \text{const},$$

where j_1 is the current at a given temperature difference ΔT and j_0 stays for $\Delta T = 0$. It has been shown experimentally that there is a different value of the coefficient q for the positive ($\Delta T > 0$) and for the negative ($\Delta T < 0$) temperature gradient for the system Au/CT/Au, see Fig. 2. The possible explanation of this difference is in the phonon

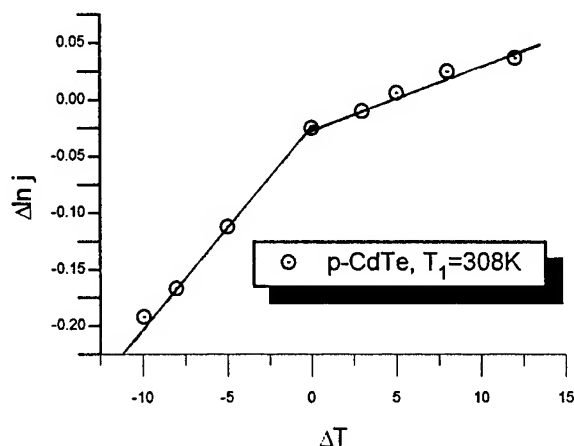


Figure 2: The asymmetrical current change in Au/CT/Au system on the temperature difference for $U = 2$ V and $T = 308$ K.

drag effect in CT, by the redistribution of holes in the sample [4]. In CZT no difference was found (see Fig. 3), because the phonon drag is negligible as it was shown

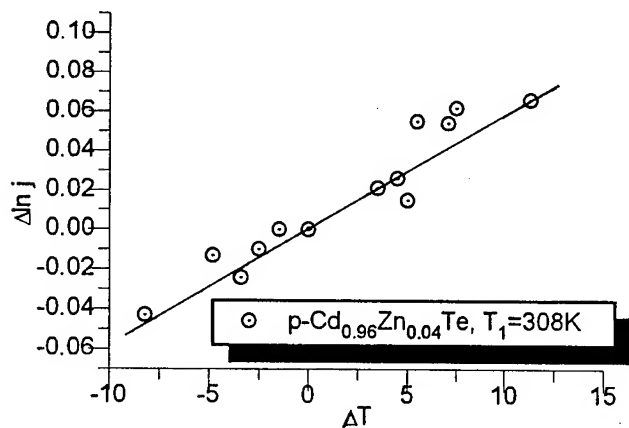


Figure 3: The current change in Au/CZT/Au on the temperature difference for $U = 3$ V and $T = 308$ K.

above from the thermopower measurements.

Acknowledgements

We wish to thank Ing. J. Racko, Slovakia, for theoretical calculations and the group of Prof. O. Panchuk, Ukraine, for large monocrystals of CdTe and CdZnTe.

- [1] J. L. Stone, *Physics Today*, vol. 46, No. 9, pp. 22 (1993).
- [2] M. Ziarri, W. H. Steier, *Appl. Optics*, vol. 32, No. 29, pp. 5711 (1993).
- [3] I. Youm, M. Cadene, M. Candille, D. Laplaze, D. Lincot, *Phys. Stat. Sol. A*, vol. 140, pp. 471 (1993).
- [4] Yu. G. Gurevich, O. Yu. Titov, G. N. Logvinov, O. I. Ljubimov, *Phys. Rev. B*, vol. 51, No. 11, pp. 6999-7004 (1995).
- [5] C. N. Plavitu, *Phys. Stat. Sol.*, vol. 12, pp. 265 (1965).
- [6] S. Kubalkova (Vackova), *Phys. Stat. Sol. B*, vol. 50, pp. 111-123 (1972).
- [7] S. Vackova, J. Racko, D. Donoval, Yu. G. Gurevich, P. Fochuk, P. Feichuk, *Proceedings of European Workshop of Thermoelectrics*, Nancy, France, pp. 133-5, Nov. 1995.
- [8] Rosenzweig, Birkholz, *Phys. Stat. Sol.*, vol. 71, pp. K41-K45 (1982).
- [9] S. Vackova, *Proceedings of 13th International Conference of Thermoelectrics*, Kansas City, USA (1994).
- [10] S. Vackova, J. Racko, D. Donoval, Yu. G. Gurevich, *Proceedings of 14th International Conference of Thermoelectrics*, St. Petersburg, pp. 331-333 (1995).
- [11] J. Racko, A. Grmanova, J. Breza, *Solid State Electronics*, vol. 39, No. 3, pp. 391-397 (1996).
- [12] A. Grmanova, S. Vackova, J. Racko, J. Breza, *Journal of Electr. Engineering*, vol. 46, No. 11, pp. 378-380 (1995).

THEORY OF PHONON DRAG THERMOPOWER

P.G. Klemens

Dept. of Physics and Inst. of Materials Science
University of Connecticut, Storrs CT 06269

Abstract

The phonon contribution to the thermopower, S_p , was first seen in germanium at low temperatures, and theoretically explained by Herring. Subsequently it was also predicted and identified in metals and alloys. In metals all phonons interact with the electron gas, and the theory is much simpler. In semiconductors only phonons of frequency below ω_c can interact with electrons, where $\omega_c \propto T^{1/2}$. The magnitude of S_p depends on the relative strength of phonon scattering by electrons compared to either phonon-phonon or phonon-defect interactions. Phonon drag thermopower is important at low temperatures, but it can be appreciable also at higher temperatures, whenever the carrier concentration is large enough for the phonon-electron interaction to be strong below ω_c . This is the case in semiconductors used for energy conversion, where S_p can be comparable to k/e or 86 V/K, thus making a significant contribution to the figure of merit. To optimize that figure, one reduces the lattice thermal conductivity by point defects, which scatter high frequency phonons, while carrier scattering limits the contribution below ω_c . Attempts have been made to scatter phonons of intermediate frequency by other imperfections. It is necessary to choose such imperfections carefully; if they scatter phonons below ω_c strongly, the advantage of reducing the lattice thermal conductivity may be offset by a reduction in the thermopower.

Phonon Drag

The electric current density in a conductor can be written as

$$j = en\lambda \quad (1)$$

where n is the electron density, e the electronic charge and λ the drift velocity. The electron distribution in momentum space is displaced, and the occupation number per electron state becomes

$$f(\lambda, E, \mathcal{E}) = (e^{\mathcal{E}} + 1)^{-1} \quad (2)$$

$$\mathcal{E} = (E - \mathcal{E} - \lambda \cdot p)/kT \quad (3)$$

where E and p are the energy and momentum of the electron, \mathcal{E} is the Fermi energy, k the Boltzmann constant and T the temperature. The phonon gas interacts with the electrons. For phonons of angular frequency ω and wavevector q , the phonon energy is $\hbar\omega/2\pi$ and its momentum $\hbar q/2\pi$, where \hbar is the Planck constant. If energy and momentum are conserved in each interaction, the phonon gas would attain a quasi-equilibrium distribution

$$N(\lambda, \omega, T) = (e^{\mathcal{X}} - 1)^{-1} \quad (4)$$

$$\mathcal{X} = \hbar(\omega - \lambda \cdot q)/2\pi kT \quad (5)$$

provided the interaction of the phonons with electrons is much stronger than the processes which bring the phonon gas into true equilibrium with the underlying crystal lattice, and which make $\lambda = 0$.

Using the shifted phonon distribution, one can calculate the phonon heat current Q , proportional to λ , i.e.

$$Q = (1/3)\lambda C T \quad (6)$$

Since Q is caused by the electric current, one can define a phonon contribution to the Peltier coefficient $\Pi_p = Q/j$, so that, in the absence of phonon-lattice interactions,

$$S_p^0 = \Pi_p^0/T = C/3ne \quad (7)$$

Here C is the phonon specific heat per unit volume.

If the phonons interact with the lattice by phonon-phonon and phonon-defect scattering processes, the drift velocity of the phonons is less than that of the electron gas. Since the phonon relaxation times τ_e and τ_p which describe the phonon-electron and the other phonon interactions may be frequency dependent

$$S_p = S_p^0 C^{-1} \int C(\omega) \tau_p(\omega) [\tau_p(\omega) + \tau_e(\omega)]^{-1} d\omega \quad \dots (8)$$

where $C(\omega)d\omega$ is the spectral contribution to the phonon specific heat. Equation (8) is obtained by equating the rate of momentum transfer from the electrons into a frequency group of phonons to the rate at which it is removed by the other processes.

Semiconductors

This relatively simple result applies to metals [1] where all phonons interact with the electrons. In semimetals and semiconductors only a portion of the phonon spectrum can interact with the electrons. This was recognised by Herring [2] whose theory for semiconductors at low temperatures actually precedes that for metals. The following simplified treatment is applicable to semiconductors in the classical limit when $C(\omega) \propto \omega^2$ and $C = 3N_a k$, N_a being the number of atoms per unit volume.

For a free electron gas of low electron density, wavevector conservation requires q to be no more than twice the Fermi wavevector or, if the gas is non-degenerate, that $q \leq \omega_c/v$, where v is the phonon velocity and

$$\omega_c = 4\pi(v/\hbar)(2mkT)^{1/2} \quad (9)$$

For a free electron mass and $v = 3 \times 10^5$ cm/s, if $\hbar\omega_c/2\pi k = T_c$,

$$T_c = 2.2T^{1/2} \quad (\text{in } ^\circ\text{K}) \quad (10)$$

Now only phonons below ω_c are being dragged

by the electrons, so that $C = N_a k (T_c/\theta)^3$, where θ is the Debye temperature, so that in place of (7)

$$S_p^0 = N_a k / n e (T_c/\theta)^3 \quad (11)$$

and in place of (8), taking the integral up to ω_c ,

$$S_p = (k/e)(N_a/n)(T_c/\theta)^3 \tau_p / (\tau_p + \tau_e) \quad (12)$$

where τ_p, τ_e are suitably averaged over the frequencies below ω_c . If $\tau_e \ll \tau_p$, $S_p = S_p^0$. Note that T_c and n both depend on temperature; also T_c varies as $T^{1/2}$.

It is now necessary to estimate τ_e and to compare it to τ_p . This is conveniently done through a momentum balance argument, that relates τ_e , the relaxation time of phonons due to electron interactions, to σ_p , the relaxation time of electrons for the same interaction. This yields

$$C_e / \sigma_p = C_p(\omega_c) / \tau_e \quad (13)$$

where $C_e = (3/2)nk$ is the heat capacity of the electron gas, $C_p(\omega_c) = 3N_a k (T_c/\theta)^3$ that of the phonons which interact with the electrons. If the electrons are in β valleys, σ_p must be increased by β . Details are given by White [3] and by White and Klemens [4]. For the electron densities useful for thermoelectric conversion [5], $1/\tau_e$ ranges from about 4 to $10 \times 10^{10} \text{ sec}^{-1}$ and phonon scattering by electrons is much stronger than other phonon scattering processes at ω_c and below. Thus S_p approaches the value of S_p^0 of equation (11). For n-type Si-Ge alloys with $n \approx 10^{21} \text{ cm}^{-3}$, S_p is around k/e or $-86 \mu\text{V/K}$ from 900 K up. This is a significant and fortuitous addition to the Seebeck coefficient, around 25 to 30% of the total. Its absence would reduce the figure of merit

$$ZT = S^2 T / (\kappa_e + \kappa_p) \varrho \quad (14)$$

where ϱ is the electrical resistivity, κ_e and κ_p the electronic and lattice thermal conductivity. Not only does a reduction in S reduce the numerator, but it also causes an increase in the Lorenz ratio $\kappa_e / \varrho^2 T$ [6].

Lattice Conductivity

Equation (14) suggests that optimum performance requires κ_p to be comparable to κ_e . A reduction in κ_p is desirable, provided it does not reduce S . The lattice thermal conductivity can be reduced below its intrinsic value, which is limited by anharmonic phonon interactions only. Point defects, such as in the Si-Ge alloys, reduce the contributions by high frequency phonons. Interactions with the conduction electrons reduce the contribution from below ω_c . This leaves a frequency window where the spectral contribution to the phonon conduc-

tivity is high, because it is limited only by anharmonic processes. As shown in the example of Si-Ge alloys, this window is now responsible for much of the conductivity. Further reductions could be made by extended defects, which would scatter phonons at low frequencies. Now, however, an important consideration would be not to scatter phonons below ω_c .

Not only would such low frequency scattering merely compete with phonon-electron scattering and not be very effective, but it would also reduce the phonon thermopower S_p .

Thus one should reconsider scattering due to mesoscopic inclusions within the grains [7]. Their contribution to the reciprocal of the phonon mean free path, expressed in terms of their overall volume fraction c , would be, if they are of spherical shape,

$$1/\ell_{\text{inc}} = 6c/d \quad (15)$$

where d is the diameter [4,8]. The smaller the inclusions, the bigger their effect for a given volume fraction c . Also, at very low frequencies, this scattering decreases rapidly, roughly when $\omega < \pi v/d$. Thus in order not to reduce S_p , the diameter d should not be larger than $\pi v/\omega_c$. This value of d varies as $T^{-1/2}$ for optimization at a temperature T . For 900°K, where from equation (10) the value of ω_c is $5.8 \times 10^{12} \text{ sec}^{-1}$, d should not exceed 16 \AA . Adding inclusions within each grain of a semiconductor alloy is far from easy, and controlling the size distribution to fit this requirement would be even harder. In any case other factors must also be considered, for example one should not reduce the electron mobility. The need to avoid reducing the phonon drag thermopower would make the optimization process even more complicated.

References

- [1] P.G. Klemens, "Contribution to the Thomson Coefficient", Australian J. of Physics, vol. 7, pp. 520-522, 1954.
- [2] C. Herring, "Theory of the Thermoelectric Power of Semiconductors", Physical Rev., vol. 96, pp. 1163 - 1187, 1954.
- [3] D.P. White, "Phonon Scattering and Thermal Conductivity in Semiconductors with Thermoelectric Applications", Storrs, CT: University of Connecticut Doctoral Dissertation, 1990.
- [4] D.P. White, P.G. Klemens, "Thermal Conductivity of Thermoelectric Si(80)-Ge(20) Alloys", J. Applied Physics, vol. 71, pp. 4258 - 4263, 1992.
- [5] C.B. Vining, W. Laskow, J.O. Hanson, R.R. Van der Beck, P.D. Gorsuch, "Thermoelectric Properties of Pressure-Sintered Si-Ge", J. Applied Physics, vol. 69, pp. 4333 - 4340, 1991.
- [6] P.G. Klemens, "Thermal Conductivity of Solids at Low Temperatures", in Handbuch der Physik, vol. 14, pp. 198 - 281, Berlin: Springer, 1956; see Section 21.

- [7] J.S. Beaty, J.L. Rolfe, J.W. Vandersande, "Thermoelectric Properties of Ultrafine Particulate SiGe Powder Alloys with Inert Additions" in Modern Perspectives on Thermoelectric Materials, Pittsburgh, PA: Materials Research Soc., Symposium Proceedings, vol.234, pp. 105 -109, 1991.
- [8] P.G. Klemens, "Thermal Conductivity of n-Type Si-Ge" in Modern Perspectives on Thermoelectric Materials, Pittsburgh PA: Materials Research Soc., Symposium Proceedings, vol. 234, pp. 87 - 94, 1991.

Thermoelectric Power in Disordered Mixed Crystals

P. J. Lin-Chung and A. K. Rajagopal
Naval Research Laboratory, Washington, D. C. 20375, U. S. A.

Abstract

In disordered mixed crystals the effect of alloy scattering is known to be of significant importance in comparison with that of lattice scattering in the consideration of electrical and thermal transport properties. In this work we consider the thermoelectric power in such isotropically disordered mixed crystals. We derive the energy current density operator for a combined electron and vibrating ions of the lattice system with the electron-lattice interaction term included. In this preliminary report, the relative importance of electrons and lattice vibrations to the thermoelectric power is discussed. The coherent potential approximation may be used to obtain the thermoelectric power of the disordered mixed crystal as function of the concentration. Our operator formulation is in coordinate space which besides containing previous formulations for metals and alloys as special cases, admits of the coherent-potential approximation methods to be applied as well.

Introduction

The performance of a thermoelectric material is characterized by the three important transport coefficients, the electrical and thermal conductivities, and the thermoelectric power. A high ratio of electrical to thermal conductivity and a large thermoelectric power are needed in selecting materials for both thermoelectric generation and refrigeration. In this work, we focus on the effect of disorder scattering on thermoelectric materials. The effect on the thermal conductivity and electrical conductivity in binary alloys have been studied extensively in the literature [1, 2]. However, the thermoelectric power in disordered mixed crystal does not seem to have been examined with the same rigor. This may be due to the fact that the correlation function expression for thermoelectric power tensor involves both charge current and energy current components, which are more complicated.

In this work we first derive the energy-current-density operator for a system of electrons and ions with first order electron-ion interaction term included by following the procedure given in [3]. The correlation function of charge-current density operator and energy-current density operator is then examined by separating the contributions from electron, lattice and electron-ion interaction terms. Coherent potential approximation (CPA) may then be employed to study the thermoelectric power in disordered mixed crystals.

Energy-current operator for a combined electron-lattice system

The correlation function expressions for the thermal transport coefficients are more general than those based on transport equation. The linear response of a system to an external electric field leads unambiguously to the Kubo formula for the electrical conductivity tensor. This derivation based on a "well defined Hamiltonian" is thus "mechanical" [4]. For a long time, there existed no mechanical formulation for thermal transport problems since there was no Hamiltonian describing a thermal gradient. Green-Kubo-Mori formulas for the thermal transport coefficients are derived based on the assumptions that local variables are controlled by a Markoff process or when "local equilibrium distribution" is assumed. Their derivations are not as rigorous but are found to be quite practical. They have been used widely in studying thermal transport. Luttinger [4] gave an essentially mechanical derivation by introducing an inhomogeneous gravitational field which produces the energy flow and temperature fluctuation. A new term which appears in the Hamiltonian as a product of this field and the local energy density operator, $h(\vec{r}, t)$, of the system is introduced and a Kubo-type theory developed.

The energy-current operator, $j^E(\vec{r}, t)$, which appears in the correlation functions is determined through the following equation of continuity

$$\dot{h}(\vec{r}, t) + \nabla \cdot j^E(\vec{r}, t) = 0, \quad (1)$$

The overdot here represents the time derivative.

Kadanoff and Martin [3] derived $j^E(\vec{r}, t)$ for superconducting electrons and expressed the correlation functions in terms of the two-particle Green function familiar in the many-body theory. Hardy [5] first derived the $j^E(\vec{r}, t)$ for a lattice system. Luttinger gave an expression for the free electron system [4]. Using the Bloch representation for electrons, Lyo [6], and Vilenkin and Taylor [7] derived the energy current. These authors also included electron-phonon interaction contributions. More recently, Jonson and Mahan [8] examined the electron-ion contribution to the thermopower of metals, who also used the Green function methods as in [3], using the harmonic approximation for the ionic vibrations. In the present work we derive the $j^E(\vec{r}, t)$ for a combined electron and lattice system in a representation free form. By choosing appropriate representation for the field operators, this reduces to the expressions found in the literature.

The Hamiltonian of the system considered here is

$$H = H_e + H_{ph} + H_{ep}, \quad (2)$$

where

$$H_e = \int d^3\vec{r} \hat{\psi}^+(\vec{r}, t) \left[\frac{\hat{p}^2}{2m} + V(\vec{r}) \right] \hat{\psi}(\vec{r}, t) \quad (3)$$

$$H_{ep} = - \sum_{\alpha, l} \int d^3\vec{r} \hat{\psi}^+(\vec{r}, t) Q_{\alpha}(l, t) \nabla_{\alpha} V(\vec{r} - \vec{R}_l) \Big|_{\vec{R}_l = \vec{R}_l^0} \hat{\psi}(\vec{r}, t) \quad (4)$$

$$H_{ph} = \sum_{\alpha, l} \frac{P_{\alpha}^2(l, t)}{2M(l)} + \frac{1}{2} \sum_{\alpha, \alpha', l, l'} \Phi_{\alpha\alpha'}(l, l') Q_{\alpha}(l, t) Q_{\alpha'}(l', t) \quad (5)$$

$$V(\vec{r}) = \sum_l V_l(\vec{r} - \vec{R}_l^0) \quad (6)$$

\hat{p} , $P_{\alpha}(l, t)$ are the momentum operators for electrons and ions, respectively. $Q_{\alpha}(l, t)$ is the displacement operator for the ion. m , $M(l)$ are the masses for electrons and ions, respectively. \vec{R}_l , \vec{R}_l^0 are the position vectors of ions at non-equilibrium and equilibrium conditions, respectively. V represents the potential energy associated with the electrons, and $\Phi_{\alpha\alpha'}(l, l')$ is the dynamical matrix of the vibrating lattice. The $\hat{\psi}^+(\vec{r}, t)$, $\hat{\psi}(\vec{r}, t)$ are the creation and annihilation field operators for the electron respectively. All the operators here are in Heisenberg representation, and obey the standard canonical commutation rules. For the sake of simplicity we have here considered harmonic approximation and leading order electron-ion interaction.

A general expression for $j^E(\vec{r}, t)$ will be derived by using the definition of $h(\vec{r}, t)$ in the form

$$h(\vec{r}, t) = \left[-\frac{\hat{p}_1 \cdot \hat{p}_2}{2m} + V(\vec{r}) - \mu \right] \hat{\psi}_1^+ \hat{\psi}_2 - \sum_{\alpha, l} \hat{\psi}^+(\vec{r}, t) Q_{\alpha}(l, t) \nabla_{\alpha} V(\vec{r} - \vec{R}_l) \Big|_{\vec{R}_l = \vec{R}_l^0} \hat{\psi}(\vec{r}, t) \quad (7)$$

In the above equation and subsequent equations, the indices, 1 or 2, denote the corresponding variables as \vec{r}_1 , \vec{r}_2 , respectively, and $\vec{r}_1 = \vec{r}_2 = \vec{r}$ at the end of the indicated operations. μ is the chemical potential of the electrons.

Eq. (1) can also be written as

$$-i\hbar \nabla \cdot j^E(\vec{r}, t) = [h(\vec{r}, t), H] \quad (8)$$

by using the standard quantum mechanical expression for the time derivative of an operator. Here H is the total Hamiltonian given by eq. (2).

From eqs. (3-8) the energy-current operator is derived and may be expressed as a sum of two terms contributed by electron and electron-ion interaction. Since the part of energy-current operator coming from phonons contributes only to the

correlation function related to the lattice thermal conductivity, and does not give contribution to the thermoelectric power we shall not consider that term in the following discussion.

$$j^E(\vec{r}, t) = j_e^E(\vec{r}, t) + j_{ep}^E(\vec{r}, t) \quad (9)$$

Our derivation gives

$$j_e^E(\vec{r}, t) = \left(-\frac{\hat{p}_1 \cdot \hat{p}_2}{2m} + V(\vec{r}) - \mu \right) \frac{\hat{p}_1 - \hat{p}_2}{2m} \hat{\psi}_2^+ \hat{\psi}_1 \quad (10)$$

$$j_{ep}^E(\vec{r}, t) = - \sum_{\alpha, l} \left[\left(\nabla_{\alpha} V(\vec{r} - \vec{R}_l^0) \right) Q_{\alpha}(l, t) \right] \hat{j}(\vec{r}, t) - \frac{i \nabla_{\vec{r}}}{4\pi} \sum_{\alpha, l} \int d^3\vec{r}' \left(\nabla_{\alpha} V(\vec{r}' - \vec{R}_l^0) \right) \frac{\dot{Q}_{\alpha}(l, t) \rho(\vec{r}', t)}{|\vec{r} - \vec{r}'|} \quad (11)$$

where

$$h_e(\vec{r}) = \frac{-\nabla^2}{2m} + V(\vec{r}) \quad (12)$$

$$\begin{aligned} \hat{j}(\vec{r}, t) &= \frac{1}{2mi} \left[\hat{\psi}_2^+ \nabla_1 \hat{\psi}_1 - (\nabla_2 \hat{\psi}_2^+) \hat{\psi}_1 \right] \\ &= \frac{\hat{p}_1 - \hat{p}_2}{2m} \hat{\psi}_2^+ \hat{\psi}_1 \end{aligned} \quad (13)$$

$$\rho(\vec{r}, t) = \hat{\psi}^+ \hat{\psi} \quad (14)$$

$j(\vec{r}, t)$ and $\rho(\vec{r}, t)$ are, respectively, the electric current density and charge density. The overdot represents the time-derivative. The second term in eq. (11) arises from the commutator of H_{ph} in eq. (5) with the second term in eq.(7), in view of the fact that $M(l)\dot{Q}_{\alpha}(l, t) = P_{\alpha}(l, t)$.

From these general expressions we may obtain those given in the literature [6, 7, 8] by expressing the electron field operators $\hat{\psi}(\vec{r}, t)$, $\hat{\psi}^+(\vec{r}, t)$ in terms of the appropriate Bloch states associated with the pertinent electron system of metals and alloys. In the present paper, we find it convenient to use Wannier representation, $\{u_m(\vec{r})\}$, to take into account the nature of site disordered mixed crystal systems. In semiconductors, similarly, one may use an effective mass representation.

It is convenient at this stage to express eq.(9) in terms of the electron creation and annihilation operators a_m^+ , a_m associated with the Wannier states. Since

$$\hat{\psi}^+(\vec{r}, t) = \sum_m u_m^*(\vec{r}) a_m^+(t) \quad (15)$$

$$\hat{\psi}(\vec{r}, t) = \sum_m u_m(\vec{r}) a_m(t) \quad (16)$$

we have

$$j_e^E(\vec{r}, t) = \frac{1}{2m} \sum_{n, n'} F(n, n') a_n^+ a_{n'} \quad (17)$$

where

$$F(n, n') \equiv \left[-\frac{\hat{p}_1 \cdot \hat{p}_2}{2m} + V(\vec{r}) - \mu \right] \left(\frac{\hat{p}_1 - \hat{p}_2}{2m} \right) u_n^*(1) u_{n'}(2) \quad (18)$$

Similarly, eqs.(11), (13), and (14) can be expressed in terms of Wannier representation since

$$j(\vec{r}, t) = \frac{1}{2mi} \sum_{n, n'} (\nabla_1 - \nabla_2) u_n^*(2) u_{n'}(1) a_n^+ a_{n'} \quad (19)$$

$$\rho(\vec{r}, t) = \sum_{n, n'} u_n^* u_{n'} a_n^+ a_{n'} \quad (20)$$

Theory of thermoelectric power of solids

Various techniques and approximations have been used in the past to describe the theory of thermoelectric power. So far no complete form is given to provide a suitable description of the experimental data. The existing works on thermoelectric power are mostly based on solving the Boltzmann equation using variational method and relaxation time approximation [9, 10]. Electron-phonon contribution to the thermopower of metals has been investigated using the Green's function technique and is found to give good agreement with the Mott's formula [8].

Here we give a general formalism applicable not only to metals but also to semiconductors. Based on the Green-Kubo-Mori formula the product of electrical conductivity, σ , and the thermopower, α , is given by

$$(\sigma \alpha)_{\mu\nu}(\omega) = \lim_{\eta \rightarrow 0^+} \frac{1}{\Omega} \int_0^\infty dt e^{-i\omega t - \eta t} \int_0^\beta d\lambda \langle j_\mu(0) j_\nu^E(t + i\hbar\lambda) \rangle \quad (21)$$

$j_\mu(0)$ is the total electric current and is given by integrating eq.(19) over all space. $j_\nu^E(t)$ is similarly the total energy current. β is related to inverse temperature, $\frac{1}{kT}$. Thus the evaluation of the correlation function in eq.(21) reduces to finding the following three types of correlation functions:

$$\langle j_\mu(0); j_\nu(t) \rangle \approx \langle a_1^+(0) a_2(0); a_3^+(t) a_4(t) \rangle \quad (22)$$

$$\langle j_\mu(0); j_\nu(t) Q_\alpha(l, t) \rangle \approx \langle a_1^+(0) a_2(0); a_3^+(t) a_4(t) Q_\alpha(l, t) \rangle \quad (23)$$

$$\langle j_\mu(0); \rho_\nu(t) \dot{Q}_\alpha(l, t) \rangle \approx \langle a_1^+(0) a_2(0); a_3^+(t) a_4(t) \dot{Q}_\alpha(l, t) \rangle \quad (24)$$

The first function also appears in the expression for electrical conductivity tensor and can readily be reduced into products of two one-particle Green's functions as an approximation [11]. The second and third ones can be reduced to products of three one-particle Green's function through the conversion of phonon displacement operators into electron operators using the following equation of motion for our combined electron phonon system.

$$Q_\alpha(l, t) = M^{-1} \sum_{\alpha', l', m, m'} \int D_o(\alpha l t; \alpha' l' t') \nabla_{\alpha'} V(\vec{r} - \vec{R}_l^0) \times \\ \times u_m^*(\vec{r}) u_{m'}(\vec{r}) a_m^+(t') a_{m'}(t') dt' d^3\vec{r} \quad (25)$$

where D_0 is the bare phonon Green's function. In the case of metals, these expressions were examined by Jonson and Mahan [8].

Coherent-potential approximation for disordered mixed crystals

In the study of disordered mixed crystal only idealized models have been solved exactly. Those results on simple systems are invaluable, both in guiding physically motivated approximations and in finding unusual features unique to the disordered systems. Coherent potential approximation [12, 13] is one of the most powerful techniques used in the calculations of electrical conductivity [1] and lattice thermal conductivity [2] of disordered binary alloys. This technique is capable of dealing with single particle properties of elementary excitations in site-disordered crystals $A_x B_{1-x}$ for arbitrary x and for moderately different characteristics of A and B.

Velicky used single band model Hamiltonian to describe the electronic structure of a disordered binary alloy. Single-site approximation in a multiple-scattering description are based to evaluation the electrical conductivity [1]. We plan to apply this method to the problem at hand.

The contributions to the thermopower are proportional to the correlation functions of the form eqs. (22-24); the first of which is similar to that appearing in the expression for electrical conductivity, and the other two are unique to the expression for thermopower, because of the inclusion of electron-ion interaction. Procedures of the configuration averaged two-particle Green's functions in ref.[1] can be generalized to determine these contributions. We plan to pursue this in the near future.

Summary

In this contribution, we have developed an expression for the energy-current-density in a general setting which unifies the results found in the literature in an elegant way. This formulation lends itself to coherent potential approximations

useful in dealing with disordered mixed crystals. In metals, Jonson and Mahan [8] found that the electron-ion contributions are negligible so that Mott's formula for thermoelectric power continues to hold. We hope to investigate if this conclusion needs modification in the case of strong coupled electron-ion systems which may occur in semiconductors and elsewhere.

This work is supported in part by the Office of Naval Research.

References

- [1] B. Velicky, "Theory of electronic transport in disordered binary alloys: Coherent-potential approximation", *Phys. Rev.* vol. 184, No. 3, pp. 614-627 (1969).
- [2] J. K. Flicker and P. L. Leath, "Lattice thermal conductivity in high-concentration mixed crystals", *Phys. Rev.* vol B7, No. 6, pp. 2296-2305 (1973).
- [3] L. P. Kadanoff and P. C. Martin, "Theory of many-particle systems. II. Superconductivity", *Phys. Rev.* vol. 124, No. 3, pp. 670-697 (1961).
- [4] J. M. Luttinger, "Theory of thermal transport coefficients", *Phys. Rev.* vol. 135, No. 6A, pp. A1505-1514 (1964).
- [5] R. J. Hardy, "Energy flux operator for a lattice", *Phys. Rev.* vol. 132, No. 1, pp. 168-177 (1963).
- [6] S. K. Lyo, "Electron-phonon enhancement of thermoelectricity in metals", *Phys. Rev.* vol. B17, No. 6, pp. 2545-2552 (1978).
- [7] A. Vilenkin and P. L. Taylor, "Theory of thermoelectric effects in dilute alloys", *Phys. Rev.* vol. B18, No. 10, pp. 5280-5290 (1978).
- [8] M. Jonson and G. D. Mahan, "Electron-phonon contribution to the thermopower of metals", *Phys. Rev.* vol. B42, No. 15, pp. 9350-9356 (1990).
- [9] L. Friedman, "Thermopower of superlattices as a probe of the density of states distribution", *J. Phys. C*, vol. 17, pp. 3999-4008 (1984).
- [10] K. Durczewski and M. Ausloos, "Theory of the thermoelectric power or Seebeck coefficient: The case of phonon scattering for a degenerate free-electron gas", *Phys. Rev.* vol. B53, No. 4, pp. 1762-1772 (1996).
- [11] R. J. Elliott, J. A. Krumhansl and P. L. Leath, "The Theory and properties of randomly disordered crystals and related physical systems", *Rev. Modern Phys.* vol. 46, No. 3, pp. 465-543 (1974).
- [12] P. Soven, "Coherent-potential model of substitutional disordered alloys", *Phys. Rev.* vol. 156, No. 3, pp. 809-813 (1967).
- [13] D. W. Taylor, "Vibrational properties of imperfect crystals with large defect concentrations", *Phys. Rev.* vol. 156, No. 3, pp. 1017-1029 (1967).

On the Role of the Bulk and Surface Recombination in the Thermopower in Bipolar Semiconductors

Yu. G. Gurevich, G. N. Logvinov,[†] O. I. Lyubimov,[‡] O. Yu. Titov

Departamento de Física, CINVESTAV—I.P.N., Apartado Postal 14-740,
México D.F. 07000, México

[†]Teacher Training University, Avenue Krivonosa 2,
Ternopil 282009, Ukraine

[‡]Kharkov State University, Square Svobodi 4,
Kharkov 310077, Ukraine

Abstract

The physical transparency of thermopower phenomenon in unipolar case and the clearness of calculation lead to the following paradoxical results: in the case of a bipolar medium the situation seems to be equally obvious, and so the same calculation scheme is used. The aim of this paper is to show that situation changes in bipolar media in principle. If a semiconductor specimen contacts with a heater with temperature T_1 on the surface $x = -a$ and with a cooler with temperature T_2 on the surface $x = +a$, the chemical potential of the electrons and holes are heterogeneous in space and different in all points of the specimen. Thus there are two Fermi quasilevels even in the quasineutrality approximation, and single common "gradient of electrochemical potential" of electrons and holes is absent. One more problem arises when bulk and surface recombinations take place: the correct determination of electron and hole equilibrium concentrations and boundary conditions when thermoelectric current flows in a closed circuit. The aims of this paper are to show the methods of thermopower calculations in case mentioned above and which physical phenomena determine its value.

Introduction

Let us begin with the unipolar situation. Dating back to the paper of Thomson¹ in 1856 the theory of the origin of the thermo-emf in this case has found its most precise description in many publications (see, for example Refs. [2,3]). It is necessary to connect the electric circuit (Fig. 1) for the determining thermo-emf in the case of the absence of electric current (broken circuit). A semiconductor sample whose thickness is $2a$ ($-a \leq x \leq a$) contacts with a heater with temperature T_1 on the surface $x = -a$ and with a cooler with temperature T_2 on the surface $x = +a$. The connecting wires are made of the same material (metal) and are hooked up to the terminals of a measuring compensating circuit which allows us to measure the difference of voltage φ_b and φ_c in the absence of an electric current. Leads of connecting wires

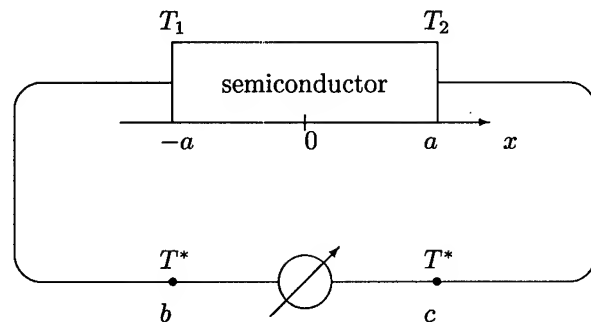


Figure 1: The electric circuit for measuring of thermopower.

have equal temperatures [for example, $T^* = (T_1 + T_2)/2$] at points b and c . As follows from Ohm's law, for a closed electric circuit $V = j(R + r)$ (V is the emf of the power source, r is source's resistance, R is the resistance of the external load, and j is the density of the electric current). If $R \rightarrow \infty$ (broken circuit), then the density of electric current $j \rightarrow 0$ and $V = jR = \varphi_c - \varphi_b$.

Since the electron's chemical potentials $\mu_n(x)$ are equal in the points b and c , then

$$\varphi_c - \varphi_b = (\tilde{\mu}_n^b - \tilde{\mu}_n^c)/e, \quad (1)$$

where $\tilde{\mu}_n(x) = \mu_n(x) - e\varphi(x)$ is an electrochemical potential. At the same time,

$$\tilde{\mu}_n^b - \tilde{\mu}_n^c = \int_c^b \frac{d\tilde{\mu}_n(x)}{dx} dx. \quad (2)$$

As is well known, the expression for the density of the electric current is of the form²

$$\mathbf{j}_n = \sigma_n(x) \left(\nabla \frac{\tilde{\mu}_n(x)}{e} - \alpha_n(x) \nabla T \right), \quad (3)$$

where $\sigma_n(x)$ is the electric conductivity and $\alpha_n(x)$ is the thermoelectric power. In the absence of an electric current

$d\tilde{\mu}_n(x)/dx = e\alpha_n(x)dT/dx$. Let us emphasize that this correlation is correct all over the circuit, where $\sigma_n(x) \neq 0$, e.g., outside the region $[b, c]$, where $\sigma_n(x) \rightarrow 0$ (this condition provides $\mathbf{j}_n = 0$ everywhere in the circuit). Therefore the expression (2) can be rewritten in the form

$$\begin{aligned}\tilde{\mu}_n^b - \tilde{\mu}_n^c &= \int_c^b e\alpha_n(x) \frac{dT}{dx} dx \\ &= \int_{T^*}^{T_2} e\alpha_M dT + \int_{T_2}^{T_1} e\alpha_n dT + \int_{T_1}^{T^*} e\alpha_M dT,\end{aligned}$$

where α_n and α_M are the values of $\alpha_n(x)$ in the semiconductor and in the connecting wires. Finally we have for the difference $\varphi_c - \varphi_b$, which coincides with the thermo-emf V of the broken circuit,

$$V = \varphi_c - \varphi_b = (\alpha_n - \alpha_M)(T_1 - T_2). \quad (4)$$

To simplify the calculations we have assumed that $T_1 - T_2 \ll T^*$ which does not restrict the generality. Since usually $|\alpha_M| \ll |\alpha_n|$, then

$$V = \alpha_n(T_1 - T_2). \quad (5)$$

The last expression coincides formally with $\int_{-a}^{+a} \nabla[\varphi - (\mu_n/e)] dx$.

Thus the general scheme of calculating the thermo-emf comes to the following for a unipolar broken circuit. The gradient of the electrochemical potential $\nabla\tilde{\mu}_n(x)$ is obtained by setting expression (3) equal to zero. Then integration of $\nabla\tilde{\mu}_n(x)$ in the anticlockwise direction (together with multiplying by e^{-1}) gives the value of the thermo-emf. It is important to emphasize that, as above, the extreme points of the circuit (b and c) would have the same temperatures.

It follows from (2), in a unipolar medium, that even if the condition of quasineutrality is not fulfilled and nonequilibrium electrons (this notion will be defined more exactly below) arise, the gradient of concentration of these carriers n does not give a contribution to the thermo-emf [the summand $(\partial\mu_n/\partial n)\nabla n$ disappears from the expression for V]. This argument confirms the following idea of Ioffe:⁴ the potential difference created by the bulk concentration's gradient is compensated by the contact potential difference ("diffusion voltages") on the boundaries $+a$ and $-a$.

Let us note in conclusion that the obviousness of the above scheme is lost when thermo-electric current flows in a closed circuit.

In bipolar semiconductors (traditional approach), the system of equations for electrons and holes are analogous to (3):²

$$\begin{aligned}\mathbf{j}_n^s &= \sigma_n(x) \left[+\nabla \frac{\tilde{\mu}_n(x)}{e} - \alpha_n(x) \nabla T \right], \\ \mathbf{j}_p^s &= \sigma_p(x) \left[-\nabla \frac{\tilde{\mu}_p(x)}{e} - \alpha_p(x) \nabla T \right].\end{aligned} \quad (6)$$

Here \mathbf{j}_p^s is the density of the hole electric current, $\sigma_p(x)$ and $\alpha_p(x)$ are the electric conductivity and thermoelectric power of the holes [$\alpha_n(x)$ and $\alpha_p(x)$ have opposite signs],

$$\tilde{\mu}_p = -\varepsilon_g - \tilde{\mu}_n = \mu_p + e\varphi \quad (7)$$

is the hole electrochemical potential,^[2] and ε_g is the band gap. It is important to emphasize that in expressions (6) $\nabla\mu = (\partial\mu/\partial T)\nabla T$ usually. The full current \mathbf{j}_0 is equal to

$$\mathbf{j}_0 = \mathbf{j}_n + \mathbf{j}_p = 0, \quad (8)$$

if a bipolar semiconductor is represented as in Fig. 1.

It is easy to obtain $\nabla[\tilde{\mu}_n(x)/e]$ from (8) taking into account (6) and knowing that $\nabla\tilde{\mu}_p = -\nabla\tilde{\mu}_n$ [see (7)],

$$\begin{aligned}\nabla \left[\frac{\tilde{\mu}_n(x)}{e} \right] &= \frac{1}{\sigma(x)} [\sigma_n(x)\alpha_n(x) + \sigma_p(x)\alpha_p(x)] \nabla T, \\ \sigma(x) &= \sigma_n(x) + \sigma_p(x).\end{aligned}$$

Then we find the thermo-emf V (it is assumed that $\alpha_{n,p} \gg \alpha_M$ and $T_1 - T_2 \ll T^*$ as above):

$$V = \int_c^b \nabla \left[\frac{\tilde{\mu}_n(x)}{e} \right] dx = \frac{1}{\sigma} (\sigma_n\alpha_n + \sigma_p\alpha_p) (T_1 - T_2). \quad (9)$$

Formulation

The expression (9), especially the method of the calculation, causes serious objections. Really, the electron concentration and hole concentration should be lower in the heating lead in the stationary state due to thermodiffusion if bulk and surface recombinations are absent. In contrast, these concentrations should increase in the cooling lead. On the one hand, this causes the appearance of appreciable diffusion currents⁵ in expression (6) [$\nabla\mu_n = (\partial\mu_n/\partial n)\nabla n$]. On the other hand, it leads to a violation of relation (7). Two Fermi quasilevels $\tilde{\mu}_n$ and $\tilde{\mu}_p$ arise instead of a single level of the electrochemical potential, and as a result $|\nabla\tilde{\mu}_n| \neq |\nabla\tilde{\mu}_p|$. In this case the procedure described in the Introduction becomes incorrect, because the single common "gradient of electrochemical potential" of electrons and holes is absent. As a result we have two equations

$$\text{div} \mathbf{j}_n^s = eR_n, \quad \text{div} \mathbf{j}_p^s = -eR_p \quad (10)$$

for both thermoelectric fields $\nabla(\tilde{\mu}_n/e)$ and $\nabla(\tilde{\mu}_p/e)$ instead of one equation (8). In Eqs. (10) R_n and R_p describe the electron and hole recombination, correspondingly.

Because $\text{div} \mathbf{j}_0 = 0$, we obtain next correlation

$$R_n = R_p = R. \quad (11)$$

One more problem arises when bulk and surface recombinations take place: the correct determination of electron and hole equilibrium concentrations.³ Really, if we write down for R equations:

$$R = \frac{n - n_0}{\tau_n} = \frac{p - p_0}{\tau_p}, \quad (12)$$

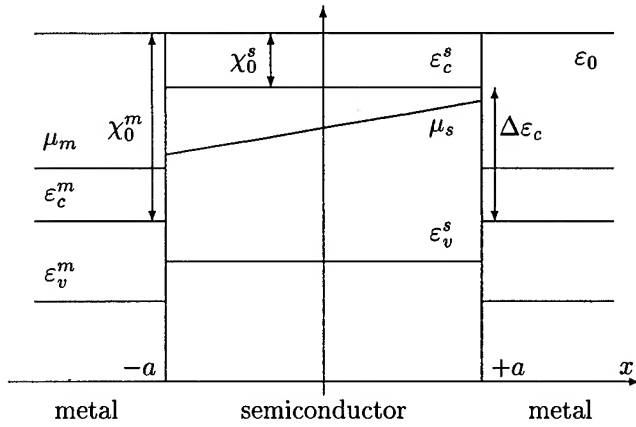


Figure 2: Band structure of metal-semiconductor-metal junction.

where $\tau_{e,p}$ are the lifetimes of electrons and holes, it should be stressed that n_0 and p_0 occurring in the terms describing the bulk and surface recombination processes are governed in a temperature field by the "equilibrium" concentrations:³

$$n_0 = n_{00} + \delta n_0, \quad p_0 = p_{00} + \delta p_0.$$

This "equilibrium" concentrations are found by solving a system of equations:

$$\bar{\mu}_n(x) = -\varepsilon_g - \bar{\mu}_p(x) = \text{const} \quad (13)$$

$$\frac{d^2 \varphi_0}{dx^2} = 4\pi e(\delta n_0 - \delta p_0).$$

Here, n_{00} and p_{00} are the local concentrations in point x with the temperature

$$T(x) = \frac{T_1 + T_2}{2} - \frac{T_1 - T_2}{2a}x. \quad (14)$$

Then the boundary conditions for Eq. (13) are (see Fig. 2):

$$\varphi_s(\pm a) = \frac{1}{e} [\mu_s(\pm a) - \mu_m] - \frac{\Delta \varepsilon_c}{e}.$$

It is possible to formulate boundary conditions for Eqs. (10) and the Poisson equation

$$\frac{d^2 \varphi}{dx^2} = 4\pi e(n - p), \quad (15)$$

if we introduce electron and hole electric conductances per unit area of the contacts of the semiconductor sample with connecting wires (ξ_n and ξ_p , respectively). If the thickness of the junction δ is negligible compared to the thickness $2a$ of the bulk semiconductor and σ_n^s (σ_p^s) is the junction conductivity of electrons (holes), we have (σ_n^s and σ_p^s are supposed to depend on δ)

$$\xi_n = \lim_{\delta \rightarrow 0} \frac{\sigma_n^s}{\delta} \quad \text{and} \quad \xi_p = \lim_{\delta \rightarrow 0} \frac{\sigma_p^s}{\delta}.$$

Then the condition of continuity of electric current in contacts in the broken circuit [considering that $\alpha_n = \alpha_p = 0$

in the connecting wires and μ_m does not depend on temperature (metal)] is reduced to⁶

$$j_n^s|_{x=\pm a} = j_0 \mp eR_s^\pm|_{x=\pm a} \quad (16)$$

$$j_p^s|_{x=\pm a} = \pm eR_s^\pm|_{x=\pm a}$$

$$j_0 = \pm \xi_n^\pm [\varphi_s(\pm a) - \varphi_m(\pm a)] \mp \frac{\xi_n^\pm}{e} [\mu_n^s(\pm a) - \mu_m] \pm \frac{\xi_n^\pm \Delta \varepsilon_c}{e}.$$

In Eqs. (16)

$$R_s^\pm = s_e^\pm (n(\pm a) - n_{00} - \delta n_0) = s_p^\pm (p(\pm a) - p_{00} - \delta p_0). \quad (17)$$

Here $s_{e,p}^\pm$ is the surface recombination velocity on the $x = \pm a$ walls.

Finally, the question remains how to obtain the thermoelectric emf in this case, and which physical phenomena determine its value. The answer to the first of these questions has been given,⁷ where the general scheme was proposed for calculation of an emf of any nature. It follows from this paper that

$$V = \oint \left(\frac{\sigma_n}{e\sigma} \frac{d\bar{\mu}_n}{dx} - \frac{\sigma_p}{e\sigma} \frac{d\bar{\mu}_p}{dx} \right) dl - \oint \left(\frac{\sigma_n \alpha_n}{\sigma} + \frac{\sigma_p \alpha_p}{\sigma} \right) \frac{dT}{dx} dl, \quad (18)$$

where integration is carried out clockwise. Let us note that expression (18) is always correct (for a broken circuit just as in the case of a flowing thermoelectric current). The second item in (18) coincides with the expression (9). The first item in (18) vanishes (it is equal to zero identically in the unipolar case) and expression (18) turns into (9) if electrons and holes have a single, common electrochemical potential level. Correlation (7) does not hold if electrons and holes flow from the hot lead to the cool one and electron and hole Fermi quasilevels appear. In this situation the first item in (18) differs from zero and the gradients of concentrations and corresponding diffusion currents contribute to the thermopower.

It should be pointed out that communication between n and p are established, when bulk and surface recombinations are not equal zero. Of course, in this case it is necessary only one of Eqs. (10) (and one of two first Eqs. (16)). It means, that the solution of the system (10), (15) obtained in the limits $\tau_{e,p} \rightarrow \infty$ and $s_{e,p}^\pm \rightarrow 0$ does not reduce to the corresponding solution in the absence of the recombination.³

In the last case it is possible to occur the current in closed circuits under conditions

$$j_p^s \equiv 0, \quad j_n^s = j_0$$

Acknowledgements

This work is partially supported by CONACyT (Mexico).

- [1] W. Thomson, *Mathematical and physical papers*, Cambridge University Press, Cambridge, England, vol. 1, p. 266 (1882).
- [2] A. I. Anselm, *Introduction to semiconductor theory*, Mir, Moscow, Prentice-Hall, Englewood Cliffs, NJ, (1981).
- [3] Yu. G. Gurevich, O. Yu. Titov, G. N. Logvinov, O. I. Lyubimov, *Phys. Rev.*, vol. 51, pp. 6999–7004 (1995)
- [4] A. F. Ioffe, *Semiconductor thermo-elements*, Izd. Ak. Nauk USSR, Moscow, p. 188 (1960).
- [5] Yu. G. Gurevich and O. L. Mashkevich, *Sov. Phys. Semicond.*, vol. 24, pp. 835 (1990).
- [6] F. G. Bass, V. S. Bochkov, and Yu. G. Gurevich, *Electrons and phonons in limit semiconductors* Nauka, Moscow, (1984).
- [7] Yu. G. Gurevich and V. B. Yurchenko, *Sov. Phys. Semicond.*, vol. 25, pp. 1268 (1991).

Interacted Electron and Phonon Thermal Waves in Semiconductors: Application to Photothermal Effects

G. González de la Cruz and Yu. G. Gurevich

Departamento de Física,
Centro de Investigación y de Estudios Avanzados del I.P.N.,
Apartado Postal 14-740, 07000,
México, Distrito Federal, México

Abstract

In this work heat transport in condensed media is examined from the theoretical point of view. We consider the heat flux at the surface of the sample as boundary condition and a fixed temperature on the other surface of the sample those boundary conditions reflect the usual experimental conditions in photoacoustic experiments. From this, we obtain explicitly the electron and phonon temperature distributions in the sample as function of both, time and position, valid for all range of the laser chopper frequency. The characterization of the thermal waves properties is discussed and some practical procedures for this purpose provide us with information about the electron and phonon thermal parameters.

Introduction

Photothermal techniques in solid materials are becoming evaluable tool in the measuring thermal parameters as well as in the semiconductor industry for characterizing process in the manufacturing of electronic devices¹. These techniques are versatile, nondestructive, and can be employed under different experimental conditions for determining thermal parameters of solid materials. Several photoacoustic cells with slight modifications, including the derivative photopyroelectric, and photothermal deflection methods, have been used in some special cases with great success². Being a photothermal technique, the detected signal is strongly dependent upon how the heat diffuses through the sample allows us to perform thermal characterization of the sample.

Recently³, thermal conductivity and thermal diffusivity of a two-layer system were examined solving the one-dimensional heat-diffusion equation with appropriate boundary conditions at the surface of the sample in the approximation of high frequency incident radiation. In the present paper, we investigate the heat diffusion in condensed media for all range of frequency of the incident electromagnetic radiation. We restrict our analysis to the case of solution of the heat transport equation considering only the continuity of the heat flux at the surface of the sample. In addition, we also take into account the continuity of the temperature distribution at the other surface of the sample. It is shown that in the limit of low frequency the variation of the temperature is quasi-static, while in the limit of high frequency, the dynamic part of temperature distribution

independen vanishes. For typical parameters of the heat conductivity of electrons and phonon in semiconductors, it is possible to obtain information about the physical parameters describing the diffusivity and electron-phonon interaction in photoacoustic experiments.

Formulation

It is well known that heat transport in solids is carried out by various quasiparticles (electrons, holes, phonons, magnons, etc.). Frequently the interactions between these quasiparticles are such that each of these systems can have its own temperature. Under certain conditions⁴ on the relaxation frequency of electron and phonon systems and size of the sample, the total system can be described by the same temperature T . In the photothermal experiments, the incident radiation is modulated on time by the chopper and in this case it is necessary to consider the dynamical contribution on the heat transport.

In one temperature approximation, which is usually the condition in most of the photothermal experiments the equation of the heat conduction in solids in one dimension can be written as

$$\frac{\partial^2 T(x, t)}{\partial x^2} = \frac{1}{\alpha} \frac{\partial T}{\partial t}. \quad (1)$$

Here α is the thermal diffusivity given by $\kappa/\rho c$ where ρ is the density and c is the specific heat of the sample. Assuming the thermal conductivity k is temperature independent, the general solution of the heat diffusion equation for the temperature distribution in the sample is given by ($0 \leq x \leq a$)

$$T(x, t) = A + BX + \theta(x, t) \quad (2)$$

the solution $T(x, t)$ should be supplemented by boundary conditions at $x = 0$ and $x = a$. In the photothermal experiments the most common mechanism to produce thermal waves is the absorption by the sample of an intensity modulated light beam with modulation frequency ω . It's clear that fixed the intensity of the radiation, the light-into-heat conversion at the surface of the sample ($x=0$) can be written as

$$Q(x, t)|_{x=0} = Q_0 + \Delta Q e^{i\omega t} \quad (3)$$

where Q_0 is proportional to incident intensity of light and the other term represents the modulation of this light. The temperature is considered fixed and continuous at $x=a$ and equal to T_1 .

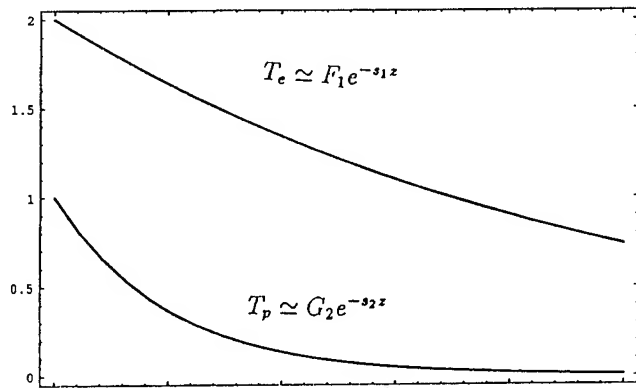


Figure 1:

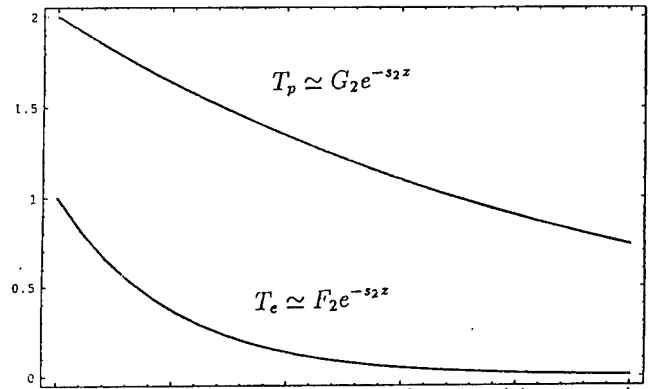


Figure 3:

Using the boundary conditions on Eq. (2) the constants A and B are given by

$$A = -Q_0/k \quad \text{and} \quad B = T_1 - \frac{Q_0}{k}a \quad (4)$$

Here $\theta(x, t)$ satisfies the heat diffusion equation with the following boundary conditions

$$-k \frac{d\theta}{dx}(x, t)|_{x=0} = \Delta Q e^{i\omega t} \quad (5)$$

$$\theta(x, t)|_{x=a} = 0$$

the general solution for $\theta(x, t)$ can be written as

$$\theta(x, t) = [f_1 e^{\sigma x} + f_2 e^{\sigma^* x}] e^{i\omega t} + [g_1 e^{-\sigma^* x} + g_2 e^{\sigma^* x}] e^{-i\omega t} \quad (6)$$

the parameter σ is determined by forcing Eq. (6) to satisfies Eq. (1) and is equal to $\sigma = (1 + i)\sqrt{\omega/2\alpha}$ and using the boundary conditions at $x = 0$ and $x = a$, the constants are given by

$$f_1 = \frac{e^{\sigma a}}{e^{\sigma a} + e^{-\sigma a}} \frac{\Delta Q}{K\sigma} \quad f_2 = -\frac{e^{-\sigma a}}{e^{\sigma a} + e^{-\sigma a}} \frac{\Delta Q}{K\sigma} \quad (7)$$

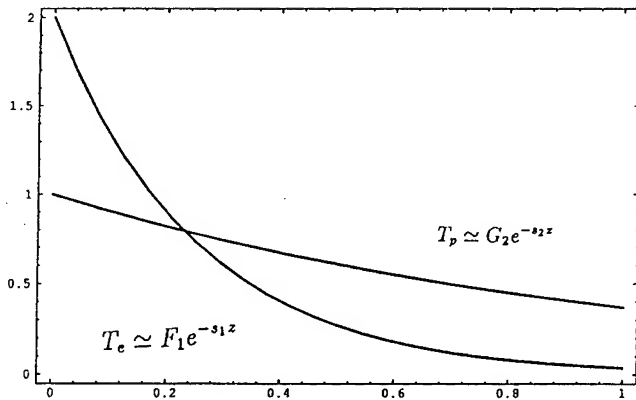


Figure 2:

For this limit, the heat flux is quasi-static and Eq. (9) can be obtained only assuming that $\partial^2 T(x, t)/\partial x^2 = 0$ with the boundary conditions mentioned before.

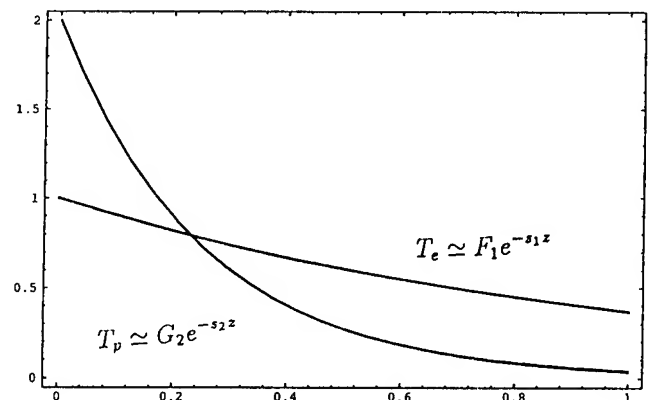


Figure 4:

On the other hand in the limit when $|\sigma a| \gg 1$ (high frequency limit)

$$T(x, t) = (T_1 + \frac{Q_0}{k} a) - \frac{Q_0}{k} x + \frac{\Delta Q}{k\sigma} e^{i\omega t - \sigma x}$$

which is similar to one obtained in Ref. 3. In this limit the dynamical part of the temperature distribution has only significant values at distance from the surface of the order $|\sigma^{-1}|$ and at this distance the amplitude of the dynamic part is $|\sigma a|$ times smaller than the static part.

Then electron T_e and phonon T_p temperatures are different instead of Eq. (1) we obtain:⁴

$$\frac{\partial^2 T_e}{\partial x^2} - k_e^2 (T_e - T_p) = \frac{1}{\alpha_e} \frac{\partial T_e}{\partial t} \quad (10)$$

$$\frac{\partial^2 T_p}{\partial x^2} + k_p^2 (T_e - T_p) = \frac{1}{\alpha_p} \frac{\partial T_p}{\partial t}$$

where $k_{e,p}^2 = \frac{P}{\kappa_{e,p}}$, κ_e (κ_p) is the electron (phonon) thermal conductivity, parameter P describes the transfer of heat between electrons and phonons.

Some possible cases of the distributions of the dynamic parts of T_e and T_p are shown on Figs. 1-4.

Acknowledgements

This work is partially supported by CONACyT (Mexico).

- [1] A. Mandelis, *Photoacoustic and thermal waves phenomena in semiconductor*, North-Holland (1987).
- [2] H. Vargas, L. C. M. Miranda, Phys. Rep., vol. 161, pp. 43 (1988).
- [3] G. González de la Cruz, Yu. G. Gurevich, Phys. Rev. B., vol. 51, pp. 2188 (1995).
- [4] Yu. G. Gurevich, O. L. Mashkevich, Phys. Rep., vol. 181, pp. 328 (1989).

Optimum design in thermoelectric cooling systems

M.Yamanashi, Y.Kibayashi, F.Toyada, M.Azechi

Komatsu Electronics Inc., 2597, Shinomiya, Hiratuka-shi, Kanagawa-ken, 254, Japan

Abstract

An optimum design is investigated to maximize the coefficient of performance(COP) for a thermoelectric cooling system(TEC system) which consists of a thermoelectric cooler(TEC) and heat-exchangers at the cold side and the hot side. Optimizing a TEC in the TEC system for the maximum COP can be performed by using the balance equations of non-dimensional entropy flow, when the thermal resistances of heat-exchangers for a TEC system are given and the system operates under a constant temperature difference. In these equations, the COP of the TEC system becomes a function of non-dimensional thermal resistance of the cold side heat-exchanger and non-dimensional entropy flow at the cold side of the TEC system. Therefore the COP of the TEC system is shown as a contour graph on these two variables. By using this graph, not only TEC design parameters for the maximum COP of the TEC system can be determined, but the degrading effect by thermal resistances of the TEC system on the COP can also be evaluated.

Introduction

When thermoelectric coolers(TECs) are used in various applications, it is important to design a TEC for obtaining the maximum COP of the TEC system in which the thermal resistance of heat-exchangers are given and which operates under a constant temperature difference. Several attempts have been done to analyze the performance of a TEC or a TEC system by various methods^{1,2,3,4}. However these methods are not convenient form to simulate the optimum TEC in a TEC system.

In this paper, a simulation method of optimizing a TEC in a TEC system is discussed by using the non-dimensional entropy flow equations⁵ which are a extension of the heat balance equations of TEC systems. In these simulations, the thermoelectric properties of thermoelements are approximated by the values determined from the average temperature of the operating TEC⁶.

Non-dimensional entropy flow equations

To generally discuss the optimization of a TEC in the TEC system shown in Fig.1, the following non-dimensional entropy flow equations for a TEC system are used:

$$q_C - j\varepsilon + \frac{1}{2}j^2 \frac{1}{ZT_C} \varepsilon \left(1 + \frac{2\beta}{1-\beta j}\right) + \frac{1}{1-\beta j} \varepsilon (\theta_H - 1) = 0, \quad (1)$$

$$q_H - j\delta - \frac{1}{2}j^2 \frac{1}{ZT_H} \delta \left(1 + \frac{2\lambda}{1+\lambda j}\right) + \frac{1}{1+\lambda j} \delta (1 - \theta_C) = 0, \quad (2)$$

$$\varepsilon = \frac{1-\beta j}{(1+\lambda+\lambda j)(1-\beta j) + (1+\lambda j)\beta}, \quad (3)$$

$$\delta = \frac{1+\lambda j}{(1+\beta-\beta j)(1+\lambda j) + (1-\beta j)\lambda}. \quad (4)$$

In these equations, q_C and q_H are the non-dimensional entropy flow at the cold side and the hot side of the TEC system respectively. The TEC system absorbs the heat flow(Q_C) at the cold side and emit the heat flow(Q_H) at the hot side. Therefore entropy flow at each side is Q_C/T_C and Q_H/T_H . q_C and q_H are derived from normalizing these entropy flow by the thermal conductance of the TEC(K). Entropy flow caused at p-n junctions by electrical current(I) is a product of Seebeck

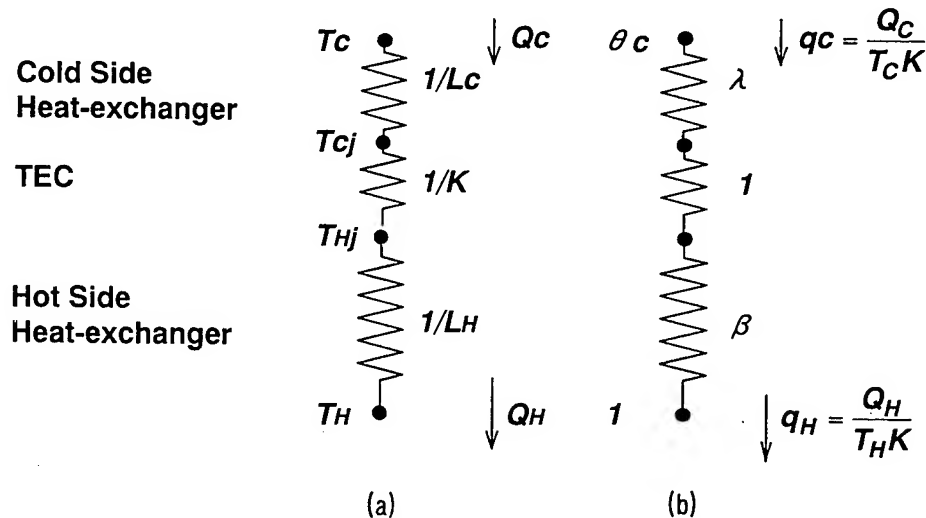


Fig.1 Schematic diagrams of TEC system : (a) heat flow scheme and (b) non-dimensional entropy flow scheme

coefficient of a TEC (A) and electrical current. This entropy flow normalized by the thermal conductance of the TEC is denoted by j . λ and β are the ratio of the thermal resistances of the hot side and the cold side heat-exchangers to the thermal resistance of the TEC. Therefore λ and β can be called non-dimensional thermal resistances of those heat-exchangers. $\theta_H (=1/\theta_C)$ is the ratio of the hot side temperature to the cold side temperature. ZT_C and ZT_H are the well-known non-dimensional figures of merits.

COP

The COP of a TEC system (η) is given below by using the non-dimensional entropy flow equations Eqs.(1) and (2):

$$\eta = \frac{Q_C}{Q_H - Q_C} = \frac{q_C}{\theta_H q_H - q_C}. \quad (5)$$

In order to simulate the optimum TEC in a TEC system of which heat-exchangers are given, it is convenient to use the non-dimensional variables λ and β/λ instead of λ and β . This TEC system has a constant β/λ . Therefore optimizing a TEC in this TEC system is replaced to determining λ to maximize the COP. In this paper we discuss optimizing a TEC in the TEC system with a constant β/λ which operates under the constant temperature difference ($\theta_H=1.1$). Since θ_H , ZT_C and β/λ are given as constant values in Eq.(5), the COP becomes a function of j and λ . Further j becomes a function of q_C and λ from Eq.(1). Therefore the COP for this TEC system becomes a function of q_C and λ . Figs.2-4 show contour graphs of TEC systems with $\beta/\lambda=1, 5$ and 10 on these variables. These contour graphs are plotted by numerical calculation that uses

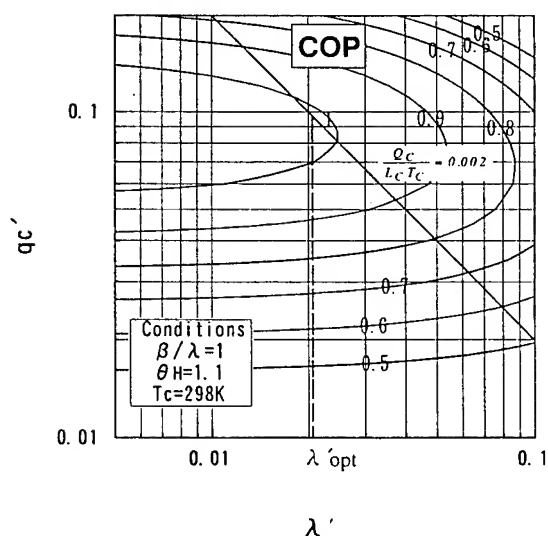


Fig.2 Contour graph of COP on q_C' and λ' for $\beta/\lambda=1$, $\theta_H=1.1$ and $T_C=298K$. The linear line shows that this TEC system which satisfies $\frac{q_C}{L_C T_C} = 0.002$ has the maximum COP at $\lambda' = \lambda'_{opt}$.

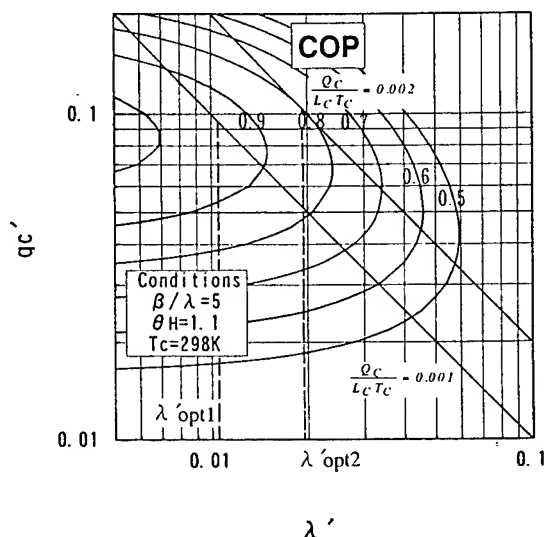


Fig.3 Contour graph of COP on q_C' and λ' for $\beta/\lambda=5$, $\theta_H=1.1$ and $T_C=298K$. The linear lines show that the TEC systems which satisfy $\frac{q_C}{L_C T_C} = 0.001$ and 0.002 have the maximum COP at $\lambda' = \lambda'_{opt1}$ and $\lambda' = \lambda'_{opt2}$ respectively.

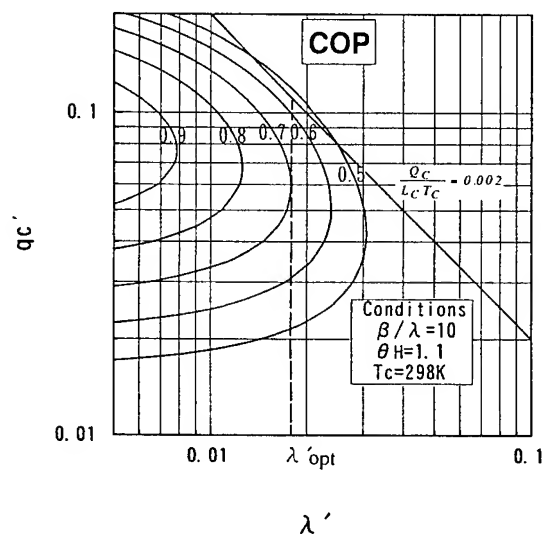


Fig.4 Contour graph of COP on q_C' and λ' for $\beta/\lambda=10$, $\theta_H=1.1$ and $T_C=298K$. The linear line shows that this TEC system which satisfies $\frac{q_C}{L_C T_C} = 0.002$ has the maximum COP at $\lambda' = \lambda'_{opt}$.

the thermoelectric properties determined from the average temperature of the operating TEC. In this approximation, q_C' and λ' are used instead of q_C and λ . q_C' and λ' are defined below by the values of q_C and λ at T_C respectively:

$$q_C' = \frac{q_C}{K(T_C)T_C}, \quad (6)$$

$$\lambda' = \frac{K(T_C)}{L_C}. \quad (7)$$

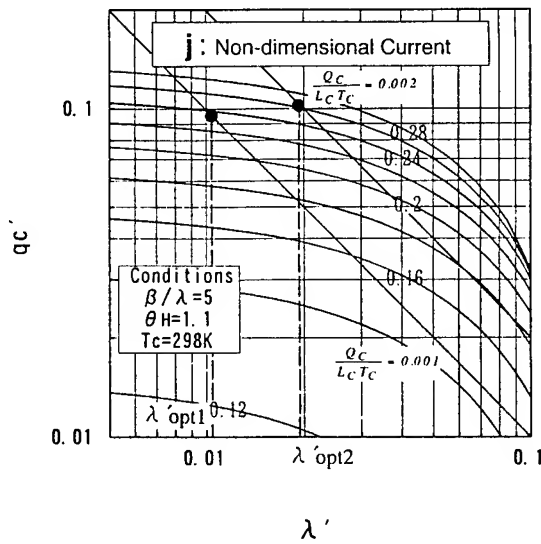


Fig.5 Contour graph of j on q_c' and λ' for $\beta/\lambda=5$, $\theta_H=1.1$, and $T_c=298K$. The linear lines shows TEC systems that satisfies $\frac{Q_c}{L_c T_c}=0.001$ and 0.002 . The solid circles is the optimum operating position for λ'_{opt1} and λ'_{opt2} .

Optimum design in thermoelectric cooling systems

In this section we discuss optimizing a TEC in the TEC system for the maximum COP by using the contour graphs, when the TEC system with a given β/λ operates under the constant temperature difference. First we investigate how the optimum TEC design are affected by the heat load at the cold side of this TEC system. On the contour graphs of the COP, the TEC system that absorbs the constant heat load are plotted by the line:

$$q_c' = \frac{Q_c}{\lambda' L_c T_c}. \quad (8)$$

This line is derived by eliminating $K(T_c)$ from Eqs.(6) and (7) and are shown as the linear line as shown in Figs.2-4. Two linear lines in Fig.2 show the TEC systems which satisfy $\frac{Q_c}{L_c T_c}=0.001, 0.002$. When $L_c=1(W/K)$ and $T_c=298(K)$, these lines mean that the TEC systems which absorb $Q_c=0.447(W), 0.298(W)$ respectively have the maximum COP at λ'_{opt1} and λ'_{opt2} . The optimum thermal conductance of a TEC (K_{opt}) is determined from substituting λ'_{opt} and L_c into Eq.(7). Furthermore to determine the design parameters of a TEC we must find the the optimum non-dimensional current which is given from the contour graph of j on q_c' and λ' as shown in Fig.5. Thus the equations to determine the design parameters of the optimized TEC are given as

$$K_{opt} = (\kappa_p + \kappa_n) \frac{S}{l} n, \quad (9)$$

$$j_{opt} = \frac{\alpha_p + \alpha_n}{\kappa_p + \kappa_n} \frac{l}{S} I. \quad (10)$$

where κ , α , l , and S are thermal conductivity at T_c ,

Seebeck coefficient at T_c , length and cross-sectional area of thermoelement respectively, n is the number of couples, and I is the electrical current. Subscripts p and n designate p type and n type thermoelement respectively. If one of the three parameters, i.e. n , l/S , and I , in Eqs.(9) and (10) is given, then the other two are derived from solving these equations. Thus by using the COP contour graphs, the procedure of optimizing a TEC in all TEC systems that satisfy the similarity condition ($\frac{Q_c}{L_c T_c} = \text{constant}$) can be performed at the same time.

Second, we investigate the effects of β/λ on the COP and λ'_{opt} . The lines satisfying $\frac{Q_c}{L_c T_c}=0.002$ in Figs.2-4 show the effect of β/λ on the maximum COP and the optimum λ' . These figures shows that the maximum COP strongly decreases as β/λ increases. Furthermore the optimum λ' is slightly affected by β/λ . This means that the optimum TEC is almost the same even if the thermal resistance of the hot side heat-exchangers increases.

Conclusion

The method determining the optimum TEC in a TEC system has been presented by using the contour graph of the COP of the TEC system on non-dimensional entropy flow and non-dimensional thermal resistance of heat-exchangers. Since this method are expressed by non-dimensional quantities, the optimum design determined on this contour graph is free from the terms such as couples, l/S , and so on. Further the degrading effects caused by thermal resistances of heat-exchangers can be easily evaluated.

References

- [1] B.Sherman, R.R.Heikes, and R.W.Ure, Jr., "Calculation of Efficiency of Thermoelectric Devices", Journal of Applied Physics, vol.31, No.1, pp1-16(1960)
- [2] P.B.Townsend and R.J.Buist, "Thermoelectric cooler performance corrections for soft heat sinks", The sixth International Conference on Thermoelectric Energy Conversion, pp80-82(1986)
- [3] K.Chen, S.G.William, B.Entezam, "Heat Transfer Analysis and Optimization of Thermoelectric Cooling Systems", The twelfth International Conference on Thermoelectrics, pp395-403(1993)
- [4] Y.Ogawa, "Breakthrough in Thermoelectric Cooling Systems", Energy and Resources, vol.16, pp410-415(1995)
- [5] M.Yamanashi, "A new approach to optimum design in thermoelectric cooling systems", now prepared.
- [6] R.J.Buist, "Design and engineering of thermoelectric cooling devices", The tenth International Conference on Thermoelectrics, Chapter16, pp84-94(1991)

OPTIMAL FUNCTIONS AS AN EFFECTIVE METHOD FOR THERMOELECTRIC DEVICES DESIGN

L.I. Anatyshuk, O.J. Luste, L.N. Vikhor

Institute of Thermoelectricity, General Post-Office, Box 86, 274000, Chernivtsi, Ukraine

Abstract

The optimal control methods are used in the present work for a search of the best function of thermoelectric material inhomogeneity. The possibility of low-temperature coolers coefficient of performance increase due to the thermoelectric material inhomogeneity use has been demonstrated.

Introduction

The best characteristics of thermoelectric modules securing is caused by the advantages in the thermoelectric material science. During last 30-40 years the investigators focussed their efforts on the thermoelectric material figure of merit Z increase at the expense of a search of new compounds, new alloying additions, change of their concentration. In technology the best homogeneity of the material samples was tried to be achieved. The advances in the material science result in the progress in thermoelectric cooling that we have today. However, in the last ten years the essential advance to the increase of homogeneous thermoelectric materials figure of merit was not observed. Therefore the reasonable question arises: how to improve the efficiency of thermoelectric conversion? In our works [1-3] we gave a number of examples supported the concept of the further progress in thermoelectricity change-over from homogeneous to functional gradients, that is, inhomogeneous materials.

The solution of the material efficient inhomogeneity search leads to the necessity of change-over to more complicated optimization methods, namely, the change-over from the optimization by a parameter to the optimal function search. Optimization by a function is a complicated problem. In thermoelectricity such problems are solved with the help of the optimal control theory [2, 4, 5]. The results of such problem solution to the *Bi-Te*-based material optimal inhomogeneity aimed to the maximum temperature difference or a cooling thermoelement coefficient of performance achievement are given in [1,2]. The energetic gain with temperature difference increase for inhomogeneous thermoelements has been shown.

At the same time the optimal control theory showed itself as the effective means for stage coolers design [2,6]. Its application allows to get the best correlation of stages power.

Thus, the new optimal problem statement becomes reasonable. It is reduced to the search for best functional inhomogeneity of thermoelectric material characteristics for multi-stage Peltier coolers.

The problem statement

The diagram for the problem of optimal control by thermoelectric material inhomogeneity for N -stage Peltier

cooler is shown in Fig. 1. This problem is formulated mathematically in the following way. The object of control is an N -stage cooler which thermoelements consist of n - and p -type legs, material properties of which are changed with the coordinate x because of their dependence on temperature and charge carriers concentration.

The starting data for optimization include cooling performance Q_0 , cooling temperature T_c , temperature of heat releasing surface T_h . Theoretical or experimental dependencies of thermo-emf α , electrical conduction s , thermal conduction k on temperature and current carriers or doping impurity concentration are to be specified as limitations for controls.

The availability of contact resistances r_0 , interstage temperature differences dT and heat exchange with environment at heat exchange coefficient a_T are also taken into account in the model.

The objective of the investigation is the determination of best functions for thermoelectric material inhomogeneity parameters and best power function for each stage.

Thus the problem spans in whole necessary parameters for the material, cooler and its operation conditions.

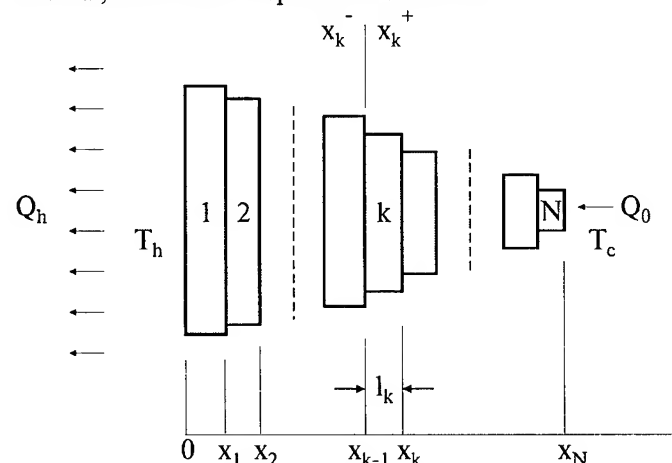


Fig.1. A model of N -stage thermoelectric cooler.

Distribution of temperature $T(x)$ and specific heat fluxes $q(x)$ in thermoelement legs is defined by the set of $4N$ -differential equations of the form

$$\left. \begin{aligned} \frac{dT}{dx} &= -\frac{\alpha i_k}{\kappa} T - \frac{i_k}{\kappa} q, \\ \frac{dq}{dx} &= -\frac{\alpha^2 i_k}{\kappa} T + \frac{\alpha i_k}{\kappa} q + \frac{i_k}{\sigma} \end{aligned} \right\} \quad k=1, \dots, N \quad (1)$$

Here $\alpha_{n,p} = \alpha_{n,p}(C_{n,p}(x), T)$; $\sigma_{n,p} = \sigma_{n,p}(C_{n,p}(x), T)$; $\kappa_{n,p} = \kappa_{n,p}(C_{n,p}(x), T)$; where $\tilde{N}_{n,p}(x)$ are the inhomogeneity

functions of n - and p -type material. This may be the carrier concentration in a semiconductor, doping impurity concentration, or other quantity that characterizes inhomogeneity of thermoelectric structure along the thermoelement leg's height.

The boundary conditions for these equations are written as temperature equalities between stages taking into consideration the interstage temperature losses, and have the form

$$\begin{aligned} T_n(0^+) &= T_p(0^+) = T_h, \quad T_n(x_N^-) = T_p(x_N^-) = T_c \\ T_n(x_k^+) &= T_p(x_k^+), \quad T_n(x_k^-) = T_p(x_k^-), \\ T_n(x_k^+) &= T_n(x_k^-) + \delta T, \end{aligned} \quad (2)$$

the placement of points x_k , $k=1 \dots N$ is there with unfixed.

The conditions when the cooling performance has its maximum value at the predetermined cooling amount are necessary to determine. Against the optimal control theory this problem is reduced to the study of the functional minimum

$$J = \sum_{k=1}^N (\ln q_1^k - \ln q_0^k). \quad (3)$$

Specific heat fluxes at junctions are determined by the expressions

$$\begin{aligned} q_0^k &= \sum_{n,p} \left[q(x_k^-) + i_k r_0 + \frac{\alpha_T}{i_k} (T_h - T(x_k^-)) \right], \\ q_1^k &= \sum_{n,p} (q(x_{k-1}^+) - i_k r_0). \end{aligned} \quad (4)$$

They depend on the controlled parameters of currents density $i_{n,p}^k$ and the function characterizing the thermoelectric material inhomogeneity $C_{n,p}(x)$.

The solution of the stated problem is made by the Pontryagin's maximum principle [7]. In accordance with this principle the next conditions must be fulfilled for J minimum :

1. Current densities in stages must satisfy the equalities

$$-\frac{\partial J}{\partial i_{n,p}^k} + \int_{x_{k-1}^+}^{x_k^-} \frac{\partial H^k(\varphi, T, q, i_n^k, i_p^k)}{\partial i_{n,p}^k} dx = 0 \quad (5)$$

where the Hamilton's function H^k has the form

$$H^k = \sum_{n,p} (\varphi_1 f_1^k + \varphi_2 f_2^k), \quad (6)$$

(f_1^k, f_2^k) are right part of expressions (1), $\varphi = (\varphi_1, \varphi_2)_{n,p}$ is the pulses vector [1].

2. Coordinates of points joint x_k satisfy the equality

$$H^k(x_k^-) = H^{k+1}(x_k^+), \quad k=1, \dots, N-1. \quad (7)$$

3. The optimal function for the material inhomogeneity must satisfy the following condition

$$\begin{aligned} H_{n,p}^k(\varphi(x), T(x), q(x), C(x), j) &= \\ &= \max_{C \in G_C} H_{n,p}^k(\varphi(x), T(x), q(x), C, j) \end{aligned} \quad (8)$$

The solution of this problem was realized by the numerical method of successive approximations. The computer program permitting to determine optimal functions for the material

inhomogeneous parameters and to use them at once for determination of the best power elaborated.

Discussion of the results

The object of the discussion is the analysis of *Bi-Te*-based the thermoelectric material of n - and p -type influence on the energetic efficiency of Peltier stage coolers.

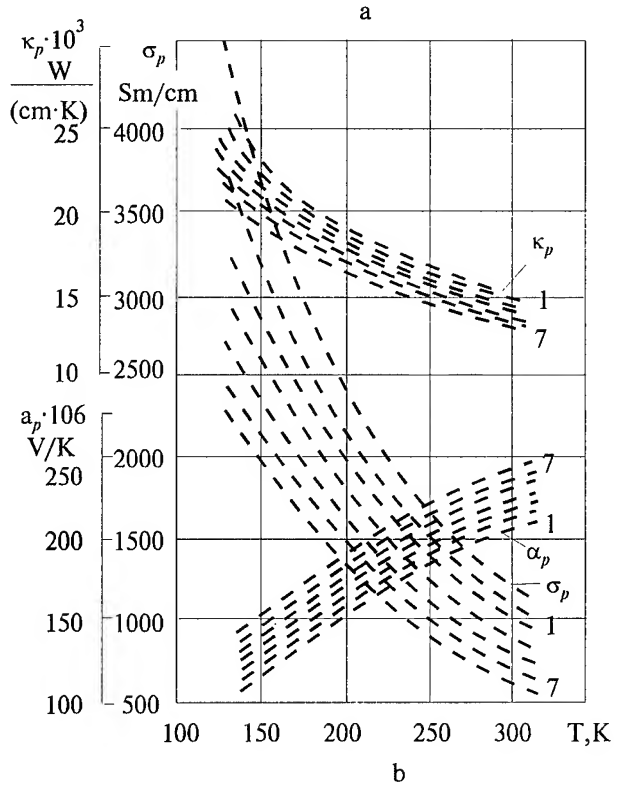
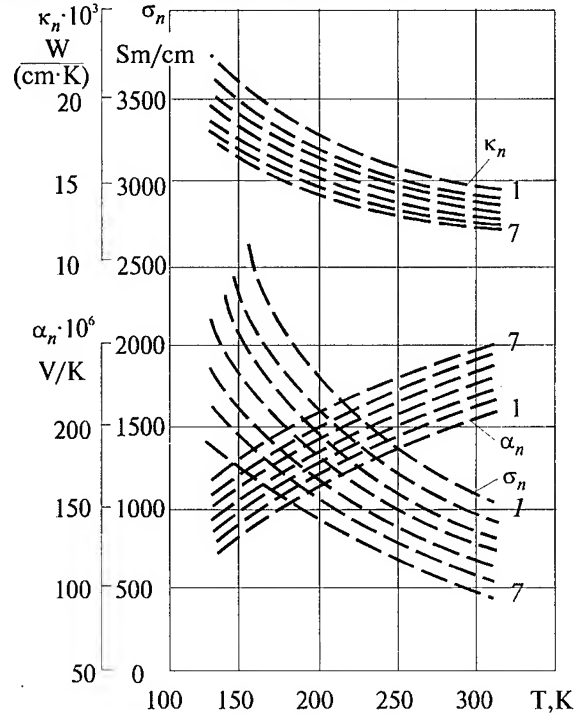


Fig. 2. Temperature dependencies of the *Bi-Te*-based material parameters for different starting electrical conductivity (at 300K): a - σ_n , b - σ_p [8]

The elaborated program was used for analysis of the coolers with different stages number, providing cooling level up to 130 K at $T_h=300$ K.

Temperature dependencies of the material parameters for different starting electrical conduction σ_n^0 and σ_p^0 (at 300 K) shown in Fig.2a, 2b were used as starting data for the optimal functions search of thermoelectric material parameters distribution along thermoelement legs' height.

These experimental dependencies of form $\alpha_{n,p}=\alpha_{n,p}(\sigma_{n,p}^0, T)$; $\sigma_{n,p}=\sigma_{n,p}(\sigma_{n,p}^0, T)$; $\kappa_{n,p}=\kappa_{n,p}(\sigma_{n,p}^0, T)$ were approximated by the method of least roots by two-dimensional polynomials and were used in the optimal control computing program. Functions $s_{n,p}^0(x)$ and parameters $i_{n,p}^k$ were assumed as controls in the studied case.

As electrical conduction of semiconductors is proportional to charge carriers concentration, and the concentration is not changed up to the intrinsic conduction achievement, then these functions of electrical conduction $s_{n,p}^0(x)$ determined at 300K characterize inhomogeneity of thermoelectric material of n - and p -type, respectively.

The results of the optimal problem solution are given in Fig. 3-5. Each variant the material inhomogeneity optimal for the given temperature range and stage number correspond to each variant of the cooler.

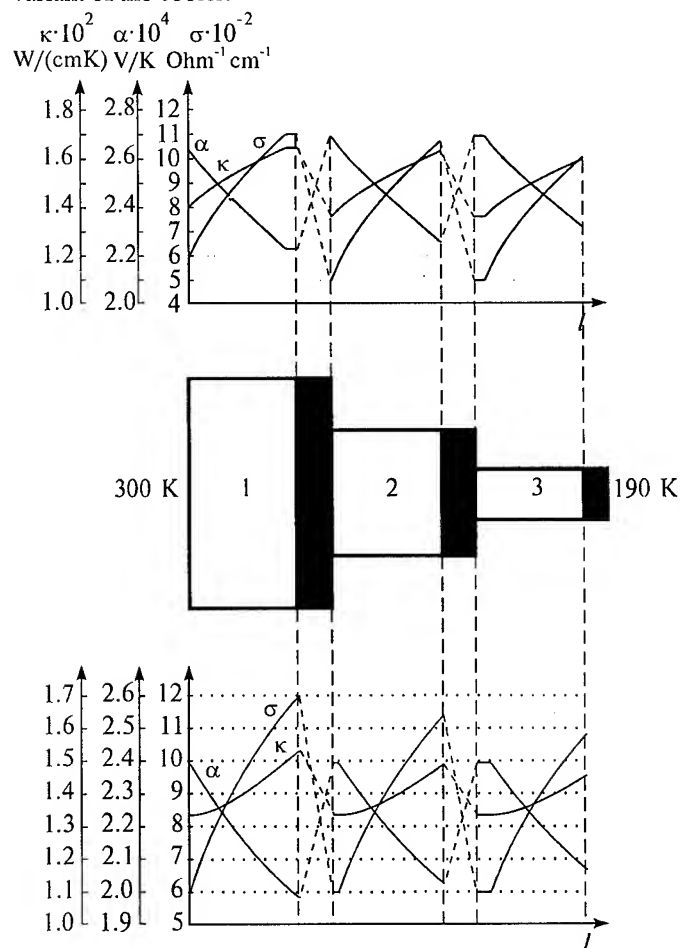


Fig. 3. Optimal distribution of thermoelectric material parameters α , σ , κ along the legs height of a thermoelement for a three-stage cooler.

Fig. 3 represents the example of the obtained optimal distributions of thermoelectric material parameters for a three-stage cooler for the level of 190K. The form of these functions is completely determined by the material parameters dependence on carriers concentration and temperature. The availability of homogeneous regions near to the thermoelements junctions is explained by the limitations imposed on the control region by the used experimental data (Fig.2a, 2b), namely, $500 \text{ Ohm}^{-1} \text{ cm}^{-1} \leq s_n^0 \leq 1100 \text{ Ohm}^{-1} \text{ cm}^{-1}$, $600 \text{ Ohm}^{-1} \text{ cm}^{-1} \leq s_p^0 \leq 1200 \text{ Ohm}^{-1} \text{ cm}^{-1}$.

Fig. 4 illustrates the increase of maximum coefficient of performance with the use of optimal inhomogeneous thermoelectric material in comparison with the best homogeneous ones depending on temperature difference and a cooler stage number. As Fig.4 suggests at the predetermined temperature difference the lesser the number of the cooler stages the larger the energetic gain

due to the inhomogeneous material. For example, at $\Delta T=110\text{K}$ the use of inhomogeneous thermoelements in a two-stage battery permits to increase coefficient of performance by 55%. The reason is that in the case of small number of stages for the given temperature difference, some stages of the battery (the upper ones in particular) operate near to their limited temperature differences, their coefficient of performance is increased by 1.5-2 due to the material inhomogeneity [2]. This results in the considerable increase of the energetic efficiency of the whole stage system.

On the other hand, the thermobattery staging itself, that is, total temperature difference distribution among separate stages, permits to have the gain in the consumed power amount [8]. At low temperature cooling (200-250 K) the increase in stages number up to some reasonable quantity is accompanied with sharp increase of the cooler energetical efficiency. In this connection the interesting is the answer the question: which of two factors - the use of inhomogeneous material or increasing of stage number has much effect on the coefficient of performance increase. Fig. 5

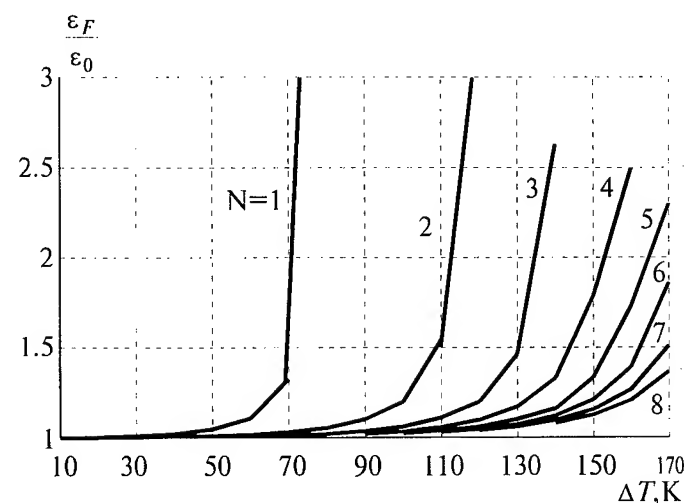


Fig. 4. Coefficient of performance increase with use of optimal inhomogeneous material e_F in comparison with optimal homogeneous material e_0 for different temperature differences on a cooler with N stage number.

gives the answer. Here solid curves represent the efficiency increase depending on TEC stages number with the use of inhomogeneous material. Dashed curves show the coefficient of performance increase at the expense of the given stages number per a unit. The results comparison allows to make the following conclusion. If for a given temperature difference

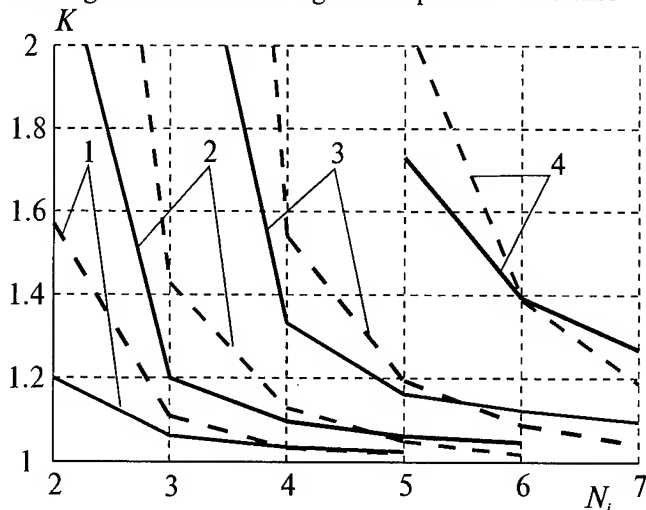


Fig. 5. Coefficient of performance K increase depending on stage number N with use of optimal inhomogeneous material (solid curves $K = \varepsilon_F/\varepsilon_0$) and stage number per a unit increase (dash curves $K = \varepsilon_{i+1}/\varepsilon_i$) for different temperature differences: 1 - $\Delta T = 100K$; 2 - $\Delta T = 120K$; 3 - $\Delta T = 140K$; 4 - $\Delta T = 160K$ at $T_h = 300K$.

stages number is far from the reasonable one, then the increase of their quantity is the more powerful factor for the increase of cooling energetical efficiency in comparison with the use of inhomogeneous material. For example, at $\Delta T = 120K$ the use of four-stage device instead of three-stage one gives the gain in 43 %, and the use of inhomogeneous thermoelements in three-stage structure permits to increase the coefficient of performance only by 20 %. If the stages number is close to reasonable one, then the effect of the both factors is comparable and is 5-15 %. In this case it is more reasonable to increase the energetic efficiency at the expense of the use of inhomogeneous thermoelectric legs because the increase of stages number undoubtedly results in the complexity of a cooler structure.

References

- [1] Anatychuk L.I., Semenjuk V.A. Optimal control in the thermoelectric coolers design. Eleventh International Conference on Thermoelectrics, Arlington, Texas, October 7-9, 1992, p.120-124.
- [2] Anatychuk L.I., Semenjuk V.A. *Optimal control by the Thermoelectric Material and Devices Properties*. Chernovthy, Prut, 1992, 264 p.
- [3] Anatychuk L.I., Vikhor L.N., Kuznetsov A.V., Letiuchenko S.D. Functional-Gradient Materials for Thermoelectric Energy Converters, in Proceedings of the XIV International Conference on Thermoelectrics, St-Petersburg, Russia, June 27-30, 1995, p.7-9

- [4] Anatychuk L.I., Vikhor L.N. Study on Cooler Design in Magnetic Field for Low Temperature Cascades, in Proceedings of the Thirteenth International Conference on Thermoelectrics, Canas, Aug., 1994.
- [5] Anatychuk L.I., Vikhor L.N. Optimal functions of magnetic field for the Peltier coolers, in Proceedings of the XIV International Conference on Thermoelectrics, St-Petersburg, Russia, June 27-30, 1995, p.461-463.
- [6] Anatychuk L.I., Vikhor L.N. Ivanov G.A. The Optimal Control Theory for Thermoelectric Cooler Design, in Proceedings of the Twelfth International Conference on Thermoelectrics, Japan, Nov., p.412-415.
- [7] Pontryagin L.S., Boltyansky V.G., Gamkrelidse R.V., Mischenko E.F. *Mathematical Theory of Optimal Processes*, Nauka, 1976, p.392.
- [8] Vayner A.L. *Thermoelectric Coolers*, Moscow, 1983, p.176.

TEMPERATURE AND TIME DEPENDENT FINITE-ELEMENT MODEL OF A THERMOELECTRIC COUPLE

Authors:

Paul G. Lau and Richard J. Buist

TE Technology, Inc.

1590 Keane Drive, Traverse City, Michigan 49686 USA

Abstract

The cooling performance of a thermoelectric (TE) couple is modeled from mathematical differential equations via finite-elements with the use of a digital computer. The finite-element model, which incorporates material property dependence on time and temperature, is presented. TE couple transient performance is investigated by applying an on-off current wave form to the model. Results from the model output are compared with experiment.

Introduction

A closed form solution of the complete differential equation for the temperature distribution in a thermoelectric (TE) pellet does not exist. This equation, of course, is further complicated when the transient of temperature with respect to time is included. Typically, simplifying assumptions are made to yield a closed form, albeit, inaccurate expression. However, the inaccuracies may be ameliorated by applying the closed-form expression to a number of finite elements which compose the TE couple.

Computational Model

The model was based on a one dimensional equation given by the following:[1]

$$SIT - \frac{1}{2} I^2 R - K(T_H - T_C) = Q_c \quad (1)$$

This equation, combined with energy conservation principles yields the following:

$$Q_p + Q_R + Q_K = \frac{m_j C_{pj} (T_j^{i+1} - T_j^i)}{t_{i+1} - t_i} \quad (2)$$

where:

$$Q_p = IT_j^i (S_{j+1} - S_j) \quad (3)$$

$$Q_R = \frac{1}{2} I^2 (R_{j+1} + R_j) \quad (4)$$

$$Q_K = K_{j+1} (T_{j+1}^i - T_j^i) + K_j (T_{j-1}^i - T_j^i) \quad (5)$$

and:

Q_c = net heat pumping

I = current

S = Seebeck coefficient (temperature dependent)

R = resistance (temperature dependent)

K = thermal conductance (temperature dependent)

mC_p = mass times specific heat (assumed constant)

T = nodal temperature

t = time

i = time index

j = node index

Figure 1 depicts a pellet within a TE module showing the practical application of this equation.[2-4] However, in nodes (-1), (0), (40) and (41), the Joule heat and Peltier heat of the copper tab was assumed negligible compared with the pellet. Therefore, the model did not include those heats with respect to the copper tab. The pellet itself was divided into 40 elements. Each copper tab and ceramic, labeled on the top and bottom of the pellet was treated as a single element. The length-to-cross-sectional-area (L/A) ratio was calculated from the length of the finite-element divided by the cross-sectional area of the finite-element. The cross-sectional area of the ceramic finite-element was determined by using the overall cross-sectional area of the ceramic for the TE module divided by the total number of pellets. The cross-sectional area of the copper tab was calculated by taking one-half the overall cross-sectional area of the tab. However, the length of the tab finite-element was composed of the thickness of the tab plus the thickness of the solder. The effective thermal conductivity of the tab finite-element was derived from combining the actual thermal conductances of the copper tab and solder.

There were two cases for which experimental results could be readily obtained: 1) testing of a suspended TE module and 2) testing of a heat-sunk TE module. The test configurations for the suspended and heat sunk cases are shown in Figures 2 and 3, respectively. Referring back to Figure 1, the heat sink and interface medium did not apply to the suspended-module configuration. However, they were, of course, applied to the heat-sunk configuration. The model treated the heat sink as a node at constant temperature. The interface medium in the test was a thin film of water. It was treated in the model as an additional thermal conductance. The cross-sectional area of the interface was equivalent to the ceramic finite-element cross-sectional area. The thickness of the interface used in the model was 25.4 μm .

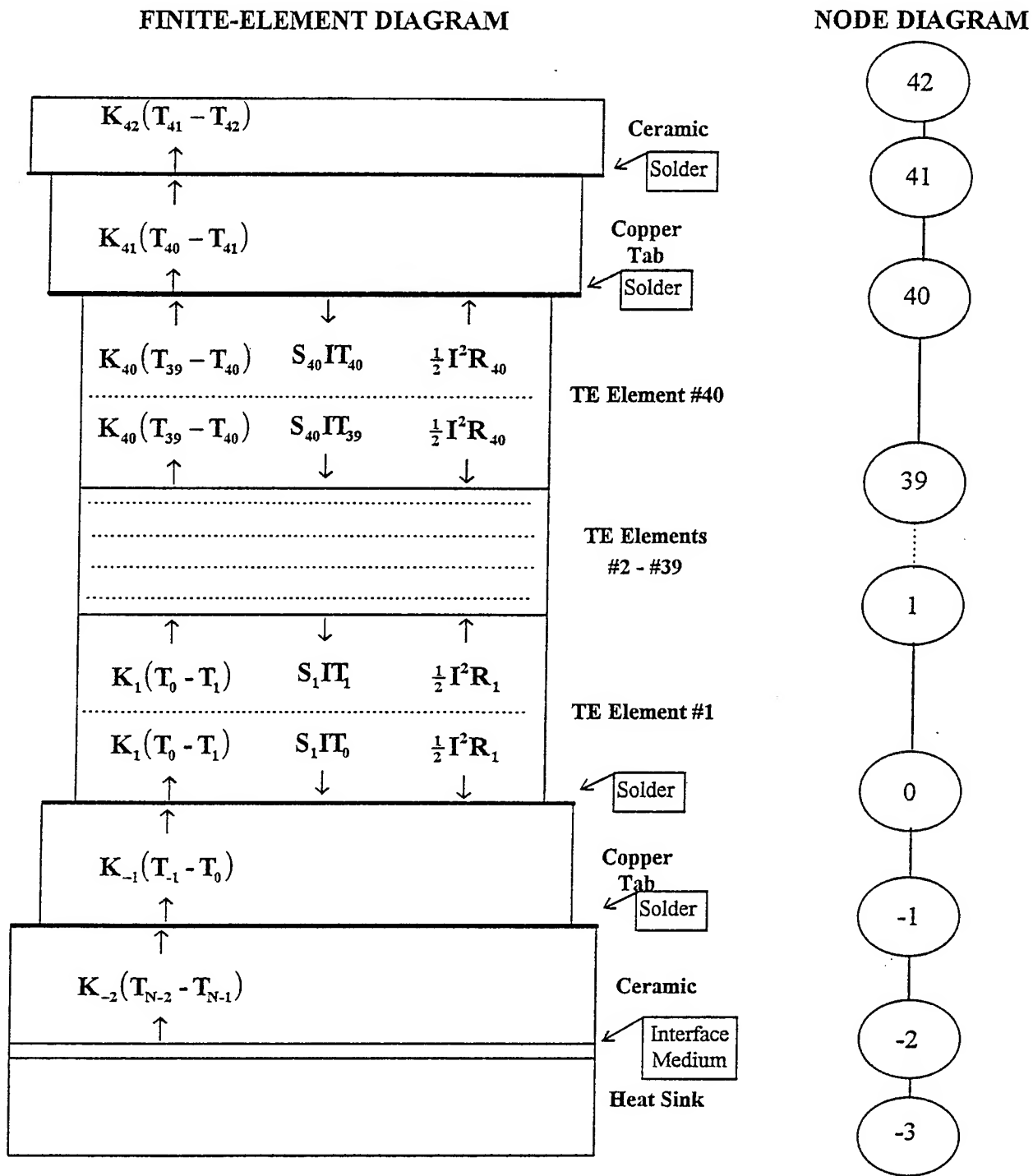


Fig. 1. Thermal Model Used for Transient Calculations

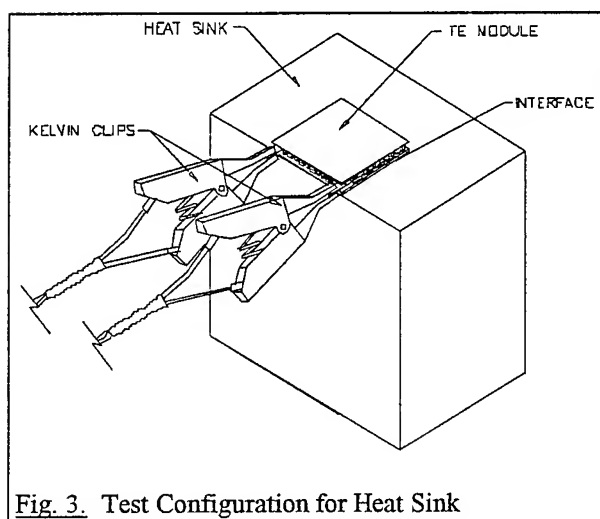
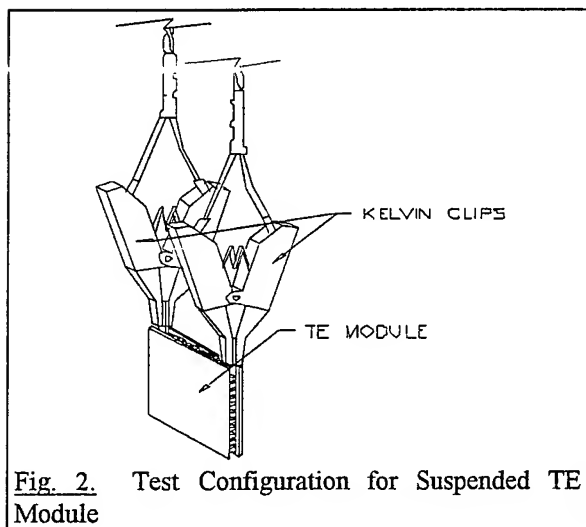


Table 1
Tested Properties Of A 71 Couple Module
Pellet Dimensions=1.37mm x 1.37mm x 3.00mm

	Temp (°C)	Seebeck ($\mu\text{V/K}$)	Electrical Resistivity ($\mu\Omega\cdot\text{cm}$)	Thermal Conductivity (mW/cm/K)	Z (1000/K)
Suspended	22.99	203.6	1077.4	16.69	2.306
Suspended	23.02	203.7	1078.2	16.70	2.304
Suspended	23.02	203.6	1076.2	16.65	2.314
Suspended	23.06	203.8	1078.4	16.67	2.309
Suspended	23.10	203.6	1078.0	16.74	2.298
Suspended	23.12	203.8	1079.3	16.69	2.305
Heat Sunk	23.34	203.8	1080.8	16.76	2.292
Heat Sunk	23.35	203.7	1080.2	16.78	2.290
Heat Sunk	23.36	203.7	1081.9	16.86	2.274
Heat Sunk	23.39	203.8	1081.0	16.75	2.293
Heat Sunk	23.42	203.6	1079.8	16.79	2.287
Heat Sunk	23.44	203.7	1080.2	16.80	2.287

Table 2
Material Property Table

Material	Density g/cm^3	Specific Heat Capacity mJ/g/K	Thermal Conductivity mW/cm/K
TE Material	7.175	178.5	See Table 1
Ceramics	3.7	775	346
Copper Tab	8.91	385.2	4000
Solder	8.56	167	326.5
Water	1000	4.18	5.89

The material properties of the TE material were obtained by directly measuring the AC-resistance, the TE figure-of-merit and the pellet geometric dimensions. Proprietary algorithms in the test software provided predictions of the temperature-dependent properties for the Seebeck coefficient, thermal conductivity and electrical resistivity.[5] Table 1 shows the results of testing six times, for each configuration, the TE module's figure-of-merit, Z, and electrical resistivity, along with the projected Seebeck coefficient and thermal conductivity. The highlighted results for the two configurations were the bases for the temperature-dependent-TE properties used in the model. Other relevant material properties used in the model are given in Table 2. However, the properties listed in Table 2 were kept constant in the model. Also, all TE material properties were based on an N and P type average.[6]

Experimental Results

The suspended module configuration, shown in Figure 2, was tested with a current of 0.0885A, which was approximately 3% of I_{max} . This same test current was also used for testing the heat-sunk configuration. A small test current was used so that the temperature of the heat sink did not measurably change. The same TE module was used in all tests. All tests were performed using a model TS-205 computer automated test system supplied by TE Technology, Inc. Figure 4 shows the test results and model results for both test configurations.

Once a steady-state voltage had been established, the current was immediately set to zero and the decay voltage was measured. Figure 5 shows the test results and model results for both test configurations.

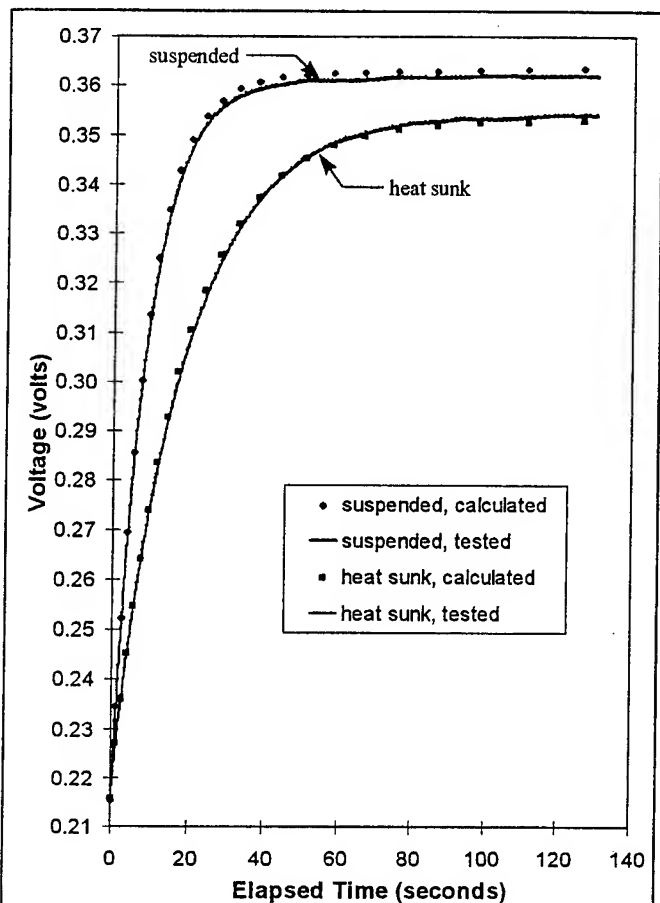


Fig 4. Transient Response of Voltage. Power on. (Current = 0.0885 A)

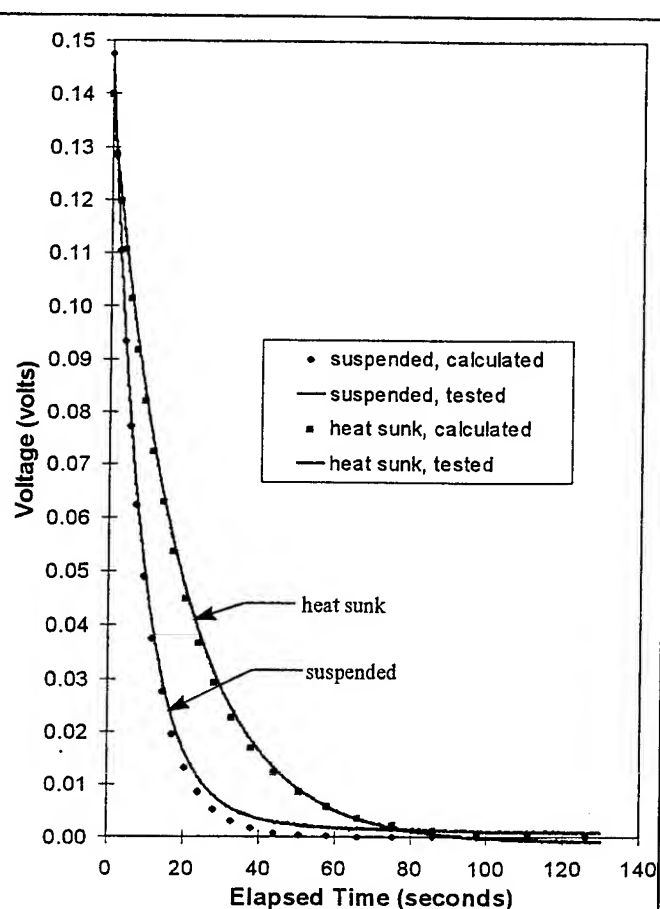


Fig 5. Transient Response of Voltage. Power off. (Initially at steady state, Current = 0 A)

Figure 6 displays the model results of suspended module for temperature profiles at given time steps for the applied test current. Figure 7 shows how each nodal temperature varied with respect to time. Figures 8 and 9 are similar to Figures 6 and 7, respectively, except are for the power-off condition.

In Figures 4 and 5, the graphs show very little change in the voltage after about 30 seconds for the suspended module. This quasi-steady-state condition corresponds to the several parallel lines graphed in Figure 6. That is, as time increased beyond 30 seconds, the temperature-profile shape remained constant. As Figure 7 shows, the rate of increase in temperature of each node was constant after about 30 seconds. This corresponded to a constant temperature difference across the TE module which corresponded to a steady-state voltage.

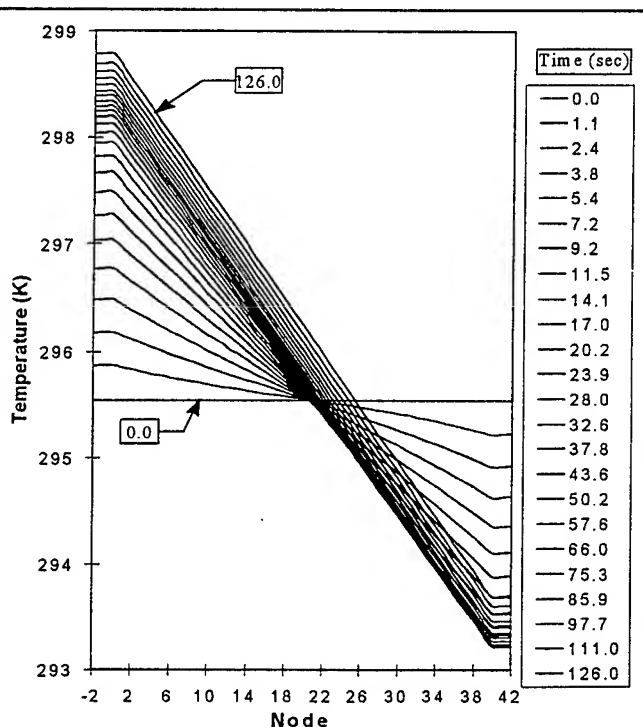


Fig 6. Temperature Profiles for Suspended Module. Power on. (Current = 0.0885 A)

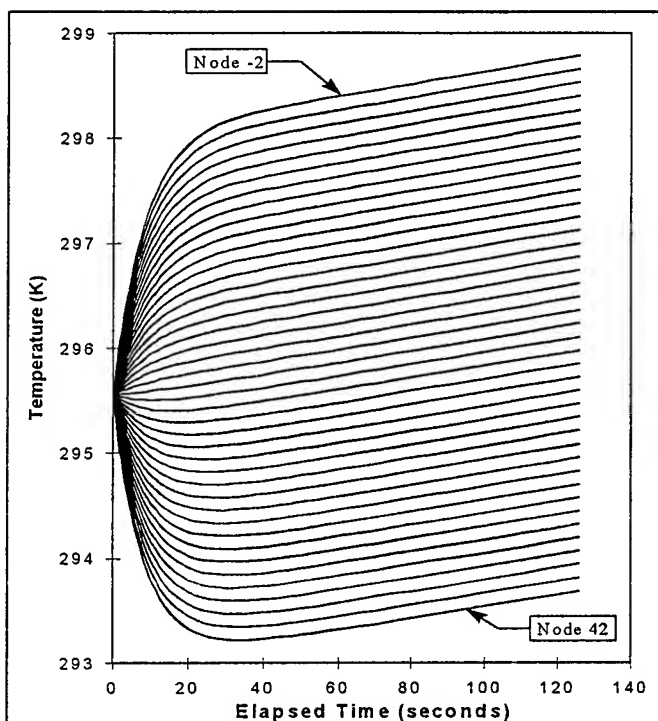


Fig. 7. Nodal Temperatures for Suspended Module. Power on. (Current = 0.0885 A)

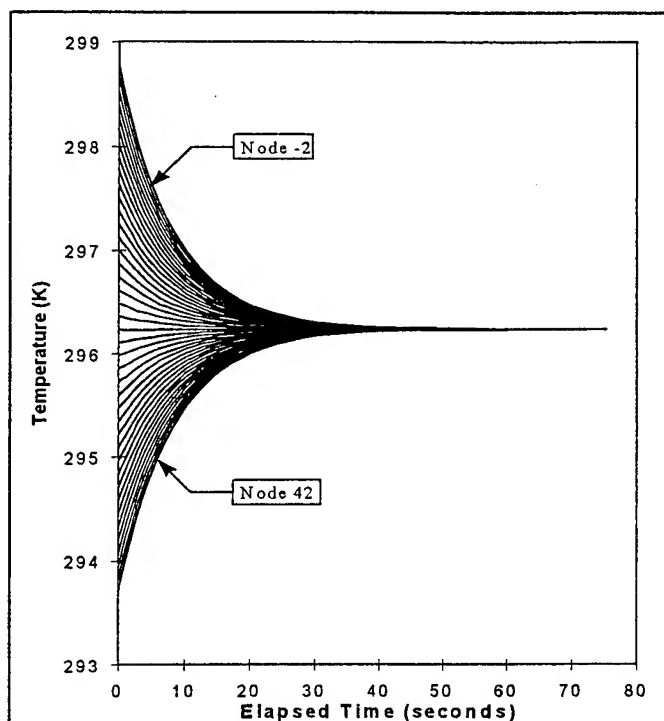


Fig. 9. Nodal Temperatures for suspended Module. Power off. (Initially at steady state, Current = 0 A)

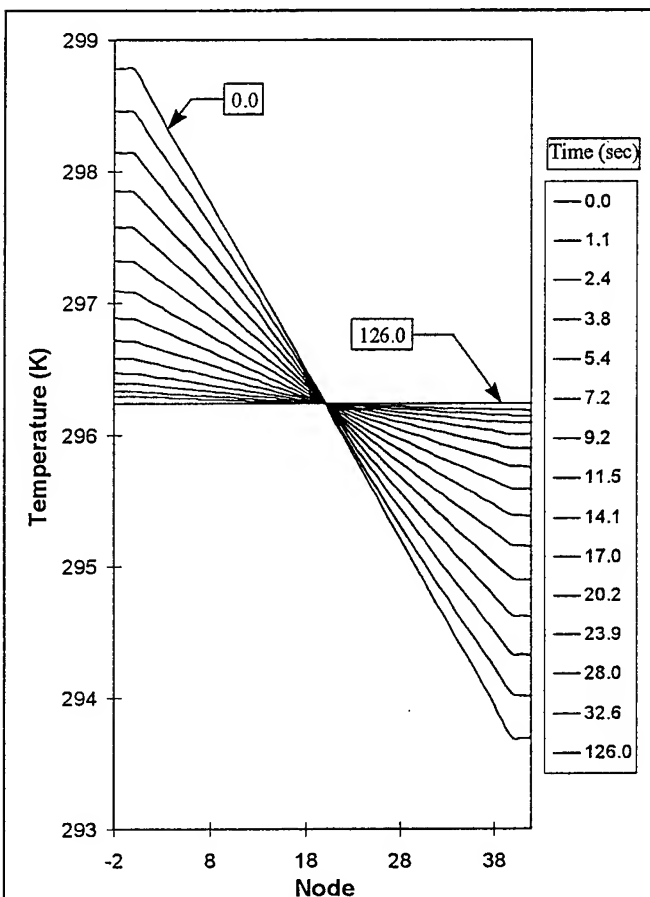


Fig. 8. Temperature Profile for Suspended Module. Power off. (Initially at steady state, Current = 0.0885 A)

Figure 10 displays the model results of the heat-sunk module temperature profiles at given time steps for the applied test current. Figure 11 shows how the nodal temperatures varied with respect to time. Figures 12 and 13 are similar to Figures 10 and 11 except are for the power-off condition.

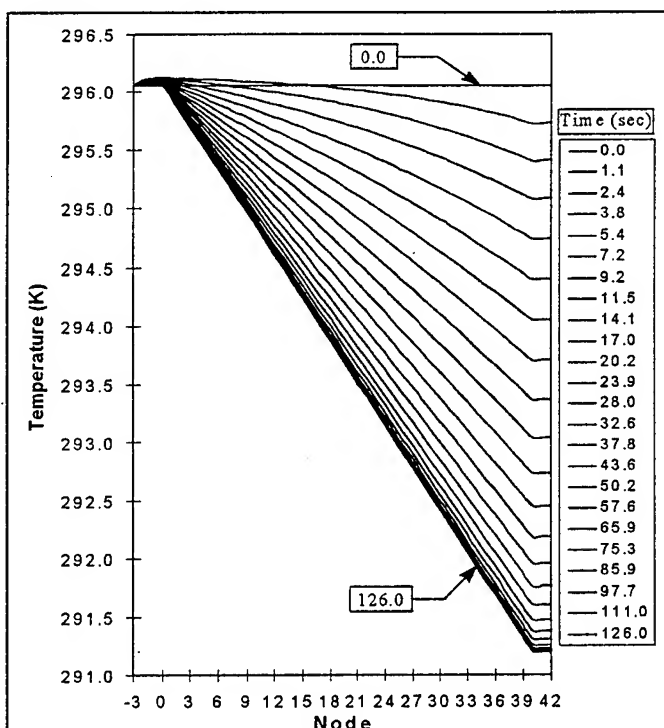


Fig. 10. Temperature Profiles for Heat Sunk Module. Power on. (Current = 0.0885 A)

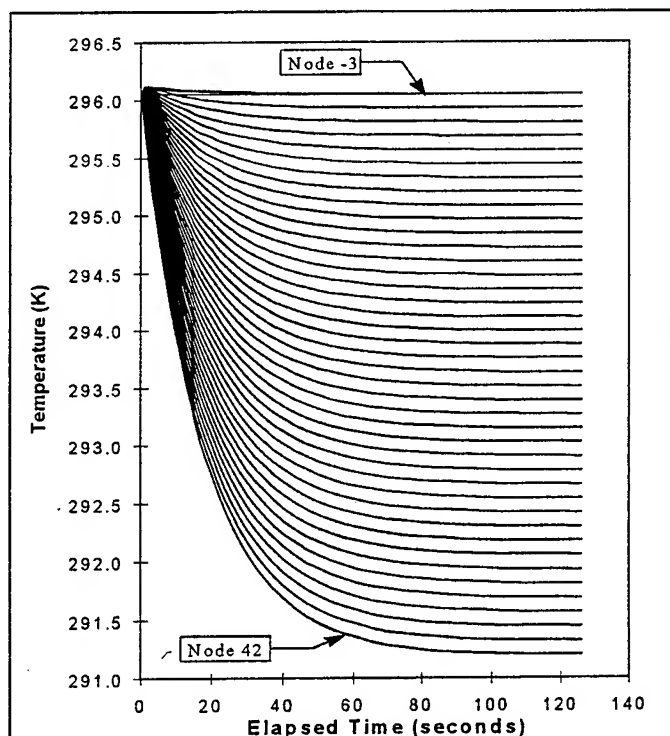


Fig. 11. Nodal Temperatures for Heat Sink Module. Power on. (Current = 0.0885 A)

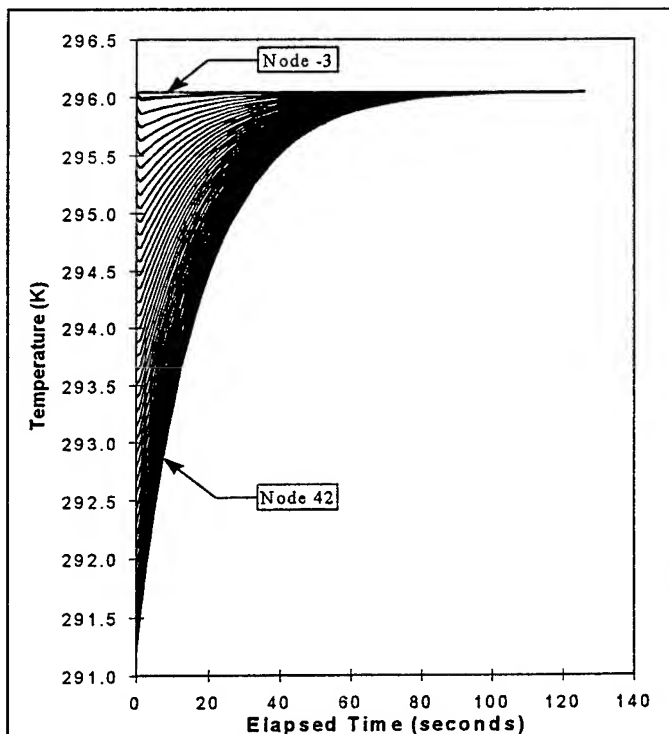


Fig. 13. Nodal Temperature for Heat Sink Module. Power off. (Initially at steady state, Current = 0.0885 A)

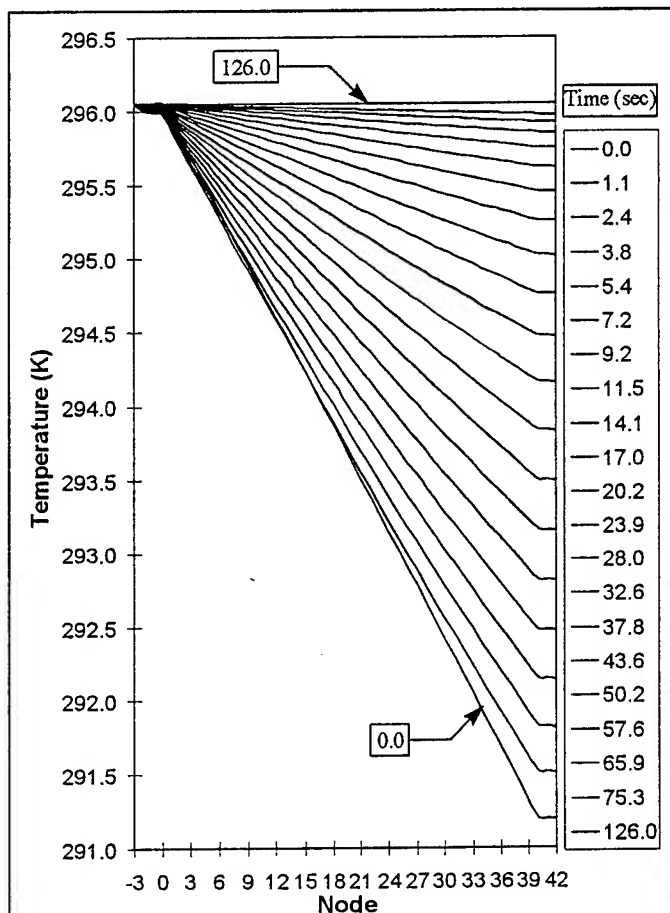


Fig. 12. Temperature Profiles for Heat Sink Module. Power off. (Initially at steady state, Current = 0.0885A)

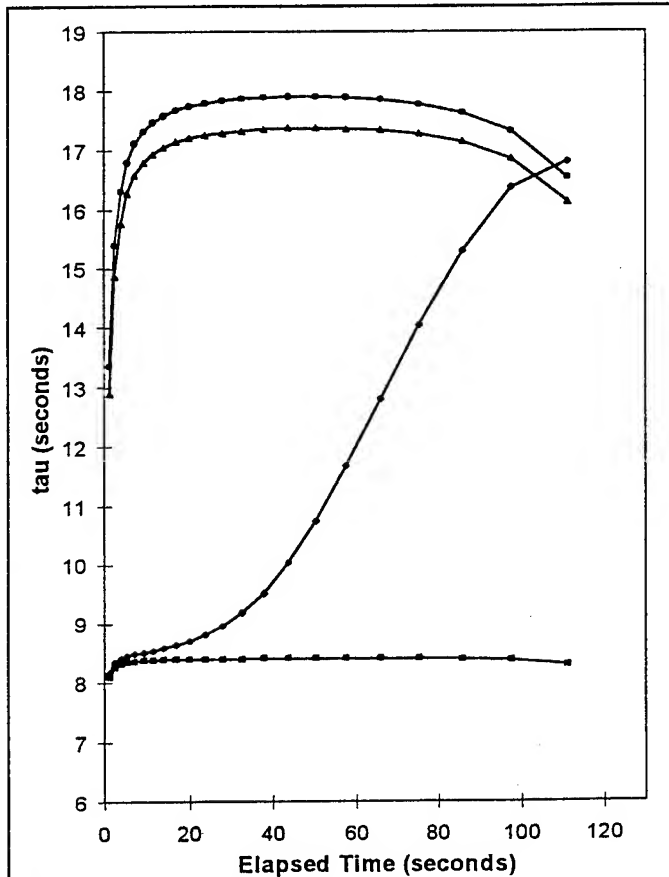


Fig. 14. Calculated Time Constants.

$$V = V_{\infty} + (V_0 - V_{\infty}) \exp\left(-\frac{t}{\tau}\right)$$

Figure 14 shows how the "time constant", τ , varied with respect to time. This time constant is based on the equation:

$$V = V_{\infty} + (V_0 - V_{\infty})\exp\left(-\frac{t}{\tau}\right) \quad (6)$$

which is normally applicable to resistance-capacitance electrical circuits. Of course, a time constant for a suspended module has no practical use. However, for the heat-sunk configuration, it was evident that a true time constant based on equation (6) did not exist.

Conclusions

The model correlated well with the test results. However, some refinements could be made to improve the model. The model used N and P-type averaged material properties. Therefore, some error was introduced by this averaging. Also, the actual TE pellet dimensions varied from one pellet to the next. The model used average pellet dimensions, so more error was introduced. Nonetheless, the finite-element model captures the fast, transient response of TE modules to an applied current.

This capability is especially important when the results presented in Figure 14 are considered. The use of a simple, time-constant analysis to characterize the transient response of a heat-sunk module would be inaccurate, especially in the first moments of applied current. However, the finite-element model is very accurate in the first moments of applied current.

References

- [1] A. Bejan, *Advanced Engineering Thermodynamics*, John Wiley & Sons, Inc., New York (1988).
- [2] R. J. Buist, "Calculation of Peltier Device Performance", *CRC Handbook of Thermoelectrics*, edited by D.M. Rowe, pp. 143-155 (1995).
- [3] S.C. Chapra and R.P. Canale, *Numerical Methods for Engineers*, McGraw-Hill, Inc., New York (1988).
- [4] F. Kiya, M. Sakai, T. Tanaka, Y. Ogawa, K. Mukasa, N. Sasa, and J. Nagao, "Computer Based Analysis of TE Cooling Device", in *Proceedings of the 12th International Conference of Thermoelectrics*, pp. 417-420 (1993).
- [5] R.J. Buist, "A New Method for Testing Thermoelectric Materials and Devices", *11th International Conference on Thermoelectrics*, Arlington, Texas, USA, (1992).
- [6] D.R. Lide, *CRC Handbook of Chemistry and Physics*, CRC Press, Florida (1992-1993).

THEORETICAL ANALYSIS OF THERMOELECTRIC COOLING PERFORMANCE ENHANCEMENT VIA THERMAL AND ELECTRICAL PULSING

Authors:

Richard J. Buist and Paul G. Lau

TE Technology, Inc.

1590 Keane Drive, Traverse City, Michigan 49686 USA

Abstract

This paper is an introduction and theoretical investigation of the fast-transient cooling characteristics of a TE module under applied high-current electrical pulses. A temperature-dependent, finite element model was developed to accurately model the fast-transient performance. Analysis of experimental data is presented to verify the accuracy and validity of the model and the conclusions derived therefrom. It has been shown that cold plate temperatures are achievable from a typical TE module beyond that obtainable by conventional, steady-state means.

The cooling enhancement is by virtue of the fact that Peltier cooling is a surface effect and extremely concentrated at the cold junction, whereas, Joule heating is a volume effect and is distributed throughout the volume of the TE pellet. As such, most of the Joule heat takes a longer time to reach the cold plate than the Peltier cooling effect. This phenomenon is theoretically demonstrated by applying a high-current pulse after the minimum steady-state cold plate temperature has been established. Calculations have shown that cold plate temperatures can be reduced by 16 K below that via steady-state means.

These transient enhancements are admittedly short-lived and have limited effectiveness. However, the results presented herein suggest that further exploitation of the fundamental differences between Peltier and Joule heat are possible. A concept is re-introduced which consists of thermally and electrically separating the cold electrode from the TE pellet. This pulse cooling concept was originally conceived over 30 years ago by Reich[1] at the Borg-Warner Research Center.

Introduction

Dr. Allen Reich[1] did a lot of pioneering work in the field of thermoelectric cooling analysis in the early 1960's. He may have been the first to recognize the potential for pulse-TE cooling by capitalizing on the fundamental differences between Peltier and Joule heat. Unfortunately, however, he preceded the age of high-speed personal computers and the accompanying analytical technologies which now provide the means for detailing the many complicated intricacies of nature. He had to rely on key, clever simplifying assumptions and solutions of difficult and complex differential equations in order to gain an analytical glimpse into the physics of thermoelectric semiconductors. Nevertheless, his work suggested the possibility of significant net cooling by thermoelectric pulsing in order to segregate the localized Peltier cooling from bulk Joule heating.

Therefore, the work presented herein is essentially computerized numerical update of a dormant, but not necessarily fruitless, idea. On the other hand, this paper is only a precursor to the real potential for pulse-TE cooling but clearly and rigorously re-establishes the existence of the potentials of enhanced TE cooling via pulsing.

Thermal Model

The key to understanding and accurately characterizing the fast-transient properties of a TE module is the development of a thermal model which incorporates as much of the real-world technical details as possible. The starting point was the finite-element, steady-state thermal model for TE pellets by Buist[2]. This model employed the speed and power of a high-speed personal computer to take advantage of simplicity but accuracy and rigor of a finite element thermal model. By making each finite element small enough, they were accurately quantified using the familiar constant parameter theory. Of course, however, the ultimate precision of this model was a consequence of accurately testing the key kinetic thermoelectric material parameters. For that model, the temperature-dependent TE material parameters were measured using the test system as described by Buist[3].

The transient model is very similar but included the added dimension of time dependence. Thermal nodes were generated for each finite element. The interactions between them were derived from the steady-state model. The details of the transient model was presented by Lau and Buist[4] together with a thorough analysis of its features and attributes. A summary of the key elements of this thermal model is given in Table 1:

Table 1

Node	Description
42	Cold Ceramic Substrate
41	Cold Copper Tabs
40	Top "Half-Slice" of TE Pellet
1-39	Imaginary "Slices" of TE Pellet from Bottom to Top
0	Bottom "Half-Slice" of TE Pellet
-1	Hot Copper Tabs
-2	Hot Ceramic Substrate
-3	Infinite Heat Sink

Physically, the configuration of system is shown in Figure 1. A typical TE module was thermally bonded to a large aluminum block which served as an infinite heat sink for the low current testing used to verify and validate the fast

transient characteristics of this system. This same module was not only used for transient testing but was also tested for its TE material properties: Seebeck coefficient, electrical resistivity, thermal conductivity and figure of merit, Z . These parameters were incorporated into the transient model.

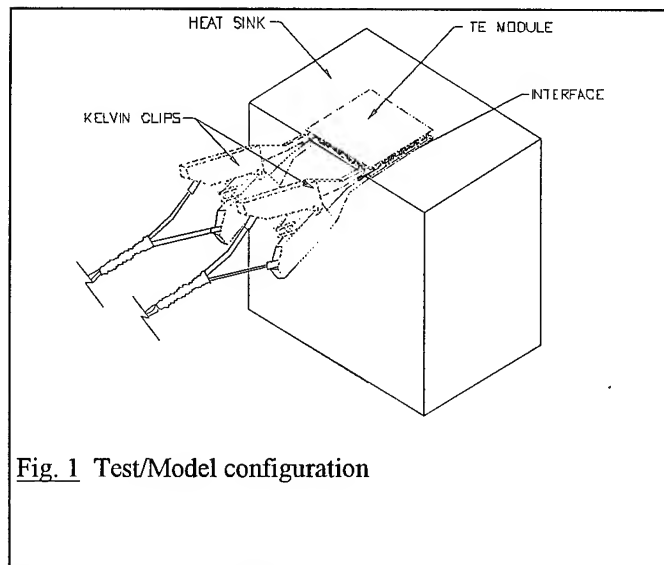


Fig. 1 Test/Model configuration

Model Verification Testing

Some initial testing at 3% of I_{max} was performed on the TE module as shown in Figure 1. This was performed by the same high-resolution, high-speed, integrating A/D board used in the test system[3]. However, it was set up to rapidly test and retest the voltage across the TE module upon the application of an applied current. These data are shown in Figures 2 and 3 together with the calculations produced but the transient model. Figure 2 clearly establishes the long-term accuracy of the model by the excellent closure throughout the entire cool-down process.

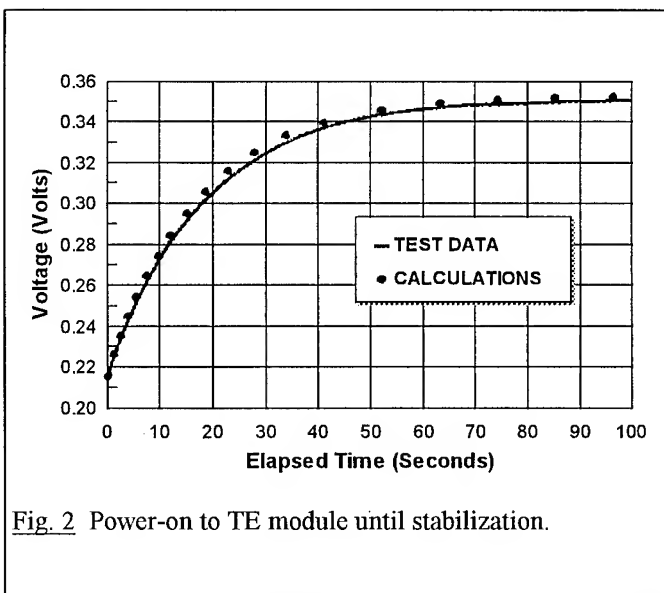


Fig. 2 Power-on to TE module until stabilization.

Figure 3 was generated to examine the accuracy of the fast-transient characteristics of the transient model. For this case, the module voltage was calculated for the same times as the test data. As observed, the calculations agreed with the test

data to within 0.5%. This closure is very good, especially since the actual time for the test points with respect to the true power-on instant was not exactly known. It could be off by as much as 0.05 seconds. In any case, the shape of the calculated curve closely matches that of the test data thereby validating the transient model for the calculations presented.

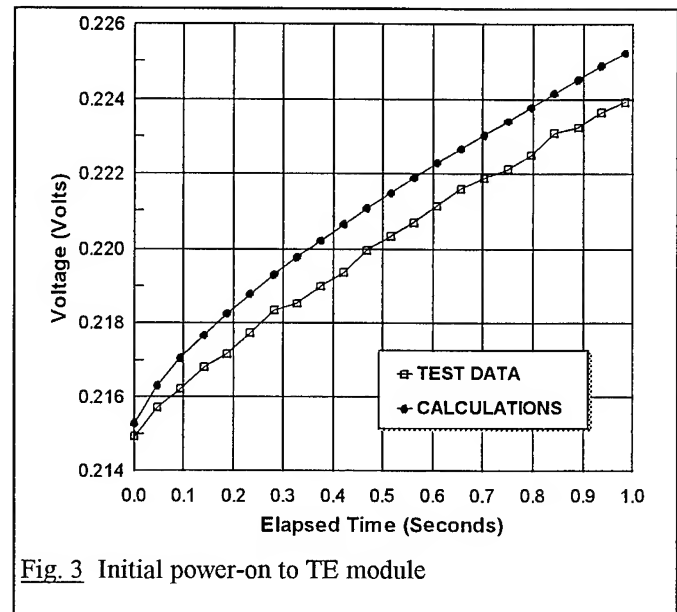


Fig. 3 Initial power-on to TE module

Calculations for I_{max}

The first step in establishing the feasibility for enhancement via pulsing was to calculate the performance of the TE module at I_{max} . I_{max} is defined as the current which produces maximum hot-to-cold temperature differential (ΔT), holding the hot junction to a constant 297K.

The calculated temperature for each node (as defined in Table 1) at selected instants of time are shown in Figures 4-6. Figure 4 depicts the temperature profiles at 10 time steps of 5 milliseconds each.

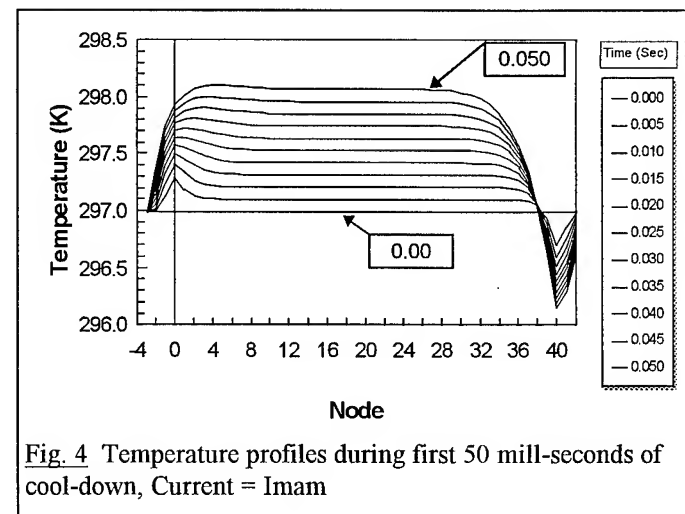


Fig. 4 Temperature profiles during first 50 mill-seconds of cool-down, Current = I_{max}

It is evident that the main body of the TE pellets is heated (even the hot junctions adjacent to the "infinite" heat sink) but the Peltier cooling is clearly overcoming Joule heat at the localized area near the cold junction. It is also clear that the

delta-T between the main body of the TE pellet and the cold junction interface is considerably larger than that between the heat sink and the cold ceramic plate. This was intuitively obvious but the cool-down speed of the cold ceramic plate was slower than anticipated. However, it did close quite well with experiment as illustrated in Figure 2.

Figure 5 illustrates the profiles over a longer time period (one second). It is observed that the Peltier cooling had greater and greater impact on the TE pellet even though Joule heating had significantly heated the main body of the TE pellet 16K above the heat sink temperature. It was also interesting to note that the TE pellet cold junction + copper tab + ceramic nodes rapidly approached a near-isotherm.

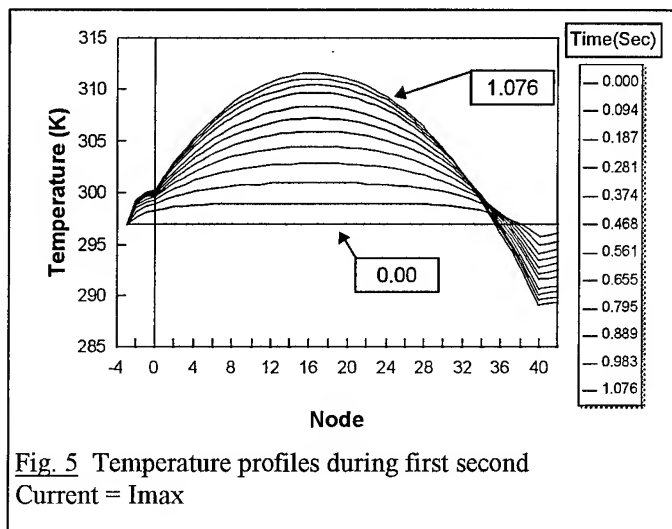


Fig. 5 Temperature profiles during first second
Current = I_{max}

The long-term temperature profiles, including the final steady-state temperature profile (96.28 seconds) are shown in Figure 6. Note that maximum heating in the TE pellet occurs in approximately 2.4 seconds. However, Peltier cooling eventually overcomes all but the nodes very close to the hot junction. It is also interesting to note that the TE pellet hot junction runs 2-3K warmer than the heat sink. This fact, of course, must be accounted for in order to accurately model TE module performance. Finally, the accuracy of the model is

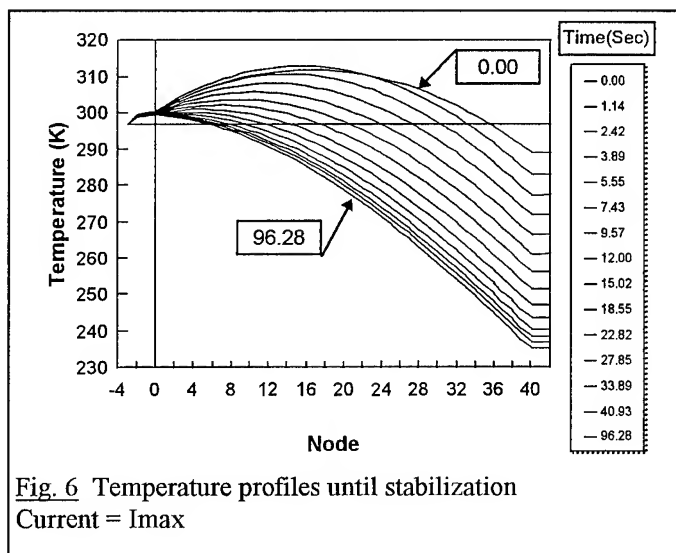


Fig. 6 Temperature profiles until stabilization
Current = I_{max}

further verified by the observed 60K delta-T_{max} that one would expect for a TE module operated in dry nitrogen from a 297K heat sink. The cold side temperature of 237K represents the lowest possible temperature for steady-state operation representing the baseline temperature from which pulsing enhancements were measured.

High-Current Pulse Cooling

Starting from the maximum steady-state cooling condition (the curve labeled 96.28), the current was stepped upward from I_{max}=3 amps in accordance with that shown in Figure 7. Obviously, if one waited until stabilization, the cold junction would be warmer than the "baseline" temperature. However, for the first few 10ths of a second, the cold junction becomes cooler.

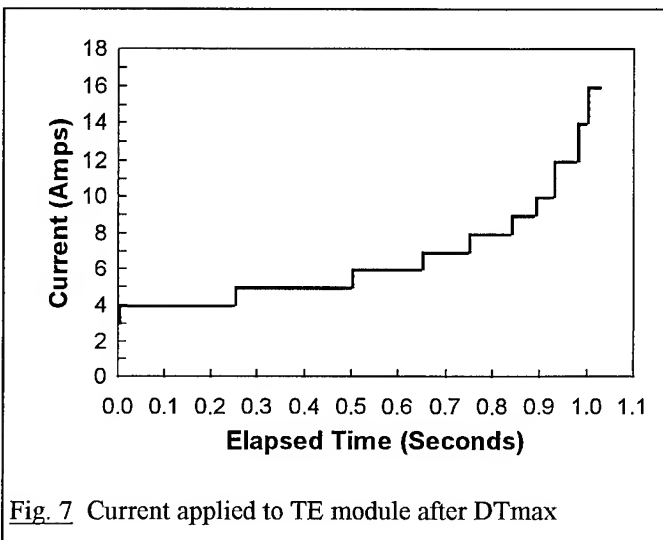


Fig. 7 Current applied to TE module after DT_{max}

This fact is illustrated by the profile data shown in Figure 8 and the lower curve shown in Figure 9. Once the delta-T enhancement began to maximize (and fall off if left in that condition), the current was stepped up to 5 amps. This process was continued by sequentially increasing current whenever each enhancement appeared to maximize.

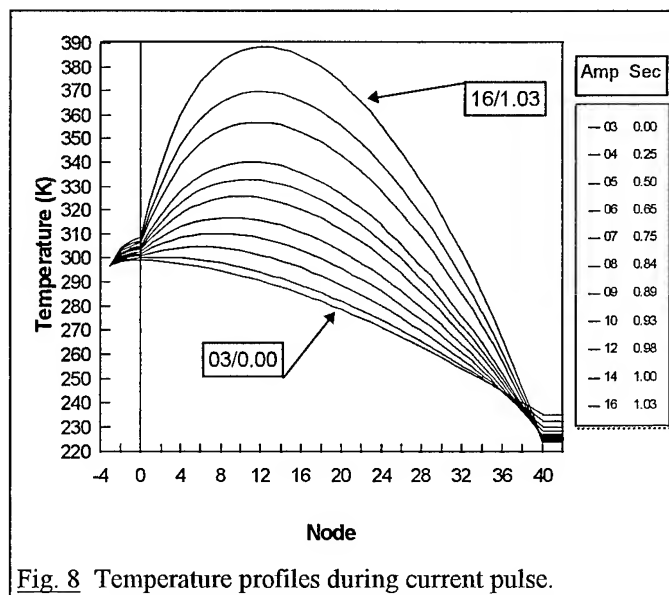


Fig. 8 Temperature profiles during current pulse.

Clearly, from Figure 8, the main body of the TE pellet heats up but the cold side gets colder with each current step. This process was repeated, but this time, neglecting the mass of the tab and ceramic. This case yielded a 16K enhancement over ΔT_{max} . See Figure 9.

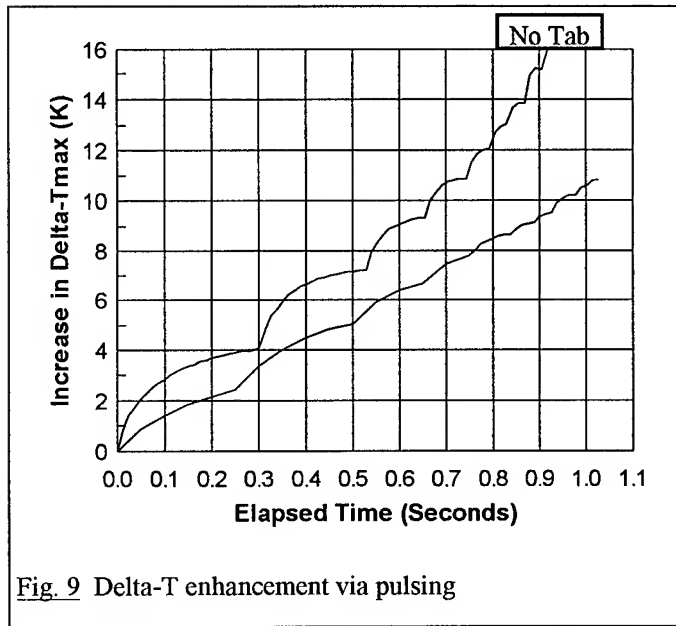


Fig. 9 Delta-T enhancement via pulsing

Conclusions

A finite element thermal model for accurately calculating the fast transient performance of a TE module has been developed. It was used to examine some possibilities for cooling enhancement via pulsing as suggested over 35 years ago. It was concluded that, indeed, enhancement is achievable but it is of such short duration it would have very limited application. Nevertheless, if a low-temperature infrared "snapshot" is ever needed, this technique could be used to boost the cooling possibly more than 15K. Actually, no attempt was made to optimize the high current pulse waveform. Therefore, it may be possible to achieve even higher ΔT enhancements than the calculated 16K case produced quite arbitrarily. Finally, the model used for these calculations can be applied to the pulse cooling concept originally conceived by Reich[1]. A possible configuration is shown in Figure 10.

Initially, the removable cold tab is thermally and electrically in contact with the N and P TE pellets. This not only completes the electrical circuit but also makes thermal contact with the TE pellet cold junctions. Now, a larger-than- I_{max} current is applied and the tab is momentarily cooled as described above. However, instead of ever-increasing the current, the cooled tab is removed and isolated (see lower sketch of Figure 10). While it "thermally coasts", the excess heat build-up in the TE pellets is conducted into the heat sink and dissipated. As soon as the TE pellet is thermally stabilized, the process can be repeated and the electrode receives another cooling "pulse". This is just a concept at this time but the means for studying this possibility has now been established.

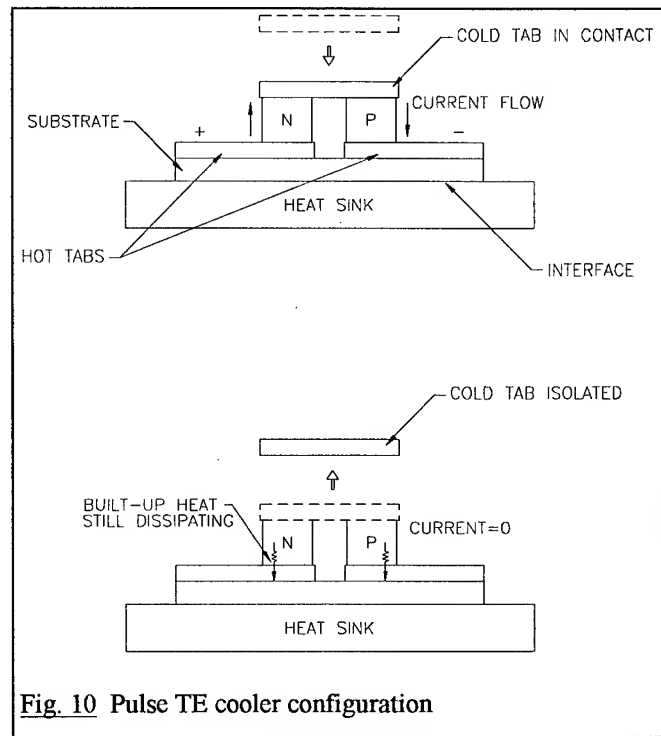


Fig. 10 Pulse TE cooler configuration

References

- [1] Allan D. Reich, Unpublished work documented in Internal Reports to the Borg-Warner Research Center, Des Plaines, IL, USA (1960).
- [2] R.J. Buist, "Design and Engineering of Thermoelectric Cooling Devices", *10th International Conference on Thermoelectrics*, Cardiff, Wales, (1991).
- [3] R.J. Buist, "A New Method for Testing Thermoelectric Materials and Devices", *11th International Conference on Thermoelectrics*, Arlington, Texas, USA, (1992).
- [4] P.G. Lau and R.J. Buist, "Temperature and Time Dependent Finite Difference Model of a Thermoelectric Pellet and Couple", *Proceedings of the XV Proceedings of the XV Conference on Thermoelectrics*, Pasadena, California, USA, (1996).

Temperature Analysis of Thermoelectric Device of Cu_4SnS_4 with Two Dimension by Boundary Element Method

S. KONDO M.HASAKA and T.MORIMURA

Department of Materials Science and Engineering, Faculty of Engineering,
Nagasaki University, Nagasaki 852, Japan

Abstract

Temperature distribution of thermoelectric device composed of Cu_4SnS_4 compound in two-dimension are evaluated by boundary element method (BEM). It is found that temperature distribution is strongly dependent on the length of thermoelectric device: temperature distribution shows very strong dependence of the direction of length of device when the length of device is very thin. In the case of small electric current density such as $-1\text{A}/\text{cm}^2$, temperature distribution can be approximately expressed as the solution of Laplace equation.

Introduction

Thermoelectric devices composed of intermetallic compound such as $\beta\text{-FeSi}_2$ ^{[1][3]}, Cu_4SnS_4 ^[4] seem to have great potential in generating electric power; especially Cu_4SnS_4 compound seems to be excellent material to change heat into electric energy because of high Seebeck coefficient ($\sim 0.5\text{mV}/\text{K}$)^[4] and the figure of merit $Z(\sim 8 \times 10^{-4}/\text{K})$ at 300K. Such a great potential as stated above is supposed to be due to Cu^+ carrier^[5].

Consequently it seems very important to evaluate temperature distribution in thermoelectric device for the purpose of running device effectively. However those calculations in two- or three dimension by BEM has not been reported and discussed. Certainly it is also possible to evaluate temperature in device analytically by Green function; however green function method can only applied to the shape with high symmetry such as cubic or rectangle and with specific boundary condition. Accordingly, in analyzing various shapes of device with various boundary conditions, it is desirable to analyze by BEM. In this article we calculate temperature distribution in rectangle shape of device (two dimension shape) by using BEM, assuming linearity.

Calculation Method

The partial differential equation on steady-state temperature distribution for thermoelectric device is given as follows:

$$\nabla \cdot (\kappa \nabla T) - \tau \mathbf{J} \cdot \nabla T + \mathbf{J} \cdot \mathbf{J} / \sigma = 0 \quad (1)$$

where κ, τ and σ are thermal conductivity, Thomson coefficient and electric conductivity, respectively. \mathbf{J} is current density.

For simplifying the eq.(1), we consider the case of κ, τ and σ having no temperature dependence. Then eq.(1) is

$$\nabla^2 T - (\tau/\kappa) \mathbf{J} \cdot \nabla T + \mathbf{J} \cdot \mathbf{J} / (\sigma \kappa) = 0 \quad (2)$$

Eq.(2) is, in the two-dimension, written down as below,

$$[(\partial/\partial x)^2 + (\partial/\partial y)^2 + \alpha \partial/\partial x + \beta \partial/\partial y] T + \gamma = 0 \quad (3)$$

where $\alpha = -\tau J_x / \kappa$, $\beta = -\tau J_y / \kappa$ and $\gamma = (J_x^2 + J_y^2) / (\sigma \kappa)$ because of $\mathbf{J} = (J_x, J_y)$. Eq.(3) is found to belong to the second order elliptic partial differential equation.

Next we introduce operator \mathbf{E}^+ and I as defined below,

$$\mathbf{E}^+ = (\partial/\partial x)^2 + (\partial/\partial y)^2 + \alpha \partial/\partial x + \beta \partial/\partial y \quad (4)$$

$$I = \iint_{\Omega} [\mathbf{E}^+ T + \gamma] W dS \quad (5)$$

where W in eq.(5) is weighting function and Ω means all domains to be calculated ($dS = dx dy$). From the view point of weighted method, I as defined in eq.(4) is zero; I can be expanded by using Green's theorem,

$$I = \iint_{\Omega} T(\mathbf{E}^- W) dS + \int_C W \partial T / \partial n ds - \int_C T \partial W / \partial n ds + \alpha \int_C W T n_x ds + \beta \int_C W T n_y ds + \gamma \iint_{\Omega} W dS = 0 \quad (6)$$

$$\text{and } ds = \sqrt{(dx)^2 + (dy)^2}$$

In eq.(6), operator \mathbf{E}^- is

$$\mathbf{E}^- = (\partial/\partial x)^2 + (\partial/\partial y)^2 - \alpha \partial/\partial x - \beta \partial/\partial y \quad (7)$$

and \int_C means the integral along curve C , where Curve C is the boundary for domain Ω . n_x and n_y are x and y component of normal vector outside to curve C , respectively. Then, yielding to usual procedures as performed in BEM, we introduce the green function $G^\infty(\mathbf{r}, \mathbf{r}_0)$ (i.e. fundamental solution) as defined in eq.(8)

$$\mathbf{E}^- G^\infty(\mathbf{r}, \mathbf{r}_0) = -\delta(\mathbf{r} - \mathbf{r}_0) \quad (8)$$

From eq.(8), green function $G^\infty(\mathbf{r}, \mathbf{r}_0)$ is deduced by

$$G^\infty(\mathbf{r}, \mathbf{r}_0) = \frac{1}{4\pi^2} \int_{-\infty}^{\infty} \int_{-\infty}^{\infty} d\xi d\eta \frac{\exp(ix\xi + iy\eta)}{\xi^2 + \eta^2 + i\alpha\xi + i\beta\eta} = \frac{1}{2\pi} \exp(\mathbf{A} \cdot (\mathbf{r} - \mathbf{r}_0) / 2) K_0(|\mathbf{A}| \cdot |\mathbf{r} - \mathbf{r}_0| / 2) \quad (9)$$

where $A = (\alpha, \beta)$ and K_0 is modified Bessel function of second kind. Therefore, based on the eq.(9), we can evaluate temperature distribution T by yielding to the procedures as usually done in BEM.

Next, let consider the temperature distribution for very thin thermoelectric device, both ends of which are contacted with hot and cold junctions with temperature of both ends being fixed. We assume that temperature difference along z axis can be negligible in the case of very thin thickness. Figure 1 shows the schematic illustration of thermoelectric device whose ends are contacted with hot and cold junctions.

we consider the case of boundary temperature being known (Dirichlet Problem) such as shown in Fig.1, namely

$$\begin{aligned} 0 \leq x \leq L_x \quad y=0 \quad T &= f(x) \\ y=L_y \quad T &= f(x) \\ x=0 \quad 0 \leq y \leq L_y \quad T &= T_L \\ x=L_x \quad 0 \leq y \leq L_y \quad T &= T_H \end{aligned} \quad (10)$$

In calculating temperature, we set $f(x)$ to $T_L + x(T_H - T_L)/L_x$

Experimental Procedure and Calculation Results

Cu_4SnS_4 compounds are prepared from oxygen-free copper(99.99%), pure tin(99.99%) and sulfur(99%). Specimen composed of Cu, Sn and S in quartz tube with the order of about 10^{-4} torr was at first heated up to 373K for the purpose of melting sulfur. After complete solution of sulfur, the specimen was heated up to 1473K very slowly so as to prevent explosion and then cooled to room temperature with very slow rate after complete formation of Cu_4SnS_4 phase. The specimen obtained by above procedures was powdered and pressed with the pressure of $2 \times 10^3 \text{ kg/cm}^2$ for 15 minutes at room temperature. After sintering treatment, the specimen was shaped into rectangle with the length in about 10mm, width in 2 to 3 mm and thickness in about 1 mm for the purpose of measuring electric resistance, thermoelectromotive force and thermal conductivity.

The measurement of electric resistance was carried out at temperature range of room temperature to 573K. In measuring thermoelectromotive force, the specimen was, as illustrated in Fig.1, held between cold and hot junction with temperature of cold junction remaining room temperature (about 296K to 300K).

Figure 2 shows temperature dependence of electric resistivity ρ for sintered Cu_4SnS_4 sample in the temperature range of 283K to 573K. Electric resistivity decrease with temperature, thus indicating semiconductive property.

Figure 3 shows temperature dependence of Seebeck coefficient S for sintered Cu_4SnS_4 sample in the temperature range of 295K to 601K. As illustrated in Fig.3, the change of Seebeck coefficient with the range of 0.25mV/K to 0.4mV/K seems to be very small in comparison with that of electric resistivity. The carrier of sample is found to be hole because of positive Seebeck coefficient; hence electric current flows high

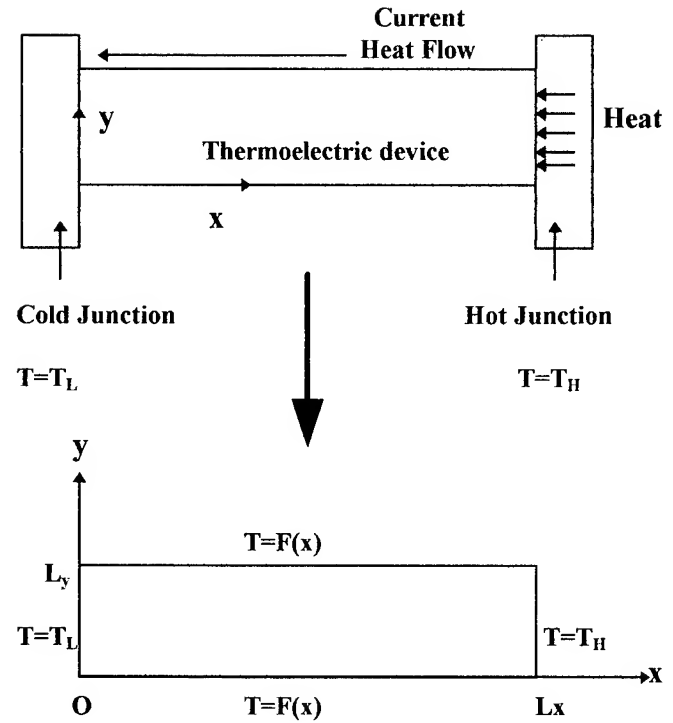


Fig.1 Schematic illustration of the two-dimension thermoelectric device connecting with high and low temperature side, where T_H and T_L are temperatures for high and low temperature sides, respectively. L_x and L_y are the length of x and y direction for device.

temperature side to low one, which means direction of electric current is negative.

In actual calculation, we fix L_y at 1cm and T_H and T_L are 283K and 583K, respectively and $J_y=0$. As described previously, we regard thermal conductivity κ , Thomson coefficient τ and electrical conductivity $\sigma (=1/\rho)$ as temperature independence, namely, constant; we substitute averaged values $\langle \kappa \rangle$, $\langle \tau \rangle$ and $\langle \rho \rangle$ as defined in eq.(11)-(13) into κ , τ and $1/\sigma$ in eq.(3).

$$\langle \kappa \rangle = \int_{T_L}^{T_H} \kappa(T) dT / (T_H - T_L) \quad (11)$$

$$\langle \tau \rangle = \int_{T_L}^{T_H} \tau(T) dT / (T_H - T_L) \quad (12)$$

$$\langle \rho \rangle = \int_{T_L}^{T_H} \rho(T) dT / (T_H - T_L) \quad (13)$$

$\langle \rho \rangle = 0.032 \Omega \cdot \text{cm}$ and $\langle \tau \rangle = 0.26 \text{ mV/K}$ are derived numerically from eq.(12)-(13). We also adopt $\langle \kappa \rangle$ for sintered Cu_4SnS_4 specimen as $0.0063 \text{ W/(cm} \cdot \text{K)}$ from the measurement of Laser Flash method, instead of eq.(11).

Adopted value is about two times as large as the reported one (0.003W/(cm·K))^{[6][7]}.

Figure 4(a)(b) and (c) show temperature distribution for Cu₄SnS₄ thermoelectric device in the case of J_x = -10A/cm². As shown in Fig.4, temperature distribution tend to be dependent upon only x with decrease in L_x: Especially when L_x=0.1cm, temperature distribution can be expressed as a function of x with showing little dependence of y direction.

Figure 5 (a) and (b) shows temperature distribution when L_x=1cm and J_x = -1A/cm² together with temperature distribution obtained by solving Laplace equation under the same boundary condition. As illustrated in the figures, there seems almost no difference between both results ; in the case of very small electric current density, solution for Laplace equation approximately expresses temperature distribution for thermoelectric device, instead of solving eq.(3).

Comparison with the results by Green function

It seems very essential to verify the solution by BEM; we try to compare the results by BEM with those by Green function. As stated previously, in the case of the specific shape of thermoelectric device with high symmetry such as cubic or rectangle and specific boundary condition, then it is possible to apply Green function to the solving of temperature distribution; thus we can evaluate temperature distribution analytically.

At first we introduce dimensionless parameter x^* , y^* and T^* as shown in eq.(14) for the purpose of making the eq.(3) dimensionless

$$x^* = x/L_y, \quad y^* = y/L_y, \quad T^* = \frac{T - T_L}{T_H - T_L} \quad (14)$$

Therefore eq.(3) is transformed into ,

$$[(\partial/\partial x^*)^2 + (\partial/\partial y^*)^2 + \alpha^* \partial/\partial x^* + \beta^* \partial/\partial y^*] T^* + \gamma^* = 0 \quad (15)$$

where $\alpha^* = \alpha L_y$, $\beta^* = \beta L_y$ and $\gamma^* = L_y^2 \gamma / (T_H - T_L)$. Then let introduce φ which is associated with T^* as below,

$$T^* = \exp\left(-\frac{\alpha^* x^* + \beta^* y^*}{2}\right) \varphi \quad (16)$$

By substituting eq.(16) into eq.(15), φ yields

$$\left[(\partial/\partial x^*)^2 + (\partial/\partial y^*)^2 - \frac{(\alpha^*)^2 + (\beta^*)^2}{4} \right] \varphi + \gamma^* \exp\left(\frac{\alpha^* x^* + \beta^* y^*}{2}\right) = 0 \quad (17)$$

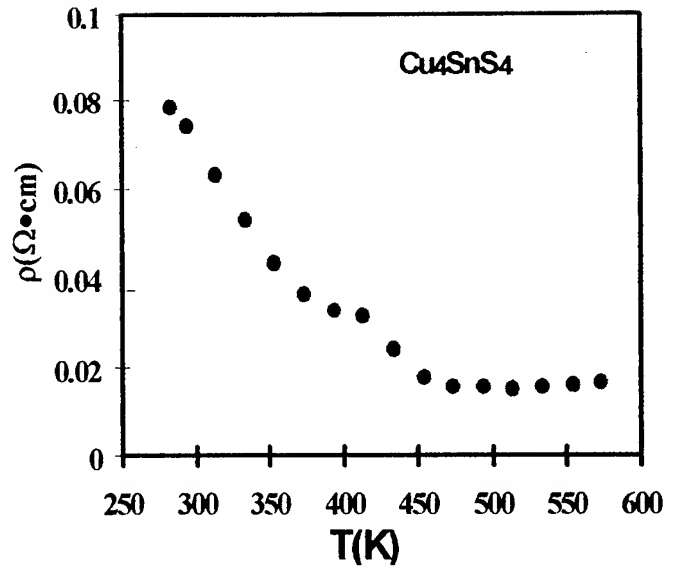


Fig.2 Electric resistivity for Cu₄SnS₄

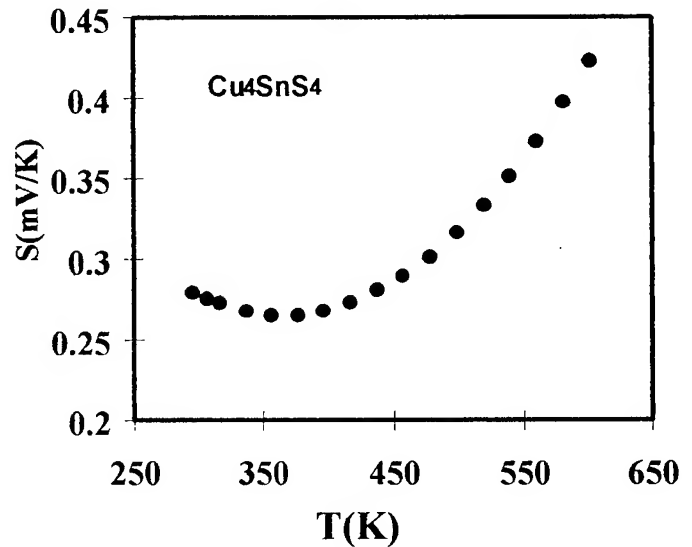


Fig.3 Temperature dependence of Seebeck Coefficient S for Cu₄SnS₄

Eq.(17) is found to be ascribed to Helmholtz type partial equation; accordingly, based on the eq.(17), we can easily define green function $G(\mathbf{r}, \mathbf{r}_0)$ as below ,

$$\left[(\partial/\partial x^*)^2 + (\partial/\partial y^*)^2 - \frac{(\alpha^*)^2 + (\beta^*)^2}{4} \right] G(\mathbf{r}, \mathbf{r}_0) = -\delta(\mathbf{r} - \mathbf{r}_0) \quad (18)$$

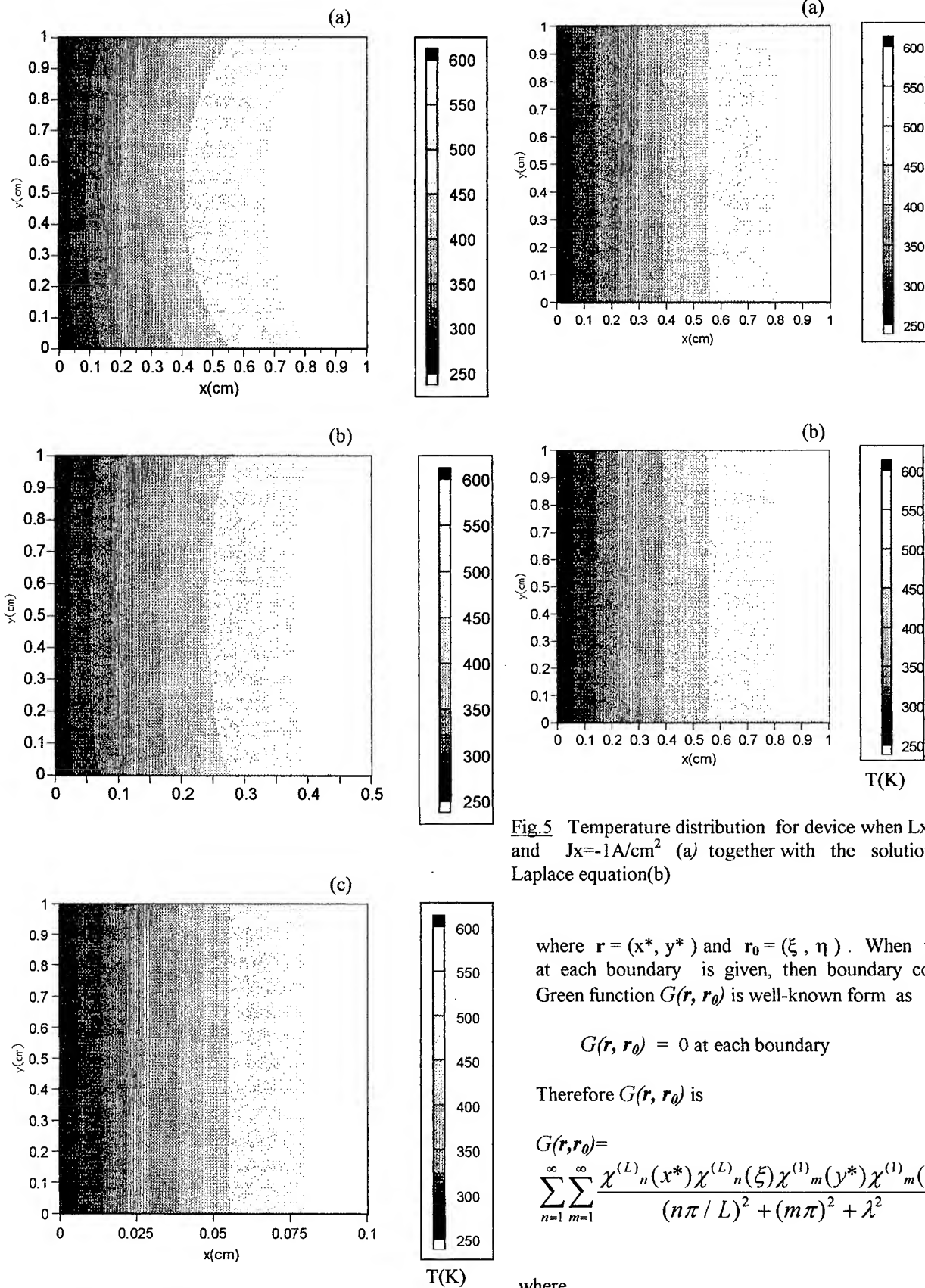


Fig.4 Temperature distribution of device
(a) $L_x=1\text{cm}$ (b) 0.5cm (c) 0.1cm when $J_x=-10\text{A/cm}^2$

Fig.5 Temperature distribution for device when $L_x=1\text{cm}$ and $J_x=-1\text{A/cm}^2$ (a) together with the solution by Laplace equation(b)

where $\mathbf{r} = (x^*, y^*)$ and $\mathbf{r}_0 = (\xi, \eta)$. When temperature at each boundary is given, then boundary condition for Green function $G(\mathbf{r}, \mathbf{r}_0)$ is well-known form as

$$G(\mathbf{r}, \mathbf{r}_0) = 0 \text{ at each boundary} \quad (19)$$

Therefore $G(\mathbf{r}, \mathbf{r}_0)$ is

$$G(\mathbf{r}, \mathbf{r}_0) = \sum_{n=1}^{\infty} \sum_{m=1}^{\infty} \frac{\chi^{(L)}_n(x^*) \chi^{(L)}_n(\xi) \chi^{(1)}_m(y^*) \chi^{(1)}_m(\eta)}{(n\pi/L)^2 + (m\pi)^2 + \lambda^2} \quad (20)$$

where

$$\chi^{(L)}_n(x^*) = \sqrt{\frac{2}{L}} \sin\left(\frac{n\pi x^*}{L}\right) \quad \text{and}$$

$$\lambda = \sqrt{(\alpha^*)^2 + (\beta^*)^2} / 2 \quad (21)$$

[5] S.Anzai and K.Ozawa, JAERI-M reports, 84-059(1984) 1.

[6] M.I.Aliev, D.G.Arasly and T.G.Dzhabrailov, Sov.Phys.-Solid State 25(1983)2009

[7] D.P.Spitzer, J.Phys.&Chem.Solids 31(1970) 19

Consequently ϕ is expressed as eq. (22) using above green function G ,

$$\phi = \int_s \gamma^* \exp\left(\frac{\alpha^* \xi + \beta^* \eta}{2}\right) G dS' - \int_c \phi (\partial G / \partial \mathbf{r}') \cdot \mathbf{n} ds' \quad (22)$$

where $dS' = d\xi d\eta$ and $ds' = \sqrt{(d\xi)^2 + (d\eta)^2}$. Hence we can calculate temperature in thermoelectric device by substituting eq.(22) into eq.(16).

Table I shows comparison of temperature distribution by Green function and BEM. As shown in Table, both agreement is fairly well, thus showing the effectiveness of BEM.

Table I Comparison of temperature distribution by Green function and B.E.M in the case of $J_x = -10 \text{ A/cm}^2$, $L_x = L_y = 1 \text{ cm}$

x(cm)	y(cm)	T(K)/Green.	T(K)/B.E.M	Error(%)
0.1	0.1	321.4783	321.4738	0.0014
0.1	0.5	331.9981	332.0002	0.000633
0.1	0.9	321.4783	321.4738	0.0014
0.5	0.1	451.2151	451.2133	0.000399
0.5	0.5	479.1847	479.1862	0.000313
0.5	0.9	451.2151	451.2133	0.000399
0.9	0.1	560.9539	560.9428	0.001979
0.9	0.5	570.4576	570.4654	0.001367
0.9	0.9	560.9539	560.9248	0.005188

Conclusion

Temperature in thermoelectric device composed of Cu_4SnS_4 compound is calculated by using BEM It is found that temperature distribution is strongly dependent on the length of thermoelectric device: temperature distribution is a function of the direction of device length when the length of device is very small. In the case of small electric current density such as -1 A/cm^2 , temperature distribution can be approximately expressed as the solution by calculating Laplace equation. Temperature distributions calculated by BEM are in very good agreement with those calculated by Green function method, even though both methods are based on the different ideas and procedures. Therefore we can conclude BEM analysis is very effective for examining temperature of device when the partial differential equation is approximately expressed as linear one.

References

- [1] T.Kojima, M.Okamoto and I.Nishida, Proc.5th Int. Conf. Thermoelectric Energy Conv., Arlington, March 1984, p.56.
- [2] R.W.Ware and D.J.McNeill, Proc.Inst.Electr.Eng. 111 (1964)178.
- [3] U.Birkholz and J.Schelm, Phys.Status.Solidi 27(1968)413.
- [4] M.Matoba, I.Inoue, T.Kamimura, M.Watanabe and S.Anzai, J.Mat.Sci.Soc.Jpn. 27(1990)299.

Reliability Theory in Thermoelectricity

L.I. Anatyshuk, O.J. Luste
(Institute of Thermoelectricity, Chernivtsi, Ukraine)

Abstract

Analysis of reliability determination methods used in thermoelectricity is carried out. These methods are based on the classical probability theory and have restricted possibilities for a description of reliability of complicated system and dynamic processes. In the present work more effective means of the random processes theory are used for creation of reliability determination methods. From the random processes theory point of view reliability parameters of thermoelectric elements and multi-element systems are considered. Possibilities of the random processes theory for determination and prognosis of thermoelectric module reliability have been considered.

Introduction

Modern theory of reliability (TR) represents a set of mathematical methods directed to theoretical support for problems solution of industrial devices reliability.

The analysis of used in thermoelectricity TR methods has been conducted in the present work on the base of the past 20 years literature data. The analysis results show that only simple TR methods are generally used. The purpose of the work is to indicate on the possibility of TR effective methods use (random processes theory, correlation analysis, optimal control theory) for the central problems of thermoelectricity solution.

1. The use the theory of reliability in thermoelectricity

Works on reliability problems constitute a small portion of the total works on thermoelectricity in the bibliography on thermoelectrics. Suffice it to note that at the International conferences on thermoelectricity not more than ten papers were devoted to this subject within last 20 years.

1.1. Probabilistic models of reliability.

To describe the reliability of thermoelectric devices in 1978, the authors of [1] have used the so-called "human-like" version of technical product failure statistics which is well-known from the general mathematical reliability theory. This approach has been used in the papers on reliability in thermoelectricity up to now [4,6-8].

According to this version, the service life of a technical product similar to a human life can be divided into three periods (Fig. 1.):

1) The infantile period.

In the infantile period the intensity of failures, i.e. the number of product failures per unit of time is large and decreases with time till the next period. In the infantile period (which reminds of children's death rate in medical statistics) rough

mistakes of product manufacturing and assembling are found. The most unreliable samples are prone to failures.

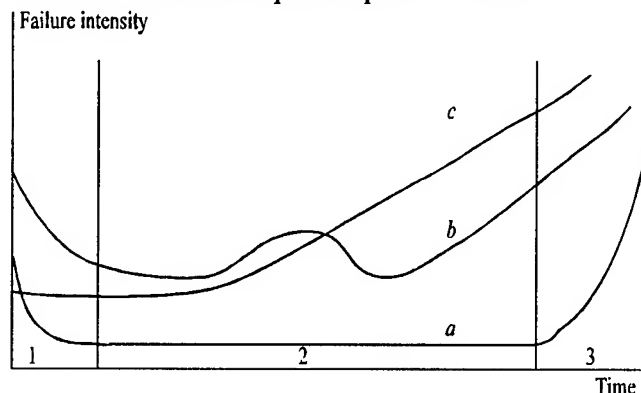


Fig. 1. Time dependencies of failure intensity.

a - human-like version of failure statistics with the exponential reliability model in useful period, 1 - infantile period, 2 - useful period, 3 - wear period; *b* - nonmonotonous failure intensity; *c* - model with latent period.

2) Useful period.

This period is characterized by a constant failure rate. As a rule, it is long and the most important for reliability analysis. For the useful period the so-called exponential model of failure intensity has been proposed in paper [1]. As far as constant failure rate λ is supposed, the probability of no-failure operation is described by the exponential time dependence

$$R(t) = \exp(-\lambda t). \quad (1)$$

Here mean time between failures (MTBF) is as follows

$$MTBF = \frac{1}{\lambda} = \text{const}. \quad (2)$$

3) The period of wear.

During this period the failure rate begins to increase. The results of product degradation accumulated during the previous periods start to tell. Generally the product service life is indicated before the onset of the period of wear.

The human-like version of life duration with the exponential failure model in the useful period has been dominating up to now in the papers on thermoelectric product reliability [6]. Note that there is no strict substantiation of this model and the assessment of its validity for thermoelectricity. This model is the simplest and most attractive from the standpoint of design facilitation. However, it does not outperform the other possible failure statistics model from the standpoint of the result validity. Modern reliability theory [9] has long been

considering other more complicated models, for instance those schematically shown in Fig.2. by curves b and c. The laws of probability distribution different from (1), for example, Weibull's law, are widely used.

$$R(t) = \alpha \lambda t^{\alpha-1} \exp(-\lambda t^{\alpha}); \alpha, \lambda > 0, \quad (3)$$

Γ - law

$$R(t) = \frac{\lambda^{\alpha}}{\Gamma(\alpha)} t^{\alpha-1} \exp(-\lambda t); \alpha, \lambda > 0, \quad (4)$$

others.

One can state that the exponential law used nowadays is only a kind of the simplest approximation, therefore for each group of thermoelectric devices the appropriate law of failure probability distribution must be determined on the basis of valid and representative statistical data.

One should note separately that the prospects and catalogues of firms manufacturing thermoelectric products never give the information about the mathematical reliability model used in these prospects and catalogues to define the parameters given therein. One can only suppose the use of exponential model. The exponential model becomes more accustomed and widely used, though valid reasons for its use still do not exist. There is a vicious circle - theoreticians consider that the exponential model is well substantiated by the experimental data and long-standing failure statistics of used products, while the manufactures and users think that the exponential model and all its consequences result from the scientific theory, and thus continue the processing of new statistical data on the basis of the same exponential model which has not been substantiated up to now.

1.2. Thermoelectric systems reliability parameters calculation.

Thermoelectric instruments and devices often contain thermoelement blocks or multi-element thermoelectric modules. Knowing the reliability parameters of individual thermal elements (or their arms) it seems possible to calculate the reliability parameters of system as a whole.

Thus, for example, in the simplest case at the series connection of N components the probability of non-failure operation of the whole system:

$$R_s(t) = \prod_{i=1}^N R_i(t), \quad (5)$$

where $R_i(t)$ is i -element probability distribution law. Note that the expression (5) is valid, if the system component failures are independent events from the standpoint of probability theory. For one type elements from (5) it follows that

$$R_s(t) = [R(t)]^N, \quad (6)$$

where $R_c(t)$ is failure probability of one component.

If we accept the exponential distribution law for the component

$$R_c(t) = \exp\left(-\frac{t}{T_c}\right), \quad (7)$$

the mean time of non-failure operation of the whole system

$$T_s = \frac{T_c}{N} \quad (8)$$

will be N times less the time of no-failure operation of one component. In paper [4] along with this simplest case a number of more complicated versions of parallel-series connection of thermoelectric system components have been considered. Among them there are also versions when the components connected in parallel add to the system reliability. These components are redundant during the non-failure product operation. But when one of the components fails they can partially fulfill the functions of the failed component. Therefore component failure does not result in the failure of the whole system, but only in the reduction of its operation parameters. If this reduction is less than the acceptable standard, the whole system does not fail. Similar circuits serve the example of using unreliable elements for the construction of sufficiently reliable systems.

The calculations made in [4] are based on a number of assumptions. The most significant assumption is that of Boolean failure model. It means that the component under consideration can be only in two states-serviceable and switched off ones. More complicated Markov failure models existing in the reliability theory [9] have not been considered. Of all the circuits considered in [4] the circuit Parallel Elements in Series has been recognized as the most efficient one. In this circuit each thermoelement arm is by-passed by the similar arm.

The second important assumption is that of the exclusive utilization in the considered circuits of one-type elements according to their reliability and functions. Meanwhile it is known [9] that the use of at least two types of active and passive components for reservation can decrease the cost of product with the increase of reliability.

The active elements here fulfill the main product functions, while the passive elements have only one function- to by-pass the open-circuit on the failed element. Therefore, the passive elements can be manufactured in the form of rather cheap resistors.

1.3. Recalculation of reliability parameters at accelerated tests

As far as temperature growth results in the failure intensity, it is only natural to use elevated temperatures to reduce the time of test. In paper [5,6] the possibilities of these accelerated tests have been considered. The recalculation of results obtained at a higher temperature T_h to determine MTBF at lower temperature T_l is based on Arrhenius law (Fig. 2)

$$\lambda(T) = \lambda_{T_0} \exp\left(-\frac{E_a}{kT}\right), \quad (9)$$

where λ_{T_0} and activation energy E_a are constants.

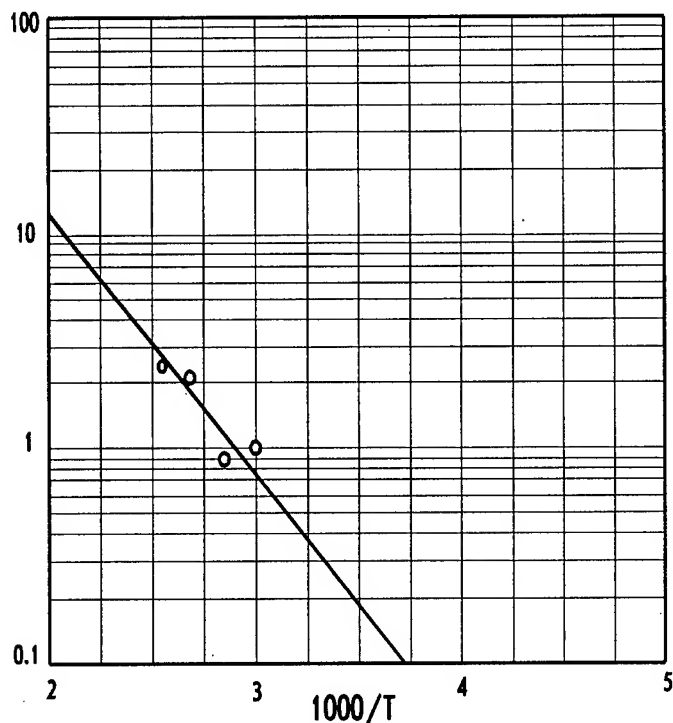


Fig. 2. An example of Arrhenius plot.

In this case, as is seen from the figure, the MTBF log dependence in temperature must be a straight line, with its slope defining the activation energy E_a . Then

$$MTBF(T_l) = MTBF(T_h)F_a, \quad (10)$$

where acceleration factor

$$F_a = \exp\left(\frac{E_a}{k} \frac{T_h - T_l}{T_h T_l}\right) \quad (11)$$

is uniquely determined by the activation energy E_a and temperatures T_h and T_l . Thus, for example, the equivalent mean time between failures at the temperature of 40°C is 30% higher than at 90°C.

Calculation of acceleration factor F_a by formula (11) can hardly be considered accurate in all the cases. The point is that Arrhenius law applicability is based on taking the logarithm of dependence (9). Admittedly, taking logs smooths considerably the spread in experimental points. Taking into account the exponential dependence (11) for acceleration factor insignificant errors in the activation energy determination can give significant deviations in the value of acceleration factor.

2. Use of the random processes theory

As the above given literature review shows only classic variants may be indicated as used ones (see Table) in the structure of RT main concepts and methods.

Table. Structure of modern reliability theory

Reliability theory		Is used in thermo-electricity
Fundamental	Probability and statistics	+
	Mathematical reliability models	
	Sets of reliability parameters	
Goals	Optimization and efficiency increase of devices and systems	+
	Estimation and prediction based on tests	
	Calculation of systems reliability	
Means	Classical probability theory	+
	Statistical estimations	+
	Random processes theory	—
	Optimal control theory	—
	Service theory	—
	Monte-Carlo method	—
	Computer modeling	—
	Correlation analysis	—

Let us show the possibilities of the modern reliability theory by the example of the failure prediction problem.

2.1. Failure area in the state systems phase space

Qualitative reliability indices based on the corresponding mathematical models were introduced into the reliability theory. A device or a system purpose, operating conditions and economical factors are taken into consideration therewith.

The main notion in the reliability theory represents the failure notion, that is, a gradual or a sudden failure of a device serviceability. The formalized theoretical description for this notion is based on the following for modern RT scheme of mathematical models structure. This scheme is based on the notion of a random process [10-12].

It is supposed that a industrial device state is defined by x point in the state phase space $X = \{x\}$. System states evolution is described by a random process $x(t)$. Among all possible states of the phase space $X = \{x\}$ states the subset X_0 corresponding to failure onset is stood out. Then failure-free performance can be measured by the time from the given moment to the moment of the phase point $x(t)$ entry into the subset X_0 which is the failure area in the phase space of the system states.

2.2. Failure prediction based on the correlation analysis

Let us examine the failure prediction on the basis of a diagram firstly used by Wiener and Kolmogorov for the solution of the random processes problem and signals filtration from interferences [10-11].

Let us consider the linear dynamic system when on its input a signal is come

$$\varphi(t) = x(t) + n(t), \quad (11)$$

where $x(t)$ is a random process of the studied device evolution, $n(t)$ is an interference. The purpose of the system is as most precise as possible prediction of the studied process at the time moment $t+\tau$. For this the signal on the system output $\mu(t)$ is to be required to be the best approximation for $x(t+\tau)$ from the point of view of the error dispersion.

Then, as it is shown in [12] the weighting function of the system $k(t)$ must satisfy the Wiener equation,

$$\int_0^t k(t, \tau) K_{\varphi\varphi}(\sigma, \tau) d\tau = K_{\mu\varphi}(t, \sigma); t_0 < \sigma < t, \quad (12)$$

where $K_{\varphi\varphi}$ is the autocorrelation function of a signal on the system input, $K_{\mu\varphi}$ is the mutual correlation function of the input and output signals.

The Wiener's equation (12) is the integral equation. Its solution $k(t, \tau)$ by the known methods of the dynamic systems theory permits to determine all parameters of the desired dynamic system capable to predict the process $x(t)$ evolution. Since all parameters of such prognosticator (at least in principle) can be found, it is also possible to perform its industrial realization as tests schedule, computer programs for measurements and data processing. It is essential that such approach takes into account errors of methods and instrumentation in measurements and prediction calculations by means of the introduced into the theory a random process of interference.

3. Conclusions

So, the classical version of the failure statistics with the exponential probability distribution law is used for reliability parameters calculation and statistical material on thermoelectric devices reliability processing.

The presently used exponential law is only some simplest approximation and hence the appropriate law of the failures possibility distribution is to be set up on the base of reliable and representative statistical data on failures for each group of thermoelectric devices.

Only circuits with the same type elements have been examined for calculation of complete thermoelectric systems with extra elements redundancy.

In comparison with such fields as electronics and measuring engineering, thermoelectricity up to now uses only simplest methods of the reliability theory and statistical material processing obtained in the process of testing and exploitation.

The random processes theory methods of correlating functions are proposed for thermoelectric devices failure prediction.

References

[1] P.Click, R.Marlow, "Reliability and failure modes of thermoelectric heat pumps", Proc. 2nd Intl. Conf. On Thermoelectric Energy Conversion, Arlington, Texas 1978, pp. 115-120.

[2] H.T.Leong, R.T.Martorana, "Finite element stress analysis of a thermoelectric cooler", Proc. 3rd Intl. Conf. On Thermoelectric Conversion, Arlington, Texas, 1980, pp. 86-91.

[3] David D.Allred, On Van Nguyen, "Accelerated life test for thermoelectric junctions: solder element interactions", Proc. 7th Intern. Conf. On Thermoelectric Energy Conversion, Arlington, Texas, 1988, pp. 137-140.

[4] D.A.Johnson, J.S.Kendrick, "Improvements in reliability of thermoelectric coolers through the use of redundant elements", Proc. 7th Intern. Conf. On Thermoelectric Energy Conversion, Arlington, Texas 1988 Ed. K.R.Rao, Ph.D., pp. 95-100.

[5] P.A.Dillon, L.McCarthy, M.I.Stephenson, "Effects of thermal cycling on thermoelectric modules", Proc. 9th Intern. Cons. On Thermoelectrics CIT, Pasadena, 1990, JPL, pp. 136-142.

[6] Richard N.Alonso, Dwight A.Johnson, Roger Devilbiss, "Predicting thermoelectric cooler reliability for the telecommunications industry", Proc. XI Intern. Conf. Thermoelectrics, Univ. Texas, Arlington, 1992, pp. 312-318.

[7] J.H.Kiely, D.V.Morgan, D.M.Rowe "Failure Analysis of a Thin Film Thermoelectric Generator", Proc. XIII Intern. Conf. On Thermoelectrics, Kansas City, Missouri, USA, 1994.

[8] R.M.Redstall, R.Studd, "Reliability of Peltier Coolers in Fiber-Optic Laser Packages", in *CRC Handbook of Thermoelectrics*, Ed. D.M.Rowe, CRC Press, Inc., pp. 641 - 645, 1995.

[9] K. Reinschke, *Modelle zur Zuverlassigkeits und Empfindlichkeitsanalyse von System*, bd.1, Berlin VEB Verlag Technik, 1973; bd.2, Berlin VEB Verlag Technik, 1974.

[10] N.Wiener., *Extrapolation, interpolation and smoothing of stationary time series*, J.Willey, N-Y, 1950.

[11] A.N.Kolmogorov, "Interpolation and extrapolation of steady-state random sequences", *Izv. AN USSR, ser. math.* v.5, # 11, 1941, p. 3- 11.(in Russian).

[12] Ya.N. Rojtenberg, *Automatic control*, M., Nauka publishers, 1978. (in Russian).

The Design Problems of Thermoelectric Heat Pumps for Transportation Facilities.

A.A. Aivazov Y.I. Stern K.B. Makhratchev, A.V. Morgal
Moscow Institute of Electronic Engineering, Terif Ltd.

Abstract.

The paper describes the problems of design and construction development of thermoelectric (TH) air chillers for different means of transport. The report contains the description of the temperature operating conditions of TH air chillers and the procedures of the TH air chiller testing. The results of the stand operation of the TH air chiller at various voltages are analyzed. The paper highlights TH modules mathematical modeling by means of equations account for the variation of the main TH properties across the thermocouple with the temperature gradient. The modeling of TH module operation is based on the numerical solution of a second order nonlinear differential equation. The solution obtained is compared with the results got by a crude method and from the stand testing.

1. Choosing of the Chiller Operation Conditions.

When developing TH air chiller one is up against a number of problems deriving, first of all, from the specificity of the use of TH systems for cooling. It has been spoken much about earlier, specifically in [1], which shows analogy between the hydraulic and the thermal pumps and emphasizes the optimization of TH modules construction stemming from the fixed operation conditions. It has also been demonstrated that the use of TH modules at rated voltages is inefficient because the rated voltage is usually calculated for obtaining the maximum temperature difference permitted by the module. This voltage corresponds to the temperature drop of 60-70 K, and it is much more than is needed for cooling ($\Delta T_{\text{module}} = 30$ K for typical air chillers). The problems of adjustment of TH modules for thereof use in the chillers are described in paper [2], but its authors described rather unusual method of heat removal (evaporated system) negating all TH advantages (compactness, lightness, ability to operate in any position in space).

We set ourselves the task of developing the TH chiller which, on one hand, would operate efficiently, on the other hand, would contain all the advantages of TH systems. It is precisely the chiller that will be suitable for the installation into an average automobile where the limited space and vibration do not allow traditional compressors. The same could be said about the trucks though the space requirements imposed on their cooling blocks are less strict.

The TH modules similar to Melcor CP1.4-127-045 TL have been used to construct the chiller. In [1] we showed that in order to increase the efficiency of operation of TH modules assembled in a chiller it is necessary to increase the area of the thermocouple cross section leaving the height invariable. The maximum ratio A_0/L (A_0 - area of TH couple cross section, L - TH couple length) distinguishes CP 1.4-127-045 module from other widely used and relatively inexpensive TH modules. All the data in

this report correspond to CP1.4-127-045.

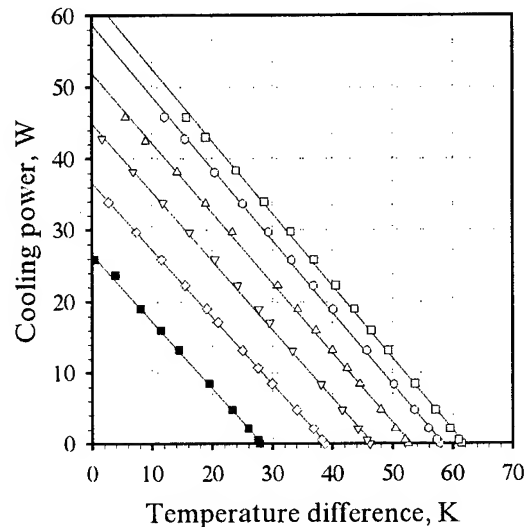


Fig. 1.1 Load characteristics of the analog of Melcor CP1.4-127-045 at various voltages.

□	15,2 Volts	▽	8,0 Volts
○	12,5 Volts	◇	6,0 Volts
△	10,0 Volts	■	4,0 Volts

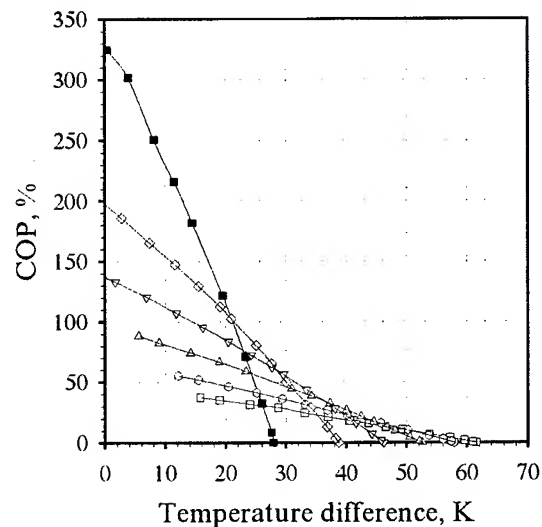


Fig. 1.2 COP characteristics. Designation is similar to that of Fig 1.1.

A series of the module load characteristics are represented on Fig. 1.1, Fig 1.2 shows COP for this module at indicated voltages. In the paper [1] we have already

proved that while constructing the chiller which is supposed to provide the temperature drop of 10 - 20 K, it is necessary to do all the calculations for the module which provides maximum efficiency at 30 - 40 K temperature difference. Basing on the above mentioned assumption and relying on Fig. 1.2 the modules used in the chiller are to operate at 8-10 V to achieve maximum efficiency.

TH air chiller TK1-06-740 has been designed and built to fit those requirements. 20 TH modules have been built into the chiller; at 12 volts/module the power consumption equals to 1680 W, at 7 V/module it is 588 W.

2. Comparative characteristics of chillers of different constructions.

A testing stand of 1 m³ has been developed and constructed to test chillers. The surface area of this volume is 6.75 m². The walls of the container have been made of veneer - 8mm and foam plastic - 50 mm. Heat penetration for the stand involved was 5 W/K. So, to maintain the temperature inside 20 K less than the environment temperature 100 W is to be removed. A heating element with maximum power of 1 kW has been installed into the stand to imitate the actual practice. The heater has been connected with a special device which provided a graduate variation of the heating power. The load on the chiller Q at temperature drop ΔT and power of the heating q has been calculated as follows

$$Q = q + 5 \cdot \Delta T \quad (2.1)$$

Both the chillers operating at usual voltage and the chiller operating at reduced voltage have been tested on that stand. The test results are showed on Fig. 2.1.

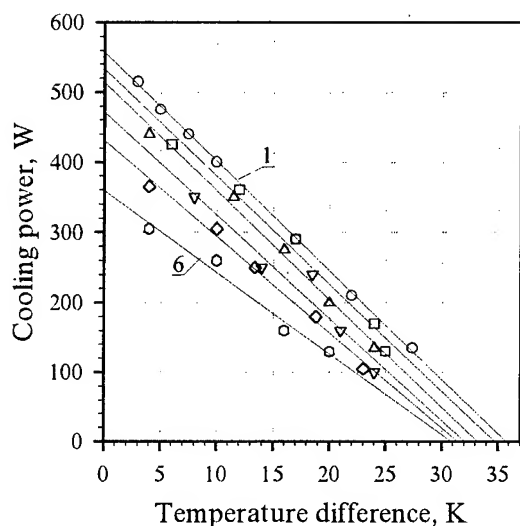


Fig. 2.1 Comparison of loading characteristics of the chillers.

- 1. ○ 12 V/module, 1680 W
- 2. □ 10 V/module, the same device
- 3. △ 9 V/module, the same device
- 4. ▽ 8 V/module, the same device
- 5. ◇ 7 V/module, the same device
- 6. ○ 12 V/module, device 960 W

As one can see from Fig. 2.1 module operation at reduced voltage results in essential increase in COP. For

instance, the chiller containing 20 modules operating at 7 V each consumes 588 W. It is also clear its cooling power in the whole range of the temperature drop is higher than the cooling power of its analog containing 12 modules operating at 12 V each and consuming 960 W.

Let us consider in details the temperature regimes of the operation of 20-module chiller in the following conditions: temperature drop: environment-cooling volume - 17 K, cooling power - 290 W, voltage at module - 10 and 12 V. Measured temperature drops at its basic blocks are represented in Table 2.1.

Voltage at module, V	12	10
Power consumption, W	1680	1160
Cooling power, W	290	290
ΔT_1 cooling volume - environment, K	17	17
ΔT_2 hot heat exchanger - hot slide, K	34.8	30.9
ΔT_3 cold heat exchanger - cold slide, K	5.0	5.6
ΔT_4 hot heat exchanger - environment, K	12.8	9.3

Table 2.1 Comparison of temperature regimes of chiller operation.

The values $\Delta T_1 + \Delta T_4$ correspond to the values $\Delta_1 + \Delta_4$ of paper [1] respectively. ΔT_1 is a temperature drop which is to be provided by the chiller. ΔT_2 is a temperature drop which the TH modules of a chiller operate at. ΔT_3 shows the efficiency of the heat exchanger at cold slide: the lower is ΔT_3 , the better is the conditions of modules operation. ΔT_4 - the same as ΔT_3 but for hot slide. So it is obvious the increase in cooling coefficient is due to twofold effect:

1. The modules operate at reduced temperature drop and thereof cooling efficiency is higher (according to Fig. 1.1).
2. The modules operate at reduced voltage and, hence, the COP is higher (it is well seen from Fig. 1.2).

In conclusion, let us consider the COP of the chiller operating at the temperature drop between the cooling volume and environment of 10 K at various voltages.

Voltage, V/module	12	10	8	7
Cooling power, W	400	390	350	305
Power consumption, W	1680	1160	736	588
COP, %	23.8	33.6	47.6	51.9

Table 2.2 Parameters of 20 - module chiller operation at temperature drop between cooling volume - environment of 10 K and various voltages.

One can see from Table 2.2 at temperature drop of 10 K the operating conditions at voltage 7 V/module are the most efficient in terms of increasing the COP. However the operating conditions are considered to be optimal at 8 V/module if the cost of the device is taken into account (it is naturally increases with the increase in the number of the modules). As a rule, the generator voltage in trucks is 24V, hence, modules of the chiller are to be commutated in a special way or (when using another power supply) a special adapter must be included in the chiller. It is obvious the first variant is more preferable in terms of economy. So, the module operation at the voltage of 8 V does not require any additional converters with the constraint the number of the modules is a multiple of 3.

3. Numerical solution of the basic thermocouple equation.

To find the temperature distribution along the thermocouple the equation (6) of the paper [3] has been used. It is follows:

$$A_0 \chi \cdot \frac{d^2 T}{dx^2} + A_0 \cdot \frac{d\chi}{dx} \cdot \frac{dT}{dx} - IT \cdot \frac{dS}{dx} + \frac{\rho I^2}{A_0} = 0 \quad (3.1)$$

$$0 < x < l, T(0) = T_{cold}, T(l) = T_{hot},$$

where T_{cold} and T_{hot} are the temperatures of the cold and hot slides respectively. Since ρ, χ, S are the functions of the temperature the equation does not have any analytical solution. Let us consider the numerical solution of the equation involved. First, let us rewrite the equation (3.1) as follows:

$$\frac{d}{dx} \left(\chi \frac{dT}{dx} \right) - \frac{I}{A_0} \cdot \frac{dS}{dx} \cdot T + \frac{\rho I^2}{A_0^2} = 0 \quad (3.2)$$

$$0 < x < l, T(0) = T_{cold}, T(l) = T_{hot},$$

and introduce the uniform grid $\{x_i = i \cdot h, 0 \leq i \leq N+1, h \cdot (N+1) = l\}$ at section $[0, l]$. At this grid problem (3.2) can be approximated by a differential scheme:

$$\frac{1}{h} \left[a_{i+1} \cdot \frac{T_{i+1} - T_i}{h} - a_i \cdot \frac{T_i - T_{i-1}}{h} \right] - q_i \cdot T_i + f_i = 0 \quad (3.3)$$

where

$$a_i = \frac{1}{2} [\chi(T_i) + \chi(T_{i-1})],$$

$$q_i = \frac{I}{A_0} \cdot \frac{S(T_{i+1}) - S(T_{i-1}))}{2h},$$

$$f_i = \frac{I \rho(T_i)}{A_0^2},$$

$$1 \leq i \leq N, T_0 = T(0) = T_{cold}, T_{N+1} = T(l) = T_{hot}$$

If we designate the left-hand side of the equation (3.3) by $g_i(T)$, where T is vector-column $(T_1 \dots T_N)^T$, and eliminate known values T_0 and T_{N+1} from the equation, the problem (3.3) can be represented as a system of nonlinear algebraic equations:

$$\begin{cases} g_1(T_1 \dots T_N) = 0 \\ g_2(T_1 \dots T_N) = 0 \\ \dots \dots \dots \\ g_N(T_1 \dots T_N) = 0 \end{cases} \quad (3.4)$$

or, in operator form:

$$AT = 0 \quad (3.5)$$

Please, note that each equation of the system (3.4) binds no more than three unknown values: T_{i-1}, T_i and T_{i+1} . For the solution of system (3.4) the modified Newton's method is applied [5]. Here is the basic idea of the method. Let's assume we have some crude solution of (3.5) and denote it as $T^{(k)}$. It is obvious that $T^{(k)}$ meets the following condition:

$$AT^{(k)} = r^{(k)} \quad (3.6)$$

where $r^{(k)}$ is a nonzero vector-column. In this case according to Newton's method close approximation $T^{(k+1)}$ can be determined resting upon the following expressions:

$$B^{(k)} p^{(k)} = r^{(k)}, \quad (3.7)$$

$$T^{(k+1)} = T^{(k)} - \tau^{(k+1)} p^{(k)}, \quad (3.8)$$

where $\tau^{(k+1)}$ is an iterational parameter which depends upon the condition of the iterational process (3.6) .. (3.8) convergence at any initial approximation,

$B^{(k)}$ is Jacoby matrix of the system (3.4)

$$B^{(k)} = \begin{vmatrix} \frac{dg_1}{dT_1} & \frac{dg_1}{dT_2} & \dots & \frac{dg_1}{dT_N} \\ \frac{dg_2}{dT_1} & \frac{dg_2}{dT_2} & \dots & \frac{dg_2}{dT_N} \\ \dots & \dots & \dots & \dots \\ \frac{dg_N}{dT_1} & \frac{dg_N}{dT_2} & \dots & \frac{dg_N}{dT_N} \end{vmatrix},$$

Matrix $B^{(k)}$ is a ternary-diagonal matrix and to deduce vector $p^{(k)}$ common methods can be applied.

So, the algorithm of the numerical solution of the equation (3.1) with a given accuracy can be described in the following way:

- 1) Assuming that ρ, χ, S are not the functions of the temperature solve the problem (3.1) analytically and use the obtained solution in the grid nodes as an initial approximation T_k for the iterational process (3.6) - (3.7).
- 2) Solve the system (3.6) for $k = 0, 1, \dots$ and find vector $p^{(k)}$.
- 3) Choose parameter $\tau^{(k+1)}$ resting upon [4] and determine $T^{(k+1)}$ by means of (3.7).
- 4) Finish the iterational process if the following condition for the approximation $T^{(k+1)}$ is fulfilled:

$$\max_{1 \leq i \leq N} \left\{ \frac{|T_i^{(k)} - T_i^{(k+1)}|}{T_i^{(k+1)}} \right\} < \varepsilon$$

where ε is a given accuracy of the equation (3.1) solution. We assumed $\varepsilon = 10^{-6}$.

This algorithm has been realized by the computer with Pentium 120 MHz processor and translator NDP Fortran 486 has been used for the compilation.

The temperature dependence of ρ, χ, S has been taken from the "Melcor" catalogue. These data are shown in Table 3.1. For the TH module the temperature description along the thermocouple has been modulated by means of the program and then the cooling power of one thermocouple and the whole module have been calculated according to the formula (1) from the paper [3].

TH property	Temperature dependence
ρ , Ohm·m	$5.37 \cdot 10^{-8} T - 4.9837 \cdot 10^{-7}$
χ , W/m·K	$-4.044 \cdot 10^{-3} T + 2.8794$
S , V/K	$3.521 \cdot 10^{-7} T + 1.061734 \cdot 10^{-4}$

Table 3.1 Temperature dependence of TH characteristics of the module.

The calculations have been carried out for currents 3.65A and 8.0A, they correspond to module voltages 8V and 15V respectively. Temperature distribution along the thermocouple for current intensity of 3.65 A is demonstrated on Fig. 3.1 - 3.2. Fig. 3.1 shows temperature distribution along the TH couple at maximum cooling power ($T_{cold} = T_{hot}$) and current intensity of 3.65 A, Fig. 3.2 shows temperature distribution along the TH couple at current intensity of 3.65 A and temperature difference 40 K. On all plots the numerical solution is designed by "1" and the analytical - by "2".

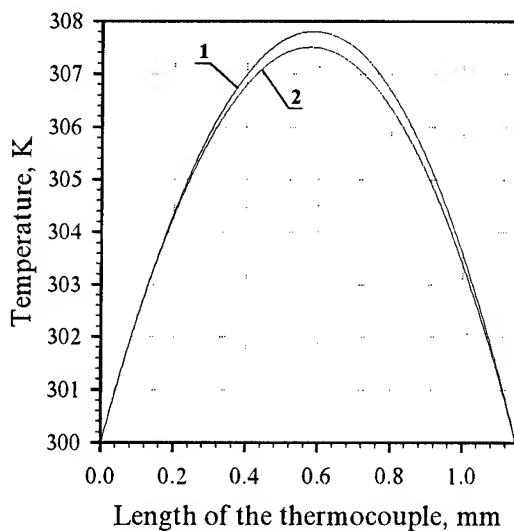


Fig. 3.1 Temperature distribution along the TH couple at current 3.65 A.

As one can see on the plot discrepancy between the numerical and analytical values increases as the temperature drop on module increases, but even at temperature drop of 40 K the difference is less than 1 K. It is clear that the values of the module cooling power differ also insignificantly for this current intensity. The discrepancy increases as the current flowing through the TH couple increases.

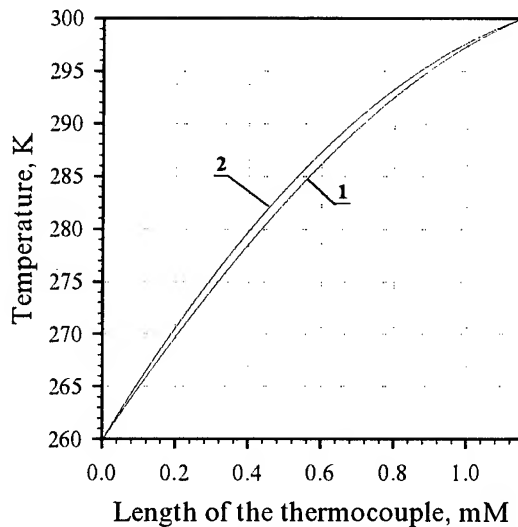


Fig. 3.2 Temperature distribution along the TH couple at current 3.65 A.

Fig. 3.3 represents the results of the calculations for current intensity of 8 A and at $\Delta T = 0$ K. Fig 3.4 demonstrates temperature distribution at the same current and $\Delta T = 40$ K. At the current of 8 A reverse phenomenon occurs: the discordance between the numerical and analytical solutions increases as the temperature drop decreases. At the temperature drop of 40 K the maximum difference is less than 5 K, at the $\Delta T = 0$ K it is 8.8 K. Naturally,

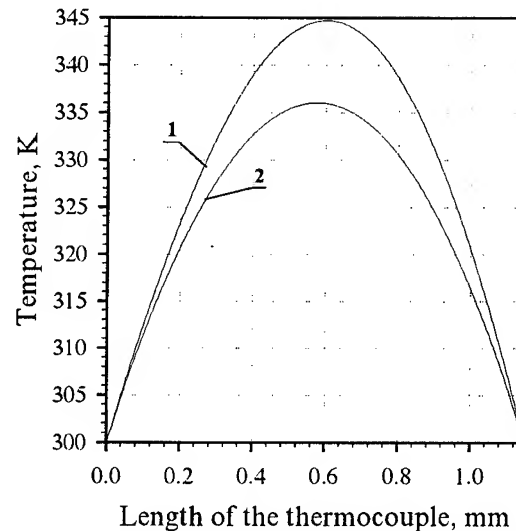


Fig. 3.3 Temperature distribution along the TH couple at current 8 A.

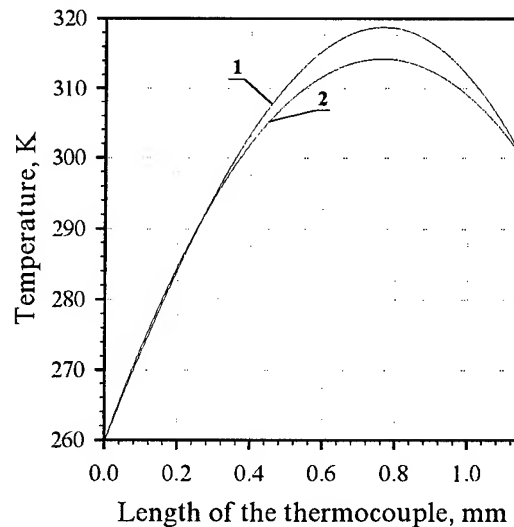


Fig. 3.4 Temperature distribution along the TH couple at current 8 A.

that the disparity between the cooling power values calculated by two different methods also increases. Fig. 3.5 conveniently illustrates that fact. As shown at Fig. 3.5 the numerical solution slightly differs from the analytical one, furthermore, at low temperature drops ($\Delta T < 40$ K) the analytical solution better correlates with the experiment. Nevertheless the numerical solution has allowed a deep understanding of the heat transfer processes in thermoelements as well as limits of module optimization. Let us illustrate it by a concrete example.

In paper [2] the authors suggested the thermocouple height should be reduced to 0.1–0.2 mm. Fig 3.3 clearly shows the effect of reduction. If module operates at current 8 A, $T_{hot} = 300^\circ\text{K}$ and temperature drop 0 K, according to the calculations, the temperature of the middle part of the thermocouple will be approximately 44–45 K higher the temperature of the hot slide. So, reducing the height of

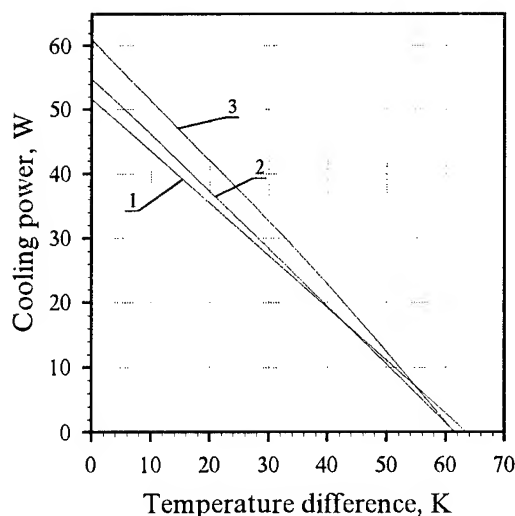


Fig. 3.5 Comparison of load module characteristics at current of 8 A. 1 - numerical solution, 2 - analytical, 3 - experimental module cooling power.

the thermocouple by half results in the same cooling power, but the temperature drop of $44 \div 45$ K. The calculation shows the cooling power equals to 51.6 W at the temperature drop of 45 K and the height of the thermocouple of 0.6 mm. It corresponds to the cooling power at the temperature difference of 0 K and the height of the thermocouple 1.15 mm. Furthermore, the part of the material will be "discarded". It will enable us to reduce the voltage drop at the thermocouple (and hence at the module) leaving the current strength invariable. Due to this measures the energy consuming will be diminished and, hence, the COP increased at the same cooling power.

Conclusions.

1. When constructing the chillers for means of transport it is desirable to use modules Melcor CP1.4-127-045 (or thereof analogs) at the voltage of 8 V.
2. For the operation conditions with the temperature drop of 40 K and high (more than 2.6 A/mm^2) currents it is desirable to produce module with the height of thermocouple 0.6 mm, and the area of the cross section of 1.4 mm^2 . Since the production of the thermocouple of the height less than 1 mm presents some technological difficulties it is possible to use modules with the equivalent ratio A_0/L , i.e. with the area of the cross section of 2 mm^2 and the height of the thermocouple 1.15 mm, for the current of 8 A. The module CP2.0-127-045 ideally suits the operation at 8 A, but, unfortunately, it is not produced commercially.

We would like to express our special thanks to the head of laboratory of difference methods of Moscow State University, professor Evgeniy S. Nikolaev, who placed at our disposal the computer with Pentium 120 MHz processor and gave some valuable remarks.

Nomenclature

T	temperature
T_{cold}	cold slide temperature
T_{hot}	hot slide temperature
$T_i^{(k)}$	temperature at i -th node of the grid at k -th iteration
x	one-dimensional Cartesian coordinate
ρ	electrical resistivity
χ	thermal conductivity
S	Seebeck coefficient
I	electrical current
A_0	cross-sectional area
L	length of the TH couple

References

- [1] A.A. Aivazov, Y.I. Stern, K.B. Makhratchev, Optimization of the Thermoelectric Air Chillers Construction: XIV ICT, (1995).
- [2] Rokusaboroh Sakai. Proposal for Electronic Air Conditioning Systems Using Semiconductor Thermo-Electric Conversion: XIII ICT, p. 511-515 (1994).
- [3] Kuan Chen, Scott Gwilliam, Behnam Entezam. Heat Transfer Analysis and Optimization of Thermoelectric Cooling Systems: XIII ICT, p. 395-403 (1994).
- [4] J.E. Dennis Jr., R.B. Schnabel. Numerical Methods for Unconstrained Optimization and Nonlinear Equations. "Mir", Moscow, p. 144-159 (1988).

Thermal Management of Power Electronics using Thermoelectric Coolers

Jan W. Vandersande and Jean-Pierre Fleurial
Jet Propulsion Laboratory/California Institute of Technology
Pasadena, CA 91109

Abstract

Many high power electronic devices, such as power amplifiers and microprocessors, operate at high temperatures close to or at the edge of their reliability, which could severely impact performance and operating lifetime. These devices thus need cooling to improve performance and reliability. Conventional thermal management techniques, most of which will be discussed, are not well suited to the specific problem of cooling discrete or localized heat dissipating devices since they generally cool the whole board. Moreover these techniques have difficulty dealing with the large heat fluxes associated with the high density packaging of power devices. The specific problem of spot cooling of power devices can be very effectively solved by using the combination of diamond substrates and a thermoelectric cooler. The highest power components would be mounted directly on a diamond substrate (ideally the top substrate of the cooler) allowing the cooler/diamond combination to maintain the temperature of the device from a few degrees to tens of degrees below that of the substrate on which the cooler is mounted (diamond or any other high thermal conductivity material). This will allow the device to operate at a low enough temperature to increase both reliability and clockspeed. It has been determined that the highest cooling power densities will be achieved with thin film coolers with cooler leg lengths on the order of 20 to 50 microns. The results of a solid state power amplifier (MMIC) cooled using a diamond/cooler combination will be presented and discussed.

Introduction

The demand for increased speeds of integrated circuits, computers etc. is accompanied by higher power levels and a higher packaging density. Combined, these requirements result in very high power densities and thermal problems, which limits integration of devices and components on the board. An example of the expected increased power levels is a Solid State Power Amplifier (SSPA), a MMIC used for microwave applications, which is expected to go from a current output of 5 W to 30 W within a few years. That increase will multiply the heat flux that has to be removed from approximately 30 W/cm² to over 100 W/cm². This higher heat flux density will result in a major thermal management problem that will have to be addressed using novel techniques. In addition, many devices are currently or will be operating at or near the edge of reliability, and so they will need to operate at lower temperatures, especially mission critical military equipment.

The demand for increased processing speed has resulted in increased packaging densities because the signal delay times are directly proportional to the physical distance between components. Additionally, faster clock rates call for faster logic, which necessitates more power, while an increase in the functional density of processors also results in a larger power requirement. At the chip level, the most performance can be obtained if the junction temperature can be maintained at a tolerable level. Ideally, a reduced temperature and a closely controlled thermal environment is needed. The best way to ensure this is by using active cooling. Several cooling techniques will be discussed below.

Cooling Techniques

Cooling techniques can be broken up into conventional and advanced cooling. Conventional cooling consists of external natural or forced convection and conduction. The most common form of convection is the use of fans whereby heat is removed by the airflow. It is best to place the hottest components in the center of the board because that is where the heat flow is the greatest. To increase cooling means more air flow, which can only be achieved by more and/or larger fans. The disadvantage of fans is that they do occasionally need repairs and that they are noisy. The other conventional form of cooling is conduction using high thermal conductivity materials such as copper, aluminum etc. Heat is conducted to the sides of the board and then to the heat sinks, so the hottest components should be at the edges of the board. In both cases there will still be hot spots on the board. These conventional cooling techniques cannot prevent that.

There are various advanced cooling techniques and some of these will be discussed briefly. Micro heat pipes use the phase change of water or methanol in a closed loop that uses the capillary effect to circulate the fluids. It is a closed loop technique with a high heat transfer coefficient. Micro heat pipes are being used in laptops, in which a copper pad at the end of the heat pipe is placed directly underneath the processor to remove the heat [1]. Micro channel liquid flow uses the flow of water through micro channels embedded in the silicon substrate to remove heat generated by the components on the board [2]. This method has a high heat transfer coefficient and can dissipate a large amount of heat but a pump is needed so there will be possible reliability problems. A method developed more recently and that holds promise is spray cooling. It uses the phase change of a dielectric fluid, such as fluorinert, that is sprayed onto the hot parts. Heat is removed during the phase change from

liquid to gas. A closed system is needed to collect, recondense, and pump the fluid. Fluorinert mist cooling is almost two orders of magnitude more efficient than forced air cooling. It takes approximately 1 W of power for 25 W of cooling (COP~25) [3]. Spray cooling can be used to spot cool single devices or the entire board. This is a promising new cooling technique but the system has to be leak tight and the reliability of the pump is an issue. A final advanced cooling method is the use of novel very high thermal conductivity materials such as diamond, AlN, and carbon-carbon composites infiltrated with diamond. Diamond, with the highest thermal conductivity known (1500-2000 W/cm-K [4]) will set the limit for passive cooling.

The cooling of power electronics with thermoelectric coolers has several advantages. One of the most important of these is the ability to spot cool discrete or localized devices and to be able to reduce the temperature of the device below ambient. This reduction in temperature increases the reliability, lifetime, and clockspeed of the device. For example, a 10 degree reduction in temperature will result in a 3 to 5 Mhz performance improvement. None of the cooling techniques discussed above have the capability of reducing the temperature below ambient. An additional advantage of thermoelectric coolers is the capability of handling large heat fluxes. The main disadvantage of using thermoelectric coolers is the introduction of additional heat into the board (could easily double the heat output of the device). This additional heat has to be removed from the heat sink so an additional cooling technique is needed, such as a high thermal conductivity substrate or a heat pipe. The large heat input is due to the low COP of thermoelectric coolers, which obviously varies over a large range depending on the temperature difference required, the thermal conductivity of the substrates and the thermal gradient. The cooling power density of SOA coolers is limited, which is why it is necessary to go to thin film coolers in the cases of large heat fluxes.

Cooling of a Power Amplifier

Solid State Power Amplifiers (SSPA) for microwave applications (MMIC) are used in spacecraft for telecommunications. A typical 5 Watt SSPA (made by Texas Instruments) is a 5.4 mm by 3.0 mm by 0.1 mm thick GaAs device that dissipates 8 Watts of thermal power [5]. In spacecraft applications the SSPA has a peak operating temperature around 110°C using PbSn solder and a moly shim bonded to the heat sink.

This temperature is too high and needs to be lowered to increase reliability and efficiency. For a GaAs device the lifetime increases by about an order of magnitude (in hours) for every 25°C drop in temperature [6]. Advanced active thermoelectric cooling is needed to reduce the temperature to more acceptable levels.

An experimental microwave setup was put together to determine the effect of advanced active cooling on an actual SSPA. The device was soldered to a metallized diamond substrate. This diamond substrate acts as a heat spreader from the small device to the larger cooler (discussed in detail earlier [7]). The diamond substrate was bonded to a non-optimal commercial "off-the-shelf" cooler using diamond-filled epoxy. The results of the test were very encouraging. The junction temperature of the device was reduced to 62°C using the cooler from a temperature of 88°C using the conventional moly shim and PbSn solder. This reduction in temperature increases the device reliability 100 fold and the efficiency was found to have increased by 10-15%. Using an optimized bulk cooler or micro-cooler, with diamond substrates instead of alumina and optimized I/A legs, would reduce the temperature even further. The key to further improvement is to go to thin film coolers.

Thin Film Coolers

The main benefit of going to thin film coolers is the dramatic increase in cooling power density since it is inversely proportional to the length of the thermoelectric legs. Heat flux densities up to several hundred watts per square centimeter can now be removed. A 30 watt power amplifier dissipates about 150 W/cm² compared to about 30 W/cm² for a 8 watt chip. Thin film coolers will allow lighter, smaller devices and higher packaging densities. Coolers could fit right under the power amplifier chips thus allowing closer packaging of components.

Figure 1 shows the cooling power density comparisons for a SOA commercial cooler with 2mm legs, for a bulk micro-cooler with 200µm legs, and for a thin film cooler with 20µm legs. These curves are for a hot side temperature of 330K and for diamond substrates, rather than alumina, on the cooler. The use of diamond, which has the highest thermal conductivity known (approximately two orders of magnitude greater than that for alumina), is necessary so that as small a ΔT as possible is dropped across the substrate. If alumina substrates are used then the top two curves would drop off substantially faster at the lower cold side temperatures. As can be seen from the figure, the cooling power density of the thin film cooler is approximately two orders of magnitude greater than that for the SOA current cooler and one order of magnitude greater than that for the bulk micro-cooler. The reason to go to thin film coolers is thus very obvious. However, considerable development work is still needed before thin film coolers are ready to be used. Areas that need development are the deposition and characterization of Bi₂Te₃-based films, bonding of metallized diamond substrates to the thermoelectric films, and the patterning, etching, bonding and testing of the cooler. Figure 2 shows the proposed schematic for the metallizations and bonding scheme for the diamond and the thin film thermoelectric material.

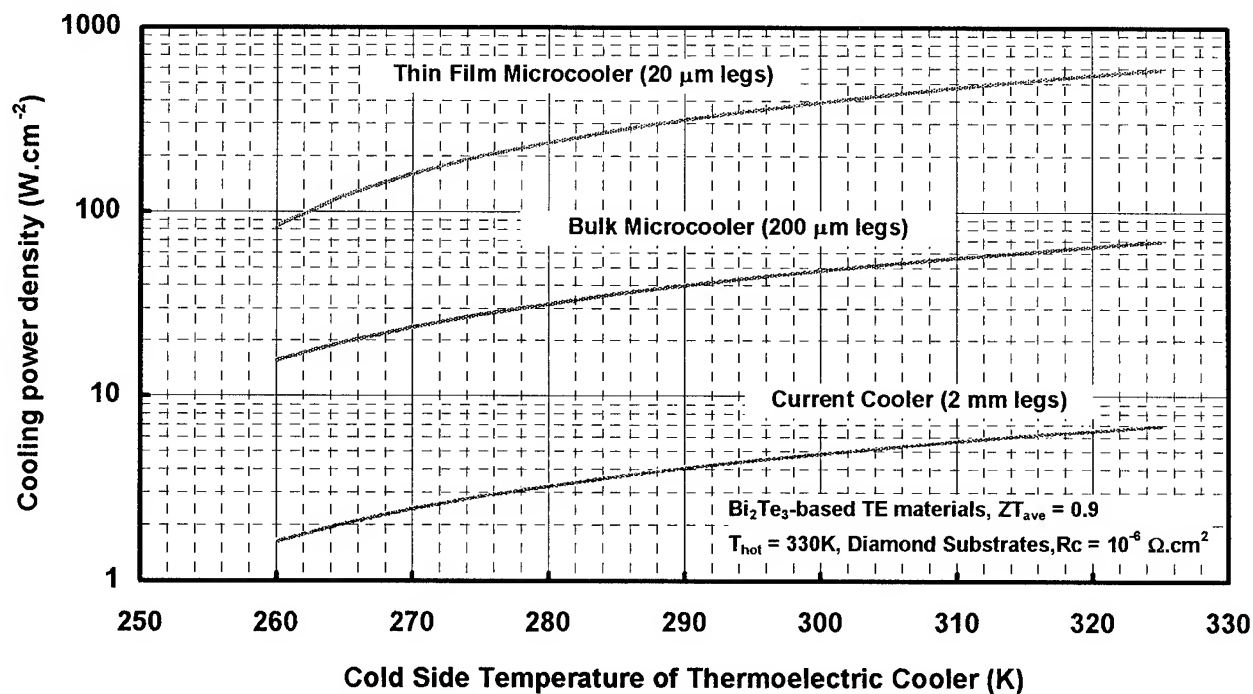


Fig. 1: The cooling power densities as a function of the temperature gradient across the thermoelectric device for three different kinds of coolers.

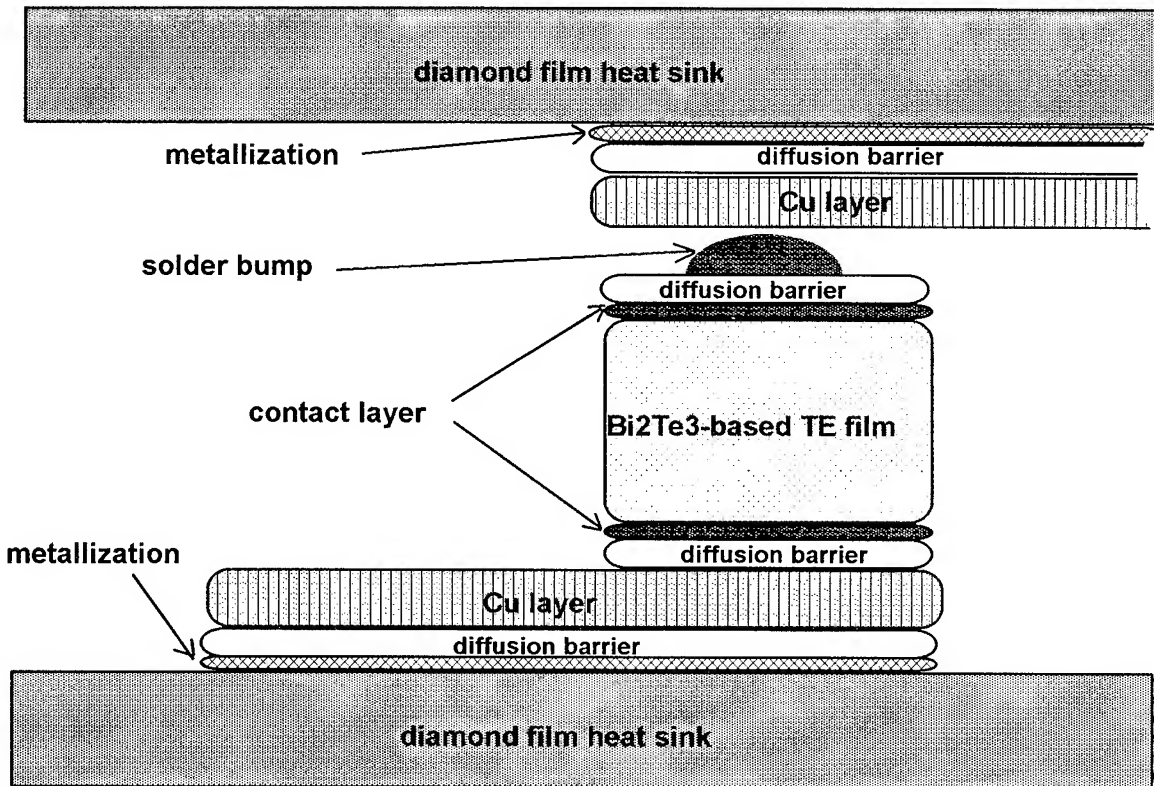


Fig. 2: Schematic of a thin film thermoelectric device with diamond substrates.

The scheme involves many layers, some of which have already been developed or are in the process of being developed. Some of the layers and barriers are fixed in composition (such as the diffusion barrier between the Cu electrode layer and the Ti metallization, which will be an amorphous silicide e.g. Ta-Si-N) while others are still in the development stage with several possibilities.

Conclusion

The demand for increased speeds and higher power levels for electronic devices such as power amplifiers and microprocessors has resulted in thermal problems on the component and board level that need to be solved. The spot cooling of these power devices and microprocessors is needed to increase reliability, efficiency, and clockspeed. Many of these devices are already operating at the limit of reliability. Thermoelectric coolers combined with diamond substrates are one of the most promising methods to spot cool these power producing devices. The highest cooling power densities can be achieved with thin film coolers (two orders of magnitude greater than SOA bulk coolers). However, thin films coolers are not available yet, but work is in progress to develop them.

Acknowledgments

The authors would like to thank Dr. Elizabeth Kolawa, Dr. Amy Ryan, and Marty Hermann for many helpful discussions. The work described in this paper was performed at the Jet Propulsion Laboratory/California Institute of Technology under contract with the National Aeronautics and Space Administration.

References

1. Thermacore Inc., private communication.
2. M.M. Sherman and G.O. Campbell, in the Proceedings of the Spacecraft Thermal Control Symposium, Albuquerque, Nov. 1994
3. Isothermal Systems Research Inc., private communication.
4. J.R. Olson, R.Q. Pohl, J.W. Vandersande, A. Zoltan, T.R. Anthony, and W.F. Banholzer, Phys. Rev. B., **47**, 14850 (1993)
5. M. Herman, JPL, private communication
6. E.A. Amerasekera and D.S. Campbell, *Failure Mechanisms in Semiconductor Devices*, pp. 7-10, Wiley-Interscience, 1987
7. J.W. Vandersande, R. Ewell, J-P. Fleurial, and H.B. Lyon, 13th International Conference on Thermoelectrics, Kansas City, MO, 1994, AIP Conference Proceedings 316, pp. 174-176.

Application of Bismuth-Telluride Thermoelectrics in Driving DNA Amplification and Sequencing Reactions

by John Hansen & Michael Nussbaum

MJ Research, Inc., 149 Grove Street, Watertown Mass. 02172 U.S.A.

Abstract

Recently a new application for low-temperature thermoelectric modules has emerged in the fields of biology and medicine. Laboratory instruments that thermally cycle small biological samples for purposes of DNA amplification are now common in research labs throughout the world, and instruments based upon several different technologies have been developed. Market forces are increasing showing that thermoelectrics are very well suited to this task, but several hurdles must first be overcome in order to build a quality instrument. Chief among these is the need to build modules optimized for thermal cycling, and data are presented here to document a particularly rugged design of module that works well in this demanding application.

DNA Amplification Technologies

In the mid-1980's, Kary Mullis of the Cetus Corporation developed a revolutionary technique for accurately identifying and synthetically amplifying specific molecules of DNA, so that sufficient quantities of the DNA could be made for easy analysis by conventional laboratory techniques.¹ The DNA molecules-of-interest serve as templates for iterative replication, which results in an exponential amplification of the DNA.

The technique, called the polymerase chain reaction (PCR)² has been rapidly adapted by investigators throughout the life sciences to conduct myriad types of DNA analysis, including determining the nature of HIV-1 infection,³ discovering the world's largest organisms,⁴ or even policing Japanese restaurants for the species of whale meat served at the sushi bars.⁵ In fact, James Watson, the co-discover of the structure of DNA, declares PCR to be a "technique that [has] transformed the way scientists work".⁶

Subsequently, several related methods of DNA amplification have been developed, most notably the *ligase chain reaction* (LCR), which is important for human diagnostic testing, and *thermal-cycle sequencing*, which is important for decoding large quantities of DNA. In fact, it appears that cycle sequencing will be the method used in the Human Genome Project to read the three billion bases of human DNA,⁷ and this methodology will likely prove to be important to the Mouse Genome and the Rice Genome Projects as well.

These biochemical techniques are all methods of synthetically amplifying DNA through an semi-automated procedure, and they have three things in common: 1) they use one or more short strands of synthetic DNA—called oligonucleotide primers—which identify the specific genetic sequences of interest and "prime" them for subsequent amplification; 2) they employ a thermostable enzyme that actively catalyzes the biochemical reaction at the molecular level; and 3) they require the use of a thermal-cycling instrument that accurately and repeatedly drives

small plastic reaction vessels (typically 0.2ml or 0.5ml in capacity) through a cyclical thermal regime, usually in a range between 4° and 95°C. The microprocessor-controlled, thermal cycler "powers" the biochemical reactions in effect, and this sort of laboratory instrument is the subject of discussion here.



Fig. 1 An early Peltier-effect thermal cycler. This is an MJ Research PTC-100 cycler, first introduced in 1988, which was camouflaged by the U.S. Marine Corps for field use in *Operation Desert Storm*. It has a temperature range of 0°-100°C, a ramping rate of about 1°C/sec, and it can hold 60 x 0.5ml plastic tubes.

History of Thermal Cyclers for DNA Amplification

The first thermal cycler specifically built for use in PCR was an instrument constructed by Larry Johnson of the Cetus Corporation, and it used thermoelectric modules to drive 0.5ml microcentrifuge tubes through a cyclical thermal regime. However, the thermoelectrics available at that time were unable to withstand for long the various stresses caused by the thermal cycling that PCR requires. In fact, the modules used in this first "PCR machine" needed to be replaced monthly, according to Mullis.⁸ Thus when the first mass-produced thermal cyclers were introduced in 1988 by The Perkin-Elmer Corporation (the strategic partner of the Cetus Corporation), they were vapor-compression machines, for it was much easier for Perkin Elmer to adapt this well-understood technology to long life in thermal

cycling applications.

However, shortly after the Perkin-Elmer introduction, two small U.S. firms, the Coy Corporation of Michigan and MJ Research, Inc. of Massachusetts, introduced thermal cycling instruments based upon bismuth-telluride thermoelectric technologies. These two companies took different approaches to lengthening the life of thermoelectrics in this application, with the Coy Corporation using a patented cam apparatus⁹ to engage and disengage the thermoelectric modules so that the modules were only used for cooling purposes. MJ Research, on the other hand, used compression-mounted thermoelectric modules bi-directionally, as reversible heat pumps, in order to better achieve the high degree of thermal precision required to drive the amplification reactions accurately and precisely. MJ Research had to conduct extensive investigation into the construction, the finishing, the quality control, and the electronic control of the modules in order to achieve the necessary life extension. This research culminated in the introduction of the "MJ Module" in 1991, which had a lifetime in this application orders of magnitude greater than what was available to Larry Johnson five years earlier.

Other companies experimented with different technologies of thermal cycler. In particular, a number of American, British and German firms constructed instruments that relied upon Joule heating of metal sample blocks, and tap water would circulate internally in the blocks during the cooling portions of the thermal regimes. The water was generally used only once, and after it became heated, it was dumped into a sink and drained as sewage. A fourth technology of thermal cycler relied upon heating the sample vessels directly by radiation and convection from a halogen light bulb or from a Joule heater, then the samples would be cooled by circulating fan-forced ambient air over the sample vessels to carry away excess heat.¹⁰

Needless to say, neither of these technologies could give the more precise, bidirectional control that can be achieved by use of vapor-compression or thermoelectric heat pumps. Nor do these designs allow incubation temperatures below ambient, which are required for certain protocols. Indeed, the manufacturers of these "heat-only" technologies have largely dropped out of the market entirely, or they have developed new instruments based upon thermoelectrics.¹¹ Of note is the fact that the Coy Corporation, with its special cam-actuated thermoelectric mechanism, also appears to have withdrawn from the market, and no other firm has mimicked their technology. Perkin Elmer and one other U.S. company continue to manufacture instruments based upon vapor compression, but this technology no longer seems to be regarded as state-of-the-art in the market.

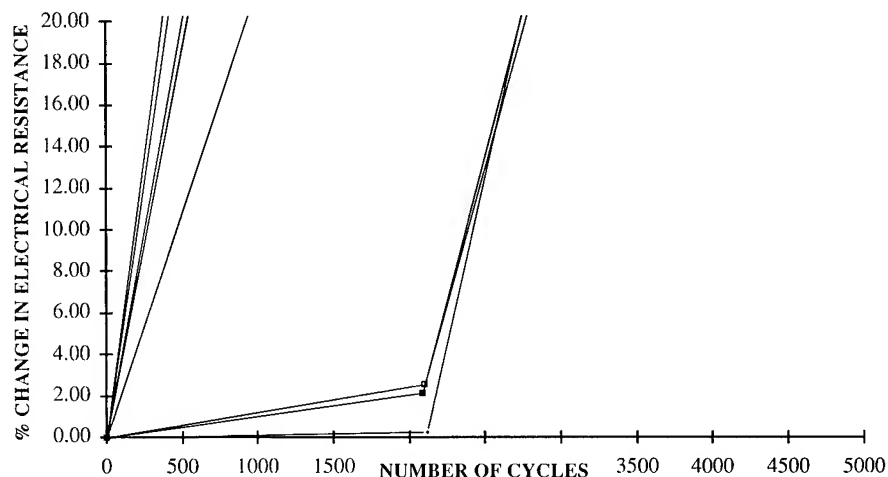


Fig. 2 Typical performance of industry-standard cooling modules in cycling regime. Nine 127-couple Bi_2Te_3 modules rated at 9 amps cycled 72g Al blocks between 70° & 30°C (with one minute holds) until failure. 6 amps constant current applied during ramping, PID loop during holds, heat sink kept between 45°-50°C.

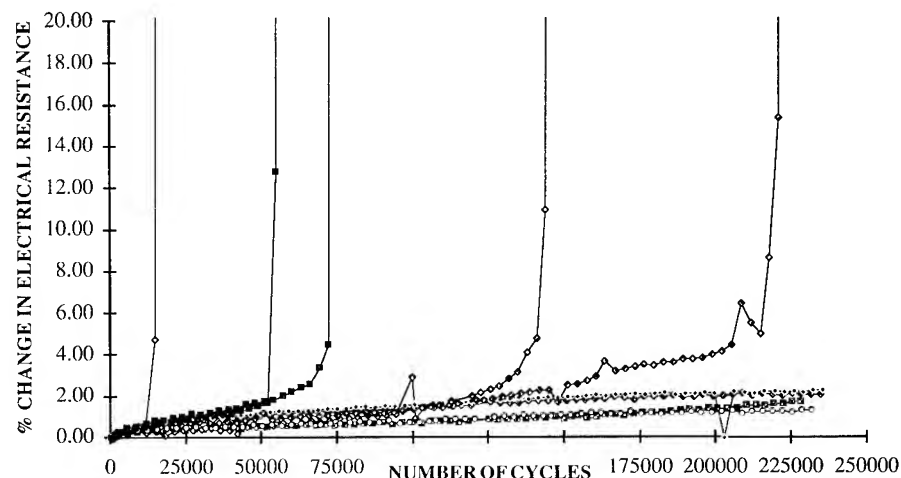


Fig. 3 Typical performance of "MJ Module" optimized for cycling. Nine 128-couple Bi_2Te_3 modules rated at 9 amps cycled 72g Al blocks in the same protocol as above, with various data points representing weekly measurements. Note average lifetime approximately two orders of magnitude greater than unmodified

Issues in the Design and Manufacture of Thermal Cyclers

Potential users of thermal cyclers generally judge instrumentation according to seven criteria: 1) the thermal uniformity across the sample block, such that each sample vessel experiences the same thermal history as its neighboring vessels; 2) the accuracy and reproducibility of thermal regimes—cycle-to-cycle, run-to-run and machine-to-machine—so that standard protocols give similar results no matter where they are used; 3) the speed of thermal ramping, which largely determines how fast an individual run can be completed and speed sometimes improves the quality of the biochemical reaction, 4) the reliability of the instrumentation, 5) the cost of acquisition and operation, 6) the physical size of the instrument relative to the number samples it holds, and 7) the versatility in the types of samples vessels that the instrument will accommodate. In general, well-engineered instruments based upon thermoelectric technology hold clear advantage in the first three and latter two categories, but it takes careful engineering and savvy manufacture to obtain

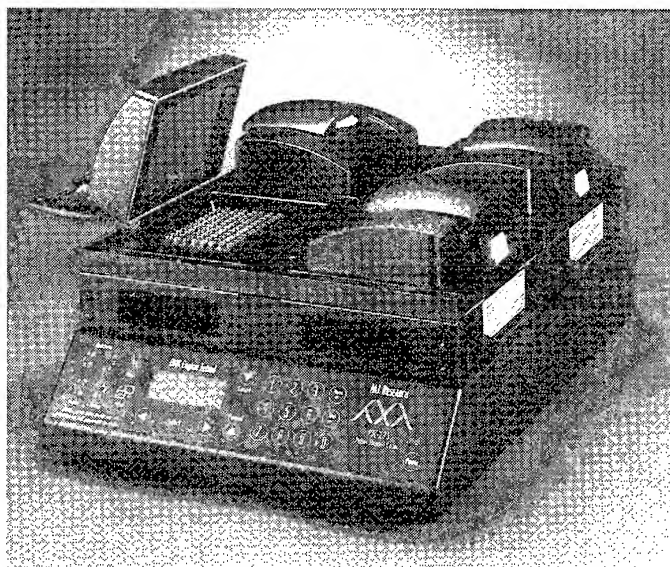


Fig. 4 A modern Peltier-effect thermal cycler. This is an MJ Research PTC-225 Tetrad, introduced in late '95, and it features 4 independent, interchangeable sample-block/heat-pump assemblies. This cycler has a thermal range of -5° – 105°C and a ramping rate of up to $3^{\circ}\text{C}/\text{sec}$. It can hold a variety of reaction vessels, with a total capacity of up to $4 \times 384 = 1536$ biochemical reactions.

advantages in reliability and cost of acquisition.

Perhaps the most important factor in constructing a world-class instrument is in the design, the construction, and the application of the thermoelectric modules used in the devices, because these are the factors that have the greatest effect on the costs and the reliability of the instrumentation. To this end, methods must be developed to reduce the various stresses experienced by the module, including the external stresses imposed upon it, as well as the internal stresses generated by the module itself. However, stresses are always going to exist to some degree in thermal cycling applications, so the module must be designed with a particular ruggedness, to better withstand these strains.

The Optimized "MJ Module" for Thermal Cycling

The results of the work we have conducted can be seen in the above graphs where the cycling lifetimes of two similar designs of bismuth-telluride modules are compared. Fig. 2 shows the results from a population of nine unmodified, industry-standard, 127-couple bismuth-telluride thermoelectric modules rated at 9 amps. The modules were put through a test protocol in which they brought 72g aluminum blocks to 70°C for one minute, then they ramped the blocks to 30°C , which was held for one minute, then brought the blocks back to 70°C for one minute and so on. The modules were supplied a constant current of 6 amps during ramping and were servoed with a PID loop during incubation. The heat sink temperature was maintained between 45° and 50°C at all times. The modules completed approximately 2200 cycles per week, their electrical resistance was measured weekly using a Wayne Kerr Model 4250 LCR Meter with a Kelvin four-terminal connection, and the resistance values were normalized to 25°C . Obviously, the standard cooling modules did not last long in this cycling protocol, with five of the modules failing before completing even 500 cycles,

one lasted about a 1000 cycles, and the remaining three were able to go about 2500 cycles before failing.

In comparison, Fig. 3 shows a population of nine "MJ Module" thermoelectrics optimized for thermal cycling being put through the same test protocol. These units are 128-couple, 9-amp bismuth-telluride modules built with special manufacturing and quality control procedures, and they last much, much longer in this application. Bear in mind that the scale on the x-axis is fifty times the scale of Fig. 2, and four of these modules are still going after nearly a quarter-million cycles. The other five modules in this population have failed at various points between 15,000 and 220,000 cycles. Advances in reducing the variance in module lifetime have since been made, and this matter continues to be the subject of ongoing investigation.

But these data clearly demonstrate the extraordinary difference in average module lifetime between industry-standard and optimized modules in cycling applications—a difference of more than two orders of magnitude. As a thermal cycler in typical laboratory use will experience 5,000 - 20,000 thermal cycles per year, optimized thermoelectric modules must be used in this application, if the instrument system is to have long life.

Conclusion

The polymerase chain reaction (PCR) and other DNA amplification techniques have led to the development of several technologies of thermal-cycling instruments for biomedical laboratories, some with active heat pumps and some without. Since initial development of these DNA techniques, market forces have led to specific criteria by which thermal cyclers are judged. Thermoelectric-based instrumentation has excelled in these analyses; however, the construction of these machines requires specialized thermoelectric modules. MJ Research has developed a specific technology of cycling modules, and these show a hundredfold increase in average lifetime in this application over standard cooling modules of similar design and materials.

- [1] Mullis, Kary "The Unusual Origin of the Polymerase Chain Reaction" *Scientific American* 262:56-61, 64-65
- [2] U.S. Patents #4,683,195 & #4,683,202
- [3] Bagasra, Omar *et al* "Detection of Human Immunodeficiency Virus Type 1 Provirus in Mononuclear Cells by *In Situ* PCR" *New England Journal of Medicine* 326:1385-91
- [4] Smith, Myron L. *et al* "The fungus *Armillaria bulbosa* is among the largest and oldest living organisms" *Nature* 356: 428-431
- [5] Baker, C.S. & S.R. Palumbi, "Which Whales Are Hunted? A Molecular Genetic Approach to Monitoring Whaling" *Science* 265:1538-1539
- [6] Watson, James in *The Polymerase Chain Reaction* (Forward) Birkäuser, Boston 1994, Kary Mullis *et al*, editors
- [7] Marshall, Eliot "A Strategy for Sequencing the Genome Five Years Early" *Science* 276:783-784
- [8] personal communication
- [9] U.S. Patent #4,865,986
- [10] *Certain Gene Amplification Thermal Cyclers And Subassemblies Thereof From the United Kingdom*, U.S. International Trade Commission Publication 2412, August 1991
- [11] Unger, Thomas "Powerful, HOT Mini Thermalcyclers," *BioConsumer Review* 2 (Summer 1995):17-22

THERMOELECTRICITY APPLIED TO THE CRYOCONCENTRATION OF ORANGE JUICE

Miguel A. Sanz-Bobi*, Rafael Palacios*, Antonio Arenas**

Universidad Pontificia Comillas

* Instituto de Investigación Tecnológica

** Laboratory of Heat and Mechanical of Fluids

Alberto Aguilera 23

28015 Madrid, Spain

Abstract

The high content of water in natural fruit juices suggests the reduction of their volume by its elimination. This is a concentration process for juices that saves space and reduces costs for storage, transport and handling. A very important part of the industry dedicated to the production of fruit juices produces concentrated juices that are obtained using conventional refrigeration cycles based on gases such as NH_3 . These technologies have been used throughout an important number of years with successful results. However, they require special care with the replacement and use of the fluids needed and for maintenance to be applied. These aspects induce to consider and to propose new ways of cooling.

This paper describes the main features of a prototype of a "cryoconcentration cell" for obtaining concentrated orange juice. This development is being supported by a research project within the program of the CICYT, a Spanish Government Agency to promote R&D activities. The prototype proposes the use of the Peltier effect as an alternative to the traditional methods of cryoconcentration using the aforementioned conventional techniques.

The cryoconcentration cell uses a set of thermoelectric elements to produce the cooling conditions able to convert the excess of water included in the juice into ice so that later it is possible to eliminate it and to concentrate the juice. The orange juice will be the hot sink in our application. The heat extracted from the orange juice will be transferred to water in circulation, which will be the cool sink.

A first prototype of this cell was constructed in aluminium [1]. From this experience another prototype was constructed in copper which is an improvement over the first one. Both prototypes of cryoconcentration cells use 16 thermoelectric elements on both main sides of the recipient that temporarily contains the juice.

A detailed description of the last prototype, its design and some initial results obtained will be presented in this paper.

Cryoconcentration of fruit juices

The contents of water in natural fruit juices is between 85 and 90 per cent of their total volume. This high content of water suggests its elimination by the concentration of the juice. This process will save important costs of packaging, transport and storage.

The most part of these concentrated juices are type "three plus one", that is, they require the addition of three volumes of water to one volume of juice to recover the original product. The degree of concentration is measured in Brix degrees. This unit indicates the content of soluble solids of the concentrated product. For example, if three volumes of water are added to a concentrated juice of 45 ° Brix a new product of 15 ° Brix results.

Two main industrial methods exist to concentrate natural juices [2][3]:

- Evaporation
Different versions of the evaporation method exist, but in any case the water is eliminated by the addition of heat.
- Cryoconcentration
This is the process of cooling juice till -8°C to obtain ice and fruit juice, because the freezing point of this is around -12°C . The next step is a mechanical separation of the ice from the juice.

The cryoconcentration of fruit juices has several advantages in respect to other methods. Some of them are the following:

- Volatile substances are not lost like in the evaporation process. This is important to keep the taste and aroma of the juice intact.
- The fermentation and growing of patogen microorganisms is diminished.
- This process is cheaper than evaporation.

Use of thermoelectricity in the cryoconcentration process as an alternative to current methods

Thermoelectricity as an alternative

The cooling requirements to be reached in the cryoconcentrated fruit juices are within a range where it is possible to think in the use of thermoelectric elements to fulfill these requirements.

In order to investigate this new application of thermoelectricity, a research project with this objective is being developed by the Instituto de Investigación Tecnológica (IIT) belonging to the Pontificia Comillas University. This

project is a subproject within another bigger project in which the objective is the study of new fruit concentration techniques. Three Spanish research centers have collaborated: Instituto del Frío, Complutense University and IIT. IIT is in charge of the investigation concerning the application of thermoelectricity techniques. The project is supported by the CICYT, a Spanish Government Agency to promote R&D activities. A first prototype of cryoconcentration cell using aluminium as the main material for heat transferring was reported in a previous publication [1]. This paper starts from this point and presents the new results obtained.

Industrial use of the cryoconcentration of fruit juices

In order to understand the details about a cryoconcentration industrial process of natural fruit juices, we visited an industry of orange juice concentration that used the cryoconcentration technique. We used the main features observed in the process as a pattern to fit our development. Such features are summarized in the following paragraph.

Once the juice is obtained from the oranges, it is processed to eliminate microorganisms and put to cool. The cooling system is based on a typical NH_3 circuit with strict requirements of maintenance for its components. This system is able to cool the juice till -10°C obtaining ice and liquid juice inside the ice. The thickness of the ice is 10 mm. The next step to obtain the concentrated juice is a mechanical separation of the orange juice achieved by pressing the ice.

Description of the cryoconcentration cell

A first prototype able to demonstrate the feasibility of the thermoelectricity application was designed and built using aluminum as the main material to transfer heat [1]. Using this experience, another prototype was built improving both the design and performance characteristics of the previous one. This new prototype, named cryoconcentration cell (in short CC), was designed using copper as the main material to transfer heat. As in the previous case, the new CC was designed according to the main parameters that we observed in the real process. These are:

- Thickness of ice produced: 10 mm
- Temperature of the ice: between -8°C and -11°C
- Recipient containing the juice suitable for human consumption

Additional requirements to the prototype were:

- Design thinking toward an industrial use
- Modularity and interchangeability of CC
- Low cost

The CC objective is to extract heat from the orange juice till freezing its water content (not the juice) and to transfer this heat to another fluid, in the present prototype water, using a set of thermoelectric elements.

The CC operation is like a heat pump [4] where the orange juice is the hot sink and the water used to take the heat extracted from the juice is the cool sink.

According to these requirements the CC prototype consists of three main parts: recipient to contain the orange juice, module of thermoelectric elements, and heat exchanger. A description of each one follows.

Recipient to contain the orange juice

This recipient has two squared parallel sides separated 10 mm to store the orange juice to be concentrated. This separation corresponds to the thickness of ice necessary to obtain. A representation of the recipient is shown in figure 1.

The recipient was made of stainless steel. This material permits a good heat transfer and is suitable to store edible products. The orange juice is introduced and removed through side A (figure 1). This side is open to the environment. The aluminium plates C_1 and C_2 permit the heat transferring from the juice to the heat exchanger using the module of thermoelectric elements.

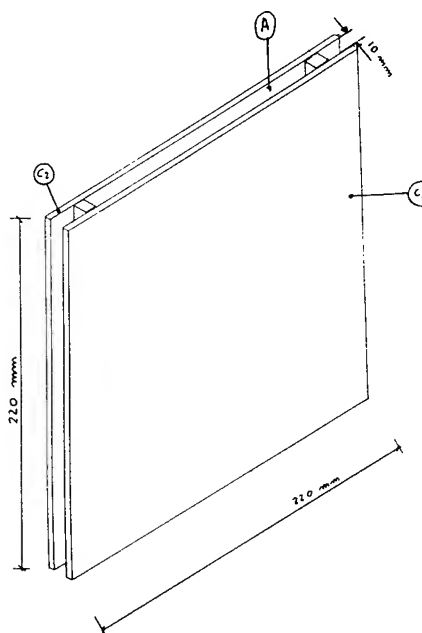


Figure 1

Module of thermoelectric elements

The CC has two modules of thermoelectric elements attached outside the recipient containing the orange juice, one to the surface of the side C_1 (figure 1) and another one to the side C_2 .

These modules consist of 16 thermoelectric elements each. The physical disposition of the elements is a squared matrix of 4×4 elements equally spaced. The 12 outer elements are type Marlow model DT-1089 and the 4 inner elements are type Marlow model DT-1069. All these elements are connected in parallel and are supported by a copper plate that fits with the side C_1 or C_2 of the recipient that contains the orange juice. A picture of this module is shown in figure 2.

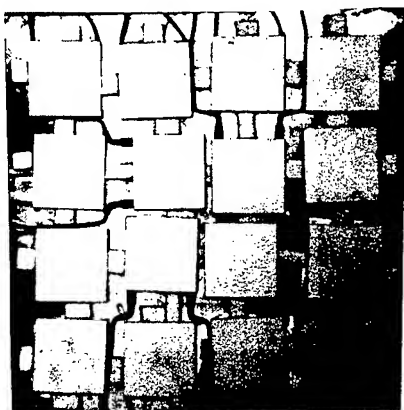


Figure 2

Heat exchanger

The heat exchanger permits the circulation of water coming from the general external water network. It is made of copper and put in contact with the hot side of the matrix of thermoelectric elements to transfer the heat to the water.

The heat exchanger consists of two elements. The first one is a squared plate that fits to the dimension of the module of thermoelectric elements covering it. The second one is a cooling coil made of copper pipe running along the surface of the plate. The cooling coil is joined to the plate by solder. The cylindrical pipe was deformed to obtain a plain side in contact with the plate.

The water flows forced through the pipe. There are two exchangers, one for each thermoelectric module. A picture of the heat exchanger is shown in figure 3.



Figure 3

Several CC can be used in an industrial process working in parallel. The modular construction of the CC allows the easy change of any element if it should be necessary.

Electric supply for the cryoconcentration cell

For the purposes of our investigation, three DC power sources of 40, 40 and 120 A supplied the 32 thermoelectric elements included in the CC. The distribution of power to the thermoelectric elements is according to the scheme presented in figure 4.

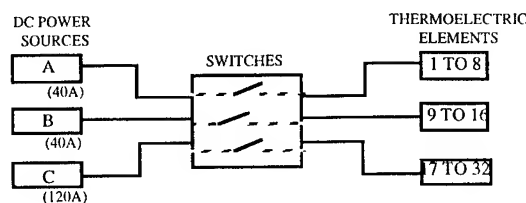


Figure 4

Cryoconcentration cell monitoring

In order to test the CC, several sensors were installed. These sensors collect the temperatures at various key points of the design. Thermocouples type K of 2 mm thickness were used for temperature measurement in the cooling side of the thermoelectric elements. The distribution of sensors in the CC is shown in figure 5.

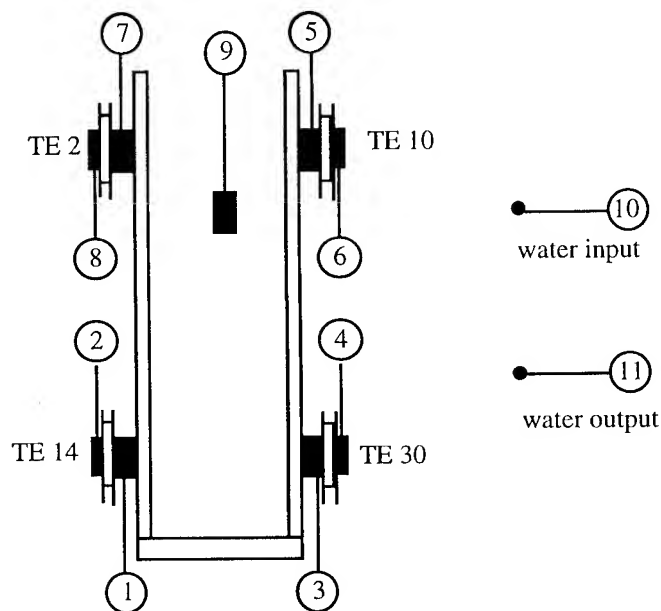


Figure 5

The description of the measurements indicated in figure 5 follows:

Thermocouple	Description
1	Cool side TE 14
2	Hot side TE 14
3	Cool side TE 30
4	Hot side TE 30
5	Cool side TE 10
6	Hot side TE 10

7	Cool side TE 2
8	Hot side TE 2
9	Juice in the middle
10	Water input
11	Water output

The TE (Thermoelectric Element) numbers 14 and 30 are on the same horizontal level on opposite sides of the recipient containing the juice. The TE numbers 10 and 30 are on the same vertical level on the same side of the recipient containing the juice.

The thermocouples were connected to a datalogger and this to a PC. A programme running in the PC was able to automatically collect the data from the sensors.

The water flow circulating inside the heat exchanger was measured using a counter not connected to the datalogger.

The consumption of electrical power used was noted reading the external panel of each DC power source.

Cryoconcentration cell performance

The CC has been tested in several working conditions and the results obtained have been analyzed to compare the performance observed with this design.

The different working conditions were obtained changing the DC current supplied to the thermoelectric elements because this parameter is the easiest to change for different tests. The temperature of the water circulating inside the interchanger is fixed by the water network. The flow of the water was also difficult to control because very small flows were required in the testing and a high precision flowmeter was not available. According to these restrictions, it was only possible to easily change the DC current.

Tests were done several times at 2, 3, 3.5, 4 and 5 A per thermoelectric element. In the entire test a pre-fixed flow of water running along the heat exchanger was used and orange juice was obtained from market oranges.

The following figures show the CC performance for 3.5 A as an example of the results obtained.

The evolution of the input and output water temperature in the heat exchanger is presented in figure 6. In this figure the temperature of the water input is constant (17.8 °C) and is fixed by the water network of the laboratory. The temperature of the water output increases to 22.8 °C when the CC is supplied by DC current. The decreasing trend of this temperature is similar to that observed in the hot side of the thermoelectric elements (see figure 8). The difference between water output and the hot side of the thermoelectric elements is around 13 °C.

The evolution of the orange juice temperature is presented in figure 7. This figure shows a decrease in the juice temperature after the thermoelectric elements are connected (90 s) till -8 °C, a temperature convenient for juice concentration by conversion of water into ice. The effect of this conversion is

observed by a change in the decreasing trend around the mark 200 in figure 7.

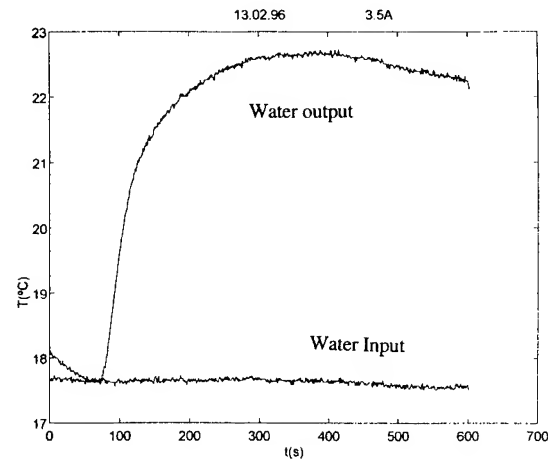


Figure 6. Water temperature

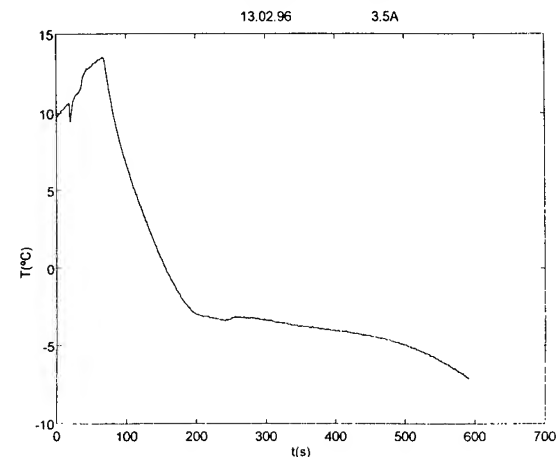


Figure 7. Juice temperature

The typical evolution on the hot and cool sides of the thermoelectric elements is shown in figure 8. The point where the water is converted into ice is discovered by the change of the decreasing slope. The difference between the hot and cool side can be observed at about 42 °C.

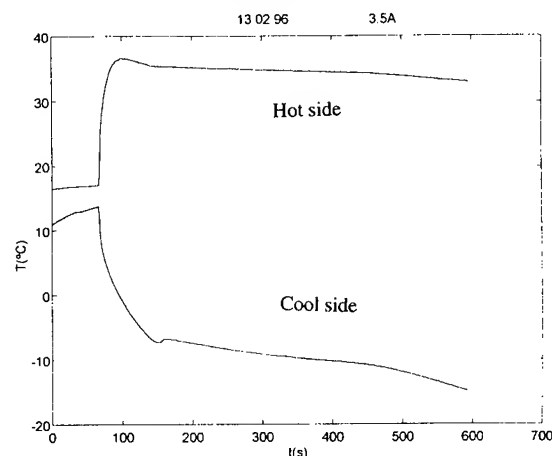


Figure 8. Thermoelectric element temperature

In figure 9, the evolution of the 4 temperatures measured in the cool sides of the thermoelectric elements is presented. The

two lower curves in the figure correspond to the monitored elements in the bottom of the CC and the other two to the elements located in the top. Also in the figure, it is possible to observe that the conversion from water to ice occurs in the bottom of the CC before it does in the top.

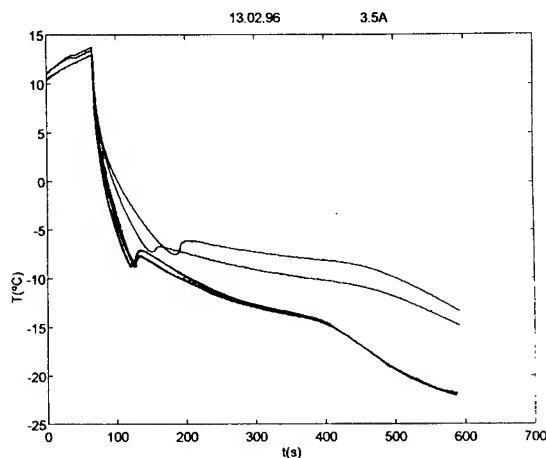


Figure 9. Cool side temperatures in thermoelectric elements

For the test analyzed in figures 6 to 9 (3.5 A), the average values measured for heat and electrical power are the following: heat in the heat exchanger 950W, heat extracted in the juice 210W, heat in the cool side of the module of the thermoelectric elements 280W, electrical power 1130W.

These results demonstrate that the CC can be used for orange juice cryoconcentration. The water is converted into ice, but the juice is liquid. The heat exchanger works heating the cool water as it was expected.

Tests for 2, 3, 4 and 5 amperes show a similar performance in the evolution of the variables. However the performance is degraded when the higher current is used. The recommendable range for an industrial application would be around 3 or 4 amperes.

The CC COP (ranged 0.3-0.2) is lower than the conventional cooling cycles used for cryoconcentration. However, the costs and requirements for operation could also be lower. Now, an economical investigation around these points is being done to complete the CC studies. The first task that it is currently being developed is the substitution of part of the energy required for the thermoelectric elements by energy coming from the sun using the photovoltaic effect.

Conclusions and future work

In this paper the investigation of the possible application of thermoelectricity to the cryoconcentration of orange juice has been presented.

For the purpose of this investigation a prototype of "Cryoconcentration Cell" able to reach the cryoconcentration objectives has been described. Design criteria, component description, test facility and performance results have also been shown.

This prototype of CC is based on a previous published experience [1]. The new prototype presented uses copper as the material for transferring heat and the design defects observed have been improved.

The performance tests demonstrate that the CC works according to the design criteria. This is to say, the CC is able to produce liquid orange juice inside the ice coming from the water, like the conventional cooling cycles used for cryoconcentration. The thermoelectric elements work cooling the juice and heating the water circulating in the cooling coil.

Now, more investigation is being done improving details to transfer this technology to industry. For this purpose, 8 photovoltaic modules have recently been installed to supply part of the DC power required for the thermoelectric elements.

Acknowledgements

The authors thank the CICYT of the Spanish Government for the economical support of the project and also Guillermo Blázquez and Juan Felipe López for their very valuable contribution in developing this project. Without their effort this work would have been impossible.

Finally, thank you to the Pontificia Comillas University maintenance personnel, especially to Pedro del Saz for his important help in the construction of the CC prototype.

References

- [1] Sanz-Bobi M.A., Palacios R. "Application of thermoelectricity to the process of cryoconcentration of orange juice". Second European Workshop on Thermoelectrics. Nancy, France. 1995
- [2] Proceedings of the XVIII TH International Congress of Refrigeration. Montreal, Canada. 1991.
- [3] Food Technology. Cuadernos CDTI. 1993
- [4] Sanz-Bobi M.A., Palacios R., Villar J., Arenas A. "Prototype of heat pump based on Peltier effect for application in ambient temperature conditioning". Proceedings 11TH International Conference on Thermoelectrics. Dallas, Texas, USA. 1992

A New Concept of Porous Thermoelectric Module Using a Reciprocating Flow for Cooling/Heating System

Shigeru Tada, *Ryozo Echigo and Hideo Yoshida

Dept. of Mech. Eng. & Sci., Tokyo Institute of Technology,
2-12-1 Ohokayama, Meguro-ku, Tokyo 152, Japan,
Phone ; +81-3-5734-2179, E-Mail ; stada@mech.titech.ac.jp

Abstract

This paper presents the conceptual design of a novel thermoelectric cooler and/or heater utilizing the heat transfer effect due to forced convection. A porous thermoelectric converter combined with a reciprocating flow system in which the flow direction of air passing through the element is reversed after regular intervals is proposed. This flow system in effect makes the thermal conductivity insignificant and contributes toward the achievement of a high efficient cooler and/or heater. For the first phase, a one-dimensional numerical analysis is performed to examine the detailed characteristics of the device by systematically varying the relevant thermo-fluid parameters. In particular, the flow velocity and the porosity of the thermoelectric elements are the most important parameters which directly affect the system performance. For example in a porous thermoelectric cooler, the lowest temperature of air is approximately -20°C for an ambient temperature of 27°C , which is attained with a flow velocity $u=0.35\text{ m/s}$, a material porosity $\epsilon=0.5$, and 2.5 cm thick thermoelectric elements. As a notable feature, the temperature of the cooling section of the system varies considerably with the velocity, and it attains a minimum at $u=0.35\text{ m/s}$. Subsequently, on the basis of the proposed cooling system, an extended concept aimed to realize commercial coolers and/or heaters is briefly discussed.

Nomenclature

A	: surface area of an equivalent particle	$[1/\text{m}]$
c_p	: specific heat of gas	$[\text{kJ}/\text{kgK}]$
c_s	: specific heat of solid	$[\text{kJ}/\text{kgK}]$
d_p	: diameter of solid particle	$[\text{m}]$
h	: heat transfer coefficient	$[\text{W}/\text{m}^2\text{K}]$
h_e	: heat transfer coefficient of end surface	$[\text{W}/\text{m}^2\text{K}]$
j	: electric current density	$[\text{A}/\text{m}^2]$
P	: input power	$[\text{W}]$
Q	: heat	$[\text{W}/\text{m}^2]$
q_c	: absorbing heat	$[\text{W}/\text{m}^2]$
r_e	: internal specific electric resistance	$[\Omega\text{m}]$
T	: temperature	$[\text{K}]$
T_0	: inlet air temperature (= 300)	$[\text{K}]$
T_{ex}	: outlet air temperature	$[\text{K}]$
T_{min}	: average temperature in the center porous	$[\text{K}]$
ΔT	: temperature difference (= $T^+ - T^-$)	$[\text{K}]$
ΔT_0	: temperature difference (= $T_0 - T_{min}$)	$[\text{K}]$
t	: time	$[\text{s}]$
u	: flow velocity	$[\text{m}/\text{s}]$
V_{Bat}	: battery voltage	$[\text{V}]$
x	: axial coordinate	$[\text{cm}]$
x_e	: thickness of thermoelectric module	$[\text{cm}]$
x_p	: thickness of porous material	$[\text{cm}]$
Z	: figure-of-merit (= $\alpha^2\sigma/\lambda_s$)	$[1/\text{K}]$

Greek Symbols

α	: Seebeck coefficient	$[\text{V}/\text{K}]$
δ	: control volume	$[\text{cm}]$

ϵ	: porosity	
λ	: thermal conductivity of gas	$[\text{W}/\text{mK}]$
ρ	: density	$[\text{kg}/\text{m}^3]$
σ	: electric conductivity (= $1/r_e$)	$[\text{S}/\text{m}]$
τ	: half cycle	$[\text{s}]$
ϕ	: coefficient of performance (COP)	

Superscripts and Subscripts

$+$: hot junction
$-$: cold junction
J	: Joule heat
P	: Peltier heat
s	: solid

Introduction

An important advantage of thermoelectric (TE) converters is that they have no moving parts; therefore they are extremely reliable. Nevertheless, the progress in the development of TE converters has stagnated because of the limitation in the efficiency of present systems and the high specific cost of power generation. To the best of our knowledge, there is not any TE device with a performance level comparable to that of conventional converters. Even for the newest TE power generators, the efficiency attained is at most 10 % which is considerably lower than any other conventional system. They are only utilized for power generation in remote locations, onboard spacecraft and in places where waste heat can be recovered. In other words, the present market for TE generators is very restricted.

Recent studies have been directed toward the development of materials in order to obtain an increase in the figure-of-merit, while proper design and optimization of TE devices in energy conversion systems have received less attention. This is because, for the development of energy conversion systems, the derivation of a thermal model employing accurate calculations for fluid mechanics and heat transfer requires versatile methods, and this tends to invest time and effort significantly for thermoelectricians. In order to realize a high efficient TE converter, one needs to discuss the thermal structure of TE devices based on the recent development in thermal engineering, in particular, in the light of thermo-fluid mechanics.

The energy efficiency of TE devices is usually described by the product of the Carnot efficiency at a constant temperature of the hot junction, and the irreversible efficiency of the system. However, the conventional Carnot efficiency of the TE device actually makes no sense, because the temperature of the hot junction is neither known or constant in real world cooling and/or heating systems. If no heat loss is exist, the Carnot efficiency is simply defined by the temperature of the hot and cold junction. In actual cases, the irreversible heat by conduction and Joule heat impose severe limitation on the improvement of the efficiency. To minimize their adverse effects, a system which includes an effective means for realizing the appropriate temperature difference between junctions is necessary[1].

As one novel approach, utilization of the convective heat transfer by introducing an air flow through a porous TE element is proposed[2]. By adjusting the flow parameters that control the convective heat transfer, the conduction heat losses can be recovered. In this way, the overall heat pattern is changed, making it possible to obtain a higher level of efficiency for TE devices. In the present study, a reciprocating flow system, in which air is introduced alternately from both ends of the device with a periodical change of flow direction, is proposed.

The detailed mechanism of the present system is examined by focusing on the trapezoidal temperature profile which is sustained through the heat balance between the convective heat exchange, Joule heat, and Peltier heat generated in solid thermoelectric elements.

Basic Concept and Comprehensive Features

Many notable characteristics of reciprocating flow in porous medium embodied in superadiabatic combustion system have been reported in past years. In particular, as a unique feature of the system, the typically trapezoidal temperature distribution in the porous medium has been demonstrated [2, 3]. This temperature profile, depicted in Fig.1, contributes greatly toward the realization of highly efficient heaters and/or coolers. For example in the TE cooler, ambient air entering from one end cools the hot junction at the inlet surface and releases the waste heat at the another end until the flow direction changes. The air flowing in this way effectively decreases the temperature of the center part of the device.

For the first phase, to find an optimum working condition for the highly efficient cooler, a one-dimensional numerical analysis is conducted to examine the detailed characteristics of the device by systematically varying the relevant parameters. As shown in Fig.1, a pair of porous TE elements with thickness x_e are located with a spacing x_p in an insulated channel, and plain porous material of thickness x_p is inserted in the space between the two elements. The insulated channel is nonporous elsewhere. For each TE element, D.C. power is supplied in order to sustain a constant electric potential between the hot and cold junctions. The flow direction is reversed at regular intervals τ , which represents the half cycle of the operation.

Further assumptions taken are that:

- the flow and heat transfer are one-dimensional.
- the flow velocity is constant during each half cycle.
- the physical properties are constant.

Mathematical Formulation

With the preceding assumptions the energy equation for both gas and solid phases, taking into account the thermoelectric terms, can be formulated as follows:

- Gas phase in free space

$$\rho c_p \frac{\partial T}{\partial t} + \rho c_p u \frac{\partial T}{\partial x} = \lambda \frac{\partial^2 T}{\partial x^2} \quad (1)$$

- Gas phase in porous medium of porosity ϵ

$$\epsilon \rho c_p \frac{\partial T}{\partial t} + \rho c_p u \frac{\partial T}{\partial x} = \epsilon \lambda \frac{\partial^2 T}{\partial x^2} - Ah(T - T_s) \quad (2)$$

- Thermoelectric porous medium of porosity ϵ

$$(1 - \epsilon) \rho_s c_s \frac{\partial T_s}{\partial t} = (1 - \epsilon) \lambda_s \frac{\partial^2 T_s}{\partial x^2} + Ah(T - T_s) + Q_J \quad (3)$$

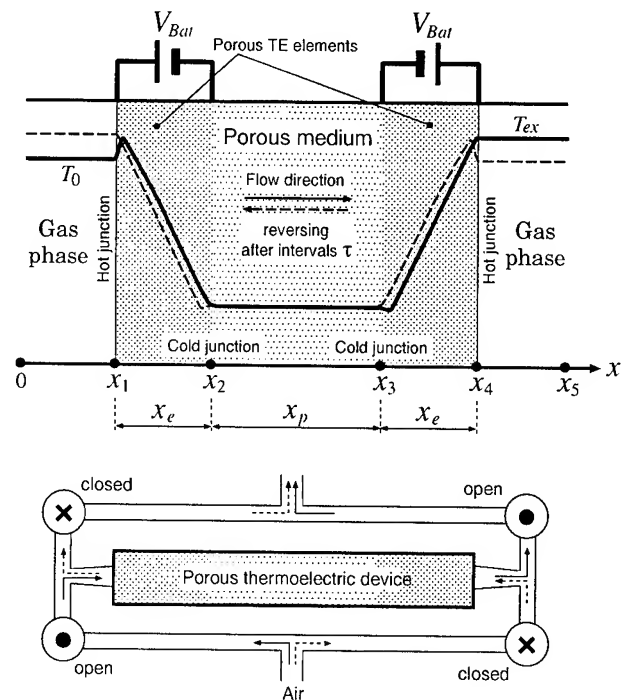


Fig.1 Schematics of the system

- Plain porous medium of porosity ϵ

$$(1 - \epsilon) \rho_s c_s \frac{\partial T_s}{\partial t} = (1 - \epsilon) \lambda_s \frac{\partial^2 T_s}{\partial x^2} + Ah(T - T_s) \quad (4)$$

The surface area of an equivalent particle per unit volume A can be written in the form:

$$A = \frac{6(1 - \epsilon)}{d_p} \quad (5)$$

The heat transfer coefficient h is given by:

$$h = 2 \frac{\lambda}{d_p} \quad (6)$$

where the constant "2" is the familiar Nusselt number in thermo-fluid mechanics[4].

For the hot and cold junctions, located at $x=x_1, x_4$ and $x=x_2, x_3$ respectively, boundary conditions are given by introducing the Peltier heat terms into the energy equations at each junction. Equations (3), (4) are integrated over the control volume δ at $x = x_1, \dots, x_4$:

- For the hot junction at $x=x_1$

$$(1 - \epsilon) \rho_s c_s \frac{\partial T_s}{\partial t} = \frac{1 - \epsilon}{\delta} \lambda_s \frac{\partial T_s}{\partial x} \Big|_{x+\delta} + \frac{Q_P^+}{\delta} + Q_J + Ah_e(T - T_s) \quad (7)$$

- For the hot junction at $x=x_4$

$$(1 - \epsilon) \rho_s c_s \frac{\partial T_s}{\partial t} = \frac{1 - \epsilon}{\delta} \lambda_s \frac{\partial T_s}{\partial x} \Big|_{x-\delta} + \frac{Q_P^+}{\delta} + Q_J + Ah_e(T - T_s) \quad (8)$$

where h_e represents the sum of the heat transfer coefficient of the porous end surface and h which is the heat transfer coefficient between porous medium and gas phase, given by eq.(6). Here, the heat transfer coefficient h is much higher than those at the end surfaces. We assume that the end surfaces have no influence on the energy balance of the porous TE device. Therefore, h_e is approximated as:

$$h_e \simeq h. \quad (9)$$

- For the cold junction at $x=x_2, x_3$

$$\begin{aligned} & (1-\epsilon)\rho_s c_s \frac{\partial T_s}{\partial t} \\ &= \frac{1-\epsilon}{2\delta} \lambda_s \frac{\partial T_s}{\partial x} \Big|_{x+\delta} - \frac{1-\epsilon}{2\delta} \lambda_s \frac{\partial T_s}{\partial x} \Big|_{x-\delta} \\ & - \frac{Q_P^-}{2\delta} + Q_J + Ah(T - T_s) \end{aligned} \quad (10)$$

The Joule heat and the Peltier heat are evaluated in terms of the electric current density j and the battery voltage V_{Bat} imposed on the open circuit of the element. They are:

- Joule heat

$$\begin{aligned} Q_J &= j^2 \frac{r_e}{1-\epsilon} \\ &= \frac{(1-\epsilon)(V_{Bat} - \alpha \Delta T_s)^2}{r_e x_e^2} \end{aligned} \quad (11)$$

- Peltier heat

$$\begin{aligned} Q_P^\pm &= j \alpha T_s^\pm \\ &= \frac{(1-\epsilon)(V_{Bat} - \alpha \Delta T_s) \alpha T_s^\pm}{r_e x_e} \end{aligned} \quad (12)$$

Results and Discussion

Basic features of the porous TE cooler

Here, the figure-of-merit of the porous TE elements is assumed to be $ZT_0 = 1$, which is the most likely performance for future TE materials. Other relevant physical properties are assumed to be the same as for Bi_2Te_3 -based TE materials. They are shown in Table 1.

Table 1 Physical properties

Specific heat c_s	0.169 kJ/kgK
Thermal conductivity λ_s	2.00 W/mK
Density ρ_s	7.67×10^3 kg/m ³
Electric conductivity σ	1.20×10^5 S/m

Because the flow velocity u (or the TE element thickness x_e) and the porosity of materials ϵ are expected to be the most important parameters which directly affect the device performance, a series of computations to systematically study their influence have been carried out. The thickness of the porous TE element x_e and of the porous material x_p are taken to be 2.5 cm and 5 cm, respectively. During calculations, a relative convergence criterion of 10^{-6} is specified for the iterations and an overall energy balance of approximately 1% (maximum 4%) is achieved for most of the cases.

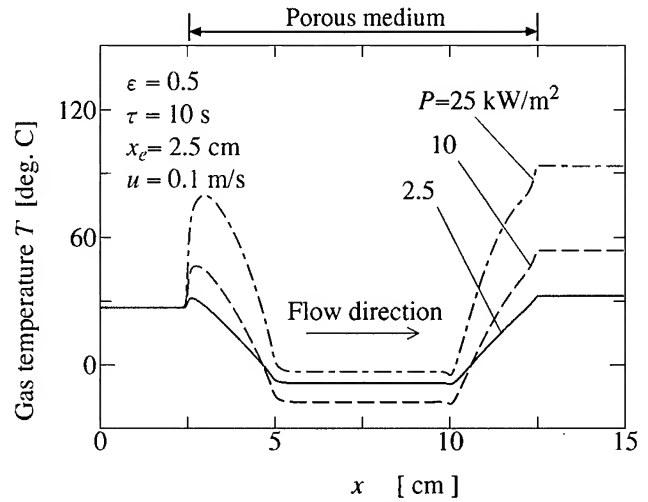


Fig.2 Gas temperature profiles in the device

Before proceeding to a detailed discussion of the results, some of the fundamental features of the reciprocating flow system are briefly introduced. Figure 2 shows the typical temperature distribution developed within the device. The figure shows temperature profiles of gas phase at the end of a half cycle τ just before the flow direction is reversed. It can be seen that inside both porous TE elements, temperature distributions with steep gradients are sustained and that the portion with the lowest temperature in the device is established along the entire length of the center porous medium ($x=5\sim 10\text{cm}$). Air of initially ambient temperature T_0 coming from the outside with velocity 0.1 m/s is heated when it reaches the hot junction ($x_1=2.5\text{cm}$). Thereafter, the temperature rapidly decreases as the air travels through the porous TE element, until it reaches the upstream cold junction ($x_2=5\text{cm}$). Then, the air passes through the center porous medium with constant temperature until it reaches the downstream cold junction ($x_3=10\text{cm}$). Here, the air is further cooled down by the Peltier heat absorption before it is heated on its way to the downstream hot junction ($x_4=12.5\text{cm}$), and finally leaves the porous body with a temperature T_{ex} at $x_4=12.5\text{cm}$. On the other hand, the effect of input power on the gas temperature profile is not monotonic; the lowest temperature is observed for $P=10\text{ kW/m}^2$. This is because, with the increasing input power P , the Joule heat becomes dominant over conduction and Peltier heat, although simultaneously the temperature difference between the center and outlet of TE device increases. It is evident that for a proper power input and flow velocity, the air passing through the device effectively decreases the temperature of the cold junction at the upstream by cooling the hot junction at the upstream face of the device.

The dependence of the average temperature in the center porous \bar{T}_{min} on the current density j of TE elements for various flow velocities u is shown in Fig.3. The broken line (—) and open circles (o) denote the variation of \bar{T}_{min} with j for a flow velocity $u=0.1\text{ m/s}$. It is found that for the value of $j=0.48 \times 10^5\text{ A/m}^2$, \bar{T}_{min} achieves its minimum. If one analyzes equations (11) and (12), the relationship between these two variables, \bar{T}_{min} and j , becomes evident. The lowest temperature in the device is achieved as a result of the heat balance between the Joule heat, which varies with the square of current density, and the Peltier heat, which varies linearly with the current density i.e. \bar{T}_{min} varies parabolically with the current density j . Therefore, the system provides an opti-

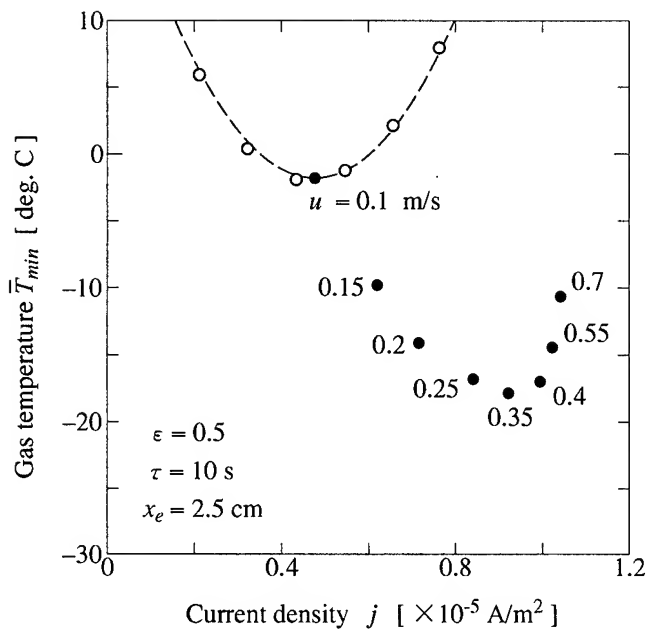


Fig.3 j vs. \bar{T}_{min} for various flow velocities u

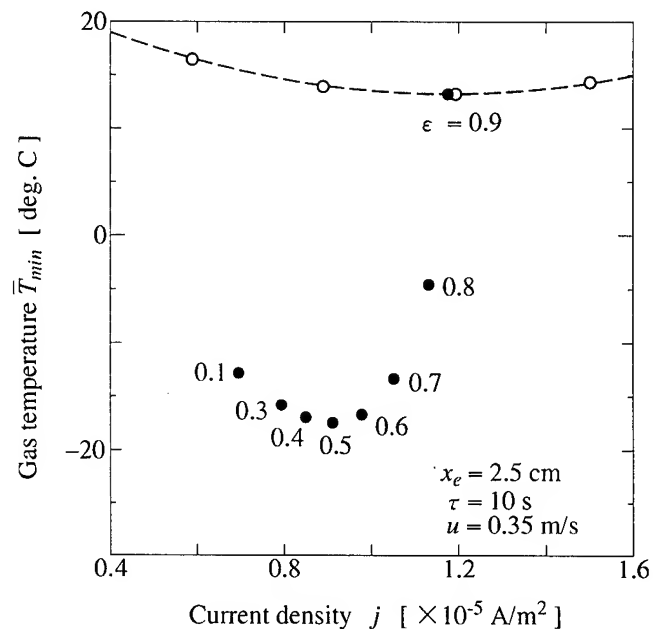


Fig.4 j vs. \bar{T}_{min} for various material porosities ϵ

imum \bar{T}_{min} at a certain current density as indicated by a filled circle (•) on the broken line. In addition, the value of the optimum \bar{T}_{min} strongly depends on the flow velocity. The variation of the optimum \bar{T}_{min} with the flow velocity u is plotted by filled circles (•) in Fig.3. In the present system, \bar{T}_{min} attains a minimum for $u=0.35$ m/s and $j=0.91 \times 10^5$ A/m². It is understood that for low flow velocities, hot junctions at both end faces are not sufficiently cooled by the air because of the low heat transfer by weak convection. Consequently, this leads to a small temperature decrease in cold junctions because the temperature difference between the cold junction and the hot junction is sustained by the constant power input through the Seebeck effect. On the other hand, for very high flow velocities, despite a sufficient cooling of the hot junctions by the air flow, the temperatures at the cold junctions do not decrease. This is because for high flow velocities, the obtainable temperature difference in the elements decreases owing to the Joule heat which transferred the downstream TE element as a result of the strongly forced convection.

Figure 4 shows the dependence of the average temperature in the center porous \bar{T}_{min} on the current density j of TE elements for various material porosities ϵ . A similar behavior as shown in Fig.3 can be observed for the relation between \bar{T}_{min} and ϵ . The value of the electrical current density which gives an optimum \bar{T}_{min} increases with an increase in the material porosity. The optimum \bar{T}_{min} has a minimum when $\epsilon=0.5$ for a flow velocity $u=0.35$ m/s and a current density $j=0.91 \times 10^5$ A/m². For this case, the electric energy in the porous body plays an important role in establishing the optimum \bar{T}_{min} . Under the condition of a constant flow velocity, an increase in the material porosity ϵ allows a decrease in the electric energy of the porous TE elements ($j \times V_{Bat}$), thus leading to a decrease in the rate of heat absorption at the cold junctions. On the contrary, the electric energy in the porous TE body decreases with decreasing material porosity; this causes a smaller temperature difference between the hot and cold junction.

Performance of the porous TE cooler

In this section, the cooling performance of the porous TE device is examined by taking into account the foregoing results which allow proper design for the optimum cooling.

After the essential thermal behavior of the cooling device has been revealed, the next step in the design optimization process is to calculate the coefficient of performance (COP) ϕ . Additional computations are conducted for the cooling device, including heat sinks q_c which are located on both end faces of the center porous medium. For the calculation, relevant parameters except for the rate of the heat absorption are specified. This includes $u=0.35$ m/s, $\epsilon=0.5$, and $\tau=10$ s. These values are expected to yield the optimum cooling in the device under consideration. On the other hand, the rate of the heat absorption is varied systematically to obtain a set of COP curves.

The device performance parameters to be calculated are specified at a constant inlet air temperature $T_0=300$ K, contrary to that conventionally specified at a constant hot junction temperature, since the hot junction temperature T_s^+ plays a minor role in evaluating the COP of this device.

Figure 5 shows both the dependence of the rate of heat absorption q_c on the electrical current density j and the COP of cooling mode for several temperature differences $\Delta T_0 (=T_0 - \bar{T}_{min})$.

The figure shows typical performance curves and a maximum cooling $q_c = 6$ kW/m², together with a COP $\phi \simeq 0.6$, which is attained for $j \simeq 1 \times 10^5$ A/m². The cooling performance remarkably decreases with an increasing temperature difference when compared with conventional TE modules. However, note that one can not simply compare the corresponding performance curves with that of conventional TE modules. This is because in conventional TE coolers which consist of heat sinks, TE modules and exchangers, significant thermal resistances existing between the cold sink and the cold junction, and between the hot junction and the exchanger, can not be avoided. Therefore, overall system efficiencies of conventional TE coolers are lower than expected on the TE "module" performance curves. In other words, in the proposed device, the

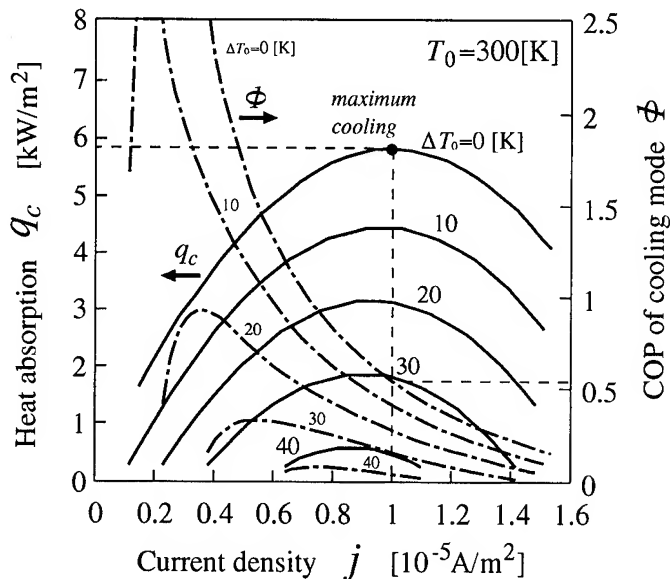


Fig.5 ΔT_0 and COP
($u=0.35$ m/s, $\epsilon=0.5$, $\tau=10$ s)

heat is mainly transferred by the effect of convection, unlike in conventional cooling systems. Therefore, thermal resistances present among constituent items have fairly small influence on the device performance. Thus good thermoelectric performance can be achieved in the present system.

Extended application of the porous TE device

The preceding discussion revealed that the present porous TE device has tremendous potential as a cooler with a high thermal efficiency. However, the analytical model developed in this paper provides only a conceptual means for optimizing the cooling system, thus more extensive parametric computations as well as detailed information about thermal engineering aspects of a favorable system design are needed before the application of this device to an actual heating and/or cooling system. In the following, the emphasis is placed on the system design rather than on the extended mathematical analysis. In Fig.6, feasible designs of coolers and heaters utilizing the porous TE element are introduced.

Figures 6-(a) and 6-(d) show the extended design of coolers, while figures 6-(b) and 6-(c) show that of heaters. For the cooler (a), a couple of porous TE elements are collocated with a spacing in an insulated nonporous channel. However, no object is inserted between elements, unlike the porous TE device which was discussed throughout this paper. The heater (b) is accomplished by simply reversing the electric polarity of the cooler (a). For systems (c) and (d), heat exchangers are installed in the center spaces. The cooler (d) is also accomplished by changing the polarity of the imposed voltage of the heater (c).

Systems (a) and (b) transfer the heat from the object to be cooled or heated to the working fluid inside the device. Conversely, systems (c) and (d) transfer the heat from the object to the air at the downstream end of the device. For example, in heater (c), when cold junctions are heated by the exchanger, the outlet air temperature increases, and there is an increase in the cold junction temperatures, owing to the sustained temperature difference between the cold and the hot junctions. This leads to an increase in outlet air. Besides, a further temperature increase in exhaust air owing to the recuperated Joule heat and the ejected Peltier

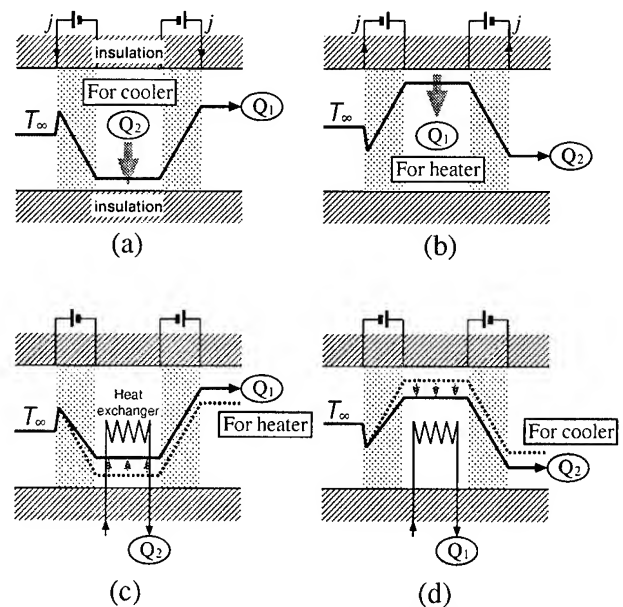


Fig.6 Extended system schemes
(a), (d) : Porous TE cooler
(b), (c) : Porous TE heater

heat is also expected.

It is interesting to note that in the heating system (c), the excess Joule heat generated in the device is effectively utilized for the improvement of system efficiency. In all systems, the excess heat due to the Joule and the Peltier heat are implicitly included in the released heat at the outlet; therefore, a system utilizing the enthalpy of the exhaust air for heating is expected to yield good efficiency.

In the above discussion, the electric power for the blower which is required to generate air flow is not accounted for in the system efficiency. However, the pressure head needed to establish a given flow rate can be considerably reduced by fabricating the porous bodies with favorable characteristics. Therefore, the required electric power for the blower has a negligible effect on the system performance.

References

- [1] R. Echigo, et al., "An Extended Analysis on Thermodynamic Cycle of Advanced Heating/Cooling Method by Porous Thermoelectric Conversion Device", 12th ICT, Yokohama, JAPAN, VI-5(1993).
- [2] K. Hanamura, et al., "Superadiabatic Combustion in a Porous Medium", Int'l. J. Heat & Mass Transfer, Vol.36, No.13, pp.3201-3209(1993).
- [3] J. G. Hoffmann, et al., "Analytical Study of Flammable Limits of Reciprocating Superadiabatic Combustion in Porous Media", Int'l. Symp. on Transport Phenomena in Combustion, San Francisco, U.S.A., 4(1995).
- [4] W. E. Ranz, and W. R. Marshall, "Evaporation from Drops", Chem. Engn. Prog., Vol.48, No.3, pp.141-146(1952).

Fabrication and Testing of Thermoelectric Thin Film Devices

Andrew V. Wagner, Ronald J. Foreman, Leslie J. Summers,
Troy W. Barbee Jr., and Joseph C. Farmer

*Chemistry and Materials Science Department
Lawrence Livermore National Laboratory
7000 East Avenue Livermore, CA 94550 USA*

Abstract

Two thin-film thermoelectric devices are experimentally demonstrated. The relevant thermal loads on the cold junction of these devices are determined. The analytical form of the equation that describes the thermal loading of the device enables us to model the performance based on the independently measured electronic properties of the films forming the devices. This model elucidates which parameters determine device performance, and how they can be used to maximize performance.

Introduction

Thermoelectric materials play an important technological role as sensors, power generators and solid-state coolers. The use of bulk thermoelectric material for cooling is becoming more widespread. For example portable thermoelectric food coolers are now becoming common place. Thermoelectrics have also found a niche where vibration free cooling is critical such as in infrared detectors and low-light CCD array cameras. They are also used as a convenient way of quickly heating and cooling for DNA synthesis by thermal cycling. These applications all make use of bulk thermoelectric materials, but there is increasing interest in thin-film thermoelectric devices.

Here we focus on the use of thermoelectrics for cooling, which is the most demanding application for such thin-film materials. Thin-film coolers could be incorporated directly into semiconductor devices in close proximity to regions such as the sensing element in IR detectors. This could greatly reduce the amount of material being cooled, thereby reducing the energy required for cooling. Low energy consumption is critical in building hand-held, battery-operated devices. A thin-film deposition technology would also be compatible with the planar technology essential to the construction of integrated circuits. Further interest in thin film-coolers stems from potential improvement in thermoelectric figure of merit from two dimensional confinement of the charge carriers in quantum well structures.^[1]

The problem of thin film deposition of thermoelectrics has been worked on sporadically since the 1950's. Numerous deposition techniques have been tried including evaporation, flash evaporation, MBE, CVD, sputtering, and laser ablation. In the case of compound semiconductors, a primary difficulty is maintaining the stoichiometry of the growing film. Keeping sufficient purity of material and controlling the dopant levels are also critical. The growth structure is another important issue

since grain boundaries and crystalline defects effect the resistivity of the deposited film by scattering charge carriers.

Recent thin-film device work has begun to show promise of producing useful devices.^[2] Much of the experimental work involves optimizing the growth parameters to achieve the best quality films.

In this work we investigate which heat transport factors are essential to consider when working with thin-film thermoelectric devices. If the heat transport to the cold junction from all sources can be calculated then the electrical conductivity and Seebeck coefficient can be used to predict the cooling achievable by the device. Here we calculated device performance based on the independently-measured thermoelectric properties of the individual films comprising a device. We compare this with experimental measurements of the maximum cooling of operating devices. The model developed and discussed here can be used as a means for optimizing device performance.

Experimental techniques

Film growth and optimization:

Magnetron sputtering was chosen for the deposition of thin film devices for two reasons. First, sputtering allows multicomponent materials to be deposited from a single source without many of the compositional shifts associated with thermal evaporation techniques. Second, the technology for large-scale deposition has been developed in industry and has been shown capable of producing large quantities of material necessary for commercially viable thin film thermoelectric devices. We discuss the sputtering process used to deposit these films in detail elsewhere.^[3]

Film quality is extremely important in growing devices. Degradation of the electrical properties of the films are reflected in reduced cooling capacity of the device. The individual p and n-type films were optimized independently. The electrical resistivity and Seebeck coefficient of the individual films was measured independently. The structural quality was investigated using x-ray diffraction, which allows the degree of orientation to be investigated, as well as the crystalline structure. Scanning electron microscopy (SEM) was used to measure the film thickness as well as characterize growth structure. The results of these measurements were used as the basis for directed changes in the sputter target composition as well as deposition parameters.

For the $\text{Bi}_{0.9}\text{Sb}_{0.1}$ film used as the n-type leg of one of the devices discussed below, the main issues were crystal quality, crystal size, and impurities. By raising the deposition temperature the electronic properties of the films were improved as a result of increased crystal size and quality. Increasing substrate deposition temperature was limited by island formation at higher temperatures. The pressure of the sputtering gas and sample bias were also found to effect the properties of the film.^[4] The $\text{Bi}_{0.9}\text{Sb}_{0.1}$ film used in the device discussed here was deposited at approximately 180°C.

Similar observations were made for the $(\text{Bi}_{1-x}\text{Sb}_x)_2(\text{Te}_{1-y}\text{Se}_y)_3$ films. The problem of island formation could be reduced by beginning deposition at a lower temperature and quickly raising the temperature during deposition. The difference in vapor pressure of the components makes deposition at these high temperatures difficult. However we have shown that by using a "hot walled" environment and excess Te concentration in the sputter target the stoichiometry of the resulting films could be controlled.^[3]

Mica was chosen as the substrate material since mica can be easily cleaved into extremely thin sheets. It is important that the substrate be thin in order to minimize thermal conductivity losses in the substrate. In addition mica has a hexagonal symmetry which is the same as the film, the cleaved surfaces are flat, and it is able to withstand the high temperature necessary for high quality deposition. The "hot walled" environment needed to control the stoichiometry also helps maintain the thin mica substrates at the desired temperature. This is particularly important since the flexible mica substrates essential to making devices do not make good mechanical contact with the stage and there is little lateral heat transport in the mica from the points where it does contact the stage. Thus, without a "hot walled" environment the temperature of the substrates would be in radiative equilibrium somewhere between the stage temperature and the chamber temperature.

The devices were prepared by first depositing one leg of the device through a mask onto the mica substrate. The chamber is then vented, the mask reset to give a small junction, and the second film deposited.

Care must be taken in depositing the second leg of the device. The existing film changes the thermal characteristics of the mica substrate and may lead to increased substrate temperature near the junction during deposition. The second film does not nucleate growth at the edge of the first deposition. A small gap is formed by atoms deposited near the junction migrating to the edge of the existing film instead of nucleating the growth of the new film. If such a small gap forms at the junction the performance of the device is destroyed. To prevent this problem, lower temperatures are used at the beginning of the deposition.

Measurement technique:

To test the device it was bridged (face down) between two copper blocks and attached with conductive silver paint which provides both electrical and thermal contact. One thermocouple is attached to the back side of the mica substrate at the cold

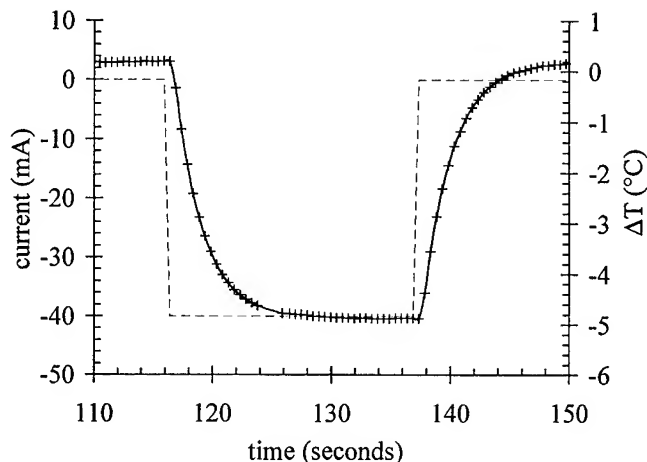


Figure 1: Measured temperature response for device 1 to a 40mA current pulse. The zero offset for the cooling for zero current is a result of slight nonequilibrium of the heat sink with the surrounding radiative environment. These small offsets show the importance of the pulsed technique.

junction. A second thermocouple monitors the temperature of one of the copper contact blocks. Both thermocouples are electrically isolated from the current pulse used to produce cooling in the device by the mica substrate material. The device is tested by sending a current pulse to the device and comparing the temperature difference between the two thermocouples before and during the pulse. The current pulses sent to the device are controlled by the data acquisition computer and can be varied in amplitude and duration. The computer allows the pulse duration to be set so that the temperature difference can be compared after the cooling transient which is typically less than a couple seconds (figure 1). Furthermore, the pulse current is varied to explore the response of the device as a function of current. It is important that the entire chamber be in thermal equilibrium with the copper blocks that are used as the "hot side" of the device. This is necessary in order for the equations governing radiative losses discussed below to apply.

Since the chosen substrate is a very good insulator, our standard measurement techniques could be used to measure the electronic properties of each leg of the device independently.^[5] This enables the independent calculation of expected device performance for comparison with measured results.

Calculations

In building thermoelectric cooling devices the relative importance of the various heat loads on the cold junction must be understood. To optimize device performance, it is useful to develop a comprehensive analytical model.

Thin-film thermoelectric devices which are designed to transport heat in the plane of the film are inherently low-power devices. Thus, small secondary heat loadings of the cold junction, which are usually inconsequential for bulk devices, are very important to consider for thin-film devices. For a device made of bulk material, thermal conductivity in the thermoelectric material is the dominant source of heat transfer to the cold junction and thus limits the minimum temperature to which the device can cool. In thin films however, other losses

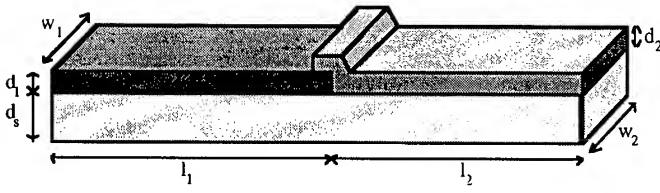


Figure 2: Schematic of a simple cooler device showing a p and n-type film on a thin substrate.

are equally important. These losses include thermal conduction in the substrate supporting the film, coupling to the environment by radiation, and conduction and convection in the atmosphere. Losses in the atmosphere were neglected in the discussion below since our experiments were conducted in vacuum. The load being cooled must also be considered, including the thermocouple used to monitor the device.

Analytical expressions for the thermal loads are developed for the simple geometry where the p-n junction is deposited on one side of a cleaved mica substrate as shown in figure 2. The load from each side of the device and each leg of the measurement thermocouple will be considered separately.

The contribution of thermal conductivity in the film and substrate to the heat transfer coefficient of the device can be calculated as follows:

$$K_{film} = \kappa_{film} \frac{dw}{l} \quad (1)$$

$$K_{sub} = \kappa_{sub} \frac{d_s w}{l} \quad (2)$$

As the surface of the device gets larger, radiation plays an increasingly important role. For small temperature differences, the coefficient of heat transfer for a surface (H) is the derivative of the radiance (\mathfrak{R}):

$$\mathfrak{R} = e\sigma T^4 \quad (3)$$

where σ is the Stefan-Boltzmann constant (5.67×10^{-12} W/cm²K⁴) and e is the emissivity. The heat transfer coefficient across the surface at the reference temperature (T_o) is:

$$H = \left. \frac{\partial \mathfrak{R}}{\partial T} \right|_{T_o} = 4e\sigma T_o^3 \quad (4)$$

Heat will be lost from both the top and bottom surfaces in an actual device. However, this factor of two will be offset by the fact that the average temperature of the device will be halfway between the temperature of the cold junction and the reference temperature. It is assumed that the whole radiative environment is at the reference temperature and therefore the radiative heat transfer coefficient for the device is:

$$K_{rad} = Hlw \quad (5)$$

Heat losses in the measurement thermocouples must also be estimated. Despite the use of extremely thin thermocouples (much thinner than a hair), they are still several times thicker than the film that is being tested. Furthermore, metallic thermocouples have a much higher thermal conductivity than any of the other components in the system. Although relatively long thermocouple wires are used to minimize thermal losses

from conduction, the heat transferred down the thermocouple is radiated away at the surface of the thermocouple. In our case the loss due to the thermocouples leads can be approximated by the analytical solution for the heat loss by radiation from a semi-infinite rod.^[6] The temperature distribution in the rod is:

$$T = T_o + (T_c - T_o)e^{-x\sqrt{pH/\omega\kappa_{Tc}}} \quad (6)$$

where p the perimeter, $2\pi r$; ω is the cross-sectional area, πr^2 ; and r is the radius of the wire. The rate of heat flow down the wire is:

$$\omega\kappa_{Tc} \left. \frac{\partial T}{\partial x} \right|_{x=0} = \pi r^2 \kappa_{Tc} (T_c - T_o) \sqrt{\frac{2H}{r\kappa_{Tc}}} \quad (7)$$

$$= (T_c - T_o) \pi r^{3/2} \sqrt{2H\kappa_{Tc}}$$

The heat flow coefficient for each leg of the thermocouple is:

$$K_{Tc} = \pi r^{3/2} \sqrt{2H\kappa_{Tc}} \quad (8)$$

To validate the assumption of the semi-infinite rod geometry, the length of thermocouple at which the temperature will be half-way between the cold junction and the reference temperature can be calculated as follows from equation 6:

$$\frac{1}{2} = \frac{T - T_o}{(T_c - T_o)} = e^{-x\sqrt{pH/r\kappa_{Tc}}} \quad (9)$$

$$x^* = -\ln\left(\frac{1}{2}\right) \sqrt{\frac{1}{2} r \frac{\kappa_{Tc}}{H}} \quad (10)$$

For the 0.001 inch diameter thermocouples used during this work, x^* is approximately half a centimeter. This is small compared to the length of the thermocouples used in the experiments. The length of thermocouple needed to remain in this approximation varies as the square root of the thermocouple radius.

The performance of a device is calculated with the figure of merit (Z) of the device. To calculate the performance of an actual device, one must sum over all the thermal losses and resistances in the system. In the simple device sketched in figure 2 several assumptions were made. First, it was assumed that the overlap of the two layers is small compared to other dimensions and can be ignored. Similarly, it was assumed that there is no junction resistance and no interdiffusion or intermixing of the two layers at the junction which could degrade the thermoelectric properties of the materials in the vicinity of the junction. Finally, the thickness of the film and substrate is small enough compared to the lateral dimensions that radiative losses from the edges can be ignored.

The Seebeck coefficient (α), resistance (R) and heat transfer coefficients for the device as a whole (K) can then be calculated, and from these the figure of merit of the device can be calculated:

$$\alpha = \alpha_1 - \alpha_2 \quad (11)$$

$$R = \frac{\rho_1 l_1}{d_1 w_1} + \frac{\rho_2 l_2}{d_2 w_2} \quad (12)$$

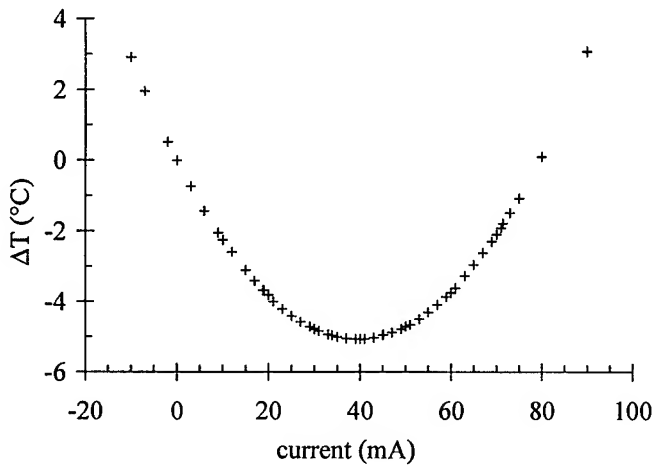


Figure 3: Measured cooling for device 1 operated at room temperature.

$$K = \sum_{p,n} K_{film} + K_{sub} + K_{rad} + K_{Tc} \quad (13)$$

$$Z = \frac{\alpha^2}{KR} \quad (14)$$

From Z the maximum cooling achievable can be calculated:

$$\Delta T_{max} = T_H + \frac{1}{Z} \left(1 - \sqrt{1 + 2ZT_H} \right) \quad (15)$$

Results and discussion

Two thin-film devices based on different materials will be discussed. The first device is a junction between a p-type $(\text{Bi}_{0.25}\text{Sb}_{0.75})_2(\text{Te}_{0.95}\text{Se}_{0.05})_3$ and an n-type $\text{Bi}_{0.9}\text{Sb}_{0.1}$ film on a 25 μm thick mica substrate. The second device is on a 10 μm thick mica substrate and uses a similar p-type material $(\text{Bi}_{0.25}\text{Sb}_{0.75})_2\text{Te}_3$ and with an n-type $(\text{Bi}_{0.95}\text{Sb}_{0.05})_2(\text{Te}_{0.95}\text{Se}_{0.05})_3$. The masks used in the deposition were arranged so that the films overlap slightly to form the cold junction of the device (as sketched in figure 2). Small devices (and their mica substrate) are then cut from the original film. Care must be taken while cutting the films to minimize damage to the thermoelectric material. In practice this damage and difficulty mounting the samples limit the minimum device size.

The electronic properties of the individual legs were measured independently on a mica witness substrate placed next to the device substrate for the deposition. The electronic properties of the witness sample and thickness were measured independently. The lateral dimensions of the device were also measured after it was mounted in the measurement jig. These measured parameters are recorded in table 1 and were used to calculate expected values for device performance.

The cooling of the actual devices was measured experimentally as a function of current (figure 3,4). The temperature response to a current pulse is also shown (figure 1). Much of the time required for response comes from the energy needed to heat the tiny dot of silver paint used to hold the thermocouple to the back of the mica substrate.

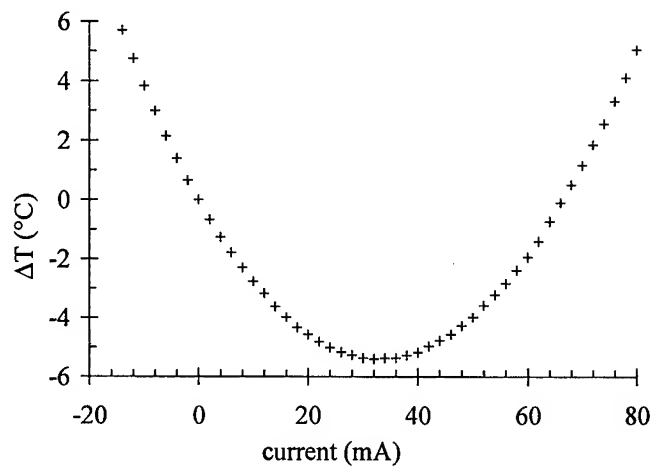


Figure 4: Measured cooling for device 2 operated at room temperature.

		device 1		device 2	
		n-type	p-type	n-type	p-type
	units	$\text{Bi}_{0.9}\text{Sb}_{0.1}$	$(\text{Bi,Sb})_2(\text{Te,Se})_3$	$(\text{Bi,Sb})_2(\text{Te,Se})_3$	$(\text{Bi,Sb})_2\text{Te}_3$
		measured values			
α	V/K	-1.00E-04	1.10E-04	-8.50E-05	1.20E-04
ρ	$\Omega \text{ cm}$	5.70E-04	1.00E-03	9.40E-04	6.20E-04
l	cm	0.25	0.18	0.28	0.28
w	cm	0.20	0.22	0.35	0.35
d	cm	9.50E-04	6.00E-04	9.40E-04	6.20E-04
d_{mica}	cm	2.50E-03		1.03E-03	
r_{Tc}	cm	1.30E-03	1.30E-03	1.30E-03	1.30E-03
		assumed values			
K_{film}	W/cm ² K	0.080	0.014	0.014	0.014
K_{mica}	W/cm ² K	0.020			
K_{Tc}	W/cm ² K	0.300	0.190	0.300	0.190
ϵ_{fts}		0.600			
ϵ_{Tc}		0.300			
		calculated values			
$Z_{\text{film}}T$		0.07	0.26	0.16	0.50
K_{film}	W/K	6.08E-05	1.03E-05	1.65E-05	1.09E-05
K_{sub}	W/K	4.00E-05	6.11E-05	2.58E-05	2.58E-05
K_{rad}	W/K	1.84E-05	1.45E-05	3.60E-05	3.60E-05
K_{Tc}	W/K	1.55E-06	1.23E-06	1.55E-06	1.23E-06
R	Ω	0.75	1.36	0.80	0.80
		whole device calculated values			
K	W/K	2.08E-04		1.54E-04	
α	V/K	2.10E-04		2.05E-04	
R	Ω	2.11		1.60	
ZT		0.03		0.05	
ΔT_{max}	K	4.39		7.32	
		measured device properties			
ΔT_{max}	K	5.10		5.30	

Table 1: At the top are the measured properties of the individual films used in the devices. Below are assumed values for the thermal conductivity and emissivity. The next section shows the heat transfer coefficients with the relative losses in each component. Finally, calculated values for ΔT_{max} from the measured film properties can be compared with measured values for the devices listed at the bottom of the table.

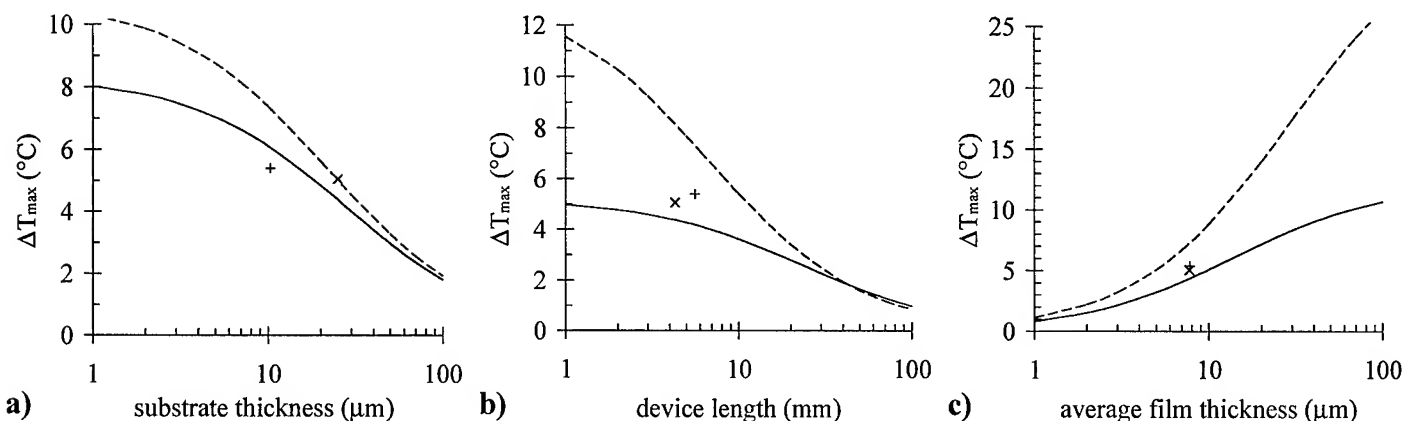


Figure 5: Derived dependence of the maximum cooling with: a) substrate thickness; b) device length; c) average film thickness. The measured electronic properties and dimensions of the films used in the two devices were used in the calculations. In b and c the device leg length or film thickness ratios are preserved. In both cases optimization in these ratios, which could be obtained from the model, could lead to further enhanced performance. Calculations based on device 1 are plotted as a solid line and device 2 as a dashed line. Measured values for device performance are also shown: (x) device 1; (+) device 2.

The cooling as a function of current (I) can also be calculated from the measured device parameters and compared with measured values:

$$\Delta T = \frac{\alpha I T_H - \frac{1}{2} I^2 R}{(\alpha I + K)} \quad (16)$$

This is approximately parabolic as seen in figures 3 and 4 if $K \gg \alpha I$, but switches to a more linear behavior at large I .

It is valuable to look more closely at the calculated values of the thermal loading for each device shown in table 1 to learn which loads are the largest, and thus what route would improve device performance the most. Table 1 shows that the thermal losses in the substrate are substantial. Thus reducing substrate thickness (or thermal conductivity) would be beneficial. The effect of substrate thickness on ΔT_{\max} is plotted in figure 5a.

Losses from radiation are less than those from the substrate in device 1. In device 2, where a thinner substrate and lower conductivity films are used, radiation is the dominant loss. The performance of each device is plotted as a function of device length in figure 5b. As the device is made larger the radiation effects begin to dominate.

Losses in the very fine 0.001 inch diameter k-type thermocouple wire used are relatively small. For a 0.003 inch diameter thermocouple, however, the thermal loss will be over 5 times larger since the loss goes as the radius of the thermocouple to the three halves power (equation 8). In this discussion we have considered the thermocouple losses to be spread over the entire cold junction of the device. In practice the thermocouple could cause a local hot spot if it were a more significant heat load.

Finally, depositing thicker films or films with higher ZT would also improve performance. As can be seen in table 1 the n-type $(\text{Bi}_{0.95}\text{Sb}_{0.05})_2(\text{Te}_{0.95}\text{Se}_{0.05})_3$ film could be improved considerably before bulk properties are reached. Increasing film thickness diminishes the importance of the parasitic thermal loads associated with thin films which we have investigated in this work. The dramatic improvement in ΔT_{\max} with increasing film thickness can be seen in figure 5c.

Conclusion

Excellent agreement is found between the values calculated for the device from the measured parameters and those measured experimentally from actual devices (table 1). This agreement suggests that all the relevant thermal loading is accounted for in the model. Using the analytical model developed here will lead to improved device performance.

Acknowledgments

Funding for this project was provided by ARPA, Larry Dubois, program manager. We would like to acknowledge D. Makowiecki for use of the sputtering chamber. This work was done under the auspices of the U.S. DOE by Lawrence Livermore National Laboratory under Contract No. W-7405-Eng-48.

References

- [1] L.D. Hicks, M.S. Dresselhaus, "Use of Quantum-Well Superlattices to Obtain a High Figure of Merit from Nonconventional Thermoelectric Materials," *Appl. Phys. Lett.* **63**, 3230-3232, 1993.
- [2] I.H. Kim, B.G. Min D.H. Lee, "Effects of Thickness and Processing Variables on the Performance of $(\text{Bi,Sb})_2(\text{Te,Se})_3$ -based Film Type Thermoelectric Modules", *Proc. of the XIV International Conference on Thermoelectrics*, St. Petersburg, Russia, 145-150, 1995.
- [3] A.V. Wagner, R.J. Foreman, L.J. Summers, T.W. Barbee, Jr., J.C. Farmer, "Synthesis and Evaluation of Thermoelectric Multilayer Film", to be published in *Proc. of the XV International Conference on Thermoelectrics*, Pasadena, CA, 1996.
- [4] A.V. Wagner, R.J. Foreman, L.J. Summers, T.W. Barbee, Jr., J.C. Farmer, "Multilayer Thin Film Thermoelectrics Produced by Sputtering", *Proc. of the XIV International Conference on Thermoelectrics*, St. Petersburg, Russia, 283-287 1995.
- [5] A.V. Wagner, R.J. Foreman, L.J. Summers, T.W. Barbee, Jr., J.C. Farmer, "Multilayer Thermoelectric Films: A Strategy for the Enhancement of ZT ," *Proc. 30th Intersociety Energy Conversion Engineering Conference*, Orlando, Florida, **3**, 87-92, 1995.
- [6] H.S. Carslaw, and J.C. Jaeger, "Conduction of Heat In Solids", Oxford University Press, 135, 1959.

Robust Thin Film Thermoelectric Devices

C.L. Chu
Tecstar
15251 Don Julian Road
City of Industry, California 91745-1002 USA

ABSTRACT

The distribution of thermal stresses in thermoelectric columns with superlattice structure was analyzed by numerical simulation. This analysis focused on Bi_2Te_3 compounds used for cooling purpose. The dimensions used for analysis are achievable by using metal organic chemical vapor deposition (MOCVD), a technology which can economically fabricate high quality thermoelectric devices. Various mechanical constraints were used for simulation. The calculated stresses within thermoelectric (TE) devices made of bulk material were also evaluated. Because the superlattice structure assembly is mechanically similar to other thin film designs, these results can be applied to TE devices made by different thin film techniques.

INTRODUCTION

In past decades some progress on improving the figure of merit has been reported by reduction of the thermal conductivity of bulk material, by methods such as alloying, microstructuring, and inclusion of inert materials. To achieve a significant breakthrough, superlattice structures have great potential to decrease the thermal conductivity of TE materials. Superlattices using Bi_2Te_3 , Sb_2Te_3 , and PbTeSe/BiSb semiconductors have been studied by the TE industry, and in laboratories such as Lincoln Laboratory and Research Triangle Institute. Theoretical evaluation of the structures was also reported by several researchers. Both approaches indicated the great potential of TE devices using these new structures(1-4).

MOCVD is the only economic manufacturing technology to fabricate TE device with superlattice structure, and the cost of MOCVD production is comparable to the existing TE processes. One technical concern of the

superlattice device structure is the cooling and heating capability. Although experimental tests can be made on prototype devices, it is necessary to analyze the reliability of these structures to validate the device robustness, and to direct the material development and assembly procedures which can ensure successful practical application.

Because TE devices with superlattice structures are not readily evaluated, numerical simulation is the most economic way to study the reliability problem. TE devices with superlattice structures of different physical dimensions were analyzed. Different thermal or mechanical constraints were assumed for simulation. The results presented in this report may not fully duplicate operating condition, but the failure criteria obtained from the studies can be used to direct further device evaluation. A NASTRAN program, which was initiated by NASA and is widely used in structural design, aerospace applications and thermal analysis, was used for the simulation. Von Mises stress profiles were generated for use in failure evaluation.

SIMULATED DEVICE AND CALCULATION SCHEME

MOCVD uses Metal Organic or Halide gaseous or liquid sources at appropriate temperatures and pressures to grow single crystal layers by chemical vapor deposition on large area substrates. Currently, high quality GaAs epi layers grown on Ge substrates and at rates of >6 micron/hour, throughput of $>3000\text{cm}^2/\text{batch}$ are being used to produce solar cells at Tecstar/ASD. To prepare TE materials with superlattice structures a faster growth rate and a higher throughput will reduce the cost of the product. Because the technology is ready for mass production, the large quantity price of gaseous/liquid sources can also be significantly

decreased to match the requirements of the TE market. MOCVD can prepare multi-layer structures on large area substrates with either homo and hetero layer structures each layer being less than 100 Å. Due to the characteristics of Bi_2Te_3 like compounds, the superlattice structure could be successfully grown on low cost Ge substrates. Figure 1 shows an X-ray diffraction picture of a 2000 Å superlattice structure epi-grown on a GaAs substrate (by Research Triangle Institute). The prominent peak is GaAs and the peaks of the $\text{Bi}_2\text{Te}_3/\text{Sb}_2\text{Te}_3$ superlattice were displaced by 0 to 5000 arc seconds (1 degree equals 3600 sec) from the main peak. Since these TE materials with superlattice structure can be grown on GaAs, the TE materials can easily be grown on Ge substrates, which have closely similar lattice spacing and thermal conductivity to GaAs. If the growth rate is improved as projected, a 25 μm (or 12 μm) thick superlattice should be a practical structure to meet both the economic and technical criteria of the TE industry. For simulation, we used one mil or half mil thick superlattice layers grown on Ge substrates sandwiched between solder coated Al_2O_3 plates.

Square cross sections (20 mil x 20 mil, Fig. 2a), and circular cross sections of (20 mil diameter, Fig. 2b) which are popular in TE industry were used for simulation. The thickness of the TE layer varied from 1 mil to 0.5 mil. The Ge substrate is 8 mils thick and the thickness of the solder and Al_2O_3 were 3 and 10 mils, respectively. 11x11x16 grids (Fig. 3) were assigned to X,Y, and Z directions for the rectangular column. For cylindrical samples, 80 grids were assigned to the bottom of the cylinder and 20 grids assigned to the Z direction. Temperatures of +70°C and -30°C were used as fixed thermal boundary temperatures to the Al_2O_3 layers at the ends of the sample, the lateral side was assumed to be adiabatic. The mechanical constraints assigned to the two ends were 1) both free, 2) one end free, one end fixed, and 3) both fixed. In addition, a cylindrical column without germanium material was used for comparison. Since the stress-free status of the sample was set at 0°C, all these calculations showed the stress difference caused by temperature variation. The calculated results indicated many interesting points for design and assembly of TE couples.

The material properties used for simulation were given in Table 1.

CALCULATED RESULTS

Square cross section was used for calculation in Case 1, other cases used the circular cross section. However, at adiabatic conditions, this variation does not affect the temperature profile of the sample (Fig. 4).

Case 1: Square Cross Section

The -30°C end was assumed to be fixed, the +70°C end was free from constraint. A 32.6°C temperature difference was generated across the TE layer. A 15.4 kpsi Von Mises (VM) stress was generated on the cold end. The hot end with nearly free expansion showed a 0.1 kpsi VM stress. In the TE layer, 2 kpsi was generated at the corners, and this decreased to 1.2 kpsi toward the center area. The largest stress gradient was created within the solder layer (at the cold end). This may indicate the possibility of easy separation at the TE/solder interface.

Case 2: Circular Cross Section

When the shape of the cross section of the column changed from square to circular shape, the same thermal/mechanical constraints generated different stresses in the sample. The largest VM stress on the -30°C end decreased from 15.4 kpsi to 14 kpsi, the stress on the TE layer decreased to 1 kpsi. The most significant change was the difference of the stress gradient caused by the corners of the square shape. Even if the magnitude of the calculated stress was excessive, the cylindrical shape is a better design to reduce the possibility of damage to the device.

Case 3: Constraint on the Hot End

In cases 1 and 2, the -30°C end was blocked. In this case, the cold end was free and the +70°C end was fixed. Because the sample was assumed to be stress free at 0°C, the +70°C temperature difference generated a greater stress (more than double) than the stress caused by 30°C temperature difference. This boundary condition generated a 38 kpsi on the hot end, and 2 kpsi on TE layer. The stress gradient still existed in the radial direction, but not in the lateral direction.

Case 4: Constraints on Both Ends

Since both the -30°C end and $+70^{\circ}\text{C}$ ends were constrained from moving, and the sample was mechanically within its elastic regime, the stresses can be superimposed. This led to estimates of stresses about 38 kpsi on both ends and 2.5 kpsi on the TE layer, greater than the stresses in both cases 2 and 3.

Case 5: Ge Substrate Replaced by TE Material

This material replacement changed the temperature profile of the sample. The TE layer became 9 mils thick. The stress calculation is also changed accordingly. This case is similar to the existing TE couple assembly. In this case, 42 kpsi VM stress was generated at the $+70^{\circ}\text{C}$ end and 14 kpsi at the -30°C end. A wide range of stress from 0.2 kpsi to 4.4 kpsi was generated in the TE layer. 8.5 kpsi VM stress was created at both solder/TE interfaces.

Case 6: Thinner TE layer

When the thickness of the TE layer grown on the Ge substrate was reduced to 0.5 mil, there was only a 20% increase of stress in the TE layer. But a TE layer of less than 0.5 mil may be impractical for application and was not included for simulation.

Case 7: Free of Mechanical Constraints

For circular cross section sample (Case 2), the VM stress on the TE layer was about 0.8 kpsi. This may be quite different from the real case but can be used as a reference.

The calculated results are shown in Table 2. The main calculation results are:

- 1) At the same thermal/mechanical constraints, less stress will be generated in TE layers with circular cross section than in square cross sections.
- 2) A greater thermal stress was generated in the thick TE layer than in the thin TE layer on Ge substrate. This may indicate that the superlattice structure will survive better than existing devices processed from bulk ET material.

DISCUSSION

Due to the discrepancies between the assumed boundary conditions and practical applications, this simulation is not perfect. We can project some modifications to the hardware and calculation scheme which will improve the prediction. These modifications include:

- 1) The material properties used for calculation are temperature dependent, but in this calculation they were to be assumed independent.

- 2) At 0°C , the assembly was assumed to be stress free. This assumption may not be valid. The real stress status of the assembly will be process dependent. The magnitude of the calculated stress will be changed by this modification. In-situ strain measurements will provide essential information to guide further analysis.

For multi-stage TE cooling assembly designed for low temperature application, significant thermal stresses generated by the different temperatures between assembly preparation and operation will severely evaluate the reliability of the device. To overcome this challenge, different material preparation and assembly technology may be required.

- 3) The adiabatic assumption can be approached by adding thermal insulation layers to the lateral sides of the column.

- 4) Bi-Te-Sb single crystals are not isotropic, and the thermal and mechanical properties are orientation dependent. The yield strength and creep phenomena of the superlattice structure need to be experimentally studied. This information will provide a solid basis for failure prediction through numerical simulation.

- 5) Other effects, such as non-uniform thermal boundaries and thickness variation of each layer, especially the solder layer, need further evaluation.

- 6) During operation, the temperature variation caused by Ohmic heating effects may add minor contribution to the stress distribution.

CONCLUSION

The MOCVD technology can form superlattices of TE materials which promise improved TE performance. This study has assumed feasible S/L structures, and using numerical analysis, the stress conditions for a variety of structures have been analyzed. The results of these calculations can be applied to direct experimental studies to fabricate practical TE devices.

ACKNOWLEDGMENT

This work was partially supported by Army Research Office under contract ATESBIR-1095.

REFERENCES

1. Hicks, L. D., Dresselhaus, M.S., "Thermoelectric Figure of Merit of a One-Dimensional Conductor," Phys. Rev. B 4724, 16631-634(1993)
2. Hicks, L. D., Dresselhaus, M.S., "Effect of Quantum-Well Structures on the Thermoelectric Figure of Merit," Phys. Rev. B 47 19, 12727-731(1993).
3. Hicks, L. D., Dresselhaus, M.S., "The Effects of Quantum Well Structures on the Thermoelectric Figure of Merit," presented at the 1st Natl. Thermogenic Cooler Conf., Center for Night Vision and Electro-Optics, U.S. Army, Ft. Belvoir, VA, 1992.
4. Venkatasubramanian, R., Timmons, M.L., and Hutchby, J.A., "Monolithically Interconnected, Superlattice-Structured Thermoelectric (MISST) in Bi₂Te₃, Sb₂Te, and BiSe Materials for High Performance Thermoelectric Cooling Devices" 12th International Conference on Thermoelectrics, 1992.

Table 1 - Material Properties of Each Layer

Material	Thermal Conduct. (W/m-C)	Specific Heat (J/Kg-c)	Density (Kg/m ³)	Thermal Exp. Coeff(10 ⁻⁶ /C)	Young's Modulus (10 ⁷ psi)	Shear Modulus (10 ⁷ psi)
Al ₂ O ₃	25.0	906.0	3890.0	7.1	5.0	2.0
Solder	50.0	212.0	7980.0	24.7	0.3	0.107
Bi ₂ Te ₃	1.75	124.0	7859.0	12.9	0.061	0.023
Ge	60.0	310.0	5316.0	5.8	1.89	1.02

Table 2 Summary of Calculation

Case #	Temperature Range	Mechanical Constraint	Thickness of TE layer (mil)	σ_{\max} (kpsi)	σ_{\max} on TE layer (kpsi)	Cross Section
1	-30°C/+70°C	-30°C	1	15.4	2	Square
2	-30°C/+70°C	-30°C	1	14	1	circular
3	-30°C/+70°C	+70°C	1	38	2	circular
4	-30°C/+70°C	-30°C/+70°C	1	38	2.5	circular
5	-30°C/+70°C	-30°C/+70°C	9	42	4.4	circular
6	-30°C/+70°C	-30°C/+70°C	0.5	38	3	circular
7	-30°C/+70°C	none	1	10	0.8	circular

σ_{\max} : Maximum Von Mises stress.

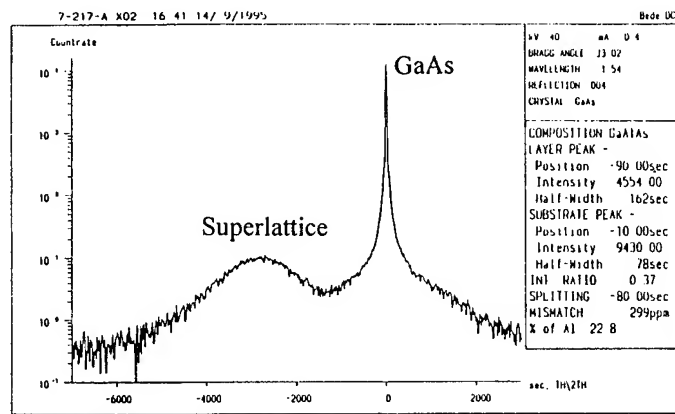


Figure 1 X-ray diffraction pattern of superlattice TE layers on GaAs substrate

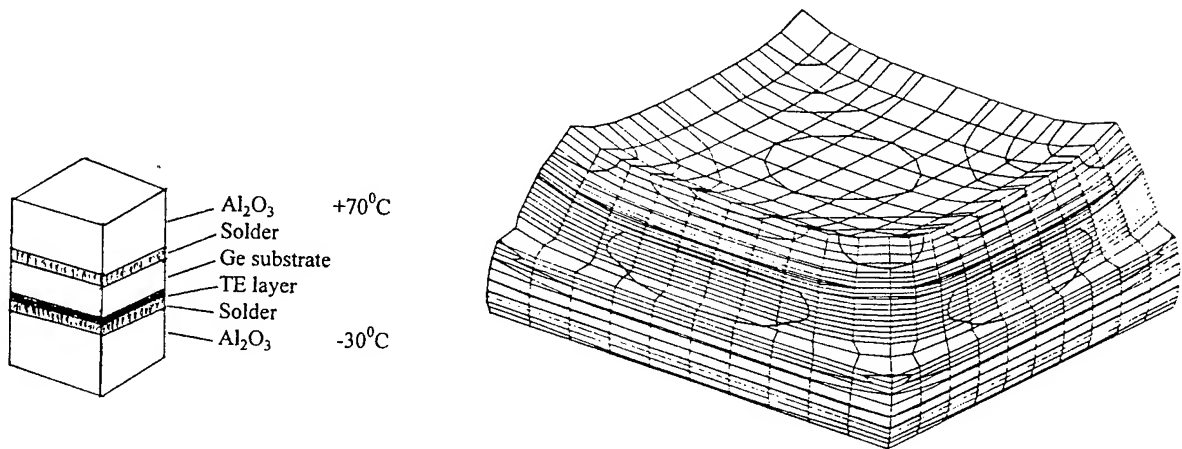


Figure 2 (a) Vertical profile of TE column of square cross section

Figure 3 11x11x16 grids used for case 1 simulation

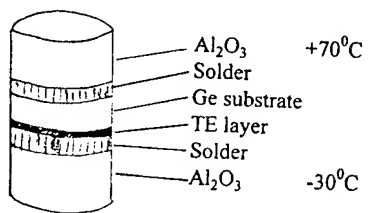


Figure 2 (b) Vertical profile of TE column of circular cross section

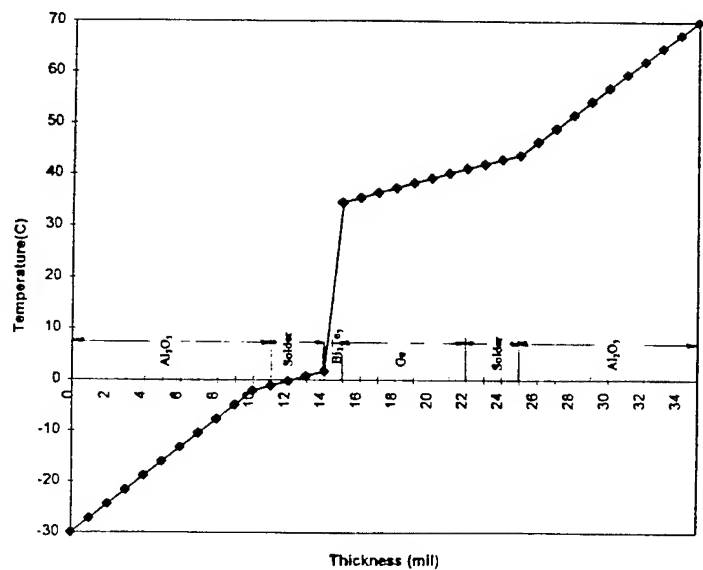


Figure 4 Temperature profile of simulated TE column

Physical Principles of Microminiaturization in Thermoelectricity

L.I. Anatyshuk, O.J. Luste
(Institute of Thermoelectricity, Chernivtsi, Ukraine)

Abstract

Factors, which promote to microminiaturization of cooling modules have been considered. Results of thermoelectric coolers investigations are presented with taking into account all classical factors: electrical and heat resistance of a commutation, contact resistance, heat resistance of heat transfers, all kinds of thermoelectric effects, temperature dependencies of material properties, etc. The influence of all factors on cooling efficiency is analyzed. New factors, which can have influence on a module work, namely strong electric field, large temperature gradient, size effects, diffusion processes are considered. The influence on microminiaturization and conditions for these factors actions are analyzed. A common analysis for microminiaturization limits and a prognosis of thermoelectric modules development is presented.

1. Microminiaturization and progress in thermoelectrics

The reason limiting the wider use of thermoelectrics appears to be the high cost of the modules for cooling and energy generation. The cost of the material is the biggest component in the module cost. At the same time the thermoelectric material itself is not involved into the energy conversion process, it is the passive heat and electricity carrier. Conversion occurs in comparatively thin layers near the interface between the thermoelectric material and metal. From this viewpoint using that big quantity of thermoelectric material is absolutely useless (Fig. 1).

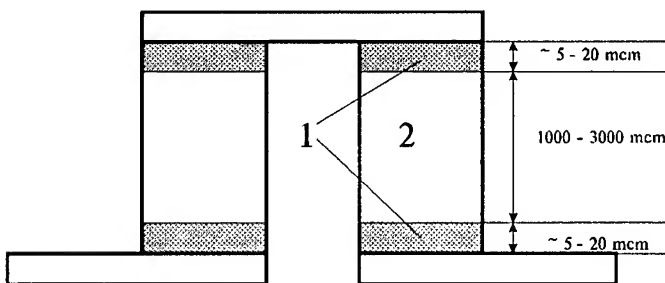


Fig. 1. Model of thermocouple energy converter.

It demonstrates the fact that only about 1% of thermoelectric material volume participates in energy conversion. 1 - material inhomogeneity areas where the conversion process occurs, 2 - passive area.

If there was such situation in electronics, the devices would be very expensive and they wouldn't be widely used.

Thereof, we should try to use less material, which means fabrication of tinier thermoelectric converters.

Beside economical factors, there are some other for miniaturization of thermoelectric energy converters. Among them the most attractive are prospective for combining thermoelectric and electronic elements all in one (Fig. 2). Analysis shows that these elements allow to increase the quality of electronic equipment, their reliability, speed, compactness, sensibility and stability of sensors, very materially.

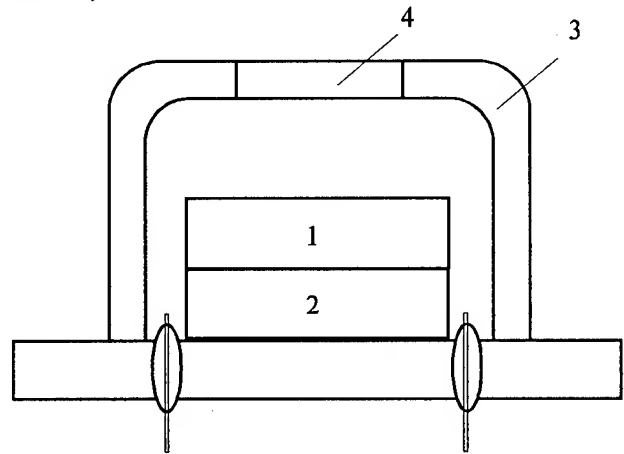


Fig. 2. A fragment of new elemental base of electronics.

1 - thermostatted and cooled components of electronics, 2 - thermoelectric cooling module compatible by size; 3 - a housing, 4 - window for radiation sensor case.

Promising is also the creation of new tiny energy sources based on microbatteries. In combination with nuclear power sources, tiny catalytic heaters, renewable low potential heat sources (temperature drops in soil, water, air, etc.) these generators appear to be in competition with chemical energy sources.

Thus, microminiaturization of thermoelectric energy converters gives the prospective for practicable thermoelectric use not only because of the price lowering, but also due to the new possibilities of thermoelectric conversion.

2. Limits for microminiaturization after classical descriptions

There were many investigations concerning the influence of different factors on thermoelectric converters properties at their microminiaturization [1-7]. Among them there are three main circumstances:

Joule heat influence in commutation plates;

Joule heat influence in contact resistances on the interface between thermoelectric semiconductor material and metal;

thermal resistances of the module structure elements influence, because heat goes in and out through them.

These reasons were studied very approximately. Lately we did precise investigations of them. Let us consider the results one by one.

2.1. Heat production in thermoelectric modules commutation plates [8].

A model for calculation is presented by Fig.3.

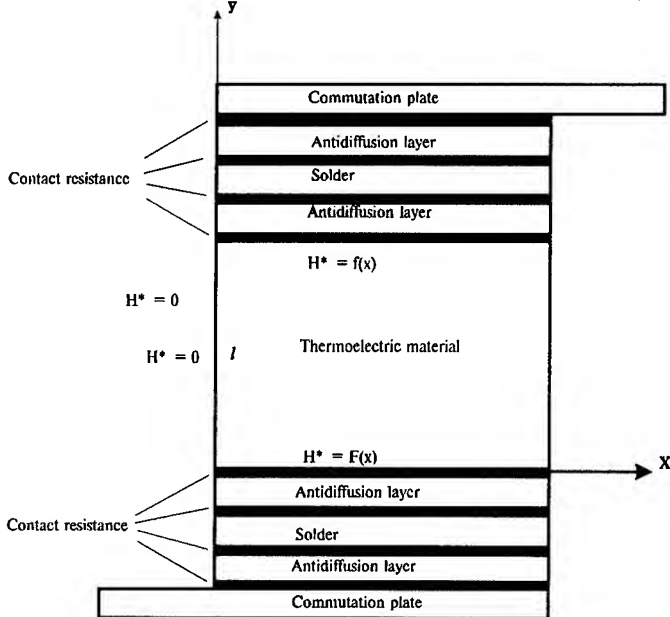


Fig. 3. Diagram of thermoelement commutation with antidiffusion and solder layers.

When an electric current is passed through a commutation plate an amount of an electric energy is expended to overcome an electric resistance of a commutation plate, that results in the coefficient of performance

$$\varepsilon = \frac{Q_0}{W} \quad (1)$$

decrease, where $W = I_2 R + \alpha(T_1 - T_2)$, Q is cooling power, I is current running along the element, R is total electric resistance (or a sum of resistances $R_{\text{legs}} + R_{\text{contact}} + R_{\text{com.plate}}$), α - Seebeck coefficient, T_1 and T_2 are hot and cold junctions temperatures.

It is necessary to account of the Joule heat production in a commutation plate when examining a general thermal picture in a thermoelectric module. Heat production in a commutation plate results in the coefficient of performance decrease because

$$\varepsilon = \frac{Q - Q_{\text{com}} - Q_{\text{cont}} - Q_{\text{heat-exchange}}}{W} \quad (2)$$

where Q - cooling power induced by Peltier effect, Q_{com} - heat produced in a commutation plate, Q_{cont} - heat produced in contacts, $Q_{\text{heat-exchange}}$ - heat losses due to heat exchange.

Commutation heat production results, on the whole, in the increase of a heat flux along a hot ceramic plate of a module,

diminishing an effective temperature differential on a module. The influence of the heat production is especially appreciable when a cooling module is used in the modes close to the maximum temperature differential mode. Therefore, when thermoelectric modules are designed, it is necessary to minimize an influence of a commutation plate electric resistances and, consequently, the Joule heat production in it. It is obtained by a commutation plate thickening when possibilities of a material use with high electric conductivity values have been already completed for this plate.

However, a commutation plate thickness increase yields to at least two disadvantages, namely, to a module increase in cost, and also to its thermal resistance value increase, since a commutation plate functions not only as an electric current conductor, but also as a heat conductor from thermobattery junctions to ceramic plates.

These circumstances are especially important at module microminiaturization.

A search of a compromise between these two counteractive factors, namely, a commutation resistance decrease and cost and heat losses increase on a commutation plate is a goal for its optimization.

To solve this problem it is necessary to know precisely the effective values for a commutation plate resistance and Joule heat production in it.

Current distributions in a commutation plate and in thermoelement branch had been determined from Laplace equation with the corresponding boundary conditions.

The simplified methods to determine a commutation plate resistance R_{plate} are known [1, 2, 3]. They can be represented by formula

$$R_{\text{plate}} = \frac{\rho_p \left(b - \frac{2a}{3} \right)}{s} \quad (3)$$

where ρ_p is resistance for a plate material, s - cross-section area, b - plate length, a - thermoelement leg width.

It is not clear, as far as this approximation is correct, and what errors may arise from its use.

The present paper considers a precise solution of the problem on an effective resistance of a commutation plate and heat production in it.

For each of the rectangular areas indicated in Fig.3 the distribution of electric currents may be determined from a steady-state conditions

$$\text{div } \mathbf{j} = 0, \quad (4)$$

where \mathbf{j} is electric current density.

Let us introduce $H(x,y)$ current function according to the following relations:

$$\begin{aligned} j_x &= H_y, \\ j_y &= -H_x, \end{aligned} \quad (5)$$

where x and y are coordinates illustrated in Fig.4 and a subscript means the differentiation by a suitable coordinate.

So, a physical meaning of the H function determined by this way is difference of this function in two points gives an electric current value, running along a plate section between these two points.

From the equation (4) it follows that H current function satisfies the Laplace equation

$$\nabla^2 H = 0, \quad (6)$$

to which the boundary conditions for a current density vector and an electric potential on the boundaries of the examined area should be added for each of the considered areas, such as a thermoelement leg, solder layers and antidiffusion layers. These conditions are the following:

$$\begin{aligned} H(x, y_{\text{boundary}})^{\text{upper area}} &= H(x, y_{\text{boundary}})^{\text{lower area}} = f(x), \\ \rho_{\text{upper}} H_x(x, y_{\text{boundary}})^{\text{upper area}} &= \rho_{\text{lower}} H_x(x, y_{\text{boundary}})^{\text{lower area}}, \\ H(x_{\text{left}}, y) &= 0, \\ H(x_{\text{right}}, y) &= 0, \end{aligned} \quad (7)$$

where subscript and a superscript defines to which boundary the corresponding expression relates to, $f(x)$ - or $F(x)$ for lower boundary - is the unknown function, indicated in Fig.2. It is convenient to solve a boundary problem for H function in a thermoelement leg as a sum of the known solution H_0 and the disturbance H^* . H_0 corresponds to a homogeneous current flux along y -axis in the considered area. The disturbance H^* is due to inhomogeneous current distribution on the area contacts. Thus, for the leg

$$H(x, y) = \frac{Ix}{ahd} + H^*(x, y), \quad (8)$$

where I - current running along a thermoelement, h is commutation plate width, d is commutation plate thickness, a is leg width. By the variable separation method the unknown disturbance $H(x, y)$ may be reduced to the form

$$H^*(x, y) = \frac{2}{a} \sum_{n=1}^{\infty} \left\{ \frac{F_n \sinh \frac{n\pi(l-y)}{a}}{+ f_n \sinh \frac{n\pi y}{a}} + \frac{\sin \frac{n\pi x}{a}}{\sinh \frac{n\pi l}{a}} \right\}, \quad (9)$$

where f_n and F_n are expansion coefficients of $f(x)$ function and $F(x)$ function into proper Fourier series.

Formulae, similar to the expression (9) may be deduced for all considered two-dimensional areas, where f_n and F_n coefficients will be introduced for the each area.

Determination of these coefficients for each examined area is the basic problem to define current and potential distributions in all areas. In fact, we have to do with a system of nine interconnected boundary problems for an every area (a number of areas indicated in Fig.3 equals to nine). To determine the unknown Fourier coefficients, it is required to solve a system of equations, which is the result of the boundary conditions similar to the eq. (7) for all contacts

between these areas. We have defined that this system of equations has one and the only solution, analytical form of which we do not adduce due to its bulky and numerous parameters.

The computer program for these equation solutions has been developed, which allows to define local and integral electric resistances and heat production for any values of geometrical sizes and material electric characteristics.

This program lets also define special distributions of current in a commutation plate and in thermoelement.

Fig. 4 to 9 illustrate current distribution in thermoelement legs and in a commutation plate. It seems from Fig 4, that if commutation plate is thick, then the current distribution is close to the uniform distribution. The deviation from the uniform distribution increases when the branch thickness decreases (Fig. 6, 7 and 8, 9).

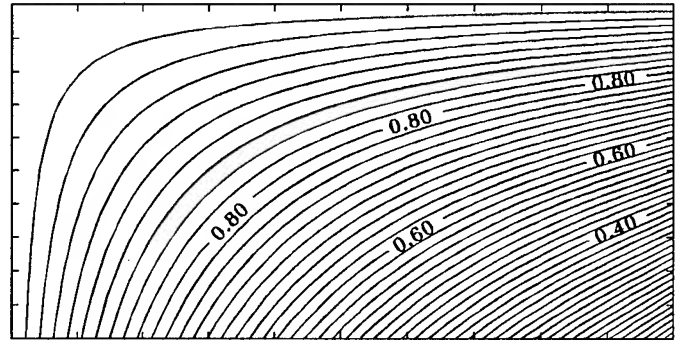


Fig.4. Current distribution in commutation plate. $l/a = 1$, $a/d = 100$.

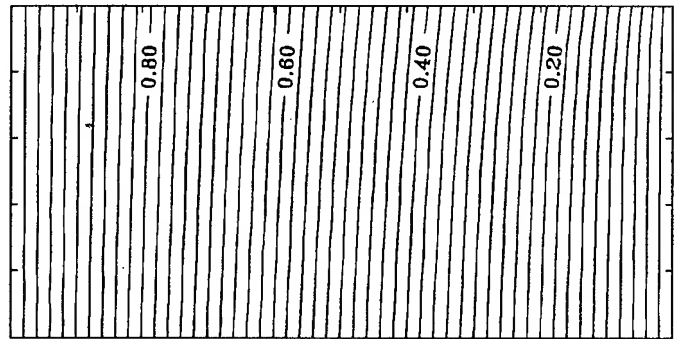


Fig.5. Current distribution in upper half of the thermoelement leg. Geometry factors are the same as in Fig.4.

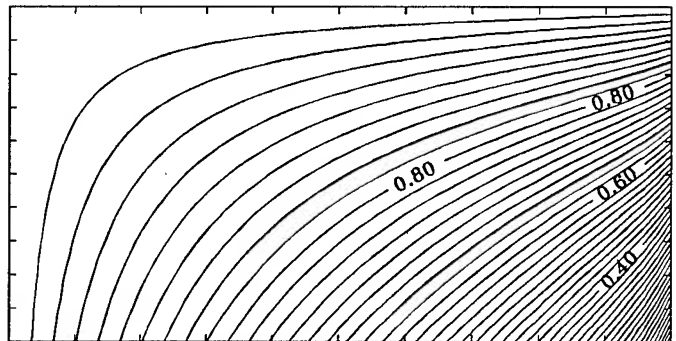


Fig.6. Current distribution in commutation plate. $l/a = 1$, $a/d = 1000$.

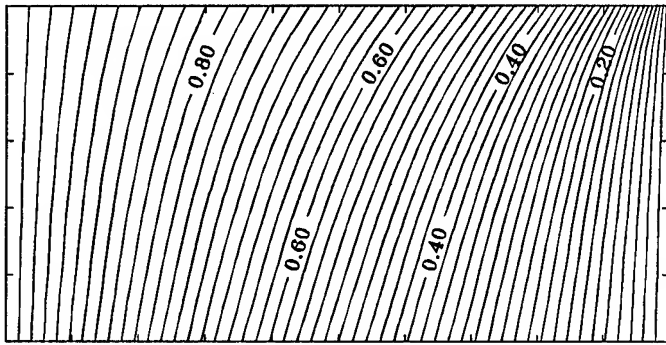


Fig.7. Current distribution in upper half of the thermoelement leg. Geometry factors are the same as in Fig.6.

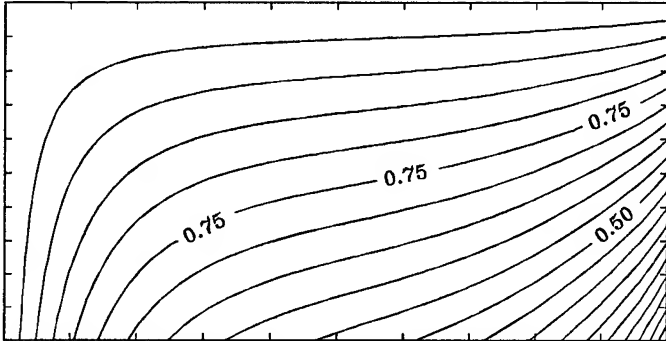


Fig.8. Current distribution in commutation plate. $l/a = 0.1$, $a/d = 1000$.

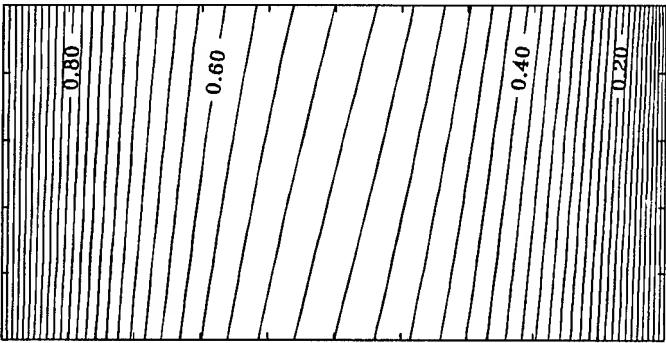


Fig.9. Current distribution in upper half of the thermoelement leg. Geometry factors are the same as in Fig.8.

The figures clearly illustrate that the calculation program allows to obtain besides the effective resistance values of commutation, heat production, and precise picture of current distributions both in thermoelement legs and in a commutation plate. The figures show, that as a commutation plate thickness eliminates, the current distribution deviates from uniform and one-dimensional one considerably. In addition, an effective resistance increase not only in commutation plate but in a thermoelement leg, that is usually not taken into consideration. This fact must be taken into account when calculating and design a cooling module.

After the aforesaid methods there was done the analysis of commutation plates' heat loss influence on COP of a cooling module. It was found that there are no principal difficulties in microminiaturization connected with commutation resistances. It is always possible to choose such cross-section area of branch, when commutation resistance is less than contact resistance. Commutation resistance forces not only

branch length miniaturization, but cross-section miniaturization also.

2.2. Heat loss on contact resistances influence.

Heat release in contact resistances results in worsening of thermoelectric modules main characteristics. For the thermoelectric cooling case the contact resistances effect is described by the equations

$$\Delta T_{\max} = T_1 - \frac{\left[\sqrt{1 + 2 \frac{Z_0 L}{L + 2r_0 \sigma}} T_1 \right] - [L + 2r_0 \sigma]}{Z_0 L} \quad (11)$$

$$\varepsilon_{\max} = \frac{T_0}{T_1 - T_0} \sqrt{\frac{1 + 0.5(T_0 + T_1) \frac{Z_0 L}{L + 2r_0 \sigma} - \frac{T_0}{T_1}}{1 + 0.5(T_0 + T_1) \frac{Z_0 L}{L + 2r_0 \sigma} + 1}} \quad (12)$$

$$q_{0 \max} = \frac{\kappa}{L} \left[\frac{Z_0 L}{L + 2r_0 \sigma} T_0^2 - (T_1 - T_0) \right] \quad (13)$$

where general designations are commonly known, L is a leg length, $r_0 = r/s$ is specific contact resistance.

The criterion for thermoelectric battery figure of merit is often introduced in the form of the equation

$$Z = Z_0 \frac{L}{L + 2r_0 \sigma} \quad (14)$$

whence it follows that with contact resistance increase, figure of merit of the thermoelectric battery decreases.

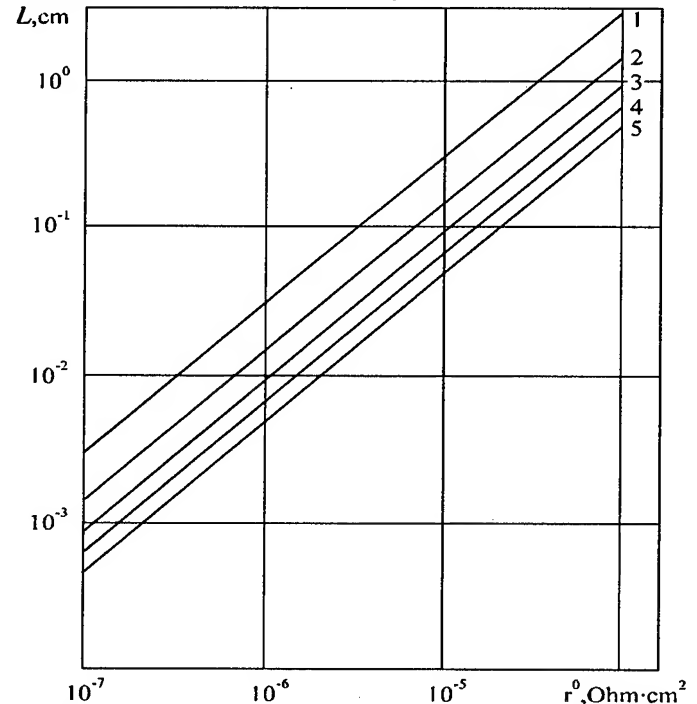


Fig.10. Z/Z_0 ratio is equal to 0.95 for the line 1, 0.9 for the line 2, 0.85 for the line 3, 0.8 for the line 4, 0.75 for the line 5.

Fig. 10 illustrates the dependencies of thermoelements figure of merit on leg's material figure of merit, and temperature difference relative decrease with a thermoelement height for different values of contact resistance.

So batteries microminiaturization depends directly on the contact resistance value.

This raises the question as to what minimum contact resistances can be obtained in principle. That is, what fundamental limitations can contact resistance impose on miniaturization. This problem has been solved in the Institute of Thermoelectricity [9]. Different variants of energetic models that describe the contact region between thermoelectric material and metal have been studied.

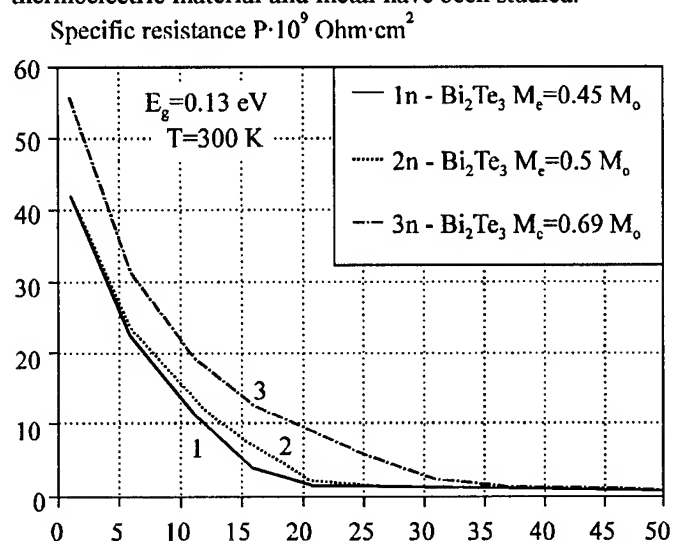


Fig. 11. Minimal specific contact resistance.

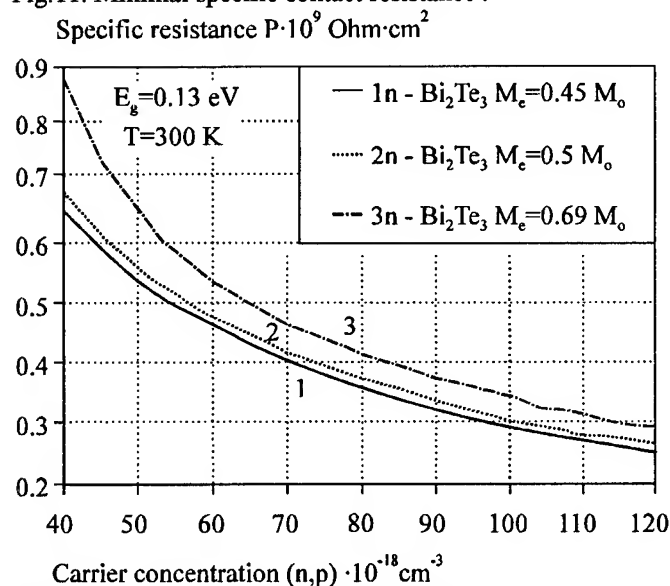


Fig. 12. Minimal specific contact resistance.

Specifically, values for contact resistances represented in Fig. 11 and 12 were obtained for thermoelectric materials based on Bi_2Te_3 alloys. It follows from the figures that values of contact resistances cannot actually be lower than $10^{-7} - 10^{-8} \text{ Ohm cm}^2$.

The possibilities of microminiaturization caused by the contact resistance effect are apparently limited by these values.

We can conclude, that there are the following tentative requirements to contact resistance

- 10-6 Ohm cm^2 for a branch length of 1000 mcm,
- 10-7 Ohm cm^2 for a branch length of 100 mcm,
- 10-8 Ohm cm^2 for a branch length of 10 mcm.

Investigations directed to the small contact resistance values achievement are essentially depend on feasibility of considerably precise measurement of contact resistance values. Contact resistance measurements against the backgrounds of relatively large legs resistance is the complicated problem and requires the creation of special methods. The Institute of Thermoelectricity has conducted the investigations on the creation of such methods.

2.3. Method for precise measurement of contact resistance.

In the work [1] L.S. Stilbans and co-workers had proposed the method of metal-semiconductor contact resistance determination by indication of thermo-e.m.f. zero equality developed by the contact when direct current pulses passed through the contact. In accordance with [1] the contact resistance equals to

$$R_k = (\alpha_1 - \alpha_2)T / I_0,$$

where $(\alpha_1 - \alpha_2)$ is the difference of semiconductor and metal coefficients of thermo-e.m.f., T is the contact temperature, I_0 is the pulse current corresponding to the thermo-e.m.f. zero signal.

The Stilbans' method unfortunately did not take into account the Joule heat entered to the contact of a semiconductor, metal and semiconductor thermal capacity, error of the used zero-indicator, and it did not give the precise assessment of the proposed method. The present paper gives the temperature dynamics temperature of thermoelectric material with metal plate contact when direct current rectangular pulses passed through the contact; compensation current corresponding to the contact zero temperature at the end of pulse action and the error of contact resistance determination by the compensation current.

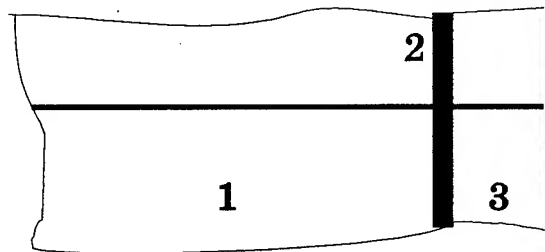


Fig. 13. Diagram of a metal-thermoelectric material contact.

Model for calculation is given in Fig. 13. It has a leg of thermoelectric material 1 which is in thermal and electric contact 2 with a commutation plate 3. Direct current pulse of j density is passed through the contact (Fig. 14).

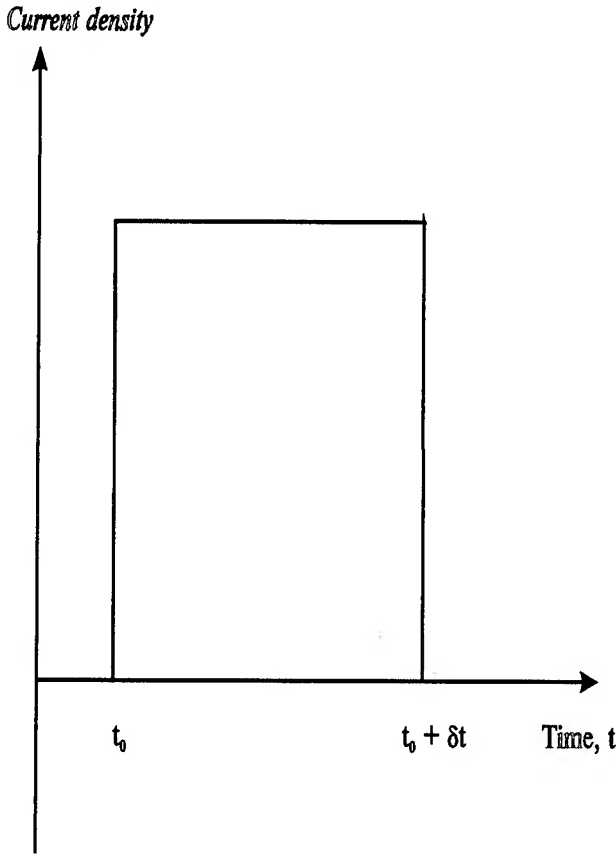


Fig. 14 Rectangular current pulse passed through the contact metal-thermoelectric material.

The contact overheating temperature can be represented as the sum (Fig. 15)

$$\Delta T(t) = \Delta T_{Joule.contact} + \Delta T_{Joule.branch} + \Delta T_{Peltier},$$

ΔT is the contact temperature change due to current passing at the end of a pulse, $\Delta T_{Joule.contact}$ is the contact temperature change due to the Joule heat release on the contact at the end of a pulse, $\Delta T_{Joule.branch}$ is the contact temperature change due to the Joule heat release in a leg at the end of a pulse, $\Delta T_{Peltier}$ is the contact temperature change due to the Peltier heat release in the contact at the end of a pulse,

$$\Delta T_{Joule.contact} = \frac{\delta t \cdot \gamma \cdot j^2}{c},$$

$$\Delta T_{Joule.branch} = \frac{4 \cdot \delta t \cdot \rho \cdot j^2 \cdot \sqrt{a \cdot \delta t}}{3 \cdot \sqrt{\pi} \cdot c},$$

$$\Delta T_{Peltier} = -\frac{\delta t \cdot \alpha \cdot j \cdot T_0}{c},$$

where δt is pulse duration, T_0 is the initial contact temperature, α is the leg coefficient of thermo-e.m.f., ρ is the leg specific resistance, κ is the leg specific heat conductivity, a is the thermal conduction, h_{Cu} the commutation plate thickness, γ is specific contact resistance, $c\delta_{Cu}$ is the commutation plate cube thermal capacity, c is the

commutation plate thermal capacity per a unit of the contact area.

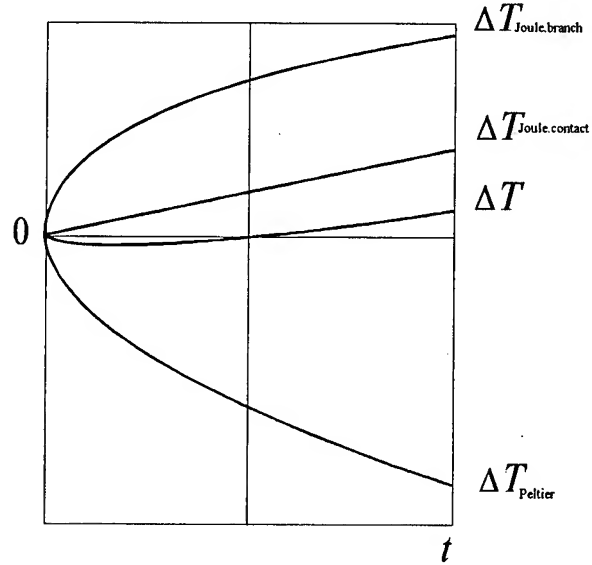


Fig. 15. Dynamics of the contact overheating ΔT and its components during a pulse of current.

2.4. Thermal resistance effect.

The thermoelement's geometric dimensions decrease is accompanied with thermal flow density through junctions increase that results in worsening of converters properties because of temperature difference in the commutating plates and other elements of module structure. The calculations for these losses effect on the limitations in microminiaturization have been given.

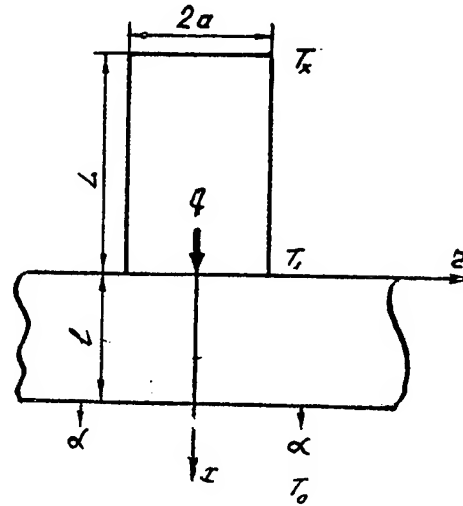


Fig. 16. Thermoelement model with an infinite flat substrate.

Several examples of module approximations have been examined, for a thermoelement model with an infinite flat substrate (Fig. 16), for a thermoelement model with a finite size substrate (Fig. 17), for a dispersal battery model (Fig. 18).

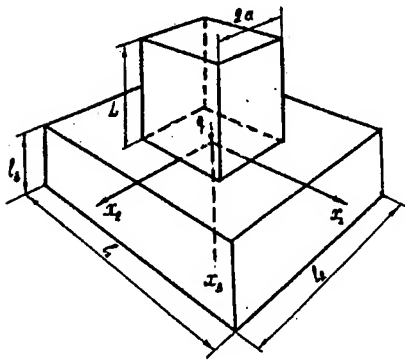


Fig. 17. Thermoelement model with a finite size substrate.

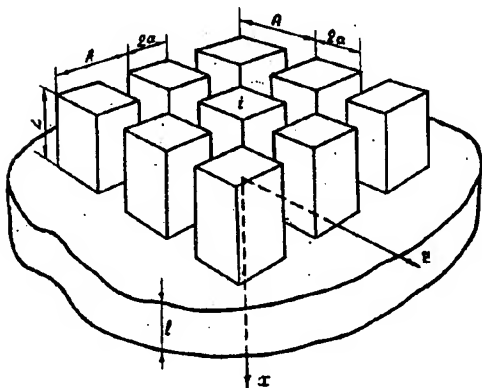


Fig. 18. Dispersal battery model.

Temperature distribution for such models was determined by the corresponding Poisson's equations with boundary conditions of the first kind. Actually, such problems have no simple analytical solutions. They were solved with the help of computers. The calculation results for a number of specific variants are given in Fig. 18, 19, 20, 21.

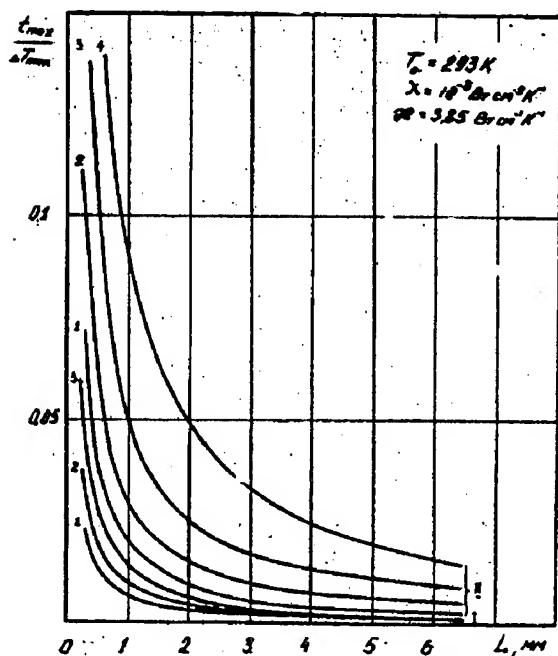


Fig. 19.

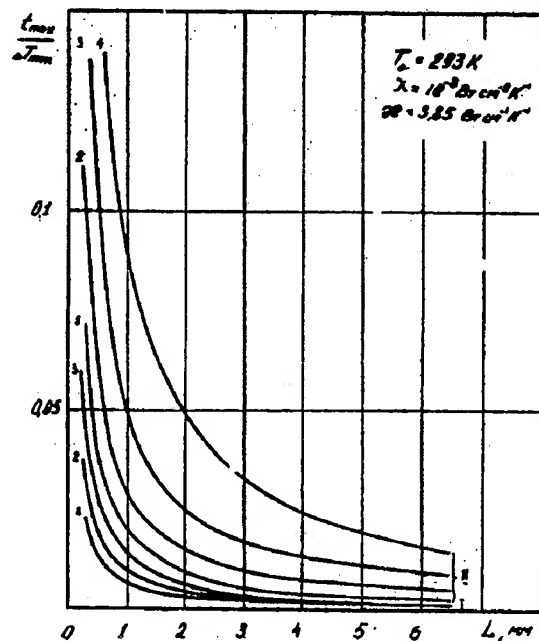


Fig. 20.

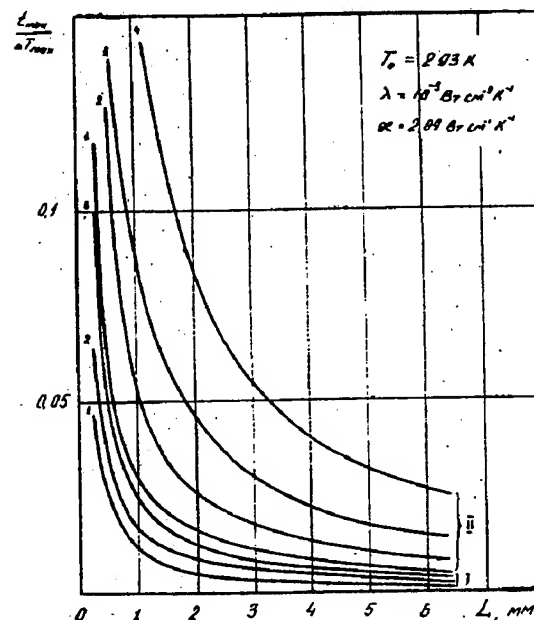


Fig. 21.

The figures illustrate relative losses in temperature difference T_{\max} at different geometric dimensions of the structure elements.

It follows from figures that losses in heat transfer are of great importance for microminiaturization when the leg's length is lesser than 1 mm. Losses in heat transfer can be only reduced by heat release intensification at the expense of materials with large thermal conduction use, of small thickness of heat transfers and heat release from the battery intensification. The factor of heat losses effect looks like one of the decisive in microminiaturization of batteries and imposes limitations on legs height of approximately up to 50 - 100 mcm.

3. New physical factors which can effect on module's operation

In order to determinate model assumptions let us consider what kind of real structures exist in thermobattery branches and in neighborhood. Sometimes at microminiaturization there is such a situation, when all the branch belongs to the near-contact area. In this case technological processes play the main role because they form near-contact areas.

Really, if near-contact area is formed by simple soldering an intermediate region appears. This region consist of solder material and thermoelectric material also. This region has very bad thermoelectric properties. The width of the region has a range between 5 and 50 mcm. It depends on technological conditions. Therefore, if temperature gradient concentrates in this region, then module properties will worsen very intensively. Therefore, such structures are not prospective for investigation and microbattery applications.

Sometimes for high reliability achievement thick antidiffusion layers are used, especially at high temperatures. These layers have continuos change from their own properties to thermoelectric material ones (for example pressed antidiffusion layers based on cobalt powder or thick layers of loose nicel of 100 mcm thickness). These structures are not very promising for microminiaturization.

The structures with a sharp boundary are interesting (for example antidiffusion layers prepared by galvanic process or obtained from gas phase, when tiny branch consist undamaged thermoelectric material). In this case new physical phenomena can take place, which are small in bulk samples. These effects can be connected with a large temperature gradient and perhaps with microscopic properties of current carriers and phonons (for example various diffusion lengths, when these lengths are close to the sample size).

It will be noted, that the theory of thermoelectric phenomena is not ready for such problem solution. In thermoelectricity a theory based on the Boltzmann kinetic equation is predominant at various approximations. It is not enough for effects which we consider. A new approach has been proposed by Dr. Gurevich and co-workers [12]. These investigations consider electron - phonon subsystems interaction, boundary conditions and sample size influence. The developing of precise calculation methods need a time in the case of tiny thermoelectric converters. These methods will be result of the theory developing.

The second difficulty in precise data obtaining about peculiarities of thermoelectric effects in micro-size samples are the information on microscopical parameters of materials absence especially for multi-component materials with developed defects. Usual optical methods are unsuccessful in this case.

Therefore, we analyze new physical factors on the base of the theory and the experiments at the present time level.

3.1. The effect of large temperature gradients

Legs height decrease under temperature difference in a module preservation results in temperature gradient increase. Macroscopic effects effecting on the physical processes in Peltier batteries can arise under these conditions.

One of possible mechanisms of large temperature gradients effect is the injection mechanism of Tauc. This mechanism consists in the appearance of nonequilibrium current carriers under the effect of a temperature gradient [10].

The other mechanism of the large temperature gradients effect on the kinetic phenomena character consists in the departure of symmetrical by electrons quasi-pulse part of the distribution function from the Fermi equilibrium function under the effect of temperature gradient [11]. The calculations show that at real values of minimum heights 10-100 mcm, values of temperature gradients increase moderately ($3-5 \cdot 10^4 \text{ K cm}^{-1}$). Under such relatively small temperature gradients the figure of merit increase is slight (0.5-0.6 %), however the material figure of merit can be essentially increased under the large temperature gradients effect, when the temperature gradient is two-three orders of magnitude larger.

That is why, such possibility must be taken into account in microminiaturization conceptually.

3.2. Consideration of size effects influence.

The investigations on size effects influence at the interface of media have been conducted. The size effect influence on the temperature length of cooling on the temperature difference in a thermoelement has been studied. Two-temperature problem has been considered. Equation sets for energy balance for electronic and lattice temperatures were starting for calculations. The calculation results showed that at leg's length of an order of 10 mcm the additional T_{max} decrease by approximately 2 K may be achieved due to size effects. Temperature difference can increase by 10-15 K at the leg's length of 1 mcm.

3.3. Consideration of phonons scattering on samples boundaries.

Besides the studied above size effect on temperature lengths of cooling, size effects connected with phonons scattering on samples boundaries (semiconductor legs) that result in the thermal conduction decrease and correspondingly the increase of the material figure of merit, can also influence on thermoelements characteristics.

The evaluations made for thermoelectric materials showed that under standard temperatures (300K) the phonon scattering effect on the sample boundary becomes appreciable at the legs size of an order of 10^{-6} cm .

4. General conclusions

1. A problem of thermobatteries microminiaturization can be separated into three basic steps, namely

Microminiaturization level of 1000 - 100 mcm branch length range;

Microminiaturization level of 1000 - 100 mcm branch length range;

Microminiaturization level of 1000 - 100 mcm branch length range.

2. The level of 1000 - 100 mcm has no principal difficulties. It is possible to reach this level by means of usual methods.

3. In the case of the level of 1000 - 100 mcm new physical regularities can begin to appear, which can compensate losses

connected with electrical and thermal contact resistances and thermobattery heat exchange.

4. At the present time the level of 10^{-1} mcm is very problematic from both the theory and application point of view.

5. The microminiaturization development will stimulate new techniques because usual known methods are ineffective for micro-size module creation.

References

- [1] A.F.Ioffe, L.S.Stilbans, E.K.Iordanishvili, *Thermoelectric cooling*, M.-L., Izd. AN SSSR, 1956, (in Russian).
- [2] E.A.Kolenko, L.S.Stilbans, "Thermoelectric coolers", in *Semiconductors in science and technology*, v. 2, M.-L., 1956, pp. 217-298, (in Russian)..
- [3] V.A.Semenyuk, *Real characteristics of semiconductor cooling devices investigation*, Candidate of Sci. Thes., Odessa, 1967 (in Russian).
- [4] V.A.Semenyuk, M.N.Tomashevich, "Choice of minimal thermoelement high", *Cooling technique and technology*, 1970, No. 9, pp.24-26, (in Russian).
- [5] V.A.Naer, "Contact resistance influence on thermobattery characteristics", *Cooling technique*, 1965, No.1, pp.9-15, (in Russian)..
- [6] A.V.Ioffe, "Influence of commutation plate resistance on thermoelectric cooling efficiency", *Semiconductors and radioelectronics in agrophysical investigations*, L., 1966, pp. 146-149, (in Russian).
- [7] L.S.Stilbans, "On commutation of semiconductor thermoelements", *JTF*, 1957, v.27, No.1, pp. 212 -213, (in Russian).
- [8] L.I.Anatychuk, O.J.Luste. "On heat production in commutation plates of thermoelectric modules", *J. of Thermoelectricity*, No.1, 1993, pp. 84 - 92.
- [10] Yu.I.Ageev, I.A.Sagaydachny, L.S. Stilbans, "Method of contact resistance measurement", *Pribory i tekhnika experimenta*, No.4, 1979, pp.253-255, (in Russian).
- [11] L.I.Anatychuk, V.I.Litvinov, V.K.Dugaev, V.L.Volkov, "On possibility of determination of minimal contact resistance between metal and thermoelectric material", *J. of Thermoelectricity*, No.1, 1993, pp. 70 - 77.
- [12] F.G.Bass, V.S.Bochkov and Gurevich, *Electrons and phonons in bounded semiconductors*, Nauka, M., 1984, 288 p.(in Russian).

TRANSIENT ANALYSIS OF THERMAL JUNCTIONS WITHIN A THERMOELECTRIC COOLING ASSEMBLY

Authors:

Michael J. Nagy and Richard J. Buist

TE Technology, Inc.

1590 Keane Drive, Traverse City, Michigan 49686 USA

Abstract

The performance of a thermoelectric (TE) heat exchanger assembly is greatly affected by the quality of the thermal junctions connecting the modules and the mounting surfaces of the heat/cold sinks. The quality of this junction, in turn, is affected by many different variables. These include heat sink surface quality, quantity of thermal grease, contaminants in the thermal grease, assembly screw torque, tapped hole quality, surface finish of the modules and the variance in module heights.

Until now, junction quality could only be verified by disassembly of the heat exchanger or inferred from a full cooling performance test of the assembly. This paper details a new, transient test method which accurately and dependably characterizes the module-to-heat-sink thermal junctions. A small current is applied to the TE modules in a thermoelectric assembly. This induces a small temperature difference across the module and between the ceramics of the module and its neighboring heat/cold sink. Power is then removed and the module's ceramics return to the temperature of its neighboring heat sink. The rate of temperature decay is directly proportional to the junction quality. Thus, the residual Seebeck decay waveform directly correlates to thermal junction quality, providing the means for rapidly and accurately characterizing assembly quality.

Introduction

The performance of a thermoelectric assembly is largely affected by the quality of the thermal junctions between the module and the heat sink and cold sink (see Figure 1).

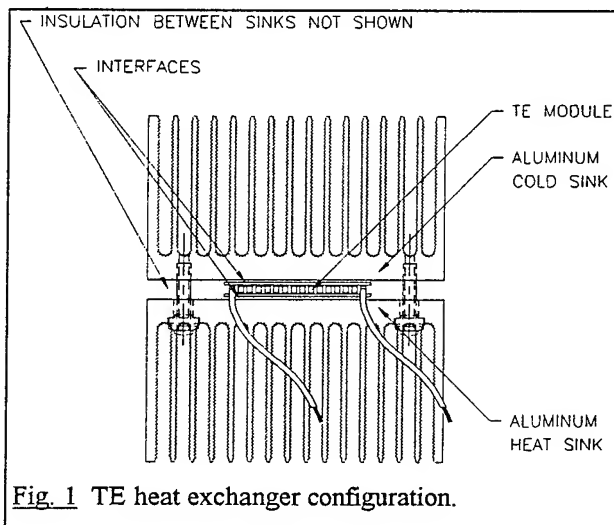


Fig. 1 TE heat exchanger configuration.

This is the most troublesome area in an assembly. Historically, it has also been one of the most difficult areas in an assembly to check for quality. Heat sinks, for example, can be visually inspected for quality. Modules can be tested prior to use. The AC resistance of an assembly can be checked to ensure the modules haven't been damaged during assembly. Thermal junctions, however, are buried in the assembly. Visual inspection of these junctions is difficult and not always accurate. For example, one may determine that a module is making contact with a heat sink, but it is impossible to know whether or not the correct compression force is being applied, even though the torque applied to each assembly screw is correct.

Typically, the only way to measure the quality of these junctions has been to actually test the completed assembly for thermal performance - either by measuring its steady-state cooling performance or by measuring its transient cool-down capabilities. Poor junctions lead to poor performing assemblies in both cases. However, these measurement techniques take a considerable amount of time and require the attachment of instrumentation to achieve proper results. Thus, a new measurement technique for determining the quality of a thermal junction is desirable. An ideal test would exhibit these criteria:

1. The test must be reproducible.
2. The test must work when the assembly is not isothermal.
3. Sensitivity must be greater than the measurement error.
4. With all other aspects of quality assured, passing the junction quality test should mean the assembly delivers acceptable performance.
5. No additional instrumentation of the assembly should be required.
6. The test should be much quicker than a full performance test.

This paper introduces a different method of testing which determines the quality of a thermal junction reproducibility and in a minimum amount of time without instrumentation.

Test Method

Figure 2 represents a simplified thermal model of an unpowered assembly. A temperature difference can be introduced between the module ceramics and their neighboring heat/cold sinks by applying a small current to the module. Removing current from the module allows the temperature difference within the module to decay. Varying thermal resistance between a module and the sinks will affect the rate at which this temperature difference decays. This phenomenon is the crux of this testing method. By analyzing

the Seebeck decay waveform of an assembly, it is possible to differentiate between assemblies of identical construction yet varying thermal junction quality.

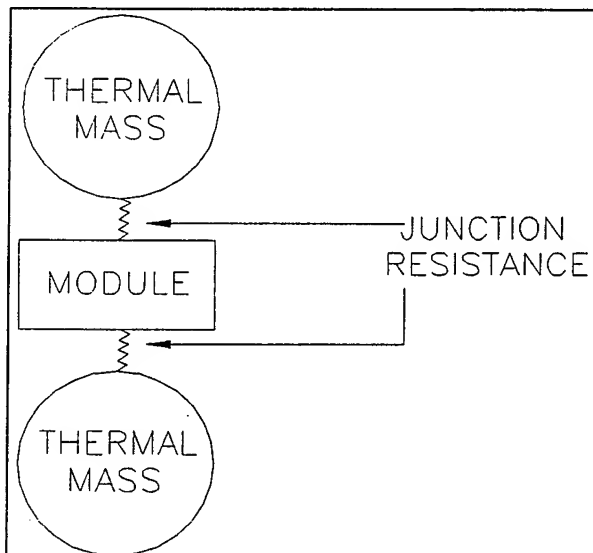


Fig. 2 Model of Heat Exchanger.

All test data gathered was taken on a TE Technology, Inc. model TS-205 test system [1]. This tester is capable of supplying a constant current to the TE assembly, switching

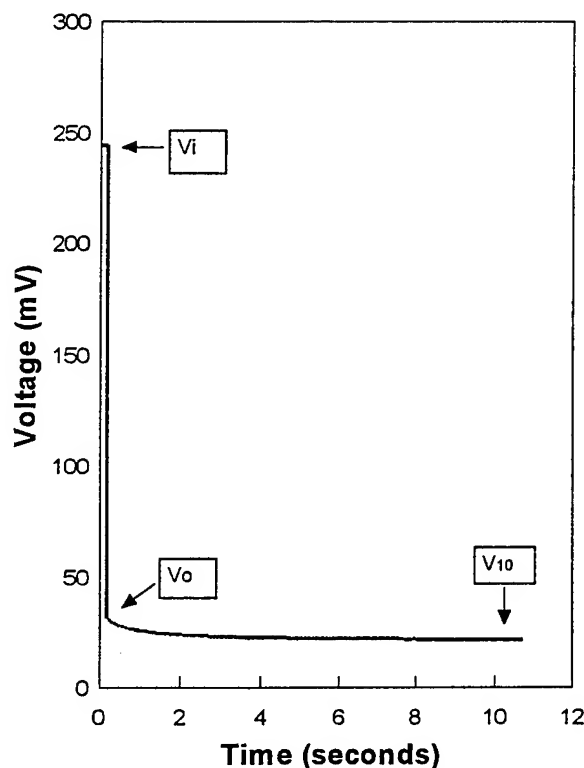


Fig. 3 Transient test waveform.

power off, and the monitoring and storing the voltage decay. A typical test waveform is shown in figure 3.

Current was applied to the assembly for 120 seconds. The magnitude of the applied current was equal to 3% of I_{max} . This current and time combination was chosen because it created a sufficiently large Seebeck voltage (temperature difference) across the modules. Current was then switched off and the residual Seebeck voltage was recorded. The decay waveform was then analyzed to produce a junction quality factor which was proportional to the quality of the thermal junctions within the assembly.

Testing

The first series of tests shows the difference between junctions of varying quality. Two aluminum heat sinks of equal size and mass were combined with a 6 amp 127 couple module to make a test assembly. For the experiments, an assembly with infinitely poor junctions was represented by a module itself (no heat sinks used). An assembly with moderately poor junctions was represented by using no grease during the assembly process. Finally, an assembly with good thermal junctions was represented by using thermal grease during the assembly process. Figure 4 shows the transient decay waveforms for these three cases.

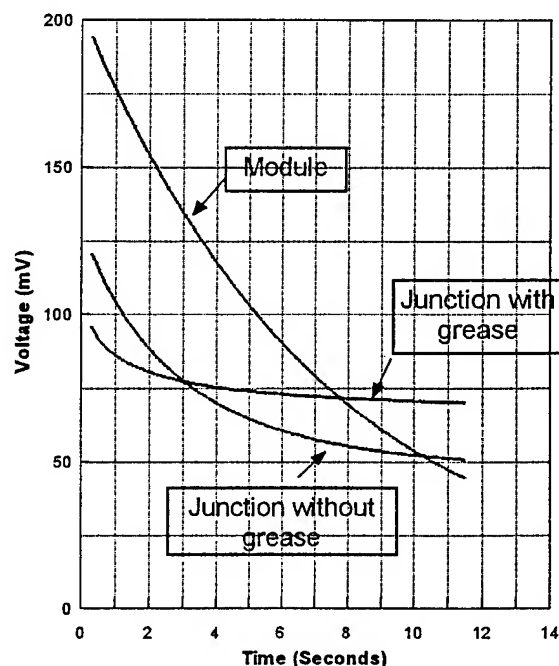


Fig. 4 Voltage decay waveforms for various configurations.

This same assembly was then tested when it was not in an isothermal state. This non-isothermal state was induced by using positive and negative test currents to create a significant temperature difference between the heat and cold sinks of the assembly. The most extreme temperature difference between the sinks took approximately one hour to create at the extreme case. This data is shown in figure 5. In the case where the voltage actually appears to level off at a negative voltage, the assembly was "charged" to allow a negative temperature difference to build between the heat sink and cold sink. Then, the leads were reversed and a test cycle was completed.

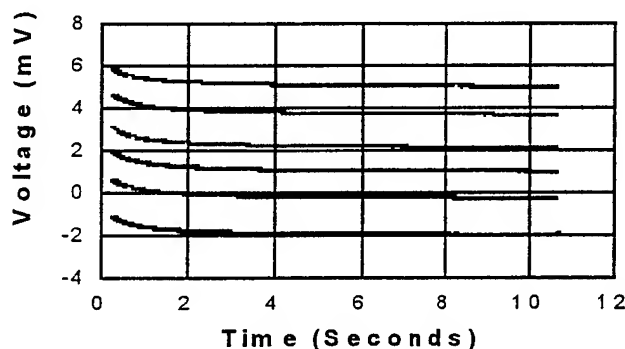


Fig. 5 Voltage decay waveforms for various starting conditions.

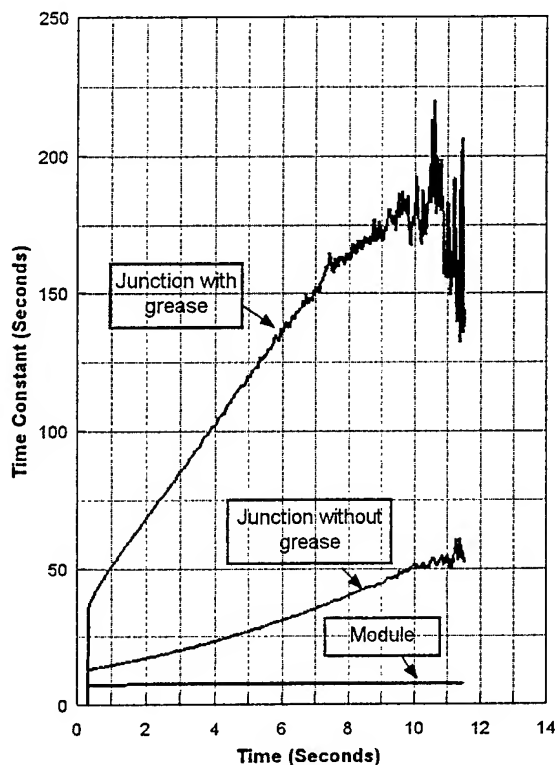


Fig. 6 Calculated time constants of various configurations.

Results

Figure 4 clearly shows the difference in transient waveforms between assemblies of varying junction quality. The general trends are as follows: for any given charge time and current, the assembly with better thermal junctions will exhibit a lower initial Seebeck voltage. The decay waveform is much slower for an assembly with good thermal junctions.

Figure 6 shows the time constants for the three waveforms of figure 4. An assembly with better thermal junctions will, in general, have a larger time constant. However, only the module exhibited a steady time constant.

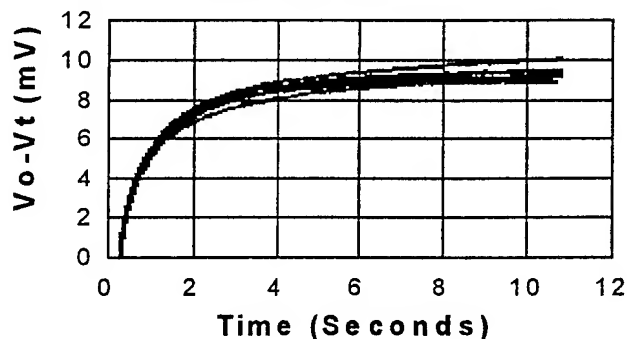


Fig. 7 Residual Seebeck decay for various starting conditions.

Figure 5 shows that, regardless of the temperature differences between the heat sink and cold sink, the shapes of the transient decay waveforms are nearly identical by visual inspection. This is further supported by figure 7. Here, the waveforms of figure 5 have been adjusted to show the amount of change in Seebeck decay as a function of time. Once again, these waveforms are nearly identical.

Derivation of Junction Quality Factor

Figures 4, 5 and 7 clearly show that an assembly will have a characteristic decay waveform and that its shape is dependent on the quality of the thermal junctions in the assembly. A formula has been created to extract a factor from the decay waveform which corresponds to the quality of the thermal junctions. This factor, called the junction quality factor, is defined by the equation:

$$Q_{jctn} = (V_i - V_o) / (V_o - V_{10}) \quad (1)$$

Where: V_i = Voltage just prior to current turn off,

V_o = Voltage immediately after current turn off,

V_{10} = Voltage 10 seconds after current turn off.

In order to understand how this formula was derived, it is necessary to understand some proposed analysis techniques which were not chosen.

A calculation of time constant was initially thought to be the choice method for characterizing junction quality. However, this proved to be impractical. Figure 5 shows that, if there is a temperature difference between the heat sink and cold sink,

the transient voltage will decay to an apparent non-zero asymptote. This shall be called V_{∞} for the sake of analysis. If we assume the decay can be characterized by a simple first order exponential equation (which it cannot), the equation would be written:

$$V_t = (V_0 - V_{\infty})e^{-t/\tau} + V_{\infty} \quad (2)$$

The equation can be rewritten as:

$$\tau = \frac{-t}{\ln\left(\frac{V_t - V_{\infty}}{V_0 - V_{\infty}}\right)} \quad (3)$$

Clearly V_{∞} must be known for τ to be calculated. Because V_{∞} is really only an apparent asymptote, and because it occurs a considerable time after current switch off in a "good" assembly, this was deemed impractical.

The ratio of V_t/V_0 was also considered. This too, was considered unacceptable because of the unknown value of V_{∞} .

One quickly calculable number which was representative of the quality of the junction was $V_0 - V_t$ where V_t represents the module voltage "t" seconds after current switch-off. This number proved to be very sensitive to junction quality. A poor junction allows a relatively high initial Seebeck voltage followed by a rapid decay. Thus, $V_0 - V_t$ is large for this case. Conversely, a good junction allows a lower initial Seebeck voltage followed by a slow decay. This causes $V_0 - V_t$ to be small for a good thermal junction. Furthermore, because $V_0 - V_t$ represents only the amount of decay in Seebeck voltage, it is insensitive to a waveform which decays to a non-zero asymptote.

Used alone, the above defined difference varies directly with both the number of couples and current in the module or series/parallel combination of modules. The resistive voltage drop measured immediately prior to current switch off was then used to normalize this difference. Thus, a series combination of n modules will increase both the resistance and Seebeck voltage by a factor of n. Conversely, paralleling n modules will reduce the resistance by a factor of 1/n. However, the current per couple (and thus Seebeck voltage) is also reduced by a factor of 1/n. Inclusion of this resistive voltage lead to the Q_{jctn} formula as defined in equation 1. By dividing the resistive voltage with the decay in Seebeck voltage a dimensionless number is derived which is directly proportional to the quality of the thermal junction yet insensitive to varying series/parallel combinations of modules.

The sensitivity and reproducibility of Q_{jctn} was measured by testing the three original assemblies. Figure 8 shows a threefold increase in Q_{jctn} between a module and an assembly made without thermal grease. Q_{jctn} then doubled when the assembly was made with grease. Reproducibility was excellent. All three repeat tests for each type of assembly yielded nearly identical results.

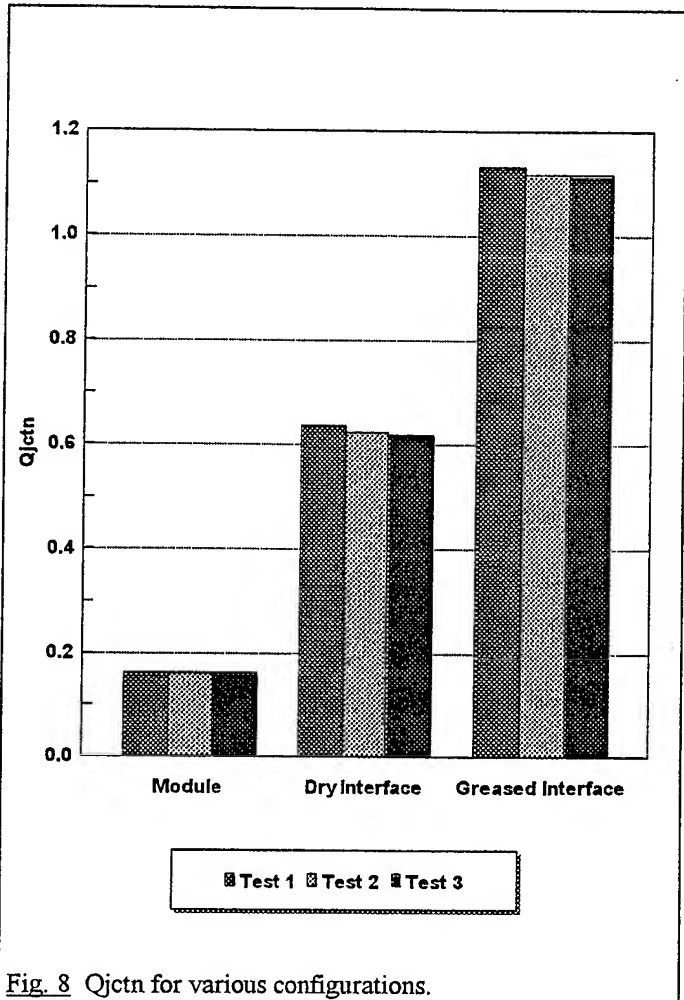


Fig. 8 Q_{jctn} for various configurations.

Discussion

Figure 5 shows that the slope of the curves, and therefore Q_{jctn} , is relatively insensitive to temperature differences that exist between the heat and cold sinks in an assembly. We can deduce from this data that the test has a strong dependence on the time constant of the module and relatively little dependence on the time constant of the assembly. As the time constant of module is orders of magnitude lower than that of an assembly, it should stand to reason that test times are orders of magnitude lower than assembly performance tests. However, this strong dependence on the module's time constant suggests that the thermal mass of a module's element length, ceramics, tabs and solder would affect the test and produce a unique Q_{jctn} per type of module.

Currently, no method exists for the prediction of Q_{jctn} . However, a transient model such as the one developed by Lau and Buist [2] could very well be adaptable for prediction of Q_{jctn} . This work is currently underway.

Finally, it should be noted that this transient test only qualifies the thermal junctions in an assembly. Therefore, it must be used in conjunction with other tests to qualify an assembly. These tests include the testing of modules for figure of merit, testing the AC resistance of the modules before assembly and testing the AC resistance of the modules after assembly. However, since the latter is easily extractable

from the same raw data base, Q_{jctn} and AC resistance are essentially tested simultaneously.

Summary/Conclusions

A new method has been developed to test the quality of the module-to-heat/cold sink thermal junctions within a thermoelectric assembly. A small current is applied to the modules for 120 seconds. The current is then removed and the residual Seebeck voltage decay is monitored. Thermal junctions of differing qualities will exhibit different decay waveforms. These waveforms differ in the amount of residual Seebeck voltage as well as the rate at which it decays. Thus, a formula for junction quality, Q_{jctn} , was defined which compares the power-on resistive voltage to the decay in Seebeck voltage 10 seconds after current is switched off. Q_{jctn} becomes larger as the quality of the thermal junction increases. The inclusion of resistance voltage drop in the equation makes Q_{jctn} insensitive to any series or parallel combination of modules.

The test has important applications as a quality control tool. Its reproducibility exhibits a high sensitivity to thermal junction quality. Furthermore, testing can be completed in about two minutes, making the test much quicker than other methods used to distinguish junction quality. This method has been evaluated by Ritzer, Nagy and Buist [3] and established as a very effective quality control tool for production.

References

- [1] R.J. Buist, "A New Method for Testing Thermoelectric Materials and Devices", *11th International Conference on Thermoelectrics*, Arlington, Texas, USA, (1992).
- [2] P.G. Lau and R.J. Buist, "Temperature and Time Dependent Finite Difference Model of a Thermoelectric Pellet and Couple", in *Proceedings of the XV Conference on Thermoelectrics*, Pasadena, California, USA, 1996.
- [3] T.M. Ritzer, M.J. Nagy and R.J. Buist, "Evaluation of Thermal Junction Quality in Thermoelectric Assemblies Using Transient Analysis Technology", in *Proceedings of the XV Conference on Thermoelectrics*, Pasadena, California, USA, 1996.

EVALUATION OF THERMAL JUNCTION QUALITY IN THERMOELECTRIC ASSEMBLIES USING TRANSIENT ANALYSIS TECHNOLOGY

Authors:

Todd M. Ritzer, Michael J. Nagy, and Richard J. Buist

TE Technology, Inc.

1590 Keane Drive, Traverse City, Michigan 49686 USA

Abstract

This paper describes the application of the Transient Analysis Test method to evaluate the integrity of thermal junctions in a thermoelectric (TE) assembly. The quality of thermal junctions (Q_{jctn}) in assemblies was measured by creating a thermal gradient in the TE modules comprising an assembly and analyzing the decay of the residual Seebeck voltage. A study was made of various junction conditions that exist between the TE module and its heatsinks which are common to most assembly techniques. Poor thermal contacts were deliberately introduced such as insufficient thermal grease, inadequate compression and improper surface finishes in test assemblies in order to simulate typical assembly defects. A direct correlation between good and inadequate thermal junctions was established and illustrated through graphic test data evaluation.

Introduction

It is essential to achieve maximum surface contact between the thermoelectric module and the mounting surfaces of its heatsinks in order to obtain optimum performance in a thermoelectric assembly. Though other conditions such as proper TE module selection and heatsink optimization should not be ignored, there are still variables that exist that can greatly affect performance in the assembly. The quality of the thermal interface at both mounting surfaces of the heatsinks and the TE module are dependent on several conditions. These are insufficient thermal grease or compound, inadequate or uneven compression, rough heatsink and module mounting surfaces and foreign material contamination in the interface medium itself. These factors make it difficult to assure that a quality thermal junction exists in all TE assemblies manufactured.

In the past, junction quality could be verified by performing a complete "cool down" test to measure transient rate and steady state cooling levels. The problem with this technique is the time, labor and equipment required to achieve accurate results. This new transient analysis test method can verify the quality of the thermal interface in only a couple of minutes.

This paper details this breakthrough in thermoelectric assembly testing, describes various test conditions used to verify its sensitivity and repeatability and illustrates results of the tests performed.

Theory

As a TE assembly is powered by a DC current, approximately 3% of I_{max} , it will create a small temperature difference within the TE module. Upon abrupt power shut-off, a measurable, residual Seebeck voltage will exist at the TE module input power leads. This voltage will decay with time. The nature of the short-term decay wave form will be affected by the quality of the thermal interfaces in the assembly. If the thermal contact with the plates were poor, the short-term rate of decay would be faster, approaching a totally isolated TE module. Conversely, if the thermal contact were good, the rate of decay would be more controlled by the thermally massive plates, and the decay would be slower. Therefore, measuring and analyzing the short-term residual Seebeck voltage as it decays offers a means of quantifying the thermal quality of the junctions between the TE module and the opposing plates. There wasn't any question as to whether this method would work or not (at least in the extreme cases). The only question was whether or not this method were reproducible and sensitive enough to work as an effective quality control tool for identifying good thermal junctions from those not quite good enough. This, then, is the subject of this paper: to test this method in a production environment and empirically evaluate its effectiveness.

The test procedure was essentially an extension of the "BURST" test described by Buist [1]. A high-speed, high-resolution A/D board was used to repeatedly test the TE module voltage before, during and after power-off in one continuous step. Thus, the data not only defined the decay wave form but also provided the key raw data needed to determine the true and accurate electrical resistance of the modules. Thus, this test method provided the data needed to not only test the thermal junction quality but also confirm the integrity of the TE modules themselves.

A dimensionless factor, Q_{jctn} , was developed by Nagy and Buist [2] via analysis of the short-term (10 seconds) voltage decay wave form. It is given in equation 1:

$$Q_{jctn} = (V_i - V_o) / (V_o - V_{10}) \quad (1)$$

Where:

V_i = The voltage just before power-off,

V_o = The voltage immediately after power-off, and

V_{10} = The voltage 10 seconds after power-off.

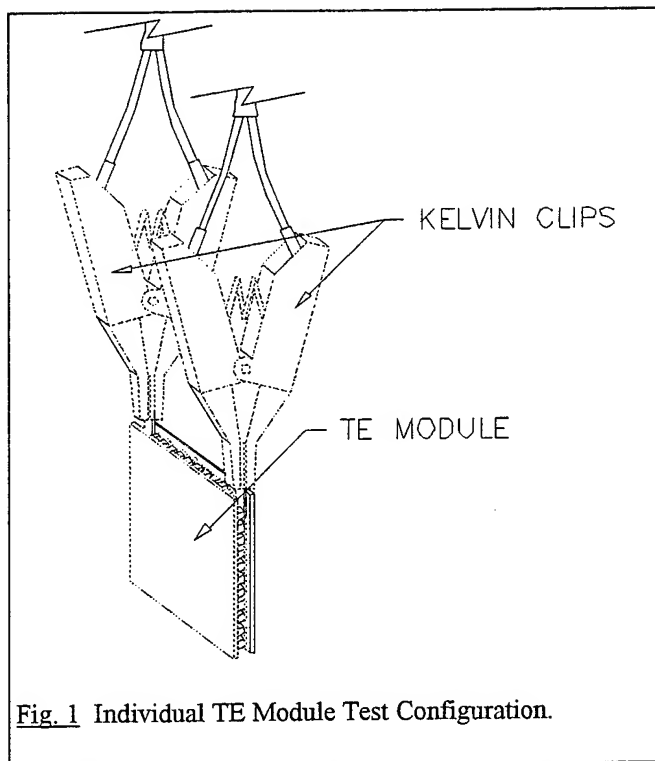


Fig. 1 Individual TE Module Test Configuration.

TE module Tests

The first series of tests were performed using a TE Technology, Inc. model TS-205 computerized test system applied to suspended, individual TE modules. These tests were performed to determine the effects of varying TE module parameters had on Q_{jctn} . Several modules were selected all having varying pellet geometry, numbers of couples and figure of merit, Z . These modules were tested while suspended in air within a small box to stabilize convection and radiation effects (see Figure 1).

Two experiments were conducted in this configuration using different TE module types obtained from various manufacturers around the world. The type of TE module selected was a 127 couple, 6 amp variety because it was common amongst most manufacturers. However, a wide variety of TE module designs were also obtained from one supplier in order to determine the impact of geometry as well TE material parameters on the parameter, Q_{jctn} .

The first of these two experiments was to measure each module's physical and thermoelectric material parameters in order to establish a base line for the subsequent analysis and assembly tests. Each TE module's physical characteristics, overall size, weight, ceramic thickness and pellet tab size were determined. The TE module lead wires were also removed to eliminate any possible variations they might have induced. They were then tested for various TE material properties, including the figure of merit, Z .

The second set of tests consisted of testing for Q_{jctn} using the same test equipment and test software as for the TE material parameter tests, but set up to determine Q_{jctn} as defined in equation 1.

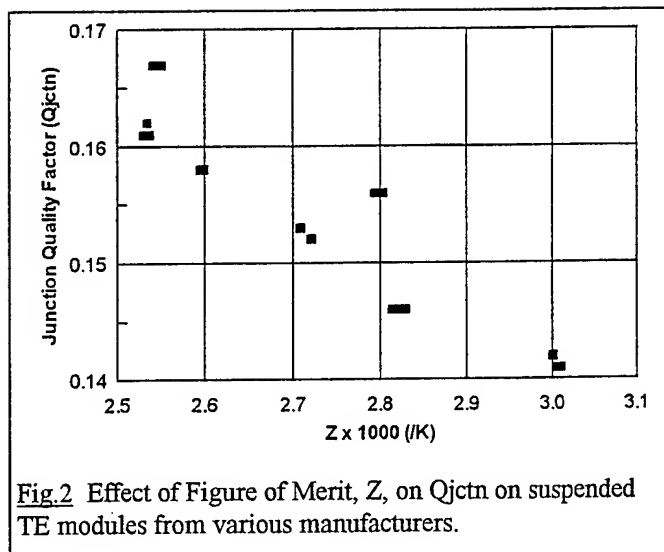


Fig. 2 Effect of Figure of Merit, Z , on Q_{jctn} on suspended TE modules from various manufacturers.

The initial results are shown in Figure 2. It was observed that Z apparently inversely affects the measured Q_{jctn} .

Figure 3 illustrates the impact of TE module geometry on the Q_{jctn} value. All modules in this data set were from the same supplier but were of widely different geometrical design. Although there was some variance with other geometrical parameters, the only obvious trend observed was the decrease in Q_{jctn} with decreasing TE pellet height as clearly evident in this plot.

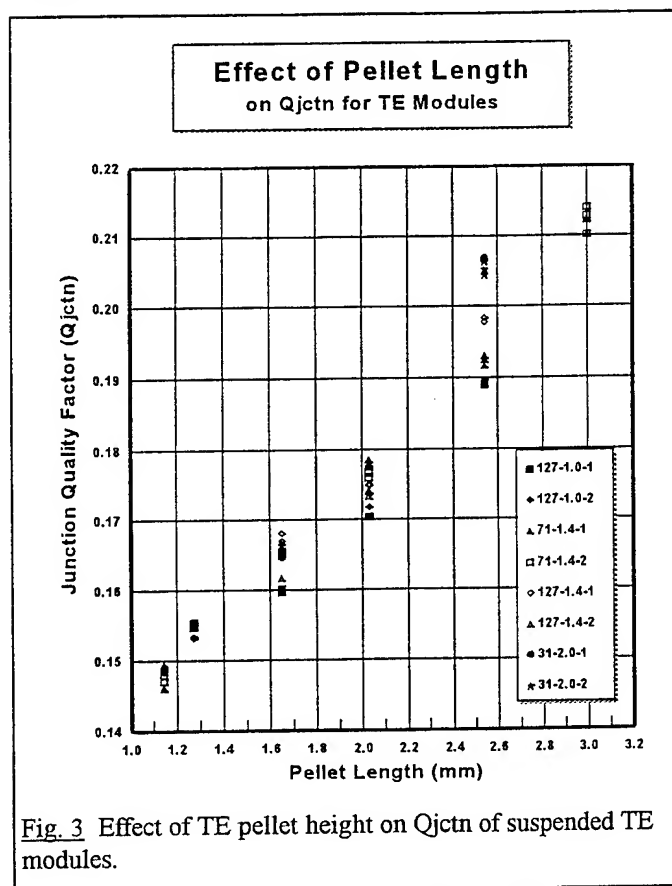


Fig. 3 Effect of TE pellet height on Q_{jctn} of suspended TE modules.

Experimental TE Assembly Tests

With the TE module baseline tests completed, the more important assembly tests were performed in order to establish the effectiveness and value of Q_{jctn} testing. The basic configuration of the experimental TE assemblies is illustrated in Figure 4.

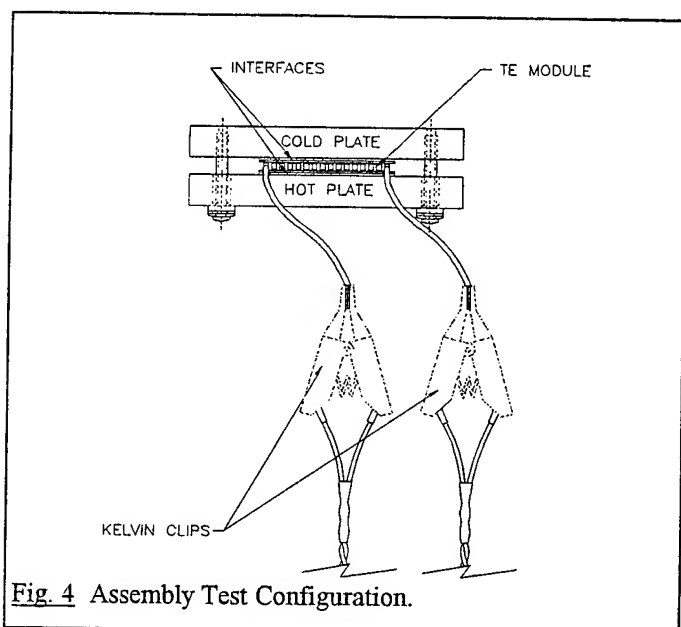


Fig. 4 Assembly Test Configuration.

The modules used were 127 couples with TE pellet sizes: 1.4mm square x 1.65mm long. All TE modules were screened for a common Z value of 0.0026 /K. The heat sinks were simple aluminum plates of the same 6061-T56 alloy. Except for the tests designed to check variability of these parameters, each assembly was fabricated using thermal grease as an interface medium and a constant predetermined torque value of 1.0 Newton-meter. The mounting surfaces were machined to a 0.8 micrometer finish.

The experimental assembly tests were conducted with the unit sitting on a piece of foam insulation with the other plate exposed to open air. Tests were conducted using the following deliberately imposed conditions in order to observe their impact on Q_{jctn} : a) different size heat sink sizes, b) different surface finishes, c) different interface media versus applied compression force, and d) contaminated interfaces.

The first experiment was designed to determine the impact of plate size on Q_{jctn} . The results of this test are given in Figure 5. In spite of the significantly different plate sizes there was not much observed variance. This was as expected since the temperature difference of module surfaces was so small, the heat sink size did not affect TE module plate temperatures. Following this test, all subsequent experimental assemblies used the smaller, 76 x 102 x 9.5 mm plate size.

The second TE assembly test was conducted using different surface finishes, but the same on both the hot and cold sides. Four sets were fabricated with surface finishes from an extremely smooth 0.8 micrometer value to a very poor 12.5 micrometer finish. The results in Figure 6 illustrate the effect surface finish had on the Q_{jctn} value.

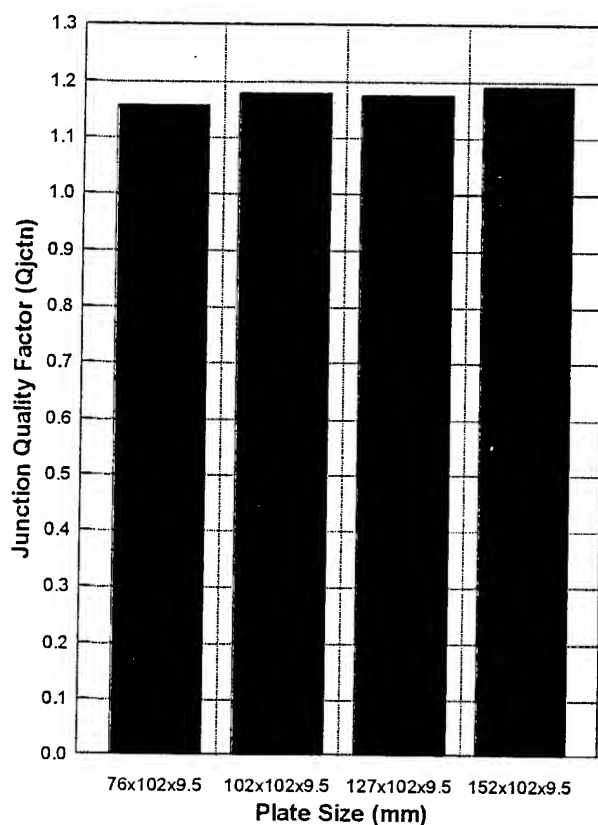


Fig. 5 Effect of plate size on Q_{jctn} of TE assemblies.

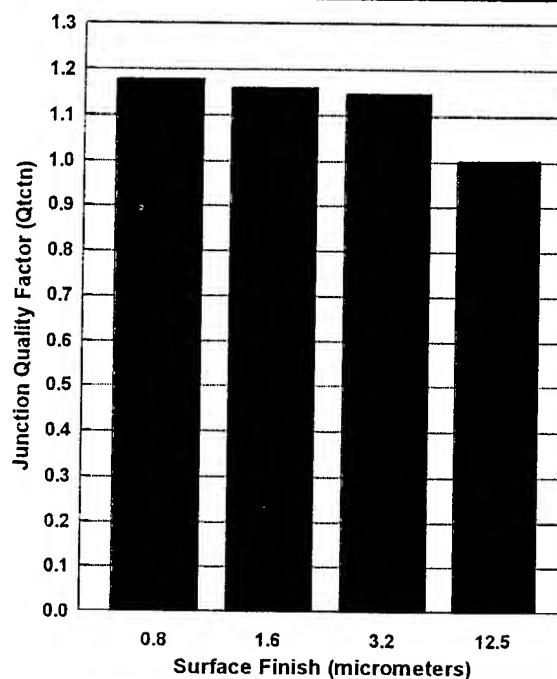


Fig. 6 Effect of plate surface finish on Q_{jctn} of TE assemblies.

The interesting thing to note by this data is that even what would be considered a poor surface finish (TE assembly standards (3.2 micrometers) still had relatively minimal effect on Q_{jctn} .

The conditions examined for the final experimental assembly test were the different interface medium between the TE module and the aluminum plate surfaces. Also, it was impossible to isolate the effects of the interface media from the amount of torque applied to the clamping screws used to compress the assembly, so these two factors were studied simultaneously.

The different interface media selected were based on some commonly suggested materials sometimes used in TE assemblies. One assembly was fabricated using a popular silicone thermal grease compound manufactured by Thermalloy, Inc. The second unit was fabricated dry, using no interface medium at all. A third unit was fabricated using a 0.26mm thick graphite sheet material manufactured by Ucar Carbon Co., Inc. known as Grafoil®. The fourth unit was fabricated using a popular Kapton® adhesive tape often used in electronic heat dissipation applications where electric insulation is required. This conductive adhesive tape measured 0.127mm thick and was manufactured by Chomerics, Inc.

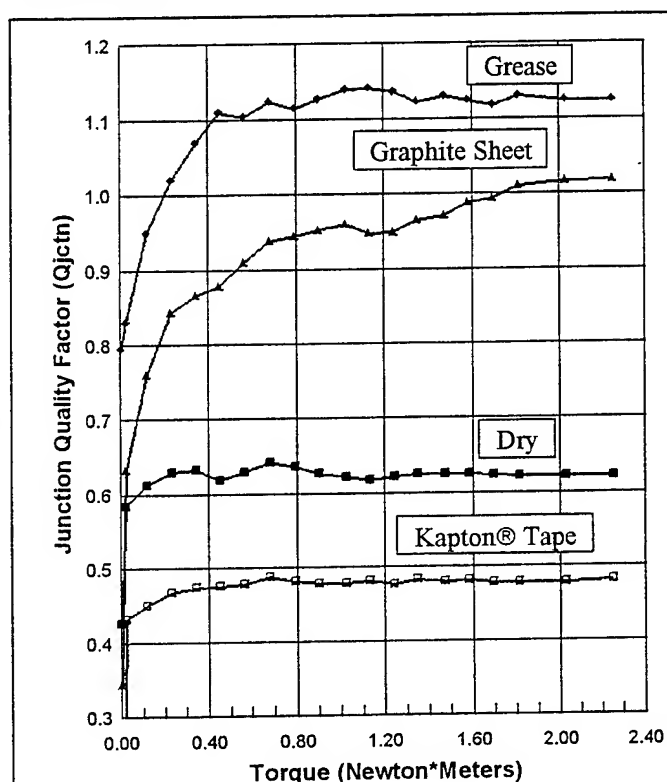


Fig.7 Effect of interface medium and applied torque on Q_{jctn} of TE assemblies.

The results of these tests are shown in Figure 7. This graph revealed some very interesting facts. The first test, where thermal grease was used as the interface medium, proved to be the configuration which attained the highest (best) Q_{jctn} value. One interesting thing to note is the Q_{jctn} value

“leveled off” at approximately 1.0 Newton-meter of torque. This translates to approximately 1.4 Mpa of compression applied to the module. This value corresponds to the specified value of compression recommended for an assembly of this nature.

The assembly configuration with the next highest Q_{jctn} value was the one in which the graphite sheet was used as the interface medium. Although the performance of this medium was not quite as good as thermal grease, it could be argued that this configuration may represent a good trade-off between performance and the benefits of a quicker, and perhaps easier, assembly time. However, it should also be noted that the torque and subsequent compression forces applied to the TE module are far beyond recommended levels.

The final two assemblies using the Kapton® sheet and no interface medium (dry) did not perform well. These interface media are not recommended for use in a TE assembly.

Production Testing

Finally, Q_{jctn} tests were performed on a small production lot of TE assemblies which consisted of a cold plate, finned heat sink and a single TE module. The results of these tests are shown in Figure 8. Notice that Q_{jctn} varied between 2.0 and 2.3 except for two assemblies. The initial Q_{jctn} for these two cases were approximately 0.8 and 1.5, respectively, and were obviously well below the average Q_{jctn} of the other units in this lot.

At first, the clamping screws were re-torqued and re-tested. However, as observed in the graph, the respective Q_{jctn} for both cases did not significantly change. Therefore, both units were disassembled and their grease patterns inspected. A human hair was discovered in the thermal grease of the first unit (H). It was removed and the unit re-assembled and re-tested. As observed in the graph, the Q_{jctn} increased to a value consistent with the acceptable (A) TE assemblies.

The grease patterns of the second unit (B) were unusually thick and it appeared that this unit was not properly compressed. Upon closer examination a metal burr was discovered in one of the tapped holes used by the clamping screws. These holes were re-tapped and the unit was re-assembled and re-tested. As observed in the graph, its Q_{jctn} value also increased to a value consistent with the other TE assemblies.

Conclusion

This paper has illustrated the effectiveness of using the transient analysis method for measuring the quality of the thermal interfaces for a TE assembly. Demonstrations have been performed to verify the sensitivity and repeatability of this technique. The main conclusion derived was that this test method is a reliable and fast tool for evaluating the thermal junction quality of literally any thermoelectric assembly.

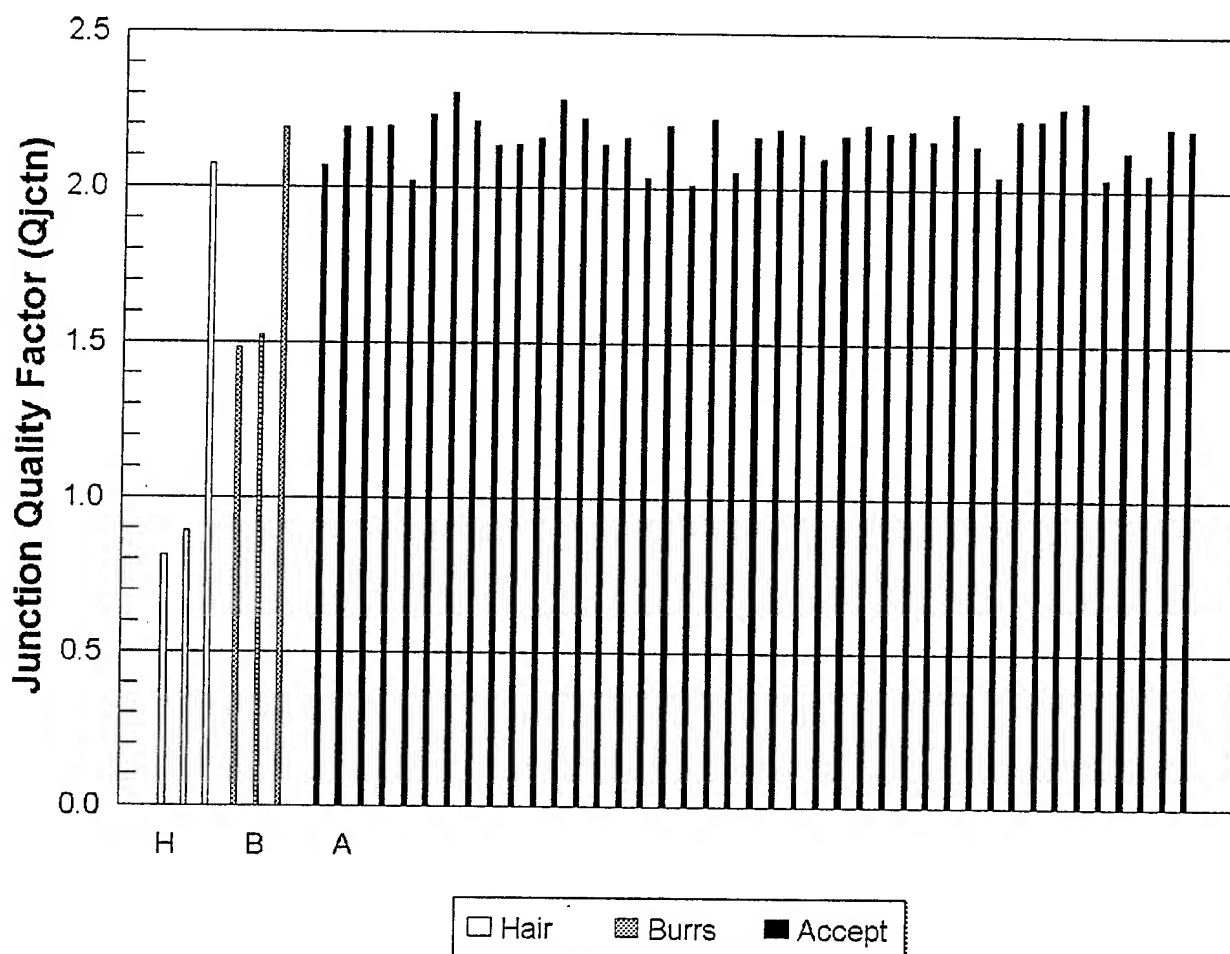


Fig. 8 Qjctn test results on a group of TE assemblies to illustrate sensitivity of Qjctn to imperfect thermal junctions.

References

- [1] R.J. Buist, "A New Method for Testing Thermoelectric Materials and Devices", *11th International Conference on Thermoelectrics*, Arlington, Texas, USA (1992).
- [2] M.J. Nagy and R.J. Buist, "Transient Analysis of Thermal Interfaces Within a Thermoelectric Cooling Assembly", in *Proceedings of the XV Conference on Thermoelectrics*, Pasadena, California, USA, (1996).

RATIONAL CONDITIONS AND PROSPECTS FOR TWO-STAGE COOLING MODULES USE

L.I. Anatyshuk, L.N. Vikhor, Kengo Misawa, Nobuyuki Suzuki

Institute of Thermoelectricity, Chernivtsi, Ukraine
Institute of Photonic and Electronic Tech. Fujitaka Co., Ltd., Japan

Abstract

The investigation results for rational fields of single- and two-stage thermoelectric cooling modules use in the context of their energetic efficiency and economical utility.

Introduction

Single-stage modules are widely used for numerous variants production of domestic refrigerators. Compactness, reliability and ease in maintenance are the attractive features of refrigerators. However, cooling degree in these refrigerators is not sufficiently high, so the further progress in thermoelectric cooling application for everyday purposes is connected with more perfect structure design which would provide lower cooling degree.

This problem cannot be solved by the use of single stage cooling modules. So it is natural to consider the problem of going to two-stage cooling in these products.

Problem solution and general discussion

A special thermoelectric module, the possible compact with minimum heat and electrical losses has been developed for this purpose, its cooling performance corresponds to standard thermoelectric modules of 40×40 mm and is 50 W. Parameters of such thermoelectric module are given in Fig.1. For comparison Fig.2 gives the parameters for standard single-stage thermoelectric module with cooling performance of about 50 W produces by the ALTEC company.

A thermoelectric module's quality, in a consumer's context, is determined by the cost of a unit of cooling performance S_0 which is defined by formula

$$S_0 = \frac{S_m}{Q_0 t} + \frac{S_e}{\varepsilon}$$

where S_m is the module's cost, Q_0 is the module's cooling performance, t is time of module's operation, ε is the module's coefficient of performance, S_e is the cost of a unit of electric energy power. The formula shows that the first term makes a considerable contribution to the cost S_0 only at not long

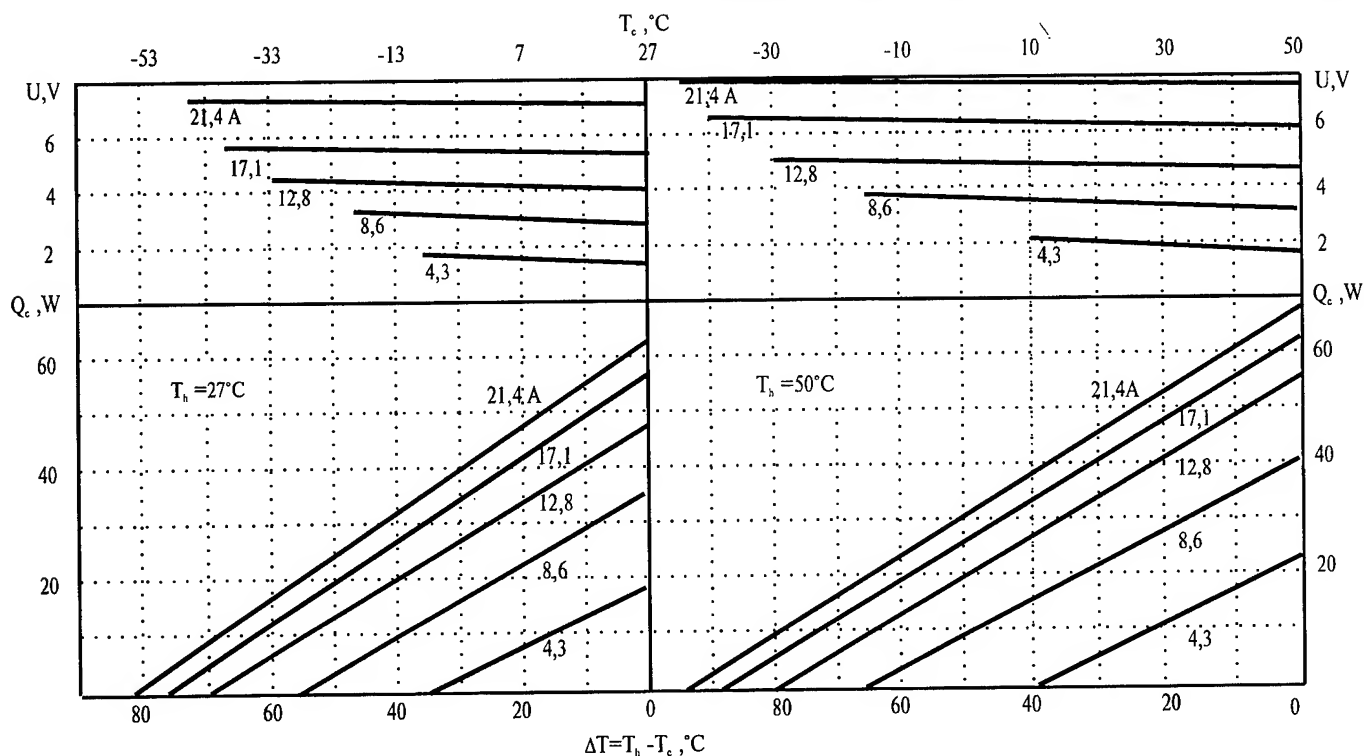


Fig. 1. Parameters of two-stage thermoelectric module.

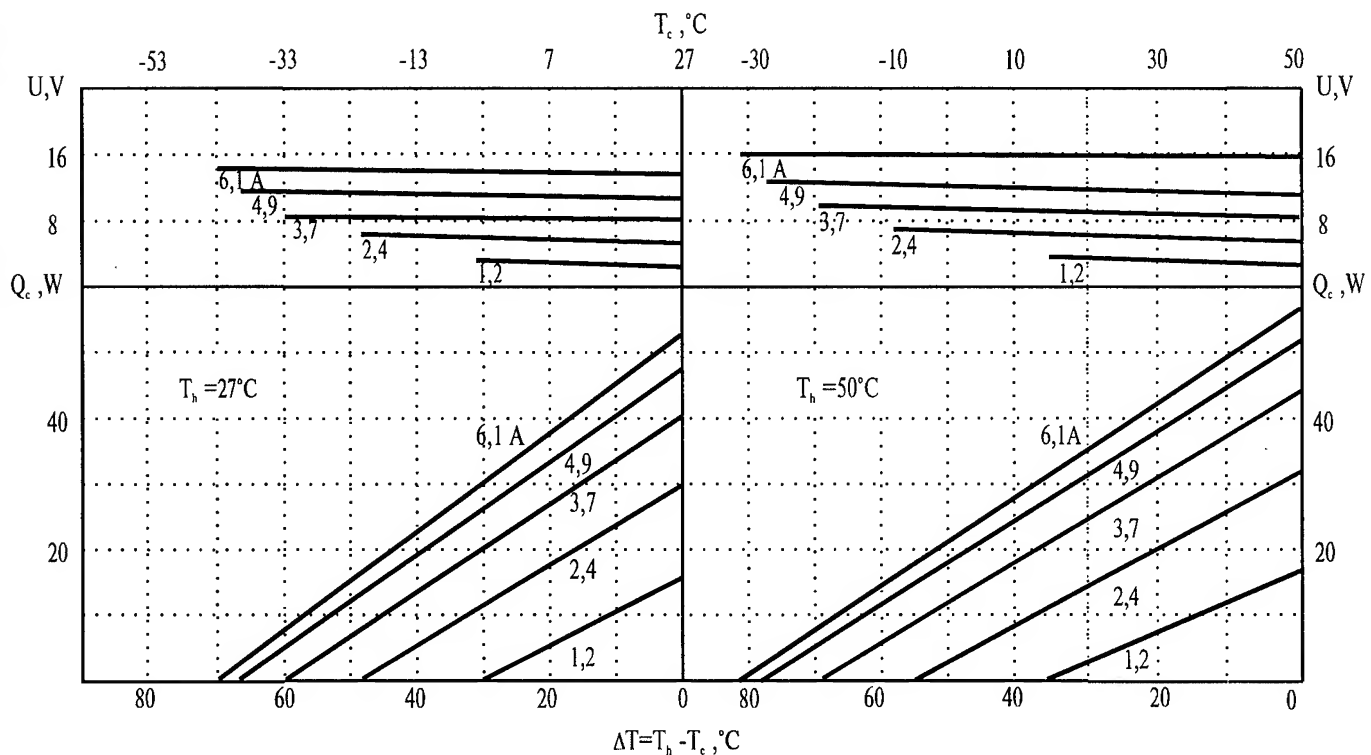


Fig.2. Parameters for a standard single-stage thermoelectric module.

periods of modules operation. As service life increases, the cost is increasingly defined by the electric energy costs,

whence it follows that the cost of a thermoelectric module is of no significance, its high reliability and large values of coefficient of performance are of more importance. That is why when design a refrigerator with long service life the more expensive but high-quality modules by reliability and energetic efficiency are more preferable.

Clearly that the S_0 value depends on the module operating conditions, that is on cooling amount, since with temperature difference increase both the value of cooling performance and the value of coefficient of performance decrease.

We have studied at what conditions is it economically reasonable to use a single-stage cooler and when a two-stage one. The computer program has been created for such analysis. In the program it was used the module operating condition under the maximum coefficient of performance. Sometimes for an apparent economy the conditions when cooling performance is increased at the cost of slight coefficient of performance decrease are used in designing. We have also studied such cases and come to the conclusion that in the context of economical expediency at long service life the preference should be given to the condition of the maximum coefficient of performance.

The results of the comparative analysis for a single- and two-stage modules are presented in Fig. 3. Temperature differences are plotted on the abscissa, and the specific cost of a unit of cooling performance are on the ordinate. The data are given for averaged costs for a single-stage module. The cost of a two-stage module is thrice as much. It should be noted that the modules values of cost are little effected on the obtained results at proper large modules service life. The energy cost is

taken as \$0.15 per 1 kW h. The departure from this cost is also little effected on the results of the comparative analysis.

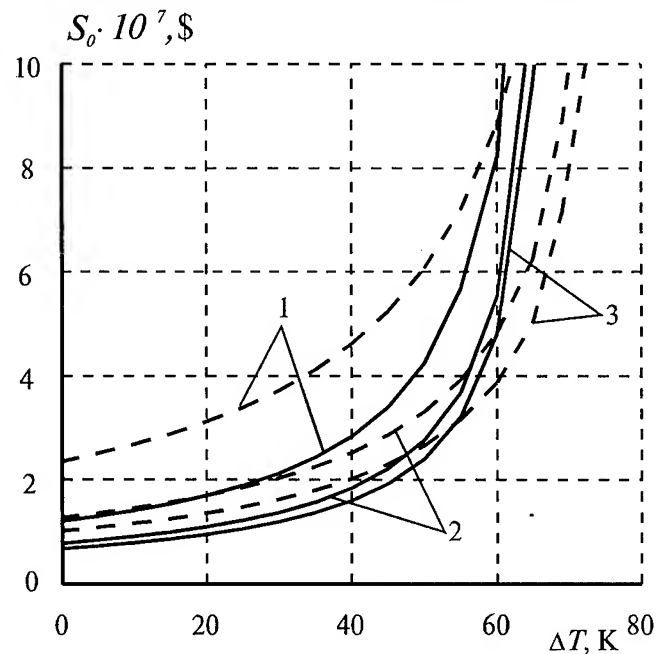


Fig.3. Module's cost dependence on temperature difference. Solid line represents a single stage module, dash one - a two-stage module.

1 - service life is 1000 hours; 2 - service life is 10000 hours; 3 - service life is 100000 hours.

It follows from the figure that there is a definite temperature difference for each service period when economical expenses are equal in the use of a single-stage module and a two-stage one. This means that at more large temperature differences

two-stage module are more preferable, at low temperature differences a single-stage is preferable. The figure shows the idealized result when losses in temperature differences are not taken into account in the module's design. Actually these losses are rather large. These are losses between the temperature of radiators and air which is used for heat sink are usually of about $10^{\circ}\text{--}15^{\circ}$, temperature difference in the radiator case that can reach $3^{\circ}\text{--}5^{\circ}$, temperature differences between surfaces of the radiator and thermoelectric module (are usually $1^{\circ}\text{--}3^{\circ}$), temperature differences in a cooler components which deliver heat to the cold surface of the module (about $1^{\circ}\text{--}2^{\circ}$) and temperature differences between cooled air and cold radiator that depending on heat exchange conditions (natural, forced) may vary from $2^{\circ}\text{--}3^{\circ}$ to $10^{\circ}\text{--}15^{\circ}$. So total losses in temperature differences can reach $20^{\circ}\text{--}40^{\circ}$.

Fig. 4 presents the study results of single-stage and two-stage modules comparison for different cases of total temperature losses when the ratio between temperature losses in cold and warm part are related as 1 to 2. The program permits to get results for any other cases. From plots follows that in the values areas higher the each curve a two-stage cooler is preferable, below the curve there is the area when a single-stage module is preferable.

The variants of thermoelectric coolers with two-stage cooling modules with operating chambers of 37 l, 65 l and 100 l volumes have been designed leaning on these results. Temperature in chambers is $-5^{\circ}\text{C}\text{--}15^{\circ}\text{C}$ at the ambient temperature of $+30^{\circ}\text{--}35^{\circ}\text{C}$.

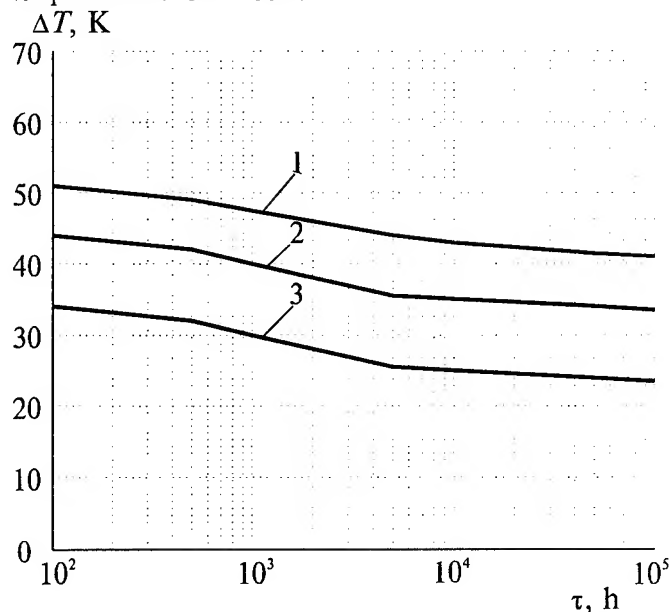


Fig. 4. Temperature difference dependence on service life at equal modules cost.

1 - temperature losses are 20°C ; 2 - temperature losses are 30°C ; 3 - temperature losses are 40°C .

Thermoelectric Coolers with Small Response Time

Vladimir A.Semeniuk*, Tatyana V.Pilipenko**

* Thermion Company, Odessa, Ukraine

** Odessa State Academy of Refrigeration, Odessa, Ukraine

Abstract

The method of evaluation of cascade thermoelectric cooler transient response is described. To check the theoretical model experimental research of a wide range of single-stage and multi-stage TE coolers was carried out. The fast response coolers providing the achievement of 90% of steady-state temperature difference for the time from 1.2 to 6.2 s have been developed. The limit speed of thermal response for cascade coolers is predicted.

Introduction

In many cases speed of response of thermoelectric coolers (TECs) under non-steady-state condition play the most important role. In particular, this parameter is significant in fast cooling of quick-response objects, such as IR detectors, various sensors and miniature semiconductor lasers.

To develop high speed response TEC it is necessary to study the transient process occurring in the cooler from switching on up to achievement the steady-state condition.

The problem of transient process evaluation for single-stage coolers is well studied [1]. As to multi-stage coolers, the satisfactory analytical solution failed to be obtained up to now even for two cascades.

In this paper the method of transient cooling effect evaluation for TECs with arbitrary cascade number is given. To check the theoretical model, experimental research of dynamic characteristics for a wide range single-stage and multi-stage coolers is carried out.

Theoretical analysis

Let us consider the transient process occurring in cascade TEC (Fig. 1) after DC switching on. We suppose that the TEC's base is maintained at the temperature of T_h , at the top the heat load Q_c being supplied, the rest TEC's surface is insulated adiabatically. At $t=0$ the whole system has the same

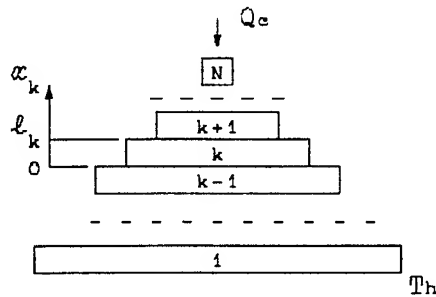


Fig.1 N-stage TEC scheme.

initial temperature T_h . Ceramic plates between cascades are supposed to have sufficiently high heat conductance so the one-dimensional model of temperature field becomes acceptable.

In such an approach the problem is reduced to finding the temperature distribution along the x -axis in each cascade at arbitrary time, corresponding differential equation being of the form

$$\frac{\partial T_k(x_k, t)}{\partial t} - a_k \frac{\partial^2 T_k(x_k, t)}{\partial x^2} = u_k, \quad (1)$$

$$0 < x_k < l_k, \quad k = 1, \dots, N,$$

where

$$u_k = \frac{a_k}{\lambda_k} \frac{i_k^2}{\sigma_k}, \quad (2)$$

a_k, λ_k, σ_k are averaged (for n- and p-type TE legs) values of thermal diffusivity, heat conductivity and electrical conductivity respectively, i_k is feeding current density, l_k is TE leg length.

The system (1) should be supplemented by the initial condition

$$T_k(x_k, 0) = T_h, \quad k = 1, \dots, N, \quad (3)$$

as well as boundary conditions which include the condition of hot side thermostating

$$T_1(0, t) = T_h \quad (4)$$

conditions of boundary temperatures continuity

$$T_k(l_k, t) = T_{k+1}(0, t), \quad k = 1, \dots, N-1, \quad (5)$$

and the heat balance equations at cascade boundaries

$$G_k \frac{\partial T_k(l_k, t)}{\partial t} - F_k q_{0k} + F_{k+1} q_{1k+1} = 0, \quad k = 1, \dots, N-1, \quad (6)$$

$$(G_N + G_c) \frac{\partial T_N(l_N, t)}{\partial t} - F_N q_{0N} - Q_c = 0,$$

where

G_k - heat capacity of ceramic plate, linked to the cold face of k -th cascade,

G_c - heat capacity of the object to be cooled,

$F_k = S_k n_k$ - total area of cascade junctions,

S_k - TE leg cross-section,

n_k - number of cascade TE legs,

$$q_{0k} = q_k(l_k, t) + i_k^2 r_c, \quad q_{1k} = q_k(0, t) - i_k^2 r_c, \quad (7)$$

- outer heat flows at cascade junctions,

r_c - contact resistance per unit contact area.

In relations (7)

$$q_k(x_k, t) = -\alpha_k i_k T_k(x_k, t) - \lambda_k \frac{\partial T_k(x_k, t)}{\partial x_k} \quad (8)$$

is the heat input along a TE leg, including heat conductance and heat transferred by charge carriers.

It should be noted, that for x -axis direction chosen, relation (8) is valid both for n - and p -legs provided that the absolute values of the Seebeck coefficient $\alpha \equiv |\alpha|$ and module of current density vector $i \equiv |\vec{i}|$ are used in this equation.

Idea of calculation method

It is impossible to obtain solution of the problem in general form. In this connection the method of approximation is used. The idea of the method is to search dependencies of boundary temperatures $T_k(l_k, t)$ upon a time in the form of approximating functions containing the finite number of free parameters

$$T_k(l_k, t) = g_k(\gamma_k, t), \quad k = 1, \dots, N \quad (9)$$

where $\gamma_k = (\gamma_k^{(1)}, \dots, \gamma_k^{(m)})$ is a m -dimensional vector-parameter with non-defined components. The class of $g_k(\gamma_k, t)$ functions must be chosen beforehand to satisfy the initial condition

$$g_k(\gamma_k, 0) = T_h \quad (10)$$

and the condition to infinity

$$g_k(\gamma_k, \infty) = T_k^s \quad (11)$$

where $T_k^s = \lim_{t \rightarrow \infty} (T_k(l_k, t))$ is the stationary temperature of k -th cascade cold junctions corresponding to the specified input current I and given heat load Q_c .

Now equations (1) can be solved separately for each cascade together with boundary conditions (9), the solution being presented in the form:

$$T_1 = f_1(\gamma_1; x_1, t), \quad T_k = f_k(\gamma_{k-1}, \gamma_k; x_k, t), \quad k = 2, \dots, N \quad (12)$$

It is clear that these relations do not satisfy boundary conditions (6) in a general case. Therefore it is reasonable to choose free vector-parameters γ_k for relations (12) to approach best of all to boundary conditions (6) for specified period of time t_0 . The problem is mathematically formulated as follows: it is necessary to find such a set of vector-parameters γ_k which provides the least square discrepancy for all boundary conditions (6) for the specified time period t_0 . Thus we have the problem of non-linear programming in the form:

$$Y(\gamma_1, \dots, \gamma_N) = \sum_{k=1}^N \int_0^{t_0} R_k^2(\gamma_{k-1}, \gamma_k, \gamma_{k+1}; t) dt = \min, \quad (13)$$

where R_k is discrepancy arising when substituting in (6) values of T_k from (9) and derivatives $\frac{\partial T_k}{\partial t}$ obtained by differentiating (12). It should be defined more precisely that the first and last components of discrepancy vector in (13) include only two sets of unknown parameters, namely $R_1 = R_1(\gamma_1, \gamma_2; t)$ and $R_N = R_N(\gamma_{N-1}, \gamma_N; t)$.

The time period t_0 for approximation can be chosen differently. In a general case the part of trajectory on which it is desirable to obtain the highest accuracy should be taken as t_0 .

Calculation algorithm

In this paper we used as approximating functions the relations of the form

$$g_k(\gamma_k, t) = T_h - \Delta T_k^s [1 - \exp(-\gamma_k t)] \quad (14)$$

where $\Delta T_k^s = T_h - T_k^s$ and vector γ_k dimension equals to unit, i.e. the case of simple variable is considered. It is easy to see, that relations (14) satisfy conditions (10) and (11).

Approximations of form (14) were used to calculate responsibility of a great number of coolers with various cascade numbers as well as to predict cooler's limit responsibility.

To calculate stationary temperatures T_k^s taking into account temperature dependence of TE materials properties, we used the method of successive approaches described in Appendix 1. Analytical solution of equations (1) with boundary conditions (14) are represented in Appendix 2. The relations given were used to calculate functional (13). The solution of the problem concerning this functional minimum was carried out by the non-linear programming method [2].

Calculations and experimental details

The above method was used to predict dynamic characteristics of cascade TECs of different configuration. We studied the influence of such parameters as cascade number, TE leg length, ceramic plates thickness, heat capacity of the object to be cooled. The maximum steady-state temperature difference $\Delta T_{\max} = \max \Delta T_N^s(I)$ was pre calculated for each cooler and parameters of TE materials $\alpha_k, \sigma_k, \lambda_k$ related to average cascade temperatures $T_{mk} = (T_{k-1} + T_k)/2$ were defined. Typical temperature dependencies of TE properties for single crystals of Bismuth and Antimony Chalcogenides [3] were used as the basic data. The resulting set of TE parameters was further used in calculations of the TEC dynamic characteristics. TE materials density and specific heat values of 6.85 g/cm³ and 0.158 J/(gK) respectively were taken and considered the same for all cascades. For ceramic based on Al₂O₃ the linear dependence of specific heat on temperature $\rho C_p = 3 + 0.01(291 - T)$ was accepted. The ρC_p value was calculated at average cooler temperature $T_m = T_h - \Delta T_{\max}/2$ and was accepted the same for all cascades.

As a first step in checking the approximation method reliability the dynamic characteristics of single stage cooler for which the accurate solution is well known [1] were calculated. Comparison of our results with those of the exact theory shows their complete agreement. As to cascade coolers, only experimental checking can answer the question of the approximation method applicability. With this aim a great number of MC coolers (Table 1) was tested. The ΔT_{\max} under steady-state condition and corresponding feeding current I_{\max} were preliminary measured for each cooler. Then

the cooler was switched off. On achieving equilibrium with heat sink the current I_{\max} was switched on again. Measurement and the recording of cold face time-temperature dependence were carried out by means of a copper-constantan

thermocouple 30 μm in diameter and XY-Recorder ENDIM 62201. All the measurements were made in vacuum of $5 \cdot 10^{-5}$ Torr at heat sink temperature of $T_h = 303$ K.

Table 1. Configuration of experimental samples and test results

No. of stages	Model	Dimensions (mm)		Ceramic thickness (mm)	Thermocouple distribution from the base to the top	TE leg cross-section (mm)	TE leg length (mm)	ΔT_{\max} condition (measured)			Time to achieve specified ΔT (s, measured)		
		Base	Top					I_{\max} (A)	U_{\max} (V)	ΔT_{\max} (K)	$0.5\Delta T_{\max}$	$0.9\Delta T_{\max}$	$0.95\Delta T_{\max}$
1	1MC06-018-1	6x8	6x6	0.5	18	0.6x0.6	1.5	1.3	2.20	75.4	1.82	6.0	7.7
							1.2	1.7	2.10	74.5	1.42	4.5	5.9
							1.0	2.0	2.28	73.9	1.20	3.7	4.6
							0.8	2.4	2.15	72.9	0.92	2.9	3.8
							0.6	3.2	2.18	72.3	0.75	2.3	2.9
							0.5	3.6	2.19	71.0	0.63	1.9	2.3
	1MC06-032-1	8x10	8x8	0.25	32	0.6x0.6	1.5	1.2	3.78	73.6	1.1	3.7	4.8
							1.0	2.0	3.89	73.5	0.9	2.6	3.4
							0.5	3.6	3.76	71.0	0.25	1.0	1.3
	1MS02-10-02	4x1	3.1x1	0.5	10	0.2x0.2	0.2	0.8	1.16	64.0	0.38	1.2	1.5
2	2MC06-021-1	6x8	2x4	0.5	17.4	0.6x0.6	1.5	1.1	2.22	102.1	3.06	10.2	13.5
							1.2	1.5	2.26	106.2	2.16	7.3	9.2
							1.0	1.6	2.13	103.8	1.92	6.3	8.0
							0.8	2.0	2.19	104.9	1.52	5.0	6.5
							0.6	2.6	2.00	100.6	1.16	3.6	4.6
							0.5	2.8	2.12	101.4	1.00	3.2	4.1
3	3MC06-080-1	12x12	2x4	0.5	59.17.4	0.6x0.6	1.5	1.0	7.22	121.0	4.10	13.6	18.0
							1.2	1.3	7.15	122.9	2.85	9.5	12.2
							1.0	1.45	6.93	121.0	2.47	8.2	10.6
							0.8	1.8	7.33	122.5	2.08	6.5	8.5
							0.6	2.3	6.50	116.1	1.52	4.8	6.2
							0.5	2.6	7.40	120.7	1.30	4.0	5.2
4	4MC06-105-1	12x12	2x4	0.5	59.31.11.4	0.6x0.6	1.5	0.72	6.92	120.9	5.40	21.4	30.0
							1.2	0.95	7.33	125.5	4.00	15.7	22.0
							1.0	1.15	7.01	124.2	3.20	12.2	16.0
							0.8	1.4	7.25	126.9	2.65	10.0	13.6
							0.5	2.05	7.19	123.6	1.70	6.2	8.1

Results and discussion

Calculation and experimental results are given in Table 1 and in Fig. 2-6.

Time temperature dependence:

As an example, experimental time dependencies of cold side temperature for a number of four-cascade MC coolers are given in Fig. 2 (solid lines). Corresponding calculated dependencies are given for the comparison (dashed lines). It is seen that the approximation method provides sufficiently good agreement between the calculated and experimental data.

Similar calculations and measurements were carried out for all MC coolers. The results of these measurements treated in the form of $\Delta T(t)/\Delta T_{\max}$ time dependence are given in Fig. 3. It is seen that for all types of coolers the rate of temperature difference rise increases with TE leg length reduction.

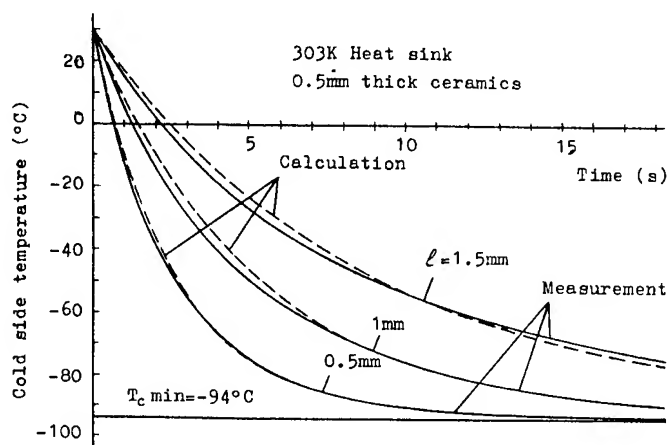


Fig.2 Recorded (solid lines) and calculated (dashed lines) cold side temperature versus time for 4-stage TECs of MC series.

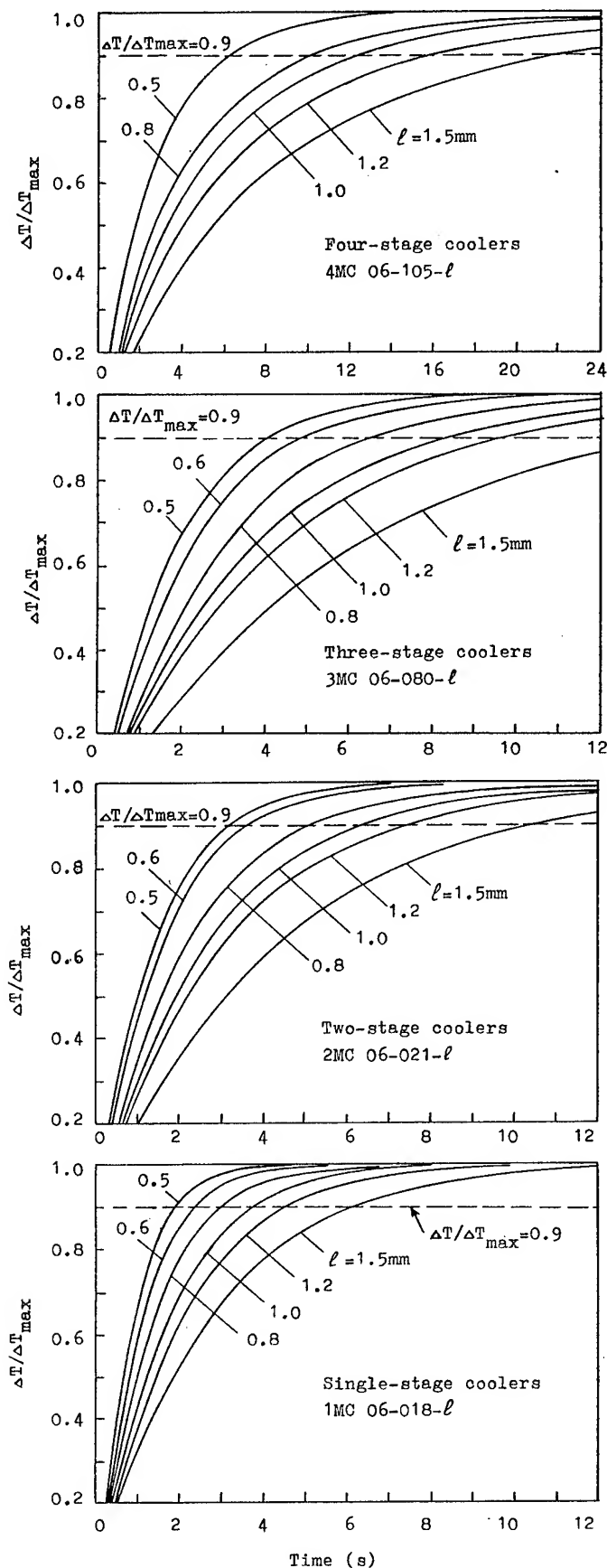


Fig.3 Dynamic characteristics of MC series TECs (measured).

Responsibility characterization:

It is reasonable to accept the time of achieving the specified value of the relation $\Delta T(t)/\Delta T_{\max}$ as TEC's fast responsibility characteristic. Table 1 gives time values necessary to achieve ΔT of 50, 90 and 95% of ΔT_{\max} . To create a unified approach for the comparison of various coolers on responsibility factor we shall accept time of achieving $\Delta T=0.9\Delta T_{\max}$ as this factor and call it briefly reference or specific cool-down time t_s .

Influence of TE leg length:

It is seen from Table 1 that specific cool-down time decreases approximately proportionally to the reduction of TE leg length. So the l reduction from 1.5 to 0.5 mm leads to the triple decrease of t_s for all kinds of MC coolers. Single stage TEC of MS series with l of 0.2 mm shows t_s of only 1.2 s, this result being near the limit one.

Fig. 4 gives the comparison of calculated (solid lines) and measured (dots) t_s values for MC coolers having various numbers of cascades with different TE leg length. One can see that there is a good agreement for all coolers of the series.

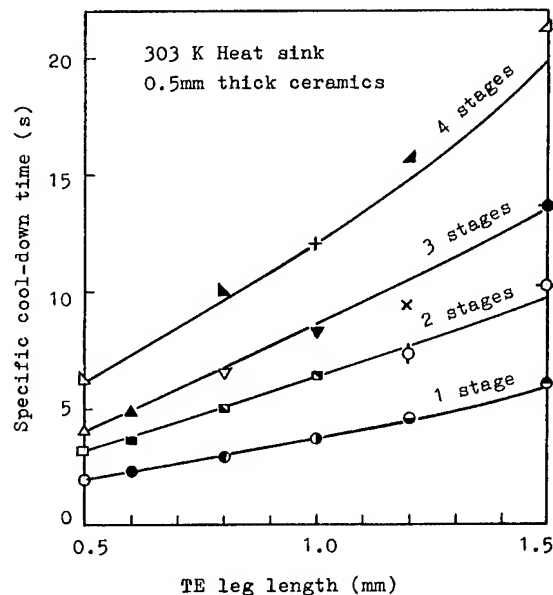


Fig.4 Specific cool-down time versus TE leg length: comparison of the experimental data (dots) and computer solution (solid lines).

Dependence on ceramic thickness:

The ceramic thickness δ_c is another factor influencing considerably the TEC's quick-responsibility. The time of achieving the specified temperature difference increases with δ_c increase, the dependence being close to the linear one for all coolers studied (Fig. 5).

TE cooler with 0.25mm thick ceramics (Table 1) shows t_s of only 1 s. This is the fastest TEC ever produced of bulk material.

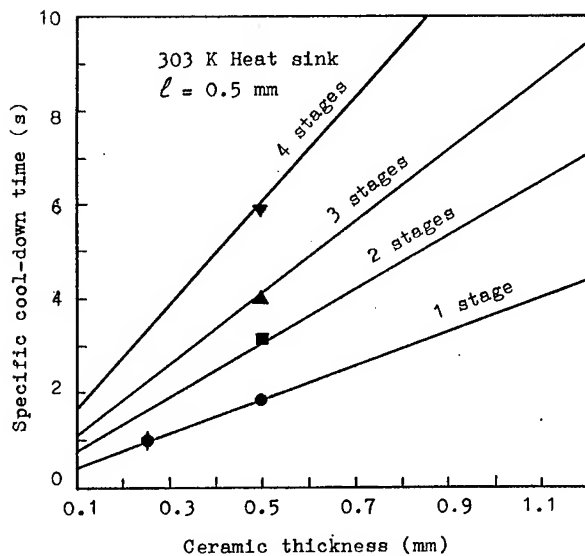


Fig.5 Specific cool-down time versus ceramic thickness: calculation (solid lines) and experimental data (dots).

Potential for further improvement

We see that the reduction of l and δ_c is the key for increasing of TEC's speed of response. It is of great interest to estimate the possibilities for further progress in this direction. We consider achieved l value of 0.2 mm as the technologically and thermodynamically justified lower limit of TE leg length. As to ceramic plates, their thickness can be reduced significantly. The lower limit of 0.1mm can be accepted, the strength condition being taken into account. To provide effective heat spread in cascade coolers with such ceramics the high conductive materials such as beryllium oxide can be used.

Table 2 gives corresponding calculated data which define the upper limit of TECs response. It is seen that cascade coolers with t_s value significantly less than 1 s can be realized.

Table 2. Upper limit of fast thermal response for TE coolers ($l=0.2\text{mm}$, $\delta_c=0.1\text{mm}$)

No. of stages	1	2	3	4
Time to achieve $\Delta T=0.9\Delta T_{\max}$ (s)	0.15	0.26	0.36	0.51

Influence of attached heat capacity:

Up to now we considered only TEC own responsibility. It is natural, to ask - in what degree heat capacity of the object attached to a cooler influences the rate of cooling. To have an idea about it the model of a cascade cooler with an attached copper layer was considered (Fig. 6). It is seen that even relatively small attached heat capacity considerably reduces TEC's responsibility, the increase of specific cool-down time being close to linear for all coolers under study.

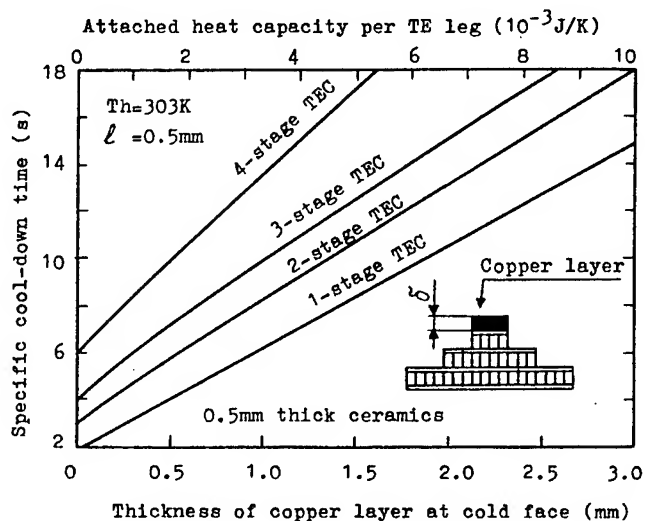


Fig.6 Dependence of specific cool-down time on attached mass heat capacity (calculation).

Conclusion

The suggested method of boundary conditions approximation provides rather high accuracy of evaluation cascade coolers dynamic characteristics.

Reduction of TE leg length is the fundamental means of TEC responsibility increasing. TE coolers of MC series with TE leg length of 0.5 mm having from 1 to 4 cascades provide achieving $\Delta T=0.9\Delta T_{\max}$ for the time from 1.9 to 6.2 s.

The reduction of ceramic thickness and heat capacity of the object to be cooled is another factor of increasing TECs responsibility. Using these means, the coolers with specific cool-down time of only 1 s are fabricated. These are fastest coolers ever produced of bulk material.

Practically achievable lower limit of specific cool-down time for cascade TECs is from 0.15 to 0.5 s.

Appendix 1

For steady-state condition

$$t \rightarrow \infty, \quad \frac{\partial T_k}{\partial t} \rightarrow 0, \quad T_k(x_k, t) \rightarrow T_k^s(x_k)$$

boundary problem (1)-(8) reduces to the linear system of the form:

$$a_{1k}T_{k-1}^s - a_{2k}T_k^s + a_{3k}T_{k+1}^s + b_k = 0, \quad k=1, \dots, N,$$

coefficients being as follows:

$$a_{11} = a_{3N} = 0,$$

$$a_{1k} = H_k, \quad k=2, \dots, N,$$

$$a_{2k} = \alpha_k I + H_k - \beta_k (\alpha_{k+1} I - H_{k+1}), \quad k=1, \dots, N,$$

$$a_{3k} = \beta_k H_{k+1}, \quad k=1, \dots, N,$$

$$b_1 = \frac{1}{2} I^2 (R_1 + \beta_1 R_2) + H_1 T_h,$$

$$b_k = \frac{1}{2} I^2 (R_k + \beta_k R_{k+1}), \quad k = 2, \dots, N-1,$$

$$b_N = \frac{1}{2} I^2 R_N + \frac{Q_c}{n_N},$$

where $T_k^s \equiv T_k^s(l_k)$ are the boundary temperatures,

$$H_k = \frac{\lambda_k S_k}{l_k}, \quad R_k = \frac{l_k}{\sigma_k S_k} + 2 \cdot r_c,$$

$$\beta_k = \frac{n_{k+1}}{n_k}, \quad k = 1, \dots, N-1, \quad \beta_N = 0.$$

For specified α_k , σ_k , λ_k the system can be solved by one-fold driving method. To solve the system with temperature dependent kinetic coefficients the iteration process with successive redetermination of boundary temperatures and TE properties is used.

Appendix 2

The solution of equation (1) with boundary conditions (14) is found by the Green's function method as follows:

$$T_k^s(\gamma_{k-1}, \gamma_k; x_k, t) = T_{k-1}^s - \frac{u_k x_k}{2a_k} (x_k - l_k) -$$

$$- \frac{4u_k}{a_k l_k} \sum_{n=1}^{\infty} \frac{\sin B_n x_k}{B_n^3} \exp(-A_{1nk} t) -$$

$$- \frac{\Delta T_k^s x_k}{l_k} \left[1 - \frac{l_k}{x_k} \frac{\sin r_k x_k}{\sin r_k l_k} \exp(-\gamma_k t) \right] -$$

$$- \frac{2\Delta T_k^s \gamma_k}{l_k} \sum_{n=1}^{\infty} (-1)^{n+1} \frac{\sin B_n x_k}{B_n (A_{nk} - \gamma_k)} \exp(-A_{nk} t) +$$

$$+ \frac{\Delta T_{k-1}^s x_k}{l_k} \left[1 + \frac{l_k}{x_k} \frac{\sin r_{1k} (l_k - x_k)}{\sin r_{1k} l_k} \exp(-\gamma_{k-1} t) \right] -$$

$$- \frac{2\Delta T_{k-1}^s \gamma_{k-1}}{l_k} \sum_{n=1}^{\infty} \frac{\sin B_n x_k}{B_n (A_{nk} - \gamma_{k-1})} \exp(-A_{nk} t),$$

$$k = 1, \dots, N,$$

where

$$r_k = \sqrt{\frac{\gamma_k}{a_k}}, \quad r_{1k} = \sqrt{\frac{\gamma_{k-1}}{a_k}},$$

$$B_n = \frac{n\pi}{l_k}, \quad B_{1n} = \frac{(2n-1)\pi}{l_k},$$

$$A_{nk} = B_n^2 a_k, \quad A_{1nk} = B_{1n}^2 a_k,$$

$$\gamma_0 = 0, \quad T_0^s = T_h, \quad \Delta T_0^s = 0.$$

References

- [1] M.A. Kaganov, M.R. Privin, *Thermoelectric heat pumps*, Energiya, Leningrad, p.176 (1970).
- [2] D.A. Paviani, D.M. Himmelblau, "Constrained Nonlinear Optimization by Heuristic Programming", *Operation Res.*, vol. 17, pp 872-881 (1969).
- [3] V.A. Semeniouk, L.D. Ivanova, T.E. Svechnikova, et al., "Thermoelectric Micro Coolers Based on Single Crystals of Solid Solutions of Bismuth and Antimony Chalcogenides", *Neorgan. Materialy*, vol. 28, No. 9, pp 1855-1860 (1992).

OPTIMIZATION OF A MULTISTAGE THERMOELECTRIC COOLING SYSTEM CONCERNING MAXIMUM C.O.P.

T. Wartanowicz, A. Czarnecki
Heat Engineering Institute, Warsaw University of Technology
Nowowiejska 25, 00-665 Warsaw, Poland

Abstract

In the process of designing multistage thermoelectric cooling systems accuracy of computations is very important. For this purpose a useful algorithm of optimization was elaborated where thermoelectric parameters of semiconductors have been concerning as temperature dependent. The presented method allows to find out the optimal solution for systems achieving maximum C.O.P.

Introduction

During designing process of a multi-stage cooling system it is particularly important to consider the respective criterion of their working conditions. Among the many known criteria three are the most common:

- maximum cooling capacity at given temperatures of the cold and hot sides of the cascade.
- minimum temperature of the cold side of the cascade at the given temperature of the hot side and the cooling capacity.
- maximum C.O.P. at a definite cooling capacity and temperatures of the cold and hot sides of the cascade.

The paper presents the third criterion where thermoelectric material properties are considered as temperature dependent.

Physical model

The scheme of enumeration of the cascade system consisting of N stages has been presented in fig.1.

The next fig.2 shows the method of indexing the heat fluxes flow between i and $i+1$ stages.

The condition of heat balance between bordering stages has to be fulfilled:

$$Q_{h(i+1)} \leq Q_{ci} \quad (1)$$

The heat output of the hot side of the upper stage $i+1$ must be at most equal or smaller than the heat absorbed by the cold side of the lower stage i . For the uppermost stage N the absorbed heat constitutes the cooling capacity Q_c of the cascade.

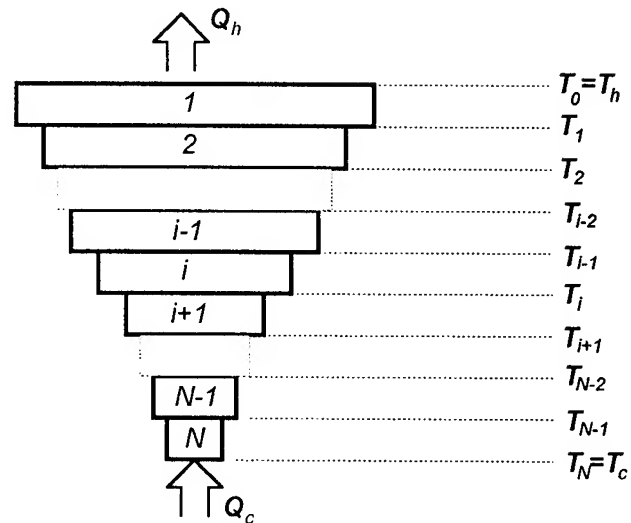


Fig.1. Numeration of stages and interstage temperatures

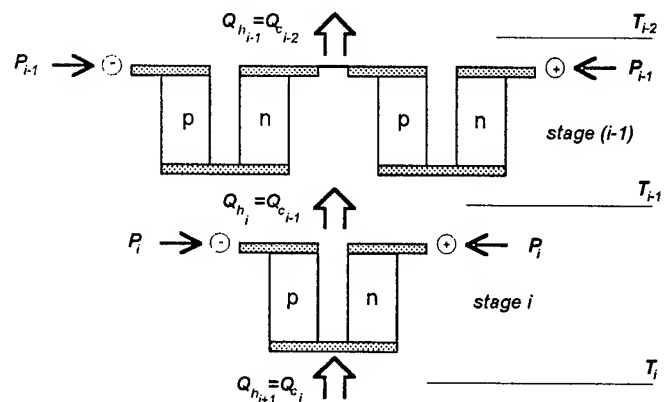


Fig.2. Scheme of heat flux flow between stages

Optimization of the cascade system according to the condition of achieving maximum C.O.P. can be performed by the method of minimizing the value of the following function:

$$\mu = 1 + \frac{1}{C.O.P.} = \frac{Q_{hN}}{Q_0} = \prod_{i=1}^N \mu_i \quad (2)$$

where:

$$\mu_i = 1 + \frac{1}{C.O.P._i} = \frac{Q_{hi}}{Q_{c(i-1)}} \quad i = 1, 2, \dots, N \quad (3)$$

$$\mu_i = \frac{M_i T_i - T_{i-1}}{M_i T_{i-1} - T_i} \quad (4)$$

The M_i parameter vs temperature can be described by the power function;

$$M_i(\bar{T}_i) = a \bar{T}_i^b \quad (5)$$

$$\bar{T}_i = (T_i + T_{i-1}) / 2 \quad (6)$$

The solution for maximum μ leads to the following form of dependence between the interstage temperatures [1]:

$$\frac{(M_i^2 - 1)T_{i-1} - bM_i(T_i - T_{i-1})}{(M_i T_{i-1} - T_i)(M_i T_i - T_{i-1})} = \frac{(M_{i+1}^2 - 1)T_{i+1} + bM_{i+1}(T_{i+1} - T_i)}{(M_{i+1} T_i - T_{i+1})(M_{i+1} T_{i+1} - T_i)}$$

(7)

where:

$$M_i = \sqrt{1 + 0.5Z_i(T_i + T_{i-1})} \quad (8)$$

$$M_{i+1} = \sqrt{1 + 0.5Z_{i+1}(T_{i+1} + T_i)} \quad (9)$$

In case when the assumption that in the considered temperature range the parameters as electrical resistivity ρ , thermoelectric power S , thermal conductivity k and the parameter M are constant is valid then the optimal solution for interstage temperatures can be reduced to the following recurrent formula [1]:

$$T_i = \sqrt{T_{i+1} T_{i-1}} \quad (10)$$

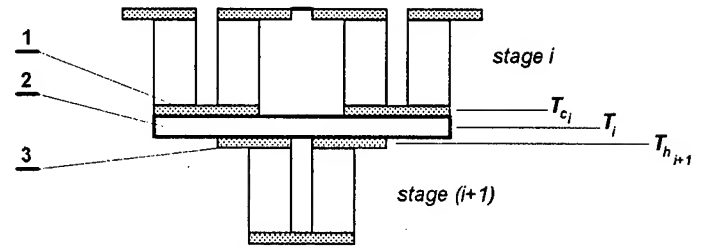
$$T_i = T_0 \left(\frac{T_N}{T_0} \right)^{\frac{i}{N}} \quad (11)$$

$$T_{i+1}/T_i = \left(\frac{T_N}{T_0} \right)^{\frac{1}{N}} \quad (12)$$

When the interstage thermal resistance has been taken into consideration the temperature drop on the interstage connections occurs. As a result the interstage temperatures means the average values of the interstage connections. Usually the heat transfer coefficient of such connections is in the range from 0.5 to 2.5 [W/cm²K].

The interstage connection has been presented schematically in fig. 3.

The input data for optimization comprise the values of cooling capacity Q_c , temperature of hot side T_h (temperature of heat sink), temperature of cold side T_c (temperature of cooled object). It can be also assumed the restrictions on supplying current I and number of thermoelements in particular stages. So the problem of finding maximum C.O.P. can be reduced to finding minimum value of electric power pumped to the cascade.



1 - cold side of stage i
2 - interstage connection
3 - hot side of stage $(i+1)$

Fig. 3. Interstage connections

Algorithm of computations

The problem of optimization can be expressed as follows:

For given input data: cooling capacity Q_c , temperatures of the hot side T_h and the cold side T_c of the cascade, electric conductivity $\rho(T)$, thermoelectric power $S(T)$, thermal conductivity $k(T)$, heat transfer coefficient of the interstage separators k_r , there should be indicated maximum C.O.P. at the following limitations:

$$0 \leq I \leq I_{max}, \quad 0 \leq n \leq n_{max}$$

The parameters $\rho(T)$, $S(T)$, $k(T)$ have been taken as temperature dependent and in view of their regular character vs temperature the approximation has been carried out by polynomial functions:

$$y(T) = p_1 + p_2 T + p_3 T^2 \quad (13)$$

The above equation has been transformed to the standard version:

$$y = y(x, \bar{a}) \quad (14)$$

in the shape required for the least square method:

$$\chi^2(a) = \sum_{i=1}^n \left[\frac{y_i - y(x_i, a)}{\sigma_i} \right]^2 = \min \quad (15)$$

Finally the following formula is used for determining the constant values of the equation (13):

$$\chi^2(p_1, p_2, p_3) = \sum_{i=1}^n \left[\frac{y(T) - (p_1 + p_2 T + p_3 T^2)}{\sigma_i} \right]^2 = \min \quad (16)$$

where:

$$\sigma_i = \sqrt{\frac{1}{n} \sum_{i=1}^n y_i^2} \quad (17)$$

where: n - number of measurements.

y_i - value of i -th measurement.

Typical characteristics of thermoelectric materials based on bismuth telluride alloys or measurements data of properties of such materials have been applied for determining the constant values of coefficients in the equation (15).

The equation (5) can be solved in the following manner:

twice logarithmization of (5) gives in result

$$\ln M(\ln T) = b \ln T + \ln a \quad (18)$$

$$Y = AY + B \quad (19)$$

where: $A = b$, $B = \ln a$.

It is a classical linear regression problem which has been solved by the least square method.

A proposal of solving the eq.(7) is worthy of notice. It has been obtained by implementation of secant method due to its very good convergence but under condition of proper choice of the starting range.

The task is as follows:

find the solution of the equation

$$T_0 = f(T_{N-1}) \quad (20)$$

where for given T_0 and T_N the function f is defined by the recurrent non-linear formula:

$$T_{i+1} = g_i(T_i, T_{i+1}) \quad (21)$$

The upper limit can be evaluated from eq. (11) but still there is a problem of the lower limit. To avoid any difficulties with the possible singularity it can be arbitrarily assumed the value of maximal μ_N . Then from eq.(4) for $i=N$ using a discret variant of the Newton method it has been possible to obtain the lower limit $T_{N-1}(\min)$.

The following steps of the optimization algorithm have been performed:

1. Find constant coefficients to approximate the thermoelectric material properties.
2. Solve the equation (7) to obtain temperature distribution across the cascade.
3. Calculate values of μ_i from the equation (4).
4. Find optimal values $C.O.P._i$ for particular stages.
5. Find values of μ and $C.O.P.$ for the cascade.

Case study

The computations have been carried out for the following data:

- thermoelectric material type: typical bismuth telluride alloys,
- the hot side temperature of the cascade $T_h = 300K$,

- the cold side temperature of the cascade $T_c = 200K$,

- maximum supplying current $I = 4A$,

- maximum number of thermoelements in the coldest stage

$$n_N = 10,$$

- cooling capacity $Q_c = 0.05W$.

The results of computations have been presented in tables 1 and 2. One- and two-stage systems have not been shown in the tables because they do not achieve the required temperature difference.

Table 1

i	μ	$C.O.P.$	μ_i	$C.O.P._i$	$\Delta T[K]$	$T_i[K]$
3	41.17	0.0249	2.829	0.547	37.93	300.00
2			3.360	0.424	33.13	262.07
1			4.331	0.300	28.94	228.94
0						200.00
4	33.58	0.0307	2.094	0.914	28.92	300.00
3			2.264	0.791	26.13	271.08
2			2.497	0.668	23.61	244.95
1			2.837	0.544	21.34	221.34
0						200.00
5	30.99	0.0334	1.780	1.281	23.37	300.00
4			1.863	1.159	21.55	276.63
3			1.965	1.036	19.87	255.08
2			2.096	0.913	18.32	235.22
1			2.267	0.789	16.89	216.89
0						200.00
6	29.73	0.0348	1.606	1.649	19.60	300.00
5			1.655	1.527	18.32	280.40
4			1.712	1.404	17.13	262.07
3			1.781	1.281	16.01	244.95
2			1.864	1.157	14.96	228.94
1			1.967	1.034	13.98	213.98
0						200.00
7	29.03	0.0357	1.496	2.017	16.88	300.00
6			1.528	1.894	15.93	283.12
5			1.564	1.772	15.04	267.18
4			1.607	1.649	14.19	252.15
3			1.656	1.526	13.39	237.96
2			1.713	1.402	12.64	224.56
1			1.782	1.279	11.93	211.93
0						200.00
8	28.60	0.0362	1.419	2.385	14.83	300.00
7			1.442	2.262	14.09	285.17
6			1.467	2.140	13.40	271.08
5			1.496	2.017	12.73	257.68
4			1.528	1.894	12.11	244.95
3			1.565	1.770	11.51	232.84
2			1.607	1.647	10.94	221.34
1			1.656	1.523	10.40	210.40
0						200.00

Table 1 (cont.)

9	28.31	0.0366	1.363	2.753	13.22	300.00
8			1.380	2.630	12.63	286.78
7			1.399	2.508	12.08	274.15
6			1.419	2.385	11.54	262.07
5			1.442	2.262	11.04	250.53
4			1.468	2.139	10.55	239.49
3			1.496	2.015	10.09	228.94
2			1.529	1.892	9.64	218.86
1			1.566	1.768	9.22	209.22
0						200.00

10	28.10	0.0369	1.320	3.121	11.92	300.00
9			1.334	2.998	11.45	288.08
8			1.348	2.876	10.99	276.63
7			1.363	2.753	10.56	265.64
6			1.380	2.630	10.14	255.08
5			1.399	2.507	9.73	244.95
4			1.420	2.384	9.35	235.22
3			1.442	2.260	8.98	225.87
2			1.468	2.137	8.62	216.89
1			1.497	2.013	8.28	208.28
0						200.00

Table 2

i	C.O.P.	C.O.P.*
3	0.0249	0.0190
4	0.0307	0.0246
5	0.0334	0.0272
6	0.0348	0.0286
7	0.0357	0.0294
8	0.0362	0.0300
9	0.0366	0.0304
10	0.0369	0.0306

Comparison of the coefficient of performance for cases with negligence of the interstage connections and when those connections are considered leads to conclusion that influence of the interstage connections significantly reduces the value of C.O.P. of the system. In the table 2 the first column corresponds to the maximum C.O.P. for systems where the interstage temperature drop can be neglected while the second column represents maximum C.O.P.* with $k_1=2[\text{W}/\text{cm}^2\text{K}]$ for interstage connections.

As a continuation of the computations from the tables 1 and 2 there can be obtained values for the number of thermoelements in the cascade and electric supplying parameters I and V . Table 3 presents the results of comparative computations for the 5-stage cascade with assumed different number of elements in the coldest stage

from 1 to 10. The first column of the table shows the number of thermoelements in the stage N , the second column determines the total number of thermoelements in the cascade, and columns 3 and 4 give the values of the supplying current and voltage to the cascade. Analysing the results it can be noticed that when the number of thermoelements in the stage N increases the total number of thermoelements and the voltage of the cascade increase while the supplying current decreases.

Table 3

n_i	n	$I[\text{A}]$	$V[\text{V}]$
3	73	0.712	2.583
4	96	0.534	3.444
5	121	0.427	4.305
6	144	0.356	5.165
7	169	0.305	6.026
8	193	0.267	6.887
9	218	0.237	7.748
10	240	0.214	8.609

Summary

On the basis of the classic assumptions concerning conditions of thermoelectric energy conversion in a multi-stage cooling system the algorithm of its optimization with C.O.P. as a merit function has been evaluated. Numerical realization of the above algorithm in shape of a useful computer program makes it possible in easy and convenient way to look for solution of the cascade systems with required features and has become a helpful tool providing the designer of such systems with the possibility of optimal choice. The results of computations have confirmed the known rule of decreasing influence of the interstage connections for maximum C.O.P.

References

- [1] A.L. Vajner, Kask. Term. Ist. Hol., Sov.Radio, 1976.
- [2] T.Wartanowicz, A.Czarnecki, Analysis of thermoelectric energy conversion in a multi-stage system, Eighth ICOTEC, pp.77-81, July 1989.

INFLUENCE OF AIR HEAT SINK GEOMETRY ON THE PERFORMANCE OF THERMOELECTRIC COOLING MODULES

Wanlie Zheng
Cannon Instrument Company

Guheng Xu
Pennsylvania State University

Abstract

Maximizing the rate of heat removal from the hot side of thermoelectric cooling modules is necessary to obtain optimum performance for any thermoelectric cooling device. The thickness, shape, height of fins and number of fins per inch are all important variables in a finned heat sink design. The area and thickness of the heat sink base plate relative to the area of the thermoelectric module is also important. This paper provides a means to calculate the effectiveness of these variables as they affect heat dissipation from the hot side of a thermoelectric module operated in the cooling mode. Although the focus is on cooling devices, the results of this model should be equally useful in evaluating power-generating devices.

Introduction

Effective heat removal from the hot side of a thermoelectric cooling module is extremely important for any thermoelectric cooling device. In the case where the heat transfer media is air, the design and manufacture of the air heat sink become significant. There are several types of air heat sinks, including aluminum extruded heat sinks, aluminum fold fin brazed heat sinks, epoxy-bound heat sinks, etc. Although the aluminum extruded heat sink is the least effective, the heat removing capabilities of the other types are quite comparable.

In general, all air heat sinks used for thermoelectric devices are finned. Many geometric factors influence air heat sink performance. Among these factors, the thickness, shape, height, and number of fins per inch are important variables. In addition to the above mentioned factors, thermoelectric modules have their own particular features. The surface area of a thermoelectric module is only approximately 20% that of an air heat sink base

plate. That means that the air heat sink is much larger than the module. As a result, those fins located on the edge of the base plate are not efficient. They become so-called "finned fins."

Since there is no simple analytical solution for general finned heat sink problems, numerical methods are usually applied. In this paper a simplified method is presented to facilitate numerical calculations involving finned heat sinks. The basic idea is to convert a finned heat sink into a flat plate. In addition, a new concept, "heat sink effectiveness, η_s ", similar to fin effectiveness, has been introduced.

Background

The most popular numerical solutions for heat conduction problems employ finite difference or finite element methods. In both cases geometric discretization is always involved. Conversion of the finned heat sink into a flat plate dramatically simplifies the numerical methods

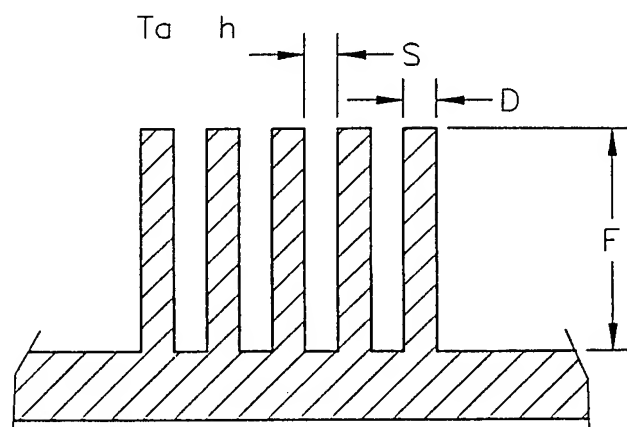


Figure 1a. Finned air heat sink.

For a finned air heat sink (see Fig. 1a), the total heat flow rate is given by the equation below:

$$Q_1 = h (A_f \eta + A_{unf}) \Delta T_{log}$$

$$\eta = \frac{\tanh n}{n}, \quad n = \sqrt{\frac{2h}{KD}}$$

where	h	convective heat transfer coefficient for finned surfaces
	K	thermoconductivity of the air heat sink material
	A_f	fin surface area
	A_{unf}	unfinned base surface area
	A_b	fin base surface area
	T_a	ambient temperature
	ΔT_{log}	mean logarithm temperature difference
	η	fin effectiveness for straight rectangular fin

The finned air heat sink can be modified and converted into a flat plate surface (see Fig. 1b) if one equalizes the heat flow rate for both cases. Then the modified convective heat transfer coefficient can be derived.

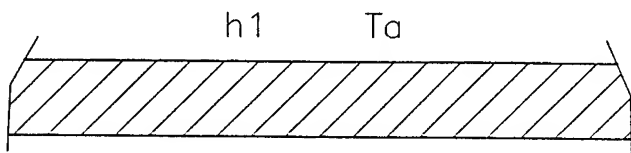


Figure 1b. Finned air sink after conversion to a flat plate surface.

The total heat flow rate of the modified flat plate can be expressed as

$$Q_2 = h_1 (A_b + A_{unf}) \Delta T_{log}$$

Since $Q_1 = Q_2$, the modified convective heat

transfer coefficient, h_1 , for a flat plate is given by the expression:

$$h_1 = h \frac{A_f \eta + A_{unf}}{A_b + A_{unf}}$$

Conversion of the finned surface into a flat plate makes numerical methods much easier and simpler. A finite difference method based on the above geometric conversion has been used for the following calculations.

Influence of geometric dimensions on air heat sink performance

As mentioned before, the fin thickness, height, and shape, and the number of fins per inch, have a significant influence on the performance of the air heat sink. In the case of thermoelectric cooling, the average temperature on the hot side of the thermoelectric module T_h^a will depend on the performance of the air heat sink. The better the performance of the heat sink, the lower the hot side temperature T_h^a .

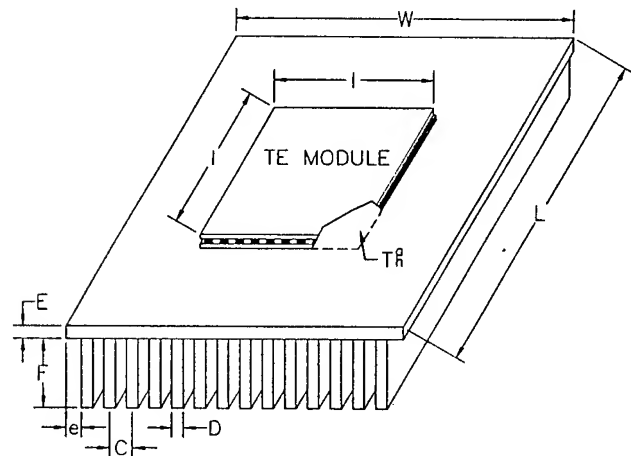


Figure 2. Thermoelectric cooling module mounted on a typical air heat sink.

In Figure 2, a typical air heat sink with a thermoelectric cooling module on top is displayed.

For different convective heat transfer coefficients (h), fin heights (F), number of fins per inch (n), and widths of air heat sink (W), the average temperatures at the hot side of the thermoelectric module T_h^a have been calculated.

The typical finite difference equation for the simplified flat plate is as follows:

$$\begin{aligned} & (T_{i+1,j,1} - T_{i,j,1}) K \frac{\Delta y \Delta z}{\Delta x} \\ & + (T_{i-1,j,1} - T_{i,j,1}) K \frac{\Delta y \Delta z}{\Delta x} \\ & + (T_{i,j+1,1} - T_{i,j,1}) K \frac{\Delta x \Delta z}{\Delta y} \\ & + (T_{i,j-1,1} - T_{i,j,1}) K \frac{\Delta x \Delta z}{\Delta y} \\ & + (T_{i,j,z} - T_{i,j,1}) K \frac{\Delta x \Delta y}{\Delta z} \\ & + \frac{Q_h}{m^2} \Delta x \Delta y = 0 \end{aligned}$$

The results T_h^a are listed in Tables 1 and 2. The air heat sink effectiveness η_a is also calculated and given in Tables 1 and 2.

The heat sink effectiveness (η) is defined as the ratio of temperature differences,

$$\eta_s = \frac{T_f^a - T_a}{T_h^a - T_a},$$

where T_f^a is the average temperature of the finned air heat sink, T_h^a is the average temperature of the hot side of a thermoelectric module, and T_a is the ambient temperature.

From Tables 1 and 2 it can be seen that when the fin height was increased from $F = 25$ mm to $F = 50$ mm, the fin effectiveness decreased from $\eta = 0.93$ to 0.78, but the average temperature at the hot side decreased from $T_h^a = 40.2^\circ\text{C}$ to $T_h^a = 35.04^\circ\text{C}$, that is, by 5.16°C . This means that the performance of the heat sink was considerably improved. On the other hand, the fin height cannot be increased infinitely. As a rule of thumb, the fin effectiveness η should be maintained at a value around 0.8.

The number of fins per inch is another important criterion for the air heat sink. In general, more fins per inch means more heat transfer area and better performance, but increasing the number of fins also restricts air flow through the heat sink and makes manufacture of the heat sink difficult. As can be seen from Tables 1 and 2, for $W = 75$ mm and $F = 50$ mm, when the number of fins per inch is decreased from $n = 10$ to $n = 6.4$, the average temperature T_h^a of the hot side of the thermoelectric module increases from 35.04°C to 38.54°C . The number of fins per inch for different types of air heat sinks can vary from 8 to 14.

In order to maximize the rate of heat removal from the hot side of a thermoelectric module, a large heat sink is usually used. As mentioned above, the thermoelectric modules occupy only about 20% of the heat sink base plate. When an extruded air heat sink is used the number of fins per inch is small, consequently the heat transfer area is also small. If the extruded air heat sink is further enlarged, the added fins do not efficiently dissipate the heat.

In Table 2, where $F = 50$ and $C = 2.5$, when the heat sink width was increased from $W = 75$ mm to $W = 100$ mm, the T_h^a decreased from $T_h^a = 35.04^\circ\text{C}$ to $T_h^a = 33.70^\circ\text{C}$, that is, by only 1.34°C (4%). When a heat sink is enlarged, fins are added only at the edges. These fins are relatively far from the thermoelectric module and become so-called finned fins. Therefore they are not efficient. It can be seen from Table 2 that the heat sink effectiveness, η_s , decreased from 0.79 to 0.68, that is, by 0.11 (14%).

Summary

This paper introduces a simplified geometric method for calculating the efficiency of heat dissipation from the hot side of a thermoelectric module. By converting a finned heat sink into a flat plate, the numerical method for calculation of heat conduction from a finned heat sink is simplified.

The influence of heat sink geometry (such as fin height, number of fins per inch, heat sink width) on performance has been discussed. A concept of air heat sink effectiveness also has been introduced to judge heat sink performance.

Table 1. Calculation results based on $h = 35 \text{ w}/(\text{m}^2\text{°C})$, $L = 75 \text{ mm}$.

F = 25 mm, W=75 mm			F=45 mm, C=2.5 mm		
C = 2.5 mm n = 10	3 8.5	4 6.4	W = 75 mm 10	89 10	100 10
$h_1 = 672 \text{ w}/(\text{m}^2\text{°C})$ $T_h^* = 40.2\text{°C}$ $\eta_s = 0.85$	566 42.67 0.87	433 47.46 0.90	1043 35.47 0.80	1043 34.59 0.74	1043 34.10 0.70

Table 2. Calculation results based on $h = 35 \text{ w}/(\text{m}^2\text{°C})$, $L = 75 \text{ mm}$.

F = 50 mm					
C = 2.5 mm			W = 75 mm		
n = 10	10	10	C = 2.5 mm	3	4
$h_1 = 1110 \text{ w}/(\text{m}^2\text{°C})$ $T_h^* = 35.04\text{°C}$ $\eta_s = 0.79$	1110 34.14 0.73	1110 33.7 0.68	1110 35.04 0.79	931 36.51 0.82	707 39.54 0.85

A View to Recent Developments in Thermoelectric Sensors.

R. Fettig

Universität Karlsruhe, Institut für Angewandte Physik, Germany

Abstract

Different types of thermoelectric radiation detectors are presented, as well as sensors like AC-power sensors, and gas pressure sensors. The suitability of thermoelectric radiation detectors for different applications is discussed and compared to photon detectors and other thermal detectors. In a systematic order, the characteristics of different device production techniques, of different thin thermoelectric films, and of different devices are listed, and their potential for further developments is discussed. The combination of thermoelectric materials and CMOS technology gave, and gives exciting new impulses to the field. For that reason, this subject takes a dominant part of the paper. Finally, some new ideas and concepts are presented to point out that thermoelectric sensors represent a living and fascinating subject.

Introduction

Sensors were the very first application of thermoelectrics, shortly after the first thermoelectric effect was discovered. In 1830 Meloni used a rather sensitive device, made from bismuth and antimony, to detect infrared radiation. Until the bolometer was invented in 1885 by Langley, thermoelectric detectors remained the most sensitive detectors. In a bolometer the fact that conductors change their resistance with temperature is utilized. The above two dates mark the beginning of a history of developments and improvements in many fields of sensor application where the both types thermoelements and bolometers shared the leading positions in the field. Today, photon detectors, pneumatic detectors and pyroelectric detectors are better alternatives for some applications. There are, however, still many fields in radiation measurement, AC-power, temperature measurement, pressure and gas flow measurement, where bolometers and thermoelements are widely used. [1]

At the time they were invented, most of these sensors were built as wire or rod devices. In the last 30 years, micro technology began to transform the old macroscopic designs into new miniaturized setups, and by that, not only improved performance, repeatability, and price/performance ratio of the devices but also extended the fields of application. The intent of this paper is to give an overview of the principles of thin film thermoelectric sensors, to show their performance limits, and to relate them to other sensors through the example of infrared detectors. Finally, the different techniques which are applied to produce thermoelectric sensors will be presented, and their advantages and disadvantages will be discussed.

Types of Sensors

In a thermoelectric sensor, a temperature difference will

arise between the junctions of a two conductor circuit depending on the energy flow introduced on the hot side of the sensor, and the energy flow distributed in the sensor, either as a flow through the cold side, or to the surroundings.

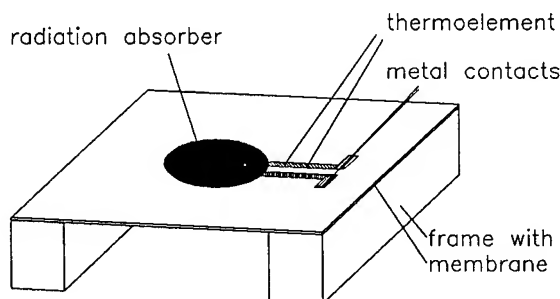


Fig. 1 Thermoelectric thin film sensor in the radiation detector configuration with an absorber.

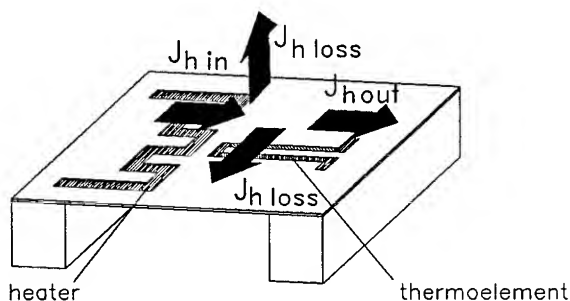


Fig. 2 Thermoelectric thin film sensor with a heater resistor. Different heat flows are shown.

In a thin film sensor, as shown in figure 1, the thermoelement, as well as the power absorber, is evaporated to a thin foil which sits on a supporting frame. The frame serves as the heat sink of the device, the foil represents a thermal short for the thermoelement.

The output voltage of a thermoelectric sensor is given as

$$U_s = n \alpha_{ab} J_{h.in} / G_h \quad (1)$$

$$G_h = (G_{h.element} + G_{h.substrate} + G_{h.surrounding}) \quad (2)$$

where n is the number of thermocouples (for simplicity only one is drawn in this paper where there might be up to several hundreds), α_{ab} the Seebeck coefficient of one thermocouple, G_h the thermal conductance and J_h the energy current.

Depending on what standard condition the device is calibrated, it can work either as a *power sensor*, or as a *power loss sensor*.

A *power sensor* is used under standard loss conditions where the losses are calibrated with a given energy flow.

The temperature difference along the thermoelement is generated either by radiation which is absorbed by an absorber (Fig. 1) or by electric power which is dissipated in a resistance, near, or on top, of the hot side of the thermocouple. (Fig. 2) Both types of sensors can be used as energy flow sensors, the one in Figure 1 as infrared detector, the one in Figure 2 as electric power sensor. The latter type is often called an AC-DC converter or true RMS-sensor.

The device shown in Figure 2 can also serve as power loss sensor if the introduced electric power is known:

- If there is an unknown gas (or liquid) under known pressure around the membrane, the thermal conductance of the gas, and through that, the gas type can be determined. ($G_{h, surrounding} \sim \lambda_{gas}$ with λ_{gas} the thermal conductivity of the gas).
- If the gas type is known the pressure (p) can be determined. $G_{h, surrounding} = f(p)$.
- If pressure and gas (liquid) type are known the flow velocity of the gas (liquid) can be determined. If the heater is located beside the thermoelement and not on top, the flow direction can be determined as well. (In two, or three, dimensions with two, or three, thermoelements).
- If there is an unknown solid film on top (or below) the sensor membrane, the thermal conductance of the film can be determined. If the thickness is known the thermal conductivity of the material can be determined, and vice versa.

Besides the properties of *external* materials, thermoelectric sensors can be used to test the sensor materials themselves. The requirement is that the production process itself be strongly reproducible. As that is the case for modern integrated circuit technology such sensors are important tools to determine thermoelectric and thermal properties of IC-process compatible materials![2, 3]

Performance Limits of Sensors.

The limits of performance for all power loss sensors are strongly dependent on the accuracy and reproducibility of device production and the stability of measurement conditions. So, all gas conductance measurements are sensitive to changes in flow and in the cleanliness of the gas.

$$\text{Responsivity} \quad r = \frac{U_s}{J_h} = n\alpha_{ab}\epsilon f(\nu)/G_h$$

$$\text{Noise Equivalent NEP} = \frac{U_n}{r}$$

$$\text{Specific Detectivity} \quad D^* = \frac{(A\Delta\nu)^{1/2}}{NEP}$$

$$\text{Response time} \quad \tau = C_h/G_h$$

$$\text{Sensitivity} \quad s = \frac{dU_s(X)}{dx}/U_{s, max}$$

Table 1 Parameters for the description of thermoelectric sensors, with the signal voltage U_s , the change in signal voltage per unit measurement parameter $\frac{dU_s(X)}{dx}$ (x for example the pressure), the Boltzmann constant k_B , n the number of thermocouples, Seebeck coefficient of the element α_{ab} , ϵ the absorption factor for the incoming energy flow, ν the measuring frequency and $\Delta\nu$ the measuring bandwidth, the absolute temperature T and the Area of the absorber A . C_h is the heat capacity of the membrane with the thermocouple and G_h the thermal conductance between the active area and the surroundings.

Intelligent design and the combination of several sensors in one device can help control these conditions.[2]

For power sensors, there are determined by fundamental effects. First, the temperature of each body which is in any thermal contact to its environment, fluctuates. This fact leads to a general limit for all thermal sensors. Table 1 gives a list of parameters which are used to describe thermoelectric detectors. The Noise equivalent power is the incident power which creates the same output signal at the terminals of a device as the internal noise sources. The NEP depends strongly on the temperature of the device and its surrounding, and on the thermal conductance with which is connected to the surrounding. The NEP is smallest, if the connection to the surrounding is smallest. For a radiation detector, there is at least a radiation coupling through the radiation receiver. As it turns out, there is a universal value which can be given to describe the performance of any type of radiation detector: The specific detectivity D^* . According [4] the maximum D^* for a given temperature is

$$D_{ideal}^* = 1/\sqrt{16k_b\sigma_s b T^5} \quad (3)$$

In Figure 3 this relation is charted vs. temperature. D^* increases strongly with decreasing temperatures. Therefore many attempts are made to build, and use, detectors for low operation temperatures. Bolometers are successful in this field, there are some available which exceed the theoretical performance limits of room temperature devices by

several orders of magnitude. For the intermediate temperature range, there is one detector type worth mentioning which is about to get wider use: the high temperature superconduction bolometer. In such devices, the strong increase of resistance at the transition edge is used. The best devices of that type are already better than any thermal detector at room temperature. [5]

For photon detectors in which radiation does not create heat but free electrons, these limits do apply differently. The detection limits are depending on the cut off wavelength of the devices, and thus on the bandgap of the semiconductors. The limits are one to several orders of magnitude smaller than those of thermal detectors. However, their sensitive range is limited to a small spectral range, as only photons of about gap energy create conduction electrons with great efficiency. With devices at liquid nitrogen temperatures, the range of 300K radiation can easily be detected. CdHgTe photo-voltaic or photo-conductive devices are therefore widely used in sophisticated detection and spectroscopic applications, often as one or two dimensional arrays. For details about the performance of photon detectors see [6]

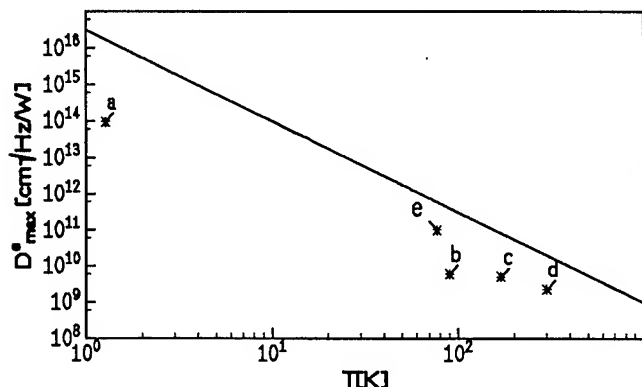


Fig.3 Theoretical limits of D^* for ideal thermal detectors for different temperatures as well as performance figures for several detector types:

- a) Al superconduction bolometer at 1.27 K according to [7]
- b) High T_c supercond. bolometer at 90K according to [5]
- c) Thermoelectric bulk detector according to [8]
- d) Thermoelectric thin film detector according to [9]
- e) CdHgTe-PV detectors at 10 μ m wavelength to [6]

As no low temperature thermoelements are known the use of thermoelectric detectors got restricted to applications where extreme low detection limits are not required, or where no low temperatures are achievable.

When the question for the performance limits is raised, for thermoelectric detectors Johnson noise, the fluctuating voltage across any resistor, must be taken into account. D^* of a thermoelectric detector can be described as [8, 11]

$$D_{max}^* = \sqrt{\frac{zT}{(\sqrt{1+zT} + 1)^2}} * D_{ideal}^* \quad (4)$$

Figure 4 shows the dependence of D^* for thermoelectric

detectors as a function of the figure of merit zT . For low values of zT , D^* goes with \sqrt{zT} and describes the influence of Johnson noise. For large values of zT , D^* approaches the limits for thermal detectors. Fig. 4 also shows the performance figures of several thermoelectric detectors. Most thin film devices remain about an order of magnitude below the theoretical limits because of parasitic losses through membranes and in contact resistances. For a list of more devices see [12].

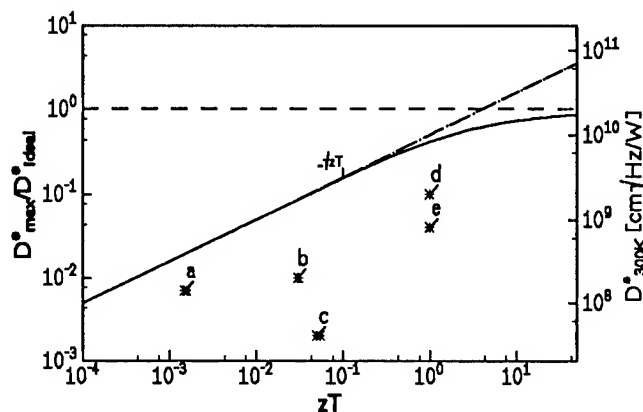


Fig. 4 Theoretical limits of D^* for ideal thermoelectric detectors for different values of zT as well as performance figures for several thin film thermoelectric detectors:

- a) Si-Al Thermopile according to [13]
- b) Bi-Sb Thermopile according to [14]
- c) p- and n-GaAlAs Thermopile according to [15]
- d) $(Bi, Sb)_2Te_3$ Thermopile according to [9]
- e) $(Bi, Sb)_2Te_3$ Thermopile according to [16]

Finally, it has to be noted, that NEP or D^* are not the only relevant numbers for thermal radiation detectors. Often it is important to have a fast device and thus either a low heat capacity, or a large thermal conductance to get a small response time.

It is the frequency behavior of pyroelectric detectors which makes them, for some fast spectroscopic applications, superior over other thermal detectors. In pyroelectric sensors the spontaneous polarisation of an material changes with temperature. The temperature change is detected by observing the moving compensation charges. Their detectivity does decrease weaker than with $1/f$, like for thermoelectric and bolometric devices. Therefore they are better at higher frequencies even if their low frequency properties are worse than that of thermoelectric devices. [10]

Especially for consumer devices, high signal levels, and therefore low amplification requirements, are often crucial in deciding whether a sensor can be used or not. Therefore, a large number of thermoelements with large internal resistances, large signal voltages and noise voltages are important. Such large numbers can be best reached by IC technology with high package density.

Production Techniques of Detectors

In order to describe developments of the production process, it is useful to group them into certain categories.

The first thermoelectric sensors and bolometers were built from bulk materials, like single crystals and wires. With such techniques, it was possible to build very sensitive devices. Because of the limited number of thermoelements, the output voltages of such devices usually are small. The production usually was labor insensitive, and there were great variations between individual sensors.

Thin film techniques show the advantage of high reproducibility, but also have the disadvantage of the demand for carrier membranes, and with them, the problem of thermal expansion mismatch. Thin film devices can be distinguished in a few categories:

Thin film metals and semi metals

They can easily be thermally evaporated to organic or ceramic membranes on metal support frames. In this category, bismuth and antimony, the materials used in the early days of thermoelectrics are the most successful materials. There are membranes available of less than 100nm thickness with very low heat capacity and conductance. Therefore, such devices can be very sensitive and fast. If very thin membranes are used, masking is limited to lift off masks which sets lower limits for the dimensions of the legs of the thermoelements.

Thin film semiconductor materials

Many attempts have been done to evaporate $(Bi, Sb)_2(Te, Se)_3$ materials because of their large value for zT of about one at room temperature. The evaporation requires high temperatures, ($> 250^\circ C$), therefore the types of membranes are limited. The best thermoelectric detectors were made from these materials. The evaporation however is complicated, and tellurium and selenium tend to spoil vacuum systems. For these reasons, these materials are not (yet) compatible with the IC-processes. [16, 17]

Thin film CMOS and other IC processes

P- and n- polysilicon either as a pair or in combination with Al as thermoelectric leg are the most successful thin film materials of the micromachining silicon processes, if they are applied on anisotropically underetched membranes. Even if such thermocouples have small values of zT , and even if the membranes of SiO_2/Si_3N_4 or poly-Si are relatively thick, their technological advantages bring them success: Because of the photo etching technology, the structure's dimensions can be very small, and therefore many elements can be integrated in a single detector. This results in high signal levels. Additionally, amplification, stabilization, and linearization electronics, can be included in the chips which can be produced in cheap batch fabrication processes [18]. Besides in Silicon processes, sensors have also been produced with GaAlAs-GaAs technology. [15]

As thermal losses through the micromachined membranes are a great drawback for silicon thermoelectric devices, technologies have been invented to avoid the disadvantages

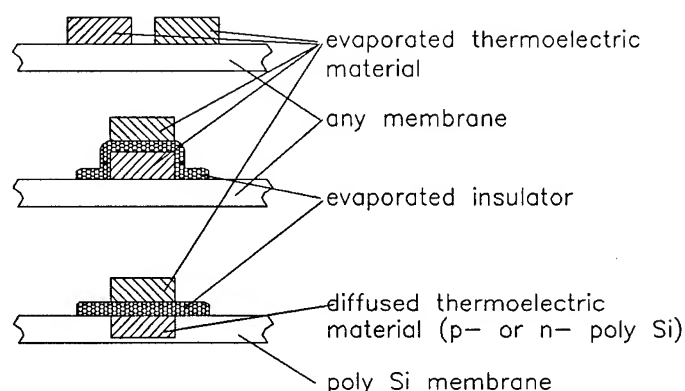


Fig. 5 Techniques to reduce membrane effects: Increase packaging density, use of the membrane as thermoelectric material

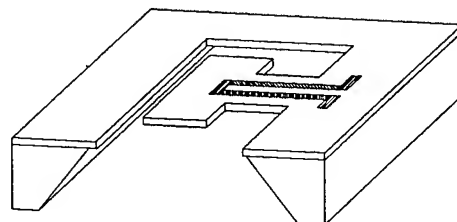


Fig. 6 Techniques to reduce membrane effects: creation of cantilever beams.

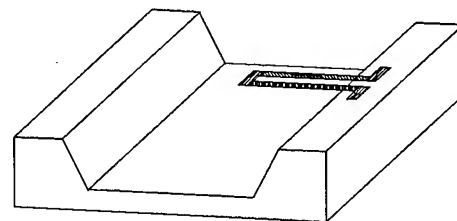


Fig. 7 Techniques to reduce membrane effects: Removal of the membrane.

Figures 5, 6 and 7 show different methods of reducing the negative effects of the additional thermal shorts to the heat sink by the supporting membrane [2, 18]. This can be done by

- increasing the packaging density through the creation of p/n double layers. Through this design change, the relative influence of the membrane on the heat conduction to the heat sink is reduced.
- using the membrane as part of an active material that is, the p or n thermoelement leg is diffused into a polysilicon membrane.
- removing all membrane parts which do not need to support thermoelements or active areas. These active area then are suspended on cantilever beams. Such

constructions allows for great heat exchange with the surrounding gas.

- removing the membrane completely.[19]

New Concepts

There are some new sensor designs which do not fit into the criteria presented here but which should be mentioned anyway.

For one the freestanding thermoelement device, mentioned as an example for avoiding membrane effects, does not fit perfectly into the above presented ordering. This technique works only for very small metal thermocouples. Such thermoelements should have low zT , but it turns out that they can have large D^* because of antenna effects of the freestanding wires.[19]

Another special development is the anisotropic high T_c thermoelectric device. [20] There, a very thin film is evaporated onto strontium titanate and grows with a tilt angle between c-axis and the surface, because of the lattice mismatch of the two materials. At room temperature, the high T_c superconductor shows high anisotropy in Seebeck coefficient, which creates voltages along the material if it is heated by radiation from top. These devices are interesting for several reasons: they belong to the few which utilize a thermoelectric effect other than the normal isotropic Seebeck effect, and they belong to the fastest thermoelectric device, however with low responsivity and D^* .

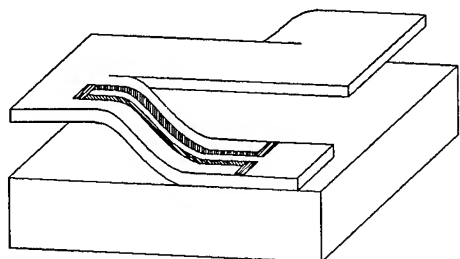


Fig. 6 Suggestion for a three dimensional membrane set up corresponding to an existing bolometer device. [22]

Most of the devices presented so far are available either as single element or as linear array sensors. No two dimensional thermoelement arrays exist so far. However, there have been very successful developments in pyroelectric[21] and bolometric detectors for imaging focal planes for infrared radiation.[22] The membrane design used for the bolometer array might be modified according to Fig. 6, to serve as a two dimensional thermoelement array, where the active area is in an elevated membrane plane and the readout circuits are in a lower plane.

Conclusions

While Thermoelements may have lost some importance in recent years in high performance radiation detection applications, due to the rapid developments of low temperature photon and bolometer detectors, thin film and

IC-technology developments have improved existing, and created new devices which are able to satisfy an increasing demand for reliable and cheap sensors. The combination of existing evaporation techniques for materials with large zT values with IC technology could bring further increase in the performance of thermoelectric sensors.

An even larger potential maybe in the application of new thermoelectric materials, especially in multi quantum well structures, which should be well suited for sensors.

References

- [1] Stevens, N.B., "Radiation Thermopiles", in: Willardson, R.K.; Beer, A.C., (Eds.) *Semiconductors and Semimetals* Springer, New York, Vol.5, pp. 287-318 (1970)
- [2] Arx, M. v.; Paul, O.; Baltes, H., "Determination of the heat capacity of CMOS layers for optimal CMOS sensor design", *Sensors and Actuators A*, Vol. 46-47, pp.428-431 (1995)
- [3] Baltes, H.; Moser, D.; Voelklein, F., "Thermoelectric Microsensors and Microsystems" in: Goepel, W.; Hesse, J.; Zemel, J.N., (Eds.) *Sensors, A Comprehensive Survey, Vol. 7, Mechanical Sensors* pp. 13-55 (1994)
- [4] Smith, R.A.; Jones, F.E.; Chasmar, R.P. *The Detection and Measurement of Infra-Red Radiation*, Oxford Uni.Press, England (1957)
- [5] Brasunas, J.C.; Lakew, B., "High T_c superconductor bolometer with record performance", *Appl. Phys. Lett.* Vol. 64, Bd.6, pp. 777-778 (1994)
- [6] Royer, M.; Midavaine, T., "IR and FIR Sensors" in : Goepel, W.; Hesse, J.; Zemel, J.N., (Eds) *Sensors, A Comprehensive Survey, Vol. 6, Optical Sensors* pp. 201-233 (1992)
- [7] Nishioka, N.S.; Richards, P.L.; Woody, D.P., "Composite bolometers for submillimeter wavelengths", *Applied Optics*, Vol. 17, No. 10, pp 1562-1567 (1978)
- [8] Fetting, R.; Lerchenmüller, H.-J.; Müller, E., "Optimization of a Thermoelectric Infrared Detector for Low Working Temperature", 12th Int. Conf. on Thermoelectricity, Yokohama, Japan (1993)
- [9] Razinkov, V.V.; Tsytko, N.K.; Gritsai, V.V., Bulat, L.P.; Vantchura, U.O.; Demtchenko, V.A., "High-Responsive Thermoelectric Radiation Receivers" *Journal of Thermoelectricity* Vol. 1, pp. 62-66 (1993)
- [10] Putley, E.H., "The Pyroelectric Detector", in: Willardson, R.K.; Beer, A.C., (Eds.) *Semiconductors and Semimetals* Springer, New York, Vol.5, pp. 259-285 (1970)

- [11] Fettig, R., *Die Temperaturabhängigkeit der Kenngrößen thermoelektrischer Infrarotdetektoren*, PhD-thesis, Fakultät für Physik, Universität Karlsruhe (1993)
- [12] Rowe, M., *Handbook of Thermoelectricity* CRC press London, pp. 452-458 (1995)
- [13] Schieferdecker, J.; Quad, R.; Holzenkaempfer, E.; Schulze, M., "Infrared thermopile sensors with high sensitivity and very low temperature coefficient", *Sensors and Actuators A*, Vol. 46-47, pp.422-427 (1995)
- [14] Eibel, Th.; Mueller, J.E.; Voelklein, F., "Miniaturisierte thermische Strahlungssensoren: Die neue Thermosaeule TS-50.1", *Feingeraetetechnik*, Vol. 34, p113 (1985)
- [15] Dehé, A.; Fricke, K.; Hartnagel, H.L., "Infrared thermopile sensor based on AlGaAs-GaAs micromachining", *Sensors and Actuators A*, Vol. 46-47, pp.432-436 (1995)
- [16] Voelklein, F.; Wiegand, A.; Baier, A., "High-sensitivity radiation thermopiles made of Bi-Sb-Te films", *Sensors and Actuators A*, Vol. 29, pp.87-91 (1991)
- [17] Mzerd, A.; Tcheliobou, F.; Sackda, A.; Boyer, A., "Improvement of thermal sensors based on Bi_2Te_3 , Sb_2Te_3 and $Bi_{0.1}Sb_{1.9}Te_3$ " *Sensors and Actuators A*, Vol. 46-47, pp.387-390 (1995)
- [18] Herwaarden, A.W.v.; Duyn, D.C.v.; Oudheusden, B.W.v.; Sarro, P.M., "Integrated Thermopile Sensors", *Sensors and Actuators A*, Vol. 21-23, pp.621-630 (1989)
- [19] Srinivas, T.A.S.; Timans, P.J.; Butcher, R.J.; Ahmed, H., "Thermal and infrared performance of a free-standing microthermocouple", *Rev.Sci.Instrum* Vol.64, Bd.12, pp. 3602-3610 (1993)
- [20] Renk, K.F.; Betz, J.; Zeuner, S.; Lengfellner, H.; Prettl, "Thermopile effect due to laser radiation heating in thin films of high-Tc materials", *Physica C*, Vol.235-240, pp.37-40 (1994)
- [21] Hanson, C.; Beratan, H., "Uncooled pyroelectric thermal imaging", in: Pandey, R.K.; Liu, M.; Safari, A. (Eds), *ISAF '94. Proceedings of the Ninth IEEE International Symposium on Applications of Ferroelectrics* New York, pp.657-661 (1994)
- [22] Wood, R.A.; Han, C.J.; Kruse, P.W., "Integrated uncooled infrared detector imaging arrays", *Technical Digest. IEEE Solid-State Sensor and Actuator Workshop* New York, pp.132-135 (1992)
- [23] Dillner, U.; Mueller, J.; Guett

Ultrafast Response and High Sensitivity Semiconductor Thermocouple

Z. Dashevsky, D. Rabinovich

Ben-Gurion University of the Negev, Materials Engineering Department

P.O.B. 653, Beer-Sheva 84105, Israel

G. Fish, S. Kokolova, A. Lewis

The Hebrew University, Department of Applied Physics, Jerusalem 91904, Israel

Abstract

The thermocouple consists of an internal wire (Pt, Au, Ag) inside a glass tube that is pulled down to a diameter of 1 - 2 μm or less. Probes are available with second electrode (leg) from film semiconductor evaporated on the outside of the glass tube. Semiconductor PbTe doping special impurity, provides constant high multitude of the thermoelectric power in the wide temperature interval (-100 - 200°C). Sensitivity of the thermocouple is from 2000 to 300 $\mu\text{V/K}$ and does not change during long time. Special protective on the base of ultrathin polymer layer permits using thermocouple in aggressive atmosphere. Calculations indicate the response time of thermocouple 1 μsec . The suitability of this thermocouple for light intensity measurements with micrometer spatial resolution is demonstrated by measuring the focused beam of the laser. In addition, such thermocouples are intrinsically suitable for applications in scanned probe microscopies. All these unique advantages make the pipette thermocouples a new and extremely promising sensor in a variety of applications include microelectronics, microbiology and others.

I. Introduction

The measurements of spatially localized rapid temperature changes are required in studies of many physical and biological processes and objects. These can include

such diverse subjects as turbulent flows, associated with processes of explosion and combustion temperature measurements in biology at the cellular and subcellular level and temperature measurements in evolving chemical reactions. For all these applications a microthermocouple is the most convenient detector. In recent publications, fast microthermocouples have been described with response times of milliseconds and spatial resolutions of from hundreds to tens of micrometers [1, 2].

Such microthermocouples may also be used as point radiation detectors in a range of wavelengths from the UV to the IR.

In the present paper, we advance these efforts in temperature measurements with the thermocouple with submicrometer contact size and a response time of a few microseconds. We demonstrate that a micropipette containing a platinum core can be coated a film semiconductor on the base PbTe (doping special impurity) to make a PbTe-platinum point thermocouple at the tip of the micropipette. The unique submicron thermocouple structure was the characterized in the terms of both its response time and its ability to image a focused laser beam.

II. Theoretical considerations

The analysis of heat distribution in point thermocouple allows one to determine restrictions imposed on the geometry of such the thermocouple. These restrictions come from the requirement for the contact temperature to be close to the temperature

of surrounding medium. For this requirement to be achieved, undesirable heat flow through the film coating (PbTe) on the walls of the pipette and platinum core should be minimized. This can be expressed in the following conditions restricting the geometry of the micropipette thermocouple (Fig.1).

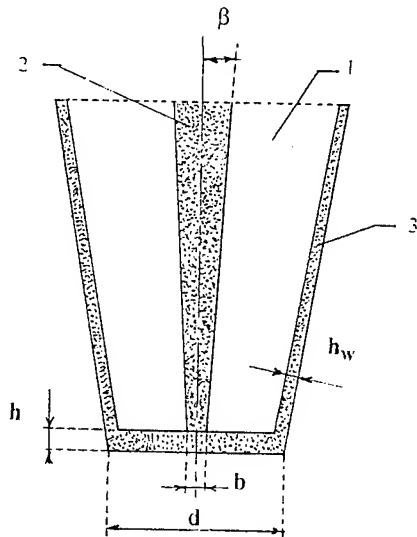


Fig.1. Schematic presentation of the sensing area of the pipette thermocouple.
1 - glass tube (pipette), 2 - platinum core, 3 - PbTe coating.

β - cone angle, b - the diameter of platinum electrode, h and h_w - thickness of disk and film coating PbTe respectively, d - the pipette diameter.

Condition 1: The heat flow through the platinum core should be smaller than the heat flow from the medium to the heat contact. This condition, interpreted in terms of the solution of the heat transfer equation, leads to the following restrictions imposed on the cone angle β :

$$\beta \ll k_m d / (k_{Pt} b), \quad (1)$$

where k_m and k_{Pt} are heat conductivity of medium and platinum respectively, b is diameter of the platinum electrode at the

contact, and d is the pipette tip diameter. For water if $b/d = 0.1$ the cone angle β should be much less than 5° .

Condition 2: The radial heat conductivity of the film coating at the tip should ensure the effective sensing temperature by the whole surface of the tip. Based on the solution of the heat transfer equation for a disk-shaped metal layer with heat outflow from its center, this condition takes the form

$$k_{Pt} (b/2) \beta \ln(d/b) \ll 2h k_{PbTe}, \quad (2)$$

where h is the thickness of the PbTe disk (see Fig.1), k_{PbTe} is the heat conductivity of PbTe. This yields $h/d \gg 2 \cdot 10^{-4}$ for $b/d = 0.1$ and $\beta = 1^\circ$.

In the case where conditions 1 and 2 are satisfied, the spatial resolution of the pipette thermocouple can be evaluated as:

$$dh_w k_{PbTe} / L \ll L k_m, \quad (3)$$

where L - the length of a sensing area, h_w is the thickness of film PbTe coating.

The response time of the pipette thermocouple with dimensions (tip diameter and thickness of film coating = $1 \mu m$, length of sensing area $L = 5 \mu m$) is as small as $< 1 \mu sec$ for the measurement in water.

III. Thermocouple fabrication

In order to obtain optimal parameters of a thermocouple it is necessary, to reduce the size of the sensor. At present, a number of methods are available for producing microelectrodes, such as electropolished platinum, carbon sealed in glass and other methods. In [3] is described method of microelectrodes fabrication with involves pulling an annealed platinum wire placed

inside a borosilicate pipette by a common pipette puller. We describe here a technique for the production of microelectrodes which allows one to control and vary its parameters. The reproducibility of this technique is about 90%. A platinum wire, 80 micrometers in a diameter, was placed inside a borosilicate tube with outer and inner diameters equal to 1.2 and 0.3 mm, respectively. The pipette-wire assembly was placed in a Sutter P-200 laser pipette puller with allowed varying of 5 parameters: temperature of heating, the length of the segment heated, delay time between turning the heat on and the beginning of pulling, the velocity of the pull and the strength of the pulling.

To find the optimal combination of these parameters, we treat our sample, consisting of a glass tube and a platinum wire inside it, as a composite material (CM). In this material the heated glass tube acts as the matrix which is more plastic than the platinum wire which acts as the frame. During the pulling procedure the surrounding glass acts to stabilize the metal and thus results in a more uniform thinning of the metal core. Therefore the metal core can be pulled down to a smaller dimension before the breaking occurs. It is also known that for CM of this type there is some critical volume fraction of the frame V_{cr} , at which the plasticity of the CM becomes equal to that of the surrounding matrix, i.e. glass in this particular case. Note that the platinum wire diameter D_w , was not varied, while the external diameter of the glass tube D_{gl} , depended on parameters that were set for the pulling program. Since the ratio $A = D_w/D_{gl}$ defines the volume fraction of the frame V , we can ensure $V = V_{cr}$ by simply varying D_{gl} . We therefore performed the pulling operation in the

following 2 steps:

First, the glass tubes were pulled to an inner diameter that was equal to the platinum wire diameter. At this point the sample was heated for several seconds without further pulling to ensure a firm connection between the glass and the platinum. Subsequently, the pulling was performed slowly, in four stages and this resulted in the formation of two glass pipettes that were filled with platinum to the end. The shape of the outer diameter was determined by the pulling program parameters at both steps. At $0.2 < A < 0.4$ it was possible to pull the glass tube and the platinum core to dimensions as small as 50 nanometers. Fig.2 shows a micrograph of pipette thermocouple.

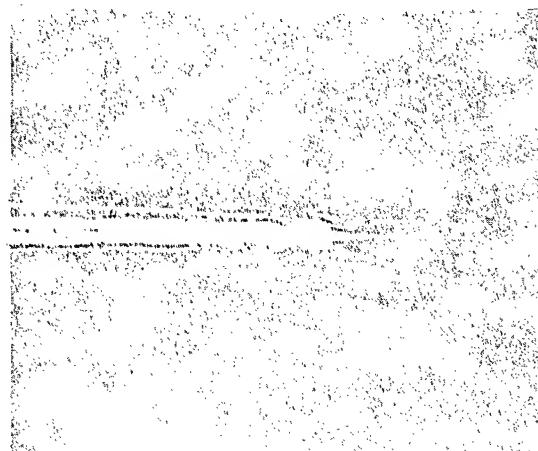


Fig.2. Light micrograph of pipette thermocouple. The magnification is 50.

The second thermoelectrode was made as a vacuum-evaporated method. Films of PbTe are of interest as the starting point for the production of high-efficiency thin-film thermoelectric elements [4]. Films of thickness from 0.5 to 1 μm , prepared by evaporation in vacuum of $5 \cdot 10^{-6}$ Torr and then subjected to different heat treatments.

The films were annealed at 350 $^{\circ}\text{C}$ in an

argon atmosphere at pressure of 0.9 atm. The substrate temperature during the evaporation was 200 - 250 °C.

Evaporation was from quartz crucible. X-ray and electron-microscopic studies of the films showed them to be polycrystalline. After annealing we observed a weak preferred orientation, with the (001) plane parallel to the plane of the film (substrate - glass). After annealing, the mean sizes of the crystalline grains in the films were 0.1 - 0.2 μm .

Polymer coating (thickness < 0.2 μm) has been deposited by the plasma-CVD techniques. Polymerization when introduced into a low-pressure glow discharge is well-documented process. Films deposited at high monomer pressure (e.g. > 0.5 Torr) low substrate bias (e.g. < -100 V to ground), and power density (e.g. < 1 Wcm^{-2}). The films grown are mechanically soft.

IV. Experimental Details

The variation of the charge carrier concentration can be achieved with the help of doping of the initial material with elements of the third group (In) and also producing solid solutions Pb-Ge-Te (In).

The high solubility of this impurity allows to observe and study the impurity state characteristic manifestations in spite of high intrinsic defect concentration. Among these manifestations are: Fermi level pinning and carrier concentration stabilization [5 - 6].

Indium impurity in lead telluride definitely manifests donor properties, but in spite of a very high solubility of InTe in PbTe the electron concentration n does not exceed several units per 10^{18} cm^{-3} . All facts and other investigations were interpreted as follows [6]:

1. With indium doping the quasi-local level appears in PbTe above the

conduction band edge, its position does not depend on the content of In up to $N_{\text{In}} < 2.5 \text{ at.}\%$. This level is very weakly broadened ($< 10^{-3} \text{ eV}$).

2. The impurity band contains two states per each atom of indium and is filled with electrons approximately by a half in the absence of other donors and acceptors.

3. When the impurity level E_i is partially filled with electrons the low-temperature Fermi level E_F practically coincides with impurity level.

4. While in case of halcogen substitution (Te -Se, S) the level shifts upwards from the conduction band edge, substitution of lead (Sn, Ge) yields an opposite effect.

The charge for preparing the thin films consisted of bulk polycrystalline samples PbTe and $\text{Pb}_{0.1}\text{Ge}_{0.9}\text{Te}$ with a constant content of the dopant indium (0.5 at.%). The profile of the film composition over the film thickness was analyzed by the method of Auger electron spectroscopy. Electrons reflected from the film surface in the energy range 250-1200 eV were analyzed. For $\text{Pb}_{0.1}\text{Ge}_{0.9}\text{Te:In}$ films, prepared by discrete evaporation, the general distribution of the elements Pb, Ge, In and Te over the thickness is similar to the distribution of these elements in the bulk material.

We investigated the Hall coefficient R , electrical resistivity ρ , Seebeck coefficient S , heat conductivity k of films PbTe:In, $\text{Pb}_{0.1}\text{Ge}_{0.9}\text{Te:In}$ (substrate - glass) at 100 - 500 K. For composition $\text{Pb}_{0.1}\text{Ge}_{0.9}\text{Te:In}$ S practically does not change from 200 to 400K and achieved magnitude -300 $\mu\text{V/K}$. The temperature dependence of the Hall mobility was T^{-1} near room temperature. The temperature dependence of the lattice heat conductivity k_l was close also to T^{-1} . The values of k_l for the films were

somewhat lower in comparison with k_l for bulk material.

The kinetic experiments were aimed at determining the response time of the pipette thermocouples. Initially we chose a technique which was based on direct laser heating of the thermocouple. The Q-switched Nd:YAg laser used as the pulsed heat source yielded 300-nsec, 1-mJ pulses at a repetition rate of 100 Hz. The emission of the laser was focused by a lens onto the pipette tip so that the pulse energy density of the infrared light was $0.5 - 2 \text{ J/cm}^2$. A part of the laser emission was directed to a pin-photodiode. Both signals, from the photodiode and the amplified thermocouple output, were processed by an identical pair of Stanford Research Model 250 gated integrators and boxcar averages. The response time of the thermocouple estimates as the rate of cooling of the thermocouple after the laser pulse. The results of measurements are presented in Fig. 3.

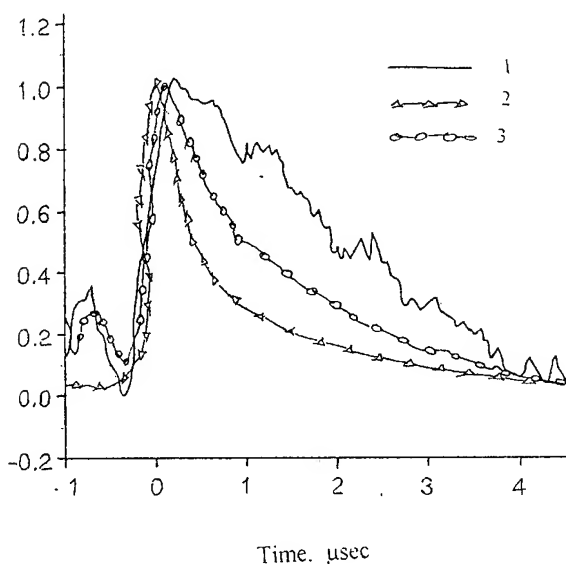


Fig.3 Response of pipette thermocouple Pt-PbTe (immersed in air 2 and water 3 respectively) to direct laser heating. The photodiode output 1 follows the temporal nature of heating laser pulse.

From Fig. 3 it is seen that the response time of the thermocouple are of the order of a few microseconds.

V. Conclusions

A new microthermocouple which consists of platinum thin wire inside a glass tube (the top pipette diameter achieves $1 \mu\text{m}$) and semiconductor thin film evaporated on the outside of the glass tube was developed.

Sensitivity Pt-PbTe thermocouple is greater than 10^2 comparing with metal thermocouples.

Calculation and measurement (focused beam of laser) indicate the response time of thermocouple $1 \mu\text{sec}$.

References

- [1] L.J. Forney, E.L. Meeks, J. Ma, G.C.Fralick, Rev. Sci. Instrum. 64, 1280-1286 (1993).
- [2] P.Beckman, R.P.Roy, K.Whitfield, and A. Hasan Rev. Sci. Instrum. 64, 2947-2951 (1993).
- [3] G.Fish, O.Bouevitch and others Rev. Sci. Instrum. 66, 3300-3320 (1995).
- [4] ZM.Dashevsky, and M.P.Rulenko, Semiconductors 27, 366-368 (1993).
- [5] T.I.Bocharova, A.N.Veis, and Z.M. Dashevsky, Sov. Phys. Semicond. 15, 1178-1180 (1981).
- [6] V.I.Kaydanov, Defect and Diffusion Forum vols. 103-105, 388-405 (1993).

MULTI-ELEMENT THERMOELECTRIC CONVERTERS

L.I. Anatyshuk, B.N. Demchuk

(Institute of Thermoelectricity, General Post Office, Box 86, 274000, Chernivtsi, Ukraine)

The study and design results of multi-element thermoelectric batteries with small section of legs for low-powered thermoelectric generators, weak current cooling modules and high-sensitive sensors have been presented.

The production technology of thermoelectric modules with legs cross-section more than 0.5×0.5 mm and length of 1-5 mm and more has been well developed up today. With such modules the problems of thermoelectric generators of more than 1-10 W and thermoelectric coolers with supply current of more than 1 A production have been solved.

At the same time there is a large class of practical problems for which solutions it is necessary to design generators of lesser powers (of milliwatt level) and miniature coolers with supply currents of tens and hundreds milliamperes.

Besides, standard modules were highly inconvenient to use as sensors in measuring systems because of their exceptionally low volt-watt sensitivity and inadequate matching with standard recording equipment by electrical resistance.

The analysis shows that possibilities for thermoelectricity practical application is substantially extended if development engineers of thermoelectric equipment have the possibility to use thermoelectric converters with small legs cross-section. In this case low-powered thermoelectric generators competitive in a number of cases to chemical electrical sources can be developed, the need in such sources is rather great.

Miniature batteries are also useful as sensitive elements for microcalorimeters, heat flow measurement devices, X-ray radiation meters of different types, etc.

There are information in literature about repeated attempts on the use for these purposes the film thermobatteries design technology. This idea is rather attracted since it assumes the possibility of mechanization of technological processes by means of microelectronics standard technologies use. However such approaches have at least two main disadvantages. The first implies that the film usage is obligatory accompanied with the use of substrates with final thermal conduction which shunt thermal flows rather energetically. This results in unjustified heat losses

and efficiency decrease of thermoelectric batteries. The more the miniaturization and as a consequence the thinner film, the larger losses increase. The second disadvantage is connected with inevitable processes of degradation in films. Properties change of films as ones knows is taken place because of re-crystallization and oxidation processes. Besides, films and substrates are differed by the coefficient of thermal expansion that results in defects formation in films due to mechanical strengths at cycling thermal conditions and at temperature gradients presence. Experimental investigations in this approach confirms our misgivings.

These circumstances bring to the fact that we have abandoned from film technologies in miniature batteries design, and have used delicate methods for legs cutting with cross-sections from 0.5×0.5 mm to 0.08×0.08 mm and their bonding in packages by high-temperature epoxy compounds (with operating temperature up to $150-250^\circ\text{C}$). Legs lengths can vary from 0.5 to 20 mm that makes it possible to make a number of thermoelectric microbatteries easily adapting for consumers demand. The package density of legs can constitute from 300 pieces to 10000 per 1 cm^2 . The technology permits to make thermoelectric batteries with different areas. Areas from $5 \times 5\text{ mm}^2$ to $20 \times 20\text{ mm}^2$ are usually used. Series of such batteries are given in Tables 1-4. But thermobatteries of other sizes within intervals given in Tables can be made without particular difficulties. The square form of batteries cross-section is also unnecessary. The batteries have no ceramics plates, heat input and output form the module is realized through compound layers filled with a thermal conductive powder.

A great number of series legs leads to the necessity to take special measures for necessary reliability of the thermobattery endurance. The use of special reserve systems permit to develop thermobatteries the reliability of which is not only competitive with standard modules reliability but significantly exceed them.

Fig. 1-3 represents modules typical characteristics in the regime of electric current generation.

As it have already noted modules can be used as sensitive sensors. Table 1-4 give values of the battery volt-watt response in the sensor regime.

Use of thermoelectric microbatteries opens up new fields of thermoelectricity widespread application.

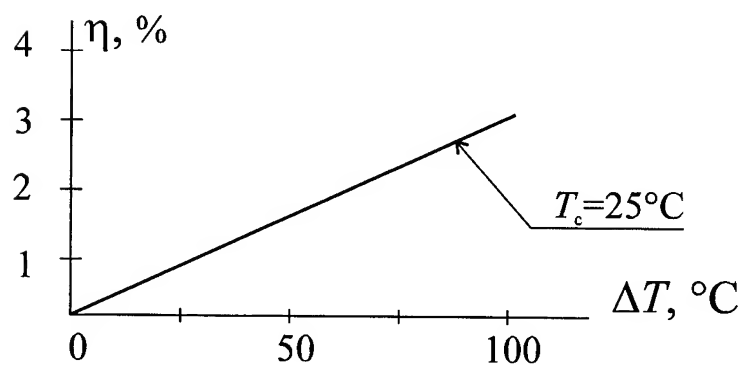
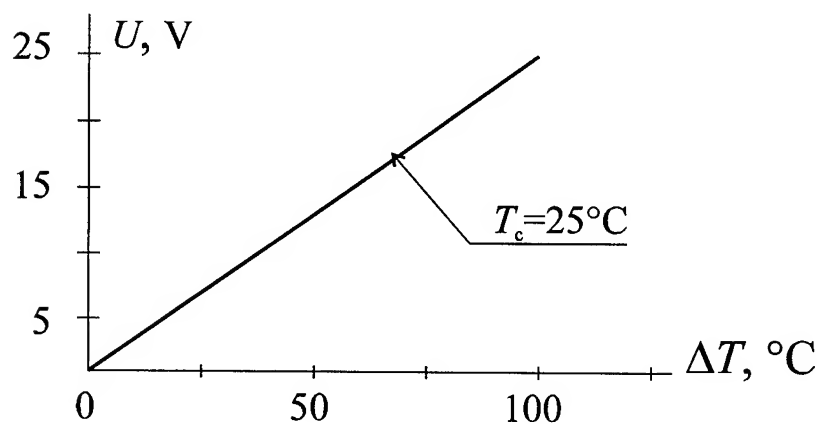
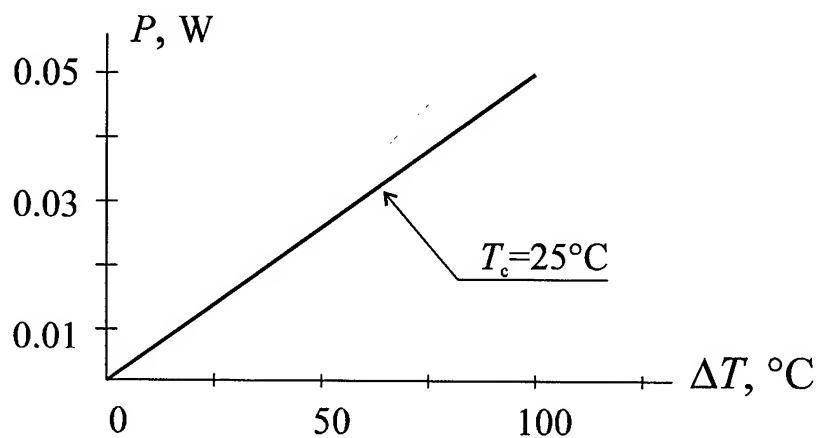


Fig. 1-3. Characteristics of module Altec-1008.
 Area of a module $S_{\text{TEB}} = 10 \times 10 \text{ mm}^2$; height - $h = 10 \text{ mm}$;
 cross-section of legs - $0.2 \times 0.2 \text{ mm}$; number of legs in a module - $N = 2162$
 T_c - TEB cold surface temperature; ΔT - temperature difference
 between TEB hot and cold surfaces.

Table 1

$$S_{TEB}=5 \times 5 \text{ mm}^2$$

No.	h_0 , mm	S_0 , mm ²	Legs number	R_{TEB} , Ohm	T_0 , °C	ΔT , °C	U_{TEB} , V	P_{TEB} , W	ε , V	E , V/W
1.	1	0.1×0.1	1890	2370.7	25	100	17.5	0.1004	40.4	11.24
2.	1	0.2×0.2	540	169.3	25	100	5.0	0.1148	11.6	2.81
3.	1	0.3×0.3	250	34.8	25	100	2.3	0.1196	5.3	1.25
4.	1	0.4×0.4	144	11.3	25	100	1.3	0.1224	3.1	0.70
5.	1	0.5×0.5	94	4.7	25	100	0.9	0.1249	2.0	0.45
1.	2	0.1×0.1	1890	4741.4	25	100	17.5	0.0502	40.4	22.48
2.	2	0.2×0.2	540	338.7	25	100	5.0	0.0574	11.6	5.62
3.	2	0.3×0.3	250	69.7	25	100	2.3	0.0598	5.3	2.50
4.	2	0.4×0.4	144	22.6	25	100	1.3	0.0612	3.1	1.41
5.	2	0.5×0.5	94	9.4	25	100	0.9	0.0624	2.0	0.90
1.	5	0.1×0.1	1890	11853.6	25	100	17.5	0.0201	40.4	56.21
2.	5	0.2×0.2	540	846.7	25	100	5.0	0.023	11.6	14.05
3.	5	0.3×0.3	250	174.2	25	100	2.3	0.0239	5.3	6.25
4.	5	0.4×0.4	144	56.4	25	100	1.3	0.0245	3.1	3.51
5.	5	0.5×0.5	94	23.6	25	100	0.9	0.025	2.0	2.25
1.	10	0.1×0.1	1890	23707.2	25	100	17.5	0.01	40.4	112.42
2.	10	0.2×0.2	540	1693.4	25	100	5.0	0.0115	11.6	28.10
3.	10	0.3×0.3	250	348.4	25	100	2.3	0.012	5.3	12.49
4.	10	0.4×0.4	144	112.9	25	100	1.3	0.0122	3.1	7.03
5.	10	0.5×0.5	94	47.2	25	100	0.9	0.0125	2.0	4.50
1.	20	0.1×0.1	1890	47414.4	25	100	17.5	0.005	40.4	224.83
2.	20	0.2×0.2	540	3386.7	25	100	5.0	0.0057	11.6	56.21
3.	20	0.3×0.3	250	696.9	25	100	2.3	0.006	5.3	24.98
4.	20	0.4×0.4	144	225.8	25	100	1.3	0.0061	3.1	14.05
5.	20	0.5×0.5	94	94.3	25	100	0.9	0.0062	2.0	8.98

Table 2

 $S_{TEB}=10 \times 10 \text{ mm}^2$

No.	h_0 , mm	S_0 , mm^2	Legs number	R_{TEB} , Ohm	T_0 , $^{\circ}\text{C}$	ΔT , $^{\circ}\text{C}$	U_{TEB} , V	P_{TEB} , W	ε , V	E , V/W
1.	1	0.1×0.1	7560	9482.9	25	100	70	0.4018	161.8	11.24
2.	1	0.2×0.2	2162	678	25	100	20	0.4596	46.3	2.81
3.	1	0.3×0.3	1006	140.2	25	100	9.3	0.4812	21.5	1.25
4.	1	0.4×0.4	580	45.5	25	100	5.4	0.4932	12.4	0.70
5.	1	0.5×0.5	376	18.9	25	100	3.5	0.4995	8.0	0.45
1.	2	0.1×0.1	7560	18965.7	25	100	70	0.2009	161.8	22.48
2.	2	0.2×0.2	2162	1356	25	100	20	0.2298	46.3	5.62
3.	2	0.3×0.3	1006	280.4	25	100	9.3	0.2406	21.5	2.50
4.	2	0.4×0.4	580	90.9	25	100	5.4	0.2466	12.4	1.41
5.	2	0.5×0.5	376	37.7	25	100	3.5	0.2498	8.0	0.90
1.	5	0.1×0.1	7560	47414	25	100	70	0.0804	161.8	56.21
2.	5	0.2×0.2	2162	3389.9	25	100	20	0.0919	46.3	14.05
3.	5	0.3×0.3	1006	701	25	100	9.3	0.0962	21.5	6.25
4.	5	0.4×0.4	580	227.4	25	100	5.4	0.0986	12.4	3.51
5.	5	0.5×0.5	376	94.3	25	100	3.5	0.0999	8.0	2.25
1.	10	0.1×0.1	7560	94828.7	25	100	70	0.0402	161.8	112.42
2.	10	0.2×0.2	2162	6779.8	25	100	20	0.046	46.3	28.10
3.	10	0.3×0.3	1006	1402.1	25	100	9.3	0.0481	21.5	12.49
4.	10	0.4×0.4	580	454.7	25	100	5.4	0.0493	12.4	7.03
5.	10	0.5×0.5	376	188.7	25	100	3.5	0.05	8.0	4.50
1.	20	0.1×0.1	7560	189657.5	25	100	70	0.0201	161.8	224.83
2.	20	0.2×0.2	2162	13559.5	25	100	20	0.023	46.3	56.21
3.	20	0.3×0.3	1006	2804.2	25	100	9.3	0.0241	21.5	24.98
4.	20	0.4×0.4	580	909.4	25	100	5.4	0.0247	12.4	14.05
5.	20	0.5×0.5	376	377.3	25	100	3.5	0.025	8.0	8.98

Table 3

 $S_{TEB}=15 \times 15 \text{ cm}^2$

No.	h_0 , mm	S_0 , mm ²	Legs number	R_{TEB} , Ohm	T_0 , °C	ΔT , °C	U_{TEB} , V	P_{TEB} , W	ϵ , V	E , V/W
1.	1	0.1×0.1	17012	21339	25	100	157.5	0.9041	364	11.24
2.	1	0.2×0.2	4866	1526	25	100	45.0	1.0344	104.1	2.81
3.	1	0.3×0.3	2266	315.8	25	100	21.0	1.0838	48.5	1.25
4.	1	0.4×0.4	1306	102.4	25	100	12.1	1.1105	27.9	0.70
5.	1	0.5×0.5	848	42.5	25	100	7.9	1.1266	18.1	0.45
1.	2	0.1×0.1	17012	42677.9	25	100	157.5	0.452	364	22.48
2.	2	0.2×0.2	4866	3051.8	25	100	45.0	0.5172	104.1	5.62
3.	2	0.3×0.3	2266	631.6	25	100	21.0	0.5419	48.5	2.50
4.	2	0.4×0.4	1306	204.8	25	100	12.1	0.5552	27.9	1.41
5.	2	0.5×0.5	848	85.1	25	100	7.9	0.5633	18.1	0.90
1.	5	0.1×0.1	17012	106695.0	25	100	157.5	0.1808	364	56.21
2.	5	0.2×0.2	4866	7630.0	25	100	45.0	0.2069	104.1	14.05
3.	5	0.3×0.3	2266	1579.1	25	100	21.0	0.2168	48.5	6.25
4.	5	0.4×0.4	1306	512.0	25	100	12.1	0.2221	27.9	3.51
5.	5	0.5×0.5	848	212.7	25	100	7.9	0.2253	18.1	2.25
1.	10	0.1×0.1	17012	213390.0	25	100	157.5	0.0904	364	112.42
2.	10	0.2×0.2	4866	15259.1	25	100	45.0	0.1034	104.1	28.10
3.	10	0.3×0.3	2266	3158.2	25	100	21.0	0.1084	48.5	12.49
4.	10	0.4×0.4	1306	1024.0	25	100	12.1	0.111	27.9	7.03
5.	10	0.5×0.5	848	425.5	25	100	7.9	0.1127	18.1	4.50
1.	20	0.1×0.1	17012	426779.4	25	100	157.5	0.0452	364	224.83
2.	20	0.2×0.2	4866	30518.3	25	100	45.0	0.0517	104.1	56.21
3.	20	0.3×0.3	2266	6316.3	25	100	21.0	0.0542	48.5	24.98
4.	20	0.4×0.4	1306	2047.7	25	100	12.1	0.0555	27.9	14.05
5.	20	0.5×0.5	848	851.0	25	100	7.9	0.0563	18.1	8.98

Table 4

 $S_{TEB}=20 \times 20 \text{ mm}^2$

No.	h_0 , mm	S_0 , mm^2	Legs number	R_{TEB} , Ohm	T_0 , $^{\circ}\text{C}$	ΔT , $^{\circ}\text{C}$	U_{TEB} , V	P_{TEB} , W	ϵ , V	E , V/W
1.	1	0.1×0.1	30244	37937	25	100	280	1.6073	647.2	11.24
2.	1	0.2×0.2	8652	2713.2	25	100	80.1	1.8392	185.1	2.81
3.	1	0.3×0.3	4030	562	25	100	37.3	1.9275	86.2	1.25
4.	1	0.4×0.4	2322	182	25	100	21.5	1.9744	49.7	0.70
5.	1	0.5×0.5	1508	75.7	25	100	14	2.0035	32.3	0.45
1.	2	0.1×0.1	30244	75873	25	100	280	0.8036	647.2	22.48
2.	2	0.2×0.2	8652	5426.3	25	100	80.1	0.9196	185.1	5.62
3.	2	0.3×0.3	4030	1123.3	25	100	37.3	0.9638	86.2	2.50
4.	2	0.4×0.4	2322	364.1	25	100	21.5	0.9872	49.7	1.41
5.	2	0.5×0.5	1508	151.3	25	100	14	1.0018	32.3	0.90
1.	5	0.1×0.1	30244	189683	25	100	280	0.3215	647.2	56.21
2.	5	0.2×0.2	8652	13566	25	100	80.1	0.3678	185.1	14.05
3.	5	0.3×0.3	4030	2808.3	25	100	37.3	0.3855	86.2	6.25
4.	5	0.4×0.4	2322	910.2	25	100	21.5	0.3949	49.7	3.51
5.	5	0.5×0.5	1508	378.3	25	100	14	0.4007	32.3	2.25
1.	10	0.1×0.1	30244	379365	25	100	280	0.1607	647.2	112.42
2.	10	0.2×0.2	8652	27132	25	100	80.1	0.1839	185.1	28.10
3.	10	0.3×0.3	4030	5616.7	25	100	37.3	0.1928	86.2	12.49
4.	10	0.4×0.4	2322	1820.4	25	100	21.5	0.1974	49.7	7.03
5.	10	0.5×0.5	1508	756.6	25	100	14	0.2004	32.3	4.50
1.	20	0.1×0.1	30244	758730	25	100	280	0.0804	647.2	224.83
2.	20	0.2×0.2	8652	54263	25	100	80.1	0.092	185.1	56.21
3.	20	0.3×0.3	4030	11233.4	25	100	37.3	0.0964	86.2	24.98
4.	20	0.4×0.4	2322	3640.7	25	100	21.5	0.0987	49.7	14.05
5.	20	0.5×0.5	1508	1513.2	25	100	14	0.1002	32.3	8.98

Investigations of the Properties of a Thermoelectric IR-Detector for Low Working Temperature

R. Fettig¹, T. Henkel¹, E. Müller²

¹ Universität Karlsruhe, Institut für Angewandte Physik, Germany

² Martin-Luther-Universität Halle-Wittenberg, Fachgruppe Angewandte Physik, Germany

Abstract

Thermoelectric IR-detectors have been developed and built to work at a temperature of 170 K in the CIRS experiment as part of the CASSINI mission to Saturn. Thermoelectric legs of p- and n-type are soldered to a metallized ceramic substrate, isolated one from another. Pyramidal legs are formed by electric discharge machining (EDM). A thin gold foil is welded to the pyramids and blackened for high absorption of radiation. Characterization measurements were carried out to correlate detector properties to the preparation process. Thermoelectric behavior is described by measuring the current-voltage characteristics from liquid nitrogen up to room temperature. Materials of the composition $(\text{Bi}_{0.4}\text{Sb}_{0.6})_2\text{Te}_3$ (for p-type) and $\text{Bi}_2(\text{Te}_{0.95}\text{Se}_{0.05})_3$ (for n-type) have been used for detector preparation. The material was doped to have maximum figure of merit at temperatures below room temperature. It has been found that the EDM process changes the properties of the thermoelectric material and that electro etching can remove degraded layers. Electro etched detectors exhibit properties which are closer to the values expected from the original material.

Introduction and Fundamentals

Thermoelectric detectors along with Golay-cells, bolometers and pyroelectric detectors belong to the most sensitive thermal IR sensors. Their construction principle is simple. They don't require any external voltage supply and exhibit a constant responsivity over a wide spectral range if an appropriate absorber is provided.

Detectors of the Hilger-Schwarz-type [1] have been built using highly effective thermoelectric material on the basis of $(\text{Bi}_{1-x}\text{Sb}_x)_2(\text{Te}_{1-y}\text{Se}_y)_3$. [2, 3, 4].

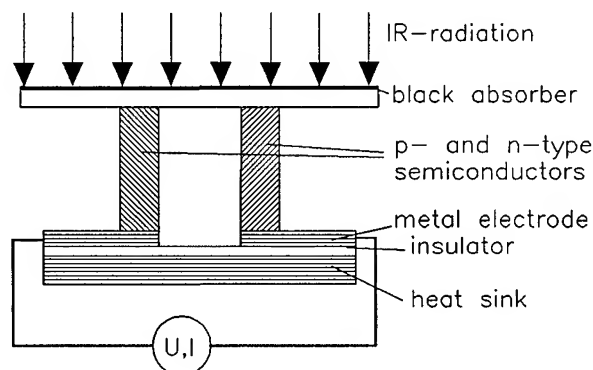


Fig.1 Principle of a thermoelectric infrared detector of the Hilger-Schwarz-type

Fig. 1 demonstrates the function principle of the detector: An absorbing structure is heated by radiation. Its temperature is measured by a thermoelement. The construction geometry in the presented way is referred to as Hilger-Schwarz-type: A thin freestanding metal foil serves as the substrate for the absorbing structure. It provides a thermal connection between the absorbing areas and the thermoelectric legs and serves as electric bridge of the thermoelement. The metal foil is linked to the two legs of thermoelectric p- and n-type materials. The legs are electrically isolated from one another and thermally connected to a heat sink at ambient temperature. To achieve maximal DC-responsivity heat losses from the absorber through surrounding gas has to be avoided, therefore the system works optimally in vacuum.

The relaxation behavior is defined by the heat capacity of the absorbing structure as well as by the heat resistance due to conduction via the thermoelement and radiation.

The detection limit of the sensor is determined by the magnitude of noise voltage (see Table 1) [5]. Johnson noise is the dominating mechanism; for high values of the figure of merit however, the influence of temperature fluctuations becomes relevant.

The dimensions of the thermoelectric legs are chosen to give the best results while taking into account the trade off between the demands for high responsivity, low response time and low resistance noise. [4]

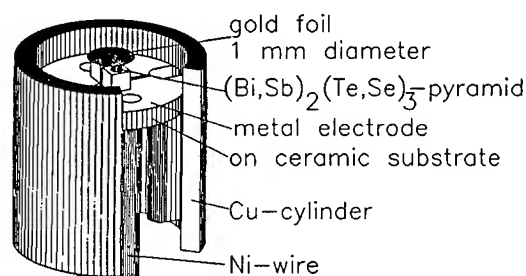


Fig. 2 Thermoelectric IR detector produced for CIRS with pyramidal geometry of the thermoelectric legs.

To manufacture detectors, cubes of thermoelectric material (edge length about 500 μm) are soldered to a ceramic carrier of Al_2O_3 coated with a structured nickel layer. This substrate sits in a copper cylinder of 5 mm diameter which is filled with epoxy in the back of the substrate. (Fig. 2). After soldering the cubes are formed into cones

or pyramids ($\approx 150 \mu\text{m}$ edge length, top area $\approx 10 \times 10 \mu\text{m}^2$) by EDM. [2]. A 100 nm thick, circular gold foil with a diameter of 1.05 mm is welded onto the tips. A layer of gold black of 20-30 μm in thickness is evaporated in inert atmosphere of several mbar onto the foil as the absorber layer [6, 7, 8].

Responsivity	$r = \frac{U_s}{I_w} = \alpha_{ab} R_w^r \epsilon f(\nu)$
Noise voltage	$U_n = \sqrt{4k_B T \Delta\nu (R_{el} + R_{p0}^r f(\nu))}$
Noise Equivalent Power	$NEP = \frac{U_n}{r}$
Specific Detectivity	$D^* = \frac{(A \Delta\nu)^{1/2}}{NEP}$
Response time	$\tau = R_w^r C_w$
Current-voltage-characteristics	$\frac{U}{I} = R_{el} + \frac{U_i(\Delta T)}{I} = R_{el} + R_p$
Peltier resistance ($I \rightarrow 0$)	$R_{p0} = \alpha_{ab}^2 R_w^p T$
	$\frac{dR_{p0}}{dT} \sim \alpha_{ab} R_w^p R_e$
Figure of Merit	$z_{eff} T = \frac{R_{p0}}{R_e}$

Table 1 Parameters for the description of a thermoelectric IR-detector with the signal voltage U_s , Boltzmann constant k_B , Seebeck coefficient of the element α_{ab} , ν the measuring frequency and $\Delta\nu$ the measuring bandwidth, the absolute temperature T and the Area of the absorber A . R_w^r , R_w^p and R_w^r are the different heat resistances relevant for the determination r , R_p and τ .

For blackened as well as for unblackened detectors responsivity r , response time τ , electrical resistance (R_{el}) and the current-voltage characteristics ($I(U)$) have been measured with an automated apparatus between room temperature and liquid nitrogen temperature. The specific detectivity and an effective figure of merit z_{eff} of the thermoelement were calculated.

For computation of specific detectivity theoretical noise values of temperature fluctuations and Johnson noise have been taken into consideration. From the ratio of measured responsivity of a detector before and after blackening the specific emissivity of the unblackened sensor can be computed. The comparison of response times at low temperatures allows for the estimation of the mass of the deposited gold black.

Detectors have been built which showed below 200 K a specific detectivity of up to $5 \cdot 10^9 \text{ cm}\sqrt{\text{Hz}}/\text{W}$ with a re-

sponse time of about 40 ms [2]. Because of the high performance figures and the simple construction and operation, these thermoelectric detectors have been selected for use in one of the Composite Infrared Spectrometers (CIRS) focal planes of the interplanetary CASSINI mission of NASA and ESA. CASSINI, scheduled to be launched in 1997 is a successor mission to Voyager II. It is expected to provide enhanced information of IR emission of Saturn and its moon Titan towards the far infrared.[9] As CIRS will operate at 170K there was demand for improvements in the performance figures of the thermoelectric detectors at this temperature.

Following theoretical considerations, material with low doping level of the composition $(\text{Bi}_{0.4}\text{Sb}_{0.6})_2\text{Te}_3$ (for p-type) and $\text{Bi}_2(\text{Te}_{0.95}\text{Se}_{0.95})_3$ (for n-type) was used to build detectors and resulted in a slight improvement of performance figures at low temperatures. [3] Even if these performance figures belong to the best values ever achieved with thermoelectric detectors, they are significantly smaller than for ideal detectors built with the same material would show.

Model fits to measured temperature characteristics and thermomicroprobe measurements show notable reduction of the Seebeck coefficient in welded detectors and EDM treated thermoelectric material. [3, 4, 10]

In the experiment described in this paper attempts were made to remove EDM-damaged surface layers from detector pyramids in order get detectors with performance figures closer to ideal theoretical ones.

Experimental

To remove the thin layer of thermoelectric material from detector pyramids which were damaged by the EDM-process an electro etching process was modified which had been developed to polish large samples. [11]

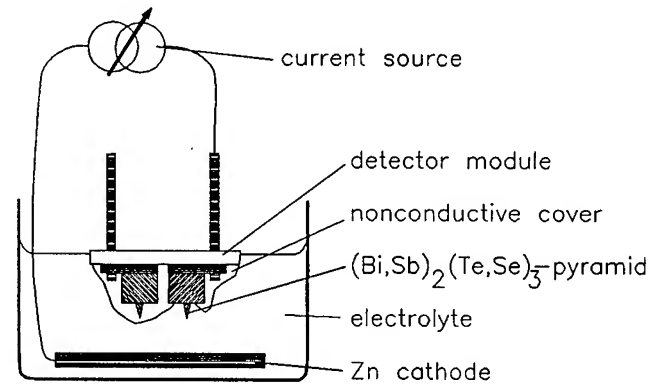


Fig. 3 Set up to remove poor quality surface layers from thermoelectric detector pyramids. The electrolyte was: 90g KOH, 55g tartaric acid, 300ml Glycerin in 1l aqueous solution for p-type material, and 83g NaOH, 67g tartaric acid in 1l solution for n-type material.[11]

Figure 3 shows the setup which was used. To remove a thin layer an electric current is sent through an electrolyte with the thermoelectric material as the anode and a Zinc plate as the cathode. In order to get appropriate results

it is important that all conductive parts except for the thermoelectric pyramids are covered with a nonconductive lacquer, that the current density is about $1\text{A}/\text{cm}^2$, that the liquid is stirred and that the electro etching process is performed only for a few seconds. If these conditions are not met, the pyramid surface gets either rough or discolored or the pyramids get desolved completely.

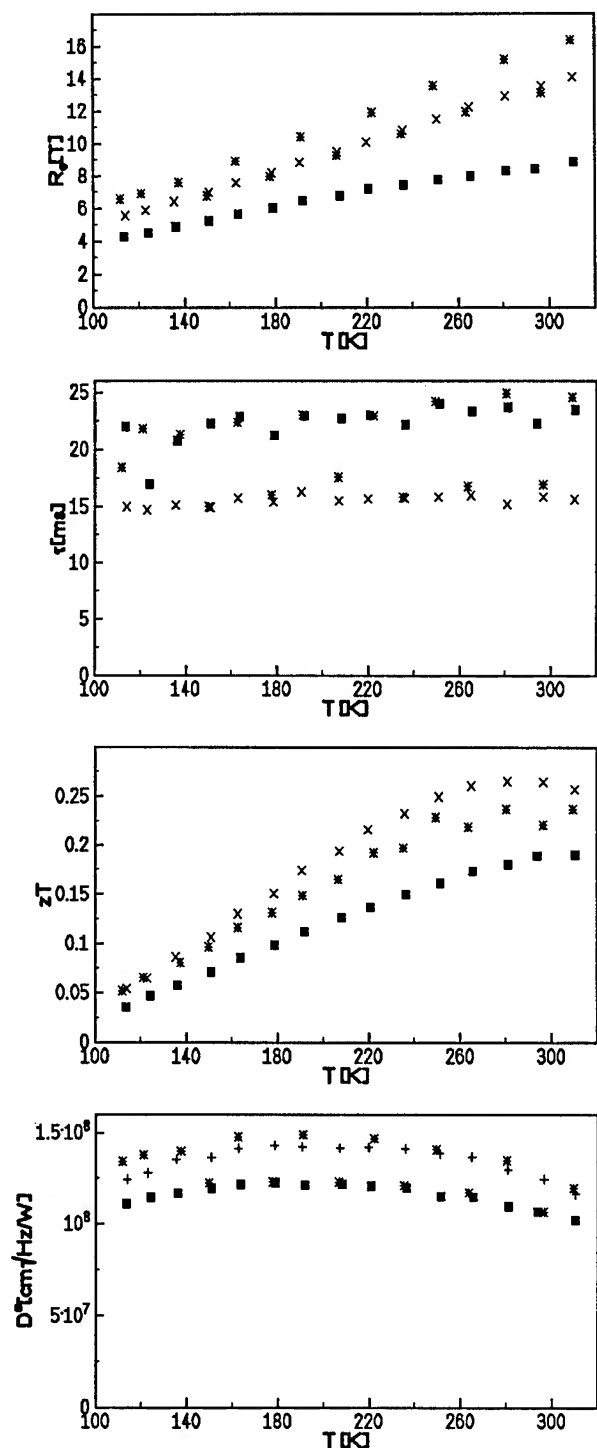


Fig.4 Temperature dependence of resistance r , response time τ , figure of merit zT and specific detectivity D^* for detector module 37, welded and characterized unblackened, before (filled squares) and after (+ and *) etching. The module was made from low temperature material: p-type: $(\text{Bi}_{0.4}\text{Sb}_{0.6})_2\text{Te}_3$, n-type: $\text{Bi}_2(\text{Te}_{0.95}\text{Se}_{0.05})_3$

To determine the effects of the etching several detector modules were treated. Before and after etching gold foils were welded to the pyramids. The performance figures of the detectors thus formed were determined at different temperatures.

Results and Discussion

Figure 4 shows the results obtained for a typical detector. A most obvious common feature for all detectors was found, that the electrical resistance was always larger after etching if the gold foil was welded in the same way before and after electro etching. However the response time of the detectors was either the same or reduced. This means that the ratio σ/κ of the thermoelement is shifted towards lower values when the EDM affected surface layer is removed. That is what is expected for weakly doped material. Another argument for low doping level is the fact that some detector resistances show a smaller temperature dependence at room temperature. This is a sign for beginning intrinsic conduction. In the sample presented in Fig. 4 the temperature dependence of the resistance gets stronger in the entire temperature range. This is what one would expect if a layer with increased boundary scattering is removed from a single crystal. The absolute value of the thermal conductance and hence of the thermal conductivity has either increase or remains unchanged while the doping level is decreased. This also could be a sign of reduced scattering.

The changes of the absolute values of $z_{eff}T$ are for all samples small, therefore the Seebeck coefficient of the detectors must have increased. The maxima of $z_{eff}T$ is shifted towards lower temperatures for all detectors which is an additional argument in favor of low doping level. Responsivity and detectivity do show a small change with the etching - an increase in the presented case, but decrease have been observed as well. To draw additional conclusions from their behavior further calculations are necessary.

Conclusions

Etching the thermoelectric pyramids of the detectors significantly changes their properties from that of a highly doped, strongly damaged semiconductor to that of a single crystal with a lower doping level. The overall improvement of the detectors however is low, which still could be an effect of the welding.

The effects of the welding spot size and the extremely thin gold foil to the detector performance have not yet been investigated in depth.

Because of the complexity of the etching process it is not useful to integrate it into the detector production process at this time. The process could give improvements where detector response time is the most crucial parameter for a particular application.

Acknowledgements

The authors are very grateful to T.E. Svečnikova and L. D. Ivanova from Baikov-Institute of Metallurgy Moscow, GUS for providing Czochralski-grown single crystals. We are obliged to the group of Dr. H. Süßmann at Martin-Luther-

Universität Halle/Wittenberg for performing of preparation procedures. The authors acknowledge NASA (NASW 4685) and DARA (50 OH 9202) for funding the project.

References

- [1] Schwarz, E., Britisch Patent Applications 57 81 87 and 87 81 88m, Research 5, 407 (1952)
- [2] Fettig, R.; Birkholz, U.; May, M., "Temperature Depending Properties of Thermoelectric Infrared Detectors", 10th Int. Conf. on Thermoelectricity, Cardiff, Great Britain (1991)
- [3] Fettig, R.; Lerchenmüller, H.-J.; Müller, E., "Optimization of a Thermoelectric Infrared Detector for Low Working Temperature", 12th Int. Conf. on Thermoelectricity, Yokohama, Japan (1993)
- [4] Fettig, R., *Die Temperaturabhängigkeit der Kenngrößen thermoelektrischer Infrarotdetektoren*, PhD-thesis, Fakultät für Physik, Universität Karlsruhe (1993)
- [5] Smith, R.A.; Jones, F.E.; Chasmar, R.P. *The Detection and Measurement of Infra-Red Radiation*, Oxford Uni.Press, England (1957)
- [6] Bly, V.; Advena, D.J.; Cox, J.F., "The Deposition and Characterization of Far Infrared Absorbing Black Gold Films", *Applied Optics*, Vol.32 No.7 pp.1136-1144 (1993)
- [7] Becker, W.; Fettig, R.; Ruppel, W., "Black Gold Deposits as Absorbers for Far Infrared Radiation", *Physica Status Solidi*, Vol. 194 pp. 241-255 (1996)
- [8] Becker, W.: *Optische Eigenschaften von Schwarzgoldschichten im fernen Infrarot*, PhD-Thesis, Fakultät für Physik, Universität Karlsruhe (1996)
- [9] Ade P.; Calcutt S.; Jennings, D.; Kunde, V.; Taylor, F., "The Composite Infrared Spectrometer", *J. of the British Interplanetary Society*, Vol 45 pp. 811-816 (1992)
- [10] Süßmann, H.; Bohm, M.; Reinshaus, P. "Scanning Thermo-Probe Technique - a Method for Determination of Concentration Profiles", 12th Int. Conf. on Thermoelectrics, Yokohama, Japan (1993)
- [11] Süßmann, H.; private communication

The Thermoelectric power on p-n junction

Z.M. Dashevsky

Ben-Gurion University of the Negev, Materials Engineering Depart.
P.O.B. 653, Beer-Sheva 84105, Israel

S. Ashmontas, L. Vingelis, I. Gradauskas

Institute of Semiconductor Physics, Academy of Sciences of Lithuania
232600, Vilnius, Lithuania

A.I.Kasian

Kishinev Polytechnical Institute
277028, Kishinev, Moldova

Abstract

The measurements of thermo-emf were performed on sharp PbTe p-n junctions with doping layer depth by order of diffusion length of minority carriers in the temperature range from 300 to 80K. The barrier thermo-emf V_b effect results in sharp output signal increase at low temperature. Moreover, at sign of V_b is opposite the sign of volume thermo-emf. The barrier thermo-emf may be explained thermodiffusion nonequilibrium carriers and its separation on p-n junction. However the difference V_b from photo-emf is opposite sign of its terms at n- and p-ranges. At our case the observation of V_b became enabled by the producing ΔT only at n-range (the absorption of short laser pulse on free carriers at surface layer). At short pulse (CO_2 - laser $\lambda = 10.6 \mu\text{m}$, $\tau = 200$ nsec) increase of output signal practically repeated the form of laser pulse, i.e. irradiation absorption of free carriers and its interaction with lattice (heat of phonon system) is acting without inertia. At same time we observed very slow decreasing in signal V (μsec and more) after switch off, connecting with inertia of phonon system cooling. This memory effect of V differs from response of photo-emf and may be very useful for concrete applications (for example measurement of power for short laser pulse).

1. Introduction

The interest to the problem of the thermoelectric phenomena at p-n junctions is still great now though first studies of the influence of the carrier injection on a thermoelectric power (thermo-emf) were published in early 60s[1]. This can be explained by searching for ways of essential increase of the thermoelectric power on the one hand and by the latest technology achievements in microelectronics on the other hand. Most of works in this field deal with different specific cases, we think the time has come for more general approach to the problem of thermoelectric properties of p-n junctions. In this case the very difficult problem is to separate volume and barrier thermoelectric power.

In the present paper we took p-n junction, produced by ion implantation method. The depth of p-n junction is not more $5 \mu\text{m}$, therefore the influence of barrier thermoelectric power in the total power may be significant. The temperature gradient came about as the result of absorption of pulses of laser radiation. For producing sharp temperature difference we used the classical thermoelectric materials which have low heat conductivity κ , as such material PbTe has κ on the order - $2 \cdot 10^{-2} \text{ W/cm}\cdot\text{K}$ at $T=300\text{K}$. Moreover this material has high absorption on free carriers (electron density more than 10^{18}cm^{-3}) and high electron and hole mobility. At low temperatures ($T < 200\text{K}$) we discover the

sign change and increase in absolute value of the output signal V of thermoelectric power, which is connected with appearance of barrier thermo-emf V_b making the primary contribution to V . Nature of V_b is connected with diffusion of nonequilibrium carriers from n-area and its separation on p-n junction (diffusion length of holes at 80 K = 10 μm). At short pulse (CO_2 -laser $\lambda = 10.6 \mu\text{m}$, $\tau = 200 \text{ nsec}$) increase of output signal practically repeated the form of laser pulse, i.e. irradiation absorption of free carriers and its interaction with lattice (heat of phonon system) is acting without inertia. At same time we observed very slow decreasing in signal V (μsec and more) after switch off, connecting with inertia of phonon system cooling (heat conductivity flux). This memory effect of V differs from response of photo-emf and may be very useful for concrete applications (for example measurement of power for short laser pulse).

II. Experimental results

The single crystals of p-type PbTe were investigated. Hole density at 80 K was $(1-2) \cdot 10^{18} \text{ cm}^{-3}$. Being polished the samples were implanted by intense Zn ion beam at energy 150 keV in a [100] direction without heat treatment. In this case ion implantation with large doses (maximum $I = 2 \cdot 10^3 \mu\text{C}/\text{cm}^2$) of Zn is accompanied by the formation of the point defects (for the most part, Te vacancies), which determine the properties of implanted layer [2 - 4]. The depth of its penetration in the host crystal is more higher than for implanted ions. These defects are very stable, after ion implantation the upper (doping) layer has electron type of conductivity. The stabilization of electron density at the value is caused by formation of quasilocal energy level of Te vacancies in conduction band of PbTe [5 - 7]. For maximum implantation

dose $I = 2 \cdot 10^3 \mu\text{C}/\text{cm}^2$ concentration N of Zn at surface layer (the thickness $d = 0.1 \mu\text{m}$) is order $1 \cdot 10^{21} \text{ cm}^{-3}$. We can assume every implanted ion produced one Te vacancy on the length of its pass (mass of Te atom is small as compared to that of Pb). Each Te vacancy produces two electrons. At these concentration N the level of Te vacancies is practically filled with electrons and low-temperature Fermi level coincides with this level (pinning of Fermi level) [8]. For special preparing specimens (wedge form) we determined the depth of p-n junction (layer of n-type conductivity). For dose from $I = 400$ to $2 \cdot 10^3 \mu\text{C}/\text{cm}^2$ depth of p-n junction increases from 1 to 5 μm . Such depth of doping layer is connected with mechanism of radiation induced diffusion of defects in sample. The diffusion coefficient D of Te vacancies at ion implantation is more higher than for standard diffusion and D can achieve $10^{-12} \text{ cm}^2/\text{sec}$.

The current - voltage (I - V) characteristics of fabricated structures are shown in Fig. 1.

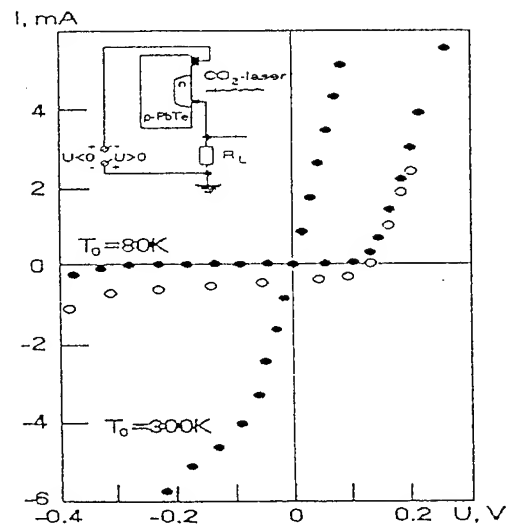


Fig. 1. Voltage-current characteristics of p-n PbTe structures.

It is seen that at room temperature the asymmetry of these characteristics is

asymmetry of these characteristics is negligible. Only at high bias voltages the tendency towards saturation of reverse current is observed. Since the intrinsic carrier concentration in PbTe at $T=300\text{K}$ is $n_i=1\cdot 10^{17}\text{cm}^{-3}$, potential barrier practically does not exhibit and such structure can be considered as double layer (the upper n-layer on p-base). When temperature is lowered to $T=80\text{K}$ the I-V characteristics of samples become typical for ordinary p-n junction.

These structures are illuminated with CO_2 - laser pulses ($\lambda = 10.6\text{ }\mu\text{m}$, $\tau = 200\text{ nsec}$) on the surface of n-layer. Oscilloscope traces of photoresponse at constant radiation power at $T=300\text{K}$ with upper five-microns- thick n-layer are showed in Fig. 2.

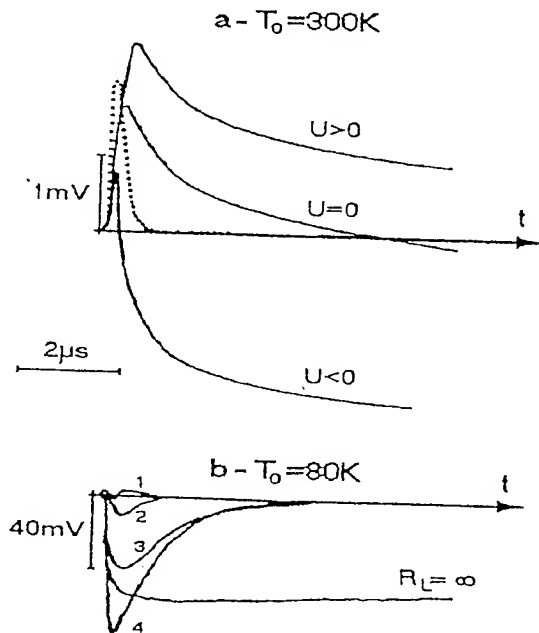


Fig.2. Oscilloscope traces of response output signal U at constant CO_2 -laser radiation power. a) $T=300\text{K}$, b) $T=80\text{K}$, 1)- V (external bias voltage $=0.8$, 2) $=0.3$, 3) $=0$. Dotted line - laser pulse. By laser radiation signal increases and achieves maximum at time some later than

time of laser pulse switch off. After pick signal drops to zero such slowly. At $t > 5\text{ }\mu\text{sec}$ signal changes sign.

Absolutely different picture is observed at $T=80\text{K}$. The photoresponse not only changes its polarity, but also increases in peak value with factor more than 20. The time dependence of photoresponse pulse changes, grows more rapidly (almost perfectly reproduces laser pulse) and drops to zero more rapidly than it was at 300K .

Fig.3 illustrates the dependence of the peak value of photoresponse on temperature.

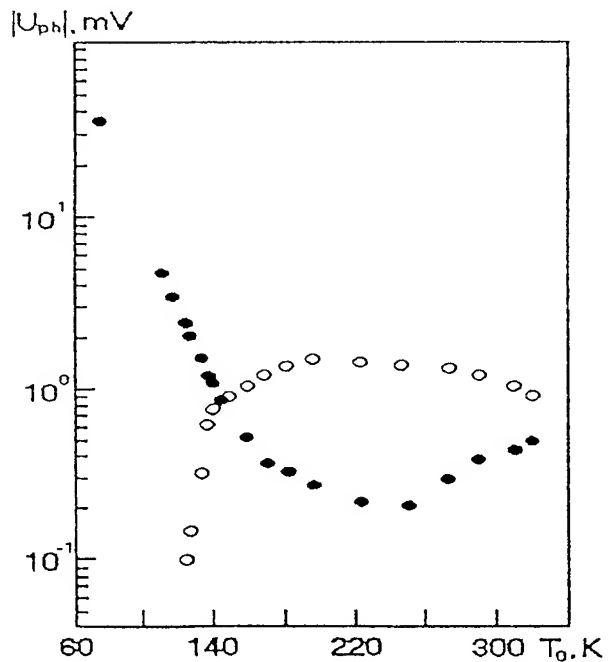


Fig.3. Temperature dependence of negative (dark dots) and positive (light dots) peak values of photoresponse.

Change of sign signal is observed at $T=150\text{K}$. The oscilloscope traces of photoresponse at different values of CO_2 - laser radiation power were shown on Fig. 4. It is seen, that at $T=300\text{K}$ photoresponse signal increases linearly with power.

At $T=80\text{K}$ at small power $V(P)$ is given by straight line, at big power dependence $V(P)$ became weak.

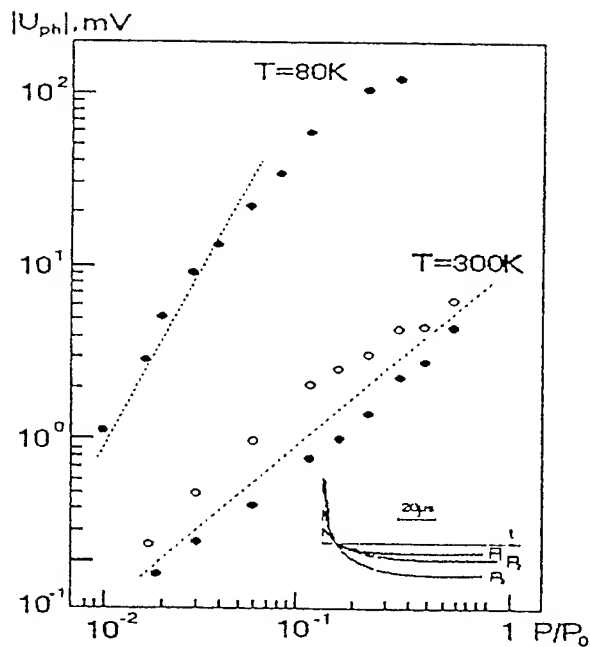


Fig.4. Voltage-power characteristics. Dark dots-negative, light dots-positive peak values of output signal. $P_0 = 1 \text{ MW/cm}^2$

III. Discussion

The observed results cannot be explained in the simple model of producing thermoelectric power. Therefore we consider the experiment more detail.

Absorption of pulses of laser radiation. In the range of radiation lying at the edges of fundamental absorption (for PbTe at 80 - 300 K $\lambda < 4 \mu\text{m}$) the major mechanism is free-carrier absorption. For carrier concentration $n = 5 \cdot 10^{18} \text{ cm}^{-3}$ and wave length $\lambda > 10 \mu\text{m}$ the absorption coefficient α for PbTe is of magnitude 10^4 cm^{-1} [9]. According to Lambert's law, the amount of absorbed energy in the layer of thickness dx is given by

$$N = N_0(1-R)e^{-\alpha x} \alpha dx, \quad (1)$$

where N_0 is the incident energy density, R is the reflection coefficient and x is the distance from the crystal surface. In our case in the order to decrease to reflection

from surface of the crystal we applied special coating. It is assumed that R is close to zero. We can think the full absorption is provided on the depth of doping layer.

The hot electrons lose the main part of the energy on the scattering with phonons. This interactions does not have inertia, therefore we can think the character of the lattice temperature is the similar to the absorbed energy dependence. Therefore we can suggest that ΔT is only in n-layer (upper layer with practically constant electron concentration of carriers).

The thermoelectric power (thermo-emf) at p-n junction. The complete thermo-emf includes contributions of a volume emf V_V , barrier emf V_b , and Benediks emf V_B . In our case we do not see thermo-edf on "hot carriers" [10]. This process is very rapid and disappears when the laser pulse switches off.

The method of barrier thermo-emf calculation is analogous to the case of barrier photo-emf, but is more enormous. The system of fundamental equations describing the development of an electromotive force across p-n junction and the passage of an electric current can be represented by equations for the electron current density j_e and hole current density j_h , the continuity equations, and the Poisson equation for the electric field intensity E . In the one dimensional approximation assuming that at each point x the equilibrium distribution of electrons and holes corresponds to the lattice temperature $T(x)$, we write these equations in the form

$$j_n = en\mu_n E + eD_n \frac{dn}{dx} + n\mu_n (Q_n^{**}/T) \frac{dT}{dx}, \quad (2)$$

$$-dj_n/(edx) = g(x) - r(n,p), \quad (3)$$

$$dE/dx = 4\pi e(p-n+N_g-N_a)/\epsilon. \quad (4)$$

V_v , barrier emf V_b , and Benediks emf V_B . In our case we do not see thermo-edf on "hot carries" [10]. This process is very rapid and disappears when the laser pulse switches off.

The method of barrier thermo-emf calculation is analogous to the case of barrier photo-emf, but is more enormous. The system of fundamental equations describing the development of an electromotive force across p-n junction and the passage of an electric current can be represented by equations for the electron current density j_e and hole current density j_h , the continuity equations, and the Poisson equation for the electric field intensity E . In the one dimensional approximation assuming that at each point x the equilibrium distribution of electrons and holes corresponds to the lattice temperature $T(x)$, we write these equations in the form

$$j_n = e\mu_n n E + e D_n \frac{dn}{dx} + n\mu_n (Q_n^{**}/T) dT/dx, \quad (2)$$

$$-dj_n/(e dx) = g(x) - r(n, p), \quad (3)$$

$$dE/dx = 4\pi e(p - n + N_g - N_a)/\epsilon. \quad (4)$$

Here e , μ_n , n and D_n are the charge, mobility, concentration and diffusion coefficient of electrons, Q_n^{**} is the amount by which the electron-transport kinetic energy exceed the mean kinetic energy, p is hole concentration, $g(x)$ is generation function, r is the recombination function, N_g and N_a are the concentrations of ionized donors and acceptors, ϵ is the dielectric permittivity. Equations analogous to (2) and (3) can be written for holes, with the subscript n replaced by p .

If the p-n junction is in thermal equilibrium at some temperature T_0 , the number g_0 of electron-hole pairs created by heat in unit

volume in unit time will be compensated by recombination, i.e., $r_0 = g_0$. If a temperature differential with a sufficiently high gradient is applied to the junction, nonequilibrium electron-hole pairs will appear within junction. The internal field of the junction separates these pairs until they recombine. As a result the n-region becomes negatively charged and p-region positively charged. The potential barrier of the p-n junction decreases by an amount V equal to the voltage will be observed in the external circuit.

Let the temperature of the n-region be equal to T , the temperature at the p-n boundary be T_0 . We shall assume that in a semiconductor the main mechanism of recombination is direct radiant recombination, the non-equilibrium-carrier concentration being small in comparison with the principal-carrier concentration. Accordingly, we transform the right-hand side of (3):

$$g(x) - r(n, p) = -[p - p_{on}(T)]/\tau_p =$$

$$\Delta p/\tau_p + G(x), \quad (5)$$

where $p_{on}(T)$ and τ_p are respectively the equilibrium concentration at temperature T and hole lifetime in the n-region, $\Delta p = p - p_{on}(T)$ and $G(x)$ plays the role of function describing the internal generation of carriers

$$G(x) = [p_n(T) - p_n(T_0)]/\tau_p. \quad (6)$$

In order to simplify the problem, assuming that the thickness d of the n-region is small (of the order or less of magnitude of the diffusion length of the minority carriers), we replace the true variation of the temperature distribution along the x -axis by a step function: $T(x) = T$ at $d < x < 0$ and $T(x) = T_0$ at $x > 0$ (for n-region x - negative, p-region x - positive). Then allows us 1) to

Here e , μ_n , n and D_n are the charge, mobility, concentration and diffusion coefficient of electrons, Q_n^{**} is the amount by which the electron-transport kinetic energy exceed the mean kinetic energy, p is hole concentration, $g(x)$ is generation function, r is the recombination function, N_g and N_a are the concentrations of ionized donors and acceptors, ϵ is the dielectric permittivity. Equations analogous to (2) and (3) can be written for holes, with the subscript n replaced by p .

If the p-n junction is in thermal equilibrium at some temperature T_0 , the number g_0 of electron-hole pairs created by heat in unit volume in unit time will be compensated by recombination, i.e., $r_0 = g_0$. If a temperature differential with a sufficiently high gradient is applied to the junction, nonequilibrium electron-hole pairs will appear within junction. The internal field of the junction separates these pairs until they recombine. As a result the n-region becomes negatively charged and p-region positively charged. The potential barrier of the p-n junction decreases by an amount V equal to the voltage will be observed in the external circuit.

Let the temperature of the n-region be equal to T , the temperature at the p-n boundary be T_0 . We shall assume that in a semiconductor the main mechanism of recombination is direct radiant recombination, the non-equilibrium-carrier concentration being small in comparison with the principal-carrier concentration. Accordingly, we transform the right-hand side of (3):

$$g(x) - r(n,p) = - [p - p_{on}(T)] / \tau_p = \Delta p / \tau_p + G(x), \quad (5)$$

where $p_{on}(T)$ and τ_p are respectively the equilibrium concentration at temperature T

and hole lifetime in the n-region, $\Delta p = p - p_{on}(T)$ and $G(x)$ plays the role of function describing the internal generation of carriers

$$G(x) = [p_n(T) - p_n(T_0)] / \tau_p. \quad (6)$$

In order to simplify the problem, assuming that the thickness d of the n-region is small (of the order or less of magnitude of the diffusion length of the minority carriers), we replace the true variation of the temperature distribution along the x -axis by a step function: $T(x) = T$ at $d < x < 0$, $T(x) = T_0$ at $x > 0$ (for n-region x - negative, p-region x - positive). Then allows us

1) to assume that, as before, the p-n junction is approximately in a state of thermal equilibrium at temperature T_0 ,

2) to take $dT/dx = 0$ in (2),

3) to describe the presence of the temperature gradient (consequently, the existence of nonequilibrium charge carriers) with aid of the internal generation function $G(x)$, in the p-region $G(x) = 0$, while in the n-region $G(x)$ has form (6), with $T(x)$ replaced by T . We note that such a simplification may be regarded as the result of expanding the expression $p_{on}(T)$ from formula (6) in series in powers of $\Delta T/T \ll 1$ and keeping the first term. As a result, we arrive at a problem analogous to the calculation of the photo-electromotive force of a p-n junction under isothermal conditions in the presence of the generation function $G(x)$. In this case, performing calculations with the same boundary conditions, approximations we obtain for current density the usual expression

$$j = j_p + j_s (e^{V/k} - 1), \quad (7)$$

$$j_p = j_s (1 + d_l/L_p) [(1 + 3\Delta T/T_0) e^{E_g \Delta T / k T_0^2} - 1] \quad (8)$$

Here j_s is the saturation-current density with

reverse bias on the p-n junction (in our case saturation-current is essentially determined by holes in the n-region), j_p is the density of the short-circuit current corresponding to the collection of the charge from the forward layer and from the adjacent space-charge region of width d_1 , L_p , τ_p and p_{0n} are diffusion length, life time and equilibrium concentration of holes in the n-region at $T = T_0$. The thermo-emf of the p-n junction is obtained from (7) with $j=0$. We shall define the efficiency coefficient α_{eff} of the thermo-emf as follows:

$$V = \alpha_{eff} \Delta T \quad (9)$$

Using (8) we find for α_{eff} the expression

$$\alpha_{eff} = (kT_0/e \Delta T) \ln \{ 1 + (1 + d_1/L_p) [(1 + 3\Delta T/T_0) e^{E_g \Delta T/kT_0^2} - 1] \}. \quad (10)$$

In the general case the value of α_{eff} depends on E_g and ΔT . However the dependence on ΔT is weak. For small ΔT , such that $E_g \Delta T \ll kT_0^2$ the expression (10) can be written as

$$\alpha_{eff} = (k/e)(1 + d_1/L_p)(E_g/kT_0 + 3). \quad (11)$$

If we compare α_{eff} at 80 K with thermo-emf for homogenic material α_e ($n = 2 \cdot 10^{18} \text{ cm}^{-3}$ absolute magnitude of α_e is not more than $100 \mu\text{V/K}$) we will see that it almost at order less than barrier α_{eff} .

The time dependence of thermo-emf We noted that pulse of laser irradiation we can describe in the form of step. Practically without inertia laser pulse warms free electrons, which during relaxation time transmitted energy to phonons. Therefore at this time temperature of crystal lattice T

and consequently thermo-emf repeats without inertia time dependence of laser pulse. Another picture we must observe at switch off of laser pulse. The cooling of crystal lattice and falling of V is connected by heat conductivity flux from surface layer to volume of crystal.

Estimates showed, dropping of ΔT in crystal PbTe with low heat conductivity (κ is practically on two orders less than for Si) flows very slow during $10 - 20 \mu\text{sec}$.

III. Conclusions

The measurements of thermo-emf were performed on sharp PbTe p-n junctions with doping layer depth by order of diffusion length of minority carriers in the temperature range from 300 to 80 K. The barrier thermo-emf V_b effect results in sharp output signal increase at low temperature. Moreover, at sign of V_b is opposite the sign of volume thermo-emf.

The barrier thermo-emf may be explained thermodiffusion nonequilibrium carriers and its separation on p-n junction. However the difference V_b from photo-emf is opposite sign of its terms at n- and p-ranges. At our case the observation of V_b became enabled by the producing ΔT only at n-range (the absorption of short laser pulse on free carriers at surface layer).

References

- [1] J. Tauc, "Photo and thermoelectric phenomena in semiconductors. Moscow, Nauka, 1962. 253 p.
- [2] Z.M. Dashevsky and M.P. Rulenko, Semiconductors 27, 366 (1993).
- [3] V.I. Kaydanov, Yu.I. Ravich, Physics-Uspekhi 51, 145 (1985), V.I. Kaydanov, Defect and Diffusion Forum vols. 103-105, 388 (1993).

THERMOELECTRIC POWER GENERATION SYSTEMS RECOVERING HEAT FROM COMBUSTIBLE SOLID WASTE IN JAPAN

Takenobu Kajikawa

Department of Electrical Engineering

Shonan Institute of Technology

1-1-25 Tsujido-nishikaigan, Fujisawa, Kanagawa, JAPAN 251

Tel:+81 466 34 4111, Fax:+81 466 35 8897, e-mail: kajikawa@elec.shonan-it.ac.jp

Abstract

The status and future prospects on the development of thermoelectric power generation systems utilizing heat from the municipal solid waste in Japan are reviewed in this paper. Two on-going research and development programs related to this application in Japan are briefly introduced. The characteristics of heat from the solid waste processing system lead to the peculiar concept of thermoelectric power generation system. The theoretical and experimental studies including small scale on-site experiment are shown to discuss several technological problems and the guideline for the development of such systems.

Introduction

In Japan solid waste per capita was discharged about 1.13kg/day in 1991. Total amount of solid waste from domestic affairs was about 5.12×10^6 ton/year in 1991. It was 1.25 times of the mount in 1985. The increment rate is gradually increasing. 72.5% of total amount of solid waste is burned, which is equivalent to 3.43×10^{14} kJ/year in energy based on 9240 kJ/kg in enthalpy of combustion. The other part is reclaimed to low ground, but this processing tends to be restricted from the environmental aspects recently.

About 2000 systems of more than 50 ton/day have been in operation for municipal solid waste management in Japan. The ratio of large scale unit processing more than 150 ton/day is about 22%. The

numbers of small scale units of several tens kg/day are more than 100,000. The numbers of the incinerators will increase year by year.

Figure 1 shows the annual variation of the enthalpy of combustion in solid waste in Tokyo, Yokohama, and Osaka. The ratio of solid waste of higher enthalpy is increasing, while the range of enthalpy of combustion is becoming wide. Recently the mean value for high grade solid waste is 10,400 kJ/kg, while that for low grade one is 4,590 kJ/kg. These data indicate that the combustion gas temperature fluctuates hourly, daily, monthly and seasonally. The range of combustion gas temperature is from 873K to 1433K. Figure 2 shows a typical case of the temperature variation at the outlet of the burner for a large scale incinerator. The temperature changes from 1433K to 1243K for one hour as an example{1}.

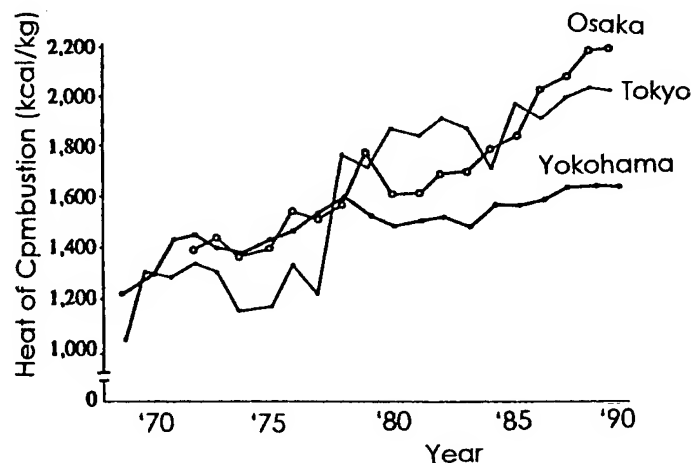


Fig.1 The annual variations of enthalpy of combustion of solid waste

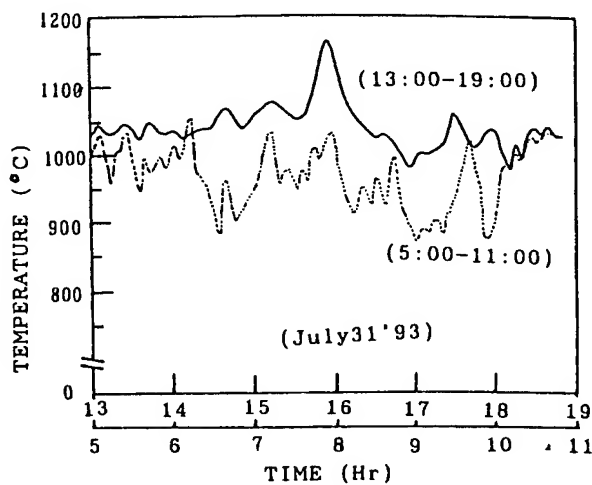


Fig.2 Temperature variation of combustion gas for a real incinerator

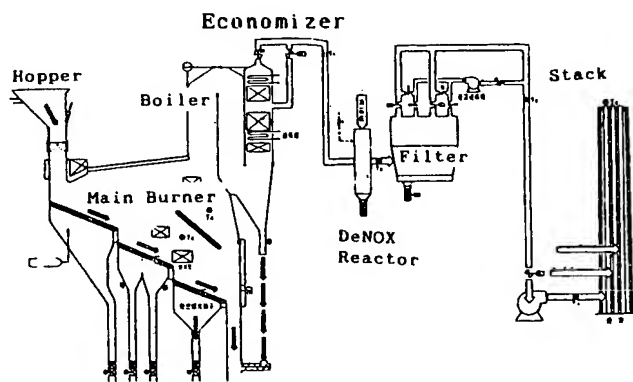


Fig.3 Conventional solid waste processing system combined with power generation system

Figure 3 shows a large scale system configuration for a conventional type combined with a Rankine cycle power generation system. The municipal systems of more than 50 ton/day in solid waste and in continuous operation are usually equipped with power generation system. For less than 50 ton/day or in intermittent operation the waste heat is not used for the production of electricity but for thermal demand such as swimming pools and green houses.

The energy conversion efficiency and gross power output are shown in Fig.4 {1}. The mean efficiency is 5.24% for the less than 200 ton/day systems, and 9.84% for more than 200 ton/day systems. Recently the energy conversion efficiency for new and large systems is higher due to several technological improvements and scale effect. The total capacity of power generation systems was about 550 MWe in

1994.

The main reasons retarding the expansion of the utilization to generate electricity are considered as follows:

- 1) Combustion gas is chemically reactive.
- 2) Combustion gas temperature fluctuates widely, frequently, and rapidly.
- 3) The operation for small scale systems is intermittent.
- 4) The capacity of most of systems is too small to equip a steam power generation system.

In consideration of the characteristics of heat of combustible solid waste resource and large amount of solid waste we have concluded that a thermoelectric power generation system has greatly the potential adaptability to this energy source. It is not said too much that for a small scale incinerator the thermoelectric power generation system is not alternative.

In this paper the status and future prospects on the development of the thermoelectric power generation system utilizing heat of municipal solid waste in Japan are reviewed.

The first is to introduce two related research and development programs in Japan briefly. The second is to present the concept of a thermoelectric power generation system combined with a solid waste processing system. The third is to review some theoretical and experimental studies. The fourth is to discuss about the technological problems and future prospects and the last is to summarize the results of this survey.

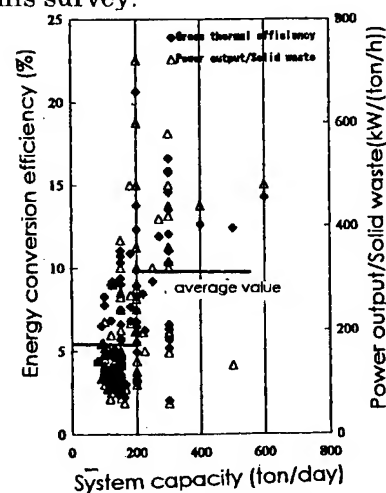


Fig.4 Energy conversion efficiency for various plants

Related Projects Summary

The national project titled "Research on Efficient Utilization of Waste Energy Such As Heat of Combustible Solid Waste" has started with the special coordination funds for promoting science and technology by Science and Technology Agency since FY 1995 {2}. The term will be six years divided with two phases (I and II). More than 10 organizations- industrial, governmental and academic have joined in it. The research budget in every year is about 300 million yen. The objective is to establish the technology on the thermoelectric power generation system recovering heat, which has hardly been used, to improve the energy conversion efficiency for local energy systems.

The major research items consist of the followings.

- 1) Development of the manufacturing technology for thermoelectric power generation module
- 2) Development of system technology for the applications to small, middle and large incinerator systems
- 3) Development of evaluation technology for various types of thermoelectric power generation systems
- 4) Development of optimum design technology

Another national project entitled "Waste Innovation 21st Century Project" has been promoted by Japan Waste Research Foundation supported by the Ministry of Health and Welfare since FY1991{3}. After three-year program (Phase I), it has been in Phase II since FY 1995. The objective of this project is to improve the energy conversion efficiency for the power generation system combined with a solid waste processing system due to various ways including thermoelectric energy conversion. Phase I program is shown in Table 1. The study committee chaired by Prof.N.Hirayama, Chiba Institute of Technology, has achieved the feasibility study including small scale experiments. More than 20 members from private sector, university and municipal office have joined in this committee.

The major research items are as follows:

1) Development of tube materials for a super heat boiler to produce steam of higher pressure and higher temperature than that for the conventional incinerator.

2) Developments of the improved Rankine cycle power generation system due to combination with fossil fuel fired system.

3) Improvement of heat recovery and heat utilization by means of thermoelectric energy conversion and /or heat pump technologies.

In this project a small scale thermoelectric power generation experiment was carried out for a real, large-scale solid waste processing system.

Table 1 Phase I program of Waste Innovation 21st C Project

Research Items \ FY	'91	'92	'93
1. R&D on Application of Conventional Power Technology to Incinerator System			
a. Tube Materials for Superheat Boiler	<u>Investigation</u>	<u>Lab. Test</u>	<u>Demonstration</u>
b. Improvement of Efficiency due to Combined Cycle	<u>Investigation</u>	<u>Conceptual Design</u>	
2. Improvement of Heat Recovery & Utilization			
a. Thermoelectrics & Heat Pump	<u>Investigation</u>		<u>Conceptual Design</u>

Concept of Thermoelectric Power Generation System

When a thermoelectric power generation system is considered to apply to the solid waste processing system, it can be classified from the view points of capacity, energy quality, operating mode, location and utilization as shown in Fig.5. The peculiar points for this system are the characteristics of the heat source and the capacity as compared with RI thermoelectric power generator. The temperature of combustion heat of solid waste is unstable as mentioned before, and the capacity is very large, that is, in the range from 100kW to more than 1000kW. These peculiar points affect the design

method and system configuration. The types of thermoelectric power generation systems are classified as shown in Fig.6. A proper type should be selected in due consideration of the given conditions for solid waste processing systems as shown in Fig.3.

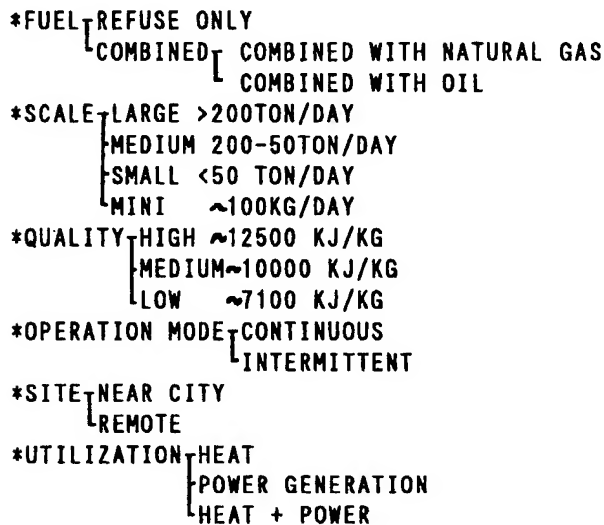


Fig.5 Classification of solid waste processing system

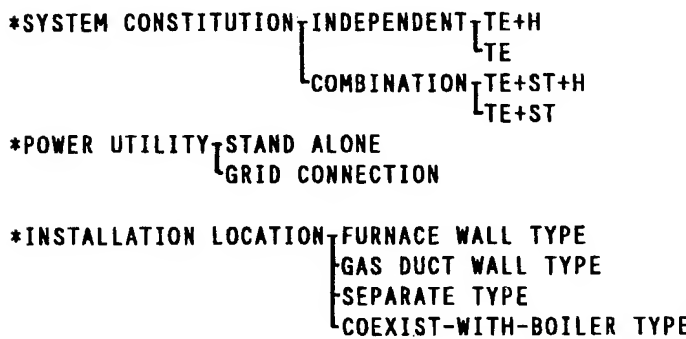


Fig.6 Classification of thermoelectric power generation system installed in a solid waste processing system

Figure 7 shows the thermal energy flow for a typical middle-scale (200 ton/day) incinerator which has 1500kW power generation system. The available heat to convert to electricity by Rankine cycle at present(Line A) is 39% of overall input energy. In the future it might be possible that the available heat becomes more than 85% (Line B)

due to the characteristics of thermoelectric system. In the case of 10% in thermoelectric energy conversion efficiency, more than 8.5 % of input thermal energy flow can be obtained in electricity. For the 200 ton/day system as shown in Fig.7, 1930 kW can be recovered. The solid waste processing system requires power to process the solid waste. Figure 8 shows the relationship between the capacity and the required amount of power. On the average 5.5 kW/(ton/day) is needed. It is desirable that each system is self-sustaining from the view point of energy by the installation of thermoelectric power generation system.

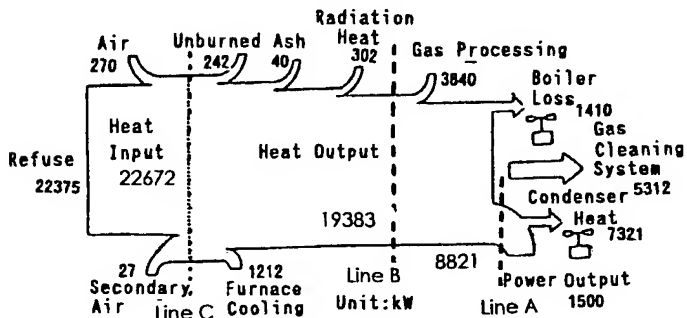


Fig.7 Thermal energy flow for a typical middle-scale incinerator

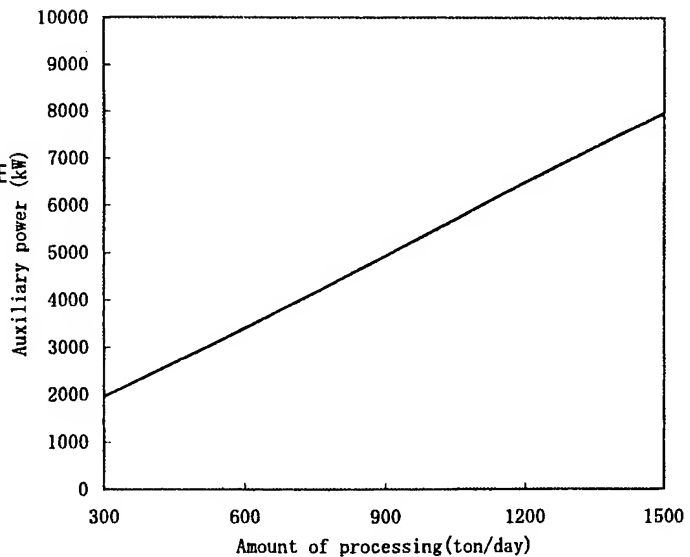


Fig.8 Auxiliary power for solid waste processing

Overview of Theoretical and Experimental Studies

The conceptual design of thermoelectric power generation system embedded in the furnace wall for a 1000kg/day class incinerator has been carried out {4}. The system configuration is shown in Fig.9. The size of a furnace for a small scale incinerator can be calculated from Eq.(1).

$$\text{Volume of a Furnace} = H G / Q \quad (1)$$

where H,G,and Q are heat of combustion (kJ/kg), processing rate (kg/s), and heat duty of a furnace (kW/m³) respectively. Heat duty of a furnace is about 290 kW/m³ for such a scale.

In the case of 200 kg/h system, the volume is 4.0 m³. The available surface area embedding thermoelectric power generation module was estimated 3.6 m². The specifications on the thermoelectric module is shown in Table 2. As the combustion temperature reaches more than 1173 K, Si-Ge elements were used. The percentage of available heat to overall input thermal energy was assumed 25%, the system energy conversion efficiency would be 2.5% based on 10.1% in thermoelectric energy conversion efficiency. The gross power output was estimated 23 kW, while the auxiliary power was about 15kW. The power density was 6.4 kW/m² at 800 K in temperature difference between the hot side thermoelectric element and the cold one.

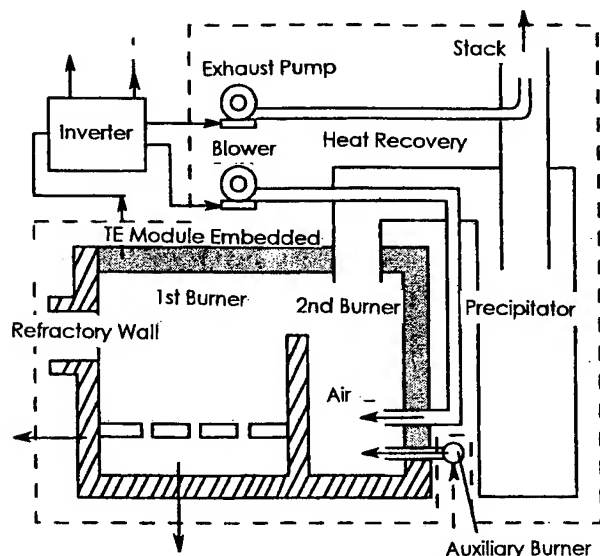


Fig.9 Configuration of small scale incinerator

Table 2 Specifications of thermoelectric module

TE Material	Si-Ge
Fig. of Merit	$0.75 \times 10^{-3} \text{ K}^{-1}$
TE Leg Hight	32 mm
Hot Junction Temp.	1123 K
Cold Junction Temp.	323 K
Temp. Difference	800 K
Efficiency	10.1 %
Heat Flux	80.4 kW/m ²

Small scale experiment on thermoelectric power generation system with fin-plate type heat exchanger has been carried out in order to obtain the design data for a waste heat recovering system for a 1000 kg/day class incinerator{5}.

In the experiment the hot air which was considered to be heated with the combustion gas as the hot side source and water as the coolant were used. The hot air temperature and water temperature were 403 K and 293 K respectively. As the temperature range is low, the thermoelectric elements could be used 101 couples made of Bi-Te element, which was the most efficient at present. The configuration of the thermoelectric power generation system is shown in Fig.10.

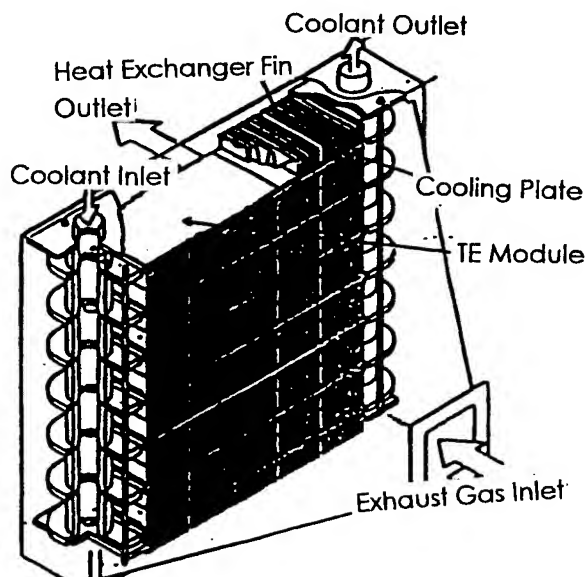


Fig.10 Fin-plate type thermoelectric unit

The electrical characteristics was obtained for various hot air velocities from 5 m/s to 1 m/s and various coolant velocities from 0.5 m/s to 0.25 m/s

as the parameters. The gross power output increases with the hot air velocity, which requires additional auxiliary power. In this case the maximum net power output can be obtained for 2-2.5 m/s in hot air velocity at 403 K in hot air temperature and 0.25 m/s in water velocity. The power density was 400 W/m².

On the basis of the experiment the construction cost and power generation cost were estimated 580,000 yen/kW and 18.5 yen/kWh in the case of 473 K in hot air temperature respectively. The overall energy conversion efficiency was also estimated 3.5%.

A small scale on-site experiment using 60 W class thermoelectric module was carried out in the real incinerator located in Yokohama.

The thermoelectric module made by Global Thermoelectric Inc., (Thermopile 5060) was installed at one of manhole near boiler section. Thermopile was equipped as a part of wall through thermal conducting cylinder made of stainless steel mounted in a durable cemented case.

The preliminary experiment was achieved during three months {6}. The time variations of electrical performance and temperatures at various points are shown in Fig.11. It took about 24 hours to reach the steady state. The power output was obtained 46.81W in maximum when the gas temperature was 871 K. Heat duty was 1.07 kW; that is, heat flux was 17.5 kW/m². The energy conversion efficiency was 4.36% based on the heat duty to the thermoelectric module. The gas temperature changed from 823 K to 973 K frequently and rapidly. In the non-stop run, the power output was suddenly dropped due to the deposition of ash and precipitation on the surface after one week.

In order to avoid the performance degradation due to the ash deposition, an improved experiment was carried out by NKK group{7}. In the experiment ten minutes air blowing per day was operated to the manhole surface. The stable characteristics could be obtained as shown in Fig.12. It can be said that air blowing is effective to keep the electrical performance stable. It is necessary to estimate optimum air blowing conditions such as flow rate,

interval and duration in consideration of temperature reduction effect and additional auxiliary power for a practical system.

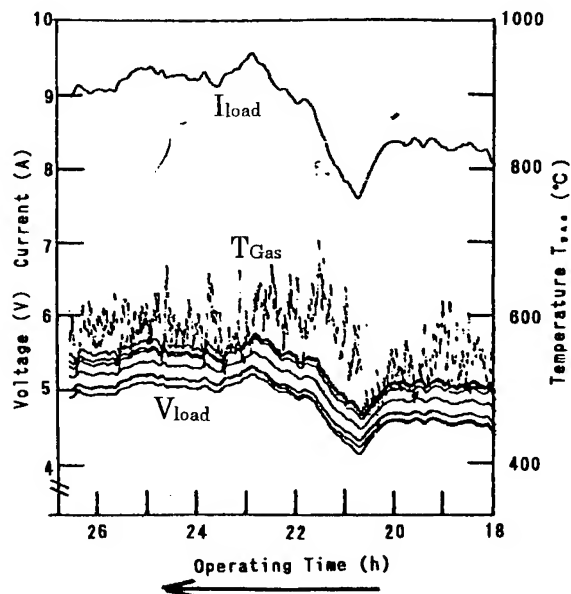


Fig.11 Variation of thermoelectric power generation performance

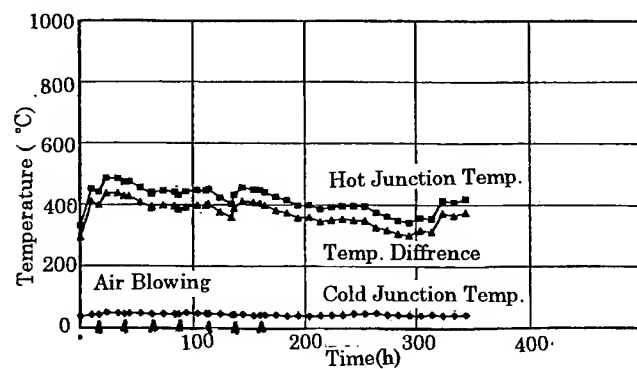


Fig.12 Air-blowing effect on the performance

One dimensional model analysis has been achieved in SIT to design a large scale thermoelectric power generation system. For this application the available temperature range is very wide from 1300 K at the inlet of the furnace to 473 K at the inlet of gas cleaning system equipped at the end of the furnace. As the solid waste is burned for less than atmospheric pressure, the heat transmission is mainly achieved by the radiation heat transfer, which is very sensitive to the temperature difference between the combustion gas and the

furnace wall. Besides, the size of the system is very large as compared with the conventional thermoelectric power systems such as RI thermoelectric power generator. Therefore, one or two dimensional analysis in steady state and transient state have been needed to design the practical system more precisely. As the first stage, one dimensional model taking account of the temperature dependencies of the heat transmission and of the thermoelectric properties along the flow direction has been developed {8}.

In the model the radiation heat transmission was considered to be dominant as compared with the forced convection heat transmission because of the low heat duty combustion in low pressure.

For heat sink side the indirect air cooling system was adopted, and each unit of thermoelectric generator was supplied with the cooling fluid separately. It means the cold junction temperature constant.

The governing equations of one dimensional model based on the heat balance between the combustion gas and thermoelectric power generation system as follows:

$$-GC1(dT_g/dx) = \pi n (\alpha_{p,n} T_h I - 1/2 I^2 R + K(T_h - T_c)) \quad \dots (2)$$

$$= \pi n B(T_g^4 - T_h^4) \quad \dots (3)$$

where G: combustion gas flow rate, C: specific heat of combustion gas, l: generating channel length, T_g: combustion gas temperature, n: number of thermoelectric couples in the vertical direction to the flow, m: number of thermoelectric couples in the longitudinal direction, T_h: hot junction temperature, T_c: cold junction temperature, I: current, R: internal resistance, K: thermal conductance, B: radiation factor related to Stefan Boltzmann's law, $\alpha_{p,n}$: Seebeck coefficient, and

Table 3 Design specifications

Incinerator	
Solid Waste	200 ton/day
Quality	9600 kJ/kg
Temp.	1273 K
Thermal Power	11724 kW
Thermoelectric Generator	
Channel Size	3mx3mx10m
Element Size	0.01mx0.01mx0.01m
TE Material	Pb-Te
Fig. of Merit	0.0015 K ⁻¹
Thermal Cond.	0.37 W/mK
No. of TE Pair	300,000

current, R: internal resistance, K: thermal conductance, B: radiation factor related to Stefan Boltzmann's law, $\alpha_{p,n}$: Seebeck coefficient, and

x: the coordinate along the flow direction.

The design specification is shown Table 3. The temperature profiles along the flow direction are shown in Fig.13. The parameter is the temperature of combustion gas. The cold junction temperature is assumed 330 K constant. The summary of the results is shown in Table 4. According to the analysis, the energy conversion efficiency is highly dependent on the figure of merit, and is relatively low because of large temperature difference between the combustion gas and the hot junction due to low heat transfer performance. If we could get the heat transfer performance between the gas and the wall by two times, the power output would be 1.48 times. In the case of 30m in generating channel, the power output is 1.35 times of that for 10m long.

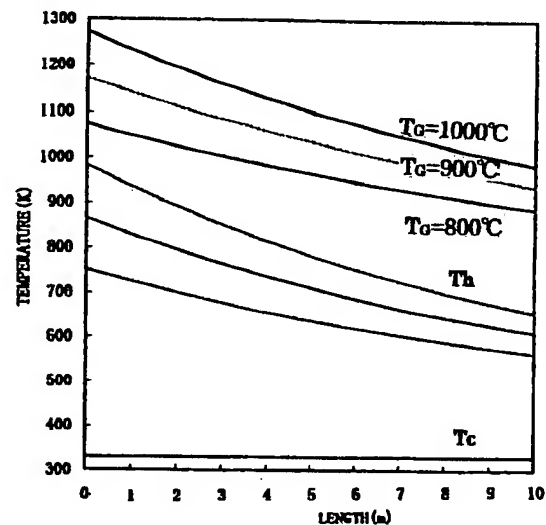


Fig. 13 Temperature profiles along the flow direction

Table 4 Power output and energy conversion efficiency due to input conditions

Temp. (°C)	Figure of Merit (K ⁻¹)	Power Output (kW)	Efficiency (%)
1000	0.001	606.0	2.72
	0.0015	792.8	3.60
	0.002	949.9	4.27
	0.0025	1073.0	4.82
	1/T	1054.0	4.74
900	0.001	432.6	2.16
	0.0015	571.0	2.85
	0.002	684.5	3.42
	0.0025	776.3	3.88
	1/T	755.4	3.77

Technological Problems and Future Prospects

The peculiar points of the thermoelectric power generation system recovering waste heat are summarized as follows:

- 1) The temperature range is wide: that is from 1300K to room temperature.
- 2) The temperature of the heat source is variable and unstable.
- 3) The combustion gas contains ash and is chemically reactive.
- 4) The power capacity is large, and total numbers of thermoelectric element are huge.
- 5) The main mission of the overall system is to process the solid waste and not to generate electricity.

The technological problems are caused by these peculiar points. These can be discussed from the points of software and hardware.

Concerning the former, these are ;

- 1) to determine the design guideline to establish the most useful thermoelectric power generation system in consideration of power generating cost and the environmental conditions such as heat sink source and site.
- 2) to select the power conditions (Power, Voltage, Current) of an unit or module in consideration of reliability, controllability and responsibility and redundancy of the system.

Concerning the latter, these are ;

- 1) to develop the countermeasure to thermal stress to the module due to variation of heat source and start-up and shut-down operation such as stress-free thermoelectric module.
- 2) to develop the countermeasure to the chemically reactive environment and the deposition of fly ash such as air blowing system.
- 3) to develop the high performance ,inexpensive thermoelectric element over the wide temperature range such as FGM(Functionally Graded Materials) element.
- 4) to develop the reliable mass-productive fabrication process of thermoelectric module and unit.

5) to develop the optimum heat exchanging sub-system for both hot side and cold side because the heat flux of the combustion gas is very low and also the water resource as the coolant is limited.

6) to establish the control of quality and quantity of the combustion gas for the incinerator to suppress the variation of the hot junction temperature.

At present the R&D stage of this application is that small scale experiments and conceptual designs have been carried out and also the national projects have been started in Japan as mentioned above. There are many technological problems to be solved for this application.

It can be said that the potential market size is very large to the thermoelectric technology and the thermoelectric system is advantageous to this application as compared with other power generation systems.

The market penetration scenarios of this thermoelectric system are considered as shown in Table 5. The key is the development of advanced thermoelectric materials and low-cost, high-reliability mass-production process.

This application will have large spin-off effect to other waste heat sources from automobile, industrial process and so on.

Table 5 Market penetration scenarios

Generation	Unit Capacity	TE Materials	Module Technology
I	< 1000 kg/day	Bi-Te	Baseline (low Temp.)
II	< 1000 kg/day	Si-Ge (Pb-Te)	Baseline (High Temp.)
III	Middle < 10-50 ton/day	Bi-Te Si-Ge	Baseline improved
IV	Middle Intermittent	Pb-Te	
	Middle	Advanced materials	Advanced Technology
V	Large scale > 200 ton/day	Advanced materials	Advanced Technology

Summary

The characteristics of solid waste resource as the energy source have been identified, which have lead to the classification of thermoelectric power generation system. For the national project supported by Science & Technology Agency the R&D program includes the advanced technology for thermoelectric materials and modules ,and also the demonstration test. For another one the program aims to demonstrate the thermoelectric system by the baseline technology for a real incinerator system. Small scale experiments and conceptual design studies have been carried out in order to obtain the basic data and the prospects. The technological problems and future prospects are summarized.

In conclusion, the thermoelectric power generation system is greatly promising and advantageous to the application to the recovery of heat of combustible solid waste as compared with other power generation systems by means of peculiar characteristics of thermoelectricity.

References

1. T.Kajikawa et al,"Conceptual Design of Thermoelectric Power Generation System Utilizing Heat of Combustible Solid Waste" Proc. of XII ICT,pp491-496(1994)
2. Science & Technology Agency,"The Plan for Research on Efficient Utilization of Waste Energy Such As Heat of Combustible Solid Waste", (1995)
3. N.Hirayama,"Waste Innovation 21st C Project" Japan Waste Research Foundation (1992)
4. T.Kajikawa et al:ed."Thermoelectric Energy Conversion Systems"p159, Realize Inc., (1995)
5. M.Niino:ed."Research on Evaluation of Super High Efficient Hybrid Direct Energy Conversion System"p121, Japanese Association of Frontier Technology (1995)
6. T.Kajikawa et al,"Development of Thermoelectric Power Generation System Utilizing Heat of Combustible Solid Waste",Proc. of XIII ICT,pp314-318 (1995)
7. NKK Inc.,"Report on Utilization of Combustion Heat of Solid Waste" (1995)
8. T.Kajikawa et al,"Development of Thermoelectric Power Generation System Utilizing Heat of Solid Waste",J. of Advanced Science (to be published in 1996)

Thermoelectric Generators in Photovoltaic Hybrid Systems

Rainer Kügele, Werner Roth,
Wolfgang Schulz, Andreas Steinhüser

Fraunhofer Institute for Solar Energy Systems
Oltmannsstr. 5, D-79100 Freiburg, Germany
Tel: +49 761 4588 227
Fax: +49 761 4588 217

Abstract

The supply of distant electric devices that can not be connected to the public electricity grid for reasons of cost, waiting time or due to the need of local flexibility has been a major problem. To date, the power supply of such stand alone systems has been based mainly on battery buffered fossil-fueled motor-generators. Apart from the consumption of limited fossil fuel reserves, the disadvantages of these systems include the creation of noise and exhaust gases, the constant need to obtain fuel and - most important - the high amount of maintenance and repairs. For these reasons, and due to the progress on regenerative energy conversion made in the last decade, battery buffered photovoltaic systems are used more and more often. Their advantages are the high reliability and the low cost of repairs. But far away from the equator, where solar radiation is very low during the winter, large photovoltaic generators are needed to guarantee sufficient reliability. Therefore the system costs are high. Another disadvantage is, that the batteries lifetime in photovoltaic systems is significantly reduced compared to the lifetime in fossil fueled systems.

To avoid these disadvantages, the photovoltaic generator can be combined with fossil fueled power generators. And here, in the medium power range from 10 W up to several hundred W, thermoelectric generators appear to be particularly qualified because of their reliability and lifetime.

In the following paper this (so called) »photovoltaic hybrid system« will be compared to an purely photovoltaic system on the basis of model calculations starting with the solar radiation situation on the earth's surface.

Photovoltaic Systems and the Winter Gap

The essential components of an exclusively photovoltaic power supply are the solar generator and the energy storage, which usually is a lead acid battery (fig. 1). During daylight, the solar generator supplies the load and - if solar radiation is high enough - charges the battery (if it is not already full). In the night or whenever

solar radiation is insufficient, the battery takes over the supply of the load. If the battery reaches the deep discharge limit, the charge controller has to turn off the supply of the load to save the battery. In this case the main objective of the system, the supply of the load, has not been fulfilled and the system is not reliable.

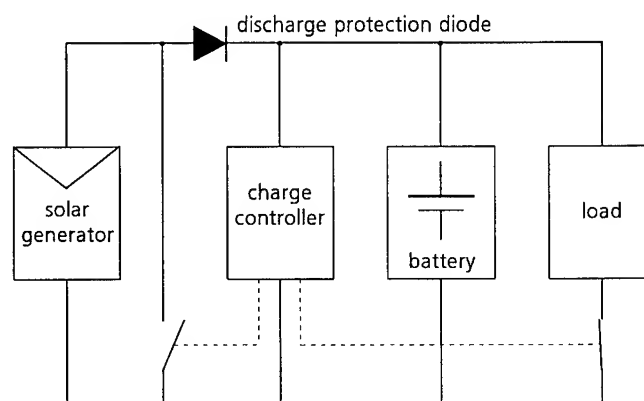


Fig. 1 Block circuit diagram of a photovoltaic system.

The reliability of the system is determined by the dimensions of solar generator and battery compared to the power consumption of the load. The dimensioning of these components strongly depends on the temporal distribution and the annual total of solar radiation at the location of the system (fig. 2).

In regions close to the equator, the monthly average of solar radiation not only is very high, but remains almost constant

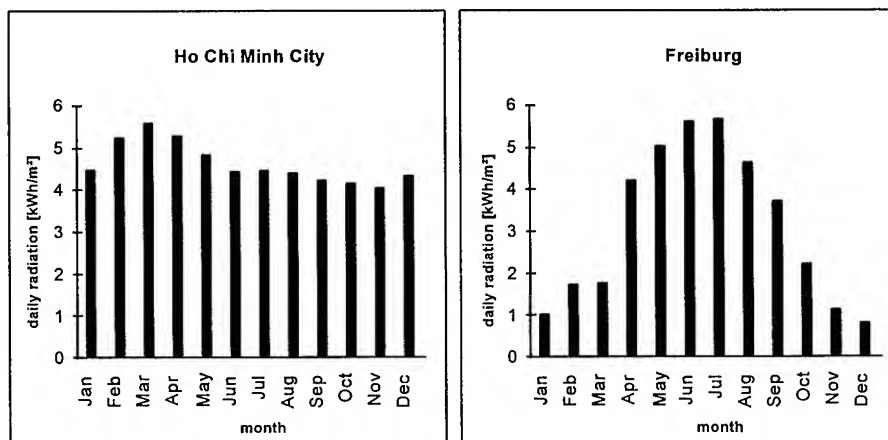


Fig. 2 Monthly average of solar radiation in Ho Chi Minh City (Vietnam) and Freiburg (Germany).

throughout the year. A continuous load of e.g. 50 W can be supplied reliably by a solar generator with about 550 W rated power size and a battery, which must be able to bridge over poor weather periods of up to 8 days.

In high-latitude regions, the monthly average of solar radiation varies strongly throughout the year. For instance, in Central Europe, the amount of solar energy incident during a winter month is about seven times lower than that of a summer month. This is called the »winter gap in solar radiation«.

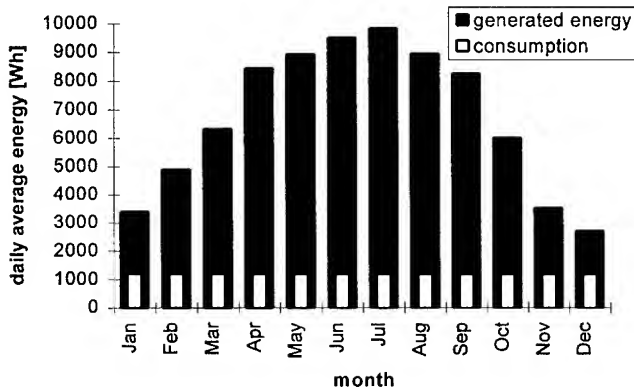


Fig. 3 Monthly energy balances for an exclusively photovoltaic power supply with a continuous power output of 50 W in Freiburg, Germany.

As there are no readily applicable and reliable forms of long-term storage for electricity, the solar generator of the exclusively photovoltaic power supply needs to be large enough to supply the load during a typical winter day. In the example of supplying a continuous load of 50 W with a theoretical reliability of 100% at a location in Central Europe, a solar generator power of about 1900 W is necessary. Although this ex-

pensive solar generator will be significantly oversized throughout spring, summer and autumn (fig. 3), the charge state of the battery is close to the deep discharge limit in the winter. During particularly unfavorable winter weather an uninterrupted supply of the electric load therefore can not be guaranteed. Also the low state of charge of the battery during many weeks of the winter strongly affects the lifetime of the battery due to recrystallisation processes in the porous electrodes.

Hybrid Systems and the Auxiliary Generator

The integration of an auxiliary generator in a photovoltaic system allows the system to compensate the solar deficit in the critical winter months; the size of solar generators therefore can be reduced. These systems are called »photovoltaic hybrid systems« due to the fact, that power generation depends not only on solar radiation, but can also utilize an auxiliary generator on demand.

Apart from wind generators, which can not guarantee the compensation of the winter gap at many locations, fossil fueled generators must be used as auxiliary generators. For large systems with a total power consumption of several kWh per day, diesel generators are usually used as auxiliary power supply. This type of hybrid system has been operated for a number of years e.g. in remote alpine lodges, where connection to the public electricity grid was impracticable. The operation of the generator is done automatically or manually, maintenance and small repairs often can be done by the inhabitants. But experience shows, that the use and transport of diesel has a high risk of pollution. Therefore gas generators are preferred in newer systems.

By contrast, an auxiliary generator is not needed for small photovoltaic systems, because the absolute size of the solar

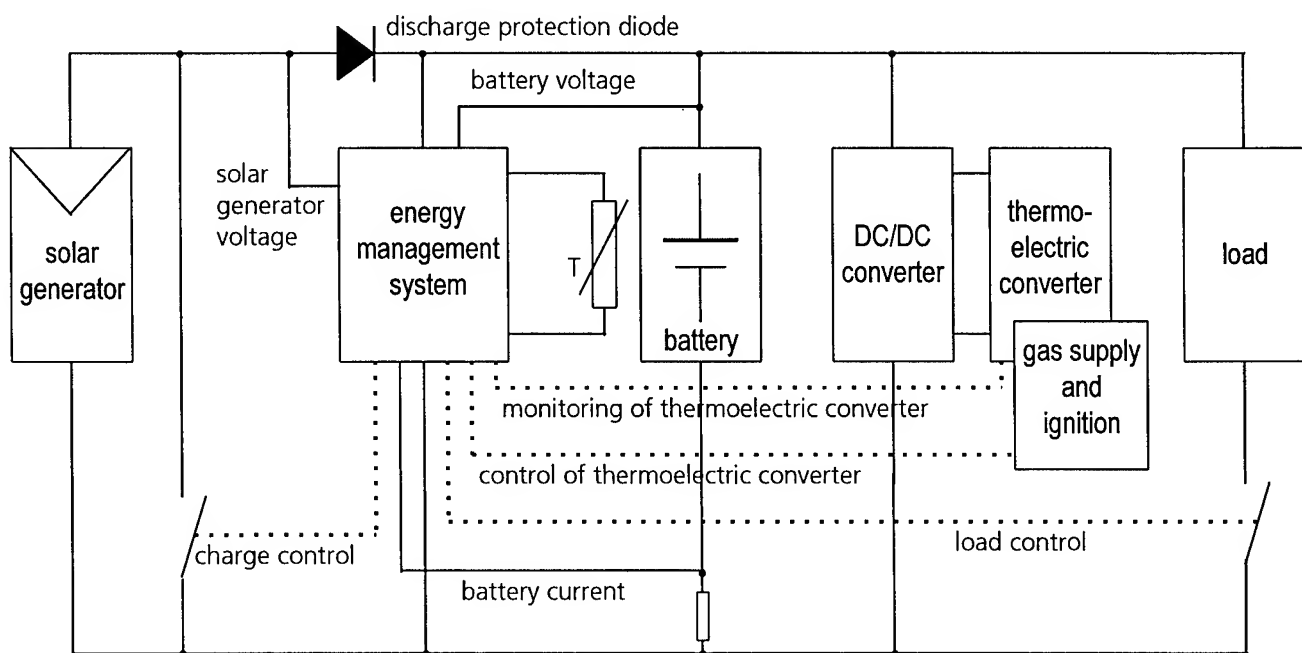


Fig. 4 Block circuit diagram of a hybrid system with photovoltaic and thermoelectric generators.

generator is rather small, even if it is dimensioned for the winter. Examples for such systems are public clocks, emergency phones or lighting systems.

Between these two extremes is the power range of e.g. local radio transmitters, environmental measurement stations or mobile telephone repeaters. They often operate under remote control at isolated sites and have to be autonomously supplied with electricity. The average power consumption of many of these systems is between 50 W and 300 W.

In this power range motor-driven auxiliary generators are unsuitable because of their high demand of maintenance, if they have long idle periods and only a few starts per year. Apart from that, even the smallest commercially available and automatically startable motor-generators are overdimensioned for systems of this size.

On the other hand, the exclusively photovoltaic system represents a high cost burden due to the large photovoltaic generator, that is needed to compensate the winter gap at locations far away from the equator. Here, the combination of the photovoltaic power supply with an auxiliary thermoelectric generator (TEG) offers a less expensive, reliable and environmentally acceptable alternative (fig. 4).

Of course systems like telecommunication repeaters can not be operated manually. Therefore the hybrid system needs to have a so called »intelligent energy management system« (EMS) (fig. 5) which has the objective to turn the thermoelectric generator on and off, so that the load is sufficiently supplied throughout the year using a minimum amount of fuel. The second objective of this microprocessor controlled EMS is to regulate the state of charge of the battery in order to

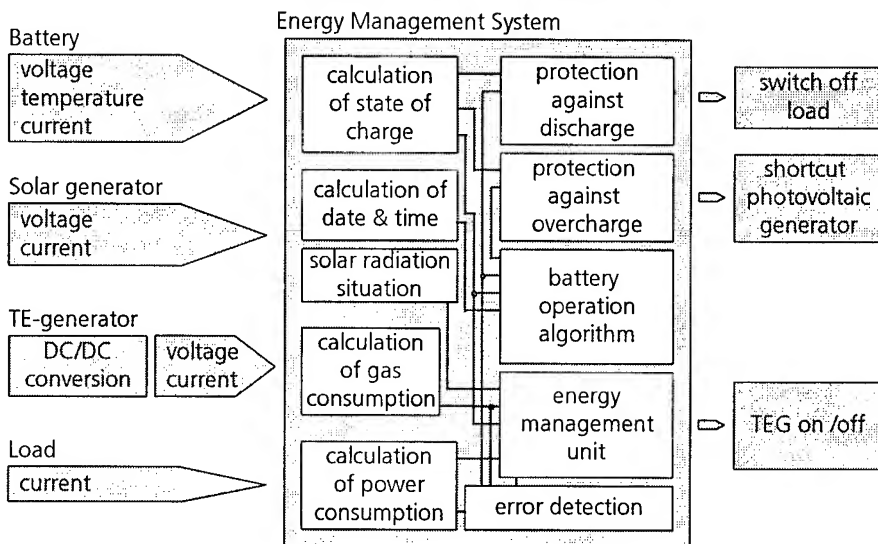


Fig. 5 Automatic energy management system for the autonomous supply of remote systems.

increase the lifetime of the battery. Further features like automatic component test, observation of the operation of the load and measurement of the fuel reserve also can be implemented.

Solar Fraction

The fraction of the annual energy consumption of the load, that is supplied by the TEG, strongly affects the solar generator size needed for 100% reliability of supply. If this fraction is e.g. only 10% and if the TEG is switched on and off at the appropriate times by the EMS, the solar generator size can be reduced by 2/3 as compared with an exclusively photovoltaic powered system (fig. 6). This represents a significant cost advantage. Updating the example, the reliable »hybrid« supply of a continuous load of 50 W at a location in central Europe requires a solar generator of about 550 W in combination with an eight-day battery and a 120 W TEG. The additional demand of electricity would be about 42 kWh per year and could be met with about 100 kg of gas (propane/butane). Due to the existence of the auxiliary generator in this system periods of bad weather now can be compensated using the TEG. Therefore the size of the battery can be reduced to one half, which allows better management of the battery and increases its lifetime. In this case, the continuous load (50 W) in the example before could be supplied by a 4 day battery with a solar generator of 830 W and the 120 W TEG using 60 kWh of fossil fuel per year.

Comparison of the System Costs

The costs of an autonomous power supply are composed of the costs for initial installation and the yearly costs for maintenance, fuel and writing off of the installation in its lifetime.

The total installation costs of the exclusively photovoltaic system (\$ 44000) with location in Freiburg consist of the cost of the 8-day battery (\$ 4000), its housing, charge controller and installation (\$ 12000) and the large photovoltaic generator (modules, framework, cabling and installation, \$ 28000). In

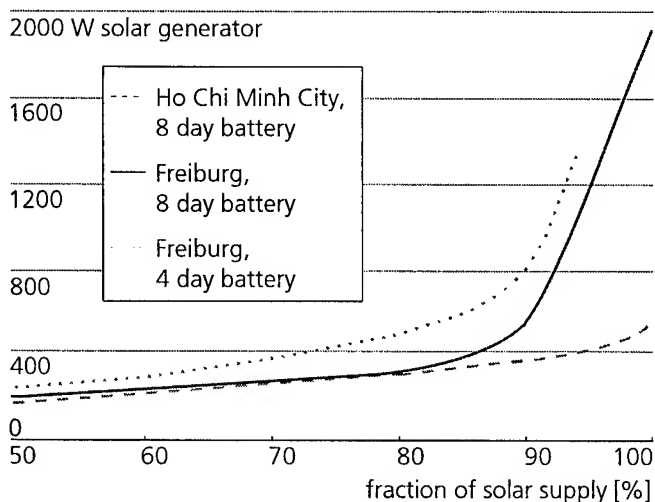



Fig. 6 Size of solar generator versus solar fraction of supply of a load (50 W, constant) in Ho Chi Minh City and Freiburg.

our experience the battery should be renewed after 5 years (\$ 800/y) and the solar generator has a lifetime of more than 20 years (\$ 1400/y). This gives a price of approximately \$ 5/kWh plus maintenance costs.

The hybrid system has a much smaller photovoltaic generator (\$ 13000) but needs a TEG in addition to it (\$ 4700). The lifetime of the smaller battery is estimated to be 7 years (\$ 285/y). Due to the smaller size of the solar generator its writing off is reduced too (\$ 650/y). The estimated lifetime of the TEG is at least 20 y (\$ 235/y). The fuel consumption of the hybrid system adds a further \$ 300/y. The refill and transport of the gas, if it is not too complex and can be done together with the required maintenance, does not raise the costs significantly. So the price of electricity in this case is about \$ 3.35/kWh plus maintenance and transport of the gas.

Due to the cost of fossil fuel, which is estimated to be 2 US\$/kg because of the small amount that is needed, this is even lower than the price per kWh of a power supply, that is totally based on thermoelectric generators or on rankine gas generators (tab. 1). Only if gas is very inexpensive, for instance as it is close to gas pipelines, these exclusively fossil fueled systems would be the better choice.

The result of this calculation shows, that far away from the equator autonomous hybrid power supplies are a financially attractive alternative to exclusively photovoltaic systems on one side, and to pure fossil powered systems on the other. If transport of the gas is very complicated, the exclusively photovoltaic system has the lowest costs, but still will not achieve the same safety of supply as the hybrid system with its two, independent sources of energy.

 Fraunhofer Institut Solare Energiesysteme	Pure Photovoltaic System (Simulation for Ho Chi Minh City)	Pure Photovoltaic System (Simulation for Freiburg)	Hybrid System (Simulation for Freiburg)	Fossil Fueled System: TEG with battery (Calculation)	Fossil Fueled System: TEG without battery (Calculation)	Fossil Fueled System: Rankine- Machine (Simulation)
	General Parameters	General Parameters	General Parameters	General Parameters	General Parameters	General Parameters
location	Ho Chi Minh City, Vietnam	Freiburg, Germany	Freiburg, Germany			
battery	9.6 kWh (8 day)	9.6 kWh (8 day)	4.8 kWh (4 day)	4.8 kWh (4 day)		4.8 kWh (4 day)
charge efficiency	80 %	80 %	80 %	80 %		80 %
lifetime in system	6 years (experience)	< 5 years (experience)	> 7 years	> 8 years		> 8 years
solar generator	550 W	1900 W	830 W			
lifetime	20 years	20 years	20 years			
fossil fueled generator:			TEG 120 W	TEG 120 W	TEG 50 W	Rankine 600 W
efficiency			4 %	4 %	4 %	< 10 %
fuel			propane/butane	propane/butane	propane/butane	propane
lifetime			20 years	20 years	20 years	30 years
load	50 W const.	50 W const.	50 W const.	50 W const.	50 W const.	50 W const.
reliability of supply	99 %	99 %	99.9 %	99 %	99 %	99 %
Electric Energy						
load consumption	438 kWh/y	438 kWh/y	438 kWh/y	438 kWh/y	438 kWh/y	438 kWh/y
photovoltaic total	731 kWh/y	2446 kWh/y	800 kWh/y			
used	520 kWh/y	515 kWh/y	450 kWh/y			
fossil total			60 kWh/y	605 kWh/y	438 kWh/y	660 kWh/y
hours of operation			ca. 600 h/y	ca. 5150 h/y	ca. 8760 h/y	ca. 1100 h/y
fuel consumption			ca. 150 kg/y	ca. 1260 kg/y	ca. 905 kg/y	ca. 807 kg/y
			Propane/Butane	Propane/Butane	Propane/ Butane	Propane
Initial Costs						
system (housing etc.)	12000 US\$	12000 US\$	12000 US\$	12000 US\$	12000 US\$	12000 US\$
battery	4000 US\$	4000 US\$	2000 US\$	2000 US\$		2000 US\$
solar generator (+framework etc.)	8100 US\$	28000 US\$	13000 US\$			
fossil fueled generator			4700 US\$	4700 US\$	3000 US\$	>50000 US\$
Operating Costs						
maintenance	1/summer	1/summer	1/summer	1/summer	1/summer	1/summer
fuel			300 US\$/y	2500 US\$/y	1800 US\$/y	1600 US\$/y
writing off on lifetime						
battery	670 US\$/y	800 US\$/y	285 US\$/y	250 US\$/y		250 US\$/y
generators	405 US\$/y	1400 US\$/y	885 US\$/y	235 US\$/y	150 US\$/y	1660 US\$/y
Price of 1 kWh	2.45 US\$ + maintenance	5 US\$ + maintenance	3.35 US\$ + maintenance + transport	6.8 US\$ + maintenance + transport	4.45 US\$ + maintenance + transport	8 US\$ + maintenance + transport

Tab. 1 Comparison of energy consumption and costs of exclusively photovoltaic systems, the hybrid system and three fossil fueled alternatives.

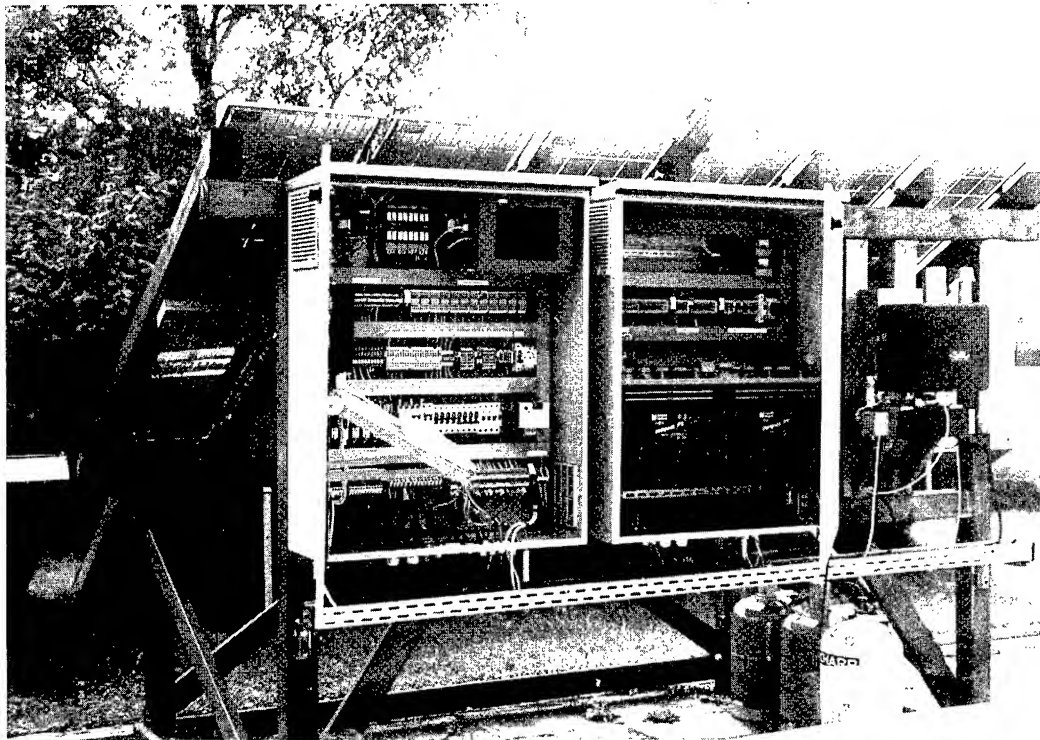


Fig. 7 Picture of the experimental hybrid system on the testing ground of the Fraunhofer ISE

Initial Operating Experience

In order to develop the system technics and to improve the microprocessor controlled energy management (EMS), an experimental hybrid system has been set up on the testing ground of the Fraunhofer Institute for Solar Energy Systems ISE in Freiburg (Germany) in 1995 (fig. 7). This system supplies a load (lamp) of 18 W continuously. The solar generator has a size of 270 W. The auxiliary generator is a TEG 5030 of Global Thermoelectric (Canada). Its rated output power at 12 V is 21.5 W but has been increased to 27 W by redesigning the control electronics and the DC/DC converter. Planning of a further system to supply larger loads has already begun.

Initial experience shows, that even simple energy management systems can achieve a high security of supply but do not use the TEG at the optimum points of time. So the development of an EMS, that reduces the gas consumption of the system is one major aim of this experiment. But there are more possibilities for an improved system management. For example, the lifetime of the batteries not only can be increased by control of complete charging and gassing but also by the use of waste heat from the TEG to warm up the battery room.

However, it has also become evident that the application in hybrid systems results in new demands on the TEG used. There is not much point in applying photovoltaics as a clean and environmentally acceptable source of energy, if the auxiliary generator can not meet high standards regarding its emission and fuel consumption. Therefore, after improvement of control electronics and voltage processing, particular attention

will be paid to the gas burner and the heat transfer to conventional thermoelectric materials. To this purpose a test stand is under construction, where heat transfers can be investigated in detail under well defined conditions. Results from this experiment will be incorporated in a computer simulation, with which the construction of the TEG and the boundary conditions for the gas burner can be optimized. Drawing on the Institute's extensive experience in the construction of highly efficient gas burners, the aim is then to construct a reliable catalytic burner with low emissions for use in thermoelectric converters.

References

- [1] Roth, W., Steinhüser, A. „Autonomie durch Photovoltaiksysteme mit Zusatzstromerzeugern (Autonomy with photovoltaic systems with auxiliary generators)“, Tagungsband Zehntes Symposium Photovoltaische Solarenergie, Staffelstein, Germany, p. 299 (1995)
- [2] Roth, W. „Autonome Stromversorgung mit Photovoltaik-Hybridsystemen (Autonomous power supply with photovoltaic hybrid systems)“, Energie/TerraTec '95, B.G. Teubner Verlagsgesellschaft, Stuttgart, Leipzig, p. 234 (1995)
- [3] Fraunhofer ISE and econcept, PVS for Windows, Simulation and Design Software for Photovoltaic Power Supply Systems (1995)

Power Performance of U.S. Space Radioisotope Thermoelectric Generators

Gary L. Bennett * and E. A. Skrabek **

* Metaspaces Enterprises; 5000 Butte Road; Emmett, Idaho 83617-9500; U.S.A.

** Orbital Sciences Corporation; 20301 Century Boulevard; Germantown, Maryland 20874; U.S.A.

Abstract

Since 1961, the United States has flown 41 radioisotope thermoelectric generators (RTGs) and one reactor to provide power for 25 space systems. Thirty-eight of these nuclear power sources on 22 space systems are still in space or on other planetary bodies. This paper summarizes the design and power performance of each of the basic RTG types that have been flown which have been based on telluride and silicon-germanium thermoelectric elements. To date U.S. radioisotope thermoelectric generators have successfully operated for over 24 years in space. These RTGs have met or exceeded their prelaunch requirements and in so doing they have greatly expanded humanity's knowledge of the universe.

Introduction

Thermoelectrics have enabled the human race to take the first exploratory steps into the outer Solar System and beyond into interstellar space. By virtue of having no moving parts (including no moving fluids) thermoelectric elements have shown themselves to be extremely reliable and long-lived. For example, the Pioneer 10 spacecraft, which has left the Solar System, has been operating since 1972, yielding over 24 years of productive scientific research thanks to four small radioisotope thermoelectric generators (RTGs). In fact, thermoelectrics have shown themselves to be so reliable that all U.S. missions involving space nuclear power (whether RTGs or nuclear reactor) have relied on thermoelectric technology for the conversion of the nuclear-generated thermal power into electrical power [1,2,3]. The only approved future U.S. mission involving nuclear power (Cassini mission to Saturn) will also rely on thermoelectric technology.

Table 1 summarizes the U.S. space systems which have used nuclear power [2]. (The early RTGs were designated by the acronym "SNAP" which stands for Systems for Nuclear Auxiliary Power. The odd-numbered SNAPS were RTGs and the even-numbered SNAPS were reactors.) Because of launch vehicle or spacecraft failures unrelated to the power source, three other systems (Transit 5BN-3, Nimbus B-1, and Apollo 13) were not able to complete their missions. However, these power sources did meet their safety criteria such that no real risk was posed by

the mission failure [4]. In general it can be stated that space nuclear power sources have been used because of their long lifetimes; their relative invulnerability to external environments (such as planetary radiation belts and Martian dust storms); their self-sufficiency (no need to rely on external sources such as the Sun); high reliability; and their capability to provide high power in a relatively compact, low-mass system [1,2,3].

The following sections will summarize the design and power performance of each of the basic RTG types that have been flown:

Telluride Thermoelectric Technology

- SNAP-3B, a 2.1-kg, 2.7-We RTG flown on the navigational satellites Transit 4A and Transit 4B
- SNAP-9A, a >25-We RTG flown on the navigational satellites Transit 5BN-1 and Transit 5BN-2
- SNAP-27, a >70-We RTG used on five Apollo lunar surface missions (Apollo 12, 14, 15, 16, and 17)
- SNAP-19B3, a 28-We RTG design flown on the meteorological satellite Nimbus III, which was then varied for
- SNAP-19, a 41-We RTG design used on the Pioneer 10 and Pioneer 11 spacecraft
- SNAP-19, a 42-We RTG design modified for planetary surface use on the Viking Mars Landers 1 and 2
- TRANSIT RTG, a 35-We RTG used on the Transit TRIAD navigational satellite

Silicon-Germanium Thermoelectric Technology

- Multi-Hundred Watt (MHW) (>150-We) RTGs used on communications satellites LES 8/9 and planetary explorers Voyager 1 and Voyager 2
- General-Purpose Heat Source (GPHS) RTGs (~300 We) in use on Galileo and Ulysses and planned for the Cassini mission

The following sections will briefly describe the different thermoelectric elements used and then show the overall power versus time performance of each of the generators. Factors affecting performance (such as decay of the plutonium-238 radioisotope fuel,

thermoelectric dopant precipitation, and thermoelectric conductivity changes) will be discussed.

The general technology trend for each of these RTG design concepts has been to improve generator performance, efficiency, and specific power. This has led to improvements in the technology of thermoelectric materials, from the telluride (Pb-Te and/or Ag-Sb-Ge-Te) used in the first five RTG concepts to the silicon germanium (Si-Ge) used in the MHW-RTGs and GPHS-RTGs. It will be shown that their performance has demonstrated that these thermoelectric-based nuclear power sources can be safely and reliably engineered to meet a variety of space-mission requirements.

Telluride Thermoelectric Technology

Five different RTG designs have been flown based on telluride (Pb-Te and/or Ag-Sb-Ge-Te) thermoelectric technology. Lead telluride was a natural choice for the early, low-powered missions because of its technical maturity and good thermoelectric properties at the lower RTG operating temperatures (<900 K) employed on these missions.

SNAP-3B RTG Design

The SNAP-3B generators (see Figure 1) were the first known applications of nuclear power in outer space. The SNAP-3B RTGs, which were an outgrowth of the earlier SNAP-3 program, supplied power to the crystal oscillator that was the heart of the electronic system used for doppler-shift tracking in the Transit 4A and Transit 4B navigational satellites [5,6,7].

Each SNAP-3B generator was designed to provide an initial power of 2.7 We with a design life of 5 years and within a mass envelope of 2.1 kg. The thermoelectric power-conversion subsystem consisted of 27 spring-loaded, series-connected pairs of Pb-Te 2N/2P thermoelectric elements operating at a hot-junction temperature of about 783 K and a cold-junction temperature of about 366 K. (The N elements were doped with lead iodide, and the P elements were doped with sodium.) This subsystem had a power-conversion efficiency on the order of 5 to 6 percent. Heat losses were minimized through the use of Min-K 1301 insulating material. The Transit 4A generator (SNAP-3B7) operated with essentially a vacuum inside it to minimize conduction heat losses through the insulation. The Transit 4B generator (SNAP-3B8) was filled with an inert-gas mixture (krypton-hydrogen) to suppress the sublimation of the thermoelectric materials and to minimize the leakage of oxygen into the generator before launch [5,6,7].

Figure 2 shows the SNAP-3B operating data which was limited by telemetry or non-RTG electrical failures on the two spacecraft. Transit 4A had the longest operating life of any satellite launched at the time by the U.S., operating at least until 1976 [6, 7]. Transit 4B was still transmitting signals until 1971 [7]. Clearly RTGs had shown that they were feasible, reliable, and long-lived. In fact, the RTGs performed better than the solar cells, particularly after a high-altitude nuclear test was conducted over the Pacific on 9 July 1962 [7].

From the test experience with the SNAP-3B and later telluride RTGs, two general modes for the degradation of RTG power output were identified:

1. Outgassing of the thermal insulation (water from the Min-K insulation), which can lead to oxygen attack on telluride elements and bonds. (The Min-K insulation can also experience structural instability caused by the loss of impurities during high-temperature service.)
2. Increases in generator internal resistance, which occur when the sublimation or loss of thermoelectric material at the hot junction leads to a reduced leg cross section and hence a higher contact resistance.

The second mode was judged to be the more probable, especially in the Transit 4A generator, which had essentially no inert fill gas [6]. Research was subsequently undertaken to minimize the magnitude of these degradation modes.

SNAP-9A RTG Design

Whereas on Transit 4A and Transit 4B the SNAP-3B RTGs were essentially auxiliary power sources supplementing the main solar power sources, a major step was taken in 1963 when the U.S. Navy launched the Transit 5BN-1 navigational satellite which obtained all of its primary power from an RTG, the SNAP-9A. The RTG approach was selected because RTGs are inherently radiation resistant in contrast to the solar-cell power system of Transit 4B which had been adversely affected by the 1962 high-altitude nuclear explosion [6].

The SNAP-9A RTG design is shown schematically in Figure 3. Each SNAP-9A was designed to provide 25 We at a nominal 6 V for 5 years in space after 1 year of storage on Earth. Seventy pairs of series-connected Pb-Te 2N/2P thermoelectric couples were assembled in 35 modules of two couples each. The hot-junction temperature was calculated to be about 790 K in space at the beginning of life (BOL). The corresponding calculated cold-junction temperature was 450 K. Argon gas was used in each generator to inhibit the

sublimation of the thermoelectric materials and Min-K-1301 insulation was used to minimize heat losses [8].

The power performance of the two SNAP-9A RTGs is shown in Figure 4. While satellite problems prevented achieving full data and operation, the satellite manufacturer, Johns Hopkins University Applied Physics Laboratory, reported that Transit "5BN-1 demonstrated the extreme simplicity with which thermoelectric generators may be integrated into the design, not only to provide the electrical power but also to aid in thermal control" [7]. (Some waste heat from the RTG was used to maintain electronic instruments within the satellite at a temperature near 293 K.)

SNAP-19 RTG Design

Building upon the SNAP-9A development program came the SNAP-19 technology-improvement program which began with SNAP-19B which was specifically designed for use on NASA's Nimbus meteorological satellites. Modifications were made to the SNAP-19B design to power NASA's Pioneer and Viking missions. The Viking SNAP-19 is shown schematically in Figure 5. The Pioneer/Viking telluride thermoelectric element is shown in Figure 6.

Nimbus/SNAP-19. To meet the deliverable power requirement of 50 We after one year in orbit, two SNAP-19B RTGs were connected in parallel, with each RTG in series with its own DC-to-DC converter. In this way a failure of either generator or converter would still permit the radioisotope power system to operate at half power. The thermoelectric elements were made of cold-pressed and sintered Pb-Te. Each RTG thermopile consisted of 90 Pb-Te 3P/2N couples distributed in six modules of three parallel rows of five couples each. The modules were connected in series and enclosed in a magnesium-thorium housing. The couples were metallurgically bonded to iron shoes and maintained under a compressive loading of some 89 N by means of a spring-and-piston assembly. Thermal insulation was provided by Min-K-1301 and the cover gas was argon with an initial fill pressure of 110 kPa. The cover gas reduced the sublimation of the Pb-Te material at its operating temperature (800 K hot junction) and minimized the diffusion of atmospheric oxygen into the RTG before launching [9].

The power performance of the Nimbus III/SNAP-19 RTGs is shown in Figure 7. The two RTGs produced a total of 56.4 We (49.4 We usable) at launch and 47 We one year later. This thermoelectrically derived power comprised about 20 percent of the total power delivered to the regulated-power bus during that time, allowing a number of extremely important atmospheric-sounder

experiments to operate in a full-time duty cycle. The RTGs maintained the total delivered power above the spacecraft load line; without them, the total delivered power would have fallen below the load line about two weeks into the mission [10].

While the Nimbus III flight paved the way for NASA to use RTGs on its planetary missions, the power performance of the SNAP-19B RTGs decreased more rapidly than predicted presumably because of gas-related effects: leakage of argon from the generator; replacement of the argon by helium leaking from the fuel; and possible release of oxygen from the plutonia-based fuel [9]. These sources of degradation were removed in subsequent SNAP-19 designs.

Pioneer/SNAP-19. As noted in the preceding section, additional improvements were made in the basic SNAP-19 design to meet the requirements and expected environments for NASA's Pioneer Jupiter flyby mission [11,12]:

- A TAGS-SnTe/2N thermoelectric element was designed to provide higher efficiency and improved longer term power performance. (The acronym TAGS is derived from the names of its major constituents: tellurium, antimony, germanium, and silver. TAGS is a solid solution of silver antimony telluride in germanium telluride. TAGS is an undoped inherent "P" material. The particular material used is sometimes referred to as TAGS-85, and it had a thin SnTe segment at the hot side. The N-leg was 3M-TEGS-2N(M) Pb-Te.)
- The electrical circuitry was modified to limit the magnetic field from the RTG to very low levels.
- The fill gas was a 75:25 helium-argon mixture, and a zirconium getter was added to eliminate any oxygen in the RTG.
- With the exception of the O-ring seal around the RTG electrical connector all gas leakage paths were removed by using welds.

Figure 8 shows the power history of the Pioneer/SNAP-19 RTGs. The excellent power performance allowed NASA to retarget Pioneer 11 for a flyby of Saturn. Pioneer 10 was the first spacecraft to visit Jupiter (passing within 42,800 km -- the closest pass ever achieved) and Pioneer 11 was the first spacecraft to visit Saturn (passing within 20,900 km of the giant planet). Pioneer 11 continued providing data for 22 years after launch out to over 6.4×10^9 km from Earth until forced to shut down because a high-voltage relay could no longer be activated. Pioneer 10, which is now about 9.6×10^9 km from Earth, is the most distant

object built by humans and it is still sending back data about the Sun's influence in deep space. Pioneer 10 should have enough power to continue providing data until 1999. This is outstanding performance considering that the prelaunch requirement for the Pioneer/SNAP-19 RTGs was to provide power for two years in space.

Viking/SNAP-19. The SNAP-19 design was again modified, this time for operation on the surface of Mars. Each of the two Viking Landers carried two series-connected RTGs for the primary source of power. These RTGs powered the scientific instruments and recharged four nickel-cadmium batteries. The RTGs also supplied the Landers with thermal power to maintain the Lander electronics at specified operational temperatures. Following the 11- to 12-month cruise to Mars from Earth, each RTG was to produce a minimum of 35 We during the 90-day mission on the surface of Mars (the primary mission) [13].

Among the modifications to the Pioneer/SNAP-19 RTG design was the addition of a dome reservoir shown in Figure 5 to allow a controlled interchange of gases to minimize heat-source operating temperatures up to launch while maximizing electrical power output at the end of mission [13]. The Viking/SNAP-19 RTGs also had to undergo a high-temperature (400 K) sterilization and have the ability to withstand the thermal cycling caused by the rapid and extreme temperature changes of the Martian day-night cycle [13].

The power history of the Viking/SNAP-19 RTGs is shown in Figure 9 [14]. All four RTGs met the 90-day requirement. Both Landers successfully operated for several years in an extended mission mode. Viking Lander 2 (VL-2) was inadvertently shut down on 1 February 1980, causing a loss of RTG data. While the continuous operation of the VL-2 relay transmitter indicated the RTGs were still operating all contact was lost when the last Viking Orbiter depleted its propellant in August 1980. In November 1982, all contact with VL-1 were lost after commands had been sent to change the battery charging cycle. The RTGs on VL-1 were capable of providing sufficient power for operation until 1994 -- *18 years beyond the mission requirement.*

Both the Pioneer and the Viking SNAP-19 RTGs demonstrated the operability and usefulness of RTGs in interplanetary spacecraft. In fact neither of these missions could have been performed as they were without nuclear power. In short nuclear power was an enabling technology for these missions. All of these RTGs performed beyond their mission requirements. The principal contribution to degradation was judged to come from gas effects. It is evident from the

outstanding performance data obtained from the Pioneer and Viking SNAP-19s that the changes made to the original SNAP-9A and Nimbus/SNAP-19 designs significantly minimized the degradation effects experienced in these earlier RTG designs.

SNAP-27 RTG.

To power the experiments of NASA's Apollo Lunar Surface Experiments Package (ALSEP) through the long lunar day-night cycle, a new RTG design, known as the SNAP-27, was developed. The requirement was to provide ≥ 63.5 We at 16 V DC one year after lunar emplacement. (In the case of Apollo 17, the requirement was 69 We two years after emplacement.)[15] A schematic of the SNAP-27 RTG is shown in Figure 10.

SNAP-27's thermoelectric conversion subsystem consisted of 442 thermoelectric couples made of Pb-Te 3N/3P elements arranged in two series strings of 221 couples connected in parallel. The couples were hermetically sealed in the converter under an argon cover gas at 172 kPa and thermally insulated from each other by powdered Min-K. Design analysis and ground tests indicated that the hot-junction temperature was about 866 K, and the cold-side thermoelectric temperature was maintained at about 547 K in the normal operating mode (lunar environment). (The Apollo 12/SNAP-27 initial data indicated a lunar night-day variation of about 855 K to 890 K at the hot junction and about 470 K to 520 K at the cold junction.)[15]

A total of five SNAP-27 RTGs were placed on the Moon by the Apollo astronauts. The performance of all five SNAP-27 RTGs is shown in Figure 11 [16]. In each case all of the RTGs exceeded their mission requirements in both power and lifetime. Through this performance beyond mission requirements, the SNAP-27 RTGs enabled the ALSEP stations to gather long-term scientific data on the internal structure and composition of the Moon, the composition of the lunar atmosphere, the state of the lunar interior, and the genesis of lunar surface features. All five RTG-powered ALSEPs were operating when NASA shut down the stations on 30 September 1977 for budget reasons.

TRANSIT RTG.

The TRANSIT RTG was developed specifically as the primary power source for the U.S. Navy's TRIAD navigational satellite. Auxiliary power was provided by four solar-cell panels and one 6-Ah nickel-cadmium battery. The power requirement on the TRANSIT RTG was to provide 30 We after five years at a minimum of

3 V. A 12-sided converter (see Figure 12) was built using low-mass Pb-Te thermoelectric panels ("Isotec") that operated at a low hot-side temperature (673 K) in a vacuum, thereby eliminating the need for hermetic sealing and a cover gas to inhibit the sublimation of thermoelectric material. Each of the 12 Isotec panels contained 36 Pb-Te 2N/3P couples arranged in a series-parallel matrix with four couples in a row in parallel and nine rows in series. The primary insulation consisted of 32 alternate layers of aluminum foil and aluminum-opacified quartz paper [17].

The short-term objectives of the TRIAD satellite were demonstrated, including a checkout of RTG performance; however, a telemetry-converter failure on 2 October 1972 caused a loss of further RTG telemetry data. The TRIAD satellite continued to operate into the 1980s by providing useful magnetometer data. This showed that the TRANSIT RTG is a dependable power source.

Silicon-Germanium Thermoelectric Technology

The use of high-temperature Si-Ge alloys as thermoelectric power-conversion materials was a direct outgrowth of spacecraft requirements for higher RTG power levels and lower RTG masses. To a first approximation, telluride alloys can be used to about 900 K before materials properties and the figure of merit become concerns. Si-Ge alloys can be used to about 1300 K and offer the potential of higher power with an improved system efficiency. The main advantage is that Si-Ge alloys allow the cold-side temperature to be raised thereby improving heat rejection which in turn improves the specific power of the RTG. Moreover, Si-Ge RTGs generally do not require an inert atmosphere for space operation because the temperatures (≤ 1300 K) are normally below those at which sublimation presents a problem to silicon-nitride-coated Si-Ge. (The use of multifoil insulation does necessitate sealing the RTG under an inert atmosphere on Earth to protect the foil against oxidation. The cover gas is then vented once the RTG is in space.) Two different Si-Ge RTG designs have been used by the U.S. in space: the Multi-Hundred Watt (MHW) RTG and the General-Purpose Heat Source (GPHS) RTG.

Multi-Hundred Watt (MHW) RTG

The MHW-RTG was designed to accommodate a range of missions. MHW-RTGs are currently in use on Lincoln Experimental Satellites 8 and 9 (LES 8/9), which required 125 W per RTG at the end of mission (EOM) five years after launch, and the Voyager 1 and 2 spacecraft which required 128 We minimum per RTG at four years after launch. The design of the

MHW-RTG, shown in Figure 13, involved a new heat source and the use of 312 Si-Ge thermoelectric couples, called unicouples. Figure 14 is a schematic of the uncouple which is used in both the MHW-RTG and the GPHS-RTG [18].

The 312 unicouples are arranged in 24 circumferential rows, each row containing 13 unicouples individually bolted to the outer case. The overall diameter of the MHW-RTG was 39.73 cm, and its length was 58.31 cm. The average MHW-RTG flight masses were 39.69 kg for LES 8/9 and 37.69 kg for Voyager 1/2. The design hot-junction temperature was 1273 K (hot-shoe temperature 1308 K) with a cold-junction temperature of 573 K. The MHW-RTGs easily met their original requirements for LES 8/9 and Voyager 1/2. All four spacecraft are still operating over 19 years after their launches. As a result of this extended operation, LES 8/9 was able to provide communications coverage for a number of Department of Defense operations and Voyager 2 was sent on an extended mission to Uranus and Neptune becoming the first spacecraft to visit the outermost two gas giants.

During and after the MHW-RTG development program, a number of analytical and experimental studies were undertaken to determine the long-term performance of the MHW-RTGs. In addition to the obvious decay of the plutonium-238 fuel, four potential contributors to power degradation were identified: (1) dopant-precipitation effects; (2) increases in the conductance of the thermal insulation; (3) degradation of the electrical insulation; and (4) carbon dioxide effects [18]. While dopant precipitation provides some contribution to the early decay of electrical power, the principal contribution to the decay comes from the natural decay of the plutonium-238 radioisotope used in the fuel. The successful performance of the MHW-RTGs led to the selection of the Si-Ge uncouple technology for the Galileo and Ulysses RTGs which are the largest, highest powered, highest specific power RTGs yet flown.

General-Purpose Heat Source (GPHS) RTG

The GPHS-RTG, shown schematically in Figure 15, is designed to provide at least 285 We at beginning of mission (BOM). (Actually, at the time of fueling the GPHS-RTG can provide over 300 We.) To achieve this power the GPHS-RTG converter contains 572 unicouples of the MHW-RTG design connected in a series-parallel network. Overall diameter of the converter with fins is 42.2 cm and the length is 114 cm. The mass of the GPHS-RTG is 55.9 kg. Three GPHS-RTGs are currently operating in space: two on the Galileo spacecraft and one on the Ulysses spacecraft. Figure 16 shows the power performance of

all the Si-Ge RTGs, both MHW-RTGs and GPHS-RTGs. To date these GPHS-RTGs have met all their requirements (especially noteworthy given the Challenger-induced launch delays of both spacecraft) allowing Ulysses to complete the first-ever polar exploration of the Sun and Galileo to conduct an extended flight through the inner Solar System and to reach Jupiter in December 1995. The continuing good performance of the GPHS-RTGs will enable Ulysses to conduct an extended mission and Galileo to conduct its long-delayed primary mission of being the first orbiting spacecraft to explore Jupiter and its principal satellites [19]. The continuing successful use of the GPHS-RTGs on Galileo and Ulysses has led to their selection for the Cassini mission to Saturn which has a planned 1997 launch date.

Some Observations on Power Degradation Mechanisms

There are only a few causes of power degradation in RTGs. One that is inherent to all of them is the gradual decrease in thermal power caused by the natural radioactive decay of the radioisotope fuel. The thermal power loss rate is approximately 0.8% per year for plutonium-238 which is the radioisotope that has been used in all U.S. RTGs. This decay is independent of the thermoelectric materials used in the RTG.

A second mechanism encountered in most of the RTGs flown is sublimation of the thermoelectric material from the hot end of the thermoelectric element or couple. This sublimation occurs because the thermoelectric materials are operated near their melting points in order to achieve the highest practical efficiency. However, operating at such high temperatures results in rather high vapor pressures at the hot end of the couple. In early generators, this led to "bullet-nosing" of the legs with a resulting increase in the internal resistance of the device. This phenomenon has been effectively eliminated with the Si-Ge systems through the use of a silicon nitride coating that covers 97% of the couple's surface. In the telluride systems, a combination of an inert cover gas and packed astroquartz fibers around the legs have greatly reduced this mechanism, although not entirely eliminating it. Fortunately, by the time that these fixes begin to lose their effectiveness, the hot-side temperature has been reduced sufficiently as a result of power decay from the plutonium-238 to reduce the vapor pressure of the legs significantly, further ameliorating the effects of this mechanism.

For Si-Ge couples the primary degradation mechanism is related to dopant precipitation along the thermal gradient of the legs. This mechanism approaches an asymptotic limit in somewhat over five years of

operation. This effect causes increases in Seebeck coefficients and electrical resistivity, and a decrease in thermal conductivity, with an overall decrease in power with time.

The remaining mechanisms are associated with the effectiveness of the thermal insulation systems in the generators. Added heat leaks through the insulation mean that less thermal power is available to the thermoelectric elements for conversion to electrical power. As mentioned above, cover gases have been used in the telluride systems to minimize sublimation. The helium gas resulting from the alpha-particle decay of the plutonium-238 fuel sources is vented into this cover gas. This helium degrades the effectiveness of the bulk insulation to some extent, but the use of strategically placed O-rings leads to a preferential loss of helium over the argon or krypton cover gases, thereby minimizing the power loss over time.

Since the Si-Ge systems utilize vacuum foil insulation, the helium is vented to space and therefore causes no problems with the insulation. However, carbon monoxide and oxygen from the heat source and astroquartz fiber spacers can eventually oxidize the molybdenum foils, reducing their reflectivity and increasing the heat loss through the insulation. All of the RTGs since the Galileo program have had their fuel processed to a plutonia stoichiometry of about $\text{PuO}_{1.98}$ to reduce the oxygen vapor pressure. This greatly minimizes the generation of carbon monoxide during operating and effectively eliminates the oxidation problem.

Concluding Remarks

As has been shown, the thermoelectric technologies used in U.S. RTGs from SNAP-3B to the GPHS-RTG have met or exceeded their mission requirements by providing power at about or above that required and beyond the planned mission lifetime. Thermoelectric conversion has not only enabled the successful operation of such challenging missions as Pioneers 10/11, Viking Landers 1/2, Apollo lunar surface experiments, Voyagers 1/2, Galileo, and Ulysses it has also enabled the first flight of a space nuclear reactor (SNAP-10A in 1965) and all but two of the former Soviet Union's space nuclear power sources [3]. Clearly thermoelectric conversion has enabled a range of reliable, long-lived power sources that in turn have enabled a range of challenging space missions that in many cases could not have otherwise been accomplished.

Acknowledgments

The authors acknowledge with deep thanks the contributions made by the staff members of Lockheed-Martin Astro Space, Teledyne Brown Engineering Energy Systems, TRW, EG&G Mound Applied Technologies, Savannah River Plant and Laboratory, Los Alamos National Laboratory, Oak Ridge National Laboratory, Sandia National Laboratories, Ames Laboratory, Orbital Sciences Corporation, NUS Corporation, the Johns Hopkins University Applied Physics Laboratory, Westinghouse Hanford Company, Battelle Columbus Laboratories, the Jet Propulsion Laboratory, General Atomic, Thermo Electron Corporation, and the 3M Company.

References

- [1] G. L. Bennett, J. J. Lombardo, and B. J. Rock, "U.S. Radioisotope Thermoelectric Generator Space Operating Experience (June 1961 - December 1982)", paper 839171, *Proceedings of the 18th Intersociety Energy Conversion Engineering Conference*, held in Orlando, Florida, 21-26 August 1983. (This paper was reprinted as "US Radioisotope Thermoelectric Generators in Space" in *The Nuclear Engineer*, Vol. 25, No. 2, pp. 49-58, March/April 1984.)
- [2] G. L. Bennett, R. J. Hemler, and A. Schock, "Space Nuclear Power: A Status Review", AIAA paper 95-0025, presented at the AIAA 33rd Aerospace Sciences Meeting and Exhibit, held in Reno, Nevada, 9-12 January 1995 (to be published in the *Journal of Propulsion and Power*).
- [3] G. L. Bennett, "Space Applications", Chapter 41 of *CRC Handbook of Thermoelectrics*, David M. Rowe, editor, CRC Press, Inc., Boca Raton, Florida, 1995.
- [4] G. L. Bennett, "Safety Aspects of Thermoelectrics in Space", Chapter 43 of *CRC Handbook of Thermoelectrics*, David M. Rowe, editor, CRC Press, Inc., Boca Raton, Florida, 1995.
- [5] P. J. Dick and R. E. Davis, "Radioisotope Power System Operation in the Transit Satellite", Paper No. CP 62-1173, AIEE Summer General Meeting, held in Denver, Colorado, 17-22 June 1962.
- [6] Hittman Associates, Inc., *Radioisotope Powered Space Systems*, NYO-3165-11, 23 August 1963.
- [7] Johns Hopkins University Applied Physics Laboratory, *Artificial Earth Satellites Designed and Fabricated by the Johns Hopkins University Applied Physics Laboratory*, JHU/APL Report SDO-1600 (revised), August 1980.
- [8] P. J. Dick, *SNAP-9A Quarterly Progress Report No. 2, Radioisotope-Fueled Thermoelectric Power Conversion System Development, December 1, 1961 through February 28, 1962*, Martin Nuclear Division report MND-P-2700-2, undated.
- [9] A. W. Fihelly and C. F. Baxter, "Orbital Performance of the SNAP-19 Radioisotopic Thermoelectric Generator Experiment", Paper 719152, *Proceedings of the 6th Intersociety Energy Conversion Engineering Conference*, held in Boston, Massachusetts, 3-5 August 1971.
- [10] H. Jaffe and P. O'Riordan, "Isotope Power Systems for Unmanned Spacecraft Applications", Paper 729088, *Proceedings of the 7th Intersociety Energy Conversion Engineering Conference*, held in San Diego, California, 25-29 September 1972.
- [11] E. A. Skrabek and D. S. Trimmer, "Properties of the General TAGS System", Chapter 22 of *CRC Handbook of Thermoelectrics*, David M. Rowe, editor, CRC Press, Inc., Boca Raton, Florida, 1995.
- [12] C. J. Goebel, "SNAP-19 Pioneer 10 and 11 RTG Deep Space Performance", Paper 759130, *Record of the 10th Intersociety Energy Conversion Engineering Conference*, held in Newark, Delaware, 18-22 August 1975.
- [13] W. M. Brittain, "SNAP-19 Viking RTG Mission Performance", Paper 769255, *Proceedings of the 11th Intersociety Energy Conversion Engineering Conference*, held in State Line, Nevada, 12-17 September 1976.
- [14] W. M. Brittain and E. A. Skrabek, "SNAP 19 RTG Performance Update for the Pioneer and Viking Missions", *Proceedings of the 18th Intersociety Energy Conversion Engineering Conference*, held in Orlando, Florida, 21-26 August 1983.
- [15] A. A. Pitrolo, B. J. Rock, W. C. Remini, and J. A. Leonard, "SNAP-27 Program Review", Paper 699023, *Proceedings of the 4th Intersociety Energy Conversion Engineering Conference*, held in Washington, D. C., 22-26 September 1969.
- [16] J. R. Bates, W. W. Lauderdale, and H. Kernaghan, *ALSEP Termination Report*, NASA Reference Publication 1036, 1979.
- [17] G. B. Bradshaw and F. D. Postula, "Beginning of Mission Flight Data on the TRANSIT RTG", Paper 739091, *Proceedings of the 8th Intersociety Energy Conversion Engineering Conference*, held in Philadelphia, Pennsylvania, 13-16 August 1973.

[18] C. E. Kelly, "The MHW Converter (RTG)", Paper 759132, *Record of the 10th Intersociety Energy Conversion Engineering Conference*, held in Newark, Delaware, 18-22 August 1975.

[19] G. L. Bennett, R. J. Hemler, and A. Schock, "Development and Use of the Galileo and Ulysses Power Sources", *Space Technology*, Vol. 15, No. 3, pp. 157-174, May 1995 (based on Paper IAF-94-R.1.362 presented at the 45th Congress of the International Astronautical Federation held in Jerusalem, Israel, 9-14 October 1994).

Table 1. Summary of Space Nuclear Power Systems Successfully Launched by the United States

Power Source ^a	Number of NPS	Initial Avg Power/NPS	Spacecraft (Mission Type)	Launch Date ^b	Initial Orbit	Status
SNAP-3B7	1	2.7 W	Transit 4A (Navigational)	29 Jun 1961 (ETR)	~890 x 1000 km 67.5°, 104 min.	RTG operated for ~15 years. Satellite now shutdown but operational.
SNAP-3B8	1	2.7 W	Transit 4B (Navigational)	15 Nov 1961 (ETR)	~960 x 1130 km 32.4°, 106 min.	RTG operated for 9 years. Satellite operation was intermittent after 1962 high-altitude nuclear test. Last reported signal in 1971.
SNAP-9A	1	>25.2 W	Transit 5BN-1 (Navigational)	28 Sep 1963 (WTR)	~1090 x 1150 km 89.9°, 107 min.	RTG operated as planned. Non-RTG electrical problems on satellite caused satellite to fail after 9 months.
SNAP-9A	1	26.8 W	Transit 5BN-2 (Navigational)	5 Dec 1963 (WTR)	~1080 x 1110 km 90.0°, 107 min.	RTG operated for >6 years. Satellite lost navigational capability after 1.5 years.
SNAP-10A	1	>500 W	SNAPSHOT (Experimental)	3 Apr 1965 (WTR)	1296 x 1329 km 90.2°, 111.5 min.	Reactor successfully operated for 43 days until shutdown by electrical component failure on spacecraft.
SNAP-19B3	2	28.2 W	Nimbus III (Meteorological)	14 Apr 1969 (WTR)	1070 x 1131 km 99.9°, 107 min.	RTGs operated for >2.5 years (no data taken after that).

**Table 1. Summary of Space Nuclear Power Systems Successfully Launched
by the United States (continued)**

SNAP-27	1	73.6 W	Apollo 12 (Lunar)	14 Nov 1969 (KSC)	Lunar trajectory	RTG operated for ~8 years (until station was shut down).
SNAP-27	1	72.5 W	Apollo 14 (Lunar)	31 Jan 1971 (KSC)	Lunar trajectory	RTG operated for ~6.5 years (until station was shut down).
SNAP-27	1	74.7 W	Apollo 15 (Lunar)	26 Jul 1971 (KSC)	Lunar trajectory	RTG operated for >6 years (until station was shut down).
SNAP-19	4	40.7 W	Pioneer 10 (Planetary)	2 Mar 1972 (ETR)	Solar system escape trajectory	RTGs still operating. Spacecraft successfully operated to Jupiter and is now beyond orbit of Pluto.
SNAP-27	1	70.9 W	Apollo 16 (Lunar)	16 Apr 1972 (KSC)	Lunar trajectory	RTG operated for ~5.5 years (until station was shut down).
Transit-RTG	1	35.6 W	"Transit" (TRIAD-01-1X)	2 Sep 1972 (WTR)	716 x 863 km 90.1°, 101 min.	RTG still operating.
SNAP-27	1	75.4 W	Apollo 17 (Lunar)	7 Dec 1972 (KSC)	Lunar trajectory	RTG operated for ~5 years (until station was shut down).
SNAP-19	4	39.9 W	Pioneer 11 (Planetary)	5 Apr 1973 (ETR)	Solar system escape trajectory	RTGs still operating. Spacecraft successfully operated to Jupiter and Saturn and is now beyond orbit of Pluto. Spacecraft shut down.
SNAP-19	2	42.3 W	Viking 1 (Mars lander)	20 Aug 1975 (ETR)	Trans-Mars trajectory	RTGs operated for >6 years (until lander was shut down).

**Table 1. Summary of Space Nuclear Power Systems Successfully Launched
by the United States (continued)**

SNAP-19	2	43.1 W	Viking 2 (Mars lander)	9 Sep 1975 (ETR)	Trans-Mars trajectory	RTGs operated for >4 years until relay link was lost.
MHW-RTG	2	153.7 W	LES-8 (Communications)	14 Mar 1976 (ETR)	35,787 km 25.0°, 1436 min.	RTGs still operating.
MHW-RTG	2	154.2 W	LES-9 (Communications)	14 Mar 1976 (ETR)	35,787 km 25.0°, 1436 min.	RTGs still operating.
MHW-RTG	3	159.2 W	Voyager 2 (Planetary)	20 Aug 1977 (ETR)	Solar system escape trajectory	RTGs still operating. Spacecraft successfully operated to Jupiter, Saturn, Uranus, Neptune, and beyond.
MHW-RTG	3	156.7 W	Voyager 1 (Planetary)	5 Sep 1977 (ETR)	Solar system escape trajectory	RTGs still operating. Spacecraft successfully operated to Jupiter, Saturn, and beyond.
GPHS-RTG	2	287.1 W	Galileo (Jupiter orbiter)	18 Oct 1989 (KSC)	Trans-Jupiter trajectory	RTGs still operating.
GPHS-RTG	1	~282 W (power inferred)	Ulysses (Solar orbiter)	6 Oct 1990 (KSC)	Solar polar orbit	RTG still operating.

^aSNAP stands for Systems for Nuclear Auxiliary Power. All odd-numbered SNAP power plants use radioisotope fuel. Even-numbered SNAP power plants have nuclear fission reactors as a source of heat. MHW-RTG stands for the Multihundred Watt Radioisotope Thermoelectric Generator. GPHS-RTG stands for the General-Purpose Heat Source Radioisotope Thermoelectric Generator.

^bKey to launching stations: ETR, Eastern Test Range; WTR, Western Test Range; KSC, Kennedy Space Center.

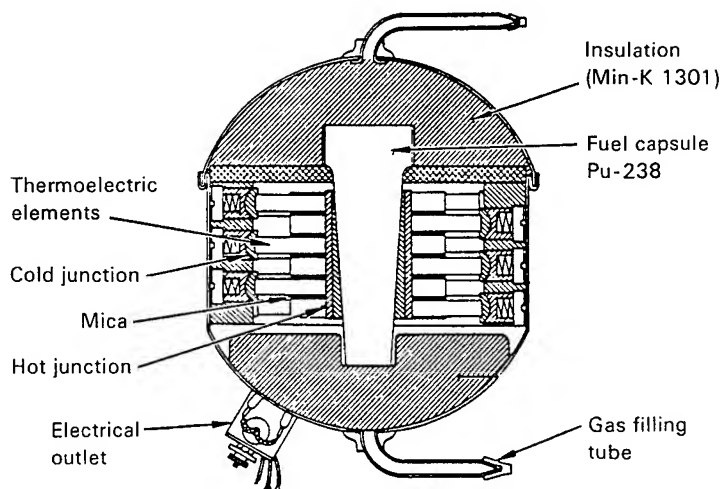


Figure 1. Schematic of the 2.7-We SNAP-3B radioisotope thermoelectric generator (RTG). The overall dimensions were 12.1 cm in diameter by 14 cm high and the mass was 2.1 kg.

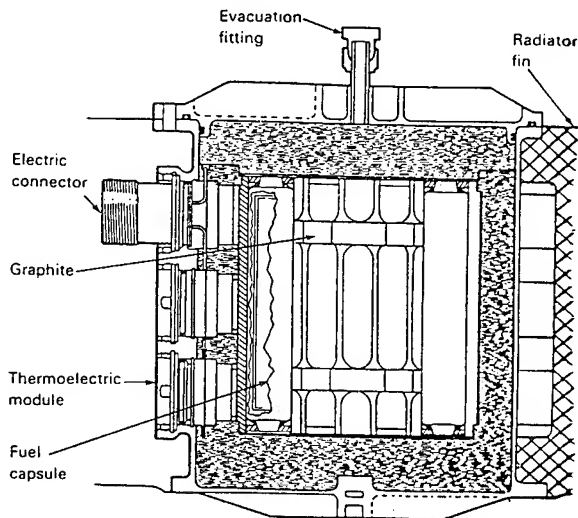


Figure 3. Schematic of the >25-We SNAP-9A RTG. The overall housing dimensions were 22.9 cm in diameter and 21.3 cm high. The fin span was 50.8 cm. The mass was 12.3 kg.

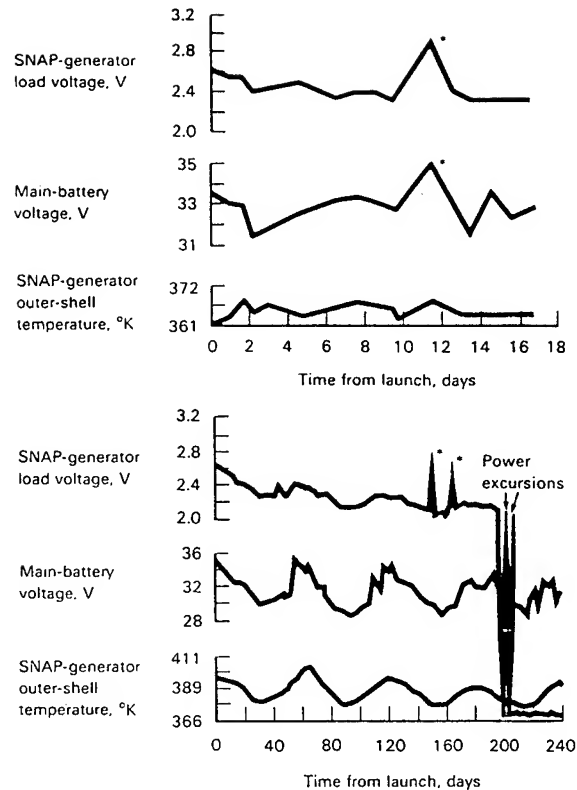


Figure 2. SNAP-3B operating data telemetered from Transit 4A (top) and Transit 4B (bottom). Voltage changes resulted from load switching. The power excursion on Transit 4B probably resulted from a capacitor failure (not on the RTG).

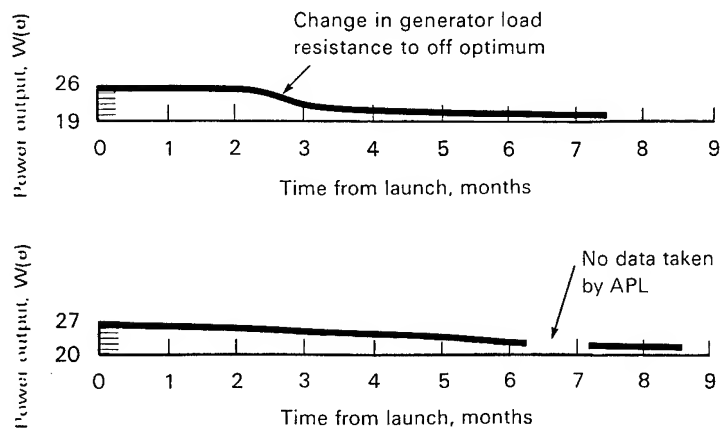


Figure 4. SNAP-9A power performance (smoothed data) as telemetered by Transit 5BN-1 (top) and Transit 5BN-2 (bottom). The gap in the Transit 5BN-2 curve reflects the period when data were not taken.

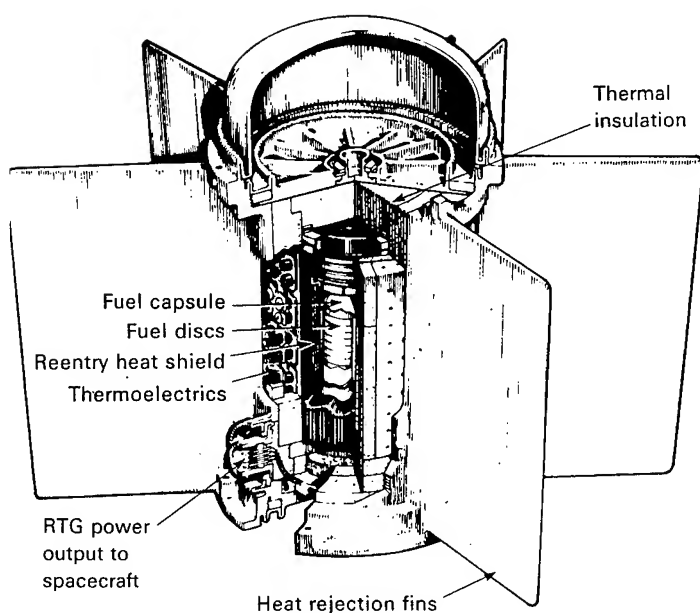


Figure 5. Schematic of the 42-We Viking/SNAP-19 RTG. The height was 40.4 cm and the housing diameter was 16.8 cm. The fin span was 58.7 cm. The mass was 15.2 kg.

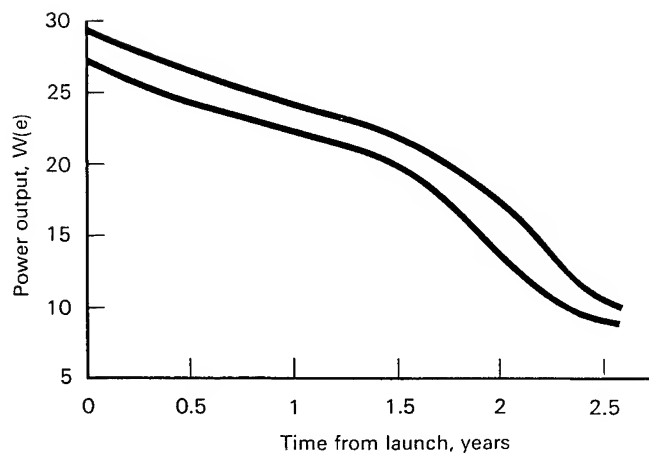


Figure 7. Nimbus III/SNAP-19 RTG power output (smoothed data).

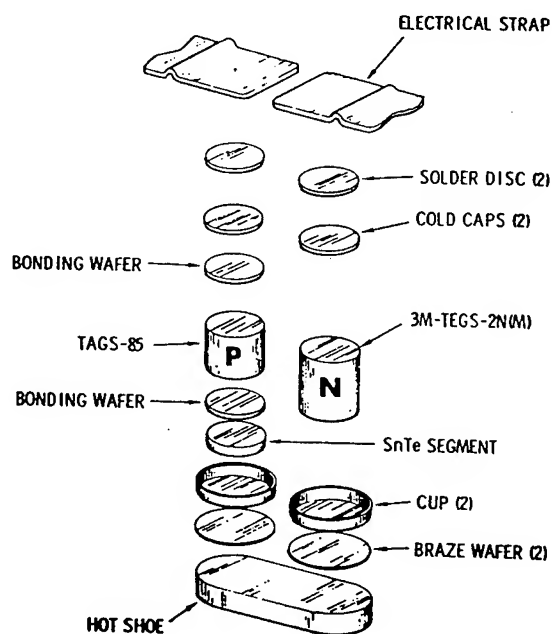


Figure 6. SNAP-19 TAGS-85/2N thermoelectric couple configuration. These couples were used in the Pioneer and Viking SNAP-19 RTGs.

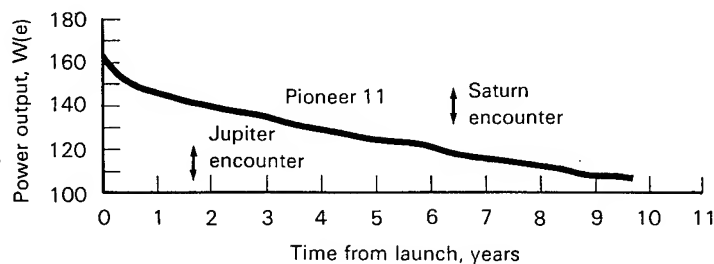
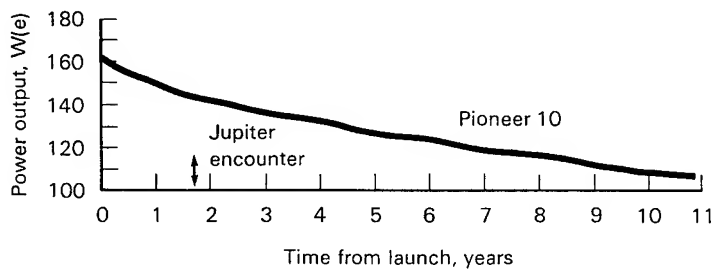


Figure 8. Power history of the Pioneer/SNAP-19 RTGs. (Smoothed and summed data). Data are available out to 1995 (≥ 22 years after launch).

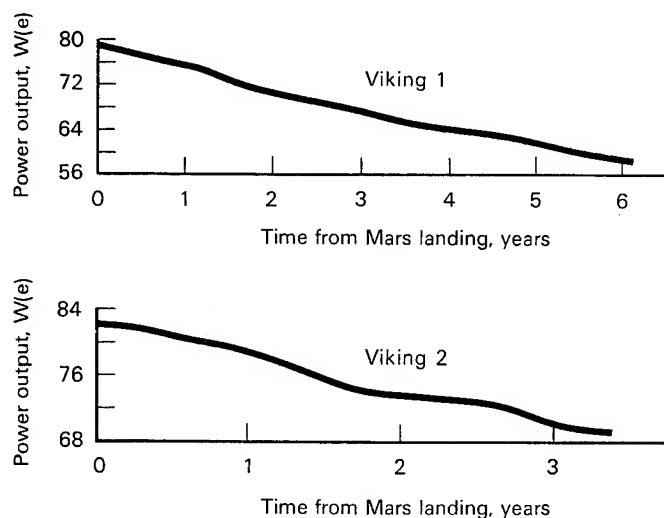


Figure 9. Power history of the Viking/SNAP-19 RTGs. (Summed and smoothed data.)

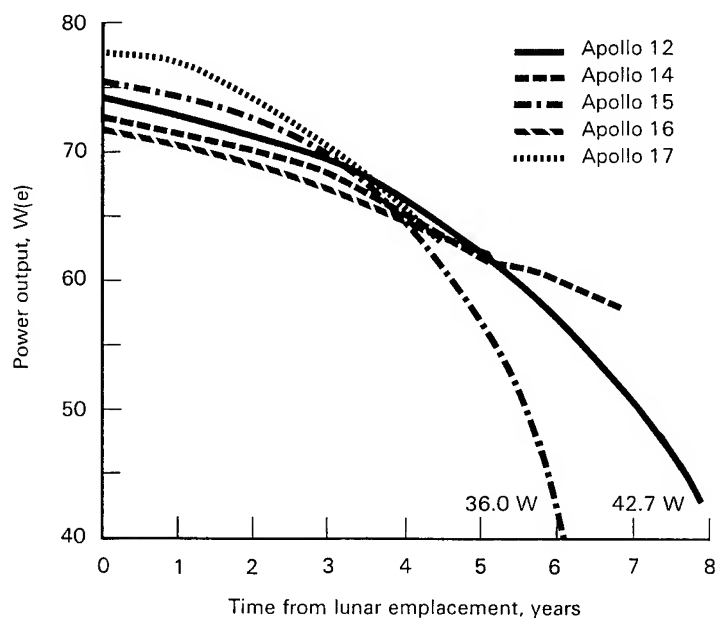


Figure 11. Power histories of the SNAP-27 RTGs. (Smoothed data.)

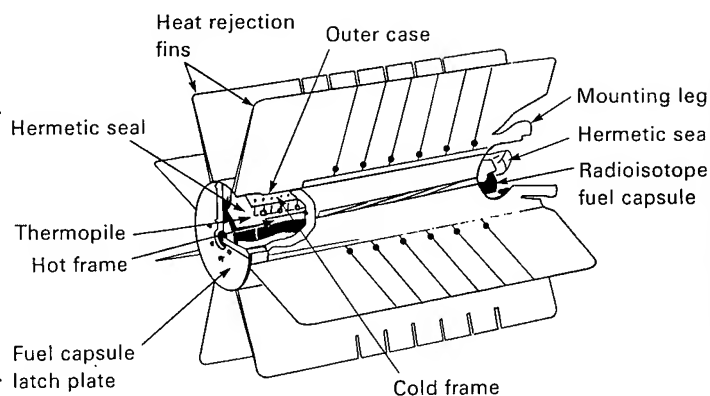


Figure 10. Schematic of the >70-We SNAP-27 RTG. The converter was 46 cm high and 40.0 cm in diameter (including fins); together with a 3-m-long cable plus connector, it had a mass of 12.7 kg. The mass of the fuel-capsule assembly without the graphite lunar module fuel cask was about 7 kg.

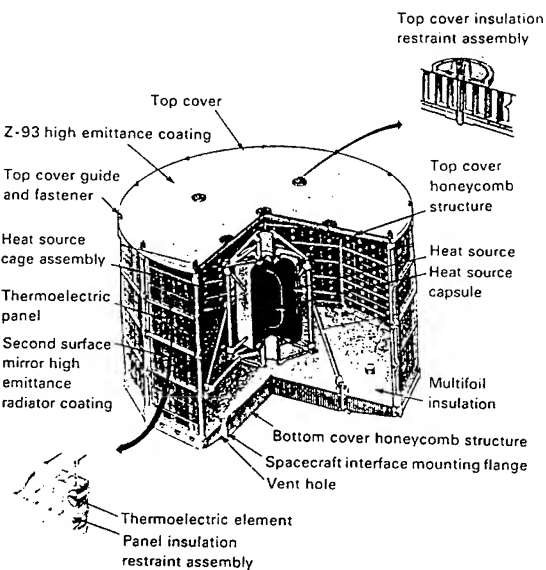


Figure 12. Schematic of the 35-We TRANSIT RTG. The distance across flats was 61 cm and the panel height was 36.3 cm. Including the heat-source cage and support structure, the mass was about 13.6 kg.

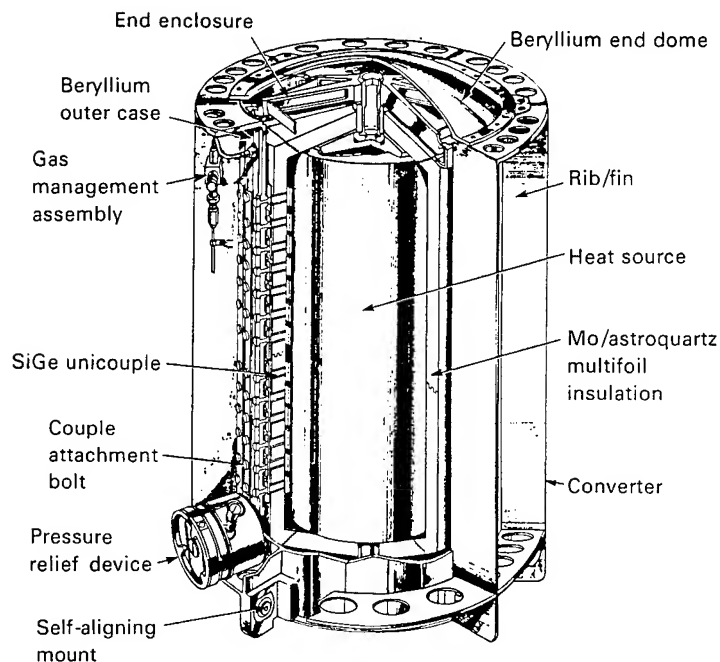


Figure 13. Schematic of the ~155-We Multi-Hundred Watt (MHW) RTG used on LES 8/9 and Voyagers 1/2. The overall diameter was 39.73 cm and its length was 58.31 cm. The average RTG flight masses were 39.69 kg for LES 8/9 and 37.69 kg for Voyagers 1/2.

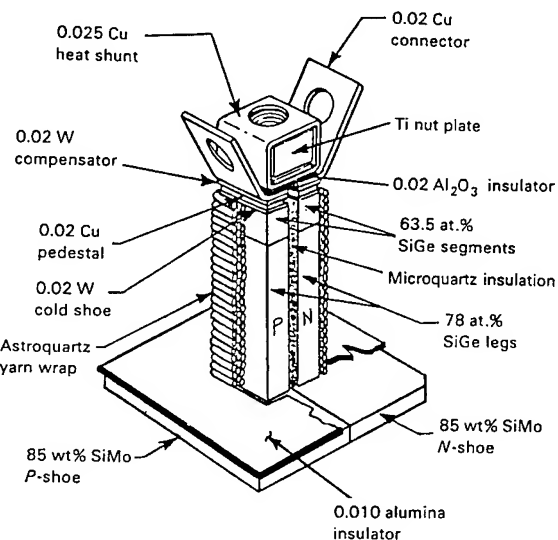


Figure 14. Cutaway of the silicon-germanium thermoelectric element ("unicouple") used in the MHW-RTGs and GPHS-RTGs. The unicouple length is 3.11 cm and the hot shoe measures 2.29 cm x 2.29 cm x 0.19 cm thick.

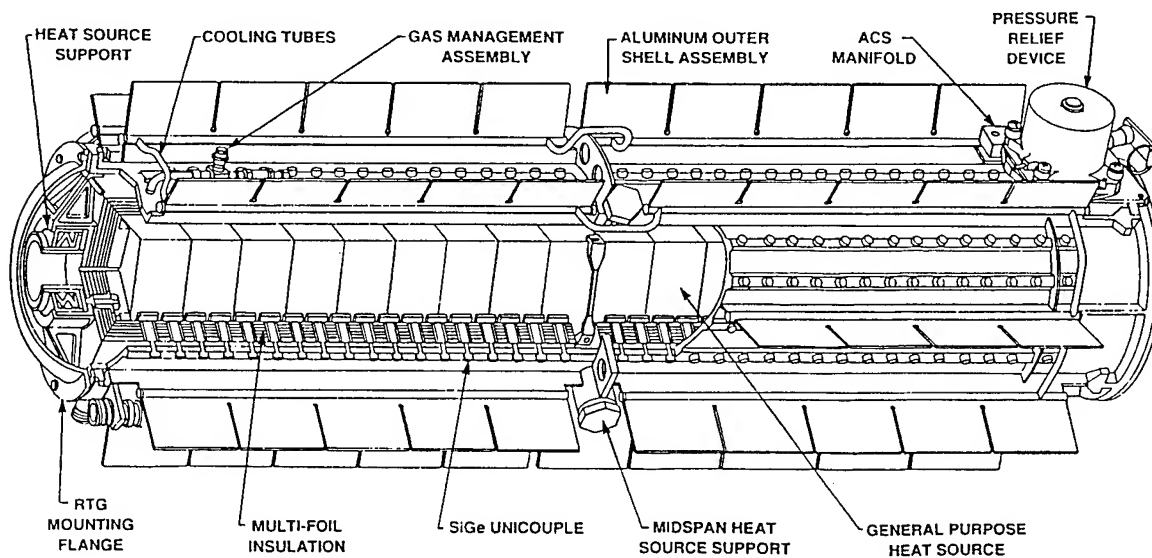


Figure 15. Schematic of the 300-We General-Purpose Heat Source (GPHS) RTG. The housing diameter is 21.8 cm with 10.2-cm-wide heat rejection fins bringing the radial envelope to 42.2 cm. The axial envelope, including end domes, is 114.1 cm. The average mass of a flight GPHS-RTG is 55.9 kg.

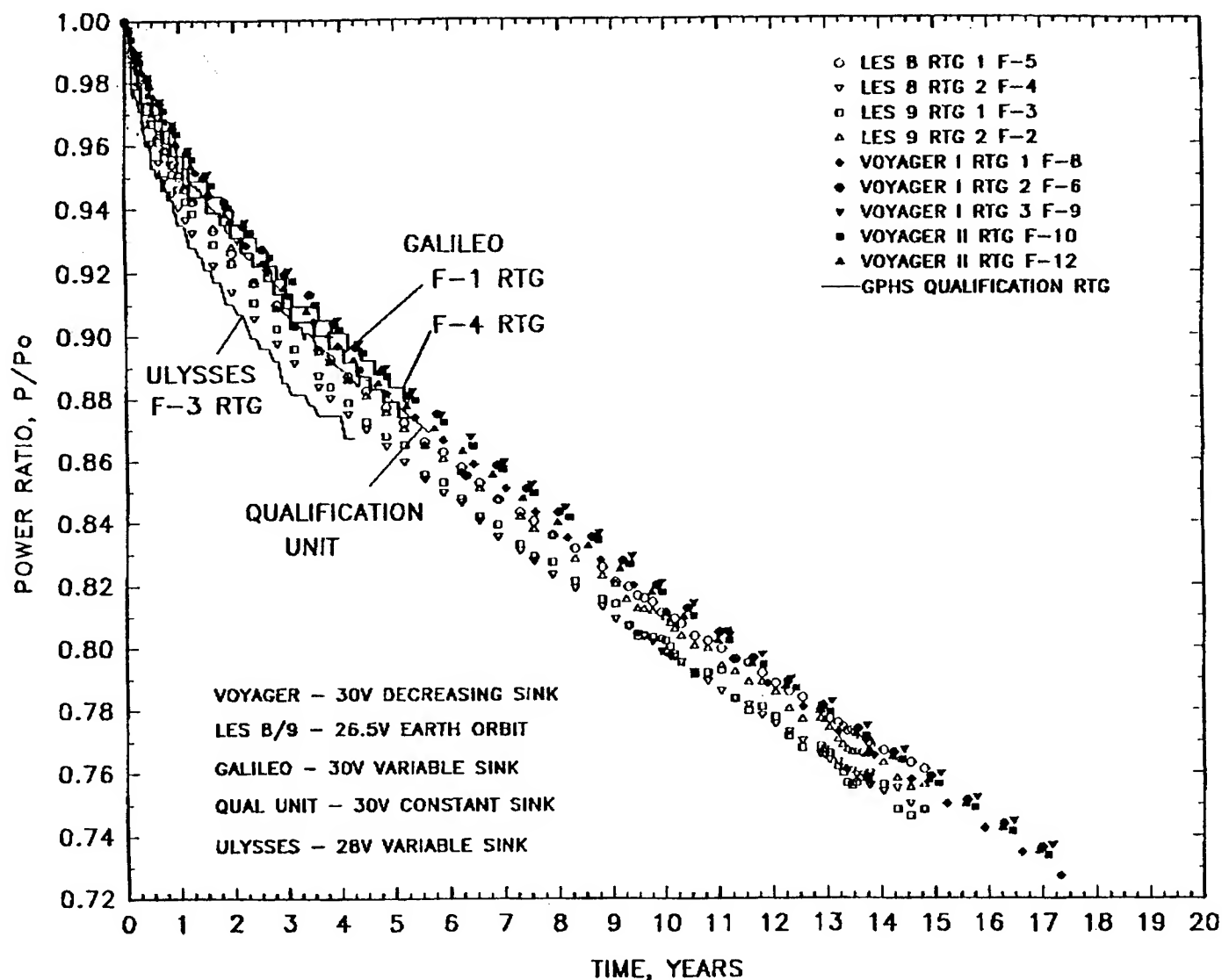


Figure 16. Power histories of all silicon-germanium RTGs (MHW-RTGs on LES 8/9 and Voyagers 1/2) and GPHS-RTGs on Galileo and Ulysses. For comparison purposes, the data are presented in terms of the ratio of the power at each time to the initial power (P_0). Initial powers for the MHW-RTGs ranged from about 153 We on LES 8/9 to about 158 We for Voyagers 1/2. Initial powers for the GPHS-RTGs, whose launches were delayed over three years, were about 289 We for Galileo and Ulysses.

Thermoelectric generation and related properties of conventional type module based on Si-Ge alloy

Masakazu KOBAYASHI, Keiko IKOMA, Kenji FURUYA,
Kazuhiko SHINOHARA, Hiroshi TAKAO,
Makoto MIYOSHI*, Yuichiro IMANISHI* and Tetsuo WATANABE*

NISSAN Motor Co., Ltd.

1 Natsushima-cho, Yokosuka, 237 Japan

*NGK Insulators, Ltd.

2-56 Suda-cho, Mizuho-ku, Nagoya, 467 Japan

Abstract

A conventional type thermoelectric module based on Si_2Ge has been made for power use. The module consists of 10 pairs of p- and n-type Si_2Ge elements in which B and P were doped ($\sim 10^{20}\text{cm}^{-3}$) respectively. The elements electrically connected in series using Mo electrodes are sandwiched between AlN plates. Each plate is $20\text{mm} \times 44\text{mm}$ in area, and the height of the module is about 12mm. The power generation of the module was evaluated as a function of temperature difference between the upper (T_u) and the lower (T_l) plates; a series circuit including the module and a reference resistance ($\sim 0.5\Omega$, comparable to the electrical resistance of the module) was used. With rising T_u , the closed circuit current (I_c), the voltage drop of the reference resistance (V_c), and the open circuit voltage of the module (V_o) were measured. Maximum power calculated from I_c , V_c and V_o was about 1.3W at $T_u - T_l \sim 400\text{K}$ ($T_u \sim 700\text{K}$). The electrical properties of Si_2Ge elements were also presented as well as the detailed experimental procedure.

Introduction

1) A General Survey

Besides the common 'energy problem', the fact has strongly attracted one's attention that almost all devices consuming fossil fuel discharge a large amount of unused energy (heat). In the case of automobile, the waste heat is about 70% of a primary energy (gasoline); consequently the energy converted into driving force is about 30%. Since a part of the driving force demands generating electrical power and running oil pressure devices, corresponding to $\sim 5\%$ of the primary energy respectively, the energy actually used for propulsion is only 20%.

So far there has been an idea to apply the thermoelectric generation to automobile because of an availability of quality heat source such as exhaust gas. For instance, if 2% of exhaust heat could be converted into electrical power with a thermoelectric generator, equal amount of driving energy that demands producing electrical power would be released; thus, we can get a driving energy by 22% totally with simultaneous reduction of emission of the exhaust heat. Under the

assumption that the weight of automobile does not change, this means that 20% of the driving energy costs about 90% of the primary energy; namely, it is possible to reduce fuel consumption by 10%. Therefore, the thermoelectric generation becomes increasingly important from the view point of making good use of energy and of conserving environment.

Recently, several practical investigations have been made according to this consideration¹⁻²⁾. Takanose et al. have pointed out an importance to improve heat transfer from exhaust gas to the hot end structure of thermoelectric generator¹⁾. They have suggested that if a thermoelectric generator producing about 200W of electrical power was obtained, it is expected to reduce fuel consumption by 4%; where they assumed that the total weight of automobile increased about 10kg. Bass et al. have reached their design goal of 1kW output by improving on heat transfer fin and by using center body with swirl fin remaining room for further refinement²⁾.

2) The Present Work

In spite of the previous investigations, it seems still difficult to make a thermoelectric generator meets the requirements of automobile use, that is, size, durability and cost. One of the reasons is that about a thousand of elements are used in a thermoelectric generator in present. For instance, it will be difficult to assemble all elements directly into a generator of good quality with saving the cost of production. Therefore, we have decided to build up a generator with some of small units (usually called module) which are assembled with some pairs of elements. Bass et al. have partially used this approach in their work; they started with finished modules²⁾.

In the present work, however, we have started to make module itself because it is necessary to optimize module for meeting the requirements of automobile. Further, we have adopted a conventional type module to make assembly of module and generator easy; we have also taken account of future mass production. Then, we have presumed the temperature of hot end of the module $\sim 1100\text{K}$ (800°C , at exit of exhaust manifold), making us to choose the silicon-germanium alloy suitable for such a high temperature use.

Under these limitations, we have selected Mo electrodes and AlN plates as a possible compositions of the module. For

settling this combination, Si-Ge alloy, AlN plates and Mo electrodes, we have noticed chiefly a matching of the linear thermal expansion coefficient (α) among them. Since mechanical and electrical connections of them are necessarily arrayed at the hot end of conventional type module, the matching of α is substantially important; any destruction of connection will cause immediate decrease of output power. We also take account of the thermal conductivity (κ) of plate, because the temperature at the junctions of elements just behind the plate is necessary to be close to the temperature of surface of the plate.

In Fig.1, κ is plotted against α for several electrical insulators. Here, α for some typical thermoelectric materials operating in a middle and/or a high temperature range is shown with vertical lines. As seen in Fig.1, α of AlN shows a good agreement with that of Si₂Ge. Moreover, it is seen that the κ of AlN is high enough to select this material for the module.

For electrodes, we have examined several metals having high melting point and have chosen Mo because α of this metal $\sim 5\text{ppm/K}$ is near to that of Si₂Ge and AlN.

With these considerations, we have made a tentative module in order to reveal problems in the module for such a high temperature use. We will show the experimental procedures and several experimental data obtained up to now and will discuss about them in the following sections.

Experimental procedures

1) Elements

Both p- and n-type Si₂Ge ingots were synthesized by a casting melt method. High purity Si, Ge, B and P were used as starting material; all raw materials were in 5N grade. A RF induction furnace and a carbon crucible were utilized for melting the raw material. Si, Ge and B were melted simultaneously for

synthesizing p-type Si₂Ge. For n-type one, P was dropped into a melt of Si and Ge for reducing evaporation of P. The mixing ratios of raw materials are shown in Table 1.

Table 1 Mole mixing ratios of starting materials.

Si	Ge	B or P
63.23%	36.36%	0.41%

After keeping the melt at $\sim 1640\text{K}$ (1370°C) for several minutes in an Ar gas, it was cast into an aluminum crucible. Temperatures were monitored with an optical thermometer.

The ingots were pulverized, milled and meshed under $32\mu\text{m}$ in diameter. Then, the raw powder was hot-pressed at 1503K (1230°C) and 200kg/cm^2 for 60min in vacuum ($\sim 10^{-5}\text{Torr}$). Black and rather porous ceramics with a nominal density of about 2.7g/cc were obtained.

The Seebeck coefficient and the electrical conductivity of the elements were measured from a room temperature to about 1000K (700°C). Specimens used were about $3 \times 3 \times 10\text{mm}^3$ bar cut from the hot-pressed ceramic body. Pt-Pt(13%Rh) thermocouples ($\phi 0.05\text{mm}$) were attached at both ends of the specimen with silver paste (Dupont-3868). Two Pt leads ($\phi 0.05\text{mm}$) were placed on the largest surface of the specimen with several millimeters spacing for the conventional 4-terminal method. Prior to measurements, the specimen was heated up to $\sim 1000\text{K}$ (700°C) and kept for 5min in an evacuated metal furnace ($\sim 10^{-5}\text{Torr}$) for sintering the silver paste.

The thermal conductivity was measured with a conventional laser-flash method in the same temperature range as that for the electrical measurements.

The active carrier densities of the elements at a room temperature were obtained from the Hall coefficient measurements; $\sim 2.0 \times 10^{20}\text{cm}^{-3}$ for p-type and $\sim 0.9 \times 10^{20}\text{cm}^{-3}$ for n-type Si₂Ge, respectively.

2) Module

A schematic structure of the present module is shown in Fig.2. In this figure, heat flows from the upper AlN plate toward the lower AlN plate. The front two electrodes ($7 \times 9\text{mm}^2$) above the lower AlN plate are concurrently output terminals. Electrical current from the left terminal flows backward along the left row of elements, then turns back through the right row. Both rows are connected at the last elements with $3 \times 19\text{mm}^2$ Mo electrode on the lower AlN plate. In the two rows, p- and n-type elements are alternately arranged and are connected in series.

Si₂Ge elements, Mo electrodes and AlN plates were stuck with a conventional brazing technique. At first Mo electrodes were put on AlN plate with a gold paste (Ishifuku, BAU-4). For increasing strength of the interface (Mo/AlN), metal Ti was sputtered on AlN plate as an activator. Moreover, for preventing Mo electrode from coming into contact with those around it, sputtered Ti was patterned with arrangements of Mo electrodes. After ordering Mo electrodes on AlN with BAU-4, they were dried at $\sim 373\text{K}$ (100°C) for 24 hours in the air. Then, they were sintered at 1303K (1030°C) for 8min

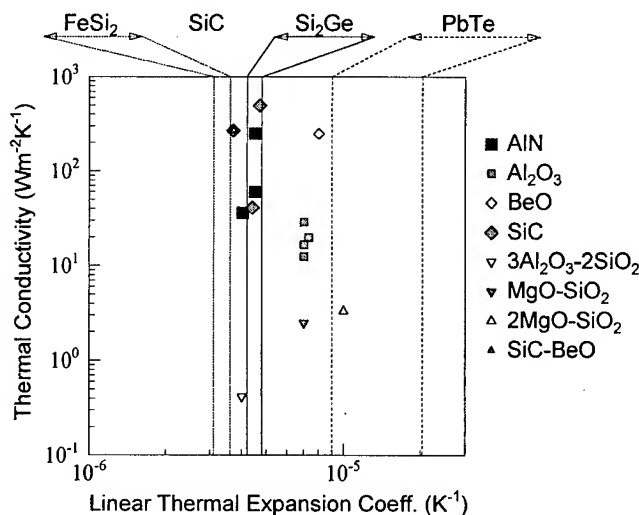


Fig.1 Correlation between the linear thermal expansion coefficient α and the thermal conductivity κ for several electrical insulators^{3,4)}. Vertical lines show the range of α for some typical thermoelectric materials used in high temperatures (see references: FeSi₂⁵⁾, Si₂Ge⁶⁾, SiC^{3,4)}, PbTe^{7,8)}).

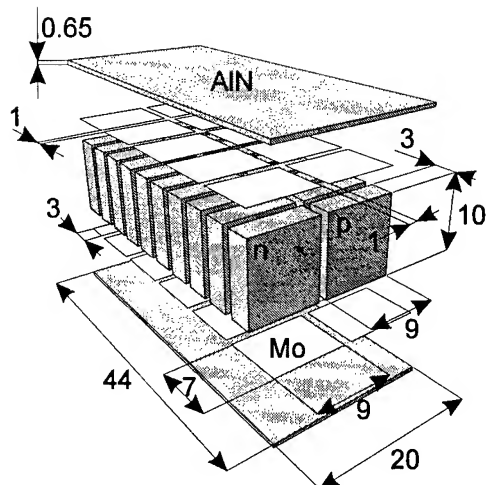


Fig.2 A schematic structure of the present module. All dimensions are shown in millimeters; Mo electrodes are 0.2mm thick. The front two electrodes above the lower AlN plate are concurrently output terminals. Heat flows from the upper AlN plate toward the lower one.

in an evacuated metal furnace at $\sim 10^{-5}$ Torr.

Next, Si_2Ge elements and Mo electrodes on the AlN plates were electrically and mechanically connected using a silver paste (ULVAC, BAG-8T). 10 pairs of Si_2Ge element were arranged between two AlN plates (see Fig.2) with BAG-8T using a mold which is made of machineable ceramic. Then, they were dried at $\sim 373\text{K}$ (100°C) for 20 hours in the air adding a vertical weight $\sim 50\text{g}/\text{cm}^2$ from the upper side. After drying, they were fired at 1083K (810°C) for 8min in an evacuated metal furnace at $\sim 10^{-5}$ Torr. Chemical compositions of BAU-4 and BAG-8T are summarized in Table 2.

Table 2 Chemical composition of brazing paste.

	Au	Ni	Ag	Cu	Ti
BAU-4	82.0%	18.0%	-	-	-
BAG-8T	-	-	36.6%	59.7%	3.7%

The electrical power of the module was evaluated as a function

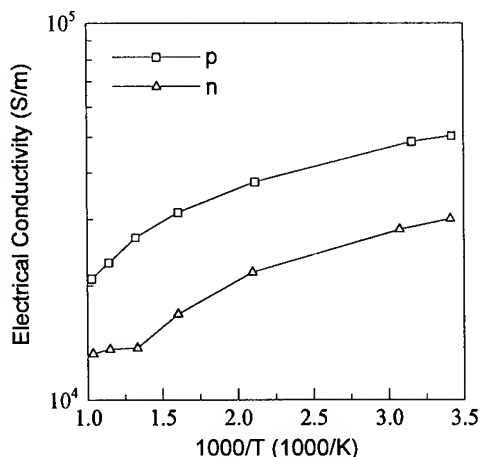


Fig.3 The Arrhenius plot of the electrical conductivity σ of p- and n-type elements.

of temperature difference (ΔT) between T_u and T_l ; a series circuit including the module and a reference resistance ($\sim 0.5\text{ohm}$, comparable to the electrical resistance of the module) was used. For increasing ΔT ($=T_u-T_l$), the module placed on a water cooled stage was heated from the upper side with a heater block. With increasing ΔT , the closed circuit current (I_c), the voltage drop of the reference resistance (V_o), and the open circuit voltage of the module (V_o) were measured. The temperature of both plates was monitored with a thin C-A thermocouple ($\phi 0.05$) inserted between each plate and the corresponding heat source. The maximum power was calculated from I_c , V_c and V_o .

Results and Discussions

Temperature dependence of the electrical conductivity (σ) and that of the Seebeck coefficient (S) are shown in Fig.3 and Fig.4, respectively. As seen in Fig.3, σ of both elements shows a metallic behavior. A small kink was observed at $\sim 750\text{K}$ ($1000/T \sim 1.3$) for n-type element; the decrease of σ becomes gradual above $\sim 750\text{K}$. The origin of the kink is still unclear though an onset of intrinsic conduction occurs around 750K . This seems to be supported by the fact that S of n-type element is almost constant in the same temperature range (see Fig.4).

The thermal conductivity κ of both types of the element was found to be roughly represented by the following linear equation above $\sim 300\text{K}$;

$$\kappa = -1.0 \times 10^{-3} T + 3.0, \quad (1)$$

where T means the absolute temperature. The calculated figure of merit, $Z=(S^2\sigma)/\kappa$, is shown in Fig.5 for p- and n-type elements; where eq.(1) and cubic polynomials of S and σ obtained by least squares were used. The absolute value of Z is rather low $\sim 4 \times 10^{-4} \text{K}^{-1}$ around 900K comparing the reported values⁹. Since we have given no special care to the preparation of elements in the present work, there is a room for further improvements on the thermoelectric properties of elements.

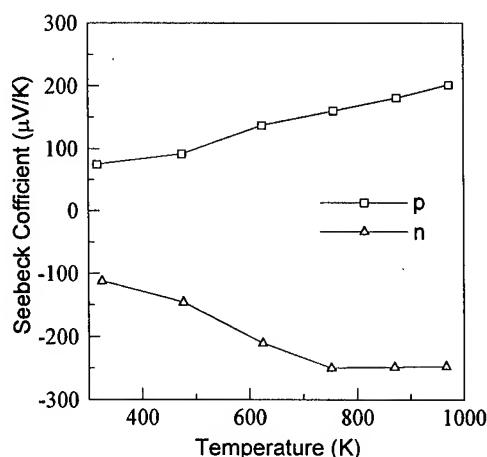


Fig.4 Temperature dependence of the Seebeck coefficient S for p- and n-type elements.

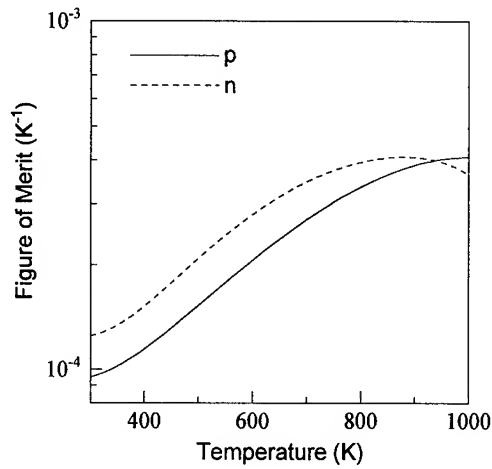


Fig.5 Temperature dependence of the calculated figure of merit of p- and n-type elements.

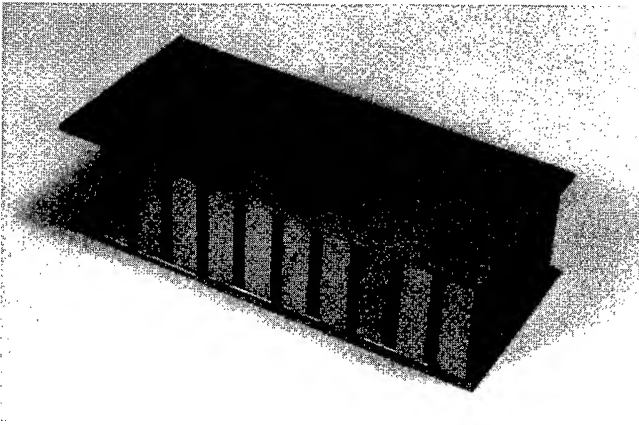


Fig.6 Conventional type thermoelectric module made in the present work.

Fig.6 shows the module made in the present work; 38 modules of the same shape and performance have been finished totally. The measuring sequence of T_u , T_l , V_c , I_c and V_o used for evaluating the electrical power produced by the module is as follows;

$$\bullet - T_u \rightarrow T_l \rightarrow V_c \rightarrow I_c \rightarrow [\text{open}] \rightarrow V_o \rightarrow [\text{close}] - \bullet.$$

The above sequence was performed at a interval of several tens of second. The circuit for measurement, where the module and a reference electrical resistance were connected in series, was closed except when the open circuit voltage V_o was measured; making and breaking circuit are indicated by square brackets.

The temperature difference of both (hot and cold) ends of the module in the closed circuit (ΔT_{close}) will be smaller than that measured with keeping the circuit open (ΔT_{open}) due to the Peltier effect. Therefore, V_o in the above sequence shows the value at ΔT_{close} when the circuit is open; then it will tend to the value expected at ΔT_{open} during the measurement. For estimating the change in V_o due to the relaxation of ΔT , V_o was

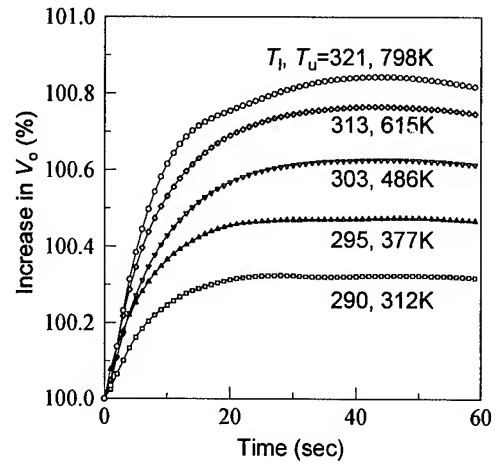


Fig.7 The increase in V_o as a function of time (t) after breaking the circuit. The measurements were performed at several sets of T_u and T_l . Where V_o is normalized to the value at $t=0$.

measured as a function of time after the circuit was open. The results are shown in Fig.7. As seen in Fig.7, it is necessary ~ 20 sec for V_o to tend to the value at ΔT_{open} ; though the increase in V_o is so small $< 1\%$ that it will be neglected in the present module.

Maximum electrical power P_{max} calculated with eq.(2) is shown in Fig.8;

$$P_{\text{max}} = \frac{V_o^2}{4R_s} = \frac{1}{4} \cdot \frac{V_o^2 I_c}{V_o - V_c}, \quad (2)$$

where R_s represents the internal electrical resistance of the module. The P_{max} increases in proportion to square of ΔT

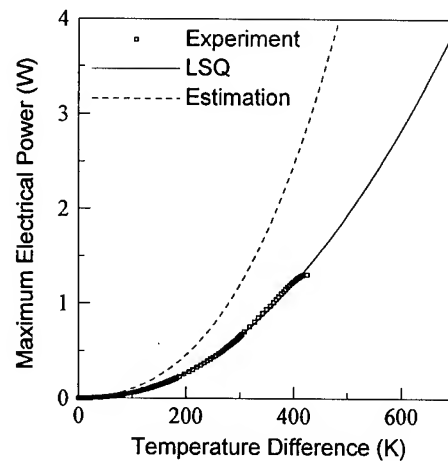


Fig.8 Maximum electrical power of the module vs. temperature difference $\Delta T = T_u - T_l$. Square markers represent the experimental results, the solid line shows a fitting curve to square equation, and the dashed line is a calculated thermoelectric power obtained from Figs.3 and 4.

($=T_u-T_l$) and shows $\sim 1.3\text{W}$ at $\Delta T \sim 400\text{K}$ ($T_u \sim 700\text{K}$). It is expected from the fitting curve that the P_{max} reaches $\sim 2.8\text{W}$ at $\Delta T \sim 600\text{K}$ (see solid line in Fig.8).

The maximum power, estimated from the thermoelectric properties of p- and n-type elements (Figs.3 and 4), is also shown in Fig.8 (dashed line). In this estimation, the temperatures of the hot end and the cold end of element are assumed equal to T_u and T_l , respectively. As seen in Fig.8, the dashed curve considerably departs from the experimental results, indicating that a large thermal resistance will exist between heat sources and both ends of element. Ohmic contacts of elements and Mo electrodes are also considered to decrease the output power. Moreover, some elements might produce less electrical power than that expected by measured T_u and T_l , because the temperature distribution on AlN plate could not be detected with only one C-A thermocouple inserted between AlN plate and corresponding heat source.

By now, we have noticed some problems being in the interface between Mo electrodes and elements; the area of contact of elements with Mo electrodes was observed to be smaller than that expected by the dimensions of elements. Therefore, large thermal and electrical resistance originating from the imperfection of the interfaces will decrease the observed output power.

Further investigations on the elements and the module are now in progress.

Conclusions

We have made a conventional type thermoelectric module based on silicon-germanium alloy. Thermoelectric properties of both p- and n-type elements used in the module were measured up to $\sim 1000\text{K}$. Maximum electrical power P_{max} of the module was measured against $\Delta T = T_u - T_l$ and compared with P_{max} calculated from the thermoelectric properties of both elements. In the present work, following conclusions are obtained.

1. The figure of merit of the present elements is rather low $\sim 4 \times 10^{-4} \text{K}^{-1}$ around 900K . There will be room for further improvement.
2. A relaxation phenomena of the open circuit voltage V_o due to the Peltier effect was observed. The relaxation intensity is so small $< 1\%$ that it will be neglected in the present module.
3. The present module produced electrical power $\sim 1.3\text{W}$ at $\Delta T \sim 400\text{K}$ ($T_u \sim 700\text{K}$); it is expected to be 2.8W at $\Delta T \sim 600\text{K}$ from a curve fitting of the experimental results.
4. The electrical power calculated from the thermoelectric properties of elements is much larger than the experimental one. We have noticed an imperfection being in the interfaces between elements and Mo electrodes, indicating that large thermal and/or electrical resistance will exist in the interfaces.

Acknowledgment

The authors wish to thank Dr. N. Masuko, a professor emeritus of Tokyo University, for his foreseeing suggestion. We are

also indebted Dr. M. Yamanaka, Dr. K. Negita and Mr. K. Aoki for their valuable discussions and advices.

References

- [1] E.Takanose and H.Tamakoshi, "The Development of Thermoelectric Generator for Passenger Car", Proceedings of The 12th International Conference on Thermoelectrics, pp.467-470 (1993).
- [2] J.C.Bass, N.B.Elsner and F.A.Leavitt, "Performance of 1kW Thermoelectric Generator for Diesel Engines", Proceedings of The 13th International Conference on Thermoelectrics, pp.295-298 (1994).
- [3] H.Sudo, *Electrode and Related Materials*, Industrial Publishing and Consulting Inc., Japan, p.53, p.58, p.324 (1990).
- [4] K.Kobayashi, *Thermophysical Properties Handbook*, Yokendo Ltd., Japan, p.131, p.133, p.230, p.257 (1968).
- [5] W.D.Wood and H.W.Deen, *Thermal Properties of High-Temperature Materials*, Horikoshi-kenkyusyo, Japan, p.243 (1968).
- [6] *Solid solution in semiconducting systems*, Nisso Tsushinsya, Japan, p.11 (1995).
- [7] B.Houston, R.E.Strakna and H.S.Berson, "Elastic Constants, Thermal Expansion, and Debye Temperature of Lead Telluride", Journal of Applied Physics, vol.39, pp.3913-3916 (1968).
- [8] R.Nii, "Cyclotron Absorption in Lead Telluride", Journal of the Physical Society of Japan, vol.19, pp.58-66 (1964).
- [9] S.L.Draper, J.W.Vandersande, C.Wood, R.Waters and V.Raag, "Effect of Ga and P Dopants on the Thermoelectric Properties of N-type SiGe", Proceedings of The 24th Intersociety Energy Conversion Engineering Conference, vol.2, pp.711-714 (1989).

USE, APPLICATION AND TESTING OF THE HZ-14 THERMOELECTRIC MODULE

Frederick A Leavitt; Norbert B Elsner; John C Bass

Hi-Z Technology, Inc.

6373 Nancy Ridge Dr., San Diego, CA 92121

(619)535-9343•fax(619)535-9350•e-mail hiz@cts.com

Abstract

The HZ-14 is a thermoelectric module that converts low grade, waste heat into electricity. To obtain optimum performance from the HZ-14 it is important to address several key points when using the module in an application. These key points in the use of the module are discussed, and methods of identifying the causes of inferior performance are addressed. The performance characteristics of the module are also described.

1.0 Introduction

The HZ-14 is a thermoelectric module that is intended to target the waste heat market. The module uses bismuth telluride based alloys and consists of 98 couples as shown in Figure 1. When applied to any heat source, the module requires a heat flux of about 8 watts per cm^2 . With a temperature difference of 200°C

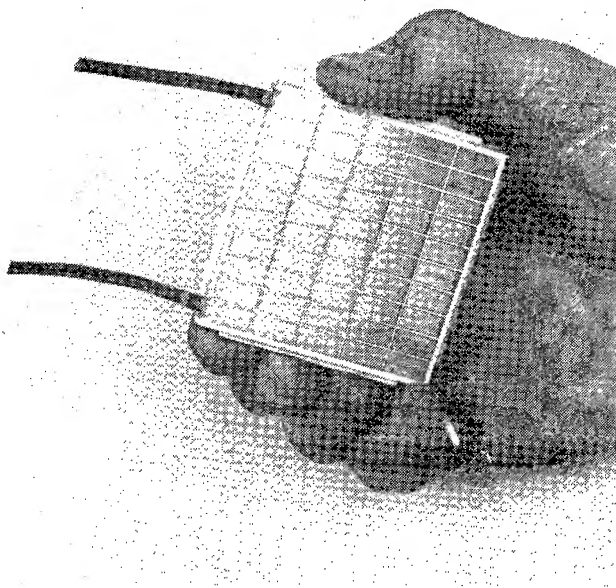


Figure 1 - HZ-14 Thermoelectric Module

the module converts 5% of the thermal energy that passes through it into electricity, generating a minimum of 14 watts of electrical power. When properly installed it will run for tens of thousands of hours.

It has been observed however that unless special attention is paid to certain details, satisfactory performance from the module is not achieved. The purpose of this presentation is to address these key points and to discuss some solutions that have been found to yield good results.

2.0 Mounting of the Module

The best method of using the module is to compressively load it between the heat source and the heat sink. A minimum load of 200 psi has been found to yield the best results. It is very important to uniformly distribute the load over the surface of the module to achieve optimum power performance and avoid damaging the module. A well designed mounting system needs to address the following issues:

- 1) Compressive Loading
- 2) Thermal Expansion
- 3) Uniform Load
- 4) Overhang
- 5) Thermal Spreader
- 6) Flatness & Thermal Transfer Compound
- 7) Thermal Bypass

2.1 Compressive Load

Putting the module under a compressive load helps in two ways, 1) it ensures that the module always remains in compression (where it is the strongest), and 2) it maximizes heat transfer across the interfaces. Experimentation shows that most of the beneficial effects on heat transfer are achieved with a 200 psi compressive load.

2.2 Thermal Expansion

In determining the compressive load it is important to accommodate the large thermal expansion of the module which is about $20 \times 10^{-6} \text{ }^\circ\text{C}^{-1}$. The best way to do this is to use springs to apply the load. If the system is simply bolted together, then the expansion of the module will apply too much pressure, or conversely, any yield in the bolts or threads will rapidly lose pressure. A typical system that can be used to mount a thermoelectric module to a hot surface is shown in Figure 2. The Belleville springs used in this example apply a large amount of force in a very compact space and at the same time they allow for thermal expansion.

2.3 Uniform Load

The clamping system used to hold the heat sink and heat source onto the module can have a significant effect on the module performance. If the module is clamped to the heat source and the heat sink by simply bolting along the edges of the heat source and heat sink, then bowing can occur, since the edge of the module acts as a pivot point as shown in Figure 3.

Bowing of the heat sink will cause excessive forces on the perimeter of the module and a gap in the center of the module. This type of mechanical loading is to be avoided since it will

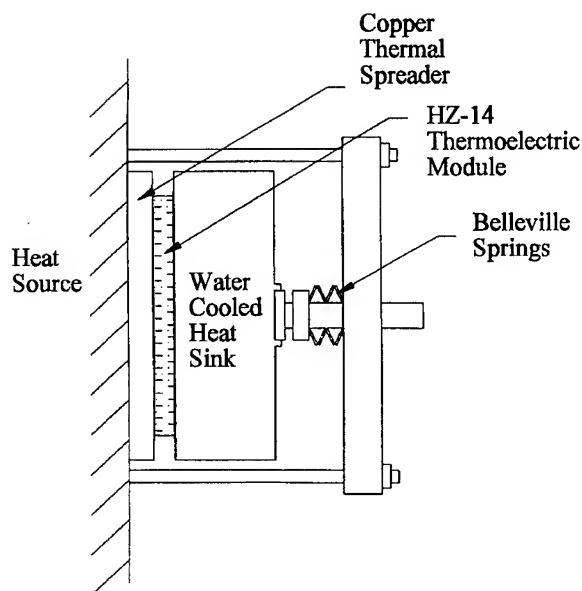


Figure 2 - Module Pressure System

result in nonuniform temperatures across the face of the module and, therefore, poor performance from the module. Also if the forces around the circumference of the module become too large, this may result in permanent damage to the module caused by microcracking of the thermoelectric material. Thicker heat sinks and heat sources will help minimize this bowing effect.

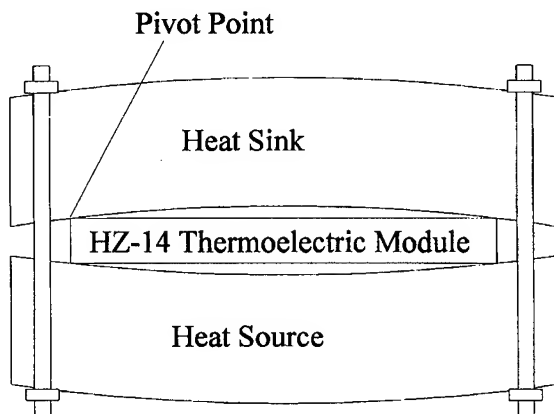


Figure 3 - Bowing of Heat Sink/Source

2.4 Heat Source Overhang

The maximum performance from the module is achieved when the temperature difference across the face of the module is zero. Since the heat source will cool near its edges, the edge of the heat source should extend well beyond the edge of the module. In a laboratory test set up an overhang of at least 0.5 inches is necessary to avoid most of the cooling effects caused by the proximity of the edge of the heat source. In an actual generator it may not be possible to allow for this 0.5 inch overhang.

2.5 Thermal Spreader

To further assist in uniform temperature distribution across the face of the module it is helpful to place a copper or aluminum plate between the module and the heat source. If the heat sink is not copper or aluminum, then a copper plate should be placed between the module and the heat sink as well. The copper plate should be at least 0.25 inches thick.

The copper plate acts as a thermal spreader and helps to minimize hot spots and cold spots and provide a uniform temperature to the face of the module.

2.6 Flatness & Heat Transfer Compound

For maximum heat transfer across the interfaces it is important that the surfaces to which the module is to be applied be as flat as possible. A flatness of ± 0.001 inches is necessary but a flatness of ± 0.0005 inches is recommended. If the heat sinks are being clamped from the sides then a very slightly convex surface will help compensate for any bowing that may occur.

In any interface, no matter how smoothly machined it is, microscopic irregularities on the surface (see Figure 4) limit the amount of contact area that can be achieved between the two surfaces.

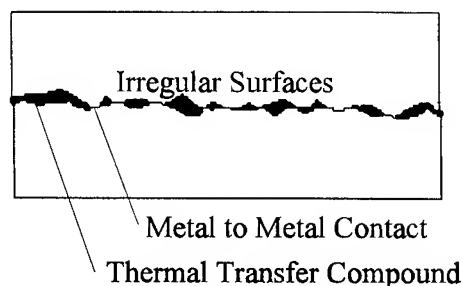


Figure 4 - Interface with Irregular Surface

Filling the voids in the interface, that are caused by the irregular surfaces, with a heat transfer compound can greatly improve the thermal conductivity across the interface. Using too much thermal transfer compound, however, will prevent metal-to-metal contact, and the thermal conductivity will actually be reduced. Conventional silicone greases, using a ZnO filler that are commonly used to heat sink transistors, work very well. If maximum performance is necessary, heat transfer greases filled with AlN or BN will decrease the thermal resistance.

Thermally conductive adhesives are available that could be used to bond modules to heat sinks and heat sources but they do not yield satisfactory results. Even though the bulk advertised properties appear to be good, the filler material often pulls away from the interface surface leaving a layer of unfilled adhesive with a very low thermal conductivity.

Another disadvantage with adhesives is that the module may not always be held in compression as it is with spring loading. If the adhesive allows the module to be subjected to tensile or shear forces it then becomes susceptible to damage.

2.7 Thermal Bypass

A significant loss of efficiency in thermoelectric systems that is often overlooked is thermal bypass. Thermal bypass is defined as thermal energy that passes from the hot side to the cold side without passing through the thermoelectric material. About 2% of the thermal energy passing through the module bypasses the thermoelectric material by passing through the module structure.

A much larger portion of the thermal energy can bypass the module by passing through the metal support structure outside the module and through the air gap between the hot and cold sides. Referring to Figure 2 it is obvious that a large amount of thermal energy will pass from the heat source to the cold side through the mounting rods. This can be minimized by making the mounting rods as small as possible, choosing low thermal conductivity materials and by increasing the length of the thermal path. One method for increasing the length of the thermal path is shown in Figure 5.

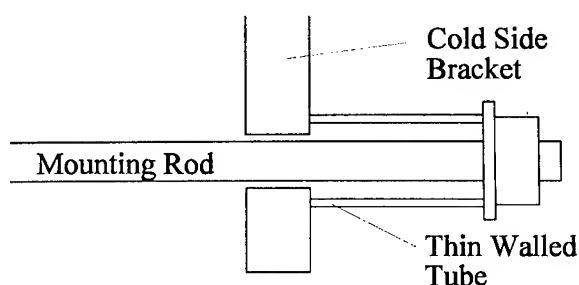


Figure 5 - Increased Thermal Path

To avoid any support structure that can conduct heat from the hot side to the cold side it is suggested, where possible, to mount a thermoelectric module on both sides of the heat source. This allows the mounting rods to go from one cold side to the other cold side without touching the heat sources as shown in Figure 6. This arrangement forces all of the thermal energy to pass through the module with the exception of the thermal energy that is lost to the surrounding atmosphere. Good thermal insulation will minimize the heat losses to the atmosphere.

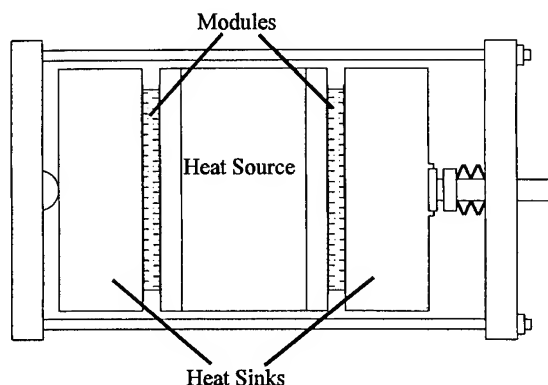


Figure 6 - Double Sided Arrangement

3.0 Interfaces

The interface between the module and the heat source and the interface between the module and the heat sink is a very critical component of any thermoelectric system. The surface of the module consists of the metallic, electrical conductors that join the "N" and "P" elements of the module. It is essential that these conductors are not electrically shorted together.

Since most heat sources (and heat sinks) are also electrically conductive, an insulating material must be placed between the module and the heat source or heat sink. If the heat source (or sink) is not electrically conductive then of course, this is not necessary.

Several options for an electrical insulator exist and they each have their advantages and disadvantages. Some of the more common alternatives are:

- 1) Impregnated silicone pads
- 2) Hard anodized Al_2O_3 coatings
- 3) Sputtered coatings
- 4) Al_2O_3 wafers

All of these alternatives require the surface to which the module is to be mated to be extremely flat. A minimum tolerance of ± 0.001 inches is suggested for the flatness of the mounting surface but a tolerance of ± 0.0005 inches is recommended. The 14 watt modules are surface finished to this tolerance. Where possible, any deviation from flat should be towards the formation of a convex surface as discussed in section 2.6.

3.1 Silicone Pads

Silicone pads are commonly used in mounting power components in electronic circuits. They are easy to work with and because of their flexible nature they can compensate for irregular surfaces. The very best pads that were available however still allowed a temperature drop of 25°C when the module was at a ΔT of 200°C . Further, these pads are not recommended for use above 210°C .

3.2 Hard Anodized Coatings

Aluminum hard anodized coatings have worked well in some cases. It is essential that a good silicone based heat transfer grease be used and that the parts are held in compression. The aluminum hardcoatings are easily scratched however making the use of hardcoatings unreliable. Some "extra hard" hardcoatings have been recently advertised but these coatings have not been evaluated.

3.3 Sputtered Coatings

Ceramic coatings sputtered onto the module or onto the heat sources (or heat sinks) are very promising. In order to be strong enough to provide reliable results the coatings become quite expensive. While this method promises good results they remain to be evaluated.

Sputtered coatings still require the use of a good heat transfer grease and compressive loading to achieve a low resistance interface.

3.4 Ceramic Wafers

The most flexible system that yields the best results and is cost effective is to use a thin ceramic wafer in between the module and the surfaces to which it is being mounted. With the proper use of heat transfer compound in all interfaces and compressively loading the arrangement, temperature drops from the heat source to the module can be as low as 15°C with a module ΔT of 200°C. A similar temperature drop between the module to the heat sink can be realized.

Suitable ceramics that are relatively inexpensive are 96%Al₂O₃ wafers that are 0.010 inches thick and available commercially from several sources. If BN filler heat transfer compound is used in the interfaces, temperature drops of less than 10°C have been achieved.

4.0 Trouble Shooting

If all of the above steps are carefully followed, a satisfactory thermoelectric system should result. If, however, the system does not perform as expected the problem can be quickly identified by following the steps described below.

4.1 Module ΔT

The first step is to determine what temperature difference has been obtained across the module. This can be estimated by bringing the module to the operating temperature and allowing it to stabilize. This should be done with the electrical load attached to the module. If no electrical load is available, connect the outputs from the module together using a jumper cable.

Next, connect the leads from a voltmeter to the outputs of the module so that the voltage can be read on the display. The voltage reading with current flowing through the module is called the load voltage (V_l). Disconnect the module from the load and quickly read the voltage on the voltmeter. The reading should be taken about 1 second after the electrical load is disconnected. The voltage on the module with no current flowing is called the open circuit voltage (E_o).

When the load is disconnected the module temperature will increase and the open circuit voltage of the module will rise. The open circuit voltage reading must be taken before the temperature rises significantly from the steady state condition.

Once the open circuit voltage has been measured refer to Figure 7 and obtain the module ΔT . Similarly, from Figure 8, the available power from the module can also be found.

Compare the actual power that you are generating from the module with the value that you recorded on line 1.3. If you are obtaining this amount of power but it is lower than what you feel you should be generating you may have a heat transfer problem at the interfaces with your heat source and/or heat sink. Proceed to section 4.3 for a discussion on this topic. If you are not generating as much power as is indicated on line 1.3 then continue on to section 4.2.

HZ-14 Thermoelectric Module

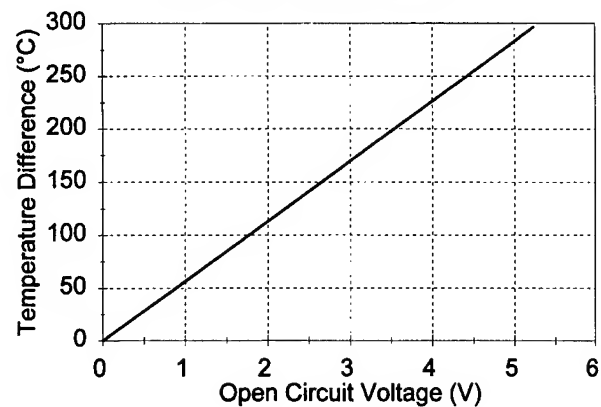


Figure 7 - ΔT vs Open Circuit Voltage

HZ-14 Thermoelectric Module

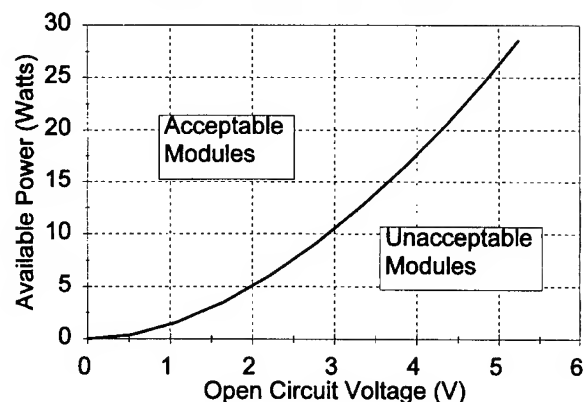


Figure 8 - Power vs Open Circuit Voltage

4.2 Module Integrity

The integrity of the module can be determined by measuring the value of the internal resistance (R_i) of the module. If the measured value of R_i is less than the value in Figure 9 that corresponds to the measured open circuit voltage then the module is making the power rated for that ΔT and E_o . If you are not sure what the internal resistance of your module is, this section will describe how it can be measured.

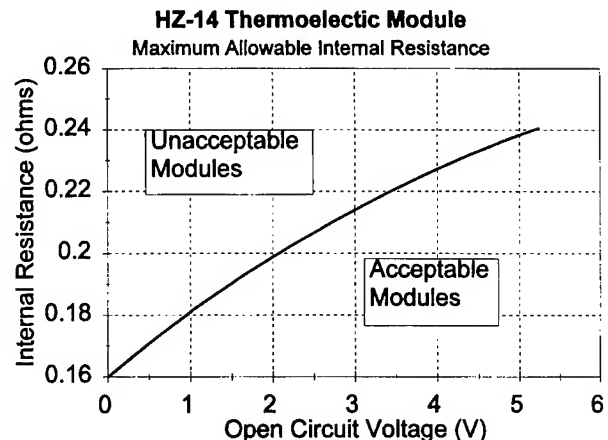


Figure 9 - Internal Resistance vs Open Circuit Voltage

It is important to understand that maximum power cannot be obtained from the module unless the load resistance is closely matched to the internal resistance of the module. The load resistance is equal to the internal resistance of the module when the load voltage is one half of the open circuit voltage. Figure 10 shows how much power is available from the HZ-14 module at different current levels (or in other words, at different loads).

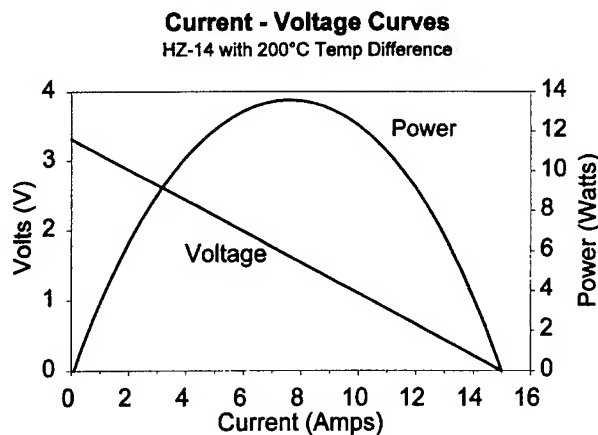


Figure 10 - Current vs Voltage

4.2.1 Precision Electrical Load: In order to accurately determine how much power the module is generating it is important to connect the module to an electrical load that can accurately measure the power being dissipated. The value of the electrical load must be close to the value of the internal resistance of the module in order to obtain maximum power from the module.

Unfortunately the internal resistance of the module is a function of temperature. For the sake of this evaluation a load resistor that is between 0.15 Ω and 0.25 Ω is suitable. The load resistor must be capable of dissipating at least 20 watts of power and have at least 5% accuracy. Record the value of the selected load resistor on line 2.1 of Table 1.

4.2.2 Connect Precision Electrical Load: The precision load that was selected in section 4.2.1 must be connected to the power leads of the module. A switch that is capable of switching the potential 15 amps of current needs to be placed in the circuit. It is preferable to solder all connections to prevent loose or high resistance joints. A 14 awg wire or larger should be used. Heat sink the resistor in an appropriate manner.

4.2.3 Measure Resistor Voltage: With the load resistor connected to the module, heat the module to the operating conditions and allow the temperatures to stabilize. Measure the voltage across the load resistor. This is the "resistor voltage" (V_r).

4.2.4 Measure Loaded Voltage: Measure the voltage of the module on the module leads. This is the "loaded voltage" (V_l). It is important to measure the voltage on the module leads.

4.2.5 Measure Open Circuit Voltage: With the meter leads still connected to the module leads, break the circuit by opening the switch discussed in section 4.2.2 and quickly measure the open circuit voltage (E_o). This value should be measured about 1 second after disconnecting the load.

4.2.6 Calculate Module Current: Using Equation 1 calculate the current (I).

$$I = V_r \div R_l \quad (1)$$

R_l is the value of the resistor in ohms.

4.2.7 Calculate Internal Resistance: Knowing the open circuit voltage (E_o) from section 4.2.5 and the loaded voltage (V_l) from 4.2.4 and the current (I) from section 4.2.6, calculate the internal resistance of the module using Equation (2).

$$R_i = (E_o - V_l) \div I \quad (2)$$

The measured value of R_i can be compared to the maximum allowable R_i as shown in Figure 9. If the measured R_i is less than the allowed R_i then the module is producing more than specified power. Using the E_o from section 4.2.5 determine the maximum allowable R_i from Figure 9 and compare this value with the measured R_i from equation (2).

4.3 Interface Temperature Drop

If the module is known to be a good module but you still can't get rated power from the module then the module is not operating at the temperatures that it needs to be at.

When measuring the temperatures of the hot and cold side it is important to position the thermocouples as close to the module as possible. It is ideal to drill a thermocouple well into the thermal spreader plate and the cold side heat sink and position the thermocouple in the thermocouple well.

Measure the hot side temperature (T_h) and the cold side temperature (T_c).

To measure the temperature drop from the hot surface of the module to the cold surface of the module follow the steps described in section 4.1. This is the estimated module ΔT .

Now that the temperature drop from the hot source to the heat sink is known and the temperature drop across the module is known the temperature drop across all of the surfaces (ΔT_i) can be calculated from Equation 3.

$$\Delta T_i = (T_h - T_c) - \Delta T \quad (3)$$

The temperature drop across all of the interfaces should be around 30°C to 50°C but due to variations in material properties the value should be used as a guide only. If large values for ΔT_i are obtained (greater than 50) then the interfaces of the system may need to be improved. Following the guidelines discussed in the previous sections should help to design a suitable system.

Potential Applications of Advanced Thermoelectrics in the Automobile Industry

Donald T. Morelli
Physics and Physical Chemistry Department
General Motors Research and Development Center
Warren, MI 48090-9055

Abstract

Several proposed applications of thermoelectric devices in the automobile industry are reviewed. The key to the realization of these technologies is the continued development of new materials with increased thermoelectric efficiency.

Introduction

With increasing environmental concerns over the deleterious effects of waste heat and the harmful nature of compressed gases and chemical refrigerants, thermoelectric devices have received renewed attention in recent years. The idea of getting "free" electrical power from waste heat or obtaining cooling power from a solid state device is at first glance very appealing from technological, environmental, and economic points of view. However, many serious challenges remain to be met before large scale thermoelectric refrigeration and power generation become a reality: Can new more efficient materials be developed? Can device design be improved and adapted to new applications? Are the thermoelectric materials themselves environmentally "friendly?" And, perhaps most importantly, can a new generation of thermoelectric devices for energy conversion on a large scale be made economically? For thermoelectric materials and devices to find application in the automobile industry, the answer to all of the above questions must be in the affirmative. In this report, we discuss the prospects of achieving this goal, present several specific proposed applications, and evaluate the likelihood that these technologies will be utilized.

A *thermoelectric generator* is a device which directly converts heat into electricity. On the microscopic scale this energy conversion can be thought of as a transfer of energy from the atoms which are vibrating in the material to free charge carriers which travel down a temperature gradient and thus produce current flow in a closed circuit situation. In a thermoelectric cooler, on the other hand, an electric current is made to flow in a thermoelectric material and results in cooling of a junction by means of the Peltier effect. Both the

amount of electrical power produced in the generator and the amount of cooling power produced in the cooler are determined by the thermoelectric figure of merit Z . This quantity is a combination of three fundamental transport properties of the material: the Seebeck coefficient S , the electrical conductivity σ , and the thermal conductivity κ , namely,

$$Z = S^2 \sigma / \kappa \quad (1)$$

Since the dimensions of Z are inverse temperature, it is convenient to define the dimensionless figure of merit ZT , where T is the absolute temperature.

The figure of merit is a direct measure of the ability of generator to produce electrical power or of a cooler to produce cooling power. In the case of a thermoelectric generator, the efficiency (i.e., the electrical power generated divided by the input thermal power) is given by

$$\epsilon = \epsilon_{\text{carnot}} [(1 + ZT)^{1/2} - 1] / [(1 + ZT)^{1/2} + T_c / T_h] \quad (2)$$

where ϵ_{carnot} is the Carnot efficiency between a hot source at temperature T_h and a sink at temperature T_c . Thus for small ZT , ϵ is small, while for $ZT \rightarrow \infty$, the thermoelectric efficiency approaches the Carnot efficiency. While physical law does not restrict the values that ZT can attain, current state of the art thermoelectric materials all have $ZT < 1$, which limits the thermoelectric efficiency to less than 30 % of ϵ_{carnot} . In view of the relative leniency of the laws of physics with regard to how large ZT can become, it is quite surprising that no materials have been found with larger values of ZT . Based on recently developed models for thermoelectric materials [1] there is good reason to believe that values of ZT in the range 2-4 can be realized, and in fact a good deal of progress in this direction has been made in the last two years. To fully appreciate the significance of such a development, one need only note that a material with $ZT = 4$ would have a $\epsilon \approx 0.55 \epsilon_{\text{carnot}}$, which represents a substantial increase in device efficiency.

For a *thermoelectric cooling device*, the coefficient of performance ϕ (which is the ratio of the rate of heat absorption to the input electrical power) is given by

$$\phi = 0.5 (T_m/\Delta T)[(1 + ZT)^{1/2} - 1]/[(1 + ZT)^{1/2} + 1] \quad (3)$$

where T_m is the mean temperature of the hot and cold junctions and ΔT the temperature difference between them. Again, for ZT small, ϕ is small, while for $ZT \rightarrow \infty$, ϕ approaches the coefficient of performance of an ideal thermodynamic machine. The maximum temperature difference that can be achieved by a thermocouple in an adiabatic enclosure ($\phi = 0$) is given by

$$\Delta T_{\max} = 2T_m [(1 + ZT)^{1/2} - 1]/[(1 + ZT)^{1/2} + 1] \quad (4)$$

For $T_m = 290$ K, this gives $\Delta T_{\max} = 100$ K for $ZT = 1$ and $\Delta T_{\max} = 220$ K for $ZT = 4$.

The above elementary discussion on the efficiency of a thermoelectric generator and the coefficient of performance and maximum ΔT of a thermoelectric cooler are not meant to be complete but should convince the reader that with the development of high- Z thermoelectrics these technologies will become very attractive alternatives or supplements to conventional power generation or refrigeration techniques, especially when the added advantages of reliability, quietness, and all solid state operation are considered. We will now turn to a brief overview of several potential applications of thermoelectrics which have been proposed for the automobile industry.

Potential Application of Thermoelectrics in Automobiles

Exhaust Gas Thermoelectric Generator

The concept of an exhaust gas thermoelectric generator is based on early fossil-fuel-fired thermoelectric generators developed by the US Army for remote field use [2]. Recently, prototype generators for automobiles were built in both Japan [3] and by Porsche [4]. The high temperature of the exhaust gas stream requires the utilization of a thermoelectric material the figure of merit of which is maximized in the 300-500 C temperature range. In the case of [3], PbTe elements for which $ZT \approx 0.6$ were employed, while [4] used FeSi₂ elements with $ZT \approx 0.2$. In spite of its rather low figure of merit, apparently the latter material was chosen because of its low cost. Both of these prototypes produced moderate (< 100 W) power output. The use

of higher figure of merit thermoelectrics would afford a significant increase in this value. Several critical issues in addition to element figure of merit must be considered in the design and construction of an exhaust gas generator:

a). *Location of the generator.* In [3] the generator was placed between the takedown pipe and the catalytic converter. While this location may be desirable from the standpoint of taking maximum advantage of the heat produced by the engine, it risks a lowering of the temperature of the catalytic converter. Whether this was in fact the case was not discussed in this reference, but should be carefully considered when such a location is chosen. The location of the generator in the Porsche prototype was not indicated.

b). *Heat transfer from exhaust gas to thermoelectric.* In both [3] and [4] it was pointed out that the heat transfer from the exhaust gas stream to the hot side of the thermoelectric generator is not large enough when the exhaust gas is just allowed to flow down the exhaust pipe. Rather, some type of internal finning or diffuser arrangement must be used in order to minimize the temperature difference between the gas and the hot side of the device. It is critical, however, as pointed out in [4], that the cross-section for heat flux remain sufficiently high to prevent a decrease in engine power. Alternatively, one might consider locating the generator in a location remote from the exhaust stream and transfer heat to it using a fluid flowing in tubing wrapped around the exhaust pipe. Such an arrangement may provide an enhanced heat transfer from the gas but would require a pump to move the fluid and a radiator to cool it before returning to the hot gas.

c). *Generator mass.* The use of a thermoelectric generator is desirable from the point of view that it can provide electrical power to supplement the alternator and thus increase fuel efficiency. In order that this be achieved, the additional weight of the generator must not be so large as to defeat this advantage. It is difficult to estimate the fractional increase in fuel efficiency with the use of such a generator, but it is reasonable to suppose that it will not exceed 5 % (or

roughly 1.5 mpg). Assuming that the weight penalty on fuel efficiency is on the order of 100 lb/mpg, it is desirable to maintain the total generator mass below about 50 pounds.

d). *Thermoelement stability.* Due to the high temperature of the exhaust gas, it is imperative that the materials used for the construction of the generator be stable in this temperature range. PbTe and FeSi₂ elements remain stable well above 500 C, and SiGe thermoelements are stable to temperatures in excess of 1000 C. In developing new materials, the thermal stability of the alloys is a critical issue deserving close attention. Frequently it is not the thermoelements themselves, but rather the electrical contacts which fail at high temperatures, and thus this is also an area of concern when developing advanced materials.

e). *Environmental friendliness.* If and when the useful life of the generator has been exhausted, can it be disposed of harmlessly or recycled? Clearly this is an issue of ever growing importance today and must not be ignored. A material such as FeSi₂ clearly can be dealt with properly from this perspective. PbTe, on the other hand, presents a potential problem with respect to heavy element contamination. In the thermoelectrics industry, Bi₂Te₃ is the most widely developed material, and methods have already been developed for recycling most of the device material [5]. Evidently, when developing new materials, the question of environmental friendliness during manufacture, use, and ultimate disposal must constantly be kept in mind.

Finally, it is to be noted that High-Z Technology has been developing an exhaust gas generator for diesel trucks for which it is claimed that a maximum power output of 1000 W is obtained [6]. This generator uses Bi₂Te₃ thermoelements and thus operates at a lower temperature than those described in [3,4]. This has the advantage of not requiring as sophisticated a heat transfer enhancement mechanism since a fairly large amount of temperature drop between the gas and the hot side of the thermoelectric can be tolerated. On the other hand the efficiency suffers somewhat since the Carnot efficiency is lowered. While this type of generator may find application in large diesel trucks, it

seems unlikely that it will be employed on passenger cars because of its large size.

Cabin/Seat Air Conditioning

Thermoelectric cooling has found widespread application for small scale applications where cooling power requirements are 10 W or less. This is because the coefficient of performance of a thermoelectric cooler increases exponentially with decreasing cooling power, and at low cooling powers exceeds that of a standard compression-type air conditioning unit. For large scale applications, such as home and vehicle air conditioning, the coefficient of performance of thermoelectrics is less than half that of standard air conditioners when one takes into account the inefficiency of the conversion of mechanical energy to electrical energy by the automobile alternator. The crossover between the coefficients of performance of the two cooling techniques occurs for cooling powers on the order of 100 W. However, with the emergence of new materials with enhanced figure of merit, it is expected that the coefficient of performance of two cooling techniques will become comparable even for cooling powers in the kW range. Then the added advantages of solid state operation, reliability, and freedom from harmful refrigerants swing the pendulum in favor of thermoelectric cooling even on a large scale. When and if this becomes the case, the issue of cost will become the most relevant, and should be a concern for those developing new materials for advanced thermoelectrics.

In the case of an electric vehicle, the outlook is a little more promising since the system COP of a thermoelectric will be larger due to the elimination of the alternator inefficiency. As such currently available thermoelectric coolers have a COP about two thirds that of a comparable vapor compression system, and at $ZT = 2$ the two methods of cooling have similar COP. An additional advantage of this type of a thermoelectric cooling unit is that it can also serve as a heating system for the cabin: simply by reversing the direction of current flow in the device, heat will be liberated at the same junction where it is absorbed in the cooling application.

Another interesting application which has been considered is the use of thermoelectrics for seat cooling [7]. The principle here is that a quick level of personal comfort of the occupants of a vehicle can be achieved even when the cabin itself is at an elevated temperature simply by cooling the seat using a thermoelectric

device. The thermoelectric device modules can be embedded in the seat and located at strategic positions to provide the maximum level of comfort. This application also enjoys the same advantage as the cabin air conditioning unit in that heating of the seat can be affected simply by current reversal.

Cooling of Microelectronics Using Thin-Film Thermoelectrics

The efficient removal of heat from integrated circuits has become a cause for concern as electronic components evolve to ever higher powers and larger packing densities. Traditional methods of brazing IC's onto a high thermal conductivity substrate such as BeO are quickly becoming incapable of handling the high heat loads generated in such applications. While the advent of chemically vapor deposited diamond was hailed as the successor to BeO for thermal management, the high cost of production of this material has precluded its widespread use. A potential niche for thermoelectric coolers would be for the cooling of high power electronics which operate only for limited periods of time [8]. The advantage of using a thin-film type thermoelectric device in this type of application is that the cooling power is inversely proportional to the length of the thermoelectric legs, which can be made very short in this geometry. The entire area of thin-film thermoelectric devices is a new one, and devices made with traditional materials are only now being investigated. In addition to the potential of new materials, unusual effects associated with the two-dimensional nature of quantum well and heterostructure systems [9] have been predicted which could improve device efficiency even more. Only time will tell whether such enhancements can be realized in the laboratory.

In summary, it is clear that an increased sensitivity to the undesirable nature of rejected heat from fossil-fired plants and engines has driven a dramatic rebirth in the interest of thermoelectric generator technology. New applications and designs have emerged which demonstrate the viability of converting heat to electricity on a large scale. At the same time, thermoelectric refrigeration is beginning to penetrate significant consumer markets (e.g., picnic coolers currently require more than half a million thermoelectric modules annually). With such increasing demand, thermoelectric module production costs have steadily decreased and will continue to do so. The engine driving this technology forward is the continued development of new materials with higher

thermoelectric efficiency. New models for enhanced figure of merit materials as well as very encouraging experimental results indicate that we are witnessing the dawn of a new era in thermoelectric technology. While the evolution from theory to everyday device will not happen overnight, with steady progress it can be expected that thermoelectrics for power generation and refrigeration will become viable and competitive technologies early in the next century.

References

1. G.A. Slack, in *Thermoelectric Handbook* (ed. M. Rowe, Chemical Rubber Company, Boca Raton, FL, 1995), p. 1.
2. A.B. Neild, Jr., SAE-645A (Society of Automotive Engineers, New York, NY, 1963).
3. E. Takanose and H. Tamakoshi, *Proc. 12th Int. Conf. Thermoelectrics* (ed. K. Matsuura, Institute of Electrical Engineers of Japan, 1994), p. 467.
4. U. Birkholz, E. Groß, U. Stöhrer, K. Voss, D.O. Gruden, and W. Wurster, *Proc. 7th Int. Conf. Thermoelectrics* (ed. K. Rao, University of Texas-Arlington, 1988), p. 124.
5. G. Knockaert, , *Proc. 12th Int. Conf. Thermoelectrics* (ed. K. Matsuura, Institute of Electrical Engineers of Japan, 1994), p. 587.
6. J. Bass, N.B. Elsner, and F.A. Leavitt, *Proc. 13th Int. Conf. Thermoelectrics* (ed. B. Mathiprakisam, American Institute of Physics, New York, NY, 1995), p. 295.
7. S. Feher, SAE-931111 (Society of Automotive Engineers, New York, NY, 1993).
8. J.W. Vandersande, R. Ewell, J.-P. Fleurial, and H.B. Lyon, *Proc. 13th Int. Conf. Thermoelectrics* (ed. B. Mathiprakisam, American Institute of Physics, New York, NY, 1995), p. 174.
9. L.D. Hicks and M.S. Dresselhaus, *Phys. Rev. B* 47, 12727 (1993).

MINIATURE THERMOELECTRIC GENERATORS (TEG) WITH CATALYTIC HEATING

Anatychuk L.I., Mikhailovskii V.Y., Konopelnyuk V.V.

Institute of Thermoelectricity, General Post-Office, Box 86, 274000, Chernivtsi, Ukraine

Modern fuel thermoelectric generators (TEG) are widely used in the range of 10 - 500 W [1]. Chemical sources of current (CSC) that not always satisfy consumers are used at lower powers. Negative factors are large weight, cost, self-discharge amount, problems in storage and maintenance at low

temperatures. CSC manufacture is power-intensive, expensive and ecologically dangerous. That is why fuel TEGs capable to compete with CSCs are of interest. Table 1 corroborates the great potentialities of this work.

The present work is devoted to fuel TEGs on liquefied gas

Table 1

Comparative characteristics for CSC and fuel TEG

Converter	Conversion system, fuel	Specific energy		Relative cost of energy
		(W h)/kg	(W h)/l	
TEG	liquefied mixture of propane & butane	180-250	100-140	1
CSC	Mn-Zn, salt	65-85	110-180	20-50
CSC	Mn-Zn, alkaline	65-200	140-400	60-85
CSC	Li	150-500	250-1000	500-1500

development for 10-100 mW power ranges.

We do not know any examples of such low-powered TEGs production in the morderm practice. The main difficulty of the problem consists in the development of an 1-10 W effective and stable heat source.

The use of a flame burner is impossible because of the problem in small fuel amouts supply (0.1-0.5 g/h) and instability of such small size flame burning. Even under small changes in fuel or air consumption such burner ceases to operate.

Small power heat sources have been developed on the catalytic counter-flow burner base which stable operates on gas and is suitable for continuous operation on a self-sufficiency basis. The flameless catalytic burner feature at separated fuel and air supply is spontaneous burning resumption after short breaks in fuel supply, changes in air supply and combustion products discharge. The burner's temperature can be maintained within 250-400°C. A high efficient promoted catalyst with service life up to 10000 hours is used in heat sources. Fig.1 represents the diagram of a heat sources structure.

The use of results of a series research works in this direction ensured the development of such catalytic heat sources (CHS) [2-4].

TEGs design was made by the computer modelling. TEGs maximum is defined by the following optimizing parameters: a collector aerodynamic drag, burner-collector distance, fuel consumption, load impedance and thermoelectric battery (TEB) properties.

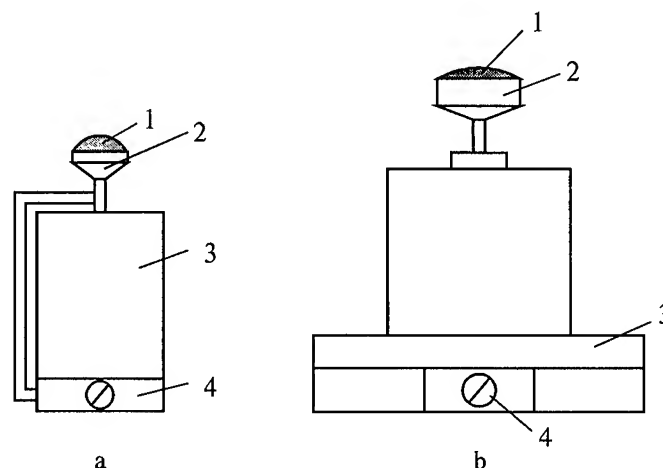


Fig. 1. a) - 1W; b) - 10 w.

1 - catalyst; 2 - a device for gas supply to the catalyst; 3 - fuel tank; 4 - controller of gas consumption.

Pilot samples of TEGs based on the structure diagram given in Fig.2 have been designed and produced.

In most cases the most important for a consumer is not such high efficiency but extended service life. For this purpose a hot juncle temperature of TEG was specified within 120-150 C and alloys based on Bi₂Te₃ were used for its development.

TEB consists of eight modules placed in series. A 15 mW module for a TEG has 44 thermocouple legs with cross-section of (0.26 x 0.5) mm² and 12 mm long, for 100 mW - 80 legs with cross-section (0.71 x 0.71) mm² and 10 mm long.

Heat regeneration method consists the structure peculiarity. A portion of a heat released from the TEB is used for its fuel tank heating. This increases CHS efficiency and stability. Complex study of 10-100 mW TEGs have been performed and a number of peculiarities in their operation were found out.

Processes of convective heat exchange in such systems have not studied yet and this hinders TEGs design. The analysis of heat exchange processes for burner-collector configuration of 1-10W catalytic heat sources showed that natural convection in heat exchange from the miniature burner to the collector is reduced to minimum and so called film regime of heat exchange bordering with heat exchange by thermal conduction is possible. Stable burning is provided therewith by forced gas supply that intensifies mass transfer in the catalyst layer and round the burner.

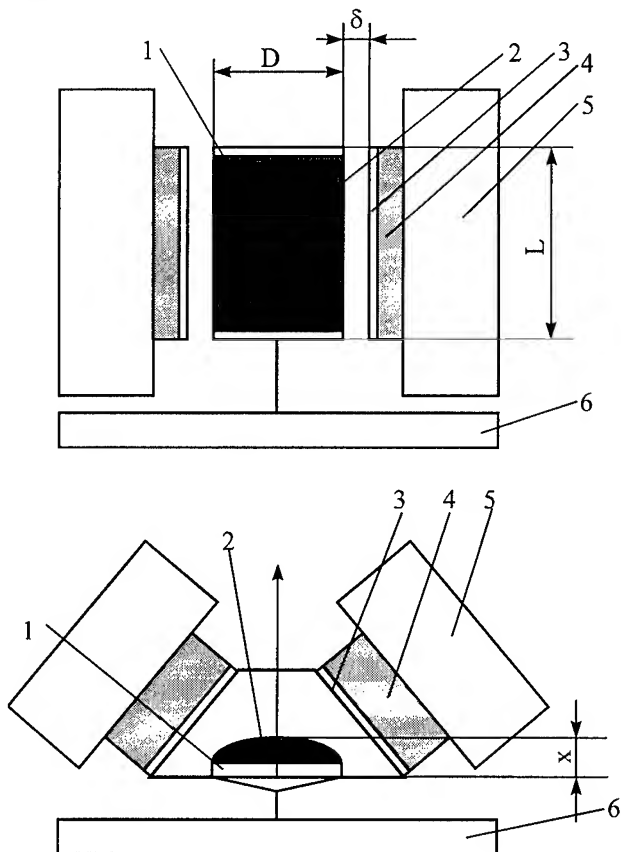


Fig. 2. Structural diagram of TEG

1 - catalytic heat source; 2 - emitting surface of the burner; 3 - heat receiving collector; 4 - thermoelectric battery; 5 - radiator; 6 - fuel tank.

TEG parameters dependence on fuel consumption has been studied and shown in Fig. 3. Maximums of electric power and efficiency are caused by maximum availability in the functional dependence of the burner temperature on fuel consumption. Causes are: the peculiarities of fuel and air supply in a counter-flow burner. First, when the fuel consumption is small and oxygen is in excess, hydrocarbon burns completely and temperature increases to its maximum value. Then, when gas speed begins to impede, the air accesses into the catalyst layer, lack of oxygen come into effect and temperature decreases. For the giving conditions the catalyst activity can also be the limiting factor for the burning process

but this factor was excluded by the use of the catalyst of obviously high activity.

More detailed study of the examined dependence showed that the maximum temperature region can be observed in considerably wide range of gaseous fuel supply speed even in the case of hydrocarbons conversion degree decrease. This testifies about the mechanism compensating the temperature decrease brought on by fuel consumption increase and decrease of the conversion. It was found out that oxidation zone transfer (maximum temperature in the catalyst layer) near to the burner surface was such mechanism. In this case the air access to the oxidation zone is facilitated and gas combustion is more complete.

Fig. 3 shows that the efficiency maximum is realized at smaller fuel consumption in comparison with the electric

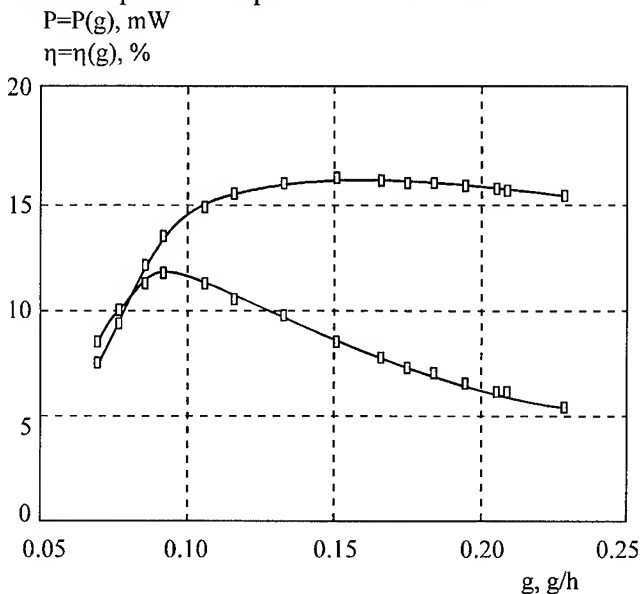


Fig. 3. Electric power P and efficiency η of thermoelectric generator with catalytic heat source dependence on fuel consumption.

power maximum. The efficiency at the TEG maximum power is about 70 % of its maximum value. The maximum efficiency condition when electric power is not less than 80 % of its maximum value is more preferable.

The main characteristics and parameters of two TEGs models on condensed propane and butane mixture are given in Table 2.

Comparison of electric power cost of catalytic generators' TK O.015 and TK O.1 with Mn-Zn chemical sources shows that thermoelectric generators' electric power cost is in 2-3 times smaller even if not to take into consideration exploiting expenses during 15000 hours. The effect value is sufficiently increased if the consumer is in a remote, inaccessible place, or if the access to it is impossible by some reasons. In this case it is reasonable to use low-powered fuel TEGs.

From the above stated one can make a conclusion about competitiveness of 10-100 mW TEGs in comparison with CHS. The decisive factors are low cost of gas fuel and TEG

Table 2

Parameter	TK 0.015	TK 0.1
nominal electric power, W	0.015	TK 0.015
matched load voltage, V	4.5	0.1
optimal fuel consumptio, g/h	0.09	9.0
catalyst service life before maintenance schedule, thousand hours, not less than	6	0.6
TEG sevice life, thousand hours not less than	15	6
Operation on one fueling, h 120 50	120	15
Mass without fuel, g not more than 70 250	70	250
Overall dimensions, mm not more than:		
diameter	45	60
height	60	120

structure, long service life and reliability, ability to operation at low temperatures and ecological purity, practically unlimited storage period.

References

- [1] Anatyчук L.I. *Thermoelements and thermoelectric devices*: Reference book. - K.: nauk.dumka, 1979. - 766 p.
- [2] Mikhailovsky V.Y. "Heat sources with catalytic combustion of hydrocarbons for thermoelectric generators." - *Journal of Thermoelectricity*, N 1, Oct., 1993, p. 51-58.
- [3] Mikhailovsky V.Y. "The gaseous fuel oxidation in countercurrent catalytic heat sources." - *Journal of Thermoelectricity*, N. 2, Oct. 1994, p. 51-58.
- [4] Mikhailovsky V.Y., Strutinskaya "Theoretical background for calculating main parameters of a catalytic element in counter-flow burners for thermoelectric generators." - *Journal of Thermoelectricity*, N. 3, Oct., 1995, p. 51-58.

A STOVE-TOP GENERATOR FOR COLD AREAS

Anders Killander, Royal Institute of Technology, Stockholm, Sweden
John C. Bass, Hi-Z Technology, Inc., San Diego, California

Abstract

This paper discusses the development and test of a prototype thermoelectric generator which is designed to use the heat of existing wood fired stoves that are typically used in the area for home heating. This generator is being developed by the Royal Institute of Technology, in Sweden, to provide small amounts of power to homes in the remote northern areas of the country which are beyond the electric grid. The paper will discuss some of the aspects of the generator design, as well as the early results obtained and some of the lessons learned from the first home test site in Skerfa, Sweden, which is located near the Arctic Circle. The bismuth-telluride thermoelectric modules used in the generator are also discussed.

Background

In Northern Sweden there are a few hundred families living in houses in areas where the electric utilities will not connect them to the grid. The cost of grid connection is estimated to be between \$5,000 and \$120,000 per house and therefore it is not economical.

The government of Sweden supports this type of rural living since it believes that a populated countryside is good for the nation. They support these families in many ways by charging them the same basic price for services as is charged to people in populated areas. However, this support does not include electricity.

Most of the homes in this area of Northern Sweden are old mountain farms which has been in continuous use for many generations without electricity but, of course, the residents desire some of the advantages and conveniences the electricity provides. Currently they use kerosene lamp for light, wood stoves for heat and small gasoline powered motor generators for electricity. However, most of the people believe these generators are too noisy, require too much maintenance, and have high fuel cost in Sweden.

Another problem with the motor-generators that are available is that their output characteristics do not match the load requirements of the farm homes. Their output is generally higher than the demand requirements. If the generators are used to charge the storage batteries, they are only run for short periods of time.

The Engineering Design group at Sweden's Royal Institute of Technology undertook the problem of providing several hundred watt hours per day of electric power. They started by investigating the different methods for producing small amounts of electric power with the energy sources available.

The result of this investigation(1) was to select thermoelectric technology as the conversion means and the home wood stove as the heat source.

Problem Definition

Typical houses in Northern Sweden are somewhat large, made of wood and are well insulated. The farmhouse in Skerfa, Arjeplog, Sweden that was selected for the test is shown in Figure 1. In the harsh winter season snow is present from November to May and during this period some families stay in an area of the house close to the kitchen and do not heat the entire house. The main source of heat in these farm homes is usually a large wood stove located in the kitchen.



Figure 1: Test Site in Skerfa, Sweden

Because the houses are located above the Arctic Circle, there are only a few hours of daylight in the winter which precludes the use of photovoltaic systems. To save energy during this period, only a few rooms are illuminated.

Families who live in the area were surveyed to determine their main desires if electricity were available. The results in order of importance were:

- Having lights such as provided by a 12v small fluorescent light
- Power for a TV 2 to 2.5 hours a day
- Power for a water pump to pump water from the lake, river, or well into a pressurized storage tank in the house
- Power for a vacuum cleaner once or twice a week
- Operate small hand tools to make repairs
- Power for small kitchen appliances such as a food processor.

The general opinion of the population was that providing the first three items would satisfy 95% of the families' desires.

A survey of the available temperatures associated with the cast iron wood stove are provided in Table 1. The positions referred to in Table 1 are shown in Figure 2.

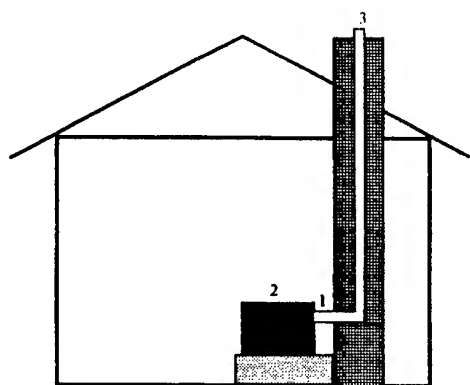


Figure 2: Temperature Positions

Table 1

Position	Location	Source Temperature	Sink Temperature
1	Behind Stove	300 - 500°	20°
2	Stove Top	150 - 300°	20°
3	Top of Chimney	140 - 200°	Sub-Zero

The daily demand for electricity was estimated to be between 200 and 300 watt-hours. This was based on providing power for 4 to 6 low-wattage lamps and a small TV. One lamp in the kitchen would be on most of the day while the lights in the other rooms would be on for only a few hours a day. Power generation from the woodstove heat source could be accomplished during 12 to 14 hours a day so that a device capable of producing 20 to 40 watts would be sufficient including the losses for a DC/DC converter.

Generator Design

The generator design developed was based on the use of two HZ-20 modules produced by Hi-Z Technology, Inc. in San Diego, California. The properties of this module, which is shown in Figure 3, are presented in Table 2.

The generators that were built and tested each used two HZ-20 modules connected electrically in series. The nominal output voltage of 4.76 Volts from the modules is converted upward to a nominal 13.5 Volts by a DC/DC converter and was used to charge four 6 Volt lead acid Exide batteries connected in series/parallel to provide a 12 Volt power source.

The generators tested consisted of a 270 x 100 mm aluminum heat collector plate 8 mm thick with two HZ-20 modules were mounted on the plate. A 0.254 mm thick wafer of Al_2O_3 was placed on each side of the module for electric isolation and Wakefield thermal grease was used on each side of the insulation wafer. A single aluminum extruded heat sink measuring 270 x 105 mm and 85 mm high was placed on the insulated modules. Two styles of heat sink were used in the

prototype generators, one heat sink contained eleven vertical parallel fins and the other contained nine parallel vertical parallel fins as well as a number of shorter angled parallel fins.

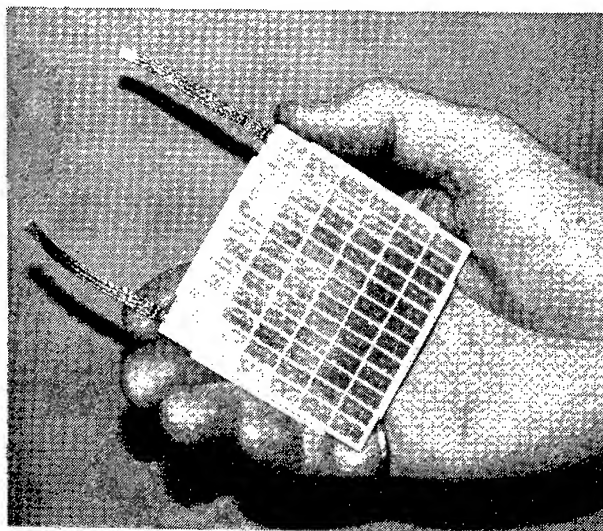


Figure 3: HZ-20 Module

Table 2: Properties of the HZ-20 Module

	Value
Width and Length	2.95" (7.5 cm)
Thickness	0.2" (0.508)
Special Order	
Weight	115 Grams
Compressive Yield Stress	10 ksi (70 Mpa)
Number of Active Couples	71 couples
Design Hot Side Temperature	230°C (450°F)
Design Cold Side Temperature	30°C (85°F)
Maximum Continuous Temperature	250°C (480°F)
Maximum Intermittent Temperature	400°C (750°F)
Thermal Conductivity	0.024 W/cm ² K
Heat Flux	9.54 W/cm ²
Power*	19 Watts
Load Voltage	2.38 Volts
Internal Resistance	0.3Ω
Current	8 Amps
Open Circuit Voltage	5.0 Volts
Efficiency	4.5%

*Minimum value at design temperatures and matched load

The heat sink was cooled by a 12 Volt fan which is mounted above the heat sink to blow cooling air down over the heat sink extrusion. Three fans ranging from 0.9 Watts to 2.2 Watts were tested. The 2.2 Watt fan was ultimately selected for use.

The heat sink and the collector plate were pressed against the modules by four sets of Bellville spring washer stacks which pressed against the end of the heat sink fins. A stud passed through each spring stack and heat sink and was threaded into the collector plate. The spring force was adjusted to provide about 14 kg/cm² of pressure on the module by a nut on the upper end of the stud which presses against the spring stack.

Test Results

Temperature of the stove top vary with both position and time. It is dependent on how and when the fire is laid, and to some extent, the outside temperature because that affects the frequency of adding new wood.

The temperature was measured at full fire and normal fire conditions for locations across the stove top. Table 3 presents the variations in the stove top temperature.

Table 3: Stove Top Temperature Variations

Location	Full Fire	Normal Fire
Left Front	320° - 340°C	195° - 200°C
Left Rear	335° - 350°C	210° - 220°C
Right Front	220° - 230°C	160° - 165°C
Right Rear	180° - 190°C	145° - 150°C

The left-rear position was selected to install the generator. This selection was made not only because of the high temperatures available, but also because it did not interfere with the Family's normal use of the stove. Figure 4 is a picture of the stove with the generator in the left rear of the stove. The person shown loading fuel into the stove is Mrs. Lasko, one of the occupants of the farm.

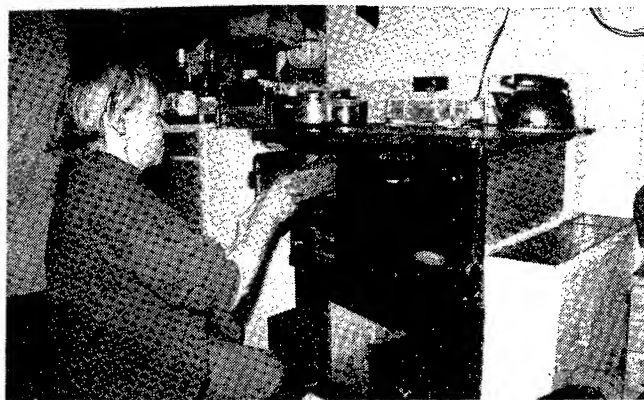


Figure 4: Wood Stove with Generator at Left Rear

A data logger was used to record the temperature variations to the stove, the heat sink, and the ambient as a function of time between 7:20AM and 10:10AM. These variations are shown in Figure 5.

Experience showed that the best generator output was obtained during the morning hours when the ambient temperature was low and the stove was being fueled frequently. During this time the output of the generator was about 10 Watts. As the temperature in the kitchen stabilized during the day, the output decreased to between 4 and 7 Watts. This generator output supplied the battery with a net input of from 1 to 5 Watts.

It was found that the generator with the heat sink with all vertical fins performed better than the one with a combination of vertical parallel fins and angled fins. This generator was therefore left for the field testing for the 1995/1996 winter season.

Problem Areas and Possible Solutions

The results provided here are for the first prototypes. Many lessons have been learned from these tests and changes will be made to improve the generator's operation.

One problem that must be face is that the top to these old cast iron stoves are not very flat and, in addition, the flatness changes with the temperature. This can cause a large temperature drop between the stove top and the heat collector. Several recommendations have been given to remedy the non-flat problem. One is to articulate the heat collector so that it can conform to the stove top more easily. Another is to provide a compliant pad possibly made of copper felt or other materials between the stove top and the bottom of the heat collector.

A related problem is that the current generator merely sits on the stove top under its own weight. The heat transfer would be improved if it could be clamped to the stove top with some type of spring loaded device.

Another option may be to make the heat collector and circular burner as one piece. In this way the heat collector would be heated directly by the fire and hot gases in the stove. This would require the removal and replacement of the existing burner cover when the generator is used.

Cooling air for the heat sink is obtained from a point directly over the stove top. The air temperature in this location is much higher than the ambient and therefore causes a higher heat sink temperature which results in a lower module efficiency. Experience has shown that, over small temperature variations, one can obtain twice the increase in power by lowering the module cold junction temperature than can be obtained in raising the hot junction temperature the same amount. This is because the peak in the figure-of-merit (Z) curve is near 100°C and, for the same temperature difference across the module, one gains more in average Z as the hot temperature is decreased than one loses from the decrease in Carnot efficiency.

One possible solution to the heat sink problem is to locate the fan remotely away from the stove top air. Cooler air would then flow to the heat sink through a lightweight duct and lower its average temperature.

Another area that needs improvement is the DC/DC converter. These devices are usually designed for optimum operation at a fixed voltage input. Since the output of the stove top generator changes over a relatively wide range during its operation, it is off optimum much of the time.

What may be required to solve the DC/DC converter problem is a fuzzy logic or smart controller which can sense the operating conditions of the generator and automatically adjust the DC/DC converter to provide optimum performance for the current input conditions.

Conclusions

The stove-mounted generator for use in remote areas is operating. While the power output today is less than the modules can produce, the prototype generator can easily be modified, as discussed above, to improve the output of the design.

The best results are that the occupants of the farm where it is installed are pleased with the unit. They now have electric light and can watch some TV during the long winter night.

An unverified side benefit of the generator is that it may have decreased the amount of fuel the Laskos burn. This is because

the small fan used to cool the generator heat sink also circulates air around the kitchen. This results in air mixing which provides a noticeably more uniform room temperature and a higher comfort level.

Acknowledgment

The authors would like to thank Mr. and Mrs. Rune Lasko for the use of their farm as the test site and Ms. Marianne Hofman for the photographs taken at the test site.

Reference

1. Killander, Anders J., "Thermo-electric Generator - Northern Sweden", TRITA-TSM R-96-1 ISSN 1104-2133 Royal Institute of Technology, Stockholm, Sweden, Feb 1996.

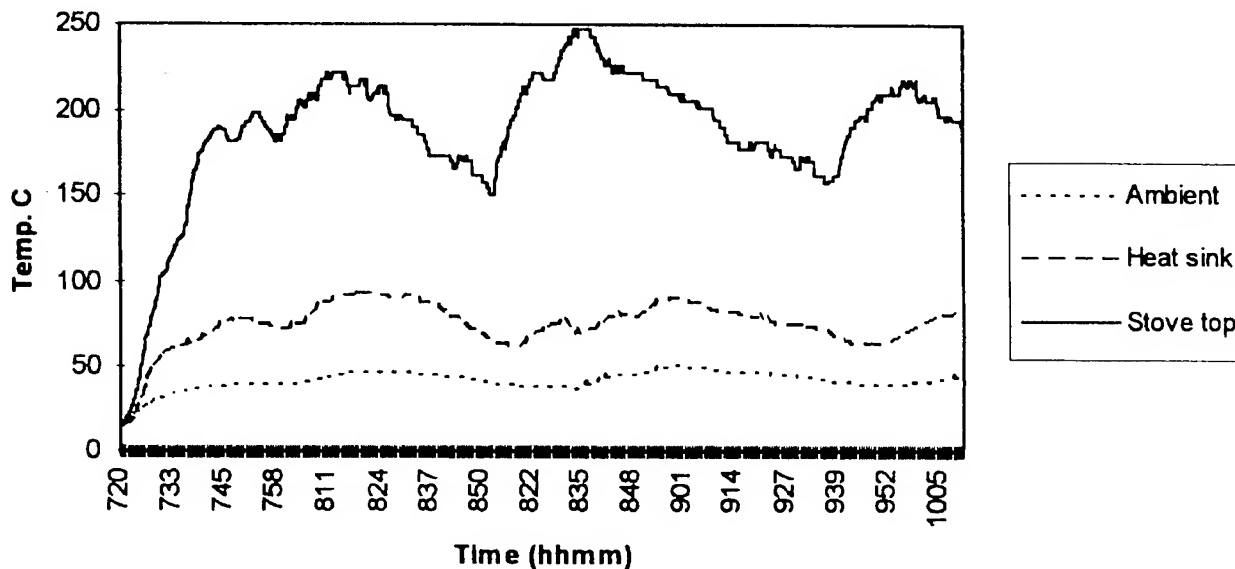


Figure 5: Variations of Stove Temperatures with Time

Free convection and electrical generation with thermoelectrics

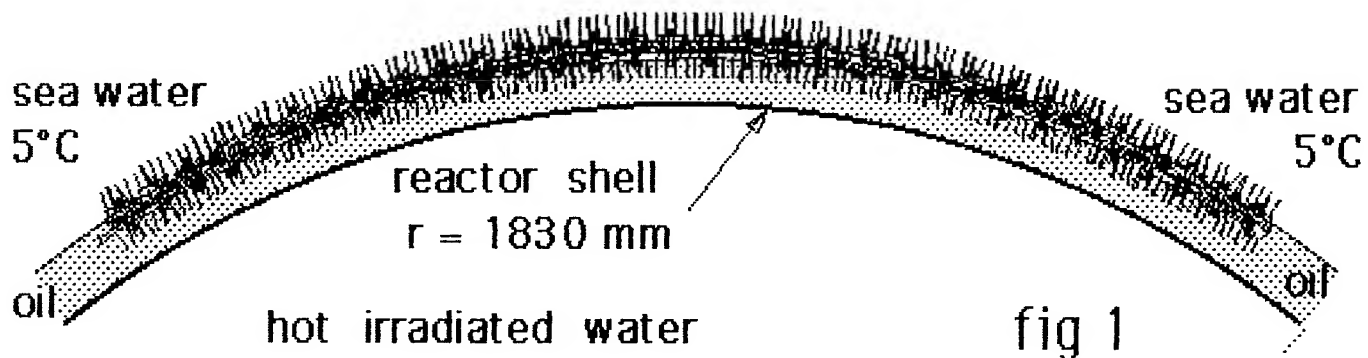
Jean BUFFET consulting engineer

Abstract The main advantage of thermoelectricity compared to conventional techniques of refrigeration and electricity generation lies in the absence of mechanical parts such as motors and compressors

Free convection based exchangers yield maximal safety due to the absence of fan or pump

We describe an electricity generating thermoelectric unit of above type ; it is designed for a small nuclear-powered submarine suitable for deep sea oil prospection

The purpose of the unit is to power an alarm system in case of reactor failure



1/ How the unit chosen as an example is expected to be used

A small 1500 kW nuclear powered submarine is designed for deep sea oil prospection especially under the northern polar ices.

In case of reactor failure , one needs to locate the submarine without using accumulators because of the toxic gases they would release in a narrow space.

As a matter of fact the temperature of the irradiated water in the stopped reactor goes down slowly from 100°C to 40°C within 140 minutes

In this critical phase , the submarine lies on the bottom of the ocean where the temperature of the water is 5°C . Thus we have two heat reservoirs (cold sea water and hot irradiated water) having a temperature difference evolving between 95 K and 35 K within 140 minutes .

A thermoelectric generator, based on the two reservoirs , can generate a DC electric current which

can activate an alarm device with which it is possible to locate the submarine.

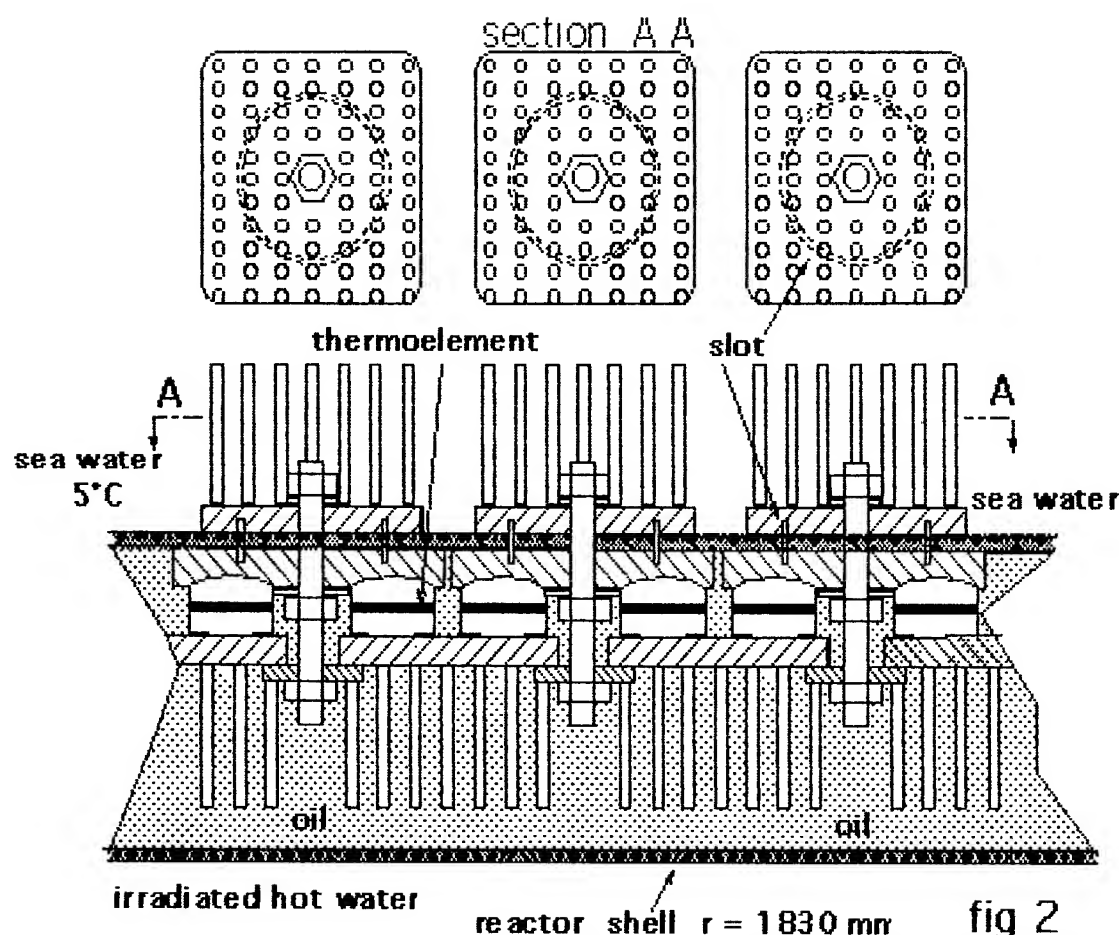
Nevertheless it is not possible, in this way , to produce an electrical power large enough to activate circulating pumps for water or another liquid like oil

Thus **free convection** is chosen for the heat transfer between liquids and exchangers in order to create a difference of temperature between the two sides of the thermoelements

Moreover free convection gives an extrasafety as electric motors and pumps are absent

2/Description of the thermoelectric unit

The reactor is placed inside a special steel sphere (HY 80) of 3,66 m diameter. It is not allowed to have bolts or pipes through the reactor shell ; consequently a second spherical shell is built over the reactor and is welded on it making a reservoir filled with oil heated by free convection from the reactor irradiated water which circulates by thermosiphon . (fig 1)



The exchangers are made of an aluminium based alloy having a good thermal conductivity ($180 \text{ W}/(\text{K}\cdot\text{m})$) and a low electrical resistivity ($4,5/10^8 \Omega\cdot\text{m}$). Each plate ($52 \text{ mm} \times 52 \text{ mm}$) is provided with 74 pins $2,8 \text{ mm}$ diameter and 40 mm long (fig 2) so that the surface area in contact with water or oil is large with a low friction power.

The plate and the pins form a single cast unit so that there is no contact resistance between plate and pins.

A bolt in the middle of the exchanger tightens the shell of the oil reservoir between two plates. These plates are made bendable by means of a circular slot which allows the exchanger to press against the spheric shell (radius 1830 mm) with a very low contact resistance.

The thermoelements (14 mm diam., $1,5 \text{ mm}$ thick) are brazed on two copper plugs and make with them a "button". The buttons have a planar side and a spherical one. By means of the central bolt the button lean on the exchanger but can slip with the thermal dilatation without dangerous shearing strain on the thermoelements.

The electric current, produced by the Seebeck effect in the thermoelements, go through the exchanger plates. A film of electrical (but not thermal) insula-

ting material is spread on the shell under the exchangers in order to avoid leakage of current.

3/ Calculating the electrical power (P_{el}) of the unit

The electrical power (P_{el}) and the thermal power (P_{th}) pumped from the hot water are computed with an approximate value of the oil temperature and free convection coefficients (H_{sw} , H_{oil}); in fact H_{sw} and H_{oil} depend on the unknown surface temperature of the exchangers.

The thermal power (P_{th}) is compared to the data resulting from the heat transfer through the shell of the reactor with the difference of temperature between hot water and oil.

A new oil temperature result in a new electrical power and so on. The iteration is repeated until a sufficiently small difference between the two values of P_{th} is achieved.

The result is summarized in the table 1 here under with:

T_{hw}	irradiated hot water temperature
T_{oil}	oil temperature
P_{el}	electrical Power
P_{th}	thermal Power pumped from irradiated hot water

TABLE n° 1 Free convection

Thw	Toil	Pel	Pth	Y	Hsw	Hoil	E
°C	°C	W	W	v	W/(m ² *K)	W/(m ² *K)	%
100	65.5	1 137	67 900	36.6	68	48	1.7
85	54.3	710	59 200	28.5	52	43	1.3
60	36.3	276	32 800	17.8	31	29	0.8
40	23.7	85	18 000	9.8	19	21	0.5

TABLE n° 2 Forced convection

Thw	Toil	Pel	Pth	V	Hsw	Hoil	E
°C	°C	W	W	v	W/(m ² *K)	W/(m ² *K)	%
100	88.6	2 740	106 116	55.6	2 798	76	2.5
85	74.5	1 860	87 300	46.0	2 798	60	2.1
60	51.4	760	58 712	30.0	2 798	52	1.3
40	33.6	220	32 804	17.2	2 798	38	0.7

_Y current voltage in TE unit

_Hsw free convection coefficient between sea water and exchanger

_Hoil free convection coefficient between oil and exchanger

E unit efficiency = P{el} / P_{th}

free convection unit

8000 TE instead of 3000 TE for the forced convection unit

4/ Comparison with a forced convection unit

When inspecting **table 1**, we see that the efficiency is very low (**0.5 % to 1.7 %**) as a result of the small free convection factors (**19 to 68 W/(m²*K)**).

A unit with a sea water pump has been computed in parallel to the free convection unit ; the results appear in the **table 2**, with the same number of thermoelements.

We see that the available electrical power **Pel** is 2.5 time higher because of the sea water forced convection factor **Hsw = 2798 W/(m²*K)** instead of 68 to 19 W/(m²*K)

It would be possible to reduce the number of thermoelements to **3000** (instead of **8000** in the free convection unit) with the same available electrical power **Pel**. However using a pump with an electrical motor results in a loss of safety

Comparing the two unities gives the price to be paid for the absolute safety of the

BIBLIOGRAPHY

1/ HEIKES R.R. URE R.W. Thermoelectricity : Science and engineering _ Interscience Publisher 1961

2/ _KLAN H. Über den Wärmeübergang bei freien Konvektion von Luft in senkrechten Kanälen _Diss. TH Darmstadt 1976

3/ _CHURCHILL S . W. Correlating equations for laminar and turbulent free convection from a vertical plate Int. J. Heat Transfer 18(1975) S. 1323_1329

Electronic Structure of Semimetals from Transport and Fermiology Experiments.

A. C. Ehrlich and D. J. Gillespie
U. S. Naval Research Laboratory, Washington D. C. 20375

Abstract

For at least thirty years most of the generic features desirable in a material to have potential for a high thermoelectric figure of merit have been known and generally not disputed. Most of these involve some aspect of the electronic structure. The latter can be measured or at least qualitatively evaluated using traditional transport and fermiology experiments. These include temperature dependent electrical resistivity, low and high field Hall effect and magnetoresistance, and the Shubnikov-de Haas (or equivalently de Haas-van Alphen) effect. In this paper the theoretical basis for this kind of an evaluation will be given, with emphasis on the semimetallic class of materials where most thermoelectrics are found but which present their own problems. The four experimental techniques mentioned above will be described and some of the subtleties of the data reduction and analysis illustrated.

Background.

An understanding of and predictive power over electronic transport properties must start with a knowledge of the electronic structure. This requires the execution and interpretation of experiments designed to elucidate various aspects of the electronic structure. When the electronic structure may be sensitive to the parameteric conditions (temperature, kinds and strengths of fields, etc.), then it is preferable that these experiments be carried out under the same conditions that obtain during the electronic transport phenomena of interest.

In good metals, which may be defined as materials whose Fermi energy, E_f , is approximately 1.0 electron volts or more from the band edge, the situation is simplest. Many experimental electronic structure determination techniques are most powerful when carried out on metals. Furthermore, because $kT \ll E_f$ will obtain over the entire temperature range, determinations carried out at low temperatures can be expected to accurately reflect the situation at higher temperatures absent magnetic, crystallographic or other phase transformations. Importantly, data acquired at all temperatures can be reliably interpreted within Fermi-Dirac (F-D) or quantum statistics. Intrinsic semiconductors may not be amenable to quite as many experimental techniques but they will, at least behave according to Maxwell-Boltzman (M-B) or classical statistics at almost all temperatures which simplifies the interpretation of experimental data.

Most of the best known thermoelectric materials are semimetals for which the situation is much more complicated. Unlike an intrinsic semiconductor, in these materials the number of charged carriers, electrons or holes, does not approach zero as the temperature, T , goes to zero. Thus, at sufficiently low temperatures $kT \ll E_f$ where E_f is measured from the nearest band edge and roughly $E_f \leq 0.1$ eV. When this inequality obtains, Fermi-Dirac statistics hold and the material will behave much like a metal so that most of the low temperature fermiology experiments can be used to study the electronic structure. Further, many of the other electronic

properties are amenable to metallic like interpretations. If the same properties are examined as a function of increasing temperature, however, unlike a good metal, they will manifest changes associated simply with the transition from quantum toward classical statistics and not necessarily with any other changing electronic structure.

In this paper we shall discuss the use of four phenomena used in the investigation of electronic structure of conducting materials, to wit; electrical resistivity, Hall effect, magnetoresistance and Shubnikov-de Haas (or equivalently de Haas-van Alphen) effect. Since all of these excepting the electrical resistivity involve the use of magnetic fields, it is necessary to define the magnitude regimes of magnetic field. In solids, the relevant magnetic field parameter is the cyclotron frequency, ω , where $\omega = eB/m^*$ and e is the charge of the electron, B the magnetic induction and m^* the (cyclotron) effective mass. The five regimes of field are generally defined as¹, (i) $\omega\tau \ll 1$, the low field limit, (2) $\omega\tau \sim 1$, the intermediate field limit, (3) $\omega\tau \gg 1$, the high field limit, (iv) $\hbar\omega \gg kT$, the quantum oscillation regime, (v) $\hbar\omega \gg E_f$, the quantum limit. Here \hbar is Planck's constant divided by 2π and τ is the electron (or hole) lifetime or scattering time. We shall have nothing more to say regarding regime (v), the quantum limit. Firstly, to our knowledge it has rarely been achieved and secondly, while interesting in its own right, it is not now a tool for the investigation of the electronic structure of materials.

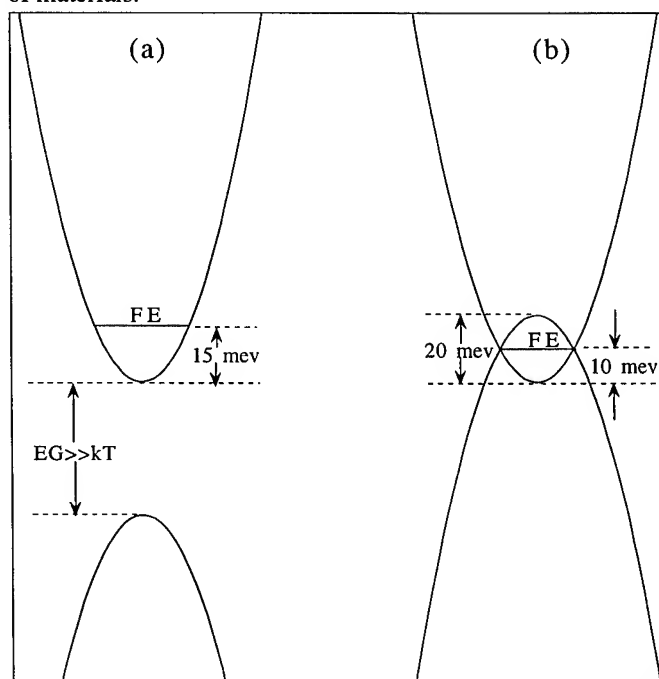


Figure 1. Model energy band diagram for two types of semimetals discussed in this paper. In 1a the energy gap, EG , between bands is much larger than any temperature of interest so that holes are never created. In 1b electrons and holes coexist at all temperatures but their numbers will increase with temperature.

It is also necessary to distinguish between two types of semimetals. In what we shall call here type 1 or one band material, an electron (hole) band, with a characteristic semimetal density of electrons (holes)/volume, is separated from the nearest fully occupied (empty) band by a gap large compared to any temperature of interest as shown in figure 1a. This could be, for example, a heavily doped semiconductor. A semimetal in which two bands overlap giving rise to equal numbers of electrons and holes (again in the semimetal density range at $T=0$) in the conduction and valence bands respectively will be called type 2 as shown in figure 1b. Bismuth is such a material. The number of electrons and holes will both increase with temperature, but of course remain equal in magnitude. There is, of course, a third category of semimetal in which there are electrons or holes but not both and temperature excitations created electron hole pairs in bands empty or full at low temperatures. This situation will not be discussed in this paper as the consequences are relatively apparent given an understanding of types 1 and 2.

Electrical Resistivity

Unlike the case of a metal or an intrinsic semiconductor, the Boltzman equation with a relaxation time mechanism representing the electron scattering processes cannot, in general, be solved in closed form for a semimetal. This is because the electron gas follows neither the low temperature F-D nor the M-B statistics, but varies between them as a function of temperature. As a consequence the position of the Fermi energy the nature of the screening of the ionized impurities and electron-phonon interaction are all functions of temperature. Ehrlich and Gillespie² developed expressions for the temperature dependent electrical resistivity for a variety of semimetallic electronic structures within the spherical band approximation and evaluated them numerically. Certain features of the resistivity are characteristic of certain features of the electronic structure and can be used diagnostically.

The simplest cases of a one band and two band (with hole and electron band masses equal) calculation are shown in figures 2a and 2b. The impurity induced resistivity and phonon induced resistivity have been calculated separately (inevitable deviations from Matthiessen's rule have not been taken into account) and their relative magnitude in figure 2 is not meaningful. Figure 2a shows a one band, 15 meV E_f at $T=0$ material. The rising impurity induced resistivity with temperature is a consequence of the increasingly less effective coulomb screening with temperature provided by a more nearly classical rather than a F-D electron gas. This feature vanishes with increasing E_f . The upward curvature with increasing temperature of the phonon induced resistivity comes from an increasing electron-phonon coupling and hence an increasing electron scattering matrix element.

Figure 2b shows the temperature dependence of a two band material with 20 meV overlap (10 meV E_f). Here the number of electrons and holes, n , both increase with temperature which is the primary reason for the fall of the impurity resistivity with temperature ($\rho \sim 1/\sigma \sim 1/n$). A second contribution is the improving screening with increasing n . The phonon induced resistivity is, of course, zero at $T=0$ and rises with temperature. Eventually, however, its rate of increase is overwhelmed by the increasing number of carriers

and the resistivity falls, somewhat akin to a semiconductor. A number of graphitic materials have exhibited peaks in their electrical resistivity not unlike that shown in figure 2b.³

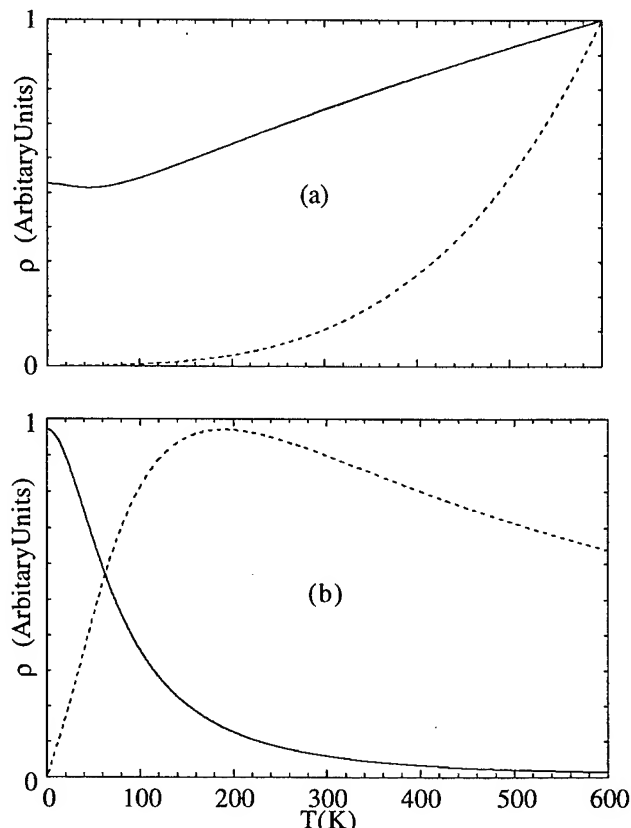


Figure 2. Model temperature dependence of both impurity induced (solid line) and phonon induced (dashed line) resistivity for the corresponding semimetals shown in figures 1a and 1b. Figure 2a represents a one band material with $E_f=15$ meV. Figure 2b represents a two band material with E_f 10 meV from both the electron and hole band edges.

Hall Effect

If a magnetic field is applied perpendicular to a current in a material, in general, a voltage (the Hall voltage, V_H) will be created in the third direction, perpendicular to both the current and the field, which is proportional to the product of their magnitudes.⁴ The constant of proportionality is called the Hall coefficient, R_H ; i.e., $V_H=R_HIB$. In the simplest models, spherical Fermi surfaces, isotropic and energy independent scattering times, τ , R_H depends only on the density of electrons and holes. In reality, τ is almost never isotropic and only in metals can one often assume energy independence. For semimetals the energy dependence of τ is critical and the spatial anisotropy is usually neglected to make the theoretical expressions, and therefore interpretation of data, manageable.

Low Magnetic Field Limit ($\omega\tau \ll 1$)

Spherical bands with isotropic, but energy dependent, relaxation times are assumed. As usual, analytical expressions can only be given if either $E_f \gg kT$ or $E_f \ll kT$. For the former, metallic expressions hold and the Hall coefficient, R_H is⁴

$$R_H = 1/ne \quad \text{single band,}$$

$$R_H = (1/e)[(1/n_1)(\sigma_1/\sigma)^2 + (1/n_2)(\sigma_2/\sigma)^2] \quad \text{two bands}$$

where σ_i is the conductivity for the individual bands, σ is the total conductivity and n_i are the carrier concentrations for the individual bands with a negative or positive sign for electrons and holes respectively.

If $kT \gg E_f$, then it is necessary to include an energy dependence in the isotropic relaxation time. Classical electron gas expressions hold which are⁵

$$R_H = (1/ne) \langle \tau^2 \rangle / \langle \tau \rangle^2 \quad (1)$$

$$\text{where} \quad \langle \tau \rangle = 4/(3\pi^{1/2}) \int \tau(E) x^{3/2} e^{-x} dx, \quad x = E/kT$$

The brackets $\langle \rangle$ indicate an average over occupied states. For the case of phonon, $\tau \sim E^{-1/2}$, and ionized impurity $\tau \sim E^{3/2}$, scattering respectively,

$$\langle \tau^2 \rangle / \langle \tau \rangle^2 = 3\pi/8 = 1.18 \quad \tau(E) \sim E^{-1/2} \quad (2)$$

$$\langle \tau^2 \rangle / \langle \tau \rangle^2 = 315\pi/512 = 1.93 \quad \tau(E) \sim E^{3/2} \quad (3)$$

It is clear from equations 1-3 that interpreting temperature dependent Hall data is not entirely straightforward. For example in measuring the Hall coefficient as a function of temperature starting at low temperatures one might find a monotonically falling R_H with increasing temperature. A plausible interpretation would be thermal excitation of electrons from lower to higher bands leaving behind high mobility holes - a kind of change of the electronic structure. However, it is also true that at sufficiently low temperatures the electron scattering will be dominated by ionized impurity scattering which will change over to phonon dominated scattering as the temperature rises. From the equations above it is clear that from this alone, a single band transitioning from quantum to classical statistics as the temperature rises, also results in a decreasing R_H .

High Magnetic Field Limit ($\omega\tau \gg 1$ but $\hbar\omega < kT$)

The Hall effect in the high field limit is perhaps the most powerful tool available for elucidating the electronic structure of conducting materials. It is relatively quick and simple to carry out and yet the results do not depend on the details of the scattering processes or on an assumption of spherical bands but only on the number of carriers in the band, or in the case of multiple bands of electrons and holes, on the difference in the number of electrons and holes. The only major weakness is that the high field limit is usually achievable only at low temperatures and in pure materials or ordered stoichiometric materials very nearly right on stoichiometry. However it is still much more easily achieved than the quantum oscillation regime and does not necessarily require single crystals to be useful. The results for either quantum or classical statistics, i.e., $kT \ll E_f$ or $kT \gg E_f$ are^{6,7}

$$R_H = 1/ne \quad \text{single band}$$

$$R_H = (1/e)[1/(n_e - n_h)] \quad \text{two bands}$$

Magnetoresistance

The magnetoresistance is usually defined as $[\rho(B) - \rho(0)]/\rho(0) = \Delta\rho/\rho$ where $\rho(B)$ and $\rho(0)$ are the resistance with and without an applied magnetic field. We consider here only effects arising directly from the action of the Lorentz force acting on charges moving through a magnetic field; i.e., we are ignoring such effects as localized magnetic spin alignments, magnetic field driven transitions, etc. For the most part, Lorentz force induced magnetoresistance can provide only qualitative information regarding the electronic structure of conducting materials. For a single spherical Fermi surface with isotropic, energy independent τ , $\Delta\rho/\rho$ will be zero. In real materials, this never occurs. In the low field limit, the theories predict $\Delta\rho/\rho \sim \rho^2$ for essentially all other electronic or scattering circumstances making unambiguous detailed interpretations of data essentially impossible. Magnitudes of magnetoresistance have been used to qualitatively evaluate "strengths" of energy dependence of τ , for example, but more can not be reliably said.

In the high field limit the magnetoresistance can provide one specific and important insight. As the magnetic field is increased, $\Delta\rho/\rho$ will initially vary as B^2 . As the condition $\omega\tau \gg 1$ is approached $\Delta\rho/\rho$ will become concave downward and approach saturation at some constant value provided the material is "uncompensated", i.e., the number of electrons does not equal the number of holes. If the two carrier types are equal in number, the material is compensated, and $\Delta\rho/\rho$ will continue to grow quadratically⁶. This is true in quantum as well as classical statistics and does not require spherical Fermi surfaces or any particular property of τ . The magnitude of the magnetoresistance will depend on these properties but not the B dependence.

So-called open Fermi surfaces are a separate case which would not be expected to occur very often in semimetals and will not be considered here. For a summary of theoretical expectations for open Fermi surfaces see Fawcett⁸.

Shubnikov-de Haas (de Haas-van Alphen) Effect

The Shubnikov-de Haas (S-dH) and de Haas-van Alphen (dH-vA) effects both arise in the quantum oscillation regime of magnetic fields where $\hbar\omega \geq kT$ and are among the most common and important of the Fermiology techniques. The S-dH (dH-vA) effect is the oscillatory magnetoresistance (magnetic susceptibility) as a function of B that arises when B quantizes the electron orbits in states whose energy is proportional to B .⁹ As B increases, a succession of clusters of permitted states separated by forbidden energy regions passes from below (in energy) to above the Fermi surface. As the permitted and forbidden levels pass through the Fermi surface the magnetoresistance, magnetic susceptibility and other phenomena that depend on the density of states at the Fermi surface will oscillate. The frequency of these oscillations, F , is given by $F = \hbar A / 2\pi e$ where A is an extremal area of the Fermi volume in k space perpendicular to the applied B . For a given direction of B relative to the crystal axes there may be multiple extremal areas due to either the shape of the Fermi surface and/or having many pieces of Fermi volume. Each area gives rise to a unique frequency which superimpose in the signal but these may be sorted out by applying a Fourier transform to the data. One then rotates

B some degrees relative to the sample, usually staying in the major symmetry planes of the sample, and repeats the experiment. By repeating this process in several symmetry planes many times one obtains extremal areas as a function of direction in the crystal.

For complex Fermi surface shapes sophisticated tomographic techniques are needed to extract the shape. For much simpler geometries, such as ellipsoidal shapes arising, for example, from a more or less quadratic dependence of energy on wave vector, i.e.,

$$E = [\hbar^2/2] \{ k_x^2/m_x + k_y^2/m_y + k_z^2/m_z \} \quad (4)$$

one can guess the shape of the Fermi volumes as ellipsoidal and calculate the predicted extremal areas as a function of the orientation of B. If the predictions fit the data, the shape is determined.^{8,9} This was done in reference 10 from which figure 3 has been taken. The circles are experimentally determined S-dH frequencies. The lines drawn through them are predicted frequencies for three separate ellipsoidal surfaces designated S1, S2 and S3. The fit is excellent and provides a high degree of confidence. Furthermore, the volume of the largest ellipsoid is equal to the sum of the volume of the two smaller ellipsoids consistent with the fact that the number of electrons must equal the number of holes in this compound. Furthermore, this indicates that no significant size piece of Fermi volume is likely to have gone undetected.

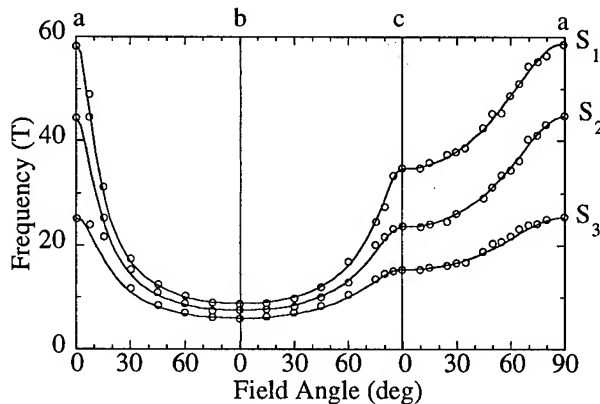


Figure 3. Shubnikov-de Haas frequencies as a function of the orientation of the applied magnetic field relative to the principal axes of the crystal from reference 10. The open circles are data and the lines are the predicted results for three specific ellipsoidal volumes.

It is also possible to obtain the cyclotron effective masses, M_i , for all the extremal orbits by measurement of the amplitude of the oscillations as a function of temperature at a given magnitude of B.^{10,11} M_i is given by

$$M_i = (\hbar^2/2\pi) [dA_i/dE]. \quad (5)$$

Using the equations 4 and 5 and the usual expression for the area of a cross section of an ellipsoid in terms of its radii, the k_i 's, one can obtain the band effective masses, m_i .^{10,11} Then assuming constant m_i from the band edge to the Fermi surface one can estimate the Fermi energy from equation (4). For a semimetal, where the E_f is relatively close to the band edge this approximation should be reasonable. It might be very

poor in a good metal where E_f is much further from the band edge.

Theoretical concepts and calculations can be invoked to assist in the final interpretation of the data. When multiple pieces of Fermi surface are present, band structure calculations even when imprecise can guide the detailed interpretation as to such things as where in k space they reside and whether they are electrons or holes. When frequencies in the data are detected that are sums and differences of other frequencies it can be an indication of magnetic breakdown¹⁰ which can further specify the location of the various pieces of Fermi surface. An even number of total electrons/cell means that the number of electrons and holes in the outer bands must be equal. This helps identify which of these the volumes detected represent. The Fermi surface must reflect at least the symmetry of the crystal. It can be more symmetric, for example a sphere, but not less.

When all of these steps can be executed, one ends with a very complete picture of the electronic structure in the conduction and valence band. What limits the power of the S-dH effect are the requirements and difficulties in carrying it out. The material must be in the form of a rather perfect single crystal, which can not always be made, and the magnetic fields must be even higher to achieve the quantum oscillation regime than in the high field limit. Very low temperatures are necessary in order to obtain measurable signals and a high density of data points in B is needed in order to carry out a meaningful Fourier transform. Finally, neither the data collection nor its interpretation is quickly done. However, if these difficulties can be overcome, one is left with a rather complete picture of those aspects of the electronic structure that importantly influences transport phenomena such as thermoelectricity.

Summary

Four experimental techniques useful in the elucidation of electronic structure of semimetals, which comprise most thermoelectric materials, have been described and discussed. The four selected are techniques requiring experimental skills largely already possessed by experimentalists working in the field of thermoelectrics and therefore feasible to incorporate into their research program. The presentation has been in order of increasing power of the technique, i.e., revealing increasingly detailed electronic structure information. It is, however, also in increasing order of difficulty of execution.

The detailed energy and directional dependence of the relaxation time, τ , must play an important role in the interpretation of the magnetoresistance and Hall effect and in fact in the thermoelectric power itself. Also of importance is the fact that in semimetals the current carriers will obey Fermi-Dirac statistics at the lowest temperatures and move toward a Maxwell-Boltzmann statistics approximation as the temperature rises. This in itself will influence the results of transport experiments and must be considered when analyzing and interpreting data.

Finally, the most powerful Fermiology techniques must be carried out on nearly perfect, stoichiometric materials so as to achieve a long mean free path and at low temperatures for the same reason, whereas the best thermoelectric materials are usually off stoichiometry and used at higher temperatures. Theoretical band structure calculations are also most easily and

usually carried out at the stoichiometric composition. Understanding the actual thermoelectric material, therefore, requires some kind of "extrapolation" of the experimental determinations with the help of theoretical band structure calculations and some model such as the rigid band model.

References

- [1] R. G. Chambers, *The Fermi Surface*, W. A. Harrison and M. B. Webb, New York, p.100 (1960).
- [2] A. C. Ehrlich and D. J. Gillespie, unpublished.
- [3] M. S. Dresselhaus, G. Dresselhaus, K. Sugihara, I. L. Spain and H. A. Goldberg, *Graphite Fibers and Filaments*, M. Cardona, Springer Series in Materials Science, Berlin, p. 188 (1988).
- [4] J. M. Ziman, *Principles of the Theory of Solids*, Cambridge University Press, p. 211 (1964).
- [5] F. J. Blatt, *Physics of Electronic Conduction in Solids*, McGraw Hill Book Company, New York, p. 286 (1968).
- [6] I. M. Lifshitz, M. Ia. Azbel and M. I. Kaganov, "On the theory of galvanomagnetic effects in metals", *Zh. Eksp. Teor. Fiz.*, vol. 30, pp 220-222 (1955) [*Soviet Phys.-JETP* (Engl. Trans.) vol.3. No. 1 pp143-145 (1956)]
- [7] *ibid.*, "The theory of galvanomagnetic effects in metals", vol. 31, pp 63-79 (1956) [*Soviet Phys.-JETP* (Engl. Trans.) vol. 4, No. 1, pp 41-54 (1956)].
- [8] E. Fawcett, "High Field Galvanomagnetic Properties of Metals", *Adv. in Phys.* vol. 13 No. 50, pp139-191 (1964).
- [9] J. M. Ziman, *Electrons and Phonons*, Oxford University Press, p.521, (1960).
- [10] G. N. Kamm, D. J. Gillespie, A. C. Ehrlich, and T. J. Wieting, "Fermi surface, effective masses and Dingle Temperatures of ZrTe₅ as derived from the Shubnikov-de Haas effect", *Phys. Rev. B*, vol. 31, No. 12, pp 7617-7623 (1985).
- [11] G. N. Kamm, D. J. Gillespie, A. C. Ehrlich, and D. L. Peebles, "Fermi surface, effective masses and energy bands of HfTe₅ as derived from the Shubnikov-de Haas effect", *Phys. Rev. B*, vol. 35, No. 3, pp 1223-1229, (1987).

DENSE SEMICONDUCTOR-INSULATOR NANOCOMPOSITES for NAVY THERMOELECTRIC APPLICATIONS

David Demske
Naval Surface Warfare Center
Carderock Division-White Oak, Code 682
10901 New Hampshire Ave.
Silver Spring, MD 20903-5640
(301) 394-1193

Abstract

This work is directed at the fabrication and optical characterization of anisotropic semiconductor composites with improved thermoelectric properties. Specifically, the quest is to dramatically improve the thermoelectric figure-of-merit, ZT , with an emphasis on the effects of "nanoconfinement", and on the crystallographic properties which provide an increase in the electrical-to-thermal conductivity ratio. Current work entails the fabrication of force-oriented nanostructural confinement of Bismuth (Bi) and Bismuth Telluride (Bi_2Te_3).

Background

In bulk semiconductor materials, under large diameter surface-size and confinement conditions, dimensional effects have such a small perturbation on the electronic and thermal (phonon) transport properties that, in practice, confinement-size effects are generally neglected. However, as the dimensions of the material and its confinement in some host material diminish, ultimately approaching sizes on the order of the thermal deBroglie wavelengths, "quantum confinement" effects ensue and a novel means to engineer the physical and electronic structural properties (density-of-status, phonon scattering, etc.) occurs.

Recently, several methods for optimizing the performance of thermoelectric (TE) coolers have turned to exploiting modern nanofabrication techniques. These push material confinement-size dimensions into the regime where conduction transport effects should drastically improve the TE material figure-of-merit.

In the early 90's, Hicks and Dresselhaus of MIT predicted the quantum confinement-size conditions under which the thermoelectric power (the Seebeck coefficient) and the electrical-to-thermal conductivity ratio could be dramatically increased [1]. These conditions have more recently been further investigated by Lin-Ching and Reinecke of NRL to include transverse quantum tunneling effects through thin insulative barriers in realistic semiconductor composite systems of quantum well and quantum wire superlattice configurations [2].

The next generation of thermoelectric materials require a dramatic improvement in the figure-of-merit (a factor of 4 or more) over those of existing bulk materials. In our present work we follow the recommendations of these investigators [1] [2] to synthesize improved thermoelectric material.

Nanofabrication

In recent years, advantage has been taken of the ability to "microfabricate" insulator-semiconductor composites down to subnanoscale sizes, thus providing a novel means to tailor basic microstructural-dependent properties. Nanofabrication techniques generally make appeal to highly sophisticated technologies such as molecular beam epitaxy (MBE) or metal organic chemical vapor deposition (MOCVD) on vicinal surfaces, and are usually combined with in situ analytical techniques that ensure proper crystallographic orientation. Using a different approach, our efforts employ high pressure injection of a liquid semiconductor melt into parallel arrays of hollow, insulate nanocapillaries or channels. The channels serve as a template for the embedded semiconductor material and provide an insulative framework, hosting bundles of nanometer-diameter semiconductive wires. On cooling, the semiconductor core-fill material is crystallographically "force-oriented" into preferentially -oriented crystallites, as described below.

In the present work we are utilizing the efforts originally initiated and established earlier at our laboratory by Carmen Huber and Tito Huber on nanocrystalline composites [3]. In this effort, both oriented Bi_2Te_3 (and Bi) crystallite aggregates, force-confined in aluminum oxide (Al_2O_3) nanochannels, and randomly-oriented Bi_2Te_3 nanocrystallites, confined in a porous-glass (Silica) honeycombed network are synthesized. In the preferentially oriented materials, crystallite orientation is made possible by the crystal lattice bonding, being weakest along the hexagonal c-axis. The crystallites will be oriented with the c-axis perpendicular to the confining wall. X-ray diffraction spectrum peaks of Bi_2Te_3 impregnated in the nanochannels is evidence of how the semiconductor is oriented in respective channels [3]. With the random-oriented Bi_2Te_3

nanocrystallites (in the nanophase glass network), x-ray diffraction spectra indicate random aggregate Bi_2Te_3 orientations.

Commercially, channel templates of 60 micron length channels, 200 nm in diameter are available [4]. In the quest toward ever-smaller wire diameters we are fabricating nanochannels employing an anodic oxidation processes, using ultra-pure aluminum as the starting material. Employing this technique, channel diameters on the average of about 10 nm are reported [5]. With the random-oriented porous-glass (SiO_2), average pore sizes down to about 56 angstroms are possible. To obtain parallel oriented channels, with different types of insulating materials (other than Al_2O_3), at these subnanometer dimensions, we have started investigating channels etched from nuclear particle track damage. The passage of heavy positively charged particles creates narrow ionization-produced defect paths on the atomic scale which are then preferentially etched out. In some inorganic insulators the channels are about 70-80 angstroms in diameter [6].

To impregnate templates of the porous glass networks or nanochannels with semiconductor material, a high temperature, high pressure autoclave is used. In most instances, the liquefied semiconductor melt is hydrostatically pressed into the channel voids at a few thousand psi. The high pressure-impregnation vessel is required to be operated at these moderately high pressures in order to overcome the surface tension between the capillary walls and the particular liquid semiconducting material being embedded. From a TE device standpoint, electrical connectivity between the ends of a large bundle of semiconductor wires in any given area of the nanochannel template is very important, yet very difficult to achieve in practice.

Optical Characterization of the Composites

In a parallel effort with the nanocomposite fabrication we have been setting up a laser system to simultaneously measure the TE material figure-of-merit transport parameters. "Contactless" electrical and thermal conductivity measurements are planned. Current efforts at the University of Maryland's Institute of Atomic and Molecular Materials Science and Engineering are directed at obtaining preliminary Z-parameter Data. Two experimental systems are set up: 1) a pulsed laser (flash) technique for measuring thermal diffusivity, and 2) a pulsed ruby laser bolometry technique for measuring electrical conductivity. These measurements provide the electrical-to-thermal conductivity ratio for the thermal diffusivity tensor component which is oriented parallel to the electrical current flow.

The experiments are configured such that the coupling of two measurements, through the change in the material specific energy, eliminates the need for an independent measurement of the specific heat in order to determine the thermal conductivity from the thermal diffusivity. Pulse laser

techniques enjoy popularity because they don't suffer the uncertainties typically associated with thermocouple methods. Thermocouple inaccuracies are generally attributed to wire thermal mass, response times and variations in composition of the wires and their junctions -even if intrinsic-type thermocouples are employed. Once more, this is especially true with the transient temperature response effects typically associated with thermal diffusivity measurements. Such considerations are even more significant in measurements conducted on heterostructured microcomposites such as those considered here, where points of secondary couples might corrupt the measurement.

Conclusion

In summary, following the direction of previous investigators, we are nanofabricating heterojunctioned composites of semiconductors embedded in nanochannel templates to improve the performance of the next generation of thermoelectrics. We are optically measuring the influences on the figure of merit transport properties of Bi and Bi_2Te_3 nanowire arrays, resulting from the diminishing nanochannel confinement of the wires. Ultimately, investigations will proceed to subnanosize channels to subsequently examine the effects of synthesized quantum confined wire structures.

Acknowledgment

This work was supported by the U.S. Office of Naval Research.

References

- [1] L.D. Hicks and M.S. Dresselhaus, "Thermoelectric figure of merit of a one-dimensional conductor", *Physical Review B*, vol. 1, No. 24, pp 16631-16634 (1993).
- [2] P.J. Lin-Chung and T.L. Reinecke, "Thermoelectric figure of merit of composite superlattice systems", *Physical Review B*, vol. 51, No. 19, pp 13244-13248 (1995).
- [3] C. Huber, M. Sadoqi, T. Huber and D. Chacko, "Micro-engineered Conducting Composites from Nanochannel Templates", *Advanced Materials*, vol. 7, No. 3, pp. 316-318 (1995).
- [4] Anopore, Whatman Laboratory Div., Clifton, New Jersey.
- [5] M. Saito and Miyagi, "Anisotropic optical loss and birefringence of anodized alumina film", *Opt. Soc. Am. A*, No. 12, pp 1895-1900 (1989).
- [6] C.P. Bean, M.V. Doyle and G. Entine, "Etching of Submicron Pores in Irradiated Mica", *Journal of Applied Physics*, Vo. 41, No. 4, pp 1454-1459 (1970).

Evaluation of metal-Bi₂Te₃ contacts by electron tunneling spectroscopy

Jiro Nagao, Eiji Hatta*, and Kōichi Mukasa*

Materials Division, Hokkaido National Industrial Research Institute, MITI

2-17-2-1 Tsukisamu-Higashi, Toyohira-Ku, Sapporo 062, JAPAN

**Faculty of Engineering, Hokkaido University*

N-13 W-8 Kita-Ku, Sapporo 060, JAPAN

Abstract

Understanding the states of the metal electrode-semiconductor junctions is important for improving the performance of the thermoelectric devices. Tunneling spectroscopy has been applied to the evaluation of metal-semiconductor Schottky junctions. In this study, tunneling spectroscopy is applied to understanding the states of a metal/Bi₂Te₃ or a metal/Bi₂Se₃ junction. Bi₂Te₃ and Bi₂Se₃ single crystals were prepared by Bridgman method. The metal contacts were made on the cleavage surface of Bi₂Te₃ or Bi₂Se₃ by the thermal evaporation in the vacuum of 10⁻³ Pa. All tunnel conductance were measured at 4.2 K. Mg/, Al/ and Ag/Bi₂Te₃ junctions exhibit V - shaped tunnel conductance curves which indicate that these contacts are the Schottky barrier. A Au/Bi₂Te₃ junction shows a flat conductance characteristic, so that we expect to be an ohmic contact formed in this junction. It becomes clear that the Schottky barrier is formed on the Mg/, Al/, or Ag-/Bi₂Te₃ junction. In the case of Au/ or Al/Bi₂Se₃ is also formed the Schottky barrier. Since Bi₂Te₃ and Bi₂Se₃, which are narrow energy gap semiconductors, form the Schottky barriers with those metals, the characterization of metal-semiconductor contacts is important to improve the performance of thermoelectric devices.

1. Introduction

Thermoelectric devices consisting of semiconductor-metal junctions have attracted considerable attention because of their high potential in energy conversion without producing any harmful substances^[1]. In general, it is required to improve a performance of the thermoelectric devices whose constituent semiconductors should have high figure of merit. Many kinds of materials have been studied to enhance the figure of merit^[2-3]. Especially, Bi₂Te₃ and its related materials have been applied to thermoelectric energy conversion devices which exhibit their high thermoelectrical figure of merit^[4-5] of $Z=3 \times 10^{-3} \text{ K}^{-1}$ in the room temperature region. On the other hand, it needs to understand the effect of electrode metals on the carrier transport since thermoelectric devices have metal - semiconductor - metal configuration. The Schottky barriers have been researched on metal - narrow energy gap

semiconductor junction, such as Au-InSb^[6], Al-Hg_{1-x}Cd_xTe^[7] and so on. Conventionally, the investigation of the Schottky barriers has been examined by capacitance - voltage (C/V) characteristics and current - voltage (I/V) characteristics. However, these evaluation techniques give only the barrier height of the Schottky barriers.

Tunneling spectroscopy has been applied to the investigation of the contact types in metal-semiconductor junctions. V-shaped tunnel conductance has been observed in the Schottky barriers^[8-10]. Furthermore, it can observe the disordered states of the metal atoms distributed in the semiconductor^[11]. In the present paper, we present the dependence of variety in electrode metals on the tunnel conductance in the metal/Bi₂Te₃ and /Bi₂Se₃ junctions. The effect of metal work function on the contacts will be discussed. We also discuss about the electron affinity of Bi₂Te₃ and Bi₂Se₃.

2. Experimental

Single crystals of Bi₂Te₃ and Bi₂Se₃ were grown by the Bridgman method using 99.9999% Bi, Te and Se. The crystals were cut into 5 mm x 5 mm in size using a wire saw with a 600-mesh silicon carbide slurry. Immediately on cleaving the crystal in air to be about 1 mm in thickness, the sample was set up in the Bell-jar of the evaporator.

Mg, Al, Ag or Au was chosen as an electrode to form an contact on the cleaved plane of Bi₂Te₃ and Bi₂Se₃ because the work function of Mg, Al, Ag and Au are 3.70, 4.20, 4.31, and 4.70 eV, respectively^[12]. The metal was evaporated through a mask having three holes of 1 mm in diameter. The metal of the same kind was also deposited on the another side of the cleaved sample. All metals of about 100 nm in thickness were deposited under a vacuum of 10⁻³ Pa.

The measurement configuration is shown in Fig.1. The tunnel conductance dI/dV was measured by the conventional

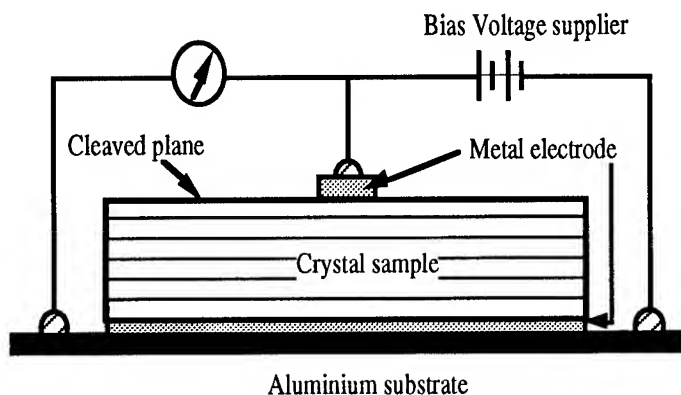


Fig. 1 Measurement configuration of tunnel conductance

modulation technique with modulated signal applied of 50 kHz in frequency and of 4 mV rms in amplitude. Experiments were carried out at liquid helium temperature. The composition of the single crystals was confirmed by electron probe micro-analysis (EPMA). Secondary ion mass spectroscopy (SIMS) was used to measure the distribution of the metal elements in the sample. The carrier concentration of the single crystals was evaluated from Hall coefficient data at room temperature with magnetic field of 0.3 T.

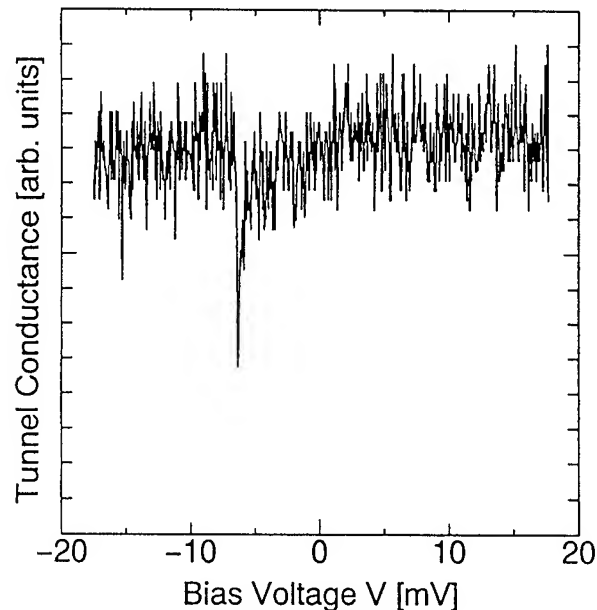


Fig. 2 Tunnel conductance of Au/Bi₂Te₃ junction

Tunnel conductance of a Mg/Bi₂Se₃ junction is similar to that shown in Fig.2. Because the measured tunnel conductance is independent on the bias voltage and noisy, the ohmic contact is formed in Au/Bi₂Te₃ and Mg/Bi₂Se₃ junctions.

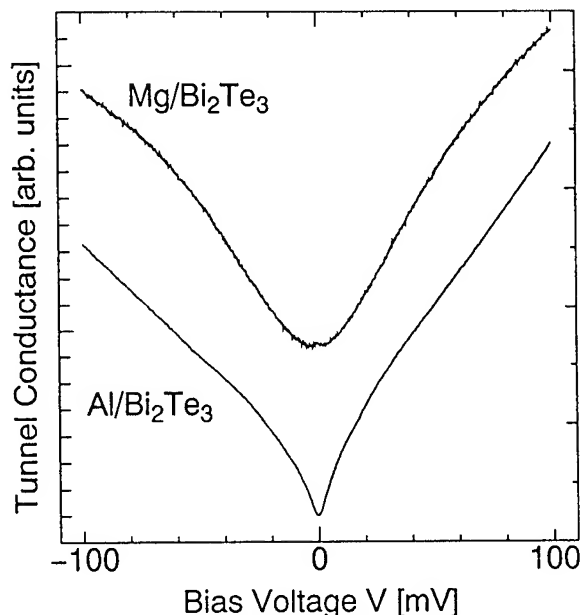


Fig. 3 Tunnel conductance curve of Mg/Bi₂Te₃ and Al/Bi₂Te₃ junctions.

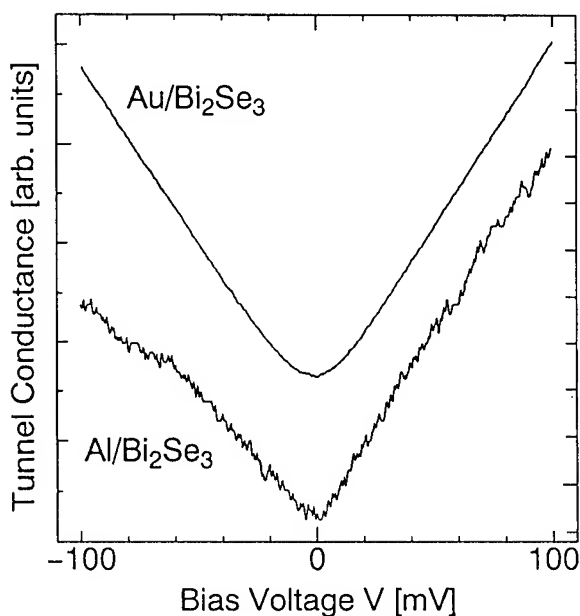


Fig. 4 Tunnel conductance curve of Au-Bi₂Se₃ and Al-Bi₂Se₃ junctions.

3. Results and discussion

Fig.2 shows tunnel conductance in a Au/Bi₂Te₃ junction. Positive bias corresponds to raising the Fermi level of the semiconductor with respect to that of metal electrodes.

Fig.3 shows tunnel conductance of Al/Bi₂Te₃ and Mg/Bi₂Te₃ junctions. V-shaped tunnel conductance was observed in these junctions and also in Au/Bi₂Se₃ and Al/Bi₂Se₃ junctions as shown in Fig.4. Therefore, it is considered that the Schottky barrier is formed in Al/Bi₂Te₃, Mg/Bi₂Te₃, Au/Bi₂Se₃ and Al/Bi₂Se₃ junctions. All tunnel conductance curves show a conductance minimum at 0mV. The bias voltage where the conductance minimum is shown corresponds to a degeneracy in the semiconductor^[13]. Therefore the Fermi level in Bi₂Te₃ and Bi₂Se₃ is located near the valence band edge and the conduction band edge, respectively. On the other hand, the carrier concentration of the Bi₂Te₃ and Bi₂Se₃ are $6 \times 10^{23} \text{ cm}^{-3}$ (p-type) and $1 \times 10^{23} \text{ cm}^{-3}$ (n-type) at 300 K, respectively. The observed carrier concentration slightly decreases with decreasing the temperature. These results demonstrate also that Bi₂Te₃ and Bi₂Te₃ are lightly degenerated.

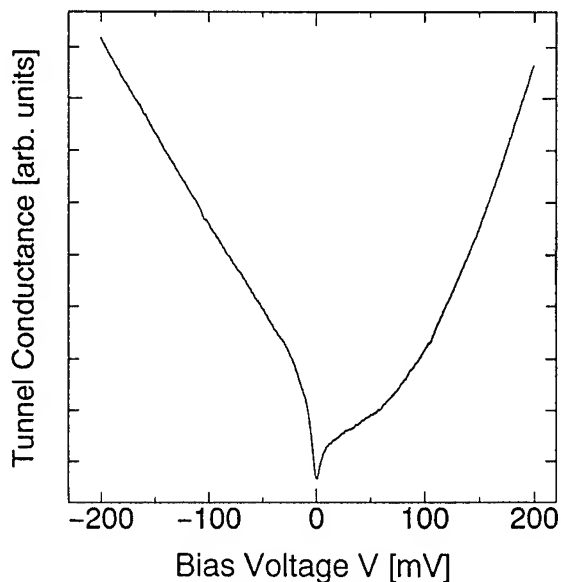


Fig. 5 Tunnel conductance of Ag/Bi₂Te₃ junction.

Fig.5 shows tunnel conductance of a Ag/Bi₂Te₃ junction. Since the measured tunnel conductance shows a V-shaped curve, the Schottky barrier is considered to be formed in this junction. On the other hand, we found a zero bias anomaly around zero bias voltage region, that is, Ag and Bi₂Te₃ consist of disordered states at their interface. Fig. 6 shows the SIMS depth profile of the Ag/Bi₂Te₃ junction. The mutual diffusion of the Ag, Bi and Te elements at interface were observed clearly. We can assume that this mutual diffusion yields to the disordered states at the interface. However, the

effects of the disordered states on the thermoelectric properties has not been clear at present.

The electron affinity will be discussed in more detail. An energy band gap of Bi₂Te₃ is calculated to be about $E_g = 0.175 \text{ eV}$ from the data^[14] of the energy gap at 300 K and the temperature coefficient of the energy gap of $dE_g/dT = -0.95 \times 10^{-4} \text{ eV/K}$. In the case of Bi₂Te₃, the Fermi level is located near the valence band edge. The ohmic contact is formed when the work function of metals is 4.7 eV. Here the energy level is measured from a vacuum level. On the other hand, the contact type of metal/Bi₂Te₃ junctions is the Schottky type when the work function of metals is lower than 4.3 eV. Therefore the top of the conduction band, which is called an electron affinity, is estimated to be between 4.125 eV and 4.525 eV. We can also estimate the Bi₂Se₃ electron affinity is between 3.7 eV and 4.2 eV.

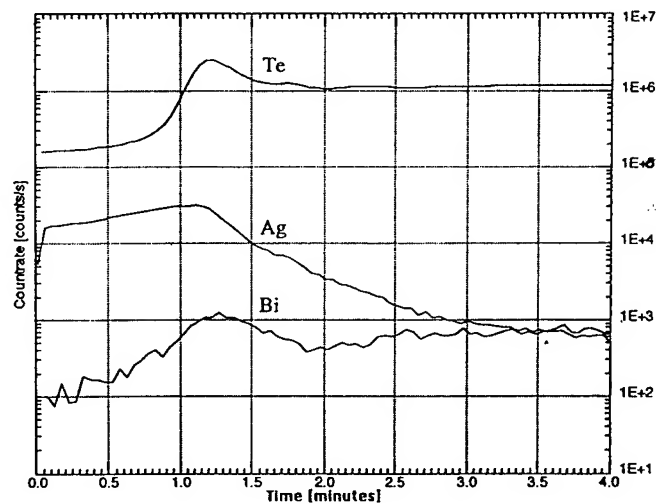


Fig. 6 SIMS depth profile of the Ag/Bi₂Te₃ junction.

As a result, it is important to choose the metal elements as an electrode considering the work function of metals for forming the ohmic contact in the thermoelectric junctions. It is also important factors that the distributed metal elements in the semiconductor exist at interfaces.

5. conclusions

The Schottky barrier can be made when Mg, Al or Ag metal of comparably low work function is brought into contact with Bi₂Te₃. The Schottky barrier also can be made in the case of Au/Bi₂Se₃ or Al/Bi₂Se₃. In these cases the electron affinity of Bi₂Te₃ and Bi₂Se₃ seem to be 4.125 to 4.525 eV and 3.7 to 4.2 eV, respectively. A kind of disordering has been found in the Schottky barrier of Ag/Bi₂Te₃ junction. SIMS measurement shows Ag atoms migrate to the surface of the

Bi_2Te_3 crystal in the Schottky barrier. The electron tunneling spectroscopy offers unique methods to obtain information on the metal - semiconductor contacts consisting of the thermoelectric semiconductors such as Bi_2Te_3 and Bi_2Se_3 .

Acknowledgements

The authors wish to thank Dr. Sueoka of Hokkaido University and Dr. Kawabata of Hokkaido National Industrial Research Institute for their useful discussion and encouragements. The authors are also grateful to Miss. Nagahara for her assistance in preparing the manuscript and to Mr. Sasamori for preparing the glass ampules.

References

- [1] H. J. Goldsmid, in *Electrical Refrigeration*, (Plenum Press, London, 1964), pp.15
- [2] D. T. Morelli, T. Caillat, J. -P. Fleurial, A. Borshevsky, J. Vandersande, B. Chen and C. Uher, *Phys. Rev. B*, 51, 9622 (1995)
- [3] Y. Sawade and T. Ohta, *Proc. 13th Int. Conf. on Thermoelectrics*, 226 (1995)
- [4] M. J. Smith, R. J. Knight and C. W. Spencer, *J. Appl. Phys.*, 33, 2186 (1962)
- [5] W.M. Yim and A. Amitk, *Solid State Electronics*, 15, 1141 (1972)
- [6] M. McColl and M. F. Millea, *J. Electronic Materials*, 5, 191 (1976)
- [7] V. V. Zav'yalov, V. F. Radantsev and T. I. Deryabina, *Sov. Phys. Semicond.*, 26, 388 (1992)
- [8] J. W. Conley, C. B. Duke, G. D. Mahan and J. J. Tiemann, *Phys. Rev.*, 150, 466 (1966)
- [9] F. Steinrisser, L. C. Davis and C. B. Duke, *Phys. Rev.*, 176, 912 (1968)
- [10] J. W. Conley and G. D. Mahan, *Phys. Rev.*, 161, 681 (1967)
- [11] W. Cabanski and M. Schulz, *Appl. Phys. A*, 50, 541 (1990)
- [12] D. C. Tsui, in *Handbook on Semiconductors*, edited by T. S. Moss, Vol.1, edited by W. Paul (North-Holland Publishing., Amsterdam, New York, Oxford, 1982) pp.672
- [13] C. R. Crowell, H. B. Shore and E. E. LaBate, *J. Appl. Phys.*, 36, 3843 (1965)
- [14] D. L. Greenaway and G. Harbeke, *J. Phys. Chem. Solids*, 26, 1585 (1965)

Tunneling Spectroscopy of Band Edge Structures of Bi_2Te_3 and Sb_2Te_3

K.Funagai, Y.Miyahara and H.Ozaki

Department of Electrical Engineering, Waseda University,
Ohkubo 3-4-1, Shinjuku-ku, Tokyo 169 Japan

V.A.Kulbachinskii

Low Temperature Physics Department, Physics Faculty,
Moscow State University, 119899, Moscow, Russia

Abstract

Tunneling study was made on Bi_2Te_3 and Sb_2Te_3 at 4.2 K, 77 K and 295 K. Energy gap of Bi_2Te_3 was estimated to be 0.25 eV, 0.22 eV and 0.20 eV at 4.2 K, 77 K and 295 K, respectively.

Introduction

Bi_2Te_3 and Sb_2Te_3 belong to the class of layer semiconductors whose structure consists of five atomic planes in the sequence of Te-Bi-Te-Bi-Te (Sb-Te-Sb-Te-Sb). These materials and their mixed materials have been utilized for thermoelectric devices widely.

Many studies have been made so far on their band structures, [1-4] especially their band edge structures.[5-8] It was clarified by many galvanomagnetic and thermoelectric measurements that the band structures of these materials were very complicated and consisted of two extrema in the conduction band and two in the valence band placed in different points of the Brillouin zone. The energy separation between the two extrema in the valence band (the upper and lower valence band) was reported as 20.5 meV by Köhler. [6] However, all data obtained from these measurements involved some models for interpretation of the experimental results. There have been rather few direct measurements of the energy gaps in these materials except for some optical measurements.[1,2,8] According to the optical measurements, the energy gap at room temperature in Bi_2Te_3 is near 0.15 eV [1] and increases with decreasing the temperature, and that in Sb_2Te_3 is near 0.24 eV [2] with similar temperature dependence.

Tunneling spectroscopy is one of the most promising technique for the investigation of band edge structure because the energy resolution is high and the energy positions of the valence and conduction band edges are measured with respect to the Fermi energy. In the present study, tunneling spectroscopy measurements were carried out in order to investigate the energy gaps and the band separations in the high quality single crystal of Bi_2Te_3 and Sb_2Te_3 at 295 K, 77 K and 4 K.

Experimental

Bi_2Te_3 and Sb_2Te_3 single crystals were grown by a modified Bridgman method from polycrystalline materials. The starting polycrystalline materials in the stoichiometric composition were synthesized from 5N purity elements in the conical quartz ampoules. The grown crystals can be easily cleaved perpendicular to the C_3 trigonal axis. Cleavage was carried out in liquid nitrogen by a razor blade. The obtained surface had large mirrorlike area.

In our tunneling spectroscopy, two methods were employed to fabricate the Metal/Insulator/Semiconductor tunneling junction. One is the point-contact type tunneling junction using tantalum oxide as the insulator. Figure 1 shows our tunneling unit. Thin polished tantalum wire, whose surface was oxidized in oxygen atmosphere, was pressed onto the sample surface. A thin phosphor bronze plate spring was used to stabilize the junction, and gold wires were attached to the sample surface by indium soldering to obtain ohmic contacts. In order to avoid the effect of the voltage drop across the series resistance, the four-terminal method was employed. In another method, vac-

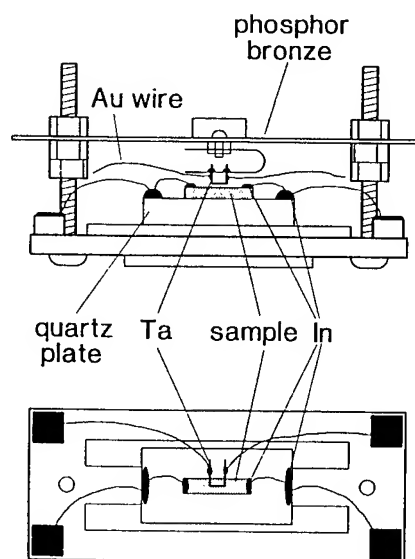


Figure 1: Tunneling unit.

uum gap was used as the tunneling barrier and evaporated silver film was used as the counter electrode. The clearance between the sample surface and the counter electrode was adjusted by the piezoelectric actuator. We mainly used the former technique, but both methods yielded basically similar results. We used the standard modulation technique to obtain the first and second derivatives of the tunneling current.

Results and Discussion

Figure 2 shows the tunneling dI/dV - V characteristics in Bi_2Te_3 . The curves at 4.2 K and 295 K were obtained by the modulation technique, while that at 77 K was obtained by the numerical integration of the d^2I/dV^2 - V curve in Fig.3, which was obtained by the modulation technique. In Fig.2, the positive bias corresponds to the higher electron energy in the sample in which the conduction band lies.

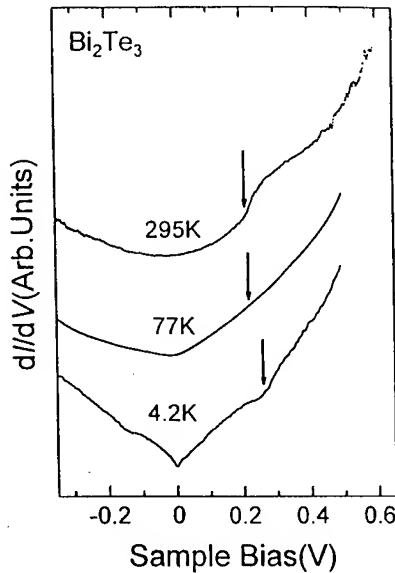


Figure 2: The tunneling dI/dV - V characteristics in Bi_2Te_3 at 295 K, 77 K and 4.2 K.

It is known that Bi_2Te_3 has two band extrema both in the conduction band and valence band. The schematic density of states is shown in Fig.4(a) as a function of electron energy. The tunneling dI/dV - V reflects the profile of the density of states, particularly, the critical energy such as the band edge.

Fig.4(b) shows the corresponding d^2I/dV^2 - V . The higher order derivative is suitable for the search of a critical energy in the density of states, because a band edge structure is shown by a peak structure. However, such peak structures are usually smeared due to the thermal fluctuations and other factors as shown in Fig.4(c). In this case the positions of the peaks in Fig.4(b) correspond to the positions of maximum slope of the curve in Fig.4(c).

Figure 3 shows the d^2I/dV^2 - V characteristics for Bi_2Te_3 . The curves at 4.2 K and 295 K are derived from Fig.2 by the numerical differentiation. The curve at 77 K is the measured one. In each curve, a peak structure is found

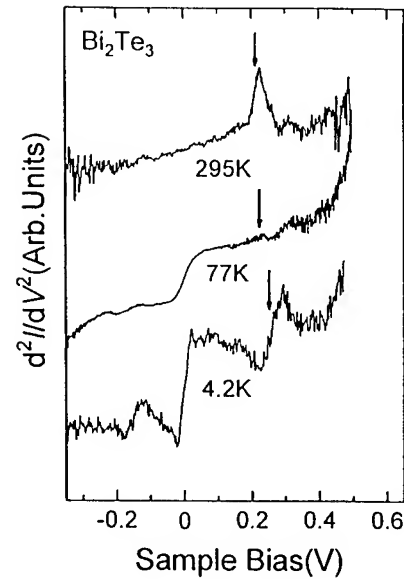


Figure 3: The tunneling d^2I/dV^2 - V characteristics in Bi_2Te_3 at 295 K, 77 K and 4.2 K.

which is indicated by the arrow. This structure is attributed to the conduction band edge, and the position measures the energy separation of the conduction band and the Fermi level. The sample is strong p -type and the top edge of the valence band structure seems to lie around $V = 0$.

The energy separation of the two extrema of the valence band is small, and due to the thermal fluctuations, it seems indistinguishable at 295 K. At lower temperature, due to the presence of a zero bias anomaly, the valence band extrema is difficult to be obtained from Fig.3.

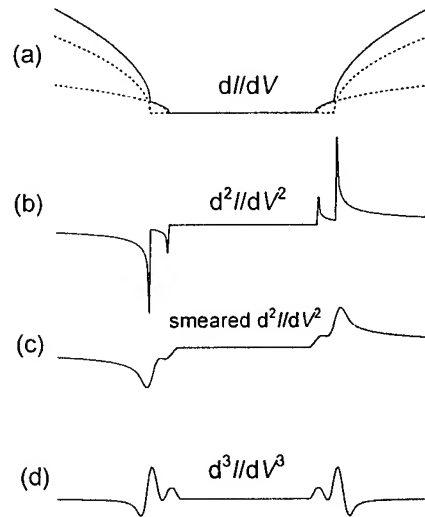


Figure 4: Schematic dI/dV - V , d^2I/dV^2 - V and d^3I/dV^3 - V characteristics, reflecting the band edge structures.

As is shown in Fig.4(d), the two extrema of the valence band will be indicated as two peaks in the d^3I/dV^3 - V plots which are derived from the d^2I/dV^2 - V curve. The experimental plots of d^3I/dV^3 near zero bias are shown in

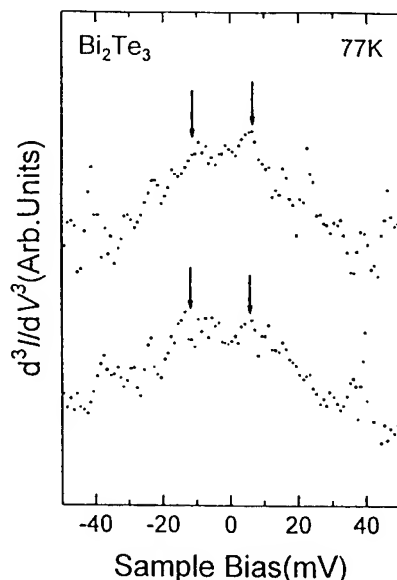


Figure 5: The tunneling d^3I/dV^3 - V characteristics in Bi_2Te_3 at 77 K for small bias voltage.

Fig.5, for two samples measured at 77 K. The overall hump structure is the zero bias anomaly.

Shoulders are seen on both sides of the bias which are indicated by arrows. If these shoulders are attributed to the two extrema of the valence band, the energy separation of them is estimated to be 18 ± 2 meV. This value is

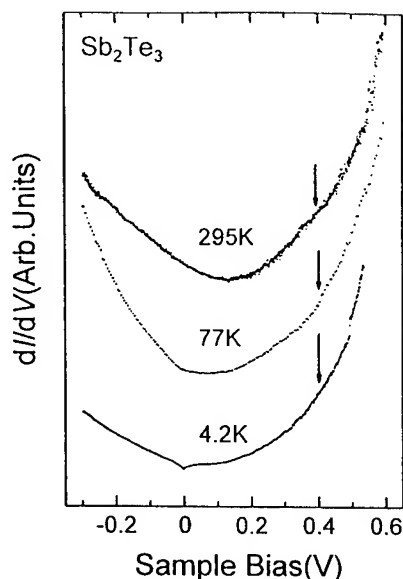


Figure 6: The tunneling dI/dV - V characteristics in Sb_2Te_3 at 295 K, 77 K, and 4.2 K.

in fairly good agreement with the value of 20.5 meV, for the energy separation of two extrema in the valence band, obtained by Köhler by means of the Shubnikov-de Haas effect measurement. [6]

According to the result in Fig.5, the top of the valence band lie at about 6 meV above the Fermi level. From this value and the positions of the conduction band edge indicated by the arrows in Fig.2, and assuming that the position of the Fermi level stays at same position for vari-

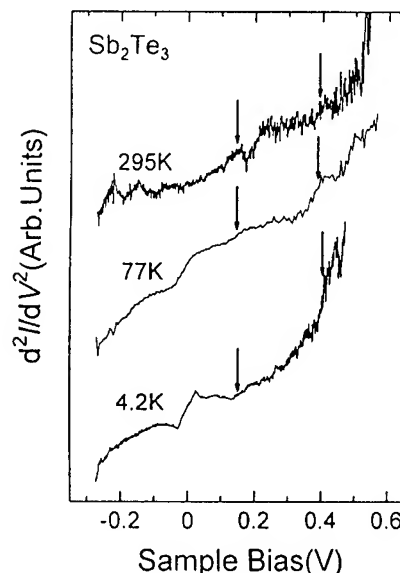


Figure 7: The tunneling d^2I/dV^2 - V characteristics in Sb_2Te_3 at 295 K, 77 K, and 4.2 K.

ous temperature, the energy gap of Bi_2Te_3 is estimated to be 0.25 eV, 0.22 eV and 0.20 eV at 4.2 K, 77 K and 295 K, respectively.

For each curve in Fig.3, a small peak structure is observed at about 90 meV higher than the arrowed peak. At present, we cannot identify this peak to the higher extremum of the conduction band, because the latter is known to have a much higher density of states than the lower extremum, and thus, the peak should be much larger than that for the lower extremum.[5]

Tunneling experiments were performed in Sb_2Te_3 similar to Bi_2Te_3 . Figure 6 shows the dI/dV - V characteristics in Sb_2Te_3 at 4.2 K, 77 K and 295 K. In this case, the minimum position of dI/dV shifts to the positive bias side. It indicates that the Fermi level of Sb_2Te_3 lie deeper in the valence band compared with Bi_2Te_3 .

Figure 7 shows the d^2I/dV^2 - V derived numerically from dI/dV - V in Fig.6. The two arrows in each curve indicate local maxima of slopes which were observed commonly on several samples. The positions of the arrows at lower biases are 0.14 V, 0.14 V and 0.14 V at 4.2 K, 77 K and 295 K, respectively. Whereas the positions of the arrows at higher biases are 0.4 V, 0.39 V and 0.39 V at 4.2 K, 77 K and 295 K, respectively. The separations of the two peaks are, thus, 0.26 eV, 0.25 eV and 0.25 eV at 4.2 K, 77 K and 295 K, respectively. These values are rather close to the optical energy gap obtained by Sehr *et al.*[2] If we attribute these values to the energy gap, the peak at lower bias means the position of the top of the valence band. However, the value of 0.14 eV seems to be rather too high for the energy separation of the top of the valence band and the Fermi level compared with the result of about 0.07 eV obtained by Sehr *et al.*[2] More detailed study is necessary in Sb_2Te_3 .

References

- [1] D.L.Greenaway and G.Harbecke, *J.Phys.Chem.Solids* **26**, pp.1585-1604 (1965).
- [2] R.Sehr and L.R.Testardi, *J.Phys.Chem.Solids* **23**, pp.1219-1224 (1962).
- [3] F.Borghese and E.Donato, *Nuovo Cimento* **LIII B**, pp.283-309 (1968).
- [4] Shin-ichi Katsuki, *J.Phys.Soc.Japan* **26**, pp.58-64 (1969).
- [5] H.Köhler, *Phys. Stat. Sol. (b)* **73**, pp.95-104 (1976).
- [6] H.Köhler, *Phys. Stat. Sol. (b)* **74**, pp.591-600 (1976).
- [7] V.A.Kulbachinskii *et al.*, *Phys. Rev.* **B50**, pp.16921-16930 (1994).
- [8] P.Lostak *et al.*, *Phys. Stat. Sol (a)* **104**, pp.841-847 (1987).

Determination of the Thermal Band Gap from the Change of the SEEBECK-Coefficient

at the pn-Transition in $(\text{Bi}_{0.5}\text{Sb}_{0.5})_2\text{Te}_3$

E. Müller, W. Heiliger, P. Reinshaus, H. Süßmann

Martin-Luther-Universität Halle-Wittenberg, Fachgruppe Angewandte Physik, Germany

Abstract

The range of existence of the homogeneous δ -phase of $(\text{Bi}_{0.5}\text{Sb}_{0.5})_2\text{Te}_3$ in the phase diagram $(\text{Bi,Sb})\text{-Te}$ intersects the stoichiometry line. N-type samples can be obtained by BRIDGMAN growth with excess of tellurium. Due to the strong tellurium segregation the transition from the p-extrinsic region through intrinsic material to n-extrinsic behavior is proceeded within a sample section of several millimeters along axial direction. The positive and negative maximum values $S_{\text{max,p}}$ and $S_{\text{max,n}}$ can be read out from a scan of the SEEBECK-coefficient by the micro-thermoprobe technique over the transition area. The p-type maximum scan value is in good agreement with the value deduced from the integral measurement of homogeneous bulk samples. The width of the thermal band gap and the ratio of the electronic parameters $\mu_B(m_d/m_o)^{3/2}$ (μ_B - non-degeneracy value of the carrier mobility (reduced to BOLTZMANN statistics); m_d/m_o - reduced d.o.s. mass) of holes and electrons are obtained from $S_{\text{max,p}}$ and $S_{\text{max,n}}$. The mobility of holes as minority carriers exhibits a strong sensitivity on doping impurities.

Introduction

Substances of the solid solution $(\text{Bi}_{1-x}\text{Sb}_x)_2\text{Te}_3$ have been well-known as p-type standard material for thermoelectric application near room temperature. Accompanying to the extension of the application range to lower and higher temperatures as well as for the development of graded material for generator application, interest increases in a solid state physics based description of the transport as a prerequisite for a systematic optimization far from room temperature. Multi-stage PELTIER cascades nowadays reach a maximum temperature difference of more than 140 K (hot side at room temperature) [1]. For $(\text{Bi}_{0.5}\text{Sb}_{0.5})_2\text{Te}_3$ with reduced carrier density advantageous thermoelectric properties can be expected below 250 K [2],[3].

With respect to generator application above room temperature the question of a possible widening of the high efficiency temperature range obtains importance especially for p-type material, because its performance descends rapidly below that of n-type at temperatures above 350..400 K.

Model of Charge Transport:

The existence of more than one sub-bands in the valence and conduction band has been proved by KÖHLER [4],[5]. Nevertheless, band structure and carrier scattering calculations for extrinsic p-type $(\text{Bi}_{0.5}\text{Sb}_{0.5})_2\text{Te}_3$ and $(\text{Bi}_{0.25}\text{Sb}_{0.75})_2\text{Te}_3$ [2] showed a good numerical applicability of a non-parabolic 1-valence band/6-valley-model with mixed elastic/inelastic scattering on acoustic phonons. The results show, that

- a small contribution of inelastic scattering leads to a slight lowering of the calculated FERMI-level,
- the FERMI-level reaches values near the expected position of the second valence band at low temperature,
- the calculated values of the FERMI-level, the effective mass and the relaxation time constant depend on temperature.

Estimations in the case of mixed and intrinsic conduction can be based on a simplified model (parabolic band structure of the conduction and valence band, pure phonon scattering). However, a discussion in this model has to take into account:

- Near intrinsic conditions a carrier transition into the more distant from the gap sub-bands occurs with rising temperature.
- A mobility difference between the sub-bands cause an additional dependence of the mean carrier mobility on temperature and FERMI-level.
- Compensation effects may cause a significant mobility restriction. Their influence decreases with rising temperature for a constant number of charged centers.

Band non-parabolicity may be neglected in the case of non-degeneracy.

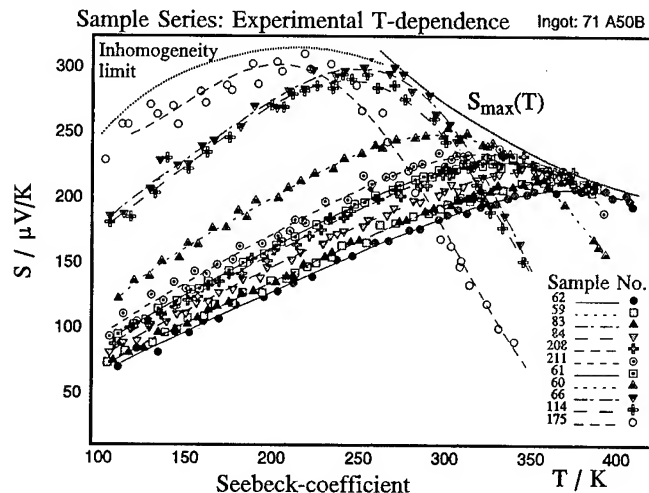


Fig. 1 Temperature dependence of the SEEBECK-coefficient of $(\text{Bi}_{0.5}\text{Sb}_{0.5})_2\text{Te}_3$ for varying carrier density

The SEEBECK-Coefficient in the Range of Mixed and Intrinsic Conduction

To estimate the maximum thermoelectric efficiency in material influenced by intrinsic conduction, the maximum reachable value of the SEEBECK-coefficient is of importance. It can be read out from a bundle of experimental temperature curves (Fig. 1) and the limiting factors can be classified. Between 100..400 K two processes are important for $(\text{Bi}_{0.5}\text{Sb}_{0.5})_2\text{Te}_3$:

- **Intrinsic limit:** The transition from extrinsic to intrinsic

conditions takes place near room temperature. The sign of the curve slope changes. The upper envelope of the curve bundle determines the extremum of the isothermal dependence on the FERMI-level.

- **Inhomogeneity limit:** Systematically occurring strong material inhomogeneity linked to the sample dimensions required by the measuring technique [3] restricts the magnitude of the thermoelectric properties at low carrier density.

However, the recording of the temperature dependence for a series of samples with tuned carrier density is laborious. At lower temperature the detection of the intrinsic limit in this way is impossible, because it is hidden by the inhomogeneity limit.

With several carrier types involved, the SEEBECK-coefficient is calculated from the partial coefficients S_i and the partial electrical conductivity σ_i of all types

$$S = \sum_i S_i \cdot \sigma_i / \sum_i \sigma_i \quad (1)$$

For mixed and intrinsic conduction near and above room temperature we can suppose, that only one type of electrons and holes each contribute to the SEEBECK-coefficient. For a p-type semiconductor with the extrinsic hole concentration p_o near the maximum of the SEEBECK-coefficient holds $\sigma_n \ll \sigma_p$ and

$$S \approx S_p + \frac{\sigma_n}{\sigma_p} S_n \approx S_p + \frac{n}{p_o} \frac{\mu_n}{\mu_p} S_n \quad \text{mit } n \approx N_c e^{-\mathcal{E}_g/k_B T} \quad (2)$$

N_c is the d.o.s. at the conduction band edge, μ_n and μ_p are the non-degeneracy values of the carrier mobility, η the reduced FERMI-level of holes, $\mathcal{E}_g = E_g/k_B \cdot T$ the reduced gap width.

The $S_{\max}(T)$ value and the belonging to it reduced FERMI-level η_{\max} depend sensitively on the gap width and on the ratio of the mobility and d.o.s. mass of electrons and holes.

x	0	0.25	0.5	0.75
$E_g(300 \text{ K}), \text{ meV}$	130 [9]		135 [7]	140 [9]
$m_p, m^2/Vs$ [6]	0.036	0.028	0.030	0.036
	0.034 (Pb)			
$m_n, m^2/Vs$ [7]	0.032 (Te [6])	0.028 (J, Te)	0.024 (0.3 J)	0.016 (J)
			0.022 (0.5 J)	
			0.018 (1.0 J)	
			0.020 (8, 12 Te)	
			0.028 (1 J, annealed)	

(Calculated values in the parabolic 1-band-model. Admixtures in at%)

Tab. 1 Thermal gap and mean values of the material parameters m_p and m_n for extrinsic conduction, $(\text{Bi}_{1-x}\text{Sb}_x)_2\text{Te}_3$ with addition of J or Te (300 K)

In the temperature range between 100..300 K SÜBMAN [6] found for the p-type solid solutions $(\text{Bi}_{1-x}\text{Sb}_x)_2\text{Te}_3$ the independence of the electronic material parameter $m_p = \mu_p(m_{d,p}/m_o)^{3/2}$ of the degree of degeneracy for samples in the whole range from strong degeneracy till the rise of the mixed conduction. UYEN [7] obtained the same result for the electron parameter $m_n = \mu_n(m_{d,n}/m_o)^{3/2}$ for n- $(\text{Bi}_{1-x}\text{Sb}_x)_2\text{Te}_3$. The values m_p and m_n are summarized in Tab. 1.

Assuming, that the independence of the majority carrier mobility of the degree of degeneracy can be extrapolated to

the region of rising mixed conduction, a change of S_{\max} at constant temperature is an immediate indication to a change of the minority carrier mobility. Its influence on S_{\max} increases with rising temperature and dominates the thermoelectric properties of $(\text{Bi}_{0.5}\text{Sb}_{0.5})_2\text{Te}_3$ above room temperature.

Significant mobility restrictions at very low carrier concentration can be expected as an effect of doping impurities. Conditions of partial compensation occur in sample areas with mixed and intrinsic conduction since the native lattice disorder persists. Band tails are formed. Carriers occupying their states exhibit a drastically reduced mobility. Particularly, this leads to a suppression of the minority conduction.

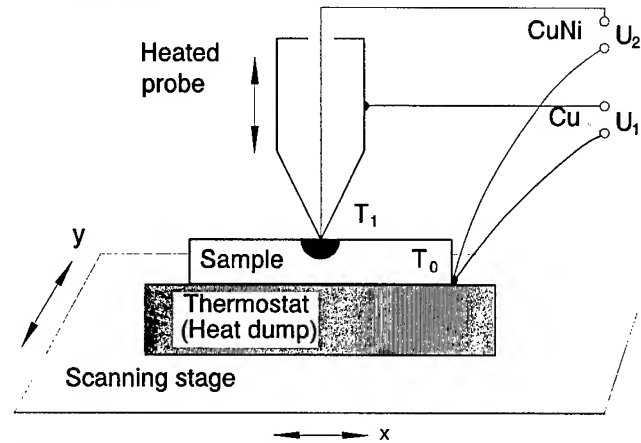


Fig. 2 Function principle of the Micro Thermoprobe

Temperature dependent characterization of carrier density graded single crystals by the micro-thermoprobe

For a locally resolving determination of the SEEBECK-coefficient a heated probe contacts the surface of the isothermal sample. The tip of the probe is formed by a thermocouple. A second thermocouple is attached to the sample with good electric and thermal contact. The setup can be thermostated between room temperature and the nitrogen boiling point. Between the Cu-Cu and the CuNi-CuNi wires the voltages U_1 and U_2 are measured simultaneously. They are determined by the temperature difference and by the local SEEBECK-coefficient of the heated sample-volume near the probe. The unknown temperature difference $T_1 - T_0$ can be eliminated from the equations and the local SEEBECK-coefficient S is obtained:

$$U_1 = (S - S_{\text{Cu}}) \cdot (T_1 - T_0), \quad U_2 = (S - S_{\text{CuNi}}) \cdot (T_1 - T_0) \quad (3)$$

$$S = \frac{U_1}{U_2 - U_1} \cdot S_{\text{Cu/CuNi}} + S_{\text{Cu}}$$

For the determination of $S_{\max}(T)$ a sample is required, in which conditions from extrinsic p-type throughout intrinsic to extrinsic n-type are proceeded by grading of the extrinsic carrier density. A suitable preparation process is given by the strong segregation of tellurium in $(\text{Bi}_{1-x}\text{Sb}_x)_2\text{Te}_3$. In the composition range $x \leq 0.5$ the conversion to n-type can be obtained simply by an excess of Te (Fig. 3), for $x > 0.6$ the addition of a donor is necessary. Addition of a low concentrated dopand modifies the segregation profiles in a characteristic way. Since the doping component is segregating as well, the resulting local dependence is a superposition of relatively independent

one from another distributions of the carrier density and the degree of compensation.

More than one pn-transition in a line scan may occur due to a nonmonotonous distribution of doping components. If only Te excess is applied, the pn-transition is formed at the end of the ingot. It is shifted to the central part of the ingot (plateau region of the Te distribution) when a donor is present (Fig. 5, Fig. 6). At lower temperatures the partial intrinsic conductivity values are very small (see (2)). Therefore, the sensitivity of the SEEBECK value to dopands is multiplied. Even very low variation of its concentration may produce a sign change of the SEEBECK-coefficient.

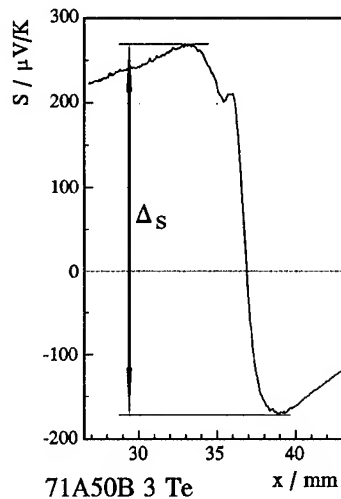


Fig. 3 SEEBECK-scan over the pn-transition of a BRIDGMAN-ingot (undoped, Te-excess)

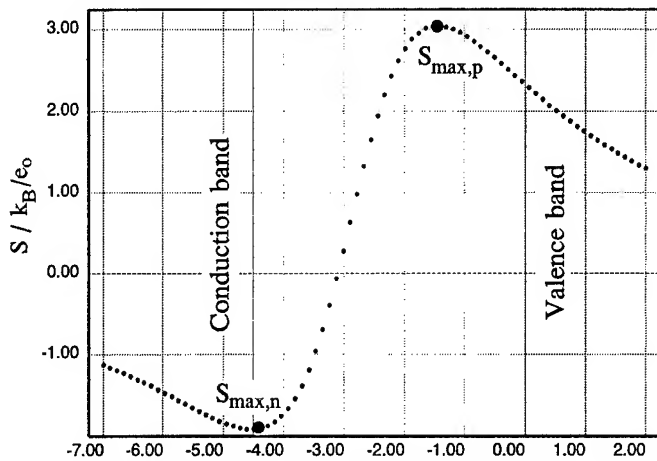


Fig. 4 Dependence of the SEEBECK-coefficient on the reduced FERMI-level (Model curve: $T=300$ K, $r_m=0.29$, $\mathcal{E}_g=4.5$)

Band Gap Determination near Room Temperature

Assuming Constant Mobility:

Relatively independently one from another, the difference of the extremum values of the SEEBECK-coefficient Δ_S (Fig. 3) is determined by the gap width while their ratio r_s is dominated by r_m (ratio of the electronic carrier parameters of electrons and holes)

$$r_m \doteq m_n / m_p, \quad m_{p,n} \doteq \mu_B (m_d / m_o)^{3/2} \quad (4)$$

Both relations are monotonous functions.

$$\begin{aligned} \mathcal{E}_g &= \mathcal{E}_g(\Delta_S), & r_m &= r_m(r_s), \\ \Delta_S &= S_{\max,p} - S_{\max,n}, & r_s &= \left| \frac{S_{\max,n}}{S_{\max,p}} \right| \end{aligned} \quad (5)$$

The evaluation of the SEEBECK scan presented in Fig. 3

(extrema: $265/-170 \mu\text{V/K}$) yields for $(\text{Bi}_{0.5}\text{Sb}_{0.5})_2\text{Te}_3$ at 300 K: $E_g=117$ meV, $r_m=0.29$ (see Fig. 4). The resulting very small gap width and the ratio r_m strikingly deviating from unity (to be expected according to Tab. 1) give evidence, that the assumption of constant m_p and m_n (independent of the FERMI-level) for mixed and intrinsic conduction is no more valid.

While the values $S_{\max,p}$ read out of SEEBECK scans and those from the curves $S(T)$ (Fig. 1) are coinciding, measurements of the temperature dependence $S(T)$ for $n\text{-(Bi}_{0.5}\text{Sb}_{0.5})_2\text{Te}_3$ [7] allow to estimate $|S_{\max,n}(300 \text{ K})| > 200 \mu\text{V/K}$, notably differing from the scan value. Comparing the scans of several $(\text{Bi}_{0.5}\text{Sb}_{0.5})_2\text{Te}_3$ samples containing a pn-transition due to Te excess resulted in a comparably constant value $S_{\max,p} \approx 255..270 \mu\text{V/K}$, while $S_{\max,n}$ varied between -100 and $-220 \mu\text{V/K}$. It has to be concluded, that

- the ratio r_m in the non-degeneracy range exhibits an essential dependence on the FERMI-level,
- r_m is sensitively influenced by donors, particularly when the FERMI-level is positioned little below the conduction band.

Using the ratio of the majority parameters (Tab. 1) which is in agreement with the largest intrinsic limits observed for $(\text{Bi}_{0.5}\text{Sb}_{0.5})_2\text{Te}_3$ at 300 K ($r_m \approx 0.8$; $S_{\max,p/n} = 270/-255 \mu\text{V/K}$), a gap energy $E_g(300 \text{ K}) \approx 150$ meV is obtained. For realistic calculations has to be recognized, that r_m takes significantly different values depending on whether conditions of extrinsic conduction ($S=S_p$ or $S=S_n$), onsetting mixed conduction ($S \approx S_{\max}$) or dominating intrinsic conduction ($S \ll S_{\max}$) occur.

Determination of the Parameter Ratio for Intrinsic Conduction:

At intrinsic conditions below room temperature the FERMI-level lies deep in the gap. With

$$\begin{aligned} S_n &= -\frac{k_B}{e_o}(2-\zeta) & \sigma_n &= N_c e^\zeta e_o \mu_n \\ S_p &= \frac{k_B}{e_o}(2-\eta) & \sigma_p &= N_v e^\eta e_o \mu_p \end{aligned} \quad (6)$$

(N_v - d.o.s. at the valence band edge, ζ - reduced FERMI-level of the electrons), several distinguished points of the SEEBECK-scans can be evaluated:

- Average of the partial coefficients: $S=(S_p+S_n)/2$
 - Zero position: $S=0$
 - Intrinsic position: $n=p$
- a) At this position, the value or the parameter ratio according to intrinsic conditions $r_m^{(i)}$ can be read out immediately:

$$\sigma_p = \sigma_n \Rightarrow r_m^{(i)} = e^{\eta-\zeta} = e^{-\frac{S_p-S_n}{k_B/e_o}} = e^{-\frac{2S}{k_B/e_o}} \quad (7)$$

- With $S_p \cdot \sigma_p = -S_n \cdot \sigma_n$ applies

$$\frac{S_p}{|S_n|} = \frac{N_c}{N_v} \frac{\mu_n}{\mu_p} e^{\zeta-\eta} = r_m. \quad (8)$$

- At the intrinsic position ($p=n$), with the relation $\sigma_n/\sigma_p = \mu_n/\mu_p = b^{(i)}$ the mobility ratio under intrinsic conditions results from (1):

$$b^{(i)} = \frac{S_p - S}{S - S_n} \quad (9)$$

Hence, the ratio of the d.o.s. masses of the electrons and holes can be obtained from $r_m^{(i)}$.

The determination of S_p and S_n has to be carried out as a geometrical extrapolation at constant temperature. The local position of intrinsicity can be determined with good accuracy from a SEEBECK-scan at low temperature. The local shift of the zero position in $(\text{Bi}_{0.5}\text{Sb}_{0.5})_2\text{Te}_3$ with changing temperature leads to the conclusion of a $r_m^{(i)}$ notably smaller than unity.

Determination of the Thermal Band Gap

The determination of the band gap from intrinsic effects influencing the temperature dependence of the thermoelectric properties ("thermal gap") is usually based on the slope of the logarithmic plot $\ln(\sigma) = f(1/T)$ in the intrinsic range or on the method by KUTASOV, SMIRNOV and MOJZHES [8],[9]. Moreover, the gap width was deduced from measurements of the intrinsic absorption in the infra-red [10] ("optical gap"). Values from both methods are in good agreement for $\text{Bi}_2(\text{Te}_{1-y}\text{Se}_y)_3$.

Literature data on the thermal and optical gap width of $(\text{Bi}_{1-x}\text{Sb}_x)_2\text{Te}_3$ reveal a discrepancy increasing with rising portion of Sb_2Te_3 in the solid solution. Contributions to the difference arise from

- the BURSTEIN-MOSS-shift of the absorption edge, which increases the experimental value of the optical gap
- the neglect of inelastic scattering, which leads to a too small thermal band gap (compare [2]),
- mobility restriction by compensation effects,
- a dependence on temperature and carrier energy of the non-degeneracy value of the carrier mobility μ_B .

Deducing E_g from the slope of the electrical conductivity in the intrinsic region [7], too low values are obtained, if $\sigma(T)$ increases steeper than according to $T^{3/2} \cdot e^{E_g/2kT}$. An increase of the occupation of the second sub-bands can be linked to a change of the mean carrier mobility. Mobility restriction due to compensation effects in doped material near intrinsic conditions is reduced with rising temperature. This contributes to a steeper dependence $\sigma(T)$.

The method according to [9] is based on a separation of the partial electrical conductivity and the partial SEEBECK-coefficient of the carrier types by extrapolating the temperature dependence from the extrinsic temperature range to the intrinsic region. E_g and μ_n/μ_p are obtained solving a system of equations. The μ_n/μ_p found is significantly smaller than the value deduced from measurements in the extrinsic region. Both methods imply the independence of the parameter $\mu_B(m_d/m_o \cdot T)^{3/2}$ of temperature.

An estimation of the BURSTEIN-MOSS-shift can be given taking into account the temperature dependence of the FERMI-level according to [2]. Consecutively, only a slight difference remains between the optical and thermal band gap value. A realistic magnitude of the thermal band gap of $(\text{Bi}_{0.5}\text{Sb}_{0.5})_2\text{Te}_3$ at room temperature is about 160 meV.

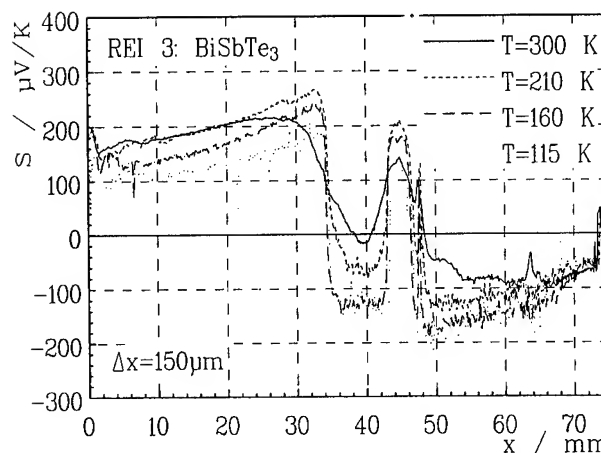


Fig. 5 SEEBECK-scans along a slightly chlorine-doped ingot (Central region)

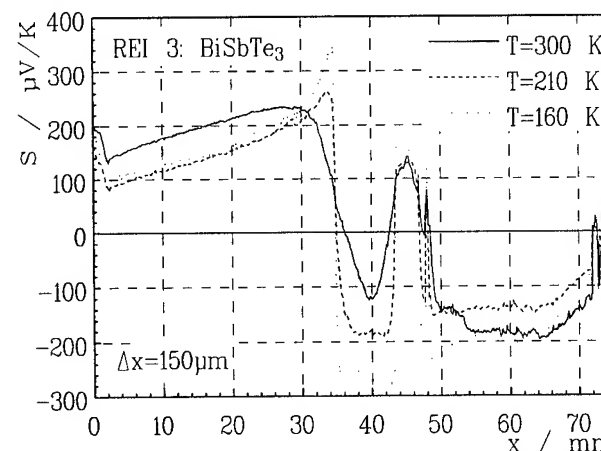


Fig. 6 SEEBECK-scans along a slightly chlorine-doped ingot (Outer region)

Thermoprobe Scans at Lower Temperature

The graded samples are BRIDGMAN ingots of about 80 mm in length and a diameter of 10 mm, grown at a rate of 2 mm/h. Overstoichiometric tellurium has been added. Several samples have been enclosed during growth by a chlorine doping coverage. At several positions of the purified surface of a cross section along the ingot, thermoprobe scans were recorded in axial direction.

With falling temperature the minority carrier effects are reduced. Therefore, the SEEBECK scans are modified:

- The absolute values S_{\max} increase and gradients get steeper.
 - The position of S_{\max} shifts towards the pn-transition, the zero position shifts towards the p-type region.
 - The sample sections with extrinsic conditions are spreading.
- The experimental image of the temperature dependent characterization of samples with doping admixtures turns out to be very complex: The intrinsic limit of the SEEBECK-coefficient S_{\max} exhibits a significant local dependence on the radial and axial coordinate due to the independent local distributions of carrier density and mobility. Near the outer surface it reaches higher values than near the ingot axis (Fig. 5, Fig. 6).

Halogen doping causes a reduction of the majority carrier mobility, which is similarly known from extrinsic bulk

samples (Tab. 1). A significant reduction of the minority carrier mobility becomes visible at something higher doping concentration (Fig. 6), as it is expected for a partially compensated semiconductor. This effect appears for minority electrons at lower temperature than for minority holes.

The local dependence of S_{\max} mainly indicates local changes of the carrier mobility. The difference between the temperature dependence of $S_{\max,n}$ and $S_{\max,p}$ is probably caused by a strong dependence of r_m with temperature. Partly, this may be linked to the different d.o.s. masses ($m_{d,n} < m_{d,p}$) and the increase of the hole mass with temperature deduced from the 1-band-model. In the range of a small SEEbeck-coefficient due to intrinsic conditions sample sections are observed, which are changing from n- to p-type with rise of temperature.

A separation of energetic and mobility-determining factors is enabled from several scans recorded at the same position for different temperatures: With falling temperature a freezing out of the mobility of the minority carriers in the band tails takes place, which reduces effects of intrinsic conduction. An influence of the band structure and the energy spectrum affecting the position of the FERMI-level and the carrier concentration becomes more and more apparent at lower temperature.

According to the desired measuring information the favorable temperature range has to be chosen:

- For the determination of the local extrinsic carrier concentration and for investigation of the energetic spectrum the range between liquid nitrogen and 200 K is suitable.
- The determination of the ratio r_m under intrinsic conditions from special scan positions has to be carried out at medium temperature (ca. 150..250 K), where mobility effects already become important and the extrapolation curve of the partial SEEbeck-coefficient is not too steep.
- The upper temperature range ($T > 200$ K) has to be preferred for the evaluation of the local dependence of S_{\max} , since there the mobility effects are most effective.

Conclusion

We have shown, that an effective way for the characterization of the material behavior of $(\text{Bi}_{1-x}\text{Sb}_x)_2\text{Te}_3$ ($x \leq 0.75$) for bipolar conduction consists in the experimental determination of the intrinsic limit of the SEEbeck-coefficient.

Segregation profiles of BRIDGMAN-grown ingots are suitable graded systems. Line scans of the SEEbeck-coefficient over pn-transitions are a convenient method to determine the intrinsic limits for both polarity in dependence on temperature (100..300 K). They provide information concerning the local and temperature dependence of the ratio of electron and hole mobility and may enable the separation of the local distribution of tellurium and doping impurities.

For the material developer the method offers an excellent tool for the determination of the temperature dependence of the SEEbeck-coefficient for material of reduced carrier concentration avoiding the disturbing influence of distribution inhomogeneity. In this way experimental evidence for the predicted increased values of the SEEbeck-coefficient at low

temperature [3] could be given. The precise local positioning setup allows to determine the temperature dependence of the SEEbeck-coefficient for an comprehensive spectrum of carrier density and mobility values within a single thermal cycle. Hence, the method represents an ideal method for the characterization of graded thermoelectric materials.

Compensation effects in doped material reduce the mobility of the minority carriers (in particular of the electrons) at lower temperature significantly. A strong dependence of the parameter ratio m_n/m_p on temperature and the degree of degeneracy was observed. For intrinsic conditions near room temperature the ratio is notably lower than unity.

Available methods for the determination of the band gap of $(\text{Bi}_{1-x}\text{Sb}_x)_2\text{Te}_3$ contain systematic uncertainties basing on the assumption of constant carrier mobility in the non-degeneracy case, the neglect of inelastic scattering and the underestimation of the BURSTEIN-MOSS-shift. Taking these effects into account reduces the discrepancy between the values of the optical and thermal gap width and yields for $(\text{Bi}_{0.5}\text{Sb}_{0.5})_2\text{Te}_3$ a thermal gap of about 160 meV at 300 K.

With respect to thermoelectric application above room temperature, an effective way for the reduction of the degrading influence of intrinsic effects consists in a limitation of the minority carrier mobility by suitable doping.

References

- [1] V.A. Semenyuk, T.E. Svechnikova, L.D. Ivanova, Journ. of Adv. Mat., vol. 1, No. 5, pp. 428-434 (1994).
- [2] H. Süßmann, E. Müller, Proc. of the XIV. Int. Conf. on Thermoel., pp. 1-6, St. Petersburg (1995).
- [3] E. Müller, H. Süßmann, Proc. of the Second Europ. Workshop on Thermoel., pp. 27-33, Nancy (1995).
- [4] H. Köhler, A. Freudenberger, phys. stat. sol. (b), vol. 84, pp. 195-204 (1977).
- [5] H. Köhler, W. Ossau, phys. stat. sol. (b), vol. 90, pp. 509-515 (1978).
- [6] H. Süßmann, W. Heiliger, phys. stat. sol. (a), vol. 80, pp. 535-539 (1983).
- [7] Ph. Uyen, Thesis, Martin-Luther-Universität Halle-Wittenberg (1983).
- [8] V.A. Kutasov, B.Ya. Mojzhes, I.A. Smirnov, Fiz. tverd. tela, vol. 7, p. 1065 (1965).
- [9] B.M. Golcman, V.A. Kudinov, I.A. Smirnov, *Poluprovodnikovye termoelektricheskie materialy na osnove Bi_2Te_3* , Izd. Nauka, Moskva (1972).
- [10] R. Sehr, L.R. Testardi, J. Phys. Chem. Sol., vol. 23, p. 1219 (1962).

Validation of Thermoelectrics Measurements II

Jeff W. Sharp, Edward H. Volckmann, Hylan B. Lyon Jr.
Marlow Industries, Inc.
10451 Vista Park Road., Dallas, TX 75238

Darrell J. Gillespie, George N. Kamm, Alexander C. Ehrlich
United States Naval Research Laboratory
Washington, DC 20375, Code 6341

Introduction

The thermoelectrics research community requires accurate and precise thermal conductivity measurements. Historically, this requirement has not been met to a satisfactory degree. At the XIIIth ICT, a discussion of discrepancies in thermal conductivity data ended with a consensus that the community should establish standard samples for calibration of these measurements. This paper reports the joint effort of Marlow Industries (MI) and members of the Naval Research Laboratory (NRL) to test the usefulness of a carefully constructed conventional apparatus for measurement of the thermal conductivity of thermoelectrics.

The sources of error in λ measurements mainly reflect the difficulty in controlling the amount of heat flowing between the locations in the sample at which the temperature is monitored. It is not easy to confine heat, which can be exchanged by many routes:

- 1] Through the sample, by conduction
- 2] Through power connections and thermocouples, by conduction
- 3] Through surrounding insulation, by conduction
- 4] Through space, by radiation
- 5] Through air, by convection or conduction

The last four routes for heat flow are unwelcome alternatives to the intended route, and they are present to some degree in any design. Their combined effect will be to increase the total rate of heat flow for a given temperature difference, leading the experimenter to calculate a λ value that is too high.

Four miscellaneous factors that can also effect λ measurements are:

- 1] Generation of heat in power connections
- 2] Non-uniform flow of heat through the sample
- 3] Inadequate heat sinking of thermocouples to sample
- 4] Thermal resistance at the contact between the sample and the heat source/sink

The usual practice is to assume that $\frac{1}{2}$ of the Joule heat from

the heater power connections flows through the sample. If this estimate is too high/low, the calculated λ will be too high/low. Uniform heat flow through the pertinent portion of the sample will occur if heat enters the sample uniformly across the cross section, or if the location of the temperature measurements is sufficiently removed from a "point" source of heat. Thermocouples, if not adequately bonded to or embedded in the sample, will register a temperature intermediate between that of the sample and the immediate environment. Thermal resistance at contacts becomes an issue if one chooses to measure the temperature of (high λ) mounting elements, rather than along the length of the sample. (This method of temperature measurement usually is more convenient, does not perturb the sample geometry, and may allow better heat sinking of the thermocouples.) Contact thermal resistance will always lead to a lower apparent λ than the true value.

We have listed four sources of heat loss and four additional possible causes of errors. Which ones are most important depends on the nominal λ of the sample. With high λ samples contact resistance can be especially bothersome, and more, rather than less, extraneous Joule heat from heater wires (or wires carrying the Peltier current in Z meters) will flow through the sample. Non-uniform heat flow is not much of a problem in long, thin samples, which are preferred for high λ samples to achieve a reasonable temperature gradient. Lastly, it is obvious that all alternative routes for heat flow diminish in importance if conduction through the sample is efficient.

In thermoelectrics research, we are interested in the opposite end of the spectrum, very low λ . We can expect to be hampered the most by alternative heat flow routes. To minimize the problem, we can measure short, broad samples, and/or we can take extreme care in frustrating all of the unwanted heat exchange mechanisms. If we use a short, broad sample, and measure temperatures along the sample length, we must be meticulous about the uniformity of heat flow. The good news is that there is more justification for measuring the temperature of mounting elements, so that it may not be necessary to bond thermocouples directly to the sample.

The design of the NRL apparatus takes into account the listed

error sources, but is especially tailored to eliminate radiative exchange. This choice is driven by the fact that the instrument is most often used to measure the thermal conductivity of metals at high temperatures. We have found that as a consequence of using insulation to prevent radiation, the apparatus is not well suited for measurement of low thermal conductivity samples, such as standard thermoelectrics.

Standard Materials

The samples used in this phase of the project were taken from ingots grown at MI by a commercial method. The p-type ingot was grown from a melt of $\text{Sb}_{150}\text{Bi}_{50}\text{Te}_{291}\text{Se}_9$ plus a few percent of excess Te. The n-type ingot was grown from a doped melt of $\text{Bi}_{20}\text{Te}_{27}\text{Se}_3$. With slight variations, these are the compositions used throughout the thermoelectrics industry. As grown, the ingots were approximately 2.7 cm in diameter. Sections of the ingots were machined (see Fig.1) to be compatible with the thermal conductivity apparatus under development at NRL.

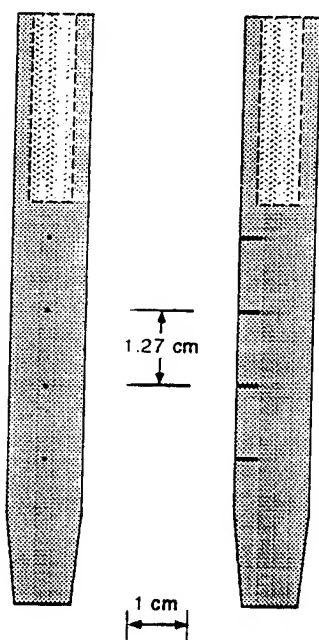


Figure 1. Rod geometry of standard thermoelectrics used in this study.

Due to segregation during solidification, the composition of these ingots varies gradually along their length. There is a corresponding variation in all of the thermoelectric properties. It is reasonable to use the nominal lattice thermal conductivity, the measured resistivity profile, and the Wiedemann-Franz law (using a Lorenz number of $2(k_B/e)^2 = 1.49 \times 10^{-8} \text{ W } \Omega \text{ K}^2$) to estimate the variation in thermal conductivity along the length of the ingot. We obtain expected thermal conductivity fluctuations of $\pm 1.5\%$ for both the n-type and p-type samples, which are 10cm in length..

Thermal Conductance Apparatus

The apparatus is illustrated in Fig. 2. Progressing outward from the axis, the arrangement consists of the sample, space shuttle tile insulation, ceramic thermal shield, fiberfax insulation, and silica ceramic foam outer insulation. The sample and ceramic shield are separately capped, but share a common heat sink at the bottom with the outer insulation. Cartridge heaters are inserted into the sample, and into the copper cap of the ceramic shield. The ceramic shield is separately heated by a wire wrapped at approximately the same height as the sample heater. Power to the wire heater is controlled to match the temperature profile of the shield to that of the sample, in the vicinity of the thermocouples, minimizing heat conduction by thermocouples and insulation. The shield cap is temperature controlled to match the sample cap to within 1/3 K. When the temperature of the shield cap was changed relative to the sample cap by 5 °C, there was little impact (1%) on the measurements, so heat exchange in this region of the instrument is negligible.

Space shuttle tile is an extremely low density solid (0.14 g cm^{-3}) with a corresponding very low thermal conductivity, $\sim 0.24 \text{ W m}^{-1} \text{ K}^{-1}$ in the radial direction at 24 °C and in air. Nevertheless, we have concluded that heat conduction through the tiles was the major source of error in these measurements.

The air gap between the sample and the space tile is very slight, $\sim 200 \mu\text{m}$. A small gap diminishes heat exchange by radiation and convection. In fact, we can expect the temperature profile of the space tile to essentially match that of the sample at equilibrium, due to the slowness of heat conduction away from the surface of the tile. If this is the case, radiative heat exchange is virtually zero because each spot on the surface views only a small portion of the tile, half of which is cooler and half of which is warmer.

The tapered end of the sample was sanded to match the conical hole in the aluminum heat sink. Thermally conductive grease is applied to the minimize thermal resistance both at this interface and in the groove in which the ceramic shield rests. It was not possible to match the temperature profiles of sample and shield without greasing both joints.

For these experiments the thermocouples were wedged into the holes drilled (0.4 mm diameter, 3.6 mm depth) in the sample using tapered Pt wires. The primary purpose of the Pt wires is to secure the thermocouples so that they do not loosen during subsequent assembly. The wedges also improve thermal contact between the thermocouples and the sample. This technique is apparently adequate, because bonding the thermocouples to the sample with epoxy did not change the measurements.

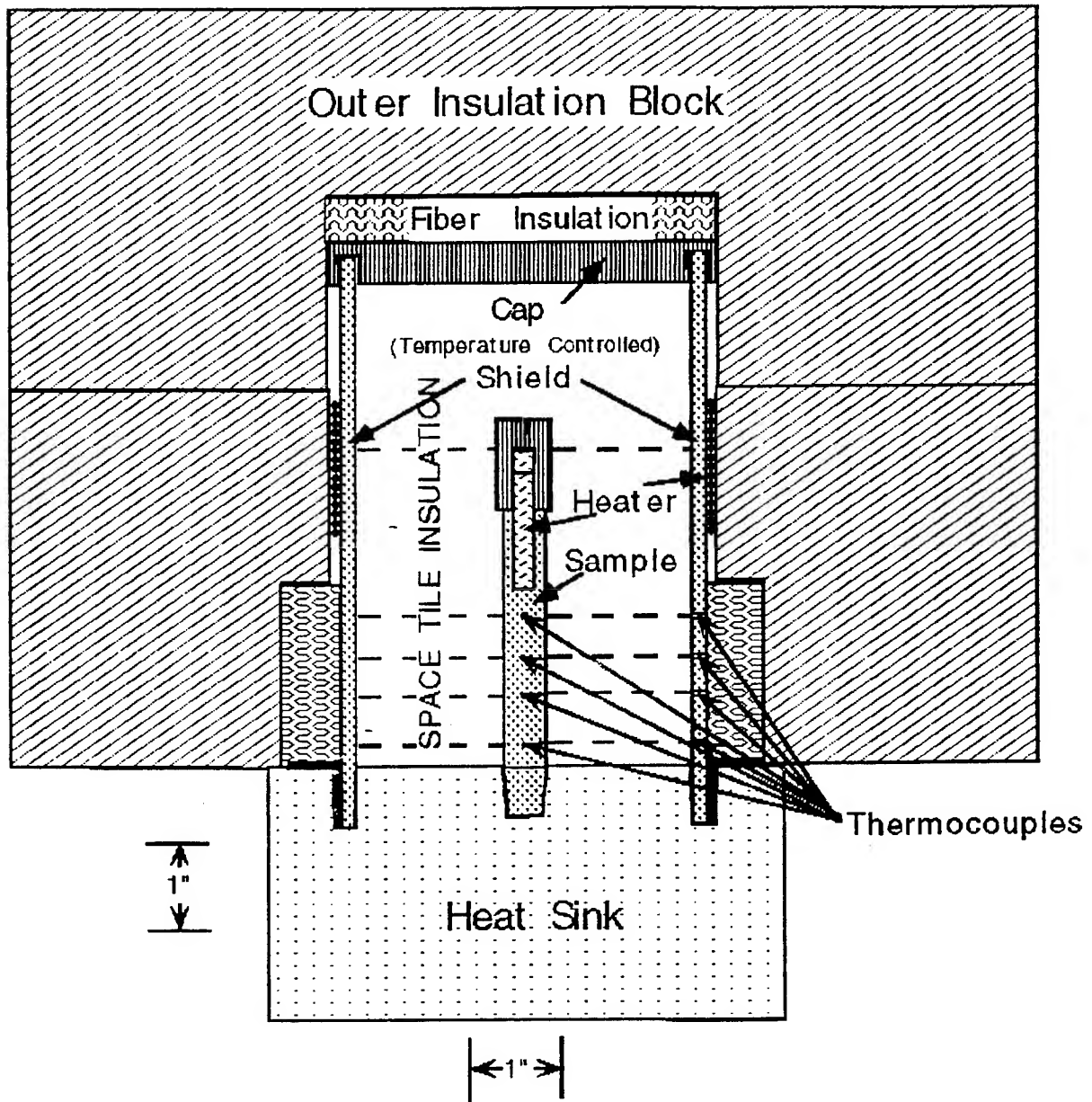


Figure 2. Schematic cross section of the thermal conductance chamber developed at NRL.

In the next section, we present the initial data taken with this instrument on the samples described earlier. The thermal conductivity values are about 6% and 22% too high for the n-type and p-type samples respectively. Most probably, the errors are due to overestimates of the heat flowing through the samples by these same percentages. There are two plausible routes for heat to "escape": through the space tile, and through the heater leads. The current and voltage leads of the heater are insulated 5 mil (127 μm) diameter chromel and alumel. Heat is introduced by a commercial ceramic cartridge heater, having internally a finely coiled resistance wire that probably transfers heat to the surrounding ceramic by radiation. The heat then is conducted to the sample across a very small air gap of $\sim 25 \mu\text{m}$. At these temperatures, radiation is relatively inefficient, so the heater coils may be as much as 20 $^{\circ}\text{C}$ hotter than the sample cap and the shield cap. Nevertheless, estimates show that it is not possible that the heater leads carry away a significant amount of heat.

The challenge that these low thermal conductivity materials present for a conventional apparatus was made clear by raising or lowering the average temperature of the ceramic shield in the vicinity of the thermocouples by 1 $^{\circ}\text{C}$ relative to the sample. The apparent change in sample λ was approximately 36%. For comparison, the precision with which the instrumentation can control temperatures is 1/3 $^{\circ}\text{C}$. Obviously, errors on the level of 10% are explained by heat loss conduction through the space tile. The extremely low λ of the space tile is offset by its large effective area to length ratio in this design, which nevertheless worked very well for measuring λ of metals.

Results

Figure 3 compares the results of the NRL measurements and Z-meter measurements made at MI. As discussed above, most of the disagreement is due to heat escaping through the space shuttle tile in the NRL apparatus. The NRL data in Fig. 3 are actually corrected for the measured temperature differences between corresponding thermocouples on the sample and the ceramic shield. (The uncorrected values were approximately 18.5 and 20.0 $\text{mW cm}^{-1} \text{K}^{-1}$ for the p-type and n-type ingots respectively.) The correction was made on the basis that an intentional 1 $^{\circ}\text{C}$ lowering of the shield temperature increased the measured thermal conductivity by 36%. One source of the remaining errors in the NRL data is believed to be heat exchange at the level of the sample and ceramic shield heaters, where the temperature profiles are not measured. Also, with a 2.4 $^{\circ}\text{C/cm}$ gradient along both the shield and the sample, a misalignment of thermocouples by 0.13 cm could yield a 10 % error.

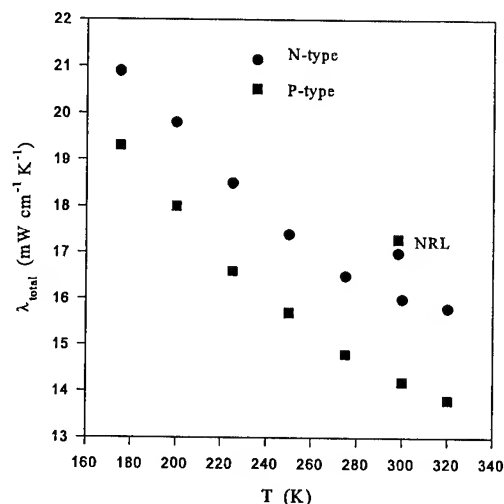


Figure 3. Comparison of thermal conductivity measurements made with the NRL apparatus and MI's Z meter.

The MI data are for parallelepipeds (nominally 4x4x5 mm^3) cut from the tapered regions. The resistivity profiles performed prior to machining the ingots indicate that the properties of these samples should differ from those of the regions measured by NRL by no more than $\pm 5\%$. The room temperature transport properties given in Table I validate this assertion for both the Seebeck coefficients and the electrical resistivities.

	Seebeck Coefficient ($\mu\text{V/K}$)	Resistivity ($\text{m}\Omega\text{-cm}$)	Thermal Conductivity (mW/cm-K)
P-type	201, 200	1.06, 1.01	14.2, 17.3
N-type	-211, -213	0.97, 0.95	16.0, 17.0

Table I. Measured room temperature properties of standard thermoelectrics (MI, NRL).

Future Work

Despite the initial setbacks, it is expected that this project will continue. The direction being taken at present is to make modest changes in the apparatus that will allow better matching of the sample and shield temperature profiles, particularly in the region of the heaters. For example, coring the outer silica insulation (which is not superb) and filling it with fiberfax insulation will greatly reduce the radial heat loss from the shield, allowing a better approximation of ideal vertical heat flow in the apparatus.

The ultimate goal is to have available an apparatus for calibrating measurements of low thermal conductivity materials. This tool will be valuable to the thermoelectrics industry as researchers begin to explore new classes of low thermal conductivity materials that, initially at least, may have a Z too low to allow accurate Z meter measurements.

Deposition of $(\text{Bi,Sb})_2\text{Te}_3$ Films by Magnetron Co-sputtering from Two Targets - First Results

M. Stölzer, V. Bechstein, J. Meusel

Martin Luther University, Dept. of Physics, 06099 Halle, Germany

e-mail: stoelzer@physik.uni-halle.d400.de

Abstract

Sputtered $(\text{Bi,Sb})_2\text{Te}_3$ films show an excellent adhesivity on Kapton substrates and are suitable for patterning by wet etching. The known problem of strong deviation from stoichiometry in these films results from both the different sticking coefficients and the resputtering of the elements during the film growth. An oversupply of Tellurium atoms is a possible and usually applied solution.

A coating system was used which enables the control of direction and intensity of the particle flux from two magnetron sources separately. The targets consist of (i) stoichiometric $(\text{Bi}_{0.25}\text{Sb}_{0.75})_2\text{Te}_3$ and (ii) pure Tellurium. The experimental arrangement allows to control the $\text{Te} : (\text{Bi,Sb})$ flux ratio R_f in a wide range.

WDX analysis of the composition shows, that the films are nearly stoichiometric in the range $1.7 \leq R_f \leq 4$ at substrate temperature $T_s \approx 300^\circ\text{C}$. A small deviation from stoichiometry was observed depending on the variation of T_s .

Introduction

The mixed crystal $(\text{Bi}_{0.25}\text{Sb}_{0.75})_2\text{Te}_3$ is known to be the best suited p-type material for thermoelectric devices like coolers or generators working near room temperature. Miniaturisation of such devices requires thin films of this material with high figure of merit easily and cheaply to produce. Furthermore, devices consisting of thousands of elements can be obtained by wet or dry chemical patterning.

There are some results published in the last years [1-3] about $(\text{Bi}_{0.25}\text{Sb}_{0.75})_2\text{Te}_3$ films having the same figure of merit $3 \cdot 10^{-3} \text{K}^{-1}$ like single crystalline material. In these publications the thermoelectric films have been produced by flash evaporation or hot wall epitaxy. These methods however have some disadvantages. Flash evaporation is difficult to control (therefore expensive) and as far as we know this process is not used in any industrial application. Hot wall epitaxy needs very high substrate temperatures, hence it excludes several substrate materials.

Mzerd et al. [4,5] studied molecular beam epitaxy of Bi_2Te_3 on Sb_2Te_3 crystals. They have found films to be nearly stoichiometric at substrate temperatures $275^\circ\text{C} \leq T_s \leq 325^\circ\text{C}$ when using a very high oversupply of Te ($R_f = 4.5$).

Magnetron sputtering is a widespread and easy-to-use film deposition method which is able to produce highly adhesive and dense films. HTSC films and amorphous Si-Ge films were successfully deposited by this method. Investigations on sputtered V_2VI_3 semiconductor films are reported [6-8]. In all cases a lack of Tellurium of several at% due to the different sticking coefficients of the elements was observed. Preferential resputtering during the film growth is supposed to cause an additional loss of Te.

In this paper an experimental arrangement is presented, which should combine the advantage of magnetron sputtering and the possibility of controlling the $\text{Te} : (\text{Bi,Sb})$ flux ratio.

Co-sputtering with two magnetrons

We used two round shaped (90 mm diameter) commercial magnetron sources which can both separately adjusted in position, angle and height over the substrate plane. Fig. 1 shows a picture of this sputtering unit.

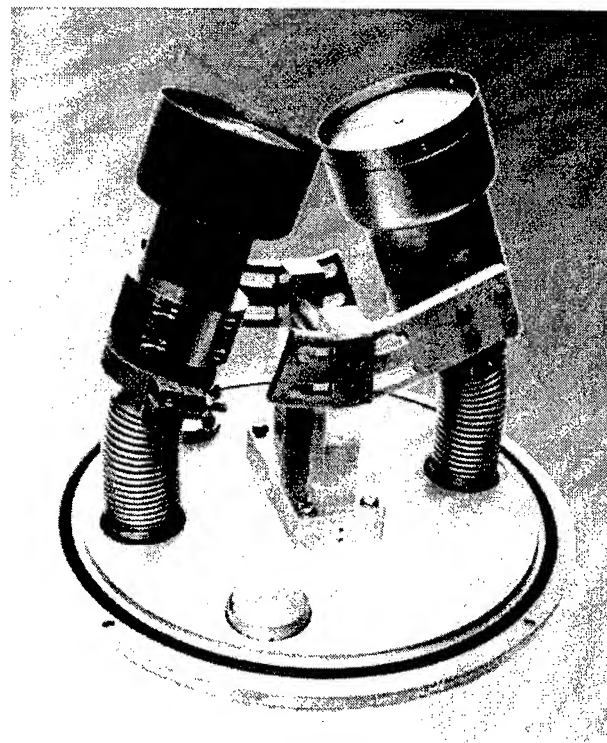


Fig. 1: The sputtering unit mounted on a 30 cm flange

Stoichiometric $(\text{Bi}_{0.25}\text{Sb}_{0.75})_2\text{Te}_3$ and pure Tellurium served as target material. The targets were produced from 99.999% pure elements (first homogenized in evacuated quartz ampouls in case of $(\text{Bi}_{0.25}\text{Sb}_{0.75})_2\text{Te}_3$) using a special melting procedure in a graphite crucible within an atmosphere of N_2 .

In a first step, the thickness distribution on a flat substrate was calculated depending on the geometrical arrangement of the sputtering sources (see fig. 2).

The sputtered particles are emitted from each point of the target surface in every direction after the usual cosine law. Scattering of these particles on the Argon atmosphere can be neglected in the calculation, because their mean free path at the working pressure of $1.8 \cdot 10^{-3}$ mbar is about 5 cm.

The sputtering rate on the target surface R_s ($\text{gs}^{-1}\text{cm}^{-2}$) is

assumed to be radial symmetric and was fitted to a Gaussian:

$$R_s(s) = \text{const} \cdot e^{-\frac{(s - 3,054)^2}{0,5 \cdot 0,732^2}}, \quad s = 0 \dots R$$

$R = 4.5$ cm is the radius of the target. The thickness at any point of the substrate plane was calculated and is then given by

$$d = \frac{t}{\varrho} \int_{s=0}^R \int_{\alpha=0}^{2\pi} \frac{s R_s}{\pi r^2} \cos \varphi \cos \theta \, d\alpha \, ds.$$

t and ϱ are the sputtering time and the mass-density, respectively. The other values are defined in fig. 2.

An additional rotation of the substrate in the $x'y'$ -plane around the origin can be taken into account by averaging the thickness d on circles to be centered in this point.

The tilt angle of the target β , the distance to the substrate h and the shift l from the substrate axis are varied during the calculations in order to reach a desired thickness distribution on

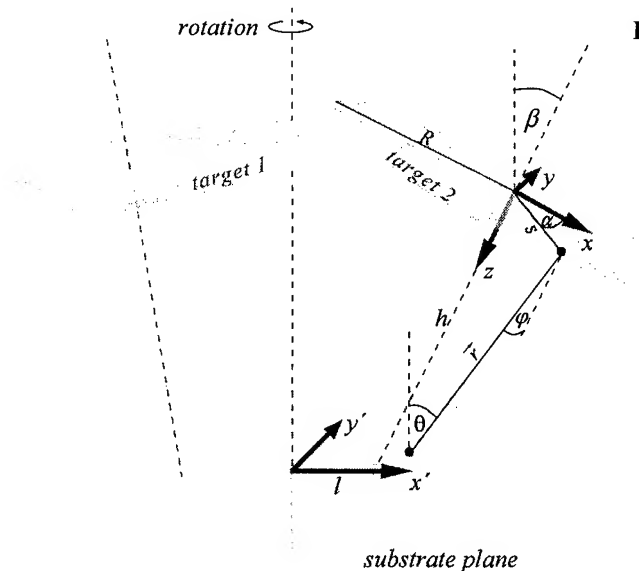


Fig. 2: Geometrical arrangement of the sputtering sources

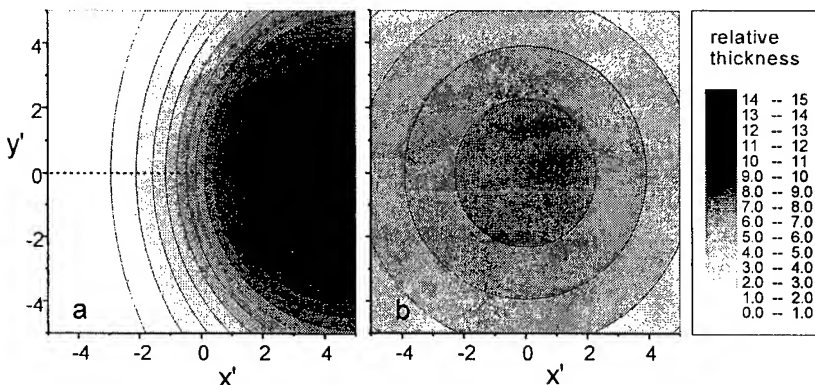


Fig. 3: Calculated thickness distribution. Parameter $\beta=15^\circ$, $h=5$ cm, $l=5$ cm
a without and b with substrate rotation (one source).

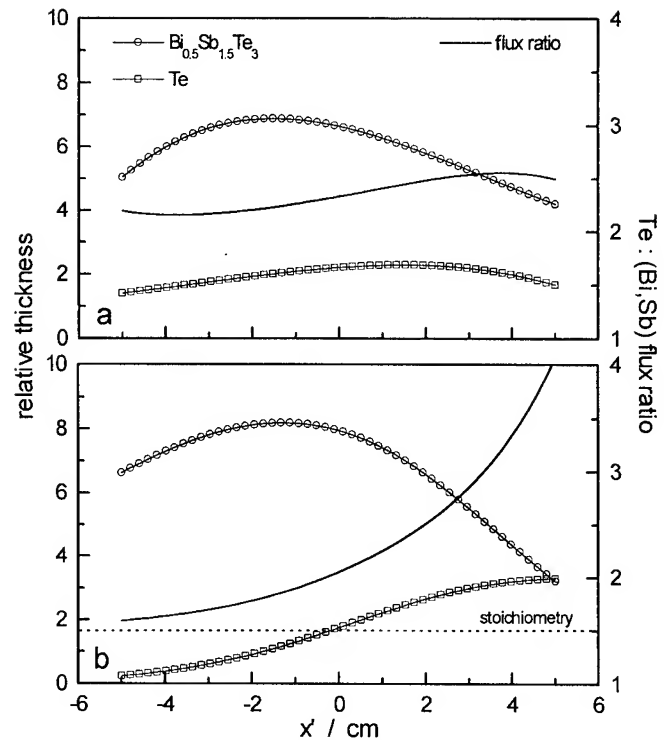


Fig. 4: Calculated thickness distribution and flux ratio along the x' axis.

a: $\beta=30^\circ$, $h=8.5$ cm, $l=0$ (both targets); b: $\beta=15^\circ$, $h=8$ cm, $l=2$ cm ($\text{Bi}_{0.5}\text{Sb}_{1.5}\text{Te}_3$) and $\beta=15^\circ$, $h=8$ cm, $l=6$ cm (Te)

the substrate.

Fig. 3 shows a typical example of a calculated thickness distribution of one target.

Two cases are of special interest: (i) a nearly constant ratio of the particle flux from both sources and (ii) a strong variation of the flux ratio over the substrate. In Fig. 4 calculations of these two cases are presented as a section of the thickness distribution in x' direction.

The arrangement calculated in fig.4a is suited for the deposition of films with constant properties over a large area as required for a production process. The homogeneity still can be improved by substrate rotation.

The arrangement in fig.4b was used in a first experiment, the results shall be presented now.

First results

The sputtering sources were arranged as written in fig.4b and power by 44W and 22W for the $\text{Bi}_{0.5}\text{Sb}_{1.5}\text{Te}_3$ and Te source, respectively, using commercial DC magnetron power supplies. The Ar pressure was $1.8 \cdot 10^{-3}$ mbar and the deposition rate in the order of magnitude of 1 nm/s.

Polyimide foil (130 μm thick Kapton) heated from the back by a radiation heater was used as substrate.

The Te : (Bi,Sb) atomic flux ratio was calculated from the measured film thickness, when each

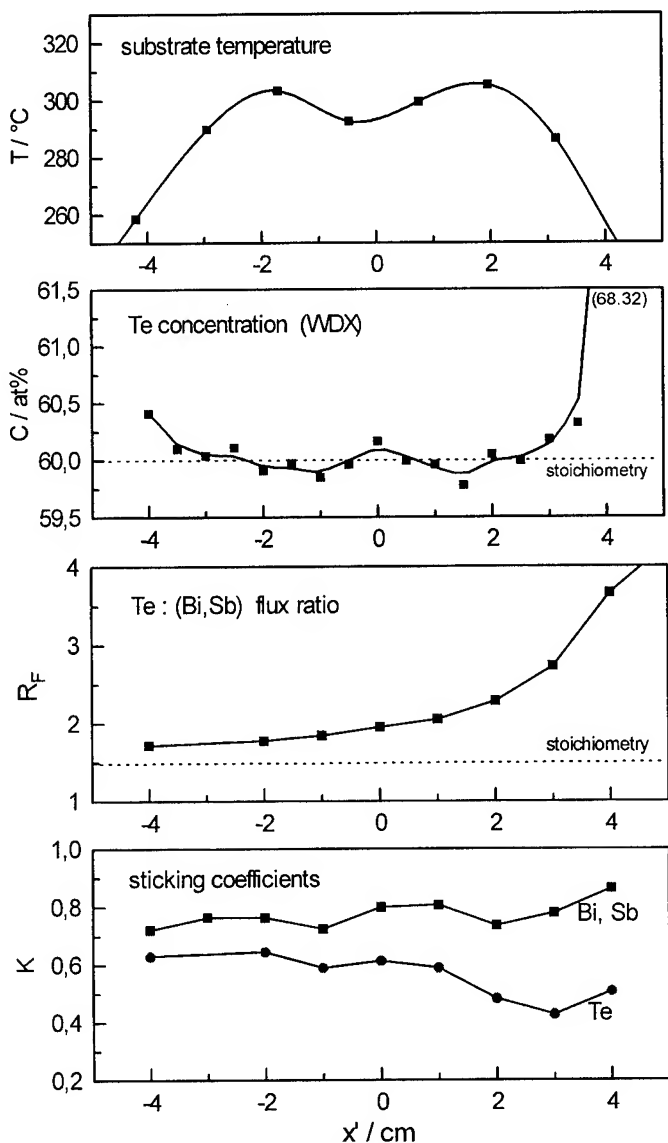


Fig.5: Growth temperature, Te concentration, atomic flux ratio and sticking coefficients of a Bi-Sb-Te film prepared by co-sputtering of $\text{Bi}_{0.5}\text{Sb}_{1.5}\text{Te}_3$ and pure Te on polyimide substrate

source sputtered separately on a cold substrate.

The concentration of Tellurium of a film deposited at 300°C was measured by WDX (wave dispersive X-ray analysis). Precision and time stability were found to be 0.1 at%, tested on a single crystal standard.

The sticking coefficients were calculated from film thickness measurements and from the element concentrations in the film. In fig.5 the results of all measurements are plotted versus the position on the sample.

The most important result seems to be the much greater impact of substrate temperature than atomic flux ratio considering the concentration of Tellurium in the film. The flux ratio varies between 1.7 and 4, which corresponds to 63 at% and 80 at% in the Te concentration scale. The concentration in the film is always near 60 at% and varies only slightly according to the growth temperature. Only at the edges where the temperature is near 260°C there is a great influence of the flux ratio. The Te concentrations determined at the edges are 60.4 at% and 68.3

at% at low and high flux ratio, respectively.

These results are similar to those achieved on epitaxial Bi_2Te_3 films on Sb_2Te_3 single crystals [4,5], which were found to be stoichiometric between 275°C and 325°C . The sticking coefficients determined are somewhat lower than those given in [4, 5]. The reason for this may be the resputtering effect.

Conclusions

A new sputtering system was put into use which enables the control of direction and intensity of the particle flux from two magnetron sources separately. The Te : (Bi,Sb) atomic flux ratio can be controlled in a wide range by simultaneous sputtering of stoichiometric $(\text{Bi}_{0.25}\text{Sb}_{0.75})_2\text{Te}_3$ and pure Tellurium.

A sample film deposited at $T_s \approx 300^\circ\text{C}$ was found to be stoichiometric, independent on the flux ratio in the range $1.7 \leq R_F \leq 4$. Its Te concentration varied between 59.78 and 60.18 (not considering the colder edges here) according to slight variations of T_s of $\pm 10^\circ\text{C}$.

The deposition of $\text{Bi}_{0.5}\text{Sb}_{1.5}\text{Te}_3$ films at $T_s \approx 300^\circ\text{C}$ with a slight oversupply of Tellurium seems to be a promising method to achieve highly effective thermoelectric films. Kapton foil is found to be a cheap substrate material that is low thermal conducting, chemical and thermal stable, and has nearly the same thermal expansion coefficient like the semiconductor. The magnetron sputtering technique guarantees an excellent adhesivity and can easily be extended to a larger scale.

Nevertheless the slight variations of the Te concentration of the sample may have a dramatic effect on the films thermoelectric properties. Further work has to be done to investigate this problem.

References

- [1] F. Völklein et al., "Transport properties of flash-evaporated $(\text{Bi}_{1-x}\text{Sb}_x)_2\text{Te}_3$ films I: Optimization of film properties", *Thin Solid Films* **187**, 253-262 (1990)
- [2] M. Stölzer, M. Stordeur and I. Stark, "Preparation of highly effective p- $\text{Bi}_{0.5}\text{Sb}_{1.5}\text{Te}_3$ and n- $\text{Bi}_2\text{Te}_{2.7}\text{Se}_{0.3}$ films", *ICT XIV*, St.Petersburg 1995
- [3] Yu.A. Boikov et al., "Electrophysical parameters of epitaxial n-type Bi_2Te_3 films", *Fizika Tverdogo Tela* **33**, 3414-19 (1991).
- [4] A. Mzerd et al., "Effect of substrate temperature on crystal growth of Bi_2Te_3 on single crystal Sb_2Te_3 ", *J. Mat. Sci. Lett.* **13**, 301-304 (1994).
- [5] A. Mzerd et al., "Optimal crystal growth conditions of thin films of semiconductors", *J. of Crystal Growth* **140**, 365-369 (1994).
- [6] Y. H. Shing et al., "Sputtered Bi_2Te_3 and PbTe films", *J. Vac. Sci. Technol. A* **1** (2), 503-506 (1983).
- [7] H. Noro, K. Sato and H. Kagechika, "The thermoelectric properties and crystallography of Bi-Sb-Te-Se thin films grown by ion beam sputtering", *J. Appl. Phys.* **73** (3), 1252-1260 (1993).
- [8] M. Stölzer and M. Stordeur, "Properties of magnetron sputtered $\text{Bi}_{0.5}\text{Sb}_{1.5}\text{Te}_3$ films", *Proc. of ICT XI*, Arlington 1992.

Thin Film Thermoelectric Generator Cell of Bi-Sb-Te-Se System

Il-Ho Kim and Dong-Hi Lee

Department of Metallurgical Engineering, Yonsei University, Seoul, 120-749, Korea

Abstract

Thin film thermoelectric generator cells (TFTEGCs) of Bi-Sb-Te-Se system were fabricated and their performances were investigated. The generator cells were composed of several layers of plate-modules, and each plate-module contained 15 p/n couples and was connected electrically in series or in parallel. Variations of the open circuit voltage, short circuit current and maximum output power as a function of temperature difference showed a linear relationship for the first two values, but there was a second-order relationship for the latter. The output power produced per couple and per unit temperature difference was $\approx 3.5 \text{ nW/K-couple}$.

I. Introduction

Thermoelements of Bi-Sb-Te-Se systems, in general, have been fabricated from the sintered blocks of the materials.¹⁻³ There is, however, certain difficulties and limitations for making highly-miniaturized modules because of the fragile nature of these materials. Moreover, the number of p/n couples fitting in the limited space available makes it impossible to obtain relatively high output voltage (order of volt) for power generation. To overcome these drawbacks, a thermoelectric module based on thin film technology has been studied.⁴⁻⁷ In the application for electronic components, a power of micro or milliwatt level at relatively high voltage has reportedly been obtained by a thin film module system.⁸⁻¹²

In the present studies, the TFTEGCs were carefully fabricated in a stacked form of individual plate-modules containing the predetermined p/n pattern. Their characteristics as well as their performances were investigated by varying the number of stacking layers and electrical connections (in series or in parallel) for the control of output voltage and current of the TFTEGC.

II. Experiments

P-type ($\text{Bi}_{0.5}\text{Sb}_{1.5}\text{Te}_3$) and n-type ($\text{Bi}_2\text{Te}_{2.4}\text{Se}_{0.6}$) films were deposited on thin glass substrates (0.15 mm thick) by the flash evaporation method^{5,13-15} using the patterning masks designed for the desired dimension and shape of p- and n-legs and their junctions. During the evaporation process, a diffusion barrier layer (aluminum; 300 nm thick) between p- and n-type material at the junctions was deposited. The dimensions of p- and n-leg were 20 mm (L) x 0.67 mm (W) x 4 μm (t) and the interleg spacings were arranged to be 0.5 mm. Overall size of a plate-module was 40 x 22 x 0.15 mm³ which contained 15 p/n couples (see Photo. 1). As shown in Fig. 1, the generator cell was composed of several layers of plate-modules (up to 20 layers) that were bonded together into a stack and connected electrically in series or in parallel. In Photo. 2 two TFTEGCs are shown, one

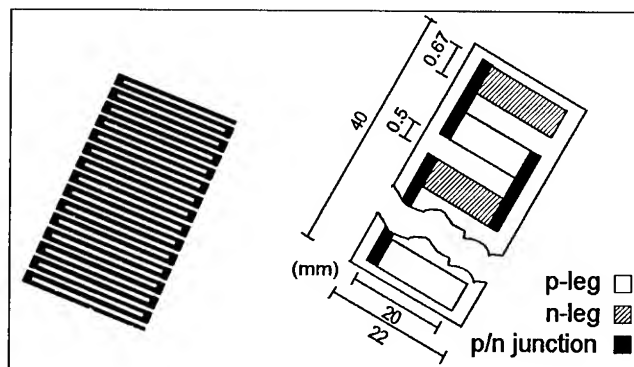


Photo. 1. Plate thermoelectric module.

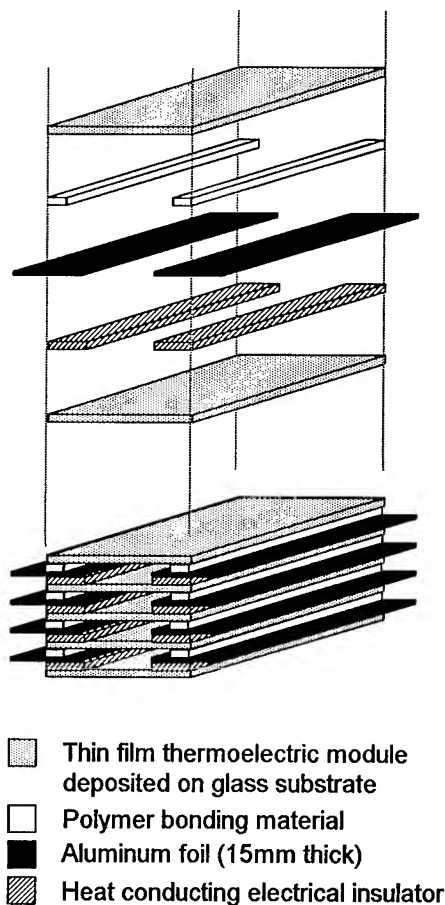
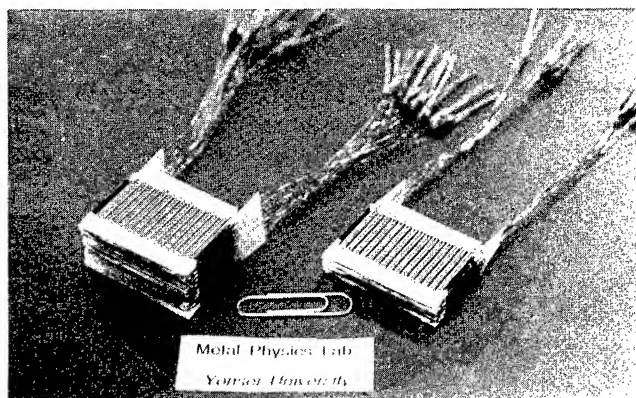


Fig. 1. Illustration for stacking procedure of the TFTEGC.



is composed of 10 plate-modules while the other is composed of 20 plate-modules. Consequently, each contains 150 and 300 p/n couples respectively. Photo. 3 shows components for assembly of the TFTEGC, together with special adhesives. In the sample designation, S and P stand for the electrical connection of each plate-module ; i.e. S for in series and P for in parallel, and the subscript after S or P indicates the number of plate-modules stacked.

Internal electric resistance (R_i), open circuit voltage (V_{OC}), short circuit current (I_{SC}) and maximum output power (P_{max}) were measured as a function of the number of plate-modules (N), temperature difference between hot and cold junctions (ΔT) and variation of electrical connections (serial or parallel). Photo. 4 shows a jig for the measurement of performance of TFTEGCs. Two parallel aluminum plates were positioned to maintain close contact with the fins (aluminum foils) attached at both sides (hot and cold side) of the plate-modules. One of the aluminum plates of the jig is for heating by a miniature heater and the other is for keeping constant temperature by circulating cold water. Temperatures of each aluminum plate were measured by T-type thermocouples attached.

III. Results and Discussion

If N_S or (and) N_P plate-modules are electrically connected in series or (and) in parallel respectively, then V_{OC} , I_{SC} , R_i and P_{max} can be expressed as follows ; $V_{OC} = N_S V_0$, $I_{SC} = N_P V_0 / R_0$, $R_i = (N_S / N_P) R_0$ and $P_{max} = N_P N_S (V_0)^2 / (4 R_0)$, where V_0 and R_0 are respectively output voltage and internal electric resistance of each plate-module.

Fig. 2 shows the variation of P_{max} with ΔT of the TFTEGC when connected in series or in parallel. Measured P_{max} varied with ΔT in a second-order relationship as predicted from one of the aforementioned equations, and P_{max} depended linearly on N , i.e. P_{max} for S_{20} or P_{20} were almost twice of S_{10} or P_{10} at a given ΔT . As presented in Fig. 3, total thermoelectric power (or total Seebeck coefficient) was almost constant over the temperature range studied in this experiment. It was ≈ 50 mV/K for S_{10} and ≈ 100 mV/K for S_{20} when connected in series. But it was only ≈ 5 mV/K for P_{10} or P_{20} because it is irrelevant to N when connected

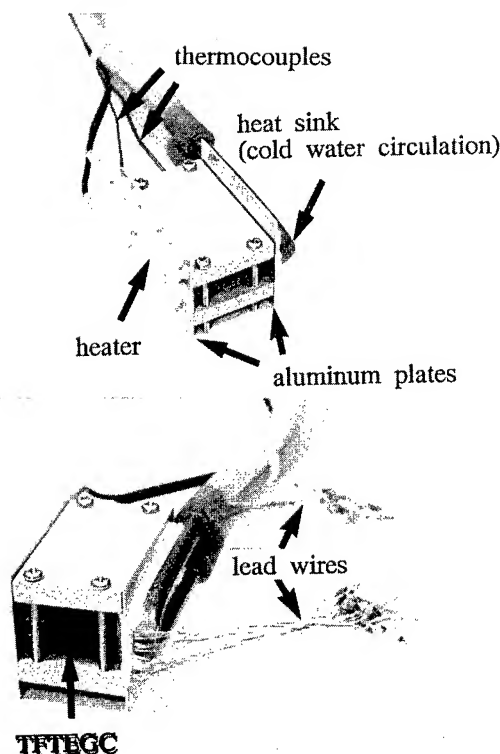


Photo. 4. Apparatus for measurement of performance of the TFTEGC.

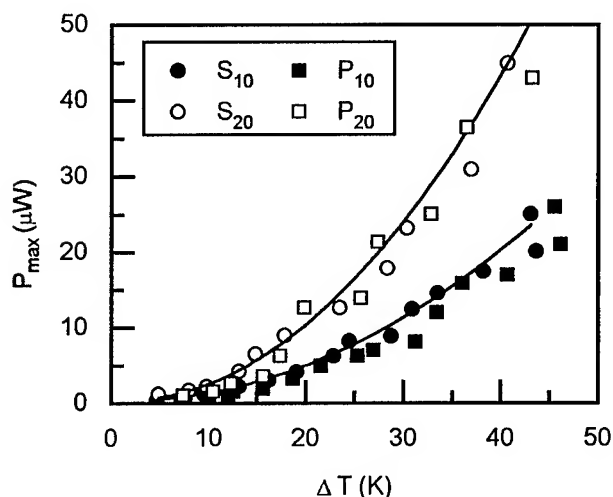


Fig. 2. Variation of maximum output power as a function of temperature difference.

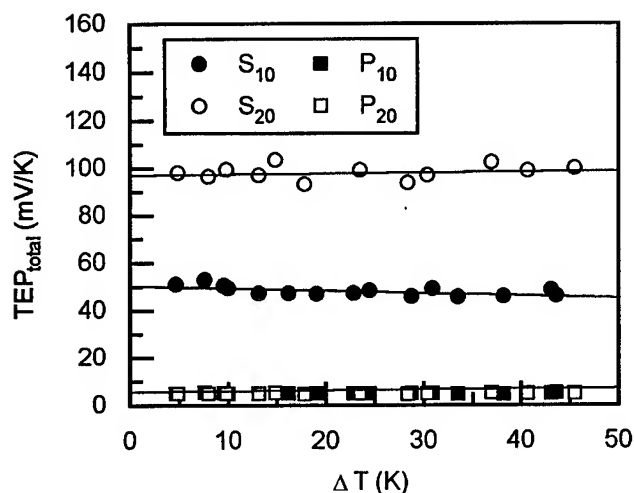


Fig. 3. A plot of total thermoelectric power against temperature difference.

in parallel. Therefore it was equal to the values of the total thermoelectric power for one plate module. Thermoelectric power per p/n couple, which equals to Seebeck coefficient of a p/n couple, was found to be ≈ 0.32 mV/K (Fig. 4).

As a mean for the evaluation of TFTEGC performance, the reported data on the Bi-Sb-Te-Se-based thin film battery for cardiac pacemaker⁸ were compared with the results of present studies. The cardiac battery, which was composed of 777 couples connected in series, was reported to have total thermoelectric power of 280 mV/K (total resistance of 180 k Ω). When considered power produced per couple and per unit temperature difference, output power of S_{20} was 3.5 nW/K-couple whereas the battery had 4.3 nW/K-couple. Reasons for the difference in output powers are believed mainly due to the compositional and dimensional differences in the thermoelectric materials used in each case. The compositions of the cardiac battery were $\text{Bi}_{0.645}\text{Sb}_{1.355}\text{Te}_{3.7}$ (p-type) and $\text{Bi}_2\text{Te}_{2.5}\text{Se}_{0.5}$ (n-type), and Seebeck coefficient of 360 $\mu\text{V/K}$ was reported per p/n couple. Thickness of the films was 4.0 μm for p-leg and 2.85 μm for n-leg respectively, while an uniform thickness of 4 μm for both

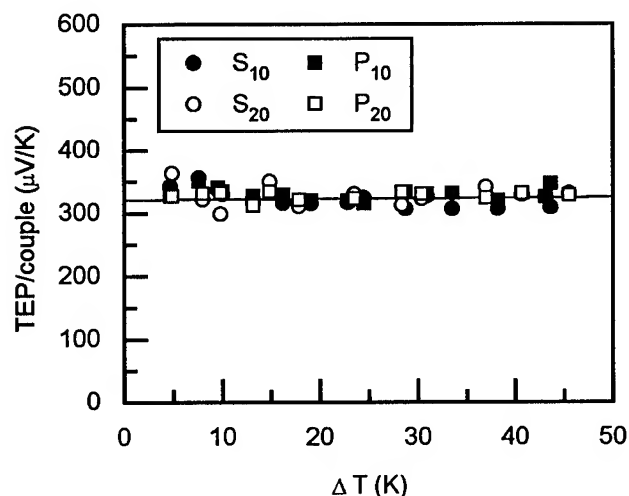


Fig. 4. A plot of thermoelectric power per p/n couple vs. temperature difference.

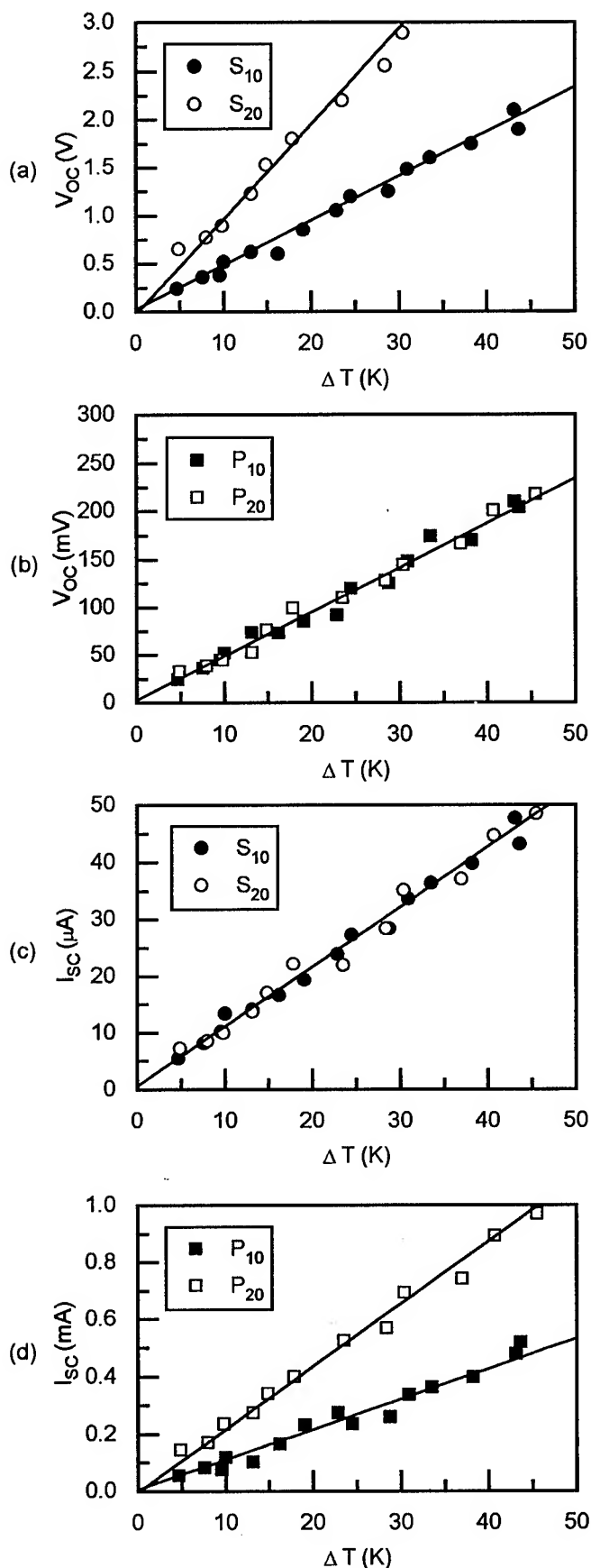


Fig. 5. Variation of open circuit voltage (V_{oc}) and short circuit current (I_{sc}) as a function of temperature difference.

(a), (c) serial connection

(b), (d) parallel connection

p- and n-types in the present case. It is, however, instructive to find similar values of output power (about 4 nW/K-couple) for both cases.

Fig. 5 shows the variation of V_{OC} and I_{SC} as a function of N , ΔT and the way of electrical connections - in series or in parallel. As shown in Figs. 5 (a) and (b), V_{OC} varied linearly with ΔT , but for serial connection its slope depends on N whereas there was only one slope for the case of parallel connection, as expected from the above equations. This implies, as found in Figs. 3 and 4, that there is little variation in Seebeck coefficients over the temperature ranges studied. On the other hand, I_{SC} (Figs. 5 (c) and (d)) behaved oppositely to the case of V_{OC} ; I_{SC} of S_{10} and S_{20} had only one slope, but I_{SC} showed two different slopes for the case of P_{10} and P_{20} .

For the case of serial connection (Figs. 5 (a) and (c)), the slopes $[dV_{OC}/d(\Delta T)]$ were ≈ 50 mV/K for S_{10} and ≈ 100 mV/K for S_{20} , and V_{OC} reached to the values of an order of volt at $\Delta T \geq 10$ K for the case of S_{20} . I_{SC} was proportional to ΔT with $[dI_{SC}/d(\Delta T)] \approx 1$ μ A/K, which was irrelevant to N .

In the parallel connection (Figs. 5 (b) and (d)), V_{OC} was proportional to ΔT with $[dV_{OC}/d(\Delta T)] \approx 5$ mV/K. The slopes $[dI_{SC}/d(\Delta T)]$ were ≈ 0.1 mA/K for P_{10} and ≈ 0.2 mA/K for P_{20} . I_{SC} , in this case, showed the values of an order of milliampere at $\Delta T \approx 50$ K for P_{20} .

Figs. 6 (a) and (b), which are an example for the combined case of serial and parallel connections, demonstrates that output voltage and current generated by the TFTEGC could be controlled by varying the connection combination or N .

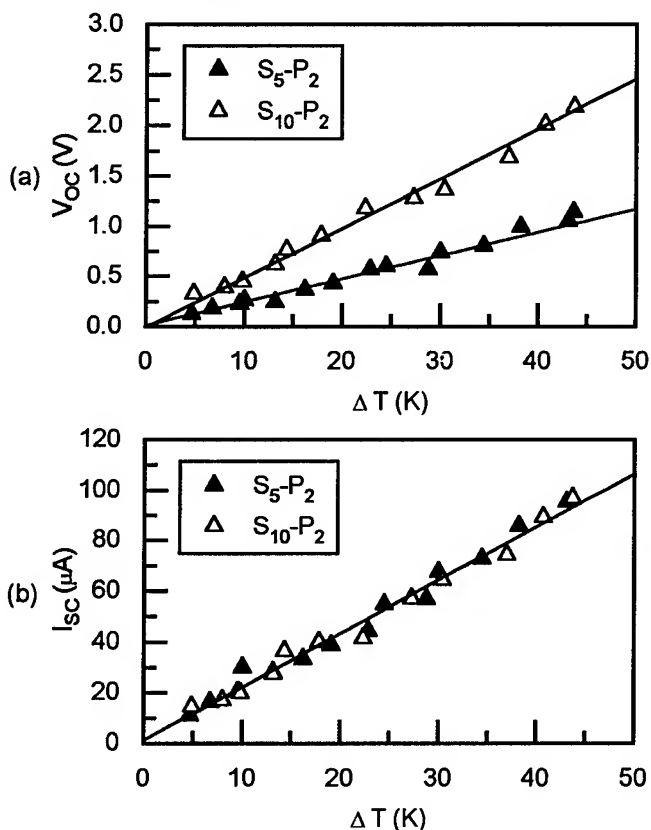


Fig. 6. Variation of (a) open circuit voltage and (b) short circuit current as a function of temperature difference when connected in series and parallel combination.

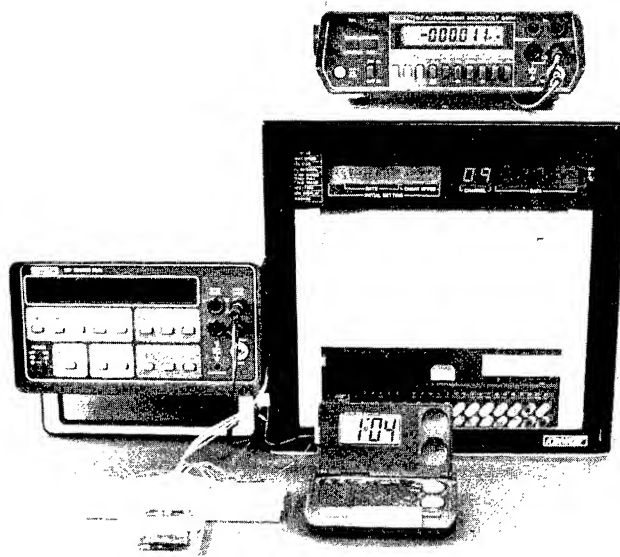


Photo. 5. An arrangement for demonstration of power generation by the TFTEGC.

An arrangement for demonstration of TFTEGC power generation was shown in Photo. 5. A LCD clock was driven by the S_{10} , where output power of 16.5 μ W (1.5 V, 11 μ A) was recorded at the temperature difference of 35 K.

IV. Conclusion

From the fabrication and an investigation into the characteristics of the thin film thermoelectric generator cells, following results were obtained :

(1) Microwatt level power at relatively high voltage (order of volt) was produced by Bi-Sb-Te-Se-based thin film generators, and output voltage and current were possible to control by changing the electrical connection manner as well as the number of stacking plate-modules.

(2) Variation of open circuit voltage and short circuit current with temperature differences showed a linear relationship. There were, however, some differences in variations ; open circuit voltages were dependent on the number of plate-modules when connected in series, but it was not for parallel connection. Short circuit current of S_{10} and S_{20} had the same dependence of temperature difference, but slopes of P_{10} and P_{20} were different each other.

(3) Maximum output power varied with temperature differences in the square-law relation. Its values were almost doubled when the number of plate-modules increases twice ; $P_{max} \propto N$ at a given ΔT .

Acknowledgments

The authors would like to show their appreciation to KOSEF and RETCAM for their financial support.

References

- [1] A.F.Semizorov, "A study of pressed thermoelectric materials based on Bi_2Te_3 - Sb_2Te_3 - Sb_2Se_3 solid solutions", *Inorganic Materials*, vol.31, No.6, pp.675-677 (1995).

- [2] Kyung-Wook Jang and Dong-Hi Lee, "Thermoelectric properties of hot-pressed p-type $(\text{Bi}_2\text{Te}_3)_{0.70}(\text{Bi}_2\text{Te}_3)_{0.25}(\text{Sb}_2\text{Se}_3)_{0.05}$ pseudo-ternary materials", J. Korean Institute of Metals, vol.32, No.5, pp.609-615 (1994).
- [3] H.T.Kaibe, M.Sakata and I.A.Nishida, "Thermoelectric cooling properties of the Π -shaped thermocouples consisting of the sintered Bi_2Te_3 and Sb_2Te_3 based compounds", Proc. 12th ICT, pp.165-168 (1993).
- [4] Il-Ho Kim and Dong-Hi Lee, "Performance of $(\text{Bi,Sb})_2(\text{Te,Se})_3$ thin film thermoelectric module", J. Korean Vacuum Society, vol.3, No.3, pp.309-315 (1994).
- [5] Il-Ho Kim and Dong-Hi Lee, "Preparation and properties of $(\text{Bi,Sb})_2(\text{Te,Se})_3$ -based film type thermoelectric modules", Proc. 12th ICT, pp.328-333 (1993).
- [6] Yu.A.Boikov, O.S.Gribanova, V.A.Danilov and I.M.Deryagina, "Thin and thick, $(\text{Bi,Sb})_2(\text{Te,Se})_3$ -based thermoelectric films", Proc. 8th ICTEC, pp.18-22 (1989).
- [7] Il-Ho Kim, Byoung-Gue Min and Dong-Hi Lee, "Effects of thickness and processing variables on the performance of $(\text{Bi,Sb})_2(\text{Te,Se})_3$ -based film type thermoelectric modules", Proc. 14th ICT, pp.145-150 (1995).
- [8] D.M.Rowe, D.V.Morgan and J.H.Kiely, "Fabrication of a miniature thermoelectric generator using integrated circuit technology", Proc. 8th ICTEC, pp.171-175 (1989).
- [9] B.Chinaglia, F.Vallana and G.Bosio, "A thin film module for thermoelectric conversion in a plutonium-238 battery", Energy Conversion, vol.16, pp.55-65 (1976).
- [10] J.H.Kiely, D.V.Morgan and D.M.Rowe, "Low cost miniature thermoelectric generator", Electronics Letters, vol.27, No.25, pp.2332-2334 (1991).
- [11] J.Przyluski and K.Borkowski, "Thin film thermoelectric Bi_2Te_3 - based modules", Proc. 6th ICTEC, pp.100-104 (1986).
- [12] D.K.Benson and C.E.Tracy, "Design and fabrication of thin film thermoelectric generator", Proc. 4th ICTEC, pp.11-14 (1982).
- [13] Sang-Youb Lee and Dong-Hi Lee, "Effect of electron transport properties on the thermoelectric power of Cu/Constantan thin film couples", J. Korean Institute of Metals, vol.28, No.7, pp.627-634 (1990).
- [14] Jae-Min Myeong, Sang-Youb Lee and Dong-Hi Lee, "Thermoelectric power of multi-junction Cu/Constantan thin film couple", Korean Applied Physics, vol.3, No.2, pp.195-201 (1990).
- [15] Myeong-Gweon Gu, Sang-Youb Lee and Dong-Hi Lee, "Thermoelectric power of mono-junction Cu/Constantan thin film couple", Korean Applied Physics, vol.3, No.1, pp.73-80 (1990).

Low Temperature MOCVD Growth of V/VI Materials Via a $\text{Me}_3\text{SiNMe}_2$ Elimination Reaction

T.J. GROSHENS, R.W. GEDRIDGE Jr., R. SCHERI and TERESA COLE

Naval Air Warfare Center Weapons Division, Research and Technology Division, China Lake, CA 93555

Abstract

The reactive precursors $\text{M}(\text{NMe}_2)_3$ ($\text{M} = \text{Sb, Bi}$) and $(\text{Me}_3\text{Si})_2\text{Te}$ were used to deposit films of M_2Te_3 ($\text{M} = \text{Sb, Bi}$) on Si(111) cut 4° off-axis, GaAs(100), and Kapton substrates between 25°C and 150°C in a low pressure MOCVD reactor. The film growth process is a novel N,N-dimethylamino-trimethylsilane ($\text{Me}_3\text{SiNMe}_2$) elimination reaction and not pyrolysis reactions employed in conventional MOCVD techniques. X-ray diffraction data show the crystalline quality and orientation of the resulting polycrystalline films were dependent on the substrate structure and growth temperature. Amorphous films were deposited below 50°C . Films deposited at 75°C for Sb_2Te_3 and 125°C for Bi_2Te_3 were highly oriented with the (015) reflection plane parallel to the substrate surface. Films of Sb_2Te_3 deposited at 150°C were highly oriented with the (002) reflection planes parallel to the substrate surface. The electrical properties and composition of Bi_2Te_3 films deposited at 125°C on Kapton were independent of the V/VI precursor ratio used. Variation in the composition of a $\text{Sb}_x\text{Bi}_{2-x}\text{Te}_3$ ternary film across the susceptor was observed due to differences in the reaction kinetics for formation of Sb_2Te_3 and Bi_2Te_3 . This unique deposition reaction provides an alternative route to prepare group V chalcogenide materials which have potential applications in solar cells, reversible optical storage, and thermoelectrics.

Introduction

Bi_2Te_3 and Sb_2Te_3 films have been deposited by various techniques including molecular beam epitaxy [1], flash evaporation [2], sputtering [3], electrodeposition [4], and ionized cluster beam (ICB) [5] methods. All of these methods require sophisticated UHV systems and careful control of fluxes to obtain stoichiometric films. We previously reported a novel technique to prepare these materials as powders and thin films directly from reactive organometallic precursor compounds using reaction 1 [6]. This method relies on the self limiting reaction to produce films of V/VI material of the proper stoichiometry. A more detailed account of Bi_2Te_3 and Sb_2Te_3 film depositions using this method will be presented in this paper.

Experimental

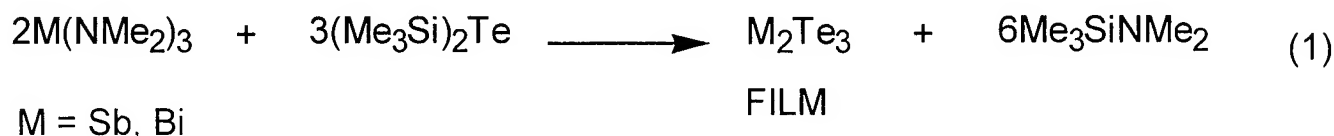
General Procedures

Polycrystalline Sb_2Te_3 , Bi_2Te_3 and $\text{Sb}_x\text{Bi}_{2-x}\text{Te}_3$ films were grown in a reduced pressure (20-100 torr) vertical MOCVD reactor with an inductively heated substrate stage using $\text{Sb}(\text{NMe}_2)_3$ and/or $\text{Bi}(\text{NMe}_2)_3$ and $(\text{Me}_3\text{Si})_2\text{Te}$ with prepurified H_2 as a carrier gas. The precursor vapors were isolated prior to entering the reactor using a coaxial inlet system which allowed the gas flows to mix 3cm above the center of the susceptor. In the first series of growth experiments, films were deposited simultaneously on GaAs(100) (high resistivity Cr doped) and Si(111) substrates placed next to each other on the susceptor. The substrates were cleaned then etched with 5% HF solution for Si(111) and $\text{NH}_4\text{OH}/\text{H}_2\text{O}_2$ solution for GaAs prior to use. The only volatile byproduct identified by proton NMR (of reactor exhaust gases collected in a liquid nitrogen cooled trap) and the Residual Gas Analyzer (in situ monitoring of reactor exhaust) was $\text{Me}_3\text{SiNMe}_2$. The V/VI inlet ratio was determined by integration of the peaks of $\text{Me}_3\text{SiNMe}_2$ and any excess group V or $(\text{Me}_3\text{Si})_2\text{Te}$ precursor in the ^1H NMR spectrum trapped byproducts. The surface morphologies of the films vary from smooth, highly reflective surfaces to dull gray. X-ray diffraction data used to characterize the structural phases and the crystallinity of the deposited films was collected on a Scintag Pad V XRD system. The Van der Pauw technique was used to measure resistivity and Hall effect (magnetic field 1.5kgauss) alternating the current between positive and negative for readings in each direction. The results are compiled in Table 1 following a detailed description of each film growth experiment.

Sb_2Te_3 FILMS

A flow rate of 50sccm H_2 was maintained through both bubblers at 24°C . The bubbler and reactor pressure was maintained at 100 torr during the deposition reactions. FILM 1 was grown at a substrate temperature of 24°C for one hour. FILM 3 was grown at a substrate temperature of 75°C for one hour. FILM 5 was grown at a substrate temperature of 150°C for two hours.

$\text{Me}_3\text{SiNMe}_2$ ELIMINATION REACTION



Bi₂Te₃ FILMS

FILM 2 was grown at a substrate temperature of 50°C for one hour. A bubbler/reactor pressure of 100 torr was maintained with a H₂ flow of 50sccm through the (Me₃Si)₂Te bubbler and a flow of 300sccm through the Bi(NMe₂)₃ bubbler which provided a V/VI precursor ratio of 1.1. FILM 4 was grown at a substrate temperature of 125°C for one hour. A bubbler/reactor pressure of 100 torr was maintained with a H₂ flow of 45 sccm through the (Me₃Si)₂Te bubbler and a flow of 120 sccm through the Bi(NMe₂)₃ bubbler which provided a V/VI precursor ratio of 0.47. FILM 6 was grown at a substrate temperature of 125°C for 1.5 hours. A bubbler/reactor pressure of 20 torr was maintained with a H₂ flow of 10 sccm through the (Me₃Si)₂Te bubbler and a flow of 50 sccm through the Bi(NMe₂)₃ bubbler which provided a V/VI precursor ratio of 0.83. FILM 7 was grown at a substrate temperature of 125°C for one hour. A bubbler/reactor pressure of 20 torr was maintained with a H₂ flow of 15 sccm through the (Me₃Si)₂Te bubbler and a flow of 50 sccm through the Bi(NMe₂)₃ bubbler which provided a V/VI precursor ratio of 0.42.

Sb₂Bi_{2-x}Te Films

A 1:1 molar mixture of Bi(NMe₂)₃ with N(SiMe₃)₃ was prepared to assist in the mass transport of the compound as well as function as an internal standard for determining the ratio of Sb(NMe₂)₃/Bi(NMe₂)₃ inlet using the H¹NMR spectrum of the trapped exhaust gases. This mixture is a yellow liquid at room temperature and a blank study showed the composition of the vapor under normal flow conditions using hydrogen as a carrier gas to be 4.9:1 (N(SiMe₃)₃ : Bi(NMe₂)₃) from the H¹NMR of the trapped exhaust gases. FILM 8 was simultaneously grown on Si(111) and Kapton film on glass substrates at a susceptor temperature of 75°C for one hour. A flow rate of 38sccm H₂ was maintained through the N(SiMe₃)₃/Bi(NMe₂)₃ and Sb(NMe₂)₃ bubblers at 24°C with a H₂ flow of 56sccm through the (Me₃Si)₂Te bubbler. A pressure of 100 torr was maintained in the bubblers and the reactor during the deposition reaction.

Table 1 **Summary of V/VI Film Growth Experiments**

Film #	V/VI Material (Substrate)	Substrate Growth Temperature (Pressure)	Growth Rate (μ/hr)	V/VI Precursor Ratio	Resistivity (ohm-cm)	Carrier Concentration (10 ¹⁸ cm ⁻³)	Carrier Mobility (cm ² /V-sec)
1	Sb ₂ Te ₃ GaAs(100)	24°C (100 torr)	5.2	1.1	0.938	p-type 0.201	33.2
2	Bi ₂ Te ₃ GaAs(100)	50°C (100 torr)	5.0	1.1	-----	-----	-----
3	Sb ₂ Te ₃ GaAs(100)	75°C (100 torr)	3.1	1.1	0.00435	p-type 10.6	135
4	Bi ₂ Te ₃ GaAs(100)	125°C (100 torr)	4.8	0.47	0.000523	n-type -873	13.7
5	Sb ₂ Te ₃ GaAs(100)	150°C (100 torr)	0.5	1.1	0.0321	p-type 0.486	401
6	Bi ₂ Te ₃ Kapton	125°C (20 torr)	2.2	0.83	0.000560	n-type -450	25
7	Bi ₂ Te ₃ Kapton	125°C (20 torr)	3.6	0.42	0.000595	n-type -490	19
8	Sb _{1.8} Bi _{0.2} Te ₃ Kapton	75°C (100 torr)	5.0	0.43*	0.0044	p-type 21	70

* Sb(NMe₂)₃/Bi(NMe₂)₃ = 7.3

Results and Discussion

Substrate Effect

The first series of film growth experiments were conducted to examine the effect of the film deposition temperature and substrate structure on the quality of the film as measured by XRD. Thus films 1-5 were grown at different susceptor temperatures and simultaneously deposited on Si(111) and GaAs(100) substrates in each of the growth experiments. Examination of the x-ray diffraction data presented in figures 1 and 2 of the resulting films shows that the crystalline quality is dependent on the substrate and on the deposition temperature.

From a comparison of the respective XRD spectra in figures 1 and 2 it is evident that the Si(111) provides a better surface for oriented deposition of the polycrystalline films. Bi_2Te_3 and isomorphous Sb_2Te_3 crystallize with a rhombohedral lattice (space group $R\bar{3}m$) however, for convenience sake their structure is referred to using a hexagonal unit cell in this manuscript. Films of Sb_2Te_3 deposited at 75°C and 150°C and of Bi_2Te_3 deposited at 125°C on Si(111) substrates exhibited better preferred orientation of the crystallites compared to the corresponding deposition on a GaAs(100) substrate. From other growth experiments it was evident that orientation of crystallites on the GaAs(100) is no different than on other substrates including Si(100), amorphous materials such as

Pyrex glass or Kapton. This is likely an effect of the threefold symmetry of the Si(111) surface which provides a better spatial arrangement of surface atoms to match the rhombohedral lattice of the V/VI materials.

Growth Temperature Effect

Within the range of deposition temperature studied three types of Sb_2Te_3 films and two types of Bi_2Te_3 films were observed. A low temperature regime (25°C to 50°C) produced specular films of both compounds with very short range order in the crystalline structure, at intermediate growth temperatures (75°C to 125°C) polycrystalline films of both compounds were grown with the (015) plane parallel to the substrate surface, and at slightly higher temperature (150°C) Sb_2Te_3 films were grown with the (004) reflection planes parallel to the substrate surface.

The Sb_2Te_3 film grown at 25°C was uniform, featureless and highly reflective, whereas the bismuth telluride films deposited at this temperature exhibited poor structural integrity and adhesion to the substrates making them difficult to characterize. The Bi_2Te_3 films cracked and delaminated unless the substrate was heated to at least 50°C during the deposition reaction. Even then, the Bi_2Te_3 film was too delicate to make adequate electrical contacts for Hall measurements. The XRD data in figure 1 and 2 of films grown at

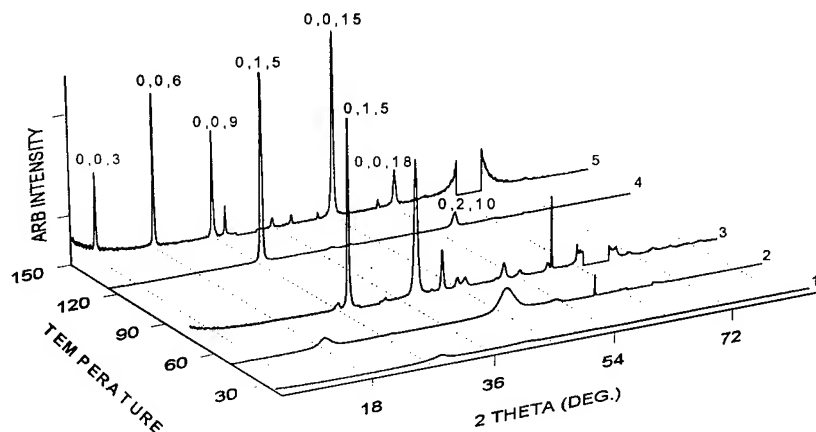


Figure 1 XRD data of Sb_2Te_3 and Bi_2Te_3 films on GaAs(100) substrates. 1. Sb_2Te_3 Film 1 deposited at 24°C, 2. Bi_2Te_3 Film 2 deposited at 50°C, 3. Sb_2Te_3 Film 3 deposited at 75°C, 4. Bi_2Te_3 Film 4 deposited at 125°C, 5. Sb_2Te_3 Film 5 deposited at 150°C.

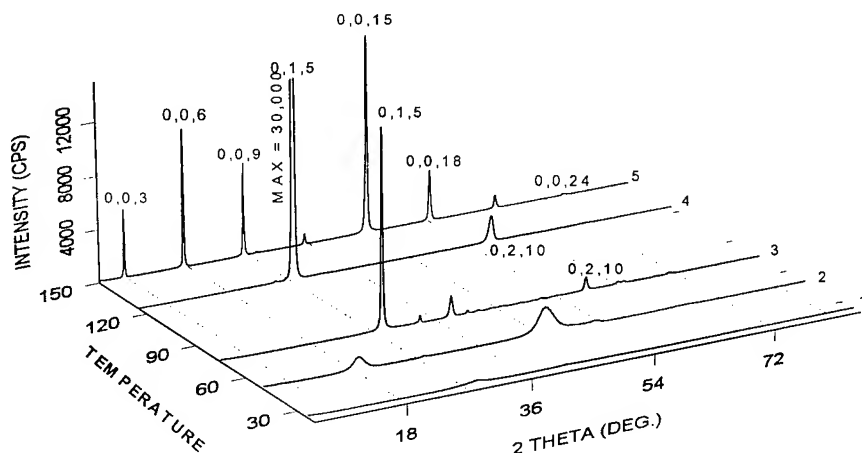


Figure 2 XRD data of Sb_2Te_3 and Bi_2Te_3 films on Si(111) substrates. 1. Sb_2Te_3 Film 1 deposited at 24°C, 2. Bi_2Te_3 Film 2 deposited at 50°C, 3. Sb_2Te_3 Film 3 deposited at 75°C, 4. Bi_2Te_3 Film 4 deposited at 125°C, 5. Sb_2Te_3 Film 5 deposited at 150°C.

low temperature indicates that the compounds either deposit in an amorphous form or with a very small crystallite size. Unlike the diffraction data for the 25°C Sb_2Te_3 film, broad diffuse reflections observed for the 50°C Bi_2Te_3 film are not at angles consistent with any long range order of the (0,1,5) reflection plane. It is possible this is a result of preferred crystallite growth in another orientation or formation of another BiTe phase.

Raising the growth temperature slightly is sufficient to produce highly oriented polycrystalline films where the (015) reflection plane is parallel to the substrate surface.

A susceptor growth temperature of 150°C was adequate to produce Sb_2Te_3 films with the c-axis perpendicular to the substrate plane, the same orientation observed in MBE grown films[1]. The deposition of Bi_2Te_3 films was limited to temperatures below 150°C due to the thermal stability of the $\text{Bi}(\text{NMe}_2)_3$ precursor. The onset of thermal pyrolysis for $\text{Bi}(\text{NMe}_2)_3$ was observed at 150°C.

In the growth experiments for Sb_2Te_3 films 1, 3, and 5, the precursor flow rates and V/VI inlet ratio were kept constant. The only variable was the substrate temperature. The data in table 1 clearly shows that as the substrate temperature was increased the film growth rate decreased. It should be noted that in all of the growth experiments the reaction was complete and film deposition occurred in all parts of the reactor at or above the susceptor stage. At higher susceptor temperature the growth rate of the film on the cooler reactor walls increased at the expense of film growth on the substrate. This indicates adsorption/desorption of precursors or reactive growth intermediates from the surface of the growing film is important. That such processes limit the film growth rate suggests surface elimination reactions produce the films under the low pressure conditions maintained in this study. At higher pressures, 1 atmosphere, evidence of gas phase nucleation reactions have been observed and the films produced had a sooty appearance. To date no intermediates in the reactions have been observed or isolated either in solution or the MOCVD reactions.

Film Composition, Hall Measurements and V/VI Precursor Ratio Effect

Films of Bi_2Te_3 were grown with V/VI precursor inlet ratio greater than and less than 0.66, the stoichiometric ratio, to examine the effect on the carrier concentration. Since the antistructure defects, and carrier concentration, of Bi_2Te_3 is reflective of the material composition [5], any significant dependence of the film stoichiometry on V/VI precursor inlet ratio should be evident in the hall data of the films. Films 6 and 7 were grown on glass substrates that had been covered with 14 μ Kapton tape.

The XRD data from the resulting films was similar to the data for film 4 deposited on GaAs(100) and there was no measurable difference in the XRD data for film 6 and 7. A comparison of the results in Table 1 for the Bi_2Te_3 films grown at 125°C/20torr under bismuth and tellurium rich flow conditions shows that the electrical properties of the two films do not vary significantly. The differences are within experimental error thus suggesting that the composition of the films is independent of the V/VI precursor ratio. AES data confirmed these results where the relative V/VI elemental composition of the films was found to be independent of the V/VI precursor inlet ratio used.

Growth of $\text{Sb}_x\text{Bi}_{2-x}\text{Te}$ Ternary Films

The growth of ternary films is possible using a mixture of the antimony and bismuth precursor compounds with an excess of the tellurium precursor compound. To demonstrate this a 5 μ thick film was deposited at a reactor pressure of 100torr and a susceptor temperature of 75°C on Si(111) and Kapton coated substrates simultaneously. The XRD data of the films in figure 3 shows that the film deposited on the Si(111) substrate was of poor crystalline ordering while the film deposited on the Kapton substrate was highly oriented polycrystalline material. EDX analysis of the films showed the composition to be $\text{Sb}_{1.8}\text{Bi}_{0.2}\text{Te}_{3.0}$ for the film on Kapton grown at the edge

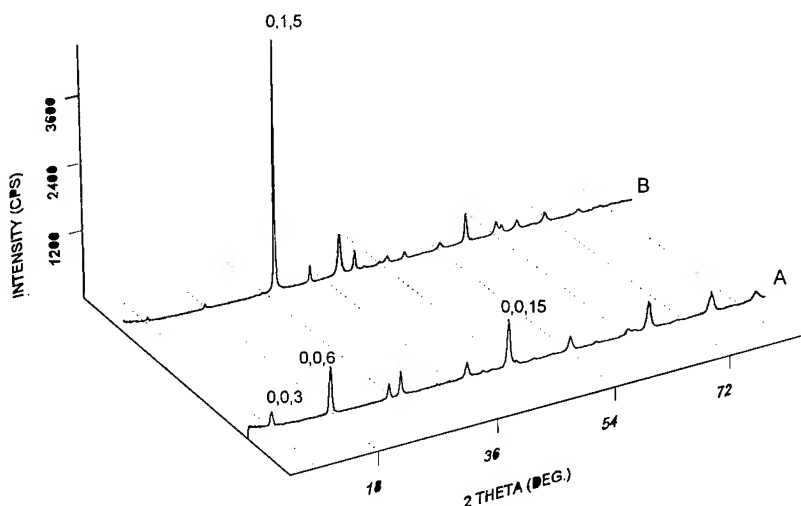


Figure 3 XRD data of $\text{Sb}_x\text{Bi}_{2-x}\text{Te}$ film deposited at 75°C, A. on Si(111) substrate B. on Kapton substrate.

of the susceptor and $\text{Sb}_{1.3}\text{Bi}_{0.9}\text{Te}_{2.9}$ for the film on Si(111) centered on the substrate stage. The difference in crystalline ordering of the film is a result of the position of the substrate on the susceptor stage during growth and their difference in composition, not the surface structure of the substrates. Growth of oriented polycrystalline Bi_2Te_3 rich material is expected to require a slightly higher substrate temperature therefore the crystallinity of the film at the center is poorer. The reason for the stoichiometric deviation across the

susceptor is not yet clear. One explanation is the vapor is depleted in bismuth precursor as it flows over the surface of the susceptor to the edge in the current reactor design due to the higher reaction rate for formation of bismuth telluride. A second possibility is that the tellurium precursor is the limiting reagent in the center of the stage in the current reactor design since the group V precursor mixture was inlet through the center coaxial inlet tube. Changes in the flow design are underway to improve the uniformity of the ternary films.

It is clear that differences in the relative reaction rates for formation of bismuth telluride and antimony telluride must be taken into account when designing a system to deposit the ternary films using these reactions. To illustrate the point, when film growth was attempted using the same precursor flow rates used for FILM 8 and a susceptor temperature of 125°C the film growth rate on the substrate dropped from 5 μ /hr to less than 2 μ /hr and the film composition was $\text{Sb}_{0.8}\text{Bi}_{1.5}\text{Te}_{2.7}$ by EDX. The film on the cooler reactor walls was likely antimony rich.

The SEM of the film edge shown in figure 4 is typical of the (0,1,5) oriented polycrystalline films. The films are fully dense with a columnar growth and the growth surface has a grainy texture. The substrate side of pieces, after removal of the substrate, is specular and featureless.

Conclusions

The $\text{Me}_3\text{SiNMe}_2$ elimination reaction provides a low temperature MOCVD method for producing highly oriented

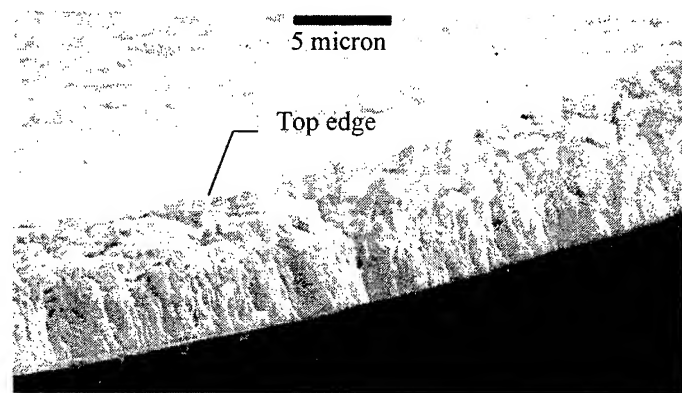


Figure 4 SEM of cleaved edge of $\text{Sb}_x\text{Bi}_{2-x}\text{Te}$ FILM 8 deposited at 75°C on Kapton with the substrate removed.

V/VI films. The Si(111) substrates provided the best growth surface although highly oriented films were deposited on all substrates. The film crystallinity and orientation were found to be temperature dependent. A lower temperature (015) preferred orientation of the crystallites changes over to a (000) orientation, a trend that was also observed in Bi_2Te_3 films deposited by MBE [1b]. The carrier concentration of the Sb_2Te_3 films is lower than values reported for other films

whereas the values for the Bi_2Te_3 films are rather high. The carrier concentration and composition of the Bi_2Te_3 films was found to be independent of the V/VI precursor ratio used reflecting the self-limiting nature of the reaction chemistry. Growth of the $\text{Sb}_{1.8}\text{Bi}_{0.2}\text{Te}_{3.0}$ film demonstrated the capability of the technique to produce ternary materials, but also illustrates the complications due to differences in the reaction kinetics that must be taken into account.

Acknowledgments

Financial support from the Office of Naval Research is gratefully acknowledged.

References

- [1] a) J. George, B. Pradeep, "Preparation and Properties of Co-Evaporated Bismuth Telluride [Bi_2Te_3] Thin Films", *Solid State Comm.*, vol. 56, pp 117-120 (1985). b) E. Charles, E. Groubert, A. Boyer, "Structural and Electrical Properties of Bismuth Telluride Films Grown by Molecular Beam Technique", *J. Material Sci. Lett.* vol. 7, pp 575-577 (1988). c) A. Mzerd, D. Sayah, J. C. Tedenac, and A. Boyer, "Effect of Substrate Temperature on Crystal Growth of Bi_2Te_3 on Single Crystal Sb_2Te_3 ", *J. Materials Sci. Lett.*, vol. 13, pp 301-304 (1994). d) A. Mzerd, D. Sayah, J. C. Tedenac, and A. Boyer, "Optimal Crystal Growth Conditions of Thin Films of Bi_2Te_3 Semiconductors" *J. Crystal Growth*, vol. 140, pp 365-369 (1994).
- [2] a) N.G. Patel, P.G. Patel, "Electrical properties of polycrystalline Sb_2Te_3 films", *J. Material Sci.*, vol. 26, pp 2543-2546 (1991). b) N.G. Patel, P.G. Patel, "Thermoelectric Power of Polycrystalline Sb_2Te_3 Films", *Cryst. Res. Technol.*, vol 28, pp 407-413 (1993).
- [3] J.C. Farmer, T.W. Barbee, Jr., G.C. Chapline, Jr., R.J. Foreman, L. J. Summers, M.S. Dresselhaus, L.D. Hicks in B. Mathiprakasham, Patrick Heenan, "Sputter Deposition of Multilayer Thermoelectric Films: An Approach to the Fabrication of Two-Dimensional Quantum Wells", *AIP Conference Proceedings 316, Thirteenth International Conference on Thermoelectrics*, p. 217 (AIP Press 1994).
- [4] P. Magri, C. Boulanger, J.M. Lecuire, "Electrodeposition of Bi_2Te_3 Films", *AIP Conference Proceedings 316, Thirteenth International Conference on Thermoelectrics*, p. 277 (AIP Press 1994).
- [5] D.M. Rowe, *CRC Handbook of Thermoelectrics*, (CRC Press, Inc., 1995)
- [6] Thomas J. Groshens, Robert W. Gedridge, Jr., and Charlotte K. Lowe-Ma, "Room-Temperature MOCVD of Sb_2Te_3 Films and Solution Precipitation of M_2Te_3 (M=Sb, Bi) Powders via A Novel (N,N-Dimethylamino)-trimethylsilane Elimination Reaction", *Chemistry of Materials*, vol. 6, 727-729 (1994).

Thermoelectric Properties of rf-Sputtered CoSb₃ Films

H. Anno, K. Matsubara, ¹Y. Notohara, ²T. Sakakibara, ³K. Kishimoto, and ³T. Koyanagi
Science University of Tokyo in Yamaguchi, ¹Kyushu Matsushita Electric Co. Ltd.,
²Aisin Cosmos R&D Co. Ltd., ³Yamaguchi University, Japan

Abstract

Film growth and electronic transport properties of CoSb₃ with the cubic skutterudite structure were studied. The skutterudite CoSb₃ films were successfully grown on Si (100) and quartz substrates by using a magnetron rf-sputtering. A preferential orientation growth along (310) plane occurs when the pressure of sputtering gas decreases. Polycrystalline films with the skutterudite structure are also obtained by annealing sputtered films at low temperature. Electrical conductivity of the films changes with the film growth conditions. Electronic structure of the films was investigated by X-ray photoelectron spectroscopy. Observed valence band structure agrees well with a recent band calculation. It is revealed that the valence band structure of CoSb₃ consists of the hybridized bands between Co *d* and Sb *p* states and a peak structure derived from localized Co *d* state.

Introduction

CoSb₃, which is a member of a large family of skutterudite compounds, has recently been identified as a candidate for advanced thermoelectric materials [1-7]. Non-doped CoSb₃ has a *p*-type conduction and extraordinarily high hole mobility, up to 3000 cm²/V·s at room temperature, compared with those of state-of-the-art semiconductors such as Si, Ge, and GaAs [2, 4, 5]. Also, the thermal conductivity of CoSb₃ is relatively low because of its large unit cell. The high potential, especially high hole mobility, of CoSb₃ is available for the application to new electronic devices using thin films and quantum-well superlattice structures as well as thermoelectric devices. It is also of interest that theoretical calculations predict the possibility of using quantum-well superlattice structures to enhance markedly the performance of thermoelectric devices [8-10]. However, no study on the epitaxial growth of CoSb₃ films has been reported in the literatures. Very little is known about the electronic transport properties and the electronic structure of this material. In this paper, we report some results of study on the film growth of the skutterudite CoSb₃ on Si (100) substrate and discuss the electronic transport properties and the electronic structure of CoSb₃ films.

Experiment

Film growth of CoSb₃ was made by a magnetron rf-sputtering in argon gas at pressures from 10⁻³ to 10⁻¹ Torr at an rf power *P*_{RF} of 50 W. Powdered CoSb₃ prepared by hot-pressing of reacted powders (HP) was used as a target [11]. Polished Si (100) and quartz substrates were used. The Si (100) substrates were sputter etched under an argon gas pressure of 8 × 10⁻² Torr at an rf power *P*_{RF} of 100 W prior to the deposition. Substrate temperature *T*_s was kept at room temperature during

the deposition. Some obtained films were annealed at 200 °C for 5 hours or 630 °C for 2 hours under flowing argon.

The crystal structure of obtained films was checked by means of X-ray (Cu Kα) diffraction. Composition of the films was determined by electron probe microanalysis (EPMA). The composition of films was found to be close to 1:3 (Co:Sb) with a slight shift towards Sb-poor side. Observation of the film surface was made by using a scanning electron microscope (SEM). Surface morphology of both films on Si (100) and quartz substrates was smooth and dense. Electrical conductivity of the films was measured by the van der Pauw technique. Electronic structure of the films was investigated by X-ray (Mg Kα) photoelectron spectroscopy. Sample surfaces were argon ion sputtered to remove surface contamination of carbon and oxygen.

Results and discussion

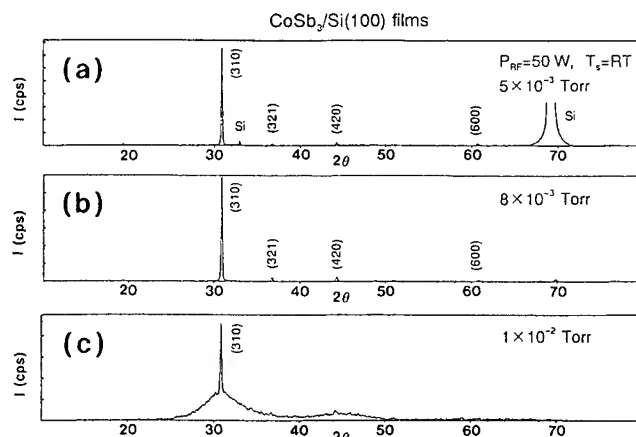


Fig.1 X-ray diffraction patterns of CoSb₃ films on Si (100) substrate sputtered under different argon gas pressures of (a) 5 × 10⁻³ Torr, (b) 8 × 10⁻³ Torr, and (c) 1 × 10⁻² Torr.

Figures 1 (a), (b), and (c) show the X-ray diffraction patterns of CoSb₃ films on Si (100) substrate sputtered under different argon gas pressures of 5 × 10⁻³, 8 × 10⁻³, and 1 × 10⁻² Torr, respectively. Observed diffraction peaks were assigned to the diffractions from the skutterudite phase, and no diffraction peak from other phases was observed. However, diffraction patterns for films sputtered at argon gas pressures of more than ~1 × 10⁻² Torr were so broad that observed peaks could not be assigned. A diffraction peak from (310) plane appeared for the film sputtered at an argon gas pressure of 1 × 10⁻² Torr. Intensity of the diffraction peak from (310) plane became larger than that of other peaks with decreasing argon gas pressure. The preferential orientation growth along (310)

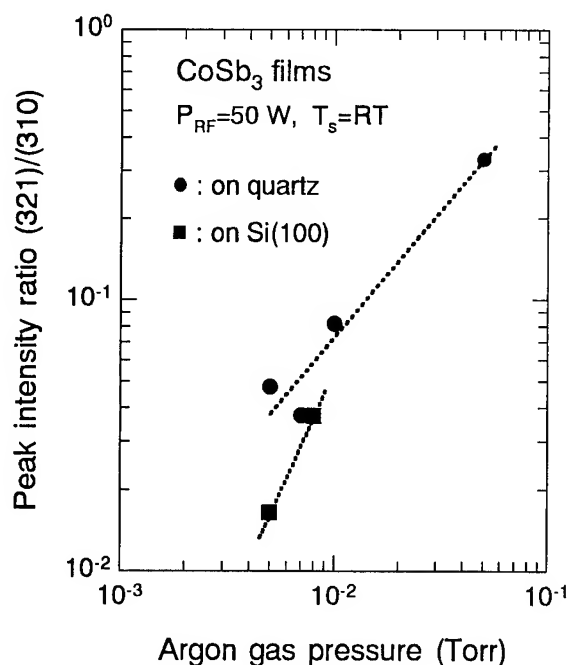


Fig.2 Intensity ratio of diffraction peaks from (321) and (310) planes as a function of argon gas pressure for CoSb₃ films on Si (100) and quartz substrates.

plane was found to occur at low argon gas pressure. Similar tendency was observed for the sputtered films on quartz substrate.

The intensity ratio of diffraction peaks from the (321) and the (310) planes is plotted as a function of argon gas pressure in figure 2. The intensity ratio for CoSb₃ powders was about 0.4. Decrease in the intensity ratio of diffraction peaks with decreasing argon gas pressure is clearly observed for both the films on Si and quartz substrates. It was found that the films on Si (100) substrate were strongly oriented along (310) plane in comparison with the films on quartz substrate.

Figure 3 shows the lattice constant of CoSb₃ films on Si (100) and quartz substrates as a function of argon gas pressure. The lattice constant was calculated from the diffraction angle of (310) peak. The lattice constant of the films on Si (100) substrate was found to be about 9.16 Å, which hardly depended on the argon gas pressure. This value is much larger than the reported value, 9.04 Å, of bulk samples [6]. On the other hand, the lattice constant of the films on quartz substrate changed widely with the argon gas pressure.

Figures 4 (a), (b), and (c) show the X-ray diffraction patterns of CoSb₃ films on Si (100) substrate before annealing, after annealing at 200 °C, and after annealing at 630 °C, respectively. Films sputtered at argon gas pressures of more than $\sim 1 \times 10^{-2}$ Torr showed very broad diffraction patterns as shown in figs. 4 (a). The films annealed at low temperature were found to have the skutterudite structure. The annealed films were considered to be polycrystalline judging from the X-ray diffraction patterns. This result reflects the fact that very short times and low temperatures are suitable for

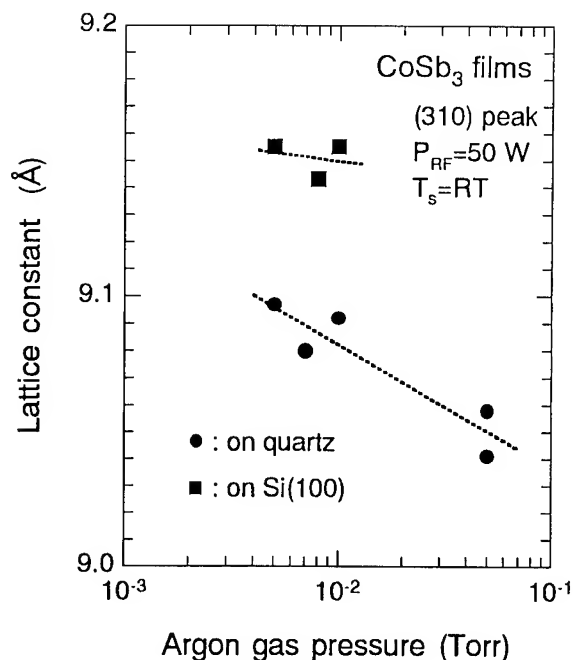


Fig.3 Lattice constant of CoSb₃ films on Si (100) and quartz substrates as a function of argon gas pressure.

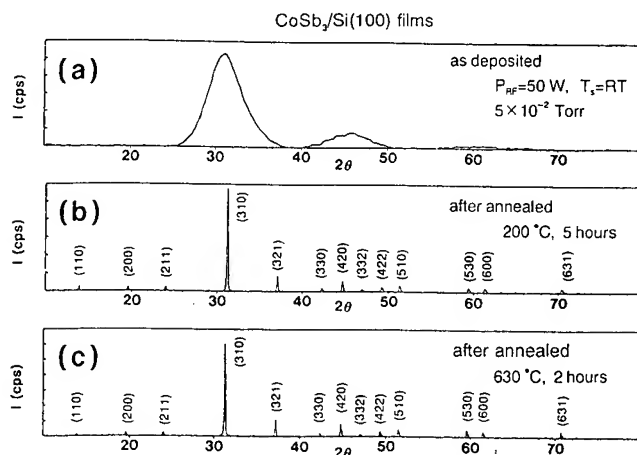


Fig.4 X-ray diffraction patterns of CoSb₃ films on Si (100) substrate (a) before annealing, (b) after annealing at 200 °C for 5 hours, and (c) after annealing at 630 °C for 2 hours.

preparing fully reacted skutterudite compounds by solid phase reaction [11, 12].

Figures 5 (a) and (b) show the core level photoemission spectra of a (310)-oriented CoSb₃ film on Si (100) substrate sputtered at an argon gas pressure of 5×10^{-3} Torr. Those of a HPed sample are also shown in the figs. 5 as a reference. Peaks of Co 2p_{1/2}, Co 2p_{3/2}, Sb 3p_{1/2}, Sb 3p_{3/2}, Sb 3d_{3/2}, and Sb 3d_{5/2} core levels were clearly observed in the spectra for both the film on Si (100) substrate and the HPed sample. Agreement in the peak energies of core levels between the film and the HPed sample is satisfactorily good. The peak energies of core levels for both the film and the HPed sample slightly

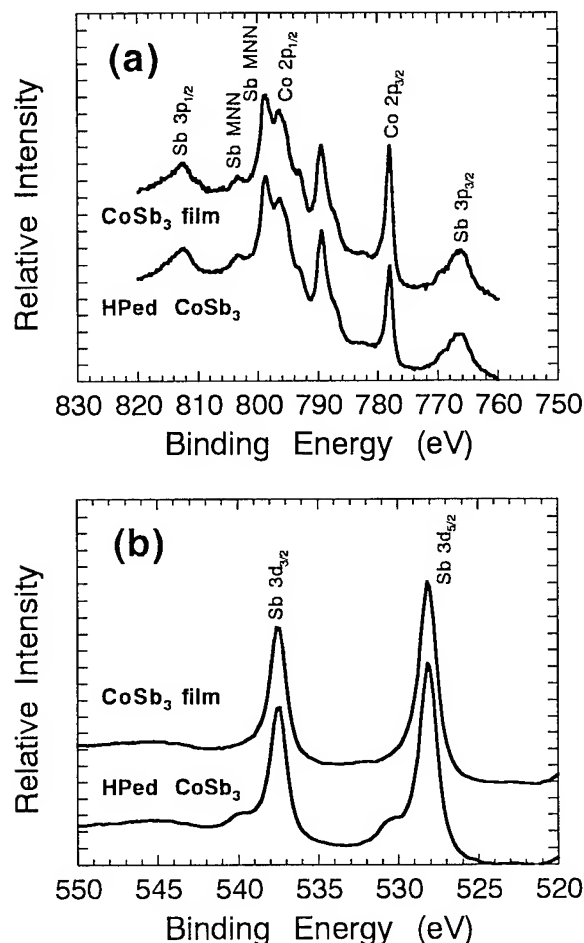


Fig.5 Core level photoemission spectra of a (310)-oriented CoSb_3 film on Si (100) substrate sputtered at 5×10^{-3} Torr and those of a HPed sample as a reference.

shift to lower binding energy relative to those for Co and Sb pure metals. Formation of predominant covalent bonds in the skutterudite structure results in the chemical shifts of core levels because of the difference in the electronegativity between Co and Sb.

Figure 6 shows the valence band photoemission spectra of as-deposited and annealed CoSb_3 films on Si (100) substrate and that of a HPed sample as a reference. Binding energy for valence band photoemission spectra was defined with respect to the valence band maximum obtained through a linear extrapolation of the leading valence band edge. The similarity of the spectra is quite good between the films and the HPed sample. This also supports that the films have the skutterudite structure in correspondence with X-ray diffraction results. The observed valence band spectra of the films and the HPed sample consist of mainly three regions of a peak at about 2 eV, a shoulder around 5 eV, and a broad peak around 10 eV.

The detailed interpretation of the observed spectra requires a theoretical calculation of the electronic structure of CoSb_3 . A calculation on skutterudite antimonides has been performed by

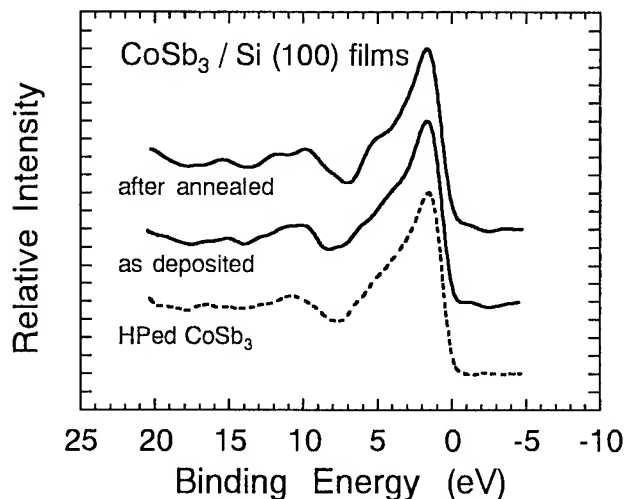


Fig.6 Valence band photoemission spectra of as-deposited and annealed CoSb_3 films on Si (100) substrate and that of a HPed sample as a reference.

Singh and Pickett [13] with an extended general-potential linearized augmented-plane-wave (LAPW) method. The calculated densities of states (DOS) of the Co-based materials are qualitatively similar. According to the calculation, both the valence and conduction band are derived from hybridized combinations of transition-metal d and pnictide p states: the p -derived component of the DOS is remarkably flat and symmetrical about the gap, while the d -derived component is peaked below the gap. The calculation quantitatively explains well the electronic transport properties of IrSb_3 and CoSb_3 , but no comparison of the calculated DOS with the experiment has been reported in the literature [4, 13].

The overall structures of observed spectra for both the films and the HPed sample were found to agree well with the calculated valence band DOS. It is, therefore, considered that the electronic structure of valence band for CoSb_3 is derived from the hybridization between Co d and Sb p states and that the observed peak at ~ 2 eV is mainly derived from the localized Co d state. Also, it is deduced from the comparison of the experiment with the calculation that the top of valence band has a p -like character [13]. This result suggests that the electronic structure of CoSb_3 belongs to a category of the charge transfer semiconductor, of which holes are light (p valence band) and electrons are heavy (d bands) [14]. This is consistent with the fact that the hole mobility is higher than the electron mobility for CoSb_3 because of the large difference in the effective mass between the electrons $m_e^* \sim 1.5m_0$ and holes $m_h^* \sim 0.1m_0$, where m_0 is the free electron mass [2].

Figure 7 shows the electrical conductivity of as-deposited and annealed CoSb_3 films on Si (100) substrate as a function of inverse temperature. The conductivity value of the Si (100) substrate was so small that one could neglect an influence of the substrate on the electrical conductivity measurements. Conductivity value for the as-deposited film increases with increasing temperature, and reaches ~ 40 S/cm at room temperature. On the other hand, conductivity value for the

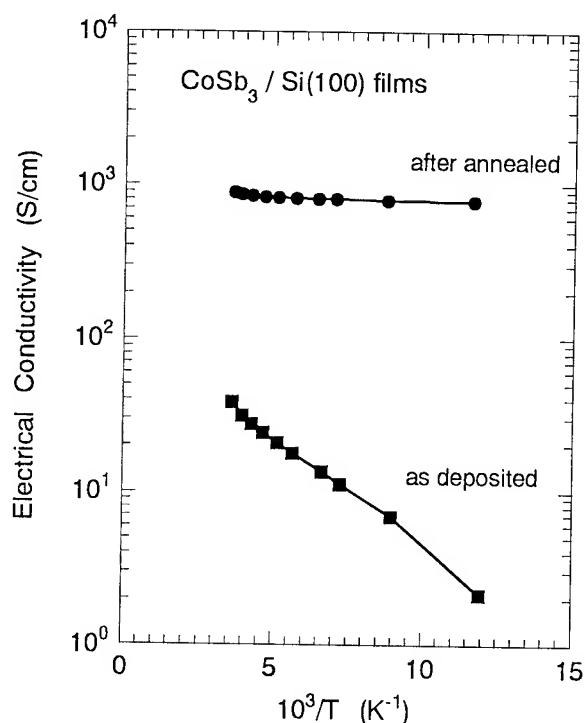


Fig.7 Electrical conductivity of as-deposited and annealed CoSb_3 films on Si (100) substrate as a function of inverse temperature.

annealed film shows a lack of temperature dependence, indicating that the annealed film behaves as a degenerated semiconductor. The annealed film has higher conductivity values, ~ 800 S/cm, than the as-deposited film. Contamination of impurity and crystallographic quality of the films significantly affect the electronic transport properties [3, 11, 15]. It is considered that the difference in the electrical conductivity between the as-deposited and the annealed films is mainly caused by the difference in the crystallographic quality of the films, for example defects and deviation from the stoichiometry.

Conclusion

Film growth and electronic transport properties of the skutterudite CoSb_3 were investigated. CoSb_3 films with the skutterudite structure were successfully grown on Si (100) and quartz substrates by using a magnetron rf-sputtering. The preferential growth direction changed with sputtering conditions and the (310)-oriented films were grown at low argon gas pressures. Polycrystalline films with the skutterudite structure were also obtained by annealing sputtered films at low temperature. The sputtered films were found to have semiconducting properties, which changed with the film growth conditions. Electronic structure of the CoSb_3 films was investigated by X-ray photoelectron spectroscopy. Observed valence band structure agreed well with a recent band calculation. It was experimentally revealed that the valence band structure of CoSb_3 mainly consisted of the hybridized bands between Co d and Sb p states and a peak structure derived from localized Co d state.

Acknowledgment

This work is supported in part by Yamaguchi prefectural government.

References

- [1] J.-P.Fleurial, T.Caillat, and A.Borshchevsky, "Skutterudites: a New Class of Promising Thermoelectric Materials", *Proc. XIII Int. Conf. on Thermoelectrics*, AIP Press, New York, Kansas (USA), pp.40-44 (1995).
- [2] T.Caillat, A.Borshchevsky, and J.-P.Fleurial, "Preparation and Thermoelectric Properties of p - and n -type CoSb_3 ", *Proc. XIII Int. Conf. on Thermoelectrics*, AIP Press, New York, Kansas (USA), pp.58-61 (1995).
- [3] K.Matsubara, T.Iyanaga, T.Tsubouchi, K.Kishimoto, and T.Koyanagi, "Thermoelectric Properties of (Pd, Co) Sb_3 Compounds with Skutterudite Structure", *Proc. XIII Int. Conf. on Thermoelectrics*, AIP Press, New York, Kansas (USA), pp.226-229 (1995).
- [4] D.T.Morelli, T.Caillat, J.-P.Fleurial, A.Borshchevsky, J.Vandersande, B.Chen, and C.Uher, "Low-Temperature Transport Properties of p -type CoSb_3 ", *Phys. Rev. B*, Vol. 51, No. 15, pp.9622-9628 (1995).
- [5] T.Caillat, J.-P.Fleurial, and A.Borshchevsky, "Bridgman-Solution Crystal Growth and Characterization of the Skutterudite Compounds CoSb_3 and RhSb_3 ", to be published in *J. Crystal Growth* (1995).
- [6] D.Mandrus, A.Migliori, T.W.Darling, M.F.Hundley, E.J.Peterson, and J.D.Thompson, "Electronic Transport in Lightly Doped CoSb_3 ", *Phys. Rev. B*, Vol. 52, No. 7, pp.4926-4931 (1995).
- [7] J.W.Sharp, E.C.Jones, R.K.Williams, P.M.Martin, and B.C.Sales, "Thermoelectric Properties of CoSb_3 and Related Alloys", *J. Appl. Phys.*, Vol. 78, No. 2, pp.1013-1018 (1995).
- [8] C.B.Vining, "The Thermoelectric Limit $ZT \sim 1$: Factor or Artifact", *Proc. XI Int. Conf. on Thermoelectrics*, K.R.Rao, Ed., Univ. Texas, Arlington (USA), pp.223-231 (1992).
- [9] L.D.Hicks and M.S.Dresselhaus, "Effect of Quantum-Well Structures on the Thermoelectric Figure of Merit", *Phys. Rev. B*, Vol. 47, No. 19, pp.12727-12731 (1993).
- [10] L.D.Hicks and M.S.Dresselhaus, "Thermoelectric Figure of Merit of a One-Dimensional Conductor", *Phys. Rev. B*, Vol. 47, No. 24, pp.16631-16634 (1993).
- [11] K.Matsubara, T.Sakakibara, Y.Notohara, H.Anno, H.Shimizu, and T.Koyanagi, "Electronic Transport Properties of CoSb_3 and Mixed Alloys", *Proc. XV Int. Conf. on Thermoelectrics*, (in this conference) Pasadena (USA), (1996).
- [12] A.Borshchevsky, J.-P.Fleurial, E.Allevato, and T.Caillat, " CoSb_3 - IrSb_3 Solid Solutions: Preparation and Characterization", *Proc. XIII Int. Conf. on Thermoelectrics*, AIP Press, New York, Kansas (USA), pp.3-6 (1995).
- [13] D.J.Singh and W.-E.Pickett, "Skutterudite Antimonides: Quasilinear Bands and Unusual Transport", *Phys. Rev. B*, Vol. 50, No. 15, pp. 11235-11238 (1994).

- [14] J.Zaanen, G.A.Sawatzky, and J.W.Allen, "Band Gaps and Electronic Structure of Transition-Metal Compounds", *Phys. Rev. Lett.* Vol. 55, No. 4, pp. 418-421 (1985).
- [15] T.Koyanagi, T.Tsubouchi, M.Ohtani, K.Kishimoto, H.Anno, and K.Matsubara, "Thermoelectric Properties of $\text{Co}(\text{M}_x\text{Sb}_{1-x})_3$ (M=Ge, Sn, Pb) Compounds", *Proc. XV Int. Conf. on Thermoelectrics*, (in this conference) Pasadena (USA), (1996).

Radiation Defects Induced by Ion Implantation as a Promising Method of Doping Semiconductor Type A^{IV}B^{IV} Films

Z.M. Dashevsky

Ben-Gurion University of the Negev, Materials Engineering Dept.,

POB 653, Beer-Sheva 84105, Israel

Tel: 972-7-472573. Fax: 972-7-472946

Abstract

Radiation defects in PbTe single crystals and epitaxial films induced by ion implantation of various impurities amounting to as much as $2 \cdot 10^4 \mu\text{C}/\text{cm}^2$ have been investigated. It has been found that the formation of point defects (for the most part, Te vacancies) running as deep as 3 μm and more determine transport properties due to the stabilization of electron concentration at a level of $2 \cdot 4 \cdot 10^{18} \text{ cm}^{-3}$. The data are interpreted based on the model of the quasi-local (doublet) energy level of Te vacancies in the PbTe conduction band. The formation of solid solutions accompanied by the increase of band gap was detected in PbTe thin layers implanted with Zn.

I. Introduction

Advances in the method of ion implantation of impurities into solids have intensified the study of properties of ion-implanted layers of semiconductors [1, 2]. To reveal the uncombined effect of ion implantation, the so-called radiation-induced defects should be subsequently removed. In practice, this is done by protective annealing of the semiconductor at elevated temperatures in a clean and oxygen-free atmosphere.

However, the radiation defects require special study. The depth of their penetration into the host crystal is higher than that of implanted ions. Of special interest is the study of intrinsic defects of A^{IV}B^{VI} semiconductors. Huge values of the static dielectric constant ($\epsilon \sim 10^3$) and small effective mass ($m \sim 10^{-2}m_0$) results in the absence of shallow impurity states (levels) in the A^{IV}B^{IV} semiconductor energy spectrum. The intrinsic defects (metal and chalcogen defects and interstitial atoms) of crystal lattice result in short-range potential form impurity levels of energy bands [3-5].

In contrast with the situation typical of wide-band semiconductors with impurity levels localized inside the energy gap, the A^{IV}B^{IV} intrinsic levels are of resonance or quasi-local nature. That is why the freezing-in of charge carriers at impurity levels had not been observed even at extremely low temperatures.

From the viewpoint of radiation defects study, thin films are preferable over bulk crystals. In some instances, their small thickness enables transport effects and optical properties of ion-implanted samples to be interpreted within the framework of the homogeneous layer model.

II. Experimental Details and Discussion

p-PbTe single crystals and epitaxial films were investigated. The crystals were produced by the Czochralsky and gas phase-growth method. The stoichiometric composition PbTe films were grown by the "hot wall" method in a vacuum chamber at a residual pressure of 10^{-9} Torr on BaF₂, KBr, and mica substrates, the thickness of films varying from 0.3 to 5 μm . X-ray diffraction and electron microscopy studies revealed the block-monocrystal structure of PbTe films with block sizes in the range of 5 to 10 μm and an angular misalignment of less than 1° in the plane parallel to the substrate surface. The size of blocks is virtually independent of the film thickness in the range of 0.1 to 5 μm . The grown films had a minimum carrier concentration of $\sim 5 \cdot 10^{17} \text{ cm}^{-3}$. Within the temperature range of 77 to 300 K, the temperature dependence of the thick film carrier mobility μ obeys the $T^{3/2}$ law typical for bulk monocrystals.

The Zn⁺, Ar⁺, and O⁺ ions were implanted with the use of a special apparatus. Parameters specifying the implantation conditions are given in Table 1, where d is the film thickness, I is the implantation dose, j is the current density, and E is the ion energy.

The implantation doses differed substantially from those given in literature for similar experiments (according to [2], typically $I < 10 \mu\text{C}/\text{cm}^2$). This generally results in the independence of characteristics of films being implanted from the implantation dose and initial characteristics of the films (see, e.g., Ar⁺, curves 7-10 in Fig. 1).

In the case of films implanted with Zn⁺ (Fig. 2), the average concentration of electrons increases with I and, dose by dose, is somewhat lower for samples belonging to the *p*-type of conductivity prior to the implantation (curves 4-6 in Fig. 2). For all PbTe <Zn> films, the absolute value of the Seebeck coefficient S decreases with the increase of I , while the electric conductivity σ increases. The temperature dependencies $S(T)$, $\sigma(T)$, $\mu(T)$, and $Q(T)$ (the coefficient of transverse Nernst - Ettingshausen effect) for films implanted with zinc and argon are free from any peculiarities and coincide with those of PbTe crystals having the same concentration of electrons. The sole exception is sample 7 of Table 1 (Ar⁺, the minimum dose $I = 10 \mu\text{C}/\text{cm}^2$), for which S and the Hall coefficient R have opposite signs, while the temperature dependence $S(T)$ is indicative of the presence of film layers having different types of conductivity.

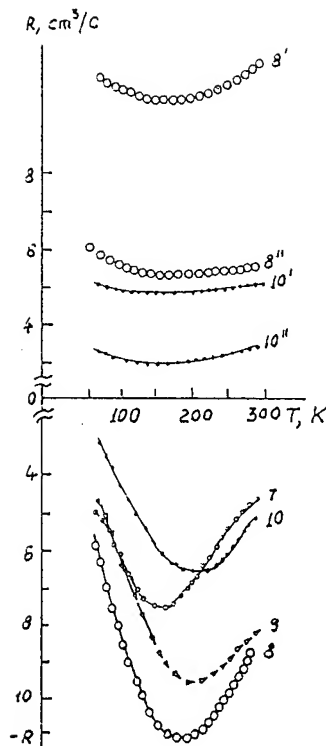


Fig. 1. PbTe film Hall coefficient vs. temperature: 8'-10' - before ion implantation; 7-10 - after ion implantation of argon; 8''-10'' - after annealing at 420°C. The numbers of curves correspond to those of samples (Table 1).

Calculations for PbTe films show that at $E = 150$ keV the maximum of impurities density distribution is located at a depth of about $0.08 \mu\text{m}$. Therefore, temperature dependencies of kinetic coefficients for $0.1 - 0.5 \mu\text{m}$ thick films should reveal features typical for layered inhomogeneous semiconductor structures. Their absence is attributable only to the fact that the properties of ion-implanted films are exclusively determined by the radiation defects. Thus, the implantation with argon results in the same changes of film properties, as that with zinc.

Taking into consideration that the ion-implanted films of different thickness have quite similar transport properties, it may be inferred that the concentration of radiation defects is sufficiently high over the whole film thickness.

This penetration depth can be explained in terms of the mechanism of radiation-induced diffusion of defects into the film. Note that the exposure time of the maximum dose is of the order of hours. The film surface temperature measured by an infra-red detector in the course of ion implantation did not exceed 200°C .

The implantation dose (and, accordingly, the exposure time) was varied from 150 to $2 \cdot 10^4 \mu\text{C}/\text{cm}^2$ for samples of different thickness in order to attain the same properties of ion-implanted films. The n -type of conductivity of ion-implanted samples is attributable to crystal lattice defects, probably, tellurium vacancies formed across the whole film thickness (the mass of Te atom is small as compared to that of Pb atom).

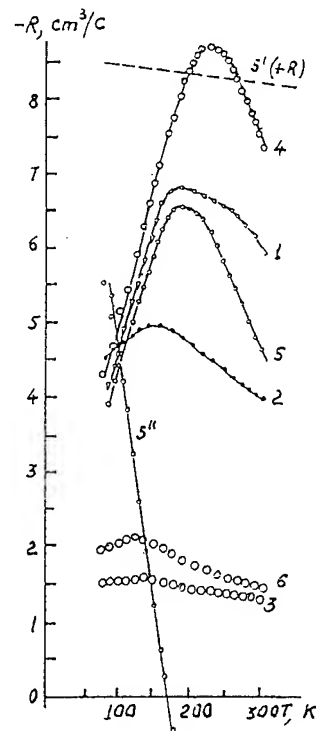


Fig. 2. PbTe film Hall coefficient vs. temperature (implantation with zinc). Pre-implantation conductivity: 1-3 - n -type, 4-6 - p -type. For curve 5' (sample 5 prior to implantation), positive values of R are plotted arbitrarily along the ordinate axis. 5'' - curve for sample 5 after annealing at 350°C .

In the simplest case, we may suggest that the Te vacancy diffuses depthwise from the surface. If the concentration N_0 of Te vacancies is held constant throughout the whole diffusion process, then the resulting profile takes the form

$$N(x, t) = N_0 \operatorname{erfc}(x / \sqrt{4D}) \quad (1)$$

where erfc is the complementary error function, D is the diffusion coefficient of Te vacancies, x is the penetration depth of Te vacancies, and t is the exposure time. Assuming that each ion being implanted produces one Te vacancy over its path length, we get the volume concentration N_0 of Te vacancies in the surface layer ($d \sim 0.1 \mu\text{m}$) of $1.2 \cdot 10^{22} \text{ cm}^{-3}$ (the maximum dose value $I = 2 \cdot 10^4 \mu\text{C}/\text{cm}^2$).

As a first approximation, we get that after the ion implantation, at the depth x equal to the film thickness ($d = 3 \mu\text{m}$) the value of N is of the same order of magnitude as the electron concentration, $\sim 3 \cdot 10^{18} \text{ cm}^{-3}$.

The calculated profile of depth distribution of Te vacancies is shown in Fig. 3. However, in this case the number of Te vacancies should be much higher than that really produced by ion implantation. Supposedly, the preferable diffusion mechanism is that acting between adjacent layers: the upper layer provides vacancies for the lower one. The profile of such a diffusion is also shown in Fig. 3.

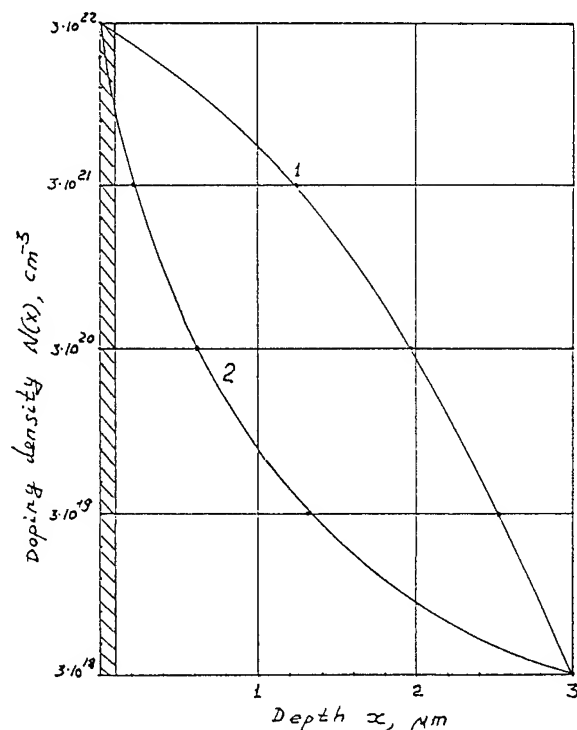


Fig. 3. Calculated diffusion profile of Te vacancies in PbTe. 1 - diffusion from a constant surface source; 2 - diffusion between adjacent layers. Total amount of diffusing vacancies is represented by shadowed area.

The nonmonotonous character of $R(T)$ dependence of ion-implanted films (Figs. 1 and 2) can be explained based on the assumption that the radiation defects under consideration form a quasi-local level, which is above the conduction band bottom at low temperatures. The position of this level E_l relative to the bottom of conduction band at $T = 0$ K and the rate of its displacement towards the forbidden band with the increase of temperature were calculated (see Table 2).

In contrast with properties of films implanted with zinc or argon, those of films implanted with oxygen undergo minor changes, the type of conductivity generally remaining the same. This behavior is attributable to a relatively low level of generation of radiation defects induced by the ion implantation due to the small mass of oxygen.

Also, a detail study of the optical absorption coefficient $\alpha(h\nu)$ was performed for films implanted with zinc and grown on the KBr substrate. Several (up to eight) samples of various thickness were used to study the $\alpha(h\nu)$ spectrum for each fixed value of implanted dose. The results were averaged using mathematical statistics methods. The optical

properties of films were compared with those of specially manufactured thin monocrystals.

Table 1

Sample No.	$d, \mu\text{m}$	Ion type	$I, \mu\text{C}/\text{cm}^2$	$j, \mu\text{A}/\text{cm}^2$	E, keV
1	0.5	Zn ⁺	50	0.2	150
2	0.4	Zn ⁺	150	0.2	150
3	0.5	Zn ⁺	300	0.2	150
4	0.3	Zn ⁺	100	0.2	150
5	0.3	Zn ⁺	200	0.2	150
6	0.4	Zn ⁺	300	0.2	150
7	0.5	Ar ⁺	10	0.5	90
8	0.4	Ar ⁺	100	0.5	90
9	0.5	Ar ⁺	300	0.5	90
10	0.4	Ar ⁺	900	0.5	90
11	0.5	O ⁺	500	0.3	150

Table 2

Initial film	Ion type	Position of level E_l at 0 K, meV (relative to the bottom of E_c)	Migration rate, $10(dE_l/dT)$, meV/K
n-PbTe	Zn ⁺	48 ± 5	$-(1.6 \pm 0.4)$
p-PbTe	Zn ⁺	47 ± 3	$-(1.9 \pm 0.5)$
p-PbTe	Ar ⁺	40 ± 2	$-(2.5 \pm 0.3)$

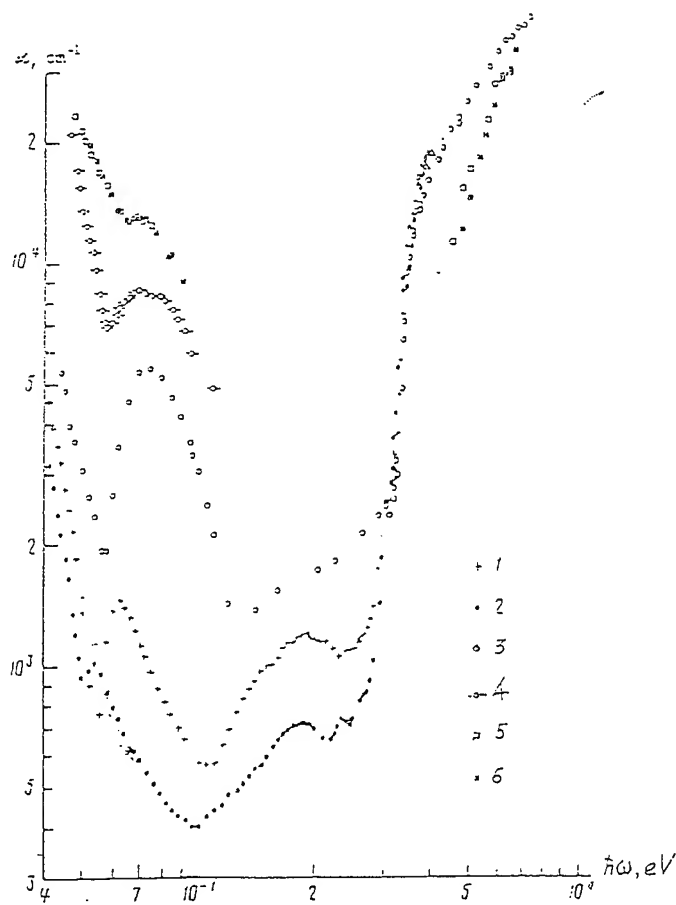


Fig. 4. Spectral dependencies of the ion-implanted PbTe absorption coefficient at 300 K: 1-2 - single crystals (foils), 3-6 - films. Impurities: 1, 3-6 - Zn; 2 - Ar; 1-300 - 100, 4 - $1.5 \cdot 10^3$, 6 - $2 \cdot 10^4 \mu\text{C}/\text{cm}^2$.

Some of the experimental results obtained are shown in Figs. 4 and 5. Fig. 4 demonstrates the similarity of $\alpha(h\omega)$ dependencies for films and single crystals. At energies of 0.1 - 0.3 eV, characteristic bands α_2 and α_3 are revealed in the central part of experimental curves, the location of these bands being independent of the kind of ions being implanted (Zn^+ or Ar^+). These bands are associated with intrinsic defects of the crystal lattice, probably, with Te vacancies V_{Te} , forming the doublet level E_2 and E_3 in the conduction band [6].

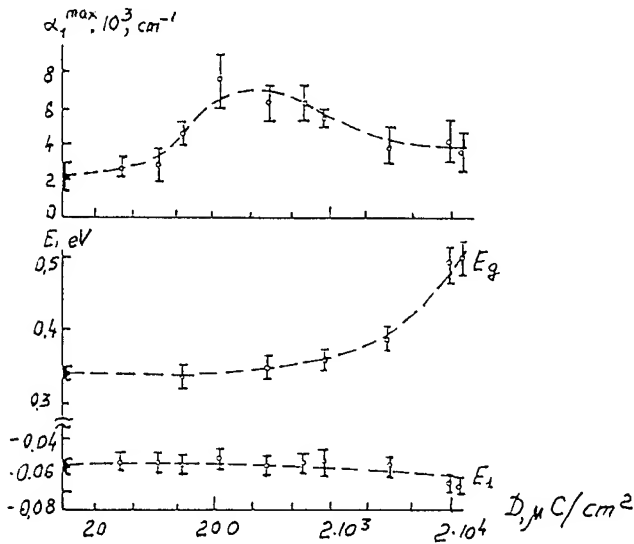


Fig. 5. Amplitude of the additional (associated with complexes) absorption band α_1 , optical band gap E_g and optical ionisation energy E_i of complexes vs. implanted zinc dose.

Asymmetric additional bands α_1 with a pronounced red border were observed in the long-wave part of the $\alpha(h\omega)$ spectrum of $\text{PbTe}(\text{Zn})$. Their character can result from a set of intrinsic defects, whose energy level E_1 lies in the upper half of the forbidden band.

The fact that the absorption intensity in the α_1 band substantially exceeds that in the α_2 and α_3 bands, implies that the absorption cross-section of the α_1 band is one - two orders of magnitude higher than that for point defects. This additionally confirms that α_1 bands are connected with complexes.

The nonmonotonous dose dependence of $\max(\alpha_1)$ (Fig. 5) gives an indication of an involved character of complexes formation in the course of ion implantation. These results may be interpreted based on the assumption that these complexes include both V_{Te} and V_{Pb} vacancies. This explains why $\max(\alpha_1)$ grows almost linearly with I in the small dose range, then attains saturation, and declines at greater doses (due to "healing" of V_{Pb} with zinc atoms).

For thin ($d < 0.3 \mu\text{m}$) $\text{PbTe}(\text{Zn})$ films, the natural absorption edge in the short-wave part of the $\alpha(h\omega)$ spectrum shifts with the increase of the dose. This indicates that the optical width

of forbidden band E_g increases monotonically with dose. (The absorption edge form analysis shows that optical transitions in $\text{PbTe}(\text{Zn})$ are direct and allowed). Changes of the natural absorption edge may arise from the two factors: changes of the Burshtein - Moss effect resulting from the increase of charge carriers concentration and (or) the increase of due to formation of $\text{Pb}_{1-x}\text{Zn}_x\text{Te}$ solid solution (the width of cubic ZnTe forbidden band is 2.1 - 2.3 eV at 300 K). Estimates show that the changes of charge carriers concentration in $\text{PbTe}(\text{Zn})$ at the minimum implantation dose may only insignificantly affect the change of natural absorption edge due to the Burshtein - Moss effect. The corresponding changes of energy spectrum of the thin PbTe films caused by the increase of zinc implantation dose are shown in Fig. 6.

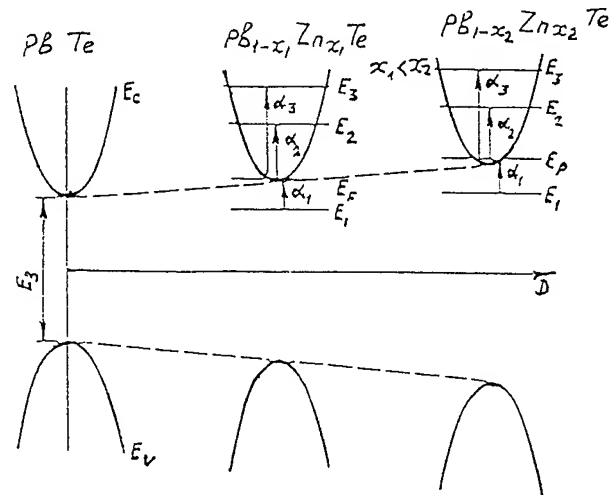


Fig. 6. Variation of the PbTe energy scheme with zinc implantation dose

In order to remove radiation defects, the ion-implanted samples were annealed at $T = 350 - 420^\circ\text{C}$ for 0.5 h in pure helium atmosphere. After the annealing of radiation defects, the values of main parameters of argon-implanted films approach to those prior to the implantation. Small qualitative differences of these parameters (see curves 8 - 8", 10 - 10" in Fig. 1) may result from repeated annealing of layers (prior to and after the implantation). In this case, structural improvements are not unlikely. These improvements are evidenced, in particular, by small increase in mobility in samples 7" - 10" after all stages of annealing.

After the annealing of radiation defects, samples 1 - 6 reveal donor effect of Zn non-uniformly distributed across the film depth. This is best demonstrated by measurements of σ , S , R , and Q for samples in which the upper (doped with zinc) and lower (initial p -type PbTe) layers belong to different types of conductivity.

In this case, the equations for kinetic coefficients are

$$\sigma = (\sigma_1 d_1 + \sigma_2 d_2) / (d_1 + d_2), \quad (2)$$

$$S = (S_1 \sigma_1 d_1 + S_2 \sigma_2 d_2) / (\sigma_1 d_1 + \sigma_2 d_2), \quad (3)$$

$$R = (R_1 \sigma_1^2 d_1 + R_2 \sigma_2^2 d_2) / (\sigma_1 d_1 + \sigma_2 d_2), \quad (4)$$

$$Q = (Q_1\sigma_1d_1 + Q_2\sigma_2d_2) / (\sigma_1d_1 + \sigma_2d_2) + \\ (S_1R_1\sigma_1^2d_1 + S_2R_2\sigma_2^2d_2) / (\sigma_1d_1 + \sigma_2d_2) - \\ (R_1\sigma_1^2d_1 + R_2\sigma_2^2d_2)(S_1\sigma_1d_1 + S_2\sigma_2d_2) / (\sigma_1d_1 + \sigma_2d_2)^2. \quad (5)$$

Here, σ_1 , S_1 , R_1 , Q_1 , and d_1 are the electric conductivity, the coefficients of Seebeck, Hall, and transverse Nernst - Ettingshausen effects, and the thickness, correspondingly, of the upper layer; σ_2 , S_2 , R_2 , Q_2 , and d_2 are the same parameters for the lower layer. Expressions for R and Q were derived under the assumption of a weak magnetic field.

For sample 5" (Fig. 2), the S and R coefficients are small or change their signs in the investigated temperature range of 77 to 300 K. In this sample, the Q value is higher than that typical for homogeneous PbTe samples. This indicates substantial changes of carrier type and concentration across the sample depth. Assuming that after ion implantation and annealing, zinc atoms replace lead in PbTe and give one electron each, we estimated the p - n junction depth (d_{p-n}) and electric activity $\beta = n/N_{Zn}$. The results are: $d_{p-n} \sim 0.1 \mu\text{m}$ and $\beta \sim 10^{-2}$, i.e., every 100 atoms give only one donor center with a unit activity. This prevents from attaining high (of order 10^{-18} cm^{-3}) electron concentrations of PbTe using the ion doping with zinc.

Doping with radiation defects (ion implantation without annealing) was used to form p - n junctions in p -PbTe single crystals and films. Local junctions were formed in PbTe crystals by photolithography. The tunnel microscopy showed that the doping layer characteristics are virtually constant throughout the entire crystal area. This high stability of parameters is due to the Fermi level pinning that results from the formation of a quasi-local energy level of Te vacancies in the conduction band.

With a ion implantation dose $I > 2 \cdot 10^3 \mu\text{C}/\text{cm}^2$, the p - n junction depth was more than $1 \mu\text{m}$. As a rule, the depth of p - n junction produced by the ion implantation does not exceed $0.1 - 0.2 \mu\text{m}$. These results are useful in producing layered and heterostructures within PbTe.

In the case of vertical p - n junctions, metallic contacts were deposited on p - and n -regions, and the produced signal V was measured using these contacts. Direct measurements of the diffusion length of carriers were carried out by the electron-beam-induced current (EBIC) method. At an applied voltage of 20 kV, the electron beam current was 10^{-8} A .

The current-induced signals from the p - n junction were measured at temperatures of 300 and 80 K. The relation describing these signals V in the p -region was found to be

$$V = V_0 e^{-x/L_e} \quad (6)$$

where V_0 is the maximum value of the signal, x is the scanning coordinate (the distance between the electron beam incidence point and the p - n junction), and L_e is the diffusion length of electrons. The values of L_e determined from the slope of the curve $\ln(V/V_0) = f(x)$ are $5 \mu\text{m}$ and $50 \mu\text{m}$ at temperatures of 300 and 80 K, correspondingly. The diffusion

length L_h of holes in the n -region (zinc-doped) is relatively small due to the presence of complexes (point defects composition). These complexes giving an energy level in the forbidden band, diminish the life of minority carriers.

III. Conclusions

1. Our studies showed that the main mechanism of ion implantation of PbTe with large ($I = 2 \cdot 10^4 \mu\text{C}/\text{cm}^2$) doses of Zn^+ or Ar^+ consists in forming point defects (predominantly, Te vacancies) that penetrate to the depth of $3 \mu\text{m}$ and more and determine the transport properties of the samples. These defects exhibit a very high stability, the film properties remaining virtually unchanged for one year and more.

2. The stabilization of electron concentration at a level of $(2 - 4) \cdot 10^{18} \text{ cm}^{-3}$ at $T = 80 \text{ K}$ irrespective of the initial type of sample conductivity and the type of ions (Ar^+ or Zn^+) is due to the formation of quasi-local (doublet) energy level of Te vacancies in the conduction band of PbTe.

3. In thin ($d < 0.3 \mu\text{m}$) layers of PbTe implanted with Zn^+ , the formation of $\text{Pb}_{1-x}\text{Zn}_x\text{Te}$ solid solutions was detected, which is accompanied with the increase of the forbidden band E_g with x .

4. The use of these materials for various detectors has a number of advantages. Noteworthy are high electric homogeneity, radioactive stability of parameters, and a high photosensitivity.

The implantation of Zn offers promise for creating heterojunctions (with $\text{Pb}_{1-x}\text{Zn}_x\text{Te}$ upper layer).

References

- [1] "Ion Implantation in Semiconductors", Solid State Phenomena, vols. B1-2, pp. 1-473 (1988).
- [2] L. Palmetshofer, "Ion Implantation in IV-VI Semiconductors", Journal of Applied Physics, vol. A34, pp 139-153 (1984).
- [3] V.I. Kaidanov, Yu. I. Ravich, Physics - Uspekhi, vol. 51, pp 145-170 (1985)
- [4] V.I. Kaidanov, "Resonance (Quasilocal) States in $\text{A}^{\text{IV}}\text{B}^{\text{VI}}$ Semiconductors", Defect and Diffusion Forum, vols. 103-105, pp 388-405 (1993)
- [5] B.A. Akimov, and L.I. Ryabova, "Metastable Electronic States Caused by Native Defects and III-d Group Impurities Semiconductors", Defect and Diffusion Forum, vols. 103-105, pp 85-104 (1993).
- [6] B.A. Volkov, and V.V. Tubushev, JETP Lett., vol. 46, pp 245-250 (1987).

Preparation of Highly Effective $p\text{-Bi}_{0.5}\text{Sb}_{1.5}\text{Te}_3$ and $n\text{-Bi}_2\text{Te}_{2.7}\text{Se}_{0.3}$ Films

M. Stölzer¹, M. Stordeur, I. Stark

¹ Martin Luther University, 06099 Halle, Germany

Abstract

$\text{Bi}_{0.5}\text{Sb}_{1.5}\text{Te}_3$ and $\text{Bi}_2\text{Te}_{2.7}\text{Se}_{0.3}$ films were flash-evaporated onto oxidized aluminium and Kapton foil substrates. The films were characterized by SEM, EDX and electrical transport measurements (electrical conductivity, Hall coefficient and thermopower in the range 85...375 K). Highly effective films grown on Kapton show a (1 0 5) texture whereas films on $\text{Al}/\text{Al}_2\text{O}_3$ are (0 0 n) texturized. With an optimal amount of excess Te in the evaporant, after an annealing procedure a power factor of $4\text{E-}3 \text{ W K(E-}2) \text{ m(E-}1)$ at 300 K was reached.

Introduction

The trigonal V_2VI_3 compound semiconductors are the most common materials for thermoelectric applications working near room temperature because of their high thermoelectric figure of merit Z .

The aim of our work is to develop films of those materials that could be used in miniaturized thermoelectric coolers or generators in the power range $< 1 \text{ mW}$. For these applications, films of several μm (1 ... 100) thickness and best available Z values are needed. Kapton foil was found to be a non-expansive substrate material with small thermoelectricity and well adapted thermal expansion coefficient.

Film deposition

Films of 1 ... 3 μm thickness were deposited on $\text{Al}/\text{Al}_2\text{O}_3$, $\text{Si}/\text{Si}_2\text{O}_3$ and Kapton (polyimide) substrates in high vacuum (10^{-5}mbar) by

means of a flash evaporation technique (see figure). The deposition rate was about 1 nm/s . The optimum substrate temperature was found to be between 200 and 250°C [1].

The substrate materials are all amorphous. They differ in their thermal conductivities and thermal expansion coefficients. Kapton foil is of special interest because of its thermal expansion coefficient $\alpha=2\cdot 10^{-5}$ is nearly the same as that of Bi_2Te_3 and Sb_2Te_3 .

The evaporant consists of either $(\text{Bi}_{0.25}\text{Sb}_{0.75})_2\text{Te}_3$ (p-type material) or $\text{Bi}_2(\text{Te}_{0.9}\text{Se}_{0.1})_3 + 0.04 \text{ J}$ (n-type material) and some at% additional Tellurium, to reach stoichiometric composition of the films. The material was homogenized at 850°C in quartz ampoules and milled to a grain size of about $200 \mu\text{m}$.

After film deposition, an additional annealing process (3 hours at 300°C in small evacuated ampoules to prevent re-evaporation) was necessary to get a high figure of merit Z .

The most important requirement in order to get high Z values is the stoichiometric composition within the solubility boundaries of the phase diagram.

The precision of common measuring methods (i. e. EDX, AAS) it is not sufficient to check the stoichiometry. In the experimental praxis, stoichiometric composition is indicated by a strong increase of the carrier mobility during the annealing process [1].

From this point of view, we obtained stoichiometric p-type films at 4...6 at% excess Te and stoichiometric n-type films at nearly 10 at% excess Te in the evaporant. The second value agrees with sticking coefficients of Bi and Te published in [2].

Texture and Morphology

XRD texture analysis and SEM pictures of $(\text{Bi}_{0.25}\text{Sb}_{0.75})_2\text{Te}_3$ films with optimized thermoelectric properties on Kapton and $\text{Al}/\text{Al}_2\text{O}_3$ substrates are presented. (the specimens correspond to the stated and hollow circled curves in the "Thermoelectric Properties" figures).

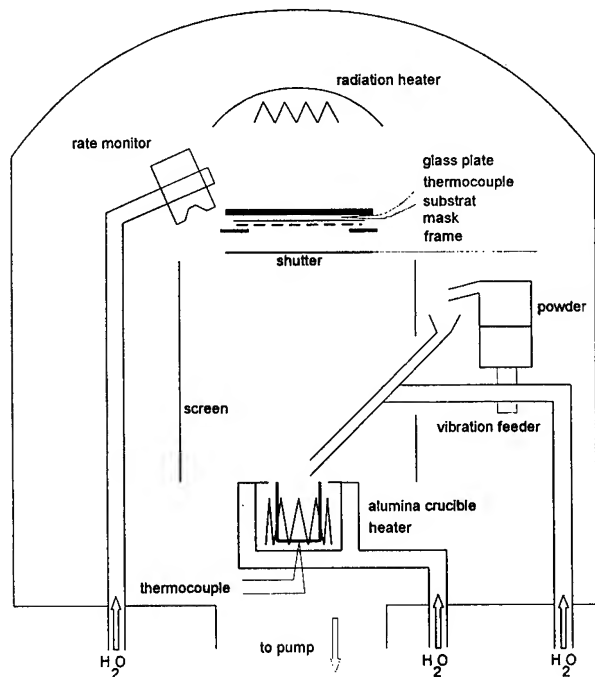


Fig. 1: Scheme of the flash evaporation apparatus.

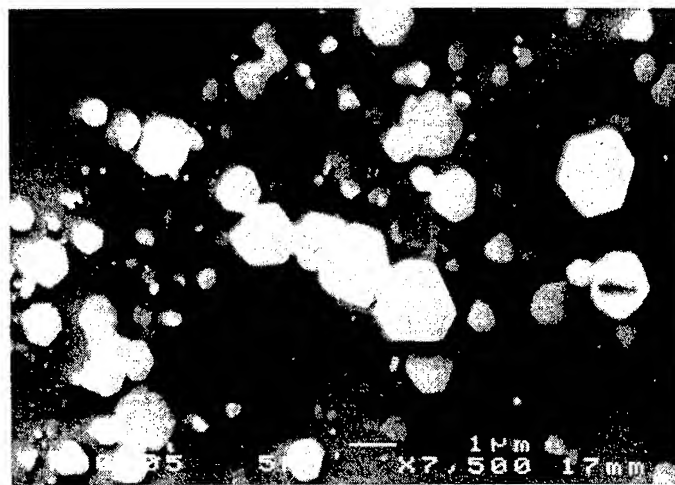


Fig. 2: (1 0 n) oriented $(\text{Bi}_{0.25}\text{Sb}_{0.75})_2\text{Te}_3$ micro crystals on oxidized silicon. Growth temperature 320°C .

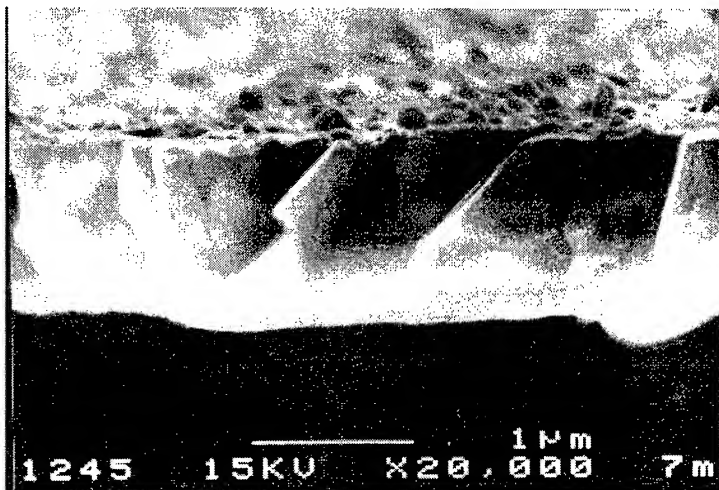


Fig. 5: $(\text{Bi}_{0.25}\text{Sb}_{0.75})_2\text{Te}_3 + 4 \text{ at\% Te}$, $T_s=250^\circ\text{C}$, $d=1\mu\text{m}$, on oxidized aluminium substrate. Edge of a broken film.



Fig. 4: $(\text{Bi}_{0.25}\text{Sb}_{0.75})_2\text{Te}_3 + 6 \text{ at\% Te}$, $T_s=230^\circ\text{C}$, $d=2.9\mu\text{m}$, on Kapton substrate. Edge of a broken film.

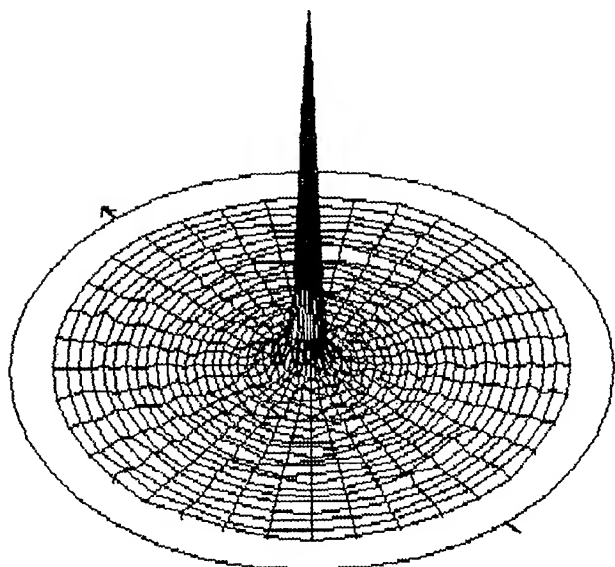


Fig. 3: Same sample as fig. 3, pole figure of the (0 0 15) reflex.

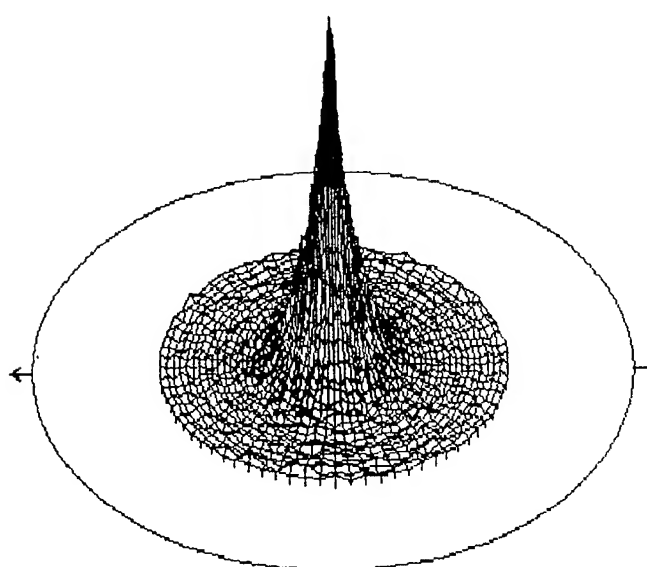


Fig. 6: Same sample as fig. 5, pole figure of the (1 0 5) reflex.

For getting SEM pictures from the edge of broken films, coated aluminium or Kapton substrates were stretched so that the films were torn up into clods and then covered with 20 nm of gold.

Stoichiometric films grown at temperatures between 200 and 300 °C are smooth and dense and consist of large grains (figs. 3 and 5).

There is a great difference in the crystallographic orientation of the grains between films on Si and Al substrates on the one hand side and on Kapton at the other. The first show a strong (0 0 n) texture (c axis \perp substrate plain) and the latter a (1 0 5) texture. That means the (1 0 5) directions are perpendicular to the substrate plain and the c axes have a tilt of 58° against the perpendicular. This is shown in fig. 2 and by the pole figure of the (0 0 15) reflex (fig. 4), and the (2 0 10) and (1 1 0) pole figures (figs. 6 and 7), respectively.

We suppose that this fact is caused by the strong difference in the thermal conductivities of the substrate materials.

The (1 0 5) plan is the base plane of a quasi-cubic elemental cell. A weak (1 0 5) texture was also observed in nonstoichiometric films and in films grown at room temperature on oxidized silicon.

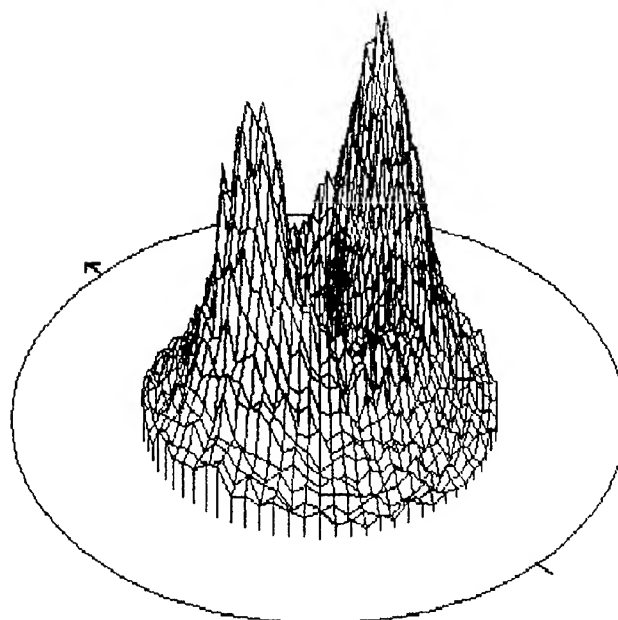


Fig. 7: Same sample as fig. 5, pole figure of the (1 1 0) reflex.

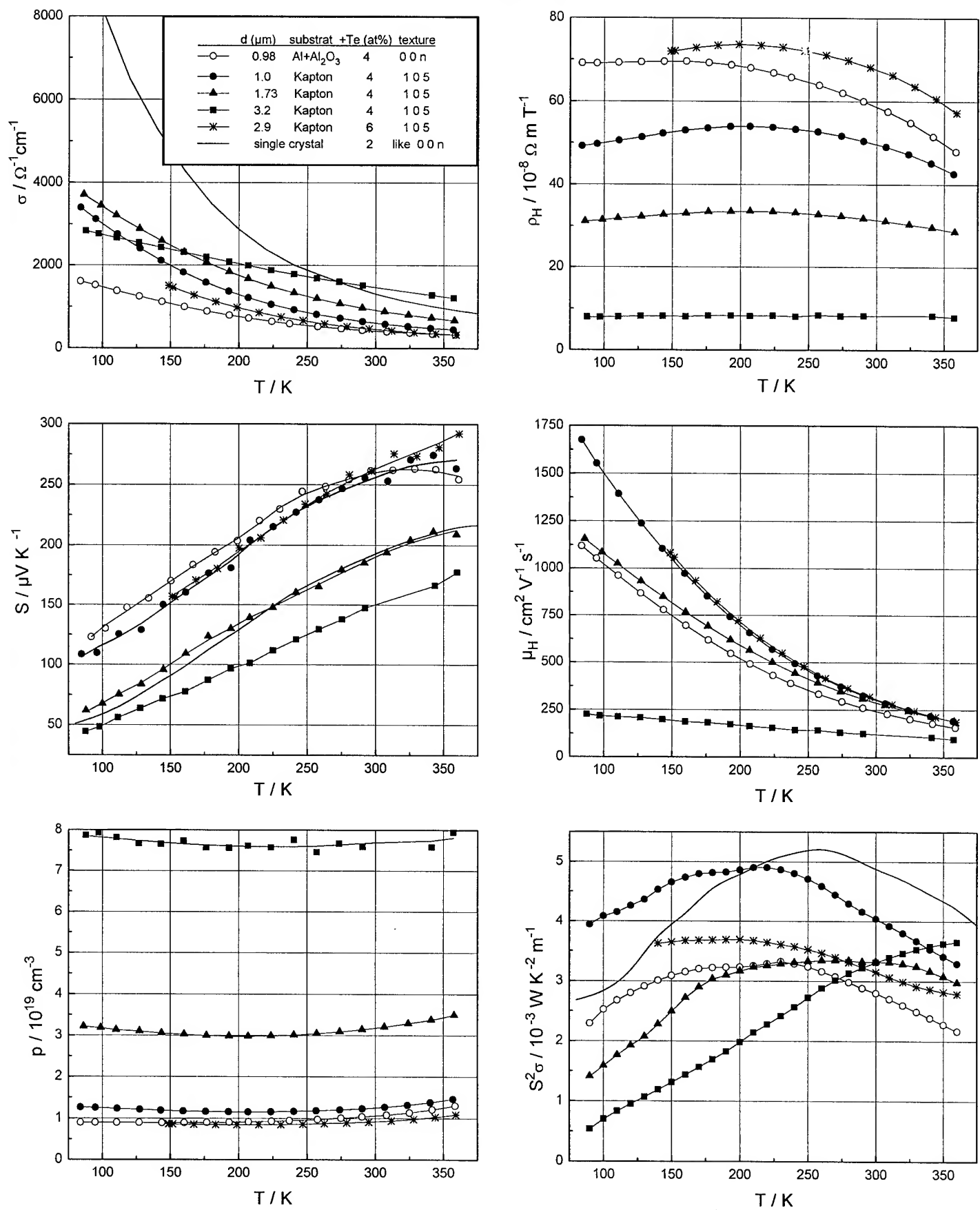


Fig. 8: p - (Bi_{0.25}Sb_{0.75})₂Te₃ films, grown at 220...250°C by flash evaporation and 3 h at 300°C annealed. Electrical conductivity, Hall and Seebeck coefficient, hall mobility, carrier concentration and power factor.

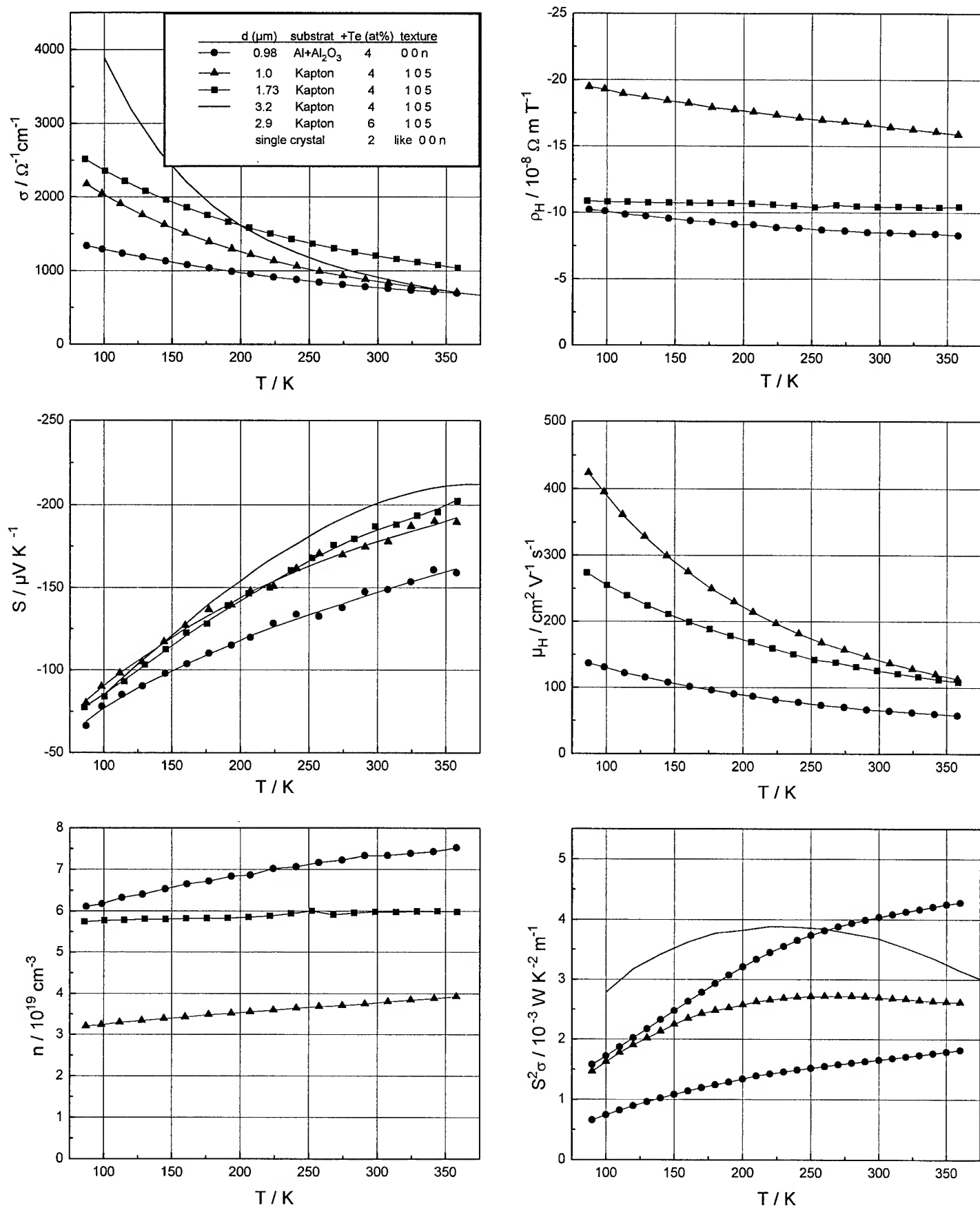


Fig. 9: n -Bi₂(Te_{0.9}Se_{0.1})₃ films (+ 0.04 at% J doping), grown at 220...240°C by flash evaporation and 3 h at 300°C annealed. Electrical conductivity, Hall and Seebeck coefficient, hall mobility, carrier concentration and power factor.

In (1 0 5) oriented $(\text{Bi}_{0.25}\text{Sb}_{0.75})_2\text{Te}_3$ films on Kapton, high carrier mobilities and power factors could be achieved.

Thermoelectric Properties

p - $(\text{Bi}_{0.25}\text{Sb}_{0.75})_2\text{Te}_3$ films (fig. 8):

1 μm thick films on both $\text{Al}/\text{Al}_2\text{O}_3$ and Kapton substrates show Seebeck coefficients near 260 $\mu\text{V}/\text{K}$ at 300 K. This is the same as the maximum value in single crystals, caused by the solubility limit of Tellurium.

Films on Kapton reach even higher mobilities as on Al_2O_3 , probably because of the better matching of its thermal expansion coefficient. However, if the thickness of the films is greater, the mobility becomes smaller and the carrier concentration increases (see solid symbols).

By considering the common defect structure model, it seems that the concentration of Te becomes smaller if the films are thicker.

Increasing the amount of additional Te in the evaporant to 6 at% (stared curve), results in a high mobility and small carrier concentration even in thick films.

n - $\text{Bi}_2(\text{Te}_{0.9}\text{Se}_{0.1})_3$ films (fig. 9):

Films without and up to 0.07 at% Iodine doping are always n-type. The behaviour of these films is more complex (an additional dopant is necessary for obtaining an optimum n-type carrier concentration) and not yet fully understood.

It was tried to optimize the thermoelectric properties by varying the contents of tellurium in the evaporant. As shown, the highest power factor was reached at 12 at% additional Te, which was the highest amount of Te within the experiments, whereas the highest mobility was reached at 8 at% Te. From published sticking coefficients [2] of Bi and Te on Bi_2Te_3 films can be estimated that 10 at% excess Te are needed to grow stoichiometric films.

At low temperatures there is only a weak increase of the mobility, indicating that carrier scattering on grain boundaries takes place.

Acknowledgements

We would like to thank C. Eisenschmidt and his colleagues from the Crystal Lab of the Martin Luther Univ. for the texture analysis measurements.

References

[1] M. Stölzer, M. Stordeur, I. Stark: Optimization of p - $(\text{Bi}_{0.25}\text{Sb}_{0.75})_2\text{Te}_3$ and n - $\text{Bi}_2(\text{Te}_{0.9}\text{Se}_{0.1})_3$ films for thermoelectric thin film components.
Proc. of the 2nd FAT Symposium on Thermoelectrics, Dreden 1994

[2] A. Mzerd, D. Sayah, J. C. Tedenac, A. Boyer: Effect of substrate temperature on crystal growth of Bi_2Te_3 on single crystal Sb_2Te_3 .
J. of Material Sciences Letters 13 (1994) 301-304

Experimental study of the effect of quantum-well structures on the thermoelectric figure of merit

L. D. Hicks

Department of Physics, Massachusetts Institute of Technology, Lexington, MA 02139, USA

T. C. Harman

*Lincoln Laboratory, Massachusetts Institute of Technology,
Lexington, MA 02173-9108, USA*

X. Sun, and M. S. Dresselhaus

*Department of Electrical Engineering and Computer Science and Department of Physics,
Massachusetts Institute of Technology, Cambridge, Massachusetts 02139*

(March 17, 1996)

Experimental investigations have been performed on the thermoelectric properties on the multiple-quantum-well structures of $\text{PbTe}/\text{Pb}_{1-x}\text{Eu}_x\text{Te}$ grown by molecular beam epitaxy. Our results are found to be consistent with theoretical predictions and indicate that an increase in Z over bulk values may be possible through quantum confinement effects using quantum-well structures.

I. INTRODUCTION

Recently, it has been shown theoretically [1] that it may be possible to increase the thermoelectric figure of merit (Z) of certain materials by preparing them in the form of two-dimensional quantum-well structures. The two-dimensional quantum confinement can significantly enhance the density of electron states, hence making possible the improvement of the thermoelectric figure of merit. The same consideration applies to one-dimensional systems [2], which have been shown to be even more promising for improvement of the thermoelectric properties. This framework of low dimensional quantum confinement allows new classes of materials, which would not be interesting for their thermoelectric properties in three dimensions, to be of interest for thermoelectric applications.

Using $\text{PbTe}/\text{Pb}_{1-x}\text{Eu}_x\text{Te}$ multiple-quantum-well structures grown by molecular beam epitaxy, we have performed thermoelectric and other transport measurements as a function of quantum well thickness and doping. Our results are found to be consistent with theoretical predictions and indicate that an increase in Z over bulk values within the PbTe quantum wells. This work shows that it may be possible through quantum confinement effects using quantum-well structures to achieve higher overall Z values compared with the bulk value.

To be a good thermoelectric material for cooling applications, the material must have a high thermoelectric figure of merit, Z . The figure of merit is defined by [3]

$$Z = \frac{S^2 \sigma}{\kappa} \quad (1)$$

where S is the thermoelectric power (Seebeck coefficient), σ is the electrical conductivity and κ is the thermal conductivity. In order to achieve a high Z , one requires a

high thermoelectric power S , a high electrical conductivity σ , and a low thermal conductivity κ . In general, it is difficult to increase Z for the following reasons. Increasing S for simple materials also leads to a simultaneous decrease in σ , and an increase in σ leads to a comparable increase in the electronic contribution to κ because of the Wiedemann-Franz law. So with known conventional solids, a limit is rapidly obtained where a modification to any one of the three parameters S , σ or κ adversely affects the other transport coefficients, so that the resulting Z does not vary significantly. Currently, the materials with the highest Z are Bi_2Te_3 alloys such as $\text{Bi}_{0.5}\text{Sb}_{1.5}\text{Te}_3$, with $ZT \simeq 1.0$ at $T = 300$ K [3]. Only small increases in Z have been achieved in this system for the last two decades, so it is now felt that the Bi_2Te_3 compounds may be nearing the limit of their potential performance.

In earlier papers [1,4], we considered theoretically the effect on Z of using materials in two-dimensional (2D) structures such as 2D multiple-quantum-well (MQW) structures, and showed that this approach could yield a significant increase in Z over the bulk value as the quantum well width is decreased. The proposed increase in Z arises mainly from the enhancement of the density of electron states per unit volume that occurs for small well widths. Other workers have extended our initial calculation and confirmed that an increase in Z over bulk values may be possible for narrow well widths [5-7]. In this paper, we report an experimental investigation to test our theoretical predictions.

The MQW system used for the investigation is the $\text{PbTe}/\text{Pb}_{1-x}\text{Eu}_x\text{Te}$ system, whose fabrication technology is relatively well-developed. Bulk PbTe is a relatively good thermoelectric material with a ZT of 0.4 at 300 K, so that a reasonable increase in Z due to 2D effects could result in a Z higher than the best Bi_2Te_3 alloys. In the $\text{PbTe}/\text{Pb}_{1-x}\text{Eu}_x\text{Te}$ system, the PbTe is

the quantum well and $\text{Pb}_{1-x}\text{Eu}_x\text{Te}$ is the barrier material. Such structures have a type I band alignment and a nearly symmetric offset between the valence and conduction bands [8]. The energy gap of the $\text{Pb}_{1-x}\text{Eu}_x\text{Te}$ barrier increases strongly with x , the Eu content [9], so only about 6% Eu can give large confinement energies and yield 2D transport for electrons in the PbTe quantum wells [10]. Since the carrier mobility of $\text{Pb}_{1-x}\text{Eu}_x\text{Te}$ also decreases rapidly with increasing Eu content [10], low values of x were used in the experiments.

Our proposed increase in Z in MQW structures occurs in the quantum wells alone. In order to extract the well transport properties easily from our MQW results, we needed to grow samples for which the transport is dominated by 2D conduction in the wells, with negligible barrier conduction. Using mobility measurements [11], we found that samples dominated by conduction in the quantum well could be obtained at 300 K using a barrier Eu content of $x > 7\%$ and barrier widths larger than 350 Å. We measured carrier mobilities of over 1400 $\text{cm}^2\text{V}^{-1}\text{s}^{-1}$ in our MQW samples, which is comparable to values in our best PbTe thick film (bulk) samples with mobilities of 1600 $\text{cm}^2\text{V}^{-1}\text{s}^{-1}$. Since the mobility of our barrier layers (45 $\text{cm}^2\text{V}^{-1}\text{s}^{-1}$) is much lower than that of the wells, the mobility of a MQW sample should be significantly less than bulk PbTe if there were significant conduction in the barrier region. This observation is used in experimental verification of carrier confinement in MQW structures.

According to our model [1], the increase in Z due to 2D quantum confinement effects arises mainly from the power factor $S^2\sigma$, while the lattice thermal conductivity is assumed to be unchanged from the bulk value except for well widths less than about 10 Å. In fact, we also assumed that the mobility of the quantum well would be the same as the best bulk value - an assumption which we verified experimentally - so any increase in Z would arise through the factor S^2n , where n is the carrier density in the quantum well. Therefore, according to our model, we would expect to observe an increase in S^2n as the well width is narrowed.

Samples were grown by molecular beam epitaxy (MBE) in a modified Varian 360 MBE system. Details of the sample preparation and characterization are given elsewhere [11]. The resistivity, Hall coefficient and Seebeck coefficient of the samples were measured at 300 K. Contacts were made with an In alloy, which results in excellent ohmic contacts for n-type samples. Chromel-Alumel thermocouples were used in measuring the Seebeck coefficient. Since we had already established that virtually all the conduction in our MQW samples is in the PbTe well and that barrier electronic conduction can be neglected, we were able to focus our attention on the transport properties of the quantum well alone. Thus the carrier density in the quantum wells could be calculated directly from the Hall coefficient and the well width. Also, the Seebeck coefficient of the wells was equal to the measured S of the MQW sample. For each sample, the

value of the well S^2n was obtained and the results are shown as full circles in Fig. 1. Here the results for S^2n as a function of well thickness are shown in Fig. 1(a), while Fig. 1(b) shows S^2n as a function of carrier density. The corresponding results for bulk single crystal PbTe obtained from Ref. [11] are also shown on these plots. The data points in Fig. 1(a) show an increase in S^2n as the well width is narrowed, and the well S^2n may reach several times the bulk value for small well widths that are experimentally achievable. These results are predicted by our theoretical model and therefore give qualitative support to the idea that MQW structures may be used to improve Z over bulk values. To obtain a quantitative comparison between experiment and theory, we used our model to calculate values of S^2n vs a and vs n for the $\text{Pb}_{0.927}\text{Eu}_{0.073}\text{Te}$ MQW system as described below.

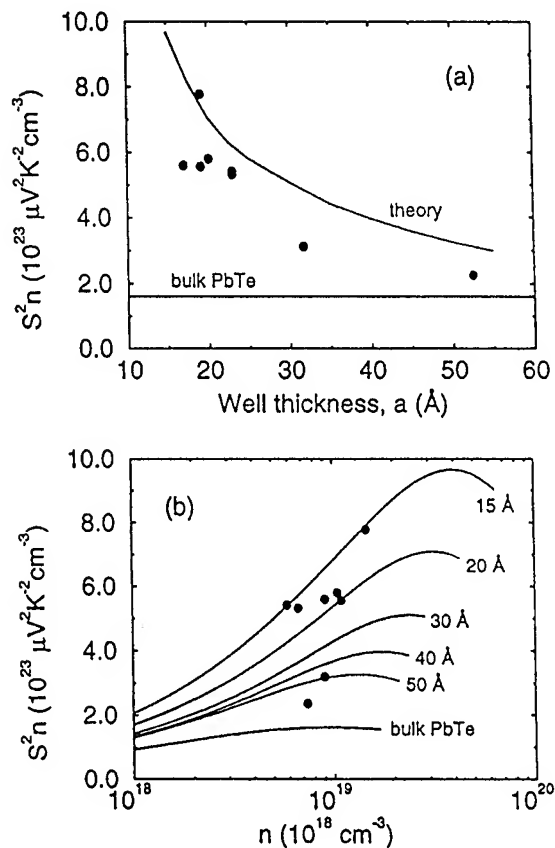


FIG. 1. (a) S^2n results for $\text{PbTe}/\text{Pb}_{0.927}\text{Eu}_{0.073}\text{Te}$ MQWs (full circles) as a function of well width a at 300 K. For comparison, the best experimental bulk PbTe value is also shown. Calculated results for optimum doping using our model are shown as a solid line. (b) S^2n results for the same $\text{PbTe}/\text{Pb}_{0.927}\text{Eu}_{0.073}\text{Te}$ MQW samples (full circles) as a function of carrier density n at 300 K. Calculated results using our model for different well widths are indicated as solid curves.

In our original model [1], we considered a quantum well in which only a single subband contributes to the trans-

port and to Z . However, in a PbTe quantum well there are multiple subbands which contribute to the transport. For example, in the case of a PbTe superlattice in the (111) direction, one of the carrier pockets will have its main symmetry axis normal to layer planes, while the other three carrier pockets will have their main symmetry axes at equivalent oblique directions. Thus, to do a realistic calculation of the transport properties of PbTe quantum wells, it is necessary to know the relative energies of all subband extrema and then to include all subbands in calculating the overall S and n . The Envelope Function Approximation (EFA) was used to calculate the positions of the energy levels in the MQW structures. The EFA calculation involves solving for the electron eigenstates in both the well and barrier materials, and matching the wavefunctions at the interface with appropriate boundary conditions to find the energy levels and dispersion relations in the quantum well. Yuan *et al.* [8] applied the EFA method to the PbTe/Pb_{1-x}Eu_xTe MQW system with great success and used it to reproduce their experimental optical data, without any fitting parameters. We used the same approach [8] to calculate the positions of the energy levels in our MQW samples. To use the EFA method, the band gaps, band offsets, interband momentum matrix elements, and far band parameters must be known. The band gap of PbTe is 319 meV at 300 K [9]. We determined the band gap for our Pb_{0.927}Eu_{0.073}Te barrier material to be 630 meV from infrared transmission measurements of single layer thick film samples. The band offsets were estimated by assuming the relation determined experimentally by Yuan *et al.* [8]: $\Delta E_c/\Delta E_g = 0.55$, where ΔE_c is the conduction band offset and ΔE_g is the difference in band gap between the well and barrier materials. Finally, the momentum matrix elements and far band parameters were obtained from Table III of Ref. [8].

Once we had calculated the positions of the energy levels in the quantum wells, the next step was to calculate values for the Seebeck coefficient and carrier density within the framework of our theoretical model, using expressions for the Seebeck coefficient S_i and carrier density n_i of the i -th subband [1] given by:

$$n_i = \frac{1}{2\pi a} \left(\frac{2k_B T}{\hbar^2} \right) (m_1 m_2)^{\frac{1}{2}} F_0(\zeta_i^*) \quad (2)$$

and

$$S_i = -\frac{k_B}{e} \left[\frac{2F_1(\zeta_i^*)}{F_0(\zeta_i^*)} - \zeta_i^* \right] \quad (3)$$

where the function F_j for a Fermi-Dirac distribution is given by

$$F_j(\zeta_i^*) = \int_0^\infty \frac{x^j dx}{e^{(x-\zeta_i^*)} + 1}, \quad (4)$$

a is the width of the quantum well, m_1 and m_2 are the principal effective mass components parallel to the lay-

ers, $\zeta_i^* = (\zeta - E_i)/k_B T$ is the reduced Fermi level measured relative to E_i , the minimum energy of each subband (calculated using the EFA method), and ζ is the Fermi level. For multiple subbands, the total carrier density and Seebeck coefficient are, respectively, $n = \sum_i n_i$ and $S = (\sum_i S_i n_i)/(\sum_i n_i)$, assuming that all subbands have the same mobility as a first approximation and for lack of better experimental knowledge.

For our S and n calculations, we used a constant barrier thickness of 460 Å, which is the average thickness of all our samples shown in Fig. 1. We did calculations for different well thicknesses varying from 15 Å to 50 Å. The effective masses were extracted from the two-band momentum matrix elements in Table III of Ref. [8]. This gave a bulk longitudinal effective mass $m_{||} = 0.620m_0$ and a bulk transverse effective mass $m_{\perp} = 0.053m_0$. For the 2D quantum well, this gives $m_1 = m_2 = m_{\perp}$ for the longitudinal subbands, and $m_1 = m_{\perp}$, $m_2 = 0.283m_0$ for the oblique subbands. For each well thickness, we used the EFA calculation to get the positions of the energy levels, E_i . Then S and n were calculated as a function of Fermi level ζ and thus S and $S^2 n$ were found as a function of n . The calculated results of $S^2 n$ vs n for different well widths are shown as solid lines in Fig. 1(b). The calculated maximum $S^2 n$ for each well width (the peak of each curve in Fig. 1(b)) is shown vs well width as a solid line in Fig. 1(a), while Fig. 1(b) shows that the optimum doping increases as the quantum well width is decreased. As can be seen from Figs. 1(a) and 1(b), there is very good agreement between experiment and theory, especially considering that no adjustable parameters were used in our calculation. Therefore our experimental results on the PbTe/Pb_{0.927}Eu_{0.073}Te superlattice appear to confirm the predictions of our theoretical model, showing that MQW structures may indeed be used to obtain an enhancement in Z .

So far, we have considered only S and n since it is through these properties that our theory predicts an increase in Z . However, Z depends also on the thermal conductivity, κ . If we assume that the quantum well κ is the same as bulk κ , our experimental results in Fig. 1 imply that the quantum well Z may be up to 5 times greater than the bulk, giving a value of $ZT = 2.0$ at 300 K, twice the value of the best bulk thermoelectric materials. However, due to the thick barriers, the overall Z of the MQW structures is about 20 times less than the well value if we assume that the Pb_{0.927}Eu_{0.073}Te has the same κ as bulk PbTe. It is very likely, however, that due to alloy scattering, the barrier κ is significantly less than the bulk value for κ , in which case the overall Z may be close to a useful value. Measuring κ of our MQW samples to determine the overall Z is underway. Although we needed wide barriers to ensure 2D well transport, it may be possible to increase the barrier Eu content to give a higher band gap so that thinner barriers can be used to confine the electrons in the wells.

In conclusion, we have done an experimental investigation to test our theoretical model which predicts an

increase in Z in MQW structures. Good agreement was found between the experimental results and our calculations, giving apparent experimental confirmation of our model. This suggests that MQW structures may indeed attain an enhanced thermoelectric figure of merit.

The authors would like to thank G. Springholz, G. Bauer and G. Dresselhaus for valuable discussions. We gratefully acknowledge support for this work by the U. S. Navy under Contract No. N00167-92-K0052. The Lincoln Laboratory portion of this work was sponsored by the Department of the Army, the Department of the Navy and the National Aeronautics and Space Administration.

[1] L. D. Hicks and M. S. Dresselhaus, Phys. Rev. B **47**,

- 12727 (1993).
 [2] L. D. Hicks and M. S. Dresselhaus, Phys. Rev. B **47**, 16631 (1993).
 [3] H. J. Goldsmid, in *Thermoelectric Refrigeration* (Plenum Press, New York, ADDRESS, 1964).
 [4] L. D. Hicks, T. C. Harman, and M. S. Dresselhaus, Appl. Phys. Lett. **63**, 3230 (1993).
 [5] D. L. Broido and T. L. Reinecke, Phys. Rev. B **51**, 13797 (1995).
 [6] D. L. Broido and T. L. Reinecke, Appl. Phys. Lett. **67**, 1170 (1995).
 [7] J. O. Sofo and G. D. Mahan, Appl. Phys. Lett. **65**, 2690 (1994).
 [8] S. Yuan, G. Springholz, G. Bauer, and M. Kriechbaum, Phys. Rev. B **49**, 5476 (1994).
 [9] S. Yuan, H. Krenn, G. Springholz, and G. Bauer, Phys. Rev. B **47**, 7213 (1993).
 [10] G. Springholz *et al.*, Appl. Phys. Lett. **63**, 2908 (1993).
 [11] T. C. Harman, D. L. Spears, and M. J. Manfra, J. Electron. Mater. (1996), (submitted).

Experimental Evidence of High Power Factors and Low Thermal Conductivity in $\text{Bi}_2\text{Te}_3/\text{Sb}_2\text{Te}_3$ Superlattice Thin-Films

R. Venkatasubramanian, T. Colpitts, E. Watko, and J. Hutchby
Research Triangle Institute, Research Triangle Park, NC 27709, USA.

Abstract

Thermoelectric properties of p-type $\text{Bi}_2\text{Te}_3/\text{Sb}_2\text{Te}_3$ superlattice (SL) thin-films grown by organometallic vapor phase epitaxy (OMVPE) are described. The electrical and thermal transport properties including, hole mobility, Seebeck coefficient and power factor as a function of SL dimension are described. It is observed that the carrier mobility, Seebeck coefficient and power factor of the $\text{Bi}_2\text{Te}_3/\text{Sb}_2\text{Te}_3$ SL structures are better than that of p-type $\text{Bi}_2\text{Sb}_{2-x}\text{Te}_3$ alloys, with similar bandgap and electrical resistivity. The improvement in carrier mobility is attributed to avoiding or minimizing alloy scattering of carriers with SL structures while the enhanced Seebeck coefficient is related to the bandstructure difference between the alloy and the SL structures. Initial measurements indicate that power factor improvement of ~50% , over corresponding alloys, can be obtained in SL structures. We have measured the thermal conductivity of the SL structures by the $3-\omega$ method and have observed a factor of four to seven reduction in thermal conductivity of optimized structures, with respect to the alloys. The electrical conductivity and Seebeck coefficient are measured in the plane of the SL structures, while the $3-\omega$ -measured thermal conductivity can potentially be dominated by a component perpendicular to the SL structures. Hence, the figure-of-merit (ZT) values are estimated with a correction for potential anisotropy of thermal conductivity. Including this correction, implying higher assumed thermal conductivities in the plane of SL's, the preliminary estimated ZT for some SL structures are in the range of 1.22 to 1.67 at 300K.

Introduction

Efficient solid state thermoelectric (TE) devices are desirable for a variety of cooling applications. The performance of a TE device at a temperature T is essentially related to the ZT of the material used to make the device. Research on improving the ZT of these bulk thermoelectric materials have met with limited success since the 1960's.

Whall and Parker [1] in 1987 suggested the possible enhancement in ZT of SiGe-thermoelectric materials by using SL structures, through carrier confinement in quantum wells to obtain an enhancement in Seebeck coefficient and by modulation doping to obtain conductivity enhancement. In 1992, a National Thermogenic Workshop was organized [2] to consider various approaches to obtain a significant breakthrough in

the performance of thermoelectric materials. Thin-film approaches using quantum-well confined structures to enhance power-factor [3,4] and SL structures to decrease thermal conductivity without deteriorating electrical conductivity [5] were proposed in this workshop. The motivation for the use of superlattice structures to reduce thermal conductivity came from the observed reduction of lattice thermal conductivity using solid solution alloying in the Bi_2Te_3 - Sb_2Te_3 and Bi_2Te_3 - Bi_2Se_3 material system. In this system, the reduction in lattice thermal conductivity has been attributed to lattice distortions that are effective in phonon scattering, thereby impeding the flow of heat. Similarly, lattice perturbations and the atomic mass fluctuations at the SL interfaces are expected to enhance phonon scattering rates. If thin-film TE materials do show a quantum jump in ZT, a planar, thin-film, thermoelectric device process technology denoted as Monolithically Interconnected, Superlattice-Structured Thermoelements (MISST) [5] has been proposed as a possible approach to achieve a practical application of thin-film, superlattice-type structures to high-performance thermoelements.

Several groups have begun a detailed theoretical investigation of the benefits of superlattices [6, 7] and some laboratories have embarked on the experimental demonstration of improved ZT at 300K in thin-film quantum-well and SL structures. In this paper, we will focus on the experimental results in the TE properties of $\text{Bi}_2\text{Te}_3/\text{Sb}_2\text{Te}_3$ SL structures. We describe the characterization of thermoelectric properties of SL structures, where the properties have been investigated as a function of the SL dimension. Such a dimensional-related quantification is important to distinguish that the improved properties result from a SL approach, rather than arising purely from an epitaxial deposition process.

Deposition of $\text{Bi}_2\text{Te}_3/\text{Sb}_2\text{Te}_3$ SL Structures

We have used the organometallic vapor phase epitaxy (OMVPE) growth process to deposit the Bi_2Te_3 and Sb_2Te_3 films [8] on both semi-insulating GaAs substrates and Al_2O_3 substrates. X-ray diffraction data indicate that the films grown on both these substrates are single crystalline and c-oriented. The x-ray full-width at half-maximum, a quality parameter, of the Bi_2Te_3 film grown by OMVPE is comparable or better than that of a recently reported MBE grown Bi_2Te_3 film on Sb_2Te_3 substrate [9]. The stoichiometry of Bi_2Te_3 and Sb_2Te_3 films have been confirmed by Rutherford Backscattering and X-ray photoemission spectroscopy, respectively. The as-grown Bi_2Te_3 films are n-type and Sb_2Te_3 films are p-type,

determined by Hall-effect measurements. However, the as-grown $\text{Bi}_2\text{Te}_3/\text{Sb}_2\text{Te}_3$ SL structures were always found to be p-type. More details of the growth of these materials will be presented elsewhere [10].

An important concern in the growth of SL structures is the possibility of inter-mixing between the constituent layers of the SL. In this regard, it is instructive to examine the crystal structure of a layered $\text{Bi}_2\text{Te}_3/\text{Sb}_2\text{Te}_3$ material along the growth direction. The periodic van der Waals bonding, as within Bi_2Te_3 and between Bi_2Te_3 and Sb_2Te_3 layers are likely to help in obtaining abrupt surface terminations and thereby leading to high-quality SL interfaces. This was evident in the XPS spectra obtained on a very thin ($< 50 \text{ \AA}$) surface- Sb_2Te_3 layer grown on a thick Bi_2Te_3 layer. The XPS data evaluated in both normal and glancing modes, indicated a negligible presence of Bi in the surface Sb_2Te_3 layer. This provided some evidence that abrupt termination of Bi_2Te_3 layer was likely achieved prior to the growth of Sb_2Te_3 layer. The quality of the $\text{Bi}_2\text{Te}_3/\text{Sb}_2\text{Te}_3$ SL structures were assessed by single-crystal x-ray diffraction. We have observed clear satellite peaks, corresponding to the periodicity of the superlattices. Good agreement (usually within 10%) was obtained between the nominal value of the period estimated from growth-rates of the individual layers and the period deduced from the position of the superlattice satellite peaks [10].

Thermoelectric Properties of $\text{Bi}_2\text{Te}_3/\text{Sb}_2\text{Te}_3$ SL Structures

In this section, we consider the properties of two types of SL structures. A schematic of the SL structures grown on a semi-insulating GaAs substrate is shown in Figure 1. One type is the symmetric SL, where the thickness of the Bi_2Te_3 and the Sb_2Te_3 layers are kept the same. The other is the non-symmetric SL, where the thickness of the Sb_2Te_3 region is larger than the Bi_2Te_3 layer.

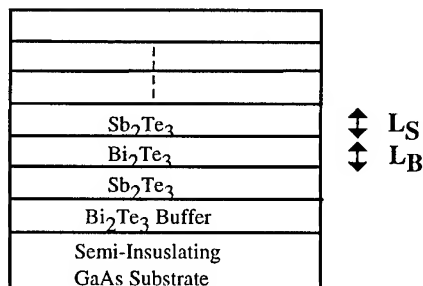


Figure 1 Schematic of $\text{Bi}_2\text{Te}_3/\text{Sb}_2\text{Te}_3$ SL Structures.

Carrier Mobility

The behavior of hole mobility of the p-type $\text{Bi}_2\text{Te}_3/\text{Sb}_2\text{Te}_3$ symmetrical SL structures, as a function of SL dimension is indicated in Figure 2a. We notice that for all the SL periods, the mobility is higher than that of a corresponding $(\text{Bi}_{0.5}\text{Sb}_{0.5})_2\text{Te}_3$ alloy, for similar resistivity values. We note

that even for a SL dimension of $\sim 10 \text{ \AA}$, the mobility of SL structure is better than a comparable solid solution alloy. This is *evidence of avoiding or minimizing alloy scattering of carriers in $\text{Bi}_2\text{Te}_3/\text{Sb}_2\text{Te}_3$ SL's*, relative to the $(\text{Bi}_{0.5}\text{Sb}_{0.5})_2\text{Te}_3$ alloy. However, we do notice a big drop in mobility when the SL dimension falls below the unit cell dimension of $\sim 30 \text{ \AA}$.

The carrier mobility of non-symmetrical SL structures, for a constant Bi_2Te_3 layer thickness of $\sim 15 \text{ \AA}$, is shown as a function of Sb_2Te_3 layer dimension in Figure 2b. We once again note that for a Sb_2Te_3 dimension $> 30 \text{ \AA}$, the mobility of the SL structure exceeds that of a solid solution $(\text{Bi}_{0.5}\text{Sb}_{1.5})\text{Te}_3$ alloy.

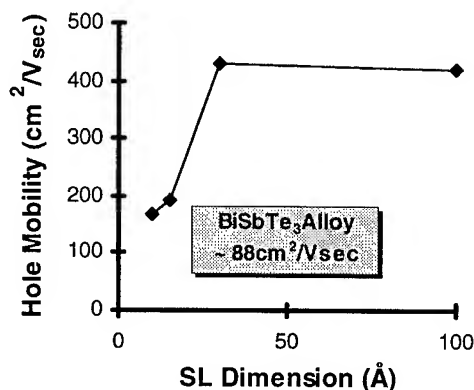


Figure 2a Carrier mobility of symmetrical $\text{Bi}_2\text{Te}_3/\text{Sb}_2\text{Te}_3$ SL structures.

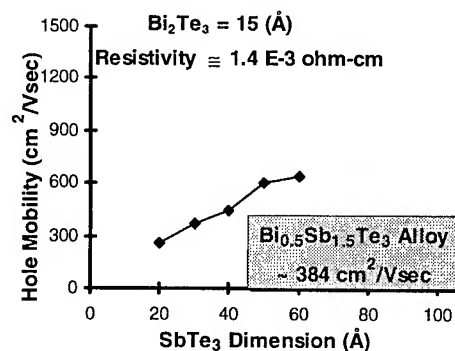


Figure 2b Carrier mobility of non-symmetrical $\text{Bi}_2\text{Te}_3/\text{Sb}_2\text{Te}_3$ SL structures.

Seebeck coefficient

The 300K Seebeck coefficient of the symmetrical and non-symmetrical $\text{Bi}_2\text{Te}_3/\text{Sb}_2\text{Te}_3$ SL structures, as a function of the SL dimension, are shown in Figure 3a and 3b. We see a near 50% increase in Seebeck coefficient with nearly a ten-fold to three-fold reduction in SL dimension, which is relatively small compared to a 100% increase in Seebeck coefficient, in going from $40\text{-}\text{\AA}$ well to $20\text{-}\text{\AA}$ well in the $\text{PbTe}/\text{Pb}_{0.927}\text{Eu}_{0.073}\text{Te}$ system [11]. This can be understood

in terms of the difference in the properties of $\text{Bi}_2\text{Te}_3/\text{Sb}_2\text{Te}_3$ and $\text{PbTe}/\text{Pb}_{0.927}\text{Eu}_{0.073}\text{Te}$ hetero-interfaces.

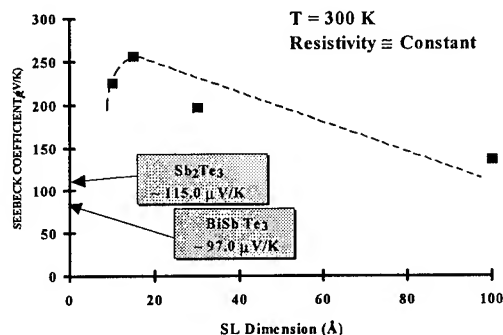


Figure. 3a Variation of the Seebeck coefficient with SL dimension in a symmetrical SL structure.

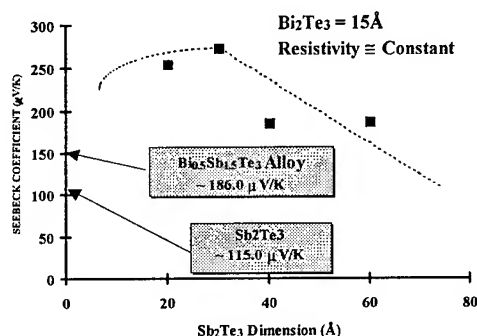


Figure.3b Variation of the Seebeck coefficient with Bi_2Te_3 dimension for a constant Bi_2Te_3 layer thickness of 15 Å.

The bandgap difference between PbTe and $\text{Pb}_{0.927}\text{Eu}_{0.073}\text{Te}$ is about 0.31 eV at 300K. In contrast, the bandgap difference between the Bi_2Te_3 and Sb_2Te_3 is expected to be about 0.08 eV at 300K. The distribution of this small bandgap difference in the $\text{Bi}_2\text{Te}_3/\text{Sb}_2\text{Te}_3$ SL system, between a valence-band offset and a conduction-band offset, has not been measured. However, at this point, we can assume that these band-offsets are expected to provide only marginal quantum-confinement effects at 300 K. This rather weak confinement could explain the relatively slow rise in Seebeck coefficient with SL dimension in the $\text{Bi}_2\text{Te}_3/\text{Sb}_2\text{Te}_3$ SL structures. We also note the eventual drop in Seebeck coefficient with decrease in SL dimension, in the range of ~15 Å to ~10 Å, probably a result of the sharp increase in carrier levels.

The 300K Seebeck coefficient of the non-symmetrical $\text{Bi}_2\text{Te}_3/\text{Sb}_2\text{Te}_3$ SL structures, as a function of the Sb_2Te_3 dimension, is shown in Figure 3b. Once again, we observe

that the Seebeck coefficient increases with a shorter SL dimension.

It is important to note in both Figs. 3a and 3b, the Seebeck coefficients of the short-period symmetrical and non-symmetrical SL structures are higher than that of BiSbTe_3 alloy and a $(\text{Bi}_{0.5}\text{Sb}_{1.5})\text{Te}_3$ alloy films, respectively. This is partly related to the bandstructure differences between the respective SL structure and the corresponding alloy.

The band diagram comparison of a p- BiSbTe_3 alloy and a p-type $\text{Bi}_2\text{Te}_3/\text{Sb}_2\text{Te}_3$ SL is shown in Figure. 4, assuming that the bandgap difference (~0.08 eV) between Bi_2Te_3 and Sb_2Te_3 splits equally between conduction and valence bands. The relation to obtain Seebeck coefficient is given by:

$$\alpha = \frac{k}{e} \left[\frac{\int_{E=E_v}^{\infty} E \sigma(E) dE}{\int_{E=E_v}^{\infty} \sigma(E) dE} - E_f^* \right]$$

We can observe that the dependence of conductivity (σ) on the energy (E) are different in the two cases in Fig. 4. For the same conductivity, the higher mobility in the SL compared to the alloy, leads to lower carrier concentration and therefore lower hole Fermi level (E_f). This potentially leads to a larger Seebeck coefficient for the SL structures.

Power Factor

The effects of improved carrier mobilities and higher Seebeck coefficients, with smaller SL dimension, act together to increase the power factor of both symmetrical and non-symmetrical $\text{Bi}_2\text{Te}_3/\text{Sb}_2\text{Te}_3$ SL structures for short SL dimensions. This is depicted in Figure 5. We note that the power factor of the non-symmetric SL structures are consistently higher than the symmetrical SL's, due to the effect of higher mobilities for the same resistivities. We have observed a best power factor of about 59 $\mu\text{W}/\text{cm}\cdot\text{K}^2$, in a non-symmetrical SL. This is ~50% better than that of a state-of-the-art, p-type, bulk $(\text{Bi}_{0.25}\text{Sb}_{0.75})_2\text{Te}_3$ alloy [12].

Thermal Conductivity Reduction in $\text{Bi}_2\text{Te}_3/\text{Sb}_2\text{Te}_3$ SL Structures

An important objective of our experimental research effort on short-period $\text{Bi}_2\text{Te}_3/\text{Sb}_2\text{Te}_3$ SL structures has been to demonstrate that phonon-scattering at the SL interfaces can

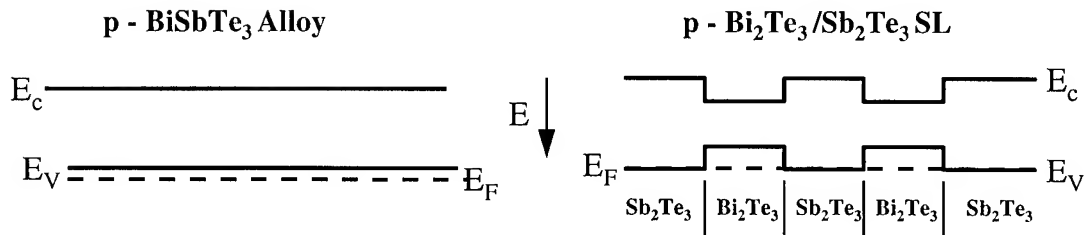


Figure. 4 The band diagrams for the p-BiSbTe₃ alloy and a p-type Bi₂Te₃/Sb₂Te₃ SL.

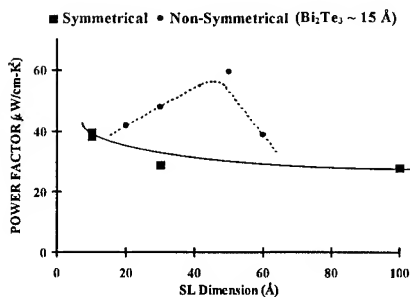


Figure 5 Variation of power factor with SL dimension.

reduce lattice thermal conductivity and then verify if it is indeed possible to obtain values lower than in solid-solution (Bi_{0.25}Sb_{0.75})₂Te₃ alloys [5] from additional phonon-scattering processes unique to periodic structures. For example, in a SL, the minimum phonon energy required to produce an Umklapp process is reduced relative to a bulk alloy. Thus, this study is important to take further advantage of the improved electrical transport and power factor of Bi₂Te₃/Sb₂Te₃ SL structures, in the overall optimization of ZT values.

The 3- ω technique [12] has been used to measure thermal conductivity (λ) of thin-films from an indirect measurement of thermal diffusivity. Essentially, a thin metal strip with four pads to measure current and voltage is deposited on the film surface. The metal strip serves as the heater (by $I^2 R$ heating) and a thermometer because of the temperature-dependent electrical resistance of the strip is related to the thermal conductivity of the thermoelectric material. Thus the thermal conductivity can be related to measured voltages. The application of an ac current (I) with an angular frequency ω causes a $I^2 R$ heating temperature wave of frequency 2ω to diffuse into the substrate. Since the film resistance itself varies with temperature, the resistance oscillation at 2ω multiplied by the excitation current at ω produces a voltage oscillation at 3ω . The 3ω voltage can be conveniently measured by lock-in amplifier techniques.

Figure 6 shows the thermal conductivity data on both symmetrical and non-symmetrical Bi₂Te₃/Sb₂Te₃ SL structures, as a function of the SL dimension. The thermal conductivity values show a fall with shorter SL dimension. We observe an apparent minimum thermal

conductivity when the Bi₂Te₃ or Sb₂Te₃ dimension approaches ~ 30 Å, the unit cell dimension. For these SL dimensions, we obtain a thermal conductivity value, as low as ~ 2.0 mW/cm-K. It is very interesting to note that when the SL dimension is less than 30 Å, the measured thermal conductivity actually increases and tend to approach the measured bulk alloy values, which are also indicated in Fig. 6.

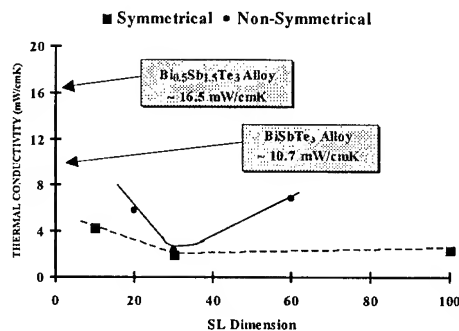


Figure 6 Variation of thermal conductivity with SL dimension.

Comments on Anisotropy of 3 ω -Measured Thermal Conductivities in SL Structures

It is worth noting that the 3 ω -measured values of thermal conductivities for the two alloy samples are approximately equal to the geometric mean of known thermal conductivities along the "a" and "c" directions in bulk crystals [13]. Thus the 3 ω -thermal conductivity method, at least for the frequencies used in this study and therefore being affected by the spread of the thermal wave in the direction parallel to the SL interfaces as well, is not likely to be dominated solely by the thermal conductivity perpendicular to the SL interfaces. This is further apparent in the fact that the 3 ω -measured thermal conductivities in GaAs/Al_{0.8}Ga_{0.2}As SL (dimension ~ 100 Å) are geometric mean of the in-plane and perpendicular thermal conductivity of a GaAs/AlAs SL [14]. A recent measurement [15] of a more-likely through-thickness thermal conductivity of a GaAs/AlAs SL for about the same SL dimension is a factor of 2.3 lower than either the 3 ω measured value or the in-plane value.

ZT in $\text{Bi}_2\text{Te}_3/\text{Sb}_2\text{Te}_3$ SL Structures

The power factors in $\text{Bi}_2\text{Te}_3/\text{Sb}_2\text{Te}_3$ superlattice structures are clearly measured in a direction parallel to the superlattice interfaces. In contrast, the 3ω -measured thermal conductivity values could be dominated by the component perpendicular to the SL interfaces. This makes the determination of ZT values of these structures not straightforward. However, we can estimate the possible thermal conductivity values in $\text{Bi}_2\text{Te}_3/\text{Sb}_2\text{Te}_3$ SL structures parallel to the superlattice interfaces based on some recent comparative measurement [16] of thermal conductivity in GaAs/AlAs superlattice structures, both perpendicular and parallel to the superlattice interfaces. This work suggests that, in a worst-case scenario, the thermal conductivity parallel to superlattice interfaces could be higher than that of perpendicular to the interfaces by a factor of about 2.6. Thus, we can estimate that the thermal conductivities of the $\text{Bi}_2\text{Te}_3/\text{Sb}_2\text{Te}_3$ superlattices are probably higher in the plane of the superlattice-interfaces by this ratio. *This leads us to estimate a three-dimensional ZT_{3D} of around 1.65, for some of the best $\text{Bi}_2\text{Te}_3/\text{Sb}_2\text{Te}_3$ superlattice samples in the direction parallel to the superlattice interfaces at 300K (Fig. 7).* The estimation of ZT_{3D} for the superlattices, in the direction perpendicular to the interfaces, is much more complicated and will require the measurement of Seebeck coefficient and conductivity in this direction; such an effort is in progress.

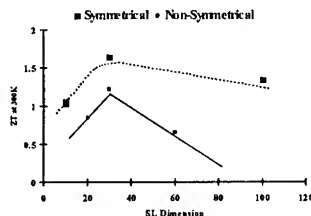


Figure. 7 Variation of ZT at 300K with SL dimension.

Summary

Thermoelectric properties of p-type $\text{Bi}_2\text{Te}_3/\text{Sb}_2\text{Te}_3$ SL thin-films grown by OMVPE are described. It is observed that the carrier mobility, Seebeck coefficient and power factor of the $\text{Bi}_2\text{Te}_3/\text{Sb}_2\text{Te}_3$ SL structures are better than that of p-type $\text{Bi}_{1-x}\text{Sb}_x\text{Te}_3$ alloys, with similar bandgap and electrical resistivity. The improvement in carrier mobility is attributed to avoiding or minimizing alloy scattering of carriers with SL structures while the enhanced Seebeck coefficient is related to the bandstructure difference between the alloy and the SL structures. Initial measurements indicate that power factor improvement of ~50%, over corresponding alloys, can be obtained in SL structures. We have observed that the thermal conductivity of the SL structures are a factor of four to seven smaller with respect to the alloys. The electrical conductivity and Seebeck coefficient are measured in the plane of the SL

structures, while the 3ω -measured thermal conductivity can potentially be dominated by a component perpendicular to the SL structures. Hence, the figure-of-merit (ZT) values are estimated with a correction for potential anisotropy of thermal conductivity. Including this correction, the estimated ZT at 300K for some SL structures are in the range of 1.22 to 1.67.

Acknowledgements

The work described in this paper was performed with the support of Office of Naval Research. The encouragement and support of Dr. John Pazik is gratefully acknowledged. We would also like to acknowledge the discussions on measurements with Dr. Ted Harman of MIT Lincoln Laboratories.

References

1. T.E. Whall and E.H. C. Parker, Proc. of 1st Euro. Conf. on Thermoelectrics, 51 (1987).
2. 1st National Thermogenic Cooler Conference, Sept. 17, 1992, Fort Belvoir, VA.
3. L.D. Hicks and M.S. Dresselhaus, Proceedings of the 1st National Thermogenic Cooler Workshop, Sept. 17, 1992, Fort Belvoir, VA.
4. T.C. Harman, Proceedings of at the 1st National Thermogenic Cooler Workshop, Sept. 17, 1992, Fort Belvoir, VA.
5. R. Venkatasubramanian, Proceedings of the 1st National Thermogenic Coler Workshop, Sept. 17, 1992, Fort Belvoir, VA.
6. D.A. Broido and T.L. Reinecke, Appl. Phys. Lett., **67**, 1170 (1995).
7. J.O. Sofo and G.D. Mahan, Proc. of the 13th International Conf. on Thermoelectrics, AIP Conf. Proc., **316**, 239 (1995).
8. R. Venkatasubramanian, T.S. Colpitts, M. Mantini and D. Malta, Proc. of 14th International Conf. on Thermoelectrics, St. Petersburg, 490 (1995).
9. A. Mzerd, D. Sayah, J.C. Tedenac, and A. Boyer, J. Cryst. Growth, **140**, 365 (1994).
10. R. Venkatasubramanian and T.S. Colpitts, To be presented at the VIII International Conf. on OMVPE, Cardiff, England, June 1996.
11. T. Harman, Proc. of ARPA Thermoelectric Materials Workshop, Arlington, VA, Nov. 1995.
12. D.G. Cahill, M. Katiyar, and J.R. Abelson, Phys. Rev. B, **50**, 6077 (1994).
13. H. Scherrer and S. Scherrer, Proc. of the 12th International Conf. on Thermoelectrics, Yokohama, H. Mastubara Ed., 90 (1994).
14. T. Yao, Appl. Phys. Lett., **51**, 1798 (1987).
15. W.S. Capinski and H.J. Maris, Presented at the 1996 Spring Meeting of Americal Physical Society, Symposium on Transport in Superlattices.
16. G. Chen, C.L. Tien, X. Wu, and J.S. Smith, J. Heat Transfer, **116**, 325 (1994).

Synthesis and Evaluation of Thermoelectric Multilayer Films

Andrew V. Wagner, Ronald J. Foreman, Leslie J. Summers,
Troy W. Barbee Jr., and Joseph C. Farmer

*Chemistry and Materials Science Department
Lawrence Livermore National Laboratory
7000 East Avenue Livermore, CA 94550 USA*

Abstract

The deposition of compositionally-modulated $(\text{Bi}_{1-x}\text{Sb}_x)_2(\text{Te}_{1-y}\text{Se}_y)_3$ thermoelectric multilayer films by magnetron sputtering has been demonstrated. Structures with a period of 140\AA are shown to be stable to interdiffusion at the high deposition temperatures necessary for growth of single-layer crystalline films with $ZT > 0.5$. These multilayers are of the correct dimension to exhibit the electronic properties of quantum well structures. Furthermore it is shown that the Seebeck coefficient of the films is not degraded by the presence of this multilayer structure. It may be possible to synthesize a multilayer thermoelectric material with enhanced ZT by maximizing the barrier height through optimization of the composition of the barrier.

Introduction

While thermoelectrics are used in countless temperature sensing applications, their use for electrical power generation or cooling is limited by their relatively low efficiency compared to mechanical heat engines and CFC/HCFC based refrigeration cycles. Theoretical predictions by Hicks and Dresselhaus suggest that using 2D quantum confinement of the charge carriers in multilayer thermoelectric materials may lead to a substantial increase in the figure of merit (Z).^[1-2] Enhanced thermoelectric properties in quantum well (QW) layers have been recently demonstrated with samples synthesized with MBE.^[3] However, to make thermoelectric multilayer materials commercially viable, it is essential to extend the MBE work and grow QW materials with a high Z by an established high deposition rate technique like sputtering.^[4,5] Expertise in the field of multilayer deposition by sputtering has been developed at Lawrence Livermore National Laboratory through extensive work on multilayer x-ray optics and other materials^[6-8].

In this work we demonstrate the effectiveness of magnetron sputtering to synthesize thermoelectric multilayer materials with potential for 2D QW behavior. Compositionally-modulated $(\text{Bi}_{1-x}\text{Sb}_x)_2(\text{Te}_{1-y}\text{Se}_y)_3$ multilayer films have been chosen for this investigation for several reasons. First, these materials have the best thermoelectric properties at room temperature. Thus, any increase in performance which can be achieved will produce a superior technological material. Second, the bandgap can be varied by changes in the Bi:Sb and Te:Se ratios without introducing any other elements. We show that the inevitable interdiffusion

between layers does not degrade the Seebeck coefficient by excessive doping of the QW material.

Experimental procedures

Deposition by magnetron sputtering:

Three characteristics of the sputtering process have enabled the deposition of multilayer thermoelectric films with abrupt interfaces. First, sputtering gives steady deposition rates which allow synthesis of multilayer samples with individual layers of uniform thickness. Second, it allows multicomponent materials to be deposited from a single source without many of the compositional shifts associated with thermal evaporation techniques. Third, the argon ions from the sputtering gas can be used to bombard the growing film at low energies by biasing the substrates. This ion bombardment can be used to change the growth morphology by imparting extra energy to the growth surface. Unlike increases in temperature, which also increase surface mobility, low energy ion bombardment does not cause interdiffusion of the layers which have already been deposited.

The films discussed here were all synthesized in a system originally designed to fabricate multilayer X-ray optics. The system is cryogenically pumped and usually achieves base pressures of approximately 1×10^{-7} torr prior to sputtering. Substrates are mounted on an electrically-isolated heated stage which rotates below two magnetron sputtering guns. The sputter sources are usually operated at an argon pressure around 0.016 torr and a power of 10 watts to give deposition rates of about 5 \AA/s directly under the gun. Multilayer samples are synthesized by alternately sweeping the substrates under the magnetron sputter sources, one depositing a conduction layer and the other depositing a barrier layer. Single-layer films are made by using a single source and either sweeping under the source or positioning the substrate directly below the source. A computer controls the position and slew rate of the stage, as well as the sources allowing automated deposition. Temperature, gas pressure, and gun parameters are logged by the computer as a function of time.

Film property measurement:

When measuring the thermoelectric properties of thin films, it is very important to make sure that substrate interference is eliminated. For this reason we have chosen to deposit all of our films on insulating substrates so that there are no possible contributions to the measured electrical properties from the substrate. The Seebeck coefficient is

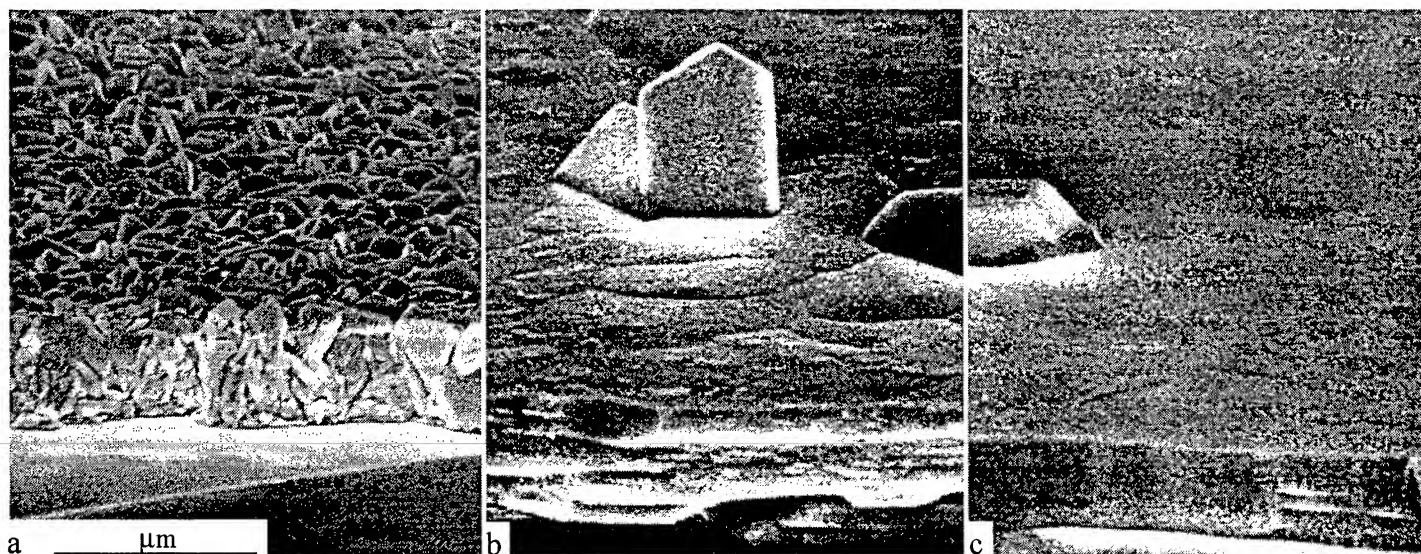


Figure 1. Effect of deposition conditions on film growth. SEM micrographs of a series of films deposited on mica substrates: a) Rough growth morphology of a film deposited at 300°C; b) film grown at 400°C. c) an isolated crystallite in an otherwise highly textured film. Deposition started at 340°C to reduce nucleation of non-textured grains while a 380°C growth temperature leads to the best thermoelectric properties.

measured by bridging the sample between two stages which are independently temperature controlled from the boiling point of liquid nitrogen 77 K to about 700 K. K-type thermocouples are attached to both ends of the sample with electrically-conductive silver paint. The thermocouple leads are used to measure the temperature of each end of the film as well as measure the potential generated between the ends of the film by the temperature gradient. The Seebeck coefficient of the thermocouple wires, which is well known can then be used to compute the absolute Seebeck coefficient of the film. Typically a temperature gradient of $\sim 15^\circ\text{C}$ is maintained by the data logging and control computer as the samples are heated through the desired temperature range. Details of this technique are described in earlier publications^[9,10].

Resistivity was measured at room temperature with a digital ohm meter. These measurements were confirmed by using an AC version of the van der Pauw technique. A two probe technique was used to measure resistivity as a function of temperature from 77°K to about 700°K. A square bipolar current pulse was passed through the sample, and a lock-in amplifier was used to measure the voltage drop between two independent probes.^[9,10]

Single-crystal mica substrates were chosen for these experiments. Although mica has the hexagonal in-plane symmetry of the films, they are not lattice matched. Mica is a particularly useful substrate since it can be acquired as large areas which are atomically smooth. The ability to work with large area films deposited on mica increases the reliability of our measurements. The characteristics of thin mica sheets which are strong, flexible and electrically insulating make it an ideal material for thin-film device applications.

The thin mica substrates do not make good thermal contact with the stage making them difficult to heat. This problem has been overcome by the use of a "hot walled" environment developed to maintain the stoichiometry of the

film. Without heating the shields around the sample, the temperature of the substrates would be in radiative equilibrium at a temperature between the temperatures of the stage and chamber. Finally, the mica substrates can withstand the temperatures required for growth of high-quality films.

Results

Single layer films:

The first step in the development of multilayer films is to deposit flat high electrical quality, single-layer films of the component materials. $(\text{Bi}_{0.25}\text{Sb}_{0.75})_2\text{Te}_3$ was used for the QW. This material was chosen so that a small amount of interdiffusion from the barrier material $(\text{Bi}_{0.25}\text{Sb}_{0.75})_2(\text{Te}_{0.5}\text{Se}_{0.5})_3$ the optimum p-type bulk material will be achieved in the QW. The primary issue arising in the deposition of the $(\text{Bi}_{1-x}\text{Sb}_x)_2(\text{Te}_{1-y}\text{Se}_y)_3$ system is maintaining the ratio of $(\text{Bi}+\text{Sb}):(\text{Te}+\text{Se})$. Slight shifts in composition change the doping and thus affect the electronic properties. In vapor deposition this is compounded by the different vapor pressures of the elements. Since Te has the highest vapor pressure, it is re-evaporated from the growing film when depositing on a hot substrate^[11]. By increasing the Te concentration in the QW sputtering target to a composition of $(\text{Bi}_{1-x}\text{Sb}_x)_2\text{Te}_4$, an overpressure of Te can be achieved. This Te overpressure is found to increase the ZT achievable in the quantum well material by allowing higher temperature deposition. An excess Te barrier target has not yet been tried. To further enhance this overpressure a "hot wall" technique has been developed. The sputtering gun and the heated substrate table are surrounded by a heated shield. The best results have been achieved when the shield temperature is from 30 to 60°C above that of the substrates.

An extensive series of samples were synthesized in order to optimize sputtering conditions both in terms of morphology and electronic properties. The effect of temperature and deposition parameters on film morphology can be seen in

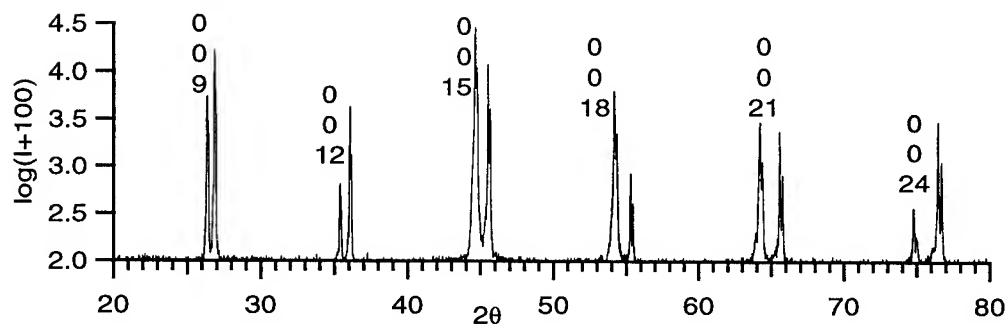


Figure 2. X-ray θ - 2θ diffraction scan of the single layer film shown in figure 1c illustrating the (003) family of peaks from the $(\text{Bi}_{0.25}\text{Sb}_{0.75})_2\text{Te}_3$ film. All the other peaks are mica substrate peaks showing that the film is extremely well textured.

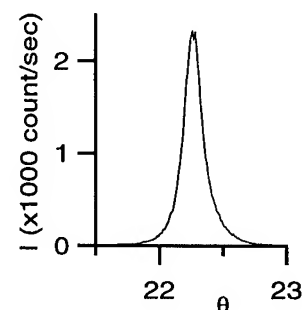


Figure 3 X-ray rocking curve taken by scanning θ with the detector set at the 2θ condition for the (0,0,15) peak. FWHM 0.15° .

figure 1. The SEM micrograph shown in figure 1a illustrates one of our first films deposited at a stage temperature of 300°C and substrate bias of -25 V . This deposition was without an excess Te target or the "hot walled" environment. The resulting rough morphology is not suitable for multilayer growth. The micrograph shown in figure 1b clearly demonstrates the improvement caused by increased deposition temperature and the "hot walled" environment. This sample was deposited at approximately 400°C in the hot walled environment with an excess Te target. The bias was lowered to -15 V and only used for the first 30 seconds of deposition. Figure 1c illustrates improved film morphology achieved by beginning the deposition at a reduced temperature. This film was deposited under the same conditions as the film shown in 1b except the deposition was started at 350°C and raised to 380°C during deposition. The sputter deposition rate was also reduce by a factor of four.

Crystal perfection was investigated using x-ray diffraction. The films are typically highly textured with the c axis along the growth direction. In a typical x-ray diffraction scan only the (003) family of peaks can be seen along with the

mica substrate peaks (figure 2). X-ray rocking curves confirm that deviations of the c axis from the growth direction are small (figure 3).

Despite the large variation in the individual electronic properties caused by variation in doping, the overall performance of the films measured by ZT (assuming a thermal conductivity of bulk material of the same resistivity $0.014\text{ W/cm}^2\text{K}$) was not nearly as variable. Increasing the deposition temperature up to about 380°C was found to improve the ZT of the films. It was not possible to control Te losses and morphology sufficiently above this temperature. Films with $\text{ZT} > 0.5$ at room temperature can consistently be grown, with values for the best films as high as 0.6. Although these values are below the value of $\text{ZT} \sim 1$ for optimized bulk material this may be partly a result of the assumed thermal conductivity. Phonon scattering at the grain boundaries in the films may reduce the thermal conductivity below that of bulk material, thus helping enhance ZT.

Multilayer experiments:

Compositionally modulated $(\text{Bi}_{1-x}\text{Sb}_x)_2(\text{Te}_{1-y}\text{Se}_y)_3$ structures have been deposited. Their structure was investigated both by x-ray diffraction and TEM. The x-ray

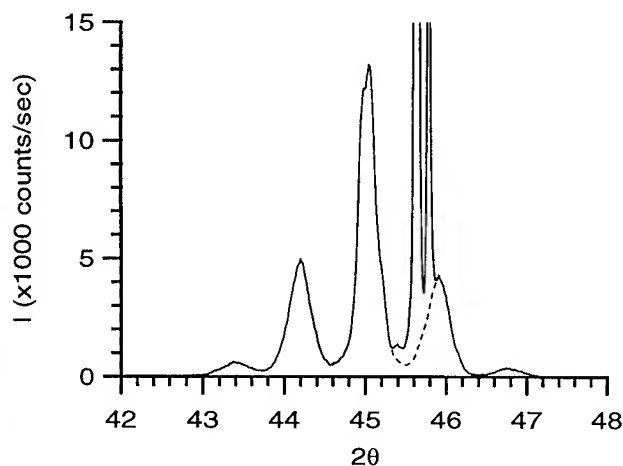


Figure 4. X-ray diffraction scan of a multilayer film. The peak at 45° is the (0,0,15) peak from the film. The mica substrate peak goes off scale to the right. The other peaks are the multilayer satellite peaks showing that the film is compositionally modulated with a period of 140 \AA . The dotted line is to aid the eye showing the mica substrate reflections for Cu K_β , $K_{\alpha 1}$ and $K_{\alpha 2}$ from left to right.

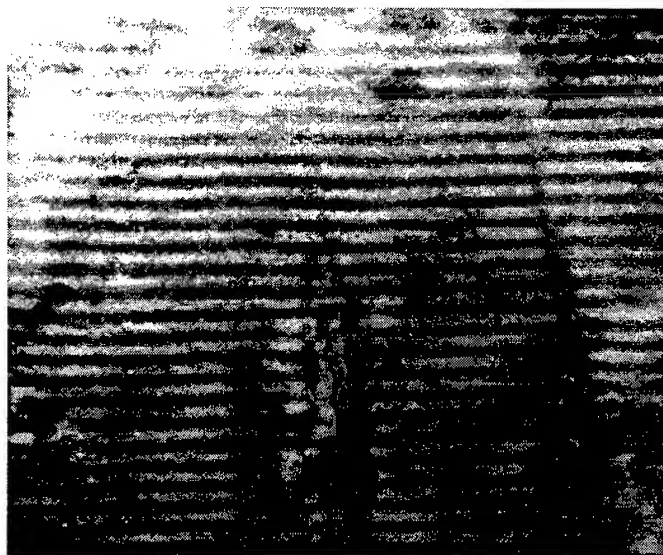


Figure 5. Bright field TEM micrograph of the 140 \AA period multilayer film. Diffraction contrast with a Fresnel defocus condition clearly shows the layering.

		Seebeck	resistivity	ZT
		$\mu\text{V/K}$	$10^{-3}\Omega\text{cm}$	
Well	$\text{Bi}_{0.5}\text{Sb}_{1.5}\text{Te}_3$	118	0.53	0.56
Barrier	$\text{Bi}_{0.5}\text{Sb}_{1.5}\text{Te}_{1.5}\text{Se}_{1.5}$	210	5.30	0.18
Multilayer		140	1.40	0.30

Table 1 Measured electrical properties of single-layer and multilayer films at room temperature. The dimensionless figure of merit was calculated assuming a thermal conductivity of $0.014 \text{ W/cm}^2\text{K}$.

diffraction scan of a 140\AA film is shown in figure 4. The intense satellite peaks on either side of the (0,0,15) peak verify the sample is a multilayer, and allows the accurate determination of the bilayer repeat length from the satellite peak separation. These satellite peaks and the main peak width prove that the layers grew epitaxially on each other. Films with bilayer repeat length as little as 50\AA have been deposited and show high-angle x-ray diffraction satellite peaks.

TEM allows the layered structure to be visualized, and verifies that the barrier and well are approximately of equal thickness (figure 5). Although grain boundaries can be seen, selected area diffraction suggests that most of the crystallites have about the same orientation in plane as well as the extremely strong out of plane orientation also observed by x-ray diffraction. This in-plane orientation suggests that during the nucleation phase of film growth there was an epitaxial relation with the mica substrate. The epitaxial relation between the layers is evident both at the resolution shown here and in high resolution TEM images where the lattice planes can be traced across the interface.

Single-layer QW and barrier films were deposited and characterized for comparison with multilayer results. Figure 6 shows the Seebeck coefficient for these films as a function of temperature. The barrier material was found to have a relatively high Seebeck coefficient. Although the barrier material has a lower ZT than the well material, it will also make a positive contribution to the ZT of the multilayer. The Seebeck coefficient of the multilayer is also shown and lies between that

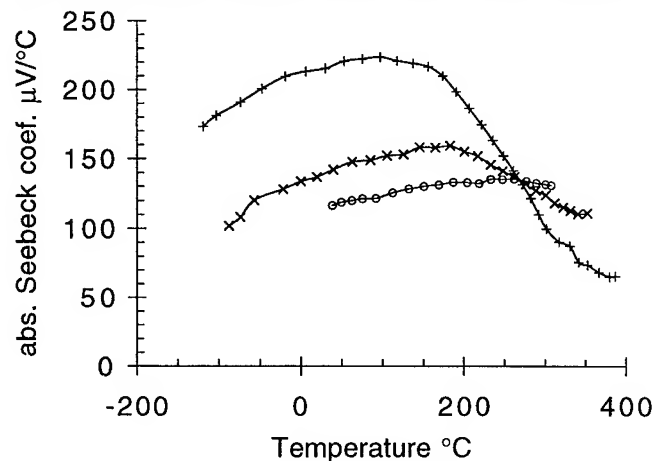


Figure 6. Absolute Seebeck coefficient as a function of temperature. (o) Single layer film of material used as the quantum well; (+) Single layer film of the barrier material; (x) with a period of 140\AA .

of the QW and barrier materials.

The resistance and dimensions were measured for these three samples. The value of the resistivity was calculated and is given in table 1. The temperature dependence of the resistivity is shown in figure 7. The resistivity of the multilayer was found to be slightly less than half that of the QW material. Making a direct comparison here is difficult since the different materials could have had different doping levels. A more informative comparison is that of ZT for each of the films. ZT for the multilayer is found to be approximately the average of the ZT of the two component layers. No evidence of an increase in ZT has been found for this combination of QW and barrier if one assumes that the thermal conductivity of the multilayer is the same as that of the components.

Discussion

Interdiffusion of the layers of multilayer samples has been found to be an important experimental problem in many of the proposed thermoelectric multilayer systems. We have explored $\text{Bi}_{0.9}\text{Sb}_{0.1}/\text{PbTe}_{0.8}\text{Se}_{0.2}$ and $\text{Bi}_{0.9}\text{Sb}_{0.1}/\text{Bi}_2\text{Te}_3$ films.^[9] In both cases it was found that small amounts of interdiffusion of electrically active species can drastically change dopant concentration and adversely affect thermoelectric properties such as the Seebeck coefficient. Here we have demonstrated that in the compositionally-modulated $(\text{Bi}_{1-x}\text{Sb}_x)_2(\text{Te}_{1-y}\text{Se}_y)_3$ system interdiffusion does not degrade the Seebeck coefficient of the films. With the experimental demonstration that thermoelectric properties of material can be enhanced by quantum confinement,^[3] the next step is showing an enhancement of performance in a system where the degradation caused by the barrier material does not outweigh the benefits achieved by quantum confinement of the charge carriers. The $(\text{Bi}_{1-x}\text{Sb}_x)_2(\text{Te}_{1-y}\text{Se}_y)_3$ system shows great promise as such a system.

The thermal conductivity in the barrier layer dictates that the barrier width must be kept as thin as possible so that losses in the barrier layer do not exceed gains made by quantum confinement. To achieve confinement with the

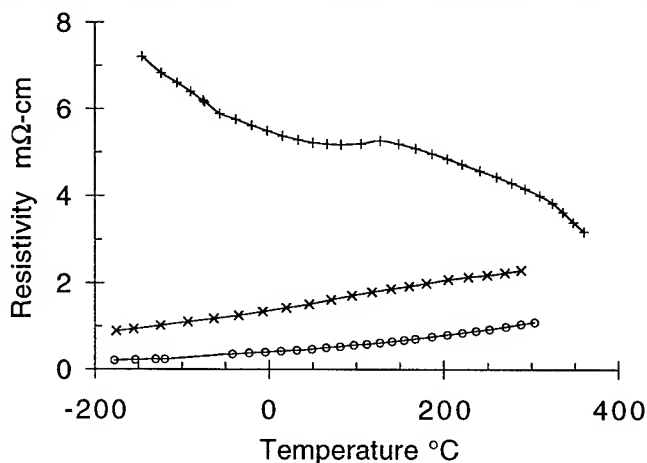


Figure 7. Resistivity as a function of temperature. (o) Single layer film of material used as the quantum well; (+) Single layer film of the barrier material; (x) Multilayer with a period of 140\AA .

thinnest possible barrier layer, a composition must be selected with the greatest possible barrier height. The failure to achieve enhanced thermoelectric properties in the measured film is probably due to insufficient barrier height. Similar observations were made during our investigation on the Bi/Bi_{0.86}Sb_{0.14} multilayer system.^[10] Although high-quality layered structures were produced, the small bandgap of the Bi_{0.86}Sb_{0.14} was not sufficient to confine the charge carriers in the Bi layer and no improvement in the thermoelectric properties was observed. Dopant and impurity states in the bandgap of the barrier material may also be degrading the structure. Efforts to optimize the barrier material, both by changing composition and by reducing states in the bandgap are continuing. Confinement with a small barrier height could also be achieved by making wider barrier layers. Characterizing the mobility of the charge carriers as a function of barrier width should help us explore these questions.

The bandgap of these materials must be studied as a function of composition over the entire phase field in order for the optimal barrier material to be determined. Sputter deposition combined with IR spectroscopy will be a powerful technique for exploring the effect of stoichiometry on the bandgap.

Along with the potential of using the multilayer structure to alter the electronic properties of the film, layering may also effect the thermal conductivity of the films. In this work we have assumed the thermal conductivity of the films to be that of bulk (Bi_{0.25}Sb_{0.75})₂(Te_{0.95}Se_{0.05})₃ with the same resistivity. It is quite possible that the multilayer structure will decrease the thermal conductivity of the films by scattering phonons. This effect would increase the ZT of the thermoelectric films. If this effect is large, it is possible that multilayer films are already superior to bulk thermoelectric materials. Techniques for accurately measuring the in-plane thermal conductivity of these thin films are currently being explored.

Conclusions

We have shown that sputtering can be used to deposit high quality (Bi_{1-x}Sb_x)₂(Te_{1-y}Se_y)₃ material. We have found that the hot walled environment and excess Te target material both are important for the synthesis of high quality films. The deposition temperature was critical. Deposition must start at a relatively low temperature to achieve wetting of the mica substrate, and then increase to provide the highest quality film growth.

We have shown that (Bi_{1-x}Sb_x)₂(Te_{1-y}Se_y)₃ multilayers are stable enough that deposition temperatures of 380°C can be used so that high quality material can be deposited. ZT of the multilayer structure shown here with a period of 140Å and approximately equal layer thickness is found to be an average of the value for the component materials.

Sputtering has been shown to be a powerful technique for depositing thermoelectric materials. Not only have we shown it to be a valuable laboratory research tool, but the ability to scale the process up for production makes it particularly attractive. Large-area, high-rate sputter deposition already plays

an important role in industry. Once it has been demonstrated that attractive thermoelectric materials can be produced by sputtering in the laboratory, the technology, equipment and trained manpower already exist to make the transition to industry.

Acknowledgments

Funding for this project was provided by the United States Department of Energy, Office of Basic Energy Sciences (OBES), W. Polansky, program manager. We gratefully acknowledge D. Makowiecki for use of the sputtering chamber. This work was done under the auspices of the U.S. DOE by Lawrence Livermore National Laboratory under Contract No. W-7405-Eng-48.

References

- [1] L.D. Hicks, M.S. Dresselhaus, "Effect of Quantum-Well Structures on the Thermoelectric Figure of Merit," *Phys. Rev. B*, **47**, 12727-12731, 1993.
- [2] L.D. Hicks, M.S. Dresselhaus, "Use of Quantum-Well Superlattices to Obtain a High Figure of Merit from Nonconventional Thermoelectric Materials," *Appl. Phys. Lett.* **63**, 3230-3232, 1993.
- [3] L.D. Hicks, T.C. Harman, X. Sun, and M.S. Dresselhaus, "Experimental Study of the Effect of Quantum-Well Structures on the Thermoelectric Figure of Merit," *Phys. Rev. B Rapid* **53**, 1996 (in press).
- [4] J.C. Farmer, T.W. Barbee Jr., G.C. Chapline Jr., R.J. Foreman, L.J. Summers, M.S. Dresselhaus, and L.D. Hicks, "Sputter Deposition of Multilayer Thermoelectric Films: An Approach to the Fabrication of Two-Dimensional Quantum Wells," *Proc. of the XIII International Conference on Thermoelectrics*, Kansas City, Missouri 217-225, 1994.
- [5] J.C. Farmer, T.W. Barbee Jr., R.J. Foreman, L.J. Summers, "Deposition and Evaluation of Multilayer Thermoelectric Films," *Proc. Symp. on Microstructures and Microfabricated Systems, 185th Electrochem. Soc. Meeting*, San Francisco, CA. **94-14**, 231-242, 1994.
- [6] T.W. Barbee, Jr., "Multilayer Synthesis by Physical Vapor Deposition," in *Synthetic Modulated Structures*, ed. L. Chang and B.C. Giessen, Academic Press, New York, 313-337, 1985.
- [7] T.W. Barbee, Jr. and D.L. Keith, "Synthesis of Metastable Materials by Sputter Deposition Techniques," *Proc. of the Fall Meeting of the Metallurgical Society of AIME*, Pittsburgh, PA, October 5-9, 1980.
- [8] T.W. Barbee, Jr., "Multilayer Optics for the Soft X-ray and Extreme Ultra-Violet," *Physica Scripta*, **T31**, 147-53, 1990.
- [9] A.V. Wagner, R.J. Foreman, L.J. Summers, T.W. Barbee, Jr., J.C. Farmer, "Multilayer Thermoelectric Films: A Strategy for the Enhancement of ZT," *Proc. 30th Intersociety Energy Conversion Engineering Conference*, Orlando, Florida, **3**, 87-92, 1995.
- [10] A.V. Wagner, R.J. Foreman, L.J. Summers, T.W. Barbee, Jr., J.C. Farmer, "Multilayer Thin Film Thermoelectrics Produced by Sputtering," *Proc. of the XIV International Conference on Thermoelectrics*, St. Petersburg, Russia, 283-287 1995.
- [11] H. Noro, K. Sato, H. Kagechika, "The Thermoelectric Properties and Crystallography of Bi-Sb-Te-Se Thin Films Grown by Ion Beam Sputtering," *Journal of Applied Physics*, **73**, 1252-1260 1993.

Thermoelectric Figure of Merit of Si-Ge Multilayered Thin Films

Atsushi Yamamoto and Toshitaka Ohta

Electrotechnical Laboratory, Umezono 1-1-4, Tsukuba, Ibaraki 305, Japan

Abstract

The electrical conductivity σ , the Seebeck coefficient α , the thermal conductivity κ and the figure of merit ZT ($Z = \sigma \alpha^2 / \kappa$) were calculated theoretically for multilayered thin film with quantum wells (QWs) made of Si, $\text{Si}_{70}\text{Ge}_{30}$ and silicide thermoelectric materials. Two-dimensional transport model for single band semiconductor was applied to these materials. As results of the calculation it is found that carrier confinement by QWs mainly have effects on increasing the carrier energy and on shifting optimizing point of power factor $\sigma \alpha^2$. The calculated figure of merit for modulated doping $\text{Si}_{70}\text{Ge}_{30}$ QWs was the same as that of bulk material at 300K. Modulated doping silicide QWs had larger figure of merit than that of $\text{Si}_{70}\text{Ge}_{30}$ QWs.

Introduction

The thermoelectric figure of merit Z is a measure of the quality of thermoelectric material and is defined as

$$Z = \frac{\sigma \alpha^2}{\kappa} \quad (1)$$

where σ is the electrical conductivity, α is the Seebeck coefficient, κ is the thermal conductivity. A good thermoelectric material should have a large Seebeck coefficient, a large electrical conductivity and a small thermal conductivity. Z has a unit of inversed temperature.

Thermoelectric materials convert thermal energy into electrical energy at the efficiency of

$$\eta = \frac{T_H - T_L}{T_H} \cdot \frac{\sqrt{1+ZT} - 1}{\sqrt{1+ZT} + T_L/T_H} \quad (2)$$

where T_H and T_L are the temperatures of hot side and cold side junction of thermoelectric materials. Thus Z contributes to the efficiency in the form of ZT , where T is the absolute

temperature. ZT is called the dimensionless figure of merit. The key to success in thermoelectric applications is to find out materials with high ZT values. The formula of ZT is as follows.

$$ZT = \frac{\sigma \alpha^2 T}{\kappa} \quad (3)$$

A conventional approach to enhancing ZT is introducing defects into the material. Formation of solid solution of same-type semiconductor⁽¹⁾, formation of fine grain⁽²⁾, introducing micro-inclusions⁽³⁾ into the material and so on are effective to scatter phonon. Thus the lattice thermal conductivity κ is reduced. Since charge carriers are not affected very much by the defects, this approach enhances the ratio σ/κ in equation (3)

Another approach to enhancing ZT is to increase the power factor $\sigma \alpha^2$. Because the values of electrical conductivity σ and Seebeck coefficient α are determined by the charge-carrier energy spectrum, there is a great possibility to optimize $\sigma \alpha^2$ by changing the spectrum. It can be achieved by nano-structural materials and materials having different scattering mechanism of charge carrier. Several theoretical estimations to verify these strategies have been made, such as an effect of increased carrier density⁽⁴⁾, an effect of energy filtering^(5,6) by using a superlattice structure and an effect of a quantum-well (QW) structure as shown in Fig. 1. Electrical carriers which energy levels are lower than the barrier height will be confined in the QW and move in the direction of parallel to the interface of the layers as two-dimensional carrier gas. A QW and two-dimensional carrier gas can also be realized by modulated doping. As shown in Fig.1 (b), distorted energy band with alternate doping can confine the carriers.

In this paper we consider three types of QWs. Type I is made of $\text{Si}_{70}\text{Ge}_{30}$ QWs and barrier layers such as silicon and 3H-SiC which have wider bandgap than $\text{Si}_{70}\text{Ge}_{30}$. Type II is made of

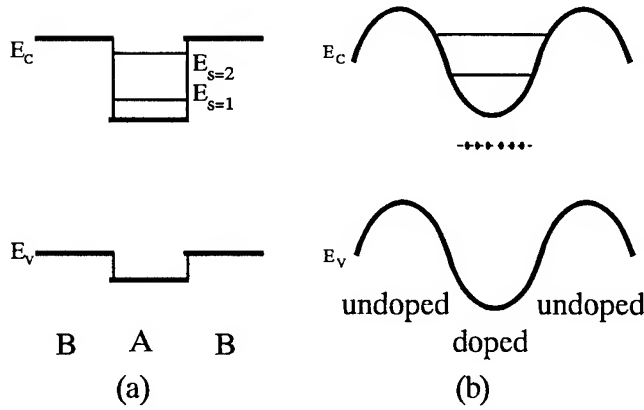


Fig. 1 A band profile Quantum Well : *TYPE I* : A/B heteroepitaxial SLS (a). *TYPE II* : Modulated Doping SLS (SiGe, b), *TYPE III* : Modulated Doping SLS (Silicides, b)

Si₇₀Ge₃₀ QWs and Si₇₀Ge₃₀ barrier layers by using modulated doping. In type III QWs are made of metal silicides, Ru₂Si₃, Mg₂(Si,Ge), CrSi₂ and Fe₂Si which are reported as good thermoelectric materials⁽⁷⁾. The barriers for them are made of the same materials and modulated doping is assumed. The purpose of this study is to evaluate the thermoelectric properties of the three types of QW structured films by using the following calculation model.

Calculation Model

In the calculations for the transport properties, we employed a single band model summarized in the paper by Hicks and Dresselhaus⁽⁴⁾. For an intrinsic semiconductor we should take into account the contributions from valence band and from conduction band because there are the same number of charge carriers in two bands. Since the semiconductor considered here is heavily doped one, the assumption of single band is consistent in the extrinsic region.

Bulk material

The equations used in the calculation of σ , α and κ are basically derived from semiclassical theory of conduction in solid⁽⁸⁾. Assuming the parabolic band, the dispersion relation of charge carrier is expressed as follows.

$$E(k_x, k_y, k_z) = \frac{\hbar^2 k_x^2}{2m_x} + \frac{\hbar^2 k_y^2}{2m_y} + \frac{\hbar^2 k_z^2}{2m_z} \quad (4)$$

where m_x , m_y , and m_z are density of state effective mass component of the carrier. For electrical and thermal conduction along x direction, we obtain

$$\sigma = \frac{1}{2\pi^2} \left(\frac{2k_B T}{\hbar^2} \right)^{3/2} (m_x m_y m_z)^{1/2} F_{1/2} e \mu_x \quad (5)$$

$$\alpha = - \frac{k_B}{e} \left(\frac{5F_{3/2}}{3F_{1/2}} - \zeta^* \right) \quad (6)$$

$$\kappa_e = \frac{\tau \hbar^2}{6\pi^2} \left(\frac{2k_B T}{\hbar^2} \right)^{5/2} \left(\frac{m_y m_z}{m_x} \right)^{1/2} \times k_B \left(\frac{7}{2} F_{5/2} - \frac{25 F_{1/2}^2}{6 F_{1/2}} \right) \quad (7)$$

where F_i is fermi integral expressed as

$$F_i = \int_0^\infty \frac{x^i dx}{\exp(x - \zeta^*)} \quad (8)$$

$\zeta^* = \zeta/k_B T$, τ , μ_x are the reduced chemical potential, relaxation time and mobility of charge carrier. Thermal conductivity κ is expressed as summation of κ_e and κ_{ph} which are the electronic and lattice thermal conductivity. Substituting these components into Eq.(3), we obtain the figure of merit for bulk materials.

2D material

For multilayered thin film shown in Fig.1, we assume perfect confinement of charge carriers. This is the case for QWs with wide bandgap barrier materials. We also assumed that there is not any carrier tunneling through the barrier layers, i.e. there is not any broadening of subband produced in QW.

In the case that the interfaces of multilayers are parallel to the x-y plane and charge carriers are confined in z direction, we obtain the dispersion relation of charge carriers as

$$E(k_x, k_y, k_z) = \frac{\hbar^2 k_x^2}{2m_x} + \frac{\hbar^2 k_y^2}{2m_y} + \frac{\hbar^2}{2m_z} \left(\frac{\pi}{a} \right)^2 \quad (9)$$

The results of the derivation are shown below

$$\sigma_{2D} = \frac{1}{2\pi a} \left(\frac{2k_B T}{\hbar^2} \right) (m_x m_y)^{1/2} F_0 e \mu_x \quad (10)$$

$$\alpha_{2D} = - \frac{k_B}{e} \left(\frac{2F_1}{F_0} - \zeta^* \right) \quad (11)$$

$$\kappa_{e2D} = \frac{\tau \hbar^2}{4\pi^2} \left(\frac{2k_B T}{\hbar^2} \right)^2 \left(\frac{m_y}{m_x} \right)^{1/2} k_B \left(3F_2 - \frac{4F_1^2}{F_0} \right) \quad (12)$$

where the fermi integral F_i is defined by Eq.(8) and the reduced chemical potential ξ_{2D}^* of 2D material is expressed as following.

$$\xi_{2D}^* = \frac{\xi}{k_B T} - \frac{\hbar^2 \pi^2}{2 m a^2 k_B T} \quad (13)$$

Thermal conductivity of multilayered film is described as a linear combination of those of materials forming QWs and barrier layers. Neglecting transversal heat flow across the interfaces and the electronic thermal conduction in the barrier layers, the thermal conductivity of whole film κ_{2D} is expressed as follows.

$$\kappa_{2D} = \frac{a \kappa_{well} + b \kappa_{barrier}}{a + b} \quad (14)$$

We assumed that lattice thermal conductivities of QWs and barrier layers are constant, respectively. From Eqs.(3), (10),(11) and (14), we obtain $Z_{2D}T$ for QW films.

Physical constants

The effective mass, the mobility and the lattice thermal conductivity are important factors in order to calculate transport properties. There are many experimental data regarding Si,Ge, and SiGe alloy, however, other silicide materials have not been investigated in detail. There are some different values on effective mass of SiGe alloys as discussed by Slack et. al⁽⁹⁾. We used $1.0m_0$ for those of hole and electron since the calculation for bulk materials using these values showed a good agreement with experimental data. Other constants such as the mobility and the lattice thermal conductivity were employed from references⁽¹⁰⁾. Physical constants used in this calculation are shown in Table 1.

Table 1 Physical constants

	m_e^*	m_h^*	μ_e	μ_h	κ_{ph}	E_g
unit	m_0		cm^2/Vs		W/mK	eV
Si	1.06	0.69	88.6	51.3	148	1.1
Si ₇₀ Ge ₃₀	1.0	1.0	71.3	47.7	4.4	0.7
Mg ₂ (Si,Ge)	1.2	2.3	108	22	2.1	0.8
Ru ₂ Si ₃	2.9	2.9	10	29	4.0	0.9
FeSi ₂	1.0	4.0	2	4	4.0	0.9
CrSi ₂	20.2	5.0	0.15	15	6.8	0.35

Results and Discussions

Calculations for ZT were made based on the model and the constants shown in Table 1. Figure of merit ZT obtained by Eqs.(3) and (10)-(14) has a maximum value when the

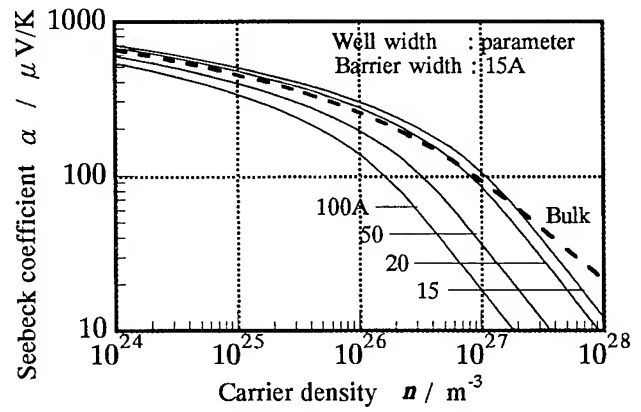


Fig.2 Seebeck coefficients of Si₇₀Ge₃₀/Si QWs as functions of the carrier density. The barrier width is 15A.

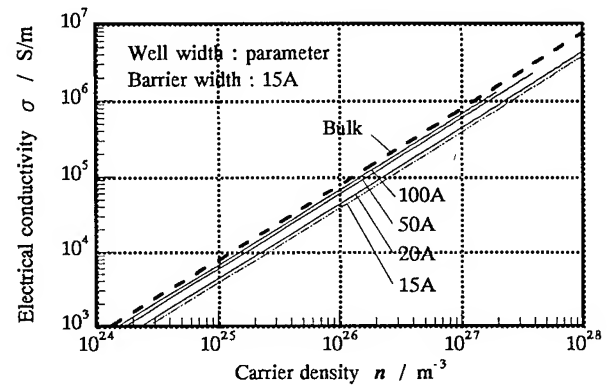


Fig.3 Electrical conductivities of Si₇₀Ge₃₀/Si QWs as functions of the carrier density. The barrier width is 15A.

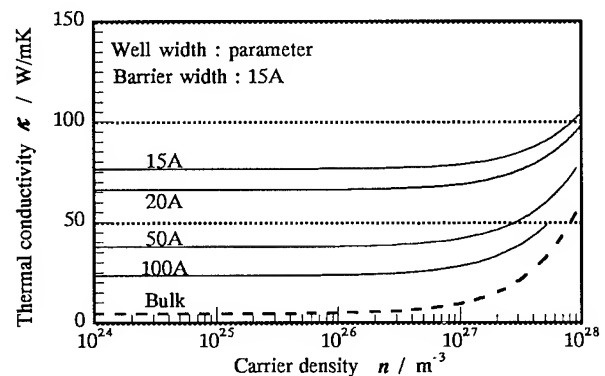


Fig.4 Thermal conductivities of Si₇₀Ge₃₀/Si QWs as functions of the carrier density. The barrier width is 15A.

reduced chemical potential ξ_{2D}^* is changed. ξ_{2D}^* values giving maxima of $Z_{2D}T$ are ranged between -2 and 3. The optimum carrier density is on the order of 10^{26} to $10^{27} m^{-3}$. In Fig. 2,3,4 and 5, α_{2D} , σ_{2D} , κ_{2D} and $Z_{2D}T$ of Si₇₀Ge₃₀/Si (type I) QWs are shown as a function of the carrier density and QW width. The barrier width is assumed constant of 15A. As shown in the

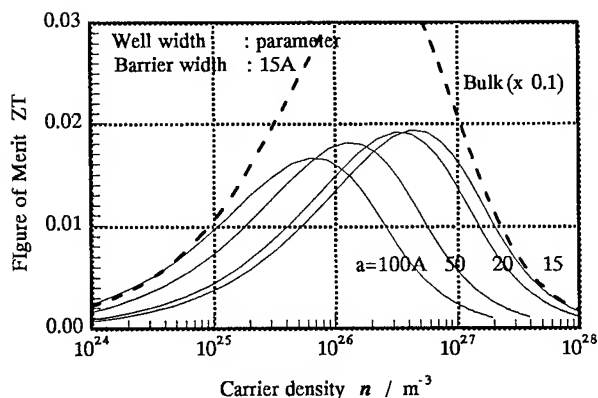


Fig.5 Figure of merit of $\text{Si}_{70}\text{Ge}_{30}/\text{Si}$ QWs (type I) as functions of the carrier density.

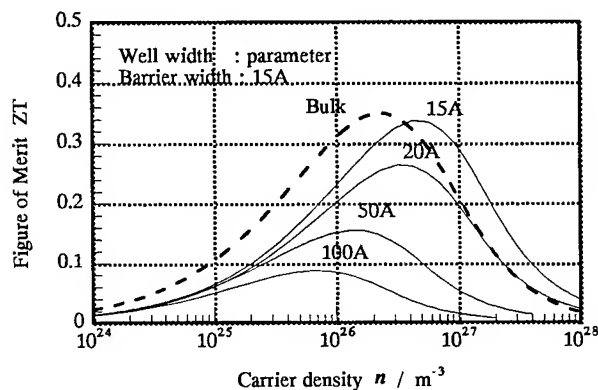


Fig.6 Figure of merit of $\text{Si}_{70}\text{Ge}_{30}/\text{Si}_{70}\text{Ge}_{30}$ modulated doping QWs (type II)

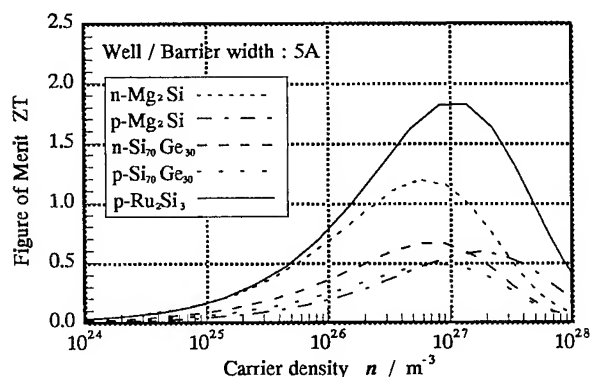


Fig.7 Figure of merit of silicide QWs (type III) as functions of the carrier density.

variations of Seebeck coefficient, reduction of the well width enhances α_{2D} . Since α_{2D} is determined by the mean carrier energy relative to the chemical potential, this enhancement is caused by the increased energy of carriers at subbands inside the well.

The electrical conductivity and the thermal conductivity in Fig. 3,4 show that an introduction of the barrier layer decreases the electrical conduction and increases the thermal

conduction since κ of the barrier layer is much higher than that of the well layer in type I QW. It is because the $Z_{2D}T$ of type I QWs is much lower than that of bulk material (Fig.5).

Fig.6 is plots of $Z_{2D}T$ of type II QWs as functions of the carrier density. In this case the thermal conductivity of barrier layer is the same as that of the well layer. Moderate enhancement of figure of merit can be expected.

Fig.7 is plots of $Z_{2D}T$ of type III QWs as functions of the carrier density. Metal silicide QWs show high figure of merit value at well width $a=5\text{\AA}$. These high $Z_{2D}T$ are quite fascinating because the type III QWs seem to be materialized by careful choice of processing technique. Several transition metal silicides such as NiSi_2 and CoSi_2 are currently used as contacting materials to silicon devices.

The high thermal conductivity shown in Fig.4 may be overestimated because there are experimental data⁽¹¹⁾ which clarified that the value of κ decreases to that of alloys of two materials in the case of thin QW and barrier layers. Accordingly the κ value could be a order of magnitude lower than the figure. Simple question is how the high carrier density n could be achieved. The maximum value of $Z_{2D}T$ will be achieved only at $n > 10^{26} \text{ m}^{-3}$. We should be careful that the maximum solubility of n-type dopant (As, P) for silicon is about 10^{27} m^{-3} ⁽¹²⁾.

Conclusion

We estimated the figure of merit value of QW structured thin films by means of a set of calculations based on single band mode. Results showed that the material for the barrier layer are the key to success, and the $\text{Si}_{70}\text{Ge}_{30}/\text{Si}_{70}\text{Ge}_{30}$ modulated doping QWs had higher $Z_{2D}T$ values than those of $\text{Si}_{70}\text{Ge}_{30}/\text{Si}$ QWs because of their low thermal conductivity. It was also clarified that QWs made of metal silicides are interesting because of their high $Z_{2D}T$ values.

References

- [1] A. Φ. Ioffe, *Thermoelement* (1960)
- [2] D.M.Rowe, V.S.Shukla and N.Savvides, *Nature* 290(30), p.765 (1981)
- [3] J. W. Vandersande and J.P. Fleurial, *Proc. of Xth Int. Conference on TE*, p.21 (1992)
- [4] L.D.Hicks and M.S. Dresselhaus, *Phys.Rev. B* 47, 12727 (1993)

- [5] Whitlow and T.Hirano, *Proc. of XIIth Int. Conference on TE*, p.39 (1993)
- [6] D.M.Rowe and Gao Min, *Proc. of XIIIth Int. Conference on TE*, p.339 (1994)
- [7] C.B.Vining, *Proc. of IXth Int. Conference on TE*, p.249 (1990)
- [8] Ashcroft/Mermin, *Solid State Physics*, p.250 (1976)
- [9] Glen A. Slack and Moayyed A. Hussain, *J. Appl. Phys.* 70 (5), p.2694 (1991)
- [10] C.B.Vining, *Handbook of Thermoelectrics*, p.277 (1995)
- [11] T.Yao, *Appl. Phys. Lett.* 51 p.1798 (1987)
- [12] F.Shimura and H.R.Huff, *VLSI Handbook*, chap.15 (1985)

Thermoelectric Performance of B₄C/B₉C Heterostructures

S. Ghamaty*, N. Elsner*,
K. Wang+ and Qi Xiang+

*Hi-Z Technology, +University of California, Los Angeles

Abstract

The electronic properties of bulk materials are altered when they are incorporated into quantum wells. Two-dimensional quantum wells have been synthesized by alternating layers of B₄C and B₉C. Such nanostructures are being investigated as candidate thermoelectric materials for high figures of merit (Z) at high temperature. The predicted enhancement is attributed to the confined motion of charge carriers in the two dimensions and separating them from the ion donors. This combination of materials is of interest since B_xC alloys are the preferred thermoelectric materials for high temperature applications because they should exhibit little diffusion.

Molecular beam epitaxy (MBE) technique has been used to prepare these multilayer films. Films have been deposited on single-crystal silicon substrates. The films have been characterized with X-ray Photoelectron Spectroscopy (XPS) and Auger spectroscopy. The thermoelectric properties of these films have also been determined over a broad range of temperatures from 4.2 K to 1200 K. When these same films were annealed at 1,050 °C for 25 hours, their α^2/ρ values increased dramatically. The α^2/ρ values for these P type films were more than a factor of 10 to 30 times higher than bulk P type SiGe. Attempts to measure thermal conductivity are being pursued. The performance of the MBE films have been systematically compared with bulk materials. Preliminary thermoelectric measurements of the multilayer structures, lead us to believe that significant gains in the thermoelectric figure of merit (Z) may be possible with this approach.

Background

Thermoelectric materials are utilized for power generation in remote locations, on spacecraft used for interplanetary exploration, and in places where waste heat can be recovered. Broader usage is limited by the efficiency of present systems and the power-specific cost (\$/W) of power generation. Materials with a $ZT \geq 6$ can lead to a factor of 2 to 3 improvement in thermodynamic efficiency. Recall that the thermodynamic efficiency, η , of a thermoelectric power generator is

$$\eta = \frac{T_h - T_c}{T_h} \left[\frac{M - 1}{M + T_c/T_h} \right]$$

where M is defined as

$$M = \sqrt{1 + \frac{1}{2} \bar{Z} (T_c + T_h)}$$

and T_h is the absolute temperature at the hot junction and T_c is the absolute temperature at the cold junction. To achieve a high efficiency with a power generator, the overall figure of merit for the device, Z , must be high. The figures of merit of the thermoelectric materials used to construct the device must also be high. For a specific material, Z is defined as:

$$Z = \frac{\sigma \alpha^2}{\kappa_{ph} + \kappa_{el}}$$

where σ is the electrical conductivity, α is the Seebeck coefficient, κ_{ph} is the phonon contribution to the thermal conductivity, and κ_{el} is the electronic contribution to the thermal conductivity. Note that κ_{ph} is also known as κ_L , the lattice thermal conductivity. Much of the effort to improve Z over the past 20-30 years has focused on attempts to reduce κ_L without adversely affecting the electrical conductivity. Some success has been achieved with solid-solution alloying. Further reductions in κ_L have been achieved by reducing the grain size of silicon-germanium alloys, however, this approach is still in its infancy and the potential benefit is believed to be relatively small.

Multilayer films of B₄C and B₉C are being investigated as a means of achieving a high Z . Models based upon quantum mechanics predict that such structures should have an unusually

high Z [1-5]. The quantum-well (QW) layer is sandwiched between two barrier layers. Typically, the QW material has a very narrow band gap and the barrier material has a relatively large band gap. Molecular beam epitaxy (MBE) has been employed to fabricate the samples, since it provides the best conditions for epitaxial growth.

For power applications, the concern is that the above materials will inter-diffuse at some elevated temperature and lose their two-dimension structure and associated quantum well properties. For power generation applications, B-C alloys appeared to be the best initial selection for the following reasons:

- B-C have very low diffusion coefficients in one another.
- B-C alloys do not have to be deposited in an exact stoichiometry to be useful thermoelectric materials.
- The B composition can easily vary from 4 to 13 (B_4C to $B_{13}C$) with no major thermoelectric property effects. With other thermoelectric materials such as PbTe and Bi_2Te_3 , the stoichiometry must be controlled exactly or the thermoelectric properties can be severely degraded.

- Since stoichiometry is not critical, the MBE process can be conducted with less critical controls.
- By using B_9C alloys, it is possible to use B_4C as the wide band gap layer material thereby allowing similar crystallographic materials to be deposited in an epitaxial manner.

Experimental

Molecular Beam Epitaxy (MBE)

The B-C multiple quantum wells were grown on 76 mm (100) Si wafers using molecular beam epitaxy (MBE) at UCLA. The B and C molecular beams were obtained from elemental sources in electron gun evaporators. Prior to growth the substrates were cleaned by a modified Shiraki process [7] which resulted in a H-terminated surface. Immediately preceding growth the hydrogen was removed by heating the sample to 650°C. The epitaxial growth was done with the substrate at 710°C. Each of the samples were grown on p-type 10-20 ohm-cm substrates. For the samples a 500 Å B_4C buffer layer was grown prior to the multiple quantum well growth. Each structure is composed of five B_9C quantum wells separated by 100 Å of B_4C .

Table 1. Thermoelectric Properties of B_4C/B_9C Quantum Wells.

- The trend of measured ρ values of B-C films agrees qualitatively with theory. Values may be lower than comparable bulk ρ .
- The α values for the B-C films are calculated from $\alpha_{combined} = f(\alpha_{sub}, \alpha_{film})$ using an equation based upon linear network theory which is discussed in the text. These corrected values may indicate a significant enhancement of α of the B-C films. It is important to note that these large Seebeck coefficients are not predicted by the theory.

Sample B_4C/B_9C	Room Temperature Properties					High Temperature Properties			Device Efficiency ⁽⁶⁾ (%) $T_{cold} \approx 300^\circ C, T_{hot} \approx 1000^\circ C$
	$\rho_{Film}^{(2)}$ (m Ω -cm) $T \approx 30^\circ C$	$\alpha_{comb}^{(3)}$ ($\mu V/^\circ C$) $T \approx 30^\circ C$	$\alpha^{(4)}$ ($\mu V/^\circ C$) $T \approx 30^\circ C$	$Pow_{min}^{(5)}$ ($\mu W/cm^2$) $T \approx 30^\circ C$	$Z^{(5)}$ (1/ $^\circ C$) $T \approx 30^\circ C$	$\rho_{Film}^{(2)}$ (m Ω -cm) $T \approx 1000^\circ C$	α ($\mu V/^\circ C$) $T \approx 1000^\circ C$	$Z^{(5)}$ (1/ $^\circ C$) $T \approx 1000^\circ C$	
UCLA#1 as fab. ⁽⁷⁾ MBE	51	1550	1600	47	0.94×10^{-3}	50	T.B.M.	—	—
UCLA#1 annealed at 1050°C for 1day	0.49	510	1000	531	10.6×10^{-3}	0.12	567	38.2×10^{-3}	29
UCLA#2 as fab. ⁽⁷⁾ MBE on SOS ⁽⁸⁾	9000	850	900	0.08	0.002×10^{-3}	T.B.M.	T.B.M.	—	—
UCLA#2 annealed at 1050°C for 1day	0.43	250	275	145	2.9×10^{-3}	T.B.M.	T.B.M.	—	—
Bulk B_9C P-Type	27	240	N.A.	2.1	0.04×10^{-3}	3.6	218	0.19×10^{-3}	5.4
Bulk SiGe P-Type ⁽¹⁾	1	130	N.A.	17	0.26×10^{-3}	2.7	276	0.62×10^{-3}	6.5

(1) INSD pages IV-36 and IV-38.

(2) ρ_{Film} is the value that includes the B_4C and the B_9C layers.

(3) α_{comb} is the Seebeck coefficient measured on the ML-QWF and the substrate.

(4) α is the Seebeck coefficient for the ML-QWF and is calculated by subtracting out the value of the substrate.

(5) Z is calculated using the same α value as the B_4C bulk material.

(6) With bulk n-type Si_3Ge_2 as the n-leg.

(7) Total film thickness is $\approx 1000\text{\AA}$ and each layer is $\approx 100\text{\AA}$ thick.

(8) SOS substrate is about .5 μ of Si On Sapphire.

Characterization

There are two classes of characterization of ML-QWFs which are being pursued at Hi-Z: 1) thermoelectric properties and 2) material properties. Thermoelectric properties include measurement of resistivity (ρ), Seebeck coefficient (α) and their respective temperature dependence. The material properties are divided into three categories: a) Morphology (SEM and/or TEM and thickness), b) Elemental /chemical composition (Auger and x-ray) and c) Crystallographic structure and defects (TEM and Auger). Results obtained with these various diagnostic methods on the B-C ML-QWFs are discussed below. The α and ρ data previously obtained on these samples are given in Table 1 and in Figs. 1 through 4.

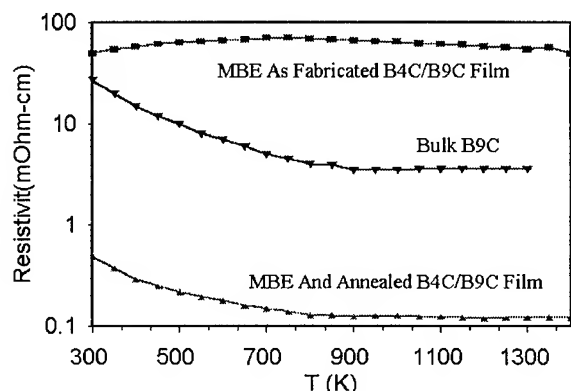


Fig. 1. High Temperature Resistivity of B₄C/B₉C Films vs. Bulk B₉C.

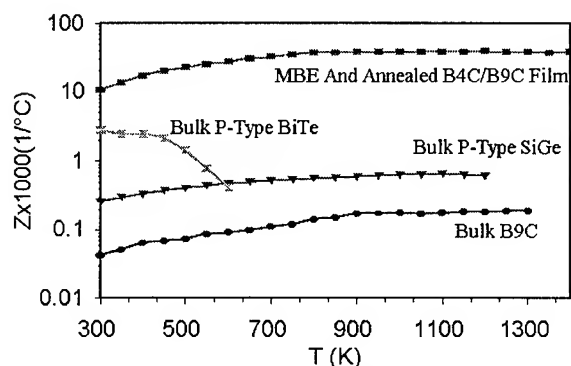


Fig. 3. High Temperature Figure of Merit of MBE and annealed B₄C/B₉C films, bulk p-SiGe, bulk p-B₉C, and bulk p-BiTe alloy. For calculating the Z of bulk B₉C was used.

α and ρ Measurements

Room temperature resistivities were measured on samples using the following method: the current was introduced at the ends of a long, rectangular cut sample and the voltage probes were near the center of the test specimen. The resistance was obtained from the voltage drop, and the resistivity was calculated by knowing the cross-sectional area of the bar and

the distance between the two voltage probes (ASTM F-43). The Allisi instrument, which uses pressure contacts, was used as the voltage probes in this case.

The high temperature α and ρ of the MBE films were measured in a system at Hi-Z and the results are shown in Figs. 1&2. The electrical resistivities of the samples were measured as a function of temperature from 300K to 1200K using a Linear Research LR400 4-wire bridge operating at 16Hz. Electrical contact to the films was made by wrapping nickel wire around the sample, and bonding the wires to the surface with silver paint. The thermocouple leads were held to the surface of the sample with the nickel wires, and bonded in place with the silver paint. Currents for the measurements were in the range of 1 to 100 mA.

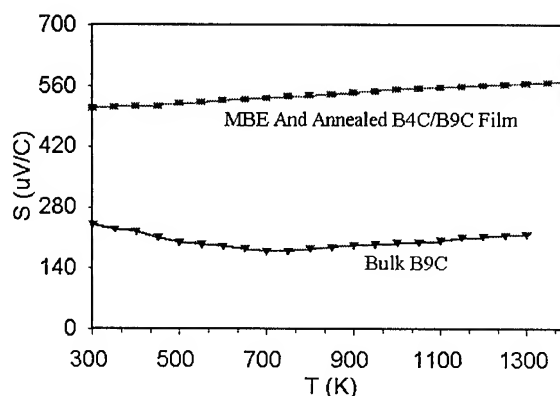


Fig. 2. High Temperature Seebeck Coefficient of MBE and Annealed B₄C/B₉C Films and bulk B₉C.

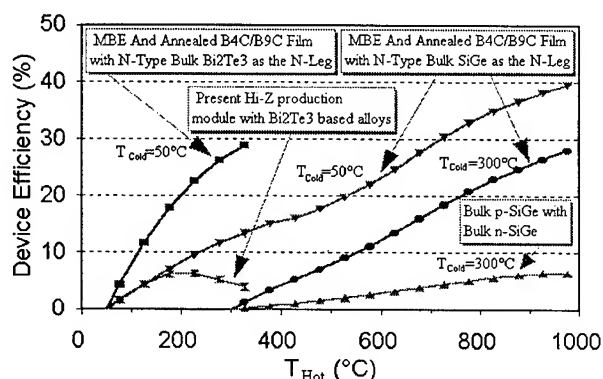


Fig. 4. Theoretical Efficiency of the MBE and Annealed B₄C/B₉C film, bulk B₉C, Bi₂Te₃ and p-SiGe. Bulk thermal k was assumed for the B₄C/B₉C films.

X-ray Analysis and Auger Emission Spectroscopy

Hi-Z is analyzing the B₄C/B₉C films by X-ray Photoelectron Spectroscopy (XPS) and Auger Emission Spectroscopy (AES), and the data generated has been very valuable in understanding why the films undergo a very large improvement in α^2/ρ when they are annealed. A summary of

the results are shown in Table 1.

It will be recalled that these multi layer films were deposited at $\sim 500^\circ\text{C}$. In the as deposited condition the films had poor α^2/ρ properties that were of little thermoelectric value. When these films were annealed however their α^2/ρ values improved dramatically as shown in Figs. 1-4 and Table 1.

B-C films deposited on Si substrates show that the films have the following characteristics:

- For the films, each period has the composition $\text{B}_4\text{C}/\text{B}_9\text{C}$ after annealing at 1050°C for 24hrs. The as fabricated film has an extra phase of B (about 20%) that disappeared when the film was annealed as shown in Figs. 5A-C.
- The annealed film appears single crystal and epitaxial, while the as fabricated film is polycrystalline.

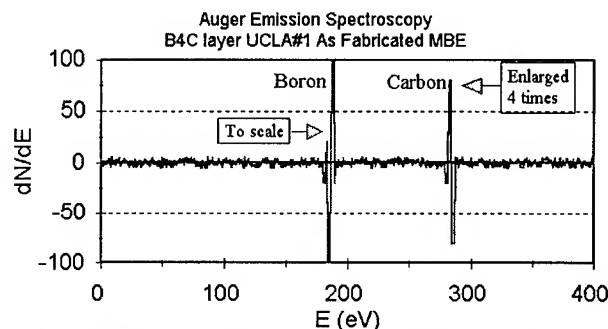


Fig. 5A. Auger Emission Spectroscopy (AES) of MBE as fabricated $\text{B}_4\text{C}/\text{B}_9\text{C}$ film. The AES of the B_4C layer is shown. The noise is an indication of the multi phase structure in the film. The Carbon peak is about 20% lower than the Boron which means the second phase has to be Boron. The number in the boxes indicates the proportion of the elements.

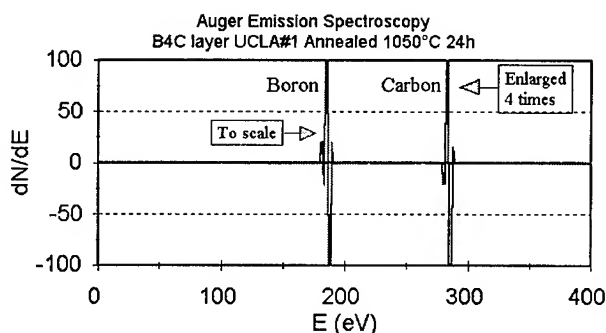


Fig. 5B. Auger Emission Spectroscopy (AES) of MBE and annealed $\text{B}_4\text{C}/\text{B}_9\text{C}$ film. The AES of the B_4C layer is shown. The low noise is an indication of the crystalline structure in the film. The number in the boxes indicates the proportion of the elements.

By using AES and XPS it appears possible to relate the films structure and morphology to their thermoelectric properties. As expected, these analyses confirmed that the more crystalline the films are, the higher will be their α^2/ρ values. Hi-Z is planning to do XPS and AES on many samples as a diagnostic tool to further correlate the films thermoelectric

properties and microstructure. TEM or other technique along with AES and XPS should be preform to confirm the results. Hi-Z has measured several types of ML-QWFs that were fabricated by MBE. Table 1 lists the α and ρ measured on these $\text{B}_4\text{C}/\text{B}_9\text{C}$ multilayers near room temperature. interpretation of the measurement techniques and how they may relate to the substrate are discussed below. The data obtained thus far is very encouraging since several of the ML-QWFs appear to have very high α^2/ρ values.

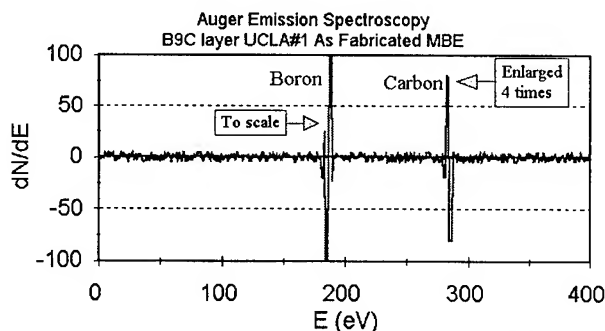


Fig. 5C. Auger Emission Spectroscopy (AES) of as fabricated MBE $\text{B}_4\text{C}/\text{B}_9\text{C}$ film. The AES of the B_9C layer is shown. The noise is an indication of the multi phase structure in the film. The Carbon peak is about 20% lower than the Boron which means the second phase has to be Boron. The number in the boxes indicates the proportion of the elements.

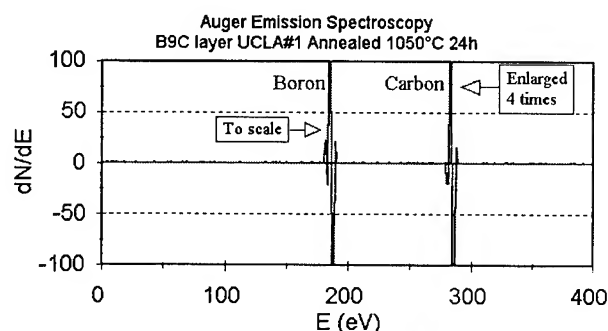


Fig. 5D. Auger Emission Spectroscopy (AES) of MBE and annealed $\text{B}_4\text{C}/\text{B}_9\text{C}$ film. The AES of the B_9C layer is shown. The low noise is an indication of the crystalline structure in the film. The number in the boxes indicates the proportion of the elements.

Results & discussion

Evaluation of Samples and Substrate Correction

In the case of the heterostructures the measurement of thermoelectric properties were complicated by the conductivity of the substrate. In this particular case, most of the films were deposited on standard $10\Omega\text{-cm}$ Si (100). The relatively high conductivity of this substrate has made it necessary to correct the result to eliminate substrate contributions to the electrical conductivity, σ , and the Seebeck coefficient, α . the measured resistance R_{total} consists of the resistance of the film, R_{films} , and the resistance of the substrate, $R_{\text{substrate}}$.

$$\frac{1}{R_{total}} = \frac{1}{R_{substrate}} + \frac{1}{R_{film}}$$

By making independent measurements of the substrate resistance, the film resistance can be calculated from the measured value.

$$R_{film} = \frac{1}{\frac{1}{R_{total}} - \frac{1}{R_{substrate}}}$$

Given the dimensions of the film the actual conductivity of the heterostructure can then be calculated directly.

$$\sigma_{films} = \frac{1}{\rho_{films}} = \left(\frac{L}{WH} \right) \frac{1}{R_{films}}$$

Similar corrections must be made in cases involving measurements of the Seebeck coefficient. The substrate and film are treated as two parallel branches of a linear circuit, each composed of a (thermal) battery and a resistor. Please see Fig. 9 for the details.

The measured thermoelectric voltage of the film, V_{film} , can be expressed in term of the measured voltage, V_{total} , the known voltage of a bare substrate, $V_{substrate}$, the resistance of the film, R_{film} , and the resistance of the bare substrate, $R_{substrate}$.

$$V_{film} = \left(1 + \frac{R_{film}}{R_{substrate}} \right) V_{total} - \left(\frac{R_{film}}{R_{substrate}} \right) V_{substrate}$$

The Seebeck coefficient is then

$$\sigma_{film} = \frac{V_{film}}{T_h - T_c}$$

Obviously, when measuring the Seebeck of thin films, it is important to minimize the substrate contribution to the extent possible by making the ratio $R_{film}/R_{substrate}$ as small as possible. Al_2O_3 is an ideal substrate for electronic measurements of thin films since no correction of the Seebeck coefficient is required for such insulating materials. In the case of 1000 Ω -cm float-zone Si (100) substrates, the uncompensated error in the measured Seebeck coefficient is on the order of 1%. In the case of 10 Ω -cm Si (100), the possible error introduced by the substrate can be much larger and must be accounted for.

Summary and Conclusions

Auger Emission Spectroscopy (AES) and X-ray Photoelectron Spectroscopy (XPS) have shown the MBE films change drastically when the as fabricated films are aged at 1050°C (fig.1) supporting the large increase in (α^2/ρ) of the aged films. The as fabricated film appears to have an extra phase of boron in both the B_4C and B_5C layers and the structure of both layers are polycrystal films. The aged sample however appears as single crystal epitaxy material with no second phase of boron. The boron might have been absorbed by the Si substrate. With future samples AES and XPS measurements will be performed on the substrate before and after aging to determine if the extra phase of boron is taken into the Si substrate.

Acknowledgement

This program was sponsored by the Department of Energy (DOE) under a Phase II SBIR grant with Dr. William Barnett the DOE Program Manager.

References

- [1] Harman, T.C., "PbTeSe/BiSb Short Period Superlattices as a New Thermoelectric Cooling Material," *Proc. 1st Natl. Thermogenic Cooler Conf., Center for Night Vision and Electro-Optics*, U.S. Army, Ft. Belvoir, VA, 1992.
- [2] Hicks, L.D., Dresselhaus, M.S., "Thermoelectric Figure of Merit of a One Dimensional Conductor," *Phys. Rev. B*, **47**, 24 (1993) 16 631-634.
- [3] Hicks, L.D., Dresselhaus, M.S., "Effect of Quantum-Well Structures on the Thermoelectric figure of Merit," *Phys. Rev. B*, **47**, 19 (1993) 12 727-731.
- [4] Hicks, L.D., Dresselhaus, M.S., "BiSb/PbTeSe Superlattices as a New Thermoelectric Cooling Material," March 15, 1993.
- [5] Hicks, L.D., Dresselhaus, M.S., "The Effects of Quantum Well Structures on the Thermoelectric Figure of Merit," *Proc. 1st Natl. Thermogenic Cooler Cong., Center for Night Vision and Electro-Optics*, U.S. Army, Ft. Belvoir, VA. 1992.
- [6] N. B. Elsner, G.H. Reynolds, J.H. Norman and C.H. Shearer in "Boron-Rich Solids", AIP Conference Proceedings 140.
- [7] A. Ishizakkaland Y. Shiraki, *J. Electrochem. Soc.* **133**(1986) 666.

Structure and Transport Properties of Ga-Doped Semi- and Polycrystalline $\text{Si}_{1-x}\text{Ge}_x$ Films

Felix Edelman¹, Mathias Stölzer², Peter Werner³, and Rainer Butz⁴

¹Materials Engineering Faculty, Technion-Israel Institute of Technology, 32 000 Haifa, Israel,

²Martin-Luther-Universität Halle-Wittenberg, Fachbereich Physik, FG Angewandte Physik, Hoher Weg 7, D-06120 Halle (Saale), Germany

³Max-Planck-Institut für Mikrostrukturphysik, Weinberg 2, D-06120 Halle(Saale), Germany

⁴Institut für Schicht- und Ionentechnik (ISI), Forschungszentrum Jülich, D-5170 Jülich, Germany

Abstract

Polycrystalline SiGe films have applications in solar cells, thermoelectrical devices and field-effect transistors for large area integration (liquid crystal displays etc.). Recently, nanocrystalline state was detected by us in heavily B-doped SiGe films after vacuum annealing. Amorphous (a) $\text{Si}_{1-x}\text{Ge}_x$ films with $x=0.25-0.60$, about 200-300nm thick and heavily doped with Ga (1%), were deposited by molecular beam on $\text{SiO}_2/\text{Si}(001)$ substrates at room temperature. For crystallization, a-SiGe/ SiO_2/Si structures were annealed in vacuum of 10^{-6} Torr at 600 to 900°C. X-ray diffraction and TEM observations in situ showed nanocrystalline (nc) structure in SiGe films with grain size of about 5-20nm. The nc- $\text{Si}_{1-x}\text{Ge}_x$ films demonstrated high hole mobility (1 to 100cm²/Vs) and Seebeck coefficient values (5 to 110μV/K).

Introduction

Polycrystalline hot-sintered $\text{Si}_{1-x}\text{Ge}_x$ was utilized first in 1970s as thermoelectric board power source element in the US Voyager's spacecrafts supplied with Pu-reactors [1].

SiGe powder used in thermoelectric applications usually has a composition varying between $x=0.2$ and $x=0.7$ and a grain size ranging from 1 to 100μm. The figure of merit of thermoelectric materials is defined as $Z=S^2\sigma/\lambda$ (S , σ and λ are Seebeck coefficient or differential thermoelectric power, specific conductivity and specific thermoconductivity, respectively). A large Z can be obtained via high doping or by entering in compact small amount of A₃B₅ compound (GaP is typical), which increase both carrier concentration up to $10^{20}-10^{21}\text{cm}^{-3}$ and S [2,3,4]. $Z_{1,2}$ which is the figure of merit of two-branches thermoelement, is given by $Z_{1,2}=(S_2-S_1)^2/[(\lambda_1/\sigma_1)^{1/2} + (\lambda_1/\sigma_1)^{1/2}]^2$ while S_1 , σ_1 , λ_1 and S_2 , σ_2 , λ_2 are the parameters of each thermoelement branch.

Distinguishing features of SiGe as a thermoelectric material are also: 1) low thermoconductivity (λ) having a minimum value for $x=0.5$; 2) high charge carriers mobility and 3) increase of Seebeck coefficient (S) with temperature up to $\sim 1000^\circ\text{C}$ [1,2,4].

Increasing the figure of merit of SiGe by decreasing the grain size from 100 to 1μm, is not effective since while the thermal conductivity is decreased with grain size, the electrical conductivity is also slightly decreased, so that no sufficient change in the figure of merit is observed[5]. Theoretical calculations, however, show [6] that further increase of Z can be expected in special monocrystalline SiGe superlattices obtained via δ -doping with compositional steps

of several Å.

Recently, we reported [7] results of detailed studies of crystallization process in undoped and heavily-doped with P and B hydrogenated $\text{Si}_{1-x}\text{Ge}_x$ films deposited in an RF glow discharge CVD system of hydrogen-diluted $\text{SiH}_4+\text{GeH}_4$ mixtures. In particular, we have discovered that the grain growth rate in SiGe films strongly decreased with B doping, independent of the Ge content. Owing to this effect even Ge-rich a-SiGe films remained nanocrystalline (grain size $<100\text{Å}$) after 800°C annealing.

In the present study we'll show that heavily Ga-doped a-SiGe films deposited in high vacuum molecular beam chamber have the tendency to form a nanocrystalline morphology. This means that strong p-doping drastically influences crystallization mechanism of a-SiGe. We'll also present some transport properties of nanocrystalline SiGe.

Experimental

Structure

Ga-doped ($[\text{Ga}]=5\cdot 10^{18}\text{cm}^{-3}$) a- $\text{Si}_{1-x}\text{Ge}_x$ films, 0.2-0.3μm thick, having compositions $x=0.27$ to 0.55, were grown at 200-250°C by molecular beam processing on oxidized Si(001) wafers where SiO_2 thickness was about 0.4μm. The Si/Ge ratio we obtained via Rutherford Backscattering Spectroscopy. The X-Ray Diffraction (XRD) analysis was performed using Philips powder diffractometer (Cu-K α radiation). XRD samples were annealed in a hot-wall furnace, having a vacuum near 10^{-7} Torr at temperatures between 600 and 900°C. Transmission Electron Microscopy (TEM) was performed by JEM-1000 microscope (1 MeV acceleration voltage) equipped with a double-tilting hot stage. In selected area diffraction imaging mode (SAD), the time t_0 (time which is necessary for a crystal to grow large enough to be detectable by TEM, see details in [7]), which describes the SiGe stability in the amorphous state, is characterized by the appearance of the second amorphous halo splitting to yield the (220) and (311) crystal rings or spots, whereas in the dark-field image, the time t_0 is characterized by the appearance of first SiGe crystals of 50-100Å in size.

Electron Transport Investigation

The electrical conductivity σ , the Hall coefficient R_H and the Seebeck coefficient S were measured in the temperature range between 85 and 375K. Fig.1 shows the structure of a sample

used for these measurements. The pattern were produced by film deposition trough steel masks, the length is 20mm.

The voltage probes as well as the copper-constantan thermocouples were glued by silver paint onto the sample. For the Hall measurements a magnetic field of $\pm 1.3T$ was used. The thermocouples served as current suppliers. All measurements were carried out in high vacuum.

The Seebeck effect is normally calculated according to

$$S = U_{Cu} S_{CuCo} / (U_{Cu} - U_{Co}) + S_{Cu} \quad (1)$$

U_{Cu} and U_{Co} are the voltages between the copper and the constantan wires, respectively. S_{CuCo} is the thermopower of the thermocouple at the samples average temperature and S_{Cu} is the thermopower of copper.

We used the following method to eliminate the error due to a little heat flow trough the thermocouples. The measurement was carried out at three temperature differences $\Delta T = 2 \dots 5$ K. $U_{Cu}(\Delta T)$ and $U_{Co}(\Delta T)$ were fitted to straight lines: $U_{Cu} = a_{Cu} \Delta T + b_{Cu}$, $U_{Co} = a_{Co} \Delta T + b_{Co}$ with the "error voltages" $b_{Cu} \approx b_{Co}$ of typical $3.5 \mu V$ at room temperature and $70 \mu V$ at 100K. Then the thermopower of the sample was calculated according to

$$S = a_{Cu} S_{CuCo} / (a_{Cu} - a_{Co}) + S_{Cu} \quad (2)$$

The overall experimental error can be estimated to be around 5% and it is mainly due to the inaccuracy of the geometrical shape and film thickness in the case of conductivity and Hall measurements.

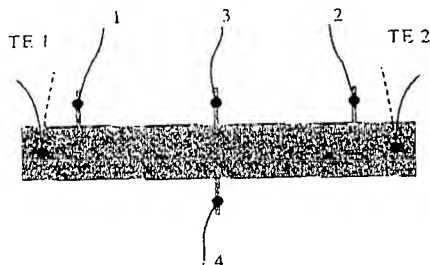


Fig. 1. Sample structure for electron transport measurements. TE - thermocouples, 1,2 - conductivity probes, 3,4 - Hall probes.

Results

I. Crystallization of Ga-doped $Si_{1-x}Ge_x$ films

I.1. XRD studies

A Vegard's law of linear dependence of the lattice parameter (d) on Ge content [8]

$$d(SiGe) = d(Si) + A[d(Ge) - d(Si)], \quad (3)$$

where A is a constant, is, in general, correct. However, the crystallized a-SiGe films present some XRD diffraction peaks correspond to interplanar spacings which are different from those of the ideal solid solution. The kinetics of

crystallization and the appearance of peaks-satellites which is related to SiGe decomposition is demonstrated in Figs. 2 and 3 by XRD spectra of Ga-doped SiGe films. XRD spectra in Fig. 2 shows also a drastic acceleration of the crystallization/recrystallization process of the a-SiGe(Ga) at 900°C compared to the partially crystallized SiGe annealed at 600-800°C.

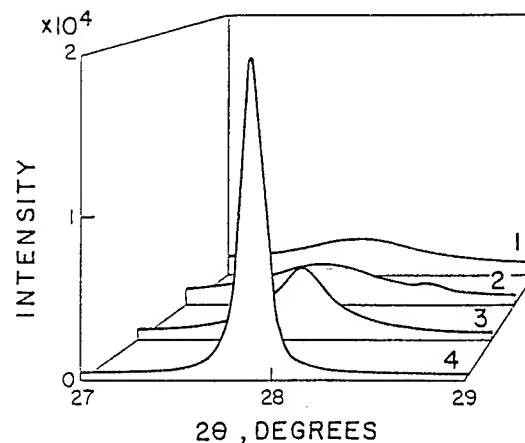


Fig. 2. Evolution of (111) XRD spectra of a Ga-doped a-Si_{0.45}Ge_{0.55} sample during annealing at 600 (spectrum 1), 700 (spectrum 2), 800 (spectrum 3) and 900°C (spectrum 4) for 1h.

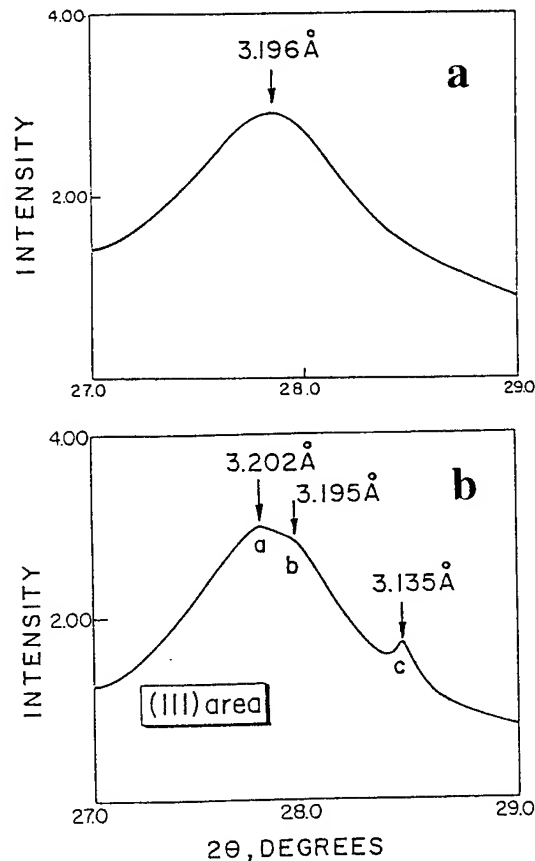


Fig. 3. Detailed XRD spectra of the same a-Si_{0.45}Ge_{0.55}(Ga) after 600°C, 1h (a) and 700°C (b) for 1h. The arrows in Fig. 3b show an example of SiGe decomposition related to the additional peaks near the main (111) reflection (with $d_{111} = 3.202 \text{ Å}$).

1.2. TEM *in-situ* studies of a-SiGe:Ga films crystallization

The typical nanocrystalline morphology which was evolved during crystallization of a-SiGe(Ga) films on SiO₂ is shown in Fig.4. This figure shows a sample of a-Si_{0.45}Ge_{0.55} which was annealed at T=700°C. Grain size in the crystallized SiGe film ranged from 50 to 250 Å. For comparison, grain size in undoped SiGe films annealed under the same conditions was about 1 μm or approximately 100 times larger. The incubation time before crystallization (*t*₀) at 700°C in a-Si_{0.45}Ge_{0.55} was about 1 min. The general *t*₀(T) dependence for different Si_{1-x}Ge_x films, undoped and doped, is demonstrated in Fig.5. It is interesting, that both p-type films, Ga-doped and B-doped are nanocrystalline (more detailed data of SiGe(B) crystallization see in Ref.7), however, compared to undoped SiGe, Ga-doping decreased incubation time while B-doping drastically increased it.

II. Transport properties of the nano-SiGe:Ga films

Well-known Ga-Si and Ga-Ge equilibrium phase diagrams [9] show maximum Ga solubility in the order of 10⁻³ and 10⁻⁴, respectively (both retrograde with temperature decrease). Therefore, the corresponding hole concentration values in SiGe films should be around 10¹⁹-10²⁰ cm⁻³, and that is what we observed in our samples (Fig.6). A weak dependence of hole concentration on temperature [p](T), as shown in Fig.6 is typical for such nearly degenerated semiconductors [10]. The attendant Si_{1-x}Ge_x films (annealed at 700°C for 1h) conductivity was also high (Fig.7) even though the film structure was mixed and characterized as a nanocrystalline with large amount of amorphous phase.

SiGe films annealed at 700°C demonstrated different hole mobilities values in the range of 0.5 to 60 cm²/Vs (largest value - for Si_{1-x}Ge_x with x=0.6; see mobility dependence on temperature in Fig.8) which were in a good accordance with mobility values specified for heavily p-doped Ge [10].

As can be seen in Fig.9, the Seebeck coefficient S values of our p-type SiGe(Ga) films at room temperature were close to 100 μV/K and which is similar to those specific for hot-pressed SiGe powder samples [2]. However, in our case S(T) dependence [10,12]

$$S = \pm k/e \{ 2 + \ln[2(2\pi m^*_{\pm} kT)^{3/2} / n_{\pm} h^3] \} \quad (4)$$

(here m^*_{\pm} is the effective mass and n_{\pm} the carrier concentration of holes/electrons) is shifted to the low temperature range with the maximum at around room temperature as compared to that for hot-pressed poly-SiGe samples [1-5]. The change of the S sign owes to the electron conductivity contribution in our p-SiGe which increased with the temperature increase.

As it is well-known [11], thermoelectric conversion efficiency η of SiGe sharply increases with grain size decrease (ten times, from 3 to 30% if the grain size decreased from 30 to 1 μm). It is obvious to expect further η improvement in SiGe materials with 100 times smaller grains.

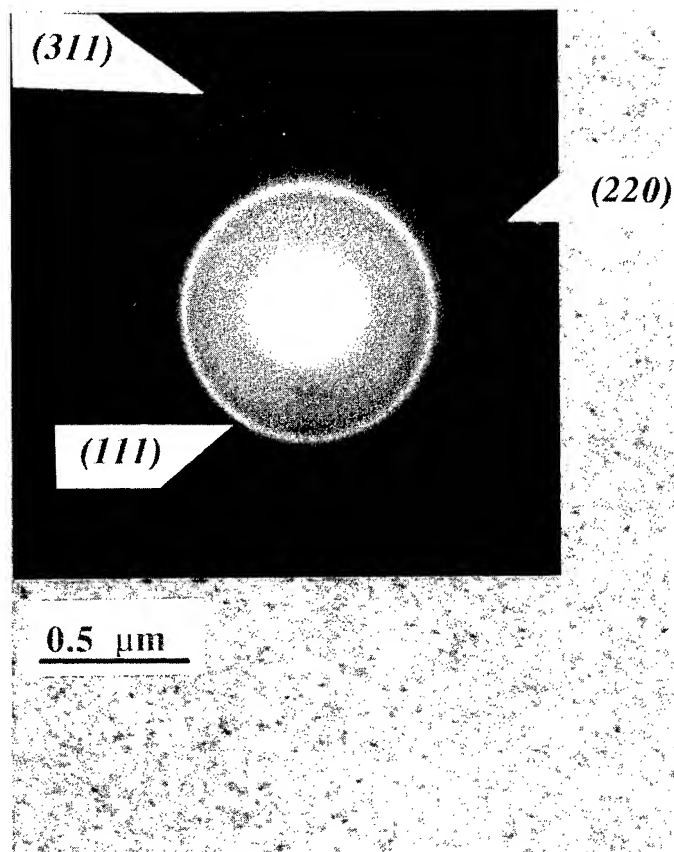


Fig.4. Plan-view TEM micrograph and selected area diffraction of Ga-doped nanocrystalline Si_{0.45}Ge_{0.55}(Ga) after annealing at 700°C for 1h.

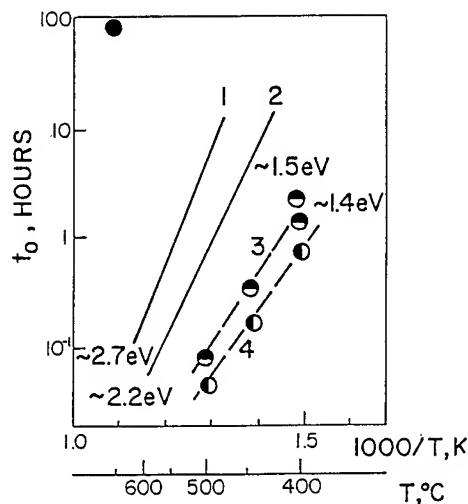


Fig.5. The temperature dependences of the incubation time *t*₀ for undoped Si_{0.74}Ge_{0.26} (1), Si_{0.46}Ge_{0.54} (2) and Ga-doped Si_{0.73}Ge_{0.27} (3) and Si_{0.45}Ge_{0.55} (4) films. Point • corresponds to the B-doped Si_{0.8}Ge_{0.2} film (interpolated data from Ref.7).

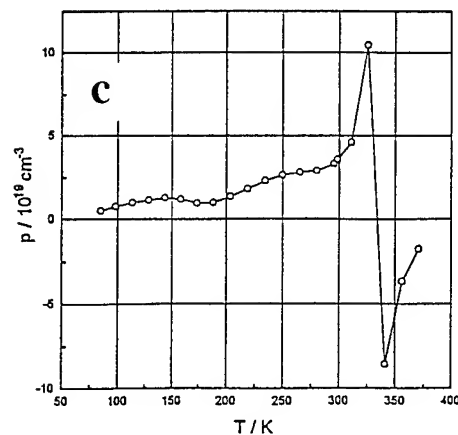
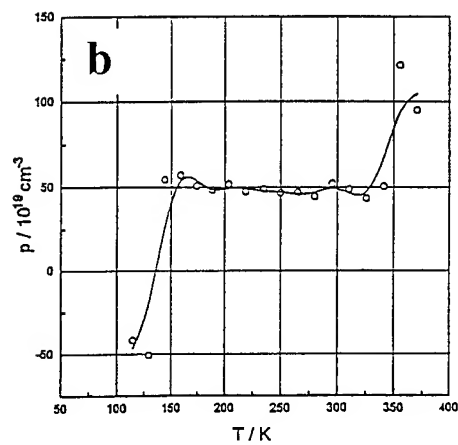
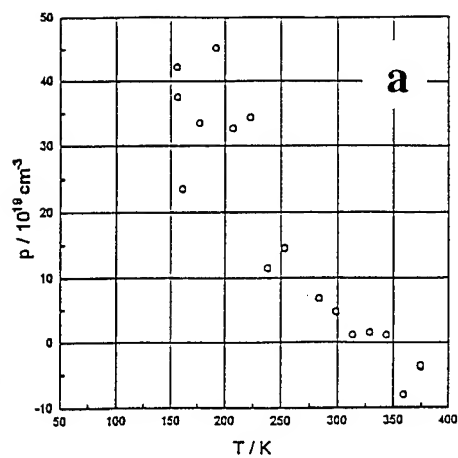


Fig. 6. The temperature dependence of carrier concentration in heavily p-doped SiGe with 27(a), 38(b) and 60%Ge(c) after vacuum annealing at 700°C for 1h.

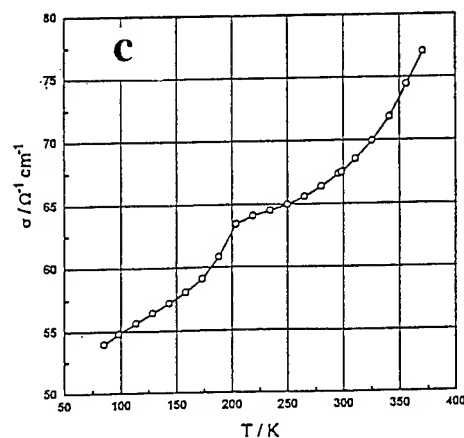
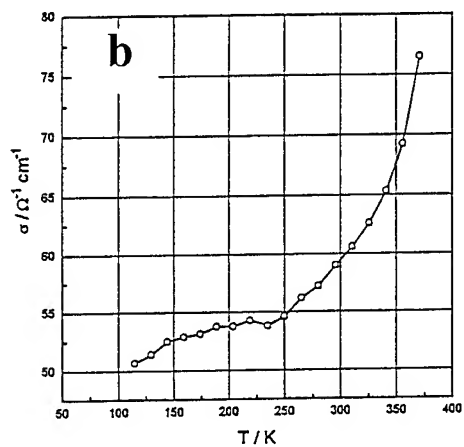
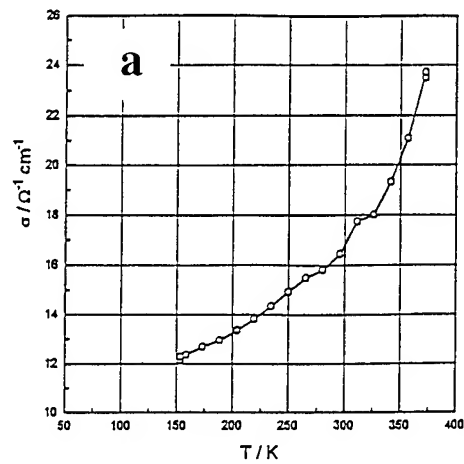


Fig. 7. The temperature dependence of the conductivity of heavily doped p-SiGe films with 27(a), 38(b) and 60%Ge(c) after vacuum annealing at 700°C for 1h, in nanocrystalline state.

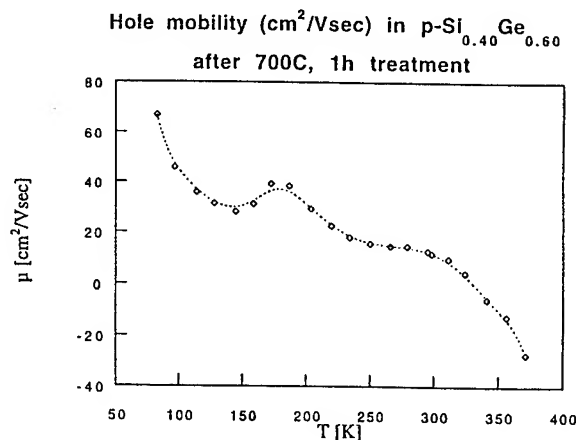


Fig.8. The temperature dependence of hole mobility in $\text{Si}_{0.4}\text{Ge}_{0.6}$ films after vacuum annealing at 700°C for 1h.

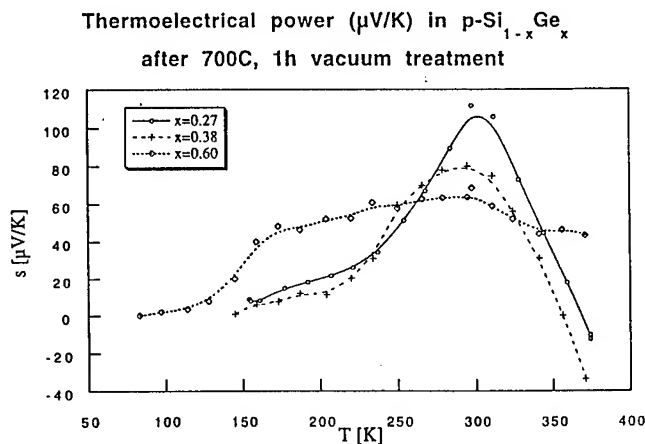


Fig.9. The temperature dependence of the thermoelectric power of heavily Ga-doped $\text{Si}_{1-x}\text{Ge}_x$ films after vacuum annealing at 700°C for 1h.

Conclusions

- (i) Ga-doped $\alpha\text{-Si}_{1-x}\text{Ge}_x$ films, independently of x , demonstrated extraordinary small grain size (in order of 100\AA) after crystallization at $700\text{--}800^\circ\text{C}$ for 1h, which was about 100 times smaller than that in undoped and P-doped SiGe films under the same treatment. This grain growth hindering effect can be, possibly, beneficial, in high-efficiency thermoelectric structure technology.
- (ii) First measurements of transport properties of nano-SiGe(Ga) films show that those stable nano-SiGe(Ga)/ SiO_2 structures can be useful in further for thermoelectric applications at low temperatures.

References

[1] C.M.Bhandari and D.M.Rove, Silicon-Germanium Alloys as High-Temperature Thermoelectric Materials, *Contemp. Phys.*, 1980, v.21, No.3, pp.219-242.

[2] F.D.Rosi, Thermoelectricity and Thermoelectric Power Generation, *Solid-State Electronics*, 1968, v.11, No.6, pp. 833-868.

[3] A.Borshchevsky and J.-P.Fleural, Growth of heavily-doped SiGe from metallic solutions, *J. Cryst. Growth*, 1993, v.128, No.1, pp. 331-337; B.A.Cook, J.L.Harringa, S.H.Han, and C.B.Vining, $\text{Si}_{0.80}\text{Ge}_{0.20}$ thermoelectric alloys prepared with GaP additions, *J. Appl. Phys.* 1995, v.78, No.9, pp.5474-5480.

[4] G.A.Slack and M.A.Hussain, The maximum possible conversion efficiency of silicon-germanium thermoelectric generators, *J. Appl. Phys.* 1991, v.70, No.5, pp.2694-2718.

[5] C.B.Vining, W.Laskow, J.O.Hanson, R.R.Van der Beck, and P.D.Gorsuch, Thermoelectric properties of pressure-sintered $\text{Si}_{0.8}\text{Ge}_{0.2}$ thermoelectric alloys, *J. Appl. Phys.* 1991, v.69, No.8, pp.4333-4340.

[6] L.W.Whitlow and T.Hirano, Superlattice applications to thermoelectricity, *J. Appl. Phys.* 1995, v.78, No.9, pp.5460-5466.

[7] F.Edelman, R.Weil, P.Werner, M.Reiche, and W.Beyer, Crystallization of Amorphous Hydrogenated $\text{Si}_{1-x}\text{Ge}_x$ Films, *phys. stat. sol. (a)*, 1995, v.150, No.2, pp.407-425; F.Edelman, R.Weil, P.Werner, M.Reiche, E.Schroer, J.Heydenreich, and W.Beyer, Transformations in $\text{Si}_{1-x}\text{Ge}_x\text{:H}$ Films on SiO_2 Substrates, *Polycrystalline Semiconductors IV*, Eds. S.Pizzini, S.Martinuzzi, H.P.Strunk, J.H.Werner, Scitec Publications, Switzerland, 1996, in press.

[8] H.Stöhr und W.Klemm, Über Zweistoffsysteme mit Germanium, *Z. anorg. und allgem. Chem.* 1939, v.241, No.4, pp.305-324; J.P.Dismukes, L.Ekstrom, and R.J.Paff, Lattice Parameters and Density in Germanium-Silicon Alloys, *J. Phys. Chem.*, 1964, v.68, No.10, 3021-3027.

[9] *Binary Alloy Phase Diagrams*, Editor-in-Chief T.B.Massalski, v.2, ASM International, 1990.

[10] V.I.Fistul', *Heavily Doped Semiconductors*, Plenum Press, N.Y., 1969.

[11] D.M.Rowe and V.S.Shukla, The effect of phonon-grain boundary scattering on the lattice thermal conductivity and thermoelectric conversion efficiency of heavily doped fine-grained, hot-pressed silicon germanium alloy, *J. Appl. Phys.*, 1981, v.52, No.12, 7421-7426.

[12] K.Seeger, *Semiconductor Physics*, Springer-Verlag, Wien-N.Y., 1973.

Optical, electrical and structural properties of polycrystalline β -FeSi₂ thin films fabricated by electron beam evaporation of ferrosilicon

H. Katsumata*, Y. Makita, H. Takahashi**, H. Shibata, N. Kobayashi, M. Hasegawa,
S. Kimura, A. Obara, J. Tanabe** and S. Uekusa*

Electrotechnical Laboratory, 1-1-4 Umezono, Tsukuba, Ibaraki 305, Japan

*Meiji University, 1-1-1 Higashi-mita, Tama, Kawasaki, Kanagawa 214, Japan

**Nippon Inst. of Tech., 4-1 Gakuendai, Miyashiro, Minami-Saitama, Saitama 345, Japan.

ABSTRACT

Ferrosilicon (FeSi₂) grains (99.9 %) were evaporated at room temperature onto the (100)-oriented n-type FZ Si substrates using electron beam deposition technique. Optical, electrical and structural properties were systematically investigated as a function of subsequent isochronal (2 hrs) annealing temperature (T_a) in the range of 400 ~ 950 °C. X-ray diffraction and Raman scattering analysis suggested the formation of polycrystalline β -FeSi₂ above $T_a=500$ °C, whereas above $T_a=800$ °C, Si agglomeration was observed to form. The electrical resistivity of these samples reached a maximum ($0.542 \Omega \cdot \text{cm}$) at $T_a=700$ °C, and then it decreased with increasing T_a . Its decrease process was explained by considering the creation of Si vacancies, which could presumably be acting as holes. It is of great interest that in $T_a=600 \sim 800$ °C, the majority carrier converts from n- to p-type. Typical carrier concentrations and mobilities were determined to be $\mu_n=39.4 \text{ cm}^2/\text{V} \cdot \text{sec}$, $n_e=6.59 \times 10^{17} \text{ cm}^{-3}$ for n-type β -FeSi₂ with $T_a=600$ °C and $\mu_h=20.3 \text{ cm}^2/\text{V} \cdot \text{sec}$, $n_h=2.22 \times 10^{18} \text{ cm}^{-3}$ for p-type β -FeSi₂ with $T_a=850$ °C. Optical absorption measurements revealed that the nature of the band-gap varies from an indirect to direct one with increasing T_a .

I. INTRODUCTION

β -FeSi₂ is a candidate material for future thermoelectric devices [1] as well as Si-based optoelectronic devices, i.e., solar cells [2] and photo-detectors [3] because of; 1) non-toxicity, good physical-chemical stability at high temperatures, and large abundance of the involved Si and Fe elements in the Earth, 2) its semiconducting properties having a supposedly direct band-gap of about 0.83 ~ 0.87 eV at room temperature [4], 3) a high optical absorption coefficient of up to 10^5 cm^{-1} near 1 eV [5-7], and 4) a possibility to grow this material epitaxially on Si substrate [8]. However, there are so many unclear points in this material, for example, although pure β -FeSi₂ is believed to be intrinsic semiconductor in the field of thermoelectric device [9], generally

unintentionally doped β -FeSi₂ exhibits p-type conductivity [5]. In addition, the nature of the band gap has been reported to be indirect according to the theoretical calculation [10], but, it was empirically demonstrated to be direct [4]. Thus, it is still necessary to investigate the fundamental properties of this material closely and systematically.

In this work, polycrystalline β -FeSi₂ was fabricated by electron beam evaporation of ferrosilicon (FeSi₂) grains onto the Si (100) substrates at room temperature, followed by a thermal annealing up to 900 °C for 2 hrs. Their optical, electrical and structural properties were investigated as a function of subsequent annealing temperature (T_a) in the range of 400 ~ 950 °C.

II. EXPERIMENTAL METHODS

Wafers used in this study are (100)-oriented FZ grown n-type Si with resistivity values higher than $1 \times 10^3 \Omega \cdot \text{cm}$. Prior to the deposition, the wafers were treated in a solution of HF:H₂O=1:50 for 30 sec. Iron silicides of 4500 Å thickness were then deposited on the silicon wafers in the vacuum around 1×10^{-5} Torr at room temperature by electron beam evaporation of ferrosilicon (FeSi₂) grains (99.9 %). Subsequently, they were isochronally annealed for 2 hrs at $T_a=400 \sim 950$ °C in constant N₂ gas flow with infrared gold image furnace, which resulted in the formation of polycrystalline β -FeSi₂ in the range of $T_a=500 \sim 900$ °C. For the structural phase determination an X-ray diffraction analysis was carried out using CuK α source. Raman scattering measurements were performed in backscattering geometry using 514.5 nm of an Ar⁺ laser in order to investigate the lattice defects and structural changes. Electrical properties were characterized at room temperature using a standard van der Pauw technique. To determine the nature of band-gap and its energy value, the optical absorption was measured at room temperature with a BOMEM DA8 spectrometer using a quartz halogen lamp as a light source. All the data were recorded as a function of annealing temperature (T_a).

III. RESULTS AND DISCUSSION

Figure 1 shows XRD spectra as a function of T_a . It presents a formation of polycrystalline β -FeSi₂ in the range of $T_a=500 \sim 900$ °C, although the as-grown sample and the sample with $T_a=400$ °C exhibit an amorphous structure. Above $T_a=950$ °C, phase transformation from β -FeSi₂ to α -Fe₂Si₅ is clearly identified. In this figure, signal from Si (111) is also recognized above 800 °C, suggesting that the Si agglomeration was formed in the β -FeSi₂ layers due to the high temperature annealing.

These features were also found in the analysis of Raman measurements as shown in Fig. 2. Two signals appearing at 198 and 250 cm⁻¹ are assigned to originate from β -FeSi₂ [11], and especially, the latter signal observed at 250 cm⁻¹ is dominant in the range of $T_a=500 \sim 850$ °C, indicating the formation of β -FeSi₂ with good crystalline quality. Another signal is found at 520 cm⁻¹ for the samples with $T_a=850 \sim 900$ °C and is attributed to Si-Si bonding, exactly indicating that the Si agglomeration was created in the formed β -FeSi₂ layers as was already discussed above.

Figures 3 and 4 show the results of van der Pauw measurements carried out at room temperature. Room temperature electrical resistivities are presented in Fig. 3 as a function of T_a . One can see that the resistivity initially increases up to 0.542 $\Omega \cdot \text{cm}$ at $T_a=700$ °C, corresponding to the previous reported resistivity value (0.3 $\Omega \cdot \text{cm}$) for an epitaxially grown β -FeSi₂ on Si [8]. This initial increase process reflects a nucleation and growth process, varying from an amorphous

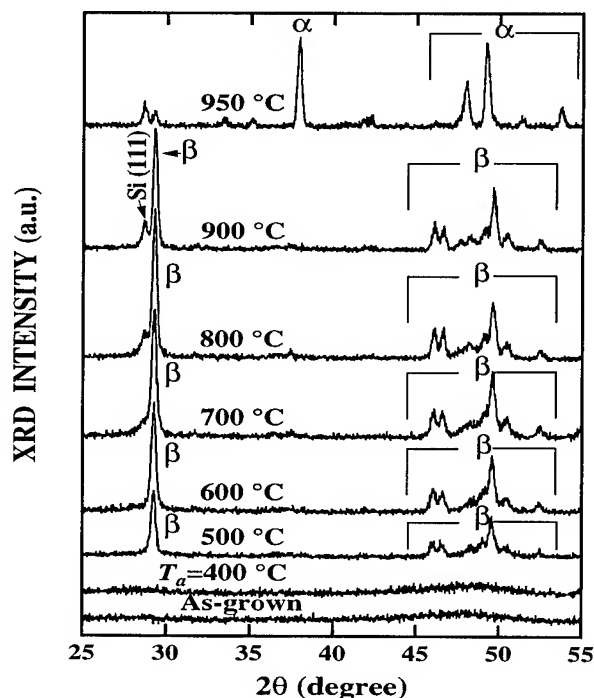


Fig.1 XRD spectra for FeSi₂ deposited on Si as a function of annealing temperature, T_a .

metallic iron silicide to semiconducting β -FeSi₂. Above 700 °C, the resistivity, however, rapidly decreases to $2.40 \times 10^{-3} \Omega \cdot \text{cm}$ at 950 °C, which is two order of magnitude higher than the typical resistivity value ($0.1\text{-}0.2 \times 10^{-4} \Omega \cdot \text{cm}$) for α -Fe₂Si₅ single crystal [12]. Si agglomeration is probably responsible for the unusual higher resistivity for the samples with $T_a=950$ °C. The reason for the resistivity reduction observed in $T_a=700 \sim 900$ °C is discussed later.

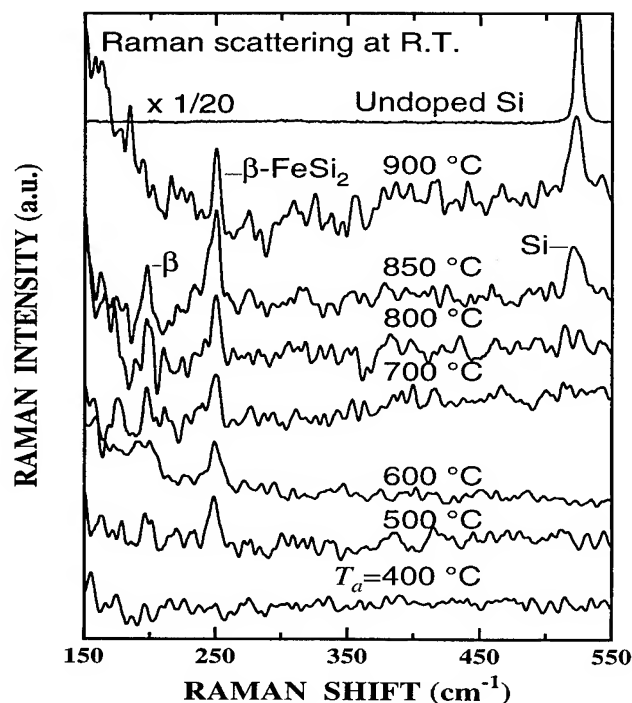


Fig. 2 Raman scattering spectra for FeSi₂ deposited on Si as a function of annealing temperature, T_a .

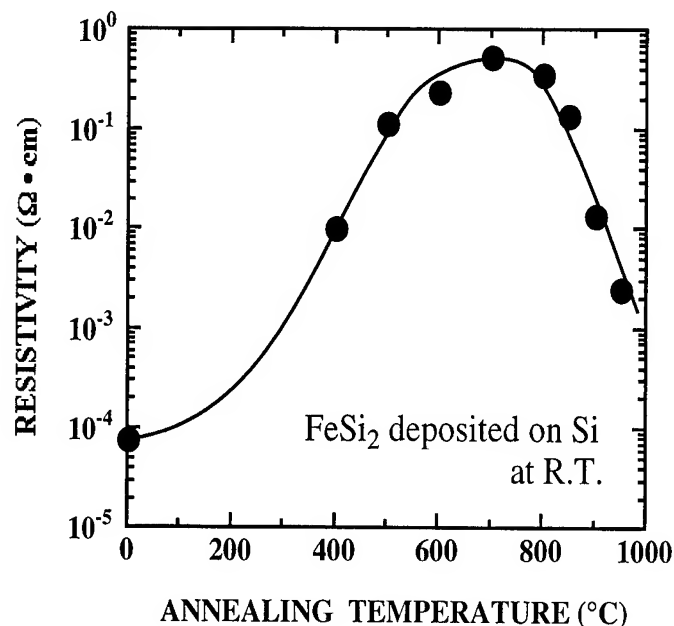


Fig. 3 Electrical resistivities for FeSi₂ deposited on Si as a function of annealing temperature, T_a .

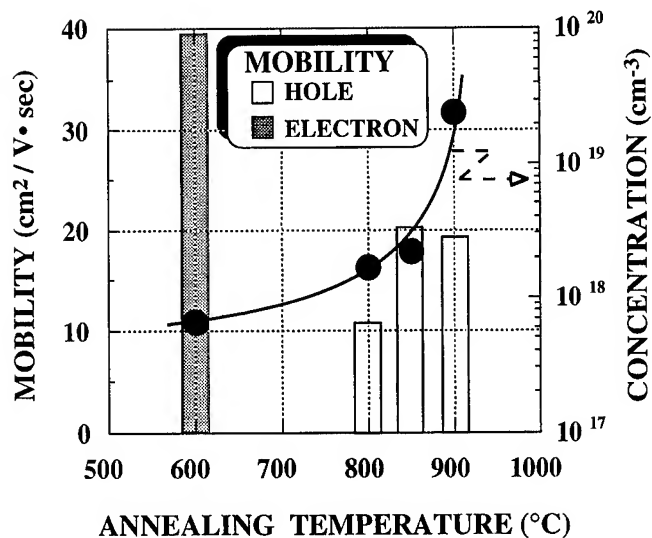


Fig. 4 Annealing temperature, T_a dependence of carrier concentration and mobilities for FeSi₂ deposited on Si.

The room temperature mobilities and the carrier concentrations for the samples with $T_a=600 \sim 900$ °C are shown in Fig. 4 as a function of T_a , in which the conductivity-type for the samples with $T_a < 600$ °C and $T_a = 700$ °C was indistinguishable. We observed a type-conversion with respect to the majority carrier from electron (n-type) to hole (p-type) in the range of $T_a = 600 \sim 800$ °C. Their mobilities were measured to be $\mu_n = 39.4$ cm²/V·sec for n-type β -FeSi₂ with $T_a = 600$ °C and $\mu_h = 10.6 \sim 20.3$ cm²/V·sec for p-type β -FeSi₂ with $T_a = 800 \sim 900$ °C, while the carrier concentration increased with increasing T_a , from $n_e = 6.59 \times 10^{17}$ cm⁻³ for n-type β -FeSi₂ with $T_a = 600$ °C to $n_h = 2.39 \times 10^{19}$ cm⁻³ for p-type β -FeSi₂ with $T_a = 900$ °C. The carrier concentration of 2.22×10^{18} cm⁻³ observed for p-type β -FeSi₂ with $T_a = 850$ °C agrees quite well with the previously reported value of 2×10^{18} cm⁻³ for an epitaxially grown β -FeSi₂ on Si [8], while the mobility value of 20.3 cm²/V·sec is one order of magnitude higher than that of ~ 2 cm²/V·sec observed for an epitaxial one [8].

In our recent results [13] of electron spin resonant (ESR)-measurements carried out for a single crystal β -FeSi₂ grown by chemical vapor transport (CVT) technique, Si vacancies were suggested to have an influence on the hole (p-type)-conductivity of β -FeSi₂. In this study, we observed a Si agglomeration for the samples with $T_a > 800$ °C as was already shown in Figs. 1 and 2, and it is consequently assumed to lead into a creation of Si vacancies in β -FeSi₂ layers. Taking this assumption into consideration, it is reasonable that the hole concentration increases with increasing T_a for the samples with $T_a = 800 \sim 900$ °C, due to the appearance of Si vacancies in β -FeSi₂ layers. Simultaneously, the reason for the rapid decrease process of resistivity for the samples with $T_a > 800$ °C demonstrated in Fig. 3 is also explained by considering an increase of the Si vacancies,

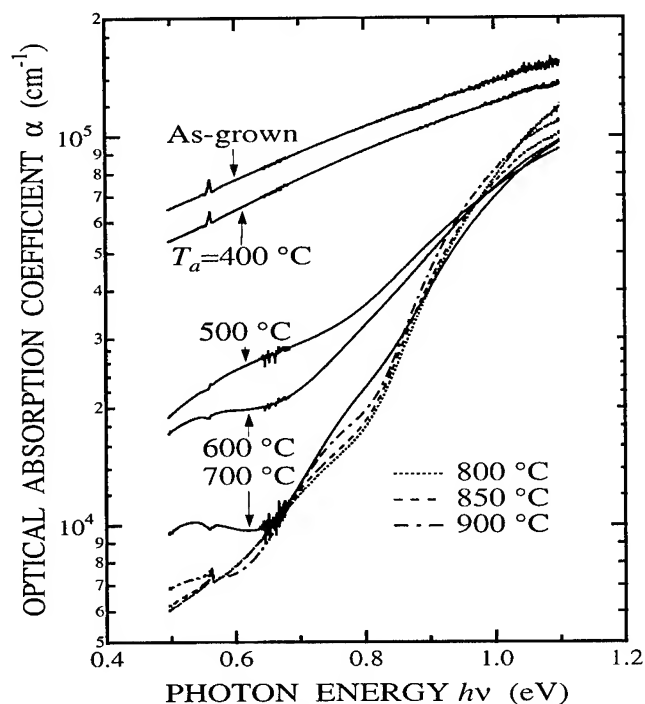


Fig. 5 Optical absorption coefficient (α) versus photon energy ($h\nu$) as a function of annealing temperature, T_a .

which could presumably be acting as holes. If Fe vacancies are supposed to act as donors, n-type conductivity is plausible to be observed for the sample with $T_a = 600$ °C.

Although the optical band-gap and its nature of β -FeSi₂ have so far been investigated by many research groups [4-8], we for the first time systematically investigated the annealing temperature (T_a) dependence of the optical absorption properties of β -FeSi₂ fabricated by electron beam deposition technique. Figure 5 shows the optical absorption coefficient (α) versus photon energy ($h\nu$). Semiconducting absorption starts to be observed from $T_a = 500$ °C, and the best crystalline quality was achieved at $T_a = 800$ °C. Above $T_a = 800$ °C, the crystalline quality was found to degrade gradually, due presumably to the appearance of Si vacancies. The high optical absorption coefficient of up to 10^5 cm⁻¹ near the energy of 1.0 eV is commonly observed in β -FeSi₂ formed by various techniques [4-8] and can be of interest in view of optoelectronics applications, i.e., solar cells and photo-detectors.

The nature of the optical band-gap and the band-gap energy can be determined by fitting the absorption data to theoretical curves that follow the relationships between optical absorption coefficient (α) and photon energy ($h\nu$) [14];

$$\alpha \cdot h\nu = A(h\nu - E_g^{\text{ind}} - E_{\text{ph}})^2 \quad (1)$$

for the materials with an indirect band-gap,

$$\alpha \cdot h\nu = A'(h\nu - E_g^{\text{dir}})^{1/2} \quad (2)$$

for the direct band-gap materials, and

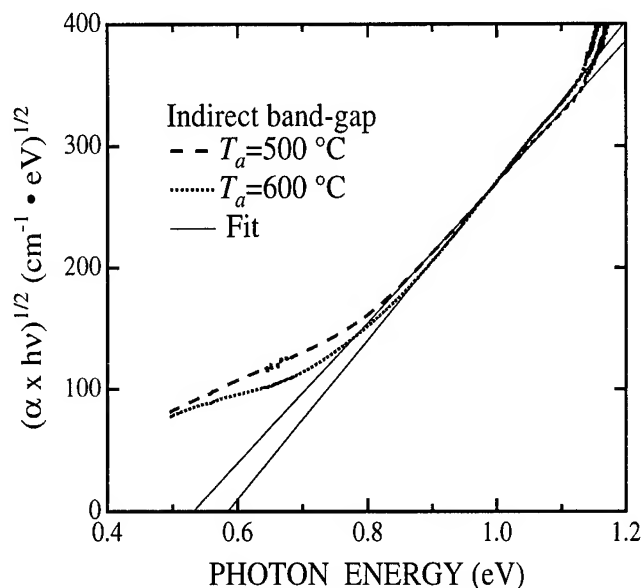


Fig. 6 The results of the fitting using Eq. (1), indicating the indirect band-gap transition for the samples with $T_a=500$ and 600 °C.

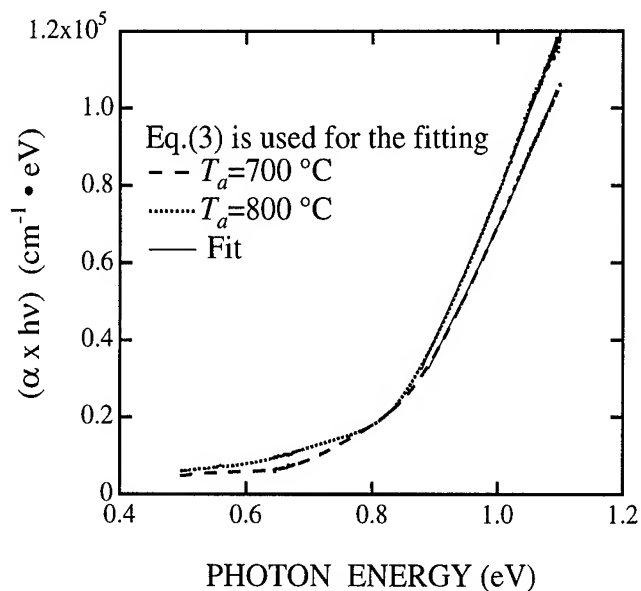


Fig. 7 The results of the fitting using Eq. (3), indicating the minimum indirect band-gap which is a few tens meV lower than direct one at Γ point, for the samples with $T_a=700$ and 800 °C.

$\alpha \cdot hv = A(hv - E_g^{\text{ind}} - E_{\text{ph}})^2 + A'(hv - E_g^{\text{dir}})^{1/2}$ (3)

for the material with a minimum indirect band-gap very close in energy to the direct band-gap at Γ . In equations. (1), (2) and (3), E_{ph} is the phonon energy, A and A' are constants which are associated with specific details of the band structure, and E_g^{ind} and E_g^{dir} are the band-gap energies for the indirect and direct transition, respectively.

The samples with $T_a=500$ and 600 °C were fitted by the equation (1) for the indirect band-gap materials as shown in Fig. 6, and those with $T_a=700$ and 800 °C were fitted by an equation

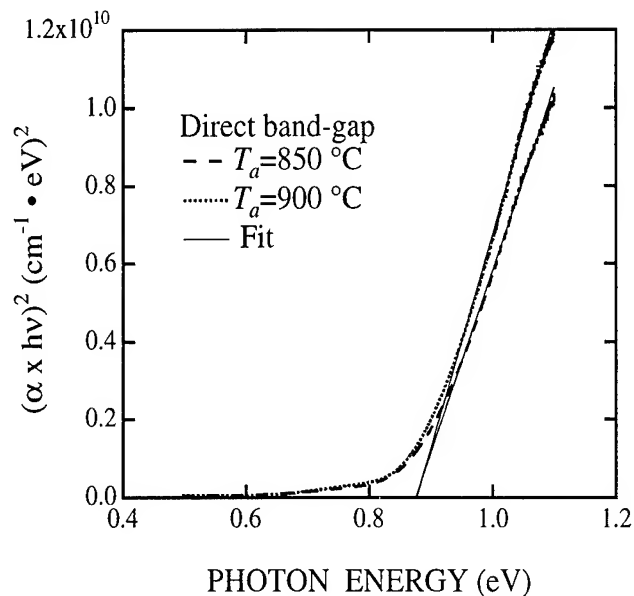


Fig. 8 The results of the fitting using Eq. (2), indicating the direct band-gap transition for the samples with $T_a=850$ and 900 °C.

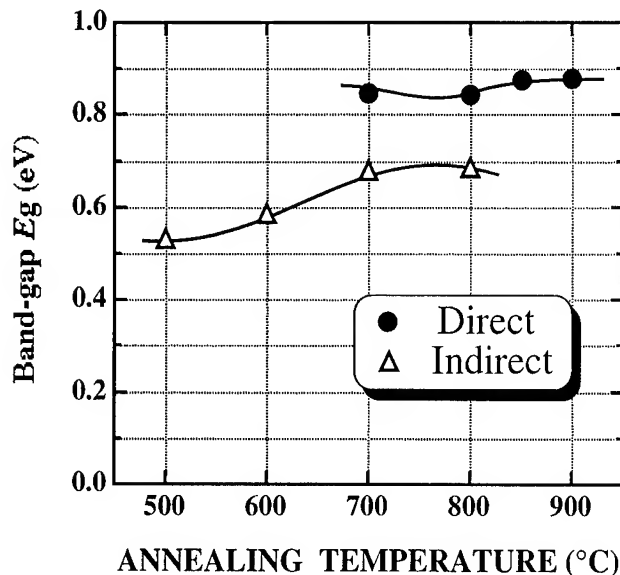


Fig. 9 The nature of the band-gap and the band-gap energies determined by the fitting.

(3) as shown in Fig. 7, while those with $T_a=850$ and 900 °C were fitted by the equation (2) for the direct band-gap materials as shown in Fig. 8. These facts indicate that the nature of the band-gap strongly depends on the annealing temperature. The results determined by the above fitting, i.e., the nature of the band-gap and their band-gap energies are illustrated in Fig. 9. The nature of the band-gap varies from indirect to direct, and their values are estimated to be $0.532 \sim 0.687$ eV for the indirect band-gap and $0.843 \sim 0.877$ eV for the direct-band-gap.

IV. CONCLUSIONS

Polycrystalline β -FeSi₂ were fabricated by electron beam evaporation of ferrosilicon (FeSi₂) grains onto the Si (100) substrates at room temperature, followed by a thermal annealing up to 900 °C for 2 hrs. Their optical, electrical and structural properties were systematically investigated as a function of subsequent annealing temperature (T_a) in the range of 400 ~ 950 °C. X-ray diffraction and Raman scattering analysis suggested the formation of polycrystalline β -FeSi₂ above $T_a=500$ °C, nevertheless above $T_a=800$ °C, Si agglomeration was observed to appear. In van der Pauw measurements, carrier type-conversion from electron (n-type) to hole (p-type) were observed in $T_a=600 \sim 800$ °C, and their typical carrier concentrations and mobilities were determined to be $\mu_n=39.4 \text{ cm}^2/\text{V}\cdot\text{sec}$, $n_e=6.59 \times 10^{17} \text{ cm}^{-3}$ for n-type β -FeSi₂ with $T_a=600$ °C and $\mu_h=20.3 \text{ cm}^2/\text{V}\cdot\text{sec}$, $n_h=2.22 \times 10^{18} \text{ cm}^{-3}$ for p-type β -FeSi₂ with $T_a=850$ °C. The resistivity reaches a maximum ($0.542 \Omega\cdot\text{cm}$) at $T_a=700$ °C, and then it decreases with increasing T_a . Its decrease process was explained by considering a creation of Si vacancies, which could be acting as holes and be expected to originate from the results of Si agglomeration. Optical absorption measurements revealed that the nature of the band-gap varies from an indirect ($0.532 \sim 0.687 \text{ eV}$) to direct one ($0.843 \sim 0.877 \text{ eV}$) with increasing T_a .

REFERENCES

- [1] E. Groß, M. Riffel, and U. Stöhrer, J. Mater. Res. **10**, 34 (1995).
- [2] M. Powalla and K. Herz, Appl. Surf. Sci. **65/66**, 482 (1993); M. Libezny, J. Poortmans, T. Vermeulen, P.H. Amesz, K. Herz, and M. Povalla, G.-U. Reinsperger, M. Schmidt, S. Brehme, J. Nijs, and H. Lange, Book of Abstracts of 13th European Photovoltaic Solar Energy Conference and Exhibition, PO8B.49 (1995).
- [3] K. Lefkl, and P. Muret, J. Appl. Phys. **74**, 1138 (1993).
- [4] C. Giannini, S. Lagomarsino, F. Scarinci, and P. Castrucci, Phys. Rev. B **45**, 8822 (1992).
- [5] C.A. Dimitrdis, J.H. Werner, S. Logothetidis, M. Stutzmann, J. Weber, and R. Nesper, J. Appl. Phys. **68**, 1726 (1990).
- [6] N. Kobayashi, H. Katsumata, H.L. Shen, M. Hasegawa, Y. Makita, H. Shibata, S. Kimura, A. Obara, S. Uekusa, and T. Hatano, Thin Solid Films, **270** (1995) 406.
- [7] H. Katsumata, H.L. Shen, N. Kobayashi, Y. Makita, M. Hasegawa, H. Shibata, S. Kimura, A. Obara, and S. Uekusa, Proc. of the 9th Int. Conf. on Ion Beam Modification of Materials, (1995) 943.
- [8] A. Rizzi, B.N.E. Rösen, D. Freundt, Ch. Dieker, and H. Lüth, Phys. Rev. B **51**, 17780 (1995).
- [9] S. Tokita, T. Amano, M. Okabayashi, and I.A. Nishida, Proc. of the 12th Int. Conf. on Thermoelectronics, 197, November, Japan (1993).
- [10] N.E. Christensen, Phys. Rev. B **42**, 7148 (1990).
- [11] K. Lefki, P. Muret, E. Bustarret, N. Boutarek, R. Madar, J. Chevrier, J. Derrien, and M. Brunel, Solid State Commun. **80** (1991) 791.
- [12] Ch. Kloc, E. Arushanov, M. Wendl, H. Hohl, U. Malang, and E. Bucher, J. Alloys & Compounds, **219** (1995) 93.
- [13] I. Aksenov, H. Katsumata, Y. Makita, Y. Kimura, T. Shinzato, and K. Sato, submitted to J. Appl. Phys.
- [14] J.J. Pankov, in : Optical Process in Semiconductors, (Dover, New York, 1971), p. 34.

Structure and thermoelectric properties of nano-crystalline $\text{Re}_x\text{-Si}_{1-x}$ thin film composites.

A. T. Burkov*, A. Heinrich, C. Gladun, W. Pitschke, J. Schumann
Institute of Solid State and Material Research, D-01171 Dresden, Germany

In this report results on phase formation and transport properties of amorphous and nano-crystalline Re-Si thin films are presented. The results imply that the partially crystallized Re-Si films i.e. films consisting of amorphous and nano-crystalline phases form a new class of heterostructures which are essentially different from binary insulator-metal mixtures. We have found that the resistivity and thermopower of the heterogeneous films consisting of amorphous and nano-crystalline phases do not follow to well known Effective Medium Approximation when the ratio between these two phases is varied. Both phase composition and crystalline grain size appear to be important parameters for the thermoelectric material optimization.

I. INTRODUCTION

Despite continuous efforts there has been not much improvement of the properties of materials suitable for thermoelectric energy conversion during recent 10 years. This resulted in a discussion whether a principle limit for the thermoelectric energy conversion efficiency has been achieved or there is still room for further improvement. Recently, new approaches to develop more efficient thermoelectrics were proposed. One of them is based on the use of quasi-two-dimensional multilayer structures made of conventional thermoelectric materials like Bi-Te-based alloys. According to the theoretical estimations one can expect an increase of the thermoelectric parameters in such multilayers to 20–30 %. We have investigated another type of inhomogeneous materials—these are nano-crystalline (NC) transition metal silicides.

Nano-crystalline materials are characterized by ultra-fine grain sizes and a large volume fraction of interfaces. These interfaces could provide an additional scattering mechanism for the conduction electrons. If the scattering magnitude on the interfaces is strongly energy-dependent then this could result in an increase of the thermoelectric parameters of a material.

We are presenting the resistivity and thermopower of thin film composites which consist of amorphous Re-Si and crystalline grains of the ReSi_2 compound. Recently, the interest in thin film rhenium silicides has considerably increased mainly because of their potential application in optoelectronic devices integrated on silicon [1–3]. Silicides are also considered as promising materials for thermoelectric applications [4].

Within the Re-Si system ReSi_2 is a narrow-gap semiconductor. The forbidden gap was found to be of 0.12 eV [1,5]. A great body of research has been devoted to the studies of bulk silicide materials, see for a review for example [6] and epitaxially grown silicide films on silicon [1,7,8]. Much less has been done in studies of polycrystalline thin films of the semiconducting ReSi_2 compound, particularly of nano-crystalline films [3].

Among variety of methods for synthesis of NC materials the crystallization from amorphous state possesses a number of advantages:

- It is very simple and convenient in this method to control the crystallization process. Conventional annealing can result in nano-crystallization with different grain sizes in dependence on the heat treatment conditions.
- The crystallization from an amorphous state provides an unique method to study interfacial phenomena in NC materials. Because in this method the crystalline phase is formed from the amorphous state via solid phase transformation the internal interfaces are clean.
- a combination of the heat treatment with in-situ transport property measurements or with in-situ X-ray investigations gives immediate and direct information about kinetics of nano-crystallization process and properties of the material.

We started with the amorphous film and have achieved the nano-crystallized structure by annealing. In dependence on the temperature and time of the annealing treatment the volume fractions of amorphous and nano-crystalline phases have been varied in a broad range.

The films with compositions close to the stoichiometric composition of the semiconducting ReSi_2 form a new interesting class of heterogeneous NC materials. In dependence of the initial film composition three distinctive types of the heterogeneous compounds could be formed in course of the heat treatment:

- Stoichiometric film consists of nanodispersed grains of semiconducting phase within an amorphous matrix of the same atomic composition. Interfaces crystalline ReSi_2 -amorphous disilicide will be realized.
- On the metal-rich side the complete crystallization will result in a formation of two- or three-phase compound consisting of crystalline disilicide and

crystalline Re. In the intermediate stages of annealing the film consists of NC disilicide within amorphous matrix with an excess of the metal in the interfaces.

- On the silicon-rich side the complete crystallization results in the formation of two-phase compound consisting of crystalline ReSi_2 and crystalline silicon. In the intermediate stages the film consists of NC disilicide and amorphous matrix with an excess of Si in the interfaces.

II. EXPERIMENTAL

The films were prepared by magnetron co-sputtering from pure component targets onto unheated substrates. As the substrates oxidized Si wafers were used. The film thickness was typically 100–150 nm. The composition analysis of the films was carried out by Rutherford Backscattering Spectroscopy (RBS) and Energy Dispersive X-ray Spectroscopy (EDXS), the former with an accuracy of $\pm 1\%$. The structure of the films was determined by in-situ X-ray diffraction measurements during annealing at temperatures up to 1250 K and also after ex-situ annealing at room temperature. From X-ray line broadening analysis we estimate the size of the crystalline grains. According to the X-ray data the as-deposited films have an amorphous structure. Transport properties (thermopower S and resistivity ρ) were measured during annealing of the films in high-purity helium atmosphere. By that means we were able to control the phase formation and to get immediately the transport properties in correlation with the phase composition of the films. Electrical resistivity was measured by conventional DC four-probe method. In case of the thermopower measurements the differential method was used. Both properties were measured simultaneously during the heat treatment of a sample as functions of the temperature and of the annealing time.

III. RESULTS AND DISCUSSION

A. Stoichiometric composites

Since in the films of stoichiometric ReSi_2 ratio between Re and Si both crystalline and amorphous phases have the same composition, no other phases appear in the course of the crystallization. Therefore the films can be considered as true binary mixtures where by annealing only the ratio between these amorphous and nanocrystalline components is changed.

Effective Medium Approximation (EMA) is commonly accepted as a theoretical basis for analysis of various properties of composite materials. Applications of EMA to describe the electrical resistivity and thermopower are

reviewed in several papers, see for example [9,10]. It has been found that, at least for binary composites, both ρ and S should vary monotonically with the component ratio in a composite and always lie between the corresponding values of the pure components [10]. Parameter $Z = S^2/(\rho\kappa)$ (κ - thermal conductivity) which determines the figure of merit of a thermoelectric energy converter should be always lower than that one of the pure components. These theoretical conclusions have been in agreement with experimental results for a variety of composite materials, including thin-film composites [9,11–13]. Most of the thin-film composites which have been investigated are binary mixtures of an insulating (or semiconducting) material and of a metal. As an example we can mention Ge-Al films consisting of amorphous Ge and crystalline Al-particles (with typical size from 5 to 20 nm) [12,13].

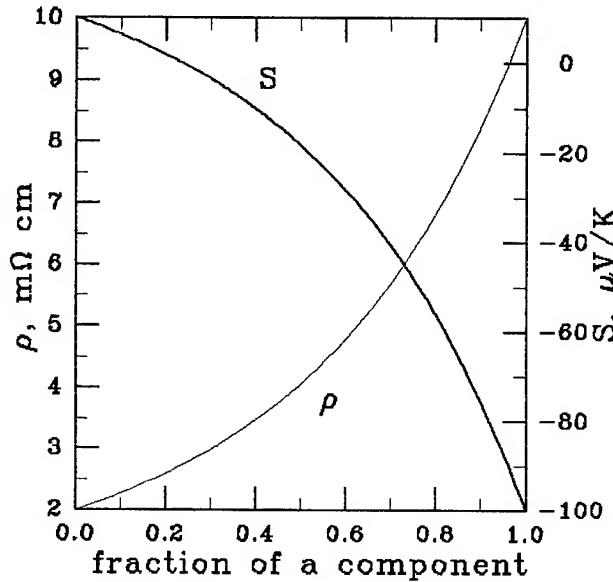


FIG. 1. Variation of the electrical resistivity and thermopower of a binary composite system according to EMA (schematically).

Within EMA the overall variation of the resistivity and thermopower can be represented by so called generalized effective medium equations [14,15]:

$$\frac{f \cdot [\rho_1^{1/t} - \rho_1^{1/t_c}]}{\rho_1^{1/t} + \rho_1^{1/t_c} \cdot f_c / (1 - f_c)} + \frac{(1 - f) \cdot [\rho_2^{1/t} - \rho_2^{1/t_c}]}{\rho_2^{1/t} + \rho_2^{1/t_c} \cdot f_c / (1 - f_c)} = 0 \quad (1)$$

$$S = \frac{(S_1 \rho_2 \kappa_2 - S_2 \rho_1 \kappa_1) + \kappa \rho (S_2 - S_1)}{\kappa_2 \rho_2 - \kappa_1 \rho_1} \quad (2)$$

with f being the volume fraction of component 1, f_c the percolation threshold of component 1, and t the critical exponent of the conductivity. Figure 1 schematically shows EMA predictions for both resistivity and thermopower of a binary metal-semiconductor compound

with the values of pure components similar to the Re-Si system considered in this paper.

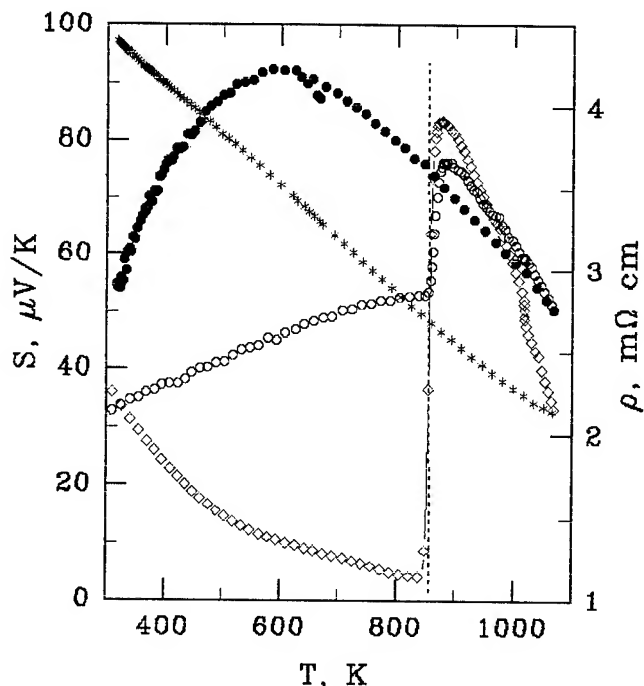


FIG. 2. Electrical resistivity (\diamond , on heating; $*$, on cooling) and thermopower (\circ , on heating; \bullet , on cooling) of the film of stoichiometric ReSi_2 composition. The broken line indicates the crystallization temperature.

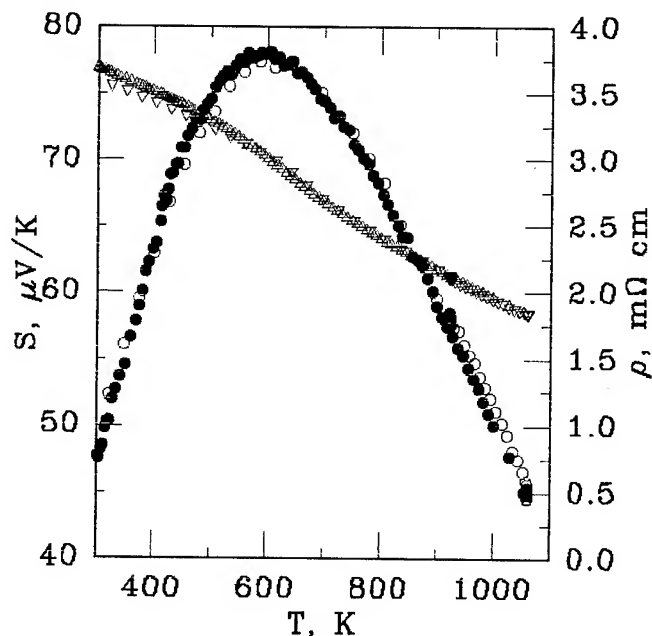


FIG. 3. Resistivity and thermopower of a single-phase ReSi_2 thin film. The data were obtained on heating (\circ , thermopower, and ∇ , resistivity) and on cooling (\bullet , thermopower, and Δ , resistivity).

In Figure 2 the transport properties of the stoichiometric film are shown in dependence on temperature. The measurements were done with a constant temperature variation rate of 2 K/min on heating and 10 K/min on cooling. The crystallization takes place at annealing temperatures of about 800–850 K. Complete crystallization can be achieved by a long term annealing of the film at temperatures above 1000 K. The resistivity and thermopower of such a single-phase ReSi_2 film are shown in Fig. 3. The film was annealed at about 1050 K for 20 hours. Good reproducibility of the results indicates the stability of the film.

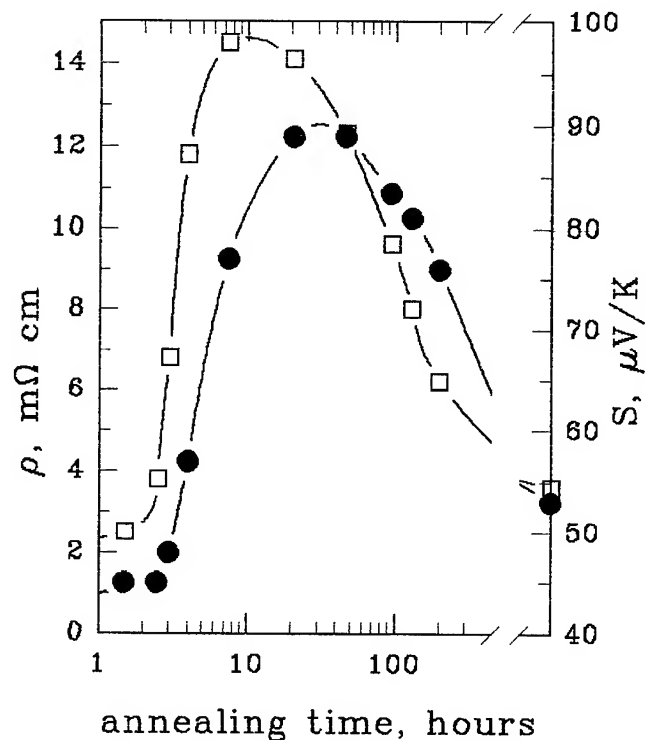


FIG. 4. Variation of the electrical resistivity, \square , and thermopower, \bullet , with annealing time. The two points after the axis break show ρ and S for single-phase crystalline film.

Figure 4 shows the variation of S and ρ with the annealing time. Each point in Fig. 4 represents the resistivity or thermopower simultaneously measured at 350 K after annealing the given time t at 810 K. At $t=0$ the film is a single-phase amorphous compound. With increasing annealing time the amount of the crystalline ReSi_2 phase increases, the film becomes a binary mixture consisting of nano-crystalline ReSi_2 phase and amorphous phase of the same atomic composition. Finally, at large annealing times we got again a single-phase film but of crystalline ReSi_2 .

The X-ray measurements revealed that ReSi_2 is the only crystalline phase formed during annealing. The X-ray

line broadening analysis yields information on the crystalline grain sizes (d) in dependence on annealing temperature. These data are summarized in Table I (second column).

In a broad range of the annealing temperatures (up to 1200 K) and annealing times the grain size of the crystalline phase in the stoichiometric composites remains constant of about 20 nm. At the annealing temperature of 810 K the grain size remains constant within the experimental uncertainty of ± 5 nm throughout the whole annealing procedure. That means that the crystallization progresses not due to a growth of individual grains but by an increasing number of NC grains within the amorphous matrix. This result is in agreement with the recent thermodynamical analysis of the crystallization from an amorphous state [16].

According to the X-ray data we can consider the results shown in Fig. 4 as the composition dependence of the resistivity and thermopower of a Re-Si binary compound consisting of amorphous and nano-crystalline ReSi_2 .

The non-monotonous dependences of both ρ and S are in obvious disagreement with the predictions of EMA which are schematically shown in Fig. 1. This implies that the interfaces essentially effect the transport properties of the heterogeneous nano-crystalline compounds. The microscopic mechanism of this behaviour is not yet known. We want to emphasize that a trivial explanation of the above result by formation of interfacial layer of Si due to a small deviation of Re/Si ratio to the Si-rich side should be excluded. We have studied the films with small but certain deviation of the Re/Si ratio to the Re-rich side and found qualitatively the same non-monotonous behaviour of resistivity and thermopower, see Figure 6.

Useful information can be obtained from transformations of the resistivity temperature dependences with annealing. These temperature dependences are shown in Fig. 5 in \log_{10} -scale for different stages of annealing.

TABLE I. Crystalline grain sizes from in-situ X-ray data at different annealing temperatures T_a .

T_a , K	$\text{Re}_{0.39}\text{Si}_{0.61}$		$\text{Re}_{0.34}\text{Si}_{0.66}$		$\text{Re}_{0.30}\text{Si}_{0.70}$	
	d , nm	Re	d , nm	Re	d , nm	Si
750	52*	-	-	-	-	-
800	51	-	-	-	-	-
850	58	-	-	15	-	-
900	69	-	24	14	-	-
950	50	22	17	15	-	-
1000	93	27	16	14	-	-
1050	83	24	18	18	-	-
1100	190	48	22	17	-	-
1150	-	-	23	20	-	-
1200	-	-	26	44	-	-
1250	-	-	37	-	-	-
1300	-	-	57	-	-	-

*This film had been annealed ex-situ at $T_a=870$ K before the in-situ measurements

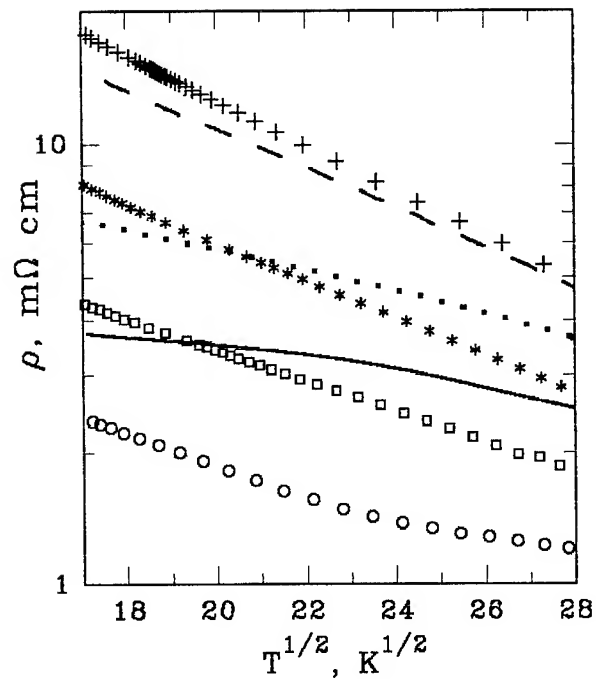


FIG. 5. The temperature dependent resistivity at different annealing stages: o, amorphous film; □, 2 hours of annealing; *, 3 hours; +, 8 hours; broken line, 47 hours; dotted line, 220 hours, and solid line, single-phase crystalline film.

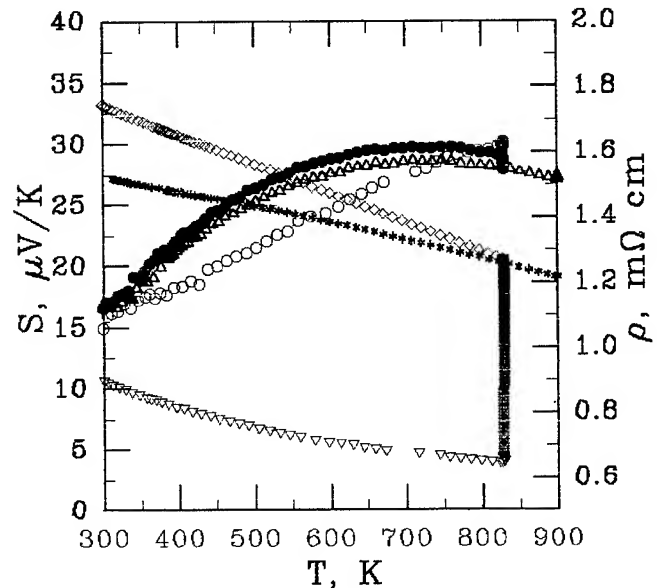


FIG. 6. Temperature dependent S and ρ of $\text{Re}_{0.39}\text{Si}_{0.61}$ film. o, S , and ∇ , ρ on heating (amorphous film); ●, S , and ◇, ρ on cooling after annealing at 829 K for 20 hours; Δ, S , and *, ρ on cooling after annealing at 900 K for 13 hours.

As it can be seen at early stages of annealing the $\log \rho(T)$ dependences are essentially parallel to each other. That means that the conductivity mechanism is the same for all these films despite different volume ratios of

the amorphous and nano-crystalline phases. Comparison with the temperature dependent resistivity of the single-phase films reveals that it is nearly the same like that of the as-deposited amorphous film but different from that of the crystalline one. Therefore we can suggest that at the early stages of annealing the nano-crystalline phase does not contribute to the conductivity of the film being isolated within the amorphous matrix by interfacial barriers. In this case the effective film cross-section will decrease with increasing of the nano-crystalline phase content.

The measured resistance of the film is determined by the specific resistivity of the amorphous phase ρ_{am} and effective film cross-section A_{am} :

$$R = \rho_{am} \frac{l}{A_{am}} \quad (3)$$

where l is distance between potential probes in the resistivity measurements. With increasing content of the nano-crystalline phase the apparent resistivity of the film ρ will be proportional to the amorphous phase resistivity with proportionality factor $\frac{A}{A_{am}}$, where A is the total film cross-section. This gives:

$$\rho = R \frac{A}{l} = \rho_{am} \frac{A}{A_{am}} \quad (4)$$

and

$$\log(\rho) = \log\left(\frac{A}{A_{am}}\right) + \log(\rho_{am}) \quad (5)$$

The increase of the first term in eqn. (5) with decreasing content of the amorphous phase results in the observed behaviour of the $\rho(T)$ temperature dependence at the early stages of the annealing.

In the measured temperature range the resistivity of those films varies with the temperature as:

$$\rho(T) \sim \exp^{-\sqrt{\left(\frac{T}{T^*}\right)}} \quad (6)$$

To our knowledge there is no microscopic theory to describe such resistivity temperature variation.

At later annealing stages (which corresponds to a larger amount of the nano-crystalline phase) the resistivity starts to deviate from the relation (6). This implies a change in the conductivity mechanism. The resistivity dependence on composition (Fig. 4) reveals that this change of the conductivity mechanism takes place at the same composition where resistivity has its maximal value. Therefore, we can suggest that this composition corresponds to the percolation threshold of the nano-crystalline phase.

B. Off-stoichiometric Compounds

In films with initial compositions different from the stoichiometric Re to Si ratio the crystallization is connected with a diffusion of one of the components to the

phase interfaces. In Re-rich films the interfaces should have an excess of Re as compared with both amorphous and crystalline phases. The temperature dependences of the resistivity and thermopower of a film with initial composition $\text{Re}_{0.39}\text{Si}_{0.61}$, which has about 5% of Re excess, are depicted in Fig. 6. From the transport properties measurements and from X-ray data (see Table I) we have found that ReSi_2 crystallizes at 800–850 K whereas crystallization of Re was observed at annealing temperatures of about 950 K. The average ReSi_2 grain size is somewhat larger than in stoichiometric films (Table I), but the Re-rich films can be still considered as nano-crystalline. The resistivity and thermopower show the same non-monotonous variation in the course of the annealing like it was found in case of the stoichiometric composites. This result suggests that the scattering on the interfaces with Re-excess also effects the transport properties and in essentially the same way as it was found for the stoichiometric films.

On the Si-rich side the completely crystallized films are expected to be composites of crystalline ReSi_2 and pure crystalline Si. However, we have not detected the formation of the crystalline Si at annealing temperatures up to 1250 K (see Table I). The reason probably is just that the amount of the excess Si was below the sensitivity level of the X-ray measurements. The interfaces in this case have a Si excess and one could suggest an enhanced influence of the interfacial scattering on the transport properties. This was indeed found experimentally as it can be seen from Fig. 7 and Fig. 8 where thermopower and resistivity of amorphous and composite films with different Si content are shown.

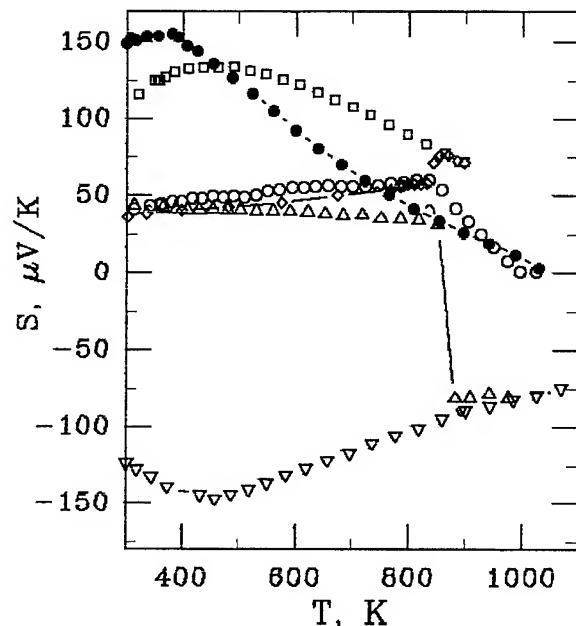


FIG. 7. The temperature dependent thermopower of amorphous and nano-crystalline composite films. $\text{Re}_{0.33}\text{Si}_{0.67}$: \diamond , amorphous; \square , composite; $\text{Re}_{0.32}\text{Si}_{0.68}$: \circ , amorphous; \bullet , composite; $\text{Re}_{0.27}\text{Si}_{0.73}$: \triangle , amorphous; ∇ , composite.

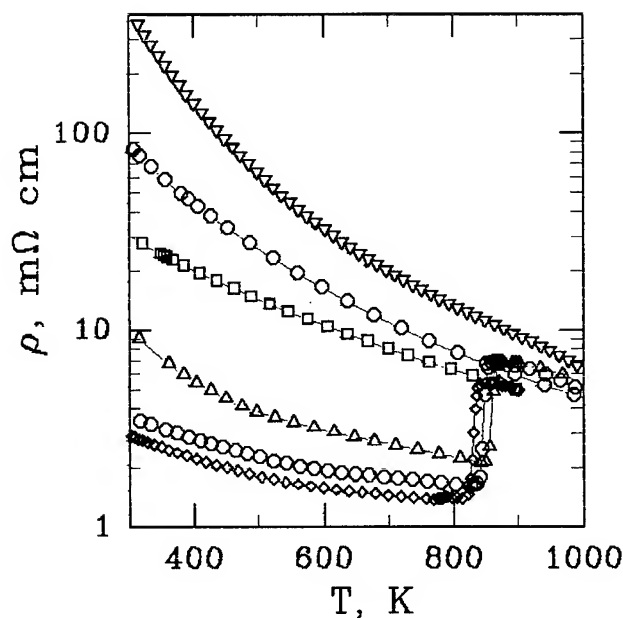


FIG. 8. The temperature dependent resistivity of amorphous and nano-crystalline composite films. $\text{Re}_{0.33}\text{Si}_{0.67}$: \diamond , amorphous; \square , composite; $\text{Re}_{0.32}\text{Si}_{0.68}$: \circ , amorphous; \bullet , composite; $\text{Re}_{0.27}\text{Si}_{0.73}$: \triangle , amorphous; ∇ , composite.

The composite films were obtained by partial crystallization of the amorphous films. From Fig. 8 one can find that the crystallization temperature is slightly dependent on the Si-content.

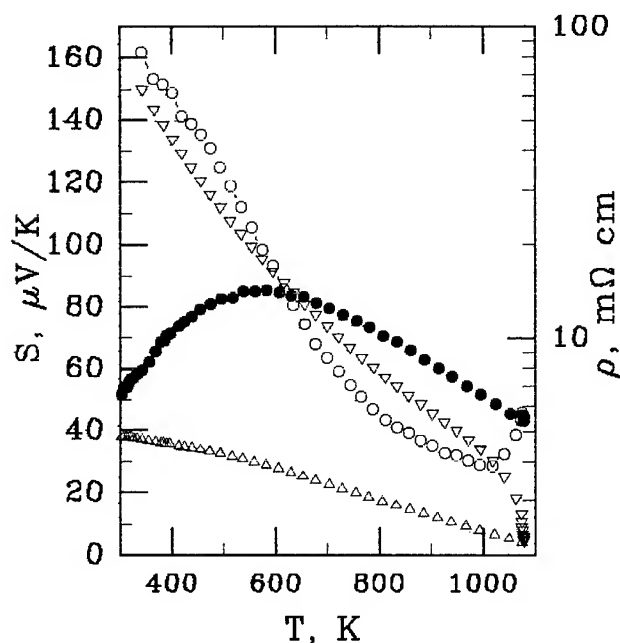


FIG. 9. The temperature dependent resistivity and thermopower of $\text{Re}_{0.32}\text{Si}_{0.68}$: \circ , S partially crystallized, \bullet , S completely crystallized; \triangle , ρ partially crystallized, ∇ , ρ completely crystallized.

The thermopower reveals very interesting variation with the Si-content. At small deviation from the stoichiometry the thermopower at room temperature is positive and increases with the increase of Si concentration. The maximum of the temperature dependent thermopower moves to lower temperatures. However at larger deviation from stoichiometric composition the thermopower of the composite changes its sign and shows comparatively large negative values. Complete crystallization of the composites results in the thermopower and resistivity which are very similar to the properties of the single-phase ReSi_2 film. Figure 9 depicts ρ and S of $\text{Re}_{0.32}\text{Si}_{0.68}$ composite before and after complete crystallization.

The microscopic mechanism which could be accounted for the observed behaviour of the transport properties of Re-Si composites is not known yet. Qualitatively the negative thermopower of the Si-rich composite can be understood on the basis of an energy-band scheme, proposed in [2]. It is reasonable to suggest that in those composites the crystalline ReSi_2 grains are separated by thin layers of Si. Due to the nature of the band bending on the silicon side of the Si- ReSi_2 junction [2] the tunneling probability for the electrons through such structure, depicted in Fig. 10 could be much larger than for the holes. This will result in a large negative thermopower as it is observed experimentally. Basically similar structure was considered in [17]. It was shown theoretically in [17] that in a cluster superlattice the dimensionless Ioffe criterion ZT can be much larger than 1.

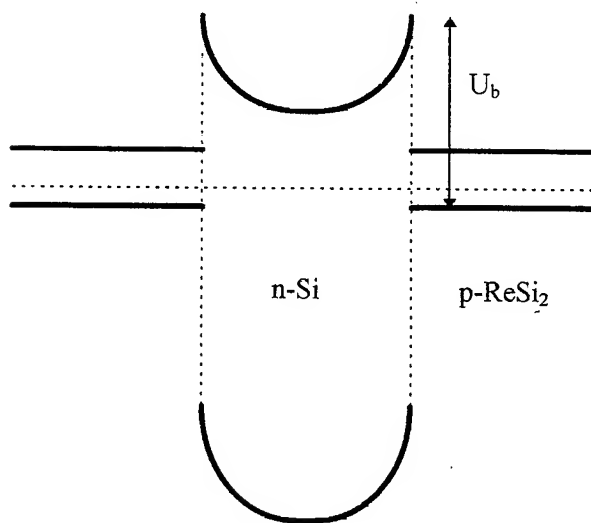


FIG. 10. A proposed energy-band diagram for the ReSi_2 -Si- ReSi_2 interface. If the thickness of the Si layer is small enough the electrons can tunnel through the interface, whereas the holes can not, since the effective barrier thickness is much larger for them. The barrier height U_b was found in [2] to be 0.59 eV but it should be different for different doping levels of Si.

IV. CONCLUSION

We have found that the transport properties of ReSi_2 thin films consisting of amorphous and nano-crystalline phases do not follow the predictions of the Effective Medium Approximation. Contrary, both resistivity and thermopower reveal non-monotonous variation with the volume ratio of the amorphous to nano-crystalline phases. This implies that the interfaces between the amorphous and nano-crystalline phases essentially influence the transport properties of the films. From the composition variation of the temperature dependent resistivity of the stoichiometric composites we have concluded that below the percolation threshold the nano-crystalline phase is isolated within the amorphous matrix by interfacial barriers and does not contribute to the conductivity of the film. The effect of the interfaces increases with the deviation from stoichiometric Re/Si ratio. The energy-band scheme of the interfaces proposed for the Si-rich composites suggests that the thermoelectric parameters of such composites could be much better as compared with those of the composite components.

V. ACKNOWLEDGEMENTS

The authors would like to thank M. Maeder and H. Thomas for performing the RBS and EDXS analysis. This work was supported in part by the Dr. Wilhelm Heinrich Heraeus and Else Heraeus-Stiftung (Germany). One of us (A. B.) would like to acknowledge the financial support of the Heraeus-Stiftung and kind hospitality of the Institute of Solid State and Materials Research Dresden, Germany.

-
- * Permanent address: A.F.Ioffe Physico-Technical Institute Russian Academy of Sciences, Sankt-Petersburg 194021, Russia.
- [1] T. A. Nguyen Tan, J. Y. Veuillen, P. Muret, S. Kennou, A. Siokou, S. Ladas, F. Lahatra Razafindramisa, M. Brunel, *J. Appl. Phys.* **77** (1995) 2514.
 - [2] J. P. Becker, J. E. Mahan, R. Long, *J. Vac. Sci. Technol. A* **13** (1995) 1133.
 - [3] A. M. Dutron, E. Blanquet, N. Bourhila, R. Madar, C. Bernard, *Thin Solid Films* **259** (1995) 25.
 - [4] C. B. Vining, *Silicides as Promising Thermoelectric Materials*, Proceedings of the IXth International Conference on Thermoelectrics, ed. by C. B. Vining (Pasadena; California Institute of Technology), 1990, p.249.
 - [5] R. G. Long, M. C. Bost, John E. Mahan, *Thin Solid Films* **162** (1988) 29.
 - [6] G. V. Samsonov, I. M. Vinitskii, *Handbook on Refractory Compounds* (IFI/Plenum, New York, 1980).

- [7] L. J. Chen, K. N. Tu, *Material Science Reports* **6** (1991) 53.
- [8] J. Derrien, J. Chevrier, Le Thanh Vinh, I. Berbezier, C. Giannini, S. Lagomarsino, M. G. Grimaldi, *Applied Surface Science* **73** (1993) 90.
- [9] D. S. McLachlan, M. Blaszkiewicz, R. E. Newnham, *J. Am. Ceram. Soc.* **73** (1990) 2187.
- [10] D. J. Bergman, O. Levy, *J. Appl. Phys.* **70** (1991) 6821.
- [11] B. Abeles, Ping Sheng, M. D. Coutts, Y. Arie, *Adv. Phys.* **42** (1975) 407.
- [12] D. S. McLachlan, R. Rosenbaum, A. Albers, G. Eytan, N. Grammatica, G. Hurvits, J. Pickup, E. Zaken, *J. Phys.: Condens. Matter* **5** (1993) 4829.
- [13] G. Hurvits, R. Rosenbaum, D. S. McLachlan, *J. Appl. Phys.* **73** (1993) 7441.
- [14] D. S. McLachlan, *J. Appl. Phys.* **68** (1990) 195.
- [15] V. Halpern, *J. Phys. C* **16** (1983) L217.
- [16] K. Lu, *Phys. Rev. B* **51** (1995) 18.
- [17] V. N. Bogomolov, D. A. Kurdyukov, A. V. Prokofiev, Yu. I. Ravich, L. A. Samoilovich, S. M. Samoilovich, *Cluster Superlattice as 3D-array of Thermoionic Energy Converters*. Proceedings of the 14 International Conference on Thermoelectrics, ed. by M.V. Vedernikov; (Sankt-Petersburg, Russia, A.F.Ioffe Physical-Technical Institute), 1995, p.280.

A Microstructural Analysis of Thin Film TiNiSn

DN Compton, AWR Leitch, JH Neethling and VV Kozyrkov
Department of Physics, University of Port Elizabeth
PO Box 1600, Port Elizabeth 6000, Republic of South Africa

Abstract

This paper reports on a structural investigation of the ternary compound TiNiSn, prepared as a thin film by electron beam deposition of a sandwich structure comprising individual layers of Ti, Ni and Sn. The effect of annealing the compound at 800 °C for times up to 72 hours was investigated. X-ray diffraction revealed the formation of TiNi₂Sn after 6 hours of annealing. The excess of Ni in the deposited structure (confirmed by EDS) resulted in the first phase of TiNiSn not being present and a shift in the lattice parameter of second phase TiNi₂Sn.

Introduction

In the field of thermoelectrics, the intermetallics of the MgAgAs-type crystal structure are a group of materials with unique properties. They are formed from metals, yet they exhibit semiconductor type properties, namely a small bandgap in their electronic spectrum [1,2]. They therefore have the potential for high temperature thermoelectric applications. An intermetallic alloy that has recently been investigated is the ternary compound TiNiSn. This compound has a high Seebeck coefficient of around $\sim 300 \mu\text{VK}^{-1}$ at room temperature and a negative temperature coefficient of electrical resistivity. The figure of merit of annealed TiNiSn has been measured to be $0.1 \times 10^{-3} \text{ K}^{-1}$ [3]. It has been found [4] that TiNiSn has a MgAgAs-type structure with symmetry $F\bar{4}3m$. It can be visualised as three interpenetrating f.c.c. sublattices, with Ti, Ni and Sn atoms at the coordinates (000), $(1/4 \ 1/4 \ 1/4)$ and $(3/4 \ 3/4 \ 3/4)$ respectively. A microstructural investigation of the bulk alloy has already been performed [3], but to date there has been no investigation of the thin-film properties of this alloy. It has been shown [5] that thin film structures may increase the efficiency of thermoelectric devices, so it is important to understand the properties of this alloy when confined to two dimensions. Due to the unavailability of structural and microstructural information of thin film TiNiSn and its phases, an analysis of this structure is presented in this paper.

Experimental Procedure

Titanium and tin of purity 99.999% and nickel of purity 99.99% were individually evaporated from graphite crucibles using a 2kV electron gun at a pressure of $\sim 3 \times 10^{-6}$ mbar. Sn and Ni were deposited at a rate of 1 \AA s^{-1} and Ti at a rate of 0.5 \AA s^{-1} . The single crystalline silicon substrates were placed ± 23 cm above the evaporation source. The substrates were

cleaned by rinsing in acetone and methanol prior to loading in the vacuum system.

Problems were experienced with the adhesion of the film onto the substrate. Initially, the films were deposited on the polished side of a (100) silicon substrate, but it was found that the film peeled off after annealing. The samples that were used in this study were deposited on the unpolished side of a Si wafer, and it appears that adhesion is good even after annealing. It can be assumed that the thin film will grow on a slightly roughened surface, but further work will need to be undertaken to ascertain the condition of the substrate that will yield optimum thin film growth.

The thin films were grown in a double sandwich-type structure on the Si substrate. Each element was sequentially deposited starting with Ni, followed by Sn and finally Ti. The thickness of each layer was $\pm 0.2 \mu\text{m}$, giving a final thin-film thickness of $\pm 1.2 \mu\text{m}$. Samples were then annealed in an Ar atmosphere at 800 °C for various times up to 72 hours.

Surface images were obtained with a Philips XL30 scanning electron microscope (SEM). An EDAX energy dispersive spectrometer (EDS) was used to acquire compositional information. X-ray diffraction was performed on a Philips single crystal diffractometer with a Cu K α source.

Experimental Results and Analysis

Figures 1 and 2 show two SEM micrographs of the surfaces of the thin films. The unannealed surface, fig. 1, exhibits a granular structure, with grain sizes of $\sim 1 \mu\text{m}$.

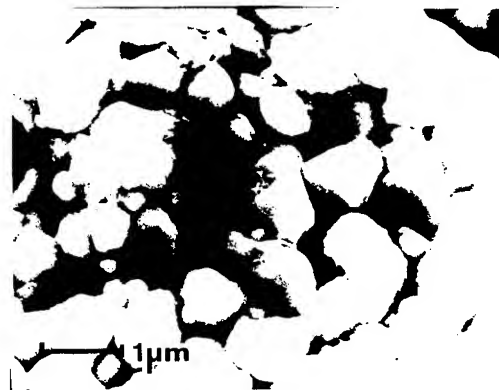


Fig. 1 SEM micrograph of the as-deposited thin film.

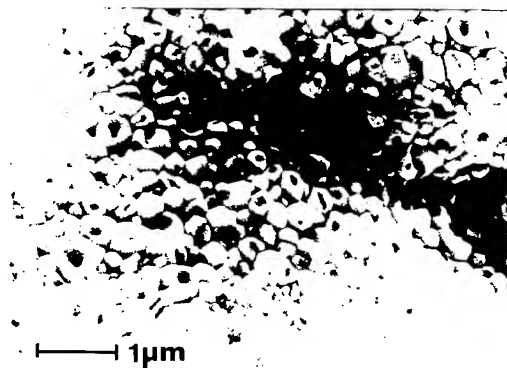


Fig. 2 SEM micrograph of the thin film after annealing at 800 °C for 72 hours.

With annealing for 72 hours, fig. 2, the grains decreased in size to less than 0.5 μm . EDS performed on the annealed grains indicated an excess of Ni. By comparison, the Ti and Sn were found in approximately equal quantities.

Fig. 3 depicts the differences between the X-ray diffraction spectra from the unannealed (curve a) and the annealed (curve b) structures. In the unannealed thin film, peaks corresponding to the elemental constituents were found, namely (200) β -Sn, (011) Ti and (111) Ni. These peaks disappear when the thin film is annealed for 6 hours or longer.

Three particular peaks in the X-ray diffraction spectrum of the unannealed sample were also found in that of the annealed sample. Two peaks at 33.20° and 35.75° 2θ remain unidentified, while the peak at 43.45° 2θ is attributed to the second phase (220) TiNi_2Sn peak. Even after a short annealing period (6 hours), peaks corresponding to different alloys can be identified, namely TiNi_2Sn , Ti_6Sn_5 , NiSn , Ti_3Sn and Ti_2Sn . The first three of these peaks are indicated in fig. 3(b). It is seen that the peaks associated with the titanium-tin and nickel-tin alloys correspond well with those given in standard diffraction tables.

Four specific peaks in fig. 3(b) are attributed to reflections from the ternary Ti-Ni-Sn alloy. Their measured (hkl) indices are listed in table 1. From the experimental d-values, it is found that the lattice parameter a_0 is 5.85 ± 0.06 Å. These peaks could be attributed to the first phase TiNi_2Sn , but it seems unlikely that this compound would form with the large amount of nickel present in the thin film (confirmed by EDS). The second phase TiNi_2Sn is thus associated with these four peaks. The Ti-Ni-Sn phase diagram database is incomplete, so the variation of the lattice parameter as a function of nickel concentration is still largely unknown. This may explain the large difference between the experimental lattice parameter obtained in this investigation and that of the stoichiometric alloy TiNi_2Sn . The experimental d-values are compared with those reported for bulk TiNi_2Sn [3] in table 1. It is also worth noting that the relative intensities of the four peaks are in the same ratios as those reported for the bulk alloy.

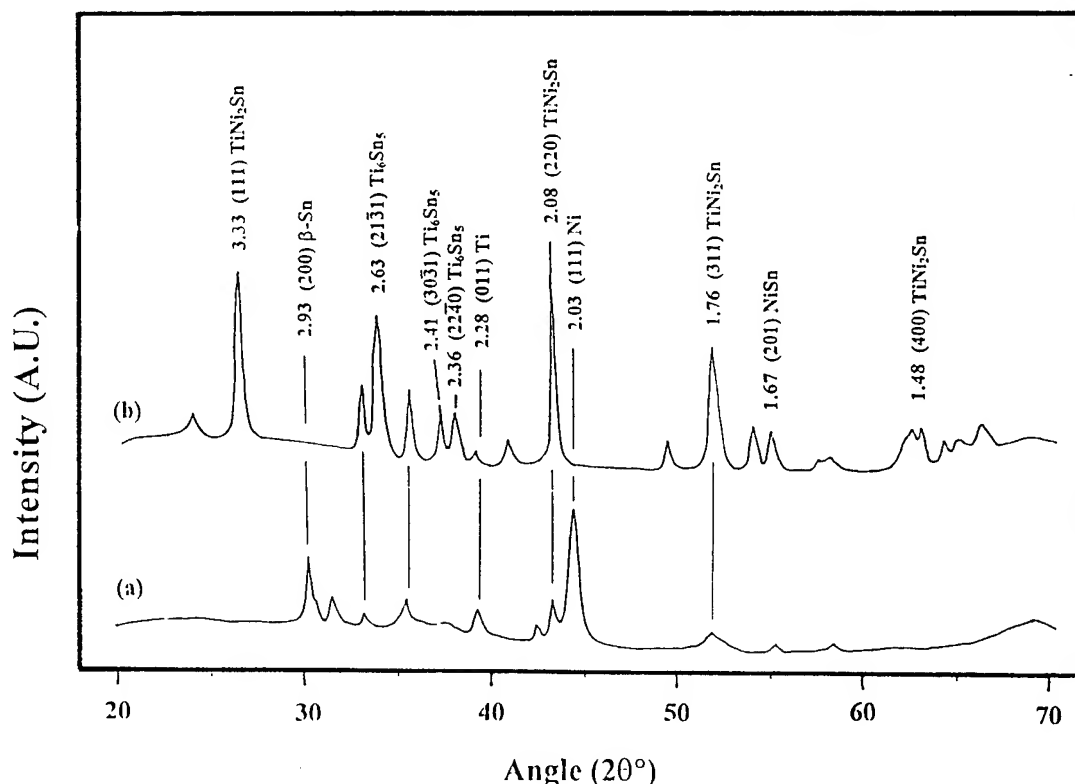


Fig. 3 X-ray diffraction spectra for the (a) unannealed, (b) 72 hour annealed thin film.

Table 1: Comparison of interplanar spacings of TiNiSn. The literature values for d were reported in [3].

h k l	d (Å) Experimental	d (Å) Literature
(111)	3.33 ± 0.06	3.49
(220)	2.08 ± 0.02	2.14
(311)	1.76 ± 0.02	1.83
(400)	1.48 ± 0.01	1.51

- [5] V.B. Yurchenko, "Enhanced thermoelectric efficiency of submicron-thick structures", Proc. of the 14th Int. Conf. on Thermoelectrics, pp. 327-330 (1995)

Finally, spectrum (b) of fig. 3 was obtained after annealing the alloy for 72 hours. Shorter anneals were also investigated. Annealing for 6 hours was sufficient for identifying the emergence of the four peaks related to the TiNi_2Sn . Longer anneals were found to increase the relative intensities of the peaks.

Conclusions

In summary, the ternary Ti-Ni-Sn alloy has been prepared as a thin film structure, and analysed for the different phases present. In a Ni rich alloy the formation of the compound TiNiSn does not occur and it is clear that an annealing period of 72 hours is insufficient for producing first phase TiNiSn. Further investigations will include the annealing time required for the first phase to appear as a function of nickel content, and the growth of thin films from a stoichiometrically correct ratio of elements. Electrical measurements as a function of annealing time will also be undertaken.

Acknowledgments

The financial support and encouragement of MINTEK is gratefully acknowledged.

References

- [1] S. Ögüt and K.M. Rabe, "Band gap and stability in the ternary intermetallic compounds NiSnM ($M=\text{Ti}, \text{Zr}, \text{Hf}$): A first-principles study", Physical Review B, Vol. 51, No. 16, pp. 10443-10453 (1995).
- [2] F.G. Aliev, V.V. Kozyrkov, V.V. Moshchalkov, R.V. Skolozdra and K. Durczewski, "Narrow band in the intermetallic compounds MNiSn ($M=\text{Ti}, \text{Zr}, \text{Hf}$)", Z. Phys. B, Condensed Matter, Vol. 80, pp. 353-357 (1990).
- [3] Z.S. Tan and W.A. Jesser, "Microstructure analysis of thermoelectric TiNiSn alloy", Proc. of the 14th Int. Conf. on Thermoelectrics, pp. 249-253 (1995).
- [4] N.D. Marchuk, R.V. Skolozdra and Y.V. Stadnyk, "Thermoelectric properties of new intermetallic compounds MMSn ", Proc. of the 14th Int. Conf. on Thermoelectrics, pp. 217-221 (1995).

Large Transverse Seebeck Voltage in Oxygen-reduced $\text{YBa}_2\text{Cu}_3\text{O}_{7-\delta}$ and $\text{Y}_{1-x}\text{Pr}_x\text{Ba}_2\text{Cu}_3\text{O}_{7-\delta}$ Thin Films

F. Lankes, E.V. Pechen, T. Honke, and K.F. Renk

Institute of Applied Physics, University of Regensburg, D-93040, Germany

Abstract

The off-diagonal Seebeck voltage of oxygen-reduced $\text{YBa}_2\text{Cu}_3\text{O}_7$ and $\text{Y}_{1-x}\text{Pr}_x\text{Ba}_2\text{Cu}_3\text{O}_{7-\delta}$ thin films epitaxially grown on strontium titanate crystals cut with a tilt angle of 20° between substrate surface and the cubic axis was measured. A temperature gradient perpendicular to the film surface was produced at room temperature by exposing the films to UV radiation pulses. The transverse Seebeck voltage, i.e. the voltage parallel to the film surface, which results from the temperature gradient perpendicular to it, was measured for varying oxygen content and Pr doping of the $\text{YBa}_2\text{Cu}_3\text{O}_{7-\delta}$ thin films. The oxygen content of the $\text{YBa}_2\text{Cu}_3\text{O}_{7-\delta}$ thin films was reduced from $\delta \simeq 0$ to $\delta \simeq 0.5$. It is shown that a reduction of the oxygen content causes a decrease of the off-diagonal Seebeck voltage. The same effect is observed for the $\text{Y}_{1-x}\text{Pr}_x\text{Ba}_2\text{Cu}_3\text{O}_{7-\delta}$ ($x = 0.1, 0.2, 0.3$) thin films, i.e. raising the partial substitution of Y by Pr results in a smaller Seebeck voltage. These results suggest that both, oxygen reduction and Pr doping, have the effect of making $\text{YBa}_2\text{Cu}_3\text{O}_{7-\delta}$ less anisotropic with respect to the thermopower. On the other hand, results of resistivity measurements of $\text{YBa}_2\text{Cu}_3\text{O}_{7-\delta}$ with different values of δ suggest that the anisotropy increases when oxygen is removed. A microscopic model for an explanation of the different behaviours of the thermopower and the resistivity is still lacking. We also have measured the transverse Seebeck voltage of $\text{YBa}_2\text{Cu}_3\text{O}_{7-\delta}$ ($\delta \simeq 0.06$ and 0.19) from T_c to room temperature. From this we can conclude that S_c of $\text{YBa}_2\text{Cu}_3\text{O}_{7-\delta}$ ($\delta \simeq 0.06$ and 0.19) increases linearly with temperature, i.e. S_c shows metallic behaviour.

Introduction

After various groups had observed giant voltaic signals of laser irradiated $\text{YBa}_2\text{Cu}_3\text{O}_7$ thin films [1, 2, 3], the origin of this effect remained a puzzle for a few years. Finally, it was shown [4, 5] that in $\text{YBa}_2\text{Cu}_3\text{O}_7$ thin films one has measured for the first time the transverse Seebeck effect. Establishing a temperature gradient on an anisotropic material leads to a thermoelectric voltage, which, in general, is not parallel to the temperature gradient:

$$\vec{E} = \hat{S} \vec{\nabla} T. \quad (1)$$

If the Seebeck tensor \hat{S} is of the following form (as it is the case for $\text{YBa}_2\text{Cu}_3\text{O}_7$ thin films grown on strontium titanate crystals cut with a tilt angle between the substrate

surface and the cubic axis)

$$\hat{S} = \begin{pmatrix} S_{xx} & \cdot & S_{xz} \\ \cdot & S_{yy} & \cdot \\ S_{zx} & \cdot & S_{zz} \end{pmatrix}, \quad (2)$$

then a temperature gradient in the z -direction results in an electric field in the x -direction

$$E_x = S_{xz} \frac{\partial T}{\partial z}. \quad (3)$$

Assuming a constant temperature gradient one finds a transverse thermoelectric voltage:

$$U = \frac{1}{2} \sin(2\alpha) \Delta S \Delta T \frac{l}{d}, \quad (4)$$

where $\Delta S = S_{ab} - S_c$. In this equation α is the tilt angle, l is the dimension of the film along the x -direction and d is its thickness. S_{ab} and S_c are the Seebeck coefficients of $\text{YBa}_2\text{Cu}_3\text{O}_{7-\delta}$ perpendicular and parallel to the c -axis of the unit cell, respectively. It is the factor l/d which gives a large Seebeck voltage even for rather small ΔT and ΔS . This effect is now exploited for the use of epitaxially grown $\text{YBa}_2\text{Cu}_3\text{O}_7$ thin films with tilt angles up to 20° as fast thermoelectric detectors for radiation from UV to FIR wavelengths. For very thin films the response is ≤ 1 ns in the UV and $\simeq 5$ ns in the FIR. Because of the wavelength dependent reflectivity the sensitivity of the films varies between 0.5 V/MW and 20 V/MW.

For two reasons further investigations of the transverse Seebeck effect in $\text{YBa}_2\text{Cu}_3\text{O}_{7-\delta}$ seem worthwhile. First, one might hope to increase the sensitivity of the detector by appropriate doping, which is difficult, however, because until now there exists no consistent model for the transport properties of the high temperature superconducting material $\text{YBa}_2\text{Cu}_3\text{O}_{7-\delta}$. This already gives the second reason for further investigating the transverse Seebeck effect in $\text{YBa}_2\text{Cu}_3\text{O}_{7-\delta}$. For an understanding of the thermopower in $\text{YBa}_2\text{Cu}_3\text{O}_{7-\delta}$ it is necessary to have reliable data about the S_c component of the thermopower. But there are only few measurements of this Seebeck coefficient. The reason being that this material has the property to grow preferably along the (a, b) -plane, so sample dimensions along the c -direction are usually very small. The transverse Seebeck effect can now be used to fill this gap. Since the measured transverse thermoelectric voltage is proportional to ΔS (Eq. (4)), and since there exist many publications about the value of S_{ab} [6, 7, 8], it is possible to receive more information about S_c . It should be noted that measurements of the thermoelectric power

(TEP) in polycrystalline samples of the high- T_c superconducting cuprates (HTSC) just give the (a, b) -plane TEP [8].

The original compound $\text{YBa}_2\text{Cu}_3\text{O}_{7-\delta}$ exists in two modifications. The first is the orthorhombic phase which is observed for $7-\delta \geq 6.4$. The second is the tetragonal phase which is stable for values of $7-\delta$ between 6.4 and 6.0. $\text{YBa}_2\text{Cu}_3\text{O}_{7-\delta}$ has a typical layered perovskite-like structure with the CuO_2 planes separated by a layer of Y ions which are bounded by the layers Ba-O4, Cu1-O1, and Ba-O4 (see, e.g., [9]). The oxygen O2 and O3 are strongly coupled with Cu2 in the CuO_2 planes, unlike the weakly coupled oxygen O1 in the Cu1-O1 chains. Upon heating, the latter readily leaves the sample. This property allowed us to vary the oxygen content of $\text{YBa}_2\text{Cu}_3\text{O}_{7-\delta}$ between $\delta \simeq 0$ and $\delta \simeq 0.5$.

It is most likely that both the normal and superconducting properties of the layered high T_c cuprates are dominated by the charge and spin dynamics in the CuO_2 planes. Now the density of charge carriers, i.e. the density of the holes, in the CuO_2 plane is directly correlated to the oxygen content of the sample. Since the oxygen O1 in the Cu1-O1 chains has a valency of -2 , the removal of oxygen can either reduce Cu1 or remove holes from the conducting planes via a charge transfer mechanism. Therewith the transport properties of the CuO_2 planes depend strongly on the amount of oxygen doping. Despite the assumption that the transport properties of the HTSCs are mainly dominated by the CuO_2 planes, studies of c -axis transport and coupling between the CuO_2 planes are also important. First, it is far from clear which role is played by the interlayer coupling for superconductivity. Second, there are several unresolved questions concerning c -axis transport. It is not understood, for example, why the c -axis resistivity ρ_c changes exponentially with doping in $\text{YBa}_2\text{Cu}_3\text{O}_{7-\delta}$ and why it shows semiconducting behavior for $\delta \geq 0.1$ [10].

Experimental Procedure

Thin films of the composition $\text{Y}_{1-x}\text{Pr}_x\text{Ba}_2\text{Cu}_3\text{O}_{7-\delta}$ ($x = 0, 0.1, 0.2, 0.3$) were prepared by pulsed laser deposition using a synchronous velocity filter [11]. The pulsed laser deposition technique is very suitable to evaporate multicomponent materials stoichiometrically. So the variation of the Pr concentration was simply accomplished by using targets with the appropriate composition. The oxygen content of the $\text{YBa}_2\text{Cu}_3\text{O}_7$ films was reduced by heating the sample in flowing oxygen ($p_{\text{O}_2} \simeq 10^{-3}$ mbar) at a temperature of about 250°C . The reduction of oxygen was almost proportional to the heating time. In this way we received $\text{YBa}_2\text{Cu}_3\text{O}_{7-\delta}$ films with $\delta \simeq 0.25, 0.30, 0.35$, and 0.50 . The superconducting transition width, which is a measure for the homogeneity of the samples, was about 2K . The oxygen content was estimated by measuring T_c and comparing the measured values with a plot of T_c against oxygen content [9]. For generation of a temperature gradient perpendicular to the film surface the films were at room temperature exposed to UV radiation

($\lambda = 308\text{nm}$, pulse duration 33ns). The thickness of the films was about 400nm and their lateral dimensions were $10 \times 10\text{mm}^2$. The tilt angle was 20° . Electrical contacts from the thin films to 50Ω coaxial cables were made by evaporating thin gold stripes on the appropriate edges of the films and by attaching copper contacts to these gold stripes. Voltage signals were recorded with a digital storage oscilloscope.

Results and Discussion

In Fig.1 the dependence of the transverse thermoelectric voltage on the oxygen content is shown. As one can see,

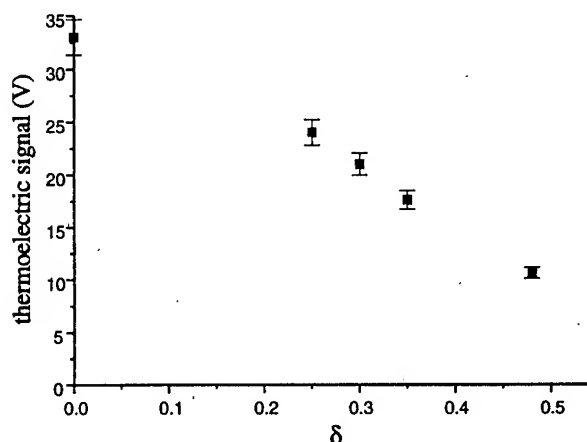


Fig. 1: Thermoelectric signal of $\text{YBa}_2\text{Cu}_3\text{O}_{7-\delta}$ thin films

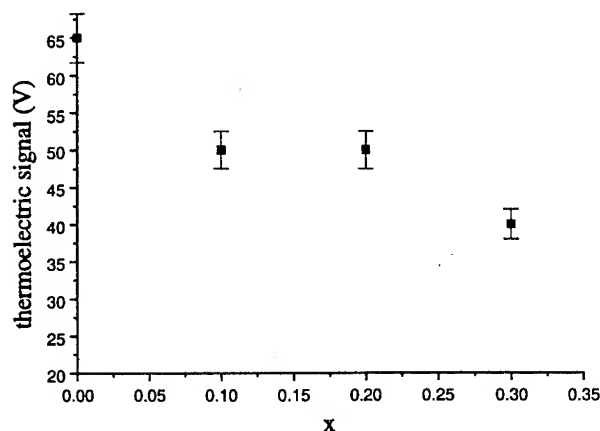


Fig. 2: Thermoelectric signal of $\text{Y}_{1-x}\text{Pr}_x\text{Ba}_2\text{Cu}_3\text{O}_{7-\delta}$ thin films

the magnitude of the signal decreases monotonously with decreasing oxygen content. For $\delta \simeq 0.5$ it is only one third of its maximum value at $\delta \simeq 0$. So the anisotropy of the Seebeck coefficient is diminished upon oxygen reduction. If we take for ΔS a value of about $30 \mu\text{V/K}$ at $\delta \simeq 0$ [12] and take into account that the value of S_{ab} changes from about $0 \mu\text{V/K}$ for $\delta \simeq 0$ to about $30 \mu\text{V/K}$ for $\delta \simeq 0.5$ [7], it may be concluded, that S_c does not depend strongly on

the oxygen content. We estimate that it only changes by an amount of about $10 \mu\text{V/K}$.

For the substitution of Y by Pr the following description is given [13]. When trivalent Y is replaced by Pr then holes of the CuO_2 plane are transferred to the Pr-sites, the hole concentration in the Cu-O chains remaining unaffected by the Pr substitution. The reason for a hole transfer from the CuO_2 planes to the Pr ions is the hybridisation of the $4f$ -Pr orbital with the neighbouring O orbitals which binds doped holes to the Pr sites. This leads to the existence of Pr^{4+} ions, whereas Y has a valence of $3+$. So in both cases, O reduction and Pr doping, the hole concentration in the CuO_2 planes is decreased. This explains the increase of the Seebeck coefficient S_{ab} when O is removed from $\text{YBa}_2\text{Cu}_3\text{O}_{7-\delta}$ or Pr is doped. In Fig.2 the transverse Seebeck voltage of $\text{Y}_{1-x}\text{Pr}_x\text{Ba}_2\text{Cu}_3\text{O}_{7-\delta}$ ($x = 0, 0.1, 0.2, 0.3$) is shown. It is seen that raising the substitution of Y by Pr up to 30% causes the voltage to decrease by one third of its maximum value at $x=0$. From the data published by Gonçalves et al. [14] we estimate that S_{ab} increases from $0 \mu\text{V/K}$ for $x = 0$ to about $10 \mu\text{V/K}$ for $x = 0.3$, suggesting that Pr-doping also does not have much influence on the value of S_c . So it is shown that neither O reduction nor Pr doping change S_c very much. This observation suggests that the value of S_c does not depend strongly on the hole concentration in the CuO_2 plane. We emphasize this observation, since it is quite different from the results which were obtained from resistivity measurements [15]. The in-plane and out-of-plane resistivities of $\text{YBa}_2\text{Cu}_3\text{O}_{7-\delta}$ were measured for $\delta = 0.07, 0.13$, and 0.18 . It was found that the magnitude and temperature dependence of the in-plane resistivity ρ_{ab} do not change very much when oxygen was removed from $\delta \simeq 0.07$ to $\delta \simeq 0.18$. The temperature dependence remained metallic and the magnitude only raised by a factor of two. Quite surprisingly, the out-of-plane resistivity showed a rather remarkable change in temperature dependence as well as in magnitude: for high hole concentration the temperature dependence shows metallic behavior whereas at lower hole concentration the T -dependence is semiconductor-like. At the same time the magnitude of ρ_c increases by a factor of about 7. So the anisotropy in the resistivity is strongly enhanced by O reduction. This is not the case for the thermopower. The anisotropy of this transport property is decreased when oxygen is removed. These different behaviors of the thermopower and resistivity are quite remarkable, and until now we do not have an explanation for this different behavior.

In Fig.4 and Fig.3 the temperature dependence of the thermoelectric signal of $\text{YBa}_2\text{Cu}_3\text{O}_{7-\delta}$ is shown for $\delta = 0.06$ and $\delta = 0.19$, respectively. Here the values for δ were calculated from the relationship [16].

$$\delta = 7 - (12.771 - c)/0.1557. \quad (5)$$

The value c for the dimension of the unit cell in z -direction was obtained from the $(00l)$ -reflections of the measured XRD spectrum. The values of δ (0.06 and 0.19) are in

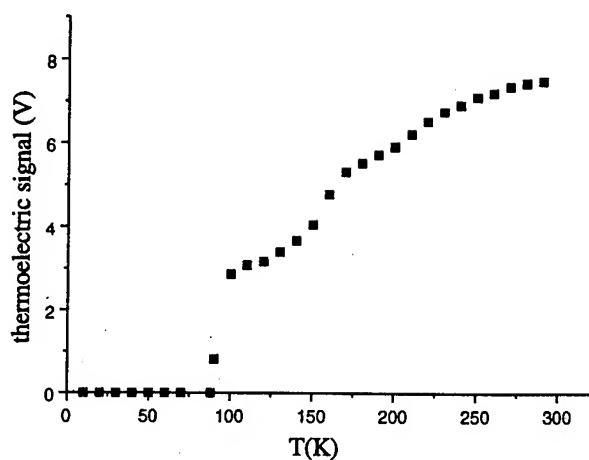


Fig. 3: Thermoelectric signal of $\text{YBa}_2\text{Cu}_3\text{O}_{6.94}$

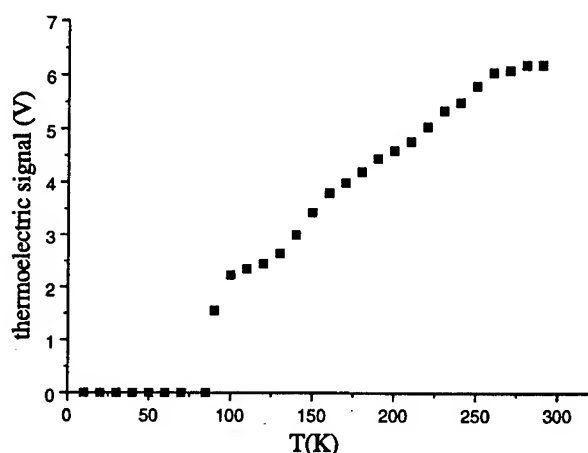


Fig. 4: Thermoelectric signal of $\text{YBa}_2\text{Cu}_3\text{O}_{6.81}$

good agreement with the measured transition temperatures ($T_c = 91.4\text{K}$ and $T_c = 90.0\text{K}$). The observed decrease of the signal with decreasing temperature is expected from earlier published data about the temperature dependence of the in-plane and out-of-plane components of the Seebeck tensor. For $\delta \simeq 0$ S_{ab} is approximately independent of temperature, whereas for $\delta = 0.19$ S_{ab} increases, showing a peak at $T \simeq 100\text{K}$ [7]. S_c decreases almost linearly with temperature for $\delta \simeq 0$ as was measured by [12].

The temperature dependence of S_{ab} was and still is the focus of much debate. Especially the peak of S_{ab} in the range $T_c < T < 150\text{K}$ has attracted much attention. The height of the peak and its width increases with decreasing oxygen content. Also the position of this peak shifts to higher temperatures with increasing δ . This behavior of S_{ab} of $\text{YBa}_2\text{Cu}_3\text{O}_{7-\delta}$ is rather different from the other HTSCs. There, for example, also exists a peak in the temperature dependence of the in-plane component of the thermopower. This peak, however is not shifted for different dopings. Cohn et al. [17] have measured the S_a and S_b components of $\text{YBa}_2\text{Cu}_3\text{O}_{7-\delta}$ separately. Their measurements reveal that S_a shows the same temperature dependence as the in-plane thermopower of the

other HTSC materials, whereas the temperature dependence of S_b is very different from that. They argue that S_a is solely influenced by the electronic properties of the CuO_2 -planes, whereas the component of the thermopower in the b -direction is also affected by the Cu-O chains in this direction. So the difference in the temperature behavior of S_{ab} of $\text{YBa}_2\text{Cu}_3\text{O}_{7-\delta}$ and the other HTSC materials, which do not possess the Cu-O chain, but otherwise have a similar structure as $\text{YBa}_2\text{Cu}_3\text{O}_{7-\delta}$, may be explained by the additional Cu-O chains in $\text{YBa}_2\text{Cu}_3\text{O}_{7-\delta}$. An argument against this conclusion might be that this peak seen in the temperature dependence of S_{ab} also shifts to higher temperatures when $\text{YBa}_2\text{Cu}_3\text{O}_{7-\delta}$ is doped with Pr [14]. As already mentioned, it was found that in this case the charge redistribution only takes place between the doped Pr atoms and the CuO_2 planes, the Cu-O chains remaining unaffected. To decide whether the doping dependence of the temperature at which the peak in the temperature dependence of S_{ab} is located, is related to the Cu-O chains or to the CuO_2 planes or to both, it would be interesting to measure the S_a and S_b components of $\text{YBa}_2\text{Cu}_3\text{O}_{7-\delta}$ for different oxygen and Pr doping. The peak in the temperature dependence of S_{ab} has been attributed to a variety of different mechanisms [18, 19]. For example, the most recent explanation for the behavior of S_{ab} in $\text{YBa}_2\text{Cu}_3\text{O}_{7-\delta}$ is given by Tallon et al [18]. They argue that the enhancement of S_{ab} results from the opening of an energy gap in the normal state excitation spectrum. Because of this energy gap, which decreases with increasing hole concentration, the transport scattering spectrum is changed in such a way that the TEP is enhanced below a temperature $T_g \sim E_g/k_B$. So with this model, both the increasing peak and its shift to higher temperatures for decreasing oxygen content might be explained by this energy gap.

The peak in the temperature dependence of S_{ab} may also be seen in the temperature dependence of the transverse thermoelectric signal. In Fig.4 the signal decreases

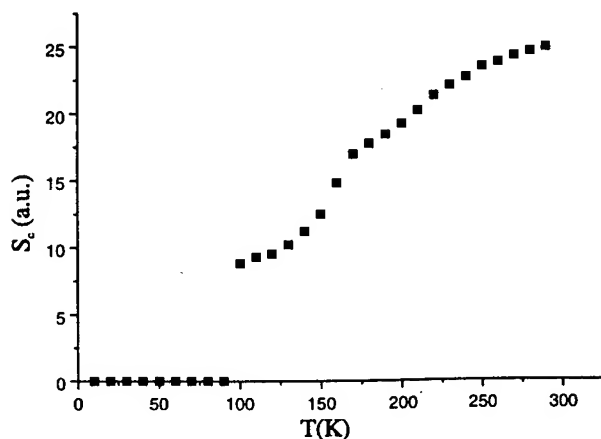


Fig. 5: Temperature dependence of the Seebeck coefficient S_c of $\text{YBa}_2\text{Cu}_3\text{O}_{6.94}$ according to [7]

more sharply at $T=150\text{K}$, which is even more pronounced in Fig.3. This change in slope might be attributed to the

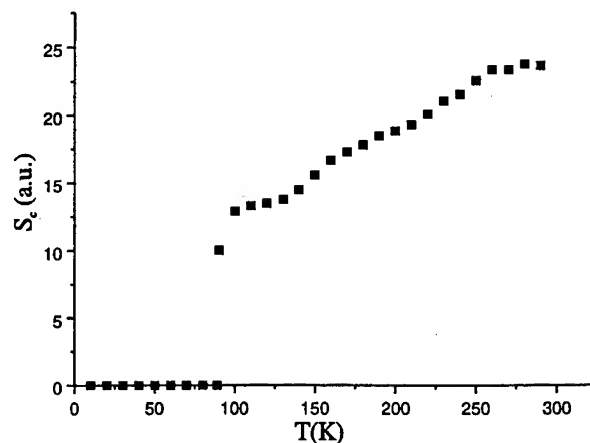


Fig. 6: Temperature dependence of the Seebeck coefficient S_c of $\text{YBa}_2\text{Cu}_3\text{O}_{6.81}$ according to [7]

peak seen in the temperature dependence of S_{ab} . But what prohibits an unambiguous attribution of this downturn in the temperature dependence to the peak seen in S_{ab} are the observations, that first, the position of this downturn is the same for $\delta = 0.06$ and $\delta = 0.19$. Second, the temperature, where the steps are located in both cases, is too high. We took the data measured for S_{ab} by Cooper et al. [7] for $\delta \simeq 0.05$ and $\delta \simeq 0.18$ to obtain plots of S_c against T for $\delta \simeq 0.05$ and $\delta \simeq 0.19$ (Figs.5 and 6). As can be seen the temperature dependence of S_c is approximately linear. To obtain a clearer picture of the temperature dependence of the transverse thermoelectric signal on one side and the temperature dependence of S_{ab} and S_c on the other side, further measurements of the transverse Seebeck voltage for different oxygen doping are currently under way.

Conclusions

In summary, we report a decreasing anisotropy between the in-plane and the out-of-plane thermoelectric power of $\text{YBa}_2\text{Cu}_3\text{O}_{7-\delta}$ with decreasing oxygen content and increasing Pr doping. This behavior is very much different from that of the resistivity, which indicates a marked enhancement of anisotropy when the oxygen content and therefore the hole concentration in the CuO_2 planes is reduced. The different behaviors of the thermopower and the resistivity are quite unusual, since in a metal, for example, one would expect a similar behavior of these transport properties upon variation of the concentration of charge carriers. From the temperature dependence of the transverse thermoelectric power of $\text{YBa}_2\text{Cu}_3\text{O}_{7-\delta}$ it is concluded that S_c decreases approximately linearly with temperature with a slightly enhanced downturn at a temperature of about 150K.

References

- [1] C.L. Chang, A. Kleinhammes, W.G. Moulton, and L.R. Testardi, "Symmetry-forbidden laser-induced

- voltages in $\text{YBa}_2\text{Cu}_3\text{O}_7$ ", *Physical Review B*, vol. 43, No. 16, pp. 11564-11567 (1990).
- [2] H.S. Kwok and J.P. Zheng, "Anomalous photovoltaic response in $\text{YBa}_2\text{Cu}_3\text{O}_7$ ", *Physical Review B*, vol. 46, No. 6, pp. 3692-3695 (1992).
 - [3] H. Lengfellner, G. Kreymb, A. Schnellbögl, J. Betz, K.F. Renk and W. Prettl, "Giant voltages upon surface heating in normal $\text{YBa}_2\text{Cu}_3\text{O}_{7-\delta}$ films suggesting an atomic layer thermopile", *Applied Physics Letters*, vol. 60, No. 4, pp. 501-503 (1992).
 - [4] H. Lengfellner, S. Zeuner, W. Prettl, and K.F. Renk, "Thermoelectric Effect in Normal-State $\text{YBa}_2\text{Cu}_3\text{O}_{7-\delta}$ films", *Europhysics Letters*, vol. 25, No. 5, pp. 375-378 (1994).
 - [5] L.R. Testardi, "Anomalous laser-induced voltages in $\text{YBa}_2\text{Cu}_3\text{O}_x$ and 'off-diagonal' thermoelectricity", *Applied Physics Letters*, vol. 64, No. 18, pp. 2347-2349 (1994).
 - [6] P. J. Ouseph and M. Ray O'Bryan, "Thermoelectric power of $\text{YBa}_2\text{Cu}_3\text{O}_{7-\delta}$ ", *Physical Review B*, vol. 41, No. 7, pp. 4123-4125 (1990).
 - [7] J.R. Cooper, S.D. Obertelli, A. Carrington, and J.W. Loram, "Effect of oxygen depletion on the transport properties of $\text{YBa}_2\text{Cu}_3\text{O}_{7-\delta}$ ", *Physical Review B*, vol. 44, No. 21, pp. 12086-12089 (1991).
 - [8] S.D. Obertelli, J.R. Cooper, and J.L. Tallon, "Systematics in the thermoelectric power of high- T_c oxides", *Physical Review B*, vol. 46, No. 22, pp. 14928-14931 (1992).
 - [9] J.D. Jorgensen, B.W. Veal, A.P. Paulikas, L.J. Nowicki, G.W. Crabtree, H. Claus, and W.K. Kwok, "Structural properties of oxygen-deficient $\text{YBa}_2\text{Cu}_3\text{O}_{7-\delta}$ ", *Physical Review B*, vol. 41, No. 4, pp. 1863-1877 (1990).
 - [10] S.L. Cooper and K.E. Gray, "Anisotropy and Inter-layer Coupling in the High- T_c Cuprates", in *Physical Properties of High Temperature Superconductors IV*, D.M. Ginsberg (ed.), World Scientific, p. 61 (1994).
 - [11] E.V. Pechen, A.V. Varlashkin, S.I. Krasnovobodtkov, B. Brunner, and K.F. Renk, "Pulsed-laser deposition of smooth high- T_c superconducting films using a synchronous velocity filter", *Applied Physics Letters*, vol. 66, No. 7, pp. 2292-2294 (1995).
 - [12] I. Terasaki, Y. Sato, S. Tajima, S. Miyamoto, and S. Tanaka, "Out-of-Plane Transport in Thick Single Crystal $\text{YBa}_2\text{Cu}_3\text{O}_{7-\delta}$ ", *Physica C*, vol. 235-240, pp. 1413-1414 (1994).
 - [13] R. Fehrenbacher and T.M. Rice, "Unusual Electronic Structure of $\text{PrBa}_2\text{Cu}_3\text{O}_7$ ", *Physical Review Letters*, vol. 77, No. 22, pp. 3471-3474 (1993).
 - [14] A.P. Gonçalves, I.C. Santos, E.B. Lopes, R.T. Henriques, and M. Almeida, "Transport properties of the oxides $\text{Y}_{1-x}\text{Pr}_x\text{Ba}_2\text{Cu}_3\text{O}_{7-\delta}$ ($0 \leq x \leq 1$): Effects of band filling and lattice distortion on superconductivity", *Physical Review B*, vol. 37, No. 13, pp. 7476-7480 (1988).
 - [15] I. Ito, Y. Nakamura, H. Takagi and S. Uchida, "Electrical conduction across CuO_2 planes in copper oxides superconductors", *Physica C*, vol. 185-189, pp. 1267-1268 (1991).
 - [16] S. Degoy, J. Jiménez, P. Martin, O. Martinez, A.C. Prieto, D. Chambonnet, C. Audry, C. Belouet, and J. Perrière, "Oxygen content of YBaCuO thin films.", *Physica C*, vol. 256, pp. 291-297 (1996).
 - [17] J.L. Cohn, E.F. Skelton, S.A. Wolf, and J.Z. Liu, "In-plane thermoelectric power of untwinned $\text{YBa}_2\text{Cu}_3\text{O}_{7-\delta}$ ", *Physical Review B*, vol. 45, No. 22, pp. 13140-13143 (1992).
 - [18] J.L. Tallon, J.R. Cooper, P.S.I.P.N. de Silva, G.V.M. Williams, and J.W. Loram, "Thermoelectric Power: A Simple Instructive Probe of High- T_c Superconductors", *Physical Review Letters*, vol. 75, No. 22, pp. 4114-4117 (1995).
 - [19] J.L. Cohn, S.A. Wolf, V. Selvamanickam, and K. Salama, "Thermoelectric Power of $\text{YBa}_2\text{Cu}_3\text{O}_{7-\delta}$: Phonon Drag and Multiband Conduction", *Physical Review Letters*, vol. 66, No. 8, pp. 1098-1101 (1991).

Structure and Phase Formation in Amorphous $\text{Ir}_x\text{Si}_{1-x}$ Thin Films at High Temperatures

W. Pitschke, R. Kurt, A. Heinrich, J. Schumann, J. Thomas and M. Mäder*

Institut für Festkörper- und Werkstofforschung Dresden e.V.

D-01171 Dresden, Germany

*Forschungszentrum Rossendorf e.V.

D-01314 Dresden, Germany

Abstract

Experimental data on the phase formation process of amorphous $\text{Ir}_x\text{Si}_{1-x}$ thin films for thermoelectric applications are presented. The composition x varies between 0.30 and 0.40. The phase formation process at temperatures from 300K up to 1223K was investigated by means of X-ray diffraction. Distinct phases were observed at the final stage in dependence on the initial composition: Ir_3Si_4 , Ir_3Si_5 , and IrSi_3 . The structure of the Ir_3Si_5 phase varies in dependence on the chemical composition of the layer. The electrical resistivity of the as-deposited and of annealed at $T=973\text{K}$ and $T=1073\text{K}$ layers was measured at room temperature and in low temperature range.

Introduction

In recent years the semiconducting compounds of the transition metal silicides found increasing interest as materials for high temperature applications in thermoelectricity [1], photovoltaics [2] and infrared optics [3]. Several promising compounds have been investigated, among others $\beta\text{-FeSi}_2$, [4] Ru_2Si_3 [5] $\text{MnSi}_{1.75}$ [6] and CrSi_2 [7]. The system Ir-Si, however, has been studied much less until now. In [8] the phase diagram and electrical behaviour of the silicon-rich iridium silicide compounds have been investigated in bulk material. Only six distinct phases could be identified by microprobe analysis and X-ray diffraction: IrSi , Ir_4Si_5 , Ir_3Si_4 , and orthorhombic and monoclinic IrSi_3 with metal-like resistivity, and the semiconducting Ir_3Si_5 . According to Korst et al. [9] the structure type of IrSi is equivalent to MnP . Engström et al. [10,11] determined the crystal structure of Ir_3Si_4 (orthorhombic) and Ir_3Si_5 (monoclinic) by single-crystal X-ray diffraction studies. They showed the structure type of Ir_4Si_5 to be Rh_4Si_5 . [10]. The structure of orthorhombic and monoclinic IrSi_3 is polymorph with the hexagonal iridium trisilicide also determined by means of single crystal X-ray diffraction [12]. The existence of other compounds such as Ir_2Si_3 [13,14], Ir_4Si_7 [15,16], and IrSi_2 [17] has been suggested, but could not confirmed in further studies [8]. Allevato and Vining [18] investigated the thermoelectric properties of semiconducting iridium silicides using Pt and Os as dopants and determined estimates of power factor values around $5.2 \mu\text{W}/\text{cm K}$ and dimensionless figure of merit ZT values up to 0.1. Most of the work about thin films was done in Ir/Si couples in connection with the

application of iridium silicides as Schottky barriers [19]. Schumann et al. [20] report about first investigations of phase formation, electrical and optical properties of sputtered Ir-Si films in a broad composition range around Ir_3Si_5 . However, the phase formation process in such layers was not understood completely. The thermoelectric properties can not be estimated because doping effects have not been studied. The aim of this paper is to investigate the layer structure of binary $\text{Ir}_x\text{Si}_{1-x}$ thin films during annealing process and to find correlations with the electrical resistivity and its temperature coefficient.

Experimental

Preparation technique

The films were prepared by a magnetron co-sputtering from two targets, an $\text{IrSi}_{1.75}$ target prepared by sintering and a high purity monocrystalline Si target onto Si substrates with intermediate $1\mu\text{m}$ thick SiO_2 layer to prevent a reaction of the film with the Si-substrate.

The deposition chamber was a cryopumped vacuum system, the unheated substrates were arranged on a disk carrying out a rotating motion relative to the two sputtering sources. The deposition conditions - power ratio $N(\text{Si})/N(\text{IrSi}_{1.75})$ and film thickness d - the electrical parameters of the film - resistivity ρ and its temperature coefficient TCR - and the chemical composition of the as deposited layers are given in Table 1.

Structure investigations

The phase formation process of the films during annealing was investigated in-situ by means of high temperature X-ray diffractometry. The measurements were done using a Philips X'Pert diffractometer PW3050 equipped with a Bühler HDK2.4 high temperature chamber (see [21] for details). Diffraction patterns were recorded using $\text{CoK}\alpha$ radiation ($\lambda = 0.17889\text{nm}$) from a long-fine-focus tube together with a graphite secondary monochromator. In order to maximize the signal level from the film and to minimize sample displacement errors, all high temperature measurements were recorded in parallel beam geometry with a fixed incidence angle of 4° . The samples were annealed in vacuum ($p < 10^{-3} \text{Pa}$) from room temperature up to 1223K.

Table 1

Sample parameters of investigated films

No.	N(Si)/ N(IrSi _{1.75})	d / nm	$\rho(300K)/$ $\mu\Omega\text{cm}$	TCR / ppm / K	c(Si) / at%
1	0.25	170	1890	-1662	60
2	0.38	182	2340	-1905	61
3	0.45	206	2565	-2018	63
4	0.50	210	2645	-2079	64
5	0.55	210	2735	-2137	65
6	0.60	206	2841	-2171	66
7	0.65	196	2786	-2196	66
8	0.70	185	2913	-2197	67
9	0.75	180	2790	-2212	68
10	0.80	190	2804	-2215	68
11	0.88	174	2900	-2189	70

Temperature measurement was done by means of a W-5%Re/W-26%Re thermocouple. Temperature scale was calibrated by reference to known phase transitions in powder samples of materials prepared on the surface of the silicon substrate. For analyzation of the crystallized state, accurate Bragg-Brentano diffraction patterns were recorded ex-situ at room temperature.

Additionally, RBS measurement were carried out in order to determine the chemical composition of the as-deposited and the annealed layers. For this purpose the films were prepared on glassy carbon substrates. TEM investigations of choosen layers deposited on NaCl carriers were carried out in order to determine residual phases with small concentrations. For this an analytical transmission electron microscop CM20FEG (Philips) was used.

Transport measurements

The electrical conductivity was measured by means of a conventional four point d.c. technique. The measurement structures were obtained by a photolithographic lift-off technique. Electrical resistivity of as-deposited and annealed at 973K and at 1073K layers was measured as a function of temperature in low temperature range.

Results and discussion

In Table 1 the investigated IrSi films are listed and characteristic sample parameters are given. In dependence on the ratio N(Si) / N(IrSi_{1.75}) of the sputtering power used for the two targets the Si concentration varies, which is connected with an increase of resistivity $\rho(300K)$ and of the value of its temperature coefficient TCR(300K).

Phase formation

All as-deposited films show in the X-ray diffraction patterns two broad reflections at $d=1.98\text{ \AA}$ and $d=3.17\text{ \AA}$, i.e. they have amorphous structure. The X-ray diffraction patterns recorded up to temperatures slight lower than the crystallization temperature are identical, which means, that

no structural changes were detectable with the X-ray diffraction method. Start of the crystallization process was observed at $T_{\text{cryst}} = 970\text{ K} \pm 10\text{ K}$ independent of the chemical composition of the layers. The layers were completely crystallized increasing the temperature a few degrees above the crystallization temperature only.

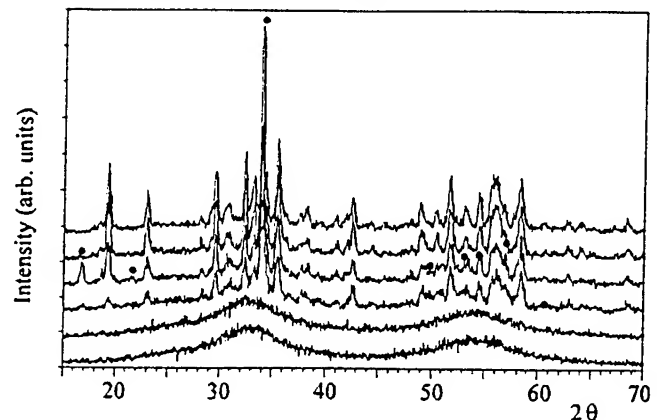


Fig.1 X-ray diffraction patterns of sample 3 recorded at T= 817K, 938K, 978K, 1060K, 1141K, and 1223K. (CoK α -radiation). The marked reflections are obviously caused by an unknown metastable phase.

Fig. 1 gives the X-ray diffraction patterns of layer No. 3 in dependence on the temperature. As a result of the crystallization process monoclinic Ir₃Si₅ was formed. In addition the marked at Fig. 1 reflections were observed. We suggest them to be caused by a metastable phase with a monoclinic primitive unit cell, $a=6.180\text{ \AA}$, $b=2.242\text{ \AA}$, $c=4.849\text{ \AA}$, and $\beta=100.12^\circ$. After increase the temperature up to 1141K the Ir₃Si₅ reflections only remained. This type of crystallization process characterized by an intermediate state above the crystallization temperature was obtained at samples No 2, 3 and 4, which corresponds to Si concentration of 61% to 64%.

In the other samples the crystalline state formed at the crystallization temperature was stable up to the highest observed temperature of 1223K.

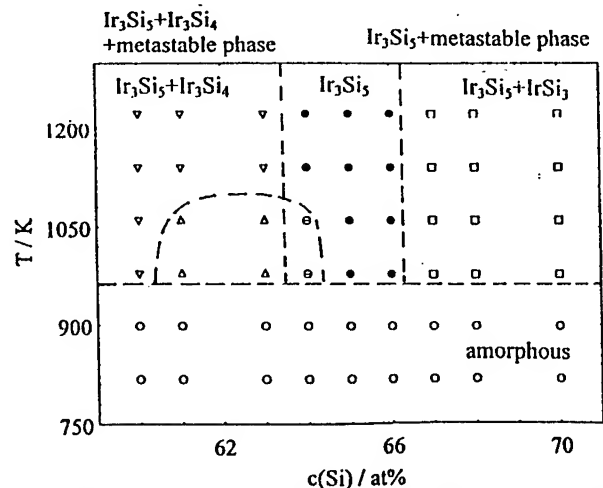


Fig.2: Phase composition of Ir_xSi_{1-x} thin films in dependence on Si-concentration and annealing temperature

Distinct phases were observed at the final stage in dependence on the initial composition: in the region $0.40 > x > 0.37$ Ir_3Si_4 and Ir_3Si_5 , in the region $0.37 > x > 0.34$ Ir_3Si_5 only, and in the region $0.34 > x > 0.30$ Ir_3Si_5 and IrSi_3 (see Fig 2).

Structure of Ir_3Si_5

The Bragg-Brentano X-ray diffraction patterns recorded after annealing at room temperature were analyzed by the Rietveld method [22] fitting the whole diffraction pattern on the basis of the crystal structure of the phases formed in the layer. For the calculations we used the DBWS9006-program [23] modified for the application to thin film patterns [24]. The structure data determined by Engström et al. [11] were used as start parameters in the fit procedure.

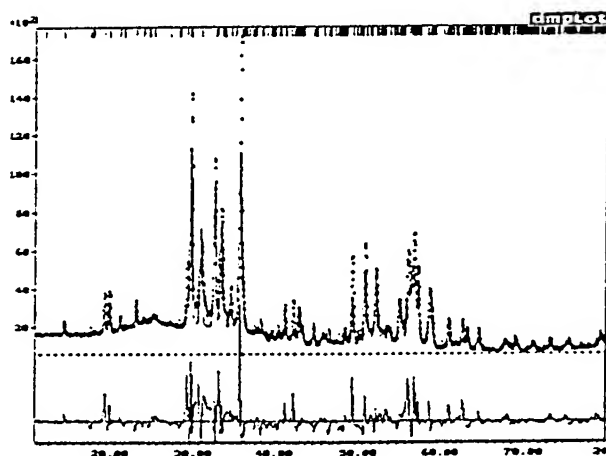


Fig. 3: Rietveld plot of sample 6 annealed up to $T=1223\text{K}$. The upper trace illustrates the observed data as dots, while the calculated pattern is shown by the solid line; the lower train is a plot of the difference, observed minus calculated intensities. The vertical markers show positions calculated for Bragg reflections.

Fig. 3 gives the resulting Rietveld plot of the diffraction pattern of sample 6 after refinement of lattice parameters and profile functions but using the fixed atom positions and occupation numbers of single crystal structure of Ir_3Si_5 [11] for the calculated pattern. All observed reflections can be explained to be caused by the monoclinic Ir_3Si_5 structure (space group $P2_1/c$). The intensities of the calculated reflections, however, differ from the observed one. This we suggest to be caused by deviations of the atom positions and the occupation numbers. Refinement of this parameters did not yield stable results because of the great number of independent, but highly correlated parameters (48 atom parameters and 16 occupation numbers).

Fig. 4 gives the resulting lattice parameters of Ir_3Si_5 phase obtained in samples 3 - 9 in dependence on the Silicon concentration of the layers. The volume of the unit cell differs clearly from the single crystal value. In layers with an chemical composition near by the ideal Ir_3Si_5 -composition

the unit cell volume is 0.5% greater than the single crystal value reflecting the disturbances of the crystal structure. With increasing silicon concentration of the layers the unit cell of Ir_3Si_5 phase decreases. This we consider to be caused by an increasing number of unoccupied Ir-positions and / or substitution of Si-atoms for Ir-atoms respectively.

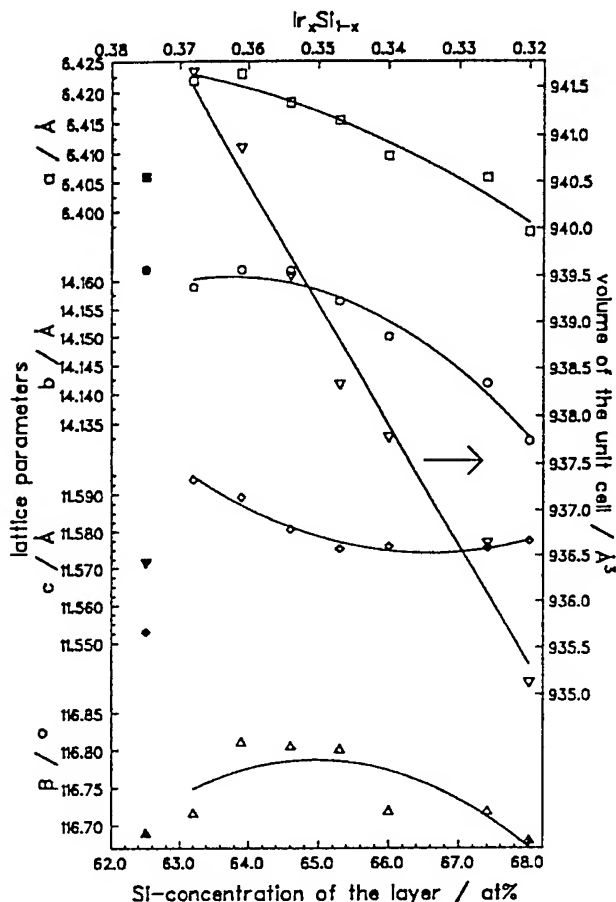


Fig.4: Lattice parameters and unit cell volume of the Ir_3Si_5 phase observed in annealed $\text{Ir}_x\text{Si}_{1-x}$ thin films in dependence on the layer composition. Filled symbols - single crystal data given by Engström et al. [11].

Microstructure

The microstructure of samples No. 4 and 6 annealed for 2 hours at $T=1073\text{K}$ in Ar atmosphere was studied by means of analytical TEM-investigations. For this the layers were transplanted onto Mo object carrier nets. The observed morphology and phase composition in both layers was similar. The layers were not homogeneous but cracked as a result of the crystallization process. Together with high diffraction contrasts at large grains this refers to high stress in the layers. Three distinct areas can be distinguished:

(a) - an area consisting of grains with typical chord lengths between $1\mu\text{m}$ and $10\mu\text{m}$ which is decorated with small perforations ($< 0.1\mu\text{m}$) (Fig. 5 a), (b) - the areas between the grains (a) characterized by a porous phase with fish-bone like contrast and typical chord lengths between $0.2\mu\text{m}$ and $2\mu\text{m}$ (Fig 5 b), and (c) - the edge of the cracks consisting of dark

areas and large gaps. The dark areas are partially covered by an layer without structure (Fig 5 c). By means of electron diffraction and EDX the large grains in area (a) were identified to be the Ir_3Si_5 main phase and the intermediate areas (b) to be an IrSi residual phase. Area (c) consists of Ir_2Si (the dark areas) and SiO_2 (the structureless layers).

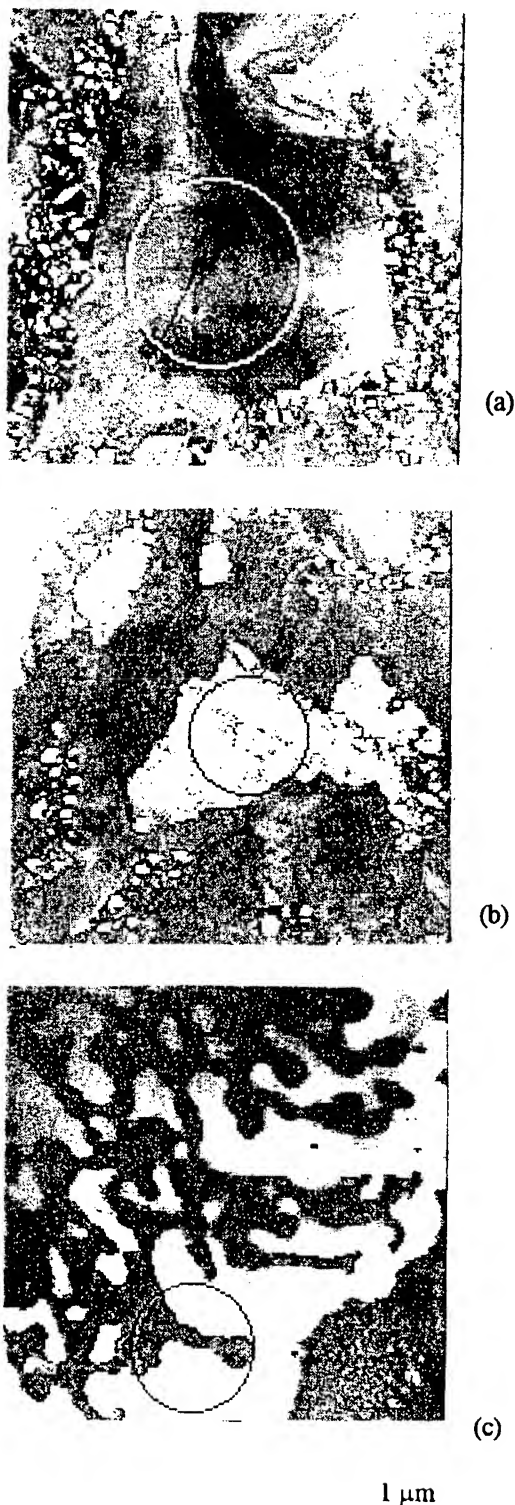


Fig. 5: Micrographs showing distinct phases observed in $\text{Ir}_{0.36}\text{Si}_{0.64}$ Si layers (sample 4) annealed at $T=1173\text{K}$ for 2 h in Ar atmosphere (a) Ir_3Si_5 ; (b) IrSi ; (c) Ir_2Si and SiO_2

Electrical resistivity

Fig. 6 shows the annealing behaviour of the resistivity and of its temperature coefficient TCR at 300 K for the investigated layers reflecting the phase composition of the investigated thin films. Layer 1,9,10, and 11 are dominated by Ir_3Si_4 and IrSi_3 respectively and show metallic character, the character of layer 2 is indifferent, and the other layers with a dominating Ir_3Si_5 phase show semiconducting-like resistivity. As a result of the formation of the metastable phase in layers 2, 3, and 4. The electrical resistivity after annealing at 973K show low values and small temperature dependences.

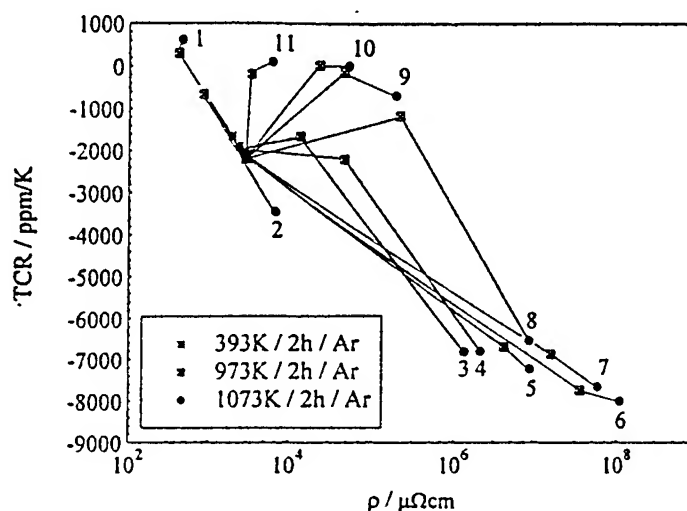


Fig. 6: Dependence of resistivity $\rho(295\text{K})$ and temperature coefficient of resistivity $\text{TCR}(295\text{K})$ of $\text{Ir}_x\text{Si}_{1-x}$ thin films on the annealing temperature

In Fig. 7 the temperature dependence of the resistivity of samples 2-5 is given for the as-deposited state and after annealing at 973K and 1073K. Due to the large disorder of the as-deposited films their transport behaviour should be determined by effects of weak and strong locations at least at low temperatures. As a result of the high disorder after annealing at 973K the polycrystalline state does not effect the electrical properties and a metallic behaviour is observed. In the final state the temperature dependence increases with increasing silicon-concentration, showing a maximum for sample 4 with Si-concentration of 64%. An activation energy of about 0.08eV was estimated for sample 3, 4, and 5 which is a typical value for a transition metal impurity state in a semiconductor.

Conclusions

The phase formation process during heat treatment has been investigated in $\text{Ir}_x\text{Si}_{1-x}$ thin films prepared by dc-magnetron sputter codeposition. The phase composition of the final state investigated by XRD measurement depends on the chemical composition of the layers: in the region $0.40 > x > 0.35$ Ir_3Si_4

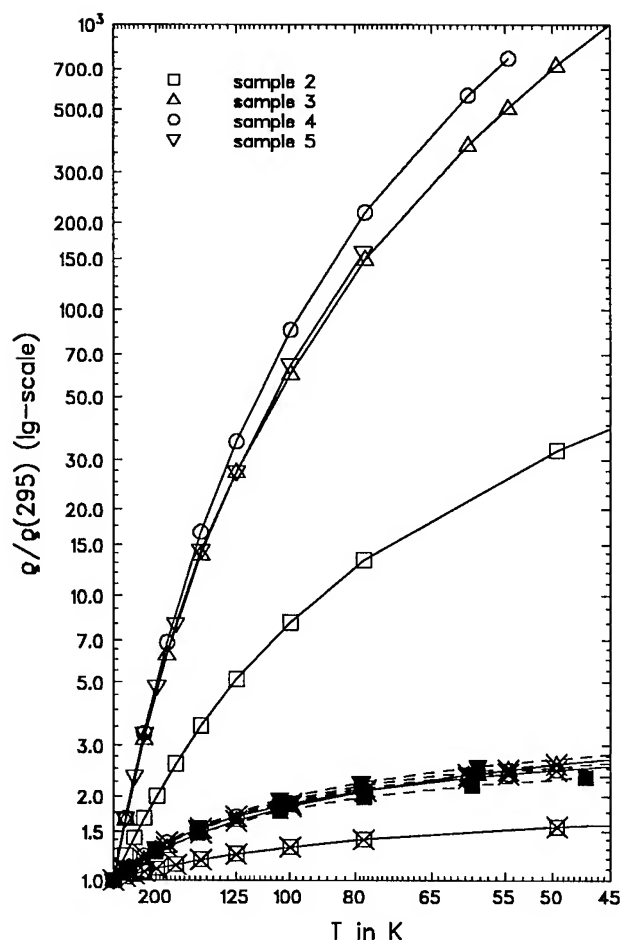


Fig. 7: Temperature dependence of the resistivity of as-deposited (crossed symbols) and annealed at 973K (filled symbols and at 1073 K (open symbols) Ir-Si films

and Ir_3Si_5 were identified, in the region $0.35 > x > 0.34$ Ir_3Si_5 only and in the region $0.34 > x > 0.30$ Ir_3Si_5 and IrSi_3 . Layers with chemical compositions near by Ir_3Si_5 were proved by microprobe analysis to contain small amounts of IrSi and, if oxygen is present, Ir_2Si and SiO_2 . In $\text{Ir}_x\text{Si}_{1-x}$ thin films with a chemical composition $0.39 > x > 0.36$ an unknown metastable phase with monoclinic unit cell was identified at a temperature range from 970K up to 1060K. The lattice parameters of the Ir_3Si_5 phase vary in dependence on the chemical composition x . The observed diffraction intensities differ from the calculated on the basis of single crystal structure parameters. This we suggest to be caused by disturbances of the crystal structure like deviations of the atom positions, unoccupied Ir-positions and / or substitution of Si-atoms for Ir-atoms. The annealing behaviour of electrical resistivity and its temperature coefficient clearly reflects the phase composition in dependence on the chemical composition.

The present study gives contributions to the understanding of the phase formation process in binary iridium silicide thin films in correlation with electrical resistivity and its temperature coefficient. Further investigations of transport properties are in progress.

Acknowledgements

We thank the Deutsche Forschungsgemeinschaft (DFG) for financial support (contract No. Pi 282/1-1)

References

- [1] C.B. Vining Proc. IX Int. Conf. Thermoel., Pasadena, Calif. Inst. Techn. (1990) 249.
- [2] M. Powalla and G. Herz, Appl. Surface Sci. 70/71 (1993) 593.
- [3] M.C. Bost and J.E. Mahan, J. Appl. Phys. 63(1988)839.
- [4] Y. Ishoda, T. Ohkoshi, I. Nishida, H. Kaibe, J. Mat. Sci. Soc. 25 (1989)311.
- [5] T. Ohta, Proc. XI th Int. Conf. Thermoel., Arlington, University of Texas, (1992) 74.
- [6] M. V. Vedernikov, A.E. Engalychev, V. Z. Zaitsev, S. V. Ordin, and M. I. Fedorov, Proc 7th Int. Conf. Thermoel. Energy Conversion, University of Texas (1988) 151.
- [7] T. Ohkoshi, Y. Isoda, H. Kaibe, S. Ichida, K. Matsumoto, and I. Nishida Trans., Jap. Inst. Met. 29 (1988) 756.
- [8] C. E. Allevato and C. B. Vining, J. Alloys and Compounds 200 (1993) 99.
- [9] W.L.Korst, L.N.Finnie, and A.W. Searcy, J. Phys. Chem. 61 (1957) 1541.
- [10] I. Engström and F. Zackrisson, Acta Chem. Scand. 24 (1970) 2109.
- [11] I. Engström, T. Lindsten, and E. Zdansky, Acta Chem. Scand. 41A (1987) 237.
- [12] J.G. White and E.F. Hockings, Inorg. Chem., 10 (1971)1934.
- [13] S. Peterson, J. Baglin, W. Hammer, F. d'Heurle, T.S. Kuan, I. Ohdomary, J. de Souza Pires and P. Tove, J. Appl. Phys. 50 (1978) 3357.
- [14] I. Ohdomari, T.S. Kuan and K.N. Tu, J. Appl. Phys. 50(1979) 7020.
- [15] S. Peterson, J.A. Reimer, M.H. Brodsky, D.K. Campbell, F. d'Heurle, B. Karlsson and P. Tove, J. Appl. Phys. 53 (1982) 3342.
- [16] M.C. Bost and J.E. Mahan, J. Vac. Sci. Technol. B 4 (1986) 1336.
- [17] B.Z. Weiss, K.N. Tu and D.A. Smith, J. Appl. Phys. 59 (1986) 415.
- [18] C.E. Allevato and C.B. Vining, Proc. 28th Intersoc. Energ. Conv. Eng. Conf., Washington, Am. Chem. Soc. 1(1993)239.
- [19] M. Wittmer, P. Oelhafen, and K. N. Tu, Phys. Rev. B 35 (1987) 9073.
- [20] J. Schumann, D. Elefant, C. Gladun, A. Heinrich, W. Pitschke, H. Lange, W. Henrion, and R. Grötzschel, phys. stat. sol. (a) 145 (1994) 429.
- [21] N. Mattern, W. Pitschke, A. Danzig, and St. Doyle, Fres. J. Anal. Chem. 349 (1994) 91.
- [22] H.M. Rietveld, J. Appl. Crystallogr. 2 (1969) 65.
- [23] D.B. Wiles and R.A. Young, J. Appl. Crystallogr. 15 (1981) 440.
- [24] W. Pitschke, Proc. IV European Powder Diffraction Conference (EPDIC IV), Chester, UK (1995) (to be published at Materials Science Forum).

OVERVIEW of the Components, Packaging, & Manufacturing Technology Society of the IEEE

The Components, Packaging, & Manufacturing Technology (CPMT) Society is a volunteer organization. Our Charter, as for all societies of the IEEE, is to advance the interests of our profession. You become a member of CPMT by first joining the IEEE, and then paying the additional \$10 fee to become a CPMT member. An alternate path to membership, open to those individuals belonging to other major scientific or engineering societies, is to affiliate directly with CPMT. The following is an overview of the organization.

The **Operating Committee** (OpCom) of CPMT consists of the President; five Vice Presidents (Technical, Administrative, Conferences, Publications, and Education); the Treasurer; and the Secretary. Eighteen at-large Board of Governors members are elected by the CPMT membership for overlapping three-year terms (six elected each year). There are thirteen **Technical Committees** (TC's), organized to pursue the varied fields covered by CPMT. In addition, there are many other standing and *ad hoc* committees: for conferences, standards, chapter development, membership, international relations, bylaws, etc.



Many of our members belong to local chapters of CPMT. We have chapters in the U.S., Canada, Japan, China, and Europe. These entities sponsor local meetings, courses, and workshops.

The officers, elected members, committee chairs, and chapter chairs, together make up the **Board of Governors**. This body meets three times a year to formulate society policy, vote on expenditures, and act as a general forum. Between meetings, the OpCom conducts pressing business.

The above structures enable us to serve our members in a way that advances their technical and professional interests. CPMT sponsors 15-20 conferences per year throughout the world, and publishes *Proceedings* for many of these conferences. We publish three quarterly *Transactions* and a quarterly NEWSLETTER, and we also negotiate discounts for IEEE members on books of interest to the membership. We administer fellowships and provide seed money for conferences, chapters, and new publications.

To carry on these and other activities, the society is always looking for new members for its committees. Membership in these committees can involve as much or as little time as you wish to put into it, and need not involve travel. Do you consider your work to be not just your *job*, but your *profession*? Are you interested in the advancement of your profession? Would you benefit from the opportunity to broaden contacts with your peers at other companies and around the world? If so, I would encourage you to contact any of the officers, to discuss opportunities for a position in the CPMT Society.

President	Ralph Wyndrum	1-908-949-7409	r.wyndrum@ieee.org
Technical Vice President	Pat Thompson	1-602-413-3295	p.f.thompson@ieee.org
Administrative Vice President	Elaine Pope	1-602-554-5368	e.pope@ieee.org
Conferences Vice President	John Stafford	1-602-897-5509	rp0014@email.sps.mot.com
Publications Vice President	Paul Wesling	1-408-285-9555	p.wesling@ieee.org
Education Vice President	Albert Puttlitz	1-802-899-4692	

CPMT Purpose: The CPMT Society's objectives are to provide a forum for the dissemination of technical information within its assigned areas. CPMT's fields of interest encompass the materials science, chemical processes, reliability technology, mathematical modeling, education and training utilized in the design and production of discretes, hybrids, and electronic packaging. Also included are fiber optics, connector technology, and semiconductor processing. Manufacturing technology includes systems, concepts, management, and quality as they relate to electronic component manufacturing.

Who Benefits? As an engineer/scientist, technologist, or student concerned with the advancement of electronic components, packaging, or manufacturing technology, you will benefit by joining or affiliating with the IEEE's CPMT Society. Through participation in Society activities you will strengthen your individual role in our profession, as well as enhance your company's reputation. When you contribute to the dissemination of technical knowledge, you contribute to society as a whole and enhance the engineering profession.

CPMT Programs and Services: CPMT offers a variety of member services: publications, specialized technical committees, chapters, conferences, educational opportunities, awards and fellowships. Join CPMT now and participate in these activities with your fellow professionals. You will be glad you did!

<http://naftalab.bus.utexas.edu/ieee/>

CPMT TECHNICAL COMMITTEES — SCOPE

One of the major benefits of belonging to an IEEE Society is exchanging technical information with peers. Our membership is served through conferences, workshops, *Transactions*, and newsletters. These are the vehicles to exchange information, with the Technical Committees acting as the "engines."

In general, certain conferences and workshops are supported by all the Technical Committees. These events include the Electronic Components and Technology Conference, and the International Electronics Manufacturing Technology (IEMT) Symposium. Several events are cosponsored by CPMT with other organizations outside the IEEE. You are encouraged to call the individual committee chairs, to address specific inquiries and interests to them; you do *not* need to be a CPMT member to request membership in a specific TC.

TC-1: Electrical Contacts Gerry Witter; Chugai USA; 3780 Hawthorn Rd; Waukegan, IL 60087; g.witter@ieee.org

The scope of this Committee is to be the focal point within the IEEE CPMT Society for electrical contacts. Its membership consists of individuals having an interest in the research, development, manufacture, and utilization of electrical contacts and devices which contain them. The Committee holds regularly scheduled meetings and functions through the Holm Organization and through task forces having specific objectives. The Committee sponsors or supports conferences, publications, educational, standardization, and other activities.

Associated activities:

1. Holm Conference on Electrical Contacts
2. Holm Course on Electrical Contacts

TC-2: Discrete Component Parts and Subassemblies Dr. Tom Reynolds, muRata, 404-433-7825

The function of the Discrete Component Parts and Subassemblies Committee is to serve as the focal point within CPMT for various activities including the design, fabrication, characterization, test, and application of electronic components. The particular devices include, but are not limited to:

Capacitors	Optical Components	Sensors
Connectors	Protective Devices	Solenoids
Displays	Relays	Transducers
Filters	Resistors	Transformers
Inductors	Semiconductor Devices	Transient Suppressors

Associated activities:

1. Capacitor and Resistor Technology Symposium (CARTS)
2. International Non-Volatile Memory Technology Conference

Contact Tom by email at 76304.463@compuserve.com

TC-3: Surface Mount Technology

Dr. Bill Wun, Hewlett Packard, 1-415-857-2988

Electronics assembly is rapidly moving from through-hole mounting to surface-mount. Challenges are increasing as lead pitch is refined, standards are debated and adopted, and processes are automated. Alternate substrates are being used: epoxy PCBs as well as advanced composites, ceramics, etc. Device power levels are increasing, so heat transfer becomes more important. This Committee explores new directions and techniques for standard and high-lead-count SMT, and the equipment developments needed to support it. A special focus is the growing application of SMT to automotive electronics.

There is a cooperation between this Committee and the Committees on materials, packaging, thermal management, and standards. This Committee is also supporting the new CPMT *Transactions on Advanced Packaging*. Please contact the chair by mail (1501 Page Mill Road; Palo Alto, CA 94304 USA) or by E-mail (at wun128@aol.com).

Associated activities:

1. Electronics Manufacturing Seminar (China Lake)
2. Surface Mount International

TC-4: Manufacturing Technology

Wyck Seelig, AT&T Bell Labs 1-908-771-2440

The focal point of TC-4 is manufacturing and the associated technologies. Automatic processes, especially robotics, control, and quality, and their management, are of prime interest. Applications of new materials which will save process time, improve quality, or lead to product manufacturing innovation, are stressed. Examples of new technologies which have been of interest recently are surface mount technology for the design and assembly of printed wiring boards, and production issues with multi-chip modules. Email: wds01!htwds@bkuxo.att.com

Associated activities:

1. Int'l Electronics Manufacturing Technology (IEMT) Symposium (U.S., Japan, Europe)

TC-5: Materials

Dr. Rajen Chanchani, Sandia Nat'l Labs 1-505-844-3482

The electronics industry has been undergoing a technical renaissance for the past two decades. The materials improvements and the introduction of new materials in answer to new needs has been one component that has fueled the change. This Committee has the responsibility to keep the membership current on materials issues and to serve as a sounding board to call attention to the introduction of an unsafe or defective material or one that is incorrectly applied. Contact Rajen by email at rajen_chanchani@sass165.sandia.gov

Associated activities:

1. Electronic Components and Technology Conference
2. Advanced Materials, Processes, & Interfaces Workshop
3. Int'l Symposium on Advanced Packaging Materials

TC-6: Electronic Packaging

Dr. Les Fox, Digital Equipment Corp. 1-508-858-3037

Electronic Packaging is concerned with the design, development, and fabrication of single and multi-component electronic assemblies. This includes the development of design systems (for layout, release, etc.), processes, and materials involved in the construction of these assemblies. Also included are the manufacturing systems and tooling for fabrication, assembly, and test adequate to meet the reliability and end-use requirements for the assembly. Contact Les by email at l.fox@ieee.org

Associated activities:

1. VLSI & GaAs Chip Packaging Workshop
2. IEEE Multichip Module Conference (MCMC)
3. International Conference on MultiChip Modules (ICMCM)

TC-7: Environmental Stress & Reliability Testing

Dr. Tony Chan, AT&T, 1-609-639-2420

This is a new Committee that has been established to assist professionals involved in assuring that their electronic system hardware is robust and meets world-class standards for design quality. Interest is from the chip package level up to fully assembled large systems, with a special emphasis on the use of environmental stress testing as a means of qualifying and systematically improving product reliability. Members share techniques for product qualification, simulation, environmental testing, and other aspects of assuring that a product is mature enough for the market. (Contact Tony at chan@pruxp.att.com.)

1. Accelerated Stress Testing Workshop

TC-8: Semiconductor Processing Technology

John Reekstin, Aerojet 1-818-812-2866

Semiconductor processing is at the heart of the industry. This committee is concerned with the establishment and standardization of processes in the manufacture of semiconductors. New processes and materials to improve quality and yield are of prime importance. In addition, new branches of semiconductor processing such as integrated optics, flat-panel displays, and micromachining are nurtured and fostered by this Committee.

Associated activities:

1. International Systems In Silicon (ISIS) Conference
2. International Symposium on Semiconductor Manufacturing (ISSM)
3. SEMICON/East & Advanced Semiconductor Manufacturing Conference (ASMC)
4. VLSI Multilevel Interconnection Conference (V-MIC)
5. Lithography Workshop
6. International Non-Volatile Memory Technology Conference

TC-9: Thermal Management

Tony Mak, Allegro Microsystems 1-508-853-5000

The Thermal Management Committee is concerned with all aspects of thermal design and analysis in science and industry. The subject is divided into Heat Transfer and Thermal Stress. The former includes thermal conductivity measurements and parameters, thermal coefficients of expansion (TCE's), and temperature distributions (both predictions and measurements). Thermal stress concerns stress/strain predictions and measurements, CTE analyses, and other issues. Contact Tony by email at mak_t@orgella.com

Associated activities:

1. Semiconductor Thermal Measurement and Management (SEMI-THERM) Symposium
2. InterSociety Conference on Thermal Phenomena (I-THERM)
3. International Thermoelectric Conference

TC-10: Fiber Optics & Photonics

Michael Lebby, Motorola 1-602-413-4826

This new TC, in formation, addresses the areas of optoelectronic and optical materials, packaging, and systems, including characterization, fabrication, assembly, reliability, and performance. Contact the chair at michael_lebby@tempeqmsps.mot.com.

TC-11: Quality

Subash Singhal, AT&T Bell Labs

This new TC serves as the focal point for all quality-related issues relevant to the IEEE membership. It affirms the goal of Total Customer Satisfaction, and works with conferences to include an emphasis on quality design and manufacture. It serves as liaison between IEEE and other organizations with a similar interest in quality, including the American Society for Quality Control, AME, etc. It maintains a mailing list of individuals with an interest in furthering the development and teaching of quality metrics, and publishes a newsletter on a periodic basis. TC-11 develops special sections for the CPMT Transactions on topics such as Design of Experiments, Statistical Process Control, and Quality, and coordinates development of short courses and tutorials for conferences or local chapters. It meets at various CPMT conferences to develop plans and share experiences.

TC-12: Semiconductor Manufacturing

Court Skinner, National Semi 1-408-721-7420)

The production of semiconductor devices becomes more exacting each year, as geometries decrease, wafer size and circuit density increase, and yields become ever more important. TC-12 provides the focus for CPMT activity in the manufacture of semiconductors, and maintains a mailing list of technical individuals from many backgrounds who share an interest in semiconductor manufacturing science and practice. Contact Court by email at l.skinner@ieee.org

Associated activities:

1. International Symposium on Semiconductor Manufacturing (ISSM)
2. SEMICON/East & Advanced Semiconductor Manufacturing Conference (ASMC)
3. The IEEE *Transactions on Semiconductor Manufacturing*

TC-13: Power Electronics Packaging

Doug Hopkins, SUNY (+1-607-777-2333)

This committee provides a focus for the development of technologies that are relevant to the electronic processing of power. Nearly all of the materials, manufacturing and process technologies developed for application to signal and data processing can be used in power processing. The committee facilitates the development of packaging technology specific to power electronics and systems, and maintains a roadmap for power packaging from chip-level to end-product. It has been established as a joint committee with the IEEE Power Electronics Society. For further information or to add your name to the data base, contact Doug at d.hopkns@ieee.org

Associated activities:

1. Electronic Components and Technology Conference (ECTC)
2. Applied Power Electronics Conference (IEEE-PELS)

You don't need to be an IEEE or CPMT member to join one of our TC's — please contact the TC chair to become associated with it's work and benefits!

PROCEEDINGS

1996 International Conference on Thermoelectrics

You are invited to propose a paper for the International Conference on Thermoelectrics in Dresden, Germany, August 26 - 29, 1997, hosted by the Institute for Solid State and Materials Research, Dresden. Deadline for abstracts is April 30, 1997; abstract acceptance is May 31, 1997. Please submit abstracts to:

Joachim Schumann
ICT97 Technical Program Chairman
Inst. for Solid State and Materials Research
Helmholtzstr. 20
D-01069 Dresden, Germany
Ph.: (+49 351) 2582 399
Fax: (+49 351) 2582 314
e-mail: ict97@ifw-dresden.de

JOIN ITS

For information on membership in the International Thermoelectric Society, please visit our Website at:

<http://www.ict.org>

or contact:

Dr. Jean Pierre Fleurial, ITS Secretary
Jet Propulsion Laboratory/California Inst. of Technology
4800 Oak Grove Drive
Pasadena, CA 91109-8099 USA
Phone: +1-818-354-4144, FAX: +1-818-393-6951

JOIN IEEE

For information on membership in the Components, Packaging, & Manufacturing Technology Society of the IEEE, a free back issue of a CPMT *Transactions*, or participation in one of the Technical Committees or local Chapters within the Society, please visit our Website at:

<http://naftalab.bus.utexas.edu/ieee/> and <http://www.ieee.org>

or contact:

Barbara Reagor
Bellcore Room 3Z-227
331 Newman Springs Road
Red Bank, NJ 07701 USA

Or, in the U.S.A., call IEEE at:
+1-800-678-IEEE